

1353

***BOEING***

1353

BOS-034

DO 6000 1935 ORIG. 8/73

1353

GAS COOLED CENTRAL RECEIVER -  
CLOSED CYCLE 1MWT BENCH MODEL TESTING

RP377-3  
FINAL REPORT

Volume: I

June 5, 1980

Prepared for  
Electric Power Research Institute  
3412 Hillview Avenue  
Palo Alto, California 94304

by  
Boeing Engineering and Construction Company  
P.O. Box 3707  
Seattle, Washington 98124

LEGAL NOTICE

This report was prepared by Boeing Engineering and Construction, as an account of work sponsored by the Electric Power Research Institute, Inc. (EPRI). Neither EPRI, members of EPRI, Boeing, nor any person acting on behalf of either: (a) makes any warranty or representation, express or implied with respect to the accuracy, completeness, or usefulness of the information contained in this report, or that the use of any information, apparatus, method, or process disclosed in this report may not infringe privately owned rights; or (b) assumes any liabilities with respect to the use, or for damages resulting from the use of, any information, apparatus, method, or process disclosed in this report.



## ABSTRACT

This report is an account of the design, fabrication and solar testing of a 1Mwt cavity receiver using metal gas-in-tube heat exchangers. The design is a scale model representation of a commercial size Brayton cycle solar thermal electric plant receiver. The DOE-Central Receiver Test Facility was used in this inaugural test. The program, from initiation of design to completion and evaluation of solar tests, was completed in a 45 month period.

Engineering design required application of existing thermal and structural analysis technology as well as development testing to determine the effects of unique operating conditions on receiver materials and components. A solar test system was developed which simulated the receiver interfaces with a Brayton cycle electric plant. Solar receiver tests included controlled parameter investigations of heat balance, non-uniform heating and transients; and demonstrations of solar load following. Test results include quantitative assessments of receiver characteristics such as thermal efficiency, operating temperatures, and dynamic response characteristics. Qualitative results are also described including observations of changes in receiver materials and components which occurred.

## TABLE OF CONTENTS

		<u>PAGE</u>
1.0	Introduction	1
1.1	Summary of Results, RP377-1	4
1.2	Contents of the RP377 Final Report	7
1.3	Division of the Report Into Three Volumes	11
2.0	Bench Model Solar Receiver Design Description	12
2.1	Arrangement and Function of Components	12
2.1.1	Configuration	12
2.1.2	Construction Materials	13
2.1.3	Steel Framework	15
2.1.4	Cavity Insulation and Aperture Rim Thermal Protection	17
2.1.5	Heat Exchanger System	20
2.1.6	Flow Control System	24
2.1.7	Instrumentation	28
2.1.8	Air Supply System	28
3.0	Receiver Design Studies	32
3.1	Thermal-Scale Modeling of the Commercial Receiver	32
3.1.1	Theoretical Requirements for Thermal-Scale Modeling	37
3.1.2	Practical Considerations for BMSR Thermal- Scale Model Design	41
3.2	Solar Interface With CRTF	57
3.2.1	Receiver Solar Input	62
3.2.2	Solar Heat Flux on Aperture Plane	62
3.2.3	Solar Heat Flux on Interior Cavity Walls	67
3.3	Thermal Analysis of BMSR Heat Exchanger Tube	77
3.4	Receiver Air Flow System	85

	<u>PAGE</u>
3.4.1	Airflow System Description 85
3.4.2	Performance of Flow-System Component 93
3.5	Receiver Thermal Analysis 116
3.5.1	General Requirements 116
3.5.2	Thermal Model Development 116
3.5.3	Pretest BMSR Thermal Model Results 127
3.6	Receiver Frame Structural Analysis 148
3.6.1	Allowable Stresses 148
3.6.2	Stress Analysis Results and Factors of Safety 149
3.7	Heat Exchanger Stress Analysis 157
3.7.1	Allowable Stresses 157
3.7.2	Deflections 163
3.7.3	Stress Analysis Results and Factors of Safety 163
4.0	Developmental Testing 175
4.1	Heat Exchanger Material Tests 176
4.1.1	Thermal Cycle Tests 176
4.1.2	Elevated-Temperature Tests 181
4.2	Receiver Thermal Insulation Testing 184
4.2.1	Insulation Test Facility 187
4.2.2	Insulation Test Activities 205
4.2.3	Measurements of Insulative Radiative Properties 221
4.2.4	Results 229
4.3	Testing of BMSR Solar Shield Materials 231
5.0	Receiver Fabrication 245
5.1	Structural Frame 245
5.2	Insulation and Shielding 256

	<u>PAGE</u>	
5.2.1	Back Cover Insulation	256
5.2.2	Main Body Insulation	261
5.3	Heat Exchangers and Manifolds	264
5.3.1	Heat Exchanger Panels	266
5.3.2	Manifolds	274
5.4	Instrumentation and Controls	282
6.0	Hot Flow Testing	297
6.1	Hot Flow Test Setup	297
6.2	Description of Tests	302
6.2.1	System Checkout Tests	302
6.2.2	Receiver Flow-Valve Calibration Tests	304
6.2.3	Receiver Observation Tests	305
6.2.4	Receiver Calibration Tests	307
6.2.5	Receiver Thermal Cycling	309
6.3	Results and Conclusions	309
7.0	Description of the Solar Test Program	311
7.1	Test Plan	311
7.1.1	Test Planning Objectives	311
7.1.2	Specific Test Plans	313
7.2	Requirements of Experimenters	332
7.3	Test Setup	339
7.3.1	Receiver Solar Input	341
7.3.2	Test Air Supply System	347
7.3.3	Data Acquisition and Control System (DACS)	354
7.3.4	Test Operations	367
7.4	Integrated Test Procedure	367
7.5	Solar Test Operations	376

	<u>PAGE</u>
7.5.1	BMSR Operating Philosophy 376
7.5.2	Test Operations 389
7.6	Test Activity Summary 389
7.6.1	Test System Checkout and Verification 390
7.6.2	Production Solar Tests 393
8.0	Test Data Base 398
8.1	Sources of Test Data 398
8.2	Test Data Processing 400
8.3	Test Data Uncertainty 403
8.3.1	Experiment Instrumentation Errors 403
8.3.2	Data Acquisition System Errors 431
8.3.3	Combined Uncertainty in Test Data Measurements 432
8.4	Receiver Solar Input Data 437
8.4.1	Experimental Measurements of BMSR Solar Input 444
8.4.2	HELIOS Analysis With Actual Test Conditions 457
8.4.3	Solar Input Data Base 461
8.5	Measurements of Aperture Rim Air Velocity 464
9.0	Results of the Experiment 472
9.1	Equilibrium Heat Balance Tests 472
9.1.1	Identification of Equilibrium Heat Balance Conditions in the Test Data 472
9.1.2	Experimental Measurements of BMSR Thermal Efficiency 479
9.1.3	Other EB Test Results 482
9.2	Nonuniform Solar Input Tests 499
9.3	Transient Heat Load Tests 505
9.4	Restricted Flow Tests 509
9.5	Cold Startup and Emergency Cooldown Tests 515

	<u>PAGE</u>
9.5.1	Cold Startup Tests 519
9.5.2	Emergency Cooldown Tests 520
9.6	Solar Load-Following Tests 521
9.7	Evidence of Exterior Convective Heat Transfer 530
10.0	Additional Results of the Solar Receiver Testing Program 544
10.1	Historical Summary of Test Activities, Inspections, and Observations During the Production Solar Tests 545
10.2	Cavity Thermal Insulation 561
10.3	Aperture Rim Solar Shielding 579
10.4	Heat Exchangers and Air Flow System 580
10.5	BMSR Instrumentation 588
11.0	Posttest Thermal Analysis 591
11.1	Comparison of Pretest Thermal Analysis With Test Data 591
11.2	Revisions to the Pretest Thermal Analysis 601
11.2.1	Insulation Temperature Profile 601
11.2.2	Posttest Thermal Model 619
11.2.3	Transient Cooldown 627
11.2.4	Independent Convective Flow Analysis 643
11.3	Thermal Analysis Conclusions 645
12.0	Test Data 647
12.1	Interpretation and Use of Test Data Tapes 647
12.2	Typical Test Run 658
12.3	Daily Activities and Test Data Summary 664

## SECTION 1.0

### INTRODUCTION

This report describes the detailed design, fabrication and assembly, operation and solar testing, and results of a 1 Mwt solar receiver development program. The report encompasses work performed for the Electric Power Research Institute from July, 1976 through March 15, 1980.

This Final Report marks the completion of EPRI Project 377 which has included research, technical and economic analyses, design development, and experimental verification of a high-temperature central receiver concept for solar thermal electric power. Figure 1.0-1 describes the objectives and periods of performance of the three major phases of RP377.

The initial phase of the Project, RP377-1, was a study of the technical and economic feasibility of a high temperature, 816°C (1500°F), central receiver. The preferred design utilized a high pressure helium gas loop for absorption of solar power in the receiver, energy transport, and electric power generation by means of a closed cycle gas turbine. Results of the study are documented in EPRI ER-629, and are summarized in Section 1.1 here. The RP377-1 work occupied a time period of 19 months, through June 1976.

The second phase of the project, RP377-2, consisted of design and fabrication of a 1 Mwt Bench Model Solar Receiver (BMSR) which would model with reasonable accuracy the design and performance characteristics of the commercial solar receiver. This was accomplished in a 24 month period of activity. A detailed design of the receiver was completed by Boeing Engineering and Construction in February, 1977, and fabrication was initiated. Two subcontractors were employed during construction, one to fabricate the steel cavity structure and the other to form and weld the refractory alloy heat exchanger panels and the stainless steel manifold system. Final assembly, instrumentation, inspection, and functional testing was completed in the Boeing shop and test facilities. A number of functional tests were conducted to verify the characteristics of the as-built solar receiver including flow tests with high temperature, high

**RP-377-1**



Phase 1

**Objectives:**

- ▣ Receiver configuration
- ▣ Materials tests
- ▣ Conceptual design for commercial plant

**RP-377-2**



Phase 2

**Objectives:**

- ▣ Design and fabricate 1 MW<sub>t</sub> receiver
- ▣ Conduct functional and hot-flow tests
- ▣ Planning studies for pilot plant

**RP-377-3**



Phase 3

**Objectives:**

- ▣ Detailed test planning
- ▣ Conduct thermal analysis of receiver
- ▣ Test in CRTF
- ▣ Analyze test data

Figure 1.0-1: Program Summary



pressure, air. This phase of the project was completed in July of 1978 with delivery of the test-ready BMSR to the solar testing site. This work is described in Sections 2 through 6.

Solar tests were conducted at the recently completed Central Receiver Test Facility (CRTF), U.S. Department of Energy facility located at Albuquerque, New Mexico, and operated by Sandia Corporation. The Department of Energy sponsored and Sandia Corporation provided the facility and the manpower required to operate the facility for BMSR tests. EPRI sponsored and Boeing provided the test article, test support equipment including equipment needed to supply high pressure, high temperature, air to the operating receiver, and personnel to conduct and direct the test activities.

All aspects of the project relating to the solar testing of the receiver were covered by RP377-3. This activity included preparation of detailed solar test plans and procedures, assisting CRTF personnel in the completion of the solar test setup, conduct of the tests, and reduction and evaluation of test results. Experience gained in the operation and maintenance of a large solar thermal system was an important part of the test program results. Testing also produced valuable technical data which defined the performance and operating characteristics of the solar receiver. This work, testing and data reduction activity, and the test results are discussed in Sections 7 through 11. Section 12 includes daily operating logs and plotted test data which describe receiver operation on each of the solar test days.

The third phase of this project, RP377-3, was essentially complete in December, 1979. Supplemental thermal insulation tests extending beyond this date will be reported as part of the ongoing insulation test program RP1521-1.

An additional task, RP377-4, included the concept definition and preliminary design of an experimental Brayton Cycle solar thermal electric plant of 10 MWe scale capacity. This task defined a central receiver system incorporating RP377 technology which is considered to be one of the logical steps leading to commercial utilization of the concepts. These results have been separately reported to EPRI.

## 1.1 SUMMARY OF RESULTS, RP377-1

The commercial solar receiver design and thermal electric conversion cycle selected as the result of the first phase of project RP377 are described in detail in Reference 1, EPRI ER-629. The receiver and plant conceptual designs are described here.

High pressure helium gas was selected for the heat transport and working fluid for electric power conversion equipment. Technology involving the use of closed cycle helium turbogenerator equipment and system controls was adopted because of the similarity of design requirements between the solar power system, and high temperature gas cooled nuclear reactor systems. When the RP377-1 study was conducted, the appropriate research and development activity, including assembly and testing of a complete 50 MWe system was underway in Europe. This highly appropriate technology used helium gas as the cycle working fluid. It was recognized that closed cycle systems utilizing air, nitrogen, or inert gas mixtures could be utilized with similar theoretical results.

The closed high pressure gas turbine cycle was selected for study because of its operating characteristics and operating flexibility. These include:

- a. Theoretically high conversion efficiency, approaching 50% with high temperature recuperated and intercooled cycle.
- b. Exceptional capability to maintain high conversion efficiency at part-power settings, by variation of cycle pressure level (via gas inventory control).
- c. Startup and transient response characteristics consistent with intermittent duty solar cycle.
- d. Excellent heat transfer characteristics of high pressure gas cycle assures feasibility of metallic receiver heat exchangers and direct working fluid interaction with thermal storage media, while accommodating pressure loss requirements and direct conversion in

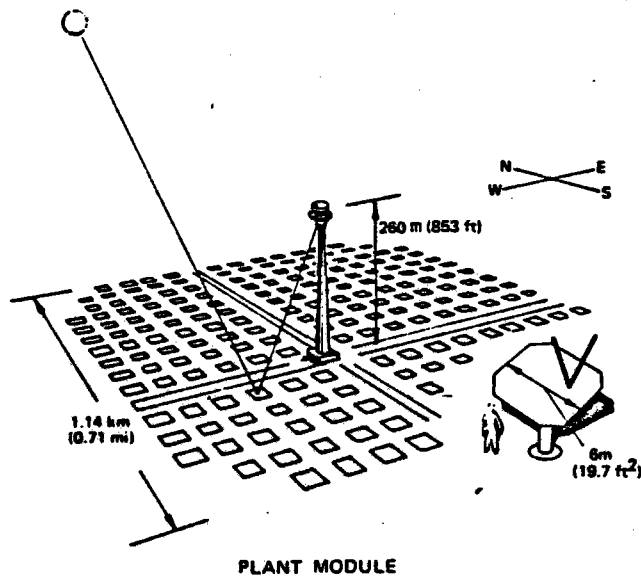
a gas turbine-generator.

In addition, recent experimental studies had indicated that efficient closed Brayton cycle systems could be designed with turbine inlet temperatures at about 800°C (1470°F) which were compatible with a metallic tube heat exchanger system desired in the solar receiver.

Two types of commercial solar thermal power systems were defined as a result of the Phase 1 study. Similar receiver, tower, and collector subsystems were used. The plant concepts are described in Figure 1.1-1. Solar receivers were mounted atop a 260 m (853 ft) tower which was located at the center of a 1.3 km<sup>2</sup> (0.5 sq mi) field of heliostat mirrors. Two alternative designs were planned with either capable of meeting the performance requirements (except capacity displacement) of a 100 MWe intermediate load plant.

Two of the collector field, tower, and receiver modules were used along with 6 hours of thermal storage capacity to power a stand-alone plant. Independent modules would utilize their own turbogenerator and waste heat rejection systems. A schematic of the stand-alone plant concept is shown in figure 1.1-2. Maximum daily solar receiver heat transfer to the working fluid varied from 259 to 315 MWt depending on season of the year. Approximately 85% of the receiver solar input was expected to be delivered either to thermal storage or to the gas turbine cycle. The mass of thermal storage media and the recuperative heat exchanger in this installation called for their location at the base of the tower. Electric power generation equipment was also located there. Insulated riser and downcomer pipes connected the tower-top receiver with this equipment.

The hybrid plant utilized a fossil fueled heater to provide approximately half of the system heat load. This allowed reduction of thermal storage capacity to 30 minutes. Fossil fuel, hybrid operation was required to extend the plant duty cycle for several hours after sunset, in the traditional intermediate load role. Once again, size and complexity of this equipment dictated use of a ground level installation for the heater, gas turbine, and system heat exchangers.



**100 MWe INTERMEDIATE PLANTS**

**STAND-ALONE PLANT**    **2 MODULES**  
**(6 HOURS STORAGE)**

**HYBRID PLANT**    **1 MODULE**  
**(1/2 HOUR STORAGE)**

**PLANT MODULE CHARACTERISTICS**

TOWER HEIGHT	260m (853 ft)
COLLECTOR AREA	0.5 km <sup>2</sup> (0.19 mi <sup>2</sup> )
AREA UTILIZATION	38.6%
TOTAL LAND AREA	1.3 km <sup>2</sup> (0.5 mi <sup>2</sup> )
NO. OF COLLECTORS	15,400
SIZE OF COLLECTORS	32.4 m <sup>2</sup> (349 ft <sup>2</sup> )

Figure 1.1-1: Commercial Size Solar Plant Concepts Defined in RP377-1

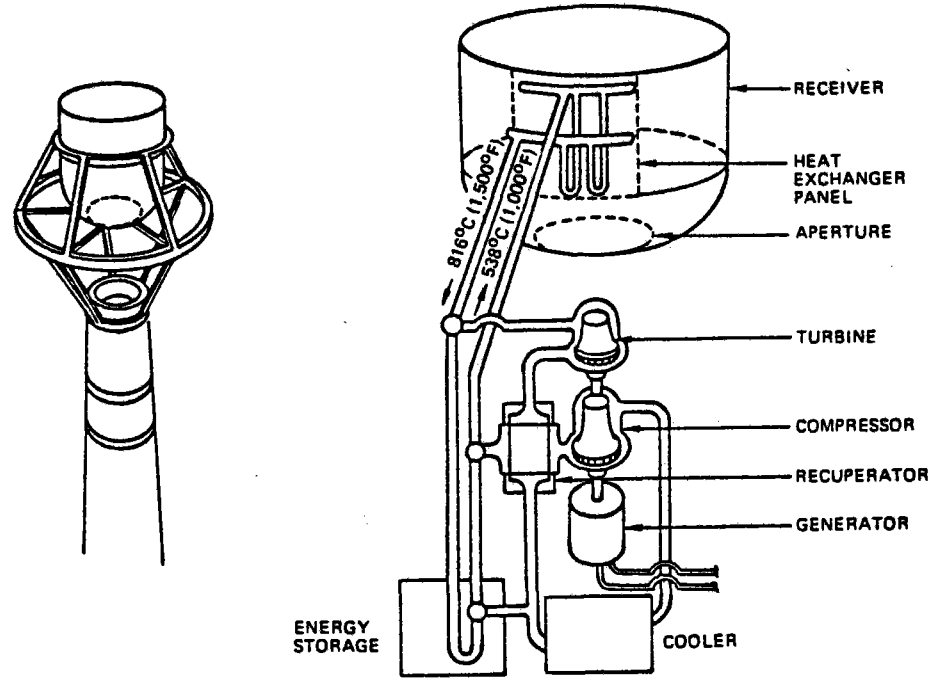


Figure 1.1-2: Design Concept and Schematic For Stand-Along Plant

The receiver design concept developed during RP377-1 is shown in Figure 1.1-3. Its arrangement atop the tower included widely spaced structural supports to allow the use of a single downward facing aperture with the tower centered in the collector field. Sunlight from the collector field entered the aperture and impinged on the lower walls of the receiver cavity. These bare insulation walls dispersed the concentrated solar flux to provide nearly uniform heating of the upper cavity walls and heat exchangers mounted on them. The receiver heat transfer system consisted of 4200 (2.4 cm [1 in] diameter by 9.5 m [334 in] long) heat exchanger tubes. They were arranged in 210 standard wall panels of 20 tubes each. These were identical modular assemblies which included gas manifolds and heat exchanger structural support, and an adjacent section of cavity wall structure and insulation, as shown in Figure 1.1-4.

This commercial central solar receiver concept, and the relevant technology, was the object of the BMSR design studies in RP377-2 and the concept verification tests in RP377-3.

## 1.2 CONTENTS OF THE RP377 FINAL REPORT

Sections 2 through 6 describe the work completed during RP377-2.

Section 2 consists of a description of the final as-built solar receiver configuration. Even though it was based upon and was a thermal scale model of the commercial receiver, it was also a self-sufficient solar receiver design. Its size and complexity required presentation and description of the BMSR independent of the commercial receiver.

Section 3 describes the technical analyses and design studies required to define the BMSR. Some of these studies were required to assure its adequacy in modeling the commercial receiver, others independently confirmed its performance in the anticipated solar testing program.

Section 4 describes the developmental tests required to determine suitability of available materials in the solar receiver operating environment. Two ceramic fiber thermal insulation applications were

210  
Gas-in-tube heat  
exchanger wall  
panels

High-temperature  
insulation wall

Circular  
aperture

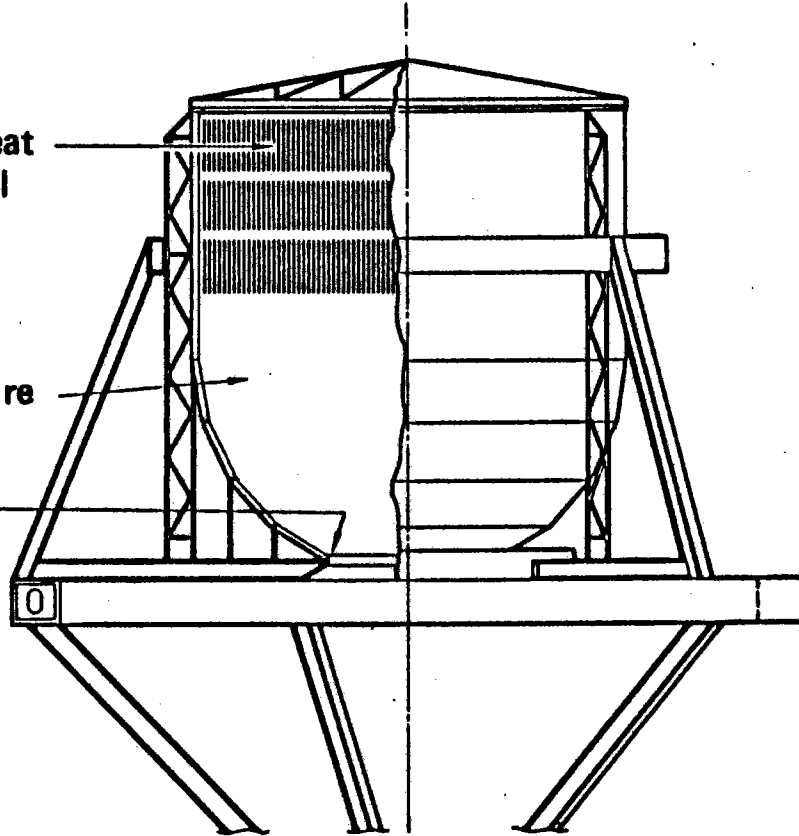


Figure 1.1-3: Closed Cycle Solar Central Receiver Concept, RP377-1

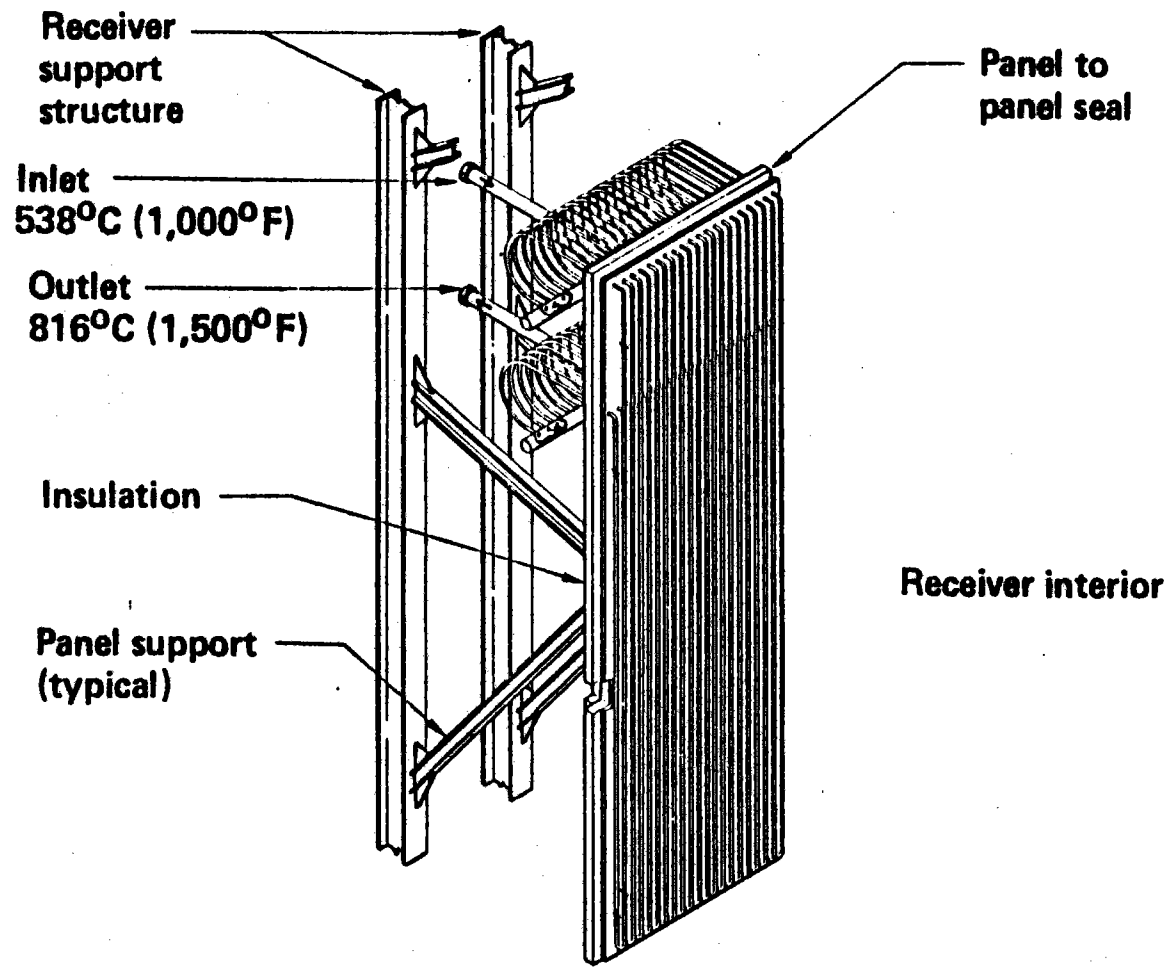


Figure 1.1-4: Heat Exchanger Wall Panel in the RP377-1 Receiver Concept

investigated including aperture rim solar shielding and high temperature cavity wall insulation. Results of tests of refractory metal alloy heat exchanger tubes conducted during RP377-1 are also described. These tests provided manufacturing development and solar receiver environmental exposure data which greatly influenced selection of the tube material and manufacturing processes used for the BMSR.

Section 5 describes the manufacturing of the BMSR. Section 6 describes the program of hot flow tests used to verify its operational readiness and as-built characteristics prior to shipment to the test site.

Sections 7 through 11 describe the work completed during RP377-3.

Section 7 provides an overview and general description of the solar testing program conducted in RP377-3. Test plans and requirements of experimenters at CRTF are described. The detailed test plans which include daily test objectives and procedures are described typically with reference to the three substantial size documents, two Boeing, and one Sandia, which were required to completely define BMSR test plans and procedures. The test setup at CRTF is described in detail. The section concludes with a summary of actual test activities which were accomplished.

Test data including test log notes, results of inspections, and records of experimental measurements are discussed in Section 8. The raw test data is described along with the posttest evaluation and processing required to define uncertainties and compare data obtained during separate tests.

Section 9 gathers together the quantitative results obtained during tests of the BMSR. Six types of tests were repeated at various times throughout the program at CRTF. Here the results of similar tests were brought together for comparison with one another, with pretest predictions, and to address the individual test objectives. Conclusions are also drawn with respect to the experimentally measured performance characteristics of the BMSR independent of analysis or thermal modeling considerations.

Section 10 describes the important qualitative test results and the changes



observed in the receiver as a result of its exposure in solar tests. These included changes anticipated due to exposure of the receiver to full operating temperatures and solar power levels. A number of unexpected changes also occurred, some caused by failure of auxiliary equipment in the test setup, and others resulting from degradation or damage to components of the BMSR.

Section 11 presents revised and updated thermal analyses of the BMSR. The pretest thermal model and analysis conditions had to be revised for two reasons. As anticipated, the actual test conditions of solar input power and receiver air inlet temperature were significantly different than pretest estimates. This is because of the lack of precise control of receiver operating conditions in the complex solar test facility. The second major impact on the pretest analysis was the measured presence of a more significant free convective heat transfer mechanism within the cavity than had been expected. This increased convective heat transfer had to be incorporated in the model.

Section 12 describes the solar test data tapes, the experimental data gathered during a typical solar test run, and the major features of each of the successful testing days at CRTF. The data tapes are a permanent record of all useable test data. A total of 200 channels of measured and computed BMSR data are recorded on four to twelve second intervals. This is the data base from which the results of Section 9 have been developed. The records have all been retained in the event that future testing or analysis show that additional information may be required.

### 1.3 DIVISION OF THE REPORT INTO THREE VOLUMES

This report is divided into three volumes. Volume I contains the introduction as well as Sections 2 through 6 which describe the RP377-2 activities prior to solar testing of the BMSR. Volume II, Sections 7 through 11, describes the solar tests and test results obtained during RP377-3. Volume III contains Section 12, which includes activity logs and plots of BMSR data obtained on each of the solar test days at CRTF.

## SECTION 2.0

### BENCH MODEL SOLAR RECEIVER DESIGN DESCRIPTION

The BMSR was a working-scale model of a commercial-size, closed-cycle, helium-gas-cooled solar receiver. The purpose of the BMSR program was to (1) demonstrate feasibility of the design concept; (2) prove the suitability of materials in a concentrated solar-flux environment; (3) demonstrate solar energy conversion by increasing the temperature of a working fluid; and (4) verify predictions of energy conversion efficiency.

Program economy dictated an open-cycle test using air as the coolant. Scale modeling of the BMSR required representing helium, the working fluid, with air, and closed-cycle design with an open-cycle test model. A major goal of the program was to use solar energy in heating air contained within a heat exchanger system from 538°C (1000°F) inlet temperature to 816°C (1500°F) outlet temperature while maintaining tubing temperatures below 871°C (1600°F). The average design solar flux on the heat exchanger tubes was identical to the commercial receiver it modeled as was the insulated wall construction and the 121°C (250°F) temperature limit of the outer steel structure.

#### 2.1 ARRANGEMENT AND FUNCTION OF COMPONENTS

The BMSR was sized to receive 1 MWt of solar input through the aperture from the collector field. From program outset, the BMSR was configured for testing at the DOE CRTF at Albuquerque, New Mexico. Figure 2.1-1 shows an artist's concept of the receiver.

The major components of the BMSR included insulated steel frame, heat exchanger panels, inlet and outlet manifolds, control system, and data instrumentation.

##### 2.1.1 Configuration

The BMSR was of welded-steel-frame construction and was lined with a

composite insulation. An eight-sided configuration with a truncated conical base section was adopted. Within the cavity were eight heat exchanger panels, one of which is shown in Figure 2.1-1. The panels consisted of a two-pass tubing arrangement and were connected by means of bolted flanges to inlet and outlet manifolds outside the cavity. The BMSR had an aperture 1.1m (43 in) in diameter and inclined 32 deg below the horizontal to best utilize the 1 Mwt north field of the CRTF. The cavity was configured to allow solar flux from the heliostat field to impinge mainly on the truncated cone portion of the insulated cavity walls, not the heat exchanger tubes. The flux was thus reflected and reradiated to provide a diffuse, evenly distributed thermal environment for the heat exchangers. The overall dimensions of the BMSR were 4m (13 ft) high by 3m (10 ft) wide and the weight was approximately 476 kg (10,500 lb).

#### 2.1.2 Construction Materials

The steel framework was constructed of ASTM-A36 structural shapes and 10-gage sheet with one exception. The leaf springs supporting the heat exchanger system were constructed of ASTM-A588 steel because of its higher yield strength.

The heat exchanger system comprised elements within the cavity. They were constructed of Inconel 617 seamless tubing. A preliminary material specification that established minimum mechanical properties, chemical composition, acceptance tests, and marking requirements was developed for control of purchased materials.

The manifold system comprised elements outside of the cavity. They provided the coolant supply and exhaust functions and were constructed of AISI 304 corrosion-resistant stainless steel.

The cavity insulation was a 15.2 cm (6 in) thick composite of block and blanket materials supplied by Babcock and Wilcox. The blanket materials were used in layers 2.5 cm (1 in) thick consisting of Saffil, a high-alumina (95%) content fiber and Kaowool, a 50-50 mix of alumina and silica fiber. The block material used in a 7.6 cm (3 in) layer was mineral wool made from

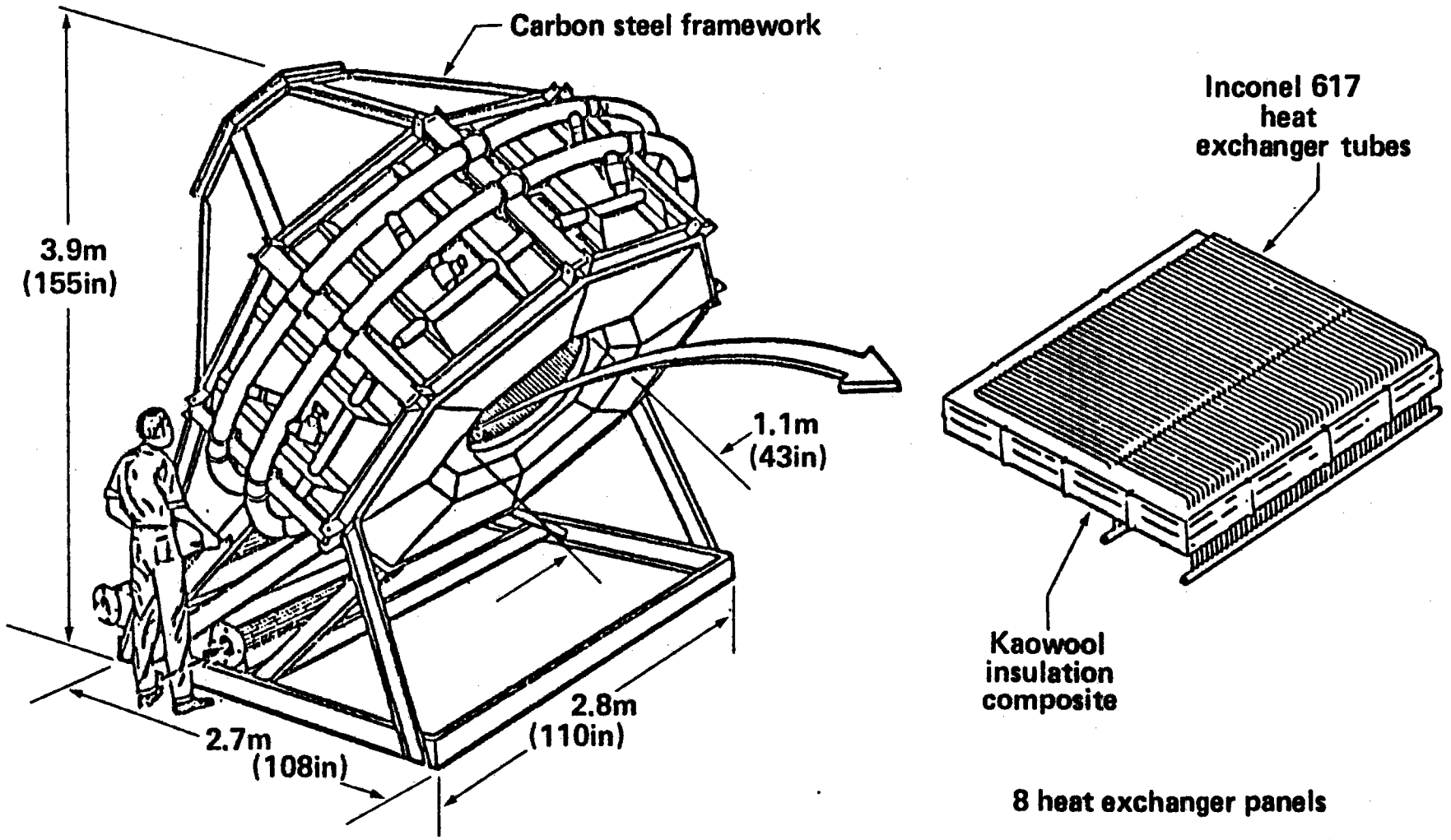


Figure 2.1-1: Artist's Concept of BMSR

blast furnace slag. Insulation retention devices included Inconel 601 studs, welded to the steel shell, and either Inconel 601 locking retainers or ceramic anchors, depending on the location within the cavity.

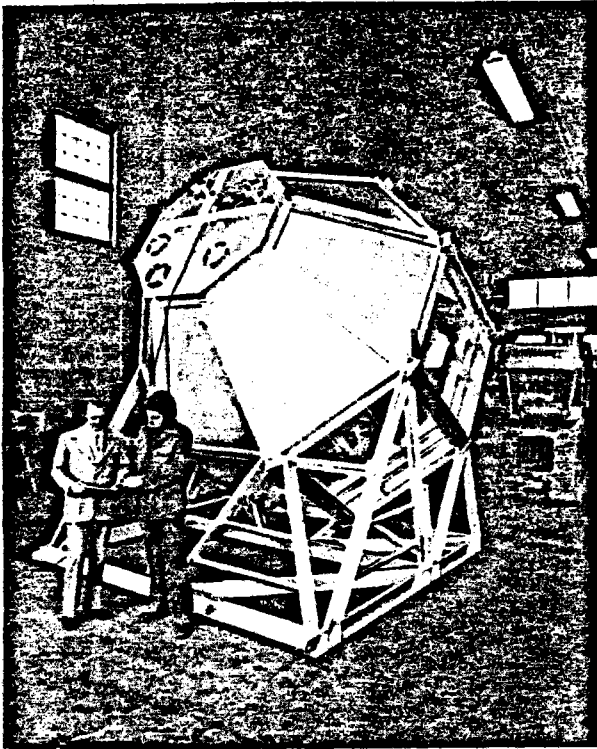
The aperture rim was insulated with Kaowool 3000 Board, 2.5 cm (1 in) thick. As discussed in Section 4, this design was later changed to include a zirconia tile overlayer, applied at the CRTF site. Mounting provisions for the aperture rim boards were 304 stainless-steel T-sections extending from a stainless-steel conical structure. This material provided the oxidation resistance needed in this high-temperature area.

### 2.1.3 Steel Framework

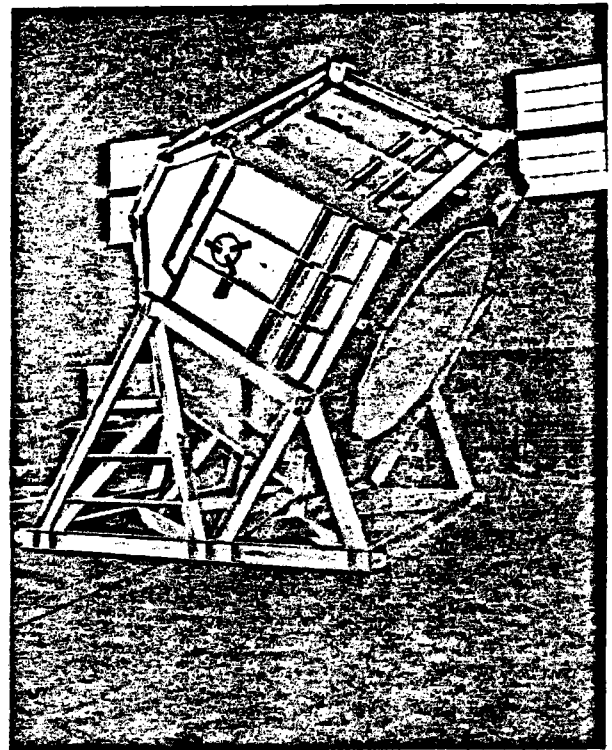
The steel framework formed the BMSR cavity and supported the heat exchanger system, as well as providing tiedown points for anchoring to the test bay floor. An all-welded construction was used. Figure 2.1-2 shows a front and back view of the BMSR framework before installation of the heat exchanger system and an interior view with the back cover removed.

The framework was constructed of structural steel and featured eight leaf springs that supported the entire heat exchanger system. The springs accommodated thermal growth of heat exchanger manifolds. The leaf springs (Figure 2.1-2) were hinged to the frame at both ends. One hinged end was also slotted to permit motion when the springs were deflected by thermal growth of the manifolds.

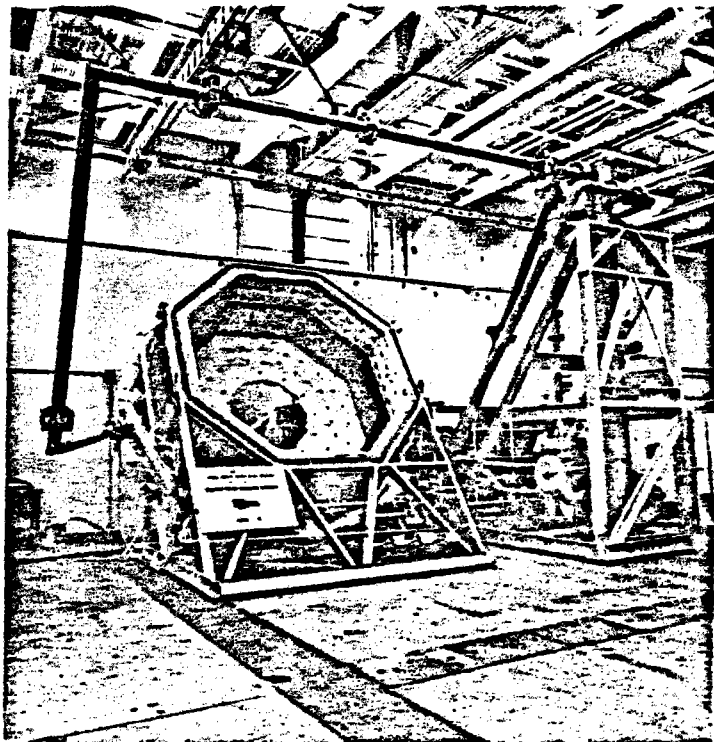
The framework was designed as two components, the back cover and the main frame. They were connected with bolts. The two components were separable and each had its own coolant lines, instrumentation, and insulation system. The heat exchangers, manifolds, and flow-control system were contained on the main frame. Upon removal of the back cover, as shown in the lower photograph of Figure 2.1-2, the heat exchanger panels were accessible for inspection or removal. The disassembly feature also diminished transportation problems, particularly trucking the completed BMSR from Seattle to Albuquerque.



Back view



Side view



BMSR with back cover removed

Figure 2.1-2: BMSR Components

#### 2.1.4 Cavity Insulation and Aperture Rim Thermal Protection

The cavity insulation was a composite of mineral wool block and three blanket layers, equaling 15.2 cm (6 in) thickness. The cavity insulation system differed between the main frame and back cover structures. Starting at the steel shell, the main frame was insulated with 7.5 cm (3 in) of mineral wool block and three 2.5 cm (1 in) layers of Kaowool blanket. The insulation thickness was selected to maintain the outer shell temperature below 121°C (250°F). The Kaowool blanket was chosen for its ease of installation, light weight, and insulating properties. Kaowool blanket has an advertised maximum-use temperature of 1260°C (2300°F). Mineral wool block is an industrial byproduct with varying mixtures of ingredients and was selected for its low cost. The advertised use limit for this material was 816°C (1500°F).

The back cover insulation, shown being applied in Figure 2.1-3, was designed to accept the direct solar flux coming through the aperture and radiate and reflect this energy to the heat exchanger panels. Starting at the steel shell, the cover was insulated with 7.5 cm (3 in) of mineral wool block, two 2.5 cm (1 in) layers of Kaowool blanket and, on the innermost surface, one 2.5 cm (1 in) layer of Saffil blanket. Surface temperatures of the Saffil blanket were predicted to be approximately 1371°C (2500°F). The material had an advertised maximum-use limit of 1649°C (3000°F).

Fasteners used to secure the insulation composite to the steel shell were Inconel 601. Figure 2.1-4 shows stud welding to shell segments. Metallic anchors were used to secure the insulation composite to the main frame. They are shown installed on the studs in Figure 2.1-4. Ceramic anchors were used to secure the insulation to the back cover, also shown in Figure 2.1-4.

The aperture rim was shielded with Kaowool 3000 Board insulation. Further protection from misdirected solar flux was provided by a layer of zirconia board 1.3 cm (0.5 in) thick bonded to the alumina board with an alumina cement, QF-180. The original BMSR design employed alumina board insulation in an annular configuration around the aperture, as shown in Figure 2.1-2. Subsequent analysis revealed the possibility of misaligned heliostats that

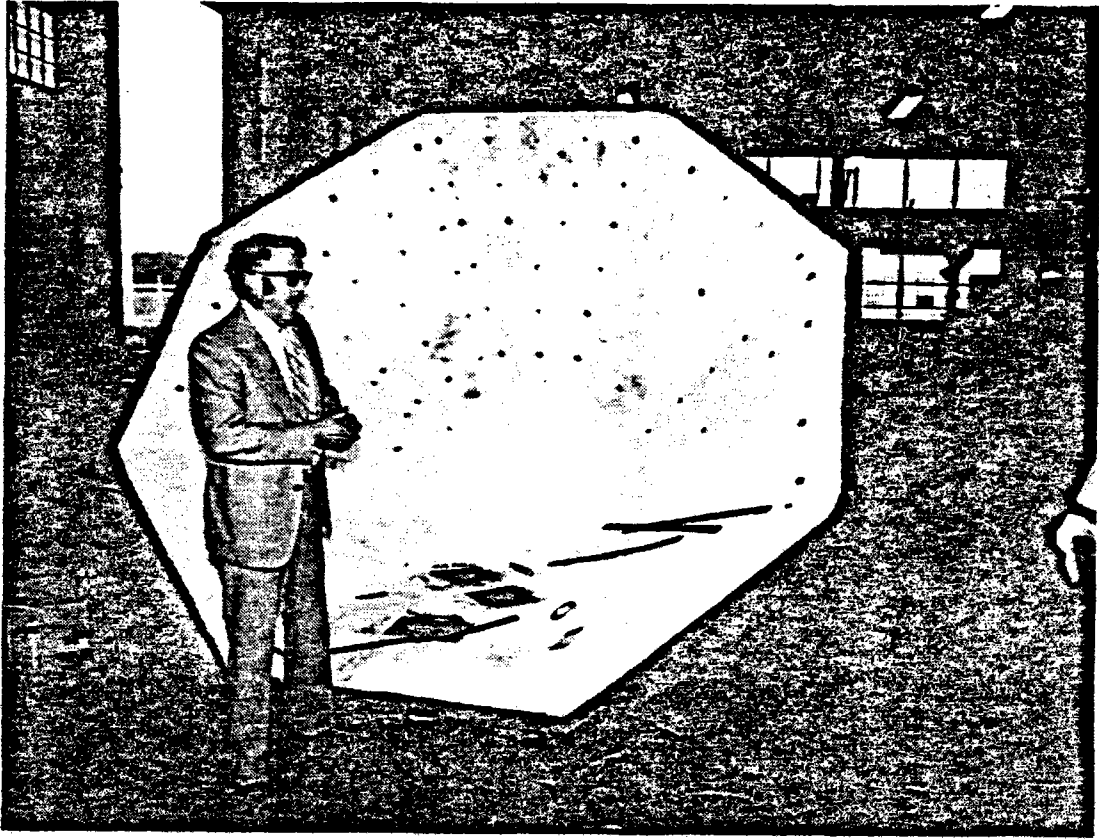
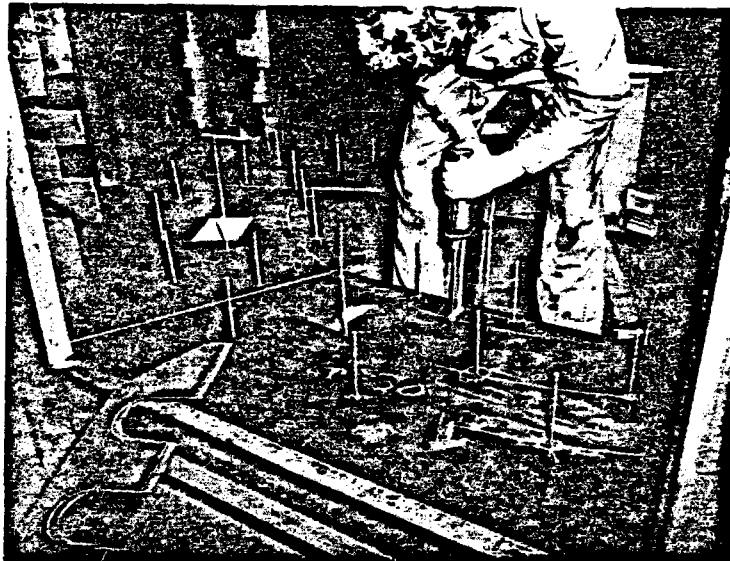
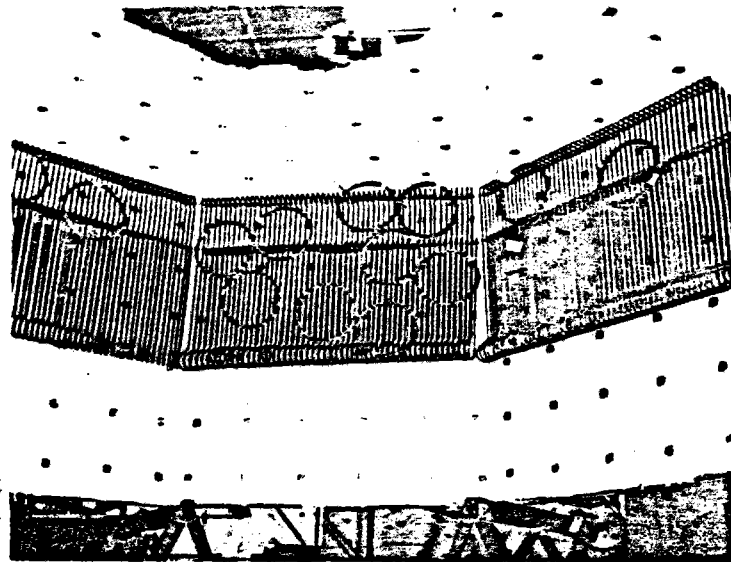


Figure 2.1-3: Back Cover Insulation in Progress





Stud welding  
insulation fasteners



Metallic  
insulation anchors

Ceramic  
insulation anchors

Figure 2.1-4: Insulation Attachment Components

could produce up to  $2100 \text{ kW/m}^2$  incident flux on the aperture rim, considerably beyond the capability of the alumina board. Therefore, when these potential facility malfunctions were considered, it was deemed advisable to protect the entire BMSR aperture face with the alumina-zirconia board laminate. The substructure supporting the aperture insulation shown in Figure 2.1-2 consisted of 304 stainless steel T-sections welded to a conical dish (Figure 2.1-5). The insulation boards were cut in a trapezoidal shape and slotted along the edges to slide onto the T-sections. Upon arrival at the CRTF site, the decision was made to insulate the entire aperture face. A metal substructure was fabricated and covered with Kaowool 3000 Board. After attaching this substructure to the aperture face, the entire surface was tiled with zirconia.

#### 2.1.5 Heat Exchanger System

The heat exchanger system comprised elements inside and outside of the cavity. The external elements consisted of stainless-steel inlet and outlet manifolds that encircled the BMSR. There were eight flanges welded to each manifold serving as the connection to the heat exchanger panels. Within the cavity were eight heat exchanger panels visible in Figure 2.1-2. Each consisted of an inlet and outlet header and 54 two-pass tubes. A flanged connector pipe was welded to each header and these protruded through the cavity wall to the outside where they were bolted to the manifolds. The entire panel assembly was of welded construction. The superalloy used for the panels was Inconel 617.

Figure 2.1-6 shows components of the heat exchanger panel before welding. When completed, the panels appeared as shown in Figure 2.1-7. The black-oxide coating was produced intentionally during the stress relief cycle. Figure 2.1-8 is a schematic of an individual panel showing the bolting flanges, the flow-control valve on the inlet, and segments of the manifolds.

The inlet and outlet manifolds served as the primary structural support for the entire heat exchanger system. The manifolds were attached to the framework leaf springs by means of brackets that mated with similar brackets

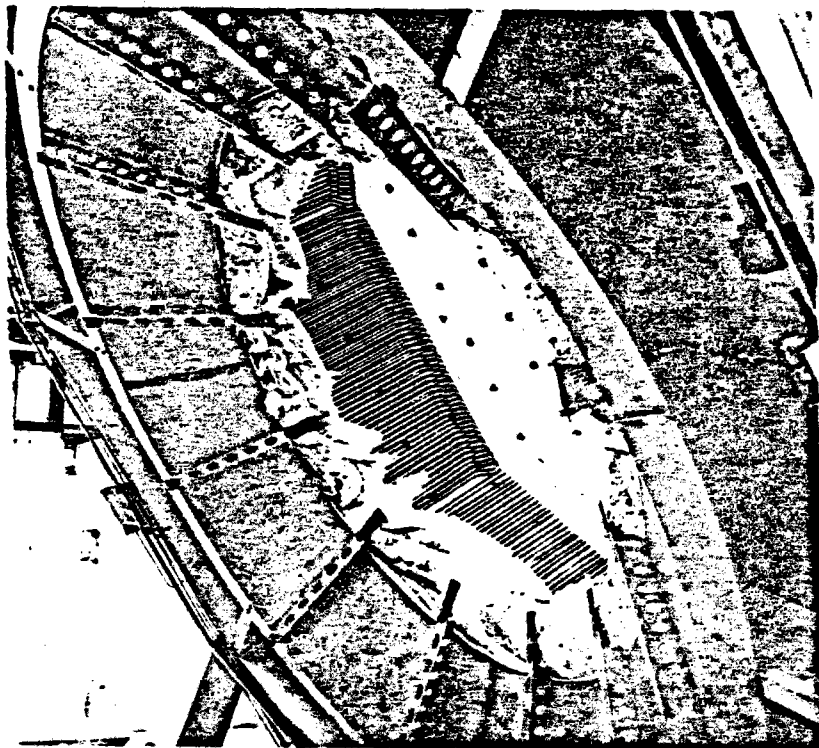


Figure 2.1-5: Aperture Face Substructure

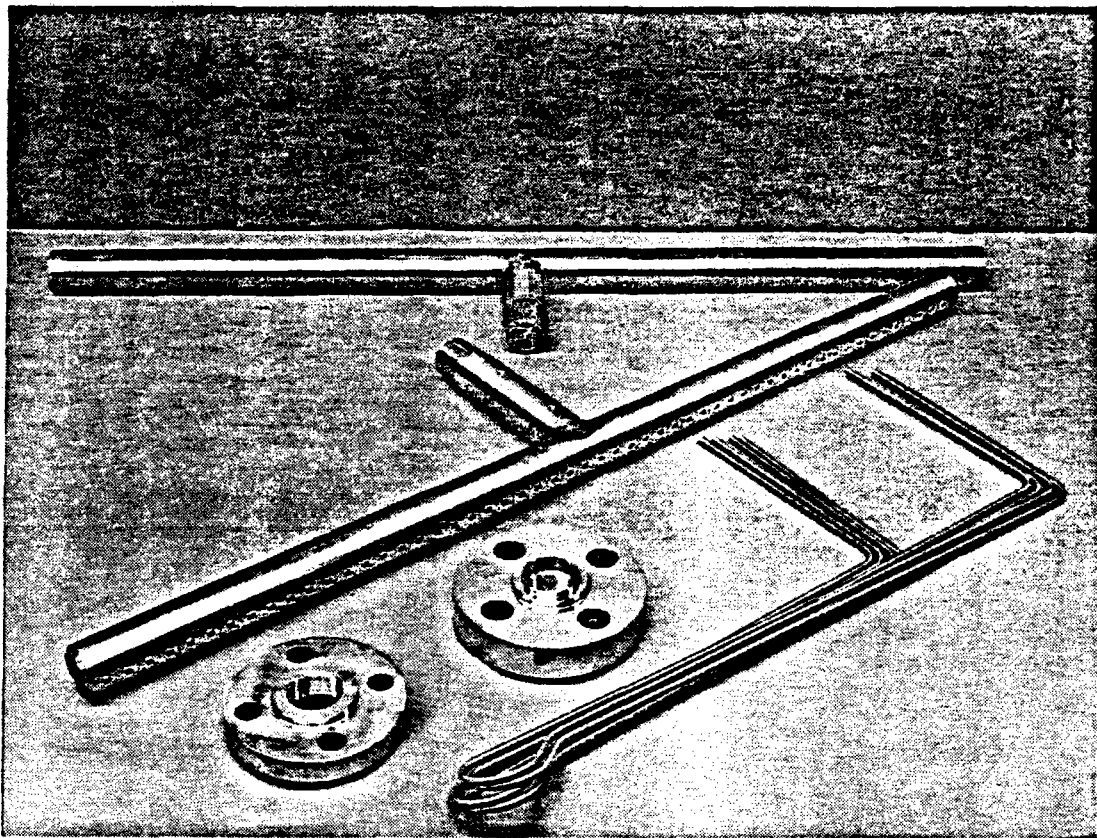


Figure 2.1-6: Heat Exchanger Components

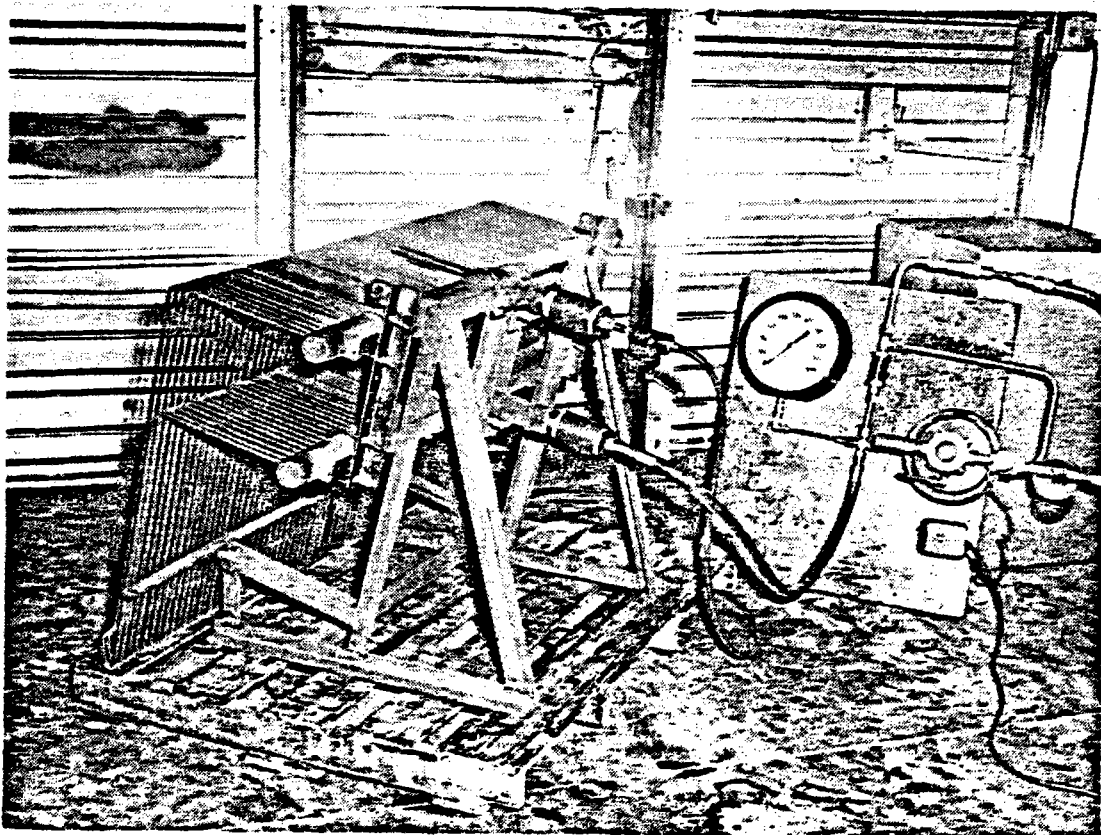
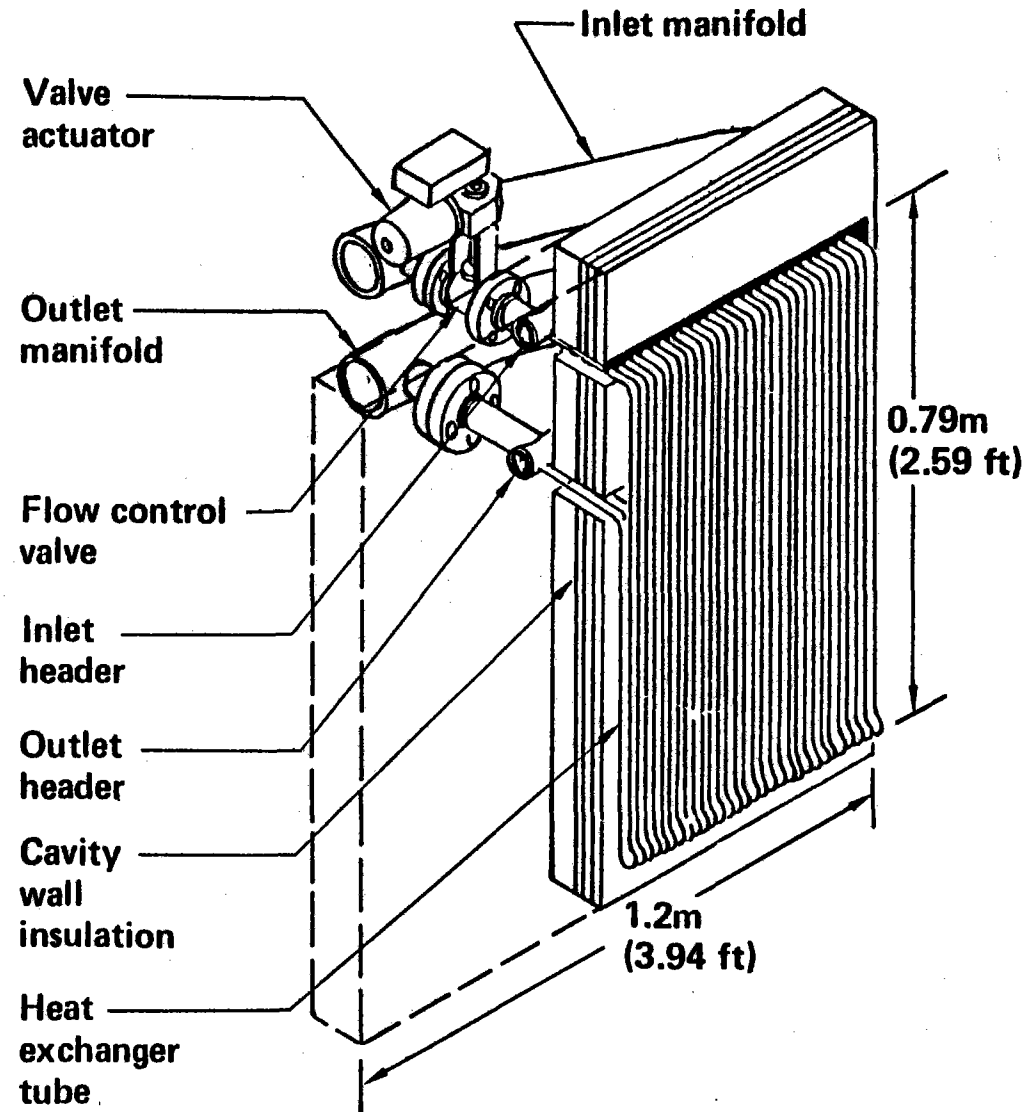


Figure 2.1-7: HX Panel During Proof Test

Figure 2.1-8. BMSR Heat Exchanger Panel Details

# BMSR Heat Exchanger Panel Details



on the springs. A titanium pin was used as the hinge member.

An interface with the supply of coolant air occurred at one point on the inlet manifold and two points on the outlet manifold. The interfaces were standard ANSI bolted flanges and because they were integral with the manifolds, were subjected to radial (thermal) motion during test. A requirement to accommodate this motion with less than a 45 kg (100 lb) load applied to the manifolds was imposed on the design of connecting supply and exhaust piping.

Inlet and outlet manifolds were insulated with Kaowool blanket wrapped in a spiral fashion. Two overlapping layers of blanket 1.3 cm (0.5 in) thick were used and were secured with stainless steel wire ties and wire mesh. The valve body and heat exchanger panel headers on the outside of the framework were also insulated with Kaowool blanket. All of these insulated elements are visible in Figure 2.1-9.

#### 2.1.6 Flow Control System

The flow control system is shown schematically in Figure 2.1-10. There were eight of these systems, one for each heat exchanger panel. The major elements were a ball valve for panel-flow regulation, a thermocouple in the panel outlet gas stream, and a setpoint controller. By means of an electropneumatic system, the valve position was regulated to maintain a selected panel outlet temperature. The selection was made by means of the proportional controller. Typical setpoint temperatures used in solar tests were 621°, 705°, and 816°C (1150°, 1300°, and 1500°F).

The control valve was contained between a pair of flanges on the inlet side of the heat exchanger panel. The valve was a wafer design, held in place by four bolts. A dummy valve, used during fabrication stages, is shown bolted in place in Figure 2.1-11. The flow control valve selected had an integral actuator and positioner. Additionally, a junction box was fitted to the positioner to house the terminal block and a valve angle potentiometer. These elements are visible in Figure 2.1-9. The valve was an off-the-shelf item, designed for a service environment of 538°C (1000°F). The sensing

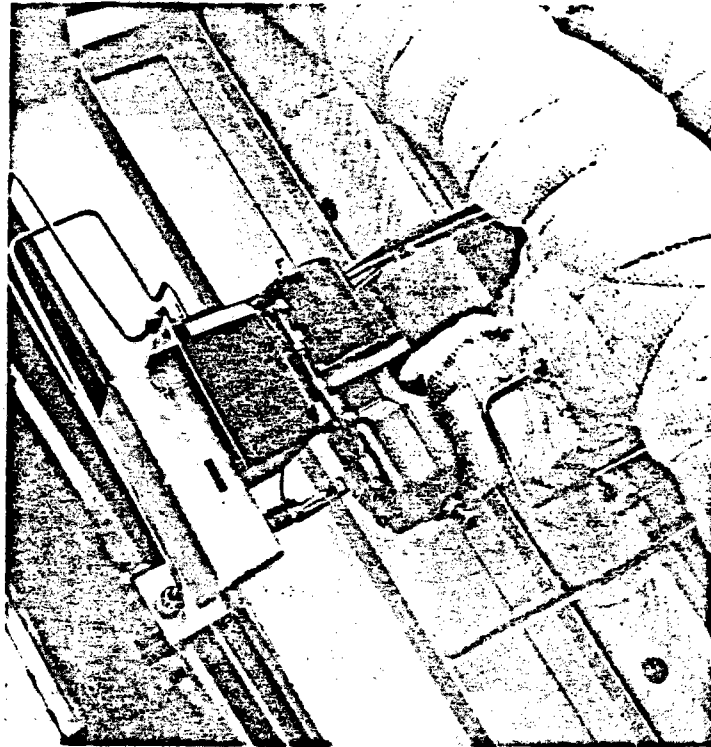


Figure 2.1-9: Flow Control Valve

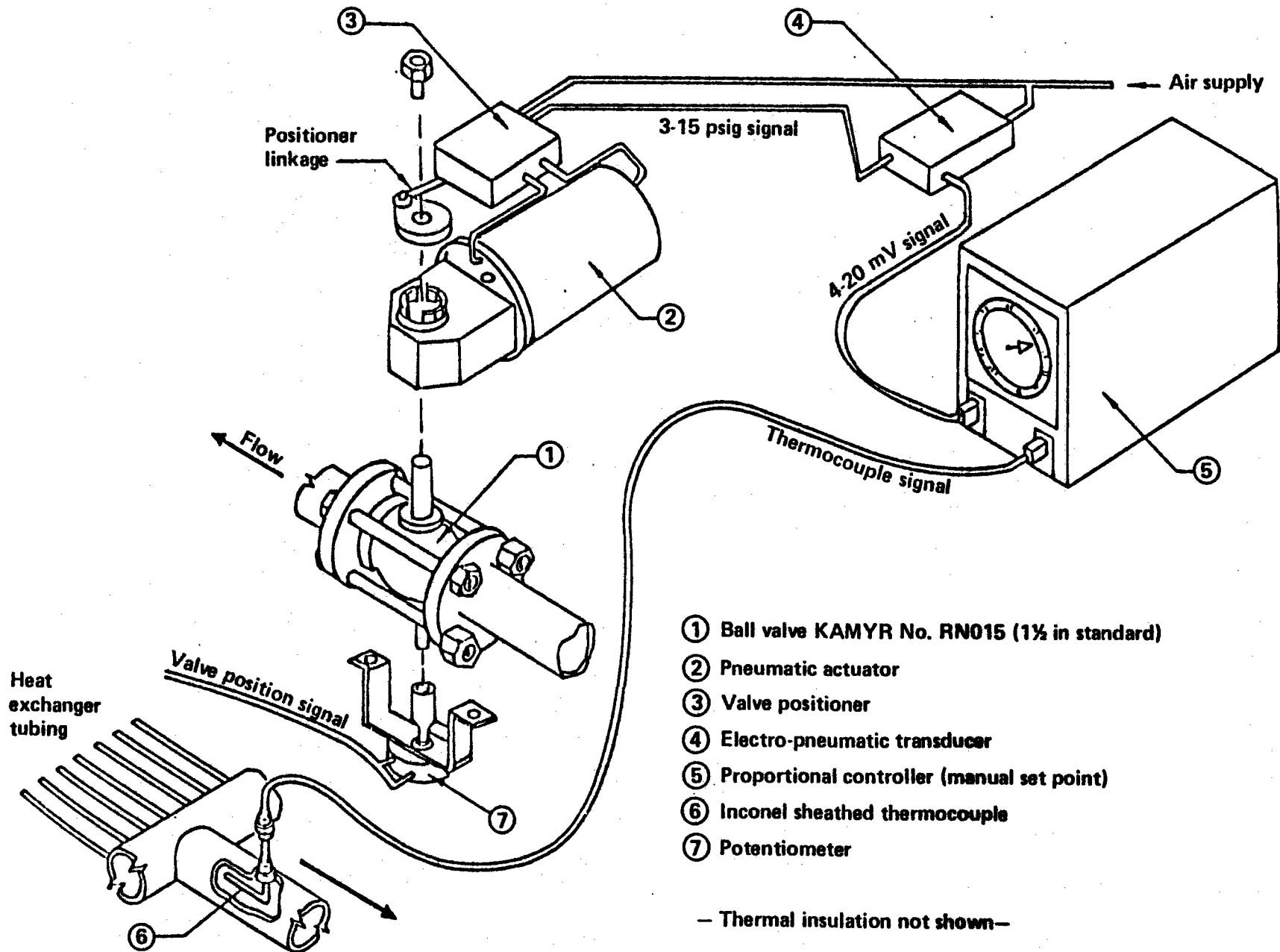


Figure 2.1-10: Gas Flow System Flow Regulation and Control Schematic



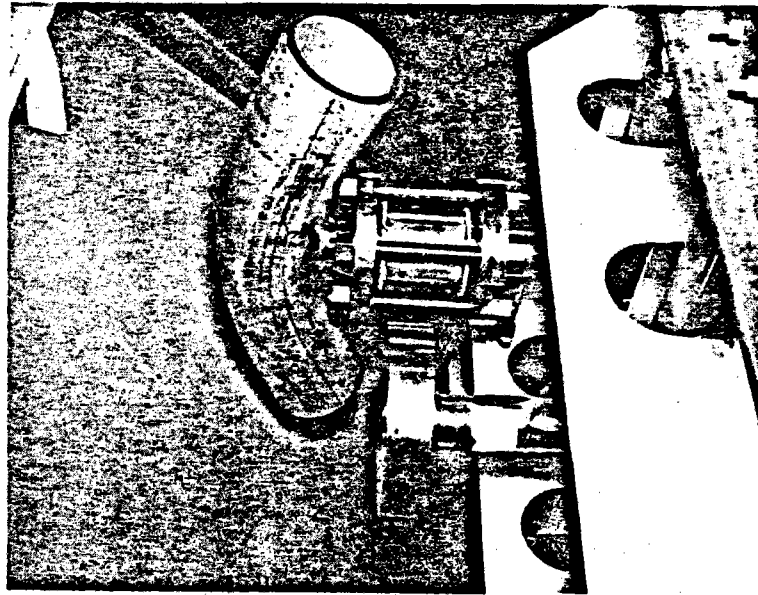


Figure 2.1-11: Dummy Valve Installation

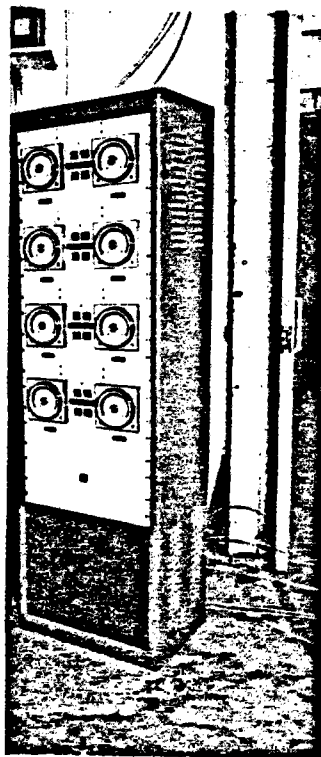


Figure 2.1-12: BMSR Control Console

element, an Inconel-sheathed thermocouple, was located in the connector pipe of the heat exchanger panel outlet. A conventional packing gland-pipe thread fitting was used for the installations.

A control console (Figure 2.1-12) housed the eight setpoint controllers and provided points for power supply and signal connections. Local and remote operational capability was designed into the control system. The control console was located in the bay immediately below the BMSR for solar testing. The local control capability allowed setpoints to be established directly on the console for checkout and initial training purposes. The remote control function, when enabled, permitted changing setpoints from the control room several hundred feet north of the test tower by means of the facility's Data Acquisition and Control System (DACs).

#### 2.1.7 Instrumentation

The BMSR was an experimental device, intended to evaluate and characterize thermal control, heat transfer, and flow behavior of a solar energy conversion system. As such, a great quantity of instrumentation was necessary to monitor performance and gather data for comparison with pretest predictions. The amount of instrumentation used was substantially greater than that anticipated for a commercial solar-electric plant.

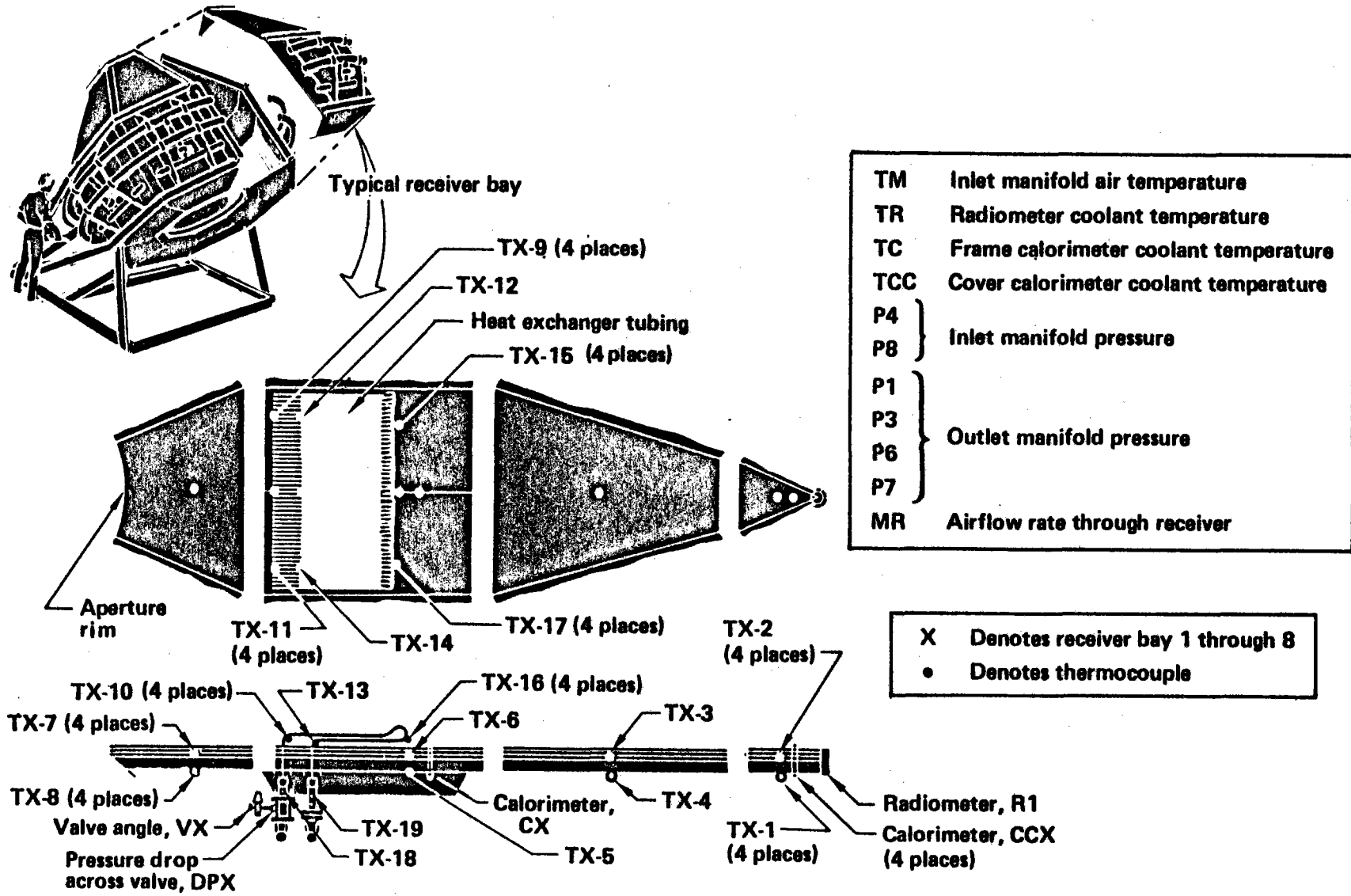
The types of data acquired were temperatures of metallic members, insulation, and heat transfer fluids; absolute pressure and pressure drop across heat exchanger panels, valves, and the total flow system; heat flux on cavity surfaces; and control valve angle. Figure 2.1-13 shows typical instrumentation for one of the eight BMSR bays.

#### 2.1.8 Air Supply System

BEC designed, fabricated and operated the air supply system that supplied coolant for the BMSR solar tests at CRTF. The work was performed on EPRI Contract RP1092-1. A schematic representation of the system, including the BMSR, is shown in Figure 2.1-14. A group of four diesel-driven, rotary-screw compressors were located at the tower base. They were

Figure 2.1-13. Bench Model Instrumentation

# Bench Model Instrumentation



TM	Inlet manifold air temperature
TR	Radiometer coolant temperature
TC	Frame calorimeter coolant temperature
TCC	Cover calorimeter coolant temperature
P4	Inlet manifold pressure
P8	
P1	Outlet manifold pressure
P3	
P6	
P7	
MR	Airflow rate through receiver

X	Denotes receiver bay 1 through 8
•	Denotes thermocouple

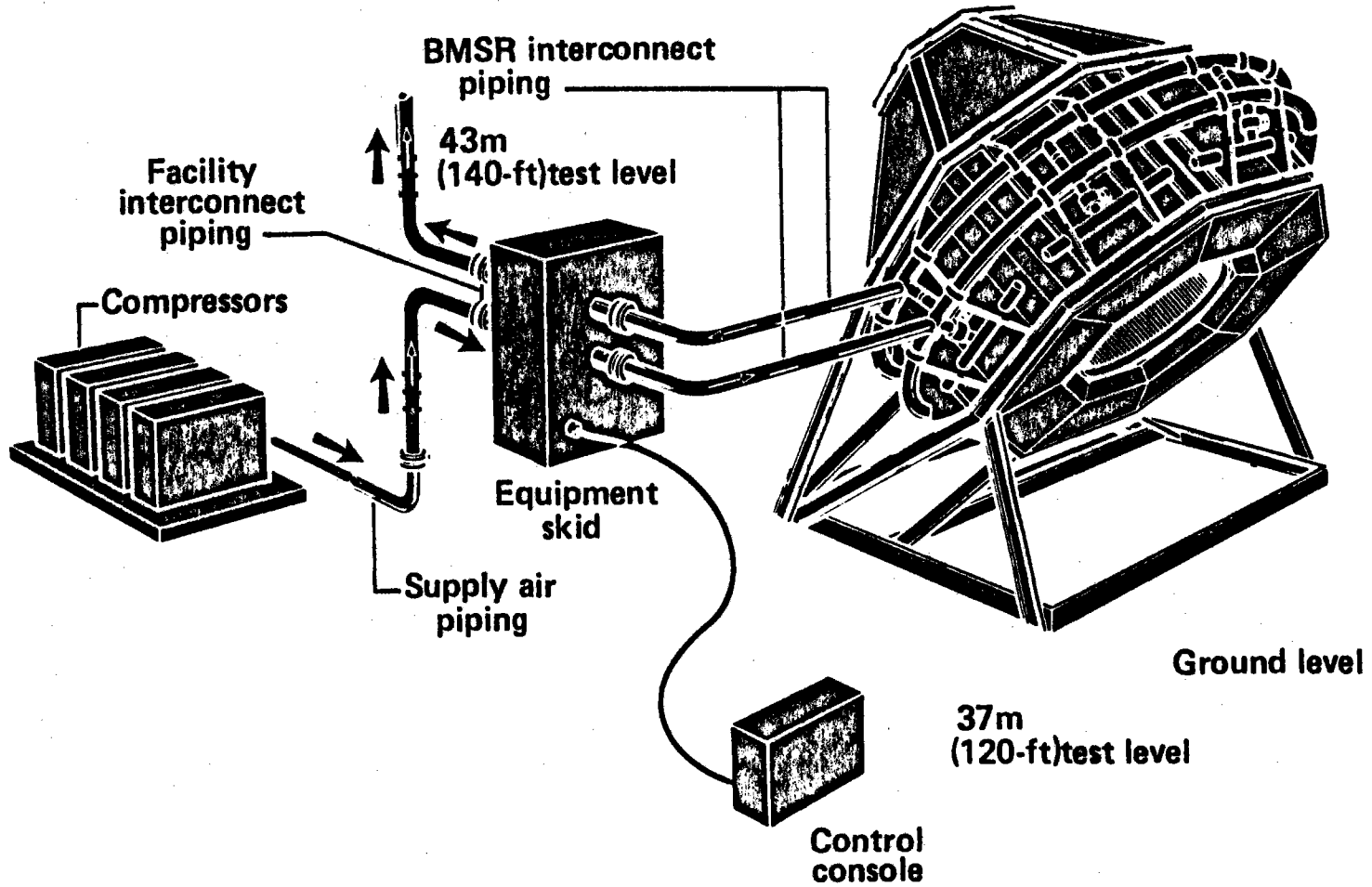


Figure 2.1-14: Air Supply System Components

connected to facility piping in the tower, which served the 43m (140-ft) test level. At the test bay, interconnects were made to the recuperative heat exchanger skid and the BMSR. Exhaust air leaving the recuperator was discharged into the facility vent stack. A butterfly control valve located at the exhaust (tube) side of the tube-shell recuperator maintained back pressure to 0.5 MPa (75 lb/in<sup>2</sup>a) within the test system. The control console for valve functions was located on the 37m (120-ft) test level, alongside the BMSR control console. Figure 2.1-2 shows the vertically mounted recuperator with interconnect piping attached to the BMSR.

The air supply system provided compressed air at 1.03 MPa (150 lb/in<sup>2</sup>a) at the compressor discharge at all mass flows. The maximum mass flow was 2.7 kg/s (6.0 lb/s) or approximately 16,844 m<sup>3</sup>/s (5950 SCFM) at 27°C (80°F) and 161m (5300-ft) altitude. The minimum flow was 0.4 kg/s (0.85 lb/s).

In a commercial plant, the hot gas would be used to drive a turbine-generator set; however, in the BMSR test, the gas was discharged through the recuperator to preheat incoming air. Design point operating temperatures at BMSR inlet and outlet manifolds were achieved by solar heating alone. This process was lengthy at the start of each test day because of the thermal inertia in piping and recuperator.

## SECTION 3.0

### RECEIVER DESIGN STUDIES

#### 3.1 THERMAL-SCALE MODELING OF THE COMMERCIAL RECEIVER

Section 1.0 describes the closed-cycle, high-temperature receiver concept for solar electric power that was developed during the course of the RP377-1 study (Reference 1). Figure 3.1-1 shows the arrangement of its cavity walls, downward-facing aperture, and gas-in-tube heat exchangers. In the solar-electric powerplant, this receiver was situated atop a 79m (260-ft) tower surrounded by 15,400 solar collectors (heliostats). During operation, the heliostats focused their reflected sunlight on the downward-facing receiver aperture, which collected approximately 300 Mwt of solar heat.

Because of the arrangement of the tower, aperture, and surround-field heliostats, virtually all receiver solar input was initially incident on the lower walls of the cavity interior (Figure 3.1-2). The solar input was diffusely reflected and reradiated by the insulation wall to provide a nearly uniform heat flux on the heat exchangers that lined the upper walls of the cavity. The metal gas-in-tube heat exchangers absorbed this heat, transferring over 80% of the receiver solar heat input into the high-pressure helium working fluid.

The heat exchanger installation consisted of a total of 4200 parallel gas-flow paths through individual tubes. These were grouped into 210 identical panels of 20 tubes each. Figure 3.1-3 shows details of a heat exchanger wall panel. Each panel was provided with some control of its gas-flow rate. This control maintained equal panel outlet temperatures despite expected variations of heat loads around the interior walls of the cavity.

Commercial-quality, readily available materials and components were used in the RP377-1 receiver. These had been used in other non-solar-heated, high-temperature commercial equipment at temperatures and working stress levels expected in the solar receiver. New technology was involved in the

Figure 3.1-1. 300-MW Closed-Cycle Solar Central Receiver Concept, RP377-1

# 300-MW Closed-Cycle Solar Central Receiver Concept, RP377-1

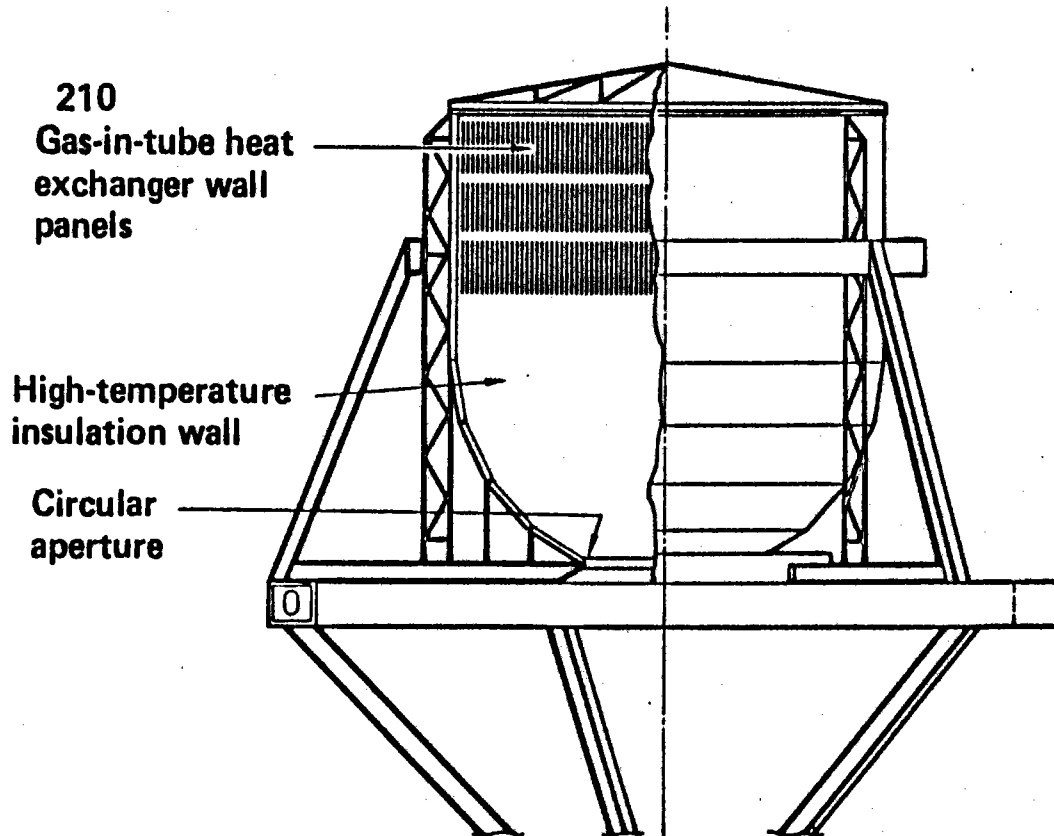


Figure 3.1-2. Solar Input Flux Distribution in the 300-MW Receiver

## Solar Input Flux Distribution in the 300-MW Receiver

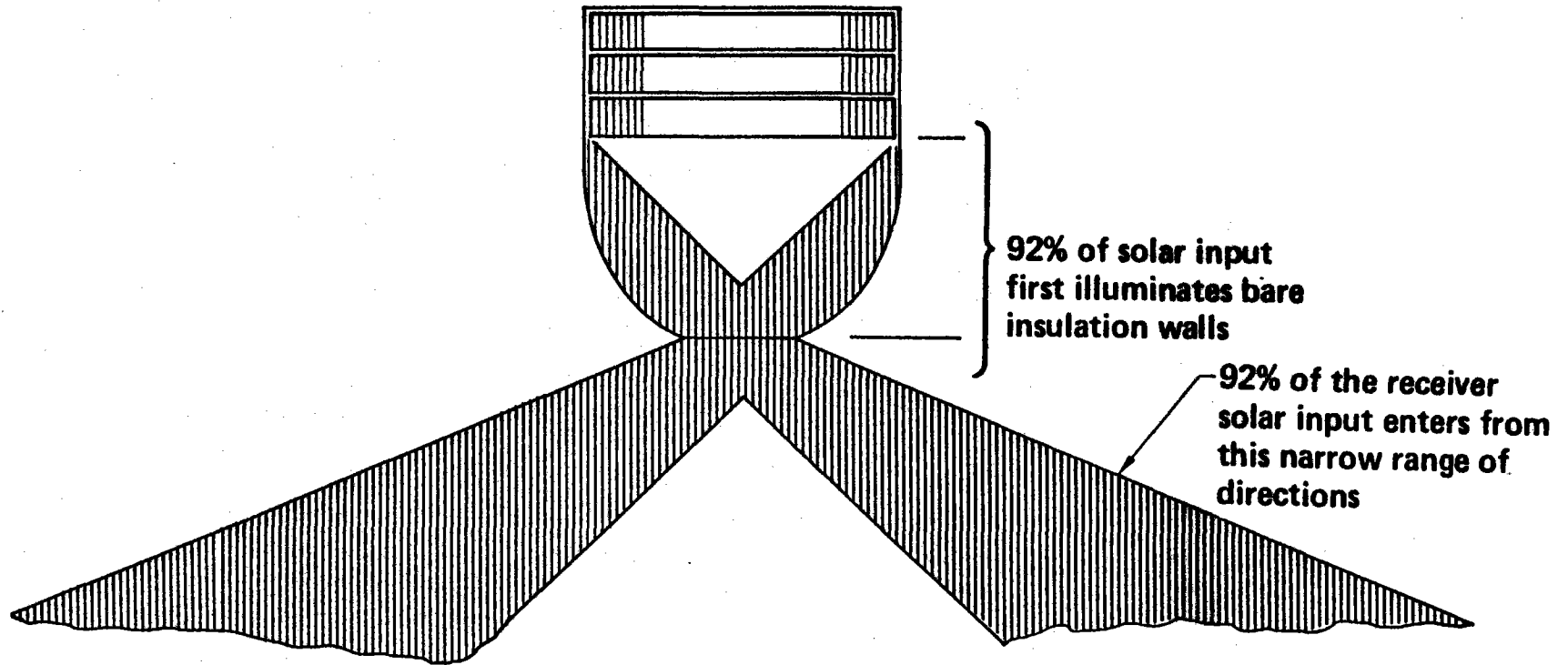
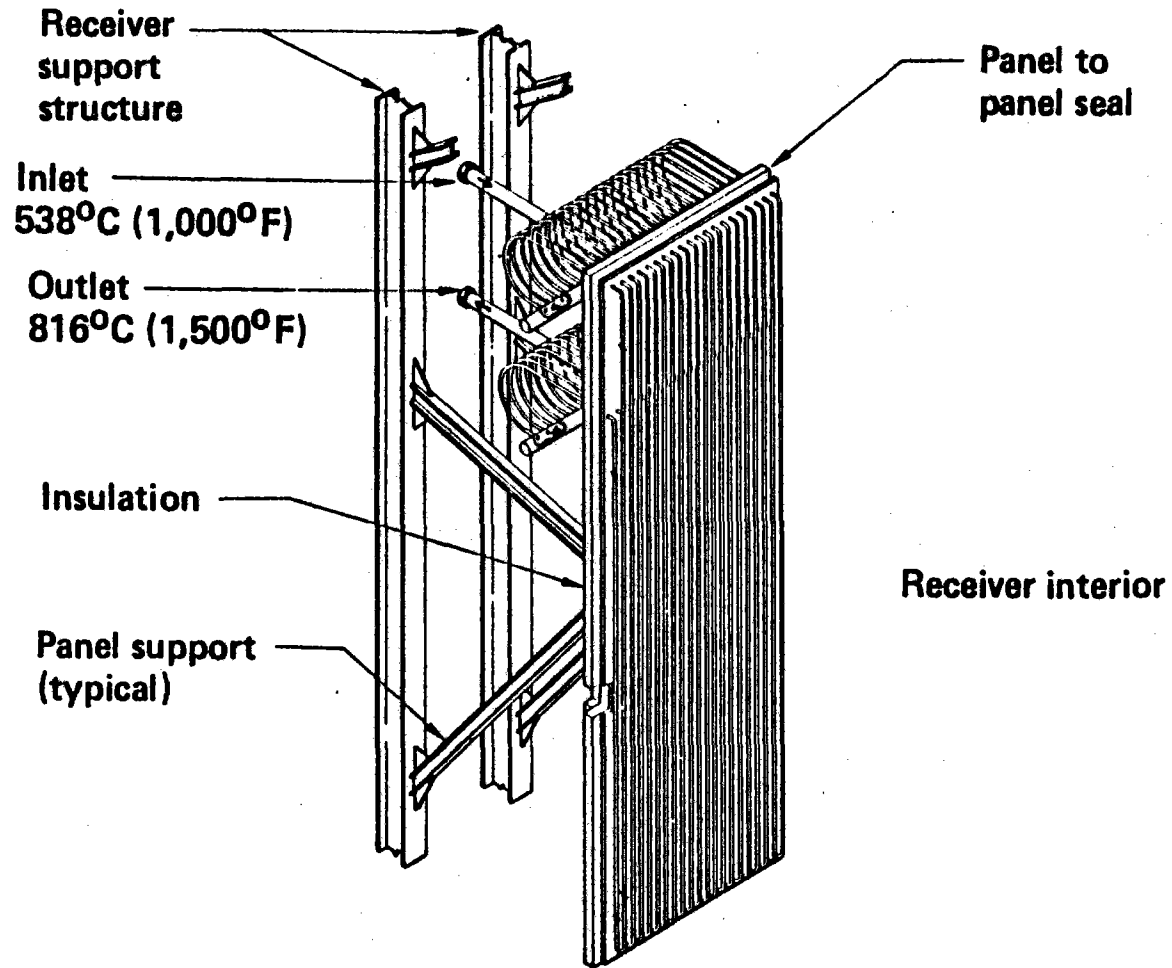




Figure 3.1-3. Heat Exchanger Wall Panel in the 300-MW Receiver Concept

# Heat Exchanger Wall Panel in the 300-MW Receiver Concept



solar receiver development program because, in addition to the usual temperatures and stresses, the components were exposed to high-intensity solar flux inside the central receiver cavity. Major technological uncertainties addressed by the BMSR program were how this solar flux would be managed by the receiver heat transfer system and how the solar flux would affect the cavity materials.

Thermal-scale-modeling requirements had to be satisfied by the BMSR, thus ensuring that the important steady-state and transient thermal characteristics of the commercial powerplant receiver were simulated by the BMSR. A model receiver was desired that would exhibit all the critical solar interface functions of the commercial receiver. These solar interface functions included--

- a. Concentrated solar flux passing through the cavity aperture
- b. Majority of cavity solar heat first incident on insulation walls
- c. Reflective redistribution of solar heat to provide balanced heat loads on heat exchanger panels

Because the BMSR was intended to verify the materials and components used in pilot-plant and commercial receivers, it had to expose them to the same operating environment. Steady-state and dynamic operating conditions of the commercial receiver were required to be duplicated in the BMSR.

In theory, thermal-scale models can be designed that duplicate heat fluxes, temperatures, transient thermal response rates, and thermal performance characteristics of any heat transfer system. This was accomplished by satisfying theoretical requirements for thermal similitude commonly available in the literature. Difficulties arose in attempting to satisfy these requirements without jeopardizing the scale-model receiver as a self-sufficient solar receiver. Compromises with the theory were required to make the model receiver compatible with available solar testing facilities, in this case the CRTF. Other compromises were required because of practical considerations of the manufacturing cost, reliability, and

service life of the model receiver.

Section 3.1.1 describes the requirements for theoretically ideal thermal-scale modeling of the commercial receiver. These are considered for a model-to-prototype solar-power scaling ratio of 1:300. Design characteristics are developed for an exact thermal-scale model. Section 3.1.2 addresses the problems that result from test interface requirements and manufacturing limitations to make the BMSR design practical. Compromises resulting from these constraints are identified and described in terms of the resultant thermal-scale-modeling errors.

### 3.1.1 Theoretical Requirements for Thermal-Scale Modeling

The goals of this thermal-scale-modeling activity were to design the model receiver for a solar input of  $1\text{MW}_t$  and to duplicate the temperatures, heat fluxes, thermal performance, and transient thermal characteristics of the full-size  $300\text{-MW}_t$  receiver. In most cases of scale modeling for engineering testing there are some commercial system characteristics that can be readily duplicated in the scale model and others that present conflicting design requirements. This section describes theoretical design requirements for the BMSR as a thermal-scale model. These were developed by consideration of the RP377-1 receiver. Some areas of conflicting model design requirements are indentified and show that all the scale-modeling requirements cannot theoretically be accomplished. Judicious compromises were required during the design of the BMSR.

The RP377-1 commercial receiver was an excellent candidate for thermal-scale modeling because its most important heat transfer mechanisms scaled down in direct proportion to the active surface area. To obtain model temperatures equal to the commercial receiver, a model receiver designed for 1/300 of the solar power of the commercial receiver needed to have its heat transfer areas reduced to 1/300 of the area of corresponding surfaces. Therefore, the linear scale size of the model was 1/17.3 of the corresponding commercial dimensions. The most important solar receiver heat transfer mechanisms preserved by this direct scaling of dimensions are discussed in the following paragraphs.

Solar heating of the cavity required matching two commercial receiver characteristics in the model. First, the directional pattern of solar flux entering the model cavity had to be scaled down in size but retain the same relative energy distribution. The solar heating pattern on cavity walls should be an exact scale model of the pattern in the commercial receiver. Secondly, the solar reflective surface properties of the internal cavity walls had to be equal to those in the commercial receiver. This was most readily achieved by using the same wall insulation and heat exchanger materials in the model as in the commercial receiver.

The same criteria necessary to match the cavity interior solar heating also provided a match of solar reflective characteristics of a model and commercial receivers. This resulted in a scale modeling of reflective solar heat losses out the aperture.

Radiant heat transfer between surfaces inside the cavity depended on their relative sizes and locations, on thermal radiative interchange factors between them, and on surface radiant properties of the cavity walls. An exact scale modeling of commercial receiver dimensions preserved the radiant interchange factors between corresponding surfaces. Radiant properties were matched by using the same wall insulation and heat exchanger materials in each receiver. Under these conditions, and assuming that the model receiver operated at the same temperature as the commercial receiver, the radiant heat loss from the model aperture was a 1/300-scale model of the commercial system heat losses.

Conductive heat losses through the insulation walls of the scale-model receiver had to be equal to those in the commercial receiver in terms of heat loss per unit area. This was accomplished by using the full thickness of the commercial insulation wall in the model. Exterior model dimensions were distorted to accommodate this thickness.

Scale thermal modeling of the gas-in-tube heat exchangers presented more difficult problems. Radiant and solar reflective heat transfer from the cavity walls to the outside of heat exchanger tubes was accurately simulated in an exact scale model using the same materials as the commercial receiver.

The commercial receiver's double row of heat exchanger tubes had to be retained in the model because the back row of tubes was shadowed by the front row. Also, the tube spacing of three diameters center-to-center affected the amount of heat received by the back row and by the cavity walls behind the rows of tubes. This relative tube spacing was also preserved in the model.

The tube-to-gas heat transfer on the inside of heat exchanger tubes depended on the local values of tube and gas temperature and on the local heat transfer film coefficient. Model heat exchanger interior tube-wall temperatures and tube-to-gas heat fluxes would be equal to those in the commercial receiver as long as the heat transfer film coefficients and gas temperatures inside the tubes were the same as the commercial receiver. This matching of film coefficients required a purposeful distortion of gas-flow conditions inside the heat exchanger tubes.

Distortions of the model heat exchangers that were potentially useful in matching the internal tube heat transfer included--

- a. Substitution of alternative working fluid in the model for the helium gas used in the commercial receiver.
- b. Distortion of model tube diameter to be greater or smaller than the ideal model tube size ( $1/17.3$  of commercial diameter). This was done while preserving the total surface of heat exchangers by correspondingly changing the number of heat exchanger tubes in the model.
- c. Distortion of model tube length to be two or three times as long as the true scale model. The three vertical rows of heat exchangers in the commercial receiver (Figure 3.1-1) could be replaced by one or two rows of corresponding longer tubes.

These heat exchanger distortions are discussed in detail in Section 3.1.2.

Tube-wall thickness also presented a problem in scale modeling of the heat exchangers. The tube wall affected heat transfer to the internal tube airstream in two ways. First, the thickness of the tube wall presented a

resistance to radial heat flow. At heat fluxes typical of the commercial receiver, this produced a thermal gradient of 10° to 20°C (18° to 36°F) between the inner and outer surfaces of the tube wall. Second, because the tubes were located alongside the cavity walls, they were heated on the sides that faced the hot cavity. The tube temperatures were 50° to 90°C (90° to 162°F) higher on the side facing the cavity. This temperature gradient was produced by the circumferential variation of solar and radiant heating. However, heat conduction around the tube wall provided a significant heat flow acting to equalize these temperatures. This equalizing heat flow was proportional to the ratio of tube-wall thickness to tube diameter. These two heat transfer mechanisms that depended on tube-wall thickness presented conflicting requirements for the model tube design. Equal tube-wall thickness was desired in model and commercial receivers to accurately simulate the radial temperature gradient. However, an equal ratio of tube-wall thickness to tube diameter was needed to match the circumferential gradient. The effective heat capacity per unit of heat transfer area in the scale model had to be equal to that in the commercial RP377-1 receiver, thus providing equal rates of response to transient thermal events. These criteria were easily satisfied for the cavity wall insulation because model wall insulation was the same as for the commercial receiver. To match the transient response it was necessary to duplicate the commercial tube-wall thickness in the model, but as described previously, this conflicted with the tube-thickness scale modeling requirement for matching of circumferential tubing thermal gradients.

It was difficult to design a thermal-scale model that simulated natural convection heat transfer. Theoretically, a large distortion of ambient air pressure or temperature was required to produce convective heat fluxes in the scale model equal to those in the commercial receiver. Fortunately, the RP377-1 receiver, with its closed cavity walls and downward-facing aperture did not allow natural circulation of ambient air through the cavity. The circulation of air trapped in the cavity tended to equalize interior temperatures but should have been of little significance compared to the high-temperature radiant heat transfer that dominated cavity heat transfer. Therefore, it was only necessary to ensure that natural convection heat transfer was sufficiently small in the scale model receiver so as not to

become a significant heat transfer or heat loss mechanism.

### 3.1.2 Practical Considerations for BMSR Thermal-Scale-Model Design

Section 3.1.1 introduced and described the following theoretical design requirements for thermal-scale modeling of the 300-MW<sub>t</sub> RP377-1 solar receiver.

- a. Interior model dimensions and aperture were a scale model of the full-size commercial receiver; scale ratio was 1/17.3.
- b. Heat exchangers and insulation were fabricated from the same materials as the commercial receiver.
- c. Solar input flux passing through the aperture was an exact scale model of the commercial receiver. Solar heating patterns on cavity interior walls were scaled-down versions of the patterns.
- d. The full thickness of commercial cavity wall insulation was used in the model.
- e. Gas-flow conditions inside the heat exchangers were distorted, and tubing lengths and diameters were distorted from exact scale-model dimensions to provide internal gas-in-tube heat transfer film coefficients equal to the commercial receiver.
- f. Natural convection heat transfer between the model cavity and ambient air was intended to be minimal to reproduce the conditions in the commercial receiver.

In addition to these theoretical requirements, an instance of conflicting design requirements for the thermal-scale-model receiver existed in the selection of model heat exchanger tubing.

#### Heat Exchanger Tube-Wall Thickness

Tube-wall thickness equal to the commercial receiver was needed to duplicate its radial temperature gradients and to match its thermal response characteristics. At the same time, an equal ratio of tube-wall thickness to tube diameter was needed to simulate circumferential temperature gradients in the full-size receiver.

Model tubing with a wall-thickness-to-tube-diameter ratio approximately equal to the commercial was selected for the BMSR. It was important to match the circumferential temperature gradient of the heat exchanger tubes because it significantly affected heat transfer and had a major influence on thermal deflections of tubes and thermal stresses developed in the heat exchangers. With this selection, the model heat exchanger tubes exhibited more rapid rates of response to thermal transient events. Also, thermal gradients from outer-to-inner-tube-wall surfaces were smaller than in the commercial receiver, resulting in a minor increase (2% to 3%) in net heat exchanger performance.

Additional cases where theoretical design requirements could not be achieved because of the inability to produce scale-model test conditions are discussed in the following paragraphs.

#### Solar Flux Matching

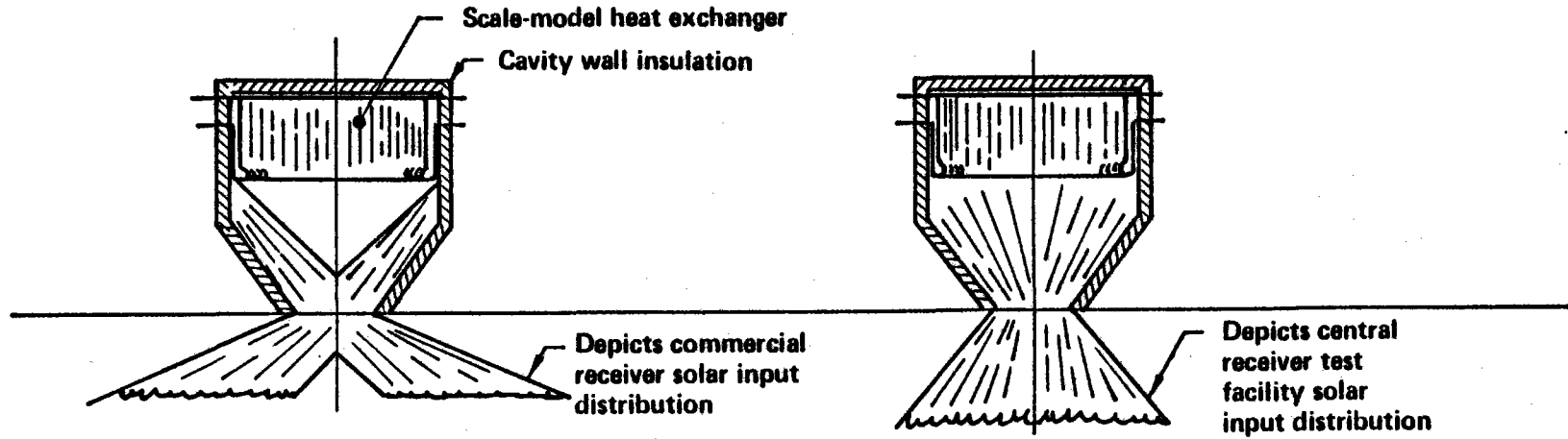
The most far-reaching discrepancy between BMSR test boundary conditions and theoretical scale-model requirements was the difference between the test receiver solar interface and the commercial receiver. The solar thermal test site capable of providing the 1-MW<sub>t</sub> solar input desired for the BMSR was the CRTF at Albuquerque, New Mexico. In this facility, it was necessary to use the Zone A north quadrant field of 78 solar collectors to simulate the surround field of the RP377-1 solar-electric powerplant. Even though the test facility solar input was correct, the sunlight passing through the receiver aperture spread out very little and preferentially illuminated the receiver inner wall directly across from the aperture. On the other hand, the sunlight passing through the aperture of the commercial receiver was rapidly spreading and incident mostly on cavity walls just adjacent to the aperture. As a result, the test receiver solar input directly illuminated a different part of the cavity interior than the commercial receiver.

Changes in the scale-model receiver design were required to accommodate the test solar interface. Sketches I and II of Figure 3.1-4 compare the CRTF Zone A receiver solar input to the ideal solar input for scale-model testing. As indicated by the sketches, the BMSR heat exchangers were



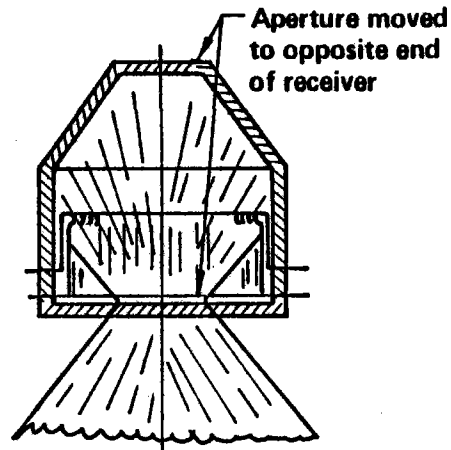
Figure 3.1-4. Thermal Scale-Model Configuration Development

# Thermal Scale-Model Configuration Development

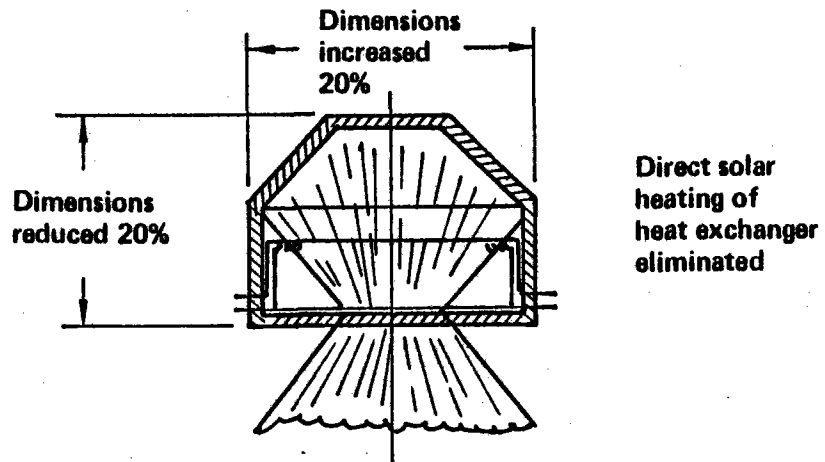


(a) Ideal thermal scale model and ideal test solar input

(b) Ideal thermal scale model and central receiver test facility solar input



(c) Inverted scale model and CRTF solar input



(d) BMSR as-built configuration and CRTF solar input

directly illuminated by the aperture solar input. This could not be tolerated by the metal-tube heat exchangers. Sketch III of Figure 3.1-4 shows a rearrangement of the model receiver that aids in accommodating the test solar input. The receiver aperture was simply relocated to the opposite wall of the cavity. With this change, most of the receiver solar input was once again first incident on the same walls (relative to the heat exchangers in the receiver) as in the commercial receiver and the theoretically ideal scale model. Reflections and reradiation from this bare insulation wall were perfectly diffuse. As far as the heat exchangers and other cavity walls were concerned, it made no difference how the heat entered the cavity as long as it was reflected and reradiated from this same surface. Moving the aperture affected its view factors to interior cavity surfaces. Its view of the hotter, directly sunlit insulation walls was increased over that of the ideal scale-model receiver. This resulted in solar reflective heat losses in the bench-model twice as great as those in the ideal receiver. Radiant heat losses were also increased, for the same reason.

Another adjustment of the scale-model receiver geometry was required to accommodate the CRTF solar input. Even with the aperture relocated, the incoming sunlight could still directly illuminate a small area of the heat exchangers. To eliminate this hot spot, the model cavity diameter was increased by 20% over the exact scale-model size. The depth of the cavity was reduced correspondingly to preserve the correct areas of model heat exchangers and side-wall insulation. These changes are shown in sketches III and IV of Figure 3.1-4. Sketch IV depicts the final selection of BMSR geometry.

To accommodate the north-quadrant field, the receiver aperture had to be reoriented from a directly downward-facing horizontal plane to a near-vertical plane. This produced a natural convective heat transfer mechanism for heat loss out of the model receiver aperture that was not present in the commercial receiver.

In summary, the following thermal-scale-model distortions were required to facilitate testing in the 1-MWt CRTF:

- a. Aperture was moved to opposite end of cavity.
- b. Receiver was turned so that aperture faced to the side rather than downward.
- c. Diameter was increased and the cavity shortened to prevent direct solar heating of heat exchanger tubes.

These changes affected the heat transfer performance of the model receiver. Its thermal efficiency was estimated to be 8% to 10% lower than the commercial receiver. In addition, the higher concentration of solar flux on bare insulation walls in the BMSR produced insulation temperatures in the back-wall region that were 200° to 300°C (360° to 540°F) higher than the corresponding walls in the commercial receiver.

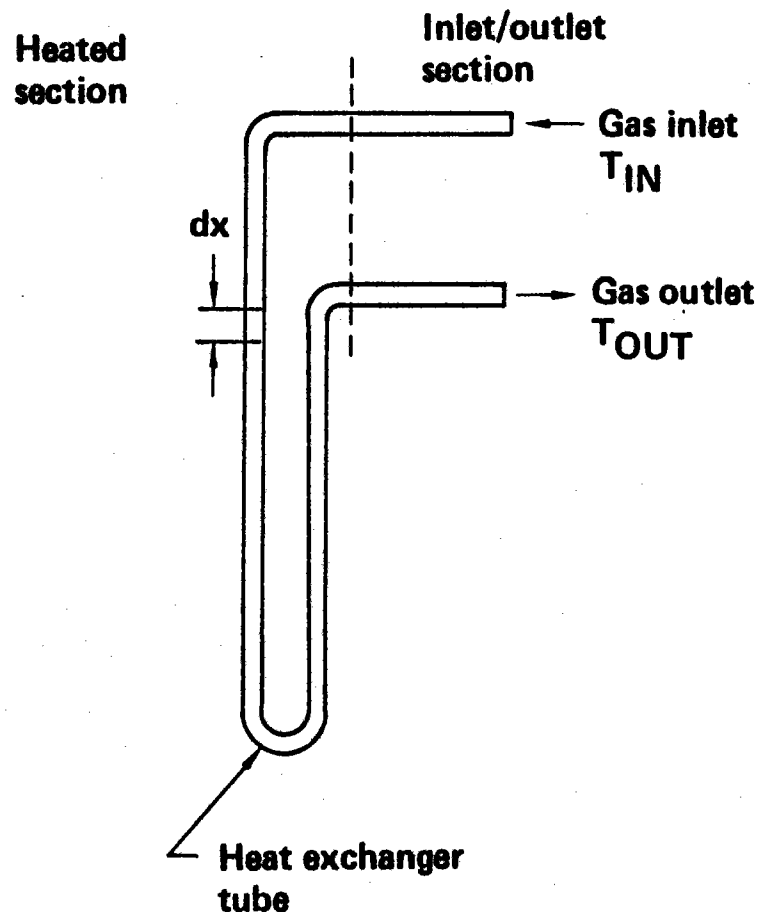
Even though the final selected cavity configuration for the BMSR was not an exact-scale thermal model of the RP377-1 commercial receiver design, compromises were made to ensure that its heat exchangers were exposed to the same environment of reflected solar and radiant thermal heating as those of the commercial receiver. The selected BMSR cavity configuration was an excellent test bed for checkout and verification of heat exchanger materials and design concepts for use in pilot-plant and commercial receivers.

#### Heat Exchanger Thermal-Scale Modeling

Thermal-scale-modeling design criteria that resulted in equal operating temperatures for scale-model and full-size commercial heat exchangers were required. As discussed earlier, the requirement that active heat exchanger surface area in the model be equal to 1/300 of the commercial heat exchanger area produced equal heat transfer conditions on the outside of heat exchanger tubes. The use of double-row heat exchanger geometry in the model with tube spacing of three diameters center-to-center ensured that heat-flux distributions around the circumference of tubes were equal. The design requirements needed to produce thermally equivalent heat transfer conditions within the tubes are developed and presented here. With internal and external heat transfer conditions equal to the commercial heat exchangers and external heat fluxes the same, the model heat exchanger tubes will operate at the same temperatures as the commercial receiver. Figure 3.1-5

Figure 3.1-5. Thermal Analysis Model of Heat Exchanger Tube

## Thermal Analysis Model of Heat Exchanger Tube



$D$  = Tube inside diameter

$L$  = Tube heated length

$N$  = Number of tubes

$\Delta T_G = (T_{OUT} - T_{IN})$

$W$  = Gas flow per tube

$C_p$  = Average gas specific heat

$Q$  (total =  $W C_p \Delta T_G N$   
cavity)

shows the heated section of a typical heat exchanger tube. It could be one of the BMSR heat exchanger tubes or one of the 4200 tubes in the commercial receiver. The overall internal heat transfer occurring in the heat exchanger tube is defined in terms of total heat transfer to the circulating gas,  $Q$ , and average temperature rise of the circulating gas,  $(T_{out}-T_{in})=\Delta T_G$

In the model, an overall heat transfer,  $Q$ , is required that is 1/300 as great as the commercial receiver. Inlet gas temperature and gas temperature increase in the receiver,  $\Delta T_G$ , are required that are exactly equal to those in the commercial receiver. Therefore,

$$\frac{\text{Model Heat Transfer, } Q_{\text{model}}}{\text{Commercial Receiver Heat Transfer, } Q_{\text{prototype}}} = \frac{1}{300} = Q^* \quad (3.1-1)$$

where the superscript \* denotes model-to-

and,

$$W^* c_p^* \Delta T_G^* N^* = Q^* \quad (3.1-2)$$

where

- $W$  = Gas mass flowrate in tube
- $c_p$  = Specific heat of gas
- $N$  = Number of tubes in receiver

Since Reynolds number,  $R_E$ , is defined as,

$$R_E = \frac{4 W}{\pi \mu D}$$

where

- $\mu$  = Fluid viscosity
- $D$  = Tube inside diameter

and

$$W^* = R_E^* \mu^* D^*$$

Also since heat flux per unit area is to be equal in model and commercial receiver

$$Q / \pi D L N = \text{Constant}$$

and

$$Q^* = D^* L^* N^*$$

Then equation (3.1-2) can be written

$$R_E^* = \frac{L^*}{\Delta T_G^* \mu^* c_p^*} \quad (3.1-3)$$

In addition to scale modeling of the overall tube heat transfer (equation 3.1-3), the local tube-to-gas heat transfer coefficient and the tube-to-gas temperature differences in the commercial receiver had to be reproduced in the scale model. Figure 3.1-6 depicts a typical segment of heat exchanger tube. Here the amount of heat added to the gas, the local heat flux,  $q$ , is proportional to the local rate of gas temperature increase  $dT_G/dx$  and also proportional to the product of the local gas-in-tube heat transfer film coefficient  $h(x)$  and the local difference between the temperatures of the tube wall and the gas  $(T_{\text{tube}} - T_{\text{gas}})_x$ .

Therefore,

$$\frac{dT_G}{dx} = \frac{\pi D h(x) (T_{\text{tube}} - T_{\text{gas}})_x}{W c_p} \quad (3.1-4)$$

integrating along the length,  $L$ , of the tube yields

$$T_G = \frac{\pi D}{W c_p} \int_0^L h(x) (T_{\text{tube}} - T_{\text{gas}})_x dx \quad (3.1-5)$$

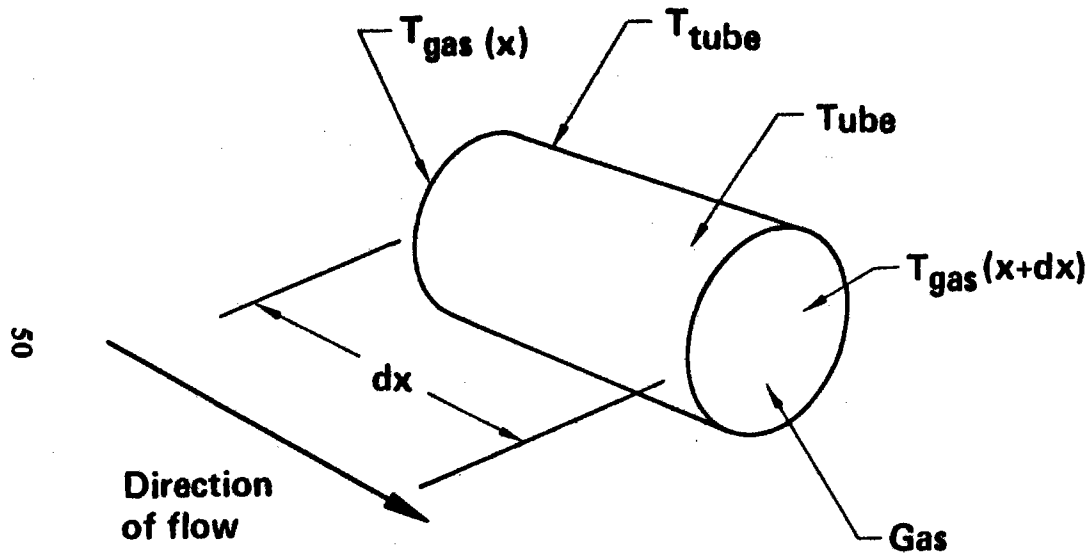
assuming that  $h(x)$  is constant and defining an average value of  $(T_{\text{tube}} - T_{\text{gas}})$  by

$$\Delta T_E = \frac{1}{L} \int_0^L (T_{\text{tube}} - T_{\text{gas}})_x dx \quad \text{yields}$$

$$\frac{\Delta T_G^*}{\Delta T_E^*} = \frac{h^* L^*}{R_E^* \mu^* c_p^*} \quad (3.1-6)$$

Figure 3.1-6. Thermal Analysis Model, Tube-to-Gas Heat Transfer

## Thermal Analysis Model, Tube-to-Gas Heat Transfer



$h$  = Heat transfer coefficient

$x$  = Distance along tube

$D$  = Tube inside diameter

$T_{\text{tube}}$  = Tube wall temperature

$$W C_p \frac{dT_G}{dx} = \pi D h(x) (T_{\text{tube}} - T_{\text{gas}})x$$



Equation (3.1-6) can be simplified by assuming that the turbulent gas-flow condition in the commercial receiver is reproduced in the model heat exchanger. In the range of interest here,

$$\text{Nusselt number, } N_U = 0.0215 R_E^{.8} P_R^{.6} = \frac{h D}{k}$$

where

$k$  = thermal conductivity of gas

$$P_R = \text{Prandtl number of gas} = \frac{c_p \mu}{k}$$

then,

$$h^* = \frac{k^* (R_E^*)^{.8} (P_R^*)^{.6}}{D^*}$$

and equation (3.1-6) reduces to,

$$\frac{\Delta T_G^*}{\Delta T_E^*} = \frac{L^*}{(R_E^*)^{.2} (P_R^*)^{.4} D^*} \quad (3.1-7)$$

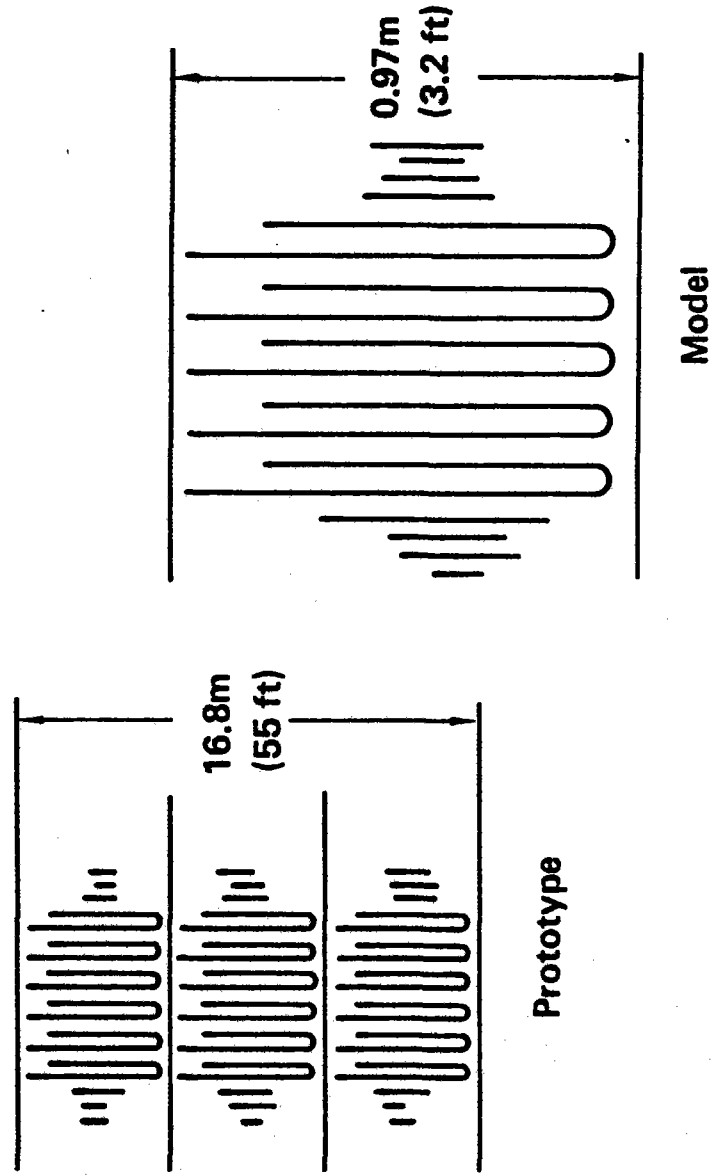
The design requirements for obtaining model heat exchanger tubing and gas temperatures equal to the commercial heat exchanger ( $\Delta T_G^* = \Delta T_E^* = 1.0$ ) are concisely stated by equations (3.1-3) and (3.1-7).

In addition to the selection of temperature ratios of unity there are other dimensional ratios in the model heat exchangers that are known. One such dimension is the heat exchanger tube-length ratio,  $L^*$ .

Figure 3.1-7 compares the heat exchanger tubing layout for commercial and model receivers. Whereas three rows of tubes occupy the 16.8m (55-ft) heat exchanger wall in the commercial receiver, the single row of tubes in the model receiver occupies a space 0.786m (2.6 ft) high. The dimensional ratio

Figure 3.1-7. Tubing Layout Comparison, Model and Prototype Heat Exchangers

## Tubing Layout Comparison, Model and Prototype Heat Exchangers



of 1/17.3 requires a model heat exchanger height of 0.971m (3.2 ft). As mentioned earlier, the BMSR heat exchangers were shortened to prevent direct solar heating of tubes in tests at the CRTF. With a model heat exchanger height of 0.786m (2.6 ft) and an individual commercial heat exchanger height of 5.6m (18.4 ft), the tube-length scale ratio is  $L^* = 0.140$ .

Another decision for BMSR solar testing involved the selection of air instead of helium as the model receiver working fluid. This change in working fluid defined the values of  $c_p^*$ ,  $P_R^*$ ,  $k^*$ , and  $\mu^*$  in equations (3.1-3) and 3.1-7). Based on the best available data in the literature and on an average heat transfer gas temperature of 677°C (1250°F), the fluid property ratios (model commercial receiver) required here are,

$$P_R^* = 1.125$$

$$k^* = 0.179$$

$$c_p^* = 0.215$$

$$\mu^* = 0.947$$

Then, using these values, and  $\Delta T_G^* = \Delta T_E^* = 1.0$ , equation (3.1-3) reduces to

$$R_E^* = 0.688$$

and equation (3.1-7) reduces to,

$$D^* = 0.144$$

The inside diameter of full-size commercial heat exchanger tubes was 2.22 cm (0.875 in). Therefore, the desired size of model tubes was 0.317 cm (0.126 in). The ratio of tubes in the model to those in the commercial receiver was:

$$N^* = \frac{\text{Number of tubes in model}}{\text{Number of tubes in commercial receiver}} = \frac{Q^*}{D^* L^*} = 0.165$$

Six hundred ninety two of the 0.317cm (0.12in) inside diameter model tubes were needed to simulate the 42 tubes in the commercial receiver.

These small-diameter heat exchanger tubes were not used in the BMSR. At the desired test operating condition of 0.86-MPa (125-lb/in<sup>2</sup>a) inlet air pressure and a receiver airflow rate of 2.61 kg/s (5.76 lb/s), there was a prohibitively high pressure loss. The basis and results of this additional compromise of scale-model heat exchanger design are discussed in the following section.

#### Heat Exchanger Design To Accommodate Test Air Supply

Theoretical criteria for thermal-scale modeling of the heat exchangers in the closed-cycle solar central receiver concept are specified by equations (3.1-3) and (3.1-7). These formulas did not place any constraints on the working pressure of the model receiver because the thermophysical properties of gases; thermal conductivity, viscosity, specific heat per unit mass; were not affected by pressure. All that was required in the heat exchanger thermal model was that the total receiver flow rate,  $W$ , be achieved through its array of heat exchanger tubes,  $N$ , each one having a diameter,  $D$ .

Because the specific volume of the heat transfer gas was reduced at lower pressures, the gas velocity required to maintain a particular flow rate was increased. The maximum practical air velocity was limited as sonic velocity was approached. In the heat exchanger tubes, therefore, the minimum specific volume (i.e., pressure of the working gas) was also limited. Even

at airflow velocities well below the maximum sonic velocity, the cumulative pressure losses for flow through slender heat exchanger tubes became prohibitive.

The air supply compressors for BMSR testing at the CRTF provided air at pressures up to about 1.0 MPa (145 lb/in<sup>2</sup>a). By the time this air was delivered from ground level to the test bay, its pressure was reduced to about 0.86 MPa (125 lb/in<sup>2</sup>a).

Figure 3.1-8 shows the pressure losses for six candidate sizes of BMSR heat exchanger tubes. The ideal heat exchanger design used 692 of the 3.17-mm (0.12-in) inside diameter tubes in the BMSR. They provided a wetted inner heat transfer area of 9.46 m<sup>2</sup> (101.8 ft<sup>2</sup>) and a D\* of 0.144 as needed for the thermal scale model. The pressure loss performance is also shown for other tubes with larger inside diameters. Fewer larger tubes are used in the BMSR to maintain the correct heat transfer area. As indicated in the figure, the pressure loss performance of these slender tubes is extremely sensitive to tube inside diameter.

The smallest of the tube sizes in Figure 3.1-8 that can support the required air-flow rate through the receiver is 4.0-mm (0.16-in) inside diameter. However, this tube lost more than half the available air pressure at full BMSR flow. It left little or no margin for error in the design of heat exchanger manifolds and piping.

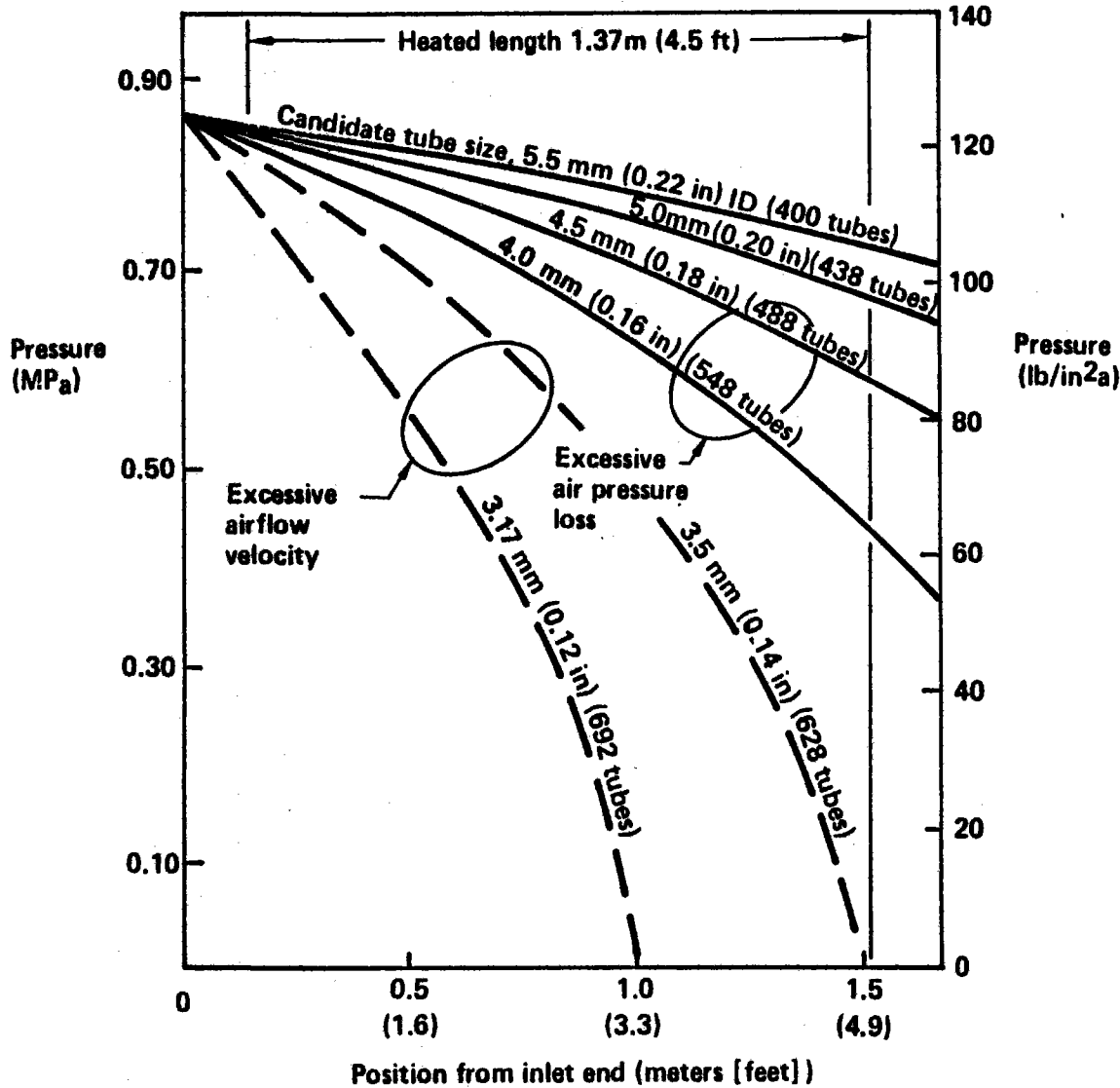
The smallest of the acceptable tube sizes in Figure 3.1-8 is 5.0-mm (0.20-in) inside diameter. This was the tube size selected for the BMSR heat exchangers. Even this tube exhibited a large pressure loss (25%) at full receiver flow rate, however, it did allow reasonable margins for design and construction of the BMSR heat exchangers.

This selection of larger-than-ideal thermal model tube size had an effect on BMSR heat exchanger tube temperatures. With a tube size of 5.0 mm (0.20 in), the model-to-commercial-receiver tube size ratio, D\*, was

$$D^* = 0.227$$

Figure 3.1-8. Pressure Losses in Candidate BMSR Heat Exchanger Tubes

# Pressure Losses in Candidate BMSR Heat Exchanger Tubes



**Basis:**

- BMSR design point operating pressure and temperatures
- Total inside tube area in BMSR, 9.46 m<sup>2</sup> (101.8 ft<sup>2</sup>)
- Total flow, 2.62 kg/s (5.78 lb/s)

Equation (3.1-3) is not affected because it does not involve tube diameters. The only place where  $D^*$  shows up uniquely is in equation (3.1-7),

$$\frac{\Delta T_G^*}{\Delta T_E^*} = \frac{L^*}{(R_E^*)^2 (P_R^*)^4 D^*}$$

and here the only independent variable that can be adjusted to accommodate nonideal values of  $D^*$  is  $\Delta T_E^*$ , the average tube-to-gas temperature difference. All other terms being equal,

$$\frac{D^*}{\Delta T_E^*} = \text{Constant}$$

Therefore, the selection of a tube size for which  $D^*$  is 57% greater than the desired value, 0.227 versus 0.144, resulted in a 57% larger temperature difference between model-tube-to-gas temperatures than was present in the commercial heat exchangers.

The effects of this compromise on model heat exchanger tube size is shown in Figures 3.1-9 and 3.1-10. Figure 3.1-9 shows the temperatures of tubes and gas in the commercial solar receiver heat exchangers. The differences in tube temperature around their circumferences are depicted by a wide band of temperatures. Figure 3.1-10 shows the predicted temperatures of BMSR heat exchangers using the larger-than-scale-model tube size. Maximum tube temperatures in the BMSR were only 19°C (34°F) higher than those of the commercial receiver heat exchanger.

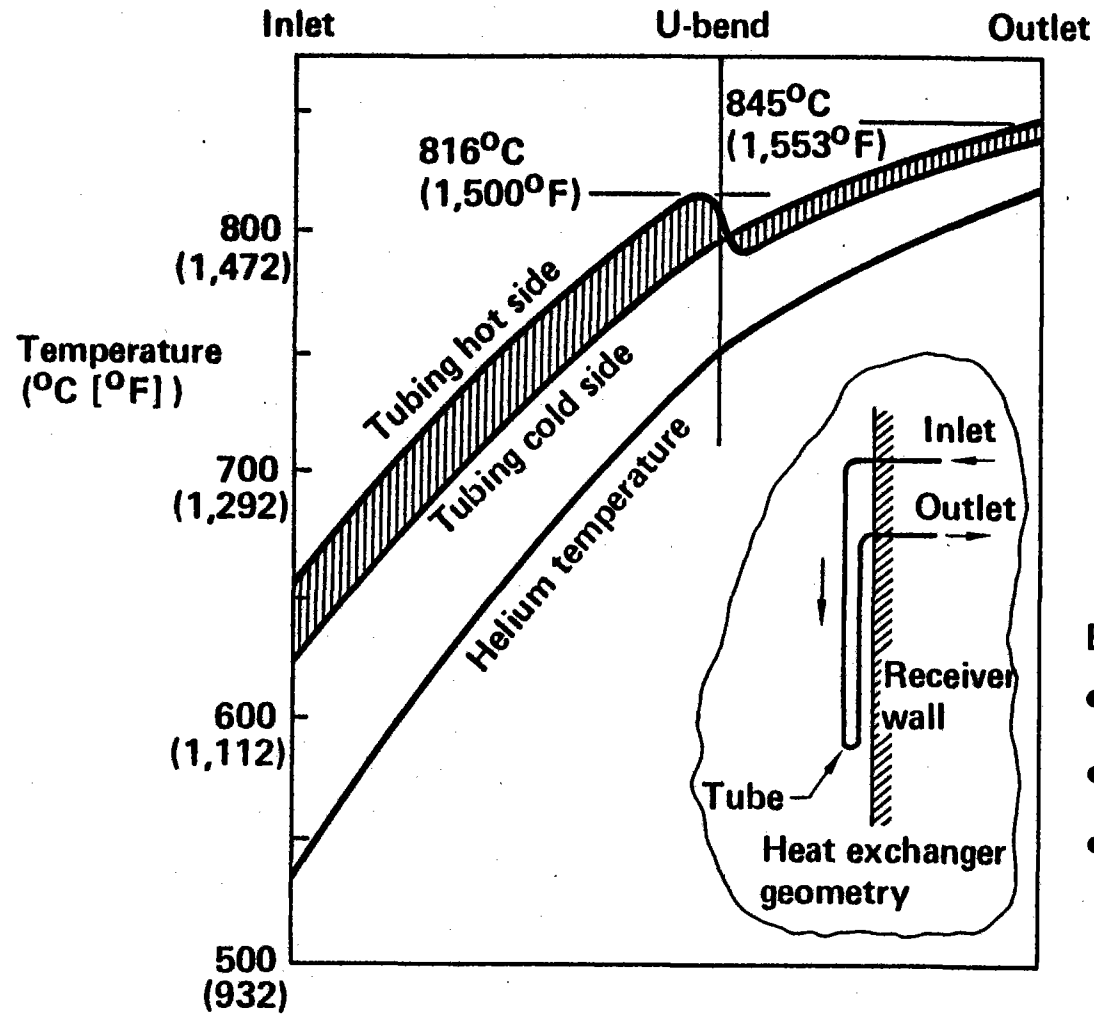
In conclusion, even though it was necessary to increase the heat exchanger tube size in the BMSR by 57% of the ideal thermal-scale-model size, the operating temperature did not exceed 87°C (1600°F), which is an acceptable temperature for Inconel 617 heat exchanger tubes.

### 3.2 SOLAR INTERFACE WITH CRTF

Figure 3.2-1 shows the arrangement and dimensions of the CRTF. The receiver test tower and the 78 heliostats included in Zone A of the collector field

Figure 3.1-9. Commercial Size Receiver Heat Exchanger Tubing and Gas Temperatures

## Commercial Size Receiver Heat Exchanger Tubing and Gas Temperatures



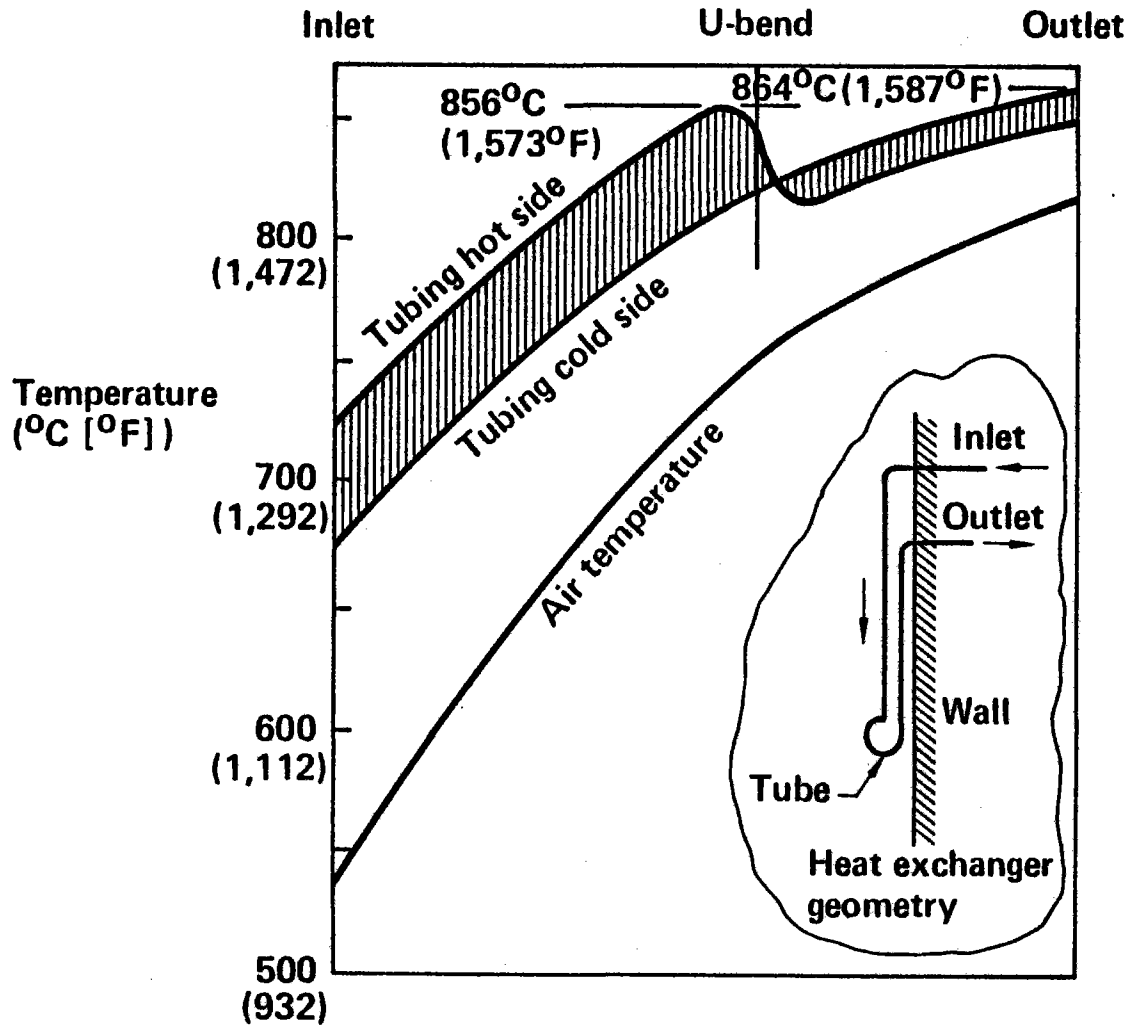
**Basis:**

- Tube ID = 2.22 cm (0.87 in)
- 4,200 tubes in the receiver
- Helium flow, 169 kg/s (373 lb/s)



Figure 3.1-10. BMSR Heat Exchanger Tube and Gas Temperatures

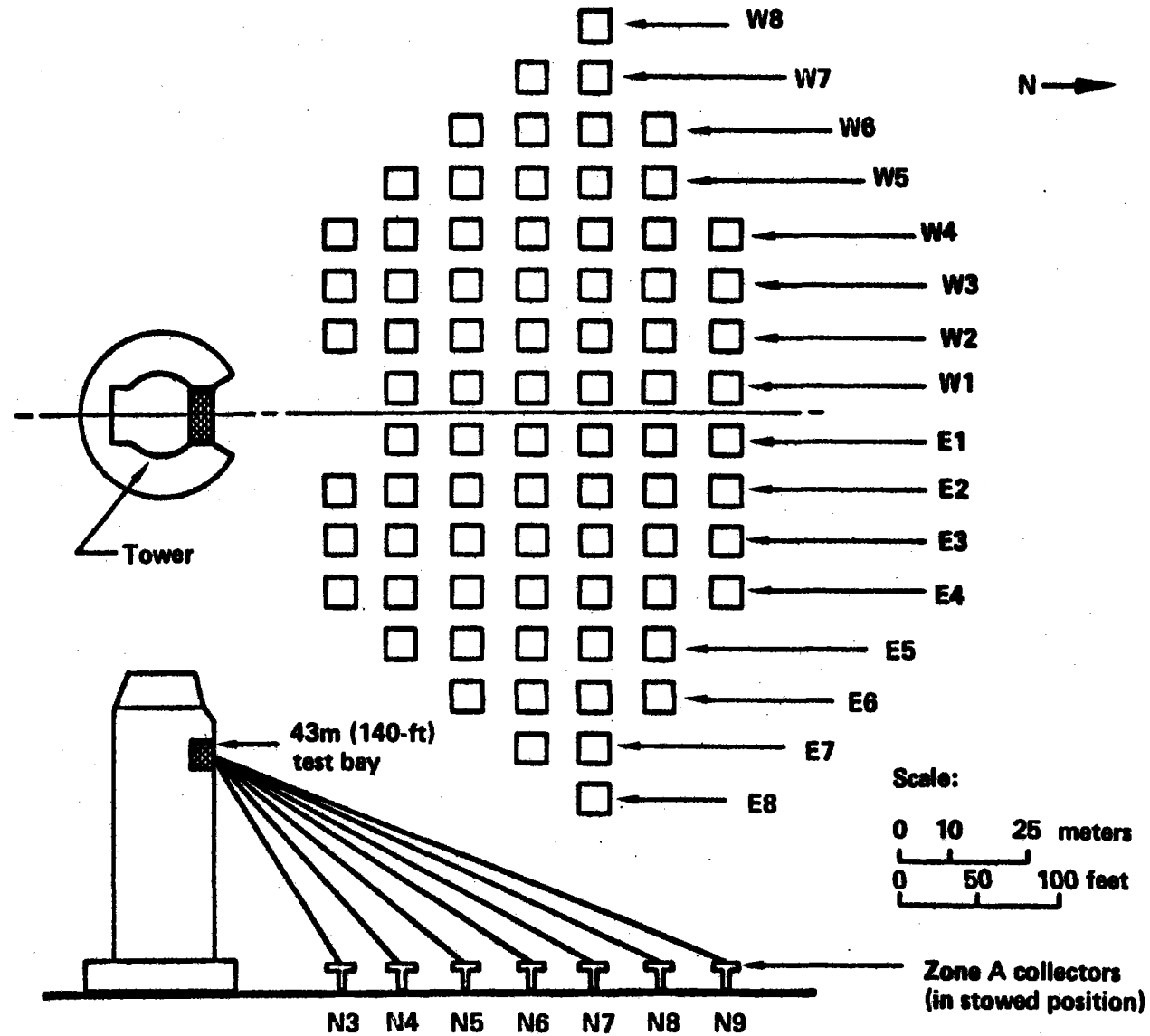
# BMSR Heat Exchanger Tube and Gas Temperatures



**Basis:**

- Tube ID = 5.08 mm (0.20 in)
- 432 tubes in the BMSR
- BMSR flow, 2.62 kg/s (5.78 lb/s)

Figure 3.2-1. Zone A of the Central Receiver Test Facility



are shown. The sketch identifies the test bay on the north side of tower that was selected for BMSR tests. This test site is nominally rated for 1 Mwt of solar power.

The BMSR was designed for a 1-Mwt solar input to its 1.1 m-diameter (3.6-ft-diameter) aperture. The tower test site and Zone A collector-field geometry were used in establishing the BMSR configuration. These configuration studies placed the center of the receiver aperture at an elevation of 44.5 m (146 ft) above ground and 8.4 m (27.6 ft) north of the tower centerline. Preliminary analyses of the heat loads on the eight receiver heat exchangers showed that significant variations could be achieved by tilting the receiver. A tilt angle of 32 deg, placing the aperture plane at an angle of 32 deg from vertical, provided the best equalization of heat loads. At this angle the aperture normal, an extension of the symmetrical centerline of the receiver, passed through the ground at a point near the centroid of the Zone A collector field.

Once the CRTF had been selected as the BMSR test site and the preliminary receiver configuration was established, studies were begun to--

- a. Verify that a receiver solar input of 1 Mwt could be achieved during tests
- b. Determine solar heat flux distributions on the aperture plane of the receiver
- c. Determine solar heat flux distributions on interior walls of the cavity receiver

The first solar thermal analyses were conducted in 1977. A data base for these studies was provided by the solar energy technology division at Sandia Livermore, Division 8184. They provided descriptions of the solar-heat-flux distributions (images) of all 78 Zone A collectors when focused on the BMSR aperture plane. Sets of data were provided for 10:00 AM, 10:30 AM, 11:00 AM and noon. Due to east-west symmetry of the collector-receiver system, these data effectively defined conditions from 10:00 AM to 2:00 PM solar time. Preliminary best estimates of heliostat performance parameters were used along with solar geometry for the equinox.

Later, in 1978, additional collector-field performance analyses were provided by the CRTF test engineers. These data agreed reasonably well with the earlier analyses.

Assessments of receiver solar interface conditions at the aperture plane were based on these two sources of collector-field performance. In addition, graphic techniques as well as the Boeing Monte Carlo ray-tracing computer code were used to determine solar-flux distributions within the receiver cavity. In general, these methods projected the spatial and directional heat-flux pattern at the aperture on into the cavity.

### 3.2.1 Receiver Solar Input

Figure 3.2-2 is based on the Sandia Livermore data. It shows the numbers of Zone A collectors out of the 78 available that were required to reflect 1 MWt of sunlight through the BMSR aperture. As shown, the number of collectors required depended mainly on the time of day (due to optical performance of the curved heliostat mirrors) and on the ambient direct solar flux. The data indicated that as long as direct sunlight exceeded  $780 \text{ W/m}^2$ , the 78 Zone A collectors were sufficient for BMSR tests. Even with 9 collectors out of service (69 available), the direct solar flux required for 1 MWt was only  $900 \text{ W/m}^2$ .

Later 1978 studies indicated that about eight more collectors were needed to produce a 1-MW<sub>t</sub> solar input to the receiver.

### 3.2.2 Solar Heat Flux on Aperture Plane

Figure 3.1-3 shows the aperture plane solar-flux predictions for 1-MW<sub>t</sub> receiver input conditions. Figure 3.2-3 shows both Sandia Livermore and Sandia Albuquerque data. The figures provided an estimate of the solar flux expected on the aperture-rim and the BMSR solar shielding. As a result of these data, the minimum heat flux for design of aperture-rim shielding was determined to be  $660 \text{ kW/m}^2$ .

Additional consideration was given to defining the design requirements for

Figure 3.2-2. Collector Requirements for 1-MW Receiver Solar Input

## Collector Requirements for 1-MW Receiver Solar Input

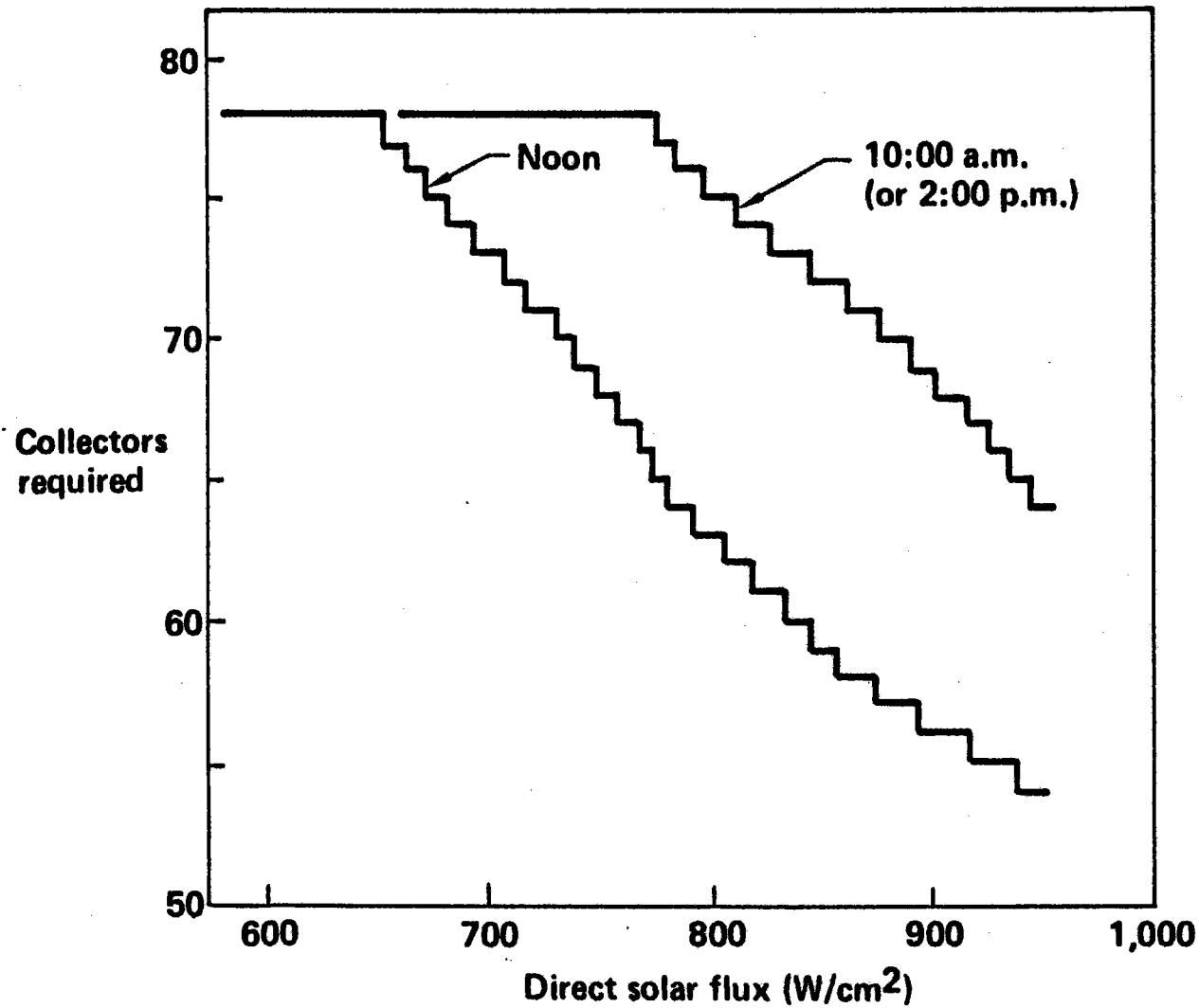
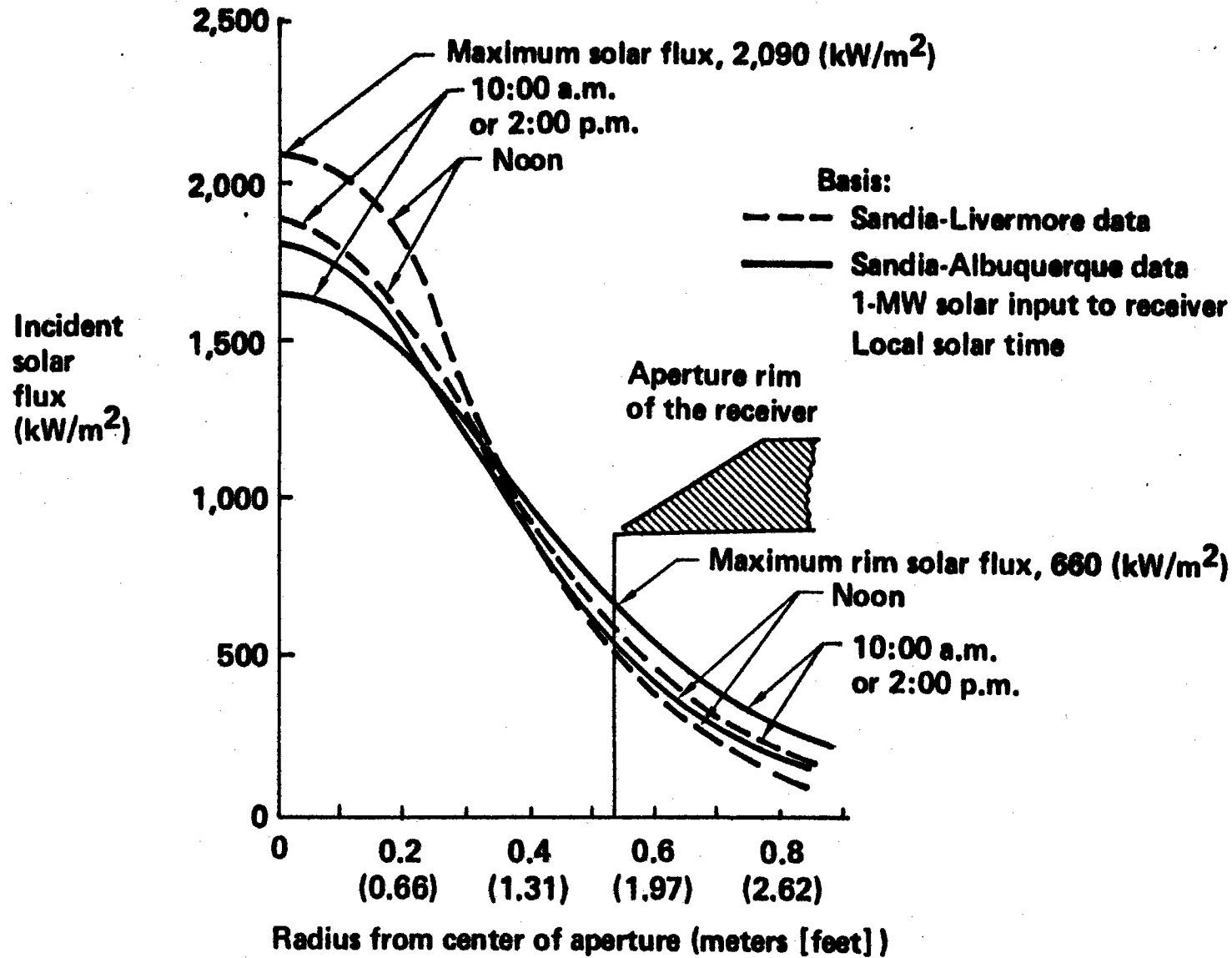


Figure 3.2-3. Aperture Plane Solar Flux

# Aperture Plane Solar Flux



aperture-rim solar shielding. First, there was the prospect, of collector-field image displacement, which could expose receiver shielding to the peak heat flux normally located at the center of the aperture. This is a natural occurrence due to motion of the Sun and could be expected whenever the collectors stop tracking and remain locked in position. If this lock-and-drift occurs, the aperture-rim solar shield is exposed to peak fluxes (Figure 3.2-3) that could exceed 2000 kW/m<sup>2</sup>.

Another reason for considering an aperture-rim heat flux higher than 660 kW/m<sup>2</sup> was that the Zone A collectors could be aligned for optimum focusing at the CRTF tower top rather than the 43 m (140-ft) test bay. This was considered to be a possibility for BMSR tests, but it never developed.

CRTF test engineers provided Zone A collector-field performance data when aligned for the tower-top test site and focused on the BMSR aperture. Figure 3.2-4 shows data for the operating condition, which produced a maximum heat flux on the aperture rim. The figure indicates that the tower-top alignment of the Zone A collector field increased the aperture-rim design flux from the previous level of about 660 kW/m<sup>2</sup> to approximately 1050 kW/m<sup>2</sup>.

In summary, these aperture plane heat-flux studies resulted in three alternative design requirements being identified for the aperture-rim shielding:

- a. 660 kW/m<sup>2</sup> for optimum collector alignment and no protection for lock-and-drift
- b. 1050 kW/m<sup>2</sup> for alternative tower-top alignment of Zone A collectors and no protection for lock-and-drift
- c. 2100 kW/m<sup>2</sup> for lock-and-drift protection of the receiver

Section 4.3 describes aperture solar-shield material tests that were conducted to evaluate candidate shielding designs. The final selection of zirconia tile for the aperture-rim shielding provided protection for all the design requirements.

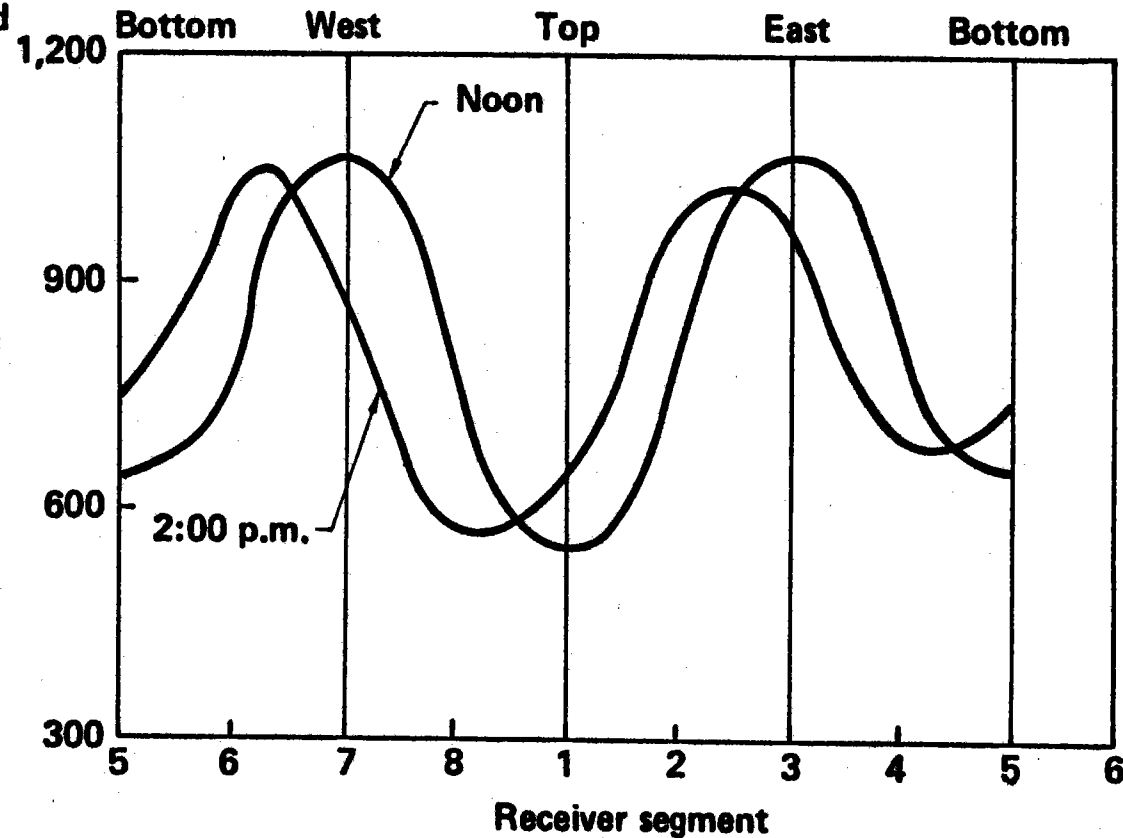
Figure 3.2-4. Aperture Rim Solar Flux With Tower Top Alignment of Zone A Collectors

## Aperture Rim Solar Flux With Tower Top Alignment of Zone A Collectors

**Basis:**

- 1-MW solar input to receiver
- Sandia-Albuquerque data
- Zone A collectors aligned for tower top focal zone

Aperture rim solar flux (kW/m<sup>2</sup>)





### 3.2.3 Solar Heat Flux on Interior Cavity Walls

The solar flux from a particular CRTF collector always approached the BMSR aperture from the same direction. After passing through the aperture it always illuminated the same area on the interior cavity wall. This area was roughly defined by the shape of the circular aperture when projected in the direction of the solar flux from the particular collector. Because of the size of the heliostat reflector, the typical 1 m-wide (3.3-ft-wide) beam of collector solar flux passing through the aperture increased in width and height by about 12.0 cm (4.7 in) as it traversed the cavity from aperture to back wall.

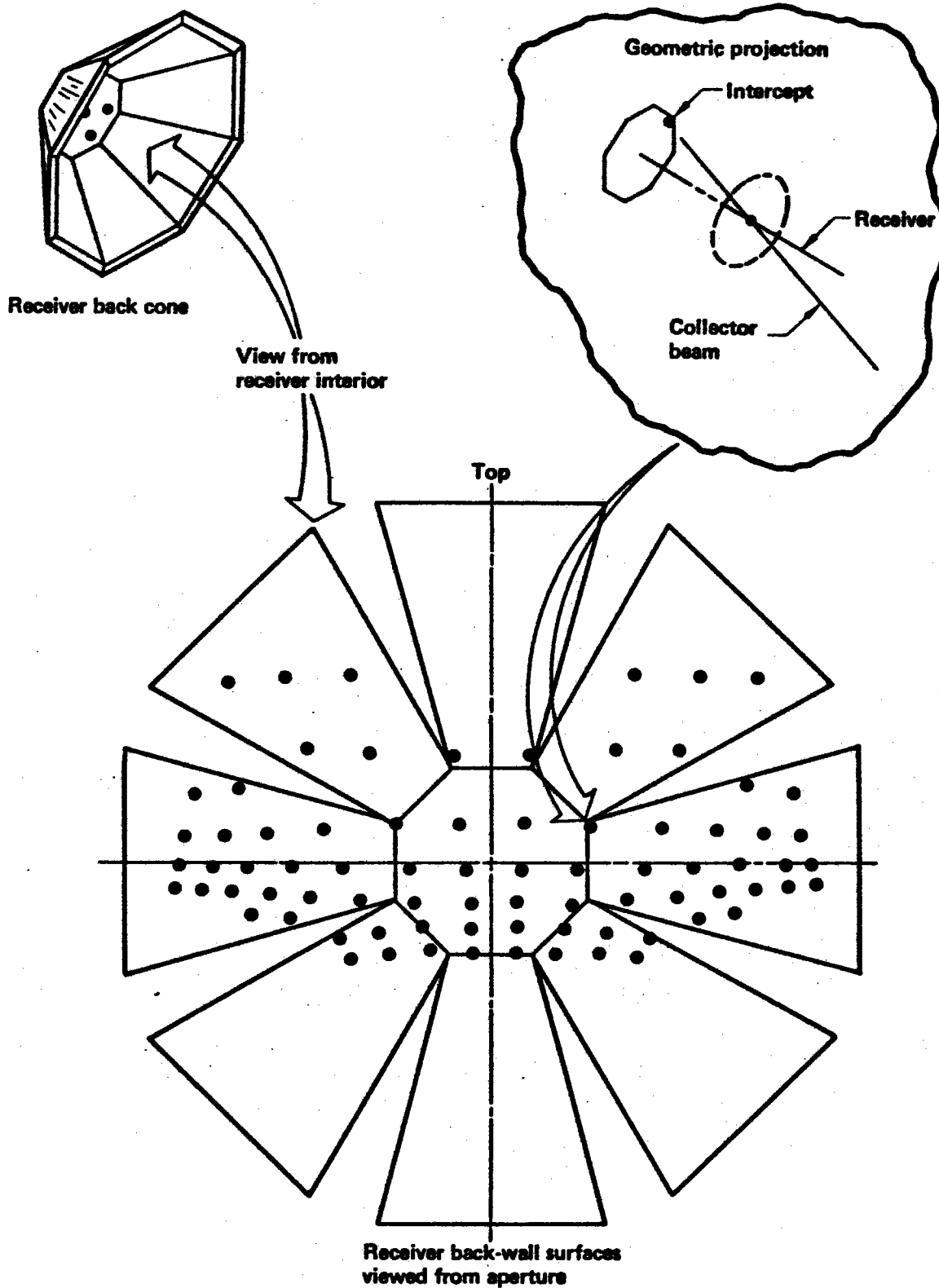
Two methods of analysis were used to determine solar heat flux on interior cavity walls. The preliminary design analysis consisted of determining the first-incident solar flux on cavity walls. This method was based on graphical projection of the beams of individual collectors through the aperture and determining where they intercepted the cavity walls. This provided a visualization and limited quantitative assessment of the solar heating patterns inside the receiver. This pattern determined if direct solar heating of receiver heat exchangers could occur. It was also used to find regions of maximum solar heat loads on the receiver walls and to establish maximum heat load design requirements for the cavity insulation. During final design, a more sophisticated evaluation of cavity wall solar heating was conducted. This analysis included the effects of solar reflections to determine the distribution of absorbed solar flux on cavity walls and heat exchangers, and to determine solar reflections back out the receiver aperture. The Boeing Monte Carlo ray-tracing computer code was used for these computations. These two analysis techniques are described and results are presented in the following paragraphs.

#### Calculations of First-Incident Solar Flux

Virtually all the solar flux entering the BMSR aperture was first incident on the conical back wall of the receiver (Figure 3.2-5). To present these data, the trapezoidal sections of the conical wall were folded out onto the plane parallel to its octagonal center section. The figure shows the points

Figure 3.2-5. Ray Intercepts for Zone A Collectors

# Ray Intercepts for Zone A Collectors



of intercept of centerline rays from each of the 78 Zone A collectors on the receiver back wall. This produces a distorted image of the collector field but the individual east-west rows of collectors can still be identified.

The areas of receiver wall illuminated by each Zone A collector were determined by projecting the aperture image onto receiver walls in the area of the collector intercept point (with a minor error because of beam spreading as it crossed the receiver). Because the receiver is made up of planar surfaces, these illuminated areas were circumscribed by a variety of elliptical shapes. Many of the areas illuminated by individual collectors overlapped one another.

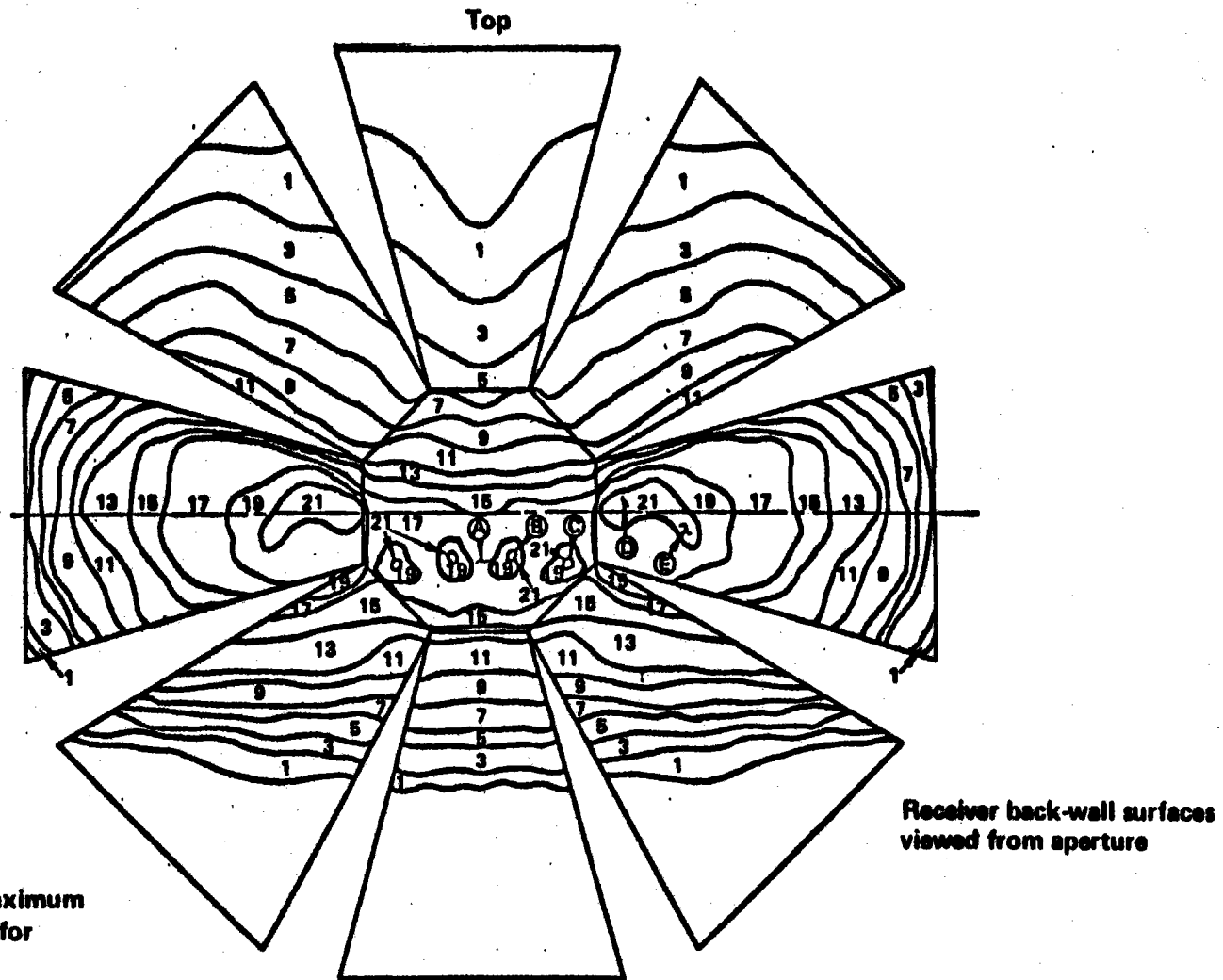
The number of illumination areas overlapping at a particular point defined the number of individual collectors that heated that area. This information is presented in Figure 3.2.6. Regions of cavity wall illuminated by equal numbers of collectors are identified. As can be seen in the figure, there are several regions on the receiver back wall that are simultaneously heated by more than 17 collectors. Five points of interest illuminated by 17 to 21 collectors have been identified in the figure for further study.

To predict the heat flux in these locations, it was necessary to consider the heat-flux profile of each of the collectors that illuminated the point of interest. These individual collector heat flux profiles were provided in the Sandia Livermore data base. Some typical profiles are shown in Figure 3.2-7. The eight profiles are typical of the range of conditions for Zone A collectors.

A typical computation of first-incident heat flux on location A (Figure 3.2-6) of the receiver back wall is shown in Figure 3.2-8. Here, the distance of point A from the center of each of the 21 collector images that illuminated point A were measured, projected onto the aperture plane, and used as radial distances from the collector-beam centerline. Then heat-flux contributions for the individual collectors were determined from their heat-flux profile. The 21 separate collector contributions for point A on the back wall added up to a total incident solar flux that depended on time of day, time of year, and direct solar-flux level. These data for point A

Figure 3.2-6. Quantities of Zone A Collectors That Heat Receiver Back Cone

# Quantities of Zone A Collectors That Heat Receiver Back Cone



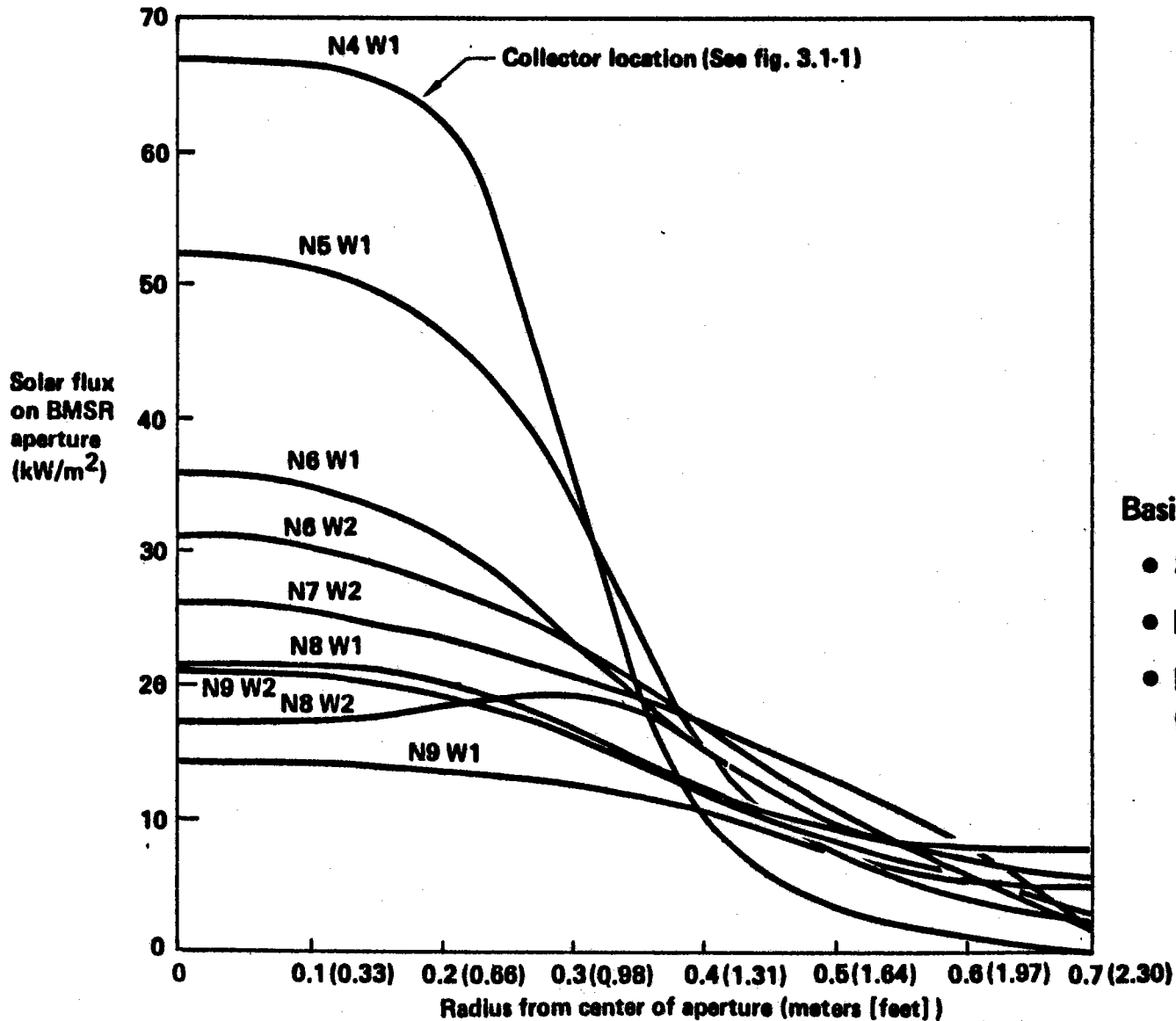
Ⓐ through Ⓔ denotes maximum heat flux zones identified for further study.

1 through 21 denotes number of zone A collectors that simultaneously heat each region.

Figure 3.2-7. Aperture Plane Heat Flux Caused by Individual Collectors

# Aperture Plane Heat Flux Caused by Individual Collectors

71



**Basis:**

- Sandia-Livermore data
- Noon, vernal equinox
- Direct solar flux (800 W/m<sup>2</sup>)

for noon on the vernal equinox are shown in Figure 3.2-8. It should be noted that these computations assumed as a worst case that all of the collectors illuminating point A were in use.

An ambient solar flux of  $950 \text{ W/m}^2$  is selected for the design condition in Figure 3.2-8. This results in a first-incident solar flux of  $372 \text{ kW/m}^2$ . Similar computations for points B, C, D, and E in Figure 3.2-6 are 393, 376, 340, and  $356 \text{ kW/m}^2$  respectively.

A design margin was added to these computed values of first-incident heat flux to establish a design requirement for insulation on the receiver back wall. This requirement was established as  $425\text{-kW/m}^2$  first-incident flux. Section 4.2 describes tests of insulation materials to certify them for use on the receiver back wall. It should be noted that in conducting these tests, it was necessary to--

- a. Create the thermal radiant environment of the operating receiver cavity
- b. Use actual BMSR materials in a test cavity to produce the multiple solar reflections that occur in the BMSR
- c. Heat the insulation with a first-incident flux of  $425 \text{ kW/m}^2$  using solar or spectrally similar heat flux

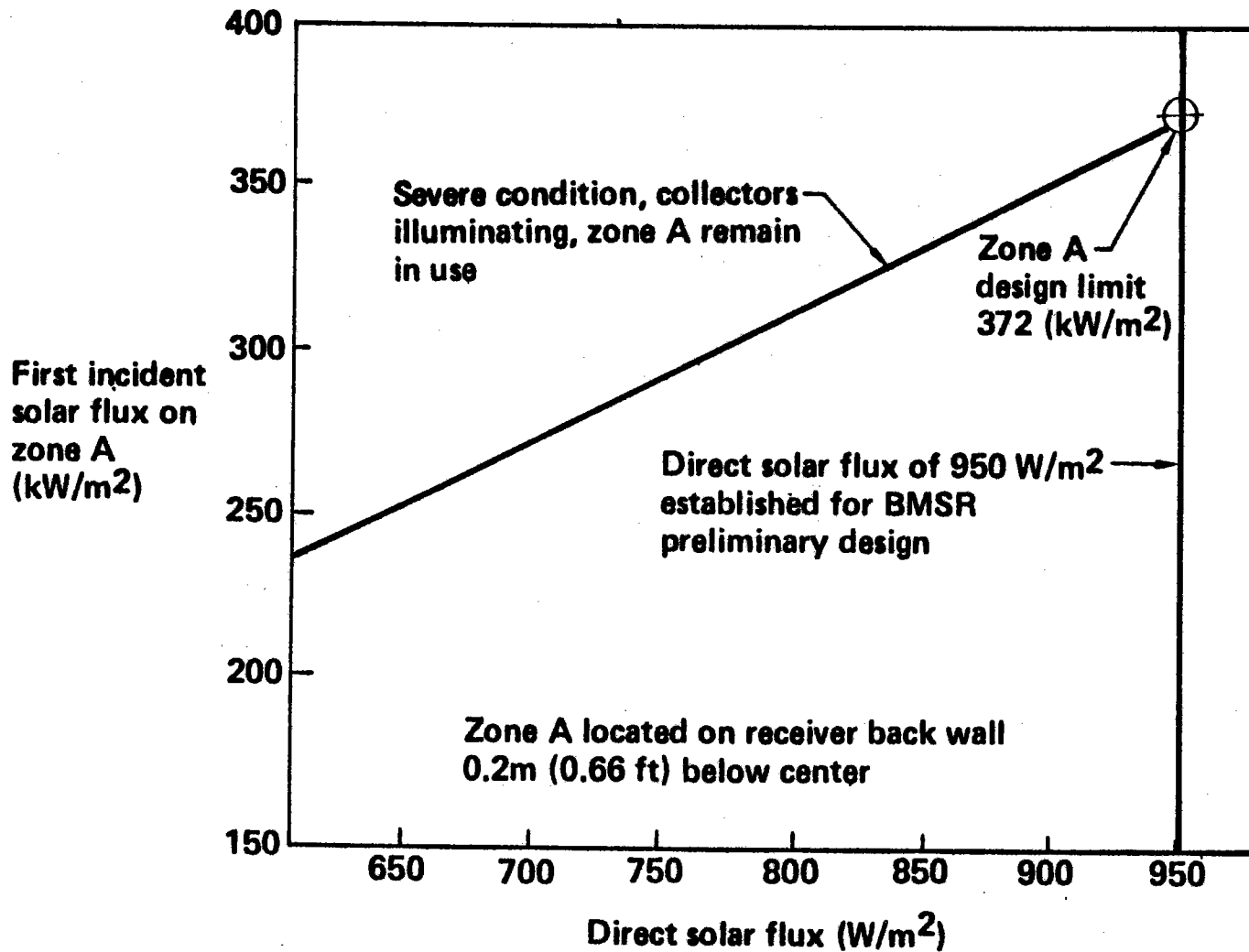
#### Calculations of Absorbed Solar Flux

First-incident solar flux is important in determining the BMSR solar interface with the CRTF. Because internal cavity solar reflections are not included, however, these analyses do not determine the final distribution of solar heat absorbed by surfaces in the cavity or reflected back out through its aperture.

The differences between first-incident and absorbed solar heat were significant in the BMSR. This was due to the highly reflective properties of cavity walls. Some of the solar energy entering the cavity was reflected several times before being absorbed or lost out the aperture. This reflective redistribution of solar flux was a desirable feature of the

Figure 3.2-8. First Incident of Zone A of Receiver Back Wall

# First Incident of Zone A of Receiver Back Wall



cavity solar receiver; however, analysis of these multiple reflections required the use of highly sophisticated computer codes for radiant heat transfer simulation.

The Boeing Monte Carlo ray-tracing computer code was used for calculations of absorbed solar flux in the BMSR. It is a generalized multipurpose code developed and used initially by Boeing Aerospace Company.

The user interface for the ray-tracing view-factor calculations consisted of two types of code inputs. First, the cavity enclosure was defined, including surface geometry and thermophysical properties. Surface geometry was defined in a three-dimensional Cartesian coordinate system. Radiant thermophysical properties of the corresponding BMSR surfaces were entered in the form of the decimal fractions of incident radiant flux: absorbed, specularly transmitted, diffusely transmitted, specularly reflected, or diffusely reflected. In addition, the user defined radiant-emitting surfaces for the initiation of ray tracing. These surfaces can be ones that make up the original enclosure or can be additional surfaces simulating external heat sources like sunlight. The rays emitted from these surfaces can be projected in a Lambertian flux distribution to simulate diffuse thermal radiation or collimated perpendicular to the emitting surface to simulate sunlight.

The view-factor geometry model used for BMSR solar heating calculations (Figure 3.2-9) consisted of 33 surface elements representing the insulation walls of the cavity, 32 surfaces representing rows of heat exchanger tubes, and a circular opening representing the cavity aperture.

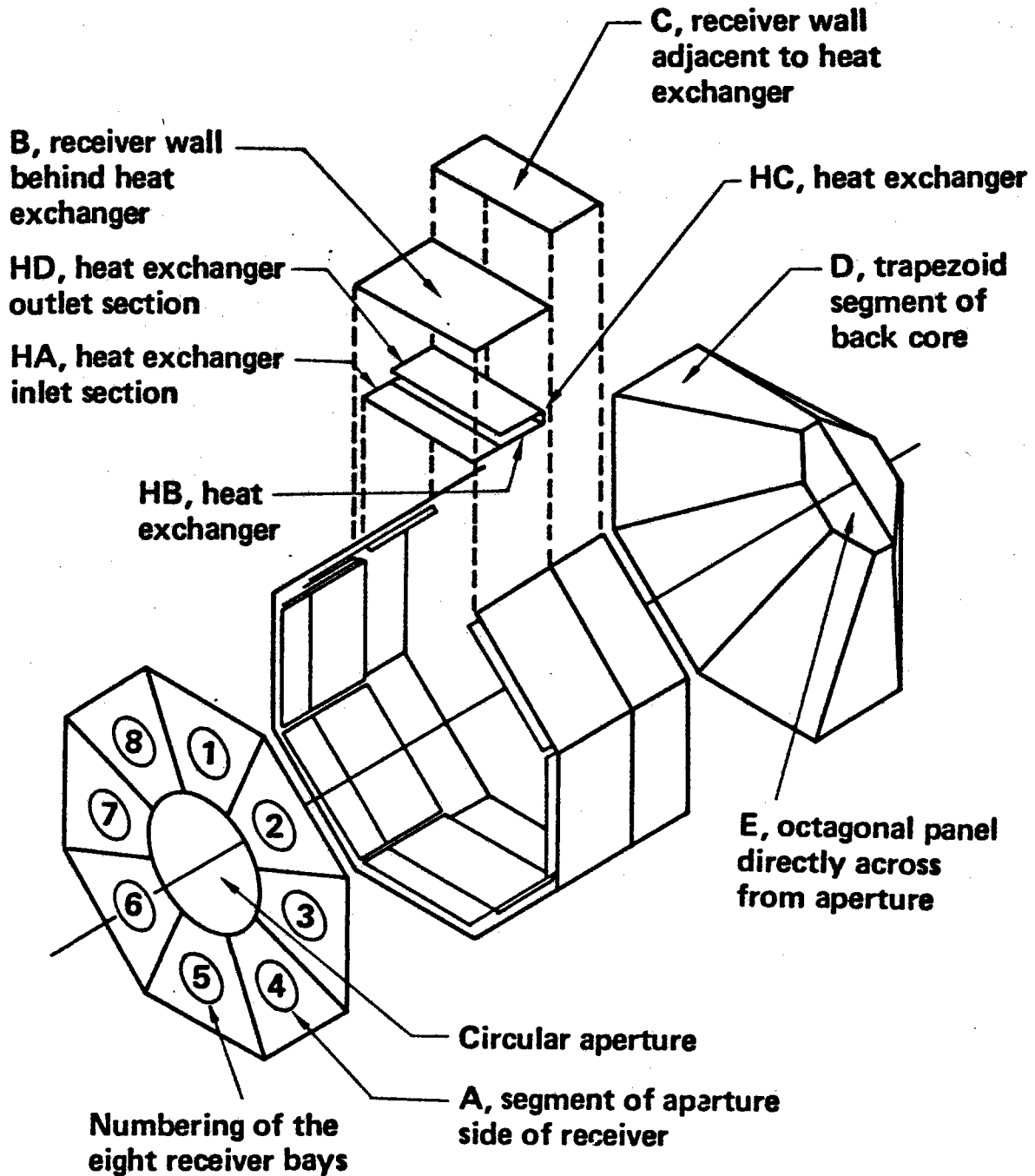
Only three materials were used in the BMSR interior: oxidized Inconel 617 for heat exchanger tubes, Kaowool blanket insulation on walls of the main frame of the receiver, and Saffil blanket insulation on the back cone. The insulation materials were assumed to be opaque diffuse reflectors of sunlight. Solar absorptances were 0.21 for Saffil and 0.29 for the Kaowool.

The rows of heat exchanger tubes were on parallel centerlines spaced three tube diameters apart. Their equivalent surface exhibited some transmittance



Figure 3.2-9 View Factor Model for BMSR Solar Heat Load Computations

# View Factor Model for BMSR Solar Heat Load Computations



due to spacing between tubes, absorptance that occurred at the tube surfaces, and a small amount of solar reflectance from the tube surfaces. The oxidized Inconel 617 tube surface absorbed 0.89 and reflected 0.11 of incident sunlight. The effective radiant properties of the row of tubes were: solar absorptance 0.40, specular transmittance 0.55, and diffuse reflectance 0.05.

Receiver solar input from a particular CRTF collector was modeled by a parallel bundle of rays entering the receiver from the direction of the collector. An emitting surface was defined for each collector so that rays emitted perpendicular to the emitting surface passed through the receiver aperture, striking the interior wall in the area of first incidence for that collector.

Because of computer time required for these ray-tracing analyses, only every other collector in the CRTF Zone A field was modeled. Furthermore, because of east-west symmetry of the receiver and collector field, analyses for the east-side collectors was used for the corresponding west-side collectors.

During ray-tracing computations, the computer code first simulated emissions of individual rays from the emitting surface. The path of these rays was projected to determine their first-incident point on the enclosure walls. Then the radiant-surface properties at the intersection point statistically determined the results of this intersection event. All the possible surface effects (absorption, specular reflection, etc.) were arranged to fill the number line from zero to one. Then a random number from zero to one was generated. The intersection event that occupied this space on the zero-to-one number line was used. If the ray was absorbed, it was tallied for the intercept surface. If it was specularly reflected or transmitted, it was projected along the corresponding new direction until a new intersection with enclosure surfaces was found. Then the intersection event was repeated. If it was diffusely reflected or transmitted, then a new direction for the ray was selected from a Lambertian weighted-distribution function and this path was projected to a new intersection with the enclosure. Thousands of these rays were traced during computation of view factors from a single surface. In large quantities, these simulated rays

produced a statistically valid representation of the radiant heat transfer process being modeled. Because a given number of rays were used to simulate the solar input to the receiver from one of the CRTF collectors, the fraction of these rays that were absorbed and tallied by each surface of the receiver was equal to the fraction of the collector heat input acting to heat that particular surface. Given the collector solar input to the receiver, which varied with time and the ambient direct solar flux, this input was always divided in the same proportions to each of the receiver surfaces.

The CRTF Zone A collectors were analyzed to determine the distribution of solar input from each one to the various interior surfaces of the receiver. These data were listed in two ways. First, assuming equal contributions of receiver heat input from each of the Zone A collectors, it was possible to define the absorbed solar heat distributions in the receiver at 1 Mwt solar heat input. These data were tabulated in Figure 3.2-10. The absorbed solar heat fluxes on back-cone surfaces were markedly lower than the maximum first-incident fluxes computed earlier because the insulation only absorbed 21% of incident flux and the rest was reflected. Data in Figure 3.2-10 are average values over relatively large surface areas; peak heat loads are averaged with large regions of much lesser heat flux. The more important use for these solar heating distribution functions is as a boundary conditions for the detailed thermal model of the BMSR. Their use in the BMSR thermal model is discussed in Section 3.6.

### 3.3 THERMAL ANALYSIS OF BMSR HEAT EXCHANGER TUBE

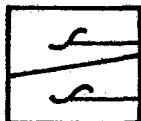
The BMSR heat transfer system used 432 parallel airflow paths through essentially identical heat exchanger tubes. The receiver thermal model (Section 3.5) simulated all these tubes by a total of 32 thermal nodes. This coarse nodal network was necessary and sufficient for an overall system analysis. However, a much more detailed thermal model of heat exchanger tubes was needed to determine exact heat transfer performance and detailed temperature distributions.

The heat exchanger tube thermal analysis described here was intended to

Figure 3.2-10. Typical Values of Absorbed Solar Flux

## Typical Values of Absorbed Solar Flux

Receiver model areas	Numbering of the receiver bays							
	1 top	2	3 east	4	5 bottom	6	7 west	8
Aperture	86.27				90.8			
A aperture side	11.74 13.9	11.92 14.1	11.59 13.7	11.16 13.2	11.69 13.8	11.16 13.2	11.59 13.7	11.92 14.1
B behind heat exchanger	6.38 6.8	6.40 6.8	6.22 6.7	6.17 6.6	6.07 6.5	6.17 6.6	6.22 6.7	6.40 6.8
C adjacent to heat exchanger	10.98 16.6	13.03 19.7	16.60 25.2	11.89 18.0	11.59 17.6	11.89 18.0	16.60 25.2	13.03 19.7
D trapezoid segment	20.95 19.0	32.74 29.7	61.63 55.7	32.49 29.5	22.57 20.5	32.49 29.5	61.63 55.7	32.74 29.7
E octagonal panel	32.43				36.2			
HA heat exchanger inlet section	8.70 30.2	9.00 31.3	8.73 30.3	8.98 31.2	8.90 30.9	8.98 31.2	8.73 30.3	9.00 31.3
HB heat exchanger	18.32 31.8	17.61 30.6	17.81 30.9	17.84 31.0	17.31 30.1	17.84 31.0	17.81 30.9	17.61 30.6
HC heat exchanger	2.68 27.9	3.36 35.0	3.06 31.9	2.73 28.4	2.63 27.4	2.73 28.4	3.06 31.9	3.36 35.0
HD heat exchanger outlet section	12.45 21.6	12.25 21.3	12.22 21.2	12.42 21.6	12.19 21.2	12.42 21.6	12.22 21.2	12.25 21.3



— Absorbed solar heat, kW, at 1-MW receiver input, noon

- - - Absorbed solar flux, kW/m<sup>2</sup>, at 1-MW receiver input, noon, based on projected area of heat exchanger panel

fulfill two important BMSR design verification requirements. First, a fine mesh of heat exchanger tube temperatures was needed for thermal stress analysis (Section 3.6). Secondly, an independent analysis was required to verify the stand-alone thermal performance of the BMSR heat exchangers. The thermal model heat exchanger configuration, tube size and length, and internal gas-flow conditions were determined by thermal-scale modeling. All performance characteristics were derived from the RP377-1 commercial solar receiver (Reference 1).

The Boeing Engineering Thermal Analyzer (BETA), a generalized heat transfer analysis computer code, provided the computational system for this analysis. A lumped-parameter nodal network was devised to represent the heat transfer characteristics of a single typical heat exchanger tube. The tube was divided into a total of 224 thermal nodes. As shown in Figure 3.3-1, the heat exchanger panel was divided into eight segments. The inlet tube pass occupied all eight segments. The outlet tube pass, from U-bend to its exit through the receiver wall, occupied an additional six segments. Each of these 14 tube-length segments were subdivided into 16 heat transfer nodes. Here the tube wall was separated into inner and outer sections and each were separated into eight circumferential elements.

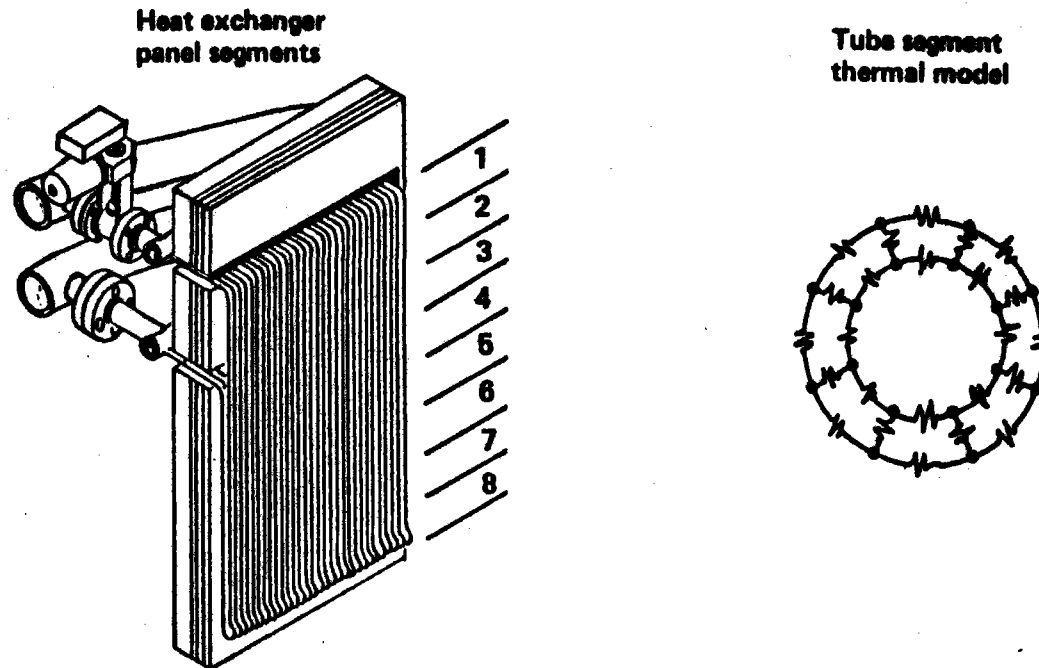
The 16-node representation of each of the tube-length segments is shown in Figure 3.3-1. The lumped-parameter nodes are connected by radial and circumferential conductors.

These conductors simulated the thermal conductance of the tube wall. Because of the slenderness of these 14 tube segments, the axial thermal conductivity from segment to segment along the tube was negligible compared to the other conductors.

The heat transfer boundary conditions used with this tube thermal model provided heat sources, heat sinks, and internal airflow simulation. They were selected in a manner that expedited BETA program calculations and at the same time provided an acceptable simulation of the receiver cavity thermal environments. The following boundary conditions were selected for this thermal model:

Figure 3.3-1. Heat Exchanger Thermal Model

## Heat Exchanger Thermal Model



### Boundary conditions:

- Inlet air temperature and flow rate
- Long row of identical heat exchanger tubes
- Receiver wall insulation
- Effective cavity temperature

### Heat transfer mechanisms:

- Tube interior
  - Radiation
  - Gas-forced convection
- Tube wall
  - Radial and circumferential conduction
- Tube exterior
  - Radiation to wall and cavity interior
  - Diffuse solar heating

- a. Air inlet at a specific temperature and flowrate.
- b. The particular tube was bounded by identical tubes on either side; it was one of a long row of identical tubes.
- c. The tube row was bounded on one side by a diffusely reflecting refractory wall. By definition, this wall neither added nor removed heat from the heat transfer system. This represented a perfectly insulating cavity wall behind the heat exchangers with no convective heat transfer.
- d. The tube row was bounded on the cavity side by a heat-source surface. This surface simulated the total radiant heating potential of the cavity. For purposes of analysis, it was assumed to be diffusely radiating at a temperature equivalent to the effective blackbody temperature of the cavity interior. An effective temperature could be assigned to this surface that represented the sum of reflected solar and thermal radiative heat flux impinging on the heat exchanger. This temperature could be adjusted to account for variations in receiver operating power.

Heat transfer mechanisms simulated in the exchanger tube thermal model included:

- a. Radiant heat transfer between areas of tube interior wall
- b. Forced convection heat transfer between interior tube-wall surfaces and the internal airstream
- c. Radial and circumferential tube-wall conduction
- d. Radiant heat transfer between tube exterior wall surfaces and the surrounding environments, including the refractory wall, adjacent tubes, and effective cavity heat source

Individual tube thermal analyses were performed by inserting a particular set of boundary conditions: inlet air temperature, flow rate through the tube, and effective receiver-cavity temperature. Then the BETA code determined resulting tube temperatures and air outlet temperatures. If the proper effective receiver cavity temperature was used, an air-outlet

temperature could be obtained that simulated the controlled air-outlet temperature in the BMSR.

These methods were used to obtain heat exchanger tube temperatures for two conditions of special interest to the BMSR design. One condition simulated the full-power receiver design point consisting of--

- a. Tube airflow rate of 0.0061 kg/s (0.013 lb/s) corresponding to a total receiver flow rate of 2.62 kg/s (5.76 lb/s)
- b. Air-inlet temperature of 538°C (1000°F)
- c. Air-outlet temperature of 816°C (1500°F)

The tube-wall temperatures for this operating condition are shown in Figure 3.3-2. The second condition of interest was one for which operating heat exchanger tube thermal stress was expected to be even higher than the normal full-power design point. Here, the receiver inlet temperature was reduced to 400°C (750°F) and the airflow rate was reduced to maintain an equal overall tube-to-air heat transfer of 1.87 kW. These tube temperature data are shown in Figure 3.3-3.

The tube temperature distributions (Figures 3.3-2 and 3.3-3) show the radial and circumferential (hot-to-cold-side) tube temperature gradients. As expected, they are very similar to the temperature gradients expected in the commercial receiver (Reference 1).

The heat transfer performance of BMSR heat exchanger tubes was verified by ascertaining that full-receiver heat loads could be transferred to the airstream without exceeding the desired range of tube temperatures. This is verified in Figure 3.3-2, where the maximum tube temperature is less than 870°C (1600°F).

The tube thermal model did not account for variations of tube thermal environment and internal tube-to-gas heat transfer in the region of the tube bend. It assumed straight-tube geometry and airflow.

Tube-bend temperatures were desired for the thermal stress analysis (Section



Figure 3.3-2. Tube Temperature Design Point BMSR Operating Conditions

# Tube Temperature Design Point BMSR Operating Conditions

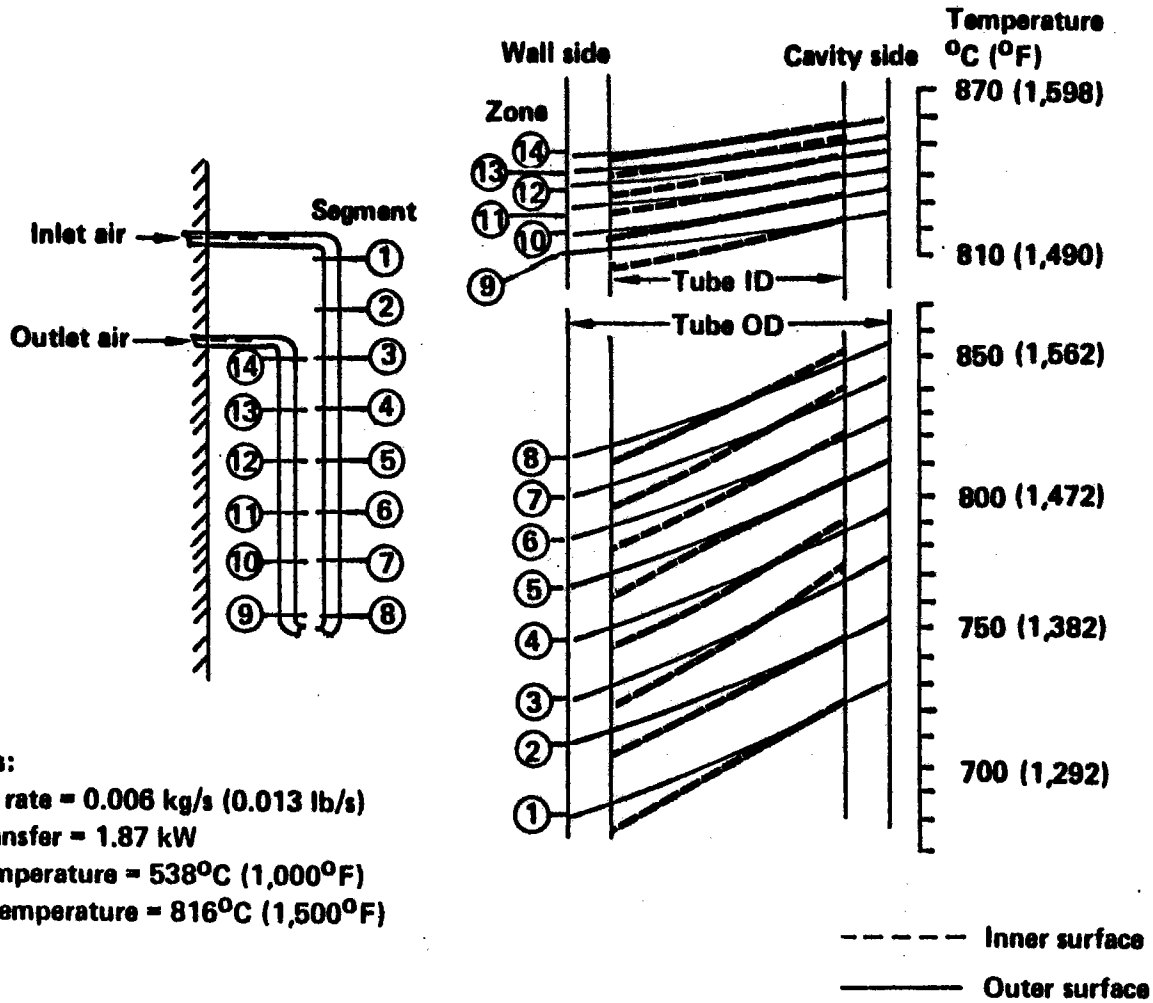
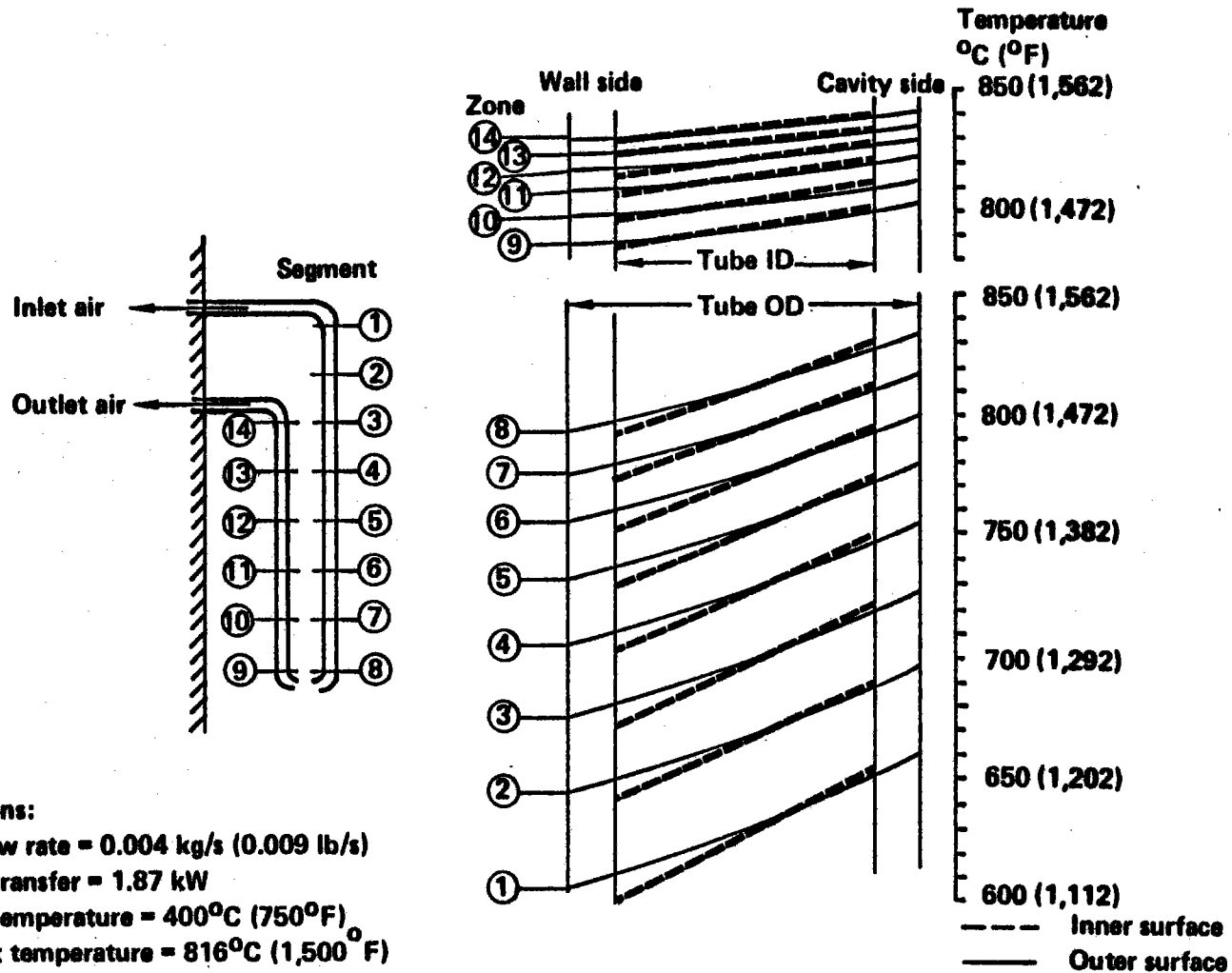


Figure 3.3-3. Worst Case Tube Temperatures for Heat Exchanger Thermal Stress

# Worst Case Tube Temperatures for Heat Exchanger Thermal Stress



3.7). These temperatures were developed by supplementing the straight-tube computer analysis with hand calculations to account for tube-bend effects. These data, for BMSR design point conditions, are shown in Figure 3.3-4.

### 3.4 RECEIVER AIR FLOW SYSTEM

#### 3.4.1 Airflow System Description

The test air supply system for BMSR solar tests is shown in Figure 3.4-1. Airflow rates of up to 2.7 kg/s (6.0 lb/s) were provided by four diesel-driven compressors. These compressors were located at ground level adjacent to the base of the CRTF tower. The rated outlet pressure of these compressors was 0.97 MPa (140 lb/in<sup>2</sup>a). The air was monitored for hydrocarbon content and carried up to the BMSR test bay via facility piping. Here it entered the air supply equipment skid.

The air supply equipment skid was used during BMSR testing to preheat the test air supply and to regulate the receiver exhaust back pressure. Another EPRI Contract, RP1092-1, covered design and fabrication of this equipment (Reference 2).

As shown in Figure 3.4-1, the hot air from the BMSR flowed through the high-temperature side of the air supply recuperator, through an automatic back-pressure control valve, and was exhausted at the top of the CRFT tower by means of facility piping. The recuperator, a cross-counterflow tube-in-shell heat exchanger, was used to extract heat from the BMSR outlet air and transfer it to the BMSR inlet airstream. Not only was the BMSR inlet airstream heated by the receiver outlet air, but its temperature was also precisely controlled by the air supply skid by diverting a portion of the supply air around the recuperator. A receiver inlet temperature controller monitored the air temperature at the BMSR inlet and operated the recuperator bypass valve. Increasing the fraction of inlet air, which was diverted around the recuperator, lowered the BMSR inlet temperature, and decreasing it increased the temperature.

The BMSR was designed prior to the air supply skid. Because pressure losses

Figure 3.3-4. Temperature Predictions for Tube Bend Stress Analysis

# Temperature Predictions for Tube Bend Stress Analysis

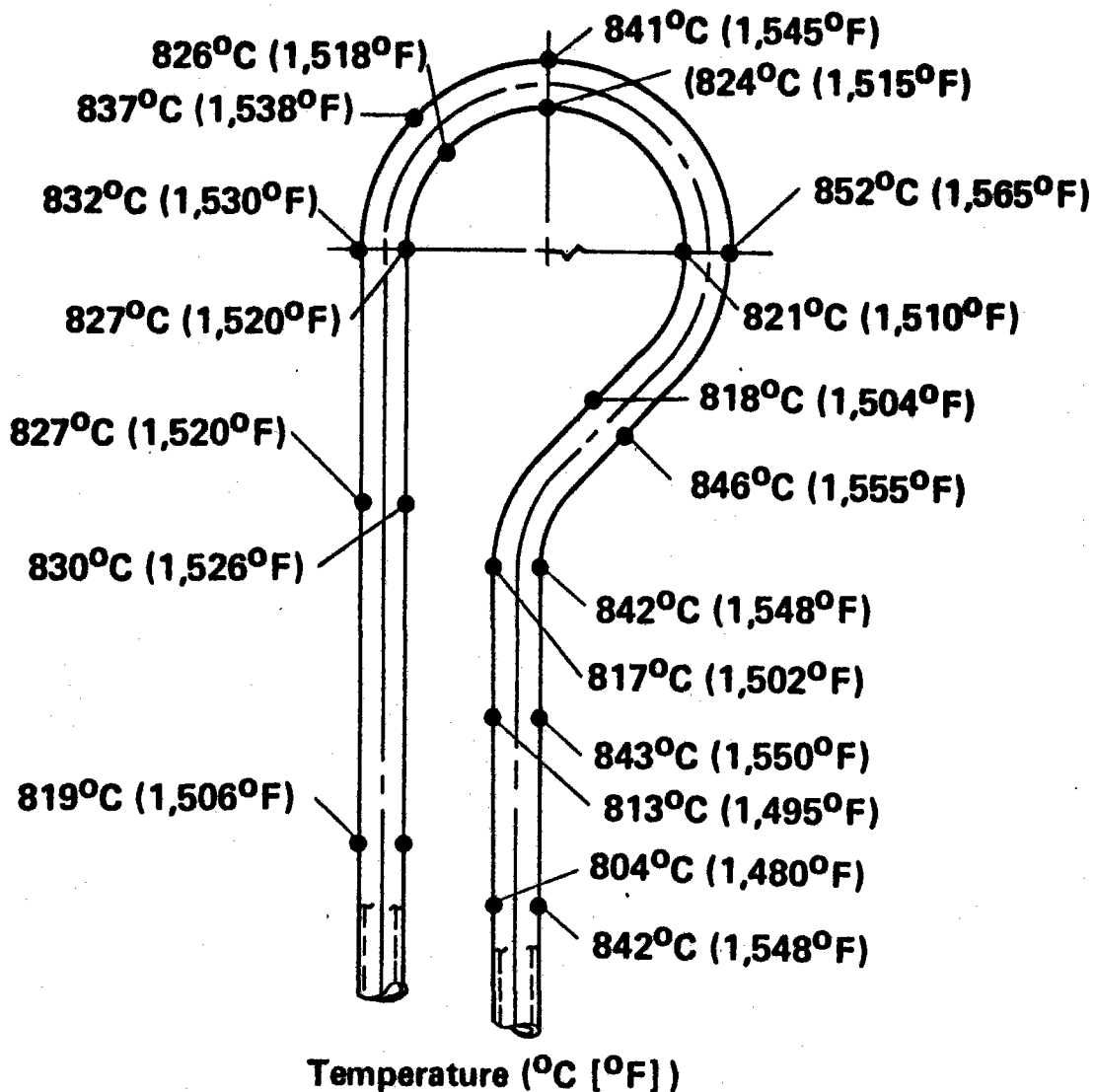
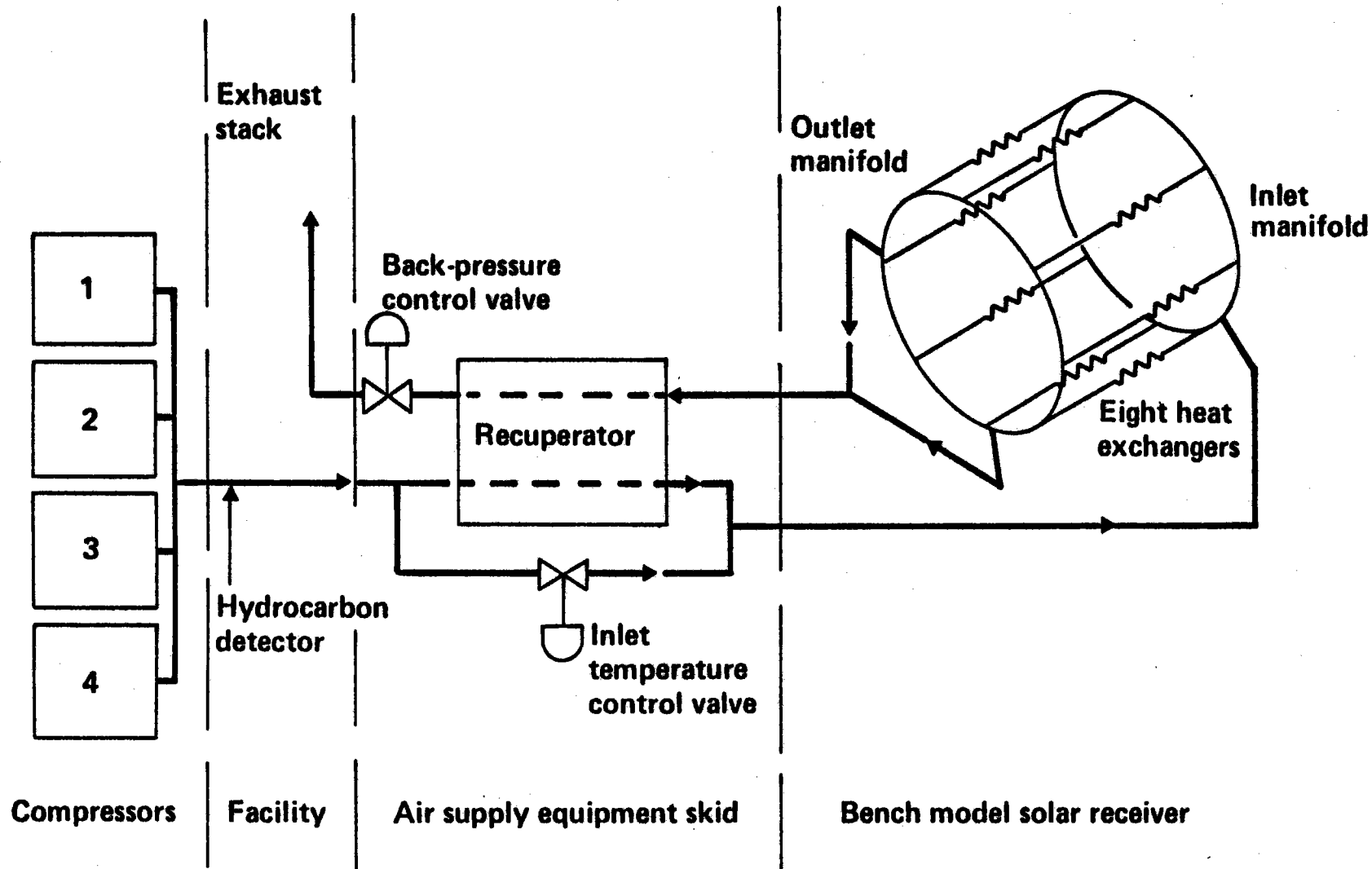


Figure 3.4-1. Test Air Supply System for BMSR Tests

# Test Air Supply System for BMSR Tests



in the air supply skid were expected to consume a significant amount of the supply air pressure, a generous pressure loss was allocated for its design. This allocation of 0.15 MPa (22 lb/in<sup>2</sup>) included piping losses from the compressors to the air supply skid, losses on the air supply side of the skid including bypass valve and recuperator, and piping losses from the skid to the BMSR inlet manifold. An inlet pressure of 0.90 MPa (130 lb/in<sup>2</sup>a) was established for the detailed design of the BMSR airflow system.

The BMSR airflow system was made up of components inside and outside of the cavity. The external components included inlet and outlet manifolds, headers, and flow-control valves. Eight sets of flow-control valves and inlet and outlet headers were used for the heat exchangers. Only the eight heat exchanger panels, each having 54 tubes, were located inside the receiver cavity.

Figure 3.4-1 shows the circular configuration of inlet and outlet manifolds on the BMSR. Figure 3.4-2 shows details of the manifolds. The inlet manifold used a single airflow inlet, distributing this flow by means of flanged connections to the eight receiver heat exchangers. The outlet manifold was essentially identical to the inlet manifold except that two outlets from the manifold were required to handle the higher volume of high-temperature receiver exhaust air.

Details of the BMSR heat exchanger panel are shown in Figure 3.4-3. The panels were attached to inlet and outlet manifolds by bolted flanges and provided inlet and outlet airflow paths as well as mechanical support points for the heat exchangers. The air supply flow-control valve was sandwiched between the pair of inlet flanges. This was a ball valve with a pneumatic actuator and a proportional valve-angle positioning system. The inlet and outlet headers spanned the width of the heat exchanger panel. Individual heat exchanger tubes were connected to the headers on 2.0-cm (0.8 in) centers. These welded tube connections provided airflow paths as well as mechanical support for the individual tubes.

Another detail, not shown in Figure 3.4-3, was the BMSR insulation wall closure around the connectors and heat exchanger tubes. A packing of bulk

Figure 3.4-2 BMSR Manifold Details

# BMSR Manifold Details

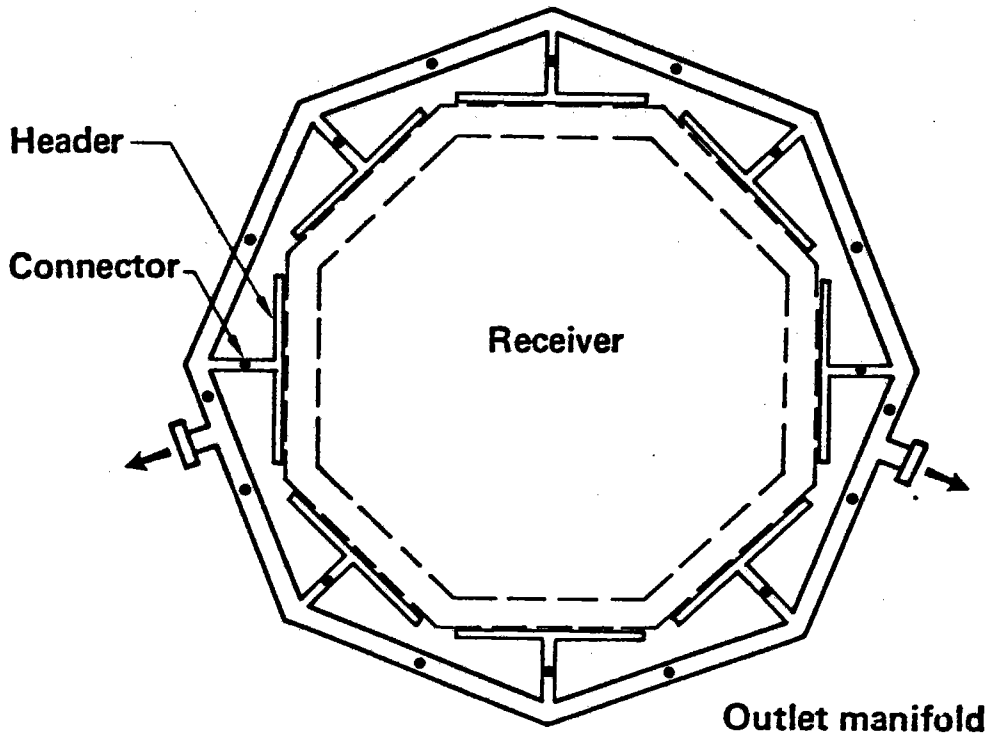
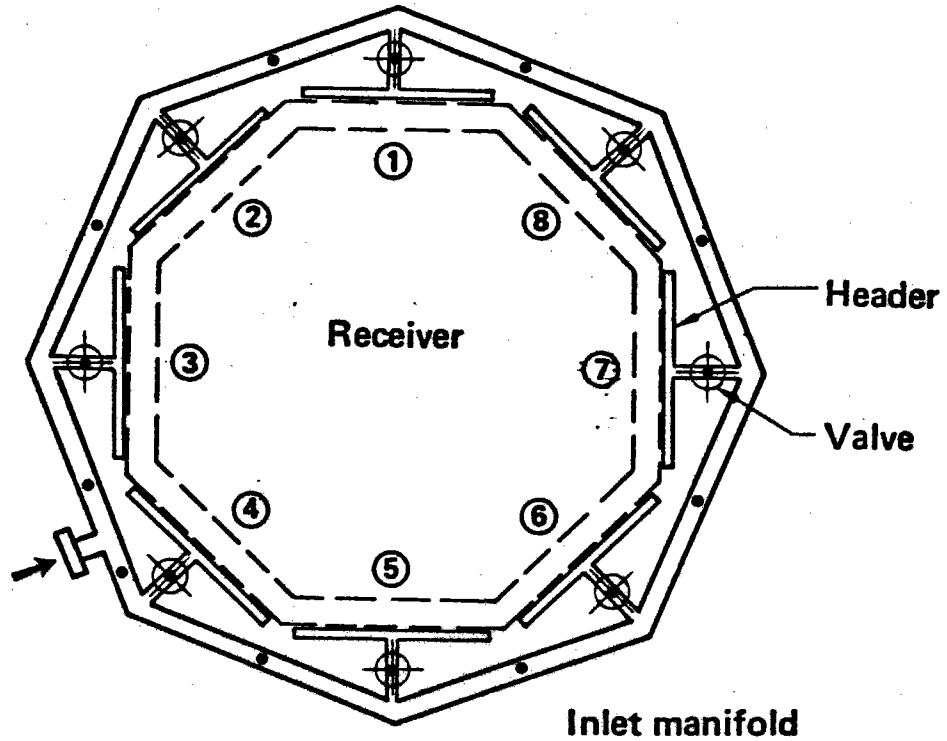
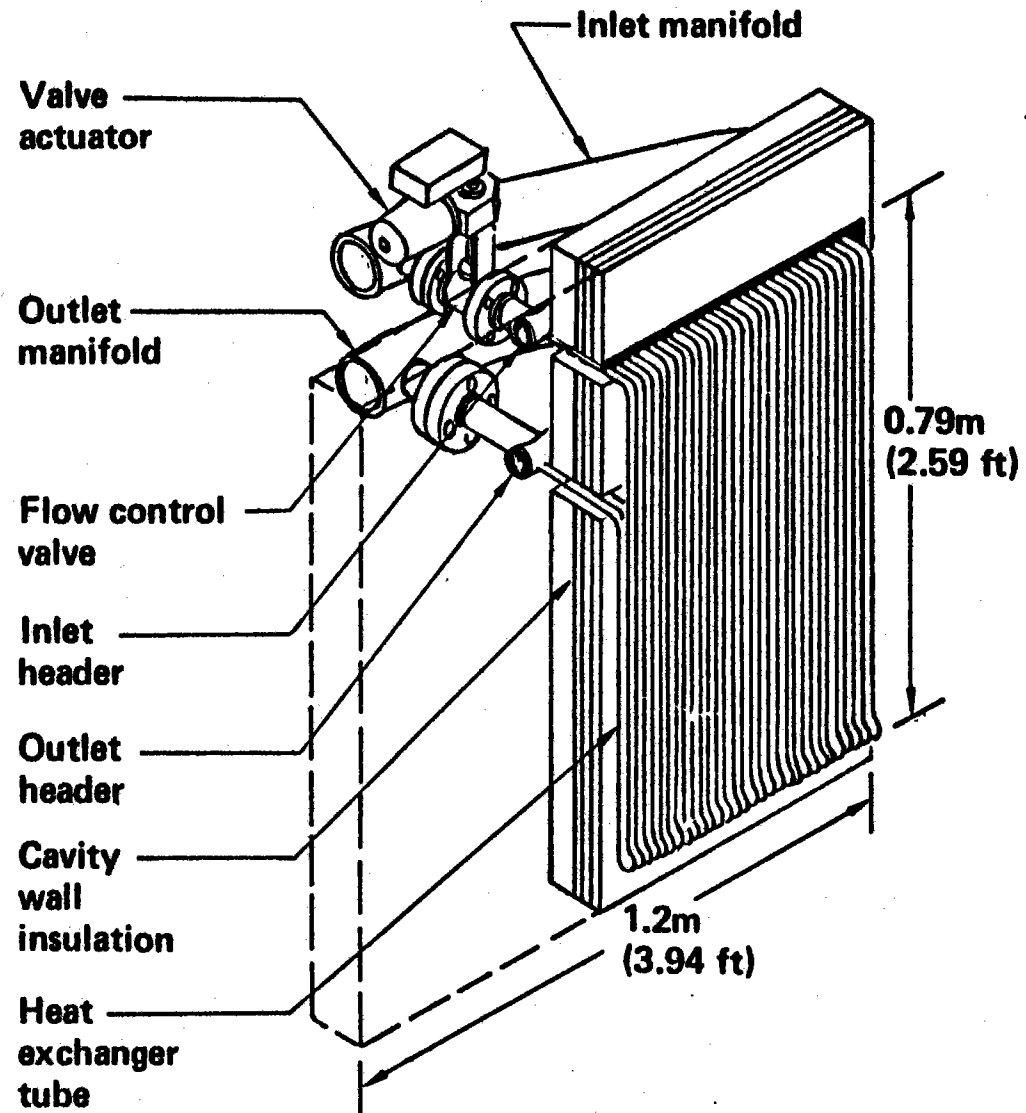


Figure 3.4-3. BMSR Heat Exchanger Panel Details

# BMSR Heat Exchanger Panel Details





ceramic fiber insulation was inserted around the tubes to fill the gap where they passed through the receiver insulation wall. Then as the manifolds expanded and contracted with thermal cycling, the heat exchanger tubes slid back and forth in this packed insulation. The total motion from this thermal expansion and contraction of manifolds was 1.0 to 2.0 cm (0.4 to 0.8 in).

The airflow system of the BMSR was made up of several parallel flow paths. The inlet manifold separated the supply airflow into eight paths for individual heat exchangers. The heat exchanger inlet headers further divided the flow into the 54 individual tube flow paths through each panel (432 total). Then the exhaust headers and exhaust manifold collected this flow back into the two BMSR air outlets on the exhaust manifold.

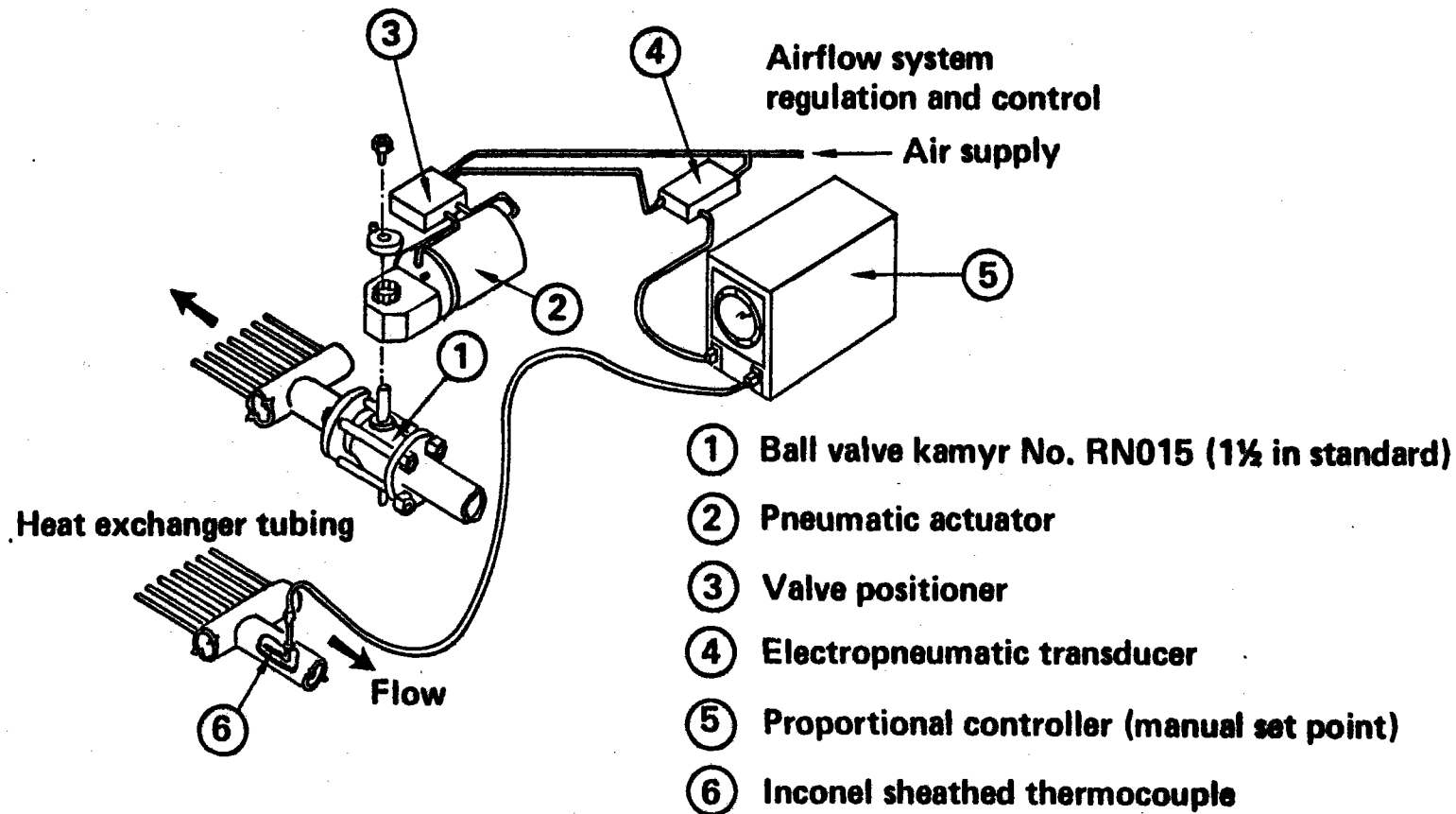
The BMSR was a variable-mass-flow, constant-outlet-temperature air heater. A precedent for this mode of operation was established by the closed-cycle, solar central receiver concept developed during the RP377-1 study (Reference 1). The RP377-1 receiver used variations of working pressure in its closed gas circuit (inventory control) to adjust mass flow and maintain constant outlet temperature during large changes in operating solar power. Small mass-flow changes to accommodate variations of solar power from panel to panel were provided by individual panel-flow valves. In the commercial receiver, these valves provided only a small range of mass-flow control.

The BMSR used flow-control valves on the individual heat exchangers for all its gas-outlet temperature controls. The electropneumatic flow-control system for an individual BMSR heat exchanger panel is shown in Figure 3.4-4. Each valve was operated by its own controller. The desired panel outlet set-point temperature was set into the controller; the actual panel outlet-air temperature was measured by the thermocouple immersed in the outlet airstream. The controller continuously adjusted the valve angle and panel flow rate so that these two temperatures were matched. Increasing the panel airflow reduced the outlet-air temperature and reducing the flow increased it.

As a result of this active control of individual panel flow rates, the

Figure 3.4-4. Panel Airflow and Temperature Control System

## Panel Airflow and Temperature Control System



airflow design requirements for inlet and outlet manifolds were quite simple. The manifold pressure losses at individual panel connections did not influence the flow distribution from panel to panel. The manifolds needed only to carry the required rates of airflow with reasonable air-pressure losses.

The panel headers that supplied and exhausted individual heat exchanger tubes presented a more critical pressure-loss design problem. Here, the inlet and outlet headers could influence the balance of the flow rates through individual tubes. Because all 54 of the tubes were in essentially equal thermal environments, flow differences resulted in variations of gas-outlet temperature from tube to tube.

Because the normal air-temperature rise in the BMSR was 278°C (500°F), a mass flow difference of only  $\pm 10\%$  produced an outlet temperature variation of about  $\pm 28^\circ\text{C}$  (50°F).

This same requirement of equal tube flows across the width of the heat exchanger panel also placed severe constraints on the individual heat exchanger tubes. The tube flow rate was extremely sensitive to tube inside diameter. For example, a 4% variation of tube diameter resulted in a flow-rate exchange, at equal applied pressures, of 10%. Once again, the gas outlet temperature variations were about 28°C (50°F).

The important component design selections and trade studies for the BMSR airflow system are described in the following section. In general, the requirements and performance of individual components were developed individually in such a way as to ensure suitable operation of the complete system.

#### 3.4.2 Performance of Flow-System Components

Design studies were conducted to verify the airflow performance of BMSR components. Each element of the receiver airflow system was allocated a pressure loss budget, taken from the 0.9 MPa (130 lb/in<sup>2</sup>a) available at the receiver inlet. Other requirements, including flow-control and

flow-distribution characteristics, were also identified. These performance requirements are summarized in Table 3.4-1.

The design studies that verified compliance of the BMSR flow system with these requirements are presented in the following paragraphs.

#### Inlet and Outlet Manifolds

The BMSR inlet and outlet manifolds were designed for 1.14-MPa (165-lb/in<sup>2</sup>a) operating pressures. At this receiver operating pressure, identical configurations could be used for the two manifolds. At the low pressures for BMSR solar tests, 0.90-MPa (130-lb/in<sup>2</sup>a) inlet and 0.52-MPa (74-lb/in<sup>2</sup>a) outlet, the inlet manifold exhibited an acceptable pressure loss. However, because of high air velocities at the 0.52-MPa (74 lb/in<sup>2</sup>a) outlet manifold pressure, it was necessary to provide two air exhausts from the manifold. This change, to accommodate low-pressure BMSR solar test operation, was adopted rather than increasing the size of manifold piping so that manufacturing commonality could be retained in both BMSR manifolds.

The pressure loss requirements, 0.014 MPa (2.0 lb/in<sup>2</sup>) for the inlet manifold and 0.028 MPa (4.0 lb/in<sup>2</sup>) for the outlet manifold, were very close to the actual pressure losses experienced during solar tests.

#### Inlet and Outlet Headers

As mentioned earlier, the most important function of inlet and outlet headers was to provide equal mass flows to their 54 separate heat exchanger tubes. This was accomplished by keeping the total pressure losses in the distribution headers much smaller than the pressure losses through individual tubes. Here the relatively high-pressure loss in BMSR heat exchanger tubes eased the requirements on inlet and outlet headers.

By restricting the effects of pressure differences in the headers to a total of 0.006 MPa (0.87 lb/in<sup>2</sup>), (Table 3.4-1), the total mass-flow variation in the heat exchanger tubes of a single panel was about +0.6%. The initial header design, with 3.81-cm (1.5-in) inside diameter, was selected to meet

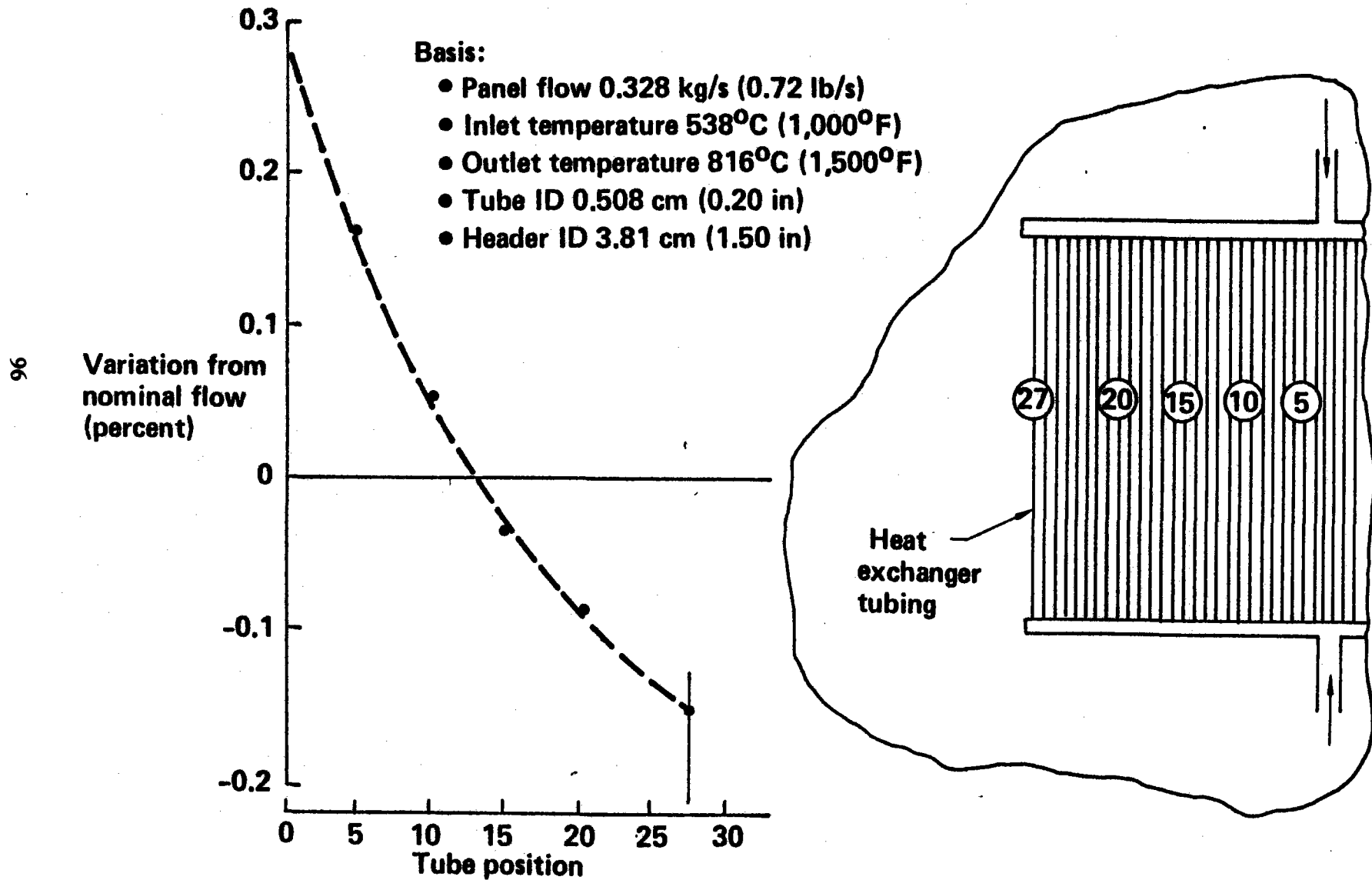
Table 3.4-1. Design Requirements of Flow System Components

## Design Requirements of Flow System Components

Component	Pressure loss budget at full receiver flow, MPa (lb/in <sup>2</sup> a)	Functional requirements
Inlet manifold	0.14 (2)	Minimize effects of individual panel flow rates on supply pressure at adjacent panels
Inlet header	0.007 (1)	Equalize individual tube inlet pressures to within 0.002 MPa (0.30 lb/in <sup>2</sup> )
Flow valve (open valve)	0.090 (13) Partially closed valve	Utilize partially closed valve at full flow to improve control stability
Heat exchanger	0.228 (33)	Acceptable manufacturing tolerances for airflow through heat exchanger tubes with equally imposed pressures is +2%
Outlet header	0.014 (2)	Equalize individual tube outlet pressures to within 0.004 MPa (0.60 lb/in <sup>2</sup> )
Outlet manifold	0.028 (4)	Minimize effects of individual range flow rate on back pressure of adjacent panels
Complete BMSR airflow system	0.381 (55)	The above constraints on headers and heat exchanger tubes ensure tube flows within 1% of each other across each heat exchanger panel

Figure 3.4-5. Influence of Inlet and Outlet Headers on Panel Flow Distribution

## Influence of Inlet and Outlet Headers on Panel Flow Distribution



this requirement. Subsequent detailed analysis of the separating and combining airstreams in inlet and outlet headers indicated the somewhat better-than-expected flow distribution performance.

Figure 3.4-5 shows part of the results of a detailed analysis conducted to determine the full-flow pressure losses in BMSR heat exchangers. A forward-difference computer code was used to proceed step by step through typical heat exchanger flow paths. Five separate paths were evaluated starting at the center of the inlet header, proceeding across the header and through the individual tubes (which were 5, 10, 15, 20, and 27 tubes away from the center of the 54-tube heat exchanger panel), and back across to the center of the outlet header. Pressure losses were computed for small downstream steps. The effects of compressible flow, flow geometry such as tube bends, inlets, and outlets into the headers and turning flow, the deceleration and acceleration of airflow in the headers, and the air-temperature increase due to solar heating were all considered in this detailed pressure-loss analysis. The flows through various tubes were adjusted to produce equal inlet and outlet pressures at the header connections to inlet and outlet manifolds.

Because all heat exchanger tubes were assumed to be geometrically identical, the differences in flow for the five typical tube flow paths examined were the differences resulting from tube position along the headers. As expected, the central tubes in the heat exchanger exhibited higher flow rates than the outer tubes.

The weighted average tube airflow was 0.0061 kg/s (0.013 lb/s). The variations of flows in the individual heat exchanger tubes ranged from +0.28% to -0.16% of this flow. The hottest tube in the panel was the one having minimum flow. This tube exhibited an outlet air temperature and tube temperature within 1°C (1.8°F) of the average panel outlet air temperature.

In this case, the detailed analysis conducted after completing the BMSR preliminary design indicated that heat exchanger panel headers were significantly oversized. Headers of a smaller inside diameter would be equally suitable for the BMSR; however, penalties for the oversize header were not severe and the large-diameter header size was retained for the final design.

## Flow-Control Valve

The panel flow-control valve is shown in Figures 3.4-3 and 3.4-4. In operation, it provided the variable-pressure-loss restriction in the heat exchanger flow path and served to regulate the panel airflow rate.

The panel flow rates desired for the BMSR ranged from about 0.045 to 0.327 kg/s (0.10 to 0.72 lb/s). The valve operating temperature, equal to the BMSR inlet temperature, was 538°C (1000°F). This 538°C inlet temperature was the most difficult requirement to meet with off-the-shelf, commercial-quality, flow-control valves. The location of these valves between the circular inlet manifold and the outer wall of the receiver also placed a serious constraint on the overall size of the valve and actuator assembly.

This combination of requirements resulted in the selection of a pneumatically actuated ball valve for the BMSR flow-control valves. Standard production valves were available that used stainless steel for the valve ball and body and stellite for the valve seats. These materials provided the required high-temperature service capability even though these construction materials were more commonly used for their corrosion resistance.

The flow-versus-pressure-loss performance of ball valves was determined experimentally where,

$$W \text{ (lb/s)} = 0.029 F_p C_v(\alpha) \left[ 1 - \frac{\Delta P}{3P X_{tp}(\alpha)} \right] \sqrt{\frac{P \Delta P}{T}} \quad (3.4-1)$$

$F_p$  = correction factor for line size vs. size of hole in valve ball

$C_v(\alpha)$  = valve flow coefficient which varies as a function of valve angle

$P$  = valve inlet pressure, psia

$\Delta P$  = pressure drop across valve, psi

$X_{tp}(\alpha)$  = pressure ratio  $\Delta P/P$  at which critical (sonic) flow occurs in valve,  $\alpha$  is a function of angle  $\alpha$

$T$  = air inlet temperature, Rankine



The constants  $F_p$ ,  $C_v$ , and  $X_{tp}$  in the valve flow formula (3.4-1) were experimentally determined.

The important parameter in sizing of the valves was the range of flow coefficient  $C_v$ , which was available as a function of valve angle. The BMSR flow and pressure requirements necessitated an operating range of  $C_v$  of about 1.8 to 35.

Figure 3.4-6 shows flow coefficients versus angle for ball valves of 2.54, 3.18, 3.81, and 5.08 cm (1.0, 1.25, 1.50, and 2.0 in) port sizes. As shown in the figure, any of these valves would be suitable for BMSR flow control.

The 3.18-cm (1.25-in) full port ball valves selected for the BMSR were a convenient compromise of availability, cost, and operational requirements. These valves, even though they were slightly larger than the minimum acceptable size, were the smallest that could be obtained in a compact configuration readily available in the small quantities needed here. The total performance envelope of the Kamyr RN-015 valve selected for the BMSR is shown in Figure 3.4-7. Here the valve inlet pressure and temperature were assumed equal to BMSR design operating values, and the valve flow rate was defined as a function of valve angle and pressure downstream of the valve.

As shown in the figure, there existed a low enough outlet pressure for every valve angle for which the mass flow reached a maximum limit. This resulted from the achievement of sonic flow in the valve. This condition was avoided in the BMSR by controlling the receiver outlet back pressure during tests.

Figures 3.4-8 and 3.4-9 show the measured flow characteristics of the heat exchanger flow-control valves after installation in the BMSR. These data were obtained during receiver hot-flow tests (Section 6.0). Figure 3.4-8 shows the combined parameters  $F_p$  and  $C_v$  as a function of valve angle, and Figure 3.4-9 shows values of  $X_{tp}$ .

Figure 3.4-6. Comparison of Ball Valve Airflow Capability With BMSR Requirements

## Comparison of Ball Valve Airflow Capability With BMSR Requirements

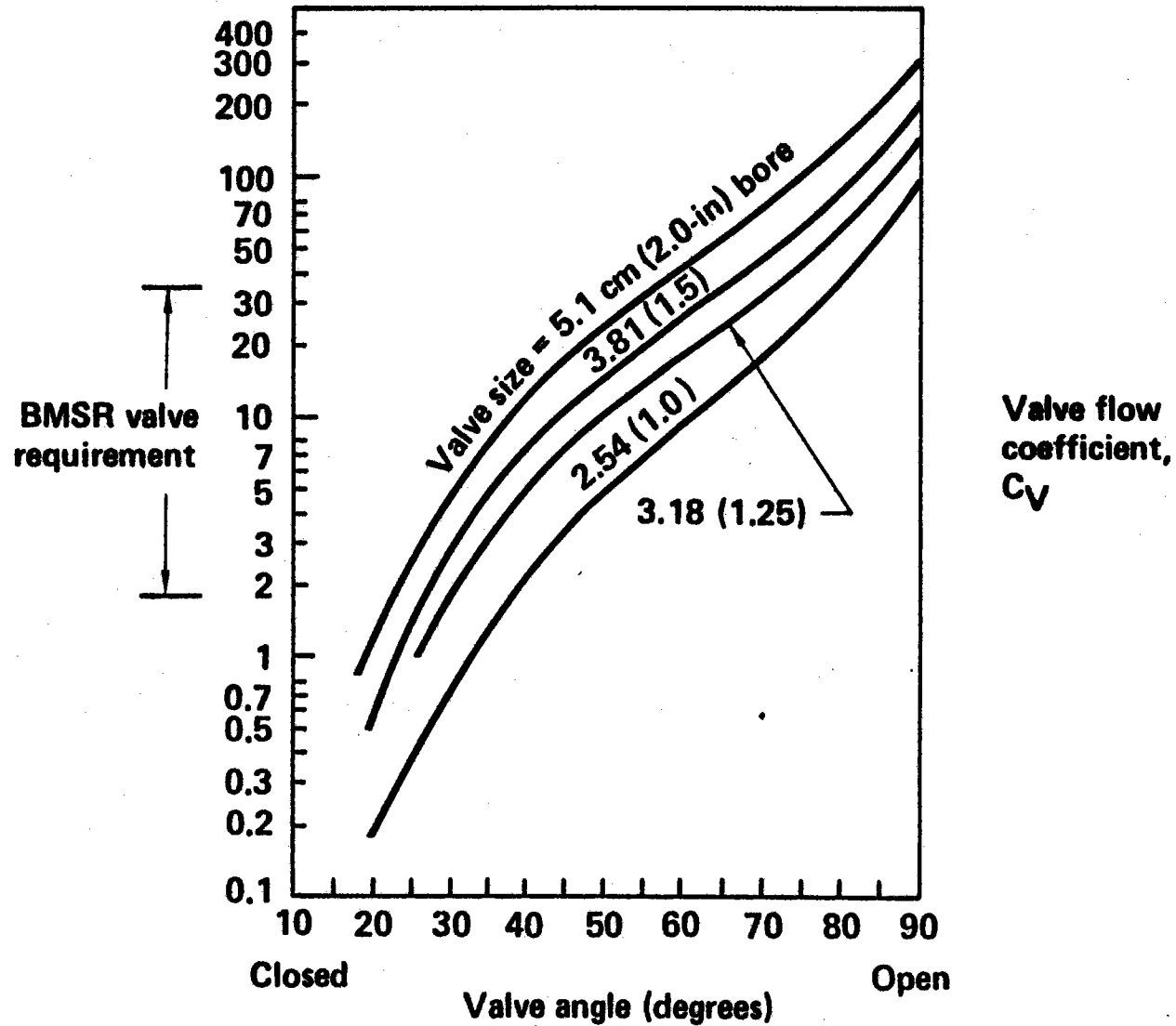


Figure 3.4-7. Flow Control Valve Performance

# Flow Control Valve Performance

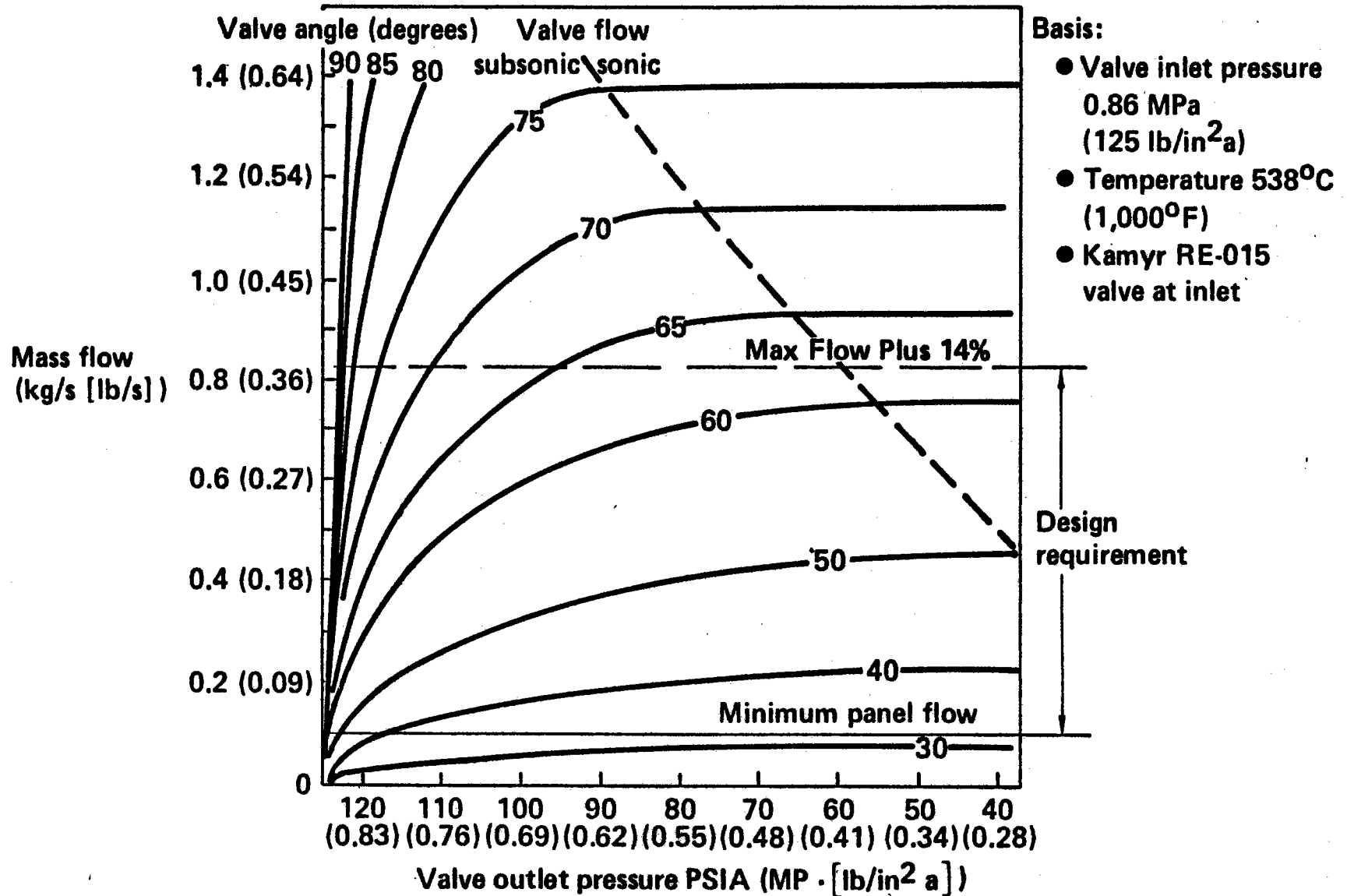


Figure 3.4-8. Flow Coefficient for BMSR Valves

# Flow Coefficient for BMSR Valves

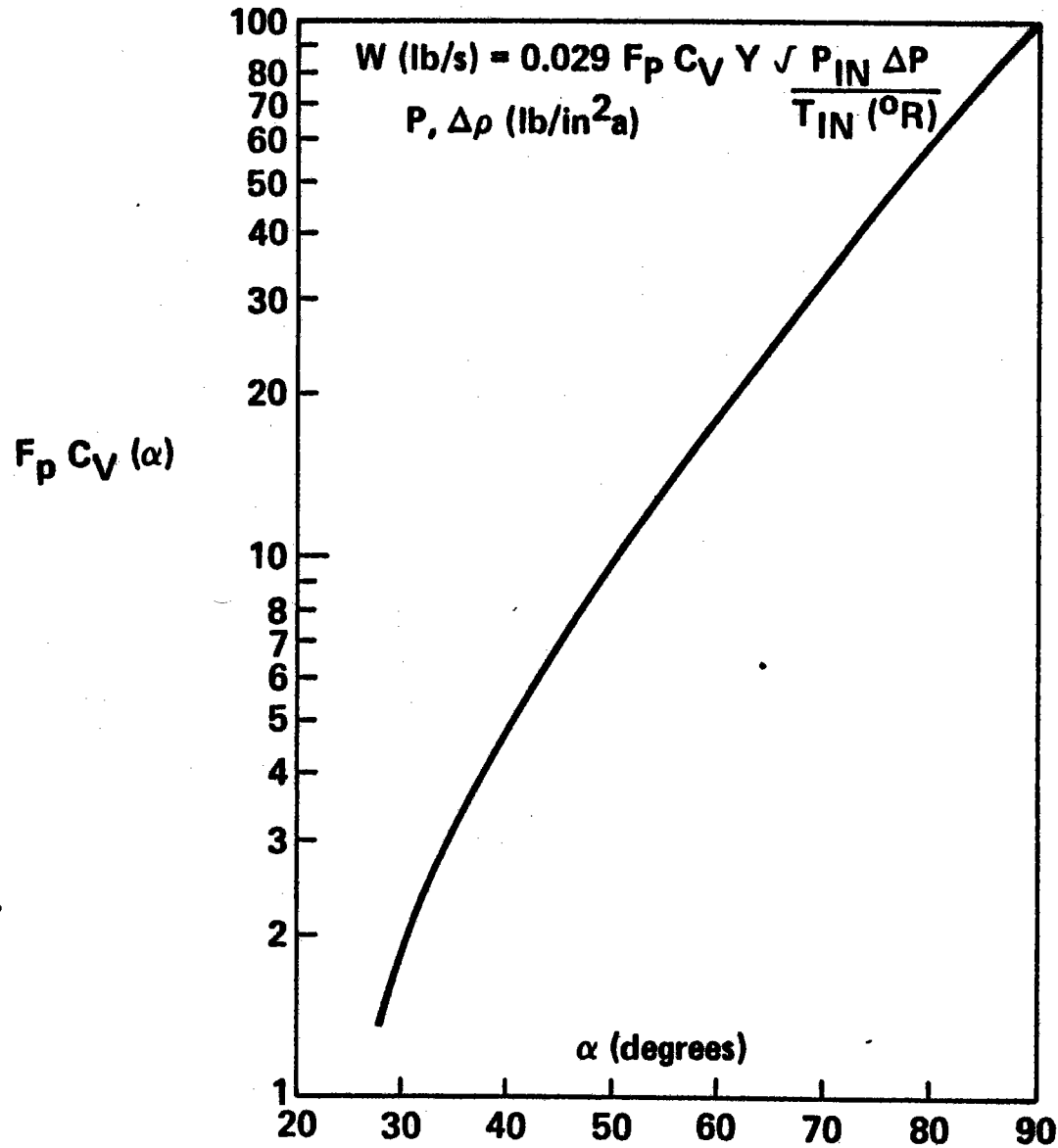
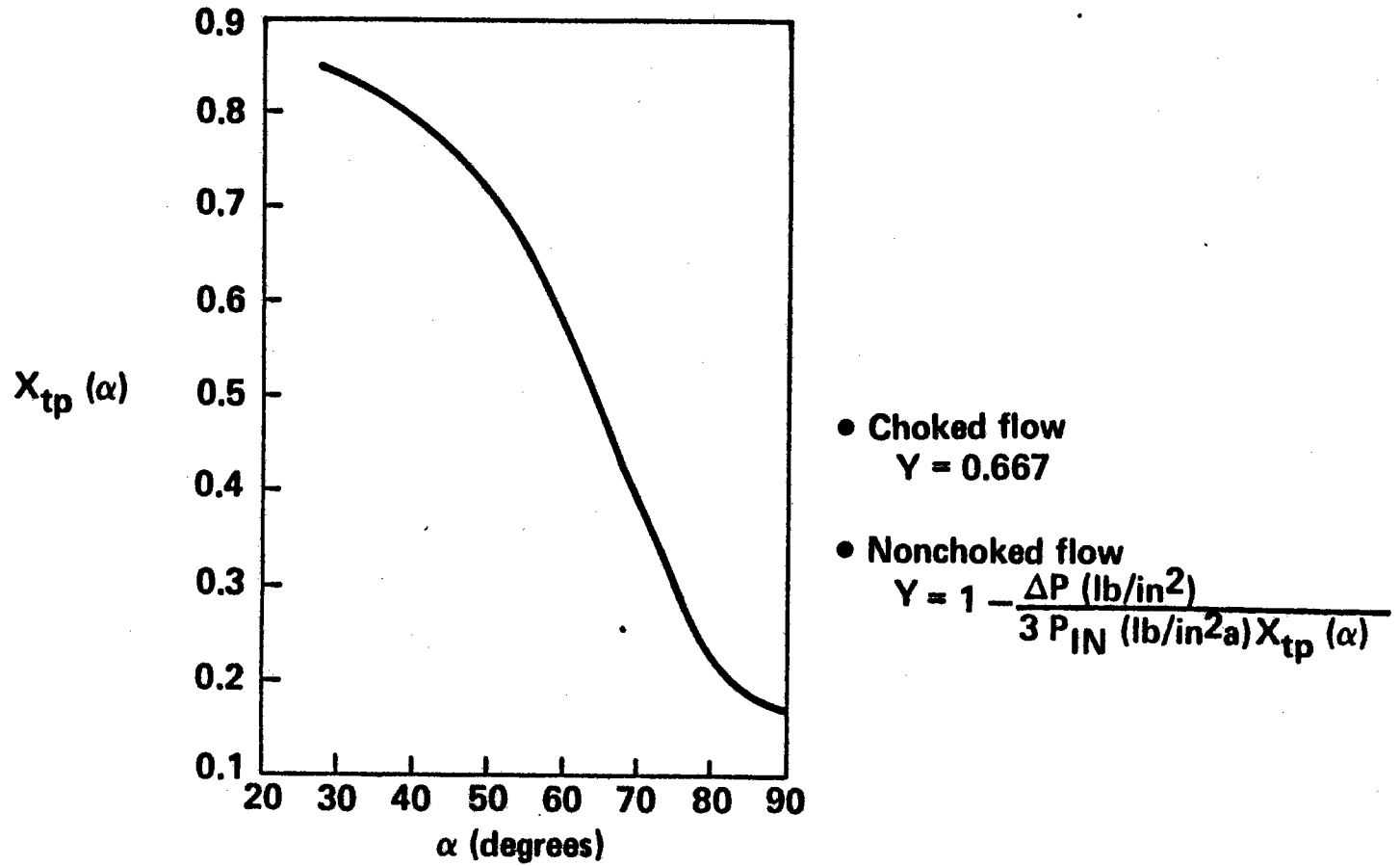


Figure 3.4-9. Critical Pressure Ratio for BMSR Valves

## Critical Pressure Ratio for BMSR Valves



## Heat Exchanger Tubes

As discussed in Section 3.1, "Thermal-Scale Modeling," the inside diameter of thermal model heat exchanger tubing had to be increased over the preferred thermal model heat exchanger tubing size to provide an acceptable pressure loss in the BMSR heat exchangers. Independent detailed studies of the heat exchanger tube pressure losses are presented here. Their objectives were to:

- a. Verify acceptability of selected BMSR heat exchanger design for pressure losses
- b. Identify manufacturing parameters critical to pressure-loss performance and establish the appropriate manufacturing tolerances for heat exchanger tubes

An independent analysis was conducted to verify heat exchanger pressure losses for the nominal heat exchanger design case assuming negligible manufacturing uncertainties. The tube pressure losses were determined by forward-difference computing methods. Here, the flow rate, local air temperature and pressure, and local tube conditions, at a position  $X$ , determined the pressure at a new location,  $X + \Delta X$ , further along the tube. In general,

$$P(X + \Delta X) = P(X) - \rho(X) V(X)^2 \left( f \frac{\Delta X}{D} + K(X) \right) \quad (3.4-2)$$

where,

$P$  = pressure at location  $X$  or  $X + \Delta X$

$\rho(X)$  = air density at location  $X$

$V(X)$  = air velocity at location  $X$

$f$  = friction factor (for frictional pressure losses)

$D$  = tube inside diameter

$K(X)$  = loss coefficient to account for local flow disturbances at point  $X$  such as abrupt expansions, contractions, and tubing bends

By continuously updating the local air density and air velocity while iterating along the length of the tube, this computational technique accounted for significant compressability effects in the BMSR heat exchangers. Local air temperatures were also varied to account for the absorption of solar heat as the air passed through the heat exchangers.

The variables in equation 3.4-2 are available in the literature covering turbulent airflow through tubes. Well-documented experimental data are available for the pressure-loss friction factor,  $f$ . The variation of air density,  $\rho$ , with pressure and temperature is also well known. However, the selection of pressure-loss coefficients,  $K$ , are subject to engineering judgment.

The assumptions used in these pressure-loss computations are presented in Figure 3.4-10. The nominal tube geometry is shown, along with the coefficients used for flow contractions, expansions, and tube bends.

Figure 3.4-11 shows the pressure-loss characteristics computed for the standard BMSR heat exchanger panel. Outlet pressures were plotted for heat exchanger panel flow rates from 10% to 115% of the 0.338-kg/s (0.745-lb/s) panel design flow rate. As indicated in the figure, the airflow mach number and the inlet-to-outlet pressure differences became excessively high at inlet pressures of less than about 0.70 MPa (100 lb/in<sup>2</sup>a). The design pressure loss for heat exchanger tubes, 0.228 MPa (33 lbs/in<sup>2</sup>a), Table 3.401, occurred at an inlet pressure of 0.81 MPa (117 lb/in<sup>2</sup>a), which was slightly less than the expected panel-inlet pressure for normal full-power operation of the receiver.

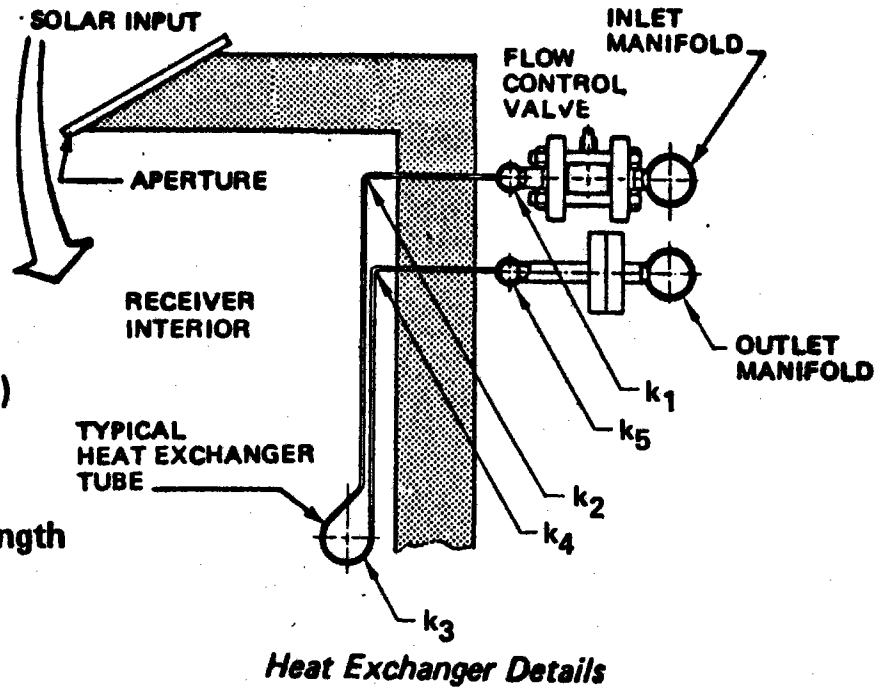
The detailed pressure-loss analysis showed that the selected BMSR heat

Figure 3.4-10. Basis for Computations of Heat Exchanger Pressure Losses

## Basis for Computations of Heat Exchanger Pressure Losses

### Assumptions

- Air temperatures
  - Inlet 538°C (1,000°F)
  - Outlet 816°C (1,500°F)
- Tube configuration
  - 5.08 mm (0.2 in) i.d.
  - 1.37m (54 in) heated length
  - 0.30m (12 in) preentry and postexit lengths
- Pressure loss coefficients



### Velocity heads lost

$k_1$ Abrupt contraction at tube inlet	1.25
$k_2$ 90-deg bend, 3.0 tube diameter radius	0.15
$k_3$ 180-deg bend, 4.6 tube diameter radius	0.22
$k_4$ 90-deg bend, 3.0 tube diameter radius	0.15
$k_5$ Abrupt expansion at tube outlet	0.30



exchanger exhibited marginally high pressure losses. The nominal configuration, not accounting for manufacturing tolerances and possible errors in the analysis, consumed all of the 0.228-MPa (33-lb/in<sup>2</sup>) pressure-loss allocation for heat exchanger tubes. The detailed design and fabrication of heat exchangers had to be carefully monitored to avoid even higher pressure losses that could result from undersized tubing, sharp-edged entry from inlet header, flow restrictions due to tube-to-header weld underbead, and ovality produced when bending tubing.

In addition to possibly exceeding the design allocation for heat exchanger pressure losses, higher than nominal pressure losses in a few tubes of the heat exchanger would reduce their airflow. As mentioned earlier, reduced flow in one tube resulted in an overheating of that tube.

Four potential sources of reduced tube flows or excessive pressure losses were studied to determine the amount of dimensional change that could produce a 2% variation of pressure loss compared to the nominal pressure loss at the design point (Figure 3.4-11). A 2% pressure-loss allowance for each of these manufacturing tolerances could accumulate to a total of +8% on any one heat exchanger tube. The resulting mass-flow variation for that tube would be about +4% and the resulting variation of gas outlet and tube temperature would be about 110C (200F).

The most critical manufacturing tolerance was on the inside diameter of the heat exchanger tubing. Figure 3.4-12 shows pressure loss variations that resulted at full receiver flow for tube sizes slightly larger or smaller than the 5.08-mm (0.198-in) nominal size. The allowance of a +2% pressure-loss variation required a tubing size tolerance of +0.017 mm (0.0007 in). A slightly higher tolerance, +0.025 mm (+0.001 in), was specified for the heat exchanger tubing. However, because the tubing was fabricated in one lot to a special order, the actual tolerance for delivered tubing was less than the 0.017-mm (0.0007-in) design goal.

Another potentially critical problem in heat exchanger manufacturing was the variation of tube-inlet geometry at the connection to header pipes. At BMSR air velocities, a sharp-edged entry could produce twice the entry pressure

Figure 3.4-11. Pressure Losses in BMSR Heat Exchanger Tubes

## Pressure Losses in BMSR Heat Exchanger Tubes

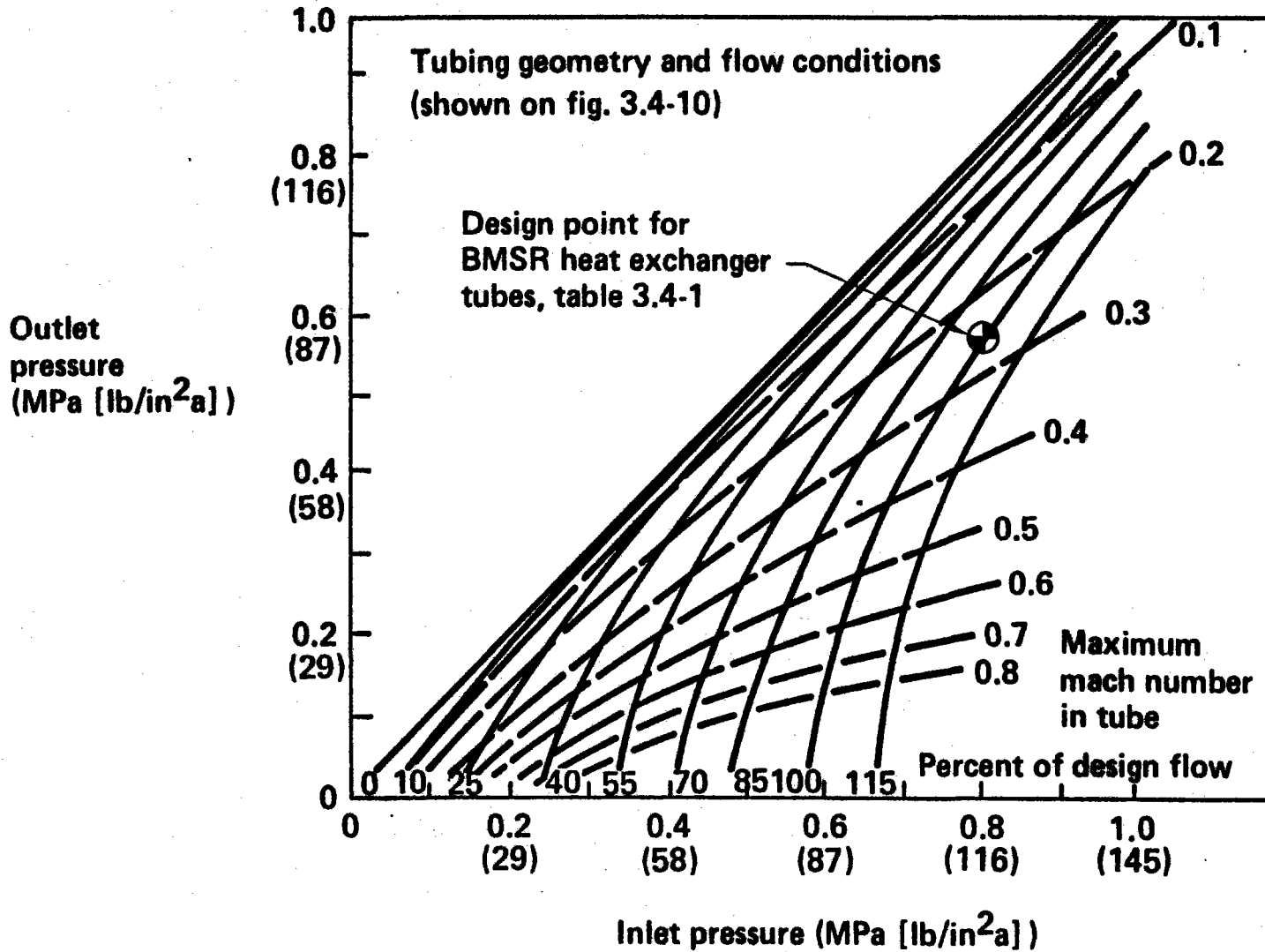
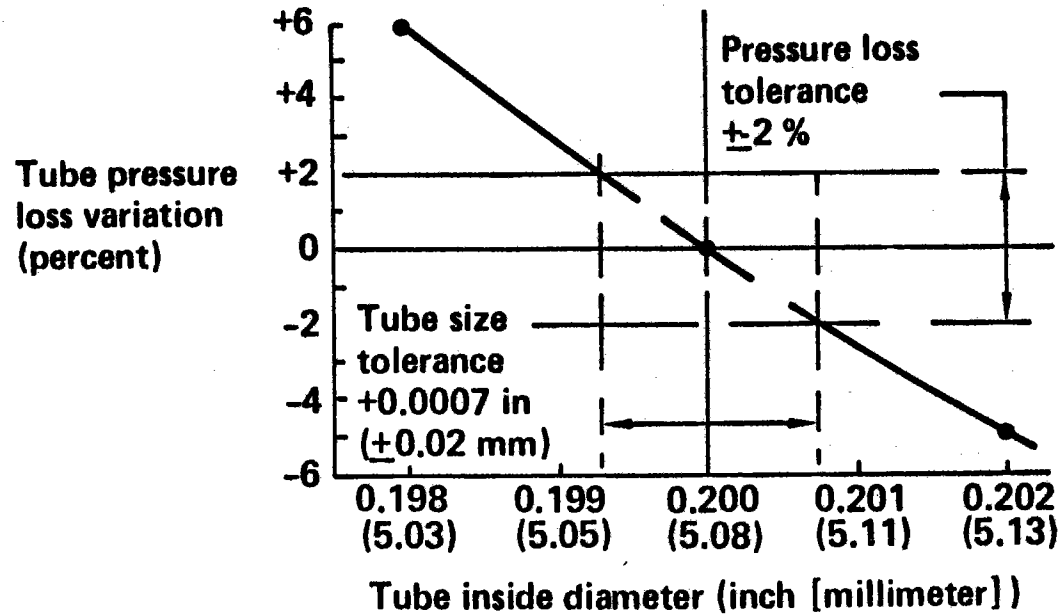


Figure 3.4-12. Effects of Tube Size Variation on Pressure Loss

## Effects of Tube Size Variation on Pressure Loss



loss as a smooth-radiused-tube entry. This corresponded to a potential of 7% variation of overall pressure loss for the heat exchanger. The details of tube-to-header welds could also produce significant pressure-loss variations. Figure 3.4-13 shows estimates of the additional pressure losses at full flow that resulted if the tube-to-header weld bead intruded, constricting the tube-inlet flow area. The airflow disturbances caused by entry geometry and weld-bead intrusion were combined rather than independent effects, as shown here. Taken individually, however, either one of these could have produced significant variations of pressure loss, flow rate, and outlet air temperature from tube to tube on the heat exchanger panel.

The potential problems with tube inlet geometry were avoided, and tube-to-header welds were simplified by the swaged-tube weld-joint design shown in Figure 3.4-14. This increase of the local tube inside diameter from 5.08 to about 6.8 mm (0.20 to 0.27 in) reduced the air-inlet velocity by 45% and the corresponding pressure losses at the tube inlet by 70%.

Finally, it was found that tube flattening (ovality) that occurred during bending of the heat exchanger tubing could be controlled by proper support. The result of ovality was to increase the local air velocity. This acceleration and deceleration of the airstream produced measurable net pressure losses. Analyses determined that a 1% increase of overall heat exchanger pressure loss would result if the ratio of minimum to maximum tube dimensions (minor to major axis ratio of the flattened tube) were 70%. Because this constituted a more severe flattening of bends than obtained by normal manufacturing practice, no special tolerances were required on the heat exchanger specification.

#### Combined Heat Exchanger and Valve

The heat exchanger and valve, operating with an inlet air pressure of 0.86 MPa (125 lb/in<sup>2</sup>a) provided a heat exchanger airflow which, upon absorption of solar heat, left the heat exchanger at the desired temperature. As solar heat loads changed due to test conditions, the heat exchanger airflow was varied. The range of flow rates achieved by the panel and valve determined the range of solar heat loads over which constant receiver outlet

Figure 3.4-13. Effects of Tube-to-Header Weld-Bead Intrusion on Pressure Loss

## Effects of Tube-to-Header Weld-Bead Intrusion on Pressure Loss

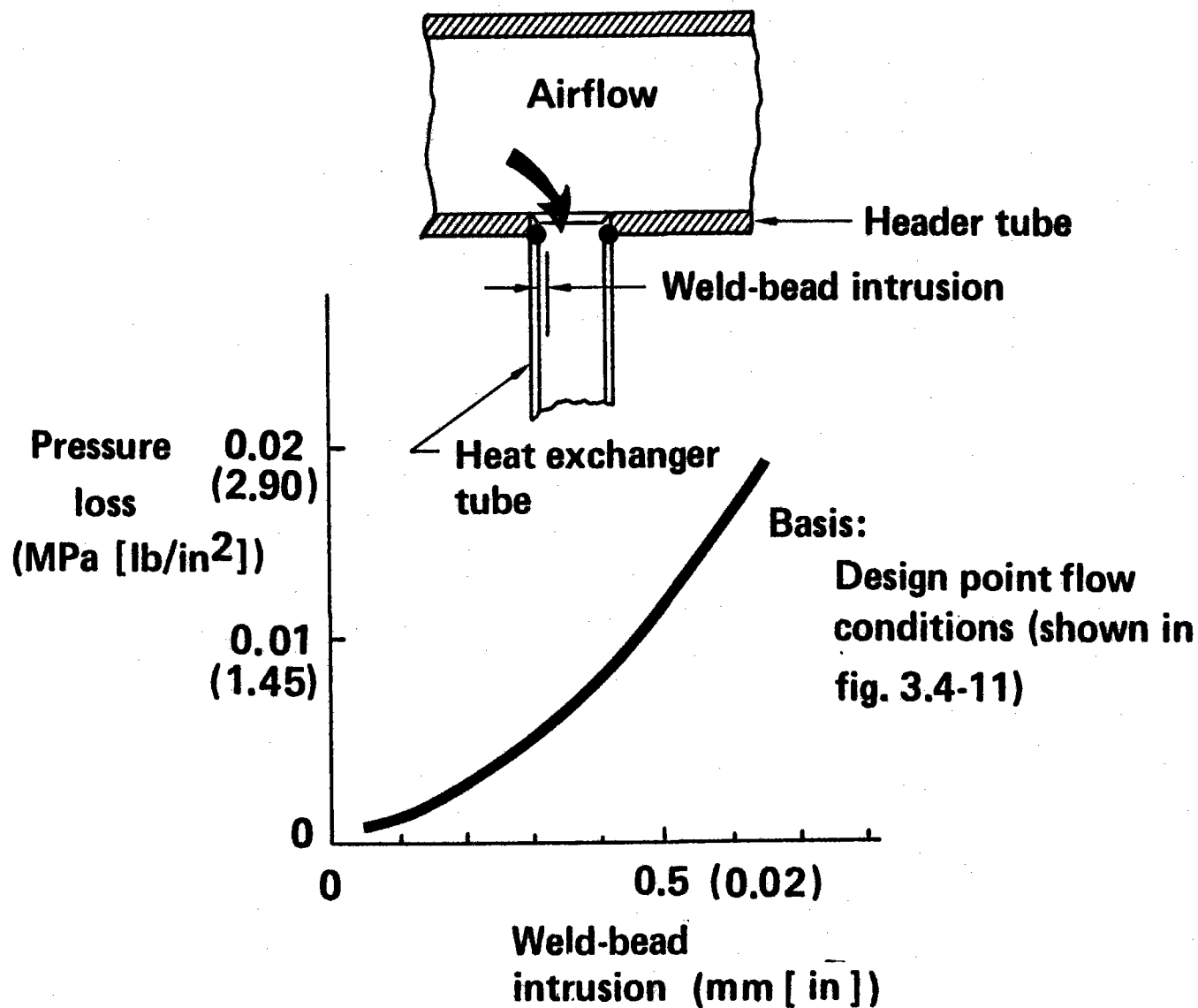
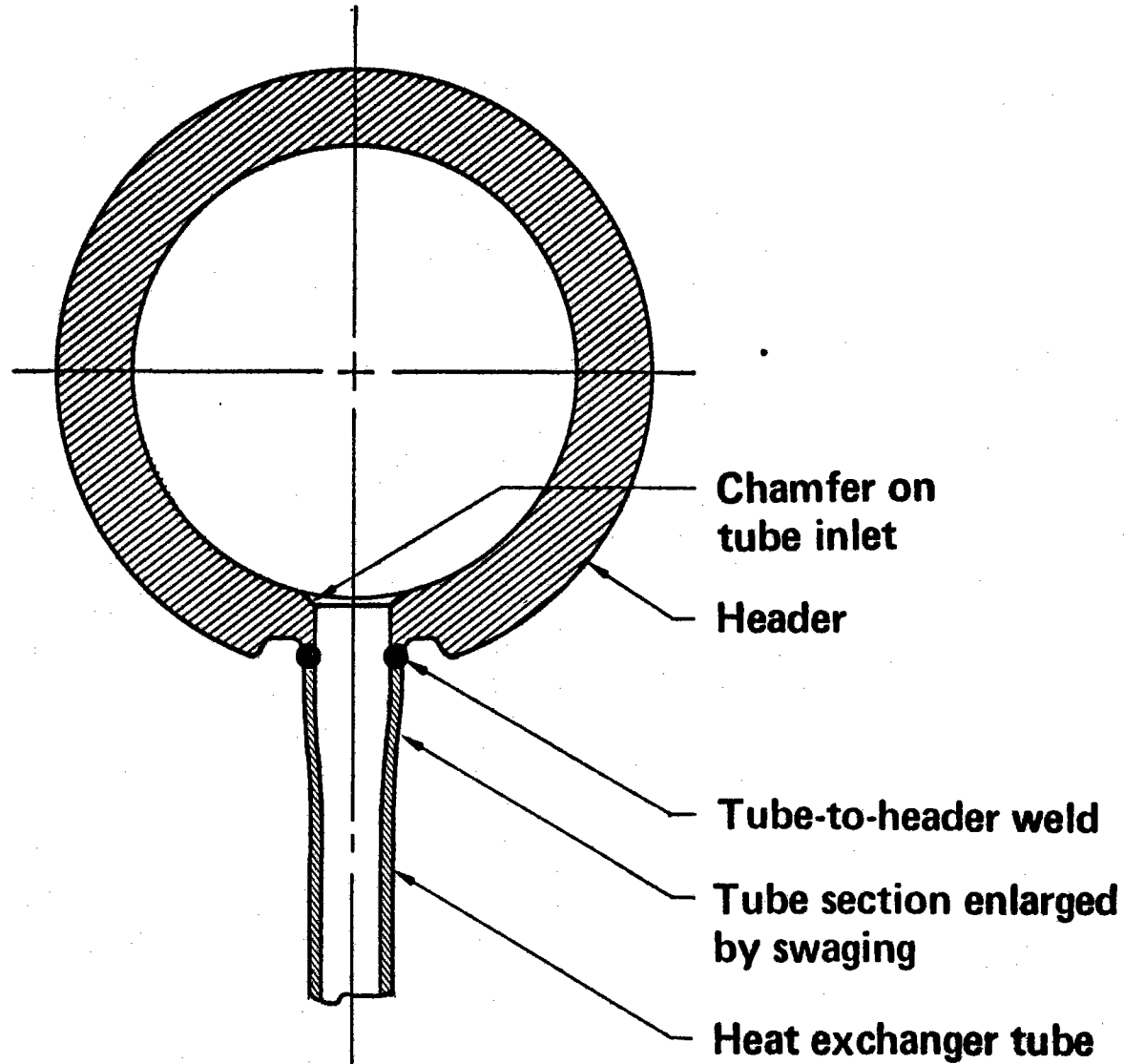


*Figure 3.4-14 As-Built Configuration of Tube-to-Header Connection*

## As-Built Configuration of Tube-to-Header Connection



temperatures were obtained.

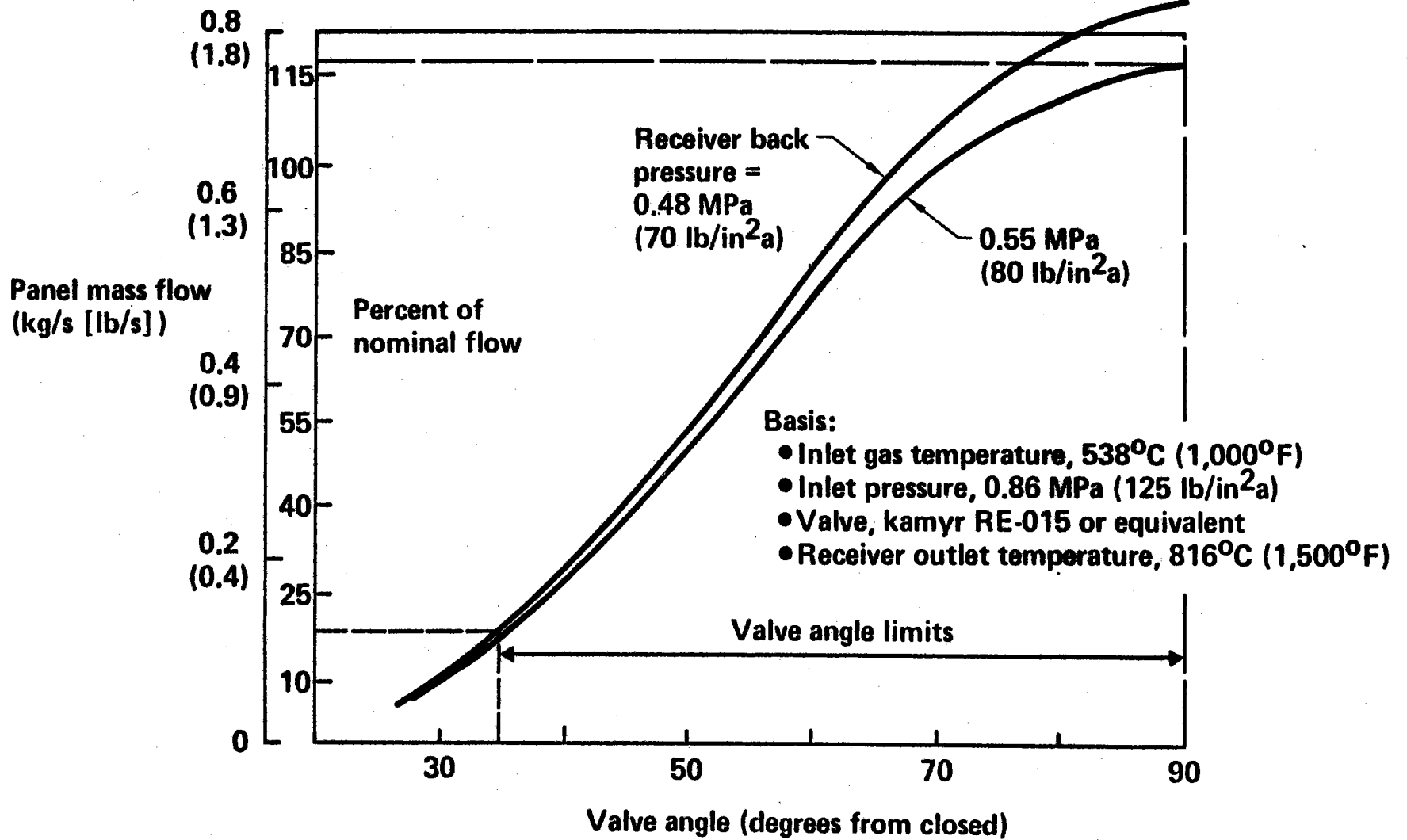
Two factors influenced the heat load and flow-control range of the heat exchanger and valve. The first of these was the BMSR back pressure, which was controlled by the back-pressure valve on the air supply equipment skid (Figure 3.4-1). The back-pressure setting affected the total inlet-to-outlet pressure difference across the receiver. If this pressure was too low, the heat exchanger pressure losses increased rapidly. In fact, with reducing back pressure, the maximum receiver flow rate with panel valves fully open increased initially but then began to decrease because of heat exchanger pressure loss. Back pressure was desired during BMSR tests, optimizing the maximum flow rate through the heat exchanger. This pressure was approximately 0.5 MPa (75 lb/in<sup>2</sup>a).

The minimum controlled flow rate through the receiver defined its lowest part load power at which the desired outlet air temperature could be obtained. Ideally, the flow could be reduced to zero; however, with no airflow, the thermocouple located in the outlet header did not sense the tube outlet air temperature. Some minimum flow was needed to ensure that air temperatures at the thermocouple were equal to those at the tube outlets. The minimum angle for which the flow ports through the ball valve began to open was between 26 and 28 deg of rotation from the mechanically closed position. Because of the uncertainty in measurements of the actual point of opening and the desire to guarantee continuous airflow past the thermocouple, a conservative minimum valve angle of 35 deg was used. The valve angular motion was limited from 35 to 90 deg by mechanical stops located inside the valve actuator.

The effect of these choices of receiver back-pressure and BMSR flow-control valve limit stops is shown in Figure 3.4-15. The back-pressure range of 0.48 to 0.55 MPa (70 to 80 lb/in<sup>2</sup>a) represented a reasonable tolerance to be placed on the back-pressure controller of the auxiliary equipment skid. The maximum panel flow rate of about 0.38 kg/s (0.84 lb/s) was 118% of the nominal design flowrate. This meant that individual heat exchangers on the BMSR could operate at up to 118% of normal solar heat load (up to 118-kW heat transfer per panel) without losing control of their outlet air

Figure 3.4-15 Flow Performance for BMSR Test Conditions

# Flow Performance for BMSR Test Conditions





temperature. The 35-deg limit stop resulted in a minimum-controlled airflow through the panel of about 18% of the nominal design flow rate. This meant that heat exchanger outlet temperature could be controlled at panel heat transfer rates as low as 18 kW.

### 3.5 RECEIVER THERMAL ANALYSIS

This section describes the pretest thermal analysis of the bench model solar receiver. Posttest thermal analysis is presented in Section 11.0.

#### 3.5.1 General Requirements

The purpose of the pretest thermal analysis was to develop operational procedures for use during the receiver testing. Being able to anticipate receiver reactions during the different tests allowed a more efficient utilization of available testing time. The thermal analysis provided data predictions that were used to establish the data-gathering system in a way to gain an critical test data in the most efficient manner. Thermal analysis also supplemented experimental data by allowing evaluation of to areas of the receiver where instrumentation was unavailable. For example, the interior cavity insulation surface temperature could be extrapolated based on the insulation thermocouple readings and thermal analysis.

Finally, an important purpose of the thermal analysis was to provide a basis from which the posttest data correlation could be accomplished. The thermal analysis refined by correlation with test data provided an invaluable analytical tool for evaluating solar receiver thermal performance.

#### 3.5.2 Thermal Model Development

The methodology used for this study involved (1) developing a thermal nodal model of the problem and (2) inputting the nodal model to a generalized transient thermal analysis computer program. The purpose of developing a thermal nodal model was to simplify the actual receiver configuration to a form that could be handled analytically. The physical system was sectioned into an array of discrete volumes. The mass of each volume element was "lumped" at a point, or node, within the volume that it represented. The paths for heat transfer by conduction, convection, and radiation from one node to another were represented by connecting elements. Figures 3.5-1 to 3.5-5 represent the thermal nodal network developed in this study. The nodal network simulated the action of the solar input from the collector field, the air supply skid and interface piping, and the BMSR. The network

Figure 3.5-1 Receiver Thermal Nodal Model

## Receiver Thermal Nodal Model

### Details of model:

- Structure, 33 nodes
- Insulation, 141 nodes
- Heat exchangers
  - Tubing, 32 nodes
  - Gas, 40 nodes
- 260 solar sources

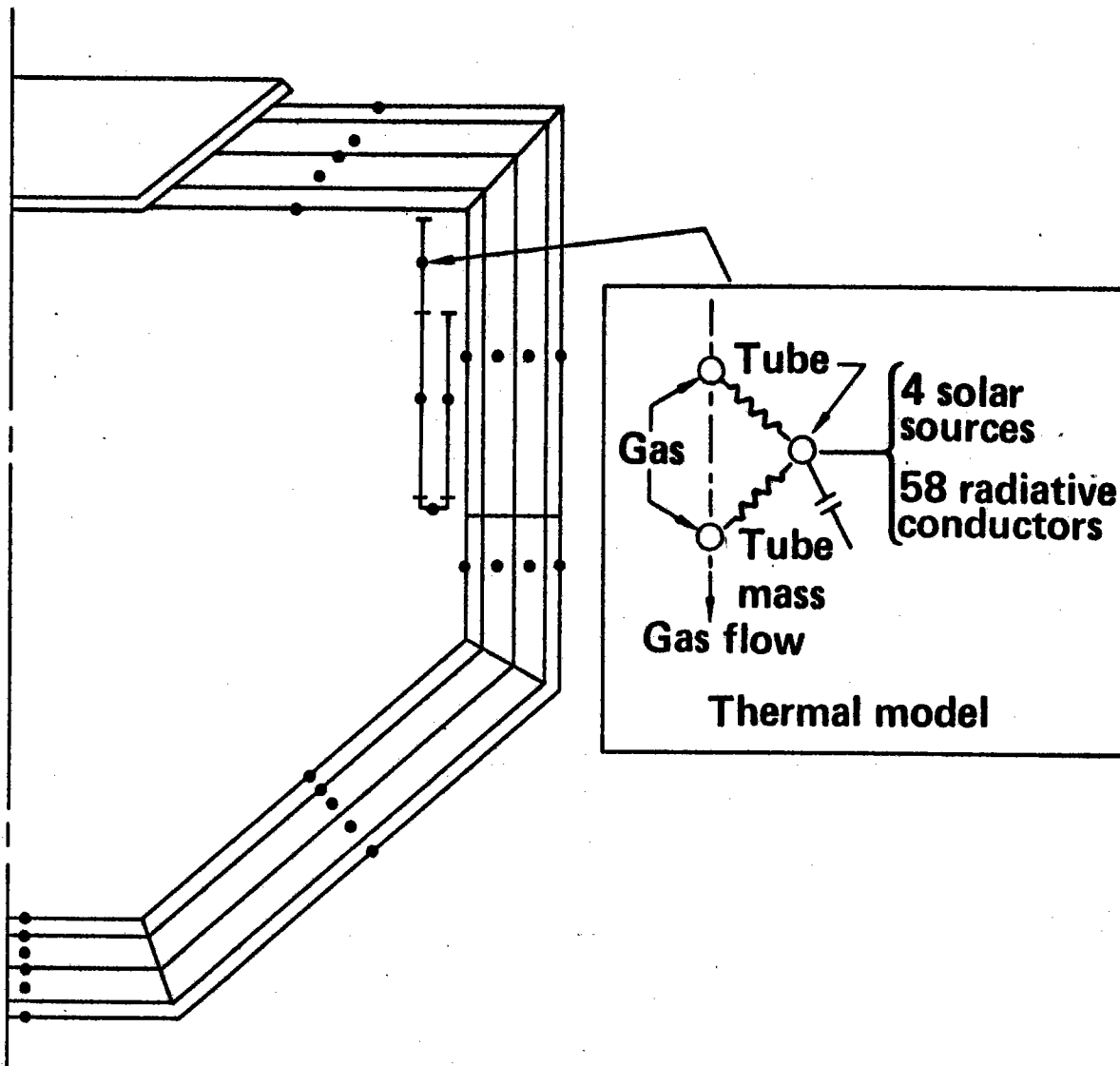
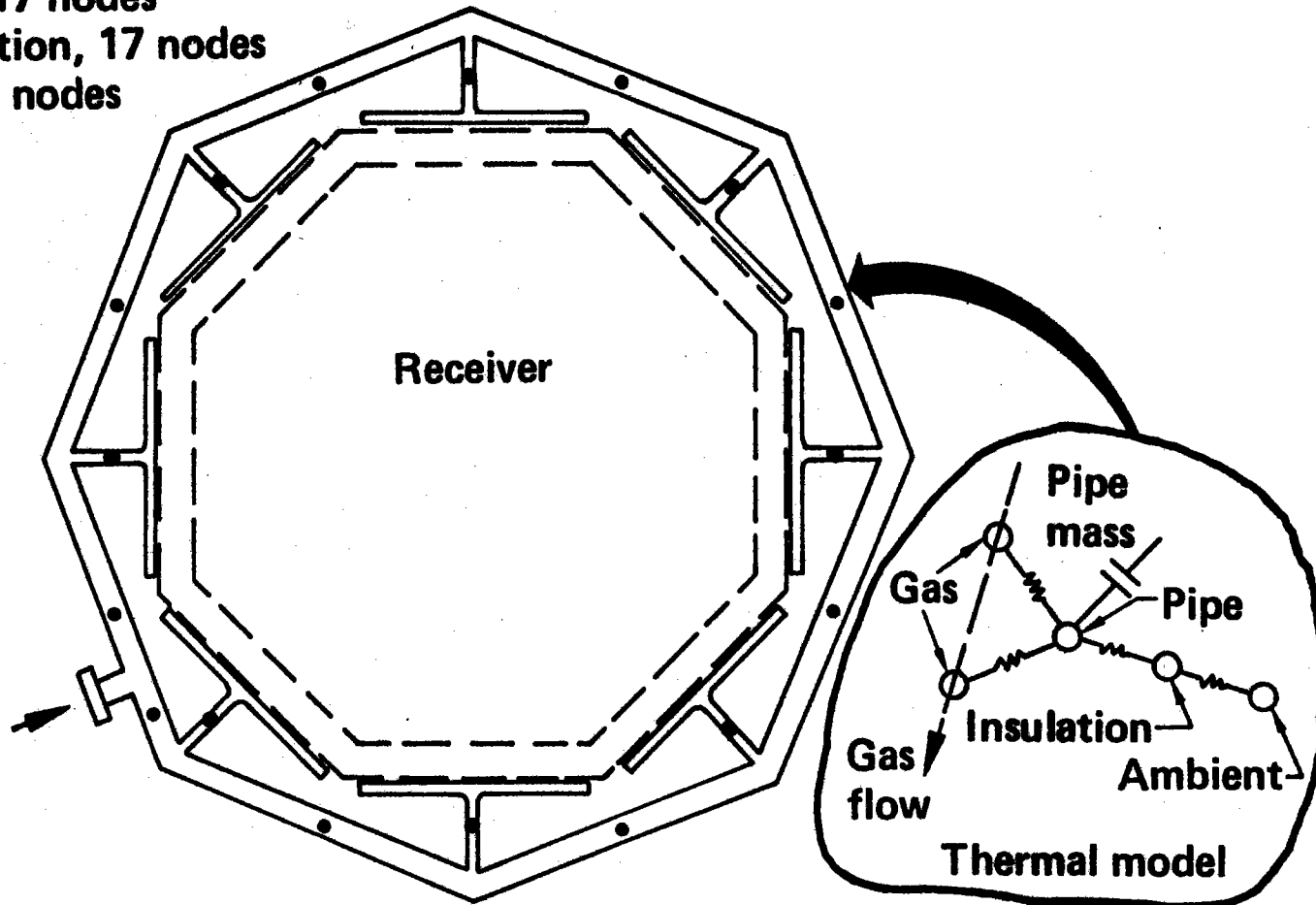


Figure 3.5-2 Inlet Manifold Thermal Nodal Model

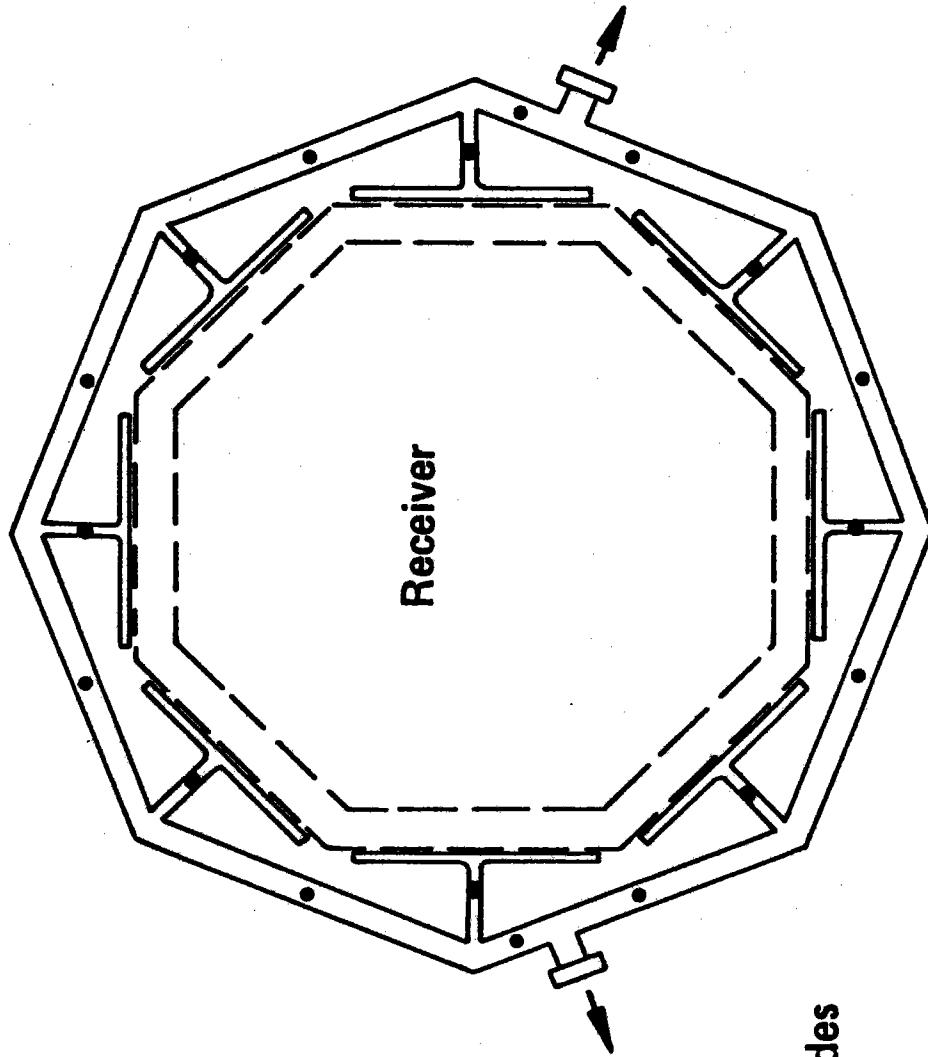
## Inlet Manifold Thermal Nodal Model

**Details of model:**

- Pipe, 17 nodes
- Insulation, 17 nodes
- Gas, 8 nodes



*Figure 3.5-3 Exhaust Manifold Thermal Nodal Model*  
**Exhaust Manifold Thermal Nodal Model**



- Details of model:**
- Pipe, 18 nodes
  - Insulation, 18 nodes
  - Gas, 18 nodes

Figure 3.5-4 Interface Piping Thermal Nodal Model

## Interface Piping Thermal Nodal Model

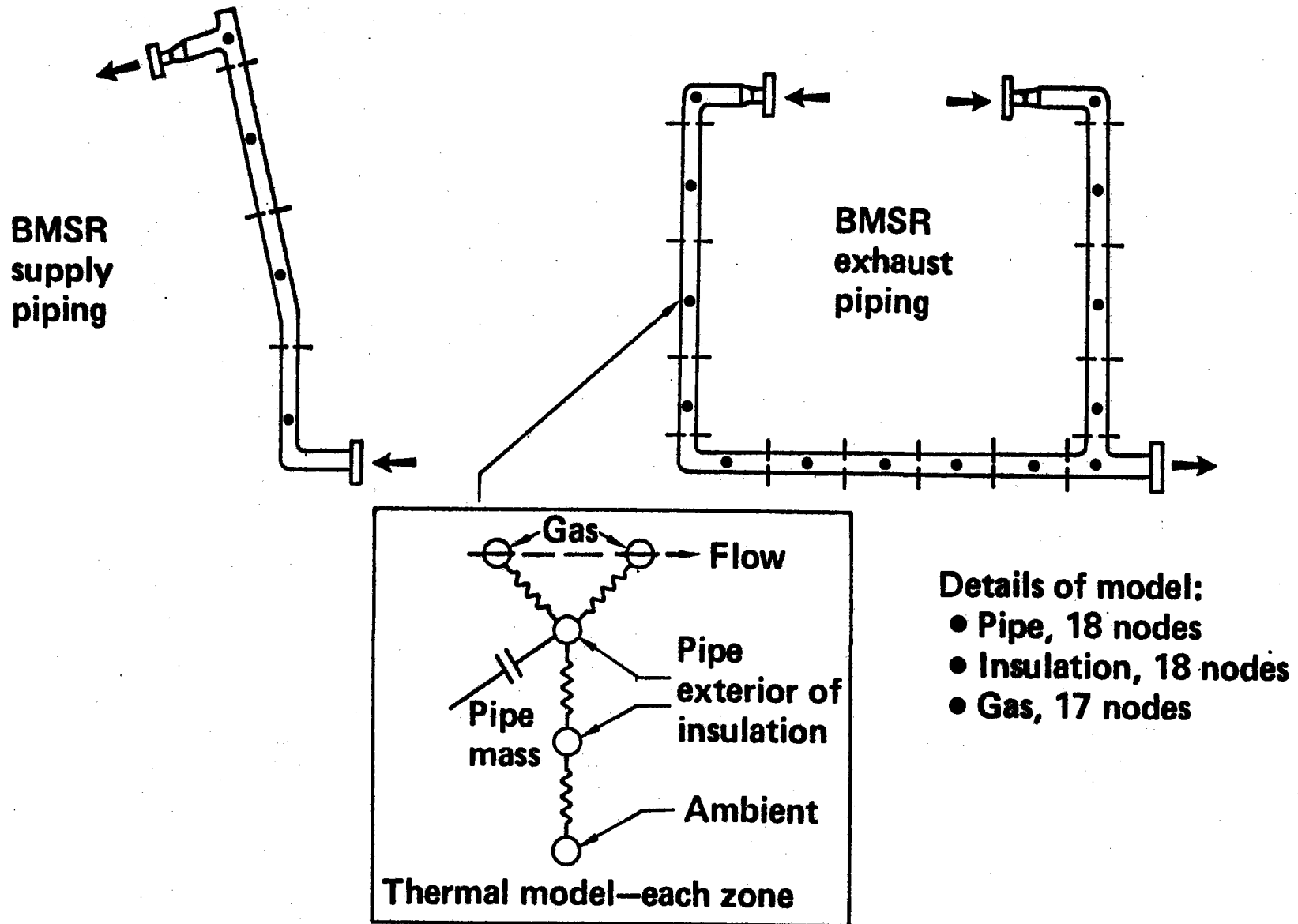
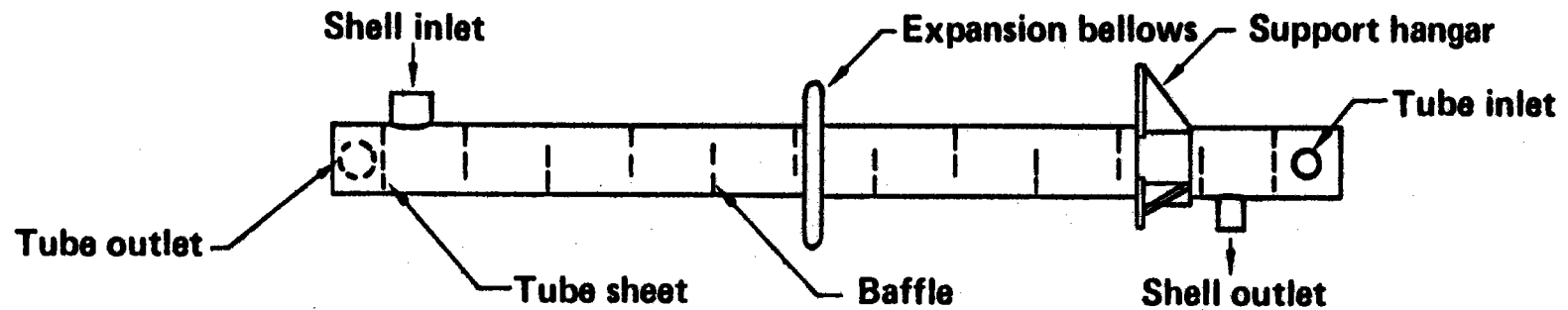


Figure 3.5-5. Air Supply Recuperator Thermal Nodal Model

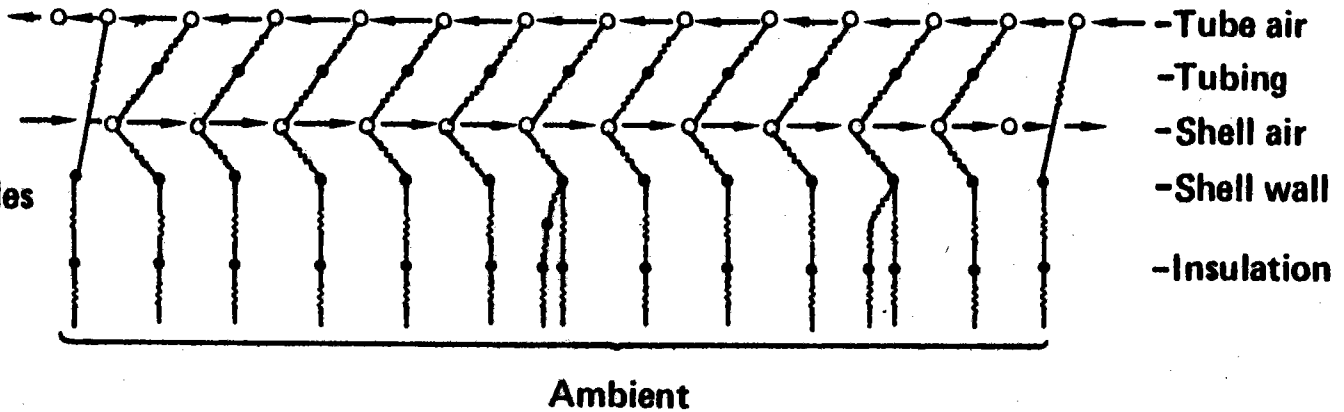
## Air Supply Recuperator Thermal Nodal Model



121

### Details of model:

- Tubing, 11 nodes
- Gas, 26 nodes
- Shell, 13 nodes
- Insulation, 17 nodes



contained 434 nodes. The number of nodes used was a compromise between increased accuracy and increased computing cost, the latter varying approximately with the square of node number. To show all the interconnections between the nodes would result in an unwieldy schematic. Representative schematics are shown in the nodal network figures to demonstrate the typical interconnection between nodes. For example, Figure 3.5-1 shows each tube wall node being connected to two gas nodes and 58 other cavity and ambient nodes by radiative connectors. Four solar sources represent the solar input from four quadrants of the heliostat field. The division of the solar field assumed is presented in Figure 3.5-6.

The thermal model contained 436 conductors that simulated conduction and external convection. Temperature-dependent thermal conductivity for the insulation was considered. Figure 3.5-7 presents the assumed thermal conductivity variations. A total of 2121 radiators were used to define the complex radiation environment inside the receiver cavity. The methodology used in calculating the radiation view factors was described in Section 3.2.3. The same Monte Carlo ray-tracing computer code was used except that infrared cavity surface radiative property values were used. A summary of the surface radiative properties for the cavity materials is given in Table 3.5-1. The effects of temperature-dependent insulation infrared emissivity were applied as corrections to the calculated view factors.

**Table 3.5-1 Cavity Surface Radiative Properties**

	<b>Solar absorptance</b>	<b>Infrared emissivity</b>
<b>Inconel 617 H/X tubes</b>	<b>0.89</b>	<b>0.83</b>
<b>Kaowool insulation</b>	<b>0.29</b>	<b>0.37</b>
<b>Saffil insulation</b>	<b>0.21</b>	<b>0.29</b>

The energy flux input to each surface element on the cavity interior was also calculated using the Monte Carlo ray-tracing program as described in Section 3.2.3. These 260 energy sources included the effects of direct and rereflected solar. These data were tabulated as a function of time of day for each of the four solar heliostat field quadrants of Figure 3.5-6. As an



Figure 3.5-6 Heliostat Field Zones Considered in Thermal Analyses

# Heliostat Field Zones Considered in Thermal Analyses

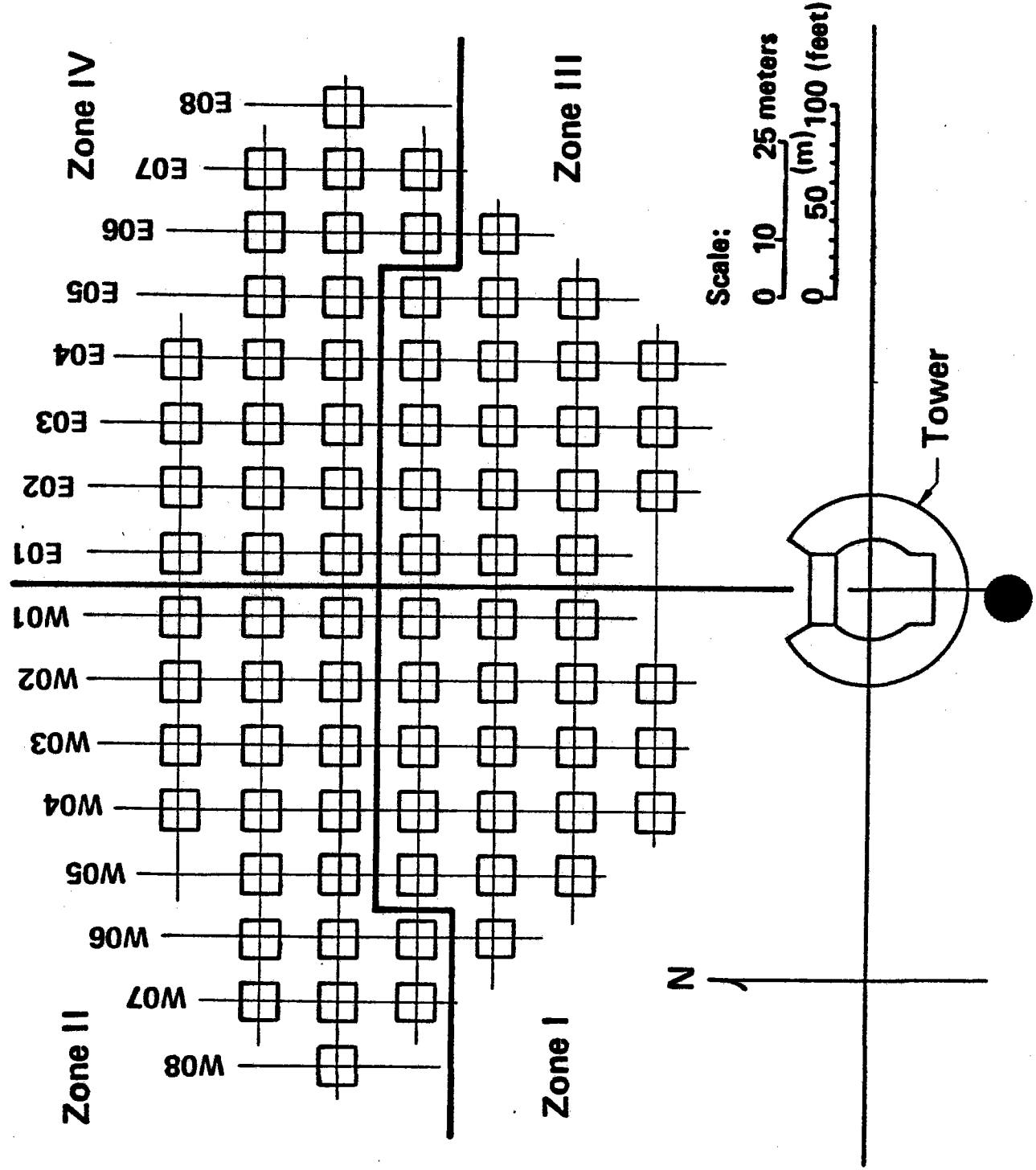
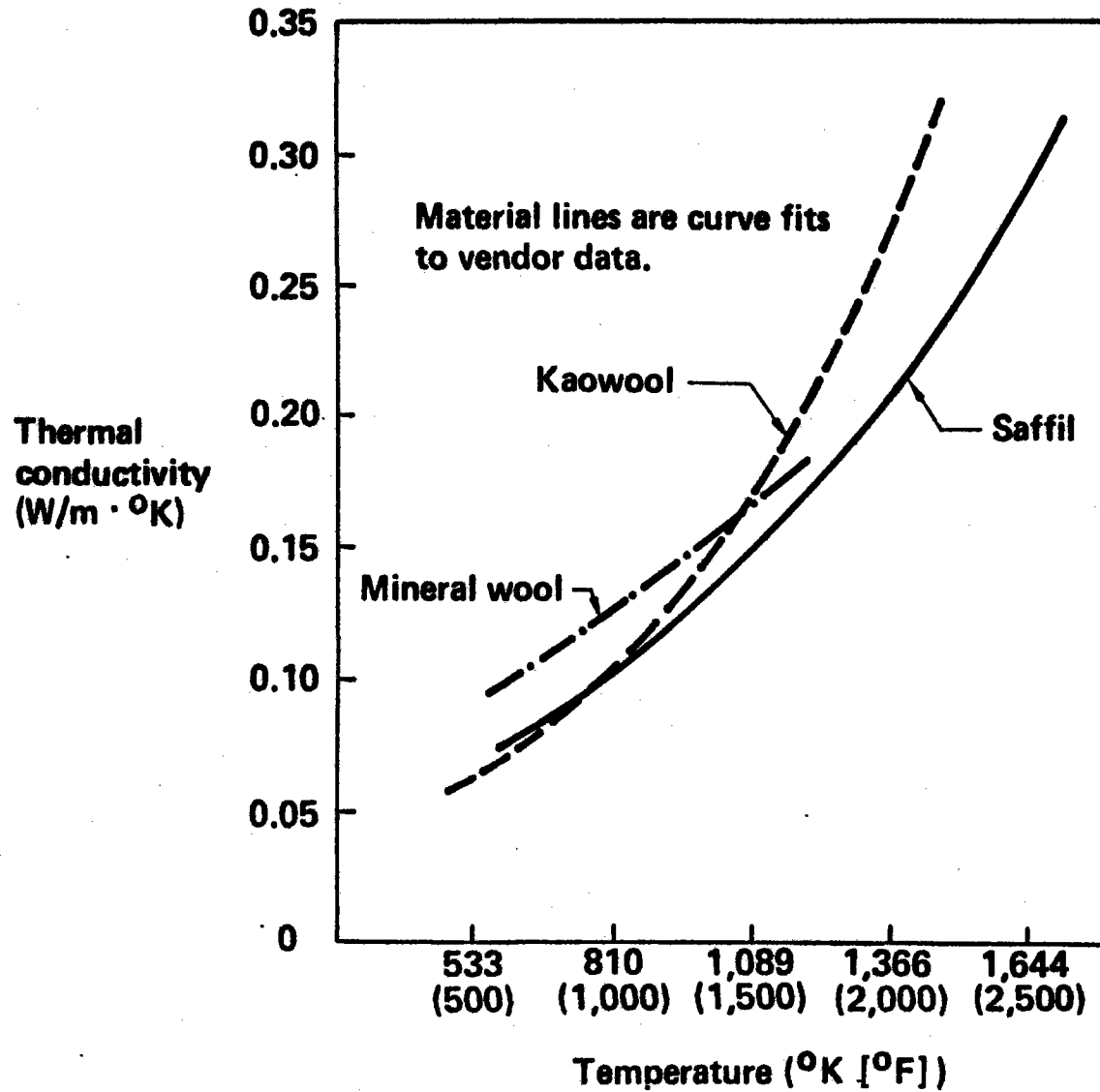


Figure 3.5-7. Thermal Conductivity of Insulation Materials Comparison

## Thermal Conductivity of Insulation Materials Comparison



example, Figure 3.2-7 presented the sum of the four quadrant energy inputs to the various sections of the receiver cavity assuming an input of 1.0 MWt through the aperture at solar noon.

The forced convective heat transfer inside the tubes was modeled by energy sources calculated from tube-wall temperature, gas mass-flow rate, gas fluid and thermal properties, and convective heat transfer data correlations. Figure 3.5-8 presents the assumed variation of heat capacity, viscosity, and thermal conductivity for the air working fluid. The heat transfer data correlation used is given by--

$$N_u = 0.0216 R_E^{0.8} P_r^{0.6} \quad (3.5-1)$$

where

$$N_u = \text{Nusselt Number} = \frac{h D}{k}$$

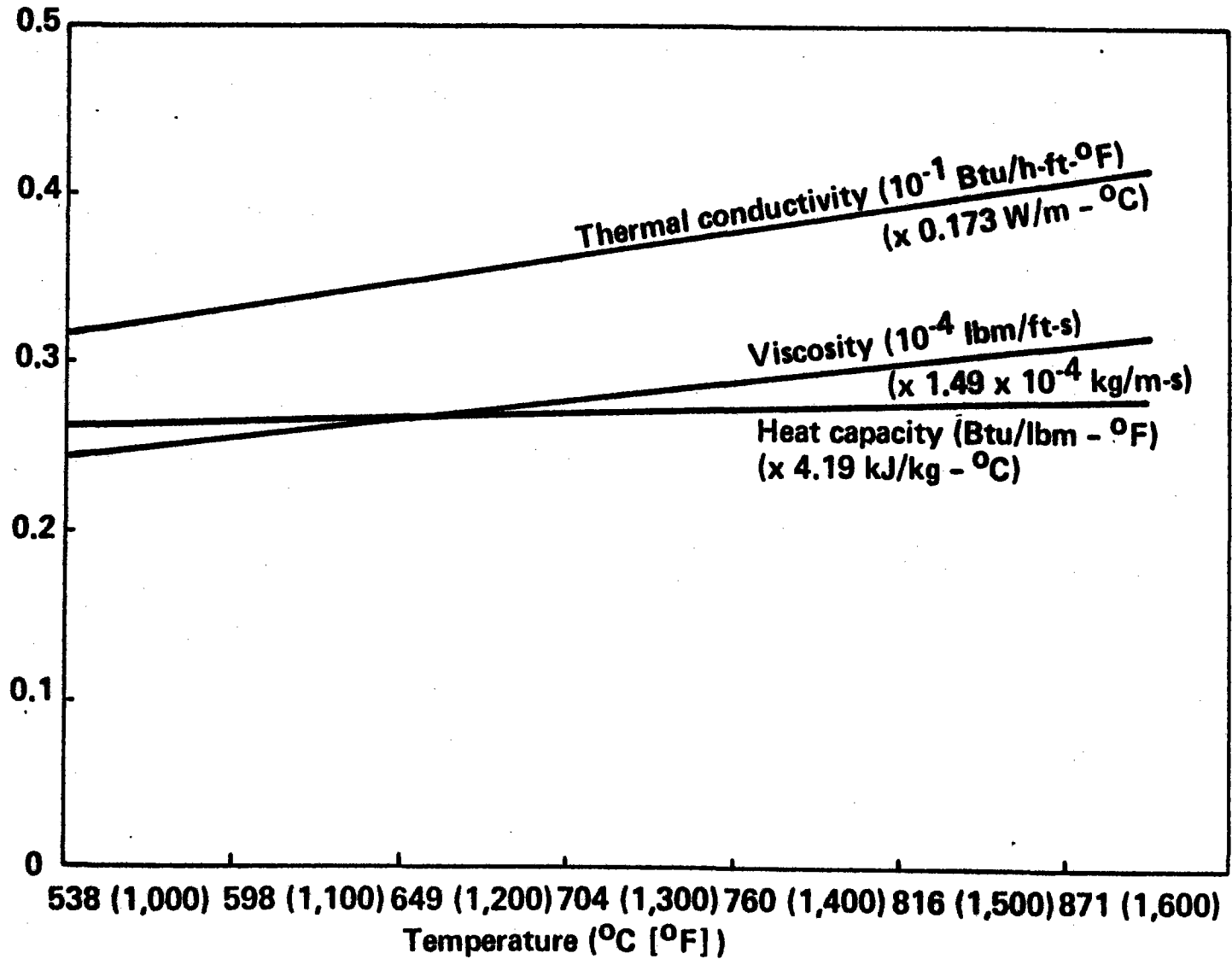
$$R_E = \text{Reynolds Number} = \frac{4 \dot{m}}{\pi D \mu}$$

$$P_r = \text{Prandtl Number} = \frac{c_p \mu}{k}$$

This correlation assumed turbulent flow and was reevaluated at each of the four nodes representing the heat exchanger tubes. The mass flow through each heat exchanger tube was assumed uniform across each of the eight panels, although the flow through the panels was not necessarily equal.

Natural convection heat transfer was calculated between the exterior receiver skin and the ambient temperature using a heat transfer coefficient based on the orientation of the receiver side walls. Natural convection in the receiver interior was not included in the pretest thermal analysis (see

Figure 3.5-8 Air Thermal and Fluid Properties Data  
**Air Thermal and Fluid Properties Data**



Section 11.0 for posttest observations).

The thermal nodal model described herein represents a sophisticated, state-of-the-art thermal analysis of the BMSR. The thermal model was input into the Boeing Engineering Thermal Analyzer (BETA) computer program. BETA's capabilities include (1) steady-state or transient analysis (2) arbitrary geometrical shape (3) heat transfer by conduction, convection, and radiation (4) internal heat generation and (5) varying physical properties. The following section presents results from the analysis.

### 3.5.3 Pretest BMSR Thermal Model Results

Representative results of the pretest thermal analysis are presented here to demonstrate the level of preparation for the testing phase of the study. No attempt was made to present the results of every computer run. Data that developed an understanding of how the BMSR-air supply combination would respond during actual testing are shown, along with data that was required for comparison with posttest thermal analyses (Section 11.0).

The planned tests were grouped into several categories, as shown in Table 3.5-2. Details of each test are more fully discussed in Section 9.0. The normal receiver startup procedure (Figures 3.5-9 through 3.5-11) was assumed for all test conditions except the cold startup (CS series). As can be seen, the inlet and outlet gas temperatures reached the desired test conditions about 1 to 2 hr after test initiation. This was an important verification of the design because a long startup (e.g., 6 to 8 hr) under the ideal solar input of Figure 3.5-9 would indicate difficulty in achieving receiver equilibrium during all but the most perfect ambient test conditions. Figure 3.5-11 indicates that the insulation surface temperatures also reached their final values in this 1 to 2 hr period. The interior insulation temperatures obviously took somewhat longer to reach full equilibrium; however, because the losses by conduction through the insulation were expected to be small, a quasi-equilibrium state was reached within 1 to 2 hr. The effects of a rapid cold startup (CS series) are shown in Figure 3.5-12. In this case, the solar input was set at 1000 kW at time zero and held constant.

*Table 3.5-2 BMSR Test Types*

## **BMSR Test Types**

- **Controlled parameter tests**
  - **Equilibrium heat balance (EB)**
  - **Nonuniform solar input (NI)**
  - **Restricted coolant flow (RF)**
  - **Transient heat load (TH)**
  - **Solar load following (SF)**
- **Demonstration tests**
  - **Cold startup (CS)**
  - **Emergency cooldown (EC)**
  - **Solar load following (SF)**

Figure 3.5-9 Solar Input Assumed in Typical Startup Analyses (Pretest)

## Solar Input Assumed in Typical Startup Analyses (Pretest)

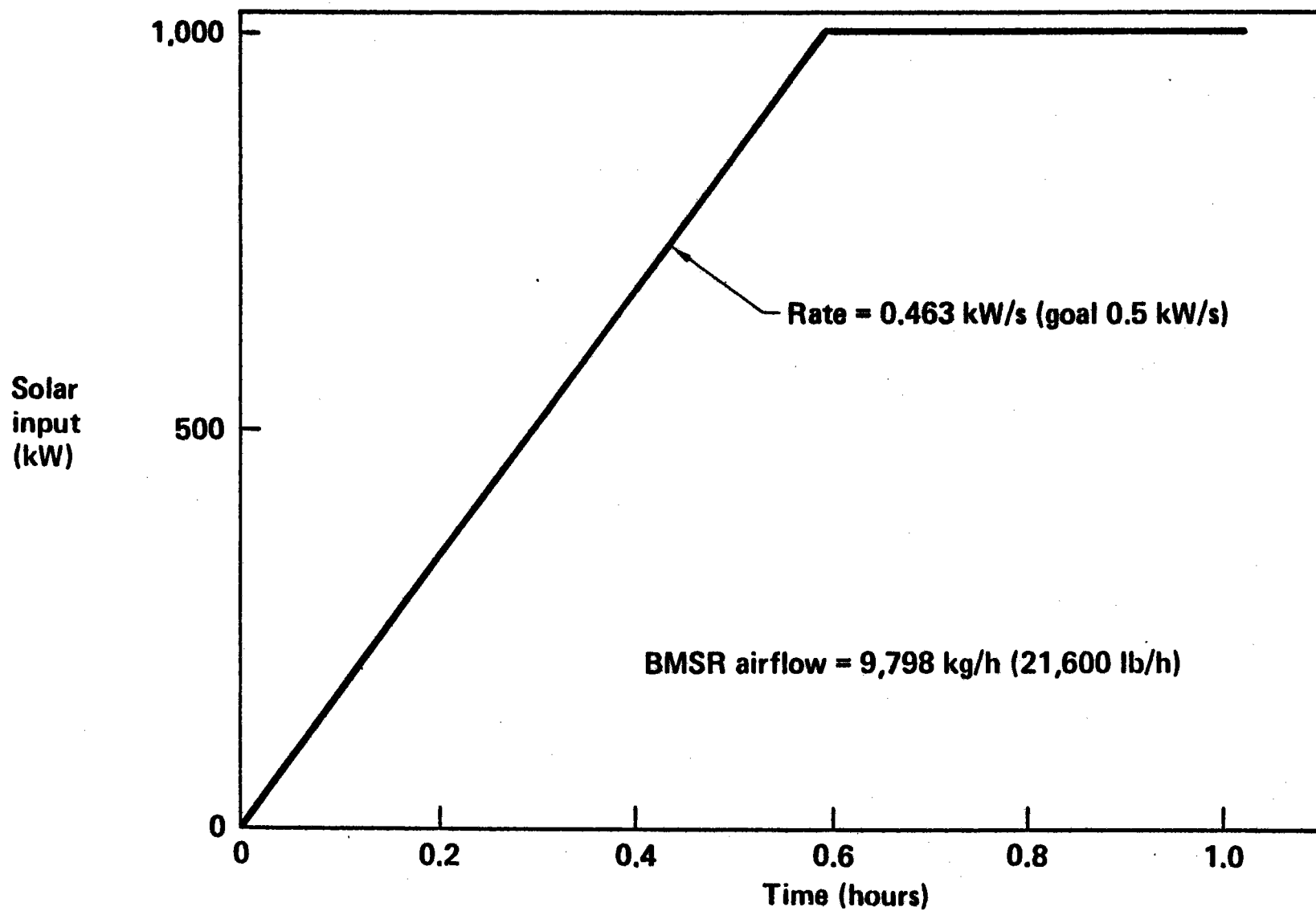


Figure 3.5-10 Typical Startup Receiver Temperature Predictions (Pretest Analysis)

## Typical Startup Receiver Temperature Predictions (Pretest Analysis)

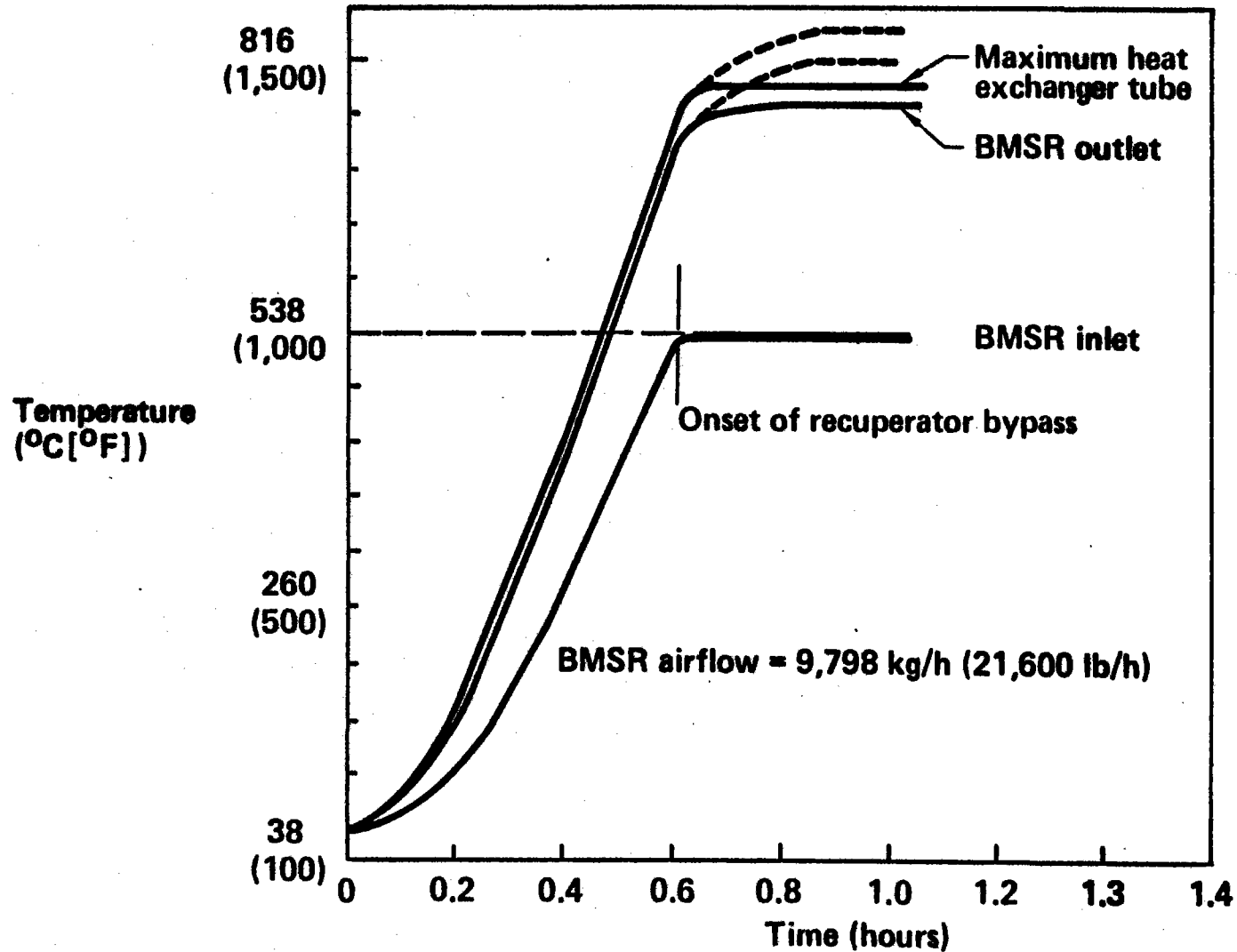




Figure 3.5-11. Typical Startup Insulation Temperature Predictions (Pretest Analysis)

## Typical Startup Insulation Temperature Predictions (Pretest Analysis)

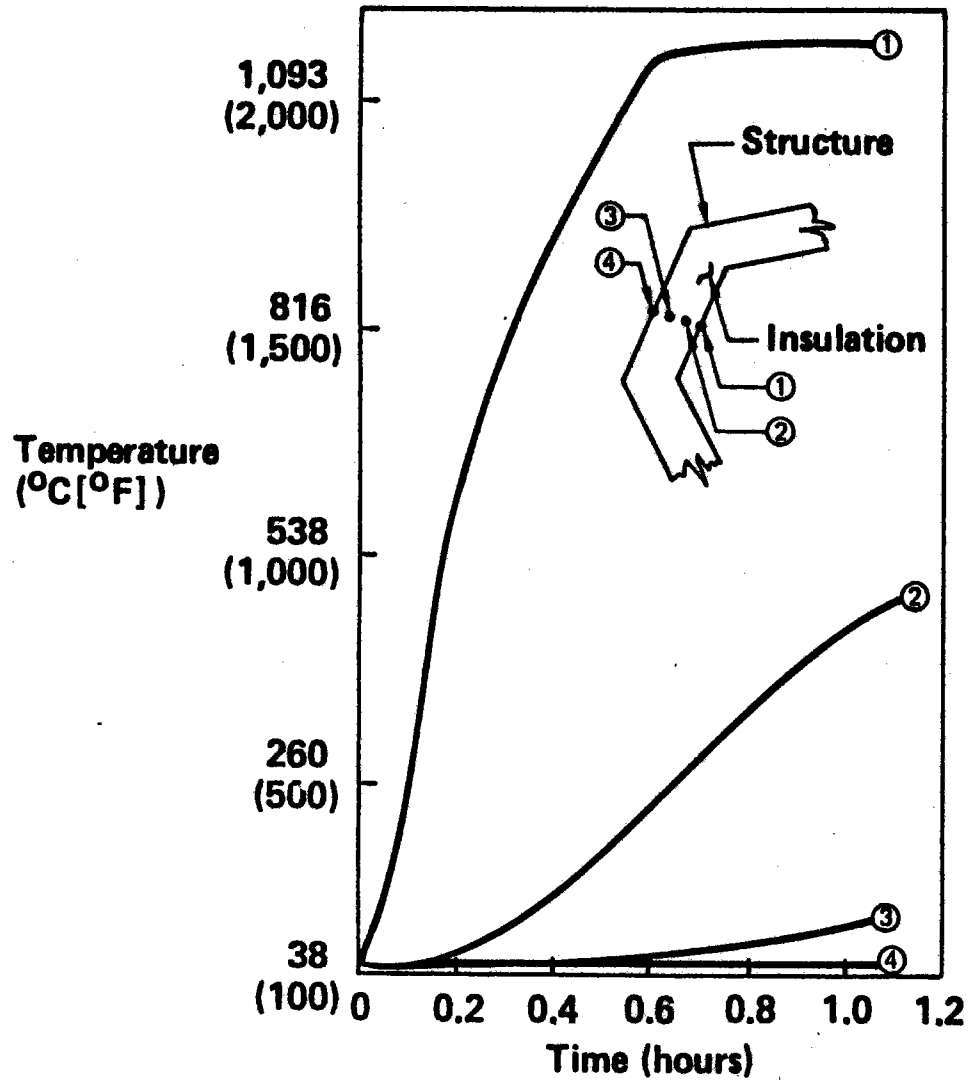
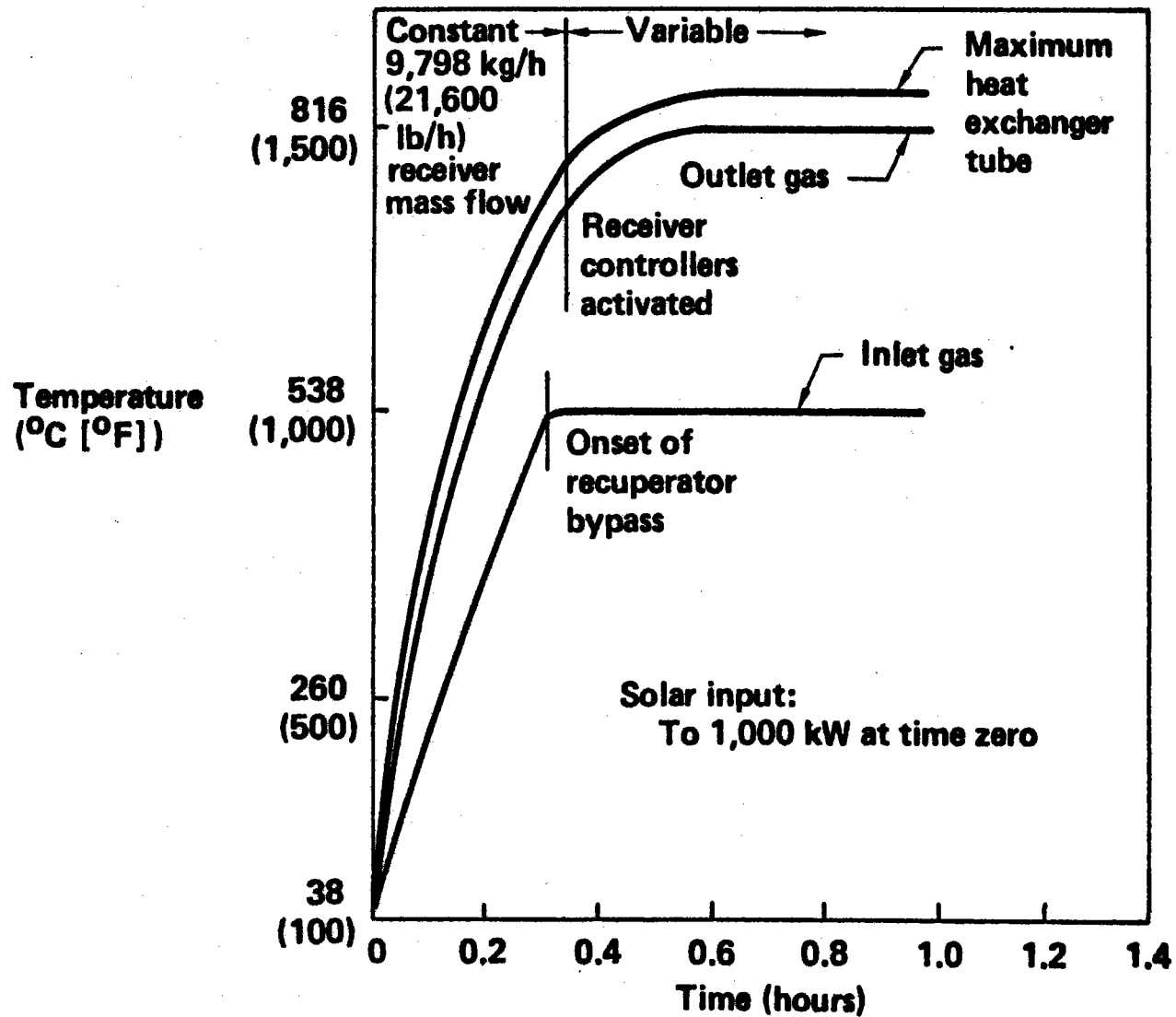


Figure 3.5-12 Cold Rapid Startup Receiver Temperatures (Pretest Analysis)

## Cold Rapid Startup Receiver Temperatures (Pretest Analysis)



### Equilibrium Heat Balance

Table 3.5-3 presents the test matrix planned for the equilibrium heat balance (EB) series tests. The important parameter to be determined from these tests was the receiver thermal efficiency. Thermal analysis predictions for receiver efficiency as a result of these pretest thermal analysis runs are presented in Figure 3.5-13. Efficiencies from 0.69 to 0.78 are indicated. A commercial Brayton cycle receiver with an optimized heliostat field would be expected to have receiver efficiencies of 0.80 to 0.85 based on these data. The design point for the BMSR was the EB-9 condition which considered a 815°C (1500°F) outlet temperature with a 538°C (1000°F) inlet temperature for 1000-kW solar input. Figure 3.5-14 presents the startup and establishment of the equilibrium point. The total mass flow decreased as the receiver panels came on control and maintained outlet temperature. The equilibrium data are for a solar input of 1000 kWt. Tables 3.5-4 and 3.5.5 present additional thermal analysis data for the same EB-9 conditions except that the solar input is assumed to be 950 kWt. The lesser insolation level is presented to facilitate comparison with the posttest data of Section 11.0.

### Nonuniform Solar Input

The nonuniform solar input tests series were intended to explore the effects of large variations in first-incident solar flux on predicted receiver performance. Cavity receivers with highly reflective walls were expected to "integrate" out the nonuniform input. Such a nonuniform solar input could be expected from the passage of a cloud over a portion of the heliostat field. Figure 3.5-15 presents the solar input assumed for the NI-3 test. Field zones I and II (Figure 3.5-6) were increased as zones III and IV were decreased to maintain the total input solar flux at a constant 500 kW. Results from the analysis revealed no perceptible difference from the uniform to the nonuniform cases, thus verifying the integrating feature of the cavity receiver concept.

### Restricted Coolant Flow

*Table 3.5-3 Equilibrium Heat Balance Test Matrix*  
**Equilibrium Heat Balance Test Matrix**

Outlet air temperature* (°C [°F])	Solar heat input (kW)		
	500	750	1,000
621 (1,150)	EB-1	EB-4	EB-7
718 (1,325)	EB-2	EB-5	EB-8
816 (1,500)	EB-3	EB-6	EB-9 **

\*Temperature increase in receiver = 260°C (500°F)

\*\*BMSR design point

Figure 3.5-13 Pretest Analysis Receiver Efficiency Predictions

# Pretest Analysis Receiver Efficiency Predictions

Pretest predictions, series EB

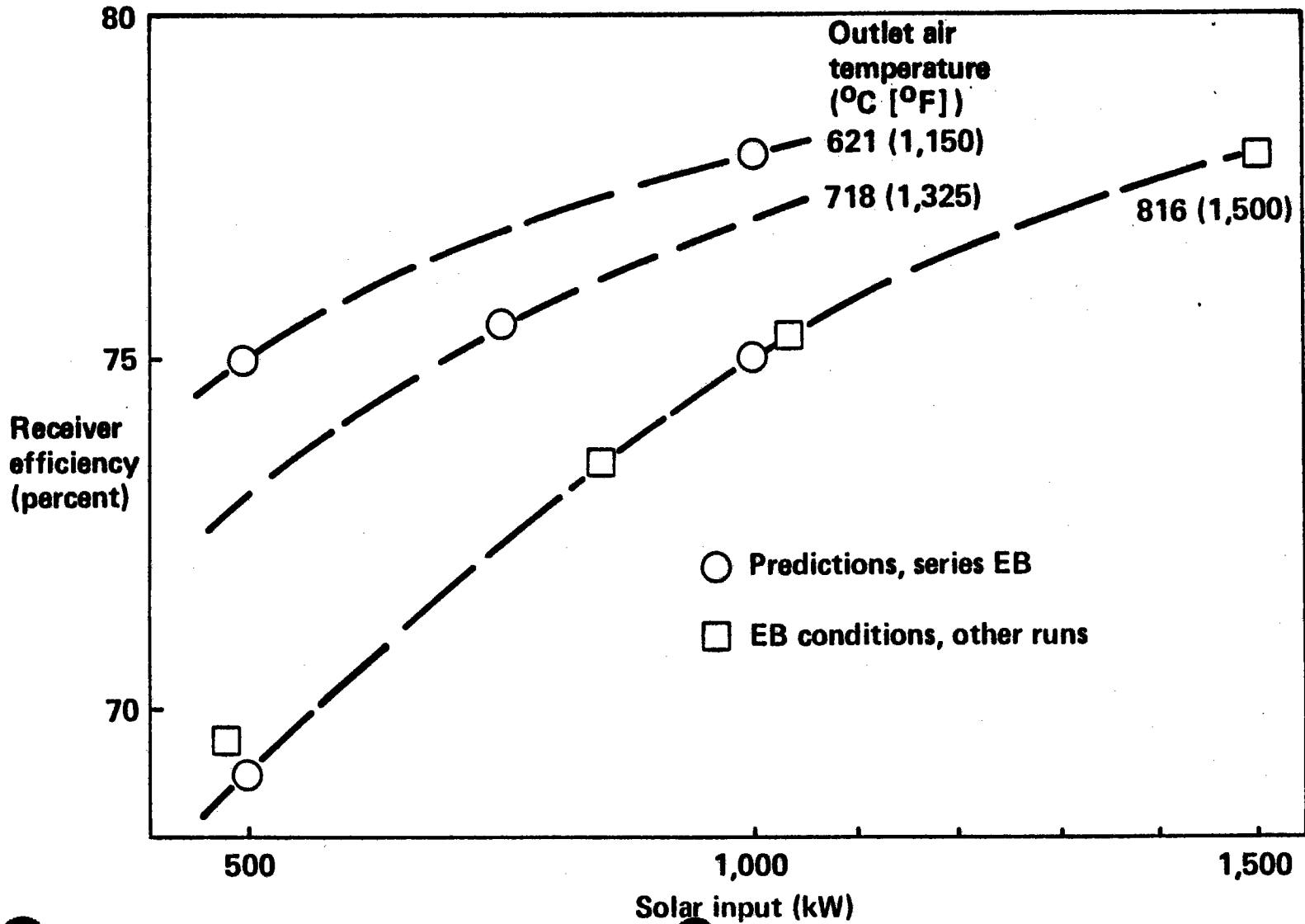


Figure 3.5-14 EB-9 Startup (Pretest Analysis)

# EB-9 Startup (Pretest Analysis)

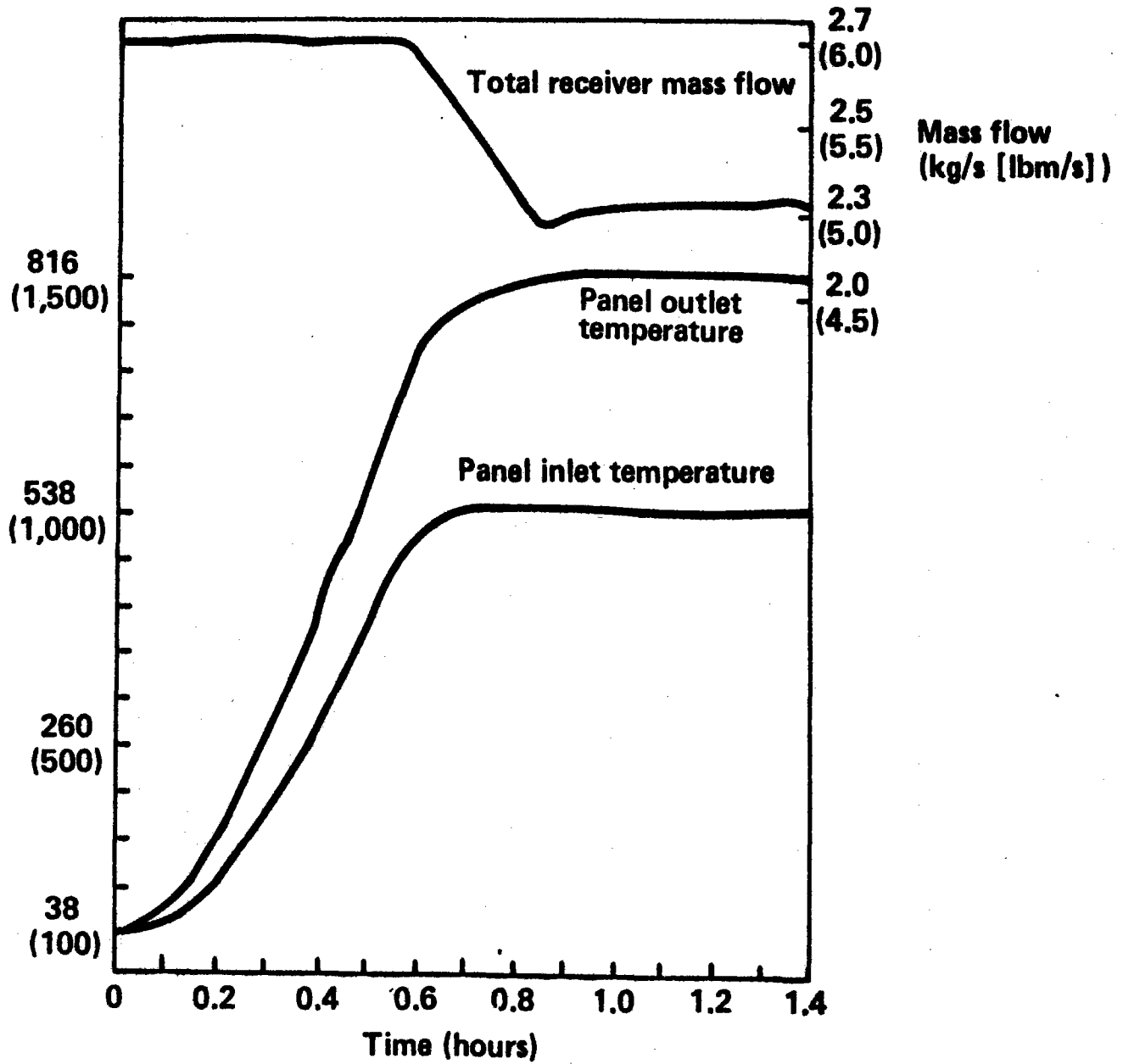
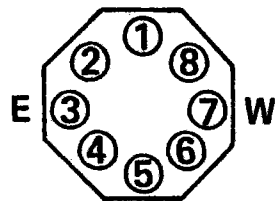


Table 3.5-4 EB-9 Heat Exchanger Temperature Predictions

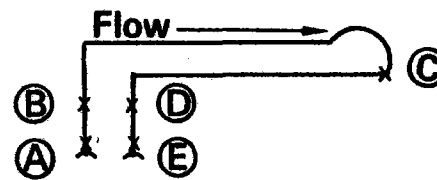
## EB-9 Heat Exchanger Temperature Predictions

	Panel number							
	①	②	③	④	⑤	⑥	⑦	⑧
Ⓐ Gas inlet (°C[°F]) Analytical	534 (993)	536 (996)	536 (997)	537 (998)	536 (996)	534 (994)	532 (989)	532 (989)
Ⓑ Tube inlet Analytical	677 (1,250)		679 (1,254)		681 (1,257)		677 (1,250)	
Ⓒ Tube bend Analytical	823 (1,514)		831 (1,527)		823 (1,514)		829 (1,524)	
Ⓓ Tube exit Analytical	849 (1,560)		843 (1,550)		848 (1,559)		844 (1,552)	
Ⓔ Gas exit Analytical	816 (1,500)	816 (1,500)	816 (1,500)	816 (1,500)	816 (1,500)	816 (1,500)	816 (1,500)	816 (1,500)

● Assumed solar input = 950 kW



Receiver panels



Heat exchanger section locations

Table 3.5-5 EB-9 Mass Flow and Thermal Output Predictions

## EB-9 Mass Flow and Thermal Output Predictions

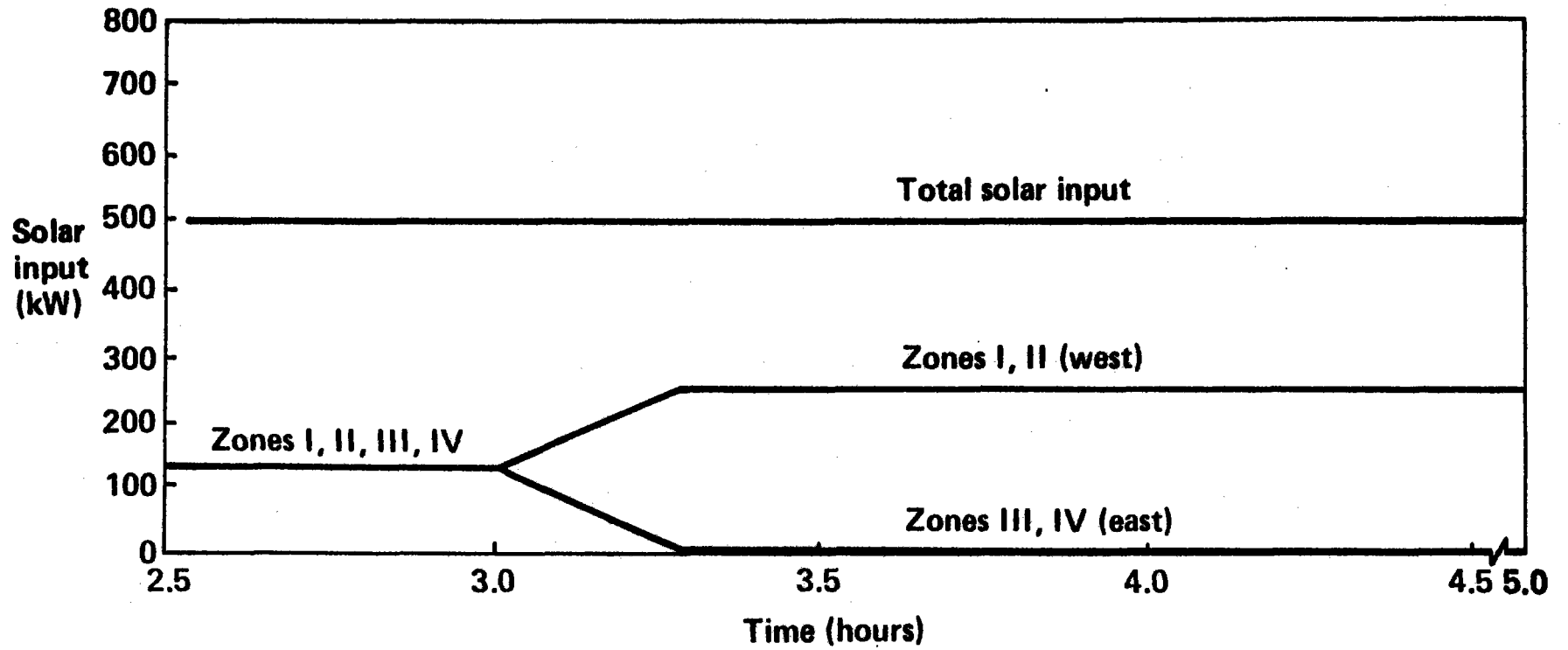
	Panel number								
	Total	①	②	③	④	⑤	⑥	⑦	⑧
<b>Mass flow rate (kg/s [lb/s])</b>									
<b>Analytical</b>	<b>2.22 (4.90)</b>	<b>0.279 (0.615)</b>	<b>0.280 (0.618)</b>	<b>0.278 (0.614)</b>	<b>0.279 (0.615)</b>	<b>0.276 (0.609)</b>	<b>0.277 (0.610)</b>	<b>0.275 (0.606)</b>	<b>0.276 (0.609)</b>
<b>Thermal output (kW)</b>									
<b>Analytical</b>	<b>720.0</b>	<b>90.6</b>	<b>90.5</b>	<b>89.7</b>	<b>89.8</b>	<b>89.1</b>	<b>89.8</b>	<b>89.9</b>	<b>90.4</b>



Figure 3.5-15 Solar Input for Nonuniform Solar Series (NI-3)

# Solar Input for Nonuniform Solar Series (NI-3)

139



The plan for this test was to explore the effects of loss of coolant flow to one of the eight panels. Figure 3.5-16 presents the predictions for RF-3. Solar input was maintained at a constant 1000 kW. Panel 3 mass flow was forced to decrease in the manner shown, resulting in an increase in gas outlet temperature and tube temperatures. These data allowed the test planner to allocate a certain amount of time for this test before maximum tube temperatures of 982°C (1800°F) or 1038°C (1900°F) were reached.

### Transient Heat Load

A transient heat load would be placed on the receiver during the passage of a cloud. The assumed solar input for TH-4 is presented in Figure 3.5-17. The resulting effects on panel gas temperature and total mass flow are shown in Figure 3.5-18. The thermal analysis showed the panel outlet and inlet temperature was maintained at set point values by an appropriate decrease in total mass flow rate. During rapid decreases in mass flow rate, oscillations in the iterative procedure of the BMSR-BETA program caused a loss of mass flow accuracy as illustrated in the initial portions of the test.

### Solar Load Following

The purpose of the solar load following (SF) series was to determine the operational characteristics of the receiver during varying degrees of cloud cover. Figure 3.5-19 presents the solar input for this test series. The top graph depicts the typical day insolation profile. The bottom graph presents the typical day insolation with two cloud series superimposed. The first grouping models the passage of two small fast clouds. The second grouping represents the passage of a large, high, stratus cloud. Figure 3.5-20 presents the thermal analysis predictions for these conditions. After the normal startup period, the inlet and outlet came onto control at about 1.3 hr. As the insolation continued to climb, the temperature setpoints were maintained by slowly increasing the total mass flow rate. At 4.0 hr, the first series of clouds was encountered (see also Figure 3.5-21). As the insolation dropped, the mass flow control attempted to maintain set-point by drastically reducing total mass flow. As the insolation

Figure 3.5-16 Restricted Flow (RF-3) Series Analysis Results

# Restricted Flow (RF-3) Series Analysis Results

141

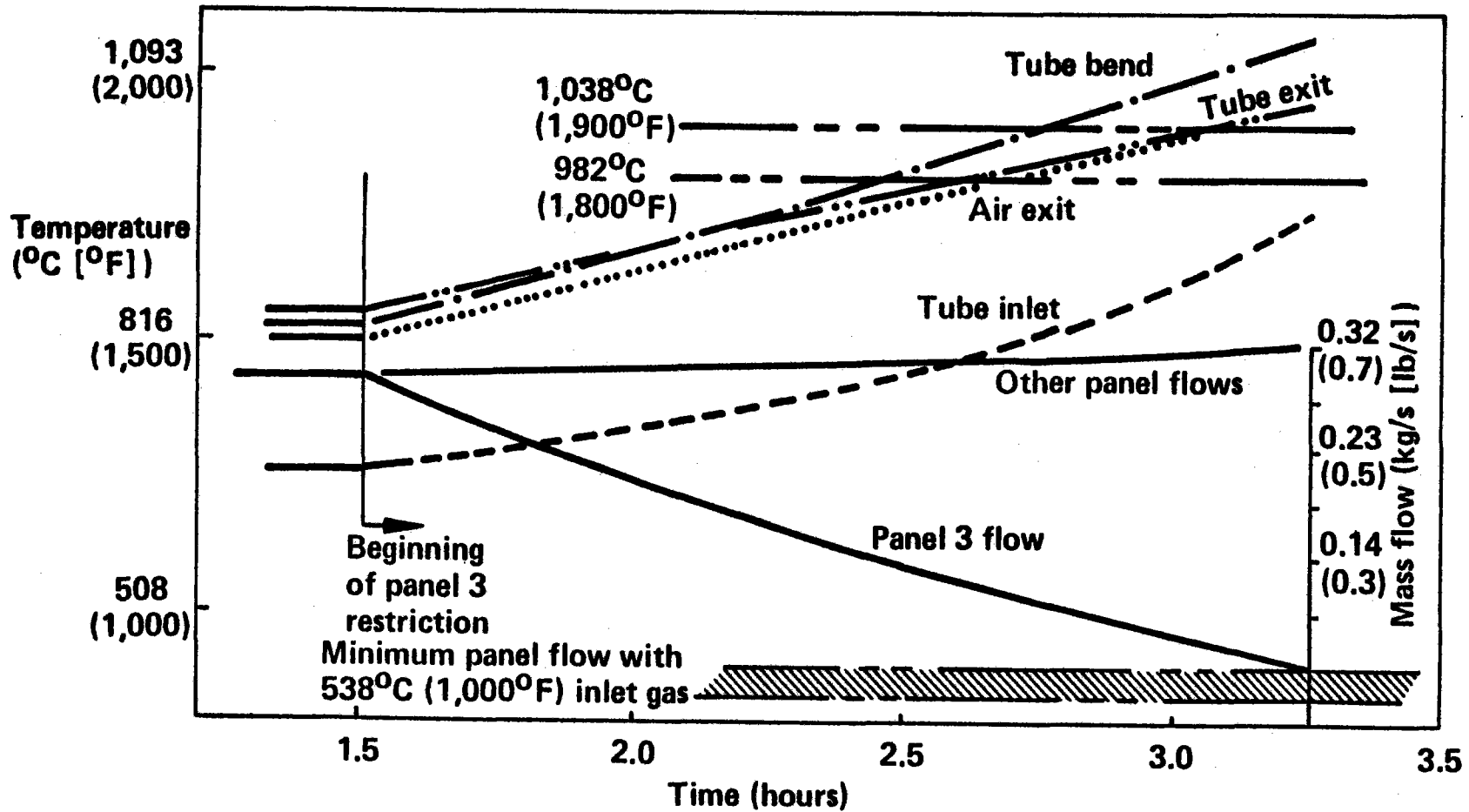


Figure 3.5-17 Solar Input for Transient Heat Loading (TH-4) Series

## Solar Input for Transient Heat Loading (TH-4) Series

142

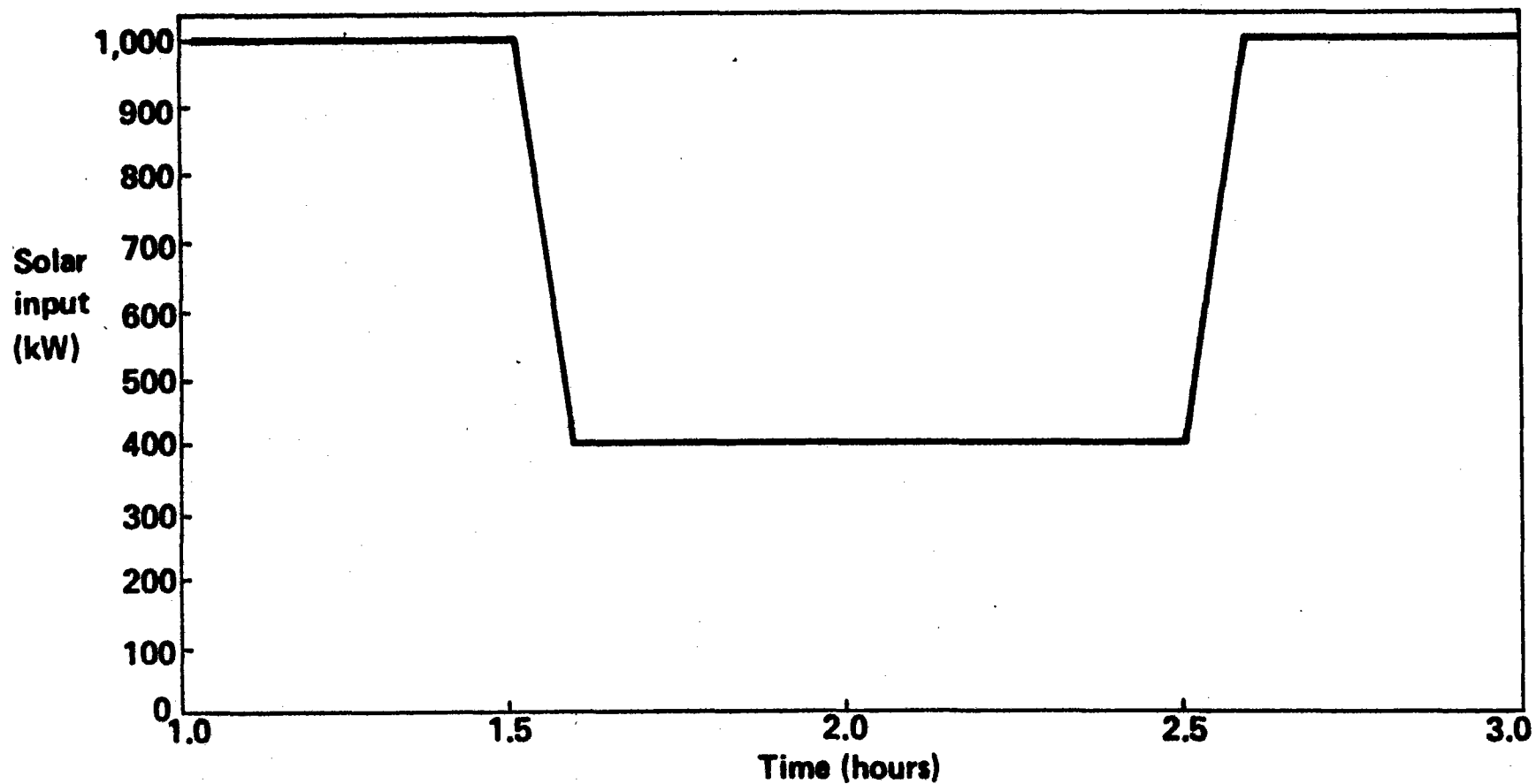


Figure 3.5-18 TH-4 Analysis Results

# TH-4 Analysis Results

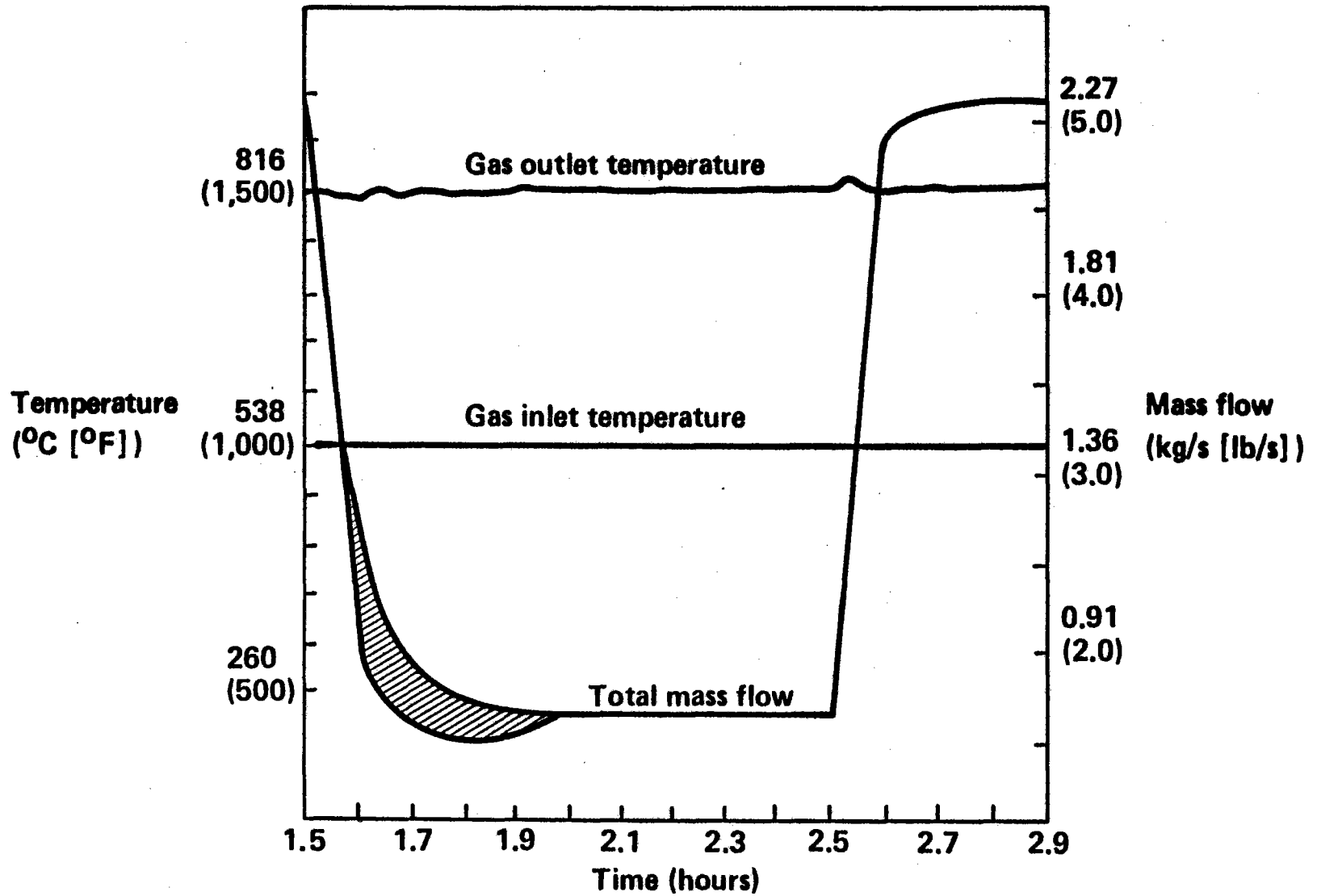


Figure 3.5-19. Solar Load Following Series Solar Input

## Solar Load Following Series Solar Input

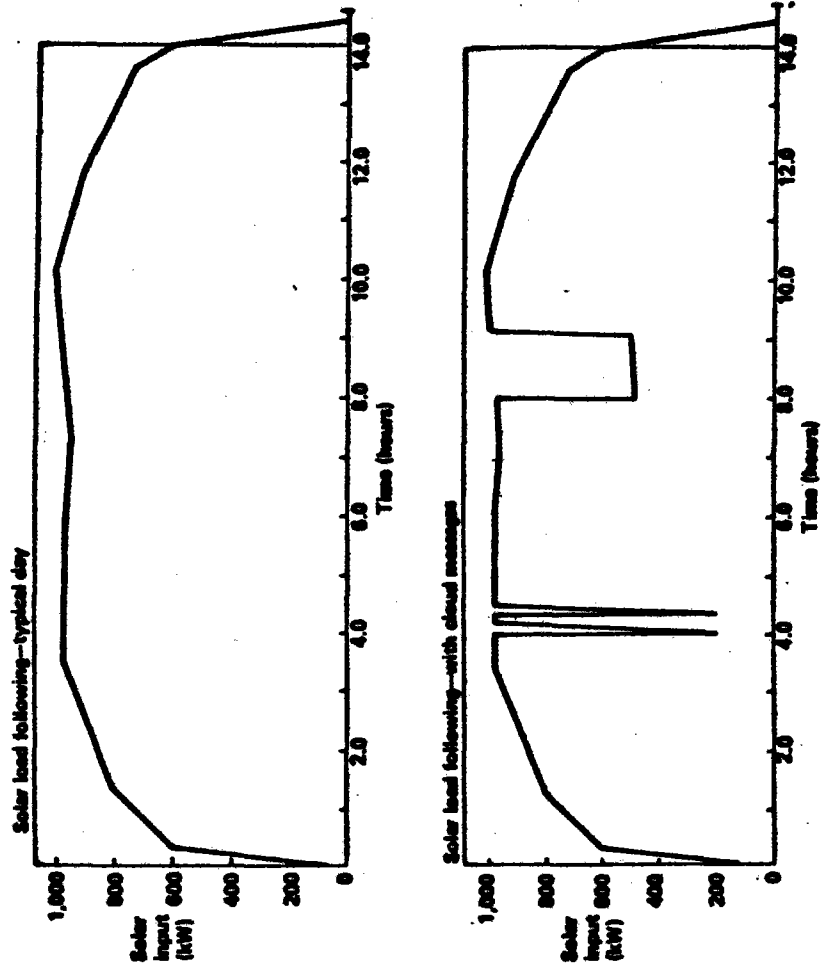


Figure 3.5-20 Thermal Analysis Predictions for Solar Load Following Series

# Thermal Analysis Predictions for Solar Load Following Series

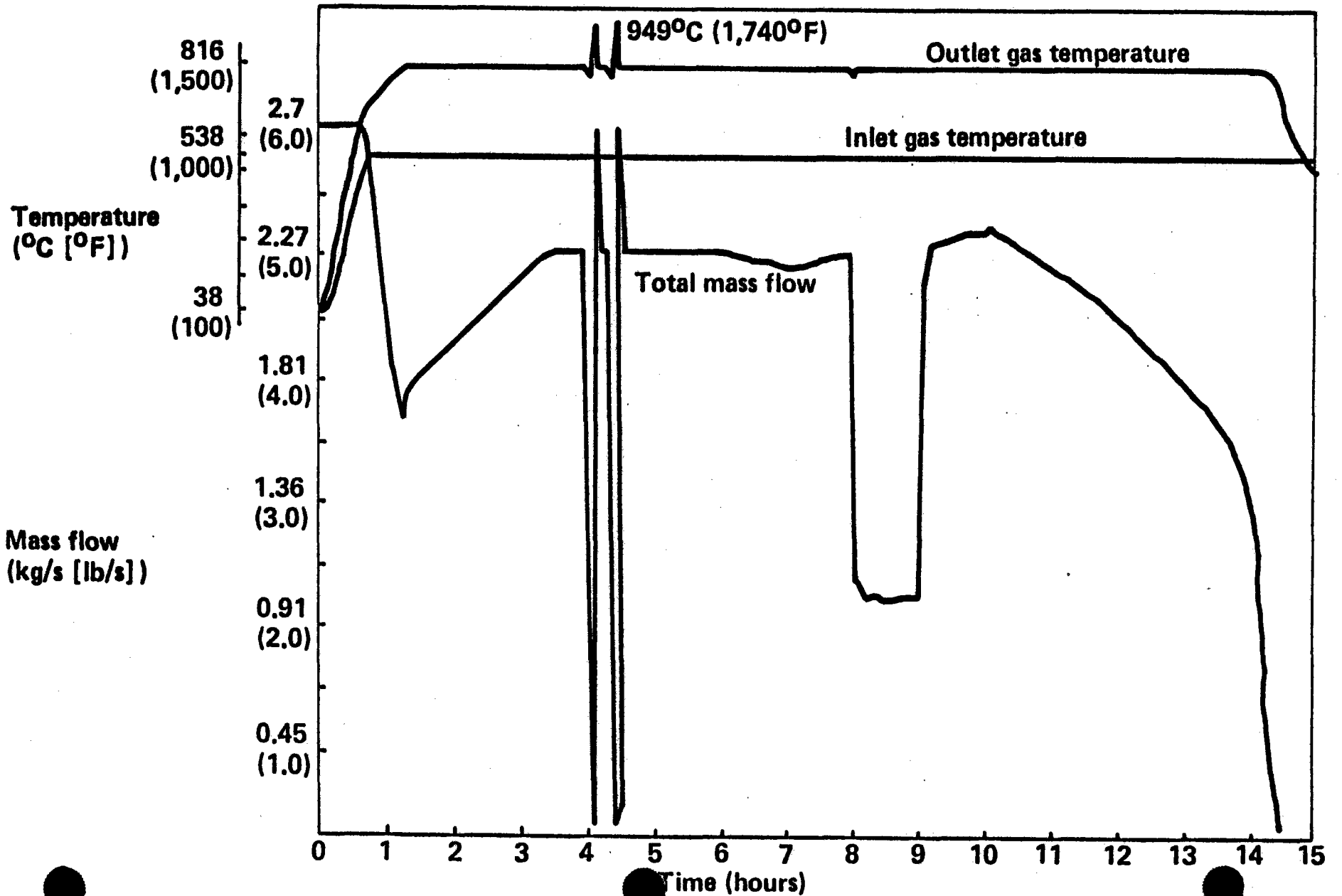
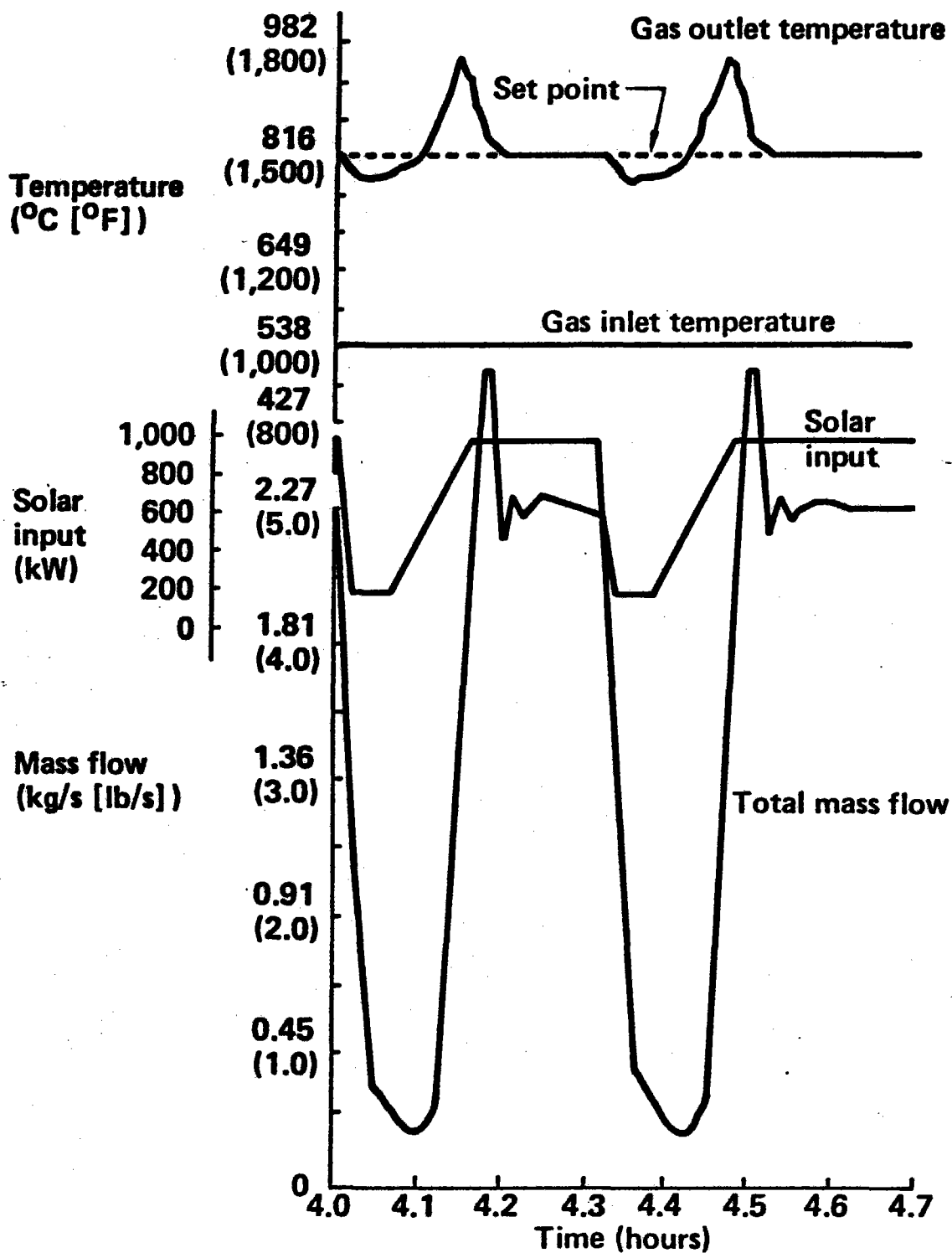


Figure 3.5-21 Thermal Analysis Predictions for Passage of Two Small Clouds

## Thermal Analysis Predictions for Passage of Two Small Clouds





returned, the gas temperature exceeded the set-point, signaling the need for additional flow. The flow control rapidly returned the gas temperature to the set-point value.

In the large stratus cloud encounter, a barely perceptible change in outlet temperature was noted. It appeared that overshooting of the gas outlet temperature would be of concern only if the dwell time of the cloud were of the same order as the response time of the mass flow control algorithm. As the insolation diminished near the end of the "day," the mass flow was decreased until the outlet temperature set-point could no longer be maintained.

### 3.6 RECEIVER FRAME STRUCTURAL ANALYSIS

The receiver frame was designed to withstand loads resulting from transportation, earthquake, handling, and wind. The frame was also designed to support the heat exchanger system and to accommodate the thermal growth of inlet and outlet manifolds that encircled the cavity body.

The receiver was designed for highway transportation with load factors of 2.5g vertical, 0.5g lateral, and 3.2g longitudinal. The fore-and-aft axis of the receiver coincided with the longitudinal direction. The receiver could be transported either in an upright position or in an inverted position, aperture face up, with the cover removed. Vertical loads were assumed to act simultaneously with either the longitudinal or lateral load. Longitudinal and lateral loads could not occur simultaneously.

The receiver was designed for a horizontal seismic load factor of 4.0g acting either longitudinally or laterally. Vertical sidewalls of the receiver body were designed to withstand a lateral acceleration of 5.6g and deflections were limited to avoid insulation damage. Headers plus heat exchanger tubes were designed to sustain a horizontal acceleration of 4.3g in any direction. The seismic load factors were derived from a Sandia-supplied design response spectrum for the 43m(140-ft) level of the CRTF tower.

Handling loads were limited to be no greater than the transportation loads by specifying a maximum allowable setdown velocity of 0.03 m/s (0.1 ft/s) and a maximum horizontal velocity of 0.70m/s (2.3 ft/s). Lifting lugs were designed for an ultimate strength equivalent to a total vertical force of five times acting downwards through the center of gravity of the receiver, in accordance with ANSI B30-16 safety standards.

The design wind loading was 171 kg/m<sup>2</sup> (35 lb/ft<sup>2</sup>), approximately equivalent to the stagnation pressure at 193 km/h (120 mi/h). In all cases, wind loadings were less than the transportation or seismic loads.

#### 3.6.1 Allowable Stresses

The receiver frame was constructed of ASTM-A36 steel having minimum ultimate tensile yield strengths as follows:

$$F_{TU} = 399.9 \text{ MPa (58,000 lb/in}^2\text{)}$$

$$F_{TY} = 248.2 \text{ MPa (36,000 lb/in}^2\text{)}$$

Allowable stresses were derived from these values using AISC specifications for design, fabrication, and erection of structural steel for buildings.

The leaf-type spring supports for the heat exchanger manifolds were of ASTM-A588 steel having minimum tensile properties:

$$F_{TU} = 482.6 \text{ MPa (70,000 lb/in}^2\text{)}$$

$$F_{TY} = 344.7 \text{ MPa (50,000 lb/in}^2\text{)}$$

Allowable stresses were derived from AISC specifications.

### 3.6.2 Stress Analysis Results and Factors of Safety

Stress analysis results for the receiver frame components are summarized in the following paragraphs. Member loads or stresses and factors of safety are given for critical load cases. Safety factors indicated in the summaries of results were ratios of allowable stress (or load) to actual stress (or load). These factors did not include safety factors inherent in the allowable stress values used. The allowable stress used for A36 steel was 148.9 MPa (21,600 lb/in<sup>2</sup>).

Margins of safety rather than factors of safety are quoted in the detailed stress notes. These margins of safety represented the amount of reserve strength based on allowable stress and expressed as a fraction of the actual stress or load level. Factors of safety are obtained by adding 1.00 to the margin of safety.

#### Main Frame and Body Members

The receiver framework was analyzed to determine member load coefficients for positive and negative 1.0g load factors in each of the vertical, longitudinal, and lateral directions. These coefficients were multiplied by the gross weight of the receiver and by the appropriate load factors and combined to obtain member loads. Alternate distributions of reaction forces at the base were assumed as necessary to permit statically determinate analyses; distributions giving highest member loads were used in the final evaluation.

Receiver framework joints and members are identified in Figure 3.6-1. Longitudinal and vertical loads were assumed equally distributed between the two main side frames, one of which is shown in the side elevation view. Lateral loads were distributed between the two lateral trusses shown in the section views. Critical load condition maximum member loads and safety factors are summarized in Table 3.6-1.

#### Miscellaneous Details

Miscellaneous structural members of the receiver framework included: side body panels, top trapezoidal panels, bottom plate, and support beams. The critical load condition for each of these members was the transportation condition with a maximum load factor for combined longitudinal and lateral loads of 4.1g. Maximum member stresses and factors of safety are summarized in Table 3.6-2.

Receiver side-body panels in addition to carrying shear loads, were required to support lateral loads from the weight of the panels plus attached insulation, with maximum lateral load factors of 4.1g for transportation and 5.6g for seismic loads. Transportation conditions required designing to AISC allowables while seismic conditions required designing to material yield. Panel lateral loads were assumed carried at panel edges and by two 0.64-cm (0.25 in) plate stiffeners. Shear continuity in the panels at the edges of the slots that accommodated the heat exchanger tubes was provided by angle stiffeners.

Receiver cover trapezoidal panels were designed to the same lateral load

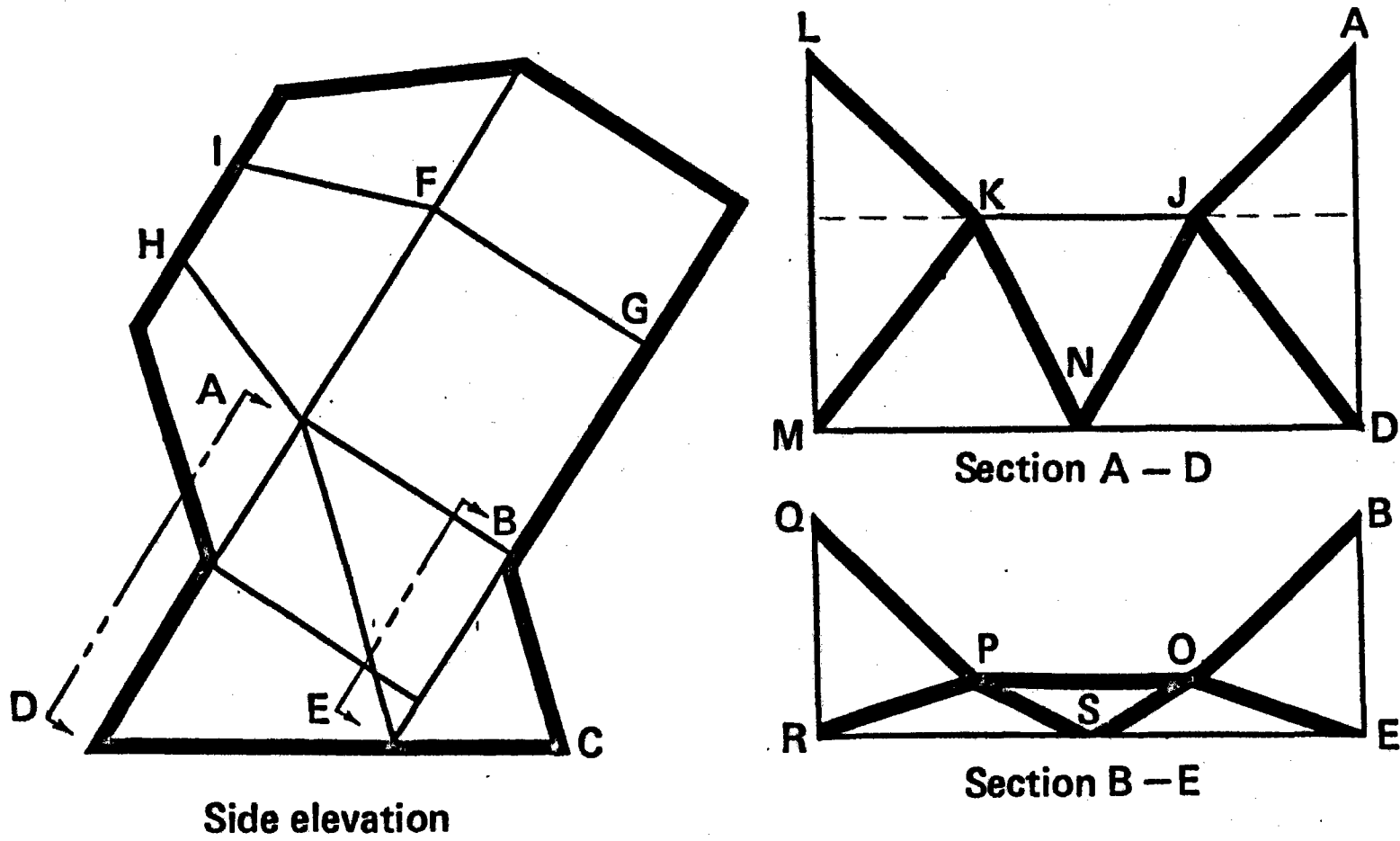


Figure 3.6-1. Receiver Framework Member Identification

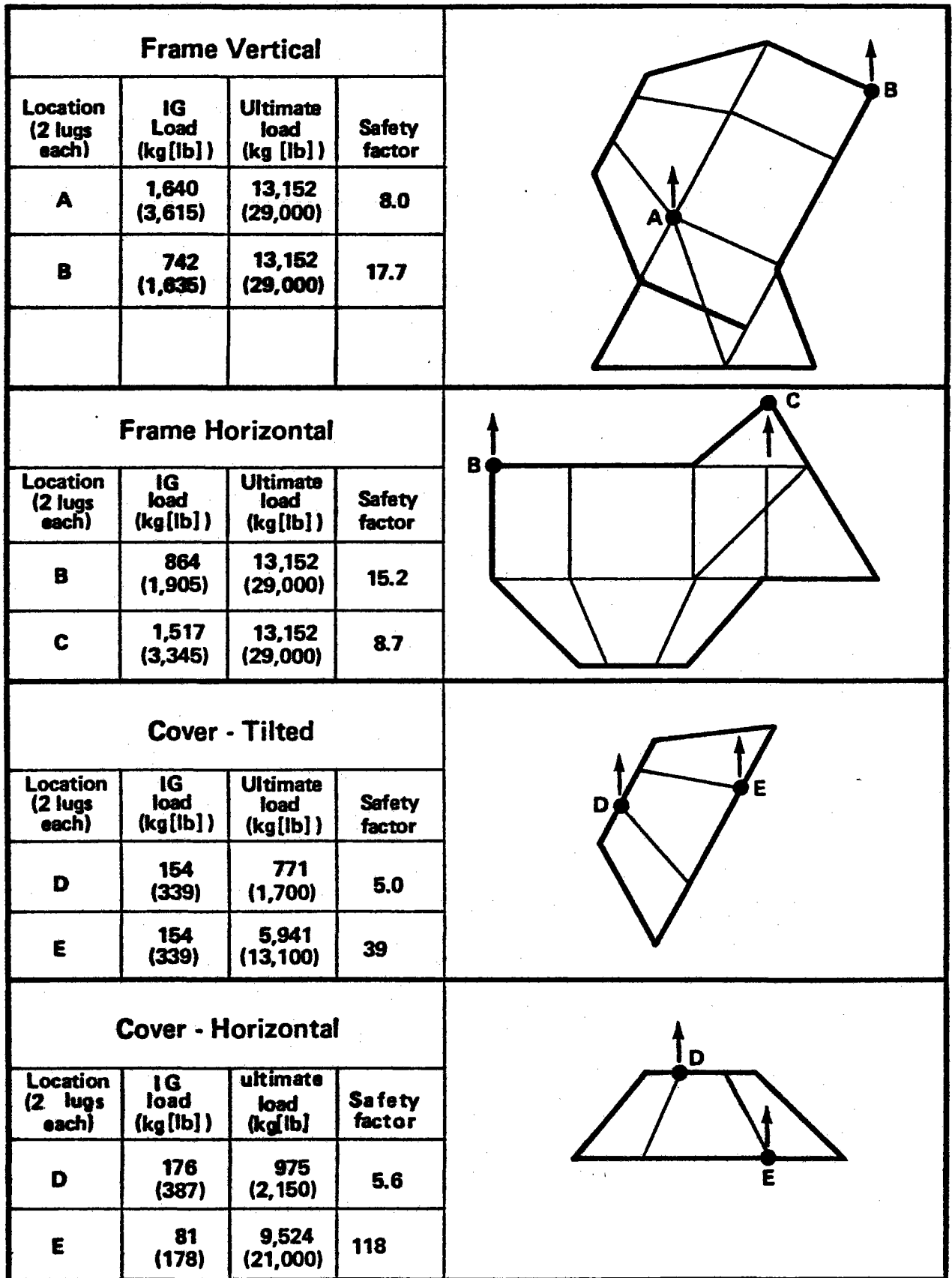










Figure 3.6-2. Lifting Lugs - Normal Loads and Factors of Safety

Table 3.6-1. Receiver Framework Loads and Safety Factors

Member	Critical Load  Condition	Member Load (kg (lb))	Factor of Safety
AB	T1	± 2728 (6016)	8.52
AD (LM)	S1	-10782 (23775)	1.44
AE	T1	± 4432 (9773)	1.91
BV BC	T1	±11029 (24319)	1.49
BE (QR)	S2	- 5367 (11835)	2.84
CE	T1	- 7439 (16403)	2.38
DE	T1	- 5367 (11834)	2.01
AJ (KL)	S2	± 6928 (15276)	3.38
DJ (KM)	S2	± 2239 (4938)	5.57
DN (MN)	S2	- 8460 (18654)	1.41
JN (KN)	S2	± 7574 (16701)	1.83
BO (PQ)	S2	± 6928 (15276)	3.38
EO (PR) <sub>q</sub>	S2	± 3043 (6709)	5.81
ES (RS)	S2	-12659 (27912)	1.24
OS (PS)	S2	- 8683 (19146)	2.26
AF	S1	± 6434 (14187)	3.64
BG	T1	± 5574 (12290)	4.20
FG	T1	± 4490 (9901)	5.21
AH (HI)	T1	- 757 (1670)	30.9
ABFG	T1	4499 (9920) 	1.46 
AFHI	T1	1075 (2360) 	3.50 

 Load condition:	 Shear load
T1 - +3.2g long. +2.5g vert.	 Buckling allowable
S1 - +4.0g long. +1.0g vert.	
S2 - +4.0g lat. +1.0g vert.	

**Table 3.6-2. Miscellaneous Member Stresses and Factors of Safety**

	<u>Maximum stress (MPa [lb/in<sup>2</sup>])</u>	<u>Factor of Safety</u>
<b><u>Side body panel</u></b>		
130cm x 18cm x .64cm L stiffener (51in x 7in x 1/4in)	±144.3 (20927)	1.03
4.5cm x 3.2cm x .5cm L stiffener (1 3/4in x 1 1/4in x 3/16in)	± 52.3 (7583)	2.64
<b><u>Top trapezoidal panel</u></b>		
10 ga. sheet	± 95.4 (13835)	1.56
<b><u>Bottom plate</u></b>		
6 L 8.2 support beams	± 16.3 (2363)	9.1
▷ 6 L 8.2 base ring	± 56.2 (8150)	2.65
▷ Combined bending and axial stress; see notes for main receiver frame member BG.		



conditions as the side-body panels. These panels were not stiffened, and lateral loads were assumed carried by plate bending.

The receiver bottom plate, insulation, and aperture assembly were supported by eight support beams cantilivered from an octagonal base ring consisting of the main receiver body frame members (see member BG in Figure 3.6-1). The support beams were of the same channel section as the main receiver frame members. A maximum lateral load factor of 4.1g for the transportation condition was assumed.

### Lifting Lugs

Lifting lug locations, load capacities, and factors of safety are summarized in Figure 3.6-2. Safety factors quoted for lifting lugs were based on 1.0g lifting loads compared to lug ultimate load capabilities rather than material allowable design stress.

### Tiedown Loads

Six receiver tiedown locations are identified in Figure 3.6-3. Tiedowns at each location were provided by Sandia at CRTF and were designed for the following loads:

Horizontal Component (any direction):	9797-kg (21,600-lb)
Vertical Component:	9797-kg (21,600-lb) down 7838-kg (17,280-lb) up

These loads were derived from seismic load factors of  $\pm 4.0g$  horizontal and  $\pm 0.25g$  vertical, combined with static 1.0g dead weight. The least favorable distribution of reaction forces was assumed to allow for variations in stiffness of frame and supports.

### Heat Exchanger Support Structure

The heat exchanger support structure consisted of eight leaf-type springs of 0.64 by 15.2 by 145-cm (0.25 by 6 by 57-in) steel plate. These springs were

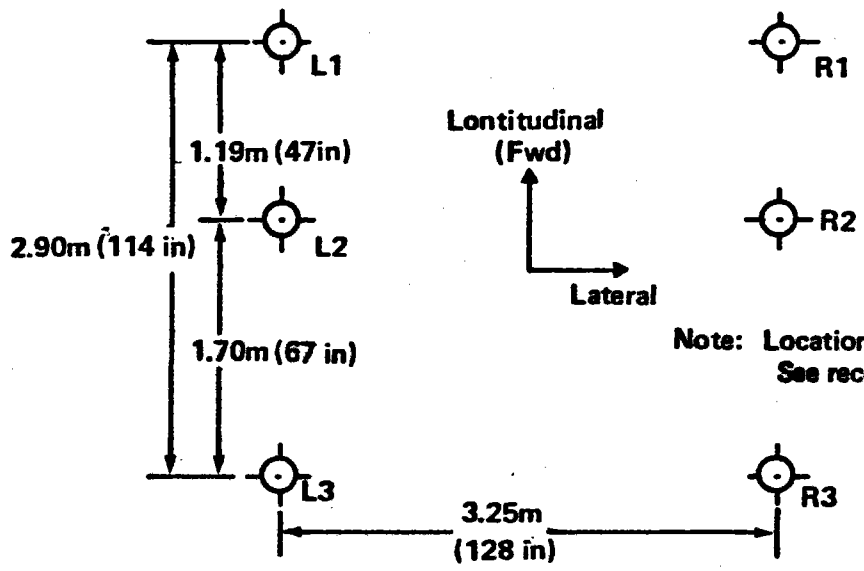


Figure 3.6-3. Tie Down Locations

located around the circumference of the receiver body, parallel to the aperture axis. They were attached at the ends by pins to the main frame so that they could support tangential and axial loads (relative to the receiver body), but would offer very little restraint to radial growth of the manifolds because of thermal expansion. The springs were made of A588 steel to obtain a high yield strength so that they could flex with manifold thermal growth without permanent deformation.

The leaf-spring supports were analyzed for tangential bending loads from heat exchanger system weight with the maximum transportation load factor of 4.1g acting parallel to the manifold plane and for axial load with the 4.1g transportation load factor acting normal to the manifold plane. The loads acting parallel to the manifold plane were assumed carried equally by four support beams, while the loads acting normal to the manifold plane were assumed distributed equally to all eight support beams. The leaf springs were also analyzed for bending due to differential expansion of inlet and outlet manifolds for the worst case of low 399°C (750°F) inlet temperature. Maximum stresses for these load cases and factors of safety are given in Table 3.6-3.

Critical load cases, maximum stresses, and factors of safety for the various heat exchanger support structure details are given in Table 3.6-4.


### 3.7 HEAT EXCHANGER STRESS ANALYSIS


Structural integrity of heat exchanger system components was ensured by using procedures and allowable stress values as given in the ASME boiler code as nearly as possible. Although specifically excluding vessels with an inside diameter not exceeding 15.2 cm (6.0 in), Section VIII (covering rules for construction of pressure vessels) was considered to be the most nearly applicable to the design of the heat exchanger system.

#### 3.7.1 Allowable Stresses

Allowable stress depended on the value of the stress intensity as defined in Division 2 of Section VIII. Stress intensity at a point was the absolute

**Table 3.6-3. HX Support Beam Stresses and Safety Factors**

<u>Load condition</u>	<u>Type</u>	<u>Max. stress (MPa [lb/in<sup>2</sup>])</u>	<u>Factor of Safety</u>
<b>Transportation</b>			
<b>4.1g</b>	<b>Tangential bending</b>	<b>155.1 (22500)</b>	<b>1.33</b>
<b>4.1g</b>	<b>Axial compression</b>	<b>7.0 (1017)</b>	<b>1.87</b> 
<b>Differential Thermal expansion</b>	<b>Radial bending</b>	<b>178.7 (25920)</b>	<b>1.16</b>

 **Conservative buckling allowable**

**Table 3.6-4. HX Support Structure Details - Stresses and Safety Factors**

<u>Item</u>	<u>Load condition</u>	<u>Type</u>	<u>Max stress (MPa [lb/in<sup>2</sup>])</u>	<u>Factor of Safety</u>
<b>Transportation</b>				
<b>Seam support lug</b>	<b>4.1g</b>	<b>Bending</b>	<b>139.9 (20290)</b>	<b>1.06</b>
<b>Beam support pin</b>	<b>"</b>	<b>Shear</b>	<b>11.9 (1726)</b>	<b>11.6</b>
<b>Manifold support bracket</b>	<b>"</b>	<b>Compression</b>	<b>50.6(7333)</b>	<b>2.45</b>
<b>Manifold support pin (Titanium, 6A1-4V)</b>	<b>Differential thermal exp. with gravity and seismic</b>	<b>Pin bending</b>	<b>291.6(42291)</b>	<b>1.11</b>

value of the difference between the maximum and minimum principal stresses at the point. The allowable value of stress intensity, denoted by  $S_m$ , was given in the code for various materials and temperatures. Stresses were classified as primary or secondary, depending on whether or not they were self-limiting. Primary stresses were those stresses caused by imposed mechanical loads such as dead weight and internal pressures, which were not self-limiting. Primary stresses that exceeded the yield strength of the material resulted in gross distortion and possible material failure. Secondary stresses were those that resulted from self-constraint or constraint of adjacent parts of the structure. Secondary stresses were self-limiting in that local yielding and minor distortions relieved the condition causing the stress. Thermal stresses were classified as secondary stresses. The maximum allowable stress intensity in a component depended on the basic material allowable,  $S_m$ , and the classification of the stress as indicated in abbreviated form in Table 3.7-1.

Two materials were used in the design of the heat exchanger system. Manifolds, connecting flanges, and valves were of Type 304 corrosion-resistant austenitic stainless steel. Heat exchanger tubes, headers, connector tubes, and flanges were of Inconel 617 superalloy. Allowable material stress intensity values for these two materials were determined as described in the following sections.

#### Type 304 Corrosion-Resistant Steel

Allowable stress intensity values for this material are only given to 427°C (800°F) in Division 2 of Section VIII. However, maximum allowable stress values are given in Division 1 of Section VIII to 816°C (1500°F). The  $S_m$  values given in Division 2 are two-thirds of the room temperature minimum yield stress,  $F_{TY}$ , for temperatures up to 149°C (300°F). Above this temperature,  $S_m$  is approximately the same as  $F_{TY}$ . The maximum stress values given in Division 1 are much more conservative, as indicated in Figure 3.7-1. The conservative value of 8.3 MPa (1200 lb/in<sup>2</sup>) at 816°C (1500°F) from Division I was adopted as an  $S_m$  value for use in a design procedure based on the alternative rules of Division 2.

*Table 3.7-1. Stress Intensity Limits*

<u>Stress classification</u>	<u>Type</u>	<u>Limit</u>
Primary	Membrane	$S_m$
Primary	Membrane & bending	$1.5 S_m$
Primary & secondary	Membrane & bending & thermal	$3 S_m$

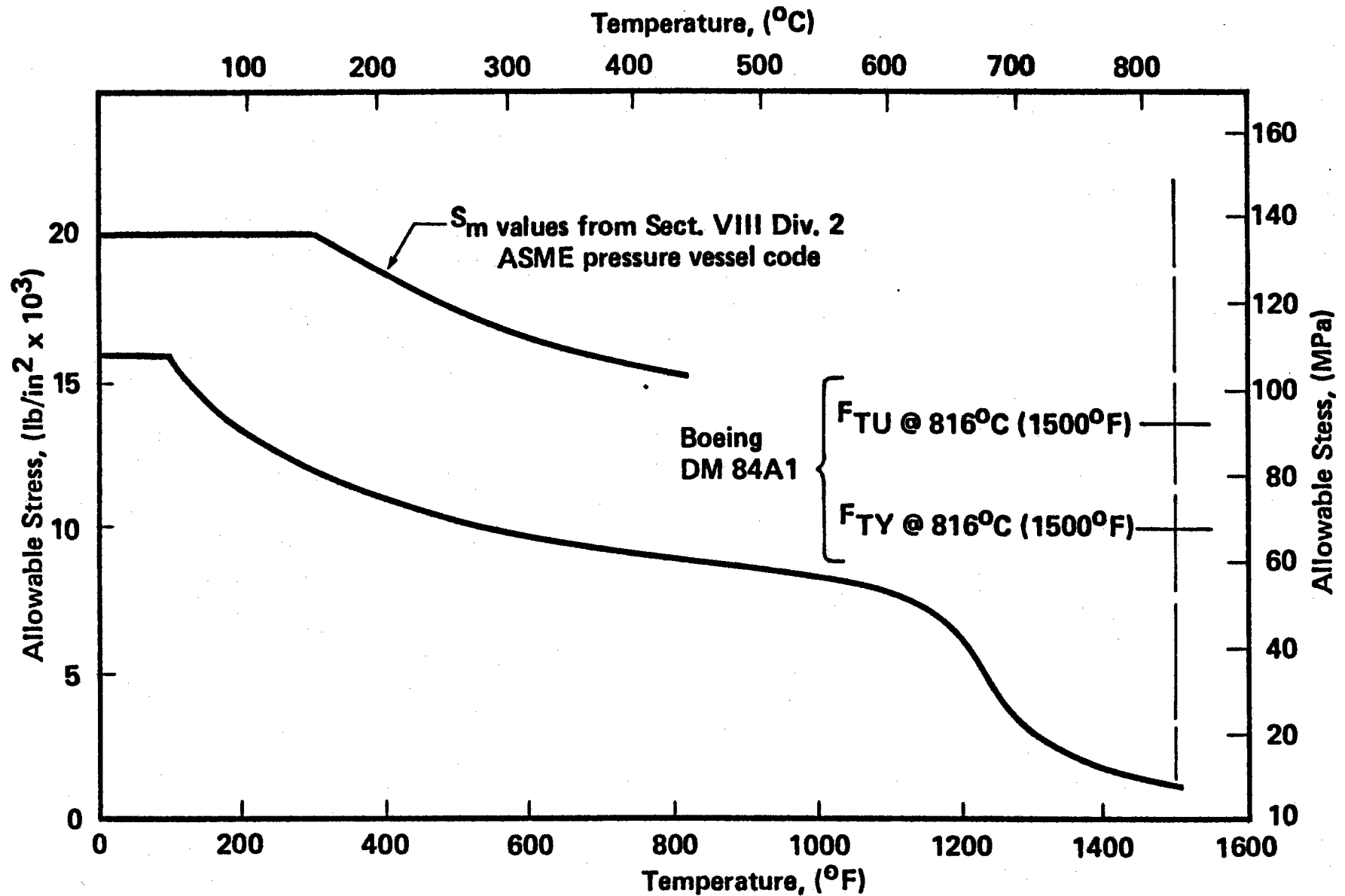


Figure 3.7-1. Allowable Stresses for 304 CRES HX Components



## Inconel 617

This material was not covered in the ASME boiler code. Allowable stress intensities were derived from vendor-furnished data as follows. Vendor typical values for 1000-hr strength-to-rupture stress were reduced to obtain an allowable stress using a factor of 69%. This factor was determined from the difference between vendor typicals and vendor  $3\sigma$  allowables furnished for HS188 tubing at 871°C (1600°F), a similar material in similar application. The allowable stress intensity value,  $S_m$ , was taken as one-fourth of the allowable 1000-hr strength-to-rupture stress. Maximum stress intensities used for design in Inconel 617 components are given in Table 3.7-2. For design of heat exchanger tubes, stress intensities were calculated from the Von Mises yield criterion,

$$S = \sqrt{1/2 [(s_1 - s_2)^2 + (s_2 - s_3)^2 + (s_3 - s_1)^2]}$$

where  $S$  was the equivalent stress intensity and  $s_1$ ,  $s_2$ , and  $s_3$  were principal stresses. This definition was used because this is the format of stress output available from the ANSYS computer code used for the detailed stress and deflection analysis of the heat exchanger tubes. The above formula gives stress intensities that may be of smaller magnitude than those given by the previous definition. However, these values are appropriate to use with a stress rupture allowable because stress rupture is a long-term creep phenomenon.

### 3.7.2 Deflections

It was required that deflections during normal operation because of pressure, gravity, thermal expansion of system components, and thermal gradients in heat exchanger tubes did not compromise a minimum clearance of 2.5 cm (1.0 in) between receiver wall and heat exchanger tubes or 0.95 cm (0.375 in) between adjacent heat exchanger tubes.

### 3.7.3 Stress Analysis Results and Factors of Safety

Stress analysis results for the heat exchanger components are summarized in

*Table 3.7-2. Maximum Stress Intensity,  $S_M$ , for Inconel 617 (Based on 1000 Hr Stress Rupture)*

<u>Temperature (°C[°F])</u>	<u><math>F_{TU}</math>, Vendor typical (MPa[lb/in<sup>2</sup>])</u>	<u><math>F_{TU}</math>, 3<math>\sigma</math> allowable (MPa[lb/in<sup>2</sup>])</u>	<u><math>S_M</math>, <math>\frac{1}{4} F_{TU}</math> (MPa[lb/in<sup>2</sup>])</u>
816 (1500)	96.5 (14000)	66.6 (9660)	16.7 (2415)
871 (1600)	69.0 (10000)	47.6 (6900)	11.9 (1725)

the following sections. Member loads or stresses and factors of safety are given for critical load cases. Safety factors indicated in the summaries of results are ratios of allowable stress (or load) to actual stress (or load). These factors do not include safety factors inherent in the allowable stress values used. A comparison of allowable stresses with short-term material yield and ultimate tensile strengths at temperature is given in Table 3.7.3.

Heat exchanger system components were designed by operating conditions because of the greatly reduced material allowable stresses associated with the high temperatures. The manifolds and connecting flanges of 304 corrosion-resistant steel were designed for a maximum expected operating pressure of 1.0 MPa (150 lb/in<sup>2</sup>). The connector tubes, headers, and heat exchanger tubes of Inconel 617 were designed for a maximum pressure of 2.1 MPa (300 lb/in<sup>2</sup>). Maximum stresses and factors of safety for heat exchanger system components are summarized in Table 3.7-4. Brief descriptions of critical load conditions and stress areas are found in the following sections.

#### Manifolds

The critical load case was the operational condition for the outlet manifold with 1.0 MPa (150-lb/in<sup>2</sup>) internal pressure at 816°C (1500°F) and with the inlet manifold at 399°C (750°F). The critical stress area was at the manifold bends where connecting flanges to the individual heat exchanger panels were attached and where maximum bending moments occurred because of restraint forces from the heat exchanger support structure.

#### Flanges and Valves

Connecting flanges and valves were rated by the vendor for the specific temperatures and pressures required. The connection of the flange to the outlet manifold was analyzed for bending from cantilevered weight of heat exchanger system components in combination with 1.0 MPa (150-lb/in<sup>2</sup>) pressure at 816°C (1500°F).

**Table 3.7-3. Material Allowables Compared to Short-Term Yield and Ultimate Tensile Strengths**

<u>Material</u>	<u>Temperature (°C [°F])</u>	<u>Allowable stress (MPa[lb/in<sup>2</sup>])</u>	<u>F<sub>TY</sub> (MPa[lb/in<sup>2</sup>])</u>	<u>F<sub>TU</sub> (MPa[lb/in<sup>2</sup>])</u>
304 CRES	816 (1500)	S <sub>m</sub> = 8.3 (1200) 1.5 S <sub>m</sub> =12.4 (1800) 3 S <sub>m</sub> =24.8 (3600)	68.3 (9900)	(93.1 (13500))
INCO 617	816 (1500)	S <sub>m</sub> =16.7 (2415) 1.5 S <sub>m</sub> =25.0 (3622) 3 S <sub>m</sub> =50.0 (7245)	—	—
INCO 617	871 (1600)	S <sub>m</sub> =11.9 (1725) 1.5 S <sub>m</sub> =17.8 (2588) 3 S <sub>m</sub> =35.7 (5175)	144.8 (21000)	206.8 (30000)

**Table 3.7-4. HX System Component Stresses and Safety Factors**

<b><u>Component</u></b>	<b><u>Pressure (MPa[lb/in<sup>2</sup>])</u></b>	<b><u>Maximum Stress (MPa[lb/in<sup>2</sup>])</u></b>	<b><u>Factor of Safety</u></b>
<b>Manifold</b>	<b>1.0 (150)</b>	<b>22.1 (3212)</b>	<b>1.12</b>
<b>Flange</b>	<b>1.0 (150)</b>	<b>10.7 (1545)</b>	<b>1.16</b>
<b>Connector</b>	<b>1.0 (150)</b>	<b>16.7 (2424)</b>	<b>1.49</b>
<b>Connector</b>	<b>2.1 (300)</b>	<b>20.1 (2914)</b>	<b>1.24</b>
<b>Header</b>	<b>1.0 (150)</b>	<b>9.9 (1436)</b>	<b>2.52</b>
<b>Header</b>	<b>2.1 (300)</b>	<b>19.8 (2872)</b>	<b>1.33</b>
<b>HX Tube</b>	<b>2.1 (300)</b>	<b>37.1 (5381)</b>	<b>1.35</b>

### Connectors and Headers

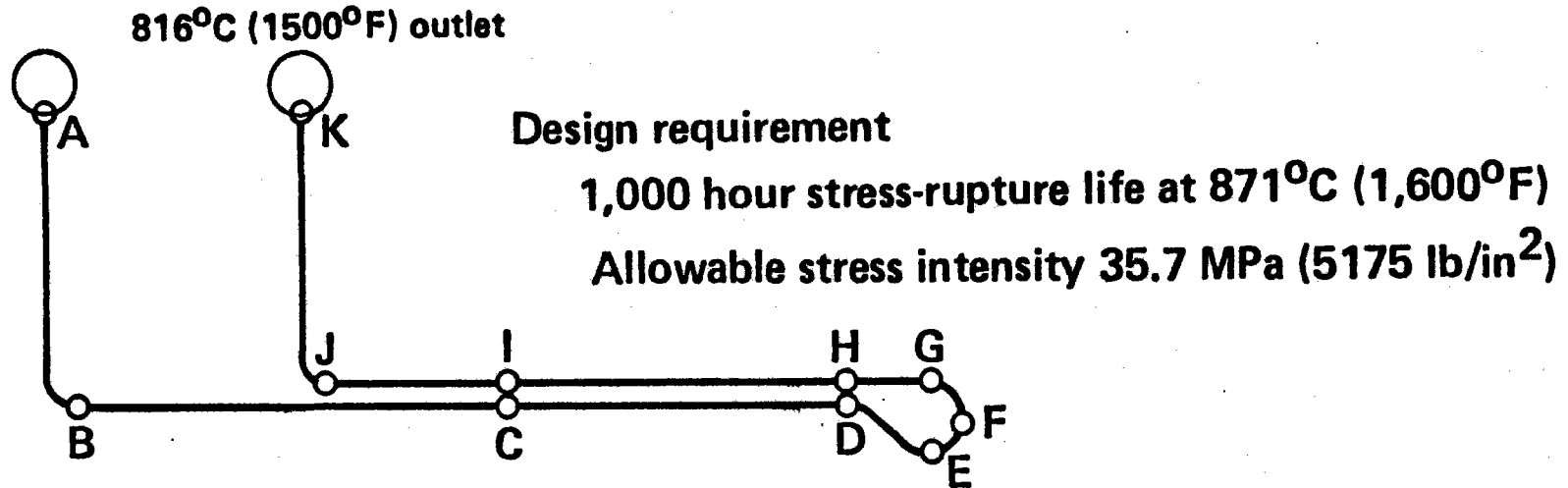
Connector tubes and headers were Inconel 617 tubing of 5.1-cm (2.00-in) outside diameter and 3.8-cm (1.50-in) inside diameter. The critical condition for the connector tube was bending due to gravity load combined with internal pressure at 816°C (1500°F), acting on the net section at the threaded connection to the flange. The critical condition for the header was internal pressure at 816°C (1500°F) with discontinuity stresses at the heat exchanger tube connections. The connectors and headers were analyzed for both the 1.0-MPa (150-lb/in<sup>2</sup>) maximum expected operating pressure and the 2.1-MPa (300-lb/in<sup>2</sup>) design pressure.

### Heat Exchanger Tubes

Heat exchanger tube stresses and deflections were analyzed using the ANSYS finite-element computer code. The analysis included effects of temperature, pressure, and gravity. Temperature inputs were determined from a thermal analysis for two inlet temperatures, 538°C (1000°F) and 399°C (750°F). Several computer runs were made to study different configurations and load conditions.

Stress results applicable to the design case of 2.1-MPa (300-lb/in<sup>2</sup>) internal pressure are shown in Figure 3.7-2. The highest stresses occurred in the region of the tube return bend, as shown in the figure. The worst case was for the 399°C (750°F) inlet temperature for tubes in the top-panel position of the cavity. The highest stress observed, 37.0 MPa (5381 lb/in<sup>2</sup>) at point E in the figure, occurred with a tube wall temperature of 822°C (1512°F). Using the 3Sm allowable stress for 816°C (1500°F), 50 MPa (7245 lb/in<sup>2</sup>) gives the safety factor of 1.35 indicated in Table 3.7-4. Figure 3.7-3 shows the stresses due to thermal expansion, alone and combined with gravity and pressure. Thermal expansion produces the major contribution to total stress in the return bend area.

The tube bend configuration shown in Figure 3.7-2 was derived as a result of several design iterations. The first configuration tried was a simple 180-deg return bend; however, stresses were substantially in excess of



2.1 MPa (300 lb/in <sup>2</sup> )–538°C(1,000°F) inlet			
Point	Stress (MPa[lb/in <sup>2</sup> ])		M.S.
A	23.2	(3,360)	+ 0.54
B	14.8	(2,142)	+ 1.42
C	18.6	(2,704)	+ 0.91
D	28.8	(4,183)	+ 0.91
E	31.7	(4,592)	+ 0.24
F	32.9	(4,774)	+ 0.13
G	31.6	(4,582)	+ 0.08
H	28.4	(4,117)	+ 0.12
I	11.6	(1,687)	+ 0.26
J	7.6	(1,101)	+ 2.07
K	6.3	(918)	+ 4.63

2.1 MPa (300 lb/in <sup>2</sup> )–399°C(750°F) inlet			
Point	Stress (MPa[lb/in <sup>2</sup> ])		M.S.
A	12.6	(1,825)	+ 1.84
B	16.8	(2,438)	+ 1.12
C	21.9	(3,172)	+ 0.63
D	32.1	(4,661)	+ 0.11
E	37.1	(5,381)	+ 0.30*
F	35.6	(5,164)	+ 0.00
G	33.5	(4,856)	+ 0.07
H	30.4	(4,412)	+ 0.17
I	12.7	(1,848)	+ 1.80
J	7.5	(1,092)	+ 3.74
K	16.0	(2,318)	+ 1.23

\* Adjusted for actual temperature (822°C[1512°F])

Figure 3.7-2. Design Case HX Tube Stresses

Maximum stress at point, (MPa[lb/in <sup>2</sup> ])											
Load condition	A	B	C	D	E	F	G	H	I	J	K
Thermal expansion only	3.1 (453)	9.1 (1,318)	16.9 (2,452)	23.2 (3,359)	25.8 (3,735)	25.6 (3,706)	24.2 (3,508)	23.2 (3,368)	16.3 (2,371)	13.3 (1,922)	7.5 (1,083)
Thermal expansion with gravity	21.6 (3,137)	12.9 (1,871)	19.6 (2,843)	26.2 (3,800)	28.1 (4,076)	29.9 (4,334)	28.8 (4,179)	26.8 (3,884)	9.7 (1,414)	0.7 (108)	2.7 (396)
Thermal expansion with gravity and pressure	23.2 (3,360)	14.8 (2,142)	18.6 (2,704)	28.8 (4,183)	31.7 (4,592)	32.9 (4,774)	31.6 (4,582)	28.4 (4,117)	11.6 (1,687)	7.6 (1,101)	6.3 (918)

*Figure 3.7-3. Tube Stress Breakdown  
2.1 MPa (300 psi)–538°C (1,000°F) Inlet*



allowable values. As the configuration was changed to increase the bend radius, a corresponding change to the thermal model was necessary to obtain correct temperatures.

Maximum heat exchanger tube deflections for the design case occurred with the 538°C (1000°F) inlet temperature condition. Tube deflections for this condition are shown in Figure 3.7-4. The maximum deflection of the tube toward the cavity wall was 3.8 cm (1.5 in) for tubes in the bottom panel position in the receiver. Maximum tube-wall temperatures at various stations along the heat exchanger tube are also shown in Figure 3.7-4.

The receiver heat exchanger system had been designed for 2.1-MPa (300-lb/in<sup>2</sup>) internal pressure capability in the event that a later test of a closed-cycle system was desired. The actual air pressure in the heat exchanger system during solar tests at CRTF was planned for 0.9 MPa (130 lb/in<sup>2</sup>). Therefore, it was necessary to conduct an ANSYS stress analysis with the actual set of test conditions. Figure 3.7-5 summarizes the results in the area of the tube return bend where maximum stresses observed (point F) occurred with a 399°C (750°F) inlet temperature. For test purposes, the largest thermal gradient allowed between inlet and outlet manifolds was then established at 399°C (750°F).

A further analysis was conducted to evaluate 30-year-life capability of the heat exchanger system in a closed-cycle, downward-facing-aperture configuration representative of the commercial receiver that it modeled. The tubes were oriented in a vertical attitude for this analysis, and the cavity interchange thermal analysis was conducted to obtain tubing temperatures at design conditions of 538°C (1000°F) inlet, 816°C (1500°F) outlet, and 2.1-MPa (300-lb/in<sup>2</sup>) internal pressure. An allowable stress value for 100,000-hr life was derived by Larson-Miller extrapolation of Huntington Alloy's 1000 and 10,000 hr of data, and using three-fourths of that value as the rupture strength at the predicted tube temperature. Figure 3.7-6 summarizes the results of the analysis. The vertical orientation reduced gravity's contribution to combined stresses in the return bend area, and positive margins of safety were obtained at all locations analyzed.

### Design loads

- Tubing temperatures at full load
- Gravity
- 2.1 MPa (300 psig) internal pressure
- 538°C (1,000°F) inlet

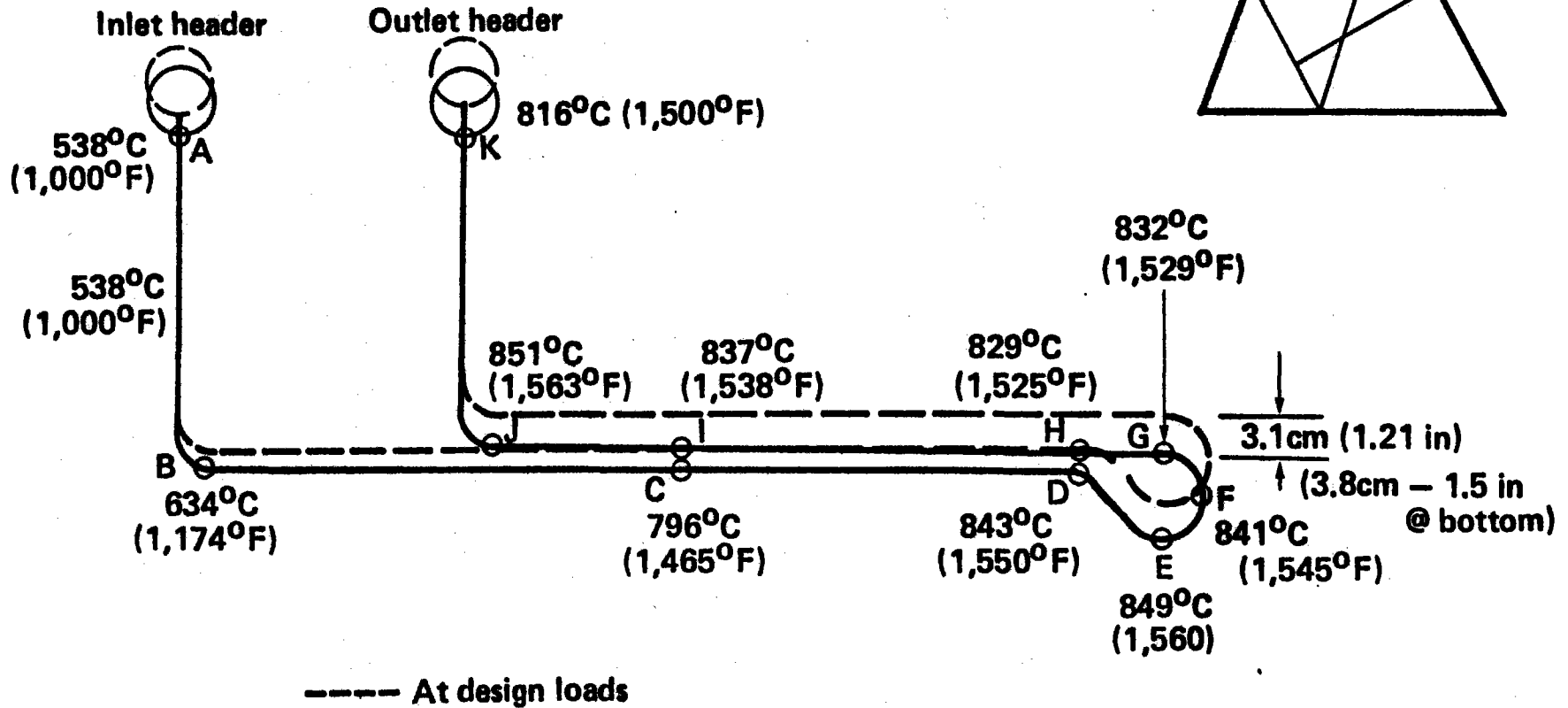
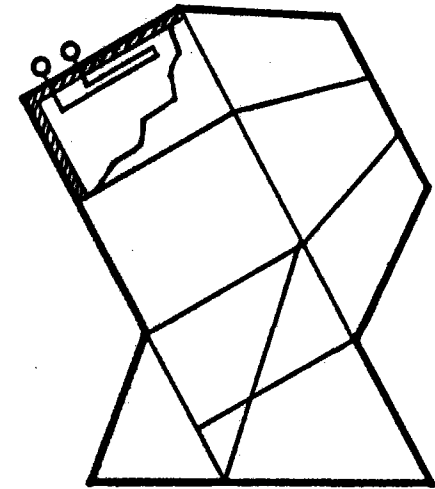
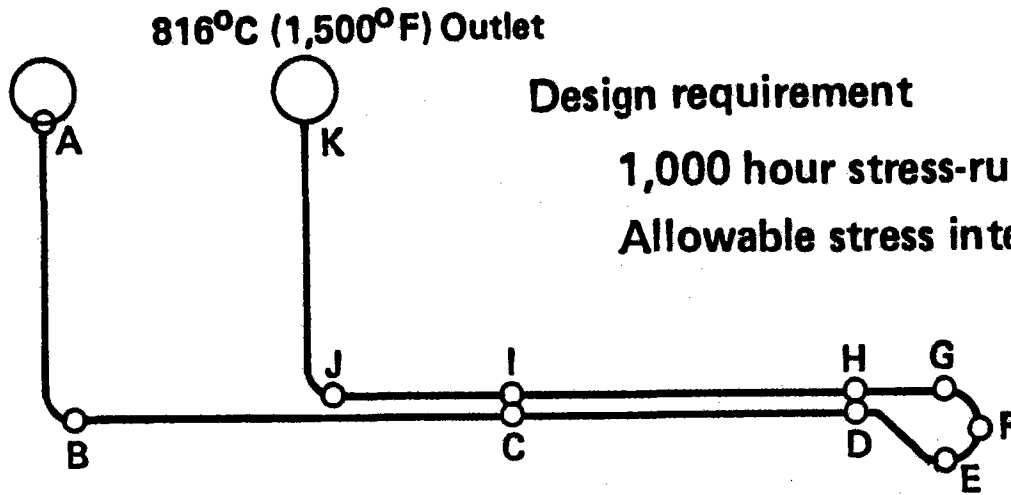


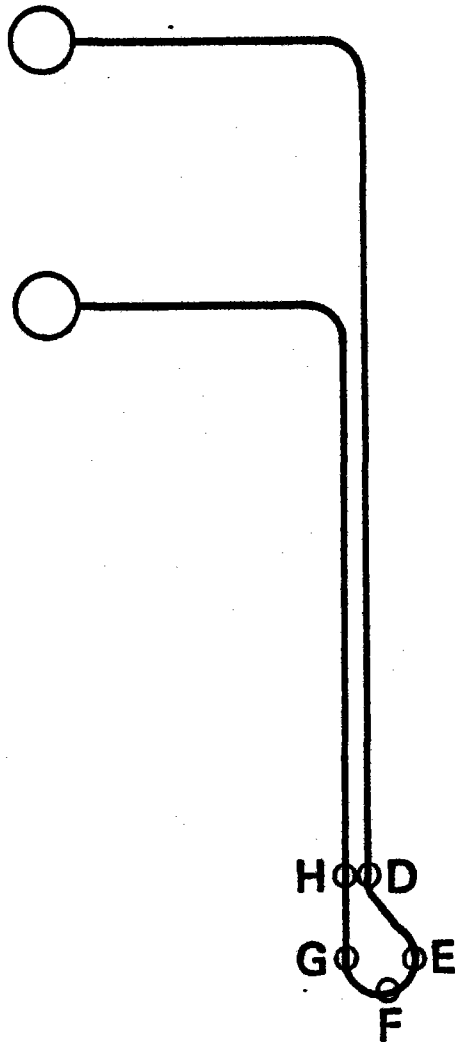
Figure 3.7-4. HX Tube Deflections and Maximum Temperatures



.9 MPa (130 lb/in <sup>2</sup> ) - 538°C (1,000°F) inlet		
Point	Stress (MPa[lb/in <sup>2</sup> ])	M.S.
D	27.1 (3,936)	+ 0.31
E	30.0 (4,353)	+ 0.19
F	31.5 (4,562)	+ 0.13
G	30.0 (4,344)	+ 0.19
H	27.8 (4,035)	+ 0.28

.9 MPa (130 lb/in <sup>2</sup> ) - 399°C (750°F) inlet		
Point	(MPa[lb/in <sup>2</sup> ])	M.S.
D	30.5 (4,425)	+ 0.17
E	35.5 (5,154)	+ 0.00
F	35.8 (5,189)	+ 0.00
G	32.1 (4,662)	+ 0.19
H	30.0 (4,347)	+ 0.67

Figure 3.7-5. Test Case HX Tube Stresses



100,000-hour stress-rupture life  
 Allowable  $3 S_m$  stress (secondary) at temperature shown

2.1 MPa (300 lb/in <sup>2</sup> )–538°C(1,000°F) inlet				
Point	Stress, (MPa [lb/in <sup>2</sup> ])	Temperature, (°C[°F])	Allowable stress, (MPa[lb/in <sup>2</sup> ])	M.S.
D	24.6 (3,569)	818 (1,505)	31.7 (4,600)	+ 0.29
E	27.5 (3,993)	839 (1,542)	27.9 (4,050)	+ 0.01
F	26.9 (3,903)	824 (1,516)	30.7 (4,450)	+ 0.14
G	25.4 (3,685)	827 (1,520)	30.3 (4,400)	+ 0.19
H	23.2 (3,369)	832 (1,530)	29.0 (4,200)	+ 0.25

Vertical Orientation

Figure 3.7-6. HX Tube Stresses Typical 30 Year Life

## SECTION 4.0

### DEVELOPMENTAL TESTING

The design, construction and testing of the 1Mwt BMSR required the extension of available commercial materials and components to a high-temperature solar environment previously not considered in their development. Three applications of state-of-the-art materials to the design needs of the BMSR required supplementary developmental testing. The tests were conducted to determine the performance limits (i.e., design allowables) for the respective materials.

Two of the developmental tests addressed the design limits for heat exchanger superalloy tubing. These included thermal cycling and elevated temperature stress-rupture tests. The alloys of interest were Inconel 617 and Haynes alloy HS188. These are commonly used in high-temperature combustor equipment subject to 800°C (1472°F) temperatures in an oxidizing environment. BMSR heat exchangers were subject to similar temperatures and oxidizing conditions. In addition, the BMSR heat exchangers were subjected to high operating stresses due to internal gas pressure and to frequent rapid changes of stress and temperature. One concern was to determine the maximum short-term temperature limit of the pressurized heat exchanger. This short-term temperature capability was needed as a design margin in the event of accidental overheating of the receiver. Another concern was the erosion of tube walls by spalling of oxidized metal scale. The thermal and pressure stress cycling of the tubes was expected to be contributory to this erosion. In this event, the losses of material must be compensated for by initially providing excess tube-wall thickness.

Developmental tests were also conducted on the highest temperature receiver wall insulation and the solar shielding around the aperture rim. In these cases, the allowable design temperature for insulation and shielding materials was well known. However, testing was needed to expose these materials to the operating environment and high solar flux heating conditions of the BMSR.

Opportunities were taken in all these developmental test programs to learn more about fabrication and installation methods applicable to BMSR construction. The test heat exchangers included tube bending and tube-to-header welds. The insulation and solar shield test samples were designed to include candidate installation fasteners and the typical seams and lap joints needed for construction.

#### 4.1 HEAT EXCHANGER MATERIALS

Heat exchanger tubes and headers in the BMSR were fabricated from Huntington Alloys Inconel 617 superalloy. This is a nickel-based alloy with 22% chromium, 12.5% cobalt, and 9% molybdenum. The Inconel 617 was one of two nickel-based superalloys that were screened and developmentally tested during EPRI Contract RP377-1, the High-Temperature, Closed-Cycle, Central Receiver Concept Definition Study ER-629 (Reference 1). The complete process of alloy selection for test and comprehensive results of heat exchanger materials tests are described in Section 7.0 of Reference 1. Those test results pertaining to the use of Inconel 617 for BMSR heat exchangers are reviewed here.

##### 4.1.1 Thermal Cycle Tests

###### Test Preparations

Lengths of seamwelded tubing of Inconel 617 were obtained for the construction of a specimen heat exchanger. Samples of the tubing were used for initial measurements of chemical composition and mechanical properties.

Prior to fabrication of the test heat exchanger, a series of tube-to-header weld joints were fabricated to establish weld control parameters and to verify weld inspection methods. The Inconel 617 tubing had excellent characteristics for machining, forming, and bending of parts to shape. Its working characteristics were similar to austenitic stainless steel. Weldability was fair, being easier to weld than aluminum, but more difficult than stainless steel. Standard practices of X-ray inspection could be used with the welded assemblies. A thermal cycling test specimen was fabricated

by bending and welding heat exchanger tubing to somewhat larger size headers. The test heat exchanger configuration is shown in Figure 4.1-1.

Thermocouples were attached to inner and outer tube walls to measure wall temperatures and thermal gradients during the cyclic testing. A pressurization system was assembled to provide a continuous internal pressure of 3.45 MPa (500 lb/in<sup>2</sup>) during tests. Both helium gas and air were used for pressurization at different times during the testing.

The heat exchanger was installed in a specially assembled radiant heat lamp test fixture. It is shown in position for testing in Figure 4.1-2. Lamps located on one side of the specimen simulated the radiant thermal environment of the cavity interior. A thick layer of high-temperature insulation blanket simulated the receiver cavity wall behind the heat exchanger.

#### Test Procedure

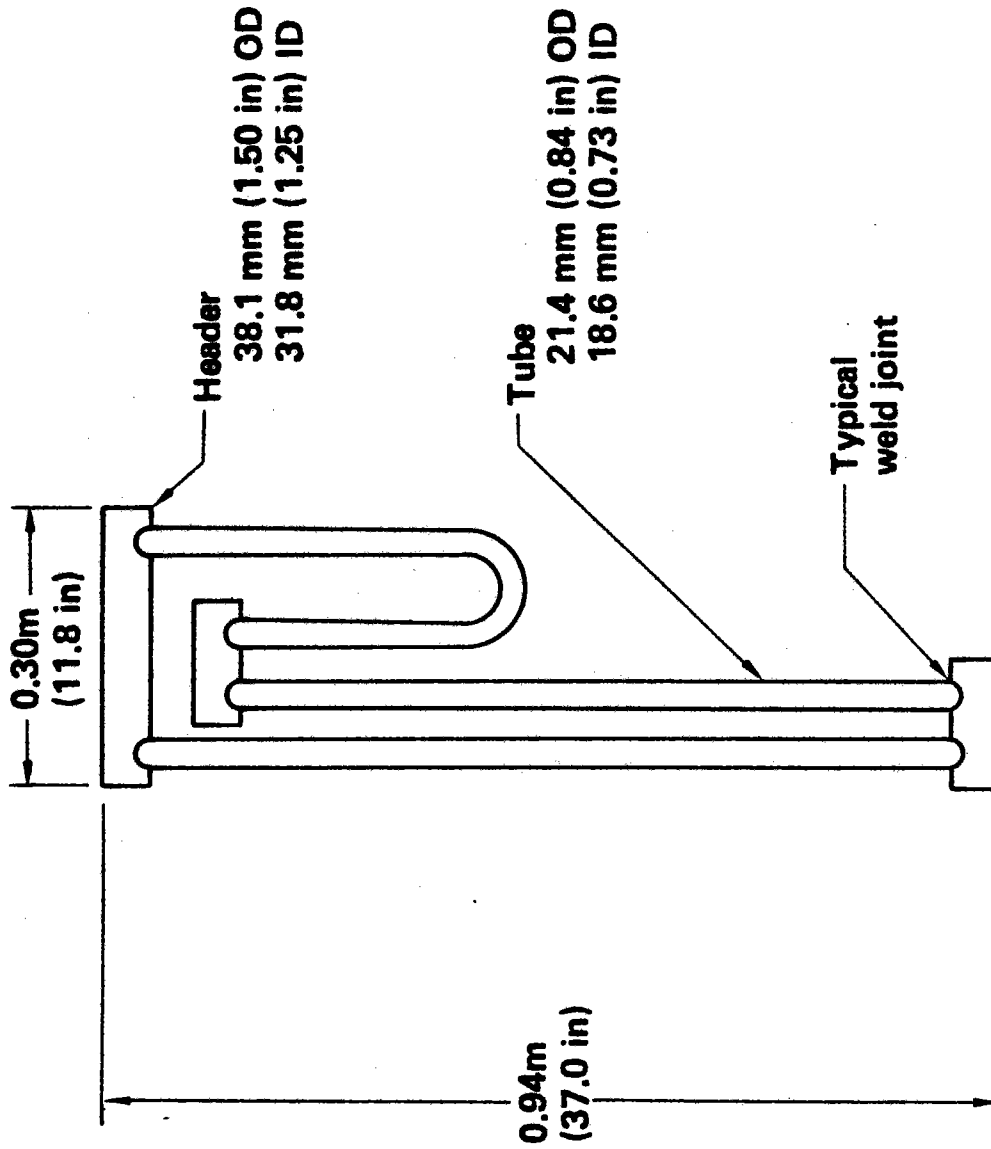
The test assembly was temperature cycled approximately 10,000 times to simulate operational conditions in the commercial solar receiver. A temperature cycle from 483°C (900°F) to 830°C (1525°F) was used. This cycle simulated the most severe portion of the receiver's diurnal temperature cycle and the operating temperature cycle to be expected when small clouds temporarily interrupt the sunlight. Pressure was held at a constant 3.45 MPa (500 lb/in<sup>2</sup>). Tube-wall thermal gradients typical of steady-state heat exchanger operation were produced during the transient heating portion of the thermal cycle. The typical thermal cycle, with a period of 7 to 9 min, is shown in Figure 4.1-3.

#### Test Results

Thermal cycling tests had measurable but acceptable effects on the Inconel 617 heat exchanger. The temperature cycling produced temperatures and thermal gradients in the heat exchanger that were typical of those expected in the BMSR. Based on the temperature-cycling experience, it was concluded that no special requirement was needed to limit heat exchanger heating or

Figure 4.1-1 Heat Exchanger Test Specimen

# Heat Exchanger Test Specimen





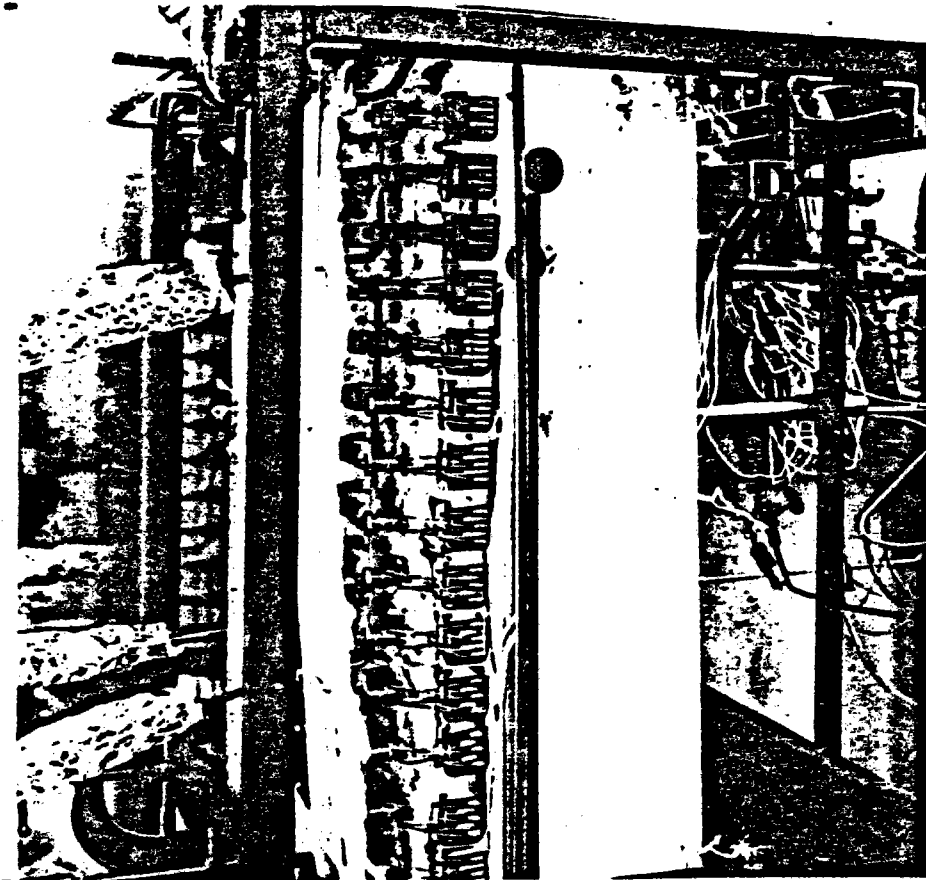
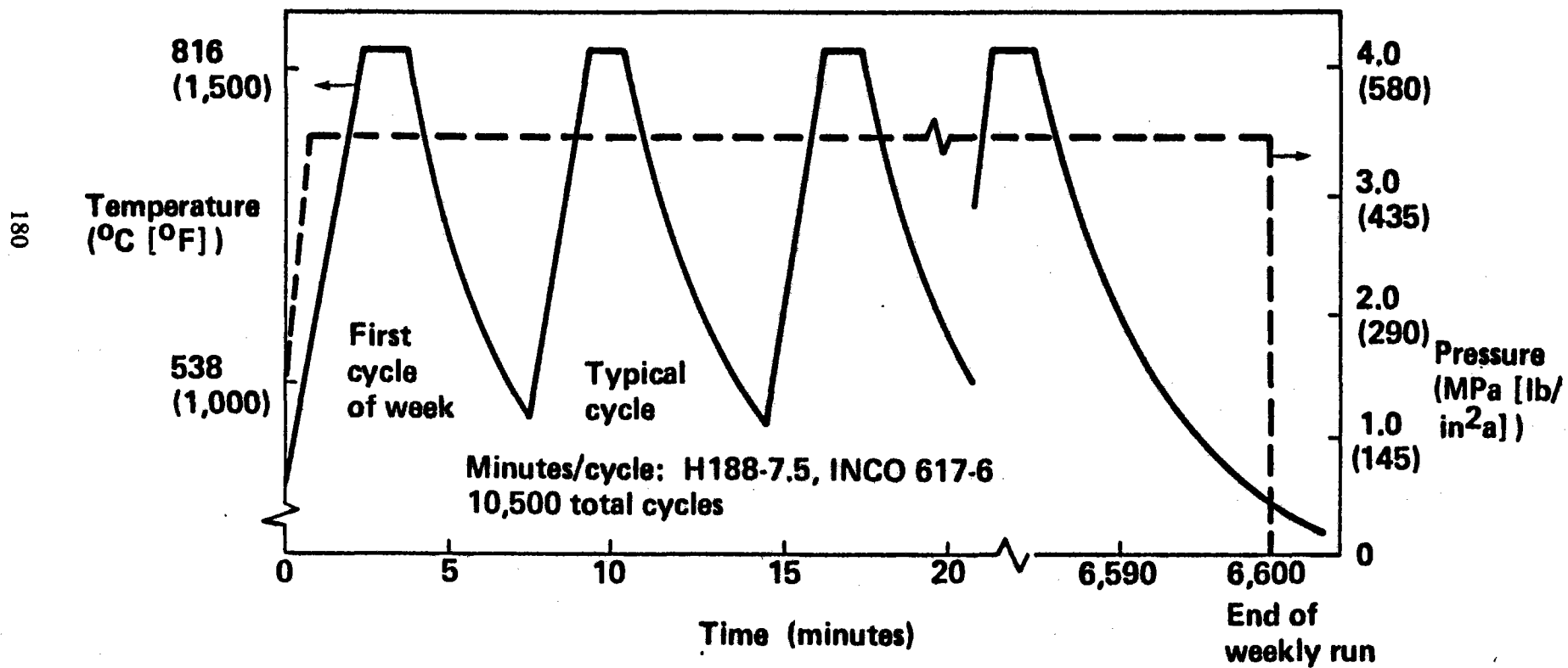


Figure 4.1-2: Test Specimens in Radiant Heat Lamp Facility

Figure 4.1-3 Thermal Cycle Test Conditions  
**Thermal Cycle Test Conditions**



cooling rates in BMSR test operations.

Upon being heated to temperatures of about 800°C (1472°F) in air, an oxide layer was produced on the surfaces of the Inconel 617 heat exchanger. This dark oxide coating was very thin and tightly adherent to the metal substructure. Tests showed that the tube-wall thickness was not measurably reduced by the development or spalling off of this oxide coating. The BMSR heat exchanger tubing did not require any additional wall thickness to compensate for scaling.

The test conditions did affect the metallurgical properties of the Inconel 617 heat exchanger alloy. Changes apparently resulted from the development of a carbide precipitate on the grain boundaries. This precipitate both strengthened and embrittled the material. Yield strength increased by 14%. Elongation-to-rupture reduced from a value of 60% before testing to a value of 43% after testing. It was determined that stress-relieving heat treatment at about 950°C (1742°F) after forming and welding the heat exchanger assembly could reduce but not eliminate this age hardening in the BMSR heat exchangers.

#### 4.1.2 Elevated-Temperature Rupture Tests

Elevated-temperature tests-to-rupture were conducted with Inconel 617 tubing during the RP377-1 study. These tests determined the effects of significantly overheating the tube beyond the planned service temperature limit of 870°C (1600°F) in the BMSR.

#### Test Preparations

Tubular test specimens were prepared from the straight tubular portion of the thermal cycling test specimen and from as-received tubing. A cap was welded over one end of these tubes and pressurization fittings were welded to the other end.

A test bed of refractory materials and high-temperature insulation was made up to house the tubular test section (Figure 4.1-4). Radiant heat lamps

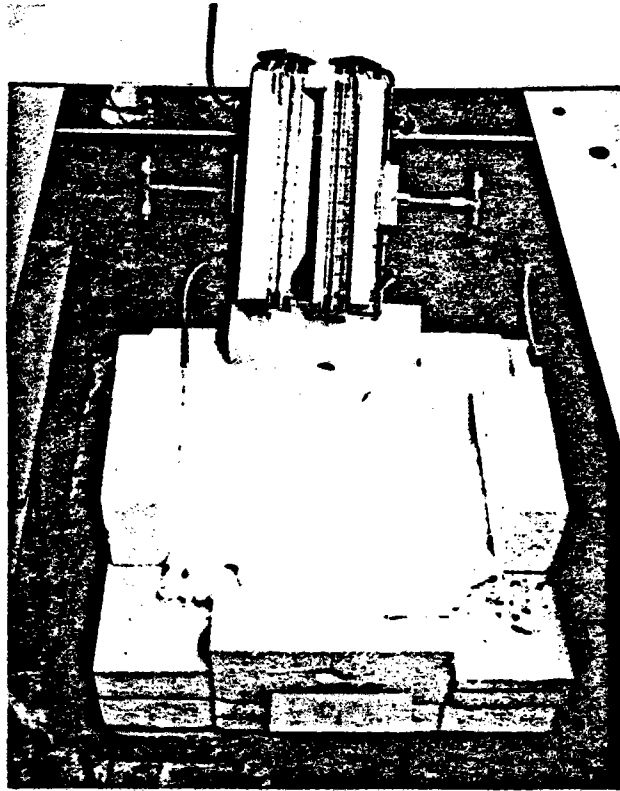


Figure 4.1-4: Test Bed and IR Lamp Arrays for Elevated-Temperature Rupture Tests

were provided to heat a central segment of the tube to uniform high temperatures.

A pressurization system was provided to maintain a gas pressure of 3.45 MPa (500 lb/in<sup>2</sup>) in the samples during tests. This provided a pressure induced stress of about 25 MPa (3600 lb/in<sup>2</sup>) which was similar to the expected stress level in heat exchangers during BMSR tests.

### Test Procedure

The tubing specimens were heated and thermally cycled during these tests. However, a longer cycle with 50 min at temperature was adopted along with a 10-min period of passive cooling between cycles. Because the purpose of these tests was to determine the temperature at which short-term failure occurred, the tests started at a temperature of 870°C (1600°F) for 50 cycles, then went up in 56°C (100°F) increments, with an additional 50 cycles of testing at each temperature level. The tubing outside diameter was checked at the end of each 50-cycle stage of testing.

### Test Results

Both of the Inconel 617 tube samples survived the 50 test cycles at each test temperature up to and including 982°C (1800°F) with no apparent changes. Their measured outside diameters remained unchanged.

The sample made from as-received Inconel 617 tube ruptured after 11 cycles at 1037°C (1900°F). The previously cyclic-tested tube lasted through 33 of the 1037°C cycles. The failures were characterized by bulging and cracking of the tube wall in the highest temperature zone. Therefore, failure presented a benign leakage condition rather than a violent rupture.

These elevated-temperature tests-to-rupture showed that the BMSR heat exchangers designed for a maximum operating temperature of 870°C (1600°F) could, in fact, be operated for short periods of the time at temperatures up to about 982°C (1800°F). This additional short-term capability was used in the planning for BMSR tests. A series of tests was formulated that aided in

the determination of receiver off-design performance by intentionally restricting the flow through one heat exchanger. As a result of these tests with Inconel 617, the maximum heat exchanger tubing temperature for short-term BMSR tests was established at 982°C (1800°F). This knowledge that unplanned short-term temperature excursions [REDACTED] could be accommodated without risk of catastrophic failure of the heat exchangers, simplified test planning activities.

#### Alloy State-Of-The-Art

Inconel 617 was a relatively new alloy at the time it was selected for the BMSR design. As such, there were no standard specifications (AISI, SAE, ASTM) available to control physical and mechanical properties, chemical composition or product form. A preliminary material specification was developed by BEC (Boeing Engineering and Construction), in conjunction with Huntington Alloys, to be used for control of purchased tubing. In this specification, minimum mechanical properties and chemical composition limits were negotiated but stress-rupture life test data was to be used for information purposes only, not as acceptance or rejection criteria. Use of this alloy in future solar components will necessitate development of more rigorous material controls.

#### 4.2 RECEIVER THERMAL INSULATION TESTING

The materials used for BMSR cavity wall insulation include mineral wool in block form along with Kaowool and Saffil ceramic fiber insulation blankets. The mineral wool and Kaowool were selected for receiver cavity insulation in the RP377-1 study of a commercial solar electric power system (Reference 1). They were selected because of their relatively light weight and high-temperature insulation capability combined with commercial availability and cost. The mineral wool block, with a long-term service temperature limit of 816°C (1500°F) and specific gravity of 0.24, was used for the outer half of the insulation walls in both the commercial receiver and the BMSR. The Kaowool blanket products, with an effective service temperature limit of 1260°C (2300°F) and a specific gravity of 0.13 to 0.20, were used for the inner half of all the insulation walls in the commercial receiver and those

insulation walls that were not directly sunlit in the BMSR. A 5.1 cm (2 in) layer of Kaowool is used behind 2.5 cm (1 in) of Saffil blanket (service temperature 1650°C (3000°F) and specific gravity of 0.09) on the directly sunlit areas of BMSR walls.

Thermal properties of these materials, such as their specific heat and thermal conductivity, were well known. These data had been used and verified in a wide range of furnace and kiln designs and other high-temperature applications. Insulation vendors routinely provide these data. Vendors also have developed and tested installation fasteners and assembly techniques that were suitable for use with materials having various service temperatures.

However, the solar thermal radiant heat transfer surface properties of these materials were not well known. Their surfaces are semitransparent; their radiant heat transfer surface properties result from a combination of effects, including absorption, transmission, scattering, and reflection from the loosely spaced matrix of ceramic fibers. As a result, the radiant thermal properties such as solar absorptivity and infrared emittance, which are critical in determining operating temperatures of solar-heated insulation, are dependent on--

- a. Radiant heat transfer properties of the ceramic fiber such as solar absorptance, reflectance, and emittance of the basic material.
- b. Characteristics of the fiber composite, such as fiber size, spacing, and orientation.
- c. Variations in fiber composite caused by differences in the past history, including differences in material from batch to batch and the packing or loosening of blanket fibers during installation and use.
- d. Contamination of the porous fiber blanket by foreign particles which are readily transported by airflow through the loosely spaced fiber matrix. Sources of this contamination in the solar receiver include high-temperature outgassing of binder and manufacturing residue in sublayers of insulation, and airborne dust and dirt.

For these reasons, it is believed impossible to analytically determine the

insulation surface temperatures in solar receiver cavities to any degree of certainty. In furnaces and kilns, the interior temperatures are reasonably uniform and the insulation surface temperatures can be assumed to be nearly equal to the internal gas temperature. In the solar receiver cavity with concentrated heat sources and dynamic cooling by heat exchangers or boiler tubes, the local surface temperatures can vary from one another and from the internal air temperature by hundreds of degrees. Furthermore, the solar receiver insulation surfaces of interest are irradiated by their surroundings. There is no way to discriminate between surface-emitted thermal radiation and reflections of heat from the surrounding areas. Infrared pyrometry is of no value in determining the actual temperature of such a surface although it can be used to measure combined emitted and reflected radiosity and to characterize the effective blackbody temperature of the surface.

The BMSR thermal insulation testing program was devised to answer these concerns. Its purpose was to directly and experimentally verify the suitability of insulation materials and fabrication details for use in the BMSR. This main goal was accomplished by design and construction of an insulation test facility that subjected a 32-cm-diameter (12.6-in-diam.) area of insulation to the radiant thermal environment expected in the hottest portion of BMSR insulation wall. This area is on the BMSR back cone directly across from its aperture. The test-zone area was as small as considered reasonable for testing insulation fasteners and seams between panels of the insulation. Details of the design and construction of the insulation test facility are described in Section 4.2.1.

Other goals accomplished during the insulation test program included the following:

- a. Gaining experience in obtaining thermocouple measurements of temperatures inside the low-density insulation wall
- b. Measuring differences in optical and thermal radiative properties of the material that may result from handling, installation, and high-temperature outgassing in the cavity environment
- c. Experimentally determining the effects of airborne dust and dirt being



artificially deposited on the candidate insulation materials prior to testing

- d. Determining the time required for cavity heat to soak through the 15-cm-thick (5.91-in-thick) insulation wall and verifying acceptability of resulting outer-surface temperatures

Test procedures, details, and direct results of the 17 individual insulation tests conducted for BMSR design development are described in Section 4.2.2. Section 4.2.3 describes measurements of the insulation radiative heat transfer properties that were conducted in conjunction with the insulation thermal tests. The overall test program results and conclusions are summarized in Section 4.2.4.

#### 4.2.1 Insulation Test Facility

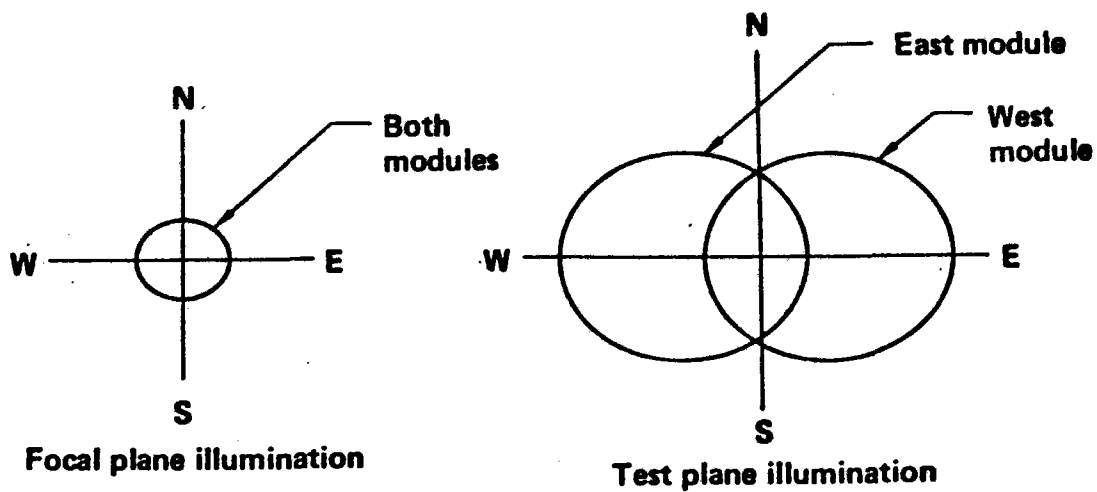
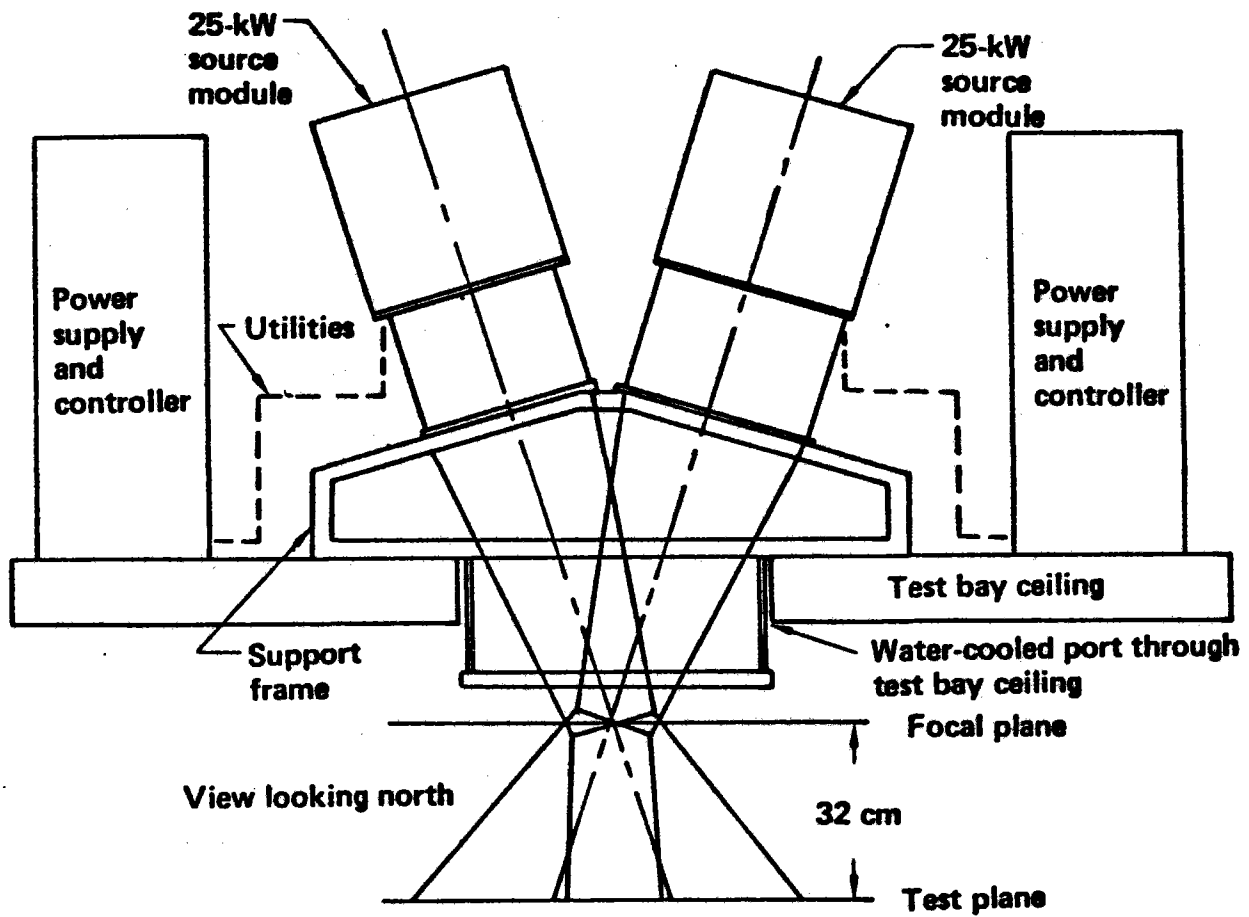
The design goal for the insulation test facility was to provide an accurate simulation of all the important characteristics of the cavity interior environment. These characteristics included the thermal conditions resulting from solar heating and radiant heat transfer to the important cavity heat sinks, including the aperture and heat exchangers. The solar heating included direct illumination of some surfaces plus the internal cavity reflections of sunlight from enclosure walls. Radiant heat losses to the aperture and heat exchangers were functions of the radiative view factors and required that the test facility receiver cavity be a geometric scale model of the BMSR. For this same reason, the internal cavity materials and radiant heat transfer properties were the same as the BMSR.

Solar heating was simulated by xenon arc-lamp modules from the Environmental Test Laboratories at Boeing Aerospace Company. These lamps are normally used as sources for solar simulation in space thermal environment chambers.

Two of the 25-kW source modules were used along with their elliptical focusing mirrors, power supplies, and controls. The module optics were adjusted to focus up to 16 kW of radiant heat onto a circular area 15 cm (5.91 in) in diameter. The arrangement to achieve simultaneous heating of the same area by both modules is shown in Figure 4.2-1.

Figure 4.2-1 Arrangement of Arc Lamp Modules for Insulation Test Facility

# Arrangement of Arc Lamp Modules for Insulation Test Facility



This arrangement of the two source modules resulted in a spreading of the arc-lamp beams as they passed through the focal plane. This image spreading simulated the solar flux as it passed through the BMSR aperture, representing both the aperture solar flux and the first-incident solar flux inside the BMSR. The source module arrangement with overlapping of module images on the test plane (Figure 4.2-1) was adjusted until a first-incident solar flux of  $500 \text{ kW/m}^2$  was achieved on the test plane. This covered the expected range of first-incident flux on hottest surfaces of the BMSR, up to  $425 \text{ kW/m}^2$ , plus providing an additional range for off-design testing.

Figure 4.2-2 shows the first-incident flux pattern produced at the test plane of the insulation test facility. This pattern can be compared with the predicted BMSR solar flux pattern in Figure 3.2-6. Both patterns show a long, narrow region of highest flux intensity. Also, by selecting a 15-cm (5.91-in) receiver aperture and a distance of 32 cm (11.81 in) from the focal plane to the test plane, the diameter of the BMSR cavity interior scales to about 32 cm (12.60 in), the reference circle shown in Figure 4.2-2.

The long, narrow region of maximum heat flux in the test facility also provided an area for uniform illumination of seams and joints in the insulation samples.

The arrangement of arc-lamp modules (Figure 4.2-1) was accomplished by mounting them on the floor, aiming them down through an existing port in the test laboratory deck, and locating the simulated receiver and test specimen base in the room below. This arrangement allowed utilization of facilities normally used for calibration of the lamp modules. The X-Y scanning radiometer normally used for source module calibration was used to measure the test solar flux at the focal plane or test plane. This instrument provided the data for Figure 4.2-2 and for frequent checks on the calibration of the facility.

Figure 4.2-3 shows the range of maximum first-incident solar flux levels that could be achieved on the test plane. Flux levels were changed by adjusting the arc-lamp power supplies. Arc-lamp current settings were

Figure 4.2-2 Arc Lamp Heat Flux Pattern on Test Plane

# Arc Lamp Heat Flux Pattern on Test Plane

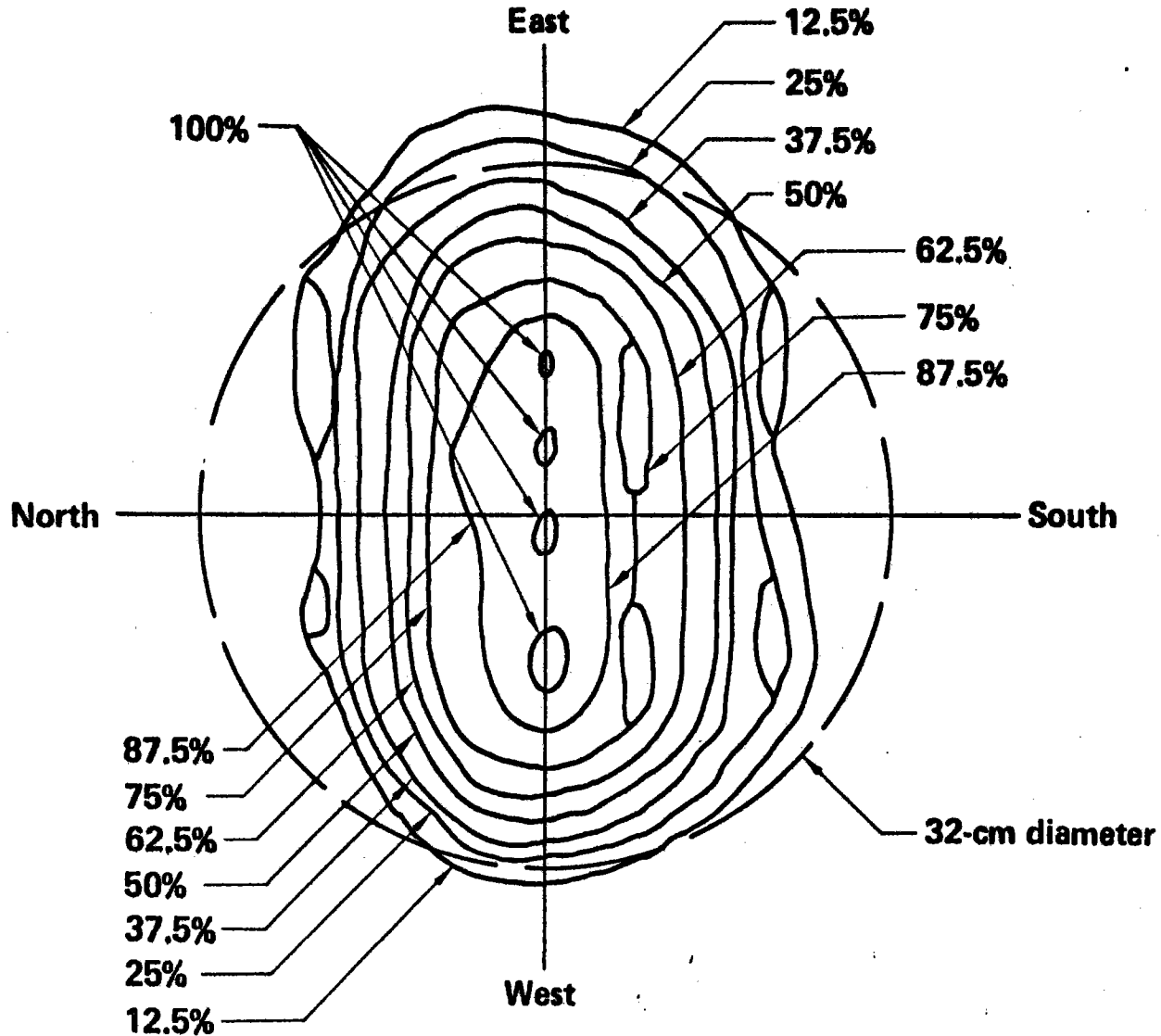
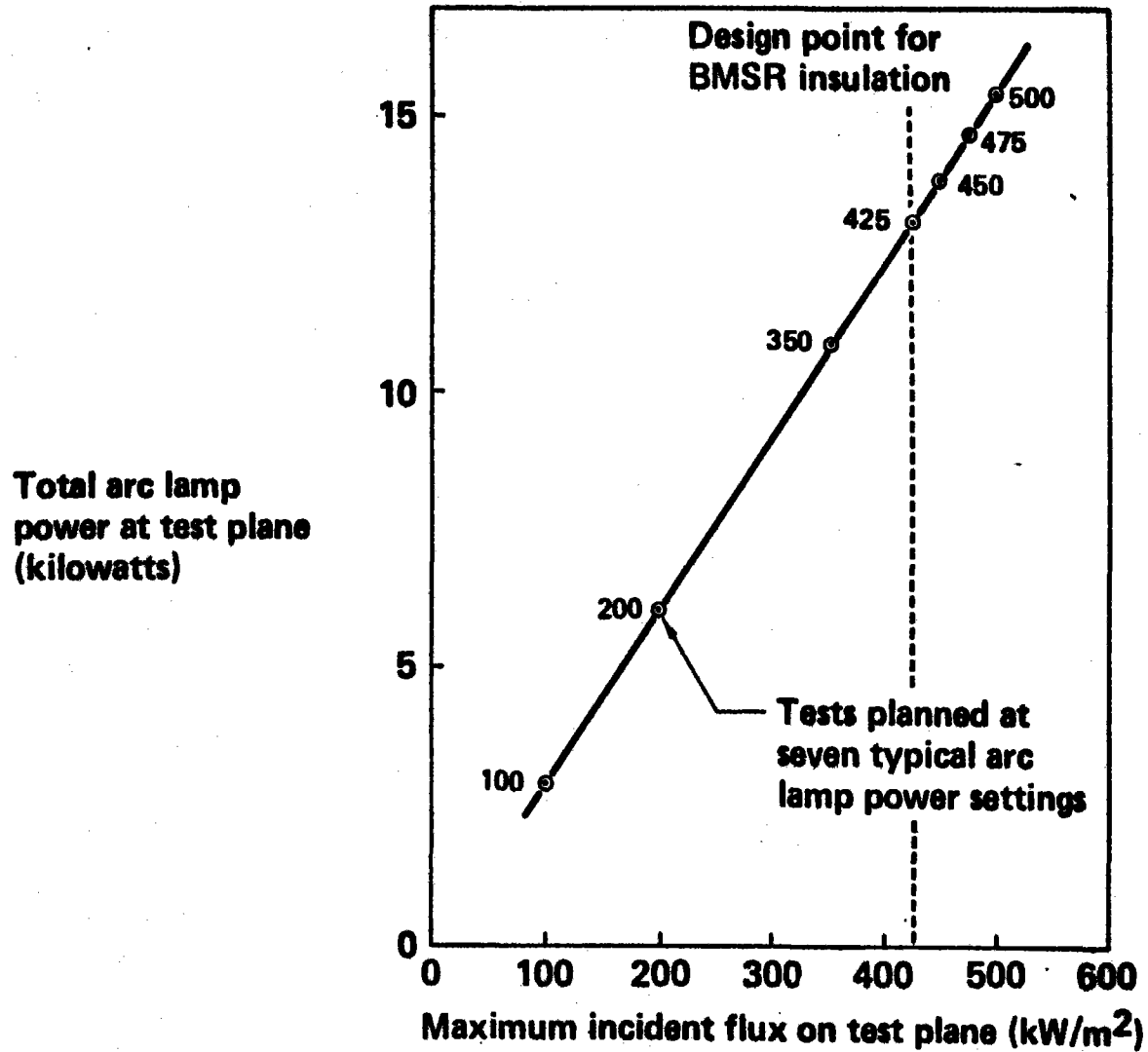


Figure 4.2-3 Arc Lamp Adjustments for Test Plane Heat Flux

# Arc Lamp Adjustments for Test Plane Heat Flux



obtained for each of the desired test points indicated on the figure; then, the test condition could be reproduced at will by adjusting each of the arc-lamp modules to the corresponding current settings.

Thermal characteristics of the BMSR were simulated in the insulation test facility by using a scale-model receiver cavity. The details of this 20-kW solar receiver are shown in Figure 4.2-4. The upper portion of the simulated receiver was permanently attached overhead in the test cell. Its aperture was located to coincide with the focus of the arc-lamp modules. As indicated in the figure, this fixed-in-place portion of the cavity included--

- a. 15-cm-diameter (5.91-in-diam.) restrictive solar aperture
- b. 15-cm-thick (5.91-in-thick) insulation side walls
- c. Metal tube heat exchanger, which geometrically simulated the cooling effect of BMSR heat exchangers
- d. Mounting flange for insulation sample holder

The insulation samples formed the bottom wall of the scale-model receiver. They were assembled inside the 15-cm-deep (5.91-in-deep) sample holder. When attached to the fixed-in-place portion of the model cavity, this fixture located the surface of the insulation sample on the test plane (Figure 4.2-1).

A number of different insulation sample configurations were tested. Four of these are shown in Figure 4.2-5. Alternative materials included the original standard composite of mineral wool block and Kaowool blanket; and high solar flux composite, in which the sunlit Kaowool layer was replaced by Saffil blanket. Other samples, all using the high solar flux composite, included lap joints, butt joints, and ceramic wall-attachment fittings.

Photographs of the fixed-in-place and sample holder structures are shown in Figures 4.2-6 and 4.2-7. Figure 4.2-8 shows the as-built cavity wall insulation and 4.2-9 shows the heat exchanger that was fabricated from stainless steel tubing and oxidized to provide a black surface coating.

Figure 4.2-4 Receiver Cavity Model for Insulation Test Facility

# Receiver Cavity Model for Insulation Test Facility

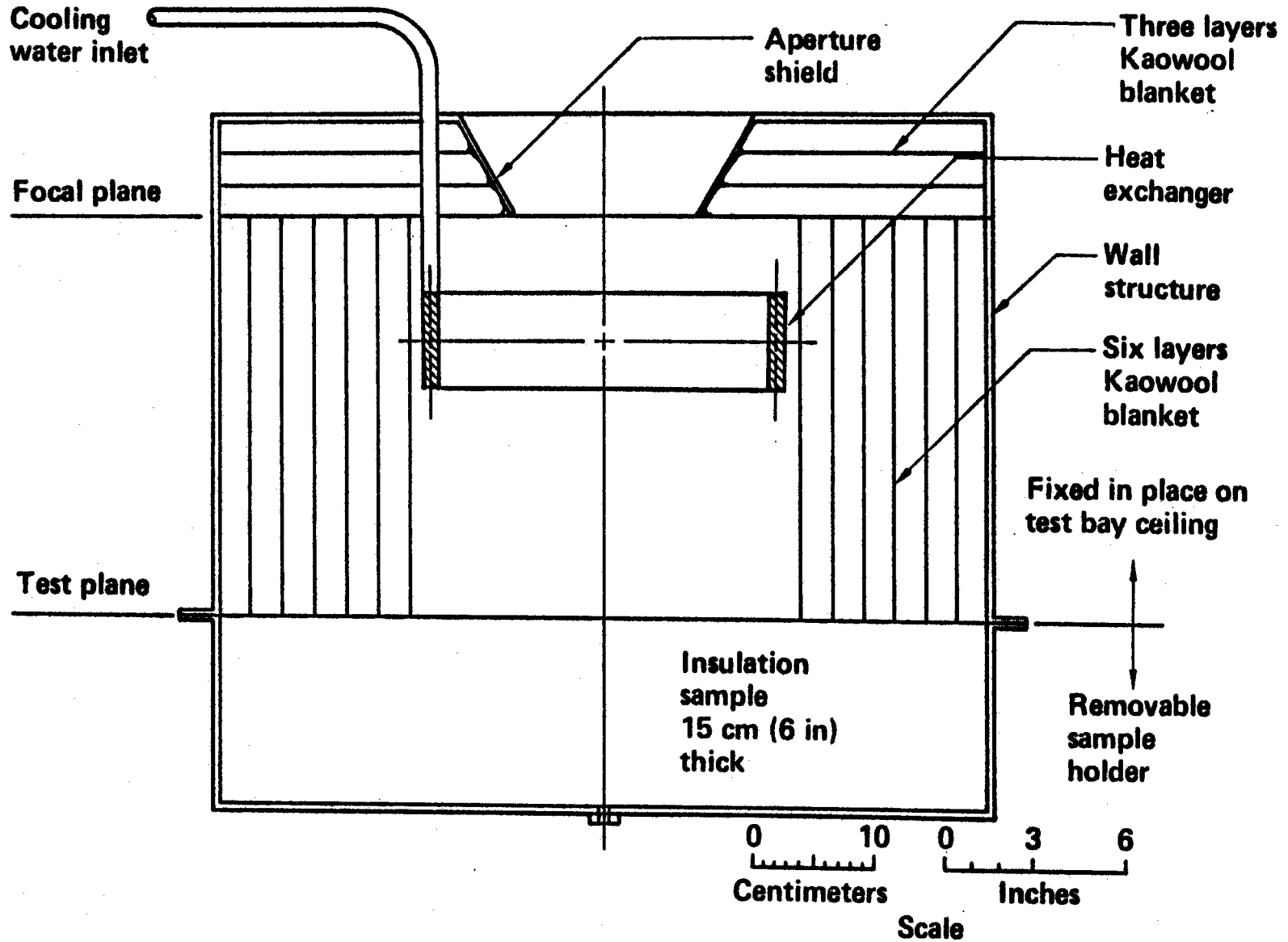
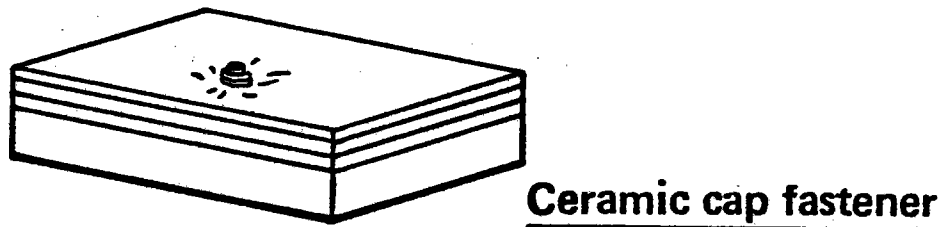
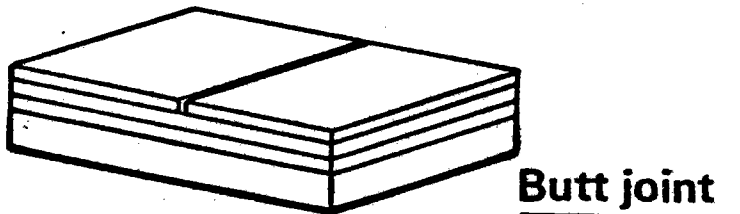
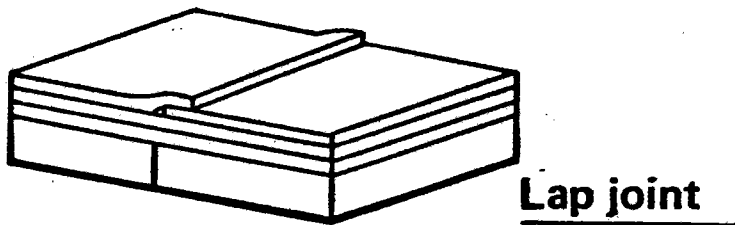
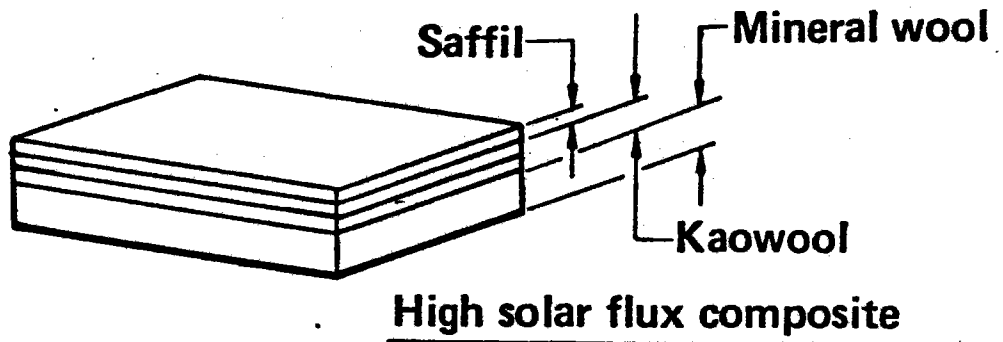
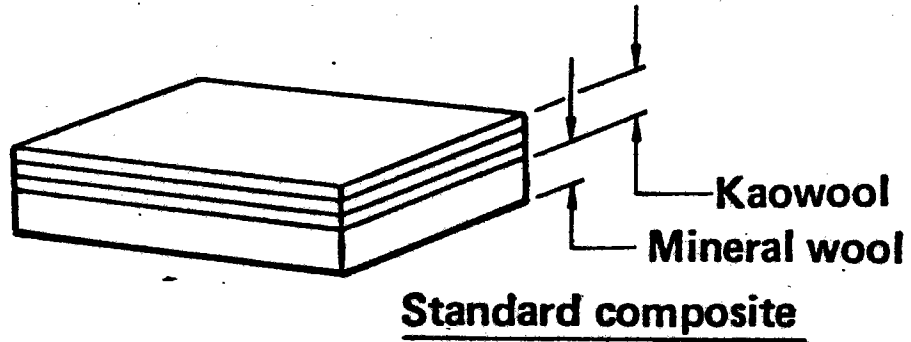


Figure 4.2-5 Insulation Test Samples

# Insulation Test Samples





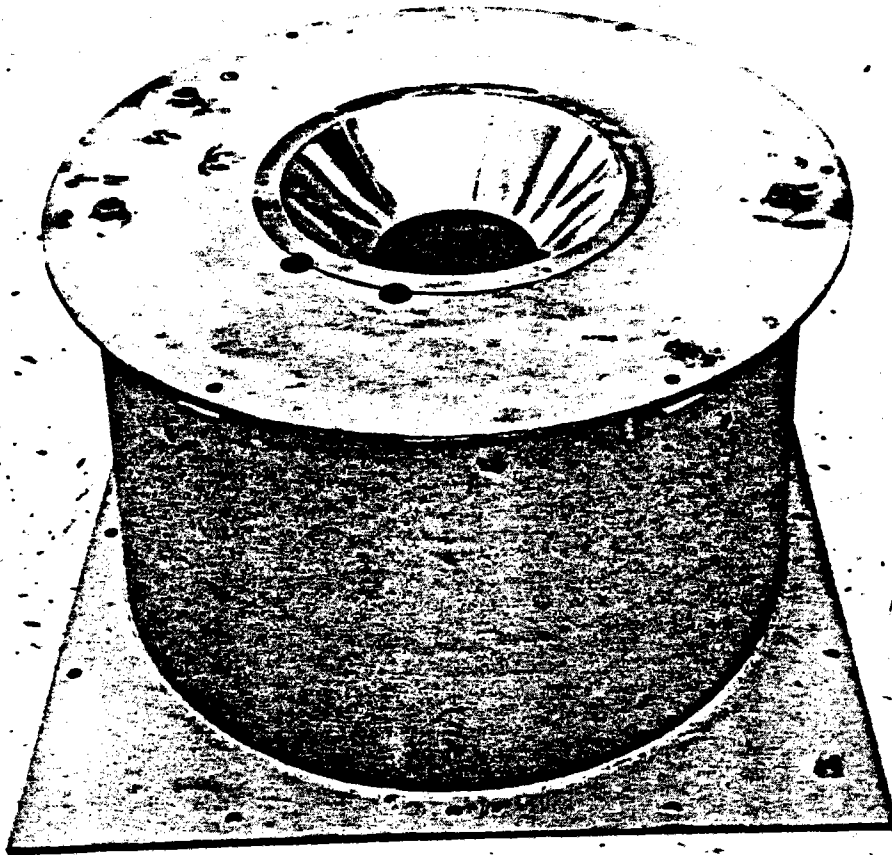


Figure 4.2-6: Fixed-in-Place Cavity Structure

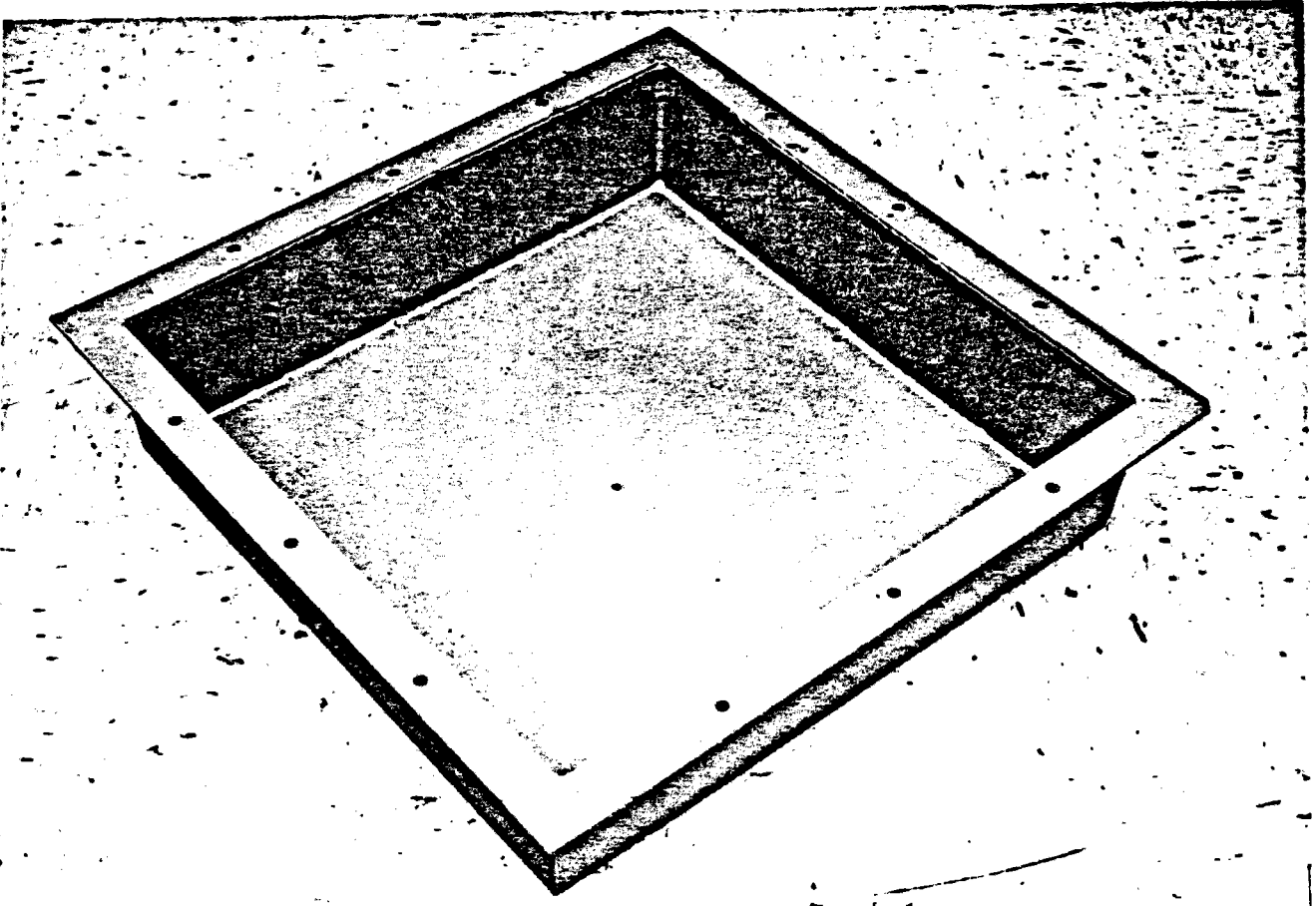


Figure 4.2-7: Sample Holder Structure

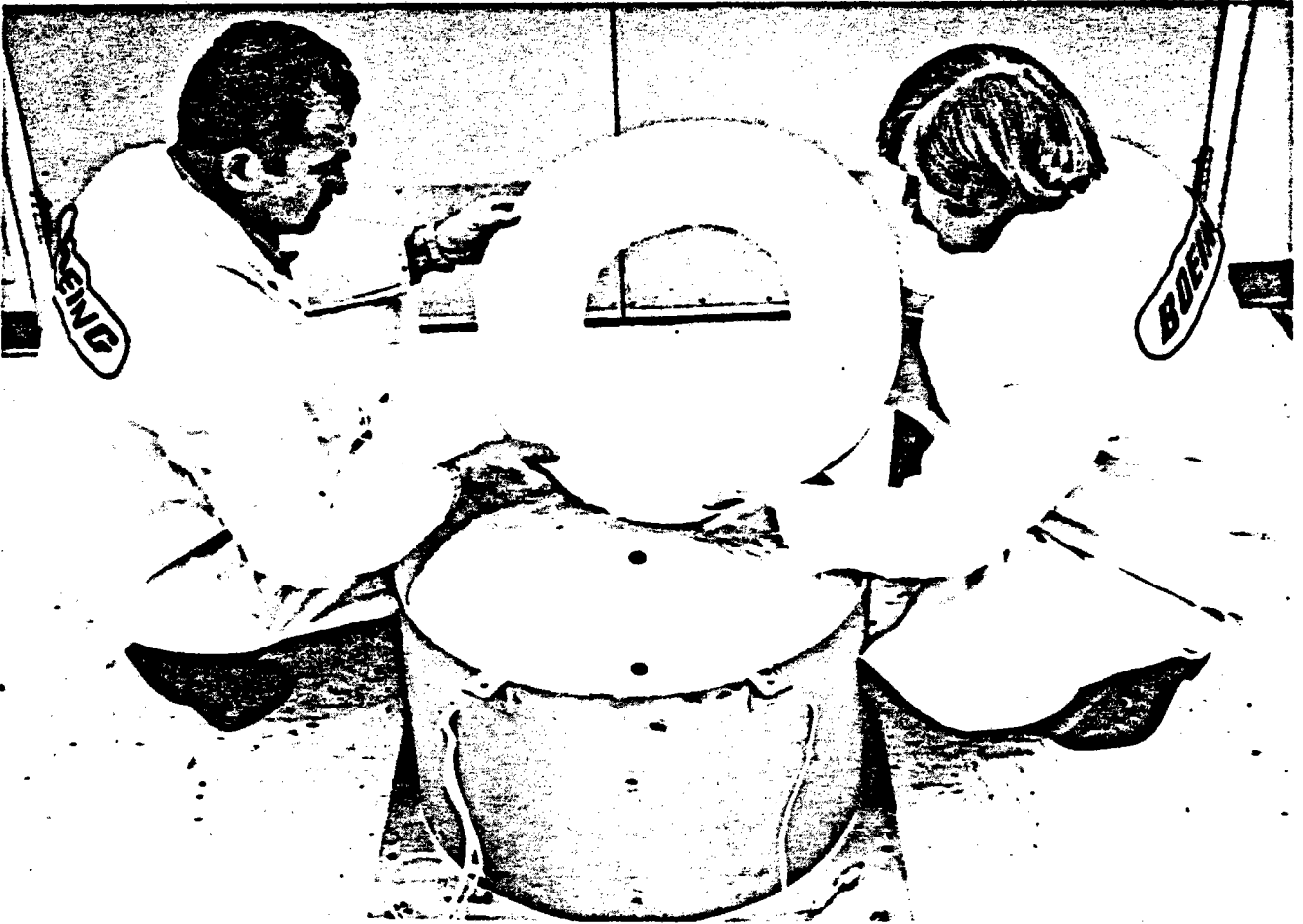


Figure 4.2-8: Instrumentation in Place

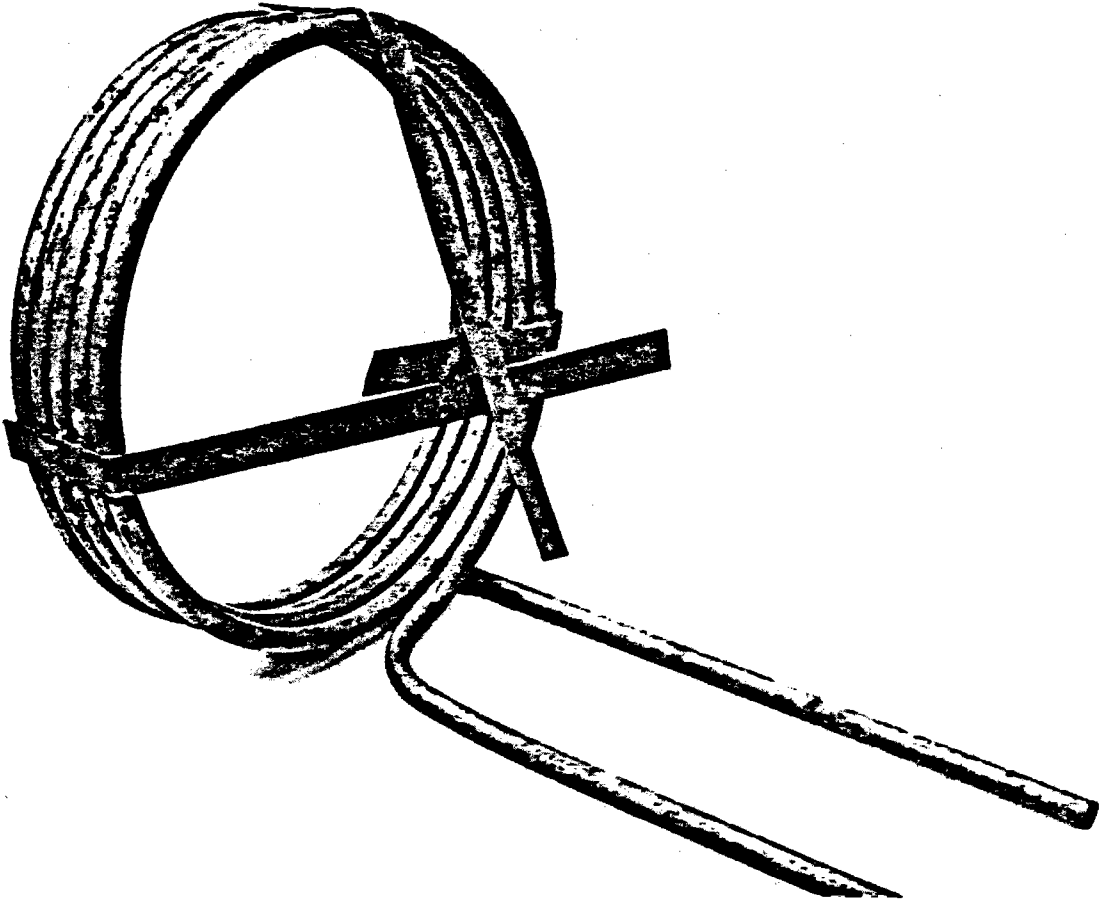


Figure 4.2-9: Heat Exchanger After Oxidation

Figure 4.2-10 shows the arc-lamp modules on the upper deck of the test setup. Figure 4.2-11 shows the model cavity with specimen holder removed during calibration of the first-incident flux on the test plane.

The model cavity was instrumented with a variety of thermocouples of specialized configurations. The four different types of thermocouple assemblies used in the insulation test facility are shown in Figure 4.2-12.

The type I thermocouple was used to measure inlet and outlet water temperatures, the temperature of the heat exchanger tubing inside the cavity, and the temperature of the outer metal shell of the receiver. The type I thermocouples were installed by resistance-welding the thermocouple junction directly to the metal surfaces of the receiver.

The type II thermocouple was used to measure insulation wall temperature in the fixed-in-place portion of the model receiver. These thermocouples, made from unsheathed wire, have a short service life at BMSR temperatures, but were acceptable for the limited service life of the insulation tests.

The type III and type IV thermocouples were prototype designs for use in the BMSR insulation. They were metal sheathed for extended service life at temperatures up to 1100°C (2010°F). They were used to instrument the insulation test samples. Type IV were standard off-the-shelf units. Type III thermocouples used a welded-on metal fin that increased the thermal contact area of the junction with the insulation blanket materials. This was intended to reduce errors that resulted from conduction of heat from the tip of the thermocouple down the metal sheath and wires.

From three to six type III thermocouples were used to measure insulation temperatures in each of the insulation samples. The basic instrumentation consisted of thermocouples located at the center of the illuminated area at positions behind each of the three 2.5 cm (1 in) thicknesses of insulation blanket. The lap-joint sample included three additional insulation thermocouples, located away from the seam, and used for measuring lateral thermal gradients. The sample, which incorporated a ceramic insulation fastener, included three additional thermocouples on the fastener.



Figure 4.2-10: Arc Lamp Modules

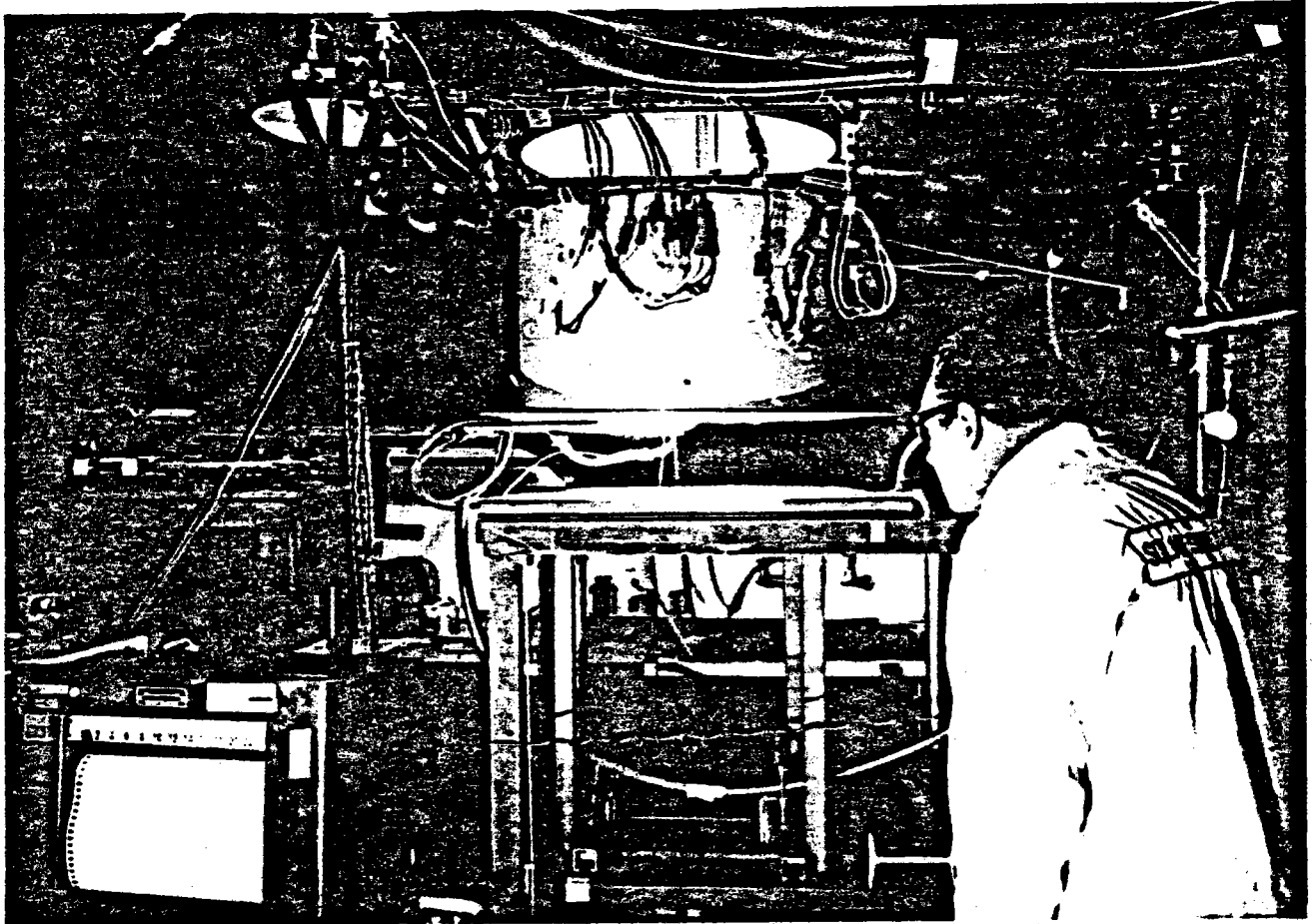
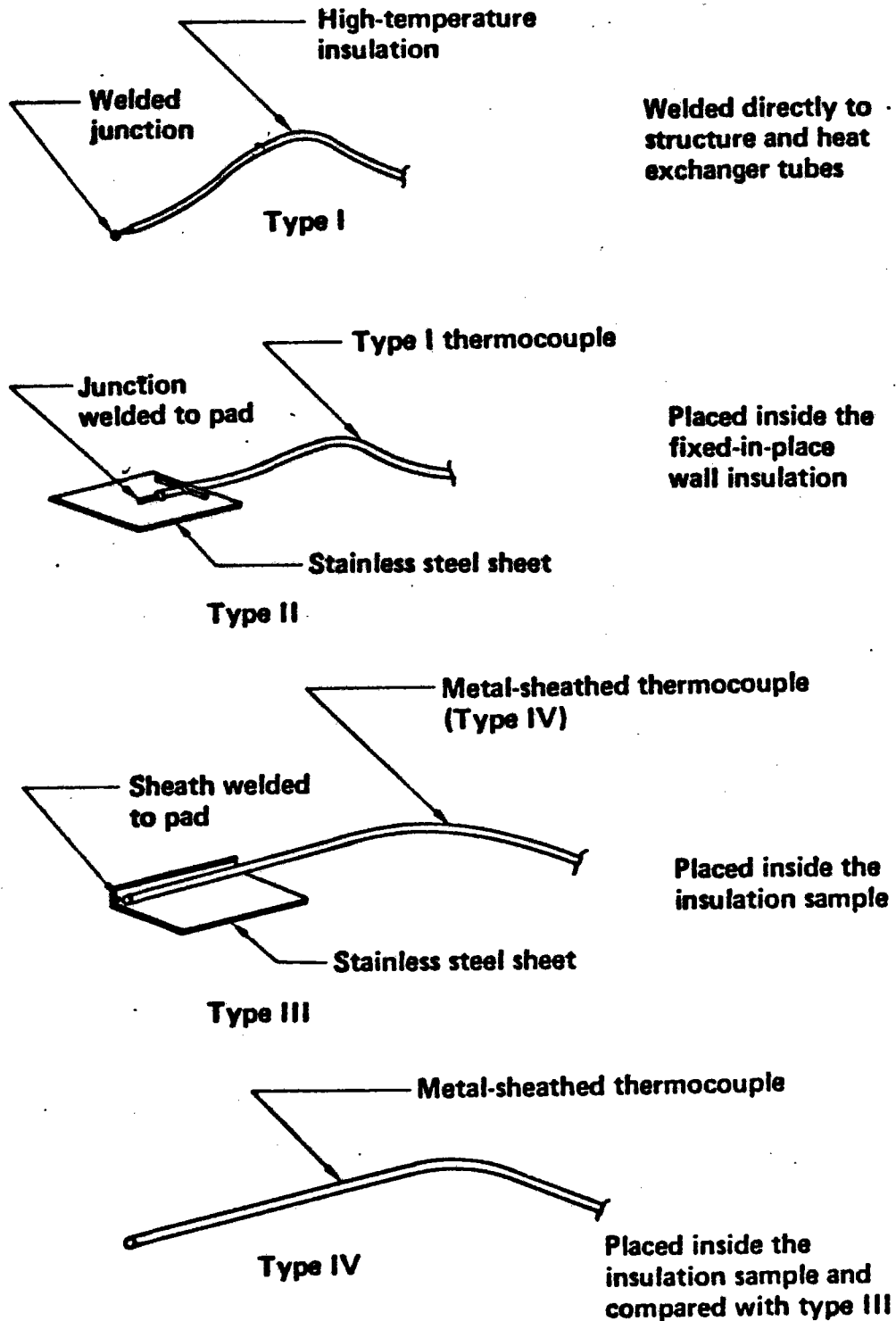


Figure 4.2-11: Test Plane Flux Calibration

Figure 4.2-12 Thermocouple Assemblies Used in the Insulation Test Facility

## Thermocouple Assemblies Used in the Insulation Test Facility





Redundant type IV thermocouples were located adjacent to the type III finned units on several tests. Their readings always closely matched those of the type III units and as a result of these checks, it was determined that standard thermocouples without the welded fins could be used in the BMSR.

Thermocouples were referenced by a 65.6°C (150°F) reference junction system and outputs were recorded on a multipoint strip chart recorder.

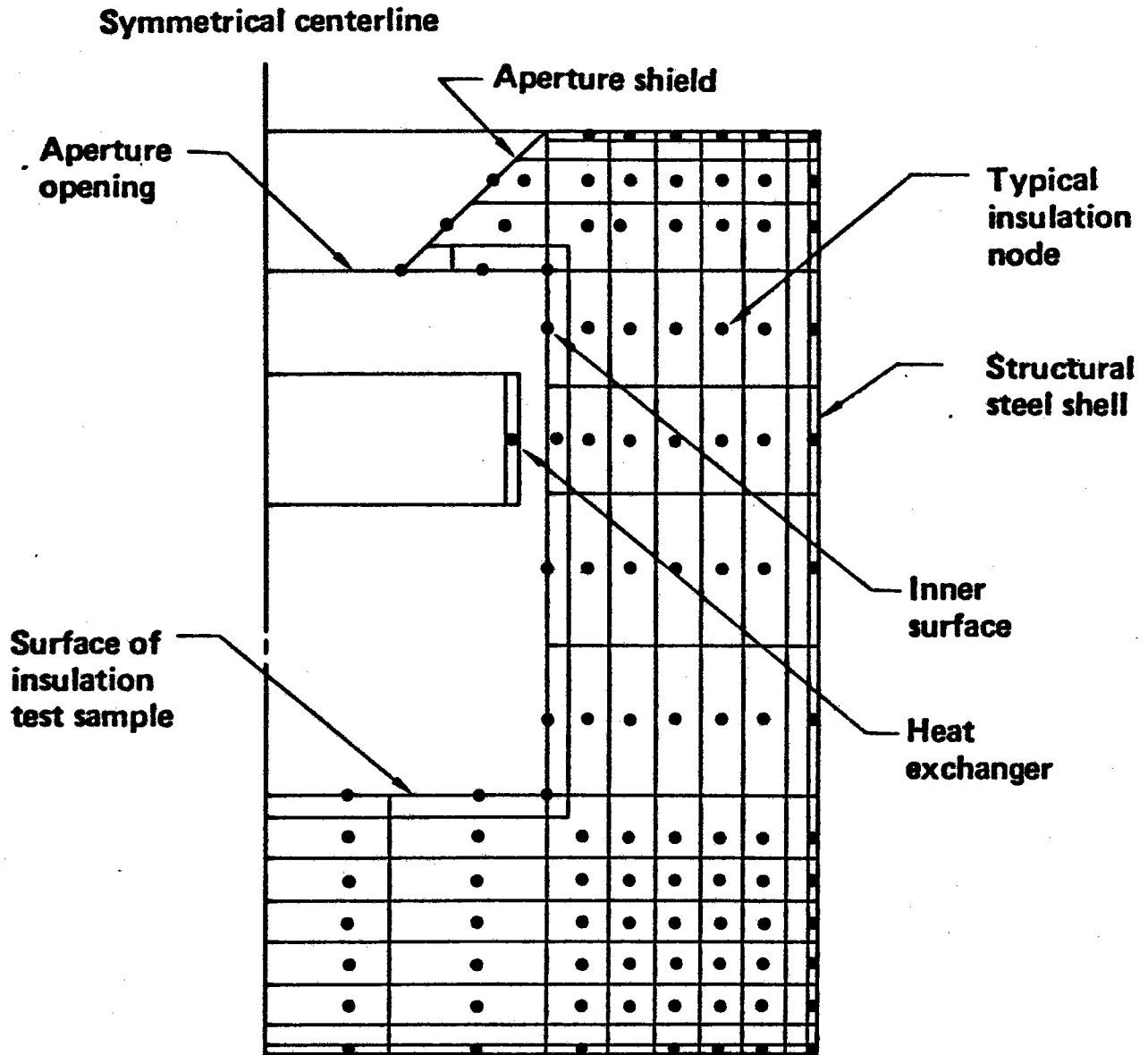
As mentioned earlier, the main goal of the insulation test program was to expose the insulation to the receiver environment and to directly observe the suitability of insulation candidates for the BMSR. Thermocouple instrumentation was not necessary to accomplish these test goals. However, these tests were also viewed as an opportunity to learn more about analyzing solar receiver temperatures and performance. The thermocouple instrumentation of the insulation test facility model receiver was required to provide data to compare with this analysis.

Thermal analyses were conducted to predict operating temperatures and heat transfer performance of the insulation test facility as a cavity solar receiver. Circular symmetry was used throughout the model to simplify its development and use. The lumped-parameter thermal node network for the model is shown in Figure 4.2-13. As indicated, the interior surfaces of the model cavity were divided into a total of nine isothermal regions. The insulation sample surface was represented by a circular area 14 cm (8.27 in) in diameter and an annular segment from 14 cm out to the cavity inside diameter of 32 cm (12.60 in). The side-wall inner surface was divided into four short cylindrical sections. The aperture wall was divided into two annular areas that extended from the 15-cm-diameter (5.91-in-diam.) aperture opening to 21 cm (8.27 in) in diameter and from 21 to 32 cm (8.27 to 12.60 in). As noted in the figure, the insulation wall behind these sections was divided into seven layers through its thickness. The heat exchanger was simulated by an opaque cylindrical surface located to correspond with the position of the water-cooled coil of heat exchanger tubes.

The lumped parameter nodes in Figure 4.2-13 were interconnected by the appropriate conduction and radiation heat transfer mechanisms. Internal

Figure 4.2-13 Thermal Model of Insulation Test Facility

# Thermal Model of Insulation Test Facility



## Heat transfer mechanisms

- Conductors between all adjacent nodes
- Conductors from shell nodes to ambient air
- Radiators between all inner surface nodes and to heat exchangers and through the aperture
- Arc lamp heat sources applied to inner surface nodes and heat exchanger

arc-lamp heat flux distributions were determined by the Monte Carlo Radiative Interchange View Factor Program previously described in Section 3.2. The exterior convective and radiative heat transfer to the test bay was accounted for by conductors from external thermal nodes to a node simulating the test bay heat sink environment. Temperatures were computed by the Boeing Engineering Thermal Analyzer (BETA) computer code operating in a transient mode with this detailed thermal model.

The initial thermal model computations were based on preliminary best estimates of the radiative solar and infrared properties of the cavity insulation. These predictions of Kaowool insulation surface temperatures are shown in Figure 4.2-14. Because of errors in radiative thermal properties of the Kaowool, these predictions were significantly lower than the early test results.

After the first series of tests, the insulation samples were removed to the laboratory for measurements of solar absorptance and emittance. These new data were used to revise the thermal analysis model, and temperature predictions were improved.

Figure 4.2-15 shows the revised predictions of insulation temperatures in the test facility. These temperatures were for insulation located on the centerline of the receiver. Surface temperatures are shown along with backside temperatures for each of the 2.5 cm (1-in) insulation layers. Thermocouple data from one of the tests at  $425 \text{ kW/m}^2$  first-incident flux compared quite closely with these analytical temperature predictions. This improved match of analysis with the test data was based on a Saffil solar absorptance of 0.14 and an infrared emittance that varied linearly with temperature, ranging from 0.385 at  $560^\circ\text{C}$  ( $1040^\circ\text{F}$ ) to 0.260 at  $1350^\circ\text{C}$  ( $2530^\circ\text{F}$ ).

#### 4.2.2 Insulation Test Activities

Eleven days of insulation tests were conducted using a variety of sample configurations and insulation heat flux levels. Pertinent features of these test runs are summarized in Table 4.2-1. The Series 1 tests, which exposed

Figure 4.2-14 Kaowool Test Results and Preliminary Analysis Results

# Kaowool Test Results and Preliminary Analysis Results

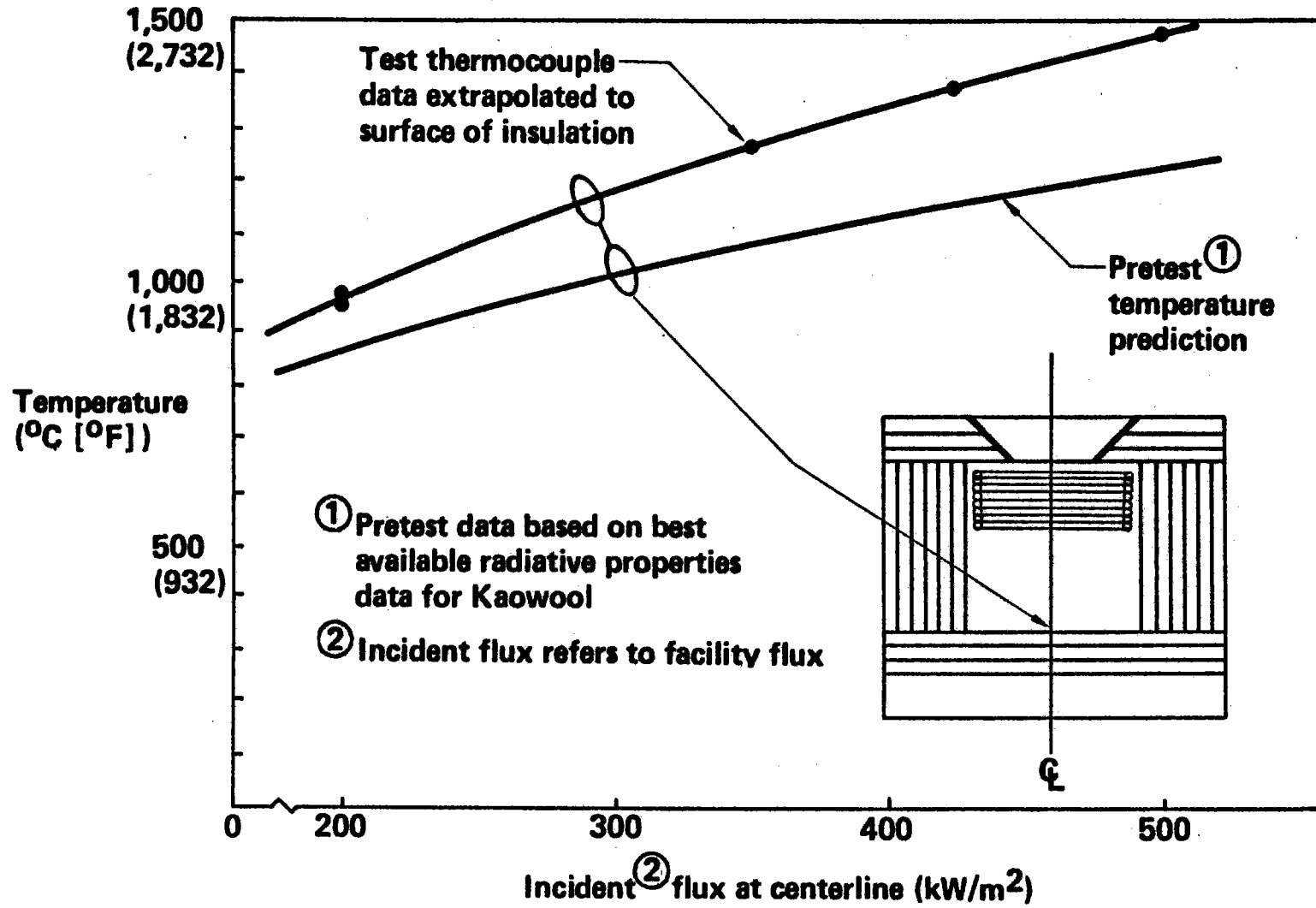


Figure 4.2-15 Test Data Correlation—Insulation Test Facility

# Test Data Correlation—Insulation Test Facility

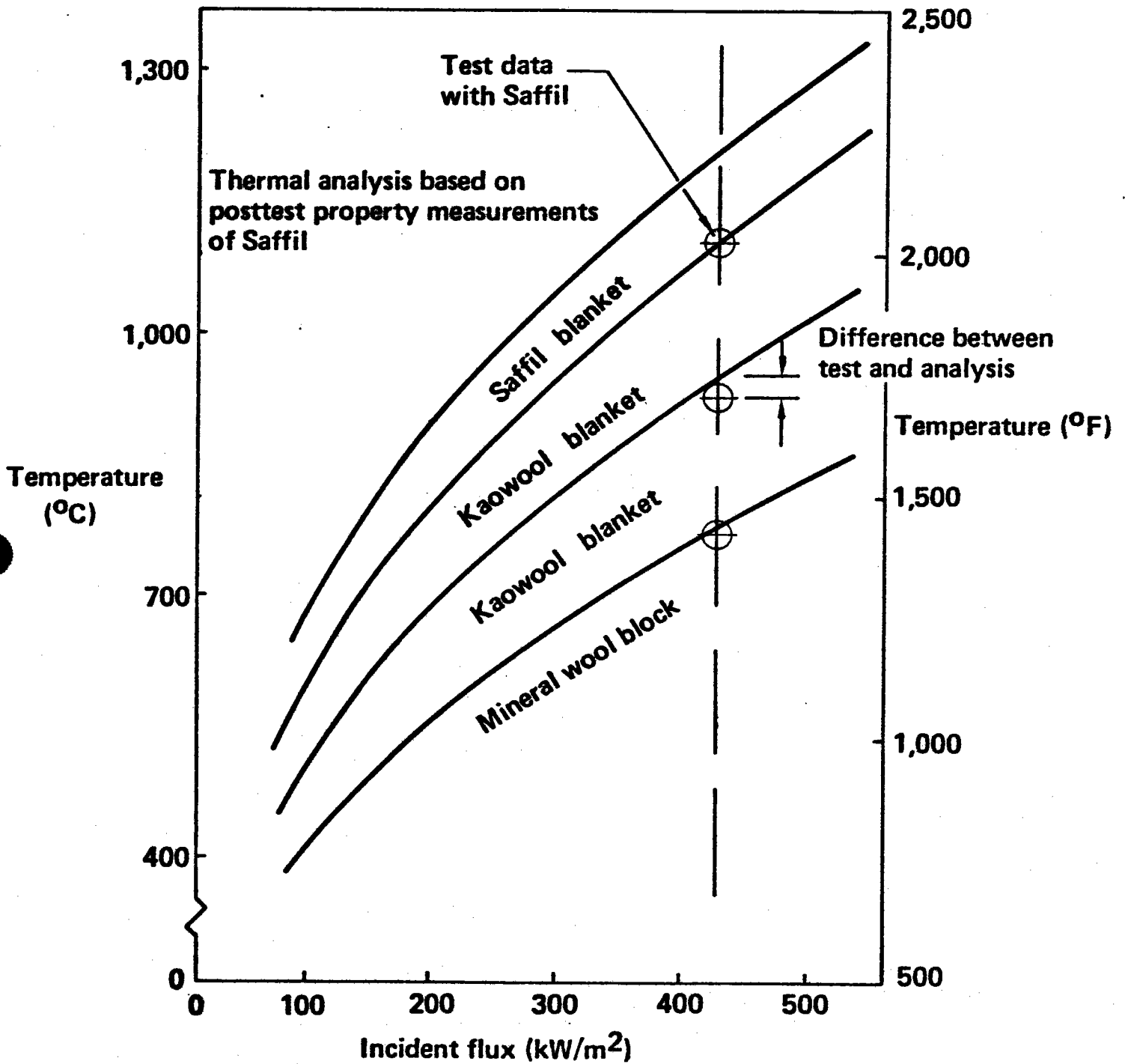


Table 4.2-1 Insulation Test Configurations and Results

## Insulation Test Configurations and Results

Test series, date	Material	Features	Flux level (kW/m <sup>2</sup> )	Results
1A, 12/20/76	Standard composite with Kaowool	Continuous tests with same plain sample	100 to 200 to 350	No damage
1B, 12/21/76			425 and 500	Surface cracking
1C, 12/22/76			Repeat of 200	No change
2A, 1/25/77	High solar flux composite with Saffil	Plain	100 and 425	No damage
2B, 1/31/77		Plain with dirt sprinkled on surface	425	Crusty surface layer
3A, 2/16/77		Lap joint	100 and 425	No damage
4A, 2/17/77		Butt joint with dirt sprinkled on one half	425	No damage on clean half; crusty layer on dirty half
5A, 3/1/77		All tests of same sample with ceramic cap fastener	100 and 425	No damage
5B, 3/7/77			450	No damage
5C, 3/8/77			475	Surface cracking of ceramic cap
5D, 3/10/77			500	

Kaowool to increasing solar flux, showed that this material was acceptable for BMSR first-incident flux levels up to  $350 \text{ kW/m}^2$ . Testing at  $425$  and  $500 \text{ kW/m}^2$  resulted in catastrophic failure of the Kaowool.

The Saffil test sample was exposed to  $425 \text{ kW/m}^2$  without apparent damage. Following this initial indication of acceptability for the BMSR, it was tested in a variety of as-built variations. These included (1) deposition of dirt on the sunlit surface, (2) simulation of a butt joint between adjacent Saffil pieces, (3) simulation of a lap joint, and (4) use of ceramic fasteners for installation. The Saffil material passed all these tests at  $425 \text{ kW/m}^2$  without apparent damage.

The duration of tests ranged from 2.5 to 6.0 hr. Figure 4.2-16 shows typical heating rates for the insulation at locations 2.5 and 5.1 cm (1 and 2 in) from the heated surface. The insulation 2.5 cm (1 in) back was near its final equilibrium temperature within about 1.5 hr. The insulation 5.1 cm (2 in) back took 3 to 4 hr to come to temperatures within about  $10^\circ\text{C}$  ( $18^\circ\text{F}$ ) of the apparent equilibrium values. Based on these data, it was concluded that the exposed surface of the cavity insulation reached a near-equilibrium temperature within 1.0 hr of the start of each test.

Individual test runs are discussed in the following paragraphs. Details of the test setup, procedures, and resulting observations of insulation performance are described.

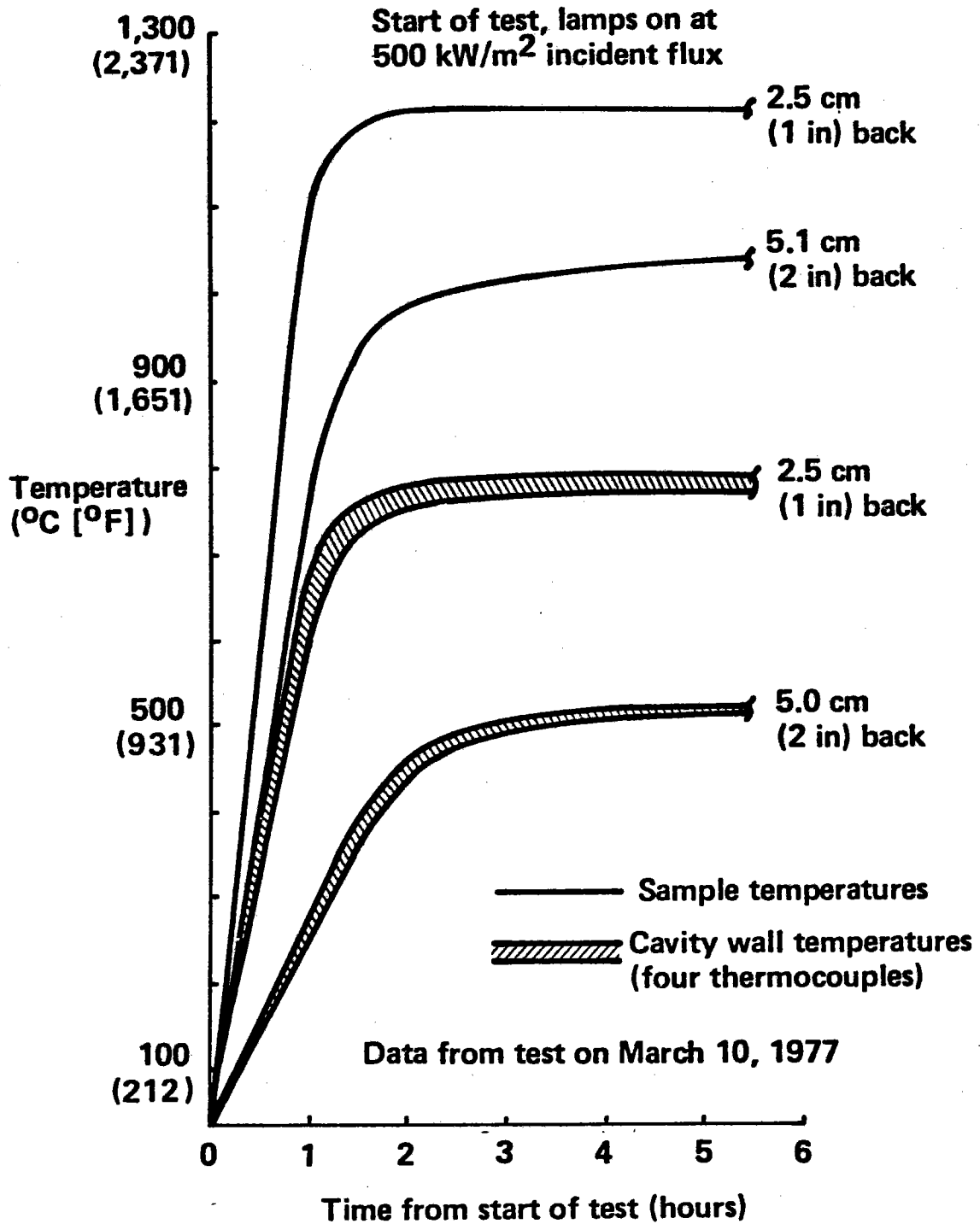
#### Test Series 1, Plain Kaowool

The Series 1 test sample consisted of three layers of 2.5 cm (1 in) Kaowool blanket backed up by 7.6 cm (3 in) of mineral wool block. Insulation temperatures were measured in the center of the heated area of the sample. Type III thermocouples (Figure 4.2-12) were placed behind each of the 2.5 cm (1 in) layers. Five sets of thermal equilibrium temperatures were obtained during Series 1 tests. These were obtained after several hours of test operation at each insulation heat flux level.

After a short period of warmup at an incident flux of  $100 \text{ kW/m}^2$ , the heating

Figure 4.2-16 Typical Heating Rates for Insulation Tests

# Typical Heating Rates for Insulation Tests





rate was increased to 200 kW/m<sup>2</sup>. Thermal equilibrium conditions were achieved and the heating rate was increased to 350 kW/m<sup>2</sup> for the remainder of the day. Arc lamps were turned off and the test setup allowed to cool overnight. Visual inspection of the insulation did not reveal any significant changes.

The same insulation sample was reheated and exposed to incident fluxes of 425 and 500 kW/m<sup>2</sup>. This again occupied a full day of testing; however, this time the cooldown was observed just as the arc lamps were turned off. The insulation, glowing red hot at the instant the lamps were turned off, appeared to be severely cracked. Cracks continued to radiate brightly after the rest of the insulation surface and turned dark, as if the sample was back-lighted.

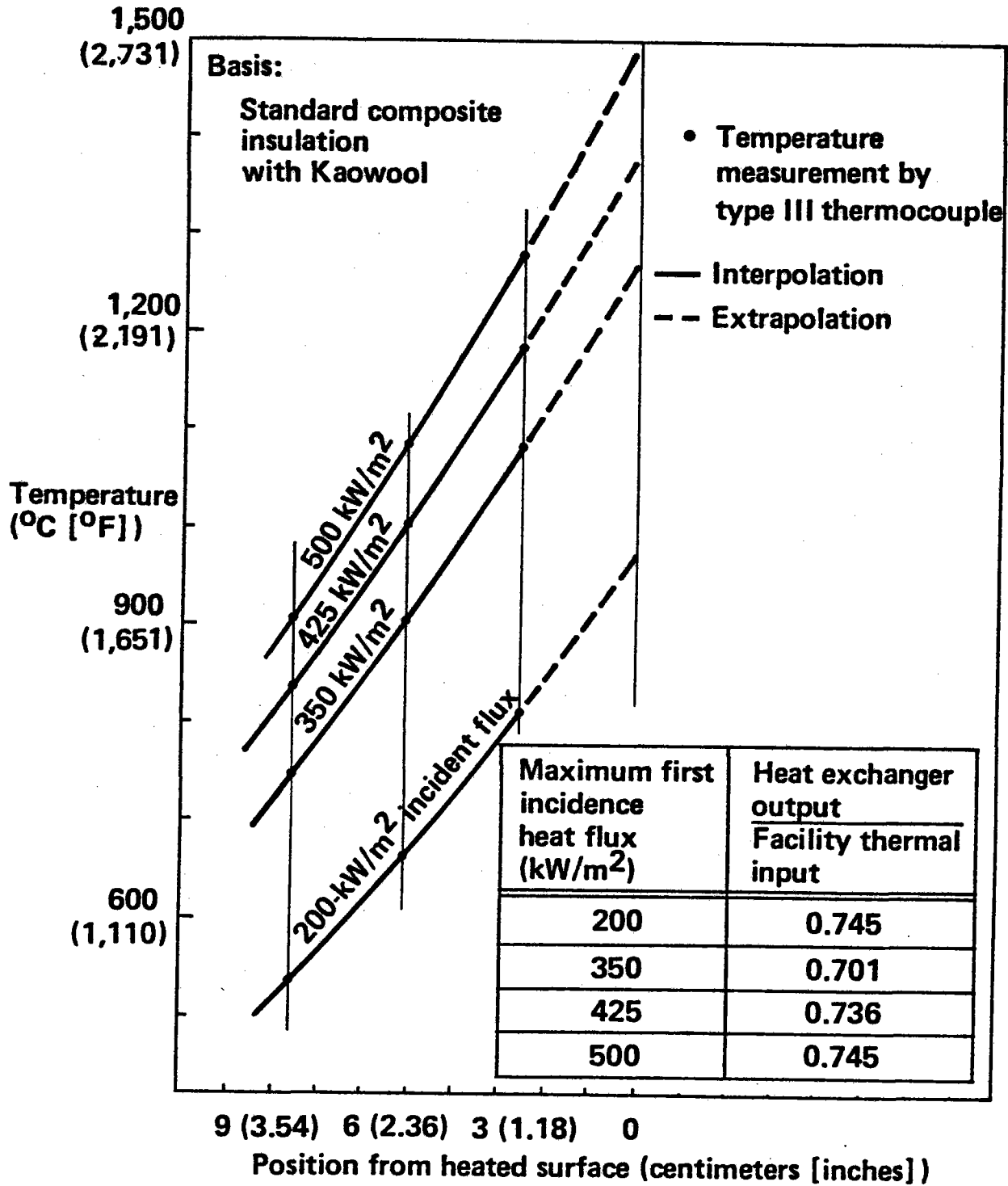
The third day of tests consisted of a repeat of the 200 kW/m<sup>2</sup> condition. This was done to determine if significant changes in insulation performance could be expected after the first exposure to BMSR operating conditions.

Insulation temperatures measured during the Series 1 tests are shown in Figure 4.2-17. The test data at each heat flux level are arranged to depict the temperature gradient through the insulation. These test data are also used to estimate temperatures of the heated surface of the sample. The data shows that the inner layer of Kaowool had been heated above the recommended short-term service temperature of 1260°C (2300°F). Furthermore, two of the insulation layers had been subjected to temperatures above 1094°C (2000°F), the preferred long-term service temperature limit.

These were serious problems, exemplified by the fact that the Kaowool surface had been severely damaged during testing. The sample-holder portion of the insulation test fixture was removed to allow close inspection of the sample. A posttest photograph of this sample is shown in Figure 4.2-18. The insulation surface was depressed in the areas of maximum heat flux and a crusty surface layer about 5.0 mm (0.20 in) thick was formed. In this damaged area, the insulation had lost all of its initial resilience and when disturbed, it crumbled into a fine powder.

Figure 4.2-17 Insulation Temperatures, Test Series

# Insulation Temperatures, Test Series 1



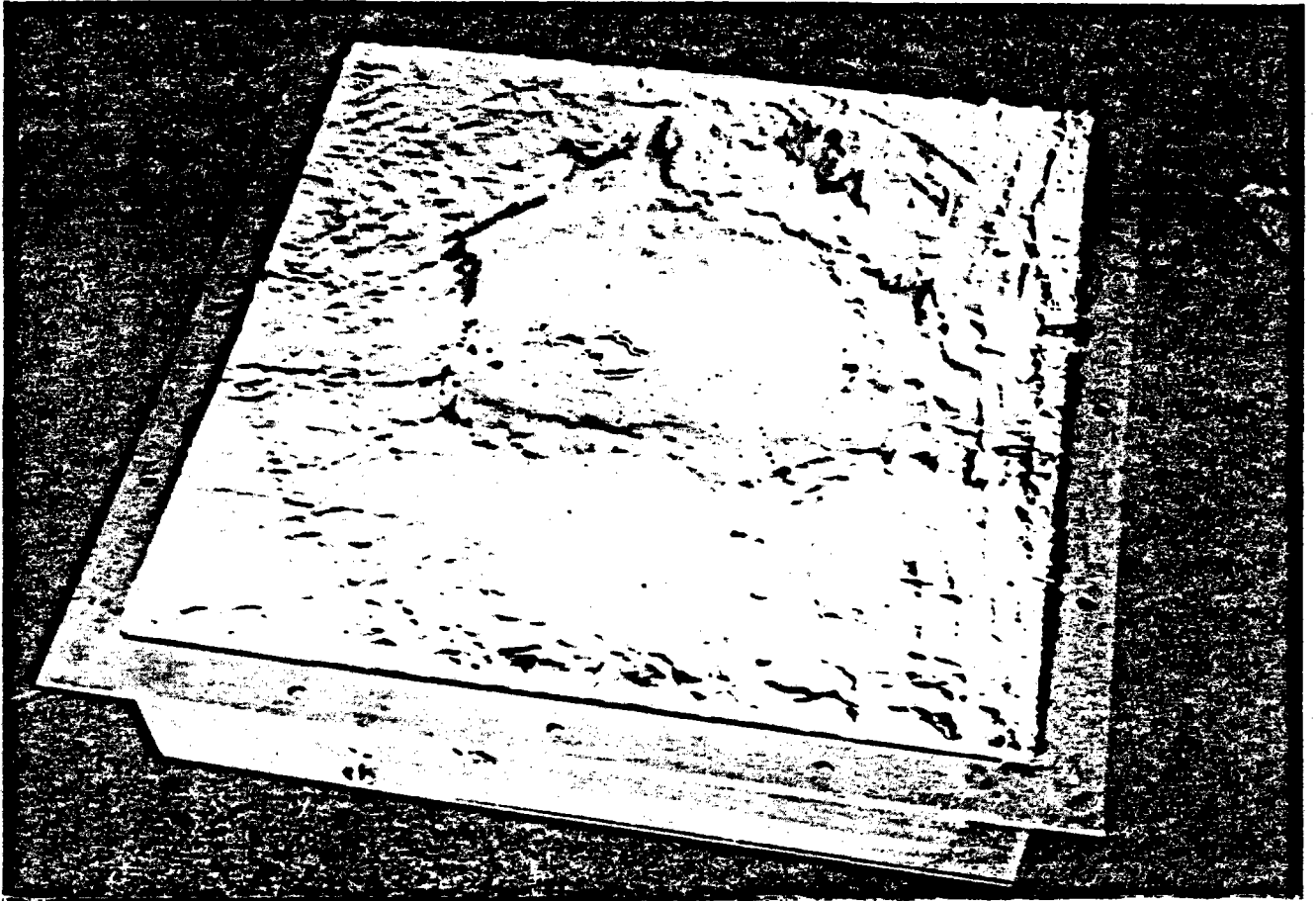


Figure 4.2-18: Kaowool Sample After Test Series 1

This significant change of the physical properties of the Kaowool was attributed to devitrification of the kaolin fibers. This occurs at temperatures well below their melting point. Given more time, this change could be expected at even lower temperatures than experienced here.

As a result of the Series 1 tests, the Kaowool was found to be of limited usefulness for BMSR wall insulation. Kaowool installations were restricted to those areas of receiver wall for which the first-incident solar flux was less than about  $275 \text{ kW/m}^2$ . This maintained the insulation temperature below  $1094^\circ\text{C}$  ( $2000^\circ\text{F}$ ), its estimated long-term service temperature limit.

### Test Series 2, Saffil

After failure of the Kaowool insulation in the highest BMSR heat flux conditions, recommendations for alternative insulation materials were solicited from ceramic engineering specialists and insulation suppliers. Blanket insulation materials were identified with higher service temperatures than Kaowool. Their improved temperature performance was achieved by increasing the alumina content from the 45% level in Kaowool. Higher temperature performance was achieved at the expense of significantly reduced mechanical strength and much higher cost. Of these candidate materials, the Saffil insulation blanket, which was manufactured by Babcock and Wilcox from 95% pure alumina fibers (produced in bulk form by Imperial Chemical Industries, Ltd.), offered the highest service temperature,  $16500\text{C}$  ( $3000^\circ\text{F}$ ).

A new high solar flux composite insulation sample was assembled with Saffil blanket replacing the sunlit Kaowool layer. New materials were used throughout the sample to provide outgassing typical of the as-built BMSR insulation. Sample instrumentation was the same as in the Series 1 tests.

After a short preheat period at  $100 \text{ kW/m}^2$ , this new sample was subjected to several hours of testing at  $425 \text{ kW/m}^2$ . The temperature measured behind the 2.5 cm (1 in) Saffil layer was  $1074^\circ\text{C}$  ( $1965^\circ\text{F}$ ), which is  $108^\circ\text{C}$  ( $194^\circ\text{F}$ ) lower than in the corresponding test with Kaowool. Not only did this new material offer a higher service temperature, but due to its increased solar

reflectivity, compared to Kaowool, it operated at a lower temperature during tests.

This fully successful test was followed by a slightly less successful test of another high solar flux composite sample. A fine layer of dirt from the location of the CRFT at Albuquerque, New Mexico, was sprinkled on the new sample. This sample was also tested at  $425 \text{ kW/m}^2$ .

A photograph of this sample after test 2B is shown in Figure 4.2-19. The photograph shows several interesting features. The two bands of lighter color near the edges of the photo are areas that were covered while the "Albuquerque dirt" was sprinkled on the sample. The highest heat flux area on the insulation surface shows as an elongated, lighter-shaded zone running parallel to these bands. Conditions in the test had somehow cleaned away the initially uniform scattering of dirt particles in this area.

Surface wrinkles are visible over the entire area. This was typical of the Saffil material. Examination of the highest heat flux area showed that these wrinkles were reduced in size and surface cracks appeared that were shorter than the wrinkles but oriented in the same direction.

The Saffil blanket tested with dirt produced significantly different results from the clean sample in test 2A. The thermocouple located behind the 2.5 cm (1 in) layer indicated  $1115^\circ\text{C}$  ( $1767^\circ\text{F}$ ), which was only  $40^\circ\text{C}$  ( $72^\circ\text{F}$ ) hotter. The insulation surface, however, had obviously shrunk and become crusty to the touch. Temperature was ruled out as the primary cause for this difference. Instead, it was the opinion of ceramic specialists that the "Albuquerque dirt" contained enough fine particles of silica and other materials to produce localized chemical contamination of the alumina fibers and to initiate the type of shrinkage and embrittlement that occurred with the Kaowool. How this chemical attack could have occurred at surface temperatures estimated to be  $1230^\circ\text{C}$  ( $2245^\circ\text{F}$ ) remained a mystery.

Questions remained as to whether the differences in samples 2A and 2B could have been caused by different test conditions. An additional test, number 4A, addressed these concerns. In test 4A, a high solar flux composite

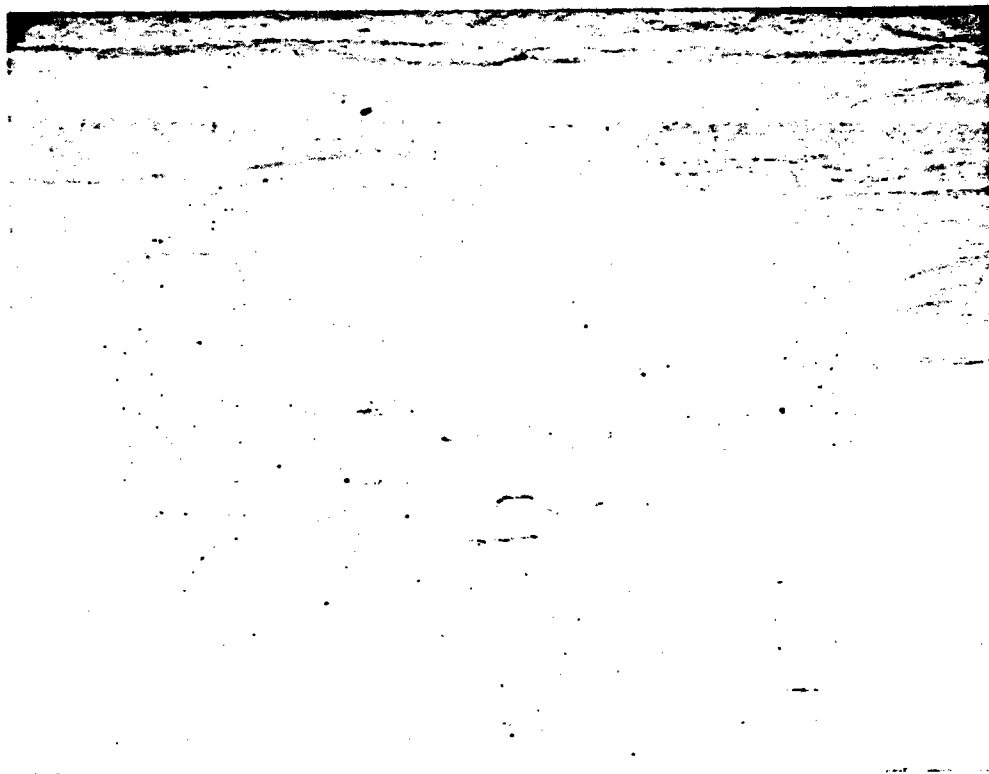


**Figure 4.2-19: Saffil After Test 2B**

sample was prepared with a butt joint in the Saffil layer. The seam was positioned to span the longer dimension of the sample heated zone. Dirt was again sprinkled on one side of the joint while the other side was left clean. After this test in which the thermal environments of the two parts of the sample were equal, the same results were observed. Just as with samples 2A and 2B, the clean side remained soft and flexible and the dirty side showed signs of shrinkage and became slightly crusty. It was concluded that the dirt was the aggravating cause of the damage.

Following these tests, it was concluded that the Saffil insulation could not be viewed as a viable commercial receiver material. However, this fault was tempered by the fact that first-incident solar flux levels in the commercial receiver are expected to be lower than  $275 \text{ kW/m}^2$ . The extra performance characteristics of the clean Saffil were needed in the BMSR. Therefore it was decided to pursue the investigation of Saffil insulation for the BMSR to the extent needed to ensure the success of the solar testing program.

#### Additional Testing With Saffil Insulation

Two more samples of the high solar flux composite receiver wall insulation were prepared and tested. Additional quantities of the Saffil insulation were subjected to BMSR thermal conditions. Acceptable methods of installing the high solar flux insulation on interior cavity walls were demonstrated.

A lap-joint sample was prepared to simulate the interface between adjacent sections of Saffil blanket in the BMSR. Figure 4.2-20 shows the condition of the lap-joint sample after completion of test 3A. This test used clean Saffil material heated at the BMSR design heat flux of  $425 \text{ kW/m}^2$ . The dark ring on the sample shows the effects of burnout of the organic binder in the blanket. The Saffil is white before testing. When heated to about  $260^\circ\text{C}$  ( $500^\circ\text{F}$ ), its organic binder material is charred, leaving behind a black carbon residue. Further heating burns the carbon, leaving a surface that is whiter than the original. The black ring on the test sample was located in an area beneath the side-wall insulation (Figure 4.2-4). A steady-state temperature gradient of about  $260^\circ$  to  $370^\circ\text{C}$  ( $500^\circ$  to  $700^\circ\text{F}$ ) is indicated by the black ring. The white areas of insulation on either side of the Saffil blanket are strips of Kaowool used as filler outside the circular heated

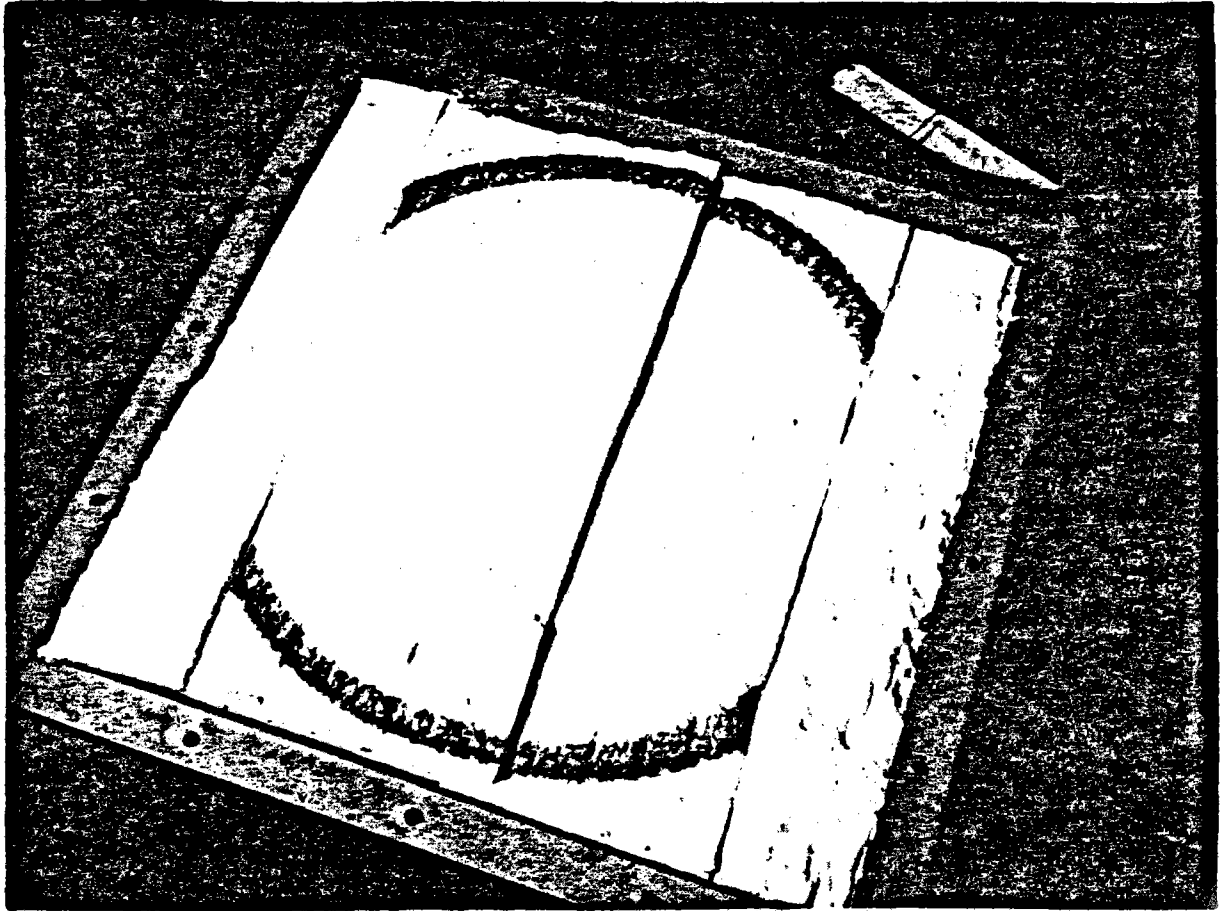


Figure 4.2-20: Photo of Lap-Joint Sample After Test 3A



test zone.

During tests, the insulation temperature behind the front layer of the lap joint was found to be 1150°C (2100°F). This temperature was 76°C (137°F) higher than the corresponding temperature without the lap joint, test 2A. The temperature behind the lap joint was acceptable for survival of the Kaowool insulation located there. This method of overlapping adjacent sections of Saffil insulation was accepted for use in the BMSR insulation design.

The final series of insulation tests were conducted to demonstrate the suitability of ceramic fasteners for attachment of high solar flux composite insulation to the metal cavity structure.

These fasteners are manufactured by Babcock and Wilcox for use with the Saffil insulation blanket in high temperature furnace and kiln applications. They consist of a metal stud which is welded to the cavity wall structure, extending to within 3 or 4 cm (1.18 or 1.57 in) of the insulation surface. Then, after the insulation has been impaled on the stud, a ceramic cap with a hollow stem is inserted over the end of the stud. The cap is held in place by rotating and locking it onto grooves in the sides of the metal stud.

The insulation fastener test sample consisted of high solar flux composite insulation with a centrally located ceramic fastener. Figure 4.2-21 shows the posttest condition of the sample. Four days of solar tests were conducted. The first test at 425 kW/m<sup>2</sup> simulated BMSR design conditions. Three additional days of testing at increasing flux levels of 450, 475, and 500 kW/m<sup>2</sup> were conducted to determine the heat flux level at which the clean Saffil might begin to degrade. During these latter tests, the arc-lamps were quickly brought to the test power level at the beginning of each test. This exposed the ceramic fastener to severe thermal shock, simulating fast startup of the solar receiver.

Insulation temperatures behind the layer of Saffil were measured as before with type III thermocouples. At the BMSR design heat flux of 425 kW/m<sup>2</sup>, the

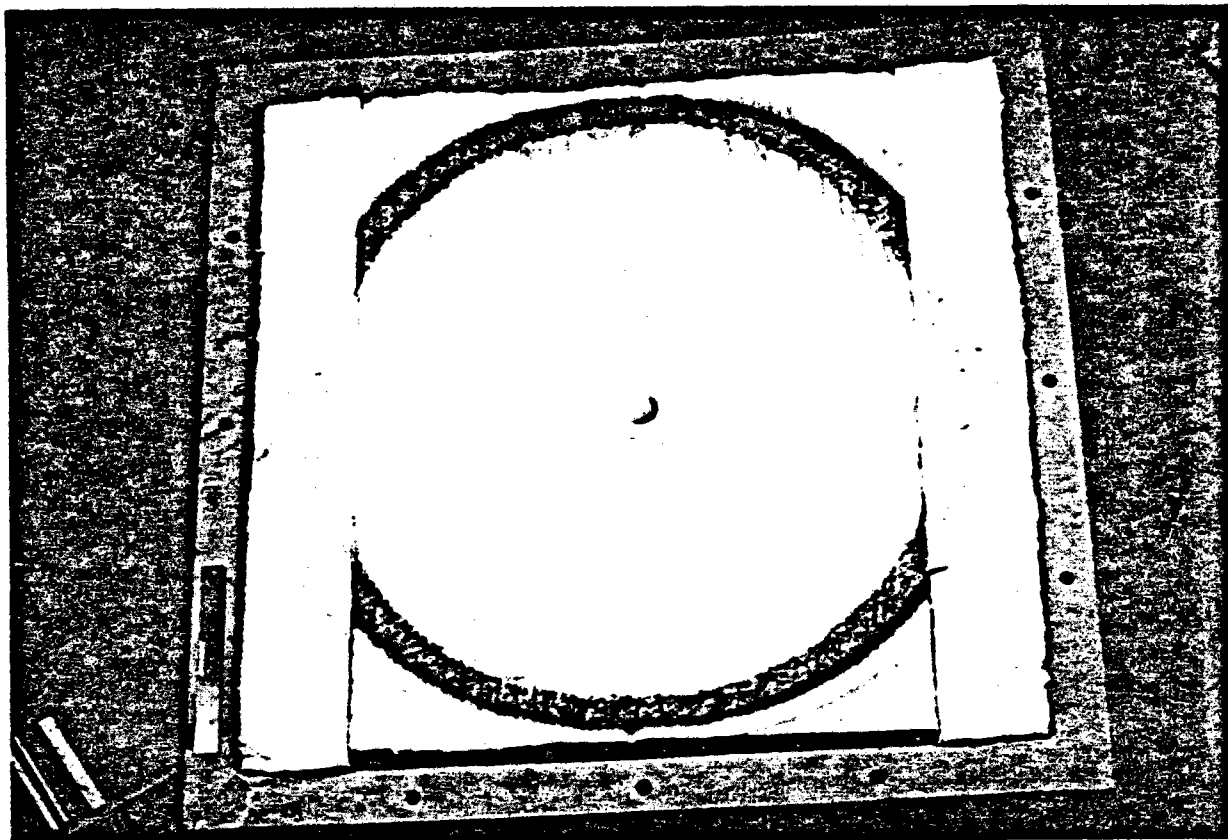


Figure 4.2-21: Fastener Sample After Test

indicated temperature was 983°C (1800°F), significantly less than the corresponding temperature in test 2A. Rather than reducing the insulation protection, the ceramic cap appears to provide better thermal protection than the Saffil blanket.

The increasing heat flux levels were intended to define the heat flux condition that begins to damage the Saffil insulation. The first indications of damage were observed after tests at 500 kW/m<sup>2</sup>. Although not detectable in the photographs, the insulation became less resilient and was clearly beginning to develop the crustiness characteristic of overheating.

Figure 4.2-22 shows the ceramic fastener after removal from the insulation sample. Two features can be observed inside the hole left by removal of the fastener. The metal stud, attached to the steel wall of the sample holder, can be seen at the bottom of the hole. It is heavily oxidized by exposure in the tests. A dark area can also be observed on the side of this hole. This is the fin area of a type III thermocouple that was form-fitted to the tapered stem of the fastener.

At BMSR design point conditions, the indicated fastener temperature was 1160°C (2122°F), which was well within its service temperature range. Heating produced hairline radial cracks on the rim of the ceramic cap, but did not appear to reduce its serviceability.

As a result of these tests, the high-temperature insulation fasteners supplied by Babcock and Wilcox were selected for use in the BMSR.

#### 4.2.3 Measurements of Insulation Radiative Properties

The thermal environment within the BMSR cavity was dominated by radiant heat transfer mechanisms, including infrared radiation heat transfer, direct solar heating in some areas, and heating by reflected sunlight. The insulation temperatures that occurred in this environment were strongly influenced by the material's solar absorptance and infrared emittance.

Efforts were made through this test program to measure the radiative surface

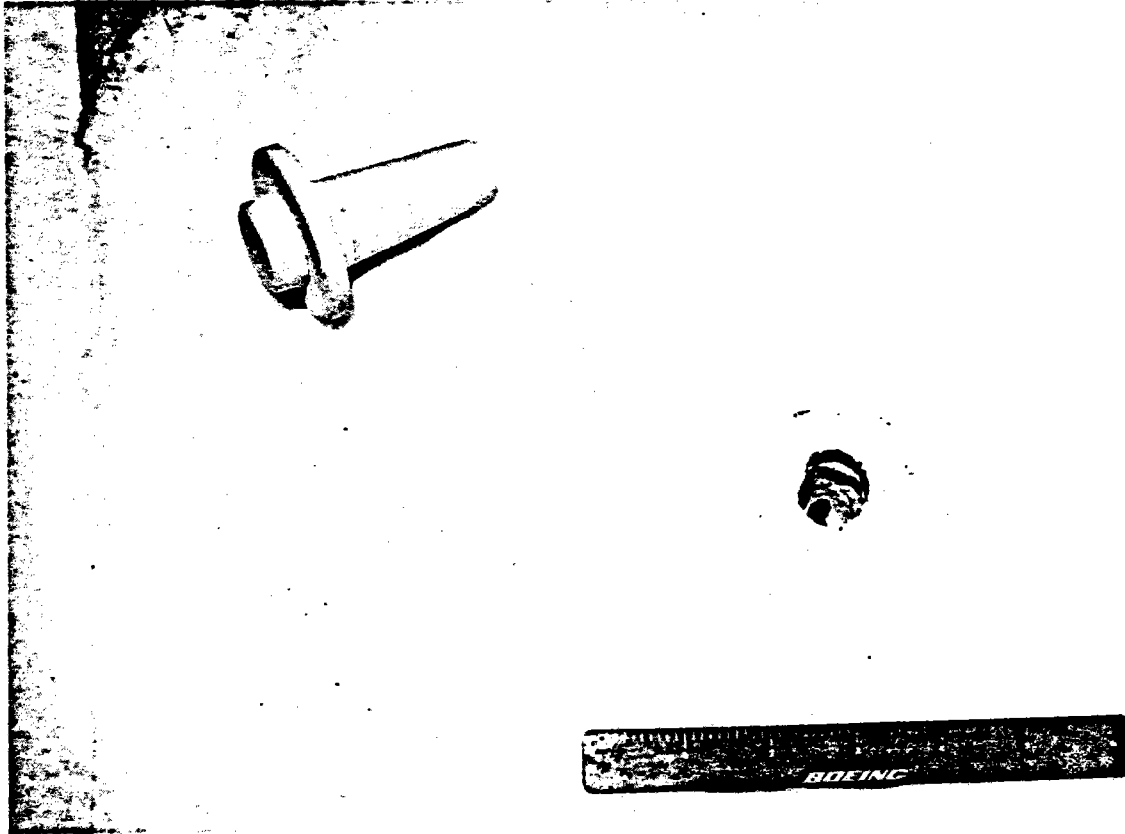


Figure 4.2-22: Ceramic Fastener After Test

properties of the insulation. Specimens were removed from the raw material stock as well as from the insulation sample after each test series. These were taken to Boeing test laboratories, which have specialized instruments to make the measurements.

The instruments that were used for these measurements provided monochromatic illumination of the sample or monochromatic detection of energy reflected from it. Therefore, measurements consisted of sample characteristics as functions of wavelength. Two different instruments were needed to measure properties over the full range of wavelengths of radiant flux in the BMSR. The first, which is based on a Beckman DK-2A Spectrometer, measures sample properties from wavelengths of about 0.3 to 2.2  $\mu\text{m}$ . The second instrument is based on the Beckman IR-4 Infrared Spectrometer and measures sample properties in the range of 1 to 15  $\mu\text{m}$ .

The soft, porous, semitransparent characteristics of the insulation samples made these measurements very difficult. The test zone in these instruments is designed to accommodate rigid opaque samples. The insulation had to be held in position by clamps and may have been packed more tightly as a result. The IR-4 instrument uses a directly water-cooled sample. The insulation could not be directly cooled. A layer of insulation material, about 2.0 mm (0.08 in) thick, had to be held in place against a water-cooled metal disk. This infrared sample thickness was a compromise between the increasing transparency with reduced thickness and the increased surface temperature due to the insulating properties of thicker samples.

Because of these difficulties, the absolute values of measurements were subject to considerable uncertainty. However, experiments were conducted to determine the repeatability that could be achieved by careful preparation and processing of identical samples. Variations of up to  $\pm 3\%$  were noted for solar absorptance data integrated over an airmass 1 or 2 spectra. Variations of up to  $\pm 5\%$  were noted for infrared emittance integrated with a 1130°C (2065°F) blackbody spectrum. In most cases, the errors in repeatability of tests were much smaller than this.

Data are reported here with these reservations as to accuracy.

Figures 4.2-23 and 4.2-24 show the spectral absorptances of Kaowool and Saffil specimens. In each case, a specimen of raw material stock is compared with one from the appropriate test sample. The changes in the Saffil are most interesting. The reduction of absorptance at short wavelengths is attributed to burnout of the organic binder material. The increased absorptance at longer wavelengths is attributed to contamination of the surface by outgassing the Kaowool and mineral wool sublayers during tests. The mineral wool which is made from blast furnace slag, contains dark-colored inorganic materials and moisture that vaporizes and could carry these materials to the surface of the insulation during tests. The integrated solar absorptance of the Saffil (for airmass 1 or 2 spectra) starts out at 0.16 and degrades to about 0.21 during tests. A laboratory experiment where the Saffil binder was burned out by a clean gas flame produced a post-burnout absorptance of only 0.12, significantly lower than either the pretest or posttest samples in Figure 4.2-24.

Measurements of spectral emittance are shown in Figure 4.2-25. These data are for posttest specimens. The pretest data were nearly identical to these curves.

These materials both exhibited low solar absorptance and high emittance in the infrared wavelengths above about 5  $\mu\text{m}$ . For this reason they were classified as selective materials. With a ratio of absorptance to emittance that was less than unity, they could be expected to operate in a cavity receiver at temperatures lower than those of a blackbody. This was a good feature because it meant lower insulation temperatures.

However, as the insulation temperature increased, the wavelengths of interest in determining its infrared emittance became shorter. This shift to the left in Figure 4.2-25 meant that as the insulation got hotter, the short wavelengths with low values of spectral emittance became more important. The integrated infrared emittance was reduced and the surface must operate at an even higher temperature to radiate away the absorbed solar heat.

This trend of the selective radiative characteristics of the insulation to

Figure 4.2-23 Measured Solar Absorptance of Kaowool

# Measured Solar Absorptance of Kaowool

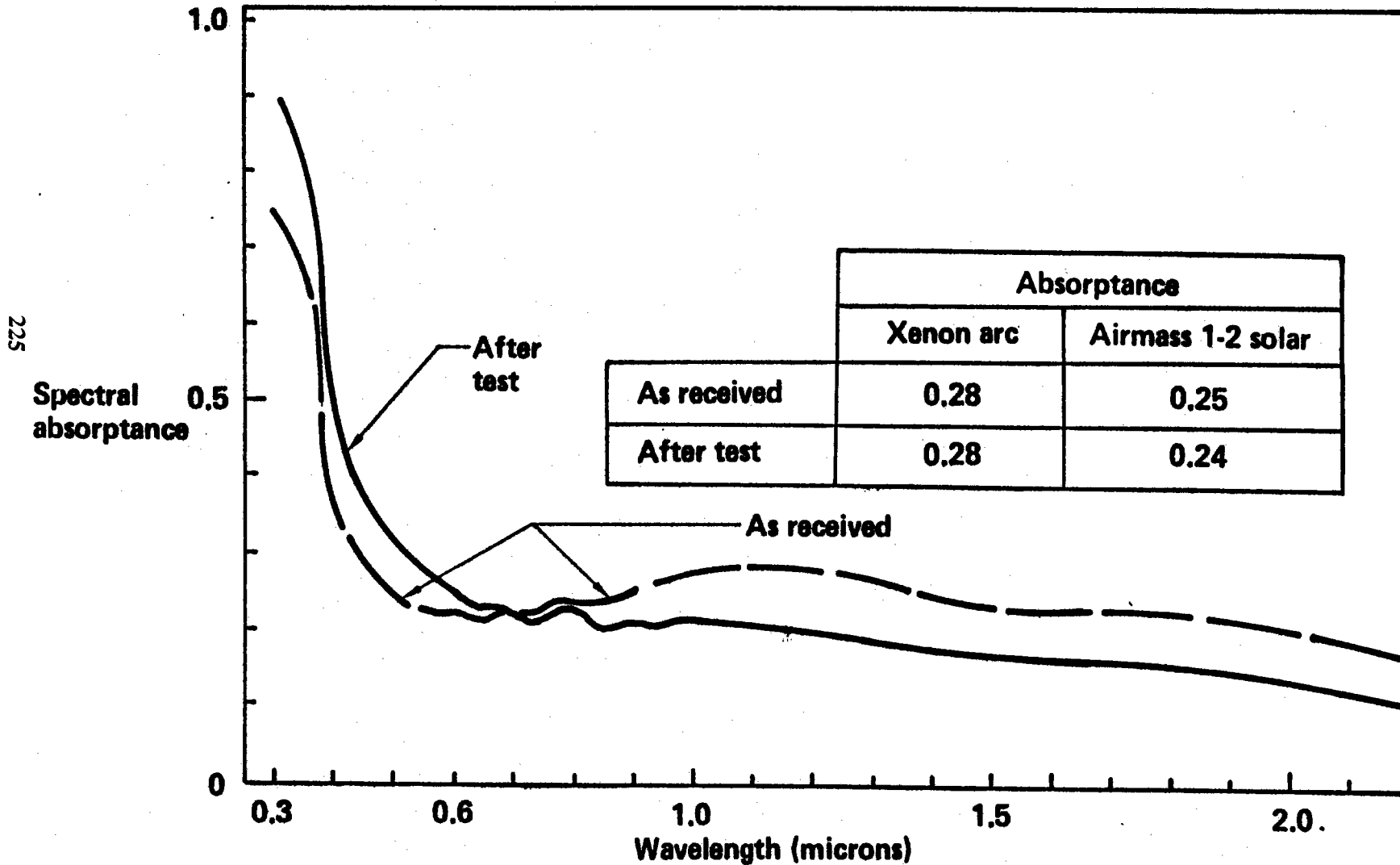


Figure 4.2-24 Measured Solar Absorptance of Saffil

# Measured Solar Absorptance of Saffil

226

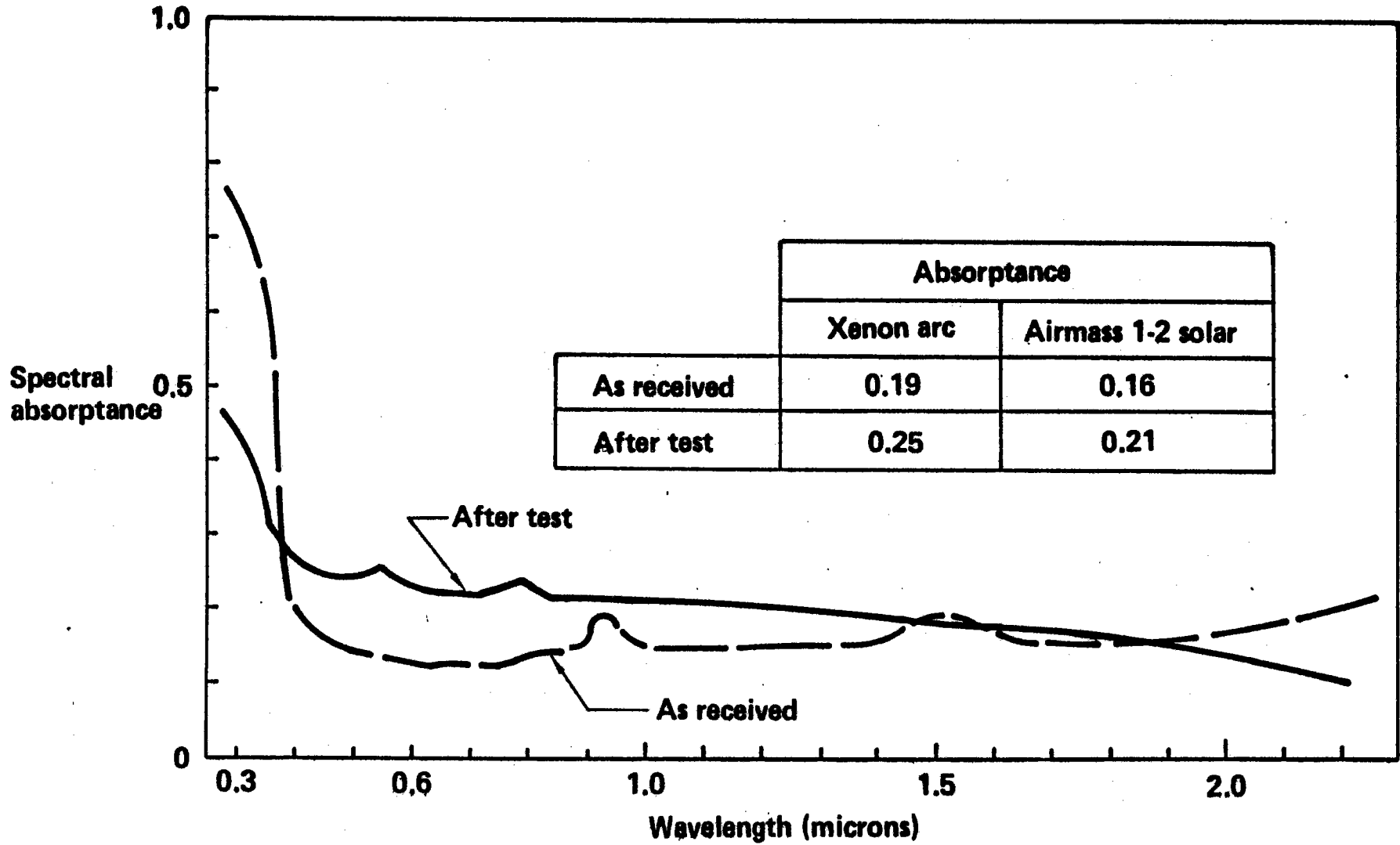




Figure 4-2-25 Measured Infrared Emittance of Kaowool and Saffil

## Measured Infrared Emittance of Kaowool and Saffil

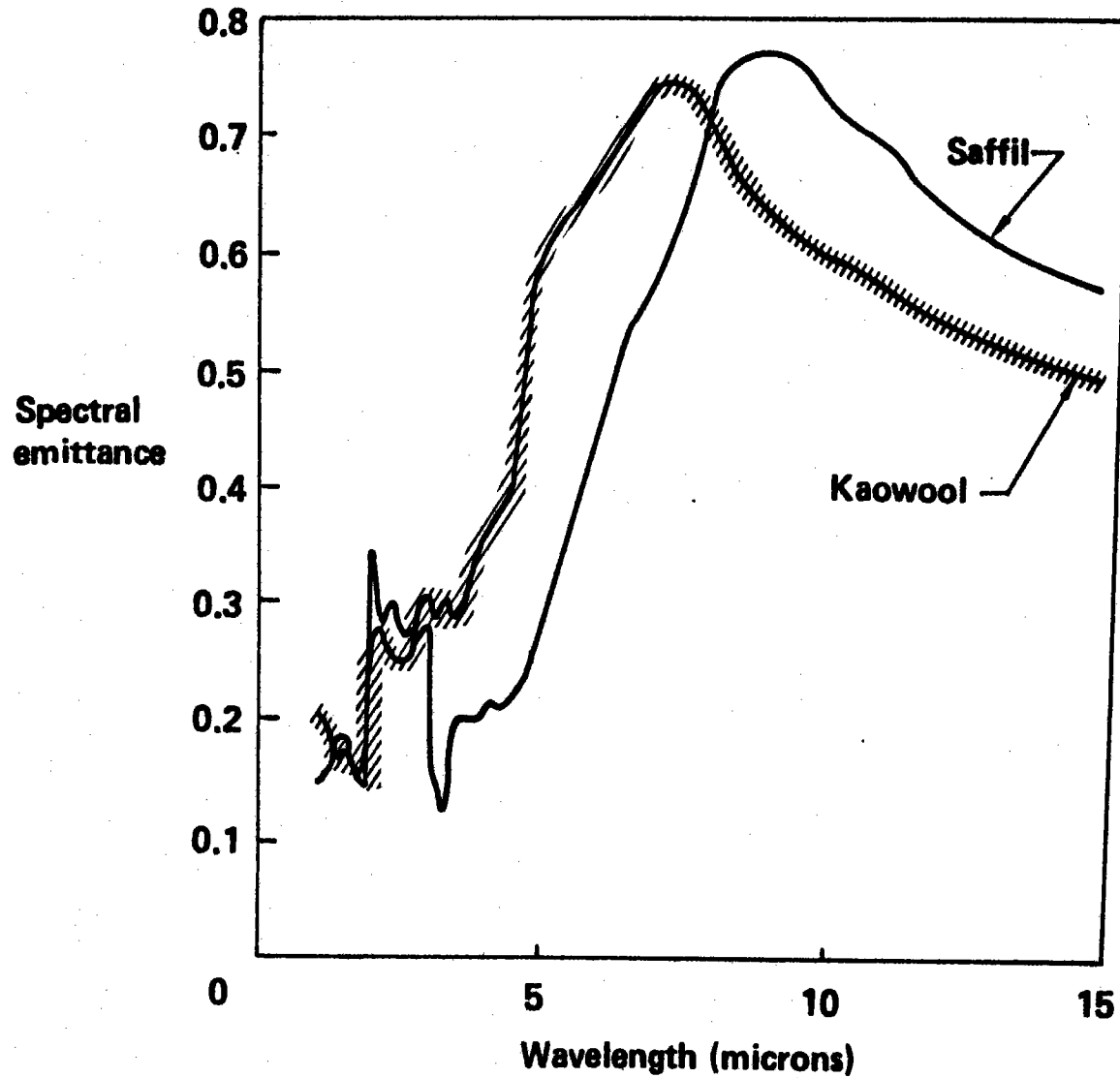


Figure 4.2.26 Emittance Versus Temperature for Kaowool and Saffil

# Emittance Versus Temperature for Kaowool and Saffil

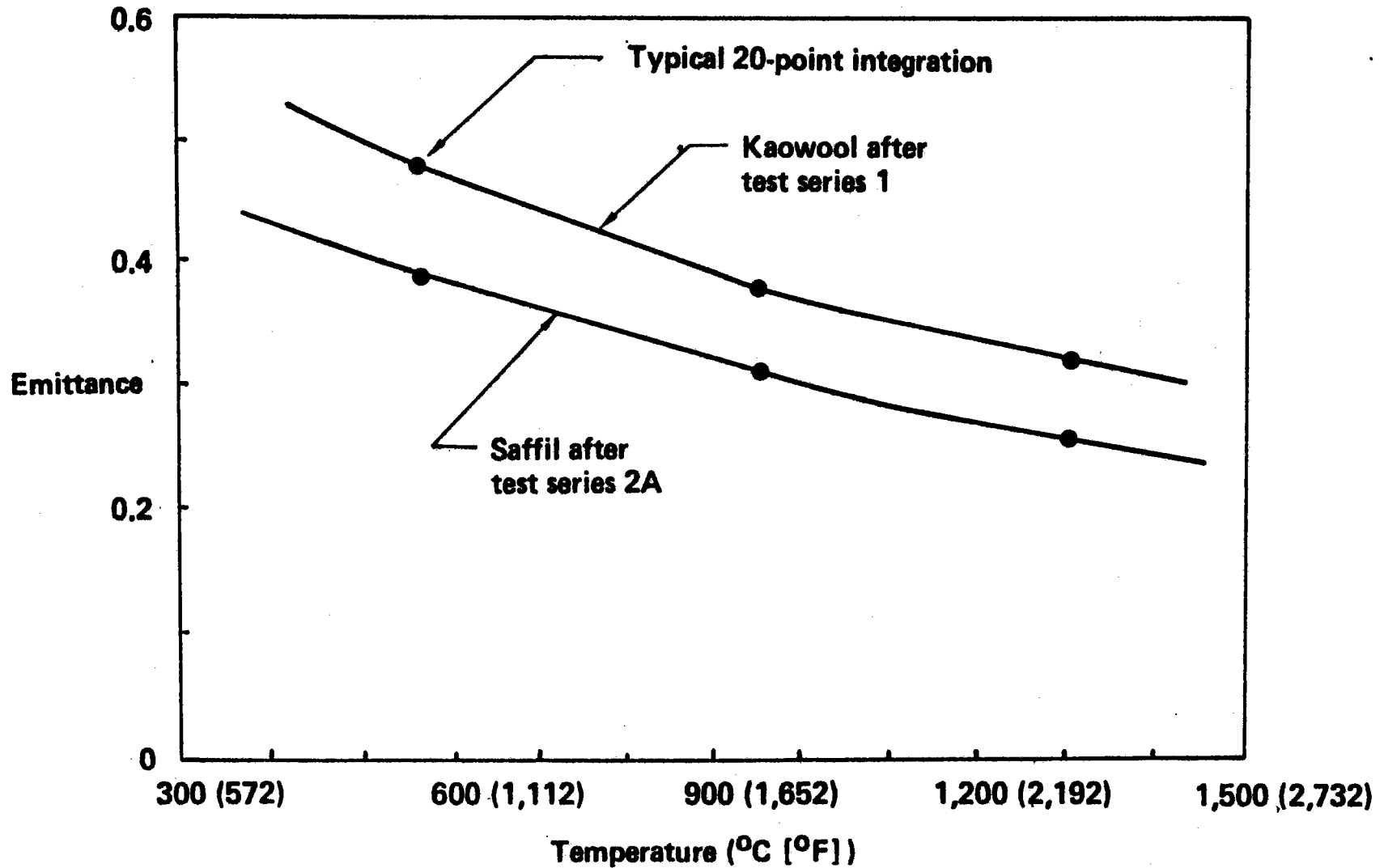


exhibit lower emittance with increasing temperature is shown in Figure 4.2-26. Here the spectral emittances have been integrated over radiation spectral characteristics of various body temperatures.

Fortunately, the total emissive power is a function of emittance and the fourth power of temperature. The reduction of emittance with increasing temperature is more than overcome by the fourth-power temperature dependence. As temperature increases, the ability to reject absorbed solar heat also increases. Otherwise, above some critical solar heat load unstable temperatures and burnout of the insulation could occur.

These data, including the temperature-dependent emittance functions, were used in thermal models of the BMSR and insulation test facility cavities. As discussed elsewhere, these models were not particularly successful in predicting insulation temperatures.

#### 4.2.4 Results

These tests were instrumental in the development of insulation designs for the walls of the BMSR. As noted, the testing program was highlighted by catastrophic failure of the baseline insulation design with Kaowool. As a result, use of this material was restricted to the low-heat-flux areas of cavity walls. Furthermore, the alternative high-heat-flux design using Saffil exhibited proclivity for failure if contaminated with small amounts of dirt and dust or if exposed to as much as 17% more than the BMSR design heat flux. The exposed Saffil layer was clearly the important link in the high solar flux composite wall insulation.

Installation details such as the lap-joint interface between adjacent sections of the Saffil and the installation of ceramic fasteners used to hold it in position were verified in test. Kaowool sublayer temperatures were measured in the vicinity of these discontinuities in the Saffil blanket and found to be acceptable. These temperatures remained acceptable, even in the off-design conditions that resulted in damage to the Saffil.

The measurements of radiative properties of the Kaowool and Saffil materials

that were conducted as part of this program constituted the only known source of these data. Large measurement errors were expected because of the adaptation of measurement techniques developed for opaque surfaces to these semitransparent matrices of fibers. This uncertainty in the determination of values for the solar absorptance and infrared emittance of the insulation materials has and will continue to cause large errors in the analytical prediction of their operating temperatures in solar receivers.

However large the uncertainty may be concerning their absolute values, the measurements conducted here did show that the solar absorptance of the insulation materials was changed by exposure to the internal cavity environment. The solar absorptance of Saffil decreased when the binder was burned out, but increased on further exposure to the hot cavity environment.

Confidence has been developed in the ability to accurately measure the temperatures of the insulation layers. Specialized thermocouple probes have been developed and standard off-the-shelf thermocouples have been adapted for this purpose and proven in test. The success of measurements with the metal-sheathed thermocouples is attributed to the exposure of a length of thermocouple sheath equal to about 200 times its diameter to a temperature essentially equal to the temperature at the thermocouple junction. The direct comparison of temperatures measured with the plain sheathed unit and the more sensitive finned unit derived the following conclusions:

- a. Measurement of the same temperature with both units showed that both installations incorporated sufficient thermal coupling to the insulation to override the effects of heat loss down the metal sheath and wires.
- b. The finned thermocouple was not needed for accurate measurements.

It should be noted that manufacturers are continuing to improve thermal insulation products. One such improvement is the development of rigid insulation board products made from the high-temperature Saffil fibers. The conversion of Saffil fibers at BMSR temperatures (conversion of the crystalline structure) caused the shrinkage and embrittlement responsible for the damage observed in the high-heat-flux tests here. The fibers used

in these new board products are converted by preheating the raw material fibers prior to forming of the board product. The fiber embrittlement is accommodated in these board products by binding fibers together, reducing their unsupported length and thereby strengthening the matrix sufficiently to allow handling and installation. These board products are promising candidates for future cavity receiver designs.

#### 4.3 TESTING OF BMSR SOLAR-SHIELD MATERIALS

High-temperature solar shielding was required to protect the BMSR from concentrated sunlight in the vicinity of its aperture. Design requirements for the aperture rim solar shielding are described in Section 3.3. The maximum solar flux on this shield was found to be either 660 or 1050 kW/m<sup>2</sup>, depending on whether the CRTF collectors were aligned for BMSR tests or tower-top tests. It was also determined that aperture rim shielding could be exposed to solar flux as high as 2100 kW/m<sup>2</sup> during a lock-and-drift failure of the collector field. The baseline design for BMSR solar shielding used a high-temperature insulation board manufactured by Babcock and Wilcox. At the time the BMSR design was developed, the product was being introduced to the commercial market. The 3000 Board is vacuum-formed from a mixture of converted (preheated) kaolin and alumina fibers. Its service temperature was stated as 1650°C(3000°F).

The solar-shield configuration and structural design are described in Section 2.0. The entire aperture face of the BMSR was covered. The area immediately adjacent to the aperture was a truncated cone made up of 12 trapezoidal, abutting segments.

Prior to the solar-shield material tests, the 3000 Board was expected to withstand the required 1050 kW/m<sup>2</sup> solar flux for an indefinite period. It was also expected to survive the 2100 kW/m<sup>2</sup> lock-and-drift flux long enough to sacrificially protect the receiver substructure. However, tests in concentrated sunlight resulted in 3000 Board failures at less than 1000 kW/m<sup>2</sup>. The board also failed by melting during tests at less than 1200 kW/m<sup>2</sup>. Its lock-and-drift protection was considered negligible after these tests.

A backup design for the aperture shield was also included in the materials test program. This design consisted of bonding zirconia tiles to the surface of the 3000 Board. The zirconia, type ZYFB3, was fabricated in 3/4-in-thick by 1-ft-square tiles by Zircar Products, Incorporated. The service temperature of the zirconia was 2205°C (4000°F). QF-180, a ceramic cement manufactured by Carborundum Company, was used to bond these tiles. This composite shield survived concentrated solar flux as high as 3700kW/m<sup>2</sup> during tests.

A total of 28 solar exposure tests were conducted on these candidate aperture rim shield materials (Table 4.3-1). The tests are described in detail in the following paragraphs.

#### Solar Test Facility

The White Sands Solar Facility (Figure 4.3-1) is operated by the Nuclear Weapons Effects Branch of the Army Material Tests and Evaluation Center. In operation, the 12.2 m by 11 m (40 by 36-ft) tracking heliostat directs sunlight onto a 9 m by 9 m (29.5 by 29.5-ft) square parabolic concentrator, which in turn focuses on a test site located just inside the experiment and control chamber. The solar image at the focal plane of the parabola is circular with a mean diameter of 15 cm (5.91 in). A nearly uniform solar flux is produced in an area 5.1 mm (2.0 in) in diameter in the center of this image. Louvers that surround the control chamber are used to adjust the test solar power. Solar intensity over the 5.1 mm (2.0 in) central portion of the image can be adjusted from zero to about 3500 kW/m<sup>2</sup>. A water-cooled shutter is provided at the solar beam entrance to the experiment and control chamber. This allows cycling of test solar flux without disturbing precise adjustments of the louvers.

An indexing table is provided at the test site inside the experiment and control chamber. The table has two stations that are automatically interchanged when the indexing mechanism is actuated. The solar-shield test sample is mounted at one station and a reference calorimeter is located at the other. The test procedure is to measure test solar flux with the calorimeter and adjust the position of the louvers to obtain the desired

Table 4.3-1. Summary of Aperture Shield Material Tests

## Summary of Aperture Shield Material Tests

Sample	Incident flux (kW/m <sup>2</sup> )	Exposure time (seconds)	Remarks
I	553	360	Back temperature stable at 202°C (395°F); surface crazing observed
I	663	360	
I	774	78	Terminated because of wind
I	751	390	Back temperature stable at 192°C (377°F)
I	857	450	Back temperature 203° to 208°C (397° to 407°F)
I	958	555	Back temperature 210° to 227°C (410° to 440°F)
I	1,064	555	Back temperature 235°C (455°F)
I	1,174	146	Observed increasing light transmission through sample; terminated test; observed 1.9-cm (3/4-in) deep hole melted in face of sample; no change in initial surface crazing
III	958	120	Metal insert exceeded 87°C (1,600°F) after 120 sec; decided to terminate and begin at lower flux level
III	746	540	Metal insert stable at 973°C (1,783°F)
III	857	420	Metal insert stable at 1,011°C (1,851°F)
III	958	510	Metal insert stable at 1,068°C (1,954°F)
III	1,059	480	Metal insert stable at 1,167°C (2,132°F); after tests, observed 1.6-mm (1/16-in diameter by 3.2-mm (1/8-in) deep hole melted in sample; location well away from parting line of sample; minor surface crazing just like sample I
IV	1,059	1,035	Backside temperature stable at 91°C (195°F); Zircar board cracked in circle around illuminated area with horizontal and vertical cracks to top, bottom, and sides of sample; minor cracks occurred all across heated zone
IV	1,336	600	Backside temperature stable at 79°C (175°F); cracks in heated zone slightly more pronounced
IV	1,589	420	Cracks more pronounced
IV	2,123	100	Terminated run because sample slipped in holder
IV	2,653	120	No change in sample
IV	3,348	130	Maximum capability of facility at 1.215 langleys
VI	1,059*	930	Metal insert stable at 574°C (1,065°F)

\*Indicates incident flux gradually increased to test level

Table 4.3-1. Summary of Aperture Shield Material Tests (Continued)

## Summary of Aperture Shield Material Tests

Sample	Incident flux (kW/m <sup>2</sup> )	Exposure time (seconds)	Remarks
VI	1,336 to 1,460*	1,600	Insert temperature 583°C (1,081°F); surface cracking observed
VI	1,856*	1,290	Terminated run because of wind gust; estimated insert temperature 669° to 677°C (1,236° to 1,250°F); surface cracks slightly more pronounced
VII	267	270	Measured backside temperature with black and white probes Black, 192°C (378°F); White, 187°C (368°F)
VII	534	255	Observed backside illumination as binder was burned out of sample; illumination confirmed to be sunlight by cycling shutter
VII	534	100+	Reversed sample to thoroughly burn out binder
II	958* to 243	2,700	Backside temperature indicated to be 793° to 199°C (380° to 390°F); calorimeter indicates 9.8 kW/m <sup>2</sup> when faced against backside Tiny pit developed on surface of sample at location of initial black spot on surface; very minor shrinkage cracks on surface of sample
VII**	539	—	Monitored backside with calorimeter; cold startup pulse due to optical transmission measured 2.96 kW/m <sup>2</sup> flux Hot steady reading is 16.9 kW/m <sup>2</sup> Hot shutdown pulse due to closing of shutter measured 3.06 kW/m <sup>2</sup>
V	3,731*	180	Spent 105 sec bringing flux to full level; sample cracked similar to IV and VI Separated two halves of sample and observed fusing of Zircar in test zone

\*Indicates incident flux gradually increased to test level

\*\*Indicates previously exposed



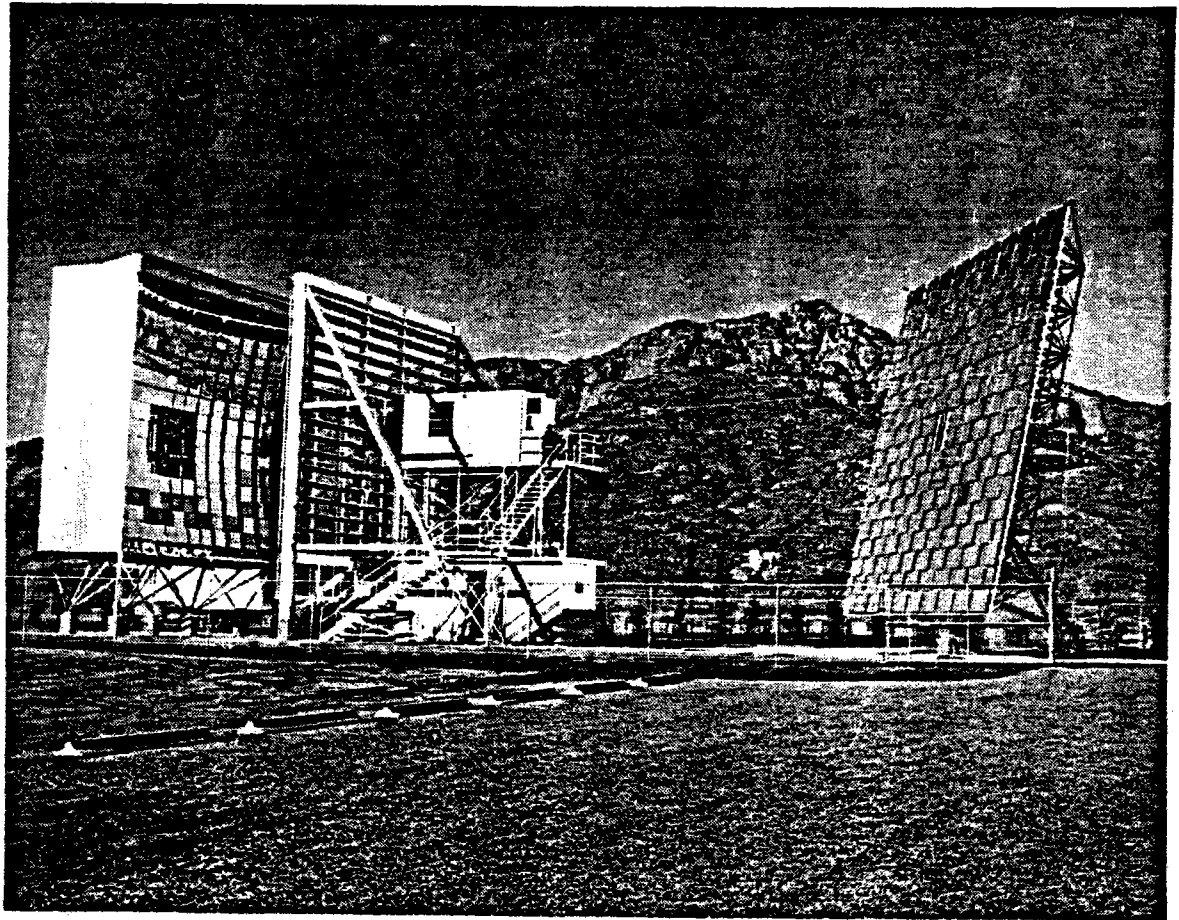


Figure 4.3-1: White Sands Solar Test Facility

test condition. Then the shutter is closed and the sample is moved to the test station. The water-cooled shutter is used to control the duration of sample solar heating.

The focal plane of the parabolic mirror is far enough inside the experiment and control chamber to allow observation of the sunlit test sample surface during exposure. The sample holder was designed to allow direct viewing of the backside of the sample in test. Both of these means were used to detect failures of samples during tests.

When test runs of up to 45-min duration were conducted, there were variations of the test solar flux due to changes in the ambient direct sunlight. These changes were monitored by a pyrhelimeter located in the solar beam between the heliostat and the parabola. Sample temperatures were monitored by thermocouples imbedded in the 3000 Board samples. Back-surface temperatures were measured by a hand-held thermocouple probe. Solar flux transmitted through the sample was measured by a hand-held calorimeter. During measurements, it was positioned directly behind the illuminated sample area but not allowed to directly contact the sample. The solar transmission component of the backside radiant flux was measured by comparing calorimeter output while quickly closing and reopening the shutter.

### Test Samples

Figure 4.3-2 shows a 10-cm (3.91-in) square segment test sample typical of the BMSR shielding. During the tests, the samples were positioned behind a 5.0-cm-diameter (1.97-in-diam.) water-cooled aperture at the test plane. The dark area on the edges of the sample is binder material that was heated and carbonized but did not reach a temperature sufficient to complete the burnout of the carbon, as the center section had.

Test samples included the following solar-shield materials and design details:

Samples I and II: 2.54-cm-thick (1-in-thick) 3000 Board.

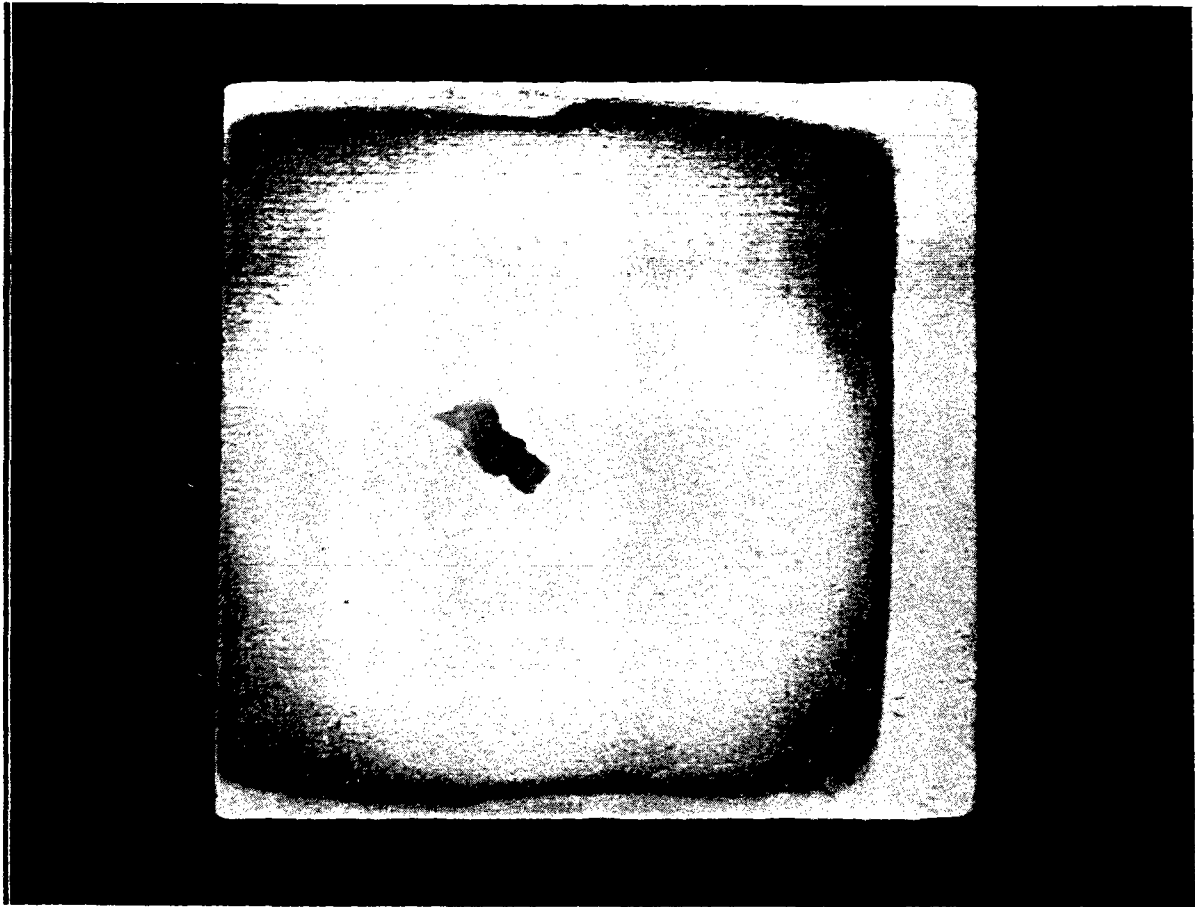


Figure 4.3-2: Sample I, 3000 Board

Sample III: 3000 Board (2.54 cm [1 in]) with a seam simulating the butt joint between adjacent panels of the BMSR solar shield. A metal disk 2.5 cm (0.98 in) in diameter was inserted parallel to the sunlit surface halfway through the sample and straddling the butt joint. The disk simulated solar-shield support structure. Its temperature was monitored during tests.

Sample IV: A zirconia tile bonded to 3000 Board. This simulated the alternative solar-shield design mentioned earlier.

Sample V: A zirconia and 3000 Board sample with a butt joint but with no metal disk or thermocouple.

Sample VI: A zirconia and 3000 Board sample with a butt joint and with the metal disk and thermocouple imbedded in the 3000 Board as in sample III.

Sample VII: A 1.270 cm thick (0.5 in thick) piece of 3000 Board. This sample was used to measure the solar transmission of the board.

These seven samples were prepared using the as-delivered insulation materials. The butt-joint seams were arranged to provide gaps of about 1 mm (0.04 in) in the heated zone. The bonded samples were air-dried and allowed to cure for several days at room temperature.

### Test Results

Table 4.3-1 describes the test conditions and results of all 28 solar exposure test runs. Results with each of the seven samples are summarized in the following paragraphs.

Sample I, 3000 Board, was tested starting at a low level at regularly increasing levels of solar flux until it failed catastrophically at 1174 kW/m<sup>2</sup>. Each of the test exposures was continued until a steady backside temperature could be observed. Sample failure occurred via melting or ablating of the fibrous insulation, which left a large pit in the sample. Figure 4.3-2 shows this sample after testing. Minor surface cracks occurred over the illuminated area. These were only a fraction of a millimeter deep

and caused no loss of mechanical integrity.

Sample III, 3000 Board, was initially tested at a high flux level, 958 kW/m<sup>2</sup>, but this first run was aborted when it appeared that the instrumented disk would experience temperatures in excess of those allowed for type K thermocouples. The test level was reduced to 746 kW/m<sup>2</sup> and tests run at incremental levels of flux up to 1059 kW/m<sup>2</sup>. Each test condition was maintained until the metal insert reached its equilibrium temperature. Examination of the sample after exposure to a flux of 1059 kW/m<sup>2</sup> revealed a small pit on the heated surface. This pit, much smaller than the failure of sample I, appeared to have initiated where minor surface cracks intersected. This sample is shown in Figure 4.3-3.

Sample IV is a 3000 Board and zirconia tile laminate. This sample exhibited thermal stress cracking of the zirconia. It was thermally shocked during exposure by rapid opening of the water-cooled shutter. After the first exposure at 1059 kW/m<sup>2</sup>, there was no change in the appearance of the sample upon exposure to solar flux levels as high as 3318 kW/m<sup>2</sup>. This sample is shown in Figure 4.3-4.

Sample VI included the same materials as sample IV, with a butt joint and metal insert. The incident solar flux was gradually applied to this sample. A period of about 2 min was spent in bringing the solar flux up to test level for each run. This procedure reduced the thermal shock to a realistic rate. The reduced heatup rate did not significantly change the surface cracking of this specimen compared to sample IV. This sample is shown on Figure 4.3-5.

Sample VII was an approximately 1.27 cm thick (1/2 in thick) piece of 3000 Board. The sample was exposed to 534 kW/m<sup>2</sup> from both sides to thoroughly burn out the binder material. Then a sensitive calorimeter was placed behind the sample and, by cycling the water-cooled shutter, determined solar flux transmission through the sample. A transmission of 0.57% was measured at ambient and operating temperature with 539 kW/m<sup>2</sup> incident flux.

Sample II was a duplicate of sample I intended to determine the effect of

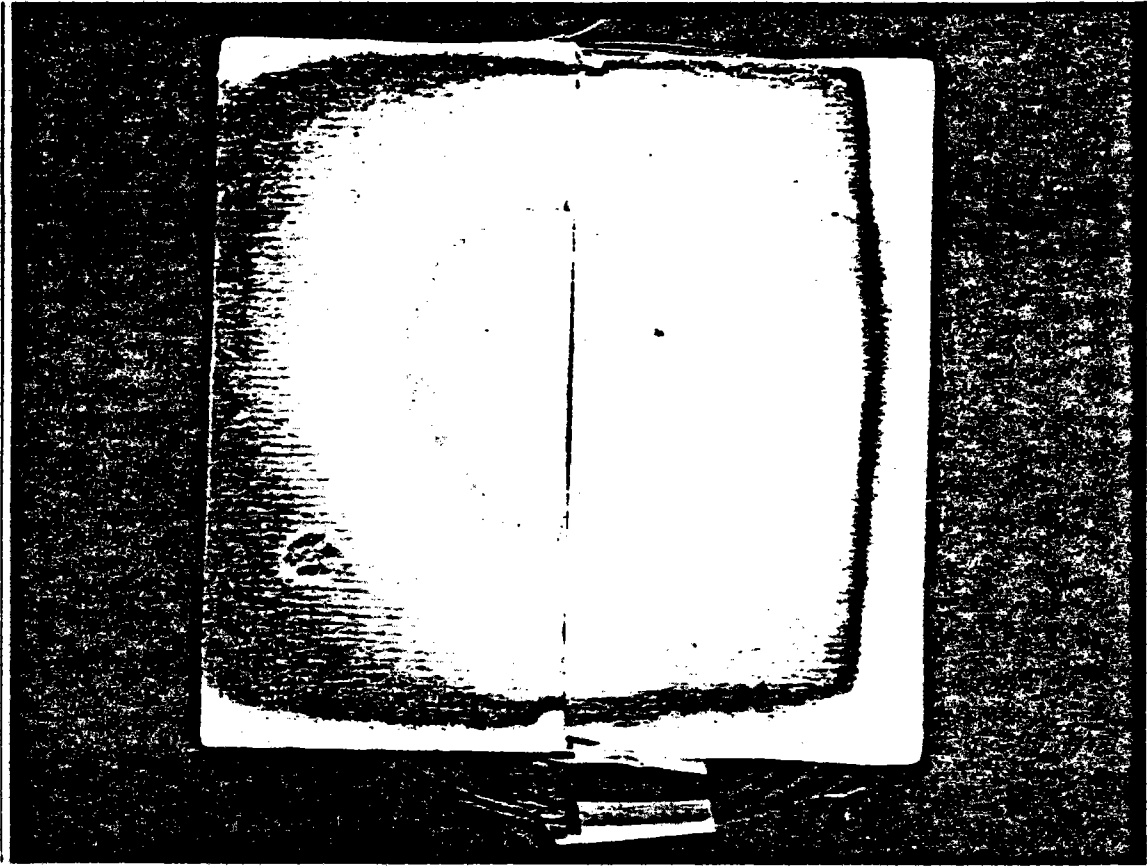


Figure 4.3-3: Sample III, 3000 Board With Seam

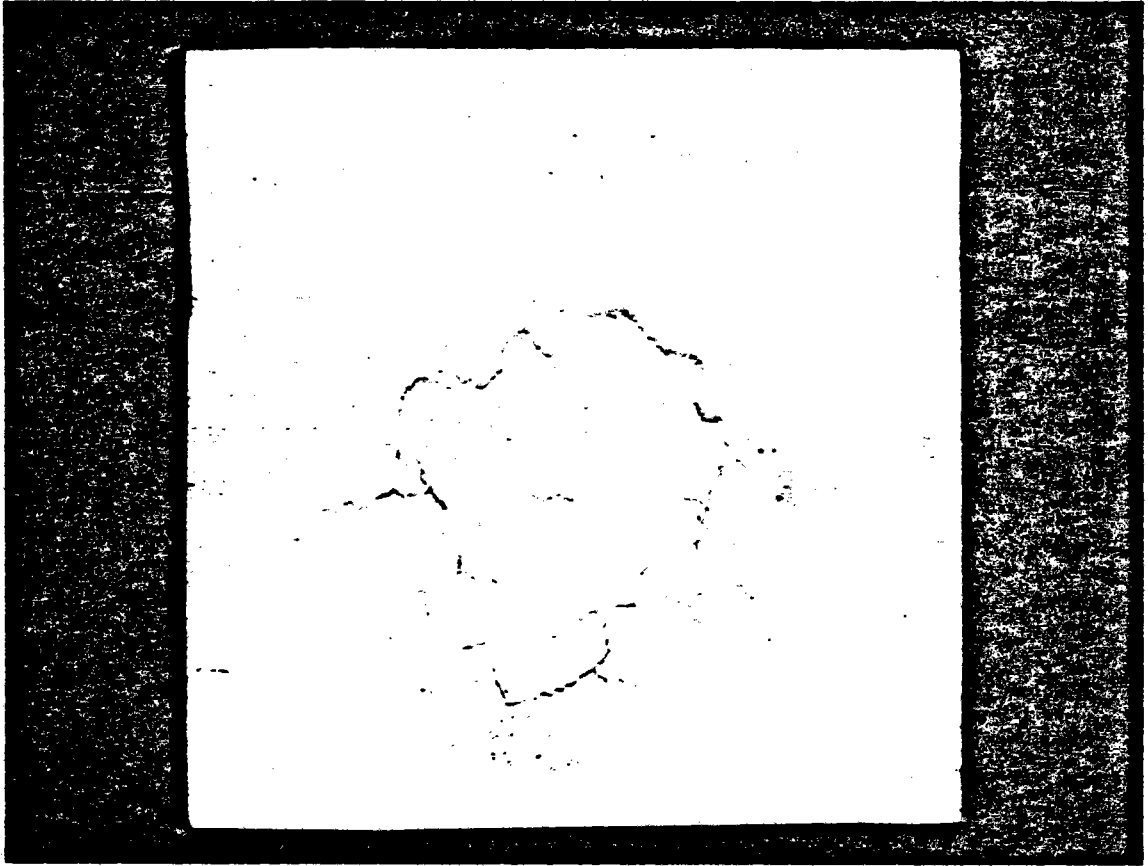


Figure 4.3-4: Sample IV, Zirconia Board

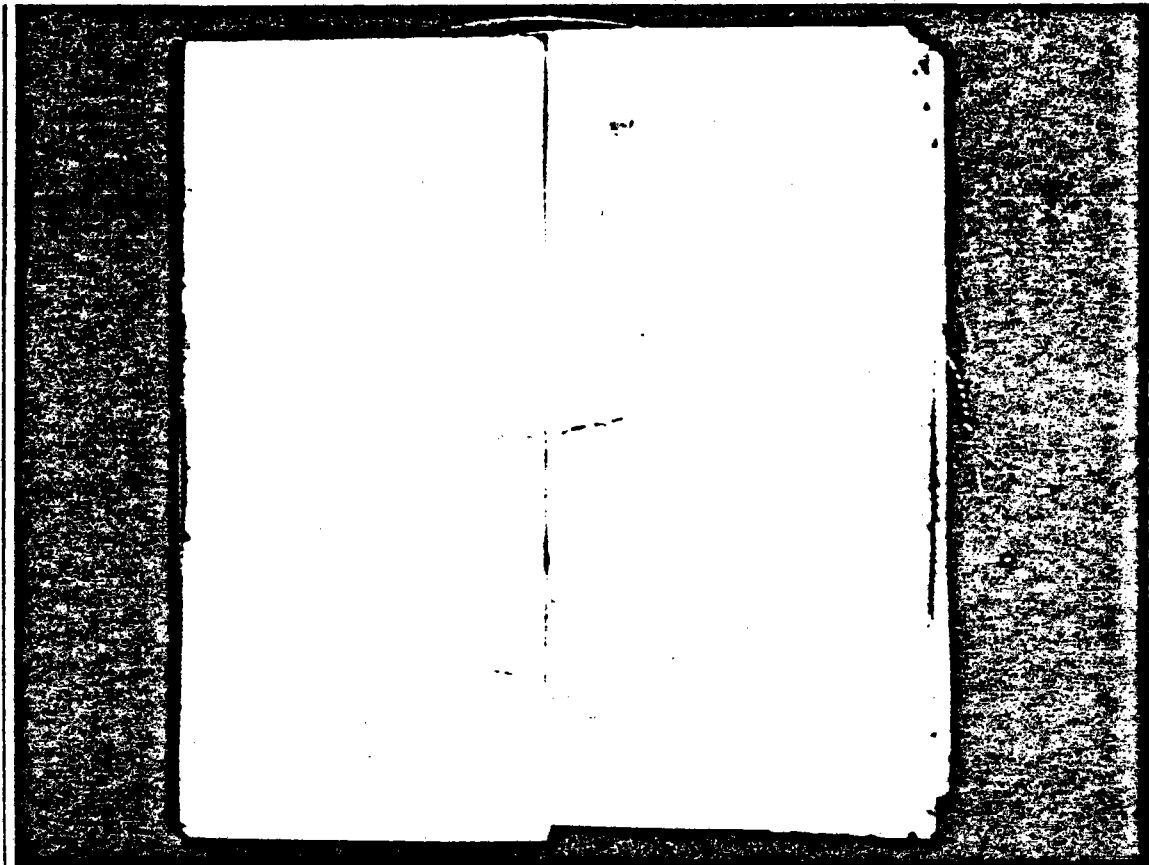


Figure 4.3-5: Sample VII, Zirconia Board With Seam



prolonged exposure on failure of the 3000 Board. The test solar flux level was chosen with the intent of achieving long term exposure without failure. Because failures had been observed to be catastrophic at  $1174 \text{ kW/m}^2$  and minimal at  $1059 \text{ kW/m}^2$ , the test level selected here was  $958 \text{ kW/m}^2$ . The sample was tested for 45 min at  $958 \text{ kW/m}^2$ . A minor surface pit was detected upon examination.

A final test was conducted on sample V to determine the effect of very high solar flux levels on zirconia - 3000 Board laminates. This sample was similar in appearance to sample VI but did not have the metal insert. It was tested at an incident flux level of  $3731 \text{ kW/m}^2$  for 3 min. The test was terminated because of minor difficulties encountered with the sample-holder cooling system. The duration was sufficient to achieve full operating temperatures on the zirconia surface. This sample survived in a condition that appeared similar to Figure 4.3-5. Upon separating the two halves of the sample, the zirconia tile was found to be fused together in a circular region the size of the solar exposed zone.

### Conclusions

These tests provided valuable new information to aid in the design of high-temperature solar shielding. Specific conclusions derived by evaluating test results are discussed in the following paragraphs.

The 3000 Board could be used with confidence for solar shielding up to approximately  $800 \text{ kW/m}^2$  incident solar flux. Solar flux levels over  $1000 \text{ kW/m}^2$  were expected to produce pitting of the board material.

Cracks and seams less than about 1.0 mm (0.04 in) wide did not necessarily precipitate damage to the 3000 Board.

A significant amount of incident solar flux was transmitted optically into the 3000 Board. The material could not be characterized as an opaque surface. Solar absorptance and infrared emittance alone were not sufficient for determining surface temperatures.

Failures induced in the 3000 Board by high levels of incident solar flux resulted in pitting of the sunlit surface. Pits appeared to be zones where the [REDACTED] fibers had melted and flowed into the surrounding medium. The initiation of this melting appeared to be triggered by localized contamination of the board or initiated from a thermal stress crack or discontinuity in the original material. Time may be a factor in the onset of these failures.

The laminated assemblies tested consisted of ZYFB3 zirconia tile bonded by means of ceramic cement to 3000 Board. The zirconia was believed to have produced bondline temperatures below 1093°C (2000°F). The bond was totally satisfactory in these tests. One sample, after being tested, was accidentally dropped 76 cm (30 in) to a steel floor. A corner was cracked but the bond remained sound.

The type ZYFB3 zirconia tile retained its strength and appearance without significant degradation up to solar flux levels of 2000 to 3000 kW/m<sup>2</sup>. However, the makeup of the tile, density, rigidity, or binder, was not optimal for use as a solar shield material. Surface cracking on about 5.0 mm (0.20 in) centers can be expected for any application of ZYFB3 above about 1000 kW/m<sup>2</sup>. The cracking did not appear to be increased by repeated thermal cycling. In applications where appearance is not critical and mechanical loading after first heating is not expected, the ZYFB3 appears suitable for use up to 3000 kW/m<sup>2</sup>.

As a result of these tests, the laminate of zirconia tile bonded to 3000 Board was adopted for BMSR solar shielding. The revised shield design has proved capable of surviving all the normally expected solar heating conditions. In addition, the zirconia provided protection for the unlikely event of collector system failure and solar image drift across the receiver.

## SECTION 5.0

### RECEIVER FABRICATION

The BMSR was constructed using typical industrial practices, materials, parts, standards, and specifications wherever possible. Subcontractors skilled in structural steel and superalloy fabrication were employed for construction of the steel framework and heat exchanger system. These firms were, respectively, Steel-Fab, Inc., of Everett, Washington, and Exotic Metals Forming Company of Seattle, Washington. Another firm, Certified Electro Manufacturing Company of Seattle, was employed for construction of portions of the control system and control consoles. Guidance on selection of insulation products and installation methods was provided by Babcock and Wilcox.

The fabrication flow path started with construction of the steel frame and subsequent insulation, all by Steel-Fab, Inc. During the installation of insulation layers, BEC personnel installed thermocouples at appropriate locations. Upon completion of this phase, the steel framework was moved to Harbor Island Machine Works in Seattle, where heat exchanger components were assembled on the framework by Exotic Metals Forming Company. Harbor Island Machine Works was used because of their overhead crane capacity and large work area; some machining of critical heat exchanger components was also provided by them. Upon completion of the heat exchanger system, the BMSR was then shipped to the Boeing Kent Space Center where the instrumentation continuity and flow-control component checks ensured proper functioning prior to performance of hot-flow testing at another Boeing facility. The following sections discuss the fabrication process steps performed in the construction flow path.

#### 5.1 STRUCTURAL FRAME

The framework was constructed of ASTM-A36 steel shapes and plate with the exception of the eight leaf springs used to support the heat exchanger system. These springs were constructed of ASTM-A588 steel. A 15.24 cm (6.0 in) steel channel section was used throughout. All joints were

full-penetration welds using metal arc-welding (GMAW) processes in accordance with the American Welding Society Specification AWS D1.1-76. Overall steel construction was in accordance with AISC specifications for structural steel for buildings.

Construction started with the front, rear, and base frame members, as shown in Figure 5.1-1. These subassemblies were then joined into the main body portion of the BMSR (Figure 5.1-2). Ten-gage steel sheets were added to close out the eight sides of the framework, as shown in Figure 5.1-3. These sheets were installed with intermittent welds, and each side or bay incorporated two slots to accommodate heat exchanger panel inlet and outlet headers to be installed at a later stage. Inconel 601 studs can be seen in Figure 5.1-4. The studs were used for insulation blanket retention, which is discussed in later sections.

Leaf springs are visible at the intersections of adjoining bays in Figure 5.1-3. These springs were fitted into brackets that were subsequently welded to the framework making the springs an integral part of the assembly. The springs (Figure 5.1-5) were single leaf with round pins at each end. When mated with the support brackets, also shown in the figure, the springs were free to rotate at each end and also to slide at one end only. In this way, the radial growth of exhaust and inlet manifolds was accommodated uniformly around the circumference of the BMSR. Brackets shown welded to the springs in Figure 5.1-5 were the points of attachment for the encircling manifolds.

The truncated prism back cover of the BMSR was fabricated in a similar manner. The channel section framework is shown in Figure 5.1-6. A typical trapezoidal steel sheet with studs in-place is shown in Figure 5.1-7. These eight sheets were installed using intermittent welds to complete the structure shown in Figures 5.1-8 and 5.1-9. In the latter photograph, insulation assembly has been started. The BMSR back cover was designed as a removable part to facilitate installation and removal of heat exchanger panels. Because there were no working flow-control components on this portion, the fabrication stage was completed by adding the insulation and instrumentation; the assembly was then stored while construction of the main

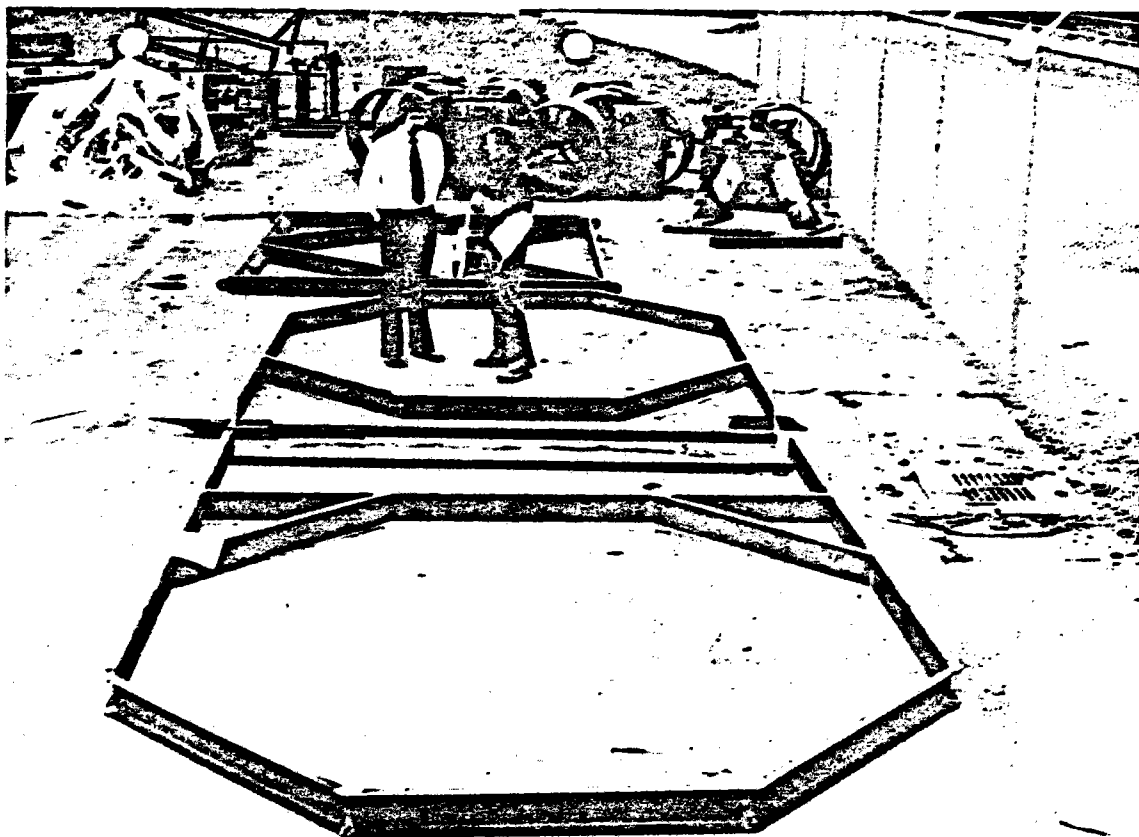


Figure 5.1-1: Steel Framework Components

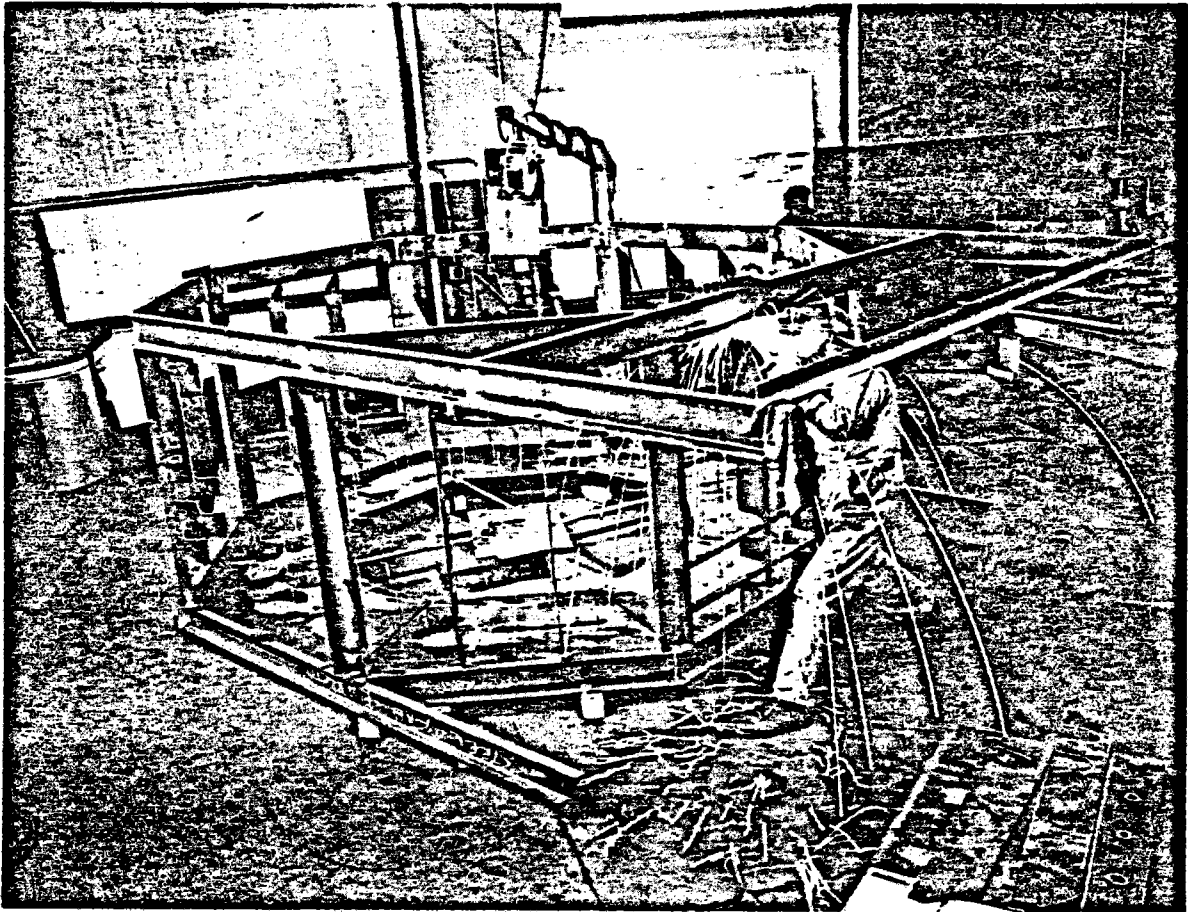


Figure 5.1-2: Welding Steel Framework

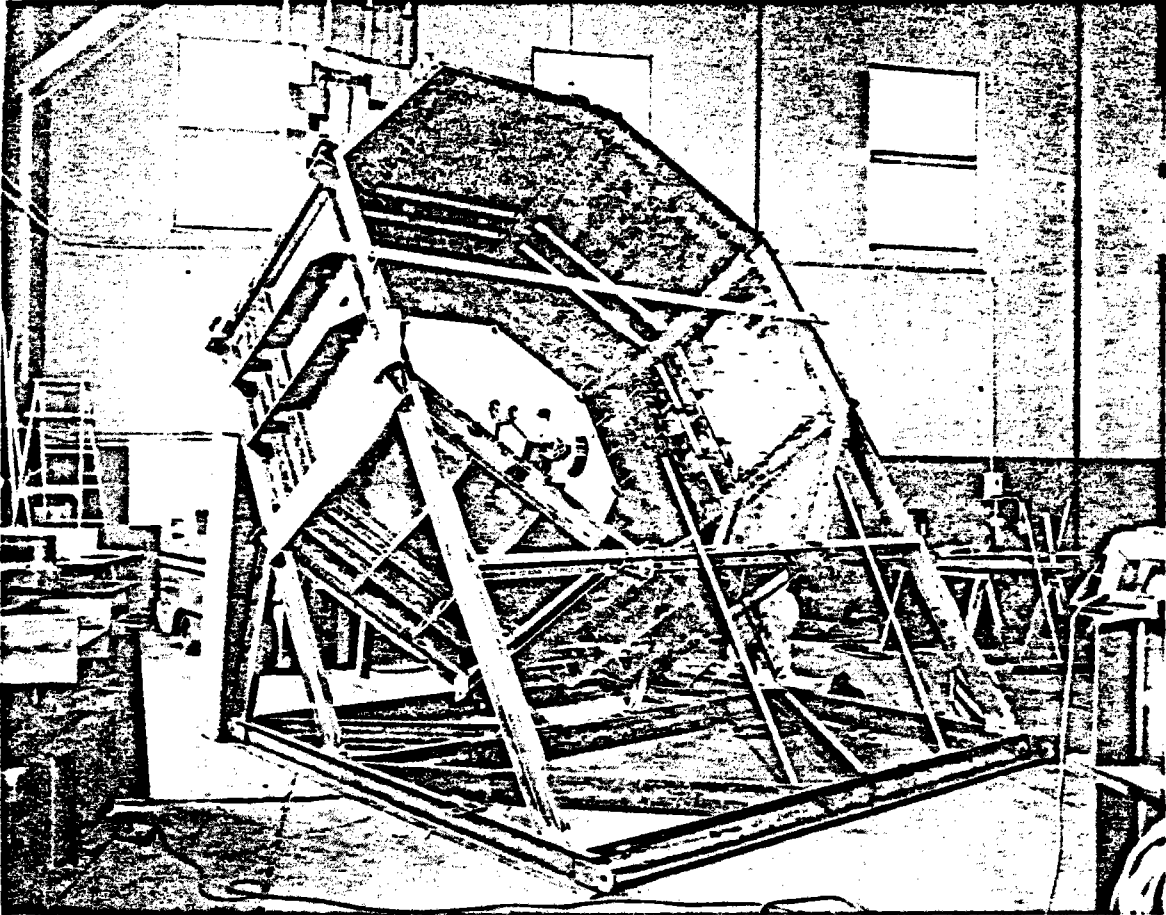


Figure 5.1-3: Framework Assembly

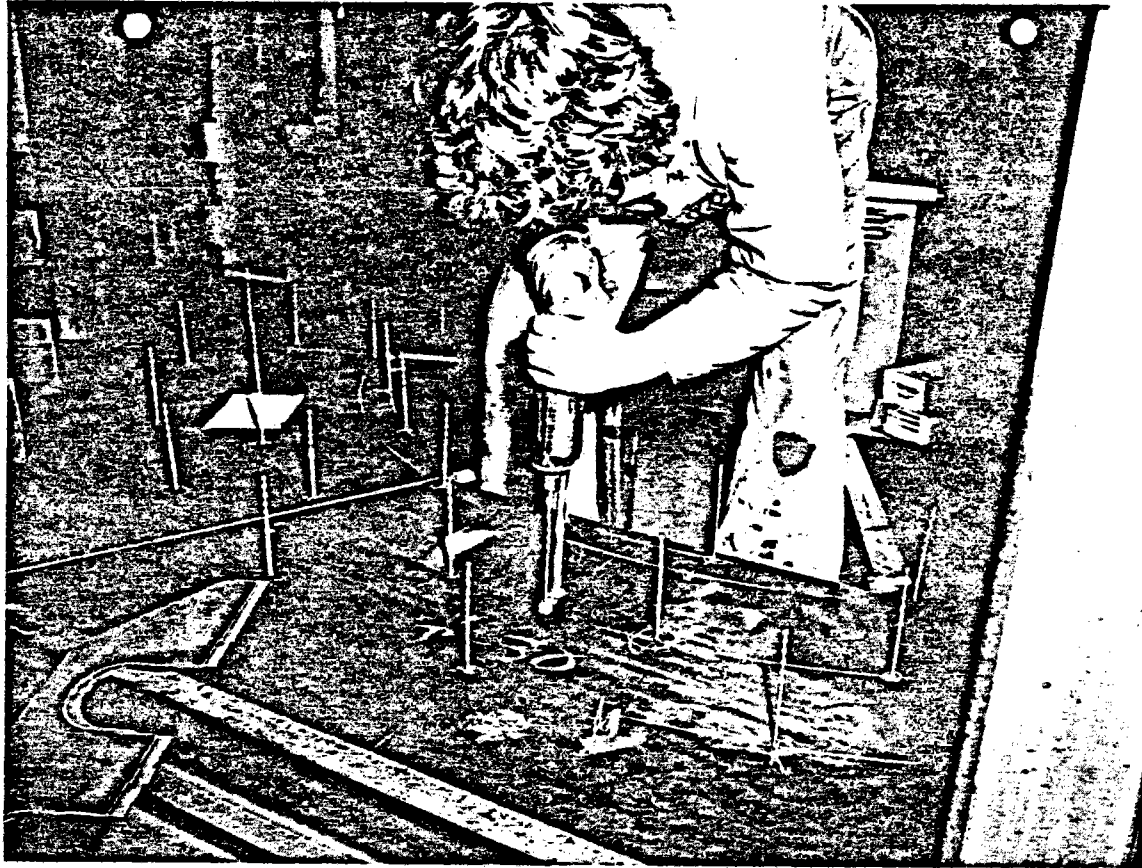


Figure 5.1-4: Stud Welding Process



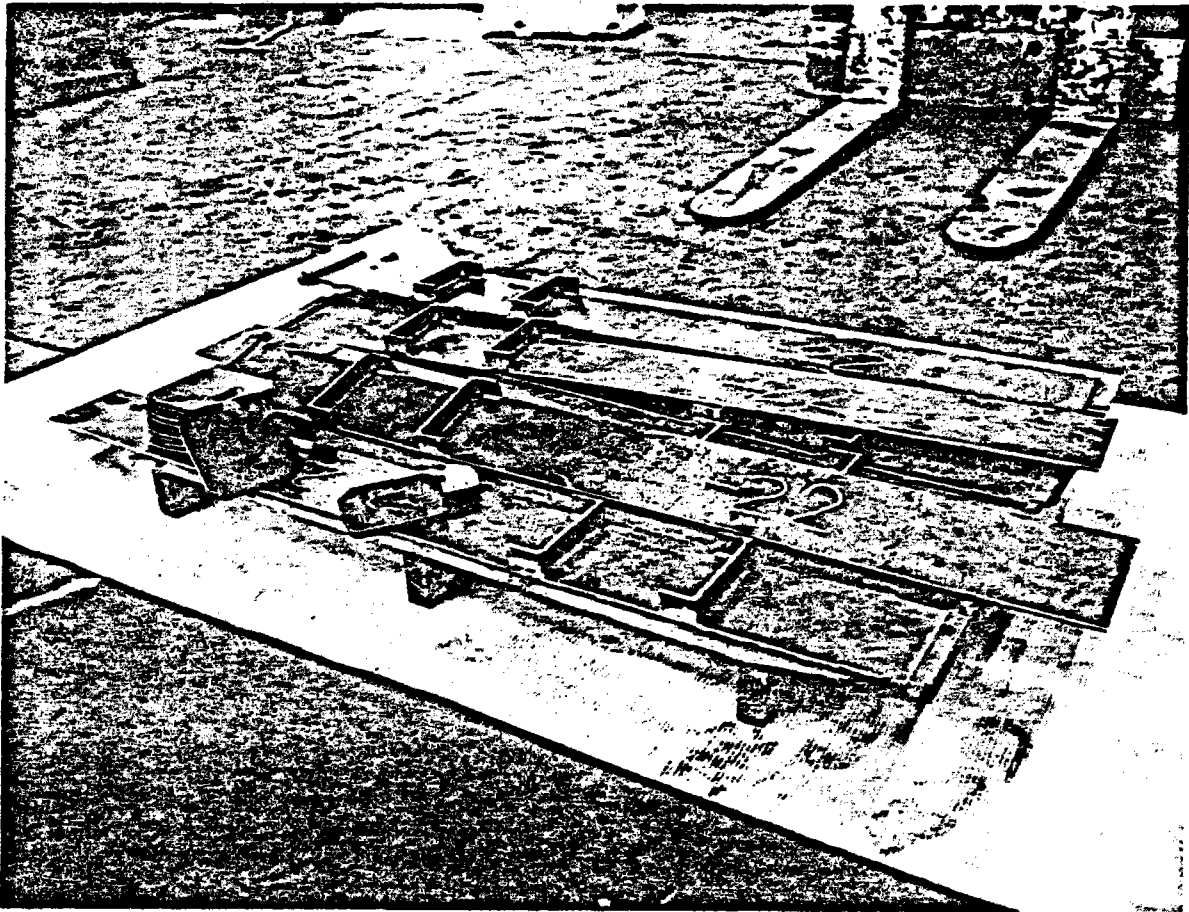


Figure 5.1-5: Leaf Spring Components

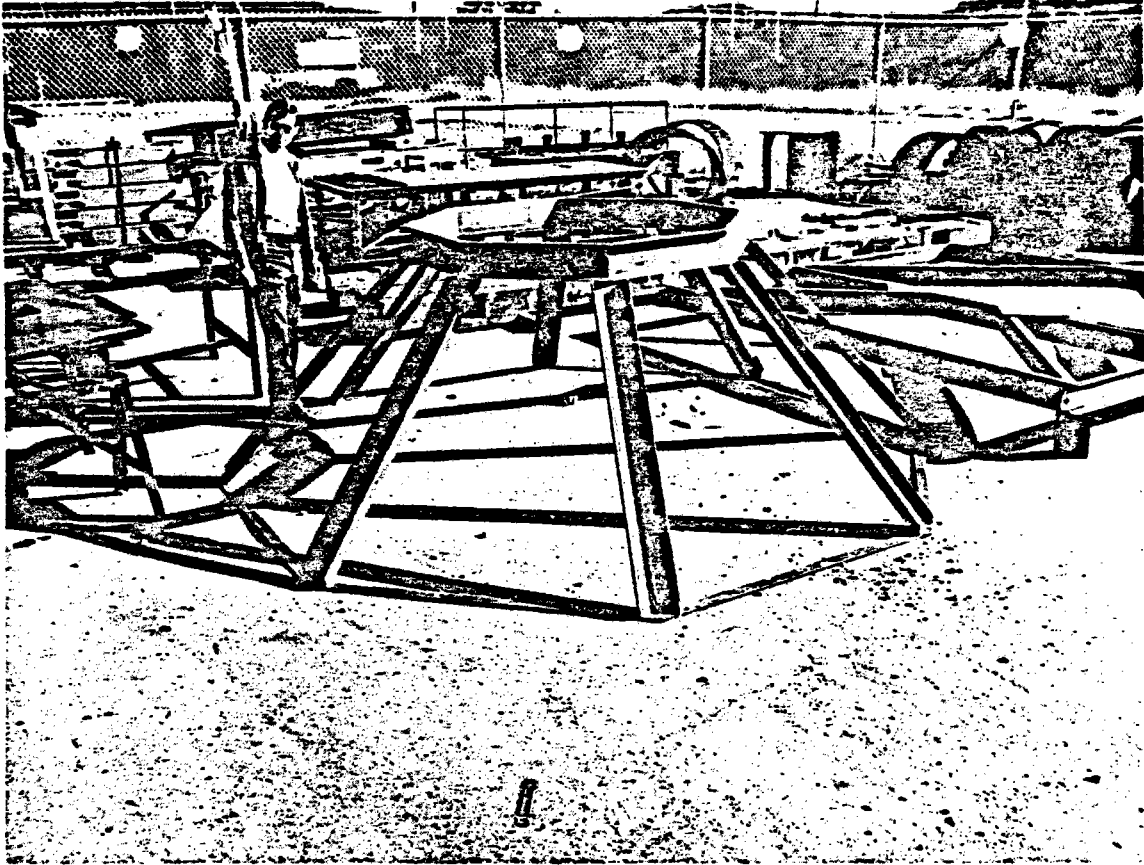


Figure 5.1-6: Back Cover Structural Frame



Figure 5.1-7: Back Cone Sidewall Assembly

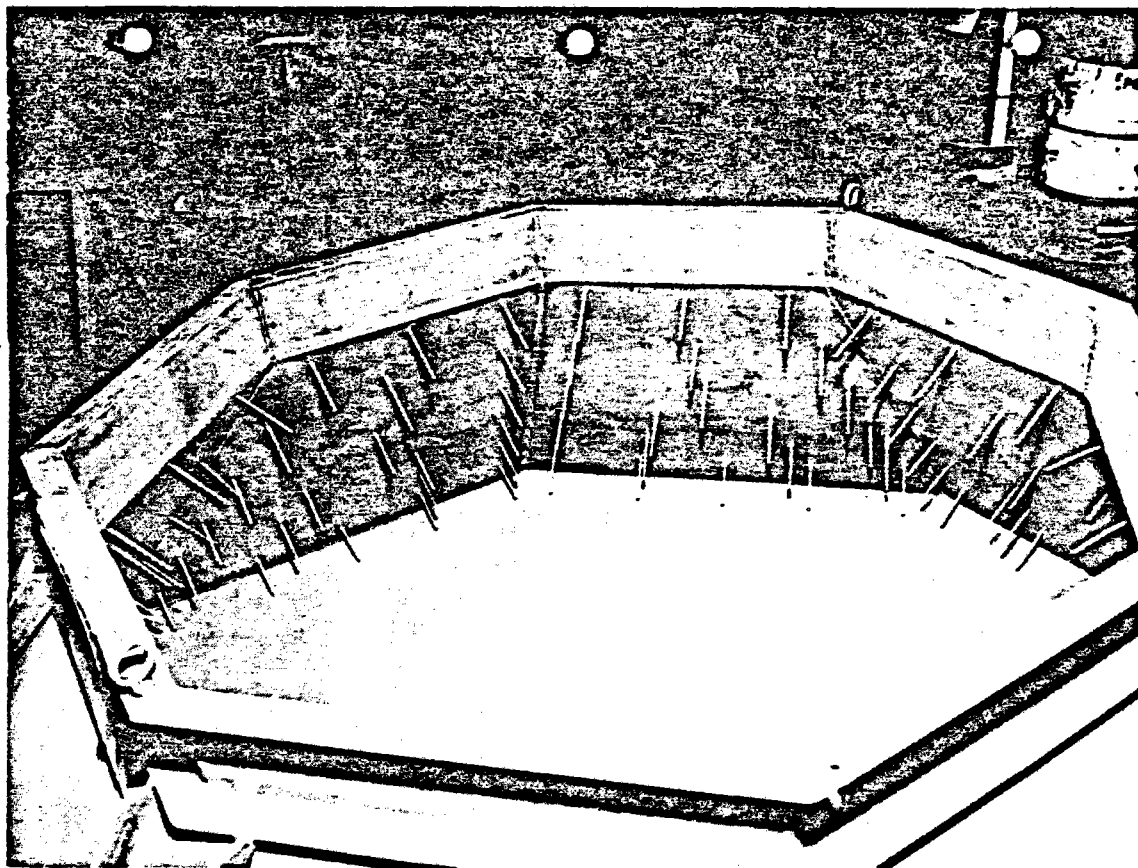


Figure 5.1-8: Interior View of Back Cover

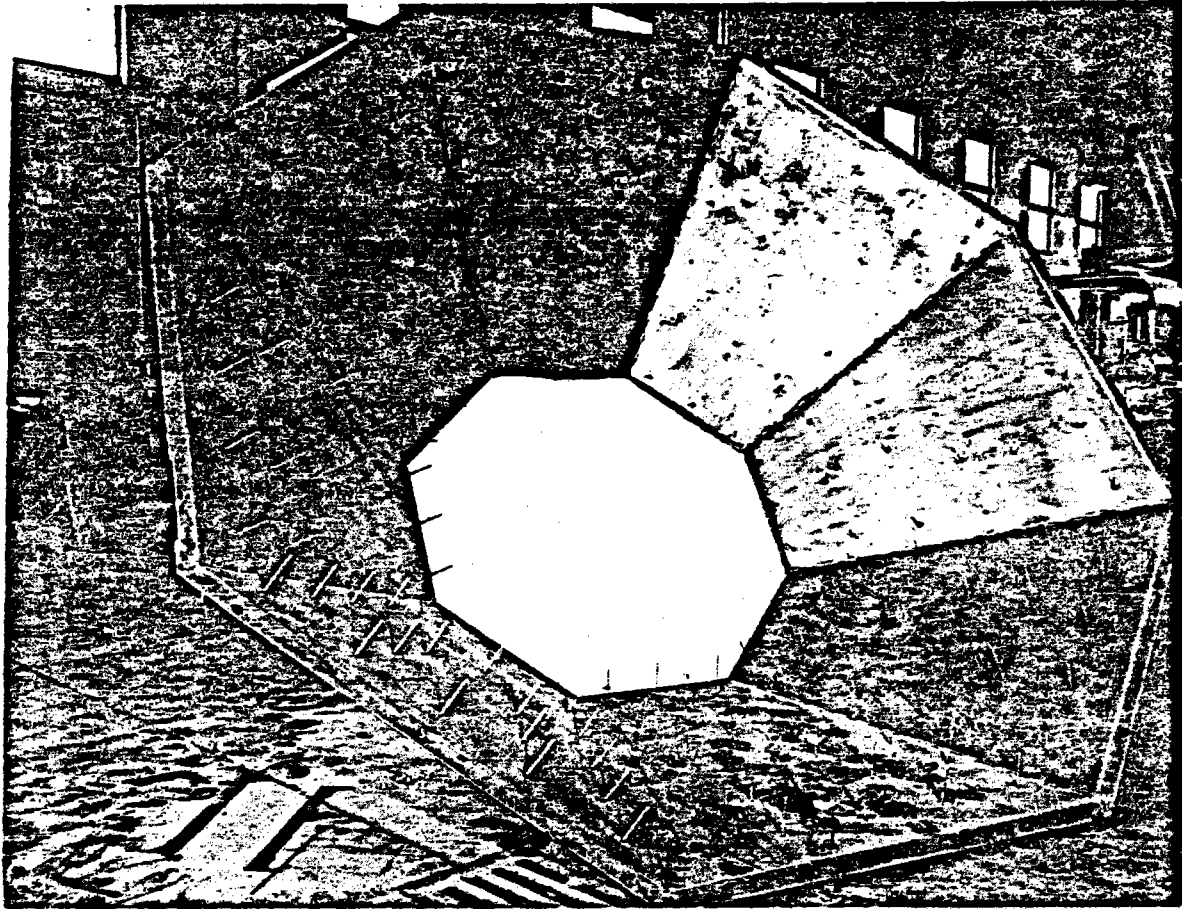


Figure 5.1-9: Back Cover Insulation Assembly

body progressed. These two parts were not mated again until they were assembled for solar testing at the CRTF in Albuquerque, New Mexico.

The aperture of the BMSR was formed by an insulated stainless-steel cone. This assembly was designed for installation on the BMSR framework with bolts, using slotted holes to accommodate thermal growth. T-section ribs stiffened the sheet metal cone and served as supports for the trapezoidal-shaped insulating boards. Figure 5.1-10 shows construction of the cone, which was made from AISI 304 stainless steel. Figure 5.1-11 shows the cone clamped in place on the BMSR aperture face, with the partially insulated cavity interior also visible. The T-sections are apparent in this photograph and the T-web has vent holes to provide free circulation of air behind the insulating boards. The insulating boards were cut, fitted, numbered, and indexed at this stage, then removed and stored for later installation at the solar test site.

Figures 5.1-12 and 5.1-13 are front and rear views of the completed BMSR insulated framework. The heat exchanger system had not been installed at this stage. Coils of thermocouple wire are visible on the outside of the shell. These thermocouples were installed within the insulation layers during construction. At this point, the two BMSR halves were separated, the main body being delivered to Exotic Metals Forming Company for installation of the heat exchanger components.

## 5.2 INSULATION AND SHIELDING

Insulation systems for the BMSR truncated prism back cover and the main body differed and will be discussed separately.

### 5.2.1 Back Cover Insulation

The insulation composite for the back cover was essentially 15.24 cm (6.0 in) thick and was composed of four layers. Starting at the steel-shell surface, a 7.62 cm (3.0 in) layer of mineral wool block was installed on the support studs. Careful attention was paid to fitup between adjacent blocks. Beveled cuts were necessary to obtain coverage, and these were made by hand

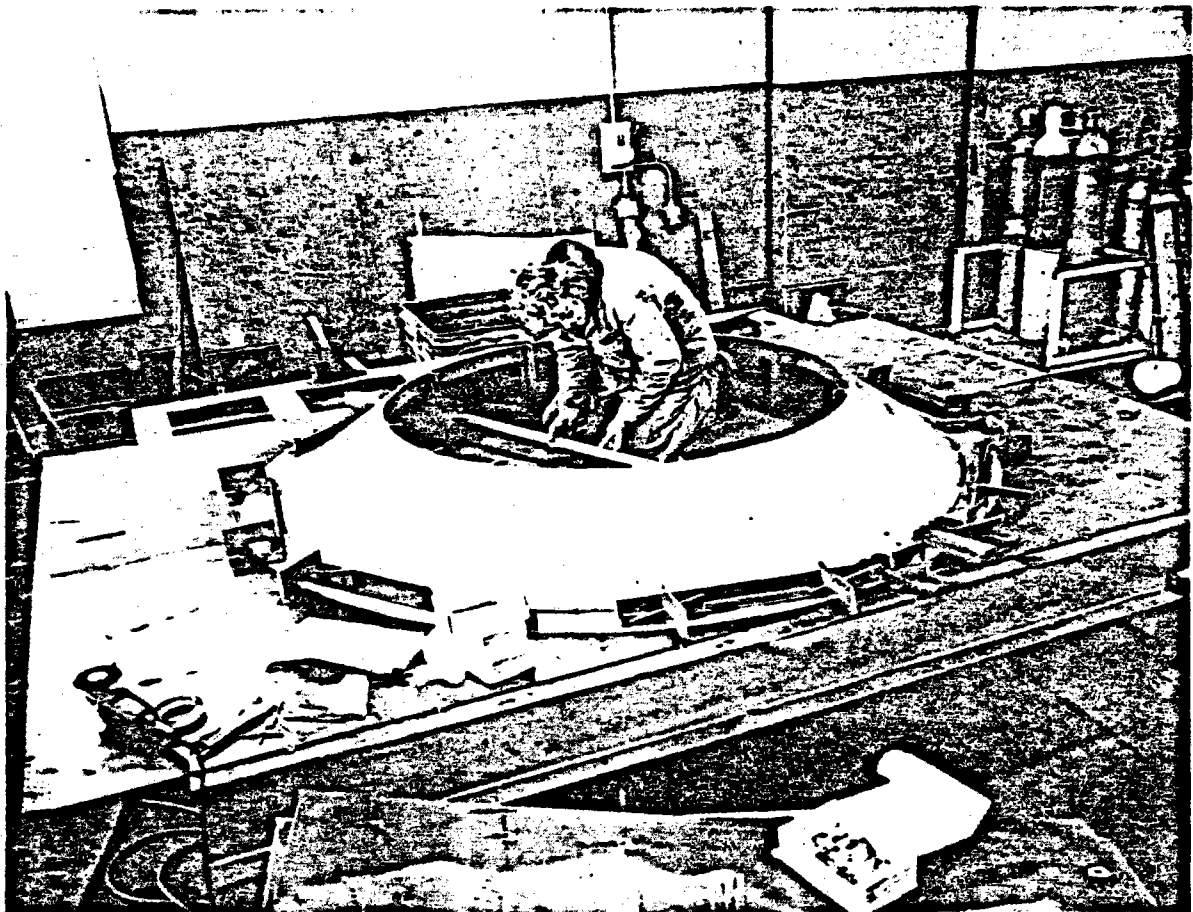


Figure 5.1-10: Aperture Cone Construction

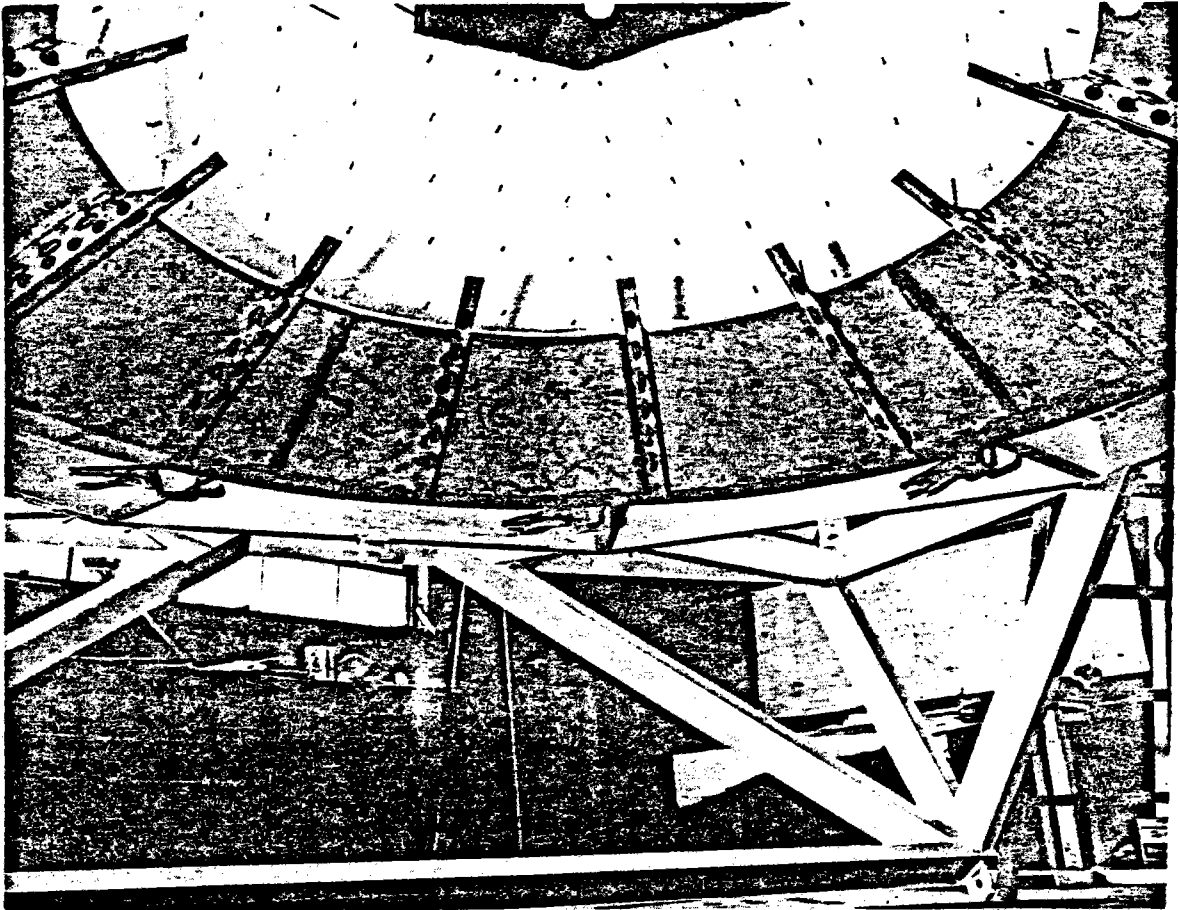


Figure 5.1-11: Aperture Cone Installation



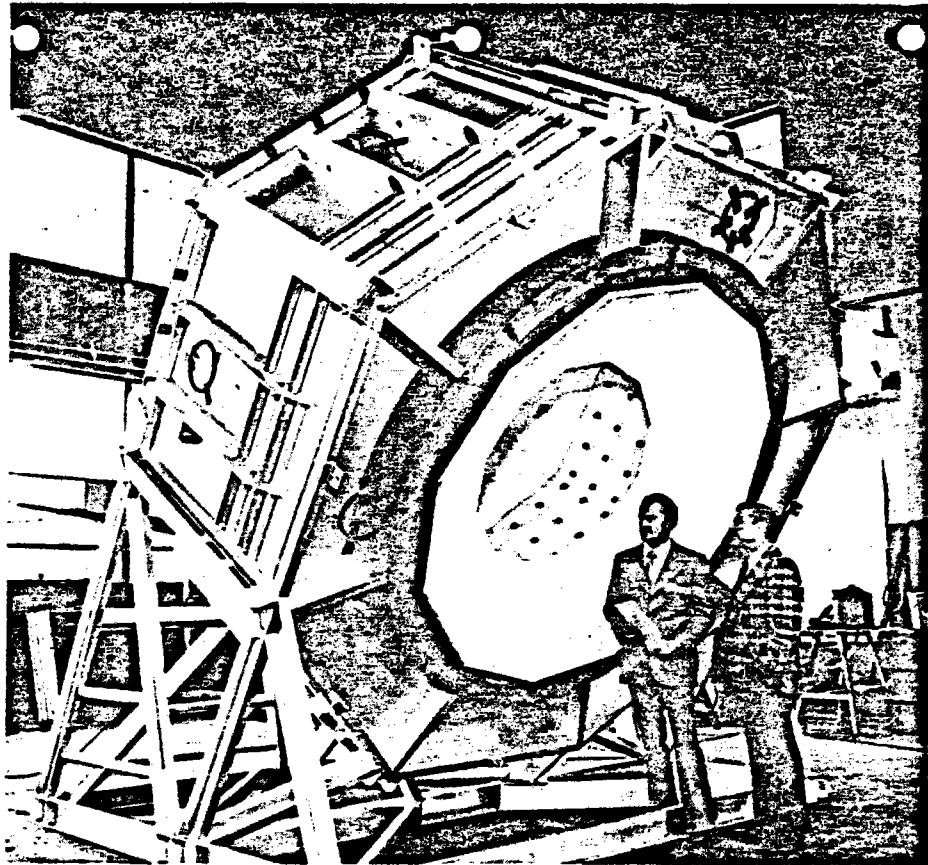


Figure 5.1-12: Front View Completed Steel Framework

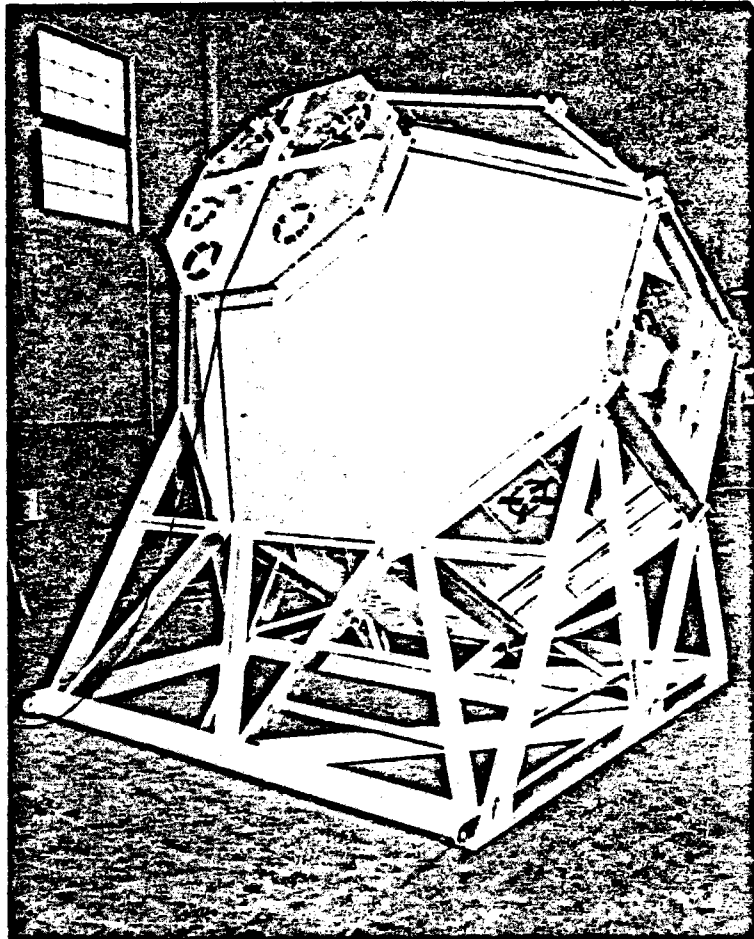


Figure 5.1-13: Back View Completed Steel Framework

using an electric knife. In areas where gaps were inevitable, the void was filled with scraps of Kaowool blanket. The following two 2.54 cm-thick (1.0 in thick) layers were of Kaowool blanket, impaled on the studs and secured with metallic "keepers". The arrangement of segments for these two layers was left to the fabricator, with the requirement that joints could not be located over joints in a preceding layer and that a minimum edge margin of 7.62 cm (3.0 in) be maintained from the nearest attachment studs. All segments of the Kaowool blanket used butt joints with a maximum gap limitation of 1.59 mm (0.06 in).

The innermost insulating layer was 2.54 cm-thick (1.0 in-thick) Saffil blanket arranged in an overlapped joint configuration with the exposed (or overlapped) edge facing away from the aperture and incident solar flux. Overlaps were also provided at the intersection of adjacent bays, anticipating some material shrinkage during test. Figure 5.2-1 shows the start of Saffil application. Preceding Kaowool blankets were held in place with metallic keepers. Installation of the Saffil started with the flat octagonal portion and then proceeded along the trapezoidal sections to the edge of the cover. One section of Saffil can be seen in place in the photograph, with another section laying on the flat octagonal portion. Upon completion of the Saffil layer, ceramic anchors were placed on the attachment studs.

The hollow centers of the anchors were filled with ceramic cement to lock them to the studs and threaded ceramic caps were installed. Figure 5.2-2 shows a closeup of the completed octagonal portion with the ceramic anchors in place. Four calorimeters and the centrally located radiometer have also been added. Figure 5.1-12 shows a portion of the insulated back cover, viewed through the aperture. The ceramic anchors are visible, as are the 601 steel washers used to secure sidewall insulation to the attachment studs.

#### 5.2.2 Main Body Insulation

The main body insulation composite was also 15.24 cm (6.0 in) thick and was constructed similarly to the cover insulation. The primary difference was

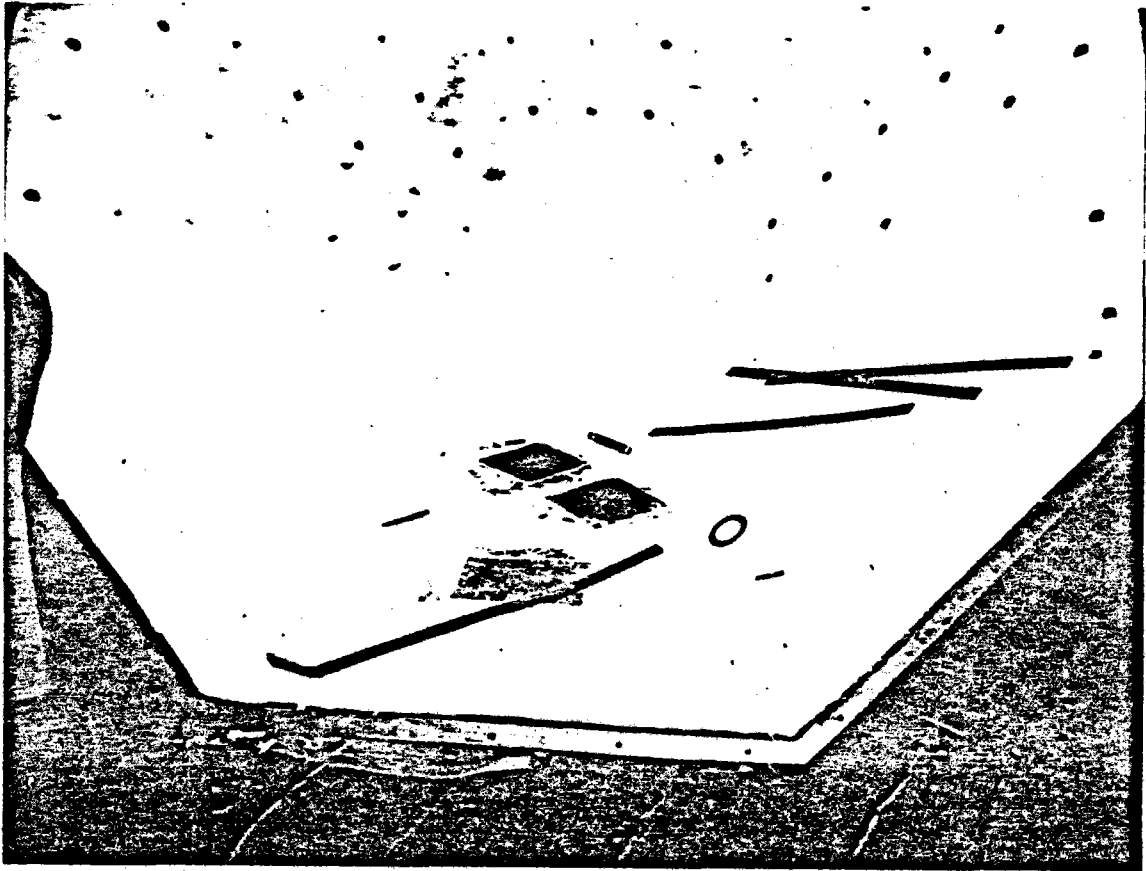
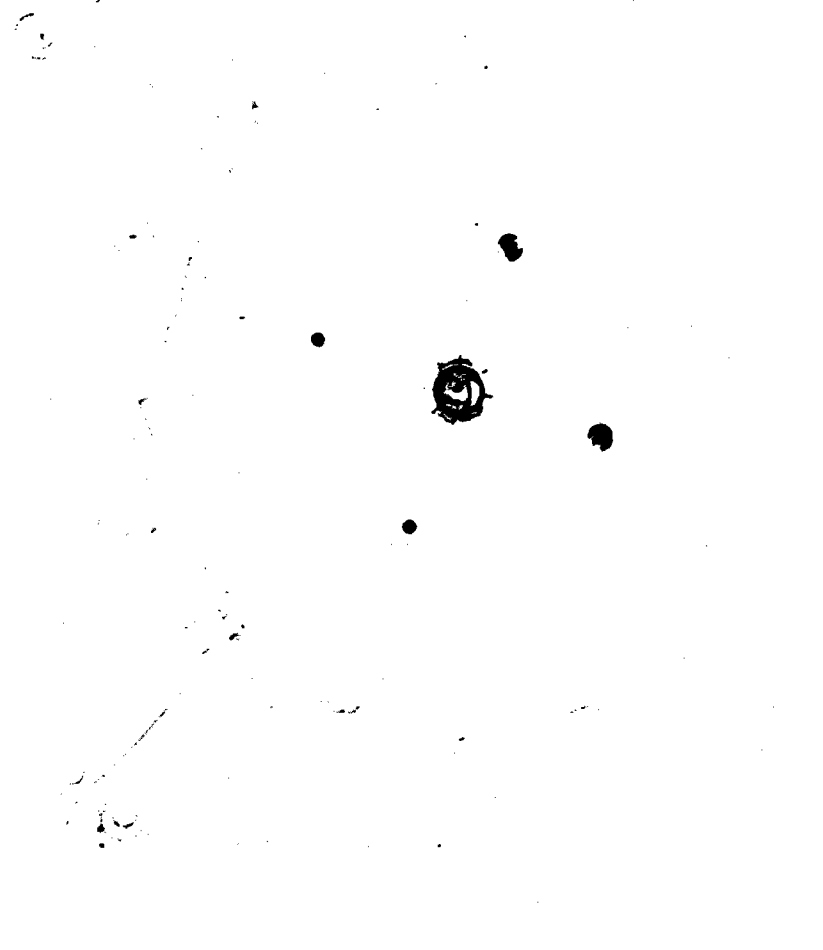


Figure 5.2-1: Back Cover Insulation Installation



**Figure 5.2-2: Back Cover Insulation Retention Method**

that the main body did not use Saffil as the innermost layer; Kaowool blanket was employed instead. Thus, the composite consisted of 7.62 cm (3.0 in) of mineral wool block against the steel shell, followed by three 2.54 cm (1.0 in) layers of Kaowool blanket. The joints of the innermost Kaowool blanket layer were overlapped 7.26 cm (3.0 in), with butt joints used for the underlying layers. A 2.54 cm (1.0 in) fold of the innermost blanket layer was provided at the edge of the main body where the truncated prism cover joined, to act as a seal when the two parts were assembled for testing. Figure 5.2-3 shows installation of a shielded thermocouple during installation layup. The view shows the inside of the aperture face and portions of two adjacent bay sidewalls. An aperture rim T-section is also visible. The thermocouples were installed 5.1 cm (2.0 in) from the exposed inner cavity surface, between two Kaowool blanket layers.

As described earlier, the aperture face was shielded externally with Kaowool 3000 board. The 3000 board was 2.54 cm (1.0 in) thick and was used as a substrate for bonding on zirconia tiles. Although not shown in Figure 5.1-12, the entire aperture face of the BMSR was insulated with the 3000-board-zirconia-tile composite to protect from misaligned heliostats. The zirconia tile was a dense 12.7 mm-thick (0.5 in-thick) product and was installed over the 3000 board by bonding with a water-soluble cement, QF 180. Bonding of the zirconia tiles was accomplished at the CRTF with the help of Sandia personnel.

### 5.3 HEAT EXCHANGERS AND MANIFOLDS

The heat exchanger system was composed of Inconel 617 elements in welded assemblies. Eight heat exchanger panels were used and these were located within the receiver cavity, each with their connecting flanges protruding from the cavity wall. Manifolds were designed to connect the eight panels into a flow system, providing inlet and exhaust functions. The manifolds were located outside of the cavity and were constructed of AISI 304 stainless steel. The manifolds were welded assemblies and were attached to the heat exchanger system by means of bolted flanges. The entire heat exchanger system (i.e., manifolds and panels) was supported by the manifolds, which were connected to leaf springs on the BMSR structure.

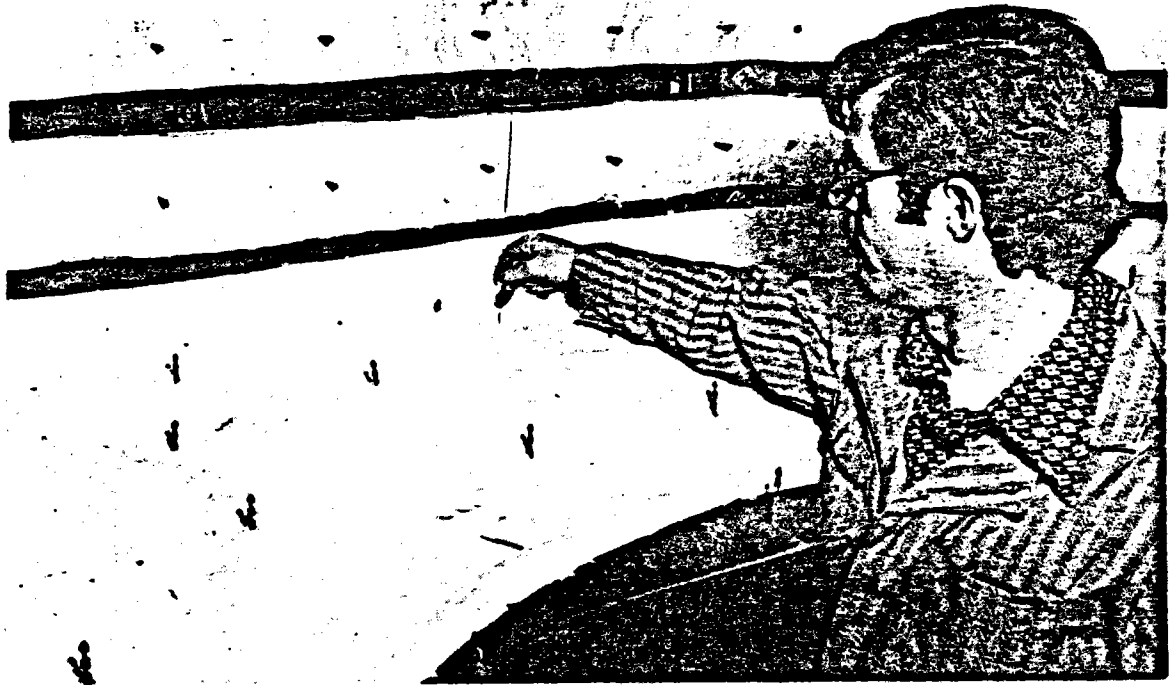


Figure 5.2-3: Installing Insulation Thermocouple

### 5.3.1 Heat Exchanger Panels

The eight heat exchanger panels were identical in all respects. The components of a panel (Figure 5.3-1) consist of two header assemblies, return bend tubes, and two internally threaded flanges. Only one lot of Inconel 617 tubing was available in the program time frame. The size of this material was 5.1 cm (2.0 in) outside diameter by 0.64 cm (0.25 in) wall thickness. The tubing was used as-purchased for the headers. A quantity of this same tubing stock was supplied to Superior Tube Company, Norristown, Pennsylvania, where the material was drawn to required dimensions for the heat exchangers. The finished dimensions of the drawn tubing were 0.5 cm (0.20 in) inside diameter by 0.97 mm (0.038 in) wall thickness.

The flanges were machined from Inconel 617 forged pancakes made by Schlosser Forge, Cucamonga, California. An internal pipe thread was provided in the design to permit final assembly adjustment when mating heat exchanger panels to manifolds on the BMSR. In retrospect, a straight thread would have been a better choice for ease of adjustment, because the pipe threads seized to the mating threads on the header assembly as the two parts were drawn together. During assembly, it became necessary to seal-weld the flange to the header pipe to prevent leakage; thus a straight thread would have been entirely acceptable.

Header assemblies (Figure 5.3-1) consisted of a T-shaped weldment constructed from tubing 5.1 cm (2.0 in) in diameter. A 45-deg bevel weld was made to add the connector tee to the header. This particular joint caused welding problems because of the varying thickness of material produced by the bevel cut. Substantial distortion was obtained in the first weld trials. The solution was to prebend the header tube, as shown in Figure 5.3-2. Subsequent weld shrinkage produced a straight header tube.



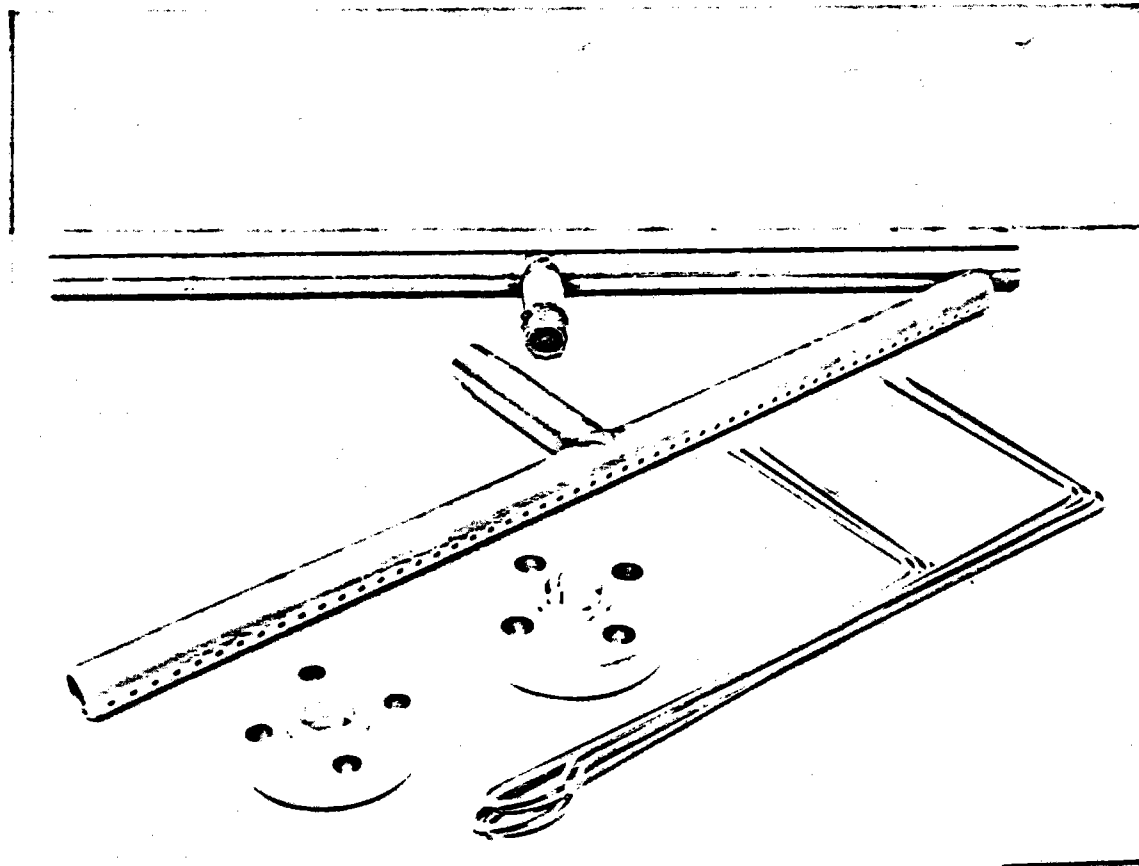


Figure 5.3-1: Heat Exchanger Components

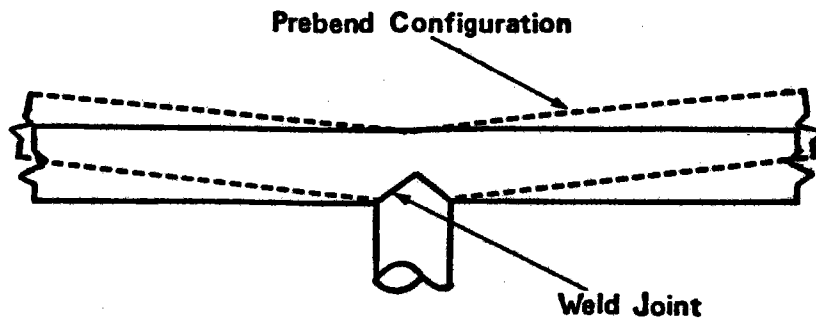


Figure 5.3-2: Header-to-Tee Weld Joint Strategy

The connector tube of the header assembly was pipe threaded externally before making the weld joint. After welding, holes were drilled and trepan edge preparations machined in 54 locations on both the inlet and outlet headers. Development of the weld-edge preparation shown in Figure 5.3-3 required considerable experimentation and research. Discussions with ORNL led to adoption of the trepan configuration whereby a thin cylinder of material was machined into the thick-wall tube to permit concentrating the welding heat. Early trials without the trepan resulted in melting of the thin-wall heat exchanger tube and lack of fusion at the joint. Several completed welds are shown in Figure 5.3-4. All tube-to-header joints were hand welded, a tedious process that required a skilled technician. The welder is shown at work in Figure 5.3-5. The same welder made all 864 welded joints in the eight heat exchanger panels, with only a few rejections because of dye penetrant indication. The limited clearance between adjacent tubes (2.0 cm [0.8 in]) required a welding technique with several stops and starts. The weld was started in the area between adjacent tubes, progressed halfway around the tube, and stopped. Then the other half of the weld was made, starting with an overlap in the area between adjacent tubes and progressing in the opposite direction to overlap the first half.

Machining of trepan weld-edge preparations in the headers was done with a cobalt steel form cutter. The cut was necessarily deeper along one axis of the trepan than the other because of the curvature of the 5.1 cm (2.0 in) tubing stock. Carbide cutters were found to work well on Inconel 617 also, provided an uninterrupted cut could be made. The trepan joint did not lend itself to use of carbide cutters.

Upon completion and inspection of tube-to-header weld joints, the header end caps (Figure 5.3-4) were welded in place. Experimentation with joint configuration and welding technique was also required to obtain a reliable process. A change of the end-cap design was necessary to eliminate a plug weld and replace it with a square butt weld. This necessitated machining the caps to produce a curved internal surface resembling a flanged head on a pressure vessel. This approach also placed the weld in an area where it could be inspected using radiographic techniques.

Figure 5.3-3. Weld Joint Detail

## Weld Joint Detail

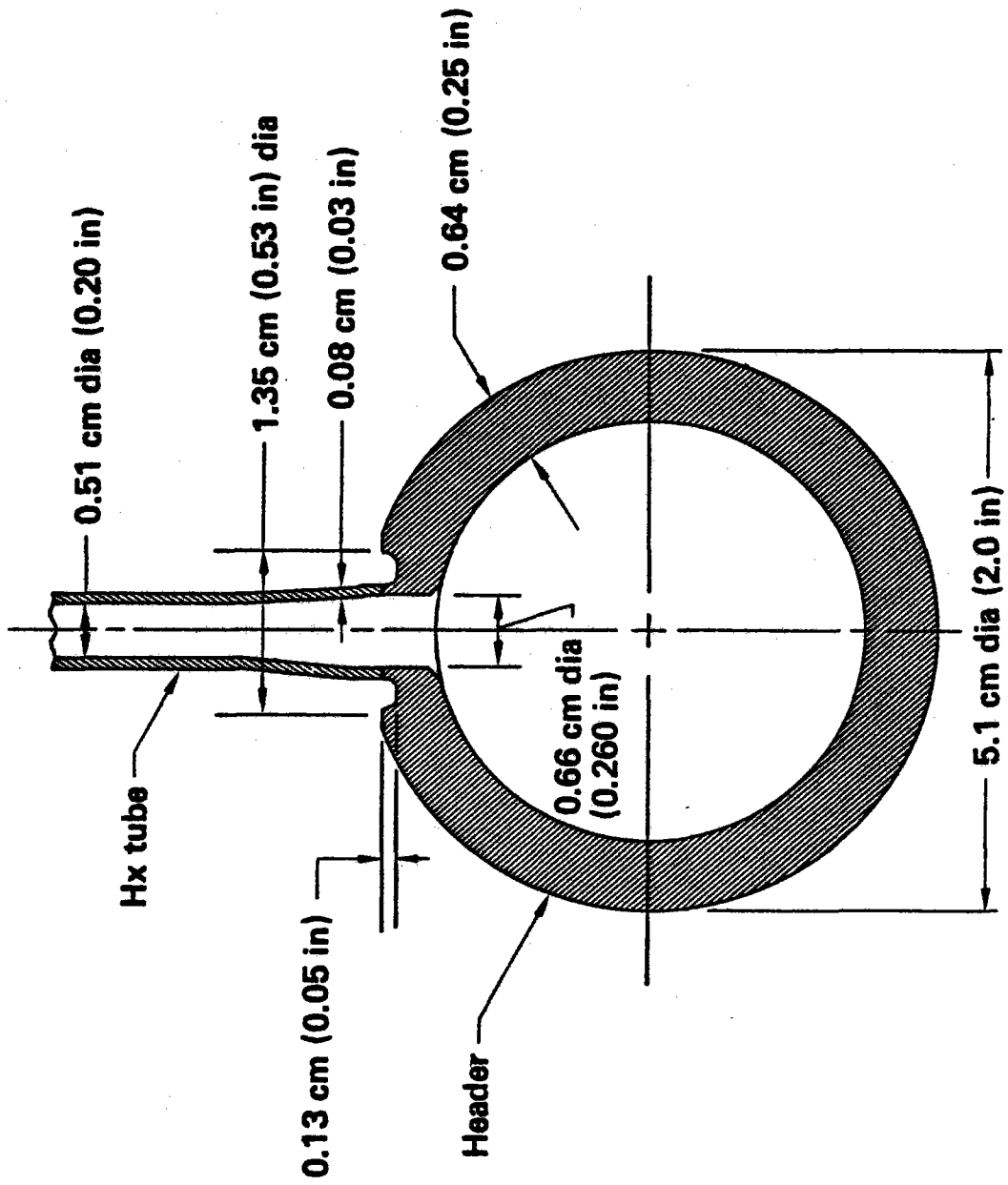




Figure 5.3-4: Tube-to-header Welds

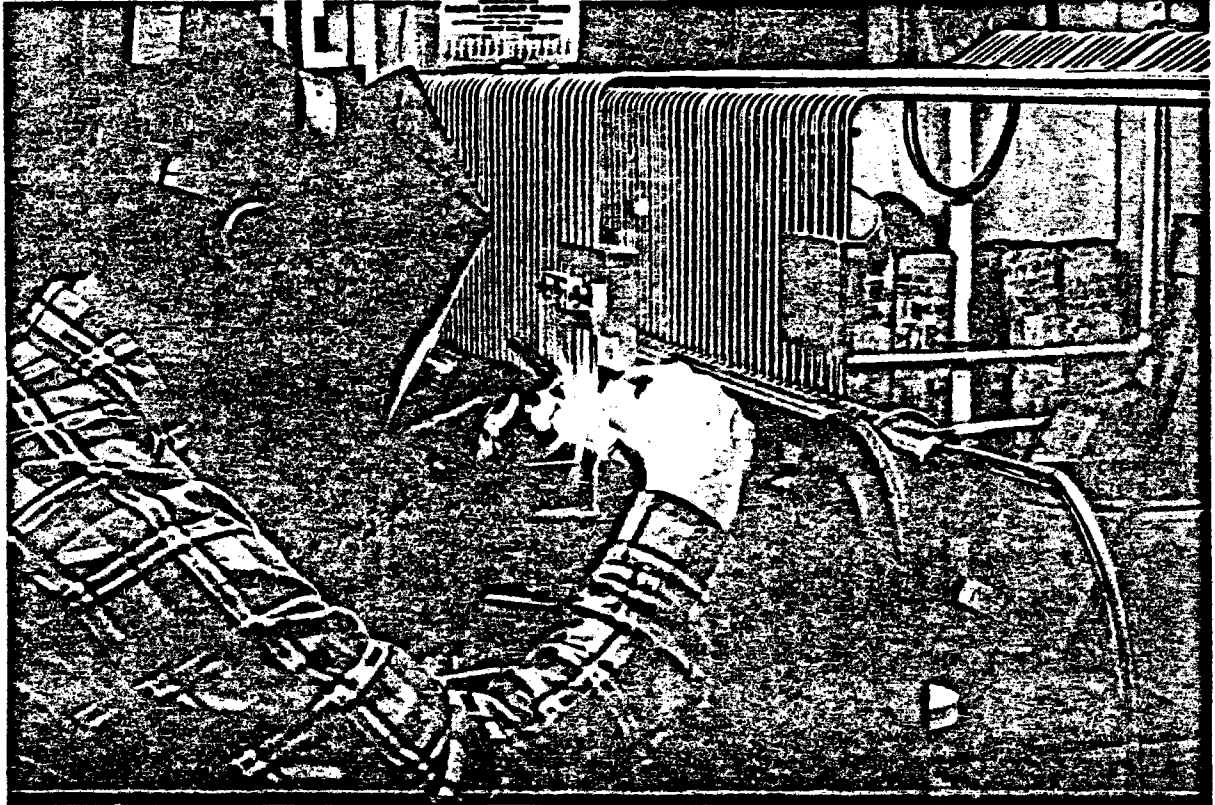


Figure 5.3-5: Heat Exchanger Tube Welding

All welds were accomplished using manual tungsten-arc processes (GTAW) as defined in Boeing Specification BAC 5975. A class A level of quality (highest level) was established owing to the severe inservice environment expected for the heat exchangers. This specification was developed for Boeing Aerospace products and is more stringent than comparable American Welding Society specifications. One requirement of the specification is that the welder must demonstrate proficiency with certain standard joint configurations to obtain certification.

Since the tube-to-header joint was considered particularly critical, an additional requirement was levied for certification wherein the welder had to qualify his process with the specific joint configuration. Acceptance was based on visual and penetrant methods of inspection of whole and sectioned weld samples. Having achieved an acceptable process, the welder was required to document the steps and inspection was performed to ensure compliance. New test welds and acceptance were required before welding each of the eight heat exchanger panels. The approach, and continued surveillance, resulted in a low tube-to-header weld rejection rate and trouble-free service during solar testing.

The nondestructive inspection techniques employed for heat exchanger welds included visual, dye penetrant, and radiographic methods. Boeing specifications were used because the subcontractor was familiar with them and they are interrelated with Boeing welding specifications. The specifications were BAC 5423, "Penetrant Methods of Inspection"; and BAC 5915, "Radiographic Inspection Methods." All welds that could be examined by X-ray were required to meet those standards. Where it was impractical to X-ray because of weld configuration, visual and dye penetrant inspection were used. Informational X-rays were taken for the critical tube-to-header joints but were not used as a basis for acceptance or rejection.

Upon completion of welding and inspection, each panel was stress relieved and oxidized in an air-heated furnace. The cycle was 2 hr at 899°C (1650°F). Following this step, the panels were hydrostatically proof-tested at 5.6 MPa (825 lb/in<sup>2</sup>), then visually leak checked at 3.7 MPa (550 lb/in<sup>2</sup>). The water was flushed from the system and warm air was circulated through

the panel until dry. Figure 5.3-6 shows a panel after stress relief in preparation for proof testing.

### 5.3.2 Manifolds

Inlet and exhaust manifolds encircled the BMSR framework in two parallel paths. The manifolds were constructed of schedule 80, 10.2 cm diameter (4.0 in-diameter) stainless-steel pipe. The specification was ASTM SA 312, type TP304 or TP304H seamless or seam-welded pipe. Connecting flanges were ANSI B16.5 forged flanges, class F304 or F304H per ASTM 182-76a. An example of the variety of flanges is shown in Figure 5.3-7.

Eight elbow sections were formed from the schedule 80 pipe and, when welded to interconnecting straight sections, formed the complete manifold. Each elbow accommodated a flange that connected to a heat exchanger panel inlet or outlet as appropriate. Figure 5.3-8 is a photograph of two elbow assemblies. The uppermost assembly is the inlet manifold; the outlet manifold is characterized by the thicker flange required for a service temperature of 816°C (1500°F). The welds shown in this photograph are only partially complete, several passes being required to fill the weld preparation completely. Accessibility was limited for welding because of the flange overhang (Figure 5.3-9). Figure 5.3-10 shows manifold components prior to assembly. The straight-pipe section has attachment brackets welded in place. These brackets, when aligned with mating parts on the leaf springs of the framework, served as the points of support for the entire manifold. A machined 6Al-4V titanium pin provided the support function.

Assembly of manifold components on the BMSR framework was initiated after the eight heat exchanger panels had been fixtured in place. Figure 5.3-11 shows headers of two adjacent heat exchanger panels held in place by fixtures. Assembly of the upper (inlet) manifold was started by bolting the welded elbow assemblies to the mating heat exchanger flange. A dummy valve body was used to achieve proper spacing, as shown in Figure 5.3-12. Fitup of interconnecting straight-pipe sections was accomplished in place, and the parts were tack welded. The weld was completed on a bench where full access was available, except for four closeout welds which, of necessity, were made



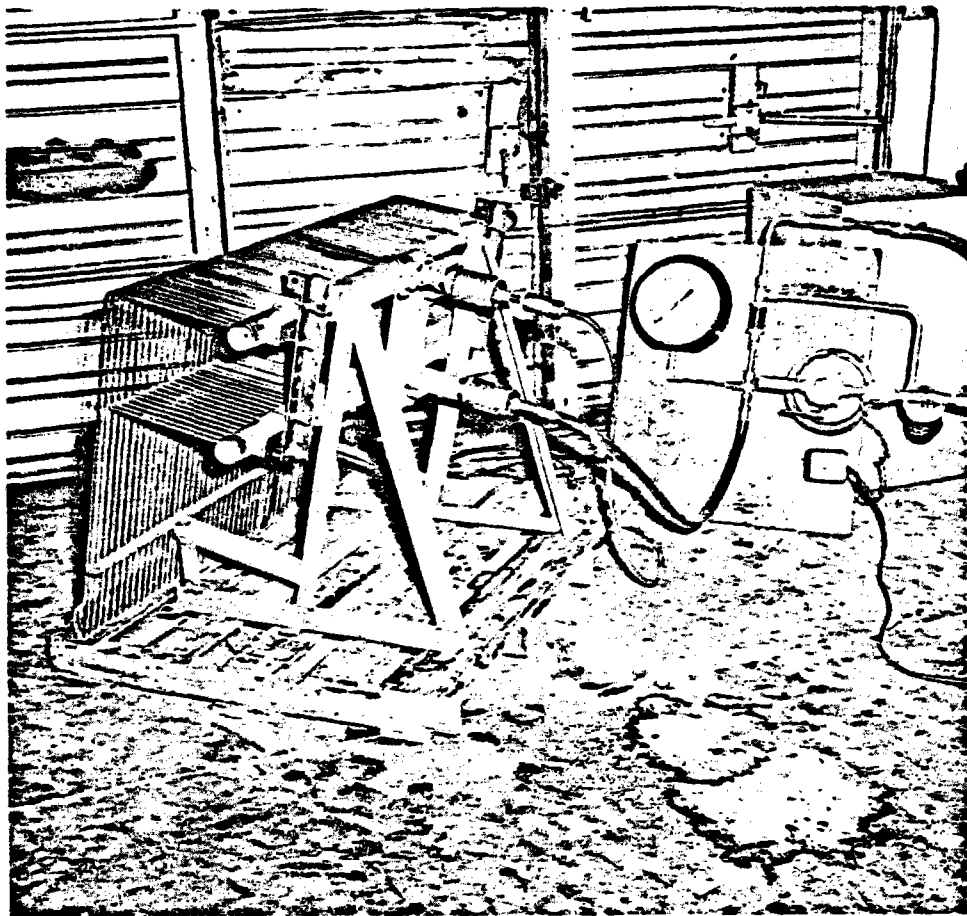


Figure 5.3-6: Heat Exchanger Panel Hydrostatic Proof Test

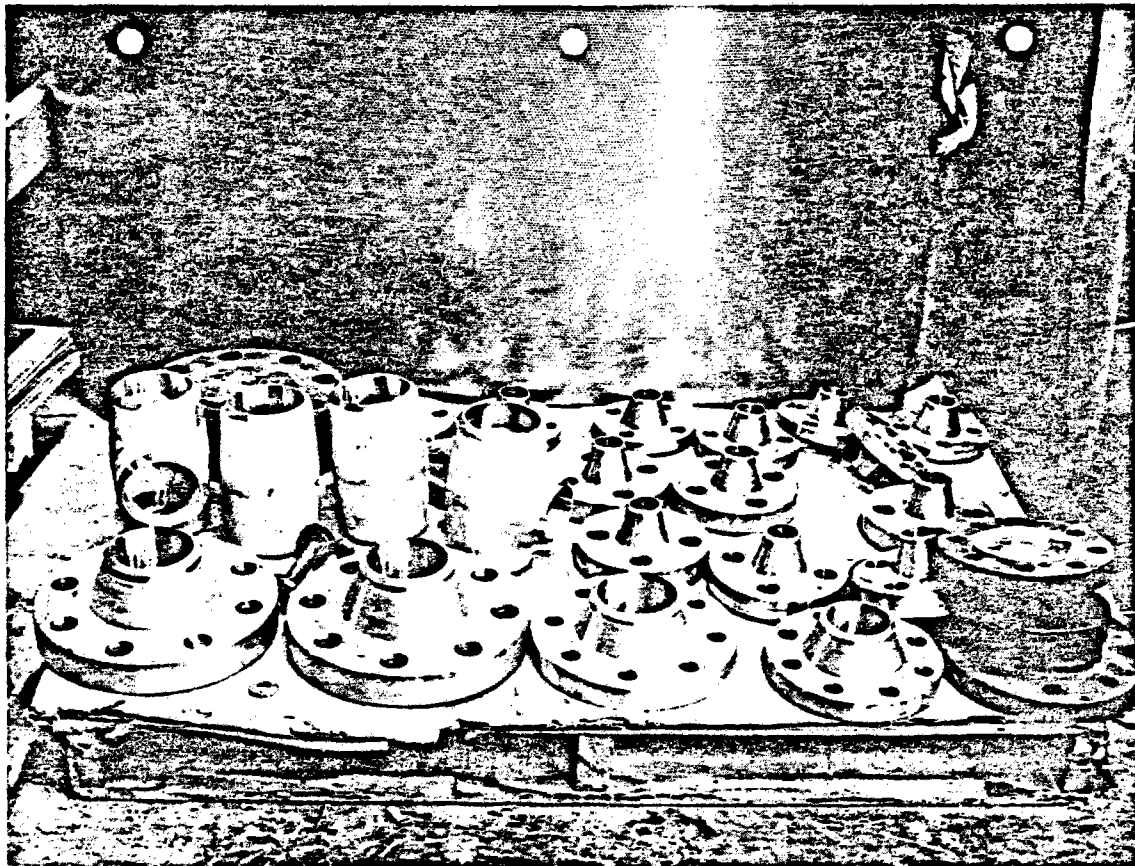


Figure 5.3-7: Manifold Components

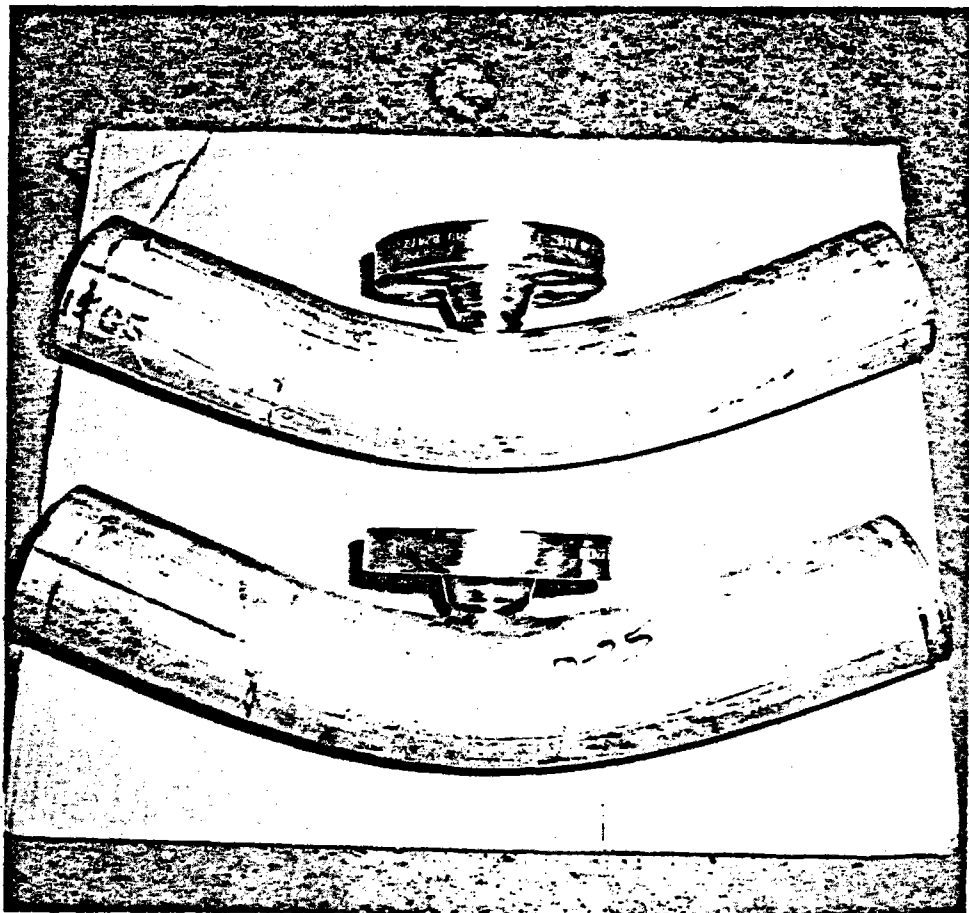


Figure 5.3-8: Manifold Elbow Assemblies



Figure 5.3-9: Welding Elbow Assembly

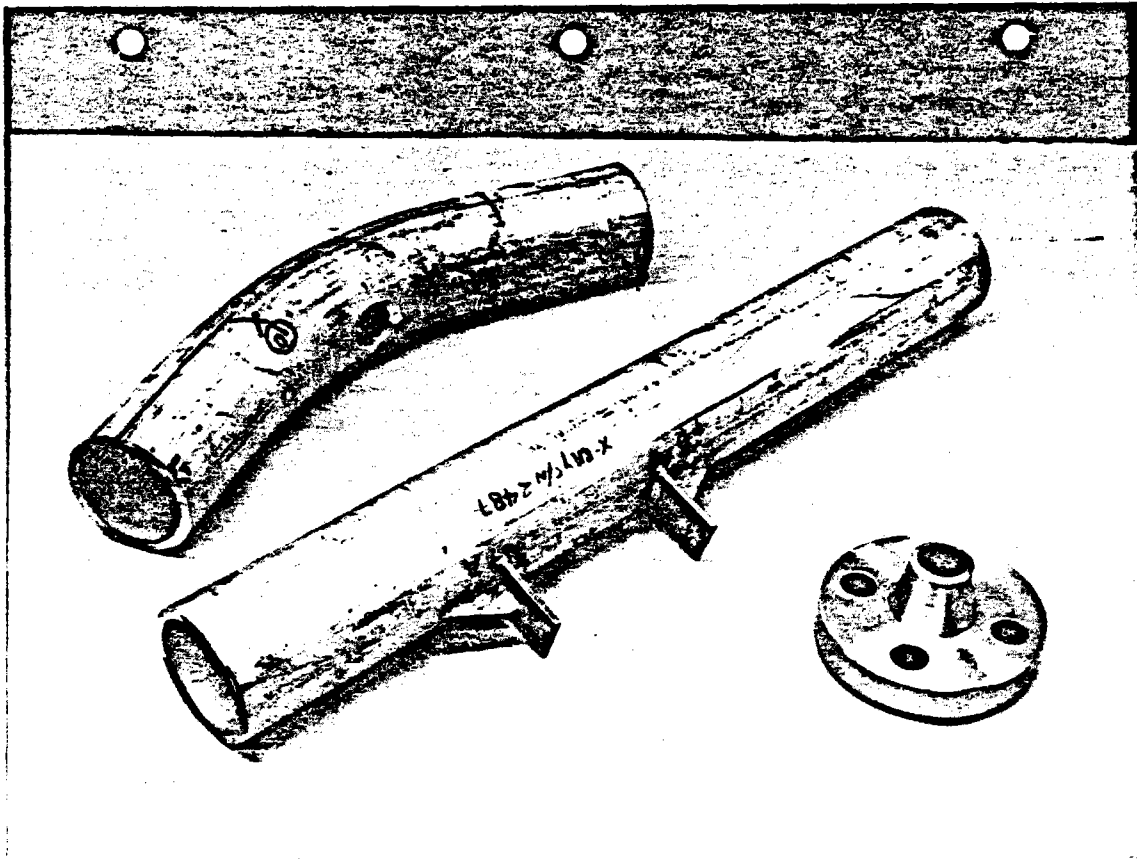


Figure 5.3-10: Manifold Piping Segments

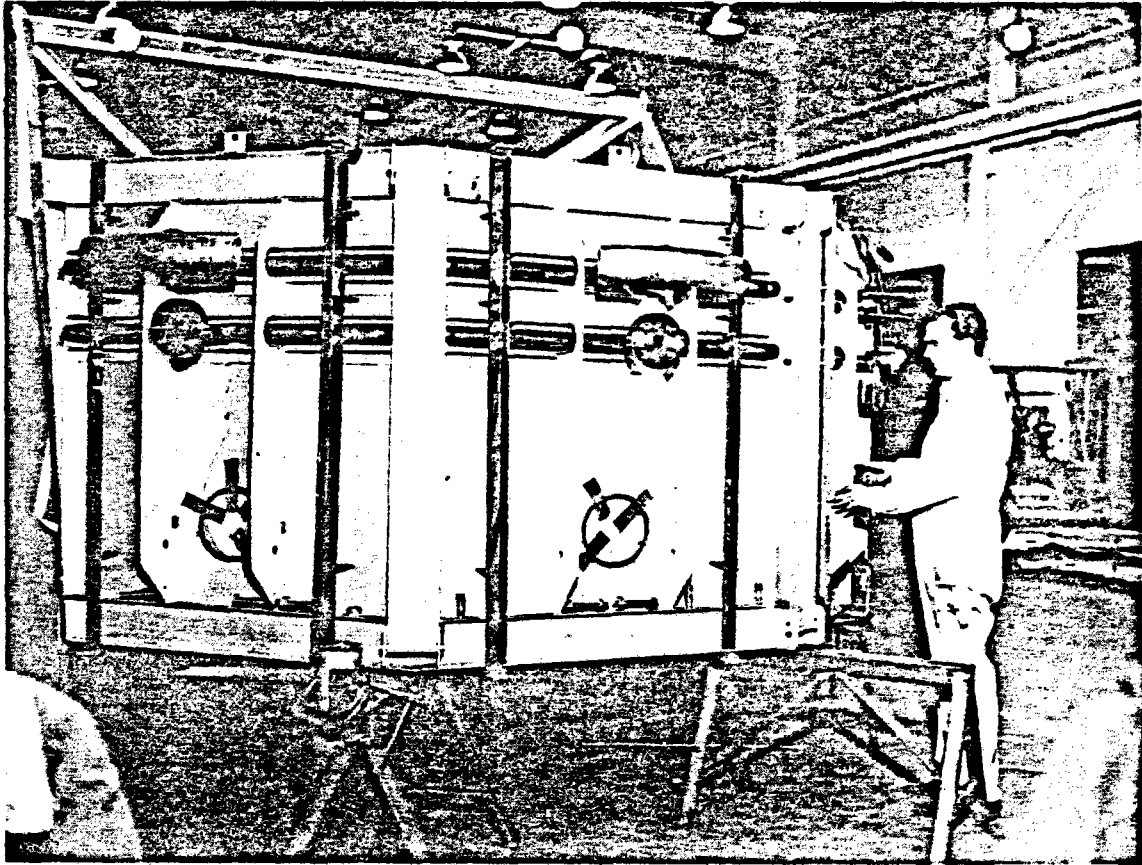


Figure 5.3-11: Assembling Manifold on BMSR Framework

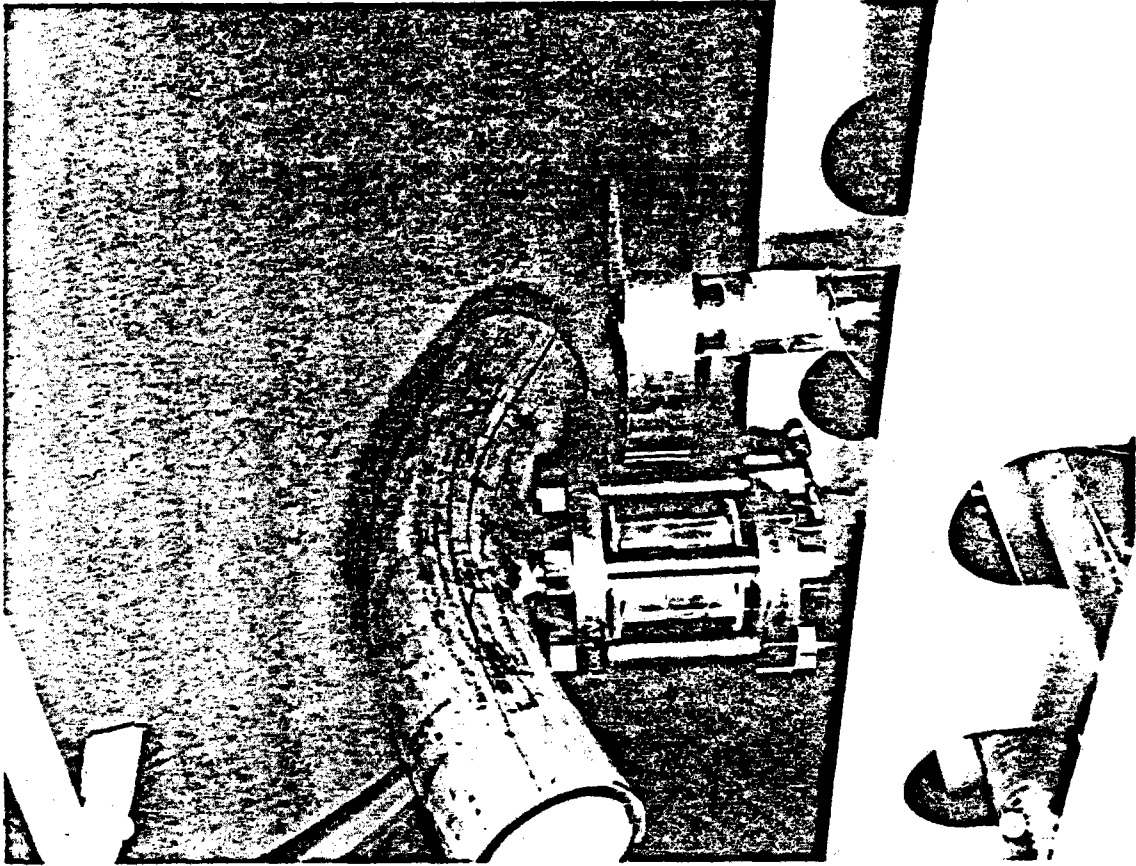


Figure 5.3-12: Valve Spaces Installation

in place on the framework. Clearances and visibility were limited for these welds, in some cases requiring welding by means of mirrors. A skilled welder was required to complete this work. Figure 5.3-13 shows welding in progress on the inlet manifold, and Figure 5.3-14 is a closeup of completed joints.

Welding was conducted in accordance with Boeing specification BAC 5975, class A, using the GTAW process. Visual, dye penetrant, and radiographic inspection methods were used except in areas where X-ray interpretation was questionable. The closeout manifold welds were inspected using a radioisotope source. This work was normally done on second shift to minimize personnel exposure hazards.

After completion of welding and inspection, the manifold flanges were connected to mating heat exchanger flanges and the manifolds were insulated. Two layers of 1.3 cm (0.5 in) Kaowool blanket were installed on the manifolds, with joints overlapping. These were spiral wrapped with stainless-steel wire. This approach produced a very durable insulation system. Figure 5.3-15 shows insulation of manifolds in progress. Figure 5.3-16 is a closeup of the completed job, and Figure 5.3-17 shows the interior of the cavity with heat exchanger panels installed and a portion of the manifolds visible.

The manifolds were fabricated with four external flanges. Two on the outlet manifold provided exhaust functions and were connected to the air supply system recuperator inlet. The inlet manifold had one supply port, which was connected to the shell (outlet) side of the recuperator; and one burst disk relief port, visible in Figure 5.3-16. These ports consisted of flanges which were welded to forged T-sections, which were in turn welded into the straight-pipe portions of the manifolds.

#### 5.4 INSTRUMENTATION AND CONTROLS

Instrumentation consisted of thermocouples, pressure transducers, calorimeters, and valve position potentiometers. The instruments were purchased items. The fabrication effort involved mounting of instruments,



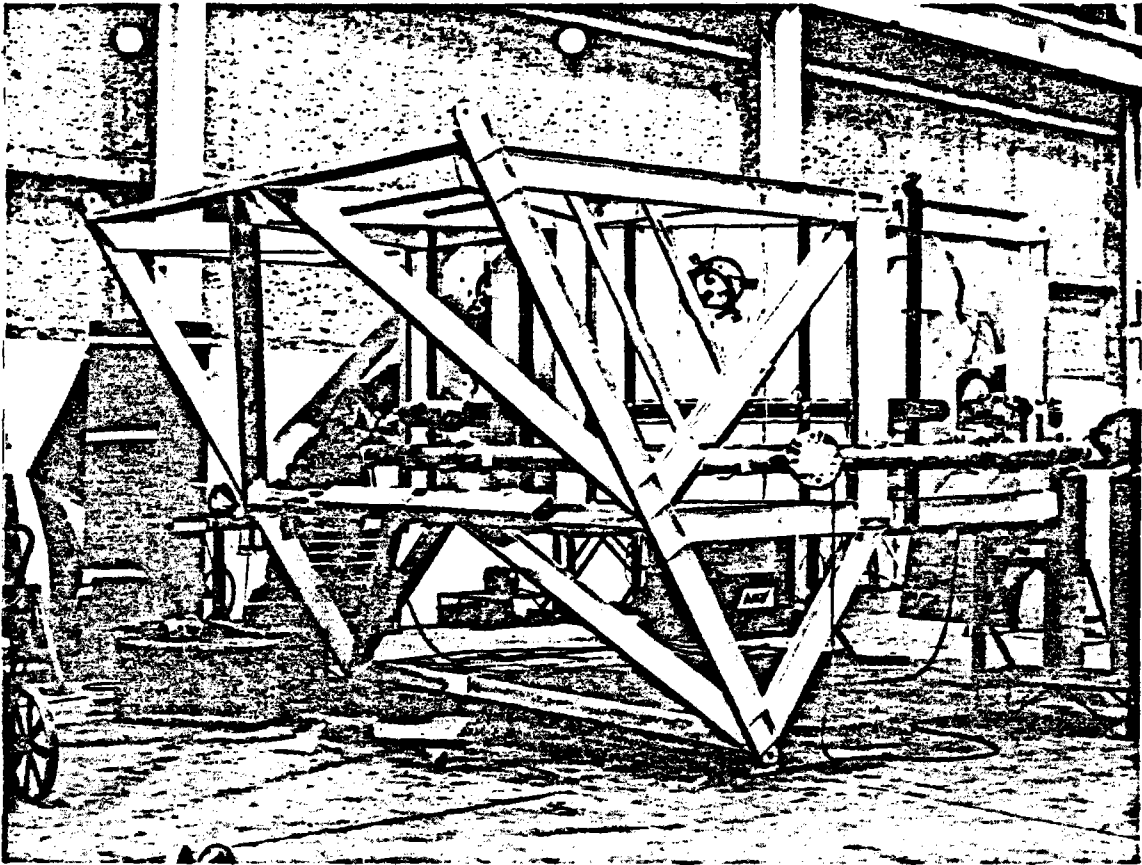


Figure 5.3-13: Manifold Welding in Progress

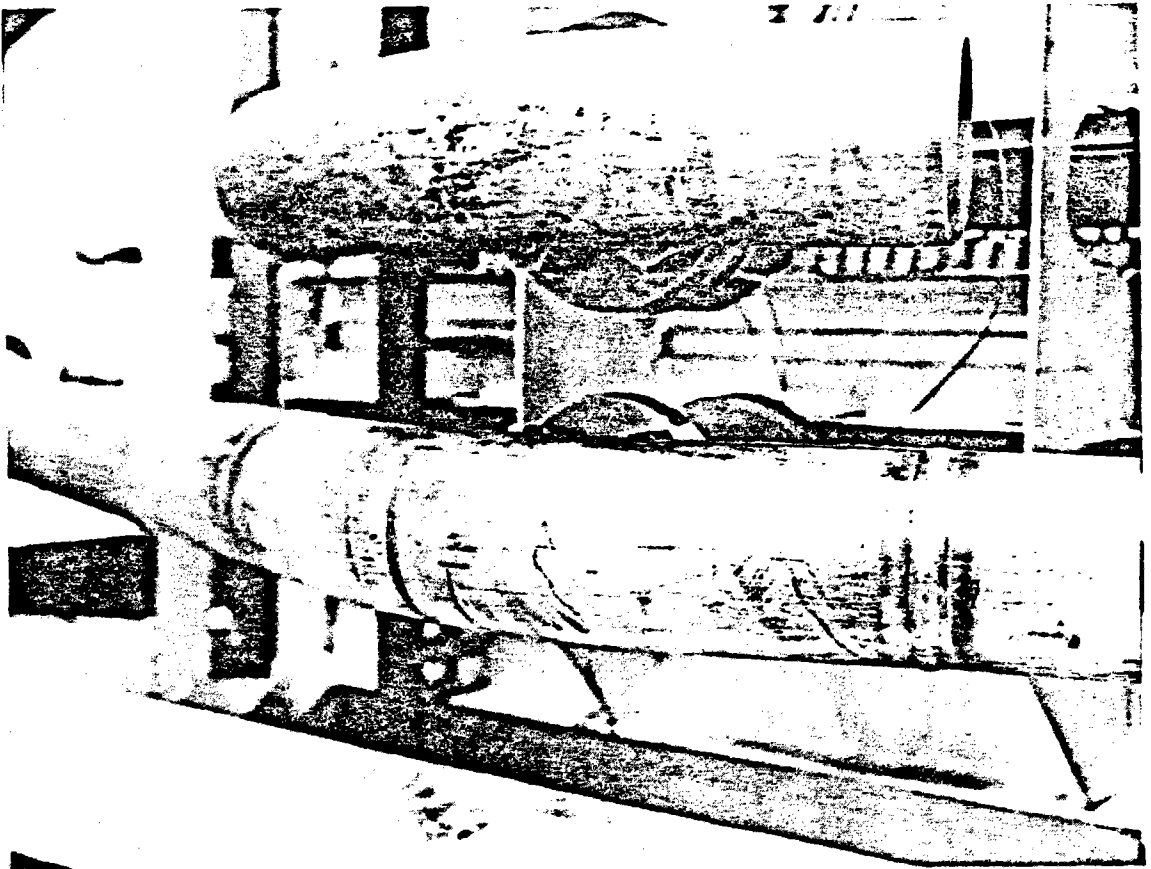


Figure 5.3-14: Manifold Weld Joints

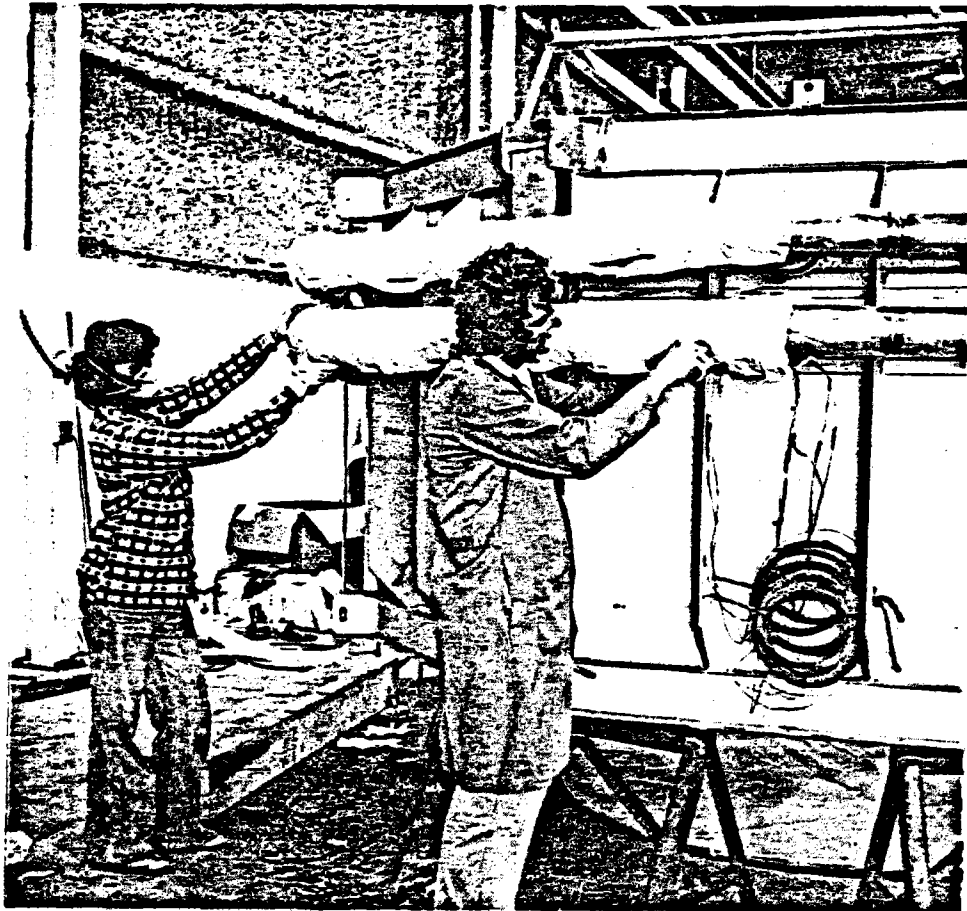


Figure 5.3-15: Installing Insulation on Manifold

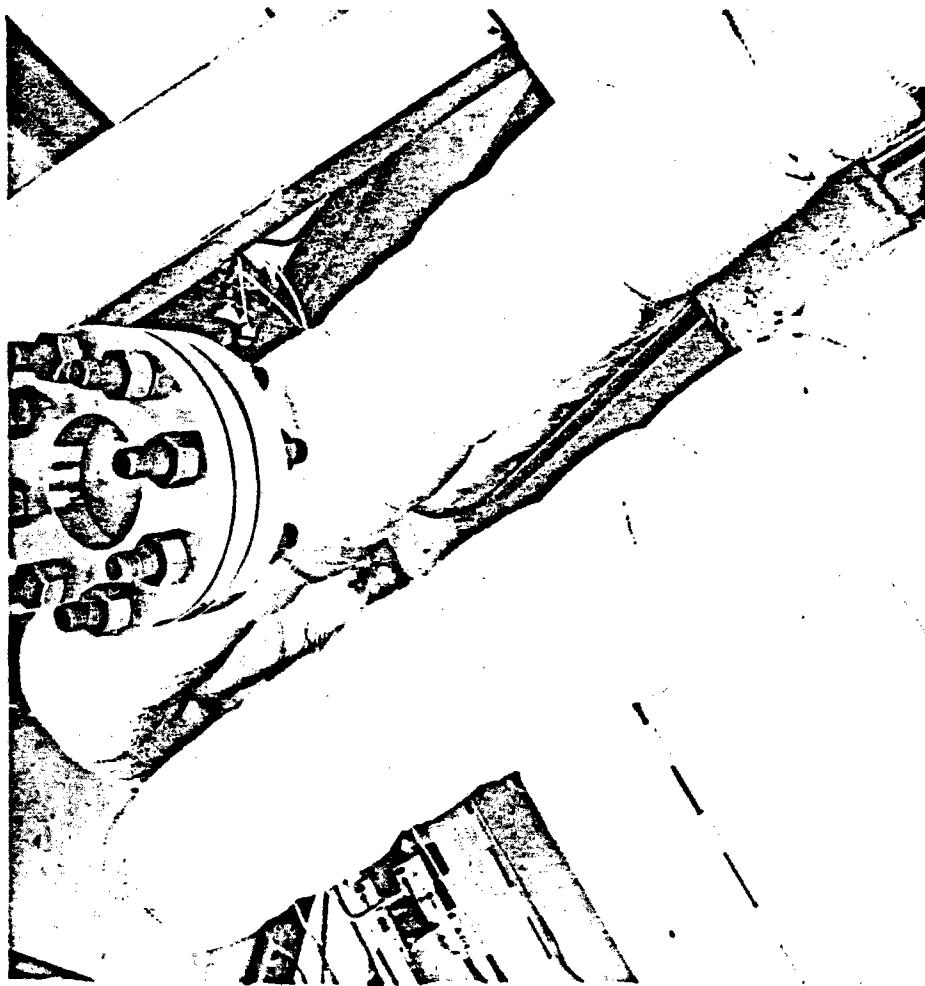


Figure 5.3-16: Insulation Wire Wrap

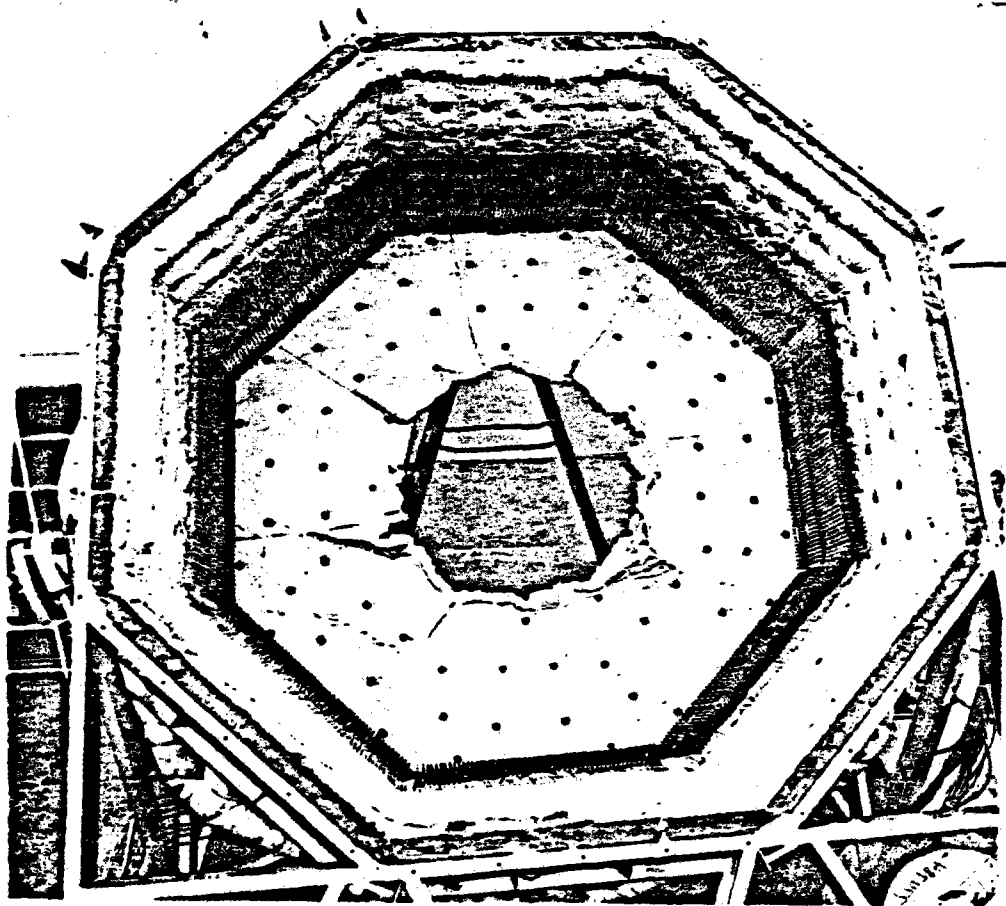


Figure 5.3-17: Cavity Interior with Back Cover Removed

connecting of leads, and routing of leads in the cable tray. Figure 5.4-1 shows the wire bundle at the cable tray exit, and Figure 5.4-2 shows the location of the cable tray on the BMSR.

Thermocouples were installed as fabrication progressed to ensure proper positioning. An insulation thermocouple was being installed in the photograph of Figure 5.2-3. Pressure taps and gas measurement thermocouples were installed in manifolds prior to applying the insulation wrap. Heat exchanger tube temperature thermocouples were special ordered from the supplier with a fin brazed on the Inconel sheath at the tip. The fin was then spot welded to the heat exchanger tube (Figure 5.4-3). Abrasive cleaning of the heat exchanger tube to remove the oxide scale was necessary to achieve an acceptable spotweld.

Calorimeters were supported by their coolant tubes, which formed an integral part of the purchased item. It was desired to have the calorimeter face flush with the interior cavity (insulation) surface. Because the insulation surface was irregular, a stainless-steel tube with a flange was used to mount the calorimeter. The flange leveled the insulation around the tube perimeter on the inside of the cavity. The tube was rigidly attached to the BMSR steel shell with screws. The inside diameter of the tube was sized to accommodate the cylindrical calorimeter body with a slight clearance. The calorimeter was inserted from the outside until flush with the interior, then the tubes were clamped to a bracket mount on the BMSR shell.

Water-coolant lines were connected to calorimeter tube projections, as shown in Figure 5.4-4. The clamp bracket is also visible in the photograph.

Figure 5.2-2 showed an interior view of the BMSR truncated cone. The four calorimeters and tube flanges are evident, arranged around the central radiometer instrument. The radiometer consisted of a calorimeter in a water-cooled shell. The shell incorporated a flange similar to the ones described previously. All calorimeter mounting devices were constructed of stainless steel.

Control system components included flow-control valves, electropneumatic transducers, valve positioners and position potentiometers, gas outlet temperature thermocouples, and set-point controllers. Each heat exchanger

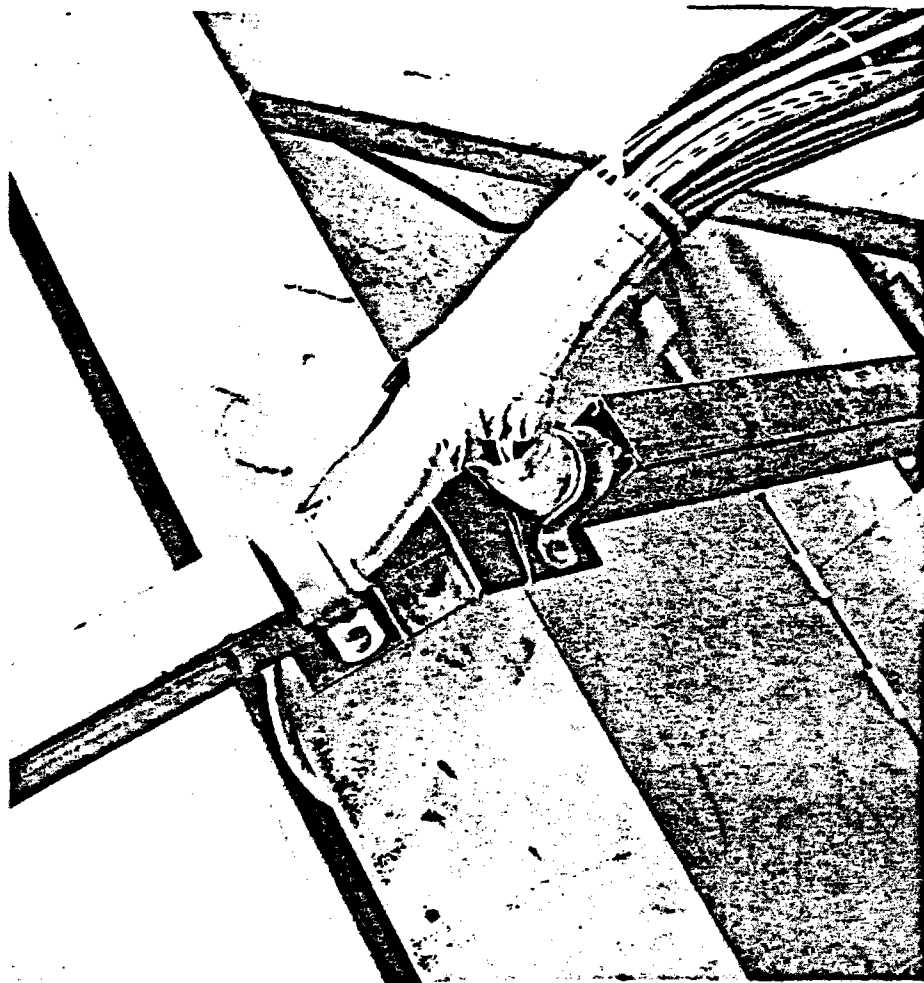


Figure 5.4-1: Cable Trays and Cabling Bundle

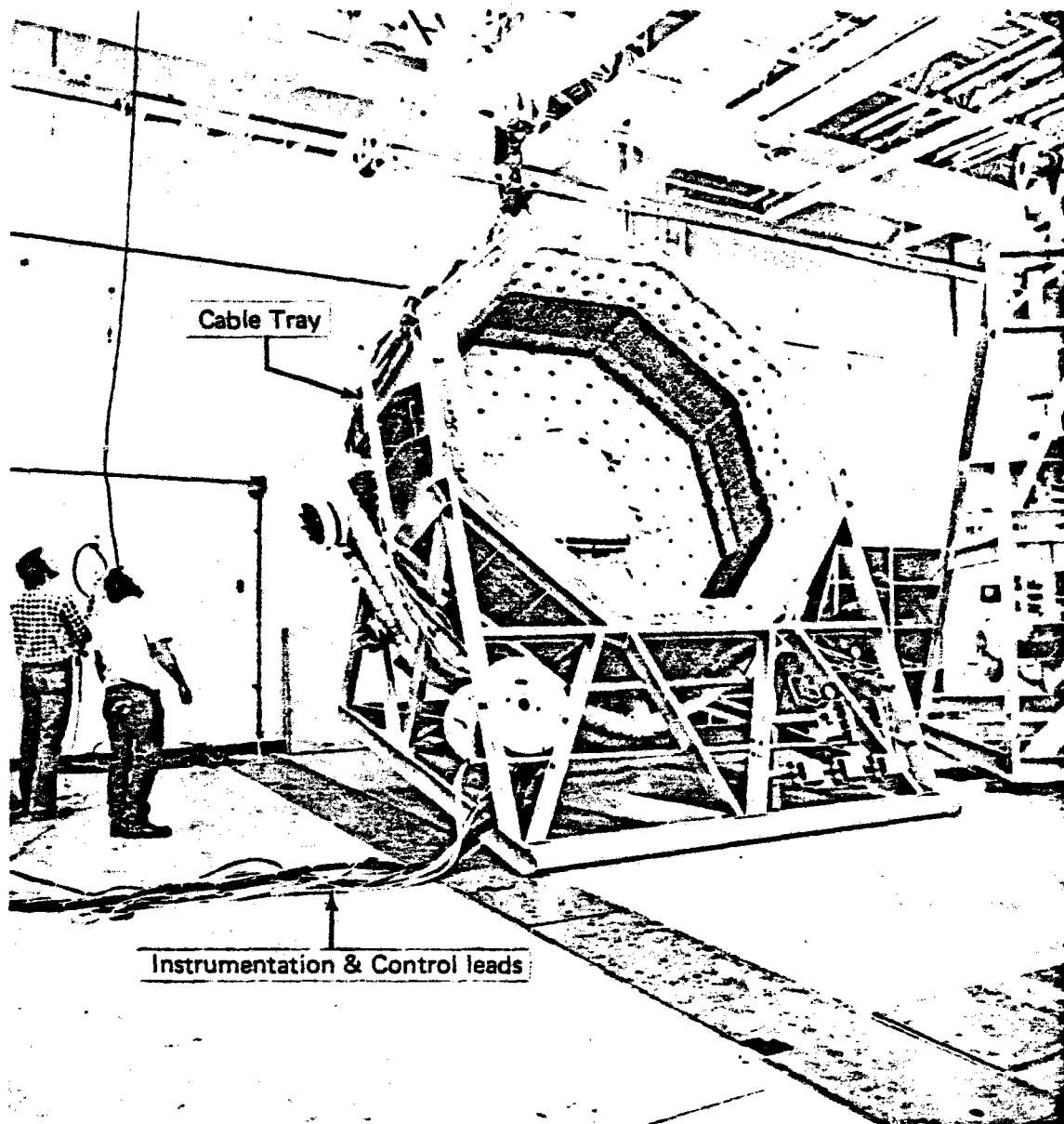


Figure 5.4-2: BMSR with Back Cover Removed



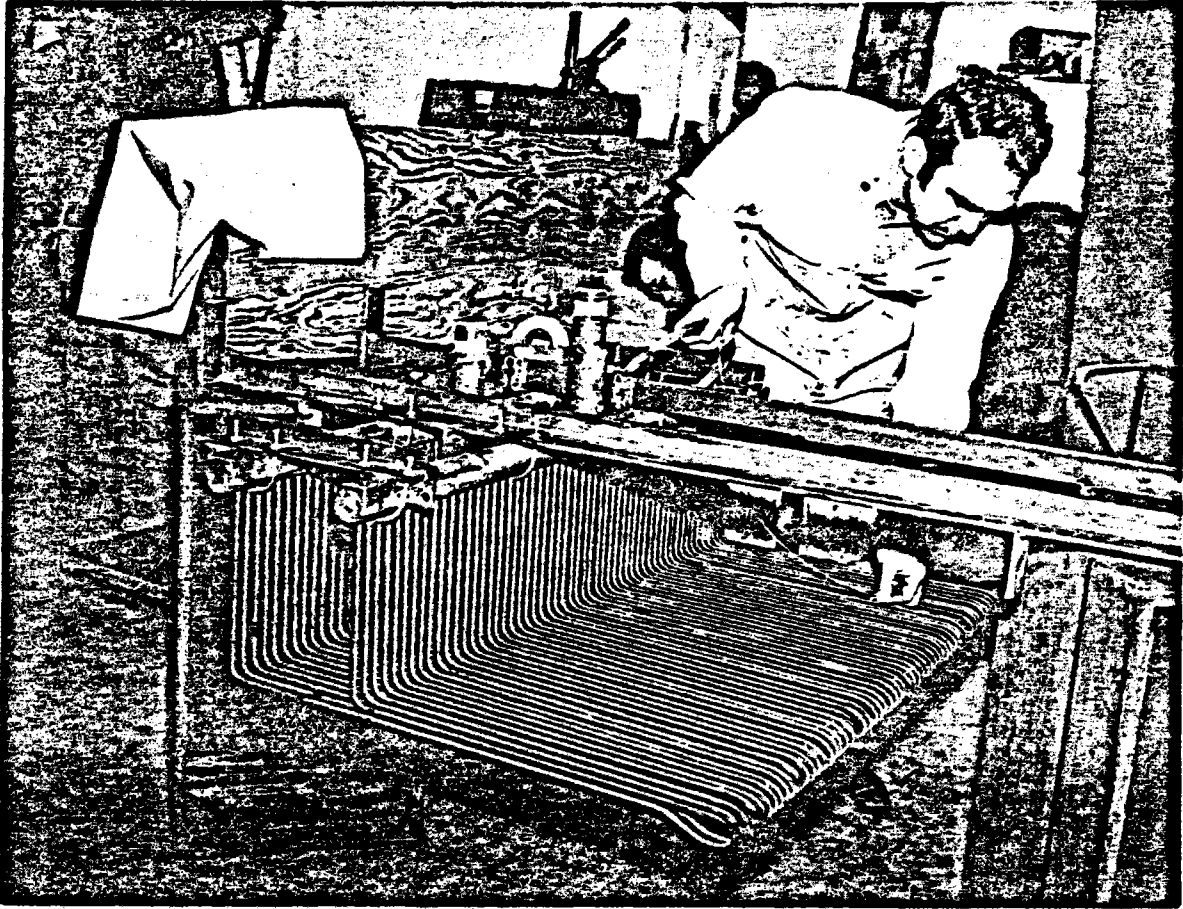


Figure 5.4-3: Installation of Thermocouples on HX Tubing

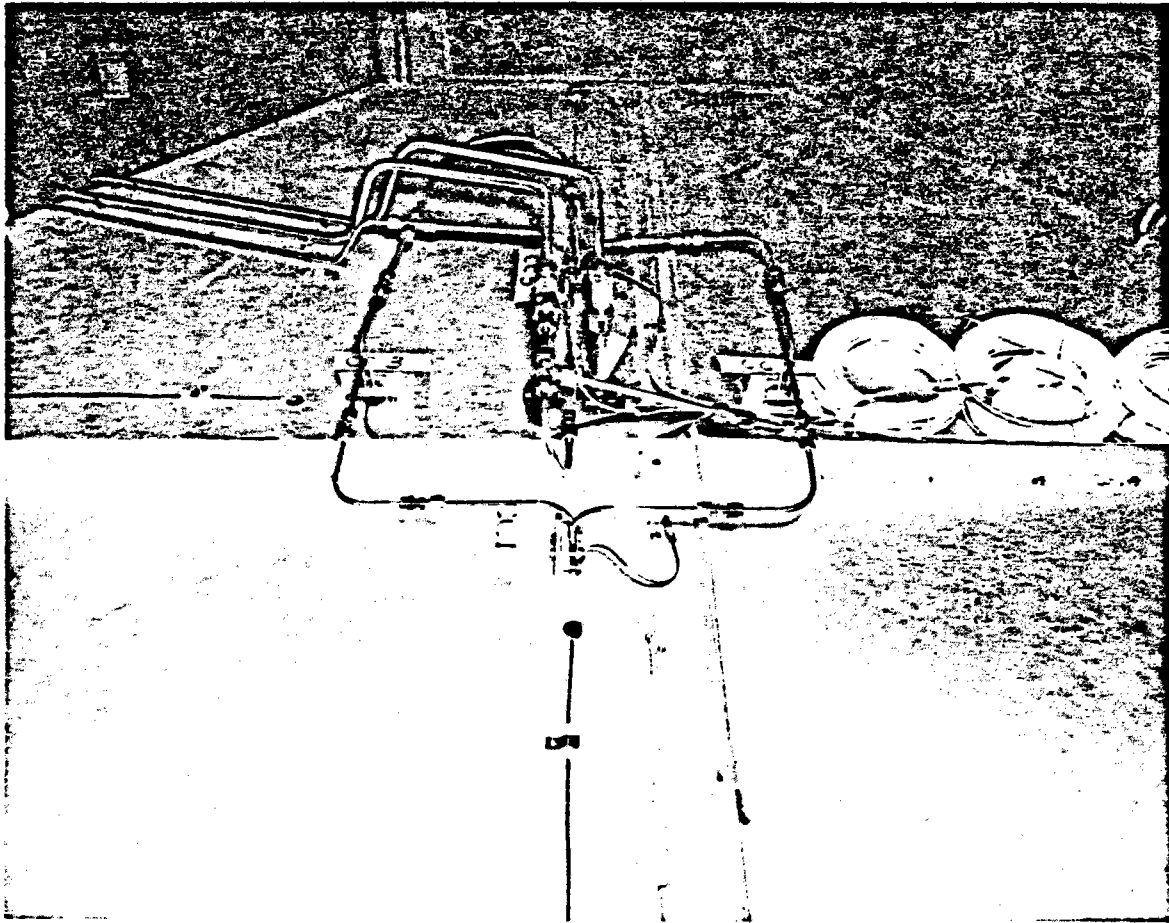


Figure 5.4-4: Calorimeter Coolant Lines on Back Cover

panel had its own flow-control system; thus there were eight of the instruments described above. Fabrication activity consisted of installing and checking the function of each component.

Flow-control valves were clamped between the mating flanges of heat exchanger panel and manifold. The dummy valve insert was removed and the valve and two gasket seals were clamped in place. The valve positioner and position potentiometer were mounted integrally with the valve. A threaded shaft and bellows coupling were added to connect the potentiometer to the valve shaft. A valve assembly is shown in Figure 5.4-5.

The electropneumatic transducers were mounted on the BMSR frame by means of U-bolts provided with the instruments. Figure 5.4-6 shows the arrangement of transducers. Two pressure gages are also visible. One measured test facility air pressure and the other measured control air pressure downstream of the regulator. Tubing runs were formed to fit between the appropriate instruments.

Set-point controllers, circuitry, and switches were mounted in a steel cabinet, shown in Figure 5.4-7. Fabrication and assembly of the control console used standard components and was accomplished by a subcontractor, Certified Electro Manufacturing Company, Seattle, Washington.

Solar testing in Albuquerque revealed several shortcomings in the control and instrumentation systems mounted on the BMSR. All wiring leads should have been encased in steel tubing to protect from overheating. Additionally, the siting of instrumentation and control components on a solar test experiment should be given serious consideration in the design phase to select; (1) the most thermally benign location without compromising function, and (2) a position which permits access for repair or adjustments.

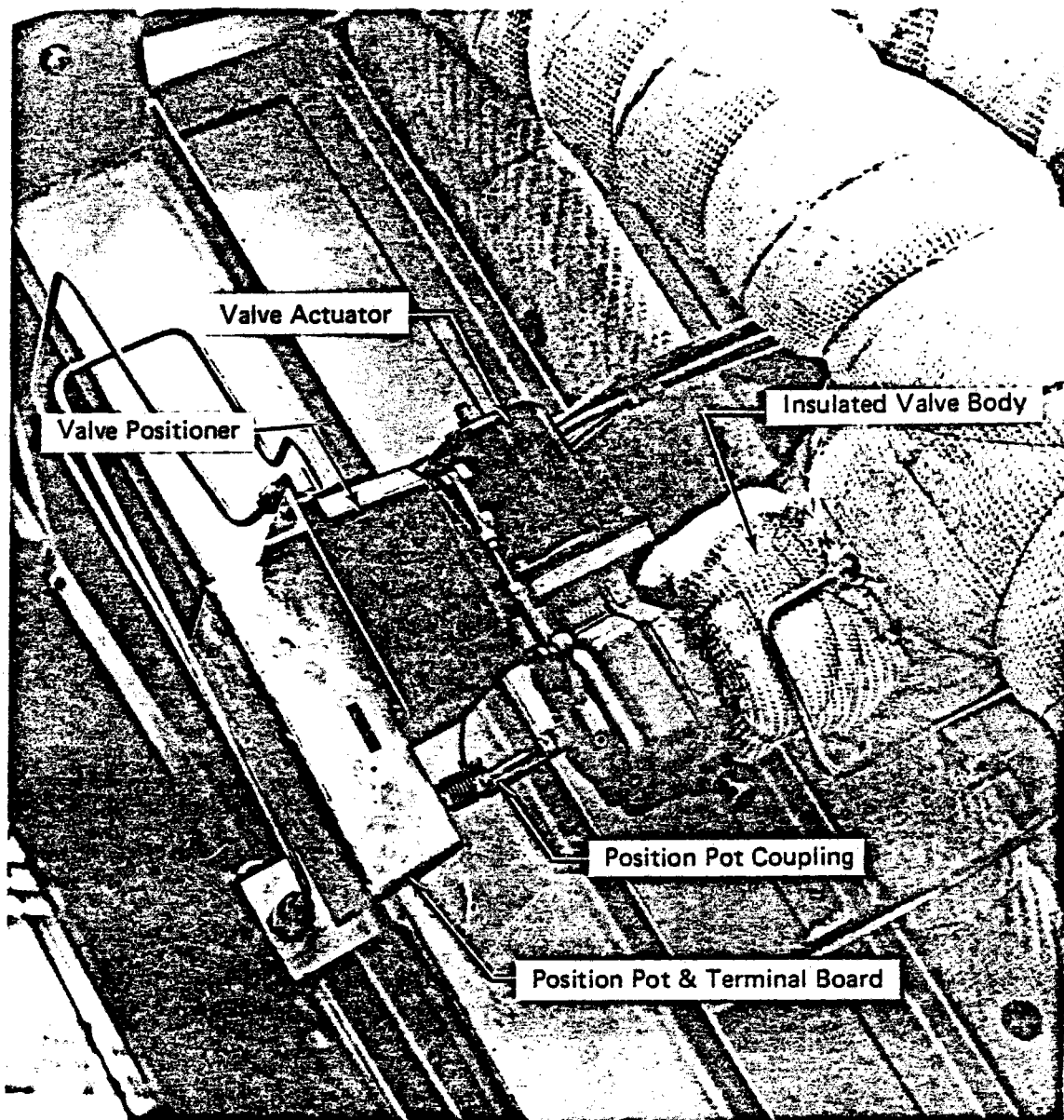


Figure 5.4-5: Flow Control Valve

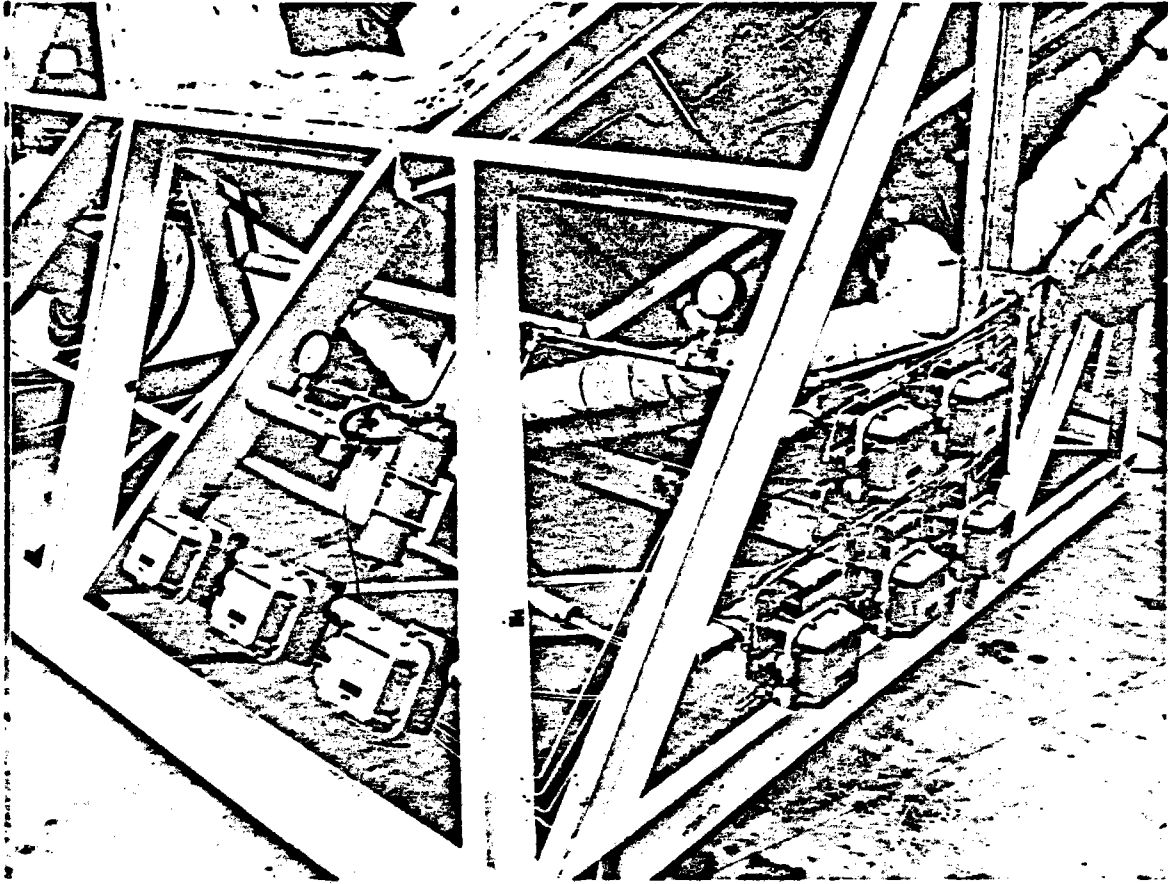


Figure 5.4-6: Control Instrumentation on BMSR Frame

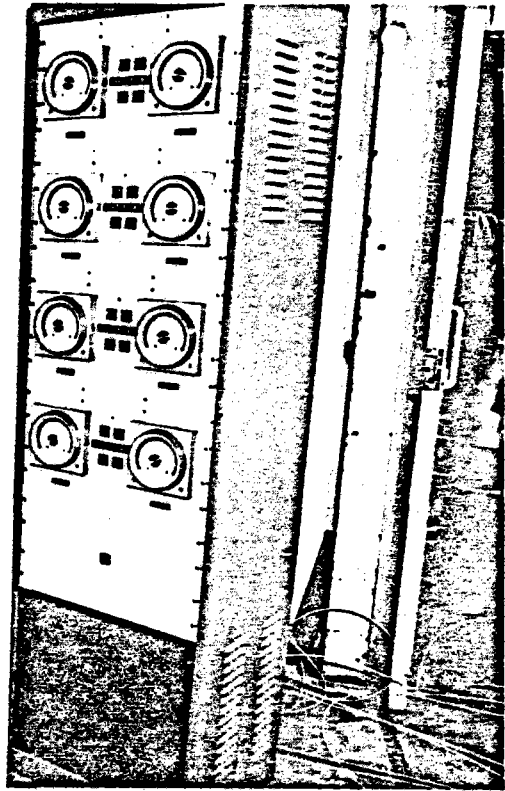


Figure 5.4-7: BMSR Control System Console

## SECTION 6.0

### HOT-FLOW TESTING

A series of hot-flow tests were conducted after the final assembly of the BMSR. They were conducted in Seattle prior to receiver shipment to the CRTF. Test objectives included--

- a. Flow calibration of the eight receiver air valves
- b. Functional testing of instrumentation and controls
- c. Verification of receiver airflows and pressure losses
- d. Measurement of insulation heat losses under controlled environmental conditions
- e. Verification of manifold and heat exchanger support structure for thermal cycling

The hot-flow testing was conducted at the wind tunnel test laboratory of Boeing Commercial Airplane Company. The test setup was completed and initial hot flow testing began on July 10, 1978. Testing was completed in 7 days and the receiver was removed from the test site on July 20, 1978.

During these tests, the receiver was subjected to about 15 hr of cold flow tests and about 18 hr of hot-flow tests. Air temperatures up to 344°C (650°F) were achieved. All the test objectives were accomplished; in addition, valuable experience was gained in the operation of receiver instrumentation and controls. Several minor instrumentation and control problems were discovered and rectified prior to shipment for solar tests.

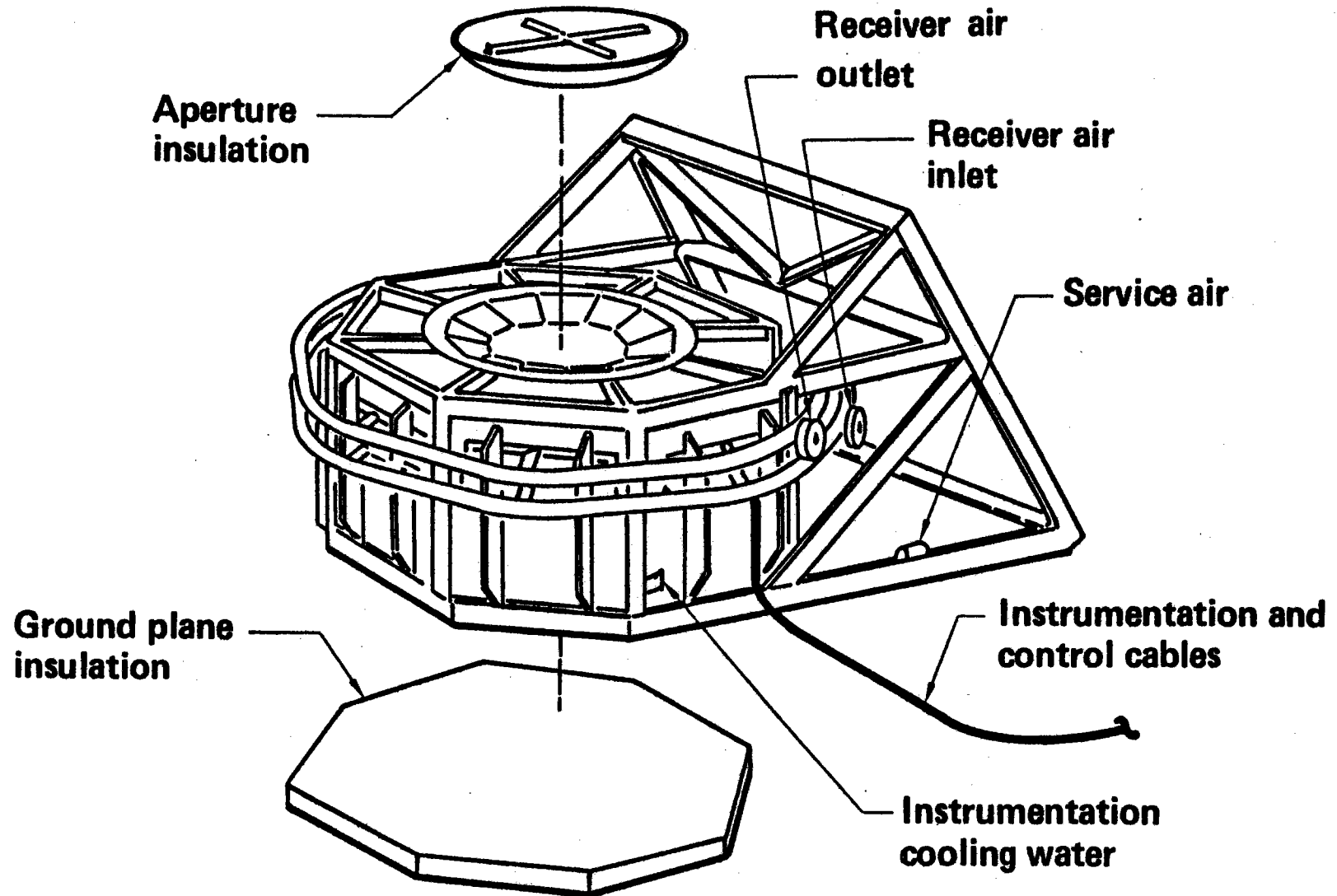
#### 6.1 HOT-FLOW TEST SETUP

##### Receiver

Figure 6.1-1 shows the receiver configuration for these tests. The frame section of the BMSR was installed, aperture side up, on an octagonal ground plane insulation pad. The ground plane insulation consisted of a 0.15 m-thick (6.0 in-thick) layer of mineral wool insulation. The receiver

Figure 6.1-1. Receiver Configuration for Hot Flow Tests

## Receiver Configuration for Hot Flow Tests





aperture was covered during some of the hot-flow tests to reduce heat losses. The cover was insulated and provided a nearly airtight seal. When in place over the receiver aperture, this cover provided effective insulation properties for the rest of the receiver walls.

The test setup included only the main frame of the BMSR. This unit contained airflow manifolds, heat exchangers, flow-control valves, all pressure and valve angle instrumentation, and most of the thermocouples and calorimeters in the solar experiment; it did not include the conical back wall of the receiver. The ground plane insulation functionally simulated the receiver back cone in these tests.

Figure 6.1-2 shows a photograph of the test setup. The receiver can be seen located inside a portable shed that was available at the wind tunnel test site. Piping can be seen that connects the receiver to the facility's 1.10-MPa (160-lb/in<sup>2</sup>g), 344°C (650°F) air supply and to the back-pressure valve and exhaust stack. Two other exhaust stacks can be seen in Figure 6.1-2. The bypass flow exhaust was on the far side of the shed, and for safety purposes, the BMSR burst disk pressure relief was exhausted by the stack on the right side of the shed. Instrument and control cables were routed overhead into the adjacent building where the test data system was located.

#### Test Air Supply

The wind tunnel test laboratory is provided with a regulated 1.10-MPa (160-lb/in<sup>2</sup>g) air supply system that can be routed through a temperature-regulated, gas-fired heater and delivered to the hot-flow test setup at temperatures up to 344°C (650°F). The test setup piping and valves shown schematically in Figure 6.1-3 were used to deliver this air to the receiver. Flow rates of air delivered to the receiver were measured by the venturi flowmeter located in the test air supply line.

#### Instrumentation

A data scanner monitored and recorded up to 40 channels of test data. Power

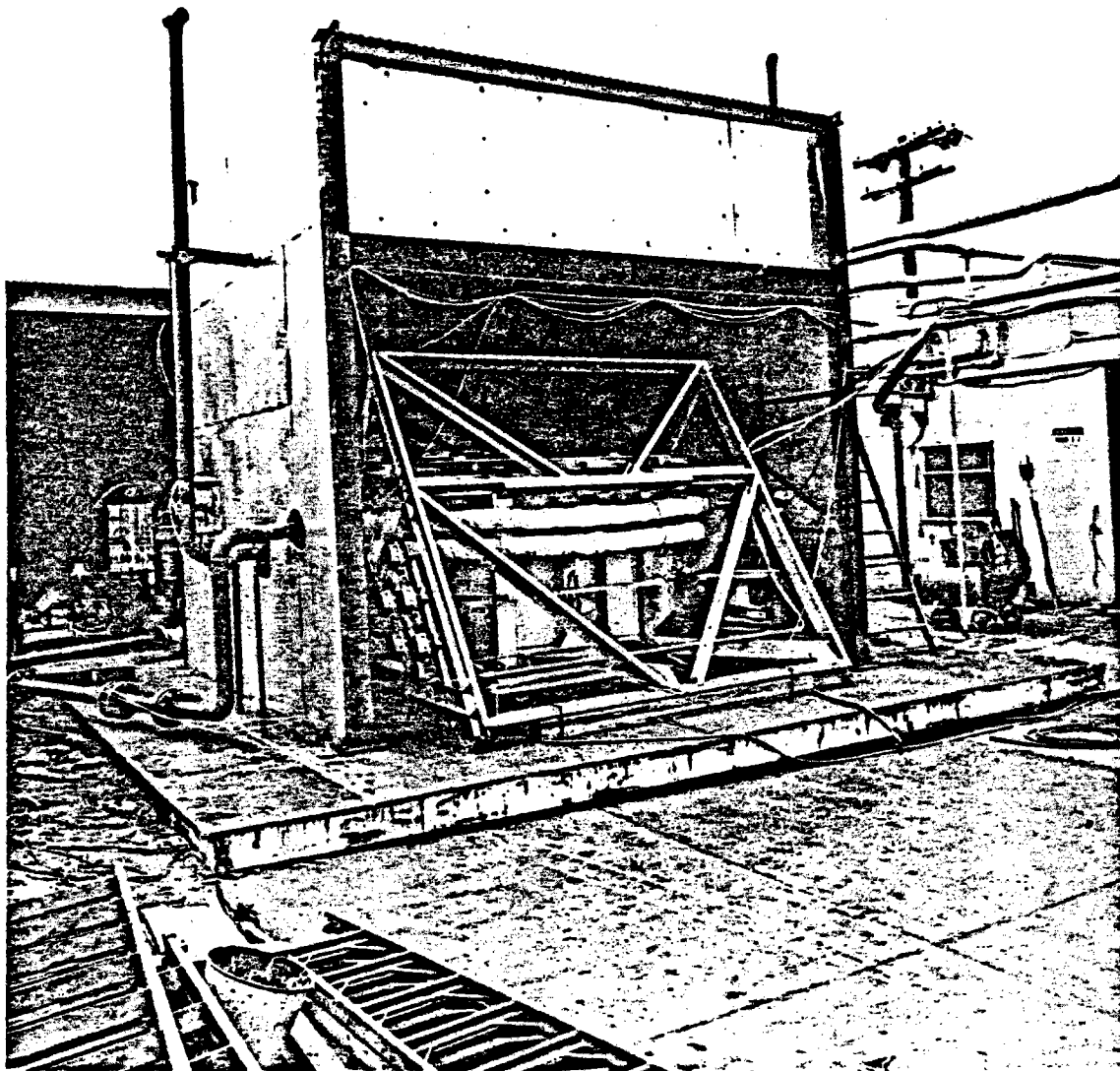
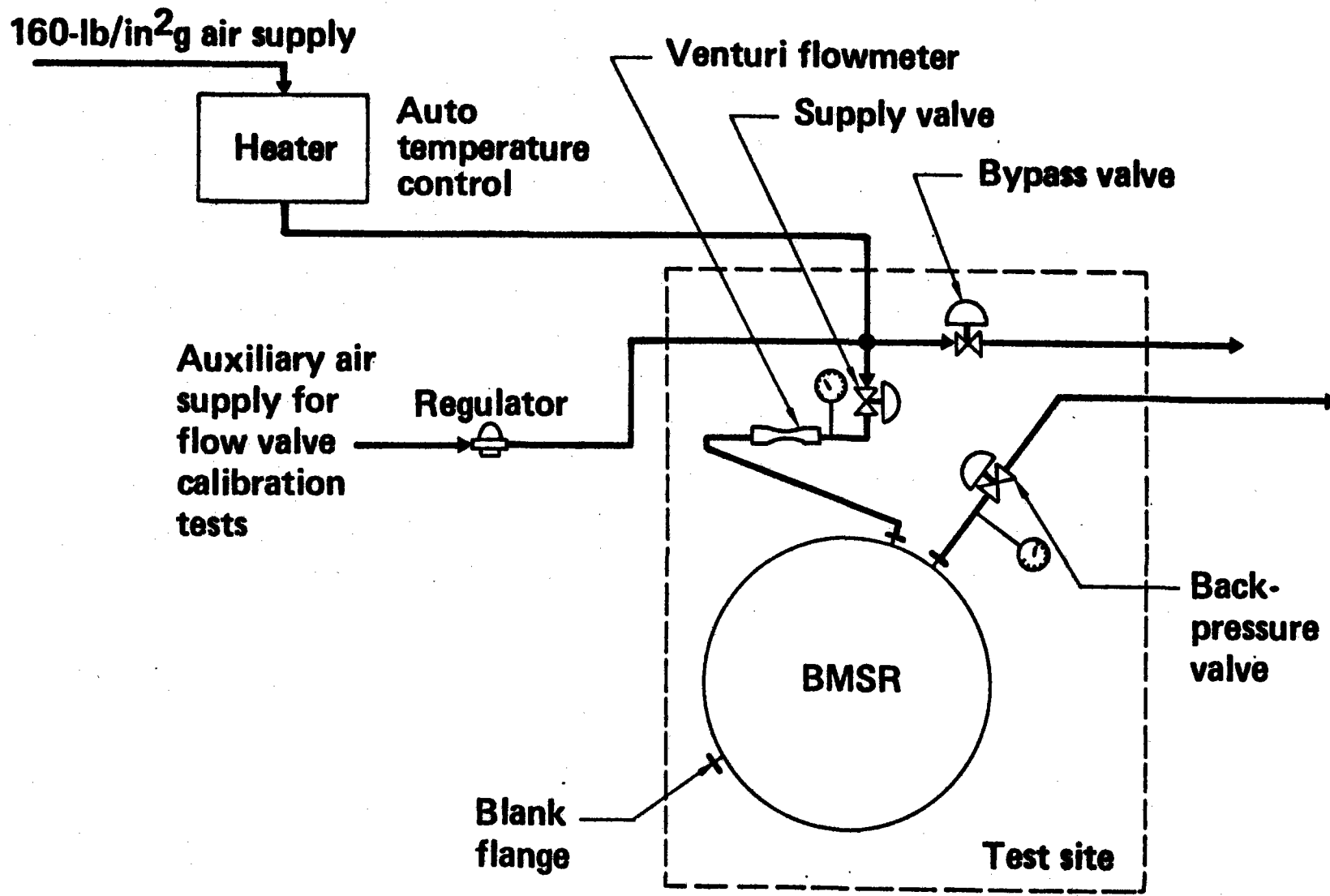


Figure 6.1-2: Hot Flow Test Setup

Figure 6.1-3. Test Gas Supply System  
**Test Gas Supply System**



301

supplies were provided for pressure measurements and pneumatic controls for remote operation of the test setup airflow valves. These controls included provisions for remote operation of the air supply, bypass, and back-pressure valves. The BMSR control console was operational in these tests and provided the means for remote operation and valve angle readout of BMSR control valves. The data channels recorded during each hot-flow test included (1) two BMSR pressure transducers; (2) up to 24 channels of BMSR thermocouples; (3) one channel of voltage readout for valve angle, calorimeter, or other purposes; and (4) test gas supply system data channels for recording mass flow, inlet pressure, and inlet temperature.

In addition, portable equipment was on hand for manual readout of individual thermocouple temperatures, output voltage of calorimeters, and voltages on the BMSR valve angle transducers.

#### Other Facilities

Cooling water was provided for the receiver frame calorimeters. Plant service air was furnished for operation of BMSR flow control valves.

### 6.2 DESCRIPTION OF TESTS

Five types of tests were conducted in this hot-flow test program. These included (1) test system checkout, (2) receiver flow-valve calibration, (3) receiver observation, (4) receiver calibration, and (5) receiver thermal cycling. Pertinent features of these tests are summarized in Table 6.2-1. The purpose, test procedures, and results of each of these tests are described in the following sections.

#### 6.2.1 System Checkout Tests

##### Purpose

The purpose of the system checkout tests was to verify test readiness of the hot-flow test site and BMSR and to conduct an initial hot-flow test that would ensure safety of the facility before allowing personnel access.

Table 6.2-1. Description of Hot Flow Tests

## Description of Hot Flow Tests

	Air inlet		Air flow	Remarks
	Pressure (MPa [lb/in <sup>2</sup> g])	Temperature (°C [°F])	(kg/s [lb/s])	
Receiver valve calibration	Variable 0.52 to 1.07 (60 to 140)	Ambient	Variable 0.10 to 0.68 (0.23 to 1.50)	Six test runs per valve (48 total)
Hot flow test system checkout	0.72 (90)	To 366 (690)	3.0 (6.6)	Initial checkout of hot flow test setup
Hot flow for observation	0.72 (90)	Initiated at 343 (650)	2.1 (4.7)	Receiver flow started with 343°C (650°F) air; observation during quick heatup
Hot flow for calibration	0.72 (90)	To 343 (650)	2.3 to 3.2 (5 to 7)	Heat-soak receiver; verify all instruments, check receiver heat losses
Thermal cycling	0.72 (90)	Cyclic 149 to 316 (300 to 600)	Variable 2.0 to 2.4 (4.5 to 5.3)	Nine cycles completed

## Test Procedures

The aperture insulation cover was removed and the receiver valves were manually positioned at 55 deg. Ambient temperature airflow of about 2.0 kg/s (4.4 lb/s) was initially established through the receiver. Then over about 1 hr, the air supply temperature was increased to its maximum level of about 350°C (662°F). The test was performed at maximum temperature long enough to confirm satisfactory operation of test system and BMSR. Airflow was continued during cooldown.

## Results

Test readiness was verified. Receiver temperatures of about 340°C (644°F) were achieved with no apparent difficulty. A heatup period of about 1 hour was needed, mainly because of thermal capacity of piping from heater to test site.

### 6.2.2 Receiver Flow-Valve Calibration Tests

#### Purpose

Each of the eight receiver flow control valves were calibrated. Flow rate versus valve angle and pressure drop across the valve at six conditions (three positions and two inlet pressures for each position) was measured. A total of 48 data points was obtained.

#### Test Procedure

The valve was manually positioned at a 35, 55, or 70 deg angle. Measured and pressure-regulated ambient temperature airflow through the valve was provided to obtain the desired test conditions. Pertinent data were monitored and recorded.

#### Results

Six calibration data points were measured for each valve. When combined

with theoretical flow versus valve-angle curve, these points showed that the minor adjustment of valve-angle position on the individual valves (corresponding to redefinition of 90-deg valve-angle position) resulted in a nearly perfect match of test data with the theoretical curve. The final match of data for all eight valves is shown in Figure 6.2-1.

### 6.2.3 Receiver Observation Tests

#### Purpose

The purpose of the receiver observation tests was to obtain rapid heatup and cooldown of the receiver. Thermal expansion of heat exchangers and manifolds was observed, freedom of motion of the manifold support structures was verified and the scanning infrared radiometer measured tube temperature variation across a typical heat exchanger.

#### Test Procedure

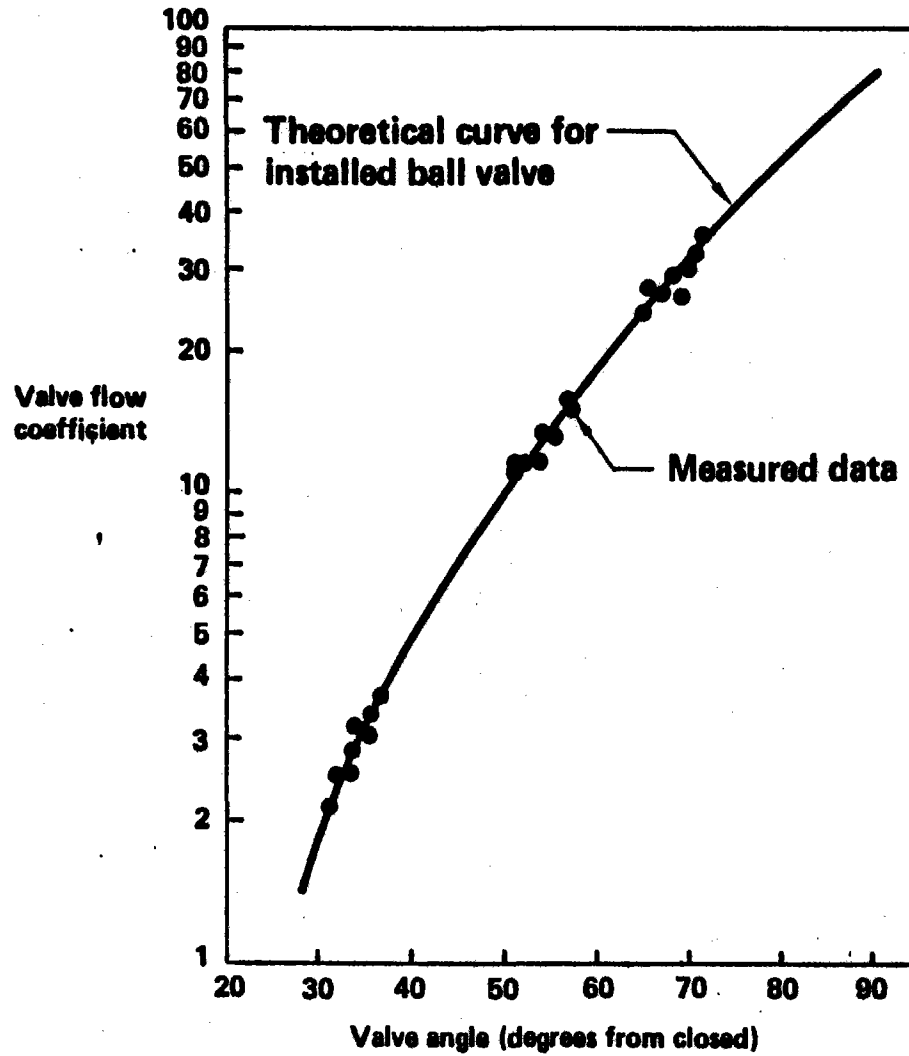
The aperture cover was removed and the manually positioned receiver valves were at an approximate 55-deg angle. Air supply lines were preheated to about 320°C (608°F) by carrying airflow through the receiver bypass. The receiver was rapidly heated by diverting about 2 kg/s (4.4 lb/s) of the high-temperature airflow through it. Effects of thermal shock and the rapid heatup cycle during the transient heatup period were observed and the infrared radiometer was swept across the full width of one heat exchanger panel and then across the outlet end of the panel tubes. The sweep began and ended on both adjacent panels so that the space with no tubes between panels was picked up.

After approximately 1 hr of hot flow, the air temperature was reduced as quickly as possible. Flow continued through the receiver to achieve rapid cooldown. Effects of thermal shock and the rapid cooling cycle were observed.

#### Results

Figure 6.2-1. BMSR Valve Flow Calibration

## BMSR Valve Flow Calibration



Panel No.	Mechanical stop angle (degrees from closed)
1	85.5
2	85.5
3	90.0
4	90.0
5	90.0
6	89.0
7	89.0
8	91.0



These tests verified the ability of heat exchanger and manifold support structure to accommodate thermal growth. Figure 6.2-2 shows one of several infrared radiometer scans that verified balanced airflow through the tubes of a heat exchanger panel.

#### 6.2.4 Receiver Calibration Tests

##### Purpose

The purpose of the receiver calibration tests was to conduct a long-duration, high-temperature heat soak of the receiver. The steady high-temperature condition was used to monitor and record all calorimeter and thermocouple outputs. Cooldown was conducted without airflow to measure receiver thermal insulation performance.

##### Test Procedure

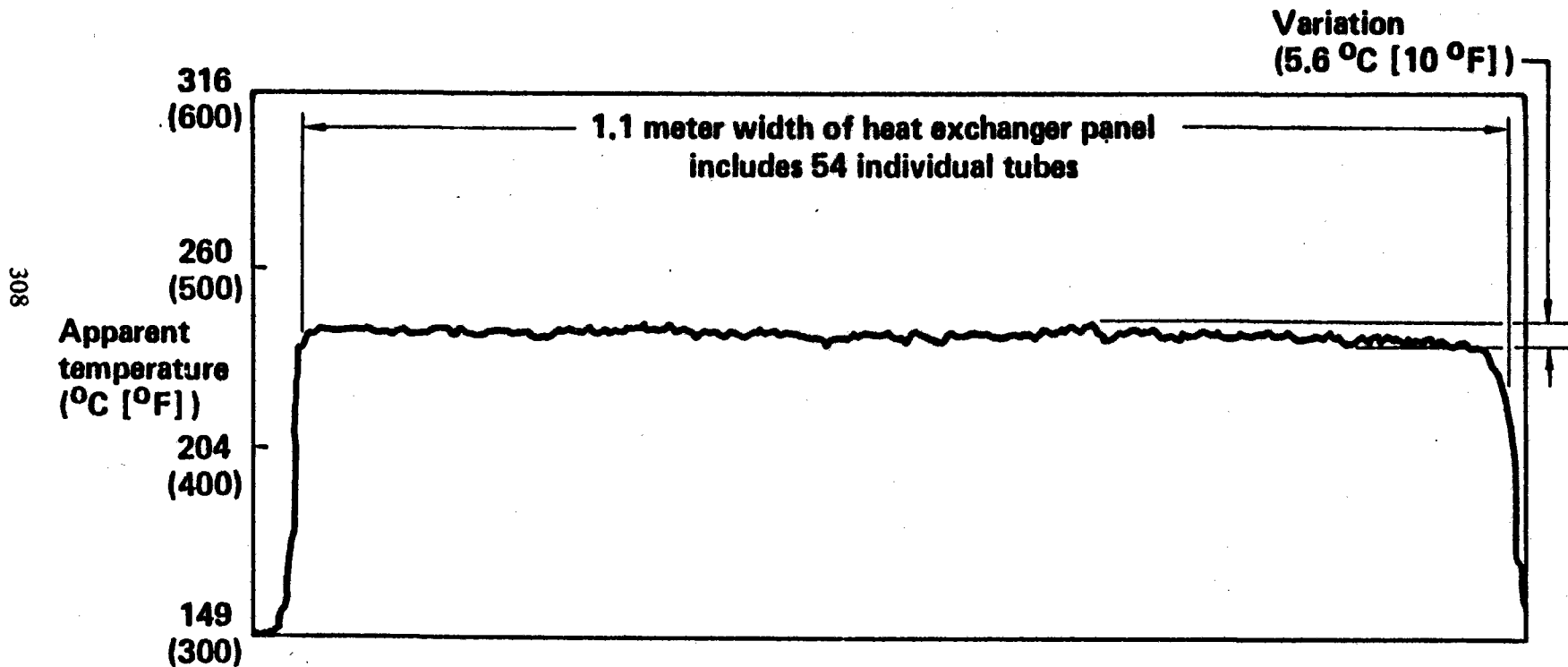
The BMSR aperture cover was installed and receiver flow valves were manually positioned at an approximate 55-deg angle. An airflow of about 2 kg/s (4.4 lb/s) at maximum 344°C (650°F) temperature was used to heat the receiver. Flow conditions were maintained for a period of 5 to 6 hr. After stable temperatures were achieved, all receiver data signals were monitored and recorded. Finally, receiver flow was terminated without lowering air temperature. Temperature during an 8-hr passive cooldown period was monitored and recorded.

##### Results

The receiver was heated to 344°C (650°F) during this test. All thermocouple outputs were measured, compared, and found to be within  $\pm 3^\circ\text{C}$  of expected values. Two mislabeled leads were discovered and corrected. The receiver heat-loss rate was determined to be 7.3 kW with an uncertainty of  $\pm 3$  kW. This was within the expected range of heat losses. Using the total temperature difference across the insulation wall and assuming constant insulation properties, the test data at 344°C (650°F) extrapolated to a heat loss rate of about 20 kW at full receiver-operating temperatures. This test

Figure 6.2-2. Infrared Radiometer Scan of Heat Exchanger Panel No. 4 During Hot Flow Tests

## Infrared Radiometer Scan of Heat Exchanger Panel No. 4 During Hot Flow Tests



- Optical spot size (9.8 cm [3.9 in] dia)
- Individual tube width (0.7 cm [0.28 in])

also verified correct operation of receiver frame calorimeters and the air-pressure transducers.

#### 6.2.5 Receiver Thermal Cycling

##### Purpose

The purpose of receiver thermal cycling was to expose the BMSR to a number of thermal cycles.

##### Test Procedure

The BMSR aperture cover was installed and receiver flow valves were manually positioned at approximately 55 deg. A cold airflow of about 2 kg/s (4.4 lb/s) was established through the receiver. The facility heater was used to cycle air temperatures. Nine thermal cycles of receiver temperatures were conducted from about 150° to 320°C (300° to 600°F) at the maximum rate that could be achieved. After test cycling, a detailed inspection of the receiver was conducted. The receiver was pressurized to 0.69 MPa (100 lb/in<sup>2</sup>g) to verify leaktight integrity.

##### Results

The required thermal cycles and posttest inspection were completed with no problems. The posttest leak check revealed a much higher leakage rate than expected. Subsequent inspection revealed several improperly gasketed flanges on the receiver. They were repaired prior to shipment for solar tests.

#### 6.3 RESULTS AND CONCLUSIONS

These hot-flow tests accomplished a thorough preshipment functional test of the receiver. A large number of low-level concerns were addressed, including operational verification of thermocouples, pressure transducers, and calorimeters. More important functional tests were accomplished on the heated receiver flow valves, including their calibration for flow-rate

measurements during the solar tests. Also, the airflow system, including manifolds, valves, and heat exchangers, was tested to verify pressure-loss performance, equal distribution of airflow across the width of the heat exchanger panels, and the ability of this assembly to accommodate movement because of thermal expansion. Finally, the cavity wall insulation performance was characterized in a way that verified the wall insulation met expectations.

The hot-flow tests were limited because of schedule pressure and the air-temperature capability of the test facility. As a result, they did not relieve all concerns as to the functional acceptability of the BMSR. Because of the apparent high quality of selected instrumentation sensors and the attention paid to details of the receiver flow system and manifold support structure design, these tests were without any dramatic results. However, the hot-flow test is recommended as an important final step in the process of receiver fabrication. Significant benefits can be derived from the most simple flow testing at ambient temperature.

**GAS COOLED CENTRAL RECEIVER -  
CLOSED CYCLE 1Mwt BENCH MODEL TESTING**

**RP377-3  
FINAL REPORT**

**Volume: II**

**June 5, 1980**

**Prepared for  
Electric Power Research Institute  
3412 Hillview Avenue  
Palo Alto, California 94304**

**by  
Boeing Engineering and Construction Company  
P.O. Box 3707  
Seattle, Washington 98124**

**LEGAL NOTICE**

**This report was prepared by Boeing Engineering and Construction, as an account of work sponsored by the Electric Power Research Institute, Inc. (EPRI). Neither EPRI, members of EPRI, Boeing, nor any person acting on behalf of either: (a) makes any warranty or representation, express or implied with respect to the accuracy, completeness, or usefulness of the information contained in this report, or that the use of any information, apparatus, method, or process disclosed in this report may not infringe privately owned rights; or (b) assumes any liabilities with respect to the use, or for damages resulting from the use of, any information, apparatus, method, or process disclosed in this report.**

## SECTION 7.0

### DESCRIPTION OF THE SOLAR TEST PROGRAM

#### 7.1 TEST PLAN

##### 7.1.1 Test Planning Objectives

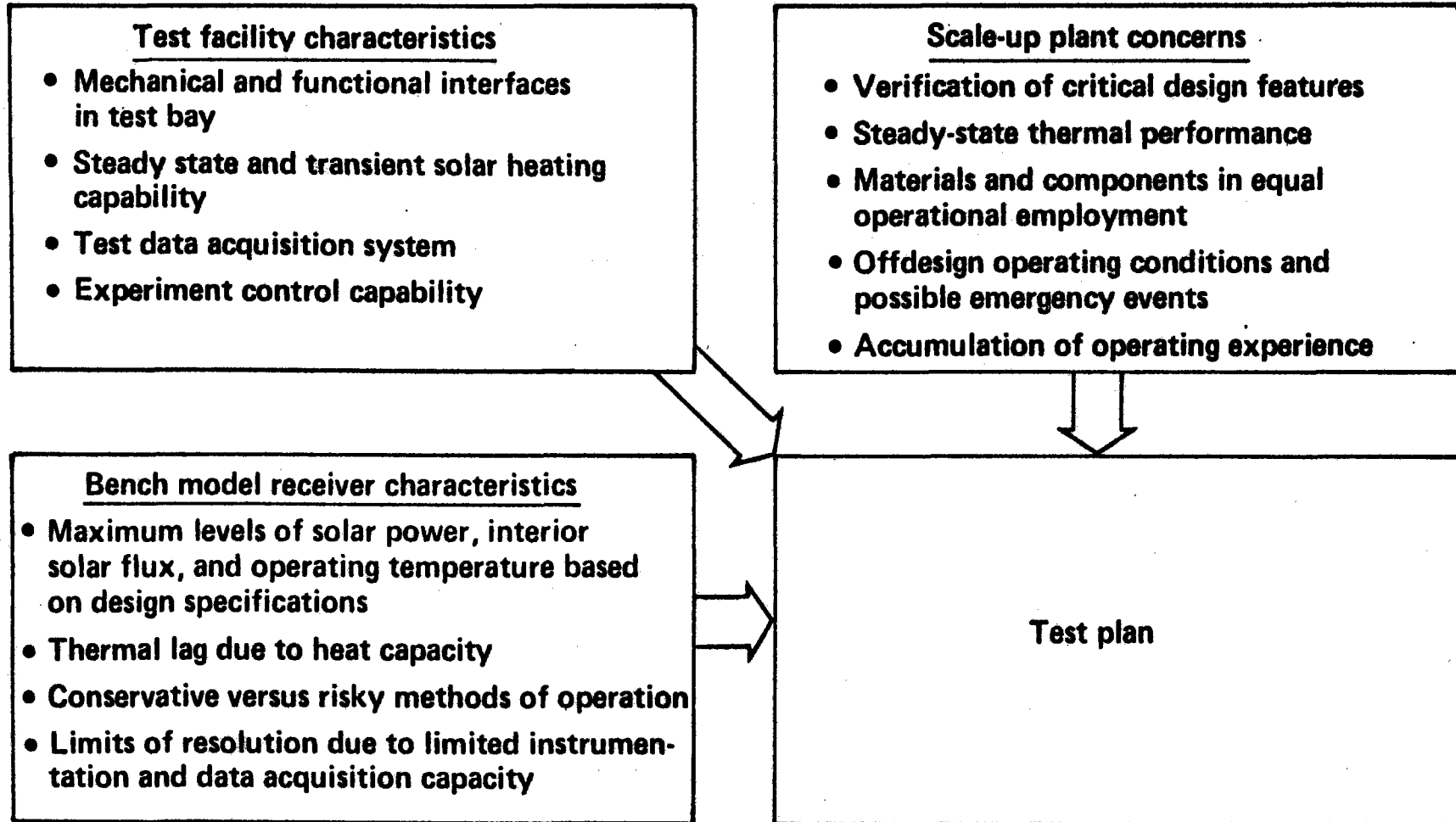
As discussed in Section 3.1, the bench model solar receiver (BMSR) used materials and design concepts that were expected to be used in the larger experimental solar power systems as well as in commercial receivers. The solar test planning goal was to formulate a series of tests where results could be used to verify these material selections and design concepts. Figure 7.1-1 describes the three sources of information considered in the formulation of a solar test plan.

Because the BMSR test program was only one step in the commercial powerplant development schedule, it had to address the most important risks and concerns of the follow-on experimental plant, pilot plant, and commercial power plant systems. Receiver operating conditions during tests needed to closely approximate those expected to be encountered in the scaled-up solar receivers. In addition to verifying performance and design features, it was important to include solar tests that investigated receiver responses to off-design operating conditions and emergency events. Importance was placed on the accumulation of operating experience under conditions as similar as possible to those expected in scaled-up solar powerplants.

Even though the BMSR was designed to reproduce operating conditions, temperatures, and heat fluxes in a commercial receiver, for test planning purposes consideration was given to the BMSR as a self-sufficient design. The BMSR had safe limits of operation that were not necessarily equal to those envisioned for the commercial receiver. Because of the transition from a surround collector field design concept (RP377-1) to the north field test site, the BMSR exhibited some operating characteristics that were not typical of the commercial receiver. These included more highly concentrated first-incident solar flux on cavity walls as well as relatively higher

Figure 7.1-1. Test Planning Considerations

## Test Planning Considerations



cavity heat losses by circulating air through the receiver aperture. Because of its scale-model design, the BMSR exhibited transient thermal response characteristics that were similar to the commercial receiver. However, the CRTF collector field covered only a fraction of the ground area of a commercial-size collector field. This meant that moving clouds obscured the test collector field quicker than the larger commercial-size collector field. As a result, the BMSR could be subjected to operating heat load transients more severe than those expected in the commercial powerplant. Transient heat loads expected during obscuration of the commercial powerplant collectors by moving clouds were determined analytically and simulated by controlled removal and addition of the test heliostats.

Finally, the solar test facility imposed physical and operational constraints on the solar receiver and the testing program. The most important facility limitations are listed in Figure 7.1-1. Aside from the obvious compromises needed to accommodate the north field collector system, the CRTF did not unduly limit any of the BMSR test objectives.

#### 7.1.2 Specific Test Plans

A test plan was developed with all the above considerations and objectives in mind. The plan included seven different types of tests as well as standardized plans for starting up and shutting down the receiver. These plans were applicable to all the tests.

Fact sheets were prepared that described each of the planned tests. These fact sheets summarized the purpose, methods of receiver operation, planned levels of solar input, receiver operating temperature, and expected results of the tests. The fact sheets are listed in Table 7.1-1, and presented in Figures 7.1-2 through 7.1-10. Individual test plans are discussed in the following sections.

##### Receiver Startup

The standard receiver startup procedure is described in Figure 7.1-2.



*Table 7.1-1. Fact Sheet Summary*  
**Fact Sheet Summary**

<b>Figure</b>	<b>Test plan</b>	<b>Number of tests included in plan</b>
<b>7.1-2</b>	<b>Receiver startup</b>	<b>Standard each test</b>
<b>7.1-3</b>	<b>Equilibrium heat balance (EB)</b>	<b>9</b>
<b>7.1-4</b>	<b>Nonuniform input (NI)</b>	<b>3</b>
<b>7.1-5</b>	<b>Transient heat load (TH)</b>	<b>4</b>
<b>7.1-6</b>	<b>Restricted coolant flow (RF)</b>	<b>3</b>
<b>7.1-7</b>	<b>Cold startup (CS)</b>	<b>3</b>
<b>7.1-8</b>	<b>Emergency cooldown (EC)</b>	<b>3</b>
<b>7.1-9</b>	<b>Solar load following (SF)</b>	<b>4</b>
<b>7.1-10</b>	<b>Receiver shutdown</b>	<b>Standard each test</b>

**Total number of tests**

**29**

*Figure 7.1-2. Fact Sheet—Receiver Startup*

## **Fact Sheet—Receiver Startup**

**Standard procedure starting each test, except SF and CS:**

- Step 1**
- Maximum airflow
  - BMSR pressure drop established
  - Compressor operation verified
- Step 2**
- Outlet temperature control setpoints at  $-18^{\circ}\text{C}$  ( $0^{\circ}\text{F}$ )
  - Solar input increased at  $0.5 \text{ kW/s}$  to desired test condition
  - Receiver inlet temperature increased to desired test level
- Step 3**
- Outlet temperature control setpoints changed to desired test condition
  - Outlet temperatures trimmed  $\pm 5^{\circ}\text{C}$  ( $9^{\circ}\text{F}$ )
- Step 4.**
- Quasi-equilibrium (state QE)
  - Receiver efficiency changing less than 2% per hour
  - Proceed to test

## Figure 7.1-3. Fact Sheet—Equilibrium Heat Balance Tests

- Purpose:** To obtain steady-state thermal equilibrium and determine—
- Operating temperatures
  - Heat balance and efficiency
- Initial condition:** QE state at desired gas temperature and solar power level
- Test duration:** Until receiver thermal efficiency changes at a rate less than 1% per hour
- Test results:** Receiver thermal characteristics over its full range of steady-state operating levels

Average gas temperature* °C (°F)	Solar heat input (kW)		
	500	750	1,000
482 (900)	EB-1	EB-4	EB-7
579 (1,075)	EB-2	EB-5	EB-8
677 (1,250)	EB-3	EB-6	EB-9

\*Temperature increase 278°C (500°F)

Figure 7.1-4. Fact Sheet—Nonuniform Solar Input Tests

## Fact Sheet—Nonuniform Solar Input Tests

- Purpose:** Effects of severe unbalanced solar input
- Operating temperatures
  - Efficiency
- Initial condition:** QE state, 500-kW solar, gas temperature
- Testing condition:** Transition to 500-kW solar from east heliostats only
- Test duration:** Thermal efficiency changing less than 1% per hour
- Test results:** Offdesign performance

Average gas temperature\*,  
°C (°F)

Solar heat input (kW)	482 (900)	579 (1,075)	677 (1,250)
500	NI-1	NI-2	NI-3

\*Temperature increase 278°C (500°F)

Figure 7.1-5. Fact Sheet—Transient Heat Load Tests

## Fact Sheet—Transient Heat Load Tests

- Purpose:** Determine limits, transient solar input
- Thermal lag and overshoot
  - Flow control system performance
- Initial condition:** QE state, temperatures, 1,000-kW input
- Decreasing:**
- Reduce solar input to 400 kW at planned rate of change
  - Maintain conditions until thermal efficiency changes less than 2% per hour
- Increasing:**
- Increase solar input to 1,000 kW at planned rate of change
  - Maintain conditions until thermal efficiency changes less than 2% per hour

Average gas temperature, °C (°F)	Rate of change of solar heat* input, kW/s	
	1.00	2.00
579 (1,075)	TH-1	TH-2
677 (1,250)	TH-3	TH-4

\*Normal rate 0.5 kW/s

Figure 7.1-6. Fact Sheet—Restricted Coolant Flow Tests

## Fact Sheet—Restricted Coolant Flow Tests

- Purpose:** Simulate loss of gas flow, single panel
- Initial condition:** QE state, solar power, temperatures
- Testing condition:** Controlled temperature increase, panel 3 (rate: 140°C/h (250°F/h) in 28°C steps)
- Test duration:** Until—
- Tubing temperature reaches 980°C (1,800°F)
  - Panel 3 flow at minimum
  - Maximum flow on other panels
- Test results:** Offdesign performance

Average gas temperature\* in undisturbed panels, °C (°F)

	Solar heat input (kW)		
	500	750	1,000
677 (1,250)	RF-1	RF-2	RF-3

\*Temperature increase 278°C (500°F)

Figure 7.1-7. Fact Sheet—Cold Startup Tests

## Fact Sheet—Cold Startup Tests

- Purpose:** Demonstrate capability of receiver to withstand the thermal transients generated by instantaneous exposure to 500-, 750-, and 1,000-kW solar input
- Initial condition:** Ambient temperature airflow through the receiver
- Test duration:** Until—
- Average gas temperature is attained (see table below)
  - Receiver temperatures change less than 5°C per hour
- Test results:** Satisfactory performance of the receiver subsequent to the startup. No degradation of materials or structure due to high temperature differentials.

320

Average gas temperature

	480°C (900°F)	580°C (1,075°F)	675°C (1,250°F)
Solar input	500 kW CS-1		
		750 kW CS-2	
			1,000 kW CS-3

*Figure 7.1-8. Emergency Cooldown Tests*

## **Emergency Cooldown Tests**

- Purpose:** Return receiver to ambient conditions from abnormal condition without damage to the receiver
- Initial conditions:**
- **EC-1:** Remove solar input and increase airflow to the maximum
  - **EC-2:** Remove solar input and shut off air supply
  - **EC-3:** Increase solar input to 1.5 MW with constant maximum airflow and then remove the solar input and reduce airflow to the minimum input
- Test duration:** Until the maximum temperature of all thermocouples on the receiver is below 400°C (750°F)
- Test results:** Receiver structural and thermal integrity not materially degraded by exposure to the abnormal conditions



## Fact Sheet—Solar Load-Following Tests

<b>Purpose:</b>	<b>Simulate daily operation with varying degrees of cloud cover</b>
<b>Initial condition (before dawn):</b>	<b>Heliostats on line for 1,000-kW maximum input; air supply system ready</b>
<b>Startup (at dawn):</b>	<b>Complete the startup procedure</b>
<b>Operation:</b>	<b>Automatic airflow control by the receiver</b>
<b>Test duration:</b>	<b>Terminate test at sunset when air outlet temperature drops below the control set point</b>
<b>Test results:</b>	<b>Satisfactory receiver operation under typical atmospheric environmental conditions</b>
<b>Note:</b>	<b>These tests are planned to be conducted in real time under actual atmospheric conditions that meet the requirements. However, should the required atmospheric conditions not occur during a reasonable period of time, cloud cover and overcast conditions will be simulated by manipulation of the collector field.</b>

*Figure 7.1-10. Fact Sheet—Receiver Shutdown*

## **Fact Sheet—Receiver Shutdown**

**Purpose:**

**Standard procedure for normally ceasing test operations, except for the solar-following (SF) test**

**Procedure:**

- **Reduce solar input at rate of 0.5 kW/s**
- **When receiver inlet temperature drops below desired level for test, reduce outlet temperature control setpoints to  $-18^{\circ}\text{C}$  ( $0^{\circ}\text{F}$ )**
- **Maintain airflow through the receiver until maximum temperature is less than  $400^{\circ}\text{C}$  ( $750^{\circ}\text{F}$ ), then secure**
- **Discontinue data recording**

During the first two steps of the startup procedure, the full flow of the air supply system was allowed to pass through the receiver. This configuration was verified prior to initiation of solar heating. A high airflow was maintained throughout the time that the solar input was gradually increased to the desired testing level. The temperature of receiver inlet air increased during this period as solar heat became available to preheat the supply air. The high airflow rate through the receiver ensured that the receiver inlet-to-outlet temperature increase was always less than 278°C (500°F) during this time.

Once the solar power and receiver inlet air temperature reached the desired conditions for test, the outlet temperature controllers for the eight receiver heat exchangers were activated. This was accomplished by increasing their temperature setpoints to the particular receiver outlet temperature desired for the test. The controllers operated heat exchanger airflow control valves and modulated the receiver airflow as necessary to achieve the desired temperature.

Startup was initially defined to be complete when the receiver thermal efficiency became stable within a rate of change of 2% per hour. During tests it was not possible to accurately assess the thermal efficiency to verify this rate of change. Therefore, the receiver startup was assumed to be complete as soon as the eight heat exchangers were all on automatic control.

#### Equilibrium Heat Balance (EB)

A series of nine EB tests were planned to obtain steady-state thermal equilibrium conditions in the receiver and to determine receiver operating temperatures and thermal efficiency. The thermal efficiency of interest for the receiver portion of a solar-thermal powerplant consisted of the heat transferred to the circulating air as it passed through the receiver and divided by the solar power that entered the receiver aperture.

The nine different EB test conditions of interest are described in Figure 7.1-3. In addition to determining thermal efficiency, a secondary reason

for obtaining data over a wide range of solar input power and circulating air temperatures was to characterize receiver heat losses, as shown in Figure 7.1-11. This additional evaluation of the EB test data was expected to improve the level of understanding of the receiver heat loss mechanisms. Receiver wall insulation temperatures could be used to analytically determine wall heat losses during each test. Then the solar reflection heat loss could be extracted from the data by assuming that it was a constant fraction of the solar input power. Finally, by evaluating data at various operating temperatures, the radiant and convective heat loss mechanisms were separated according to their different exponential dependence on operating temperatures.

Initially, these EB tests were to be conducted at constant solar input. However, during the tests it was difficult to maintain steady solar input conditions for more than a few minutes. Continuous adjustments of the number of collectors on line were required to maintain relatively constant solar input to the receiver. As a result, the EB test conditions in the data were all characterized by 1 to 2 hr of operation at constant outlet temperature and similar but variable solar input. Then, the particular time for data evaluation was determined by a detailed examination of test data (Section 9.0).

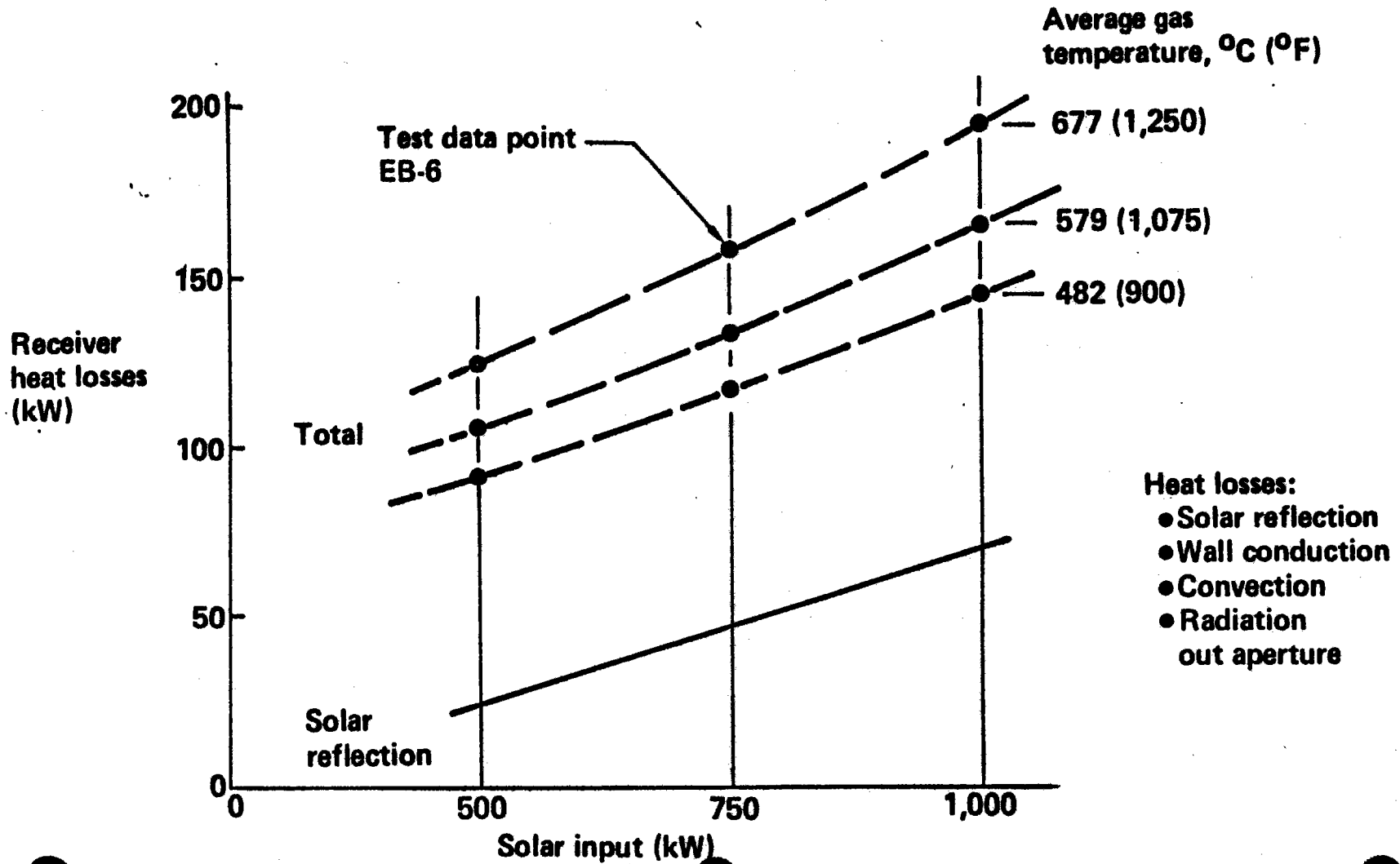
#### Nonuniform Input (NI)

The nonuniform input test plans are summarized in Figure 7.1-4. A series of three tests investigated the effects of unbalanced solar input from the collector field. All three tests started with a uniform distribution of heliostats throughout the CRTF collector field. However, only about half the available collectors were used. Then, after reaching stable operating conditions in the receiver, the heliostats on the west side of the collector field were taken off target. Equal numbers of eastside collectors were brought on target during this time to maintain a nearly constant solar input to the receiver.

The three NI tests used similar operation of the collector field. The three different receiver operating temperatures used for the EB tests were also

Figure 7.1-11. Typical Results Expected From EB Test Series

## Typical Results Expected from EB Test Series



used here.

The purpose of the NI testing was to demonstrate the capability of the BMSR to accommodate off-design collector field performance. The reflective redistribution of solar input to the receiver, which provided nearly equal heat exchanger heat loads during normal operating conditions, received its most severe test during these conditions. The verification of reflective redistribution in the receiver cavity provided a solid basis for similar design concepts in larger commercial receiver configurations.

#### Transient Heat Load (TH)

Transient heat load testing of the BMSR determined the effects of rapidly changing solar input power on the receiver flow control system and temperatures. Two conditions were of particular interest, both of which were induced by the receiver's design concept of self-regulation of airflow to obtain desired outlet temperatures. The control system had to have enough time to remain stable during steady-state operation at power. However, this stability could not be gained if the system could not accommodate realistic short-term transient events. Thermal lag and overshoot occurred if the airflow controls were slow to respond to changes of solar input power. In addition, the operating receiver was expected to exhibit internal temperature gradients of several hundred degrees during normal full-power operation. The rapid reduction of receiver airflow expected during rapid solar power reductions reduced the capability of the circulating air to control heat exchanger tube temperatures. A short-term increase of heat exchanger tube temperatures was expected during rapid reductions of solar input power.

The transient heat load test exposed the BMSR to solar input variations typical of pilot plant and commercial-size powerplants. Because of the thermal-scale-model qualities of the BMSR design, the temperature excursions that occurred in these tests were at least as severe as those expected in the scaled-up solar receivers.

Four transient heat load tests were planned. They are described in Figure

7.1-5. Test conditions included rates of change of solar input that were equivalent to a 2 m/s (6.6 ft/s) rate of cloud shadow progression over a large (1 km [0.6 mi]) field of collectors, or a somewhat higher rate of shadowing of a smaller pilot plant collector field. The test plans incorporated initial tests at reduced receiver temperature to provide significant temperature margins in the BMSR during its first exposures to these transient heat loads.

#### Restricted Coolant Flow (RF)

The purpose of the restricted coolant flow testing was to simulate the effects of airflow loss in one of the eight BMSR heat exchangers. This is an off-design condition that is very likely to occur during the operational lifetime of a commercial or pilot plant receiver.

During normal operation, the receiver temperature levels were limited and controlled by the high rate of solar heat removed by the circulating air. Margins were built into the BMSR heat transfer and airflow design to allow maintenance of this required airflow and solar heat removal with only seven of the eight receiver heat exchangers in operation. This principle of design provided for continued control of receiver operating temperatures. As a result, the heat exchanger with reduced airflow was subjected to a limited temperature increase over normal operation. This increase was the difference between normal heat exchanger operating temperature and the effective receiver cavity temperature, an increase of about 125°C (225°F) at full-power conditions. The metal heat exchangers were expected to survive short-term exposure to these higher-than-normal temperatures.

Three of the restricted flow tests were included in the BMSR test plan. Test parameters are described in Figure 7.1-6. The initial tests at lower solar power levels provided results that were evaluated before exposing the receiver to increasingly severe off-design conditions.

Because of the mechanical limit stops used to prevent full closure of the receiver flow control valves, the airflow through the restricted heat exchanger could not be completely turned off. Therefore, test data were

collected at a number of operating conditions with increasing amounts of flow restriction. These data can be extrapolated, as shown in figure 7.1-12, to determine the heat exchanger temperature with no airflow.

#### Cold Startup Tests (CS)

The standard method of receiver startup included a very conservative 0.5 kW/s rate of solar power increase. It also included a conservative mode of initial receiver operation with full airflow and the smallest possible temperature difference between inlet and outlet air. Cold startup tests verified acceptable receiver operation under startup conditions that were typical of the pilot plant and commercial powerplant receivers.

Three different tests were planned with increasing solar input power levels and increasing receiver operating temperatures. Figure 7.1-7 shows the power and temperature levels for these tests. In each test, the facility solar collectors were brought on target at once rather than one at a time.

#### Emergency Cooldown (EC)

The standard procedure for shutting down the receiver included a very conservative 0.5 kW/s rate of solar power removal. It also provided for maintenance of high airflow rates through the receiver during the cooling period. Emergency cooldown tests exposed the BMSR to shutdown procedures more typical of the normal operation of pilot plant and commercial receivers. In addition, tests were planned that investigated the effects of emergency shutdown of these plants from a full-power operating state.

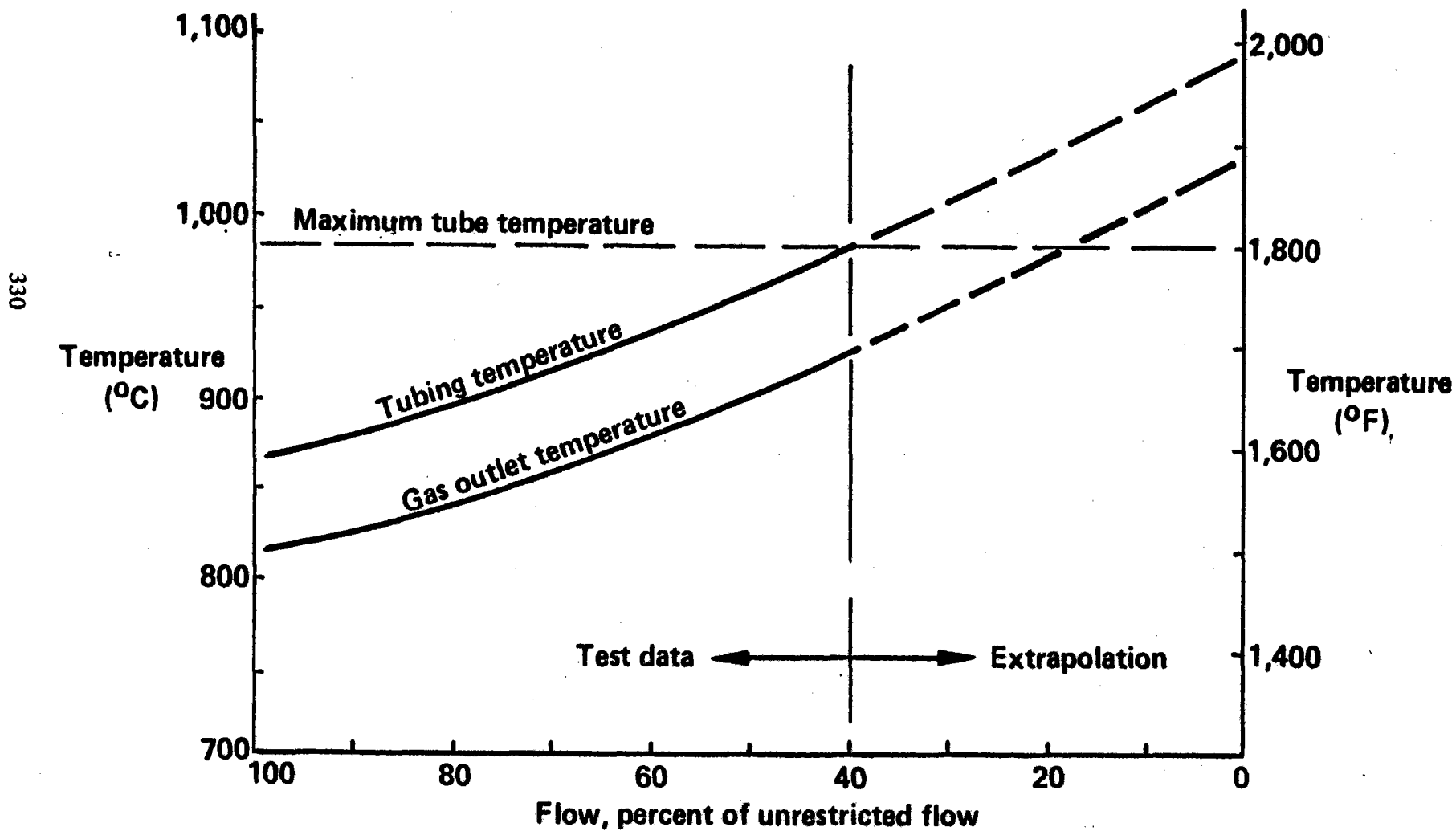
Each of the emergency cooldown tests was a continuation of a corresponding cold startup test. The three EC tests incorporated the solar power and operating temperatures as shown in Figure 7.1-8. All three of the tests incorporated solar heat removal as rapidly as could be accomplished by the test facility. Each of the EC test plans included a different plan for control of the receiver air flow during cooldown.

Test EC-1 at low temperature and solar power also utilized the most



Figure 7.1-12. Planned Extrapolation of Restricted Flow Test Data

## Planned Extrapolation of Restricted Flow Test Data



conservative plan for receiver airflow control during cooldown. Here, the receiver airflow was increased to a maximum rate as soon as possible after terminating the solar heating.

Test EC-3 used reduced airflow rates during cooldown. Rather than fully opening the receiver flow control valves, as in EC-1 and normal BMSR shutdown, the valves were allowed to close down to their minimum opening angles defined by mechanical limit stops. With these valves at minimum opening angles, the airflow through the receiver was 20% to 30% of the EC-1 airflow. The plans to increase the receiver solar input to 1.5Mwt for this test were discarded because the test facility was unable to provide this input.

Finally, test EC-3 incorporated simultaneous shutdown of both the solar input to the receiver and its air supply. The test simulated a failure of the airflow system or piping in the pilot plant or commercial powerplant. Higher-than-normal heat exchanger temperatures were expected to occur during this emergency shutdown condition. Without internal airflow, the heat exchanger tubes were quickly subjected to the residual heat in the cavity wall insulation. In the worst instance, tube temperatures could have approached the levels predicted by extrapolation of the restricted flow test results to zero flow.

#### Solar Load Following (SF)

Four days of tests were planned to include continuous receiver operation at or near its design point condition, 1 Mwt solar input and 816°C (1500°F) outlet air temperature. The test plans are summarized in Figure 7.1-9. The main purpose of these tests was to accumulate operating time at receiver design conditions. A secondary objective was to obtain operational experience with environmental effects such as scattered cloudiness and wind that were expected to influence the performance of the scaled-up solar receivers. These effects were expected to produce marginally acceptable operating conditions in the solar power systems. The test plans were not specific but assumed that the receiver and test facility operators would take all precautions to ensure the safety of the test and make every effort

to continue operating and learning about the system response to off-design conditions.

In the absence of suitable off-design environmental conditions during solar load following the tests plans called for the collector field to be operated to produce the effects of clouds.

### Receiver Shutdown

The standard plan for receiver shutdown is described in Figure 7.1-10. The important features of this test plan were the conservative methods of operation of the collector field and the receiver airflow during cooldown. The gradual reduction of solar input, 0.5 kW/s, reduced the risk of damage to insulation and solar shielding materials because of rapid cooling. The high airflow through the receiver quickly lowered the heat exchanger temperatures while minimizing thermal gradients in the heat exchangers, manifolds, and air supply piping.

## 7.2 REQUIREMENTS OF EXPERIMENTERS

During the early stages of test planning, the Central Receiver Test Facility (CRTF) was identified as the preferred location for conducting BMSR tests. This Department of Energy Facility is operated by the Sandia Laboratories and is located on Kirtland Air Force Base, near Albuquerque, New Mexico.

Initial discussions with test site personnel resulted in the preparation of the BMSR solar test plan (Section 7.1). During this process, the Sandia personnel were provided with information to assess the feasibility of the experiment. Once the planned experiment was determined to be acceptable by Sandia, the experimenter was asked to prepare a test proposal that described the objective, test setup, and duration of the solar test program, along with financial assistance that may be required.

The BMSR experiment proposal was approved by Sandia Laboratories and the Department of Energy. DOE also authorized funds and other resources to be expended by Sandia Laboratories in the execution of the BMSR test plan.

The requirements of experiments accepted for tests at the CRTF are described in Reference 3, the Central Receiver Test Facility Experimenters Manual. This consists of a series of documents prepared by the experimenter and submitted to Sandia Laboratories. The schedule for these submittals was synchronized with the date of arrival of the experiment on site and its removal date. Table 7.2-1 lists these documents and shows the required submittal schedule. Contents of the documents are summarized in the following paragraphs.

The data package and test plan were required 90 days before arrival of the experiment. The data package included drawings and sketches of the experiment; engineering analyses demonstrating its integrity; descriptions of utility interfaces and thermal shielding requirements; a comprehensive experimenter's safety analysis; and general descriptive operating procedures for the experiment. The test plan included a description of the desired sets of conditions to be obtained during tests including such variables as solar-flux distributions, flow rates, and temperatures; the complete sequence of activities on site including all events necessary to implement, conduct, and dispose of the experiment; a description of the data acquisition display and control needs of the experiment, including data and control channel interfaces and display requirements; and a listing of the special needs from other CRTF systems such as heat rejection or meteorological data. Data package compliance was accomplished by the preparation and delivery of document D277-10068-1, "Data Package, 1Mwt BMSR" and several sets of receiver drawings to CRTF along with reports in letter format that presented results of the various engineering and safety analyses. A Boeing document was also prepared and published pursuant to the CRTF test plan schedule. This document, D277-10069-1 "Test Plan, 1Mwt BMSR", described the test plans in about the same degree of detail as Section 7.1. It described the instrumentation system channel by channel, including transducer wiring schematics and calibration data. Experiment data displays required for BMSR operation and control were defined and described as in Section 7.3.3.

There were four additional experimenter inputs to Sandia Laboratories that were scheduled to precede the experiment onsite by 60 days. These included

Table 7.2-1. Requirements for Experimenters

Table 7.2-1. Requirements for Experimenters

Experimenter input to STTF (CRTF)	Chapter reference	Minimum lead time prior to receipt of experiment at STTF (CRTF)
1. Discussions with STTF (CRTF) staff	II, C	—
2. Data package and codes and standards input	IV, A and B	90 days
3. Test plan	IV, C	90 days
4. Installation, QA, and checkout procedures	IV, D, 1	60 days
5. Operating procedures	IV, D, 2	60 days
6. Maintenance procedures	IV, D, 3	60 days
7. Operator training input	IV, D, 4	60 days
8. QA records, reports, and as-built drawings	II, C and IV, E	30 days
9. Unpacking and receiving inspection	IV, D, 5	15 days
10. Manufacturer's drawings, literature, and manuals	IV, D, 6	With hardware
11. Experiment removal and handling	IV, D, 7	60 days prior to removal

installation, operation, and maintenance procedures for the experiment and operator training input. The most important of these inputs were the procedures for conduct of the individual solar tests. A third Boeing document was published pursuant to these requirements. This was document D277-10070-1, "Test Procedure, 1Mwt Bench Model Solar Receiver."

The test procedure document described a step-by-step sequence of events developed for the execution of each of the planned tests. During this process, the physical and operational interfaces with the test facility became increasingly well defined. The necessity of verifying test system status by reference to prepared checklists became apparent as well as the need to standardize procedures as much as possible from day to day. To ensure coordinated operation of the experiment and the test facility, it was necessary to include procedural signoffs by both the experimenter and the CRTF test engineer at certain critical stages of the test operations.

A typical test procedure is duplicated in Figure 7.2-1. This shows the 17 procedural steps employed during normal receiver startup. All of the steps were initialed upon completion by the experimenter. Those that required test system cognizance were also initialed by the CRTF test engineer.

Additional experimenter requirements included submitting updated descriptions of the as-built solar receiver and the experiment receiving and removal instructions. These required inputs were transmitted by hand or letter. Because these inputs documented procedural activities, they did not constitute the major engineering effort required to prepare test plans and procedures.

An additional important experimenter requirement became apparent after arrival of the BMSR at CRTF. The CRTF operating procedures called for publication of an integrated test procedure (ITP) prior to the initiation of any solar test. Because it was not described in the experimenters manual and it played such an important role in the pretest preparations, it is described here in Section 7.4.

Figure 7.2-1. Typical BMSR Test Procedure—Normal Startup

## Typical BMSR Test Procedure—Normal Startup

Step	Procedure	TE	EXP
<ol style="list-style-type: none"> <li>1.</li> <li>2.</li> <li>3.</li> <li>4.</li> <li>5.</li> </ol>	<p><b>Activate DACS per STTF procedures.</b></p> <p><b>Input the following settings to the DACS computer:</b></p> <ol style="list-style-type: none"> <li>a. Command the 10 experiment controllers to use their local setpoint.</li> <li>b. Insert remote (computer) setpoint values for the 10 experiment controllers into the DACS computer memory. Use the desired values for this day's test.</li> </ol> <p><b>Turn on and verify house air supply at experiment. The high-pressure actuator "muscle" air should be 90 to 110 lb/in<sup>2</sup>g. Control air should be regulated to 20 lb/in<sup>2</sup>g. Check each at both the receiver and the air supply equipment skid.</b></p> <p><b>Turn on the 10 experiment controllers. Position pushbutton controls to enable local or remote operation at the command of DACS computer. Position the local setpoint dials as follows:</b></p> <ol style="list-style-type: none"> <li>a. Eight receiver controller setpoints at 0°F</li> <li>b. Air supply temperature TA1 setpoint at 0°F</li> <li>c. Air supply back-pressure setpoint PA2 at 0 lb/in<sup>2</sup>g (0 on 100% scale for 0 to 150 lb/in<sup>2</sup>g)</li> </ol> <p><b>Verify DACS output by inspection of displays.</b></p> <ol style="list-style-type: none"> <li>a. Setpoint status should be on local. Setpoint valves should be correct for this day's test.</li> <li>b. Receiver valves should be at about 90 deg. Bypass valve VA1 should be in the full bypass position to pass air around the recuperator. The back-pressure valve should be open.</li> <li>c. Pressure channels should read 0 ±0.5 lb/in<sup>2</sup>. If not, the transducer zero bias should be checked by measuring at the tower DACS, and the revised value inserted in the DACS computer program.</li> </ol>		
Run	Experimenter (EXP)      Boeing      Date	Test engineer (TE)	STTF      Date

Figure 7.2-1. Typical BMSR Test Procedure—Normal Startup (Continued)

## Typical BMSR Test Procedure—Normal Startup (Continued)

Step	Procedure	TE	EXP
<p>6.</p> <p>7.</p> <p>8.</p> <p>9.</p> <p>10.</p>	<p>d. Temperatures should be near the ambient temperature in the test bay.                      e. Heat fluxes should be near zero.</p> <p>Command the 10 experiment controllers to the remote setpoint while observing motion of valves via DACS display.</p> <p>a. Receiver valves should close to about 35 deg.                      b. Recuperator bypass valve should move to full recuperator flow position.                      c. Back-pressure valve should close.                      d. Remote setpoint should be indicated at the controllers and the color graphics display.</p> <p>Return the receiver controls (eight) to local setpoint function, and verify opening of receiver valves.</p> <p>When RTAF chiller is started, check flow of coolant through BMSR instruments by observing discharge from BMSR coolant return hose.</p> <p>Verify operation of emergency shutdown data channels, DPM, and T1-19 through T8-19. Use input from tower data system to activate automatic shutdown on DPM and one of the TX-19 thermocouple channels.</p> <p>Note: With no flow, DPM is out of limits at less than 30 lb/in<sup>2</sup>. Automatic shutdown should follow activation of alarm.</p> <p>Start compressors, referring to section 5.1.1 of the compressor operation and maintenance manual (ref. 2.4). As compressors are brought on line, their output flow passes directly through the experiment. The back-pressure controller PA2, using the back-pressure valve, will maintain the system back pressure at the value that was given to the DACS computer as the remote setpoint, step 2 above.</p>		
Run	Experimenter (EXP)      Boeing      Date	Test engineer (TE)	STTF    Date



Figure 7.2-1. Typical BMSR Test Procedure—Normal Startup (Concluded)

## Typical BMSR Test Procedure—Normal Startup (Concluded)

Step	Procedure	TE	EXP			
	<p>Monitor and verify operation of valves and control during air compressor startup. Note stability of back-pressure level and valve angle. Note hydrocarbon detector reading. Quantity of compressors to be determined for each day of tests.</p> <p style="text-align: center;">_____</p> <p style="text-align: center;">Compressors on line</p>					
11.	Remove environmental curtain from the test bay door.					
12.	Minimum pretest airflow rate to be determined for each day's test.					
	<p style="text-align: center;">_____</p> <p style="text-align: center;">Initial airflow rate</p>					
13.	Verify DPM in excess of 30 lb/in <sup>2</sup> and activate emergency shutdown system.					
14.	Activate the collector field. Move a sufficient number of collectors to standby to meet the requirements of the daily test file for this day's test.					
	<p style="text-align: center;">_____</p> <p style="text-align: center;">Quantity of collectors on line</p>					
15.	Switch collectors to Sun tracking to provide the desired solar input to receiver. The collectors shall be brought on line one at a time such that the average rate of change will not exceed 0.5 kW/s.					
16.	After the air supply outlet air temperature reaches desired test inlet temperature and the recuperator bypass valve (VA1) begins to open, switch to remote setpoint control on receiver valves.					
17.	Trim outlet temperatures to ±9°F of desired condition as required. When a quasi-equilibrium (QE) state is attained, start the specific test.					
Run	Experimenter (EXP)	Boeing	Date	Test engineer (TE)	STTF	Date

### 7.3 TEST SETUP

The test setup at CRTF included components provided by Boeing under contract to EPRI; several CRTF subsystems, including the collector field, data acquisition and control system, and the central receiver tower; and a variety of additional instruments and equipment provided by Sandia Laboratories. These elements of the test setup are listed in Table 7.3-1. Three persons were required to operate the test system and conduct the tests: The experimenter, responsible for the BMSR and its air supply equipment skid; the CRTF console operator, responsible for the collector field; and the CRTF test engineer, responsible for operation of the remainder of the test system. During tests these persons were stationed in the CRTF control building. The test equipment was operated remotely by means of computer data links and displays. Test operators were also in radio communication with test support personnel stationed in the collector field and in the CRTF tower.

As noted in Table 7.3-1, EPRI/Boeing provided the set of four diesel-powered compressors that supplied high-pressure air, the receiver heat transfer medium. Also provided was the air supply equipment skid used to preheat the high pressure air to the desired receiver inlet temperature during tests. Sandia Laboratories provided the remainder of the test setup. The CRTF tower subsystem housed the BMSR and provided protection from the elements as well as utility services needed for electrical and pneumatic operation of the receiver and air supply skid. Most of the electrical wiring and piping required for the test setup were available as part of the test support systems built into the tower. The collector field subsystem provided solar input to the receiver during tests. As many as 118 of the 210 heliostats in the CRTF collector field were used during BMSR tests. The CRTF data acquisition and control system (DACS) stored and displayed about 200 channels of BMSR and air supply skid data during the tests. This system also provided the control channels needed for remote operation of the receiver from the CRTF control building. The real-time aperture flux (RTAF) system provided measurements of the solar-flux incident on the receiver during tests and provided approximate measurements of the receiver solar input. The CRTF heat rejection system (HRS), a water-glycol cooling loop

*Table 7.3-1. Elements of the Test Setup*  
**Elements of the Test Setup**

<b>Element</b>	<b>Supplied by</b>	<b>Operated by</b>
<b>Solar collector field</b>	<b>CRTF</b>	<b>CRTF console operator</b>
<b>Bench model solar receiver</b>	<b>Boeing/EPRI</b>	<b>Boeing experimenter</b>
<b>Air supply equipment skid</b>		
<b>Air supply compressors</b>		
<b>Real-time aperture flux system</b>	<b>CRTF</b>	<b>CRTF test engineer</b>
<b>Receiver tower and test bay</b>		
<b>Water-glycol cooling system</b>		
<b>Data acquisition and control system</b>		
<b>Additional equipment</b>		
<ul style="list-style-type: none"> <li>● Panalarm system</li> <li>● Short-wave radio network</li> <li>● Metrology tower</li> <li>● Eppley pyrhelimeter</li> <li>● Barnes infrared radiometer</li> </ul>		

that was piped throughout the CRTF tower, provided coolant for the diesel-powered air compressors and for the solar-heated frame of the RTAF, as well as some of the BMSR instrumentation.

Section 7.3.1 describes the solar heating components of the test setup, including the collector subsystem and the RTAF. Section 7.3.2 describes the receiver airflow circuit and Section 7.3.3 describes the CRTF data acquisition and control system.

### 7.3.1 Receiver Solar Input

#### CRTF Collector Field

The CRTF collector field and tower are shown in Figure 7.3-1. The BMSR can be seen in the 43m (140 ft) level test bay of the tower. This test bay was designed to accommodate receivers up to 1Mwt in size. Those receivers that required only a part of the 5Mwt collector field capacity utilized the 78 heliostats in Zone A, nearest to the base of the tower. Heliostats not required for a test remained in their downward-facing stored position. All the heliostats are north field (i.e., the tower is on the south edge of the collector field).

The CRTF heliostat design is shown in Figure 7.3-2. Each heliostat had 25 separate mirror facets with a total reflective area of  $37 \text{ m}^2$  ( $400 \text{ ft}^2$ ). The mirror facets were curved and individually adjustable to reduce the size of the heliostat solar image. The individual mirror facets were supported near their edges and pulled inward at the center to make them concave. As facets were mounted on the heliostat structural frame, they were aligned to provide optimum focusing. Also, the facet alignment could be changed to provide an optimum collector field image at each of the alternative test sites on the tower. During BMSR tests, the Zone A heliostats were aligned to provide an optimum focus on the 43m (140 ft) level test bay at noon on an equinox day. The remainder of the heliostats, Zone B, were aligned for an optimum focus at the tower top test site. As a result, when targeted on the BMSR, their images were significantly larger than the Zone A heliostat images.

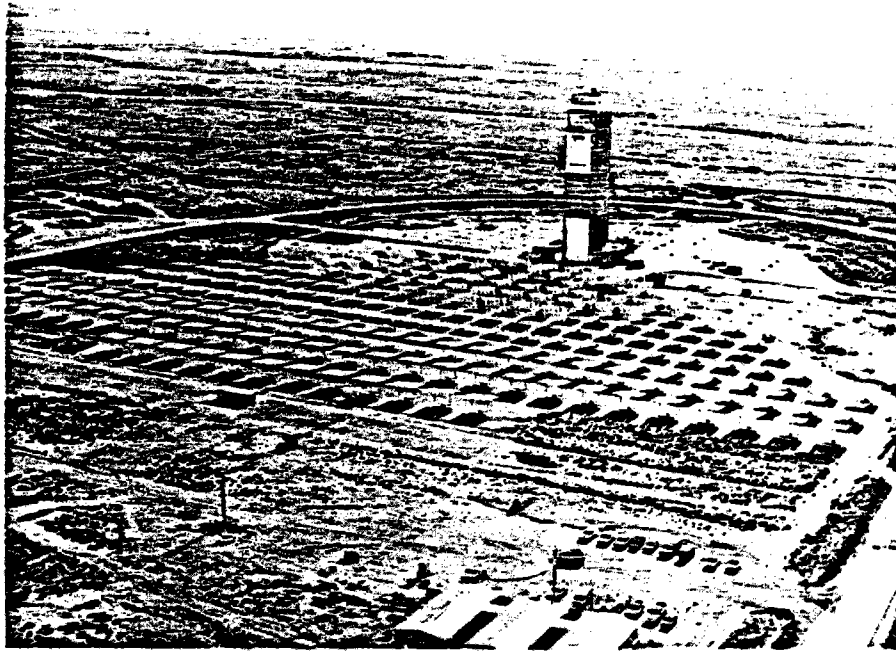


**Figure 7.3-1: CRTF Collector Field and Tower**

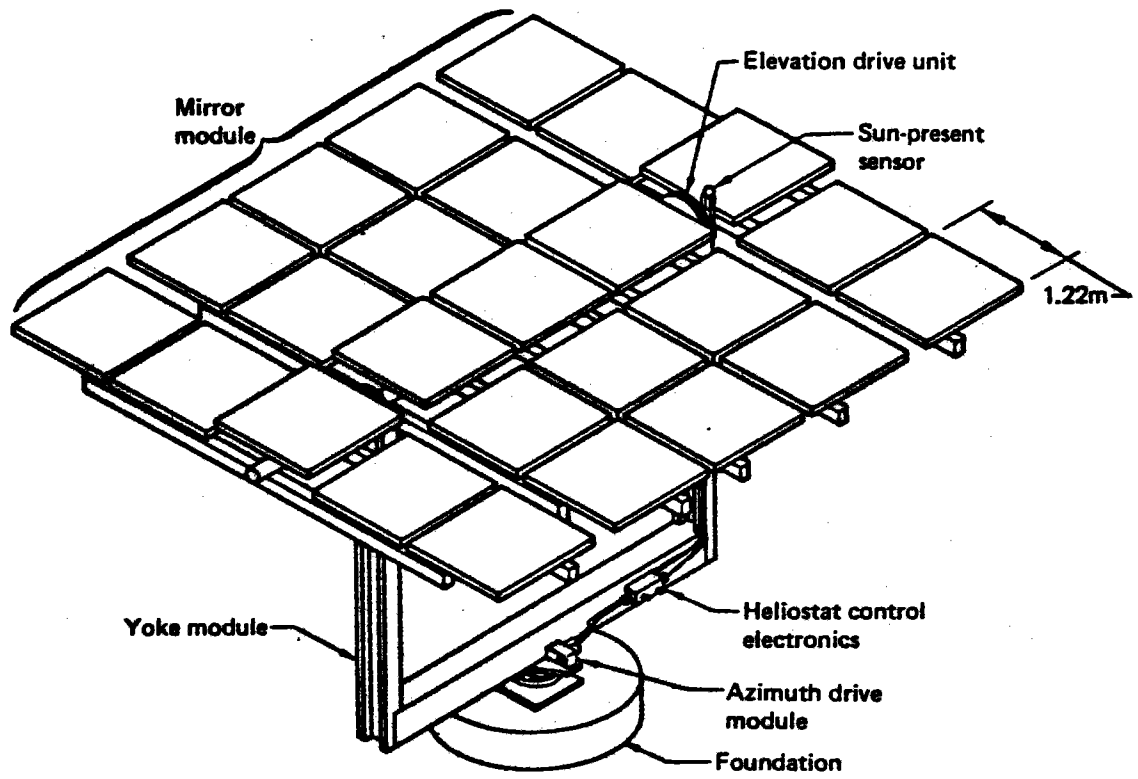


*Figure 7.3-2. CRTF Heliostat*

The curved mirrors and optimized facet alignment were needed to achieve solar concentrations of 1000 to 1500 suns with only 78 heliostats. Collector field performance with curved mirrors and optimized facet alignment dropped off rapidly at times of day more than 2 hr from solar noon. As a result, Zone B heliostats were needed to supplement the Zone A field during many of the late afternoon tests of the BMSR.

The CRTF collector field subsystem included its own computer system for field operations and control. The computer maintained a continuously updated location of the sun. It received operator commands for the targeting (in three-dimensional coordinates) for the reflected solar image from each heliostat. These commands were relayed from a stored list of commands or individually submitted by the CRTF console operator. Then the computer determined the orientation of each heliostat that was required to place its solar image at the desired location. This orientation was defined in terms of heliostat azimuth and elevation angles. The system then drove the heliostat so that its azimuth and elevation angle encoders agreed with these values. New azimuth and elevation angles were continuously computed for each heliostat as the sun moved. Whenever the difference between actual and desired angles exceeded 1 data bit (the resolution of the digital encoder system), the computer recognized an error was present and moved the heliostat to compensate. With Zone A heliostats, this 1 digital-data-bit resolution error amounted to a 10 cm (4 in) displacement of the heliostat image from the center of the receiver.

Heliostat pointing errors developed because of mechanical or electrical problems occurring in the drive units or encoders. When suspected, a heliostat was reoriented to focus on a target on the side of the CRTF tower. The heliostat system was flexible enough so that fixed errors that may have developed over time could be compensated for by reprogramming the software to obtain an accurate alignment on this target.

During a test, all collector field computer system activity was programmed and controlled by the CRTF console operator. The CRTF console operator was stationed inside the control building without a direct view of the collector field. Television cameras with monitors in the control room provided

limited viewing of the collector field. A color CRT display was also provided for the console operator and showed the operational status of each heliostat along with other pertinent collector system data.

A nearby computer terminal printed out the results of a continuous diagnostic test conducted by the field computer.

During tests, a field monitor was stationed in the collector field behind the farthest north row of heliostats in use. Staying in radio contact with the control room personnel, this monitor acted as the outside test observer checking on the operation of individual heliostats for the console operator as well as informing the test operators of changes in environmental conditions.

#### Real-Time Aperture Flux System (RTAF)

Another test subsystem, the real-time aperture flux system, measured the amount of sunlight reflected onto the BMSR by the collector field. Figure 7.3-3 shows the RTAF in place in front of the BMSR on the 43m (140 ft) level test bay. The outer frame of the RTAF was made of hollow steel members cooled by water-glycol from the CRTF heat rejection system. The frame was installed in front of the receiver in a plane parallel to the BMSR aperture plane. Along its top and bottom horizontal members the frame housed tracks that guided the ends of a vertical scanning bar. Normally the scanning bar was housed behind an actively cooled solar shield on the east side of the RTAF frame. In Figure 7.3-3, the bar has been moved to the center of the frame to be serviced.

Heat-flux gages were located on 10 cm (4 in) intervals along the full length of the scanning bar. The bar and gages were actively cooled by a refrigerated water-glycol cooling system, the chiller, which was located in an adjacent test bay in the tower. Coolant lines were carried by the scanning bar as it transversed across the RTAF frame. The RTAF system also had its own data acquisition, control, and data processing computer.

At times during the test program, when solar flux measurements were desired,



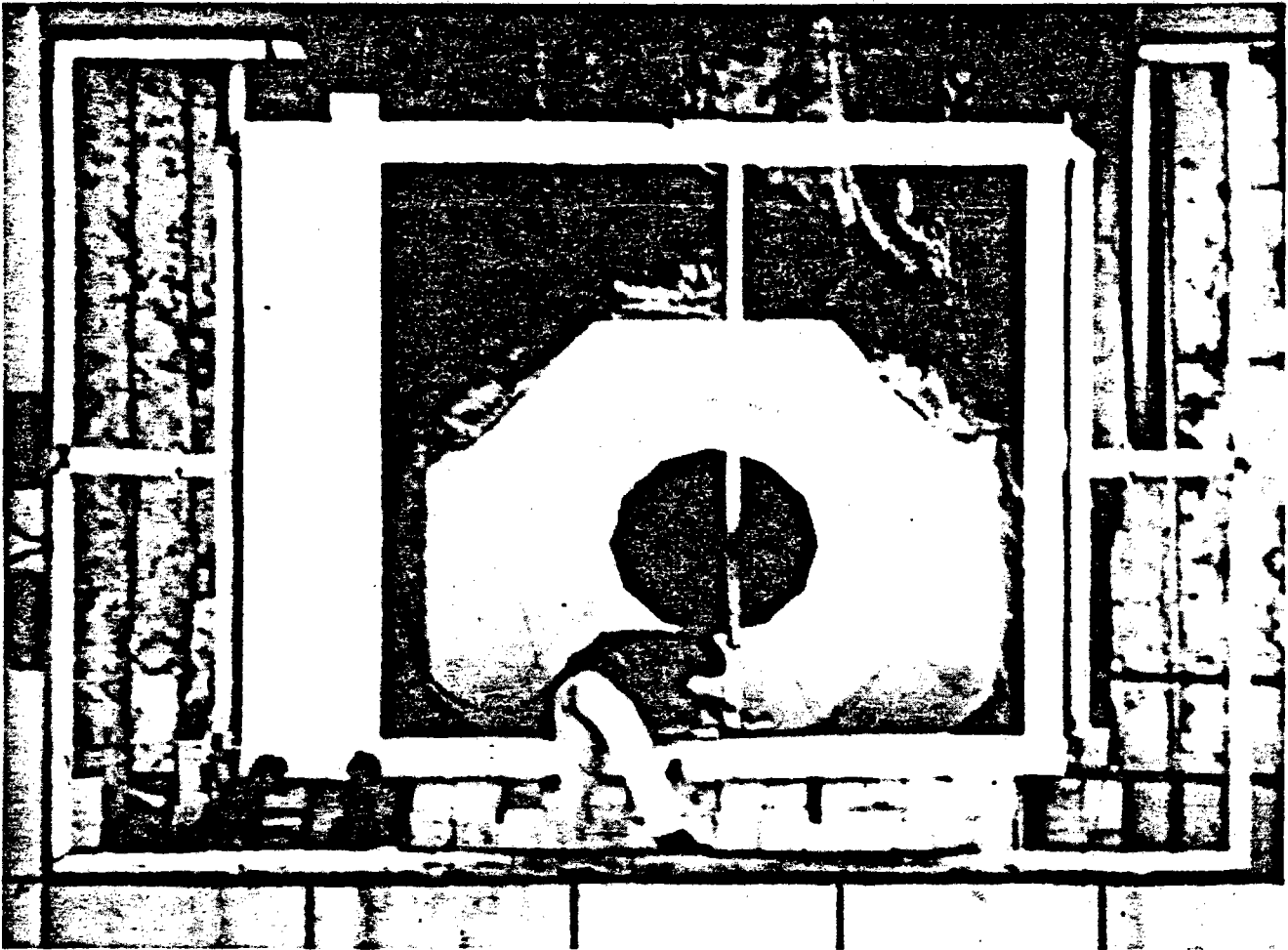


**Figure 7.3-3: RTAF Frame and Scanning Bar**

the RTAF was commanded to scan. The bar moved in 10 cm (4 in) steps, pausing at each step to allow heat flux gage readings to stabilize and be recorded. At the end of a scan it returned to its protective housing.

Data from a single scan of the RTAF included heat flux measurements on a 10 by 10 cm grid spacing across the full vertical and horizontal width of the solar beam. These data were stored on a magnetic tape for future reference.

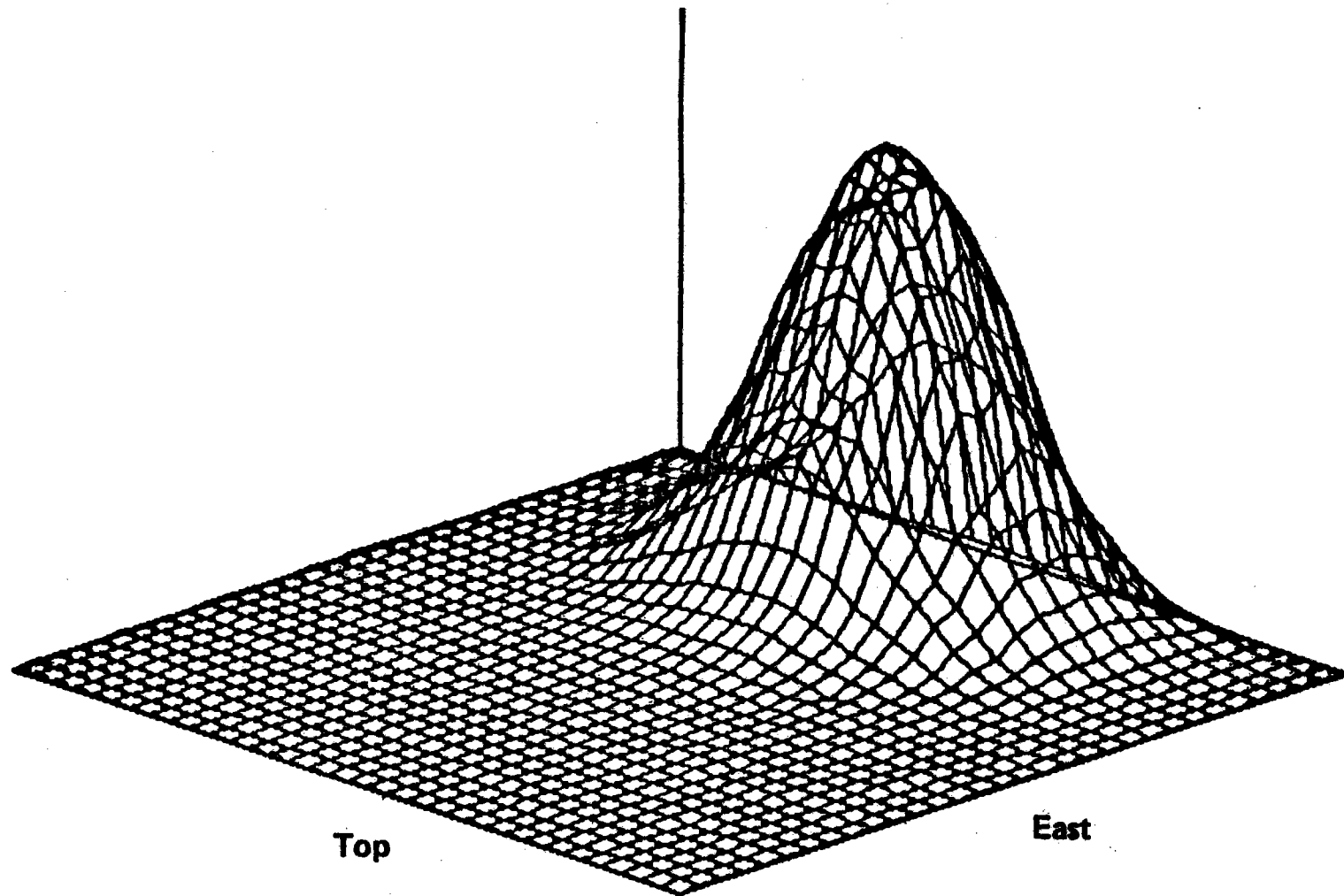
The RTAF computer could also reduce and display the solar flux data during the test. Figure 7.3-4 shows a typical three-dimensional plot of the solar flux at the aperture plane as measured by the RTAF.

During BMSR tests, the RTAF was operated by the test engineer and other CRTF personnel. It served two purposes. First, the real time data were integrated to determine the total solar energy being delivered to the RTAF scanning plane by the collector field. The data were used along with a geometric transfer function, to estimate the solar input to the 1.1m diameter (3.6 ft) receiver aperture. These estimates were used to adjust the number of collectors on target and to obtain the desired receiver solar input. Unfortunately, the geometric transfer function required to extrapolate solar flux at the RTAF plane to the receiver aperture 0.64 m (1.0 ft) farther along the solar beam was a complex function that changed depending on the exact collectors in use, the position of the CRTF tower shadow in the collector field, and other factors. As a result, the real time solar estimates were subject to 10% uncertainty. The RTAF scans provided an experimental data base suitable for use with sophisticated methods of posttest analysis to more accurately determine the solar input for each test. These data processing activities are described in Section 8.0.

### 7.3.2 Test Air Supply System

The BMSR was designed to operate as an element of a closed-cycle gas turbine powerplant. In such a plant it was located in the thermodynamic cycle in place of the traditional coal-fired or oil-fired heater, similar to the boiler in a steam powerplant. In the closed-cycle solar powerplant, the

*Figure 7.3-4. Typical Plot of RTAF Solar Flux Data*  
**Typical Plot of RTAF Solar Flux Data**



BMSR received air at temperatures up to 538°C (1000°F) and heated this air to the desired turbine inlet temperature of 816°C (1500°F). Owing to the aerodynamic design characteristics of the gas turbine, a constant air supply temperature was preferred, with power variations accommodated by changes in flowrate.

Therefore, the BMSR was designed to regulate its airflow rate and produce constant outlet air temperatures in spite of variations of the solar input power. The control valves and sensors used to obtain this outlet temperature control are described in Section 2.0. The significance here is that this mode of operation of the BMSR established the requirements for design of its test air supply system. The components of the test air supply system are described in Figure 7.3-5 and in the following paragraphs.

Diesel-powered air compressors supplied the receiver airflow during tests. The output of four compressors were combined in an air manifold system so that they operated singly or together in any combination. Each of the units was self-contained with its own engine speed control and outlet air pressure regulation system. These controls provided for compressor operation at constant outlet air pressure, about 0.95 MPa (138 lb/in<sup>2</sup>g), over a range of flow rates from about 10% to 100% of capacity. Together the four compressors delivered air at a rate of up to 2.7 kg/s (5.9 lb/s) to the receiver.

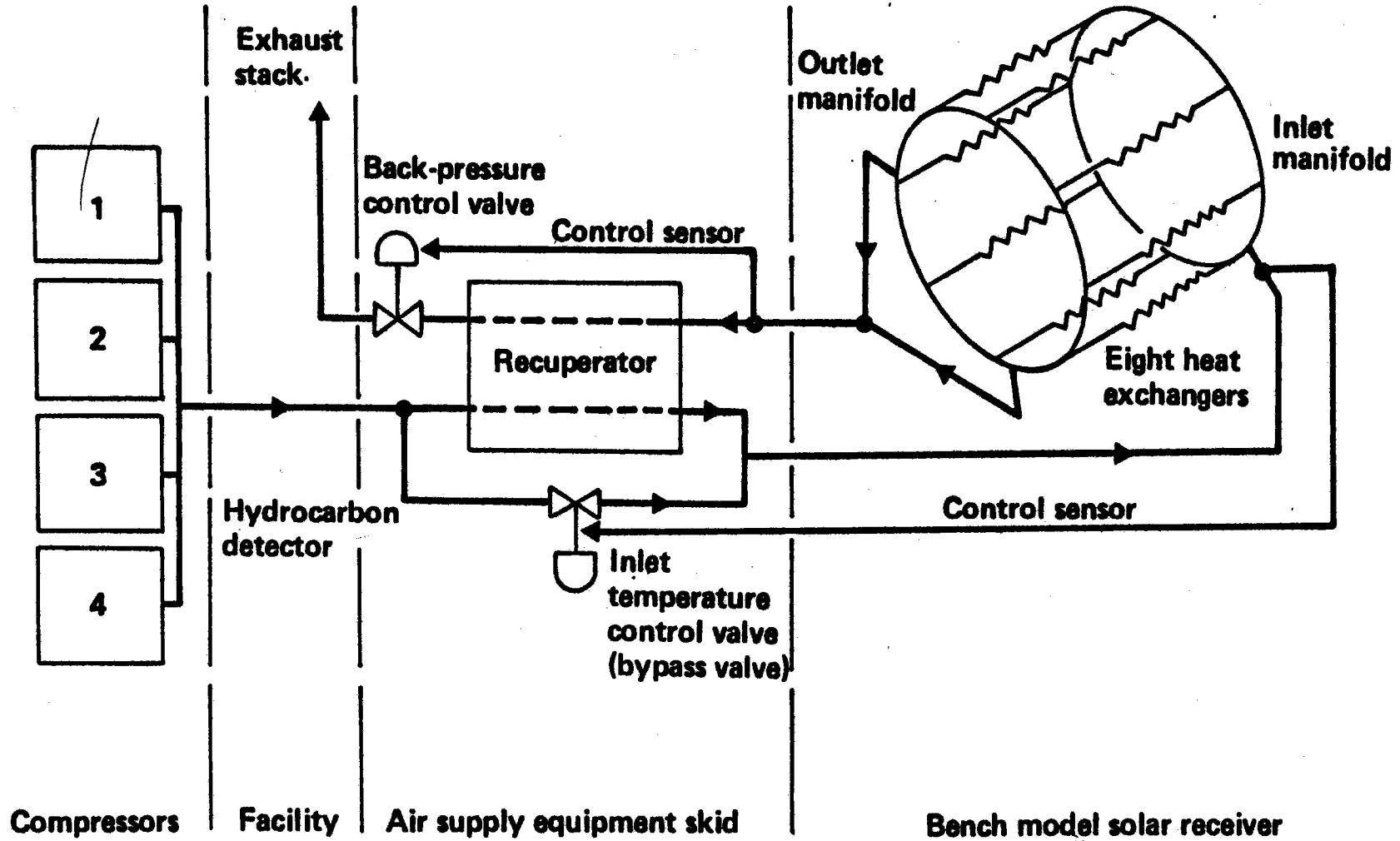
The diesel engines and oil-cooled, screw-type compressors required active cooling during operation. The CRTF water-glycol heat rejection system (HRS) provided this cooling. Piping installed by Sandia Laboratories connected the engine and compressor heat exchangers to the HRS piping system built into the CRTF tower. Coolant circulation pressure was provided by the HRS coolant pump and regulated by individual thermostatic valves on the engine and compressor oil heat exchangers.

Each of the engine-compressor units had its own self-contained system of pressure and temperature sensors to detect operating malfunctions. They protected the equipment by shutting down the unit whenever problems were detected.

Figure 7.3-5. Test Air Supply System for BMSR Tests

# Test Air Supply System for BMSR Tests

350



Because the BMSR was critically dependent on a continuing airflow for its cooling, some means were needed to alert the experimenter if a compressor shut itself down. A CRTF alarm system, the panalarm, located in the control building, was wired to the compressor shutdown relays. Separate alarm circuits were provided for each of the compressors. The HRS coolant pump was also provided with a panalarm display as part of the HRS installation.

The air compressor output passed into the equipment room at the base of the CRTF tower. Because they were oil-immersion, screw-type compressors, they required an extensive system of air filters to remove oil from the compressed air. These filters were mounted on each of the air compressor skids. However, because failure of these filters could result in fire or explosion in the air piping, an air monitoring system was provided by Sandia that detected hydrocarbon contents as low as one part per million in the compressed air. Because mixtures of 3000 to 5000 parts per million are hazardous, the hydrocarbon detector system also included an airflow shutoff valve that automatically closed at a level of 2000 parts per million.

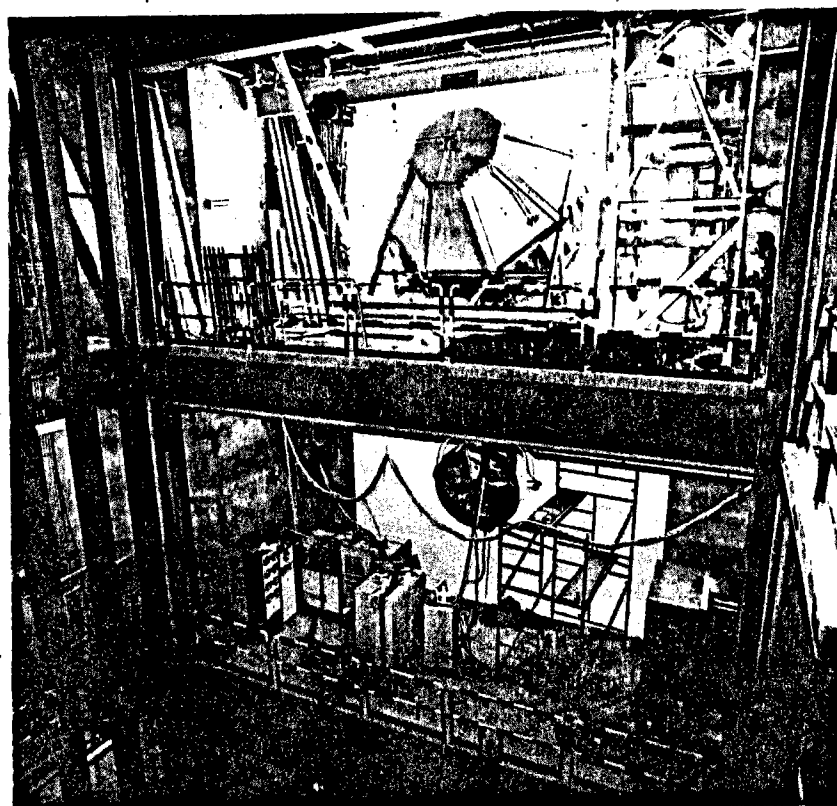
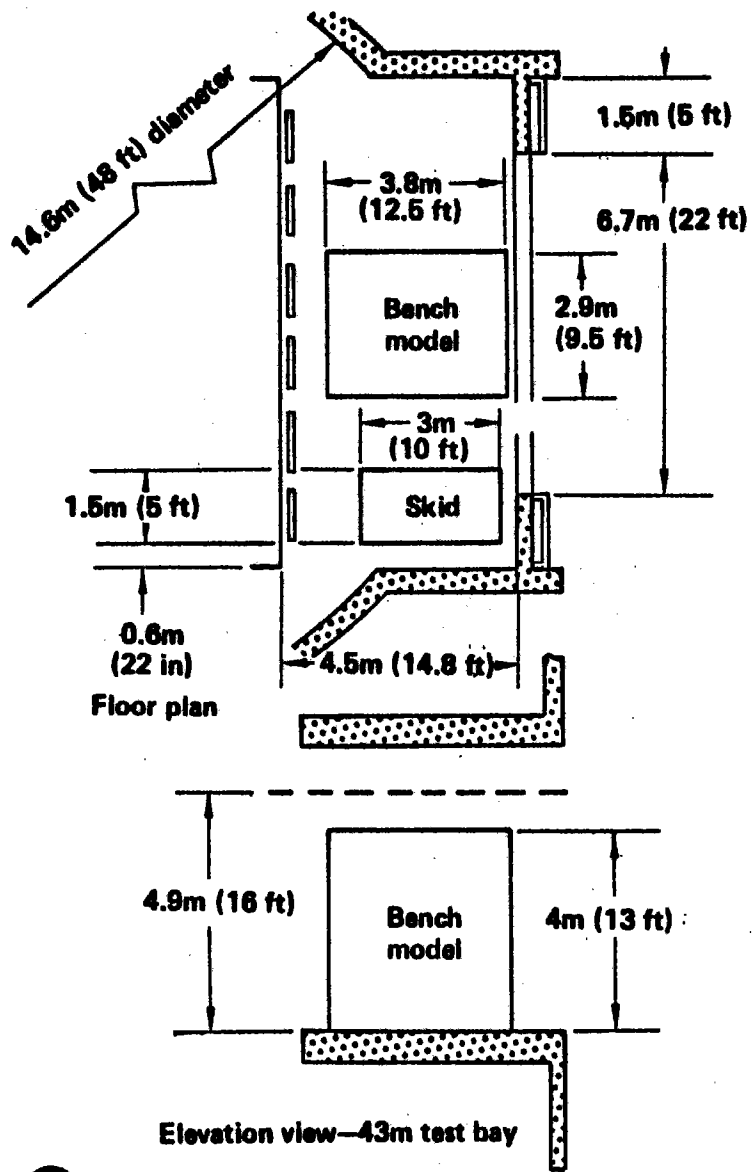
This automatic shutoff valve, however, increased the possibility that receiver cooling airflow could be lost during a test. Therefore a data channel was added to the experimenter's display to indicate hydrocarbon content and to provide an early warning to allow normal test shutdown if more than the normal 2- to 3-parts-per-million hydrocarbon level was observed.

The hydrocarbon detection equipment was part of the CRTF tower system, which also included piping design to carry the compressed air from ground level up to the 43m (140-ft) level test bay. Normally the test air left the compressors at a temperature of 88°C (190°F), but by the time it reached the test level, its temperature was about 65°C (150°F).

A short length of pipe, supplied by EPRI/Boeing and installed by Sandia laboratories, connected the tower air supply piping to the air supply equipment skid. Figure 7.3-6 shows the equipment skid, receiver, and interface piping in the 43m (140-ft) level test bay. Test operation and functions of the equipment skid during tests are described in the following

Figure 7.3-6. Arrangement of Equipment in the CRTF Tower

# Arrangement of Equipment in the CRTF Tower



paragraphs.

The air supply schematic (Figure 7.3-5) shows the airflow paths and major components of the equipment skid. Its central element was a high-temperature tube-in-shell heat exchanger used as a recuperator. The heat exchanger shell was 0.3m (1.0 ft) in diameter by about 4.0m (13.0 ft) long. It was supported in a vertical position, as shown in Figure 7.3-6. Rigidly mounted near its upper end, the shell was free to expand downward into a fitting that allowed vertical movement but constrained lateral motion at its base. The tube side of this heat exchanger received all the BMSR outlet air by means of interface piping connected near its upper end. This air passed through the heat exchanger tubes and out the bottom end of the heat exchanger. Then it passed through a high-temperature butterfly valve, the back-pressure valve, and out through the exhaust piping built into the CRTF tower.

The back-pressure valve and its controller were designed to monitor and control the receiver outlet pressure at a constant level in spite of changes in airflow rate through the system. As shown in Figure 7.3-5, the control pressure sensor was located on the interface piping between the receiver and the equipment skid. As a result, the actual pressures at the location of the back-pressure valve were always slightly less than the valve controller setpoint.

Heat given up in the heat exchanger by the receiver outlet airflow was available to preheat the air supplied to the receiver. Once the receiver, the interface piping, and the heat exchanger were up to normal operating temperatures, there was always more than enough heat available to provide the necessary preheat. Because excess heat was available, the air supply preheat and BMSR inlet temperature control system were relatively straightforward. Upon entering the air supply equipment skid, the receiver test air supply flow rate was measured by a venturi flowmeter built into the air piping. Then the flow was divided by a three-way flow-control valve. A portion of the flow was directed through the shell side of the heat exchanger where it picked up receiver outlet heat. This air was heated to a temperature in excess of the desired receiver inlet temperature. Then it



was mixed with air that had been bypassed around the heat exchanger. The final mixed-air temperature was measured by a thermocouple immersed in the airstream near the inlet to the BMSR. This thermocouple operated the three-way bypass valve by a temperature controller. When receiver inlet temperature was higher than the desired setpoint temperature, the valve was moved to increase the bypass flow and reduce the heated airflow. The split-flow method of operation of this temperature control system was highly desirable because it was not severely affected by, or coupled to, changes in flow rate. A bypass valve angle suitable for one rate of receiver airflow was not much different than the angle needed for higher or lower rates of airflow at the same temperatures.

The air supply equipment skid was considered by Sandia Laboratories to be part of the BMSR experiment. Its instrumentation and controls were connected to the CRTF data acquisition and control system and were stored and displayed along with BMSR data.

### 7.3.3 Data Acquisition and Control System (DACs)

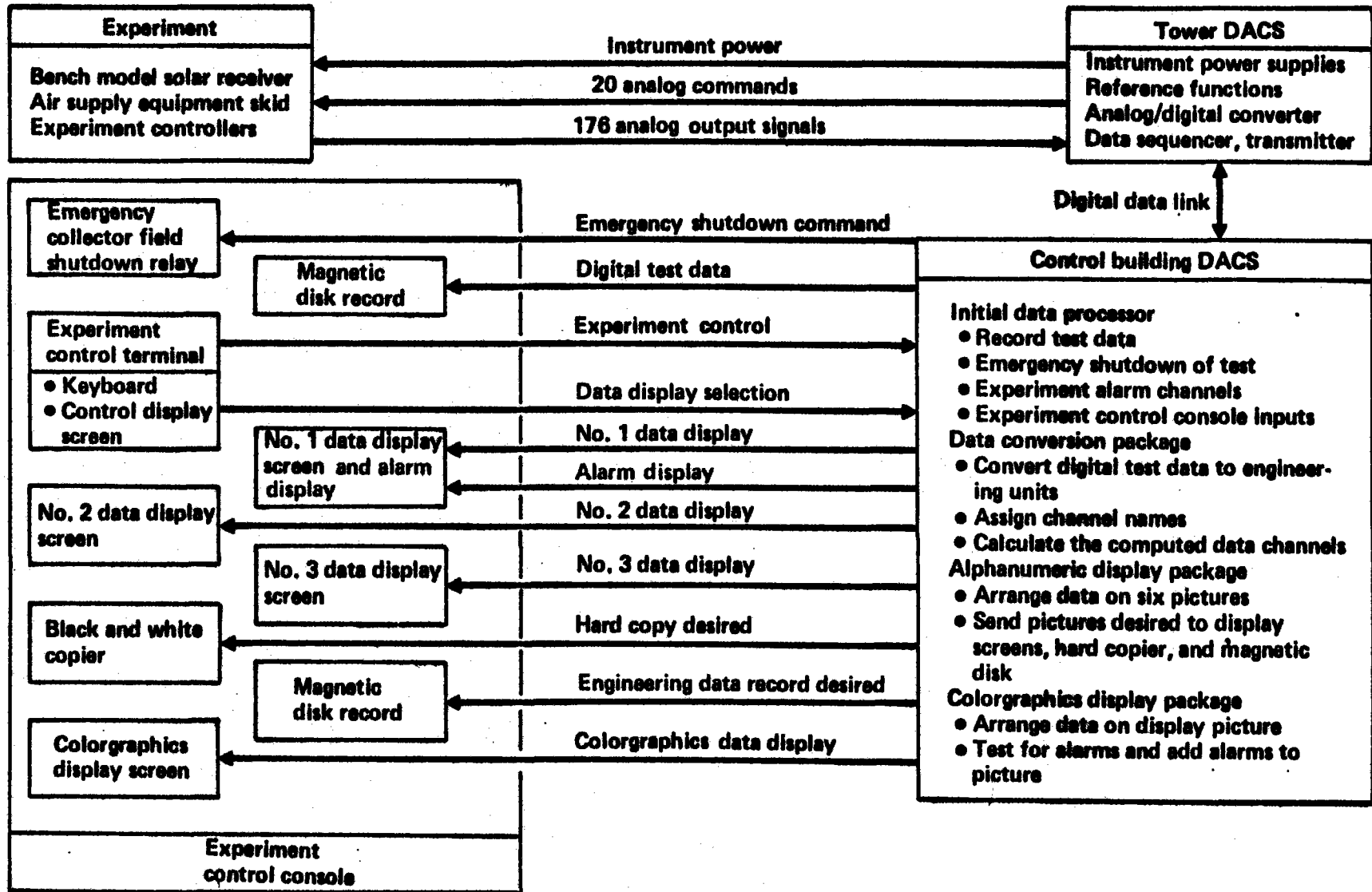
The data acquisition and control system used for these tests at CRFT is shown in Figure 7.3-7. The system included instruments and controls located on the experiment: a data system terminal located at the CRTF tower that provided the CRTF-experiment data interface and transmitted the test measurements to the CRTF control building, the main body of the CRTF data processing equipment located in the control building, and an experiment control console, also located in the control building, which included visual (CRT) displays and a computer terminal used by the experimenter to operate the experiment controls.

### Experiment Instrumentation and Controls

The experiment instrumentation, which is described in Section 3.0, consisted of 172 measurements, including pressures, temperatures, heat fluxes, and valve angles. Experiment control during tests included the capability to remotely adjust the temperature and pressure set-points used by the eight receiver outlet temperature controllers and the receiver inlet temperature

Figure 7.3-7. CRTF Data Acquisition and Control System

# CRTF Data Acquisition and Control System



and back-pressure controllers located on the air supply equipment skid. The instrumentation and control interface between the experiment and the CRTF consisted of cables and wires provided with the experiment that were connected to the DACS equipment located in the tower. Figure 7.3-6 shows the arrangement of these components in the 43m level (140 ft level) and the 37m level (120 ft-level) test bays at CRTF.

### Tower DACS Equipment

The DACS terminal in the test tower provided signal conditioning power to the pressure transducers and reference junctions for the 128 thermocouples used on the experiment. All analog data signals (voltages corresponding to temperatures, pressure, etc.) were converted to digital output. Digital data transmission was required because of the 400m (1312-ft) distance from the tower test site to the control building. The tower DACS scanned through all the data channels in a preprogrammed sequence, creating a string of digital words that corresponded to a full set of experimental data at that point.

The 192 data channels in the BMSR experiment were separated by priority code into three groups. The first group of most important data (heat exchanger air outlet temperatures) was monitored and updated with each scan of the tower data system. The second group of lower priority channels (heat exchanger tube temperature) was monitored and updated every second scan. The lowest priority data channels (structural shell temperatures) were monitored and updated every third scan. In this way, the scanning rate on the highest priority data was faster than with equal priorities on all 192 channels. The scanning rate depended on a number of experiment-sensitive variables; in this test it was 4 sec.

This data string was then transmitted to the control building. Because of this scanning process, the test data received in the control building were not continuous. New sets of values were made available with each scan of the tower data system.

In addition to transmitting measured test data, the tower DACS terminal

received digital command signals from the control building and converted them into analog output for the controller setpoint adjustments.

### Control Building DACS

The digital data stream produced by the tower DACS terminal was received by another set of DACS equipment located in the control building. There the data was recorded in its original digital format and stored on magnetic tape at the end of each test day. This raw data tape was of great value because the only time delay built into the data at this point was the scanning rate of the tower DACS terminal. As a result, the information on the raw data tape was accurate to within a few seconds of the scan time shown on the tape (4 to 12 sec).

The test data were processed for display on four CRT monitors that made up the experiment operator's console in the data control building (shown in Figure 7.3-8). Other data system functions were provided in the data processing system, including warning the experimenter of data channels exceeding their normal operating limits and automatically commanding the removal of heliostats from target on the receiver if BMSR outlet temperatures exceeded 844°C (1550°F), or outlet pressure dropped below 0.3MPa (40 lb/in<sup>2</sup>).

Immediately after being scanned, the data channels corresponding to receiver outlet temperature were checked to see if any of them exceeded 844°C (1550°F). This was accomplished by comparing channel voltage with the thermocouple output voltage at 844°C (1550°F). In case of excessive temperature, a relay was triggered that paralleled the console operator's emergency test shutdown switch. Activating this switch caused a rapid but controlled movement of the heliostat solar images to converge at a point just east of the CRTF tower, the standby point. All heliostat solar images left the vicinity of the receiver within a period of 4 sec from initiation of this command. Severe damage to the receiver was almost certainly avoided by this automatic shutdown on two occasions when control valves on the receiver closed because of actuator malfunction.



Figure 7.3-8: Experiment Control Console

The next event in the data processing sequence was the preparation and display of the experiment alarm channels, which were 15 of the experiment data channels selected each day for special display priority. These data channels were listed on the screen of the display (CRT) monitor adjacent to the experimenter's computer terminal. The display showed measured test data in engineering units and channel alarm levels. This was the most up-to-date of the five visual data displays provided for the experimenter. A time delay of about 8 sec occurred from the time the data was scanned by the tower DACS equipment until it showed up on the experiment alarm display.

The next step in the data processing sequence was the conversion of all the digital format test data into engineering data. This function was performed by a computer program written for BMSR tests, the data conversion package.

The data conversion package assigned proper engineering units identification to each test data channel. It used instrument calibration constants and formulas to convert measured voltages into measurements in the proper engineering units. Some of the calibration constants were adjusted based on daily recalibration of instruments. Others, such as the thermocouple conversion tables, were permanently programmed into the conversion package. In addition, new data were produced by the conversion package, including data obtained by combining two or more of the measured data together to produce new information. For example, the receiver airflow rate was computed by the use of flowmeter inlet temperature, inlet pressure, and pressure drop in a formula provided by the flowmeter supplier. Other new data included summaries of measurements such as the highest tubing temperature on each of the receiver heat exchangers. With the addition of these new computed data, the test data consisted of 213 channels of measured or computed data.

### Experiment Control Console

Figure 7.3-8 shows the experiment control console at CRTF. The items shown in this photograph include (1) the experiment control computer terminal, an off-line copier capable of producing black and white copies of alphanumeric data display pictures, (2) two of three small black and white CRT monitors

used for alphanumeric data display pictures, and (3) the color CRT monitor used for colorgraphics display. A third black and white CRT monitor, used for alphanumeric data display, was located to the right of the colorgraphics display. One of the overhead television monitors was used to remotely observe the experiment controllers in the tower test bay.

The keyboard of the experiment control computer terminal provided access to the DACS computer. Different functions of the terminal were as follows:

- a. Revise calibration constants used in the conversion package.
- b. Select the 15 experiment alarm data channels to be processed and displayed on monitor number 1.
- c. Insert remote set-point values for the 10 experiment controllers and execute the commands to use local or remote set-points.
- d. Select three of the six alphanumeric display pictures to be shown on the three black and white CRT monitors.
- e. Command the data system to store the contents of the six alphanumeric displays on disk storage for posttest review.
- f. Use the off-line copier to produce a copy of any of the six alphanumeric display pictures.

The three black and white CRT monitors were used with six preprogrammed alphanumeric display pictures. Once a new set of test data was processed by the conversion package, it replaced the old values on these display pictures. All six pictures were continuously available, even though only three of them could be viewed at any one time. The nomenclature established during the fabrication and instrumentation of the BMSR was also used on these displays. This system of nomenclature is shown in Figure 7.3-9. Because the receiver instrumentation is symmetrical around the aperture centerline, the variable "X" in all the labels is replaced by the appropriate receiver bay numbers, 1 through 8.

Contents of the six preprogrammed alphanumeric pictures are listed in Table 7.3-2. Picture 1 included receiver structural shell temperatures and the temperatures of the eight receiver valve actuators. Picture 2 included all the receiver insulation temperatures and the cavity heat flux gage readings.

Figure 7.3-9. Bench Model Instrumentation

# Bench Model Instrumentation

361

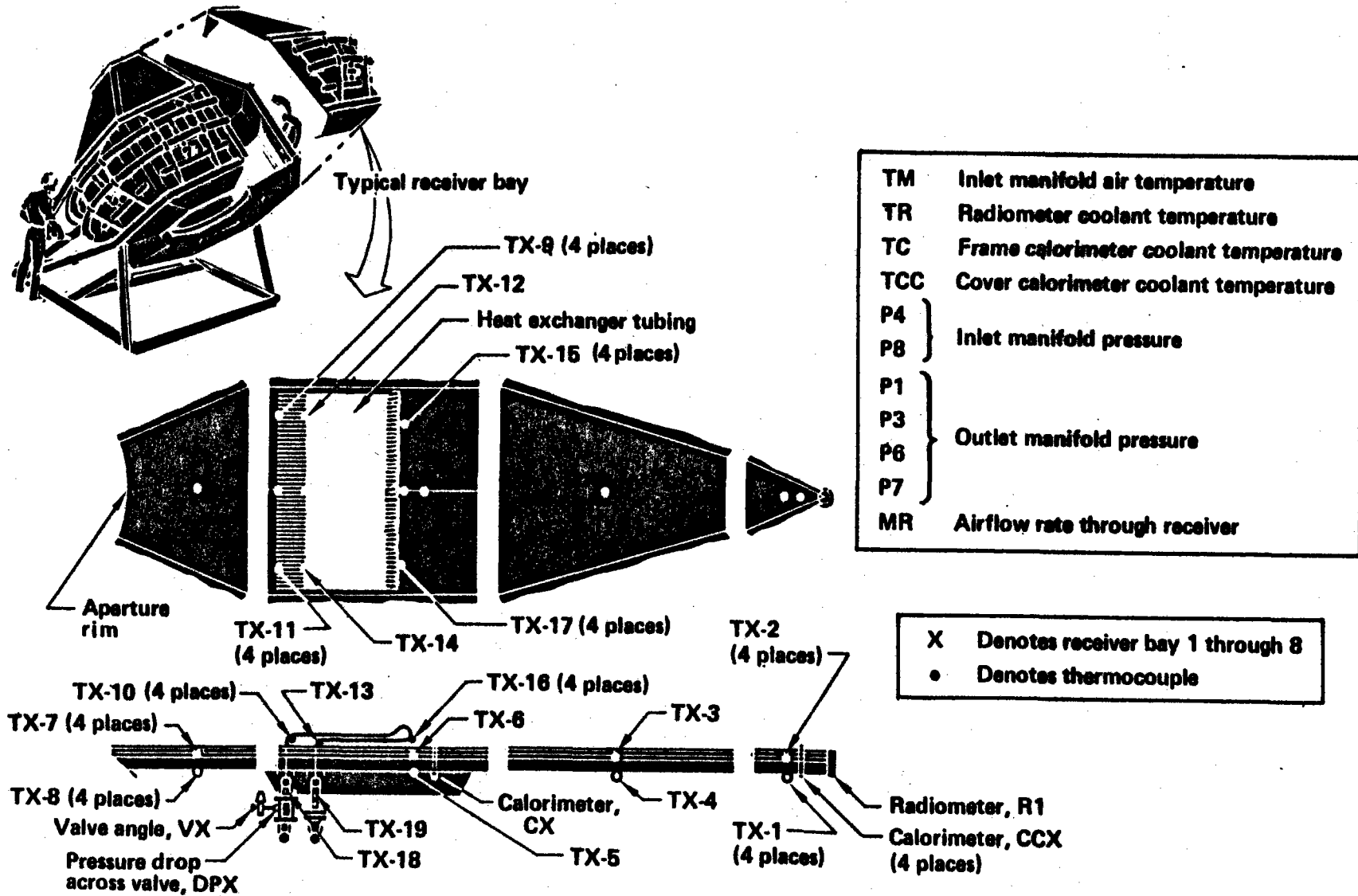




Table 7.3-2. Alphanumeric Display Pictures

## Alphanumeric Display Pictures

	Sensor	Description	Range	Alarms
Picture 1	TX-1	Temperature of outside surface of receiver cover, bays 1, 3, 5, 7	0° to 400°F	—
	TX-4	Temperature of outside surface of receiver cover, bays 1-8	0° to 400°F	—
	TX-5	Temperature of outside surface of receiver frame, bays 1-8	0° to 400°F	—
	TX-8	Temperature of outside surface of receiver frame, bays 1, 3, 5, 7	0° to 400°F	—
	TP	Temperature of valve actuator in bays 1-8	0° to 400°F	240°F
	TCON	Temperature of steel cone behind zone II shield	0° to 400°F	—
	TR	Temperature of radiometer coolant outlet	32° to 212°F	160°F
	TCC	Temperature of cover calorimeter coolant outlet	32° to 212°F	160°F
	TC	Temperature of frame calorimeter coolant outlet	32° to 212°F	160°F
Picture 2	R1	Solar flux, radiometer at center of receiver cover	0 to 500 kW/m <sup>2</sup>	400 kW/m <sup>2</sup>
	CCX	Solar flux, calorimeter in receiver cover, bays 1, 3, 5, 7	0 to 650 kW/m <sup>2</sup>	—
	CX	Solar flux, calorimeter in receiver frame, bays 1-8	0 to 200 kW/m <sup>2</sup>	—
	TX-2	Temperature within cover insulation of bays 1, 3, 5, 7	0° to 1,800°F	1,800°F
	TX-3	Temperature within cover insulation of bays 1-8	0° to 1,800°F	1,800°F
	TX-6	Temperature within receiver frame insulation of bays 1-8	0° to 1,800°F	—
	TX-7	Temperature within receiver frame insulation of bays 1, 3, 5, 7	0° to 1,800°F	—
Picture 3	TX-18	Temperature of inlet air to bays 1-8	0° to 1,300°F	—
	TX-9	Temperature of heat exchanger tubes at inlet in bays 1, 3, 5, 7 (near bays 2, 4, 6, 8)	0° to 1,300°F	—
	TX-10	Temperature of heat exchanger tubes at inlet in center of bays 1, 3, 5, 7	0° to 1,300°F	—
	TX-11	Temperature of heat exchanger tubes at inlet in bays 1, 3, 5, 7 (near bays 2, 4, 6, 8)	0° to 1,300°F	—
	TX-15	Temperature of heat exchanger tubes at bend in bays 1, 3, 5, 7 (near bays 2, 4, 6, 8)	0° to 1,800°F	1,700°F
	TX-16	Temperature of heat exchanger tubes at bend in bays 1, 3, 5, 7 (at center of bay)	0° to 1,800°F	1,700°F
	Picture 4	TX-17	Temperature of heat exchanger tubes at bend in bays 1, 3, 5, 7 (near bays 2, 4, 6, 8)	0° to 1,800°F
TX-12		Temperature of heat exchanger tubes at outlet of bays 1-8 (near bays 8 and 1-7)	0° to 1,800°F	1,700°F
TX-13		Temperature of heat exchanger tubes at outlet in center bays 1-8	0° to 1,800°F	1,700°F
TX-14		Temperature of heat exchanger tubes at outlet of bays 1-8 (near bays 2-8 and 1)	0° to 1,800°F	1,700°F
TX-19		Temperature of outlet air from bays 1-8	0° to 1,800°F	1,550°F(auto)

Table 7.3-2. Alphanumeric Display Pictures (Continued)

## Alphanumeric Display Pictures (Continued)

Sensor	Description	Range	Alarms	
Picture 5	DPX	Delta pressure across panel control valves in bays 1-8	0 to 150 lb/in <sup>2</sup>	—
	VX	Valve position indicators on panel control valves in bays 1-8	0° to 90 deg	Over 75 deg open
	TX-18	Temperature of inlet air in bays 1-8	0° to 1,300°F	—
	MX	Mass airflow through designated bays 1-8	0 to 1 lb/s	—
	TX-19	Temperature of outlet air from designated bays 1-8	0° to 1,800°F	1,500°F
	PX	Pressure of air in outlet manifold (P1 top, P3 east, P5 bottom, P7 west)	0 to 150 lb/in <sup>2</sup>	Low 58 lb/in <sup>2</sup> High 68 lb/in <sup>2</sup>
	S	Reading from pyrhelimeter atop tower	0 to 1.2 kW/m <sup>2</sup>	—
	MR	Total mass flow rate of air through receiver	0 to 7 lb/s	—
	TM	Temperature of air in inlet manifold	0° to 1,300°F	1,200°F
	P-4	Pressure of air in inlet manifold (far from inlet direction)	0 to 150 lb/in <sup>2</sup> <sub>g</sub>	Low 118 lb/in <sup>2</sup> <sub>g</sub> High 128 lb/in <sup>2</sup> <sub>g</sub>
P-8	Pressure of air in inlet manifold (near inlet direction)	0 to 150 lb/in <sup>2</sup> <sub>g</sub>	Low 118 lb/in <sup>2</sup> <sub>g</sub> High 128 lb/in <sup>2</sup> <sub>g</sub>	
HCAR	Hydrocarbon content of inlet air	0 to 500 ppm	200 ppm	
Picture 6	TA4	Temperature of air from compressors	0° to 1,800°F	—
	TRCO	Temperature of radiometer coolant outlet	32° to 212°F	160°F
	TA1	Temperature of air to receiver	0° to 1,800°F	—
	TA2	Temperature of air from receiver	0° to 1,800°F	—
	TA5	Temperature of air back-pressure valve	0° to 1,800°F	—
	PA4	Pressure of air from compressors	0 to 150 lb/in <sup>2</sup> <sub>g</sub>	—
	PA6	Pressure of air in bypass line	0 to 150 lb/in <sup>2</sup> <sub>g</sub>	—
	PA1	Pressure of air to receiver	0 to 150 lb/in <sup>2</sup> <sub>g</sub>	—
	PA2	Pressure of air from receiver	0 to 150 lb/in <sup>2</sup> <sub>g</sub>	—
	PA5	Pressure of air to back-pressure valve	0 to 150 lb/in <sup>2</sup> <sub>g</sub>	Less than 50 lb/in <sup>2</sup> <sub>g</sub> Less than 40 lb/in <sup>2</sup> <sub>g</sub>
	DPA4	Delta pressure across main flowmeter	0 to 15 lb/in <sup>2</sup>	—
	DPA6	Delta pressure across bypass flowmeter	0 to 15 lb/in <sup>2</sup>	—
	DPM	Delta pressure between inlet and outlet manifold	0 to 60 lb/in <sup>2</sup>	40 lb/in <sup>2</sup>
	MR	Mass flow rate total through receiver	0 to 7 lb/s	—
	MB	Mass flow rate through bypass line	0 to 7 lb/s	—
	VA1	Valve angle to recuperator (90 deg full recuperator flow)	0° to 90 deg	Less than 25 deg
	VA2	Valve angle of back-pressure valve (90 deg = open)	0° to 90 deg	Less than 25 deg
PAIR	Pressure of house air to regulators	0 to 150 lb/in <sup>2</sup> <sub>g</sub>	Less than 80 lb/in <sup>2</sup>	

Pictures 3 and 4 were usually displayed together; they showed all the receiver heat exchanger temperatures, including inlet and outlet air temperatures (repeated here for convenience) and total receiver airflow. Picture 6 showed all the air supply equipment skid data channels, including pressures, temperatures, and valve angles.

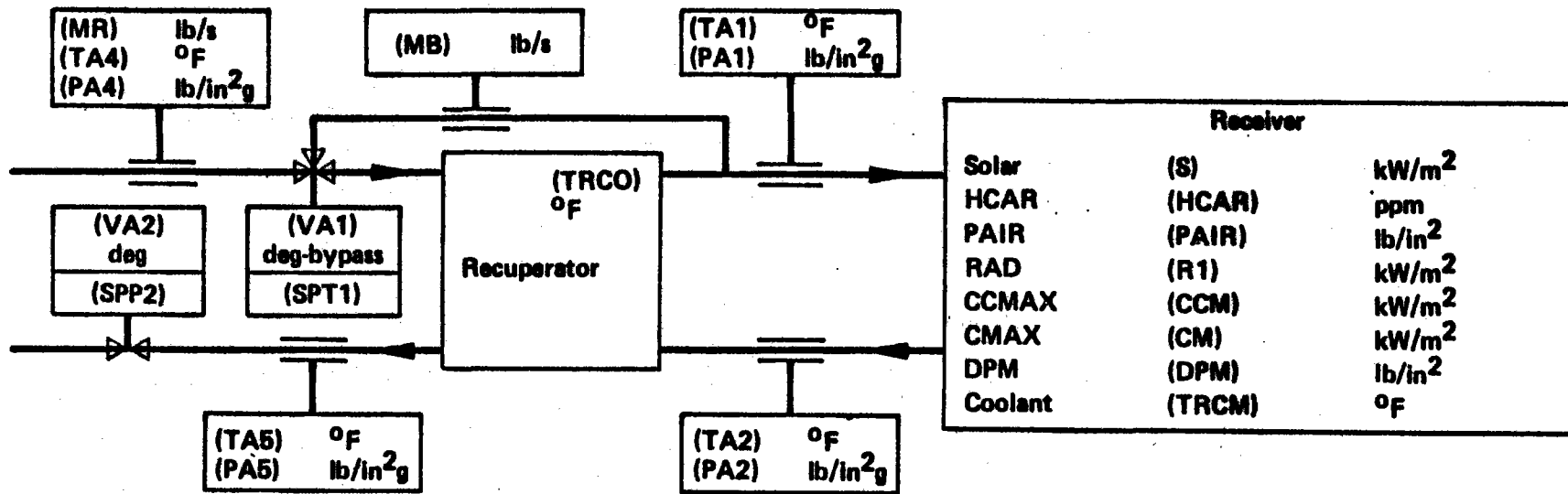
Because of the time required to produce these alphanumeric display pictures, they lagged behind the test events by about 16 sec. Therefore it was frequently desirable to use the 15 operator alarm channels (within 8 sec of test events) to observe rapidly changing conditions in the experiment rather than wait for the alphanumeric display to be updated.

The colorgraphics CRT display was the most readily used of the visual data displays at CRTF. This system was programmed to display all the data needed to monitor and control the experiment on one viewing screen.

The layout of the colorgraphics display screen is shown in Figure 7.3-10. The upper portion of the screen shows a block diagram of the test airflow system. Locations of air temperature and pressure transducers are readily apparent by their location on the schematic. The positions of the two control valves in the air supply system are described, along with the measured valve angles and the temperature or pressure setpoints used by the valve controllers. Some of the solar receiver data are included within its block diagram on the upper portion of the colorgraphics screen. These include maximum readings of heat-flux gages on the receiver back cone (CCMAX) and the receiver frame (CMAX), the maximum temperature of coolant returning from the heat-flux gages (coolant), and other test equipment parameters such as Epply pyrliometer reading (SOLAR), air supply pressure to the pneumatic valves on the experiment (PAIR), and hydrocarbon content in the test air supply (HCAR). The lower half of the colorgraphics display included all the data needed to determine receiver operating conditions. Data are shown for each of the eight receiver bays.

Most of the data shown on the colorgraphics display were provided with visual alarms to indicate when the data exceeded expected limits. These alarm levels were programmed into the colorgraphics display package. When

Figure 7.3-10. Colorgraphics Display  
**Colorgraphics Display**



Receiver conditions.

Data channel	Description	Units	1 Top	2	3 east	4	5 bottom	6	7 west	8
MX	Panel flow	lb/s	(M1)	(M2)	(M3)	(M4)	(M5)	(M6)	(M7)	(M8)
PX	Inlet pressure	lb/in <sup>2</sup> g		(P4)				(P8)		
VX	Valve angle	deg	(V1)	(V2)	(V3)	(V4)	(V5)	(V6)	(V7)	(V8)
DPX	Valve pressure	lb/in <sup>2</sup>	(DP1)	(DP2)	(DP3)	(DP4)	(DP5)	(DP6)	(DP7)	(DP8)
PX	Outlet pressure	lb/in <sup>2</sup> g	(P1)		(P3)		(P5)		(P7)	
TX-18	Gas inlet temperature	°F	(T1-18)	(T2-18)	(T3-18)	(T4-18)	(T5-18)	(T6-18)	(T7-18)	(T8-18)
TXX	Maximum tube temperature	°F	(TT1)	(TT2)	(TT3)	(TT4)	(TT5)	(TT6)	(TT7)	(TT8)
TX-19	Gas outlet temperature	°F	(T1-19)	(T2-19)	(T3-19)	(T4-19)	(T5-19)	(T6-19)	(T7-19)	(T8-19)
SPX	Setpoint	°F	(SP1)	(SP2)	(SP3)	(SP4)	(SP5)	(SP6)	(SP7)	(SP8)

any data channel exceeded its alarm limits, an area on the display screen around the out-of-limit data was changed from black to red. These alarms were readily observed by the experimenter. The limits were established for operating flexibility with sufficient margins from the point of failure of the receiver to allow the experimenter to take note of conditions and observe for some time before taking corrective action or shutting down the test.

Because of the extra computer time needed to produce the colorgraphics picture, these data lagged the farthest behind the test events. Typically, the data on the colorgraphics screen were 24 to 30 sec old.

#### Posttest Data

Three types of posttest data records were produced by the data acquisition and control system. By initiating a store data command through the experiment control computer terminal, the experimenter caused the contents of all six alphanumeric display pictures to be stored. These commands were used on 1- to 5-min intervals to produce records that were printed out and reviewed immediately after each day of testing. These records were used to examine the day's activities and to plan future tests. The second test data record was the raw data tape mentioned earlier. This record had the advantage of 4-sec intervals between data records, but the disadvantage was that it was in the form of digitized signals (as received from the tower DACS).

Finally, the most useful of the posttest data records was produced after each day's test by reading the raw data tape (using the conversion package) and converting the raw data to engineering units. These converted test data were recorded on a new magnetic tape. These engineering data taped from each test formed the basis for test data processing described in Section 8.0.

#### 7.3.4 Test Operations

Figure 7.3-11 describes the operational relationship between the three test operators (CRTF console operator, CRTF test engineer, and experimenter) and the various test data acquisition and control systems on hand at CRFT. The experimenter used the DACS to monitor conditions in the experiment and to adjust experiment controls. The console operator used the collector field display system and information from the field monitor to direct the action of the collector system. The CRTF test engineer used the RTAF data acquisition and control system to measure solar flux on the receiver.

The integrated test procedure provided a description of the events desired for completion of each test. Using this as a guide, the collector field and receiver activities were coordinated to achieve the desired results. Because of the unusual operating and weather conditions expected during a solar receiver test, the successful achievement of desired test conditions depended quite strongly on the flexibility, willingness, and judgement of these three test operators.

#### 7.4 INTEGRATED TEST PROCEDURE

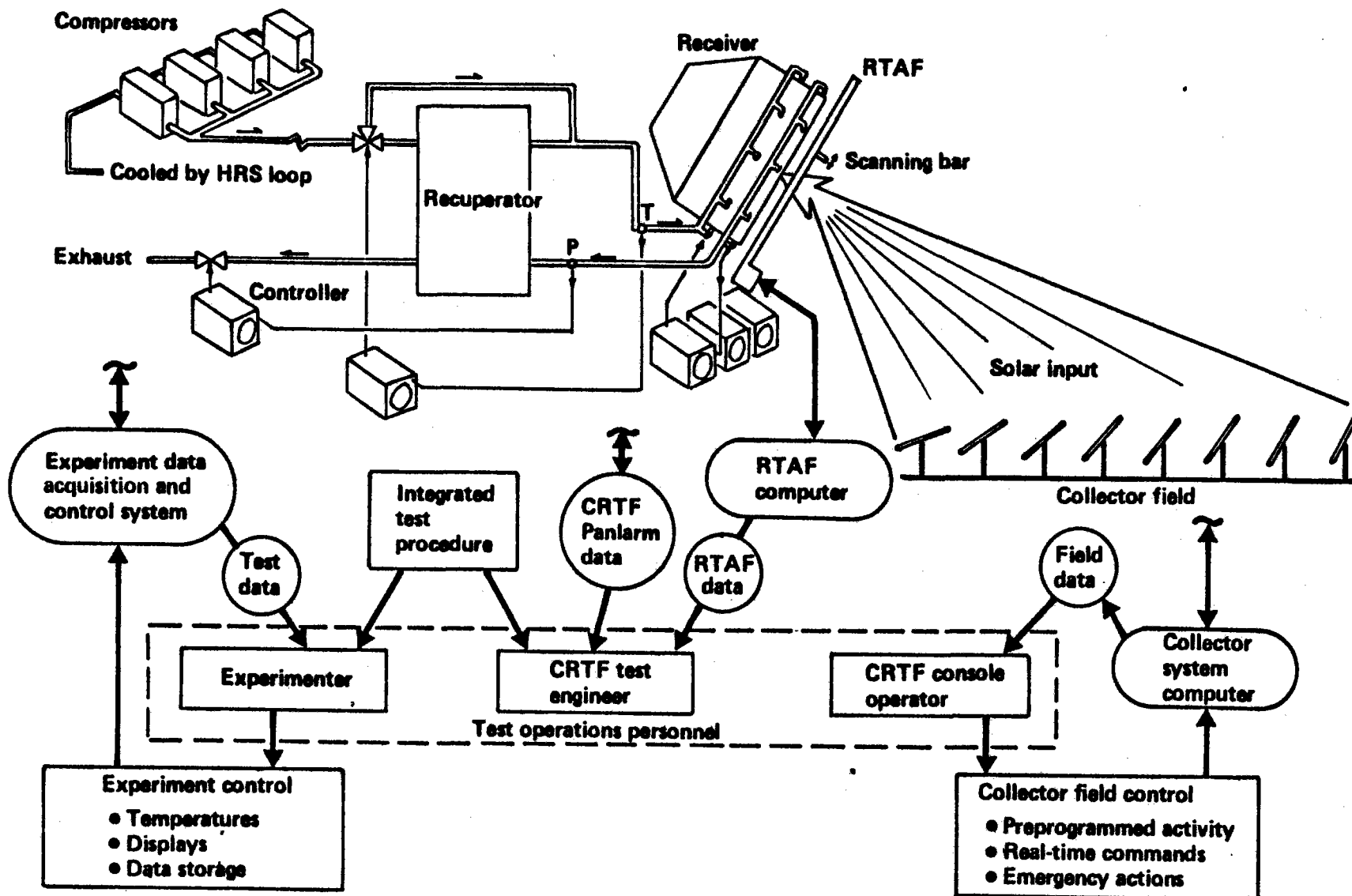
The objective of the integrated test procedure (ITP), Reference 4, was to combine CRTF operating procedures, experiment test plans and procedures, and other procedures necessary to perform the experiment, into a single system-level test procedure. Preparation of the ITP was one of the responsibilities of the Sandia test engineer assigned to the experimenter, the CRTF operations and safety engineer, the CRTF supervisor and the Safety Engineering Division at Sandia.

Because it was the first major solar receiver test program to be conducted at CRTF, the preparation of the ITP required dealing with new and challenging problems. Both the CRTF engineering staff and the experimenter had separately considered the sequence of events and courses of action to be taken with their respective equipment in order to execute the test plan while ensuring personnel safety and equipment survival. Several problems were encountered while attempting to combine these subsystem procedures into

Figure 7.3-11 Test Operations

# Test Operations

368



an integrated procedure.

One problem that had been overlooked during design of the test setup and during pretest planning was the need to provide backup equipment, failure alarms, or fail-safe modes of operation for all the test systems whose failure could lead to catastrophic damage to the experiment. These concerns became clear during ITP preparation. Several last-minute changes were made in the test setup, including adding provisions for automatic collector field shutdown upon detection of excessive receiver outlet air temperature or lower-than-normal outlet pressure; addition of visual and audio alarms in the control room to warn the experimenter in the event of inadvertent shutdown of any of the air supply compressors; addition of a hydrocarbon sensor data channel with visual alarm on the experimenter's data display to warn of imminent automatic shutdown of the receiver air supply because of excessive oil in the air; addition of a redundant backup cooling supply for the receiver heat-flux gages; and modification of the electrical wiring to provide power to the receiver controllers from the same high-reliability source as used by the collector field computers and the data acquisition and control system.

Another problem arose during ITP preparation when it was discovered that collector field operation needed to be formalized and preprogrammed for each test. During the CRTF acceptance tests it was determined that collector field operation by means of individual real-time heliostat commands was excessively time-consuming and subject to possible human error. Instead, an entire day's sequence of test activities in the collector field needed to be prescheduled and preprogrammed. Then during the test, the field operator could interact with this plan by inserting pauses, jumping over steps, or adding to the preplanned sequence. Because this collector field sequencing test file was determined to be an integral part of the ITP, the test files for the entire test program were technically required at the outset. The experimenter was not prepared to deal with this multitude of decisions without gaining at least some of the operating experience from initial receiver tests.

Another discrepancy that showed up was the need to establish jointly



acceptable procedures for checkout and verification of the test system. Six new procedures were developed and included in the ITP to provide for a thorough step-by-step checkout of the test system. These included end-to-end verification of control and data channels; checkout of the pointing accuracy of individual collectors and groups of collectors when targeted on the BMSR; verification of the air supply compressors and the test air supply piping and controls, including a variety of experiment and facility hardware; checkout of the real-time aperture flux system provided by Sandia Laboratories; and verification of the correct operation of all test backup systems, operator alarms, and automatic shutdown provisions of the test setup.

Finally, a large number of unscheduled events could be foreseen to occur during the course of the solar testing program. At CRTF there were several alternative courses of action for the heliostats following an unscheduled event. These are shown in Table 7.4-1.

To minimize the risk of indecision playing a part in the response to unscheduled events, it was decided to document preferred courses of action for all the unscheduled events that could be envisioned. Resolution of these preferred courses of action required full and complete understanding of CRTF operating and safety procedures by the experimenter and an awareness of the experiment operating and control characteristics by the CRTF test engineer.

After considerable deliberation, three alternative courses of action were defined to cover all the unscheduled events which could be foreseen. These unscheduled events are shown in Figures 7.4-1 through 7.4-3, along with their respective courses of action. As an example of the distinction between procedures 2 and 3, the execution of a "him stow" was a somewhat more reliable means of shutdown than the "emergency standby" procedure; however, recovery to a test status from "him stow" took more than an hour, while recovery from emergency standby could be accomplished in minutes.

All of the problems and concern described in the preceding paragraphs would have been resolved without the formal preparation of an ITP. Nevertheless,

Table 7.4-1. Alternative Courses of Action for Heliostats Following an Unscheduled Event

## Alternative Courses of Action for Heliostats Following an Unscheduled Event

<u>Action by heliostat field operator</u>	<u>Heliostat movement</u>	Time interval to resume testing (time span from initiation of action until targeted heliostats are again aimed at aperture)
<p><b>Pause for evaluation</b> Field operator inserts pause in test file.</p> <p><b>Emergency standby</b> Field operator manually pushes red button at console, also can be initiated automatically for certain events.</p> <p><b>Emergency shutdown</b> Field operator types in ES command at console.</p> <p><b>HIM stow</b> Automatically initiated if HAC is delayed; operator can manually initiate by switching HAC to "half" position.</p> <p><b>Fail-safe</b> Operator opens switch to each target heliostat.</p>	<p>Targeted heliostats remain aimed at aperture. No additional heliostats are brought on target.</p> <p>Targeted heliostats collectively move to standby in a few seconds. They are held at standby until commanded either to move back on target or to move down to the stow position.</p> <p>Targeted heliostats collectively move to standby in a few seconds and then move to stow in about 20 min. Regular startup required to resume testing.</p> <p>All heliostats, including targeted heliostats, move to stow within seconds. (Elevation motors move in slew mode.)</p> <p>Those heliostats for which switches were moved to stow (elevation motors move in slew mode).</p>	<p>0 min (targeted heliostats remain aimed at aperture)</p> <p>5 to 35 min<sup>a</sup></p> <p>45 to 75 min<sup>a, b</sup></p> <p>Approximately 60 min<sup>a, b</sup></p> <p>Approximately 60 min<sup>a, b</sup></p>

<sup>a</sup>Normal on-target sequence from standby takes 35 min, can be reduced to 5 if desired.

<sup>b</sup>Requires about 20 min to go from standby to stow or vice versa.

Figure 7.4-1. ITP Unscheduled Event Procedure 1—Pause for Evaluation

## ITP Unscheduled Event Procedure 1—Pause for Evaluation

### Action

1. Field operator inserts pause in test file.
2. Experimenter delays any planned changes in receiver status.
3. Evaluation of problem.

### Events leading to pause for evaluation

1. Cloud shadowing the heliostats.
2. Loss of control of one or two heliostats in use.
3. Loss or malfunction of instrumentation or control data system channel (except for T1-19 through T8-19, PA5, high-level hydrocarbon detector, and automatic air supply shutoff valve, each of which requires standby action as per procedure 2).
4. Loss of alphanumeric display (does not include color graphics).
5. Evidence of minor damage to test bay or receiver solar shielding (e.g., smoke, cracking, falling fragments).
6. Evidence of minor leakage of coolant to RTAF. (Major coolant leaks require emergency standby action per procedure 2.)
7. Temporary absence of either the experimenter or the heliostat field console operator from their respective control console posts without being replaced by their approved backup. (These absences are for short periods [i.e., a few minutes] and require designation of a temporary backup to monitor the control console during this time interval.)
8. Loss of communications with heliostat field monitor.
9. Hydrocarbon content in air supply to experiment in excess of 40 ppm, as measured on the low-level hydrocarbon detector. (Hydrocarbon content in excess of 2,000 ppm, as measured on the high-level hydrocarbon detector, will require emergency standby action per procedure 2.)

Figure 7.4-2. ITP Unscheduled Event Procedure 2—Emergency Standby

## ITP Unscheduled Event Procedure 2—Emergency Standby

### Action

1. Collector field quickly brought to "standby" condition.
2. Experimenter determines if coolant flow of compressed air is adequate. If adequate, flow controls are not adjusted. If inadequate, BMSR panel valve controls are transferred to the local set point; panel valves then go to full-open position to provide maximum cooling.

### Events leading to emergency standby action

1. Loss of generator power. (Power for heliostat field should immediately switch to commercial power; console operator should immediately command active heliostats to standby as a precautionary measure.)
2. Panelarm indication or picture-display indication of unplanned shutdown of any compressor being used in a test. (For loss of two or more compressors, the entire field should be taken to standby. For loss of only one compressor, a predesignated block of heliostats, representing only a portion of the active field, should be taken to standby. This predesignated block of heliostats to be removed should be large enough so that the solar power input from the remaining targeted heliostats can be accommodated by the remaining operational compressors.)
3. Hydrocarbon content in air supply to the receiver in excess of 2,000 ppm. (This causes automatic closure of air inlet valve at base of tower, and field then is automatically commanded to go to standby.)
4. Any alarm on channels T1-19 through T8-19 (high temperature on outlet air of panels 1 through 8) or PA5 (pressure below 30 lb/in<sup>2</sup>).
5. Loss of control of several heliostats aimed at receiver aperture.

## ITP Unscheduled Event Procedure 2—Emergency Standby (Continued)

Events leading to emergency standby action (continued)

6. Loss of DAS involving just the experiment (does not apply to loss of any computer-controlling solar field as this is covered under HIM stow procedure 3).
7. Loss of receiver-air-temperature control, loss of indication of receiver inlet or outlet temperature, or loss of receiver back-pressure control.
8. Loss of all data displays, color graphics, and CRT displays on the experiment.
9. Evidence of major leakage of coolant from components such as compressors, RTAF, chiller line, or aperture instrument. (Minor leakage calls for pause for evaluation procedure 1.)
10. Loss of instrument (house air) to receive control valves.
11. Loss of 1-MW<sub>t</sub> circulating pump (panalarm). This calls for emergency standby plus immediate manual shutdown of compressors.
12. Loss of chiller cooling system and backup domestic water cooling of calorimeters and radiometers. (Testing is not to be interrupted when chiller cooling system fails if backup domestic water cooling operates satisfactorily.)

Figure 7.4-3. ITP Unscheduled Event Procedure 3—HIM Stow

## ITP Unscheduled Event Procedure 3—HIM Stow

### Action

1. Emergency collector field shutdown to stow. If not initiated automatically, control room personnel can initiate HIM stow by moving switch on HAC from "run" to "halt".
2. Experimenter determines if coolant flow of compressed air is adequate. If adequate, flow controls are not adjusted. If inadequate, the BMSR panel valve controls are transferred to the local set point; panel valves then go to full-open position to provide maximum cooling.

### Events leading to HIM stow

1. Loss of commercial power. This causes HAC computer to lose update capability leading to an automatic HIM stow.\*
2. Loss of collector field control including MCS, HAC, and HAS. (Automatic HIM stow if HIM is still powered; if HIM is not powered, then must activate fail-safe switches.)
3. Burst of rupture disk on receiver or air supply skid.\*
4. Flooding of either the receiver, its controls, or associated DAS components by water from sources such as the fire sprinkler system.

\*For events 1 and 3, the air compressors supplying coolant air to the receiver should be shut down as soon as possible. This is particularly important during event 1 because the pumps in the 1-MW<sub>t</sub> coolant loop will stop functioning when commercial power is lost and the compressors and their diesel engine drives could then overheat.

it was the integrated test system frame of mind inspired by the ITP that provided the cooperative environment needed to deal with them efficiently.

The ITP also became a repository for sets of step-by-step integrated test procedures. These new procedures were based on the BMSR step-by-step procedures described in Section 7.2. In addition, they provided timely references to established CRTF operating procedures and checklists. Being no more than a page or two in length, these procedures effectively referred to all the dozens of pages of detailed procedures. An example of the integrated test procedure for equilibrium heat balance tests of the BMSR is shown in Figure 7.4-4.

Once the ITP was written and approved, BMSR solar-thermal testing could proceed.

## 7.5 SOLAR TEST OPERATIONS

### 7.5.1 BMSR Operating Philosophy

Section 3.0 describes the detailed engineering studies that were conducted to define and verify the BMSR design. The requirements used for these design studies were based on the best estimates of solar test operating conditions available at the time. Even at this early stage of consideration, some test operating conditions were recognized to be hazardous to the receiver. These hazards, identified during the course of receiver design and solar test planning, carried over into the testing program and significantly affected the BMSR test activities and test operating philosophy.

The heat exchanger tubes and the directly sunlit insulation on the cavity wall across from the aperture were determined to be the most susceptible to failure during testing. At solar input power and temperatures corresponding to the receiver design point, both the Inconel 617 heat exchanger tubes and the Saffil blanket insulation were found to operate at temperatures within a few hundred degrees of their maximum service temperatures.

Receiver operating conditions were found that either increased the temperatures of these critical components above their safe levels or increased their operating stresses so as to make operation at the design temperature levels hazardous. Once these conditions were found, the test operations were modified to either completely avoid the hazardous condition or at least postpone it until late in the testing program.

### Heat Exchanger Considerations

The most important problem with the Inconel 617 heat exchangers was the sensitivity of their service life to operating stress and temperature. For example, the BMSR heat exchangers, which exhibited a design lifetime of at least 1000 hr at an operating temperature of 871°C (1600°F), would have a design lifetime of about 100 hr at 927°C (1800°F). This dependence of lifetime at equal stress level on temperature was quantitatively defined by the Larson-Miller parameter for the alloy. These elevated-temperature, stress-rupture characteristics of Inconel 617 have been published by Huntington Alloys, Incorporated, the manufacturer of Inconel metals. They have also been qualitatively demonstrated in the heat exchanger material development tests described in Section 4.0.

Several receiver operating conditions and test events were discovered during the pretest analysis and test planning that could significantly shorten the service life of the BMSR heat exchangers. These conditions are described in the following paragraphs, along with the test planning and operating philosophy used to minimize their effect.

During receiver operation, the temperature of BMSR heat exchanger tubes was controlled by the air flowing inside them. During operation, the airflow rate inside heat exchanger tubes was continuously adjusted to maintain a constant outlet air temperature. The test air supply system provided a constant receiver air inlet temperature. As a result, the air temperature at any point down the length of the heat exchanger tubes was nearly constant. The cavity heat received by these tubes was transferred to the internal airstream by means of turbulent-flow forced convection. A tube-to-air temperature difference resulted as a consequence of this heat



transfer. Therefore, the tube temperature at any point on the heat exchanger depended on three factors: the local air temperature inside the tube, the magnitude of the convective heat transfer coefficient, and the amount of cavity heat received by the local area of tubing wall.

While acting to control heat exchanger outlet air temperatures at constant values, the BMSR control system varied the airflow rate through the heat exchanger tubes in proportion to the amount of solar heat absorbed by the air. As more heat was absorbed by the heat exchanger tube, the airflow rate increased by an equal fraction. As a result, the tube internal convective heat transfer coefficient increased, but at a rate slightly lower than the rate of airflow increase. Therefore, the highest tube temperature (largest tube-to-air-temperature difference) occurred when the receiver was operating at design point airflow rate and outlet temperature and at its maximum (1000 kWt) solar input power level. Lower-than-design-point tube temperatures occurred during steady-state receiver operation at lower solar power input. The conditions of concern for the heat exchanger tube temperatures were outside of this normal operating regime.

All of the restricted flow (RF) tests and one of the originally planned emergency cooldown tests (EC-3) described in Section 7.1 involved receiver operating conditions for which some of the heat exchanger tube temperatures exceeded their normal design temperatures. During the RF tests, the outlet temperature of heat exchanger panel 3 was to be intentionally increased so that its control system would throttle down the airflow through the panel. This process was to be continued until the maximum panel 3 tubing temperature reached a level of 982°C (1800°F). After consideration of the significant reduction of heat exchanger lifetime at this elevated temperature, it was decided to redefine the RF test conditions and to postpone this test until late in the solar testing program. Revisions to the test plan included lowering the overall receiver outlet temperature during these tests from 816°C to 705°C (1500°F to 1300°F) and shortening the time spent with tube temperatures above the normal limit of 871°C (1600°F) by accelerating the test procedure.

The original plan for EC-3 called for increasing the receiver solar input to

1500 kW just before the start of the cooldown transient. This receiver solar input was difficult to obtain because of the large number of CRTF heliostats required. Higher-than-normal design point tube temperatures were also expected during this high solar power operating condition. Both of these concerns influenced the decision to modify the EC-3 test plan, reducing the solar input power level to 1000kWt.

Another receiver operating condition was found to disrupt the normal means of heat exchanger tube temperature control. This was a transient event that occurred every time the temperature set-point was increased on the heat exchanger outlet temperature controllers.

During normal steady-state operation, the BMSR air outlet temperature controllers set the heat exchanger flow control valves at the precise angle needed to obtain outlet air temperatures equal to their set-points. When the temperature controller set-points were suddenly increased, to increase the receiver air outlet temperature, they responded instantly by closing the flow-control valves so that heat exchanger outlet temperatures would rise. Once the temperature increased and became equal to the new set-point, the controller began opening the valve to hold the temperature constant. After a short period of time, the valve position stabilized at the angle corresponding to the new flow rate and outlet temperature. Similar events occurred when the controller set-points were suddenly lowered, except the valves instantly opened rather than instantly closed.

Heat exchanger outlet air temperature was detected by an immersion thermocouple located in the heat exchanger outlet connector. This was in the piping outside the receiver cavity. The control valves were not allowed to close completely because, with no airflow, the thermocouple did not sense the heat exchanger outlet temperature. A mechanical limit stop, located in the valve actuator, was used to prevent the valve from closing beyond an angle of 35 deg.

Another reason for limiting the closing angle of the control valves was to limit the tube temperature increase, above normal operating temperature, which occurred from the sudden increase of temperature controller

set-points. As mentioned earlier, when the set-point was suddenly increased, the controller closed the valve as far as possible. This caused a reduction of the airflow rate through the heat exchanger tubes and a corresponding reduction of the convective heat transfer coefficient within the tube. Because the cavity heat absorbed by the outer surface of the tube and the internal air temperature remained unchanged, the tube-to-air-temperature difference and the tube wall temperature had to increase. The magnitude of the nearly instantaneous tube temperature increase varied in proportion to the magnitude of the instantaneous change of heat transfer coefficient caused by the flow reduction.

Ball valves were used for flow control in the BMSR. Their flow was shut off at a mechanical angle of about 26 deg. The 35-deg minimum valve angle used in the receiver provided for a flow capacity through the closed valve that was about 30% of the flow through a wide-open valve. This meant that if a heat exchanger was operating at receiver design point conditions and its outlet temperature set-point was suddenly increased, its airflow was instantaneously reduced to about one-third of the original rate. If the heat exchanger was initially operating at 90% of its maximum flow capacity with an outlet air temperature of 805°C (1480°F) (ready, for example, to be adjusted to an 816°C [1500°F] outlet), its maximum tube temperature would be about 850°C (1560°F). The instantaneous reduction of airflow through the heat exchanger caused by set-point adjustment increased the tubing temperature to about 916°C (1680°F), well above the normal level. This was the tube temperature overshoot mentioned above that proved to be a hazard to the heat exchangers.

The angular setting of the valve limit stop was increased. This reduced the amount of flow reduction experienced when the outlet temperature setpoints were changed. Tube temperature overshoot was reduced. However, the valve limit stop restricted the range of solar power input over which the receiver maintained its outlet temperature under control. As solar input power was reduced, the controllers reduced the airflow through the receiver to maintain the desired outlet temperature. The 35-deg minimum valve opening was originally expected to carry less than 10% of the maximum receiver airflow; however, increases in the compressor outlet pressure at low

flowrates increased this minimum flow to about 30% of the maximum receiver flow. This meant that the receiver, which was designed to operate at constant outlet temperature over a range of solar input from about 400 to 1000 kW<sub>t</sub>, only maintained its outlet temperature over a range of about 700 to 1000 kW<sub>t</sub>. The valve limit stops were adjusted to a 28- or 30-deg opening angle and the desired 10% to 100% range of flow control was restored. However, this increased the tube temperature overshoot problem and resulted in transient tube temperatures of about 1040°C (1900°F) occurring when the temperature controller set-points were adjusted upward.

The tubing temperature overshoot problem that occurred during adjustment of temperature control set-points was not foreseen during the BMSR design activity. Neither was the action of the test air supply compressors, which caused the minimum receiver flow rate to be 30% of the design point flow rate, rather than 10% as planned. However, the higher level of minimum receiver flow most certainly prevented severe tube temperature overshoot problems from occurring.

For whatever the reason, the 35-deg minimum opening of receiver valves turned out to be a fortuitous choice. However, with a flow control range of 30% to 100% rather than the 10% to 100% originally expected, it was necessary to narrow the range of solar input used during the various tests. Tests for which a 500-kW<sub>t</sub> solar input was originally planned had to be conducted at solar power levels of more than 650 kW<sub>t</sub> to obtain outlet temperature control of all the receiver heat exchangers. Although the tube temperature excursions during temperature set-point adjustments were not so severe or of sufficient duration to significantly reduce the heat exchanger service life, the frequency of these temperature adjustments was reduced as much as possible without compromising test results.

Another BMSR operating hazard, one which was identified during the course of design studies, involved subjecting the heat exchanger tubes to higher-than-normal operating stresses. These higher stresses could cause heat exchanger tube failures at temperatures equal to or less than their normal operating levels.

During the heat exchanger design studies (Section 3.0), it was found that tube stresses were sensitive to the magnitude of the difference between heat exchanger inlet and outlet air temperatures. A stress analysis with 538°C (1000°F) inlet temperature and 816°C (1500°F) outlet temperature showed that stresses in the tubes were 13% less than the allowable stress for Inconel 617. However, a similar analysis using an inlet temperature of 400°C (750°F) showed zero stress margin. These data are shown in Figure 7.5-1.

As the inlet-to-outlet temperature difference increased, the heat exchanger thermal stresses became significantly larger. At first this was not a concern because all the receiver tests called for a 278°C (500°F) difference between inlet and outlet air temperatures.

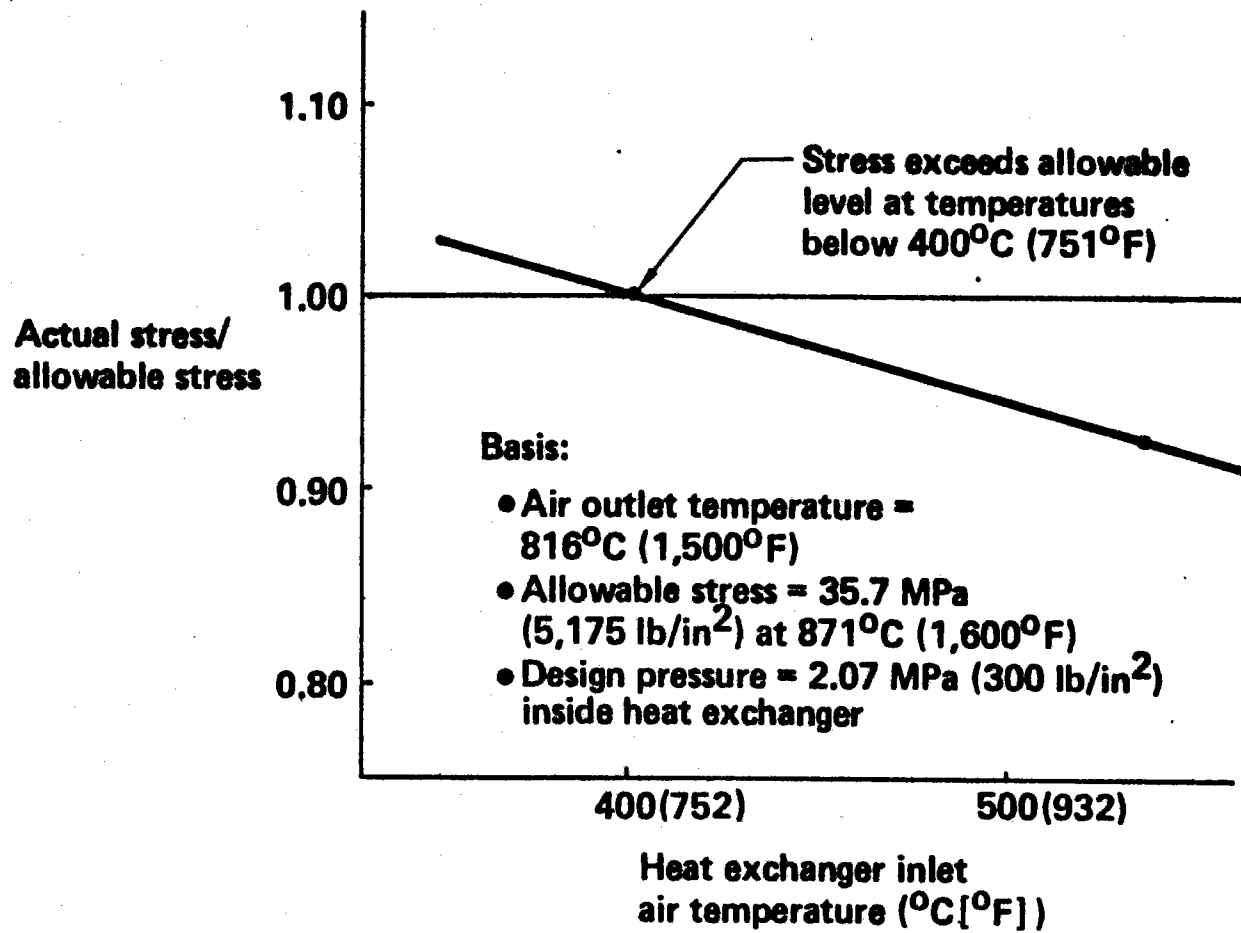
A series of comprehensive transient thermal analyses of the BMSR test setup were conducted as part of the solar test planning activity. The analytical model for these studies included the receiver, the air supply equipment skid, and the receiver interface piping. This model is described in Section 3.0 and shown in Figures 3.5-1 through 3.5-4. During analyses of the receiver startup conditions, this model showed differences between receiver inlet and outlet temperatures of more than 444°C (800°F), thus posing a hazard to the heat exchangers.

When the receiver outlet temperature controllers were in operation during startup, they closed the heat exchanger flow-control valves and reduced the receiver flow rate in an attempt to increase the receiver outlet temperature as rapidly as possible. Because of the valve actuator limit stops, the controllers succeeded in reducing the receiver flow rate to about 30% of the normal design-point flow rate. If the receiver solar input during startup was at or near the 1000kWt normal design level, the air flowing through the receiver heat exchangers had to absorb about three times the normal amount of heat per unit mass. Hence, rather than exhibiting a temperature increase of about 278°C (500°F), the air temperature increased by as much as 900°C (1620°F) as it passed through the heat exchangers.

As a result of the large inlet-to-outlet-temperature difference, it was not difficult to quickly achieve the 816°C (1500°F) receiver outlet temperature

Figure 7.5-1. Effect of Inlet Air Temperature on Heat Exchanger Stress Level

# Effect of Inlet Air Temperature on Heat Exchanger Stress Level



during startup. Even at low solar input power levels, the airflow rate through the receiver was reduced to achieve full outlet temperature.

However, with capacitive heat storage in the air supply piping, the receiver inlet temperature lagged far behind the outlet temperature. The desired control of BMSR inlet-to-outlet-temperature difference during startup could only be accomplished by matching the receiver airflow to its solar-power input. For example, when the BMSR temperature controllers reduced the flow to 30% of full flow during startup, it was necessary to conduct the startup with a solar input, which was also only 30% of the design maximum level, about 300 kWt.

Studies determined whether the experiment system could be brought up to operating temperature more quickly at low solar input power and flow rate or high power and high flow rate. Surprisingly, there was not a great deal of difference in startup time for these two extreme cases; however, the high power and high flow rate startup was faster.

A receiver operating plan was defined that called for startup at an airflow rate equal to or greater than the required maximum level expected during the day's tests. A system of remote controls was devised for adjusting the receiver temperature controller set-points from the CRTF control building. They were added to the CRTF test setup, allowing the normal controller functions to be changed during startup so that control valves would open and airflow rate would be maximized. Once the receiver was up to operating temperature, the controller functions were returned to normal.

The problem of limiting the receiver inlet-to-outlet-temperature difference to 278°C (500°F) or less also affected the receiver operating philosophy during periods when the CRTF collector field was subjected to intermittent shadowing by clouds.

Many of the nearly ideal testing days during the months of December and January were plagued by a scattering of small but opaque clouds interrupting the receiver solar input for a few (5 to 30) minutes. Continuing to operate in spite of these disruptions seemed to be a reasonable design condition to

be required of the solar powerplant. Great difficulty in maintaining receiver operating temperature during these periods was experienced.

As soon as the collector field became shadowed and the solar input to the receiver was reduced, the receiver flow-control valves were closed by their controllers in an effort to maintain desired outlet temperatures. The receiver flow rate would be reduced to about 30% of the maximum design flow rate. This, of course was not sufficient to maintain outlet temperature with no solar input. Within a few minutes after the solar input was reduced, the receiver outlet temperature began to decrease. This loss of receiver outlet temperature marked the beginning of a rather rapid cooldown of the entire test system. This occurred because the high-temperature receiver outlet air was needed to preheat the inlet air.

Once the outlet air temperature began to drop, the inlet temperature followed suit, resulting in even more rapid cooling of the receiver. Then, as the inlet temperature became lower than normal, a serious operational hazard developed: the risk of the collector field being suddenly reilluminated with sunlight and the receiver solar input returning to normal.

Because the CRTF heliostats continued to track during periods of cloud shadowing, their input to the receiver returned to normal as soon as the Sun came out. With the receiver flow rate reduced to 30%, the heat exchanger outlet temperatures quickly returned to their precloudiness level. However, just as during startup, the heat exchanger inlet temperatures were slow to increase because of the thermal capacity of the air supply equipment and piping. The receiver inlet-to-outlet-temperature difference exceeded 278°C (500°F) and tube stresses were greater than normal.

The test operating procedures adopted to prevent excessive thermal stress of the heat exchangers during these periods of intermittent cloudiness were identical to the procedures used during startup. As soon as the receiver inlet temperatures began to drop below the desired test level, the receiver temperature controller set-points were changed to cause them to open the flow-control valves. At full flow rate the receiver accommodated the return



of full solar input without overstressing the heat exchangers.

This was a fail-safe method of operating the receiver on days with intermittent cloudiness. However, opening the flow valves accelerated the rate of cooldown to such an extent that more than an hour of reheat was needed to recover from the cooling effects of a 15-min period of cloudiness.

A different type of test air supply system (e.g. a fossil burner) capable of maintaining the receiver inlet temperature without relying on solar heat delivered by the receiver would have significantly affected the receiver operating procedures during test startup and periods of intermittent cloudiness. Receiver startup time would have been reduced from the 1- to 2-hr periods that were experienced to less than 30 min. The losses of operating time that occurred on days with intermittent cloudiness could have been significantly reduced as well.

#### Receiver Wall Insulation Considerations

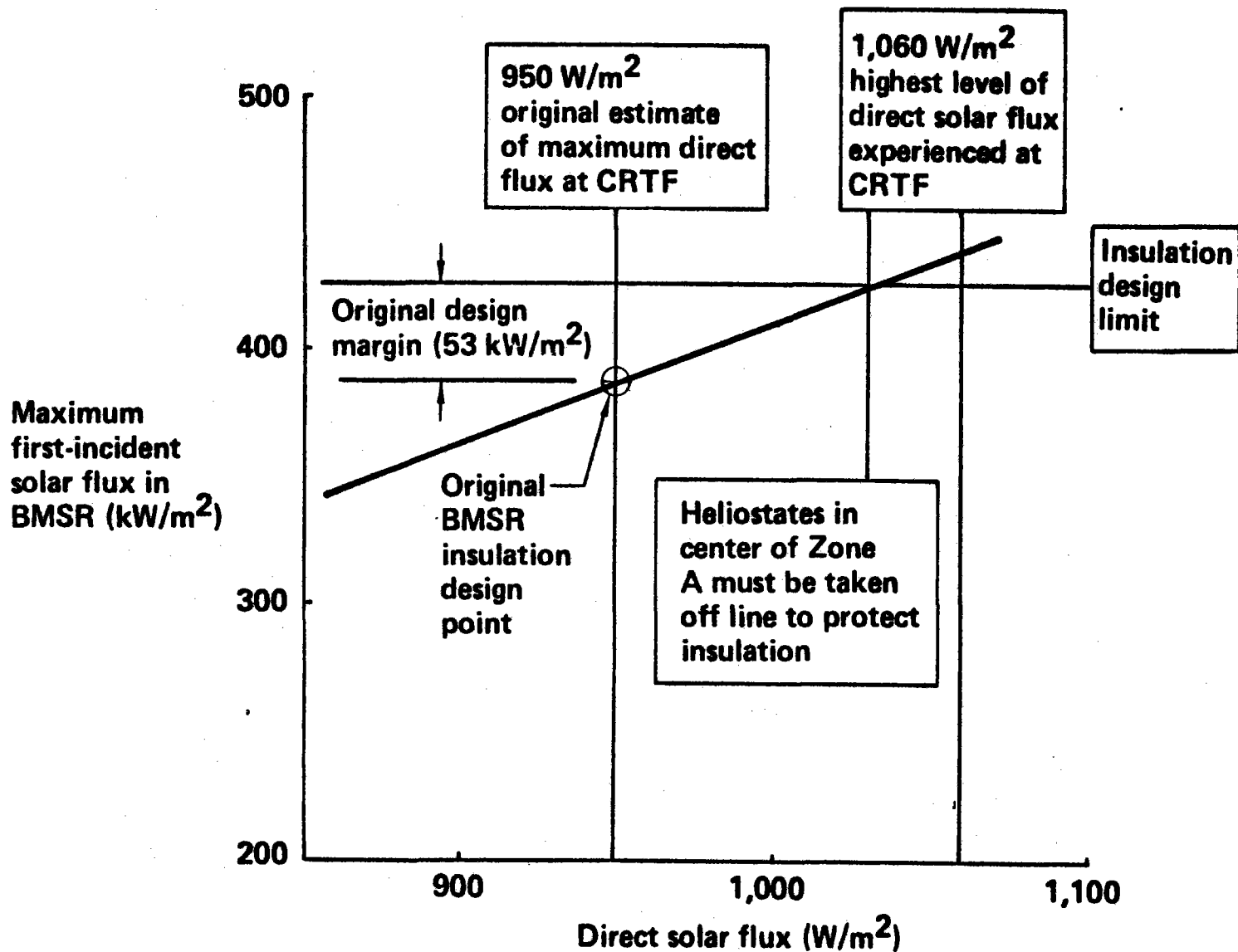
Another operational hazard discovered during the receiver design involved the exposure of the receiver back-cone insulation wall to excessive direct solar flux. Because the reflected sunlight from a particular CRTF heliostat always entered the receiver aperture from the same direction, the same area of the back-cone insulation wall was illuminated by the heliostat. The areas illuminated by various heliostats overlapped one another on the receiver back wall. As many as 21 heliostat images overlapped one another in some areas of the back-cone.

During the BMSR design studies, the assessment of direct solar flux available at CRTF was mainly concerned with the capability of the facility to produce a 1Mwt solar input to the receiver. Conservatism resulted in the establishment of a clear day direct solar flux level of  $950 \text{ W/m}^2$  for design. This design guideline carried over into the evaluation of the maximum direct solar flux to be expected on the back-cone insulation wall.

The data from Figure 3.2-8 is reproduced in figure 7.5-2. Additions to the original figure show the effects of new information obtained after the

Figure 7.5-2. Effect of Higher-Than-Expected Levels of Direct Solar Flux at CRTF

# Effect of Higher-Than-Expected Levels of Direct Solar Flux at CRTF



completion of the BMSR design and before the start of solar tests. This figure describes the direct solar flux that was incident upon a particular point on the receiver back cone. Twenty-one of the CRTF heliostats located near the center of the collector field acted together to produce this heat flux. As the direct solar flux intercepted by the heliostats increased in intensity, the solar flux on the back cone increased proportionally, forcing the insulation wall to higher and higher surface temperatures.

A maximum direct solar flux of  $950 \text{ W/m}^2$  was used for BMSR preliminary design. At the same time, concerns as to the adequacy of the back-cone insulation design and materials showed that they were capable of withstanding first-incident solar-flux levels of  $425 \text{ kW/m}^2$ . This provided an insulation design margin of  $53 \text{ kW/m}^2$  in excess of the first-incident flux initially expected. However, as test plans were being developed, it became evident that even though the  $950\text{-W/m}^2$  direct solar flux was a reasonable upper limit for most parts of the world and an optimistic average value for clear days anywhere, the exceptional atmospheric conditions in Albuquerque during clear winter days could result in direct solar-flux levels as high as  $1070 \text{ W/m}^2$ . As shown in Figure 7.5-2, this increase used up the insulation design margin.

A test operating philosophy was adopted that was intended to retain the insulation heat-flux design margin. It was found that as direct solar flux exceeded  $950 \text{ W/m}^2$ , fewer of the CRTF heliostats were needed to obtain a 1MWt receiver solar input. This was verified during tests at about  $950\text{W/m}^2$  solar flux when only about 56 of the 78 Zone A heliostats were needed to produce a 1MWt solar input to the receiver. Provisions were made in the daily operation plan for the collector field, the daily test file, to be sure that the last few heliostats added in achieving full solar power were from the central region of the collector field. These heliostats, which contributed to all areas of maximum first-incident solar flux on the back cone, would not be required on the days with high levels of direct insolation.

It must also be stated that this plan could not be as rigorously adhered to as was originally intended. Six heliostats in the first ray of the Zone A collector field were severely shadowed by the RTAF frame. They were not used

during the tests. Also three heliostats in the center of the east side of Zone A were always out of service. The original plan to leave 13 of the centrally located heliostats off target on clear days was necessarily changed to include only four heliostats.

#### 7.5.2 Test Operations

Figure 7.3-11 describes the interfaces between the three solar test operators and the various data acquisition and control systems used at CRTF. The CRTF console operator used the collector field display and control console to monitor and direct the action of the CRTF heliostats. The experimenter used the CRTF data acquisition and control system displays and the experiment control console to monitor and direct the operation of the BMSR. The CRTF test engineer used the RTAF data acquisition and control system to conduct scans of the solar-flux incident on the receiver and obtain approximate measurements of the receiver solar input. Using the pretest checklists and top-level procedures of the ITP, the CRTF test engineer was responsible for directing the test activities.

#### 7.6 TEST ACTIVITY SUMMARY

The EPRI/Boeing 1Mwt BMSR was the first experiment to be conducted at the CRTF. The four diesel-powered air compressors provided by EPRI/Boeing for these tests were delivered to the test site during the summer of 1978. They were installed and connected to the CRTF tower piping system while the tower was in its final stages of construction. The BMSR and air supply equipment skid were on site by August 3, 1978. Test preparations commenced at this time, even though the CRTF tower contractor was still at work and the final acceptance testing of the CRTF was yet to be completed.

Pretest activities included positioning of the receiver, air supply equipment skid, and RTAF assembly in the test bay. The experiment controllers, data acquisition and control equipment, and RTAF chiller were installed in the test bay just below the experiment. Then, 84 calendar days were required for the completion of the test setup. Tasks included testing the air compressors to verify flow capacity; testing to verify vendor

calibration of the air supply flowmeters; installing experiment interface piping; completing the piping insulation; connecting and checking out the experiment controls; completing the DACS interfaces by connecting experiment wires and cables to the tower DACS; and installing test bay solar shielding. Sandia laboratory personnel completed this work under the direction of CRTF engineering personnel and the Boeing test engineers who remained on site. The time required for completion of the test setup was longer than had been originally planned. However, the delays were understandable, considering the heavy work load imposed on these personnel by the CRTF acceptance tests that were conducted during this time.

#### 7.6.1 Test System Checkout and Verification

BMSR testing was officially started on October 21, 1978, with the first of three non-solar-heated system checkout and verification tests. The first solar heating of the receiver was accomplished on October 27, 1978.

A calendar of BMSR solar tests is shown in Figure 7.6-1. The solar testing included 21 days of system checkout and verification tests with solar heat, a 77-day period of production testing that ended on February 1, 1979, and 7 days of supplemental production tests conducted in March, 1979.

The checkout and system verification tests are described in Figure 7.6-2. This program of tests was developed as part of the integrated test procedure. As indicated in the figure, the objectives were to provide a step-by-step sequence of increasing complexity as more of the test system was brought into operation. The primary objective was to systematically check out the test system, but this also proved to be a learning period for the test operators.

Sets of data were also obtained to determine the targeting accuracy and solar image characteristics of groups of CRTF heliostats. An aperture flux detector was fabricated by Sandia Laboratories and installed in the receiver aperture for these tests. It had heat-flux gages mounted on 10-cm (4-ft) centers over the lengths of its vertical and horizontal members. They provided solar-flux data used to determine if the heliostat image was

Figure 7.6-1. Solar Testing Calendar

# Solar Testing Calendar

391

	October	November					December					January					March
	30	6	13	20	27	4	11	18	25	1	8	15	22	29	19		
<b>Checkout testing</b>	[Bar from Oct 30 to Nov 13]																
<b>Production testing</b>			[Bar from Nov 20 to Jan 29]														
<b>Conditions preventing test:</b>																	
Experiment not ready			[ ]	[ ]	[ ]	[ ]	[ ]									[ ]	
Facility not ready	[ ]	[ ]	[ ]	[ ]		[ ]	[ ]	[ ]			[ ]					[ ]	
Test personnel not ready	[ ]			[ ]	[ ]	[ ]		[ ]	[ ]	[ ]						[ ]	
Weather prohibitive		[ ]	[ ]	[ ]	[ ]	[ ]	[ ]	[ ]	[ ]	[ ]	[ ]	[ ]	[ ]	[ ]	[ ]	[ ]	
<b>Test opportunities</b>	[ ]	[ ]	[ ]	[ ]	[ ]	[ ]	[ ]	[ ]		[ ]	[ ]	[ ]	[ ]	[ ]	[ ]	[ ]	
<b>Conditions preventing success:</b>																	
Facility problem	[ ]	[ ]	[ ]			[ ]	[ ]				[ ]	[ ]	[ ]	[ ]		[ ]	
Weather				[ ]		[ ]	[ ]	[ ]		[ ]	[ ]	[ ]	[ ]			[ ]	
Experiment problem					[ ]											[ ]	
<b>Usable test data</b>	☆		○○☆	☆☆		☆	○ ☆				☆☆	☆☆	○☆	☆☆☆	☆☆	○☆○	

- ☆ Met test objectives
- Partial results, incomplete test

Figure 7.6-2. Checkout and System Verification Tests

## Checkout and System Verification Tests

Completed tests	Solar input (kW)	Outlet temperature, °C (°F)	Features
CO-1	0	Ambient	Check out DAS and BMSR controls
CO-2	0	Ambient	Check out RTAF
SV-1 (3 tests)	} 30 to 600	} Up to 371° (700°F)	Verification of airflow and controls
SV-2 (4 tests)			Single heliostat targeting
SV-3 (9 tests)			Targeting groups of heliostats
SV-4 (18 tests)			

centered on the receiver aperture.

During the system verification tests with groups of heliostats, it became possible to measure the aperture solar flux while simultaneously conducting an RTAF scan. These data were used for the development of the RTAF transfer function (Section 8.0).

#### 7.6.2 Production Solar Tests

As shown in Figure 7.6-1, the first production solar test was conducted on November 17, 1978. This marked the beginning of a period of time during which each day's goal was the accomplishment of one of the 29 tests defined in the test plan (Section 7.1).

As indicated in Figure 7.6-1, these daily test goals were frustrated by a variety of events. For the purpose of discussion, these events are separated into two categories: those that prevented even the start of a test and those that interfered with its successful completion.

Accurate records of onsite activity were expected to be useful to those planning future solar testing programs. An effort was made to keep track of weather conditions even though other conditions might exist that prevented testing. The solar tests of the BMSR occupied a period of 105 calendar days, 35 of which were ruled out because of weather conditions severe enough to ensure that there was no possibility of accomplishing a test. Even though the weather might be prohibitive at sunrise, the test system was usually brought to pretest status and maintained in a ready-to-test condition until about noon. Some of the successful tests were achieved by using this method to obtain rapid startup when the weather cleared. Successful tests were started as late as 11:00 AM.

Figure 7.6-1 shows other conditions such as experiment and facility problems and test personnel absence prevented testing on other days. The test system was operated on a total of 31 of the 105 calendar days of the solar testing program. These test opportunities were the days for which the system and personnel were ready and the weather was at least good enough to justify



starting up the test system.

Of the 31 test opportunities, 23 resulted in the production of usable test data. Conditions preventing success are shown in Figure 7.6-1. As the test crew became more skilled, it became possible to complete more than one of the 29 planned tests in one good day. As many as four of the planned tests were conducted in 1 day.

Test program highlights and major test events are summarized in Table 7.6-1. A total of 109 hr of solar receiver operation was accumulated during the test program. Because of the good test conditions required and the time needed for the receiver thermal output to heat up the entire test setup, only about 32 hr of this time were spent with the receiver under full control of its outlet air temperatures.

Production solar tests completed during the BMSR test operations are summarized in Figure 7.6-3. This record of completed tests compares favorably with the initial test plans described in Section 7.1. All the planned equilibrium heat balance (EB) tests were conducted. Two of the three planned nonuniform solar input (NI) tests were conducted. Test NI-3 was deleted when the earlier test results showed nonuniform input to have such a minor effect that no further information was expected.

The original plan called for a total of four transient heat load (TH) tests. Two of these tests were to be conducted at conservatively low rates of change of receiver solar input, and two at rates typical of cloud shadowing of pilot plant collector fields. The more conservative of these tests were deleted to accelerate the test program.

The restricted flow (RF) tests were not scheduled to be conducted until rather late in the solar testing program. They were considered to be high-risk tests because of the increased operating temperature of panel 3 heat exchanger tubes. It was also determined that the automatic emergency collector field shutdown feature of the DACS could not be used after the panel 3 outlet temperature was increased to above 844°C (1550°F). This was considered to be extremely risky. As a result of these considerations, the

*Table 7.6-1. Major Test Events*

## Major Test Events

<b>Day</b>	<b>Event</b>
<b>August 3</b>	<b>All test equipment on site</b>
<b>October 27</b>	<b>First solar heating of receiver</b>
<b>November 17</b>	<b>First production test complete</b>
<b>November 19</b>	<b>Calorimeters damaged</b>
<b>November 28</b>	<b>Major damage to BMSR wiring</b>
<b>December 10</b>	<b>Long-term, 40-min operation on control Major damage to DAS</b>
<b>January 11</b>	<b>First full-power test</b>
<b>January 20</b>	<b>Full power at maximum temperatures</b>
<b>January 28</b>	<b>Operated until sunset</b>
<b>January 31</b>	<b>4.6-hr receiver operation at design point</b>
<b>March 1</b>	<b>Back cover reinsulated</b>
<b>March 24</b>	<b>&gt;8-hr solar load following</b>
<b>March 25</b>	<b>Test program concluded</b>

Figure 7.6-3. Summary of Production Solar Tests

## Summary of Production Solar Tests

Completed tests	Solar input (kW)	Outlet temperature, °C (°F)	Features
EB-1	650	816 (1,500)	Heat balance at thermal equilibrium conditions
EB-2	640	705 (1,300)	
EB-3	710	816 (1,500)	
EB-4 (3 tests)	620 to 700	621 (1,150)	
EB-5	800	705 (1,300)	
EB-6	840	816 (1,500)	
EB-7 (2 tests)	830 to 980	621 (1,150)	
EB-8 (3 tests)	910 to 1,030	705 (1,300)	
EB-9 (3 tests)	970 to 1,100	816 (1,500)	
NI-1	775	621 (1,150)	Transition from uniform to east side solar input
NI-2	840	705 (1,300)	
TH-2	1,050	705 (1,300)	Controlled transients
TH-4	1,000	816 (1,500)	
RF-2	830	705 (1,300)	Restricted flow through panel 3
RF-3	1,000	705 (1,300)	
CS-2, -3	1,000	705 and 816 (1,300 and 1,500)	Simulated pilot plant startups and shutdowns
EC-1, -2, -3	750 to 1,000	621 to 816 (1,150 to 1,500)	
SF-2 (3 tests)	950 to 1,100	816 (1,500)	Solar load following

receiver operating temperature for restricted flow tests was reduced from 816°C to 705° C (1500°F to 1300°F). The lowest power case, RF-1, was also deleted to accelerate the testing program.

One of the cold startup (CS) tests was deleted. This was the most conservative CS test in the plan. Other shaving higher initial solar heat loads were conducted with no difficulty. One change was required that deviated from the planned emergency cooldown tests when it was learned that the collector field could not routinely produce a 1.5 MWt solar input to the receiver. Even with all the CRTF heliostats in operation, the system could only provide 1.5 MWt for a short period of time around noon. It was determined that this prime testing time was better utilized by conducting other tests. An emergency shutdown test would have cost several hours for restart of the system; instead, an emergency cooldown was conducted from a 1MWt solar input condition using all other features of the EC-3 test.

During the test program there were only 2 days on which full days of solar-load following were accomplished. These tests extended from early morning to late afternoon under generally clear skies. However, partial days of solar-load following were accomplished on three other occasions. These included two mornings and one afternoon of testing.

Section 8.0 describes the BMSR test data acquired during these solar receiver tests. Solar heat load measurements are also discussed along with the other test measurements that were obtained. Section 9.0 presents a detailed evaluation of results of each of the six groups of tests (Figure 7.6-3) as well as the other more general results of observations of test effects on the receiver.

## SECTION 8.0 TEST DATA BASE

### 8.1 SOURCES OF TEST DATA

Six different types of documentation were used to record test events and data during the solar testing program. These included: (1) engineering data tapes, (2) heliostat field operation records, (3) real-time aperture flux data, (4) meteorological data, (5) daily logs, and (6) test logs. They are described in the following paragraphs.

Data recorded during the BMSR testing provided documentation of the receiver performance during each test event. These data were used to check receiver performance under various conditions and to help determine preferred operational procedures for future solar receivers. The most comprehensive of these test records were the engineering data tapes produced at the CRTF using the data acquisition and control system (DACs). During a test, the BMSR instrumentation, the command and control functions of the experimenter's console and a number of test facility sensors such as the Eppley pyrheliumeter interfaced actively with the DACs. One of its functions was to record these data (on 4 to 12 sec intervals) throughout the duration of the test.

These data were "raw" data (voltage signals from each sensor) and were not conveniently usable in this form. It was made usable by posttest processing by conversion to engineering unit format. These processed data were recorded on magnetic tape for storage and future examination. A great deal of posttest data processing has been conducted with the engineering data tapes and is described in Section 8.2. Section 7.3.3 contains a more detailed description of the DACs.

In addition to BMSR data acquisition, there were three other computer controlled activities in progress during the solar tests. The heliostats in the CRTF collector field were operated by computer, processing commands from the field operator. These commands were printed out during the test along with diagnostic and operational feedback from the heliostat field computer.

A typical listing of activities showed the exact time each heliostat was brought on target or removed. These records provided a direct means of posttest assessment of the heliostats on target at any particular time. The record also showed the periods of time when the collector field alignment on target, was held constant to obtain steady-state conditions in the receiver. These records have been used to determine the exact heliostats in use during each of the equilibrium heat balance tests. Use of these data is described in Section 8.4.

Another computer-controlled activity during testing was the use of the real time aperture flux system (RTAF). This system is described in Section 7.3.1. On command, the RTAF scanning bar would pass across the solar image just in front of the receiver aperture. Heat flux sensors spaced along the scanning bar would measure solar flux profiles along their line of action. Data from all sensors along the bar were stored in the form of a solar flux map. These data, in the form of computer printouts of the flux patterns, were available for each of the several dozen scans conducted during the tests.

The CRTF system periodically scanned and recorded ambient meteorological data from the on site weather station. This record provided the wind speed and direction information used to evaluate effects of wind during the various tests.

Additional handwritten records were available, including two types of log books maintained by the experimenter as well as various manually recorded test and calibration data.

The experimenter's daily log summarized the highlights of each day's activities on site at CRTF. This included results of daily visual inspections of the receiver, notations of changes in transducers used for pressure measurements, and the results of frequent leak tests conducted on the receiver and air supply system.

The experimenter's test log consisted of an annotated record of all pertinent activities that occurred during each day of testing. Changes in

receiver operation (i.e., temperature set-point adjustments) were noted as well as the changes requested in the operation of the collector field such as adding or removing collectors. Also noted were any unusual events such as interruption of tests by clouds or anomalies observed in the receiver operation. In addition to the daily written record of test activities, the experimenter's test log was supplemented by all pertinent information, which had to be recorded by hand. These data included pretest zero-pressure calibration of all the pressure measurements in the experiment. These daily calibrations were instituted early in the test program when it was noted that pretest zero calibrations had changed by a significant amount. The changes were attributed mainly to environmental effects and aging of the transducers and were too large to be ignored. These daily calibrations were instrumental in posttest processing of the pressure data. Also, the experimenter's test log was a convenient repository for supplementary measurements conducted during the tests. During various tests, these measurements included scans of the aperture radiosity, effective cavity temperature, and aperture air velocity.

## 8.2 TEST DATA PROCESSING

During the testing of the BMSR, 25 engineering data tapes were produced at the CRTF. Of these 25 data tapes, 18 were chosen for more detailed posttest examination and analysis (the remainder of the tapes corresponded to unsuccessful test days). However, because of differences in computer systems, the CRTF engineering data tapes required special processing to be made usable at Boeing. The data tapes, in their final form, were condensed and restructured for optimum access of data. A description of the processing of these tapes follows in this section. The interpretation and use of the test data tapes is described in Section 12.

The raw data tapes provided by the CRTF were inconvenient to use. This was because each datum had system information coded into it that had to be extracted, and a conversion factor had to be applied to resolve the data from voltage signals to engineering units. CRTF personnel devised a method whereby an engineering unit data tape could be produced from the raw data tape using an existing computer program.

The creation of these engineering data tapes seemed to solve the problem of accessing and interpreting the test data. However, it turned out to be only a partial solution. The first difficulty came about when it was realized that the tapes were written in a format unique to the type of computer system the CRTF used. This meant that for posttest data reduction, either a similar computer system had to be used, or the tapes had to be rewritten. Because easy accessibility to the data was essential for test analyses, it was decided to process the tapes with the Boeing computer system. Figure 8.2-1 shows the relationship between the three levels of data tape produced.

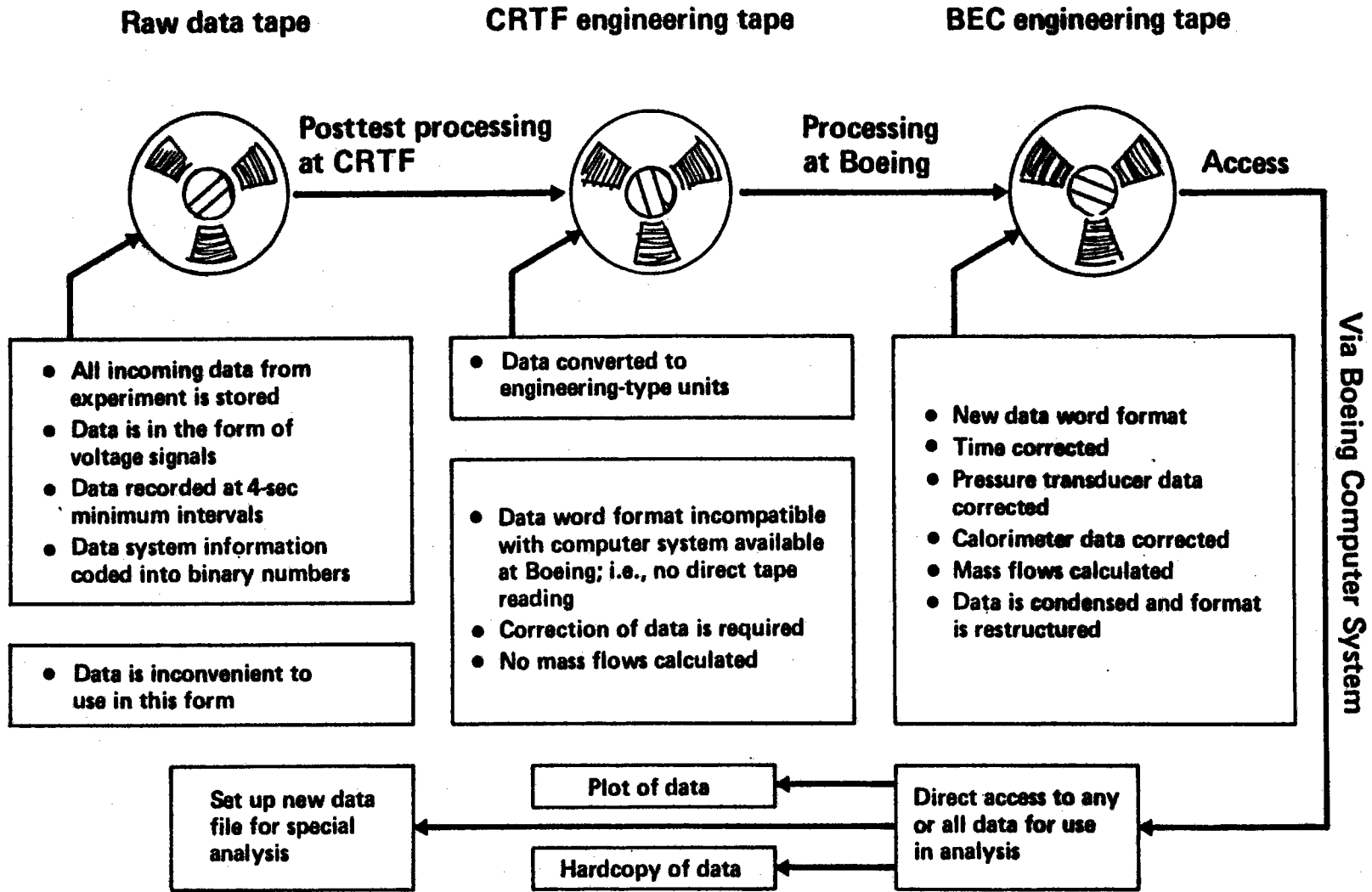
The data tapes were rewritten in a more universal format. It was learned, however, after beginning the process, that several inconsistencies were present in the CRTF engineering tapes. With EPRI/Boeing being the first to test at the facility, there were many "bugs" in the system that would only surface as a result of actual usage. Corrections and improvements to the software were continually being made as the test progressed. Each tape had its own particular problems and each had to be treated individually.

The largest single error was in the pressure transducer conversion factors. These readings in themselves were not critical, but all the mass flows were calculated with these numbers. A small deviation in pressure reading could produce a large error in a mass flow calculation. The DACS display package normally read the conversion factors from a table. There were two variables required for each transducer: a voltage offset and a conversion factor ( $\text{lb/in}^2$ ). Originally (before testing of the BMSR began), these values were programmed into the display package, not expecting to have to change them. However, it was soon realized that the transducer offsets tended to vary from day to day, and if a transducer went bad it would have to be replaced (requiring a new conversion factor). This meant the transducer variables might be changed on a frequent basis, as it turned out, offsets were changed on a daily basis. Therefore, the display program was changed to include a variable table that could be updated at any time. A modified version of the display package program was used to create the CRTF engineering tapes but all the problems had not been resolved. When the program was used, the original pressure transducer conversion factors were read. This was further complicated because some of the transducers were moved or replaced.



Figure 8.2-1. Data Tape Processing

# Data Tape Processing



Fortunately, a chronological map of the transducer positions was kept, along with the daily offsets and conversion factors. To correct these data then, a pressure transducer datum was read from the CRTF tape, the original millivolt signal was extracted (using the old values), and then recalculated with the correct values. Other less critical errors were also discovered, but most of them did not affect the data, only the reading of the tape.

In addition to the corrections made, calculated data (mass flows) not present on the CRTF tapes were added, the data was condensed to include only pertinent test data, and the data format was restructured for easier and faster access. At this point, the data were accessible for analysis as shown in Figure 8.2-1. Data plots could be computer generated, a hardcopy of all the data on 5-min intervals had been produced (see Section 12 for example), and data at any time interval could be reproduced and either printed or set up on a new file for further analysis.

Figures 8.2-3 to 8.2-8 are examples of computer-generated plots of test data. Figure 8.2-2 is a time chart for the test day. A set of computer-generated plots for all the successful test days is in Section 12.

### 8.3 TEST DATA UNCERTAINTY

#### 8.3.1 Experiment Instrumentation Errors

Table 8.3-1 lists the 10 different types of instrumentation devices used on the BMSR and air supply equipment skid. There are four varieties of thermocouples, strain-gage pressure transducers with high and low measurement ranges, water-cooled circular foil heat flux gages, precision potentiometers to measure valve angles, and flow measuring devices, including venturi flowmeters on the air supply equipment skid and calibrated ball valves on the receiver heat exchangers. Correction factors were required to compensate for the measurement offsets that occurred with some of the thermocouples and all of the pressure transducers. They are described in the following paragraphs, along with estimates of the maximum errors expected from all these devices.

#### Thermocouples

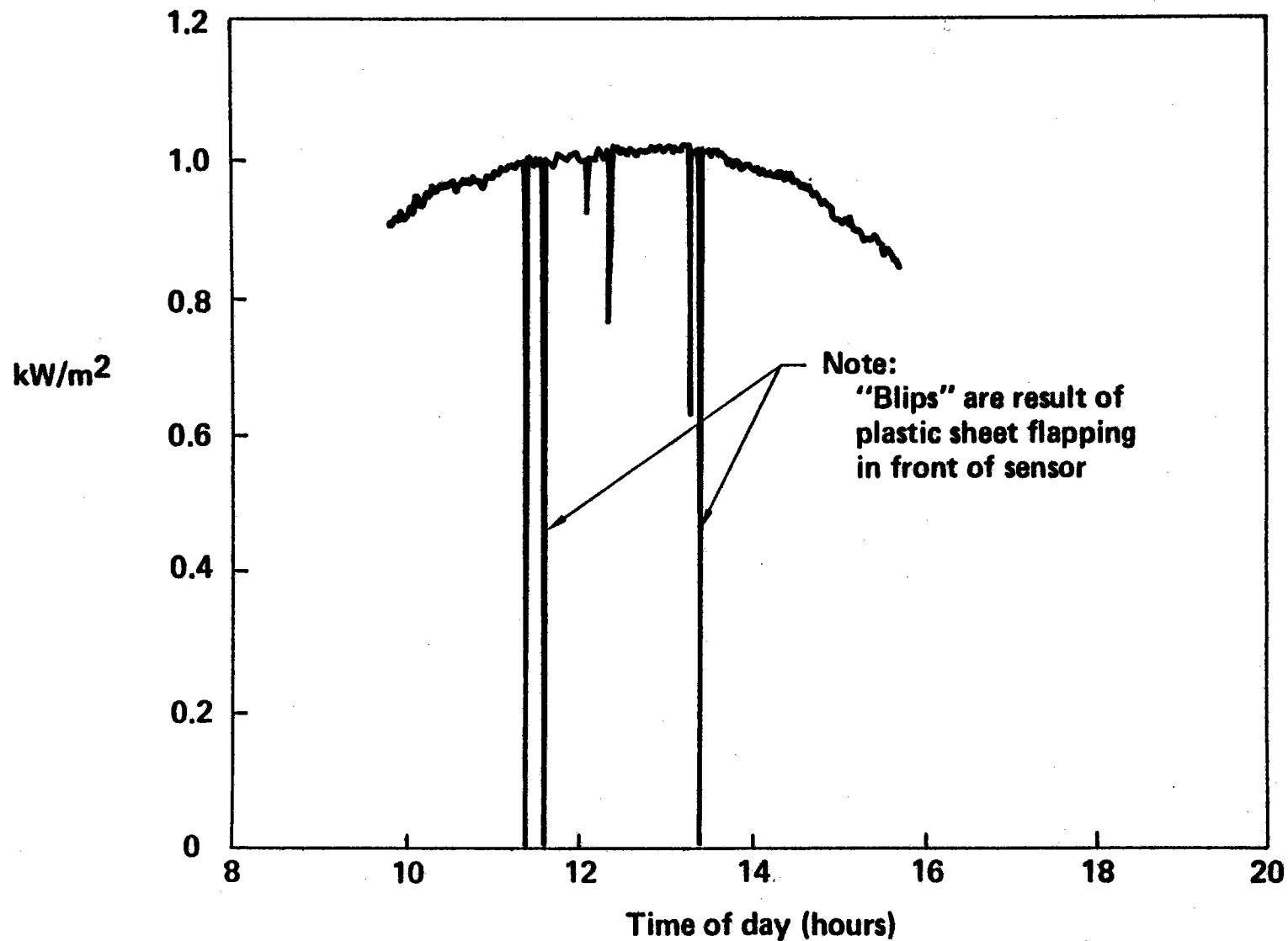
*Figure 8.2-2. Time Chart for January 20, 1979 Solar Test*

## **Time Chart for January 20, 1979 Solar Test**

<b>9:45</b>	<b>Field at standby</b>
<b>9:50</b>	<b>First collector on target</b>
<b>10:26</b>	<b>58 collectors on target</b>
<b>10:58</b>	<b>62 collectors on target</b>
<b>11:31</b>	<b>Receiver on control</b>
<b>12:10</b>	<b>Steady test conditions, EB-9A</b>
<b>12:52</b>	<b>Steady test conditions, EB-9B</b>
<b>13:25</b>	<b>53 collectors on target</b>
<b>13:49</b>	<b>Steady test conditions, EB-6A</b>
<b>14:03</b>	<b>47 collectors on target</b>
<b>14:21</b>	<b>49 collectors on target</b>
<b>14:23</b>	<b>55 collectors on target</b>
<b>14:44</b>	<b>51 collectors on target</b>
<b>14:53</b>	<b>Steady test conditions, EB-3A</b>
<b>15:29</b>	<b>Field at standby</b>

Figure 8.2-3. Plot of January 20, 1979 Test Data, Eppley Pyrheliometer

# Plot of January 20, 1979 Test Data, Eppley Pyrheliometer



405

Figure 8.2-4. Plot of January 20, 1979 Test Data, Air Supply Gas Temperatures

# Plot of January 20, 1979 Test Data, Air Supply Gas Temperatures

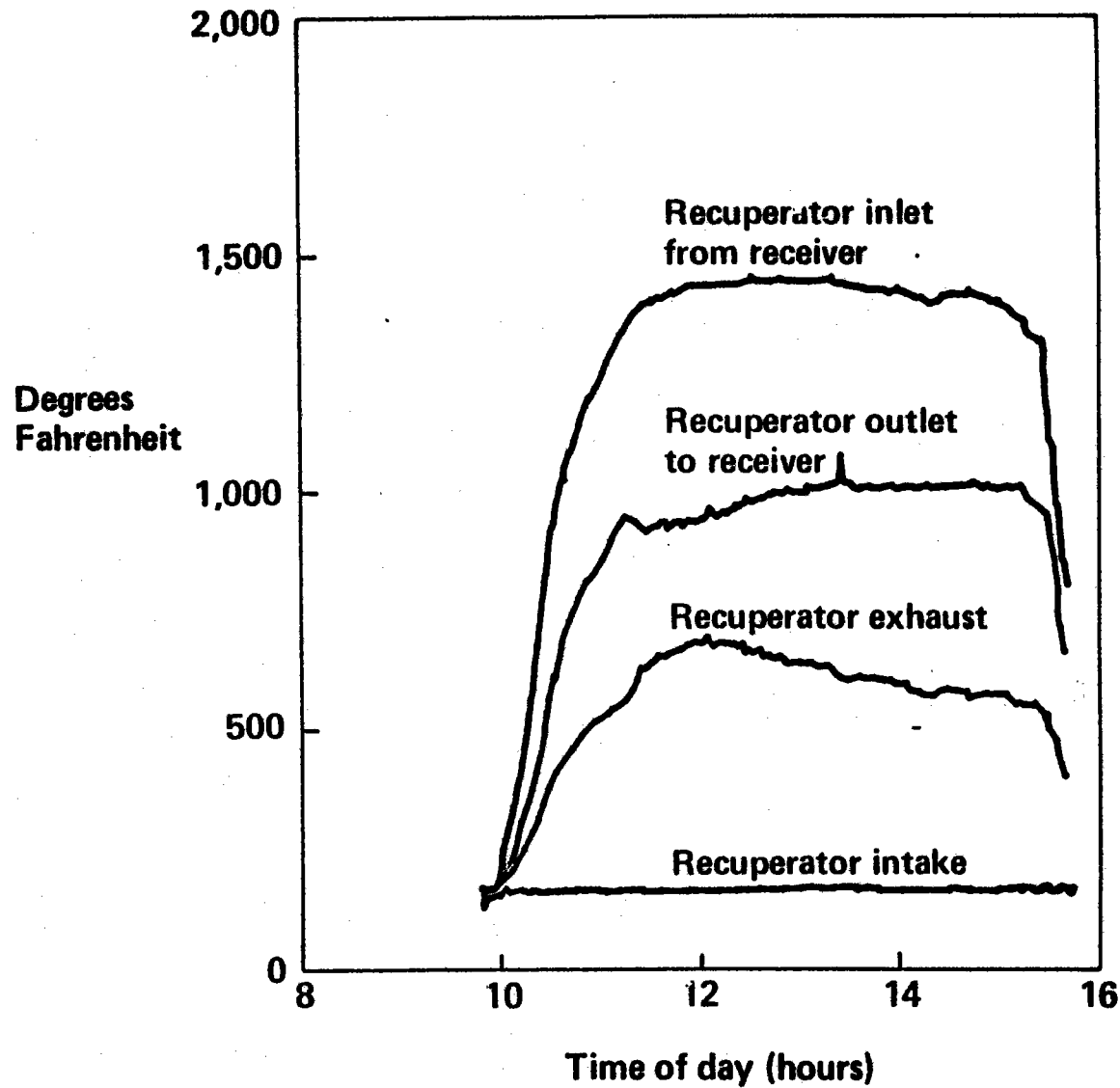


Figure 8.2-5. Plot of January 20, 1979 Test Data, Frame Calorimeters

## Plot of January 20, 1979 Test Data, Frame Calorimeters

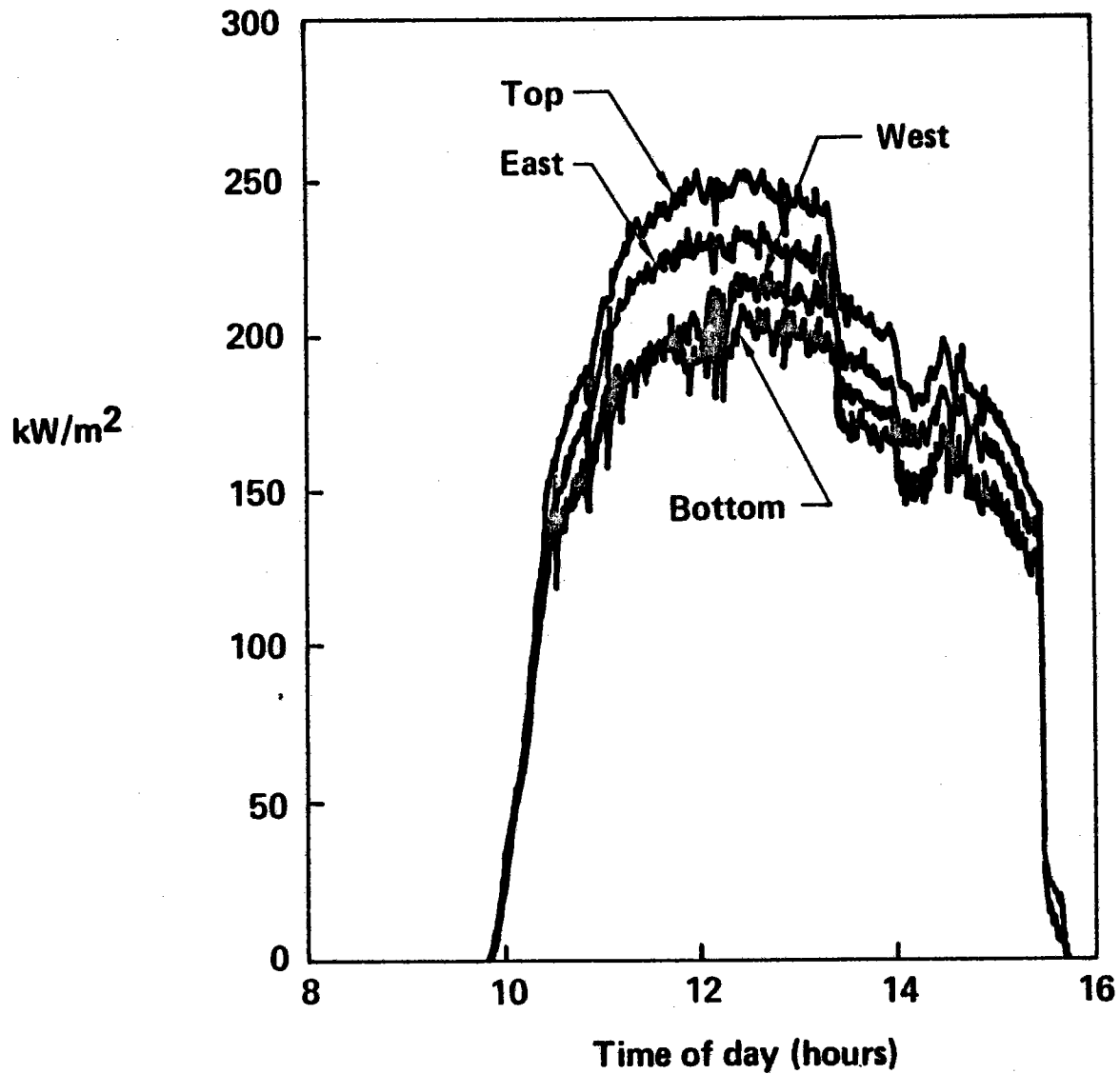


Figure 8.2-6. Plot of January 20, 1979 Test Data, Receiver Mass Flow

# Plot of January 20, 1979 Test Data, Receiver Mass Flow

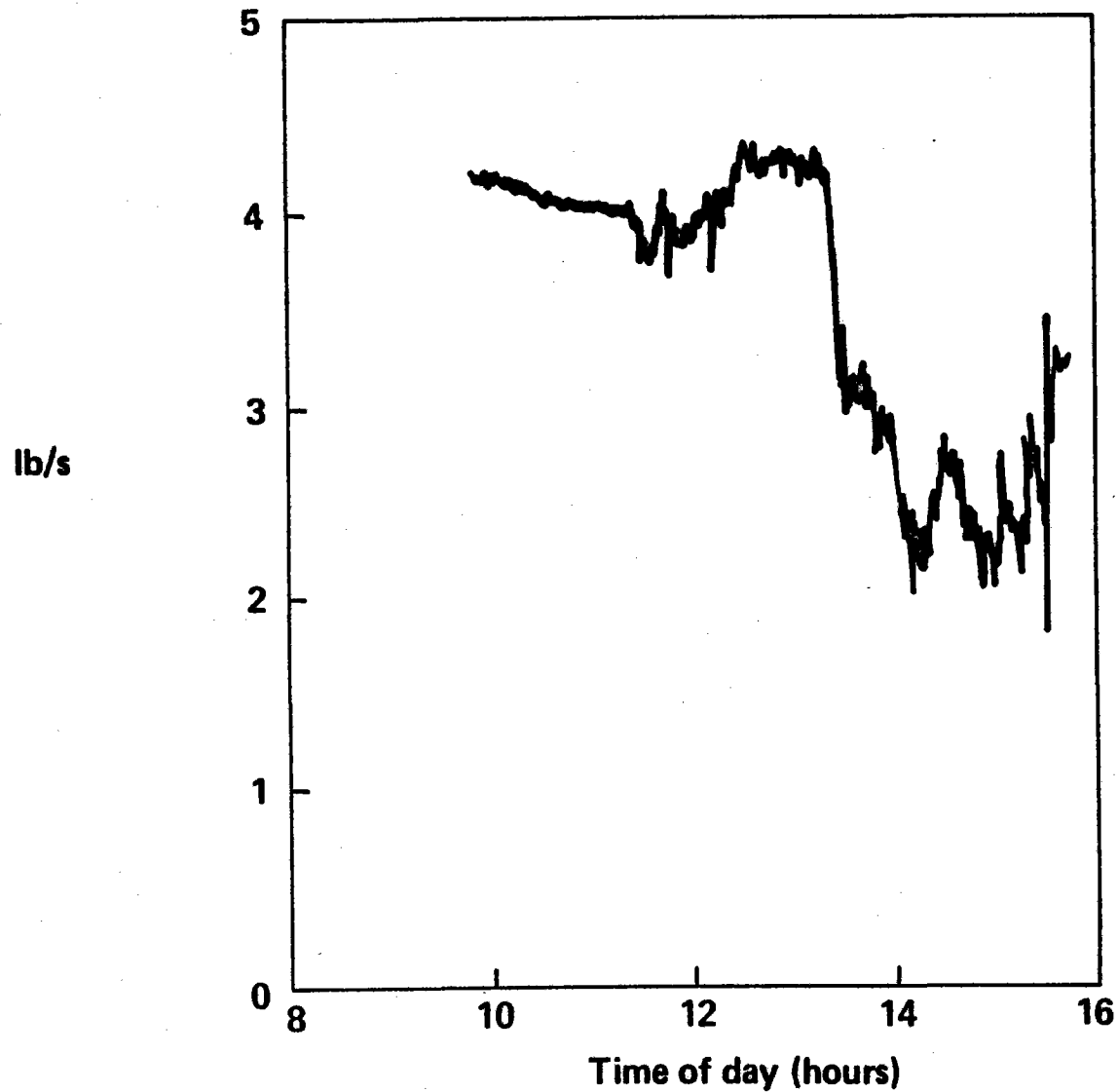


Figure 8.2-7. Plot of January 20, 1979 Test Data, H/X Panel Three-Valve Angle

### Plot of January 20, 1979 Test Data, H/X Panel Three-Valve Angle

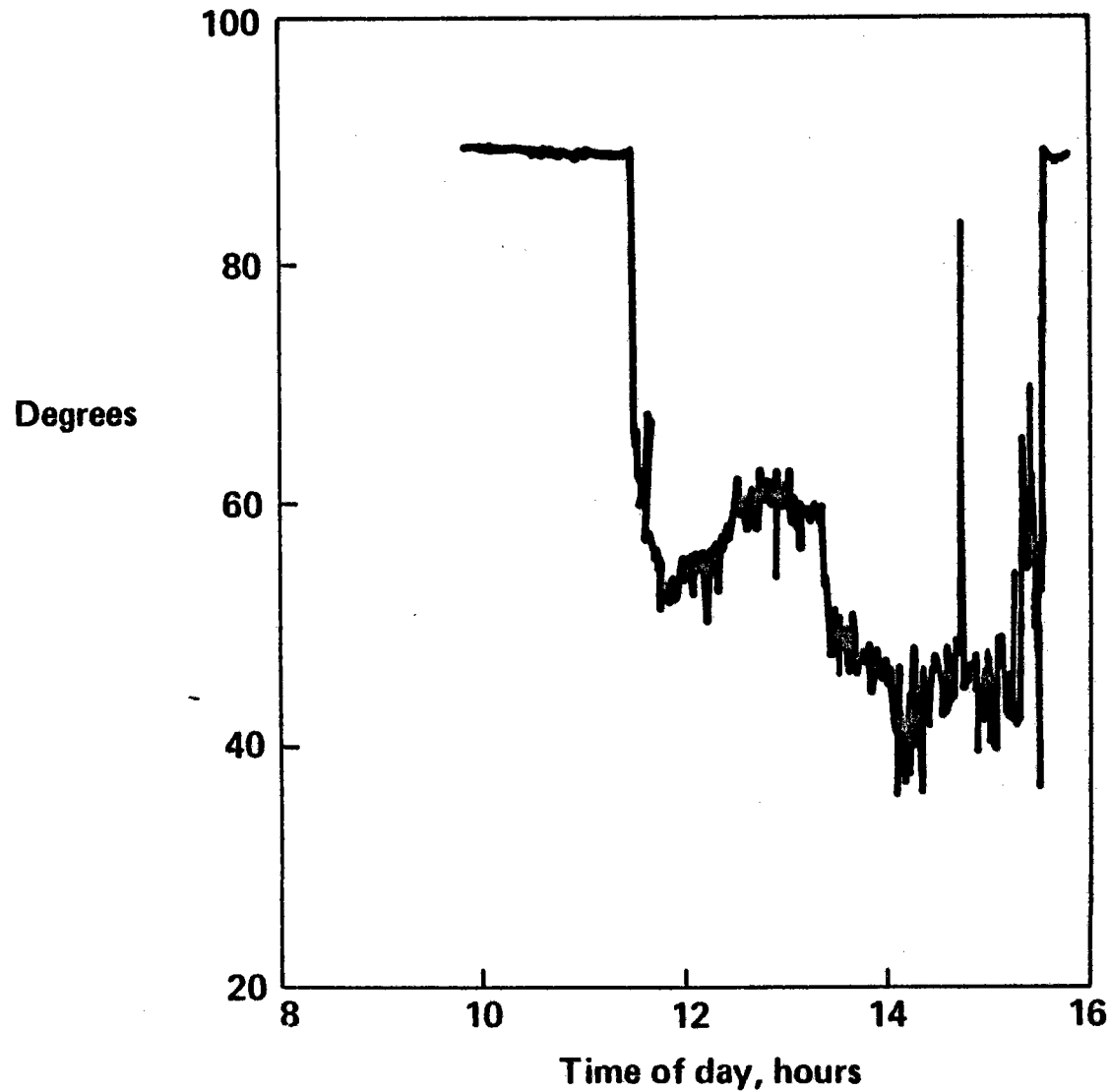
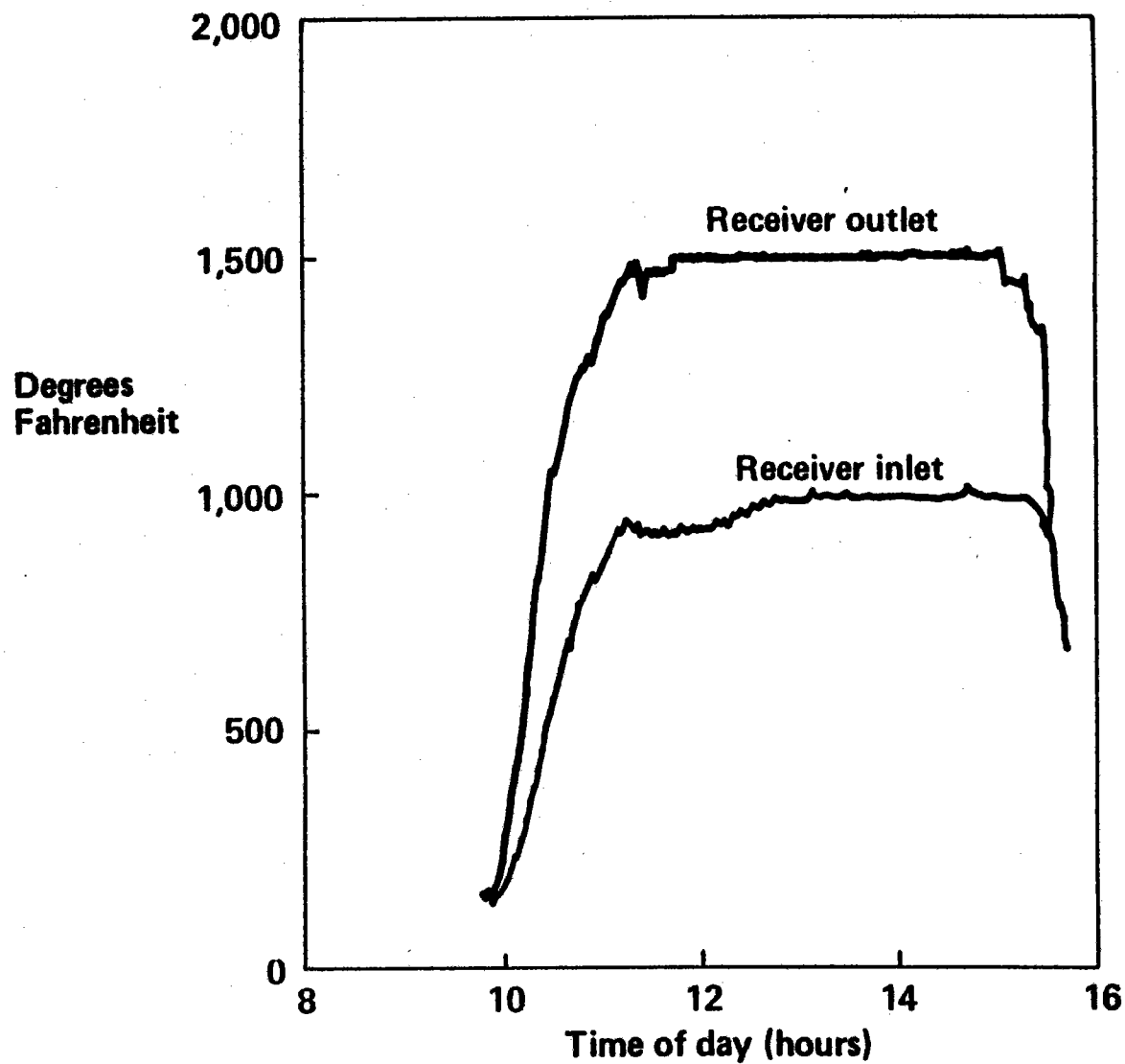




Figure 8.2-8. Plot of January 20, 1979 Test Data, Air Inlet-Outlet Temperatures, Panel 3

## Plot of January 20, 1979 Test Data, Air Inlet-Outlet Temperatures, Panel 3



## BMSR Instrumentation

### 1. Thermocouples

- ⊙ Heat exchanger air inlet and outlet
- ⊙ Heat exchanger tubes
- Insulation
- Receiver frame structure, valve actuators, metal cone behind aperture, heat flux gages, calorimeter coolant

### 2. Pressure transducers

- ⊙ Gage and differential pressures to 1.0 MPa (150 lb/in<sup>2</sup>)
- ⊙ Differential pressures to 0.17 MPa (25 lb/in<sup>2</sup>)

### 3. Heat flux gages

- Receiver wall calorimeters, back cone calorimeters, radiometer

### 4. Valve angle potentiometers

- Receiver flow control valves, backpressure and recuperator bypass valves on the air supply equipment skid

### 5. Flow measuring devices

- Universal venturi flowmeters for total receiver flow and recuperator bypass flow
- Calibrated ball valves for individual receiver heat exchanger flow rates

- ⊙ Correction required to compensate for zero offset and systematic errors

Two types of transducer errors were associated with thermocouple temperature sensors. Differences in the chemical and metallurgical composition of the wire and the fabricated thermocouple junctions accounted for differences in their voltage output at equal junction temperatures. The most effective methods of reducing these errors were to use wire for which specific limits of quality were guaranteed by the manufacturer and to use standardized and accepted processes of fabricating the welded thermocouple junctions. All the BMSR thermocouples were manufactured by a qualified supplier using "ANSI Special Limit Grade" thermocouple wire. Four different types of wire, all chromel-alumel having different conductor sizes and electrical insulation, were used to fabricate the thermocouples on the experiment. The ANSI-specified limits of error for the resulting thermocouples (not including installation errors) were  $\pm 1.1^{\circ}\text{C}$  ( $\pm 2^{\circ}\text{F}$ ) or  $\pm 0.38\%$  of their reading, whichever was greater. These limits of error applied for thermocouple operation over the range of  $0^{\circ}$  to  $1260^{\circ}\text{C}$  ( $32^{\circ}$  to  $2300^{\circ}\text{F}$ ).

Installation effects accounted for the other errors that occurred with thermocouple temperature sensors. These errors were caused by the existence of a heat flow and corresponding temperature gradient between the point of interest and the thermocouple junction. Two of the four types of thermocouple installations on the experiment exhibited significant offset because of temperature gradients, and two of them did not.

Thermocouple junctions consisting of bare wires fused into a spherical weld bead were used for all the low and intermediate temperature measurements. This included thermocouples on the structural frame, coolant lines and heat-flux gages, and the valve actuator temperature sensors. All these thermocouple junctions were either welded or mechanically clamped to the measurand with sufficient force to ensure accurate measurements.

The suitability of sheathed thermocouples for use within the cavity wall insulation was thoroughly investigated during the insulation development tests (Section 4.0). Plain sheathed thermocouples with a length of sheath equal to 200 times the sheath diameter and located in the same insulation layer as the junction, were found to exhibit negligible thermal gradient error.

The two types of BMSR thermocouple installations found to exhibit thermal gradient errors were the heat exchanger tube temperature and the heat exchanger inlet and outlet air temperature thermocouples.

#### Heat Exchanger Tube Temperature Measurements

The heat exchanger tubing temperatures were measured at 48 locations within the receiver cavity. Thermocouples were installed near the outlet end of the 9th, 27th, and 45th tube ( as measured from the outermost tube on one end) on each of the eight 54-tube heat exchangers. Inlet and U-bend temperatures were measured on tubes next to these on the four (top, bottom, east-side, and west-side) heat exchangers. Similar thermocouples and installation techniques were used throughout. These are shown in Figure 8.3-1.

Small-diameter (0.16 cm [0.6 in]) Inconel-sheathed chromel-alumel thermocouples were used for the heat exchanger tube temperature measurements. Thermocouple reliability was increased by using ungrounded junctions throughout. Special fittings were fabricated from Inconel sheet material and nicel brazed to the tip of these thermocouples. Their installation on the heat exchanger tubing involved positioning of the sheath and junction on the back (nonsunlit) side of the tube, routing the sheath out of the cavity by passing it alongside the heat exchanger tube, and thoroughly spot welding the tip fitting to the tube. These details are shown in Figure 8.3-1.

The tip of the sheathed thermocouple that indicated heat exchanger tube temperature was thermally coupled to the tubes by conduction through the welded-tip-fitting attachment and was radiatively heated by the solar and radiant flux in the receiver cavity. The conductive heat transfer path from the tip fitting to the tubing was not large enough to prevent temperature differences from occurring between the thermocouple junction and the adjacent tubing wall. However, the tip-fitting design provided well-defined heat transfer paths; the conduction, convection, and radiant heat transfer mechanisms involved were readily analyzed.

Figure 8.3-1. Details of Heat Exchanger Thermocouple Installation

## Details of Heat Exchanger Thermocouple Installation

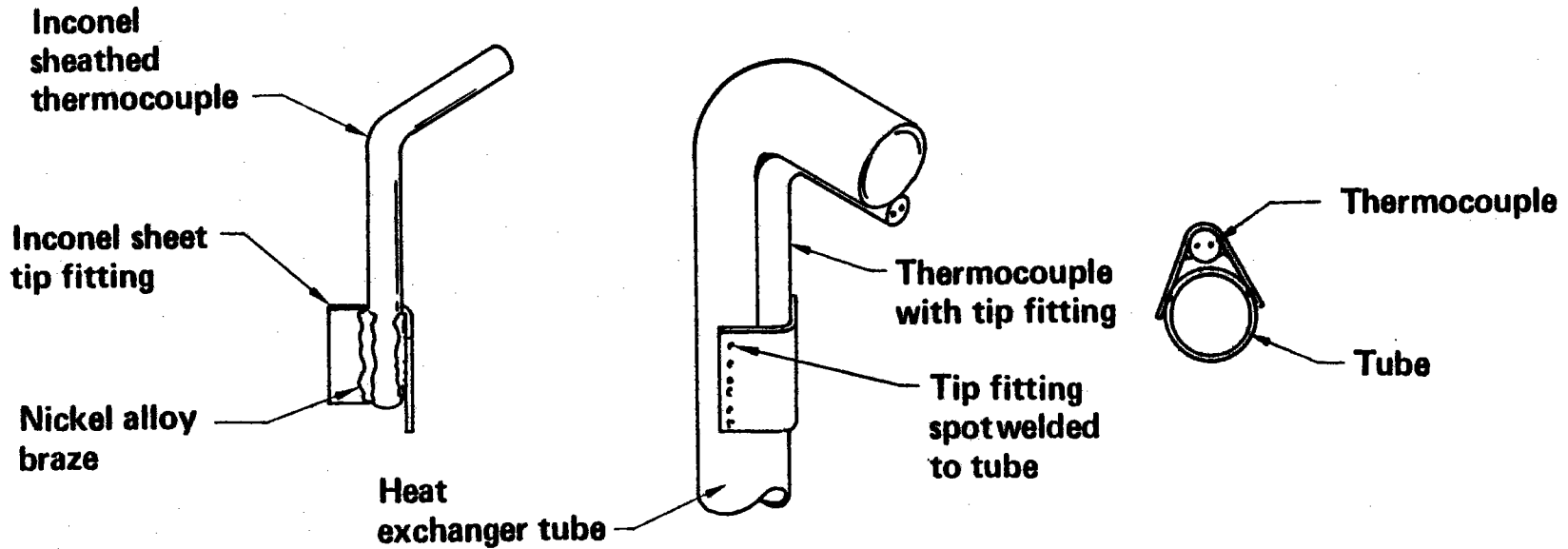
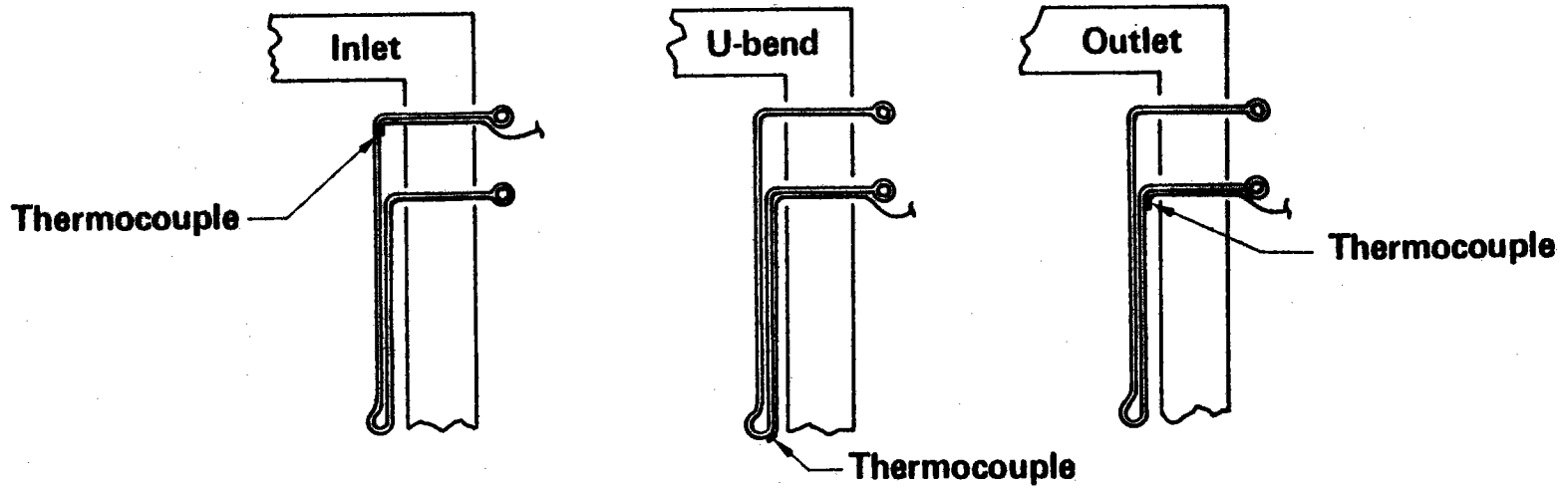


Figure 8.3-2 shows the results of analyses of the thermocouple installations used to indicate heat exchanger tubing temperatures. Because of their locations on the back of the heat exchanger tubes, the thermocouples were affected by the heat radiated from the adjacent region of cavity insulation wall. The temperature of this wall was always equal to or greater than the heat exchanger tubing temperature. As a result, heat from the wall increased the thermocouple temperature so that it always indicated a temperature higher than the tubing temperature. This excess temperature error is plotted in Figure 8.3-2 as a function of the indicated tube temperature and the effective cavity wall temperature.

These temperature corrections were subtracted from the indicated thermocouple temperature to define heat exchanger tube temperatures. Examination of test data showed that these corrections ranged in value from 60°C (108°F) at low tube and wall temperature conditions to as much as 180°C (324°F) at high solar input power and receiver design point operating temperatures.

The measured tubing temperatures provided valuable information on the distribution of heat within the cavity. Compared with one another, the 24 measurements of tube temperature near the outlet provided indications of the relative heat transfer occurring in each of the heat exchanger panels that agreed with other methods of measurement (Section 9.0). However, they were not accurate enough to determine differences between tube wall and internal air temperatures for the purpose of quantitatively evaluating the gas-in-tube heat transfer coefficients in the heat exchangers.

#### Heat Exchanger Air Temperature Measurements

The other BMSR thermocouple installation for which test data were corrected to compensate for thermocouple installation effects was the measurement of heat exchanger inlet or outlet air temperature. These thermocouples were installed in the connector pipes that extended between the heat exchangers and the receiver inlet and outlet manifolds. The details of this thermocouple installation are shown on Figure 8.3-3. The connector pipe was 51 cm (2.0 in) in diameter with a 6.4 cm (0.25 in) wall thickness. The

Figure 8.3-2. Corrections Required for Heat Exchanger Tube Temperatures

# Corrections Required for Heat Exchanger Tube Temperatures

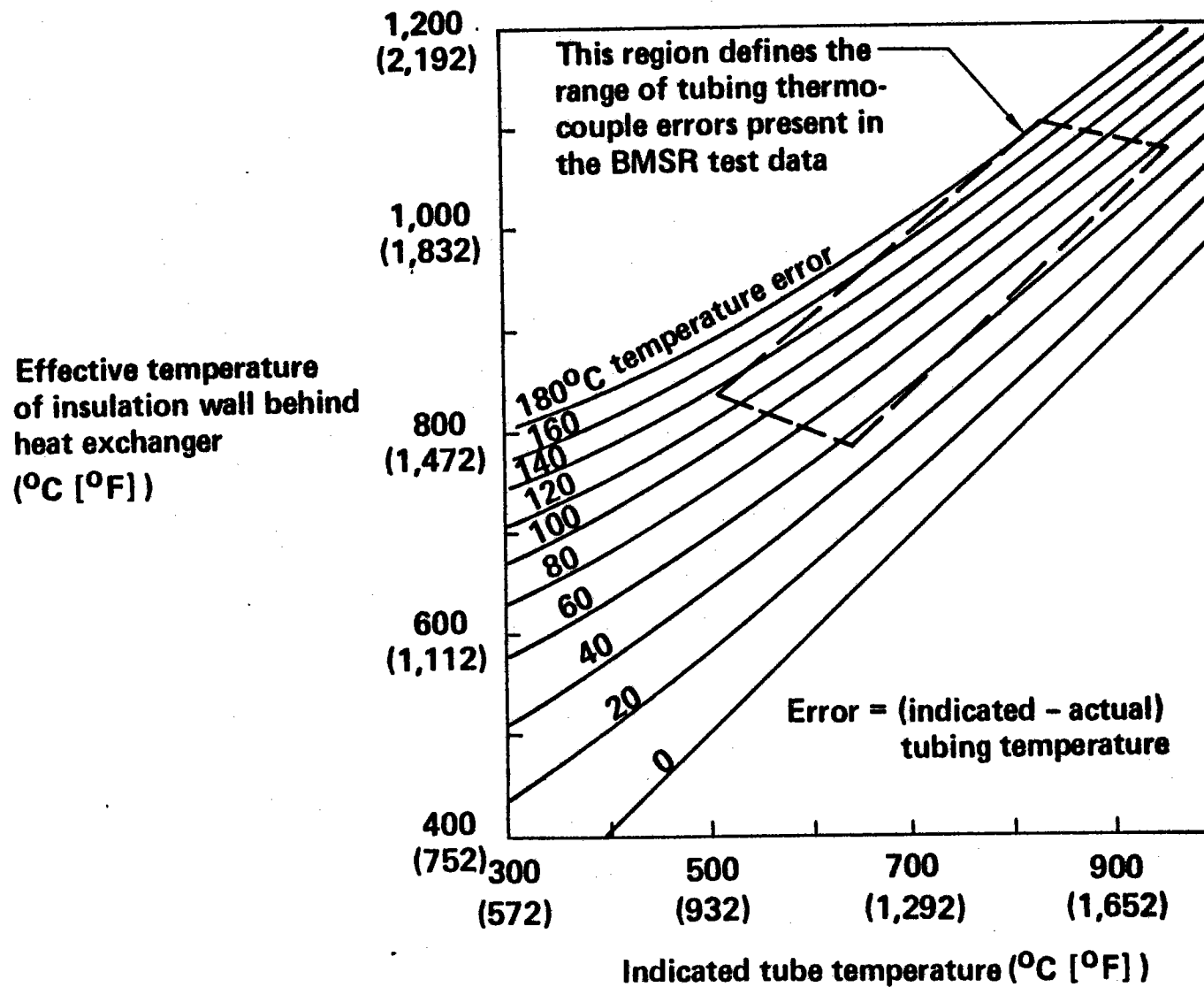
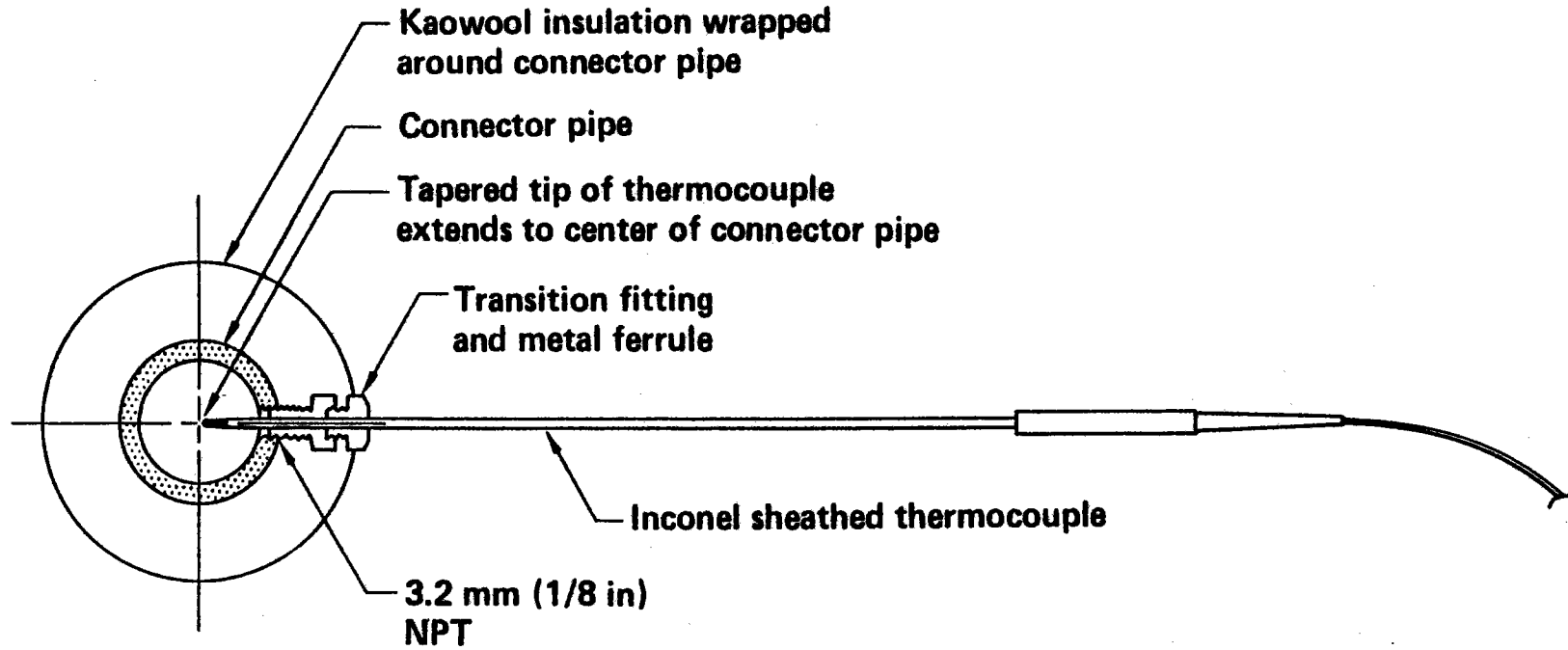


*Figure 8.3-3. Details of Air Temperature Thermocouple Installation*

## Details of Air Temperature Thermocouple Installation





thermocouple design for these installations was an Inconel-sheathed unit with a nominal sheath diameter of 3.2 cm (0.125 in), which tapered to half this diameter at the tip. The tip of the thermocouple was positioned inside the connector pipe where it was directly exposed to the air flowing through the pipe. It was thermally coupled to the connector pipe by the stainless-steel ferrule of the wall transition fitting that crimped on the sheath during installation. Other significant heat transfer mechanisms that affected the temperature of the thermocouple junction included convective heat transfer with the air flowing through the connector, and radiative heat transfer with the surrounding interior walls of the connector pipe.

The connector pipe and thermocouple were both heated by the air flowing through the connector. The pipe, in turn lost heat to the surrounding air by conduction through its 2.5 cm (1.0 in) layer of protective insulation. The effect of this heat loss was to depress the temperature of the connector pipe below that of the internal air. Connector pipe temperatures 10° to 50°C (18° to 90°F) lower than the internal air temperature were typical. Because of its high heat transfer coefficient with the air flowing through the connector pipe, the thermocouple temperature remained close to the air temperature in spite of its radiative and conductive heat losses to the connector pipe. The depression of thermocouple junction temperature below the air temperature in the connector pipe is shown in Figure 8.3-4. As indicated in the figure, these thermocouples located inside the heat exchanger inlet and outlet connector pipes indicated temperatures that were 1° to 4°C (1.8° to 7.2°F) lower during design point operation of the receiver. Larger errors, up to 12°C (21°F), occurred during operation at high temperature and low flow rates.

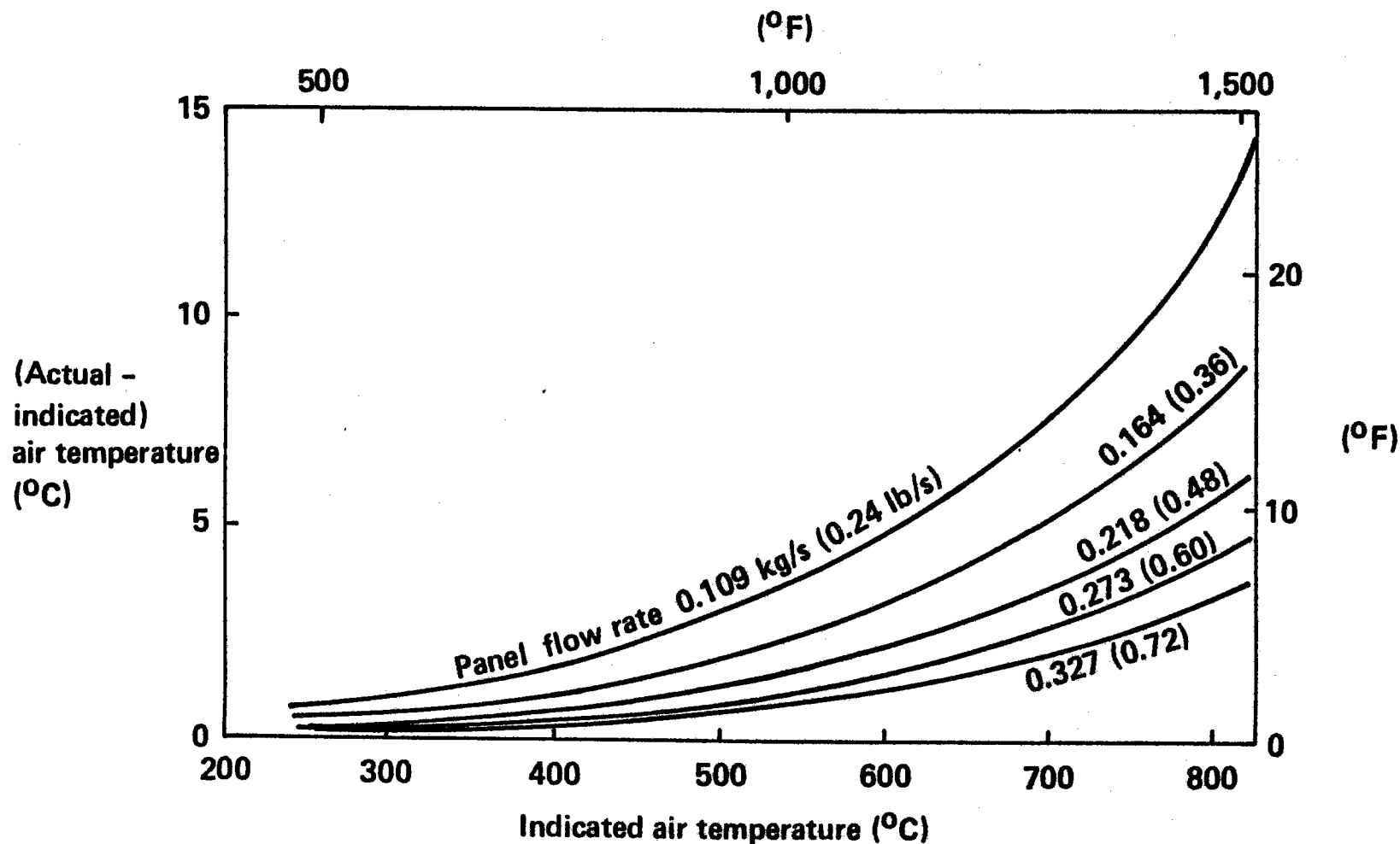
Thermocouple errors resulting from heat flows and thermal gradients at their point of installation were present in all the tubing temperature and heat exchanger inlet and outlet air temperature data recorded during tests. These corrections have not been made to the test data on record (Section 8.2). It remains necessary for users of the BMSR test data to apply these corrections.

Reference junction errors, which also affected the accuracy of thermocouple

Figure 8.3-4. Corrections Required for Heat Exchanger Inlet and Outlet Air Temperatures

## Corrections Required for Heat Exchanger Inlet and Outlet Air Temperatures

419



measurements, were treated as data system errors and are discussed in Section 8.3.2.

### Pressure Transducers

A total of 20 strain-gage pressure transducers were used on the BMSR experiment; 18 of these transducers were essentially identical industrial-quality units with pressure measurement ranges of 0 to 1.03 MPa (0 to 150 lb/in<sup>2</sup>). Two other units measured the difference between the inlet and throat pressures in the venturi flowmeters on the air supply equipment skid. Initially, lower measurement range transducers (0.10 and 0.17 MPa [15 and 25 lb/in<sup>2</sup>]) similar to the 1.03-MPa (150-lb/in<sup>2</sup>) range units were used for these measurements, but they proved to be unreliable. The transducer on the receiver flowmeter was replaced by a 0 to 0.69-MPa (0 to 100-lb/in<sup>2</sup>) transducer of aerospace quality. The other low-range transducer was retained on the bypass flowmeter, but readings were significantly discounted and used only for purposes of operation and control of the receiver.

All of the pressure transducers were accurately calibrated prior to installation on the experiment. A typical set of calibration data consisted of:

- a. Recommended linear output slope in pounds per square inch per millivolt of output at constant 10V applied voltage,
- b. Total deviation from recommended linear output slope, 95% confidence, expressed in difference between indicated and actual pressure,
- c. Offset of millivolt output at zero pressure and 10V applied voltage.

The linear output slope was determined by least-squares fitting of a linear function to 11 precisely measured sets of pressure and millivolt calibration points. The total deviation from this recommended function consisted of hysteresis errors and systematic nonlinear response characteristics.

The 95% confidence deviation from linear output for the 18 transducers used on the experiment ranged from 0.00076 to 0.00104 MPa (0.11 to 0.15 lb/in<sup>2</sup>). The average value of the corresponding three-sigma deviation was 0.0014 MPa (0.20 lb/in<sup>2</sup>).

Besides their deviation from linear output response, other sources of pressure measurement errors were attributed to the pressure transducers, including changes of their millivolt offset at zero pressure and possible variations of the energizing voltage applied to their strain-gage bridges. The power supplies for these transducers were provided as part of the CRTF data system. Once connected to the transducers, they were left turned on for the duration of the testing program. Occasional checks of their output confirmed steady output voltages with variations of less than 0.001V (0.01%), which constituted a negligible contribution to errors.

The zero offset of the 18 industrial-quality pressure transducers was found to vary significantly with time. These values were found to be affected by transducer temperature and history of operation. Steadily increasing or decreasing offset values were noted during the first few months of operation of the transducers. It was subsequently learned that this initial burn-in characteristic is commonly present with these devices. The "well-used" aerospace quality transducer on the venturi flowmeter did not exhibit any measurable zero drift.

As mentioned in Section 8.2, variations of zero offset were accommodated by daily, and often twice daily, measurement of new offset values. Basically, the transducer outputs were all measured before pressurization of the receiver and offset data was recorded for use during the posttest data processing activities. An additional uncertainty of 0.0103 MPa (1.50 lb/in<sup>2</sup>) was added to the three-sigma standard deviation of the industrial-quality pressure transducers to account for zero offset errors not eliminated by their daily calibration.

#### Heat-Flux Gages

A total of 13 heat flux gages were used in the BMSR to measure the solar and

infrared radiant heat-flux incident on the walls of the cavity. These devices used a small, directly heated metal disk to measure the heat flux. The rim of the disk was welded to a water-cooled heat sink. The temperature difference between the center of the disk and the rim varied in proportion to the heat flux absorbed. This temperature difference was measured by a pair of thermocouple junctions, one at the center and one at the rim. All these devices exhibited a 0 to 10mV range of output signal over their design range of heat fluxes.

Calibration of these instruments consisted of measuring their responses to various levels of direct radiant heat flux. These data were provided by the instrument supplier; however, maintenance of accurate measurements depended on preservation of the optical properties of the black coating on the exposed surface of the sensor disk.

The heat-flux gages that were initially delivered to CRTF with the BMSR were damaged by the loss of coolant flow during one of the initial solar tests. Eight of the original 13 gages were destroyed and the remainder were overheated sufficiently to damage their coatings. Subsequently, the four calorimeters on the back cone that were destroyed were replaced with new units, and the four usable calorimeters on the receiver main frame were recoated and moved to the top, bottom, east, and west sides of the receiver.

Coolant that leaked into the back cone insulation in the region of the four calorimeters during the failure of the first set of calorimeters remained a problem throughout the test program. In spite of frequent cleaning of the calorimeters, this material continued to outgas and deposit on the surface of the four back cone calorimeters. Their accuracy remains in question.

The four calorimeters installed on the main frame of the receiver remained clean and black, but because they had been recoated with black paint, it was necessary to completely recalibrate them. This was accomplished at the end of the first series of tests (February 1979), and the new calibrations have been used for data processing (Section 8.2).

An exact evaluation of the measurement uncertainty of these instruments was

not feasible. Examination of posttest calibration data allowed establishing limits of confidence to the four-frame calorimeter readings. This range was 8 kW/m<sup>2</sup>. The absolute values of measurements by the other heat flux gages located on the back cone had to be discounted because of the continuously varying state of their surface coatings. These measurements were useful during tests, but were of little scientific value.

### Valve-Angle Measurements

The experiment system used a total of 10 proportionally controlled valves to maintain proper airflow rates and pressure levels in the BMSR. A precision potentiometer was fitted to the operating shaft of each of these valves. The potentiometers were energized by a 20V dc power supply. The ratio of potentiometer wiper terminal voltage to total applied voltage was used to indicate angular position of each valve.

Considerable effort was expended during the hot flow tests (Section 6.0) to calibrate the flow-versus-valve-angle and pressure-drop characteristics of the receiver flow valves. The similarity of the flow characteristics through these eight valves allowed their flow rates to be defined by a common calibration curve (Figure 6.2-2).

Reference angles were provided for the heat exchanger flow-control valves by the adjustable limit stops. These stops were fixed during the hot flow test to provide identical, wide-open (90-deg), valve-angle flow characteristics for all the valves. The remaining errors that accrued to the valve-angle measurements included nonlinearity, hysteresis, and resolution errors of the potentiometer supplier as an angular resolution uncertainty of 0.063% of full scale, or 0.23 deg of angular position.

### Airflow Measurements

The BMSR test instrumentation included capability for measuring airflow rates at 10 different locations in the experiment. Eight of these locations were measured by calibrated heat exchanger flow valves and two used venturi flowmeters installed on the air supply equipment skid.

Details of the flow-valve installation are schematically described in Figure 8.3-5. The airflow rate through a full-flow ball valve is defined by the formula:

$$M_p = C_1 C_2(\alpha) C_3 \left[ \frac{P_{IN} \Delta P}{T_{IN}} \right]^{1/2} \quad (8.3-1)$$

where

- $M_p$  = heat exchanger panel flow rate
- $C_1$  = constant accounting for units used
- $C_2(\alpha)$  = flow coefficient, which varies as a function of valve angle (Figure 6.2-2)
- $P_{in}$  = valve inlet pressure, absolute
- $\Delta P$  = pressure difference across valve
- $T_{in}$  = inlet temperature, absolute
- $C_3$  = coefficient accounting for compressible flow effects in flow through valve, the larger of,

$$C_3 = \left[ 1 - \frac{\Delta P}{3 P_{in} C_4(\alpha)} \right] \quad \text{OR, } C_3 = 0.667$$

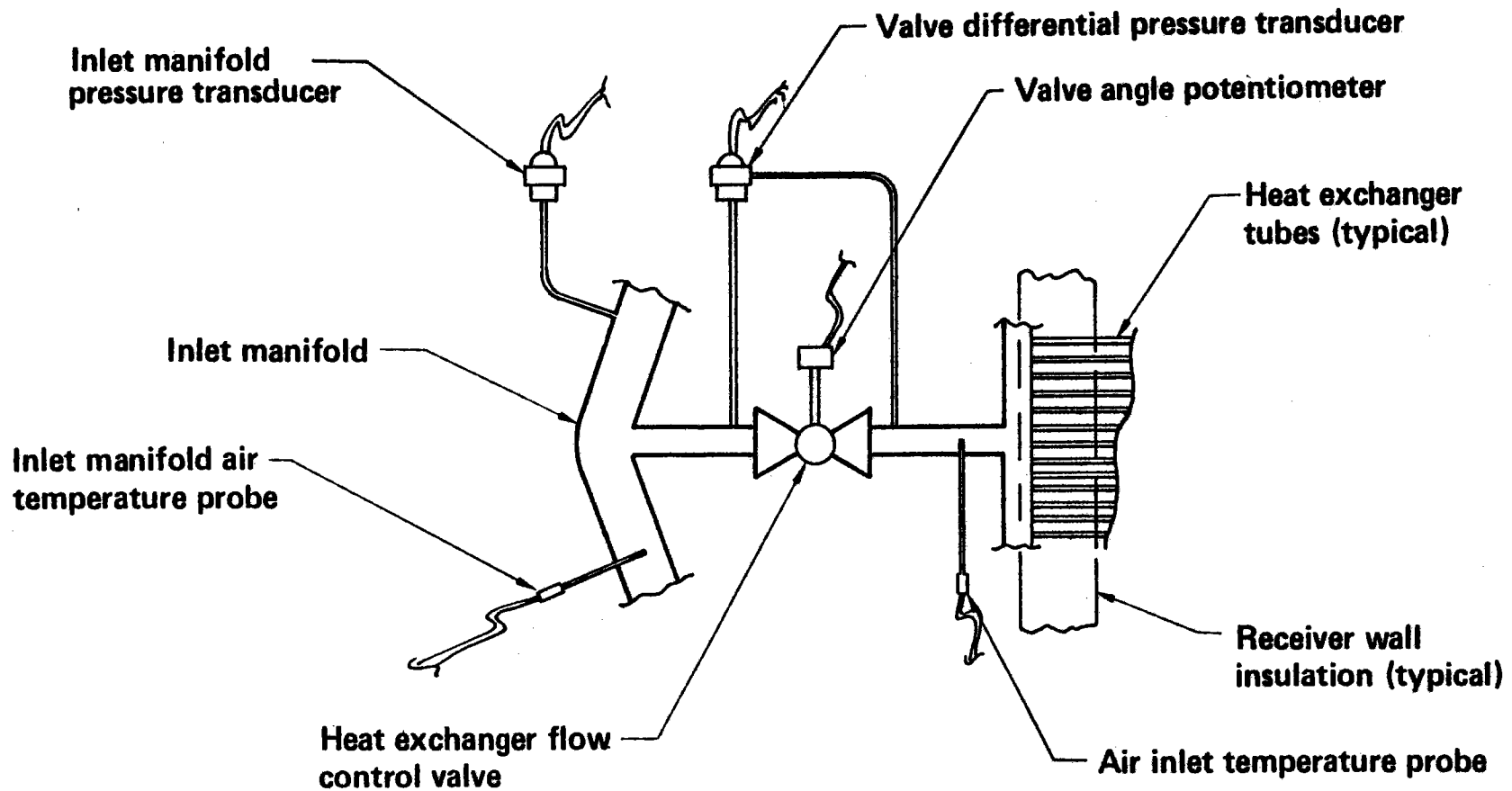
where

- $C_4(\alpha)$  = valve pressure ratio, which produces choked flow as function of valve angle (Figure 3.4-9)

Values of coefficients  $C_1$ ,  $C_3$ , and  $C_4(\alpha)$  for the BMSR flow valves were obtained from the literature. The values of coefficient  $C_2(\alpha)$  were defined during hot-flow tests. This was accomplished by accurately measuring the airflow and factoring out the assumed values for all the other terms on the right side of equation 8.3-1. The result was an experimentally measured value of  $C_2(\alpha)$ , which compensated for minor errors in the values of the other constants. The accuracy of this method of valve calibration depended on the ability to independently and accurately measure flow rates in the hot-flow test setup. A 3% uncertainty was assigned because of the

Figure 8.3-5. Instrumentation Used for Measurement of Airflow Through Heat Exchangers

## Instrumentation Used for Measurement of Airflow Through Heat Exchangers





probable errors in these flow measurements, and an additional 3% uncertainty was assigned because of the apparent differences between the eight receiver valves, as indicated by the data scatter in Figure 6.2-2.

The resulting large uncertainty in the measurement of airflow rate through individual heat exchangers was not a critical problem. This was because the total receiver flowrate was simultaneously measured by an accurate flowmeter on the air supply equipment skid. Because inlet and outlet temperatures of the individual heat exchangers were maintained nearly equal to one another, the flow rate through individual heat exchangers was of secondary importance in determining the overall rate of heat transfer to the air.

The flowmeter on the air supply equipment skid was the most important instrument on the experiment. As will be shown in the following sections, a major effort was expended to make sure that total receiver flow rates were accurately measured by the device.

The particular device selected for these airflow measurements was officially defined as a universal venturi tube (UVT). The hydraulic shape of the UVT is shown in Figure 8.3-6. Figure 8.3-7 shows details of its installation in the air supply equipment skid piping.

Developers of the UVT claimed an extremely high level of uncalibrated accuracy. Values of the discharge coefficient, which totally described the flowmeter's hydraulic characteristics, remained essentially constant over wide ranges of size, construction materials, and machine finish. Reference 8 describes measurements of the discharge coefficients for 51 UVT's in sizes ranging from 7.5 cm to 1.06 m (3.0 in to 3.5 ft) in diameter that incorporate full and partial machining of their interior walls and a variety of construction materials, including cast iron, steel, and plastic. Their discharge coefficients were all within  $\pm 0.75\%$  of the average value, 0.9797. Other groups were compared for which materials and fabrication details were more similar. Discharge coefficients for these were within a  $\pm 0.5\%$  range.

Except for the possibility of a major error in BMSR experiment design or data processing at CRTF, the uncalibrated accuracy of the UVT flowmeter was

Figure 8.3-6. Configuration of the Universal Venturi Tube

## Configuration of the Universal Venturi Tube

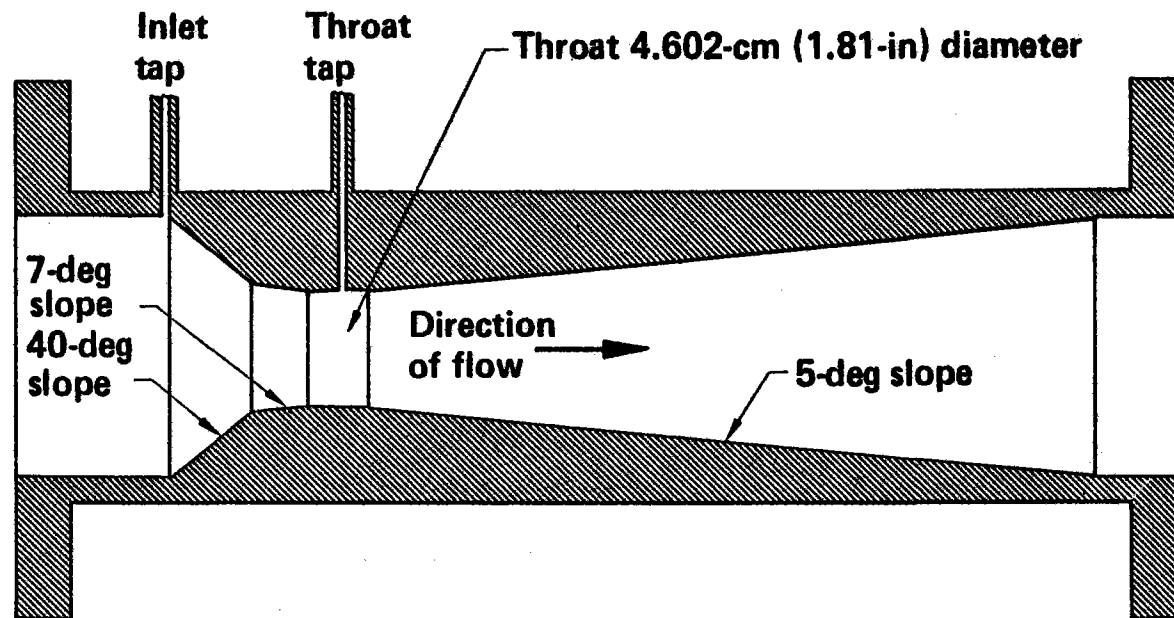
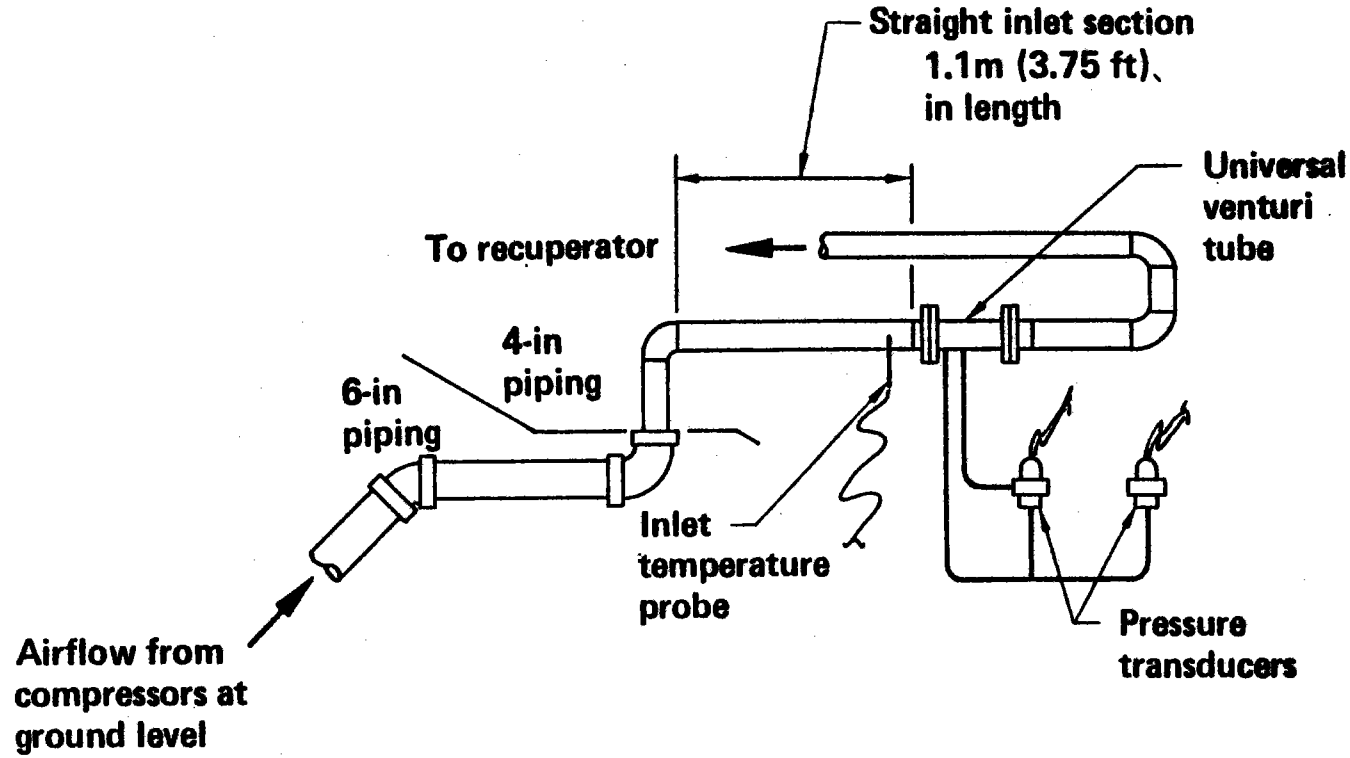


Figure 8.3-7. Flowmeter Installation Details

## Flowmeter Installation Details



better than could be measured by the experiment data system. Checkout testing was conducted to verify the accuracy of the flowmeters, but it must be noted that these tests were intended to uncover the type of major errors that could occur rather than act as a calibration of the UVT.

A test rig was borrowed from the Boeing test laboratories that included a critical venturi flowmeter assembly. The venturi was a special unit traceable to NBS standards. The critical venturi meter was installed on the outlet of the air supply equipment skid, temporarily replacing the BMSR in the airflow circuit. A manual valve was installed in the line between the UVT and the critical venturi, allowing variation of the pressure level and flow rate through the critical venturi.

The results of these flowmeter checkout tests are summarized in Figure 8.3-8. Some difficulties were encountered with the differential pressure transducers on the UVT flowmeters. This accounted for the uncertainty reported at 1.5 kg/s (3.3 lb/s). However, the conclusions were clear; the test system design and test data reduction methods were verified. The +0.75% accuracy claimed for the UVT could not be disputed by these data. Indeed, when the realistic uncertainties associated with pressure and temperature measurements were taken into account, the result was quite remarkable.

Based on these measurements and the substantiating data in Reference 8, the flowmeter accuracy of the UVT was assumed to be +0.75%. Pressure and temperature transducer errors did, of course, add to this uncertainty.

Receiver flow rates were computed by the vendor's recommended formula:

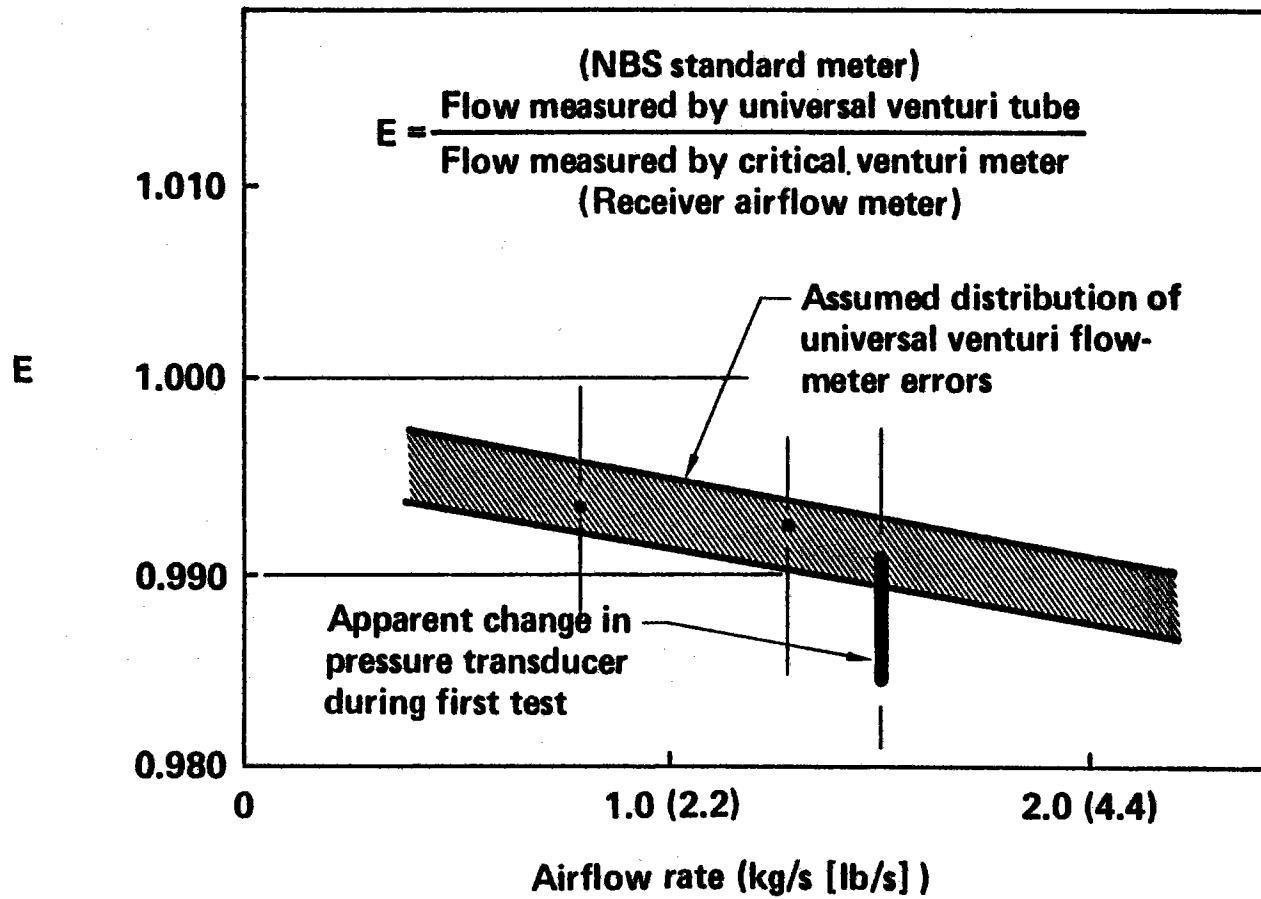
$$M_r = \left[ A - B \left[ \frac{\Delta P}{P_{in}} \right] \right] \left[ \frac{P_{in} \Delta P}{T_{in}} \right]^{1/2} \quad (8.3-2)$$

where

- $M_r$  = receiver flow rate
- $A$  = flowmeter constant
- $B$  = flowmeter constant

Figure 8.3-8. Results of Checkout Testing of Receiver Airflow Meter

## Results of Checkout Testing of Receiver Airflow Meter



$P_{in}$  = flowmeter inlet pressure, absolute  
 $\Delta P$  = inlet-to-throat-pressure difference  
 $T_{in}$  = flowmeter inlet temperature, absolute

### 8.3.2 Data Acquisition System Errors

The instrumentation transducers described in Section 8.3.1 are similar to one another in that they all produced electrical output signals that varied in voltage to indicate measurement levels. Output voltages ranged from a few millivolts for the heat-flux gages, to 30 to 50 mV for pressure transducers and thermocouples, to 1V to 5V for the valve-angle potentiometers. These voltage signals were amplified and converted from analog to digital format by the signal-conditioning equipment in the tower data system. This signal conditioning added to the instrument errors that already existed.

Reference 3, the CRTF Experiment Manual, defined the maximum errors to be expected during normal operation of the DACS signal-conditioning equipment based on vendor specifications. Calibration checks on these components were conducted prior to and during the BMSR tests. When connected to properly ungrounded instrumentation transducers having appropriate transient response and electrical resistance, the signal-conditioning equipment consistently performed within these error limits. Problems and failures of the equipment occurred but they consistently resulted in large, easily discovered offsets of measured values caused by poor electrical connections or outright failure of the signal-conditioning electronics.

Some problems occurred with the tower data system during the course of BMSR tests. A sprinkler head in the tower fire control system failed and deluged the tower DACS with water. Replacement, drying, and repairs to equipment were considered adequate when the spurious signal-to-ground levels in the analog signal-conditioning equipment was reduced to less than 0.0005 mV.

Two types of multiplexers were used for BMSR signal conditioning. High-level multiplexers were used for valve-angle potentiometers and were accurate to  $\pm 0.09\%$  of the measured signal level. Low-level multiplexers

were used for all the millivolt data signals. These were rated at  $\pm 0.38\%$  accuracy.

Reference junctions used with the experiment thermocouples were rated at  $\pm 0.25$  °F accuracy, which converts to about  $\pm 0.14$  °C. Up to 36 of the experiment thermocouples were connected to each of the reference junctions. Those temperatures that were to be compared with one another, such as heat exchanger inlet and outlet air temperatures, were connected to the same reference junction. As a result, the reference junction errors were considered negligible for temperature-difference measurements.

The analog-to-digital conversion introduced a rounding-off error with a maximum value equal to one-half of its least significant digital bit. This amounted to  $\pm 0.024\%$  of the full span of the converter. The corresponding analog data span varied to match the range of the transducer output. Applicable ranges were  $\pm 10$ ,  $\pm 40$ , and  $\pm 80$  mV and  $\pm 10$ V. Table 8.3-2 shows the analog-to-digital roundoff errors for the various channels of test data.

### 8.3.3 Combined Uncertainty in Test Data Measurements

Preceding sections of this report have defined the measurement errors to be expected from the experiment transducers and the various components of the data acquisition and control system. Individual error contributions of all the elements of a data measurement channel must be combined to define the data channel uncertainty.

The term "maximum error" has been used in different ways during the preceding discussions. It has been consistently used to describe the largest expected error; however, a variety of definitions of maximum error have been encountered. The most fundamental difference between the various definitions was whether the maximum error was a fixed percentage of the indicated measurement, percent of value, or a fixed interval of the measured parameter such as a dimensional tolerance. Furthermore, some of the error data were described as 95 percentile or three-sigma confidence intervals. Others were component specifications without stated confidence levels. Still others, such as the analog-to-digital roundoff errors, were quantities

Table 8.3-2. Resolution of Analog-to-Digital Conversion

## Resolution of Analog-to-Digital Conversion

Data channel	Range of data channel	Resolution
Temperature	0-2,000	1.7°F
Pressure	0-25	0.016 lb-in <sup>2</sup>
Pressure	0-150	0.10 lb/in <sup>2</sup>
Heat flux	0-400	0.20 kW/m <sup>2</sup>
Voltage	0-10	0.005V

Resolution errors affect fourth significant figure



with absolute rather than statistically defined intervals. This was the first problem encountered in attempting to determine combined uncertainties in the test measurements.

Reference 9 describes statistically valid methods for the propagation (combination) of errors in computing. The author's introductory comments are appropriate here.

"When using direct measurement values to compute final results, such as to reach indirect measurements, it is necessary to guard against carrying excessive random error into the result. Thus it is necessary to know the size of the error in the result after arithmetic operations have been performed on any measured value or the mean of several values. The general rules of error propagation refer to three-sigma or any similar random errors."

(Which are independent of one another)

For the purposes of development, error, E, was defined as the tolerance assigned to a measuring or data processing function. Confidence levels and rationale for the conversion of previously described limits of "maximum error" to this format will be described in later paragraphs.

According to the laws of probability, when quantities are added or subtracted from one another, the result contains an error equal to the square root of the sum of the squares of the errors of the individual quantities. Thus,

$$E = \left[ E_A^2 + E_B^2 + \dots + E_N^2 \right]^{1/2} \quad (8.3-3)$$

Similarly, when quantities are multiplied together, their product has the error,

$$E = \pm A \cdot B \cdot C \dots N \left[ \left( \frac{E_A}{A} \right)^2 + \left( \frac{E_B}{B} \right)^2 + \left( \frac{E_C}{C} \right)^2 + \dots + \left( \frac{E_N}{N} \right)^2 \right]^{1/2} \quad (8.3-4)$$

When quantity A is divided by quantity B, then

$$E = \frac{1}{B^2} \left[ (E_A B)^2 + (E_B A)^2 \right]^{1/2} \quad (8.3-5)$$

When quantity a is raised to the power B, then

$$E = B \cdot A^{(B-1)} \cdot E_A \quad (8.3-6)$$

The error propagation formulas produce values (the E values) that are equivalent to tolerances. The confidence interval of the resulting E values is a composite of the confidence intervals of the terms  $E_A$ ,  $E_B$ , etc. Equal (i.e., three-sigma) confidence intervals are desired for  $E_A$ ,  $E_B$ , etc., to precisely define the confidence interval of the result. Definitions of error intervals of the form  $E_A/A$ , such as percentage error, are useful, but individual values of error,  $E_A$ , and nominal value, A, are more generally required. Therefore, it is necessary to translate the previously defined "maximum errors" into average values and tolerances of value. Tolerances with small confidence intervals, such as 95 percentile, will be increased by appropriate amounts to define new three-sigma confidence intervals. The work sheet for these computations is reproduced in Figure 8.3-9.

As may be noted in Figure 8.3-9, a standard assumption (Reference 9) was made to accommodate those maximum error values for which no confidence level was available. It was recommended that a three-sigma limit of a normal distribution of errors was assumed to be equivalent to specified tolerances beyond which individual observations of errors larger than these limits virtually never occurred.

The method used to define individual errors that were combined together affected the manner in which they were to be combined. Figure 8.3-9 is an example of this principle. Here the nominal final value of the data channel is defined in the engineering units to be finally displayed. The

Figure 8.3-9. Combined Errors in BMSR Data Channels

## Combined Errors in BMSR Data Channels

Measured data channel	Nominal value	Transducer tolerance <sup>a</sup>	DACS multiplexer tolerance	Analog-to-digital roundoff tolerance	Combined tolerance
High temperature	2,000	$7.6 + (0.25)^b$	7.6	1.7	10.88
Intermediate temperature	1,250	$4.8 + (0.25)^b$	4.8	1.7	7.00
Low temperature	300	$2.0 + (0.25)^b$	1.1	0.85	2.45
High pressure	80	$0.20^c + 1.50^d$	0.30	0.100	1.54
Low pressure	10	$0.20 + 1.50$	0.038	0.100	1.52
Flowmeter pressure	10	$0.10 + 0.40$	0.038	0.016	0.414
Valve angle	50	0.23	0.045	0.088	0.25
Heat flux (receiver frame)	200	8.0	0.76	0.20	8.04

<sup>a</sup> $3\sigma$  or converted to  $3\sigma$  confidence interval

<sup>b</sup>Reference junction tolerance

<sup>c</sup>Nonlinearity

<sup>d</sup>Zero offset residual after daily calibration

three-sigma maximum-error interval introduced by each element of the data system is also described in terms of a tolerance (in engineering units) to be applied to the nominal displayed value. Errors defined in this way add together (equation 8.3-3).

Alternately, the individual data system functions were assigned values and tolerances. Separate values described the initial electrical output of the transducer, the electrical multiplying factor (gain) of each of the signal-processing components, and a final value used to multiply (and convert) the final electrical voltage to engineering units. In the case of the high-temperature channel, the nominal value of the product of these terms was 1093°C (2000°F). When defined in this way, the quantities and error intervals of the data system elements were multiplied together, as by equation 8.3-4. However, the combined error interval defined in this way was the same 10.88 deg as previously determined by RMS addition of the individual contributions to the errors in final data channel reading.

Other test measurements involved computations with more than one measured test data channel to determine airflow rates and receiver heat transfer. The principles of combining random errors were used to determine three-sigma error intervals for these data as well. Worksheets for these computations are reproduced in Figures 8.3-10, -11, and -12. The measurement uncertainty for these data were +9.2% for individual heat exchanger panel flow rate, +2.4% for total receiver flow rate, and +3.2% for receiver heat transfer to circulating air. Nominal receiver operating conditions were assumed during the computation of these measurement uncertainties. However, the measurement uncertainties were not significantly changed over the normal range of receiver operating conditions.

#### 8.4 RECEIVER SOLAR INPUT DATA

During tests at CRTF, a solar image produced by 40 to more than 100 heliostats was concentrated at the circular aperture of the BMSR cavity.

Because of the thermal-scale-modeling requirements imposed on the BMSR design, its solar aperture was smaller than the solar image produced by the

Figure 8.3-10. Combined Uncertainties in Heat Exchanger Panel Flow Rate Computations

## Combined Uncertainties in Heat Exchanger Panel Flow Rate Computations

Computational formula

$$M_p = C_1 C_2 (a) C_3 (a) \sqrt{\frac{P_{IN} \Delta P}{T_{IN}}}$$

$$C_3 (a) = \left( 1 - \frac{\Delta P}{3 P_{IN} C_4 (a)} \right)$$

Combined errors

Variable or grouping	Nominal value	3σ error interval	3σ error percent
$P_{IN}$	92	1.55	1.68
$\Delta P$	10	1.52	15.2
$T_{IN}$	1,000	5.64	0.56
$a$	50	0.25	0.50
$C_4$	0.715	0.020 <sup>a</sup>	2.80
$C_3 (a)$	0.9493	0.0079	0.83
$\frac{P_{IN} \Delta P}{T_{IN}}$	0.630	0.0964	15.30
$\sqrt{\frac{P_{IN} \Delta P}{T_{IN}}}$	0.794	0.0541	6.81
$C_2 (a)$	9.75	0.598 <sup>b</sup>	6.14
$C_1$	0.029	—	—
$M_p$	0.213	0.0196	9.21

<sup>a</sup>Caused by uncertainty in value of  $a$

<sup>b</sup>Combined uncertainty in  $a$  and in  $C (a)$

Figure 8.3-11. Combined Uncertainties in Receiver Air Flow Rate Computations

# Combined Uncertainties in Receiver Air Flow Rate Computations

## Combined errors

Variable or grouping	Nominal value	3σ error interval	3σ error percent
A	2.852	0.0214	0.75
B	1.734	0.0130	0.75
ΔP	10.0	0.414	4.14
P <sub>IN</sub>	92.0	1.546	1.68
T <sub>IN</sub>	510	2.450	0.48
(P <sub>IN</sub> ΔP)	920	41.12	4.47
$\left(\frac{P_{IN} \Delta P}{T_{IN}}\right)$	1.804	0.0811	4.495
$\left[\frac{P_{IN} \Delta P}{T_{IN}}\right]^{1/2}$	1.343	0.03019	2.248
$\left(\frac{\Delta P}{P_{IN}}\right)$	0.1087	0.00486	4.47
$\left(B \frac{\Delta P}{P_{IN}}\right)$	0.1885	0.00854	4.53
$\left(A - B \frac{\Delta P}{P_{IN}}\right)$	2.664	0.0230	0.864
M <sub>R</sub>	3.578	0.0861	2.408

Computational formula

$$M_R = \left[ A - B \left( \frac{\Delta P}{P_{IN}} \right) \right] \left[ \frac{P_{IN} \Delta P}{T_{IN}} \right]^{1/2}$$

Figure 8.3-12. Combined Uncertainties in Receiver Heat Transfer Computations

## Combined Uncertainties in Receiver Heat Transfer Computations

Computational formula

$$Q_R = M_R (T_{OUT} - T_{IN})$$

$Q_R$  proportional to the receiver heat transfer to circulating air

Combined errors

Variable or grouping	Nominal value	$3\sigma$ error interval	$3\sigma$ error percent
$M_R$	3.578	0.0861	2.408
$T_{IN}$	1,000	5.64	0.564
$T_{OUT}$	1,500	8.24	0.549
$(T_{OUT} - T_{IN})$	500	9.99	2.00
$Q_R$	1,789	57.0	3.19

CRTF collector field. Observations during tests and posttest examination of the aperture-rim solar shielding showed that the heliostat field image was usually about 1.4m (4.6 ft) across. The receiver aperture, designed to model the aperture of a commercial receiver, was 1.1m (3.6 ft) in diameter. As a result, a large fraction (20% to 30% of the sunlight that focused on the aperture plane did not enter the cavity.

Figures 8.4-1 and 8.4-2 show comparable photographs of the face of the BMSR with and without the collector field in operation. The bright area of the collector field image is elliptical and is offset to the left of the center of the receiver aperture, toward the east. The intensely heated area of the aperture-rim shield can also be observed in the nonsunlit photograph. Here the intensely heated areas of shielding are first darkened and then become white. A dark rim remains that frames the highest temperature region on the shield. This oval-shaped rim can be observed in the nonsunlit photograph (Figure 8.4-1).

The aperture-rim shield on the BMSR was conical in shape. It sloped inward at an angle of approximately 30 deg. This shape was not intended to concentrate or redirect solar flux into the aperture. In fact, because of the diffuse reflective properties of the aperture-rim shield, only about 3% of the sunlight striking the shield was reflected into the receiver cavity. The slope allowed thinning of the aperture shield to approximately 3.0 cm (1.2 in) at its rim, providing a more precisely defined opening for solar input computations.

To date, three different methods were used to determine the solar input to the BMSR, including combinations of analysis and experimental measurements. The different methods produced significantly different results, with variations of as much as 19% between them. As will be apparent in the ensuing discussion, the solar-flux measurement and analysis technology was in an early stage of development, with much remaining to be learned concerning characterization of the collector field and measurement of the solar-flux patterns produced in three-dimensional space at the focal zone of the collector system.



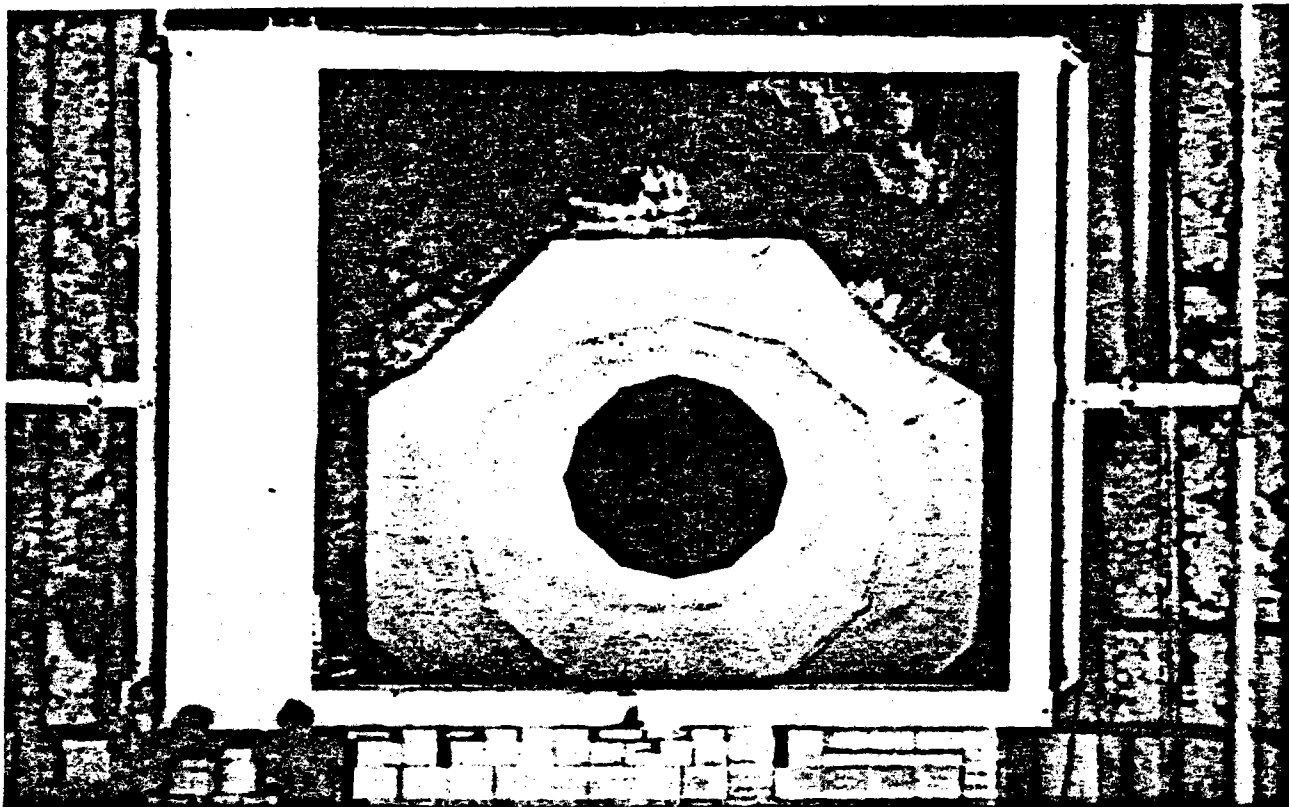
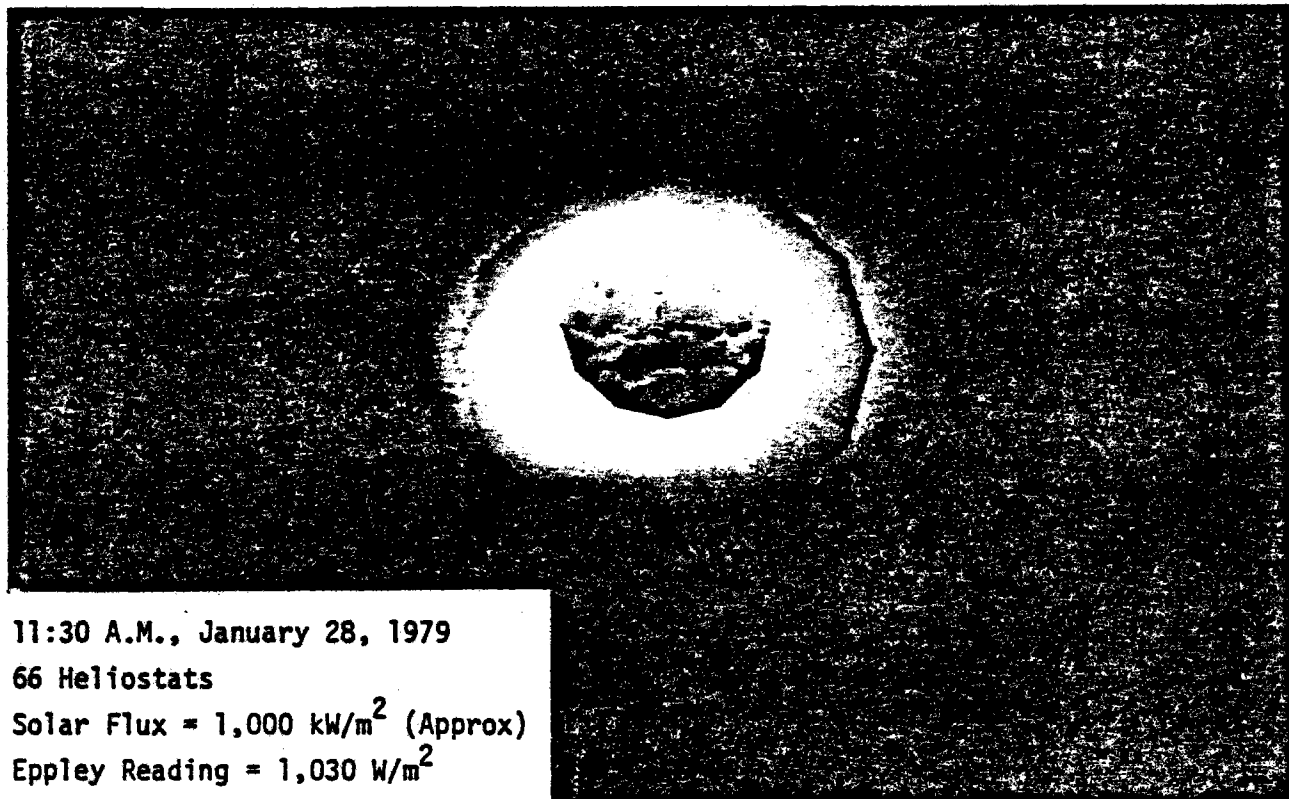


Figure 8.4-1: Receiver Aperture, Solar Shielding, and RTAF, January 28, 1979



11:30 A.M., January 28, 1979  
66 Heliostats  
Solar Flux =  $1,000 \text{ kW/m}^2$  (Approx)  
Eppley Reading =  $1,030 \text{ W/m}^2$

Figure 8.4-2: Collector Field Image on Receiver During Typical Solar Test

The three-dimensional solar-flux pattern produced at the focal zone of the collector field was extremely complex. The solar flux reflected from a particular heliostat and directed onto the receiver aperture exhibited certain distributional characteristics of interest. Because the CRTF heliostats were curved to focus sunlight, their reflected beam converged to a minimum area and then spread out. The distance from the heliostat to the minimum convergence area of its beam was variable, subject to the pretest focus and alignment of the heliostat. During the BMSR tests, the 78 Zone A CRTF heliostats were aligned for optimum focusing of their reflected solar flux on the BMSR aperture at noon on the vernal equinox, March 21. Because the alignment process was subjective, essentially an art learned with experience, the focus at this time was not ideal. Certainly it was even less optimal on other days of the year.

The image produced by this single heliostat on the aperture plane of the BMSR was a coarse, optical reflection of the Sun. Because atmospheric conditions produced attenuation and spreading of the effective width of the solar disk, these conditions also produced attenuation and spreading of the image from a single heliostat.

Zone A heliostats were located at angles up to 45 deg from the normal to the BMSR aperture plane. Therefore, considerable apparent beam spreading occurred when the solar flux from one of these off-axis heliostats was projected onto the aperture plane.

The combined image of several heliostats incorporated all of the above complexities plus at least two other major effects. First, the converging combined beams filled a region in front of the receiver approximately 90 deg wide from side to side and 40 deg high. This resulted in an optical system with a very shallow focal zone. The projected area of the converging solar beam, which was about 1.5 m<sup>2</sup> (16.1 ft<sup>2</sup>) at the receiver aperture plane, increased to about 4.0 m<sup>2</sup> (43.0 ft<sup>2</sup>) at the plane of the RTAF, only 0.64 m (25 in) in front of the aperture plane. Also, with this rapid convergence of the combined collector-field image, the solar-flux distribution at locations other than the focal plane clearly depended on the relative energy contribution of individual heliostats, including the possibility that some

of them may not be in use.

Sandia Laboratories provided solar input data during BMSR tests. The HELIOS computer code under development at Sandia-Albuquerque was extensively used for computations for these solar tests. Also, a real-time aperture-flux system representative of the first stage in the development of high-solar-flux measurement devices for general use at CRTF was developed, checked out, and installed as part of the BMSR test setup (Section 7.0).

The planned method of determining solar inputs to the BMSR during tests and for upgrading the accuracy of these measurements by posttest analysis is described in Section 8.4.1. Other solar input data obtained by analysis of test conditions during 16 events of particular importance for the evaluation of receiver performance is presented in Section 8.4.2. Solar input data from various sources is compared in Section 8.4.3 in an attempt to establish limits of uncertainty for these data.

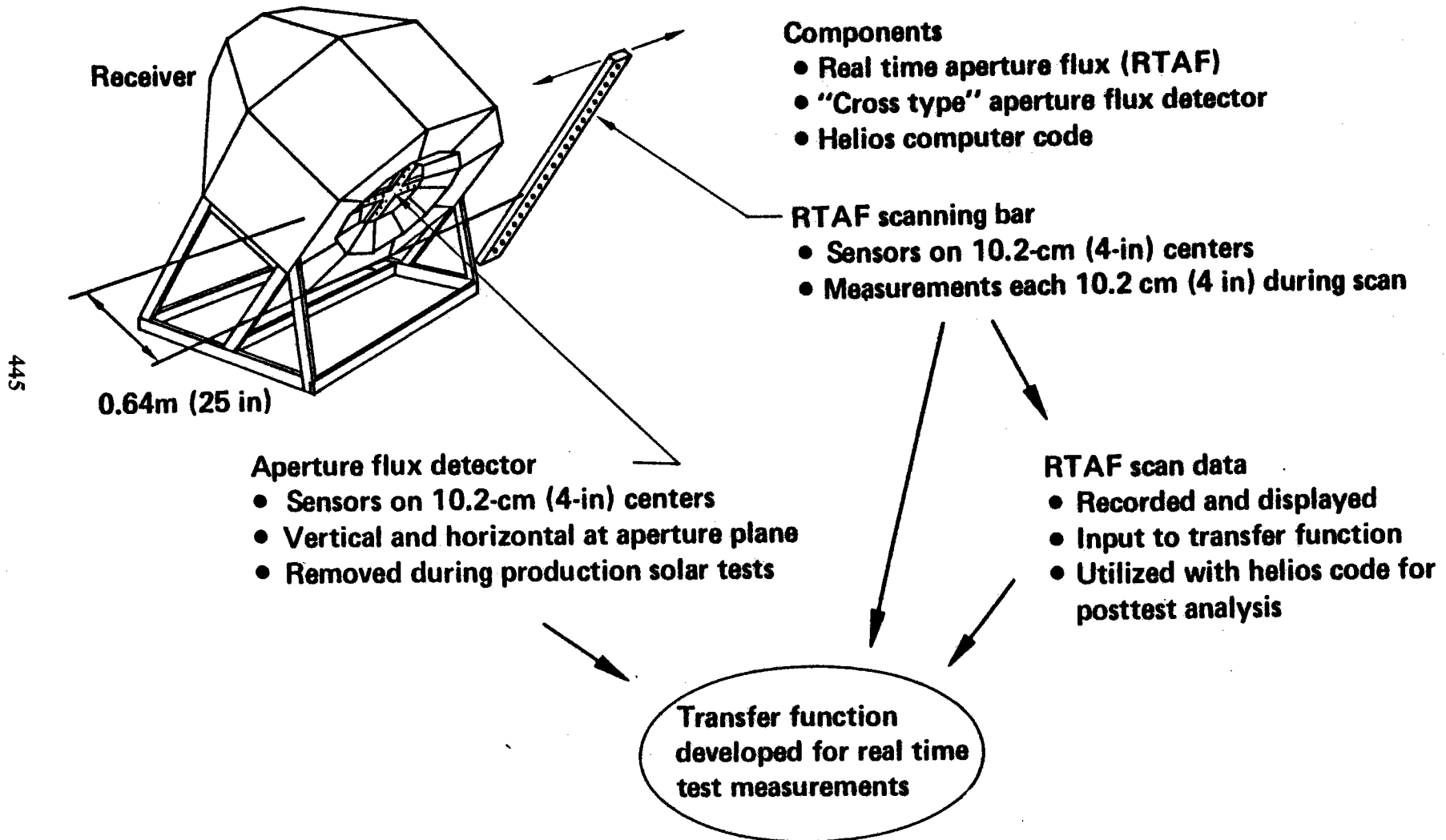
#### 8.4.1 Experimental Measurements of BMSR Solar Input

The test system provided by Sandia Laboratories for the measurement of BMSR solar input is described schematically in Figure 8.4-3. Major components include the RTAF, a cross-type aperture flux detector, an analytical transfer function developed for real-time estimation of receiver input from RTAF measurements, and the HELIOS computer code separately developed by Sandia Laboratories, which was used for detail posttest analysis of RTAF data.

As depicted in Figure 8.4-3, the RTAF scanning bar with heat-flux sensors located on 10-cm (4-in) centers was passed across the solar beam in a plane located 0.64m (2.1 ft) in front of the receiver aperture. The solar beam at this plane occupied a projected area about 2.5 times its size at the aperture plane. Nevertheless, an area of the RTAF scanning plane through which all the solar flux entering the receiver must pass, was defined and designated as the "RTAF aperture." The RTAF aperture was 2.43m (8 ft) wide and 1.52m (5 ft) high. Provisions were made in the RTAF software to integrate the solar-flux measurements in this region of the RTAF scanning

Figure 8.4-3. Components of the Solar Input Measurement System

## Components of the Solar Input Measurement System



plane, thereby defining the "RTAF aperture power."

The cross-type aperture-flux detector consisted of a water-cooled mount with heat-flux sensors located on 10-cm (4-in) centers on its vertical and horizontal members. It was used during the checkout and system verification tests to determine the amount of solar flux passing through the receiver aperture. Initially, a series of calibration tests were conducted using groups of heliostats in various regions of the collector field to determine the fraction of their reflected solar flux passing through the RTAF aperture, which also passed through the receiver aperture. These data were tabulated and stored for later use as functional descriptions of the solar-flux transmission from the RTAF aperture to the receiver aperture, the transfer functions.

With these transfer functions on record, the BMSR test setup was considered to be ready for production tests. The cross-type aperture-flux detector was removed.

Scans of the solar flux entering the RTAF aperture were conducted at approximately 1-hr intervals throughout the first 3 months of BMSR solar tests. These data were recorded on magnetic tapes and remain available for evaluation and assessment.

A transfer function computer code was used during tests to estimate the solar input to the receiver aperture. This computer code was developed using the solar transmission functions previously measured by the cross-type aperture-flux detector. Inputs to the transfer function computer code included the collectors in use, the direct solar intensity, the time of day, the integrated RTAF aperture flux, and the local maximum solar flux measured by the RTAF. Its output consisted of maximum solar flux in the region of the BMSR aperture as well as the estimated solar input to the 1.1m diameter (3.6 ft-diameter) aperture of the BMSR. These values were used to monitor and control the receiver solar input. The number of heliostats focused on the receiver was increased or decreased to obtain the receiver solar input desired for the particular test.

The real-time transfer function was an approximate method of dealing with the many variables involved in the transmission of solar flux from the plane of the RTAF to the plane of the receiver aperture. For this reason, the initial plans for BMSR test data evaluation called for posttest analyses of several sets of RTAF data using HELIOS. In these studies, the HELIOS computer code fills the role of the transfer functions.

The HELIOS computer code was capable of independently analyzing the CRTF collector-field performance and determining the solar flux entering the BMSR aperture. However, the BMSR data evaluation plans called for a more sophisticated approach. The HELIOS code was to be used and adjusted as reasonable and necessary to reproduce the measured solar flux in the RTAF aperture at the time of interest. Then, the same values of HELIOS code parameters would be used to determine the solar input to the BMSR aperture.

This work was begun during February 1979, after completion of the first series of BMSR solar tests. Tests conducted on January 20, 1979, were selected as the first to be analyzed in detail. These included test EB-9A, completed at 12:10 PM, EB-9B, completed at 12:52 PM, EB-6A, completed at 1:49 PM, and EB-3A, completed at 2:48 PM.

Input parameters required for the HELIOS computer code used in these studies are listed in Table 8.4-1. The HELIOS analysis procedure consisted of insertion of known parameters such as sunshape and intensity, target configuration (the RTAF aperture), and a list of the heliostats in use at the time. Best estimates of the remaining HELIOS input parameters were used for the initial computer run. Then the computed flux distribution on the RTAF plane was compared with the RTAF measurements. HELIOS input parameters were varied until a reasonable match was achieved between the analytical and experimental data. The results of this RTAF-HELIOS correlation for test number EB-9A are described in the following sections.

The operating conditions for test EB-9A were--

- a. Time: 12:10 PM MST on January 20, 1979
- b. Direct solar flux (at top of tower):

*Table 8.4-1. Helios Input Parameters*

## **Helios Input Parameters**

### **Collector field configuration**

- Heliostats in use
- Heliostat alignment characteristics

### **Target**

- Orientation
- Configuration

### **Time**

- Time of year
- Time of day

### **Solar flux characteristics**

- Direct intensity
- Sunshape

### **Heliostat characteristics**

- Curvature of facets
- Pointing error function
- Reflector error function
- Directional and total solar reflectance

### **Aim point**

- Coordinates
- Offset if appropriate

- 1010 W/m<sup>2</sup>, by Eppley pyrhelimeter
- c. Ambient wind speed: 6.5 m/s (21.3 ft/s) from the north
  - d. Receiver operating temperatures: inlet air, 532°C (990°F); outlet air, 816°C (1500°F)
  - e. Receiver airflow rate: 1.9 kg/s (4.2 lb/s)

A total of 62 of the Zone A heliostats were in use. These are shown in the collector field diagram, Figure 8.4-4. Because of the time of the EB-9A test event, almost exactly solar noon, and because a nearly balanced group of east-field and west-field collectors were in use at the time, the east and west sides of the solar-flux patterns on the receiver interior and the RTAF plane in front of the receiver should have been symmetrical.

The circumsolar telescope, installed and operated at the CRTF by Lawrence Berkley Laboratories (LBL), was in operation on January 20. LBL personnel have provided sunshape data that they collected during several of the BMSR tests. Sunshape measurements obtained during test EB-9A are shown in Figure 8.4-5. As indicated in the figure, the circumsolar ratio during EB-9A was only 0.66%, indicating clear-sky conditions. This was an average test day at CRTF. Circumsolar ratios from 0.2% to as much as 3% were observed on other test days.

An RTAF scan was also conducted during test EB-9A. These data are shown in Figure 8.4-6. Individual solar-flux profiles are shown for each of the heat-flux gages on the RTAF scanning bar. The RTAF software was used to produce smooth curves from the 34 discrete measurements produced by each flux gage during a scan. The maximum solar flux measured on the RTAF plane during this scan was 1686 kW/m<sup>2</sup>. The integrated solar power passing through the 1.52m (5.0-ft) high by 2.43m (8.0-ft) wide RTAF aperture was 1566 kW. The transfer function for real-time estimation of solar input to the BMSR aperture indicated a solar input of 1059 kW.

This test and other tests on January 20, 1979, were the first to be evaluated by the RTAF-HELIOS data-processing technique. The results of the RTAF/HELIOS correlation analysis for EB-9A are described in Figures 8.4-7 and 8.4-8. Several horizontal and vertical solar-flux profiles through the



Figure 8.4-4. Heliostats in Use During Test EB-9A

# Heliostats in Use During Test EB-9A

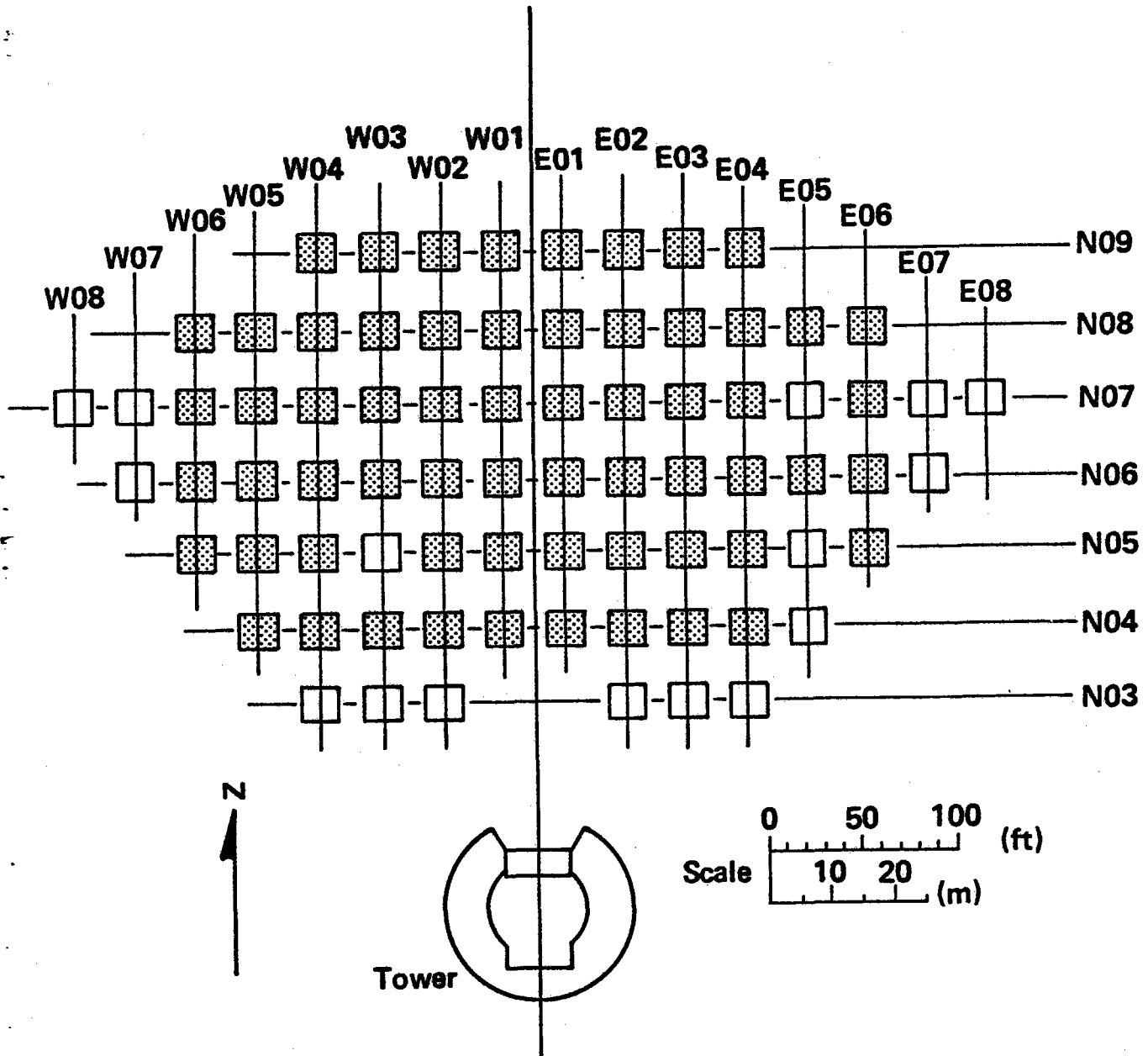
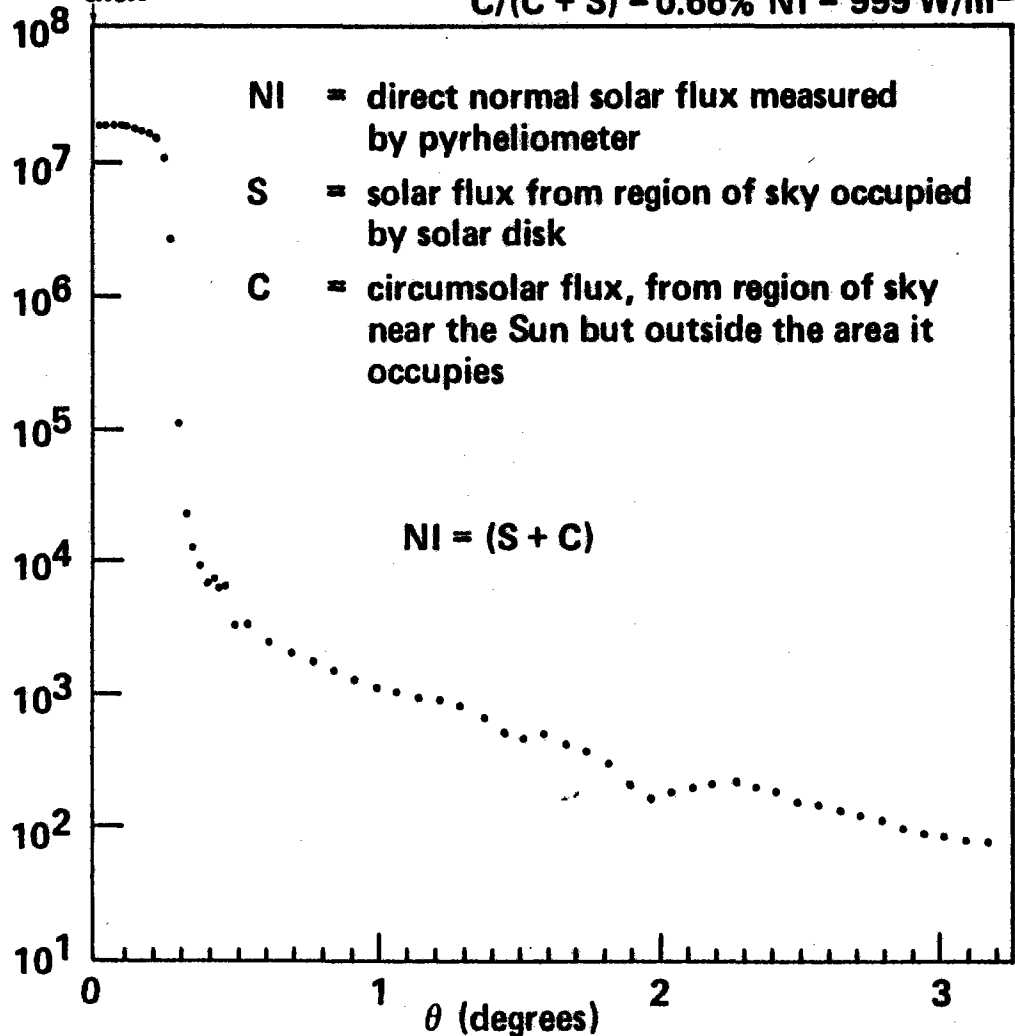


Figure 8.4-5. Sunshape During Test Event EB-9A

# Sunshape During Test Event EB-9A

Center of solar disk  
Albuquerque (scope 2)  
79/01/20 12:05 solar time  
 $C/(C + S) = 0.66\%$  NI = 999 W/m<sup>2</sup>



451

W/m<sup>2</sup>  
steradian

Figure 8.4-6. RTAF Scan During Test EB-9A

# RTAF Scan During Test EB-9A

Solar  
flux  
(kW/m<sup>2</sup>)

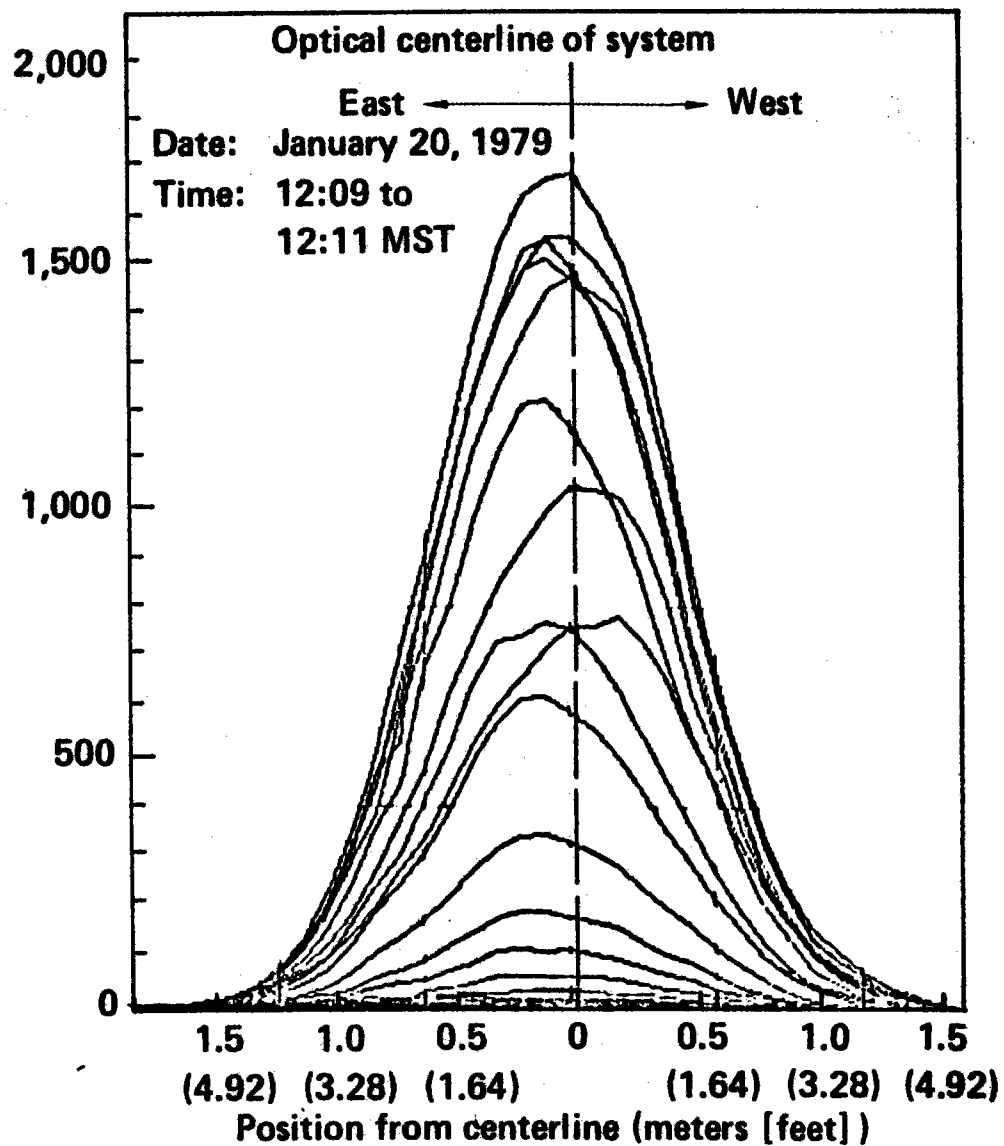


Figure 8.4-7. RTAF/Helios Correlation, Horizontal Scan Through Optical Centerline of System

# RTAF/Helios Correlation, Horizontal Scan Through Optical Centerline of System

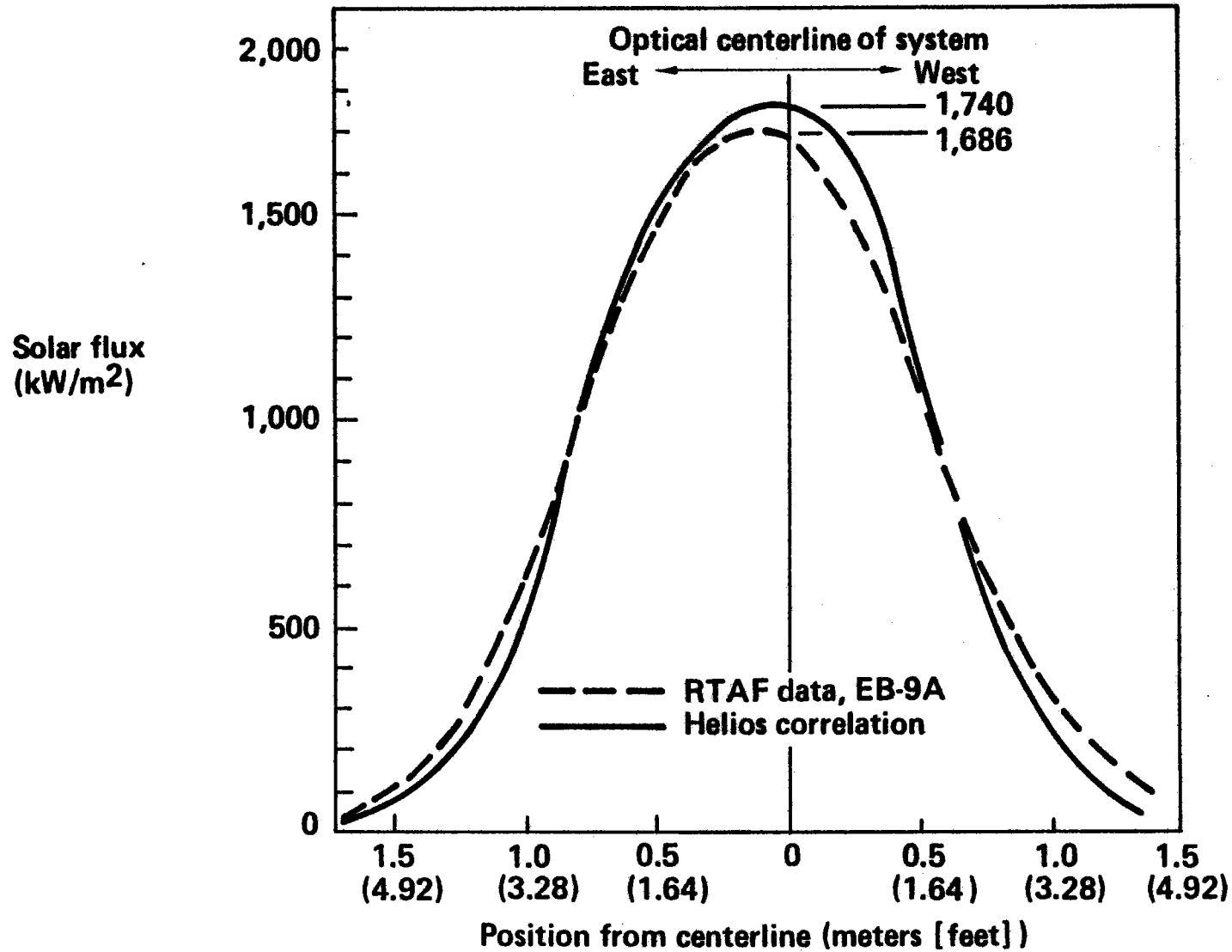
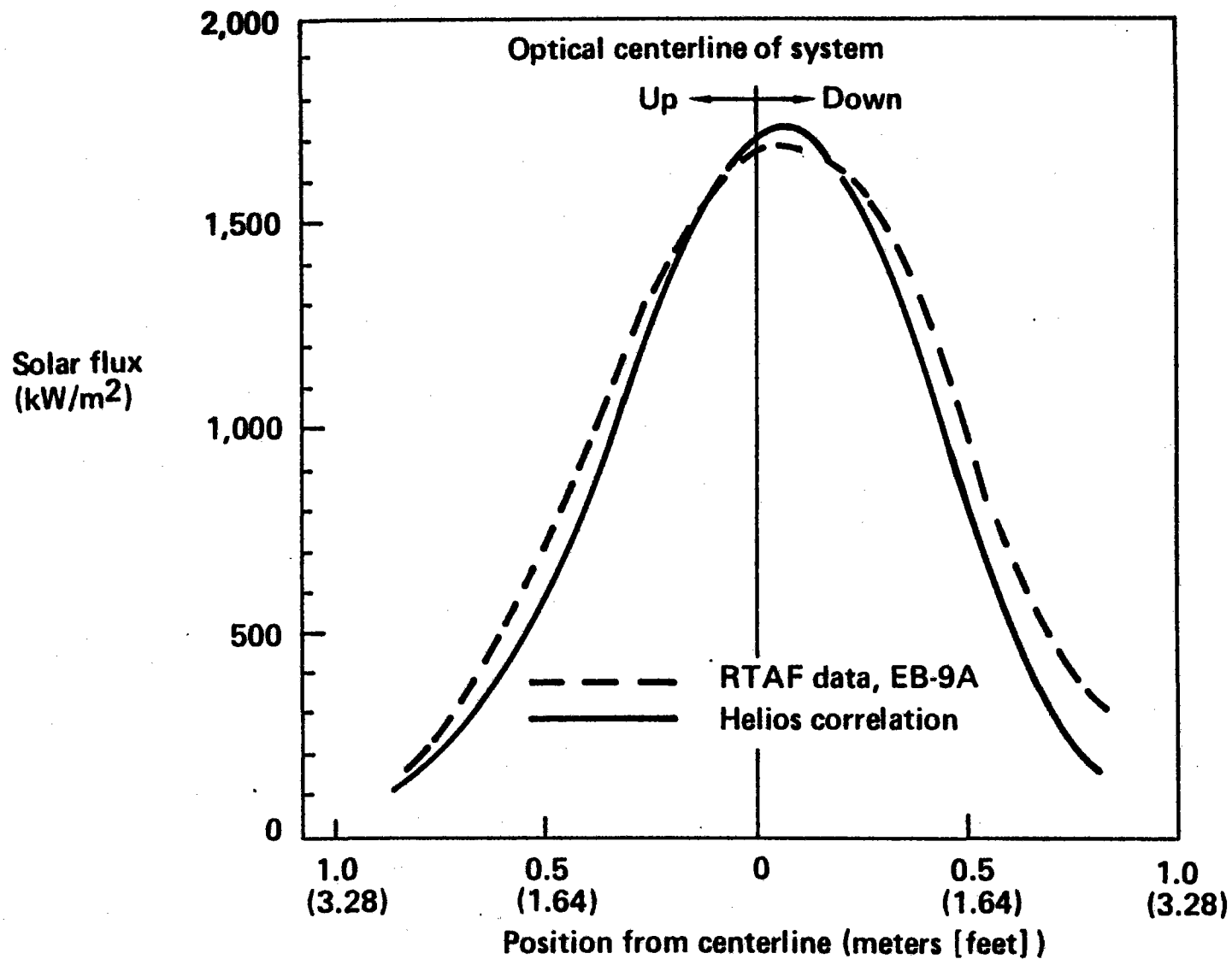


Figure 8.4-8. RTAF/Helios Correlation, Vertical Scan Through Optical Centerline of System

## RTAF/Helios Correlation, Vertical Scan Through Optical Centerline of System



RTAF plane were correlated with HELIOS data. Two of the profiles, vertical and horizontal through the centerline of the CRTF/BMSR optical system, are shown here. Differences between the experimental and analytical solar-flux values range from zero, where the flux profiles cross over, to as much as  $150 \text{ kW/m}^2$  in the regions of greatest mismatch. The integrated solar flux in the RTAF aperture was 1566 kW for the experimental data and 1490 kW for the HELIOS analysis data.

Initially it was expected that HELIOS correlations of experimental RTAF data could be produced by a few iterations of the HELIOS code for each test case. However, the first two correlations, EB-9A and EB-9B, consumed several weeks of programming activity and most of the computer time allocated for the posttest data processing. During this time it became clear that the HELIOS inputs needed for correlating were far from the initially expected values.

The most severe problem encountered in these RTAF-HELIOS correlations was that the CRTF solar image was nonsymmetrical, being spread out to the eastern side of the RTAF plane (Figure 8.4-6) and the eastern side of the receiver aperture (left side of Figure 8.4-2). The only way this performance could be reproduced by HELIOS analysis was to retarget some of the heliostats to an aimpoint displaced to the west of the center of the BMSR aperture. This multiple aimpoint technique was used to produce the HELIOS data in Figures 8.4-7 and 8.4-8.

Use of this tactic to correlate RTAF data caused a loss of confidence in the targeting accuracy of the CRTF collector system and clearly showed that the HELIOS computer code was not characterizing all the variables in the collector system. Suggestions as to the cause of this unexpected performance were as follows:

- a. Long-term drift of the collector pointing accuracy caused by uncorrected nonorthogonality of their azimuth and elevation axes. Long-term tests of pointing accuracy were not conducted during the initial system checkout. When spot checks of the long-term heliostat pointing accuracy were conducted they showed significant pointing errors developing after several hours of operation. CRTF personnel are

continuing to evaluate this problem.

- b. Aiming offset because of systematic roundoff of digital angular measurements during collector-field alignment. This offset was caused when collector aiming parameters were being updated in the collector-field computer. The digital encoders used to aim the heliostat exhibited a least significant bit that amounted to several inches of image displacement at the target. Upon investigation, it was learned that this error had been systematically rounded off in the same direction. This factor was not incorporated in the HELIOS pointing error algorithm.
  
- c. Systematic bias of collector field aimpoint to the east due to motion of the Sun. Initially when being brought onto target, the collector-field computer placed the heliostat image directly on target. Then, as the sun moved in the sky, the heliostat image moved off the target in an easterly direction. When the pointing error became equal to 1 data bit of the heliostat encoders, the heliostat was moved to again be directly on target. Because eastward pointing errors were allowed to develop in this way, the effective target point was slightly to the east of the actual target point. Apparently, this bias was not accounted for in this HELIOS code.

These concerns were revealed after the completion of just two of the planned correlations of RTAF and HELIOS data. Tests EB-9A and EB-9B were conducted within a period of about 40 min of one another. They used the same collector-field heliostats. Other conditions such as the direct solar intensity were nearly identical. RTAF scans were similar and correlated equally well with HELIOS computer runs.

The transfer functions estimated receiver solar input at 1059 and 1075 kW for EB-9A and EB-9B, respectively. The HELIOS code indicated that the receiver solar input consistent with RTAF data should be 950 kW for both of these tests.

The experimental measurements of BMSR solar input ended on January 28, 1979,

with the failure of the RTAF scanning mechanism. Even though a major effort was expended by CRTF personnel to return it to operational status, it was not available during the very productive test days in late January and the three days of tests in March.

#### 8.4.2 HELIOS Analysis With Actual Test Conditions

Because RTAF measurements were unavailable and RTAF-HELIOS correlations were impractical for many of the BMSR tests, it was necessary to exercise other optional means of defining BMSR solar input. The BMSR thermal performance data were evaluated and found to contain a total of 21 events of special interest. They were the equilibrium heat balance test conditions desired for assessment of receiver thermal efficiency. Solar input data were desired for these events that were consistent with one another and as accurate as possible.

Even though only two cases had been completed, the RTAF-HELIOS correlation methods described in Section 8.4.1 were expected to provide the most accurate assessment of receiver solar input. Supplemental analytical methods of determining receiver solar input by the use of the HELIOS computer code were adopted. In adopting an analytical data base it was understood that the RTAF-HELIOS correlation cases could be used to verify its accuracy.

CRTF personnel agreed to run the HELIOS code to analyze the performance of all the CRTF heliostats and to provide individual heliostat solar inputs to the BMSR as functions of time of day. The HELIOS input parameters included those for which the previous RTAF-HELIOS correlations had been accomplished. An environmental parameter, the direct solar flux, was referenced at 1000 W/m<sup>2</sup>. Adjustments of the heliostat performance data were made to correct for the actual direct solar flux on the day and time of interest. Two characteristic days of the year were selected for these analyses. One was in January, to characterize field performance during those tests, and another for tests in March.

The data base was provided in the form of a three-dimensional matrix of



performance values for the individual heliostats. One dimension of the matrix covered times of day from 7:00 AM to 5:00 PM in 1-hr increments. Another dimension consisted of a listing of all the heliostats that were ever used in BMSR tests. The third dimension to this matrix of data consisted of two elements, January data and March data.

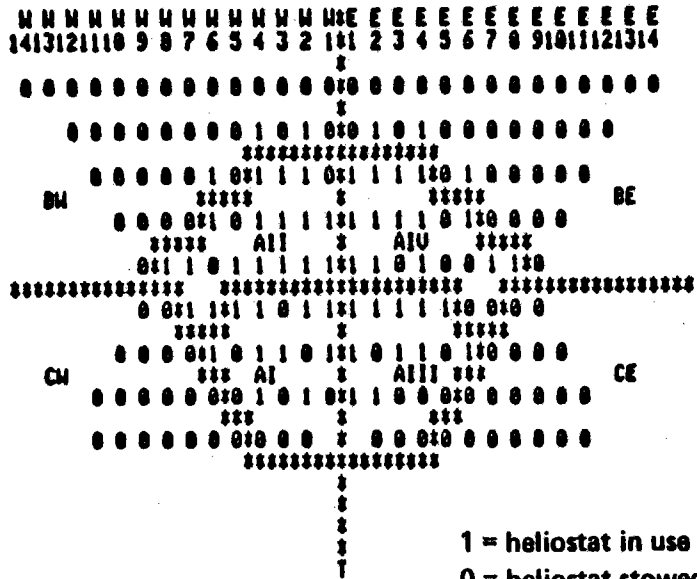
A computer code was written at Boeing to provide access to this data and compute the receiver solar input for particular tests. Inputs included date, time of day, heliostats in use, and direct solar flux, all of which were available from the BMSR test logs. An example of the computer code output is shown in Figure 8.4-9. The day, date, and time are shown along with the test identification, in this case EB-9F. A diagram of the CRTF collector field is produced with rows of heliostats identified and 0's or 1's designating heliostat status, on or off. The BMSR solar input contributed by each heliostat in operation is listed (only a part of this list is included in Figure 8.4-9). A summary of the BMSR solar input from various zones of the collector field is shown along with the total BMSR solar input.

Figure 8.4-10 compares the receiver solar inputs computed for 16 applicable test cases with one another and with an independent test measurement. The calorimeters located on interior sidewalls of the BMSR received reflected and reradiated solar heat from the receiver back-cone. They also received radiant heat from the heat exchangers. As indicated in Figure 8.4-10, the calorimeter readings at similar heat exchanger temperatures were directly proportional to the solar inputs computed by these specialized HELIOS computer runs. This provided an independent verification of the relative accuracy of the HELIOS computations.

As mentioned earlier, the RTAF-HELIOS correlations for tests EB-9A and EB-9B provided base points to check on the absolute value of these new HELIOS computations. Whereas the RTAF-HELIOS correlations indicated solar inputs of 950 kW for these tests, the new analyses indicated values of 900 and 905 kW. As a result, it was decided to increase all the nominal values obtained by these HELIOS computations by 5%, keeping in mind that uncertainty assessments as to absolute accuracy of the data must be increased

Figure 8.4-9. Example of Helios Analysis With Actual Test Conditions

# Example of Helios Analysis With Actual Test Conditions



CRTF field  
EB-9F

- Heliostats in use found from CRTF field test file.
- Insolation value found from test data tapes.

Day = 70  
 Time = 11.54 hr  
 QSOL = 1030.0 kW/m<sup>2</sup>  
 Test EB-9F = March 24, 1979  
 Equilibrium heat balance

Nonzero power input heliostats:

Heliostat No.	Power input (kW)	Efficiency	Zone	Row
29	16.56	0.16079E + 02	AI	4
31	20.94	0.20333E + 02	AI	4
39	23.98	0.23280E + 02	AI	5
41	22.03	0.21387E + 02	AI	5

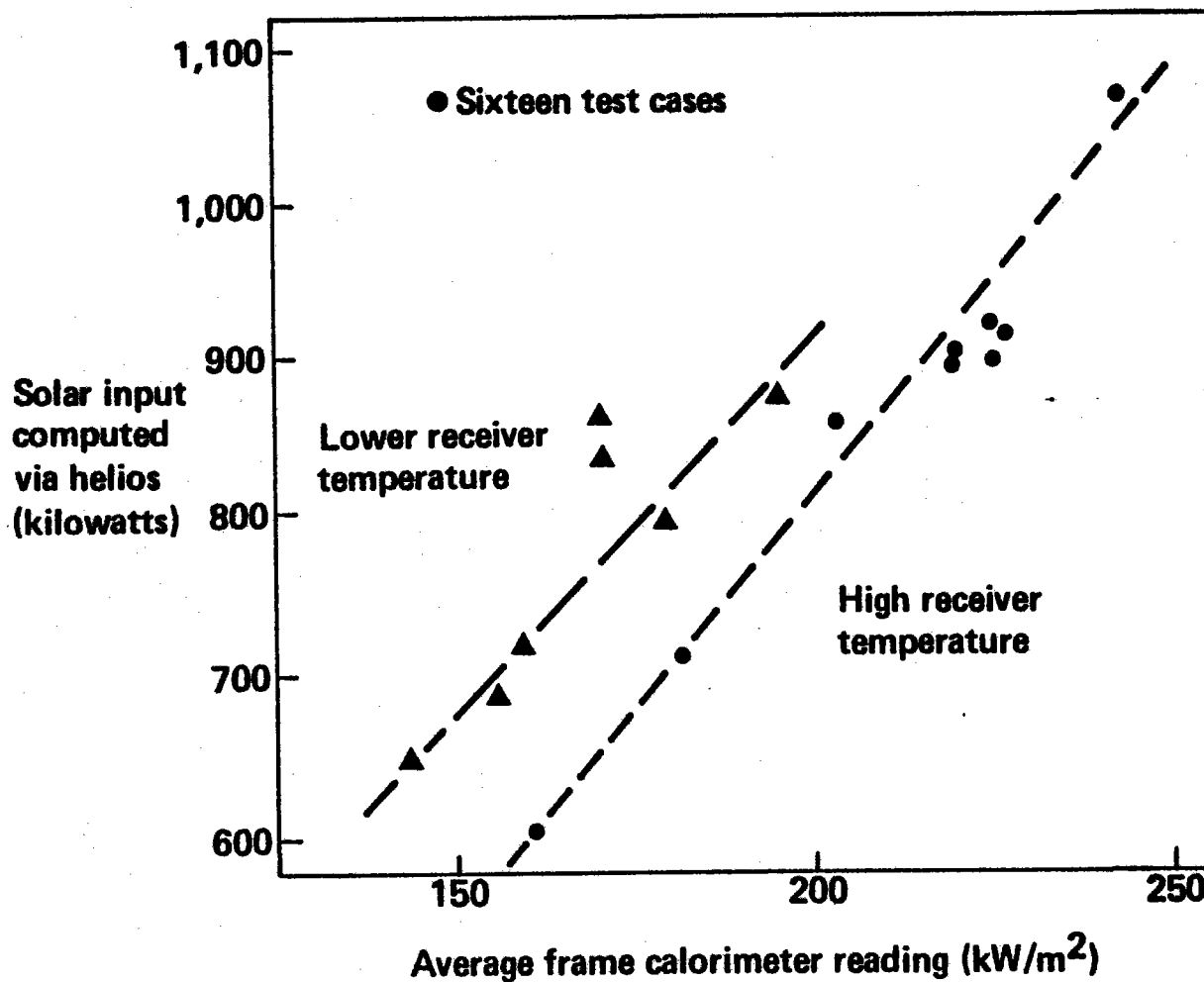
Note: For all heliostats

Summary:

Zone	No. of heliostats	Heat input (kW)	Percentage
BW	3	30.68	3.4
BE	3	29.73	3.3
AI	10	196.47	21.8
AII	17	239.93	26.7
AIII	11	214.16	23.0
AIV	14	188.32	20.9
CW	0	0.00	0.0
CE	0	0.00	0.0
Total	58	899.28	100.0

Figure 8.4-10. Comparison of Helios Analysis Results With Independent Test Data

## Comparison of Helios Analysis Results With Independent Test Data



correspondingly.

#### 8.4.3 Solar Input Data Base

Collector-field operating conditions and receiver solar input data for 19 cases of particular interest are listed on Table 8.4-2. These were all test conditions for which receiver thermal efficiency data was desired. Ten of the test cases included RTAF scan data; two included RTAF scans and RTAF-HELIOS correlations and analysis of the receiver solar input. The 16 test cases occurring in January and March included comparable HELIOS computations of the receiver solar input that were adjusted (increased by 5%) to achieve agreement with the two RTAF-HELIOS correlation solar input values.

Receiver solar input data for seven similar tests are compared with one another in Figure 8.4-11. Data from three different sources are compared. The two receiver solar inputs determined by means of the RTAF-HELIOS correlation analysis, EB-9A and EB-9B, are shown. The comparable HELIOS analysis data are shown in their original form (values shown are 5% less than in Table 8.4-2). Also, measurements of the cavity wall heat flux (Figure 8.4-10) have been scaled up by an equal factor to independently describe the effects of the receiver solar heat input. The pattern of values of these scaled-up heat-flux data agrees reasonably well with the test-to-test variation of solar inputs computed by HELIOS.

As shown in Figure 8.4-11, all these indications of receiver solar input were contained within a 10% uncertainty interval with its lower boundary colocated with the solar input values computed by means of the HELIOS code. This placed the values obtained by RTAF-HELIOS correlation analysis squarely in the center of the uncertainty interval.

A 10% uncertainty interval was definitely the smallest that could be substantiated. Some additional observations were pertinent to the consideration of larger uncertainty intervals. There was no cause to consider solar input values less than the minimums included in the 10% uncertainty band. The transfer function used during tests consistently

Table 8.4-2. Solar Input Data Base

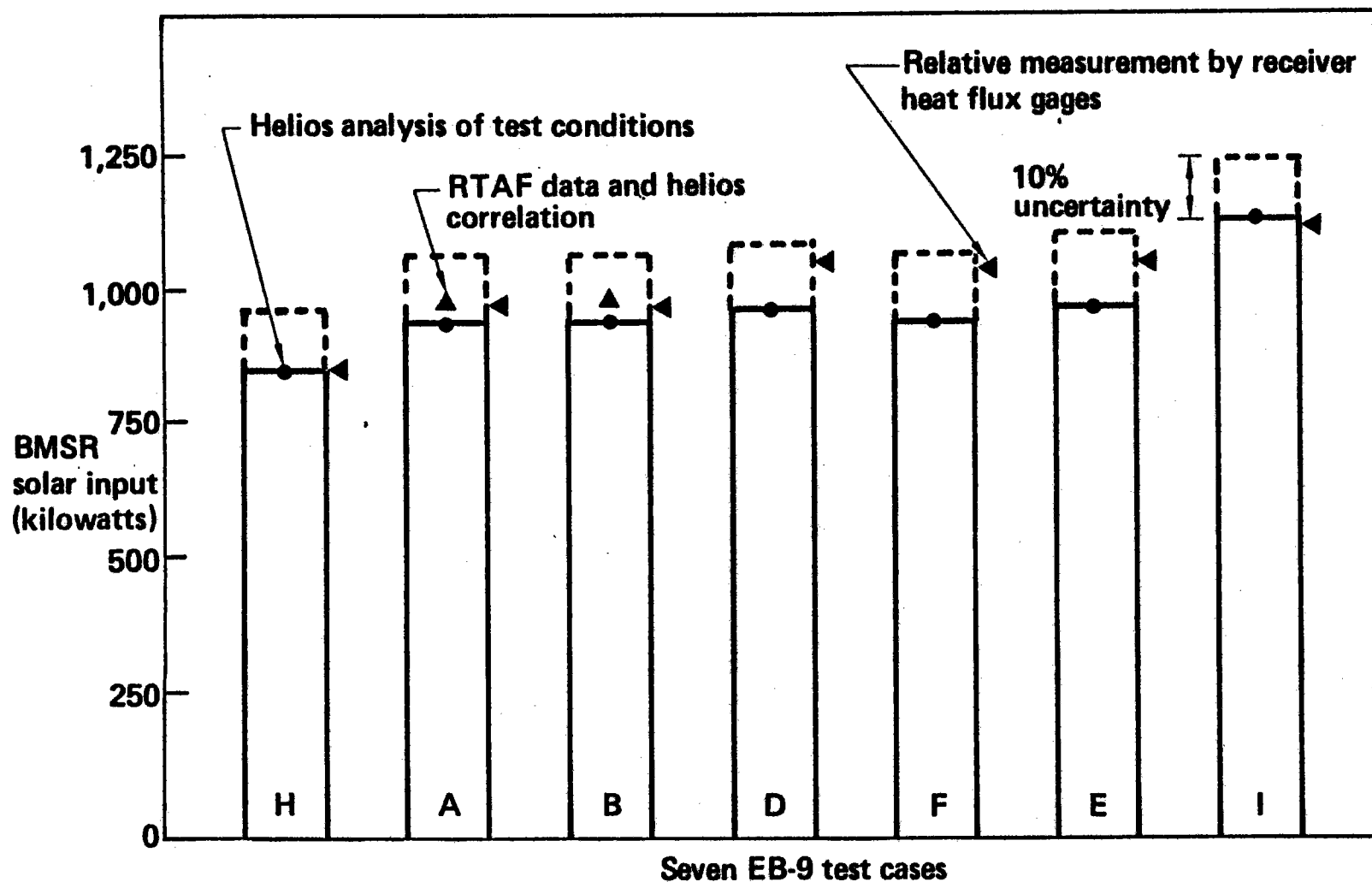
## Solar Input Data Base

Test case	Date	Mountain standard time	Heliostats in operation	Direct solar flux (W/m <sup>2</sup> )	RTAF scan	BMSR solar input (kW)	
						RTAF/helios	Helios*
EB-1A	11/17/78	12:17	34	1,030	Yes	—	—
EB-2A	11/28/78	12:18	40	930	Yes	—	—
EB-4A	12/10/78	14:49	53	970	Yes	—	—
EB-5A	1/4/79	13:06	47	1,000	Yes	—	671
EB-7A	1/7/79	14:25	61	900	No	—	718
EB-8A	1/10/79	12:21	59	1,000	Yes	—	835
EB-8B	1/11/79	11:50	65	990	No	—	920
EB-7B	1/13/79	14:20	65	980	No	—	879
EB-9A	1/20/79	12:10	62	1,010	Yes	950	945
EB-9B	1/20/79	12:52	62	1,020	Yes	950	950
EB-6A	1/20/79	13:49	53	1,000	Yes	—	744
EB-3A	1/20/79	14:53	51	940	Yes	—	624
EB-4B	1/23/79	12:54	50	1,040	Yes	—	749
EB-8C	1/30/79	14:20	68	1,020	No	—	904
EB-9D	1/31/79	12:00	65	1,070	No	—	961
EB-9E	3/23/79	12:00	60	1,010	No	—	966
EB-9F	3/24/79	11:50	58	1,030	No	—	944
EB-9H	3/25/79	11:00	55	1,030	No	—	902
EB-9I	3/25/79	11:20	68	1,040	No	—	1,128

\*Values increased by 5% to agree with RTAF/helios correlations

Figure 8.4-11. Comparison of Solar Input Data From Three Sources

## Comparison of Solar Input Data From Three Sources



indicated solar inputs higher than the values shown in Table 8.4-2. Typically, they were 10% to 13% higher. In addition, a series of HELIOS analyses conducted independently by CRTF personnel for EB-9D, EB-9E, EB-9F, EB-9H, and EB-9I also indicated higher solar input values than those that were adopted.

The most recent HELIOS computations used an updated version of the HELIOS code with improved means of defining the heliostat pointing errors and other concerns described in Section 8.4.1. These newest solar-input computations provided values between 21% and 24% greater than the values in Table 8.4-2. They are direct computations because there were no RTAF data for these tests. These high values are not consistent with any of the previous studies, including the pretest analyses. The major difference between these new computations and the other posttest analyses with HELIOS is the use of a single target point for the heliostats. A second target point to the east of the aperture center had been used for some of the CRTF heliostats to obtain HELIOS correlations with measured RTAF data. The return to a single aimpoint would only be justified if all the previous problems had been caused by HELIOS. Considerable doubt remains as to the long-term tracking accuracy of the CRTF collector system as configured during BMSR tests. Until this issue is resolved, reliance will be placed on the experimentally based RTAF-HELIOS correlation data rather than this new, purely analytical data.

#### 8.5 MEASUREMENTS OF APERTURE-RIM AIR VELOCITY

As mentioned in Section 8.4, the real-time estimates of BMSR solar input by means of the transfer functions were about 10% higher than the values obtained by the more accurate posttest correlation with RTAF data. These real-time solar-input estimates caused a great deal of concern at the time because the additional solar input could not be accounted for. It did not show up in the heat transfer to circulating air, nor was it measured in the radiant thermal and solar reflected heat loss out the receiver aperture. Convective heat losses much higher than the 2% to 4% that had been predicted before the tests were suspected to be the cause of these higher-than-expected heat losses.

Studies were conducted to determine the magnitude of the air velocities needed to transport this heat out through the BMSR aperture. If the transfer function solar input data were to be believed, the BMSR convective heat loss at design point operating conditions had to be approximately 140 kW. An air transport mechanism was visualized whereby ambient temperature air was assumed to be entering the lower part of the BMSR aperture forcing hot cavity air out the upper part of the aperture. The pressure gradient resulting from the buoyancy of the in-cavity air was assumed to be counteracted by velocity-head pressure losses caused by acceleration and deceleration of the air as it passed through the aperture.

A preliminary analysis was conducted based on the assumption that heat was being transported out of the receiver aperture at a rate of 140 kW. The study showed that rather high air velocities into the bottom and out the top of the aperture were needed to accomplish this heat transport. The outward velocity near the top of the aperture had to be approximately 5.0 m/s (16.4 ft/s).

Normal means of measuring air velocities would not work in the high solar-flux environment of the BMSR aperture. However, high-temperature insulation materials were available that could survive in the heat-flux environment near the rim of the opening. Because the air velocities of interest were quite high, it was concluded that a simple pendulum air-vane device could be used to detect their presence.

Initially, a small piece of the high-temperature insulation board used for aperture-rim solar shielding (3000 board manufactured by Babcock and Wilcox) was placed in the upper rim of the cavity aperture. The sample remained intact after a full day of solar testing. Some pitting was observed on the sunlit surface of the insulation board sample, but it retained its shape and mechanical integrity. A piece of Inconel 617 weld wire 1.0 mm (0.04 in) in diameter was used to hold the sample in place. The wire remained intact but was found to be fully oxidized and brittle, with little strength.

A small wind tunnel was fabricated that simulated the interior shape of the upper rim of the BMSR aperture. A cooling fan and flow straightener were



used to provide airflow. The test zone velocity was modulated by adjusting the exit area of the tunnel. Air velocities were measured by a hand-held velometer. This facility worked well at velocities up to about 3.5 m/s (11.5 ft/s) where fan surging was experienced. The wind tunnel calibration facility is shown in Figure 8.5-1.

The first anemometer to be calibrated and tested in the receiver aperture had a very high sensitivity. Full deflection to a horizontal position occurred at less than 1 m/s. During BMSR testing, it quickly assumed this fully deflected position and remained there for the duration of the day's testing.

The second anemometer to be constructed is shown in Figure 8.5-1. The ceramic spacers on either side of the anemometer were part of a free-swinging trapeze of wire used to visually estimate its position. The wind tunnel was in operation in Figure 8.5-1 and the anemometer was displaced about 3.8 cm (1.5 in), indicating an airflow of about 1.4 m/s (4.6 ft/s).

Figure 8.5-2 shows the BMSR aperture with the anemometer in place. No air velocity is present and the bottom of the anemometer is parallel with the bottom of the trapeze. The 2.5 cm-long (1 in-long) ceramic spacers used to indicate displacement of the anemometer can be clearly seen in this photograph.

The photograph in Figure 8.5-2 was taken through a telescope located on the observation platform of the CRTF control building. This same telescope was used to observe anemometer deflections during the tests.

Anemometer measurements of the aperture-rim air velocity existed for just one of the BMSR test days. After the testing of the first anemometer, it was decided that an instrument with a velocity sensitivity in the range of 1 to 3 m/s (3.3 to 9.8 ft/s) was desired. This new anemometer was also fabricated from 3000 board. It was calibrated in the wind tunnel and installed in the aperture rim on January 19, 1979. During the day of tests, its displacement was observed through the telescope and recorded in the test

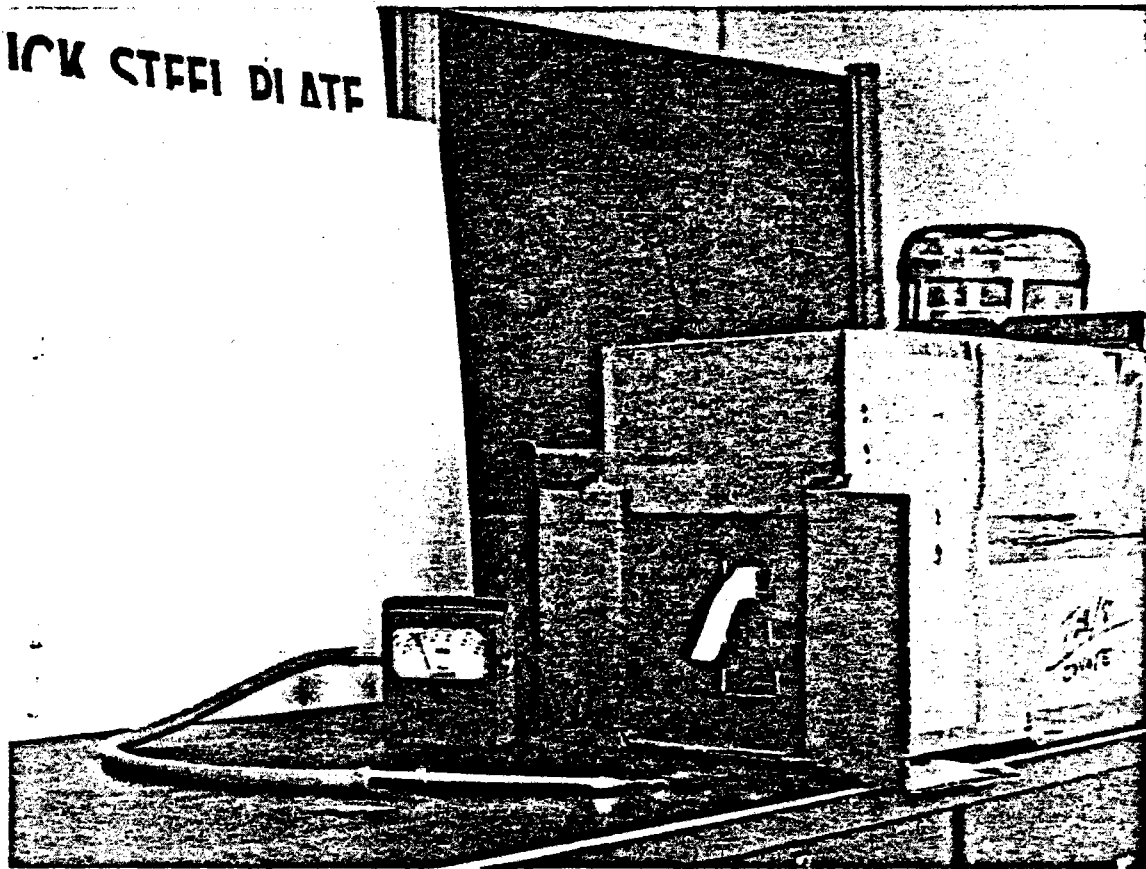


Figure 8.5-1: Aperture Rim Anemometer Calibration Facility

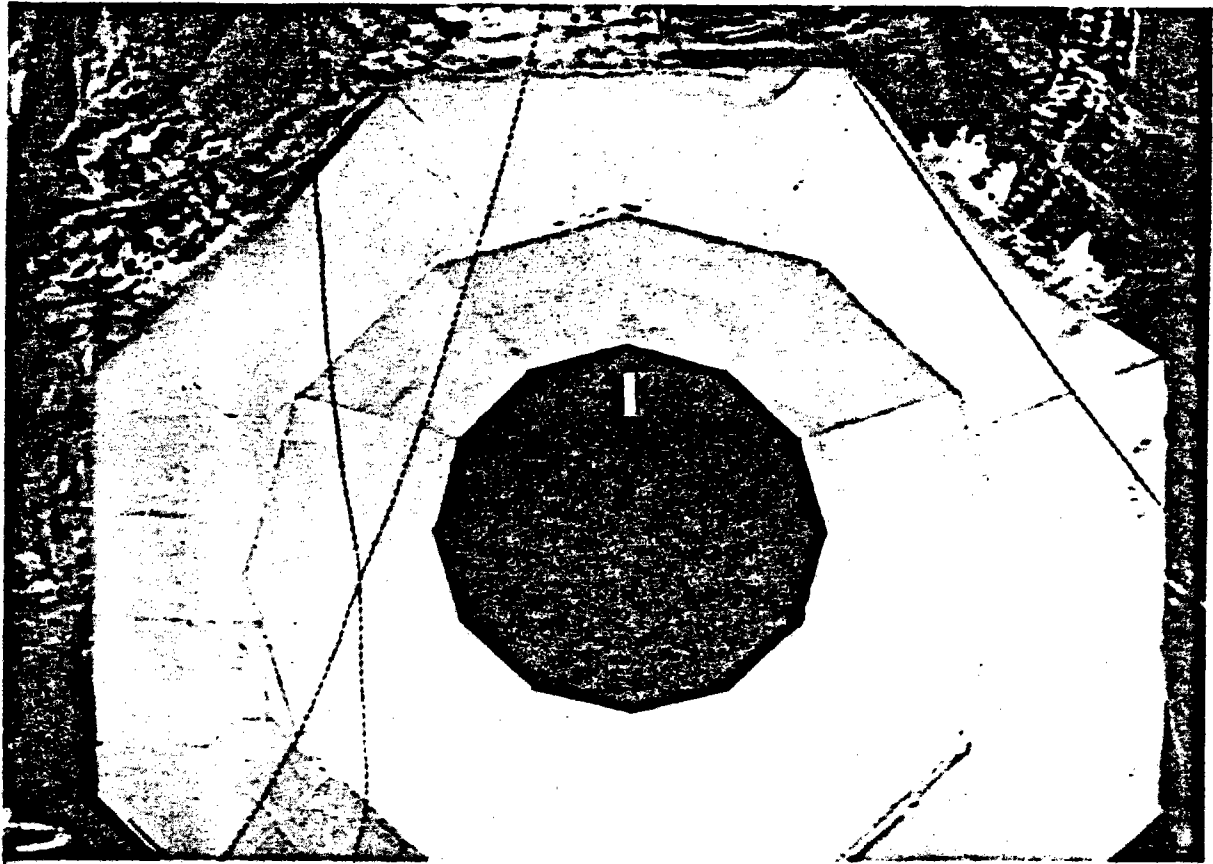


Figure 8.5-2: Anemometer Installed in BMSR Aperture

log. Upon removal from the receiver aperture, the anemometer was replaced in the wind tunnel and recalibrated. This was necessary because of pitting of the insulation board, which affected its weight distribution. These pits can be seen in Figure 8.5-1.

The posttest anemometer calibration data are shown in Figure 8.5-3. The data spread at equal air velocities was attributed to two factors. First, the width of individual calibration data lines was typical of the different displacement readings obtained by three different observers. Second, after testing, the anemometer exhibited measurable hysteresis. Values measured with increasing air velocity tended to be lower than the nominal value and those measured with decreasing air velocity were higher.

Figure 8.5-4 shows the aperture-rim velocity measurements obtained during tests on January 20, 1979. A total of seven observations were recorded. The uncertainty intervals shown for these data include the calibration uncertainty described above as well as the observer's own estimated range of uncertainty.

Ambient wind velocity and direction during January 20, 1979, are also noted in Figure 8.5-4. The windspeed was quite high on this test day. It consistently came from an azimuth within a few degrees north, placing the receiver aperture in a stagnation zone on the north side of the CRTF tower. For this reason, ambient wind should not have affected the aperture velocity.

These measurements showed that the aperture-rim velocity was from 1.0 to 1.5 m/s (3.3 to 4.9 ft), considerably less than the 5 m/s (16.4 ft) required to transport 140 kW. Subsequent posttest analyses discussed in Section 11.0 concluded that the measured velocities could account for convective heat transport of about 60kW out the receiver aperture. This heat loss was also consistent with the receiver heat balance based on RTAF-HELIOS correlation and subsequent HELIOS predictions of solar input to the receiver.

Figure 8.5-3. Posttest Calibration of Aperture Rim Anemometer

## Posttest Calibration of Aperture Rim Anemometer

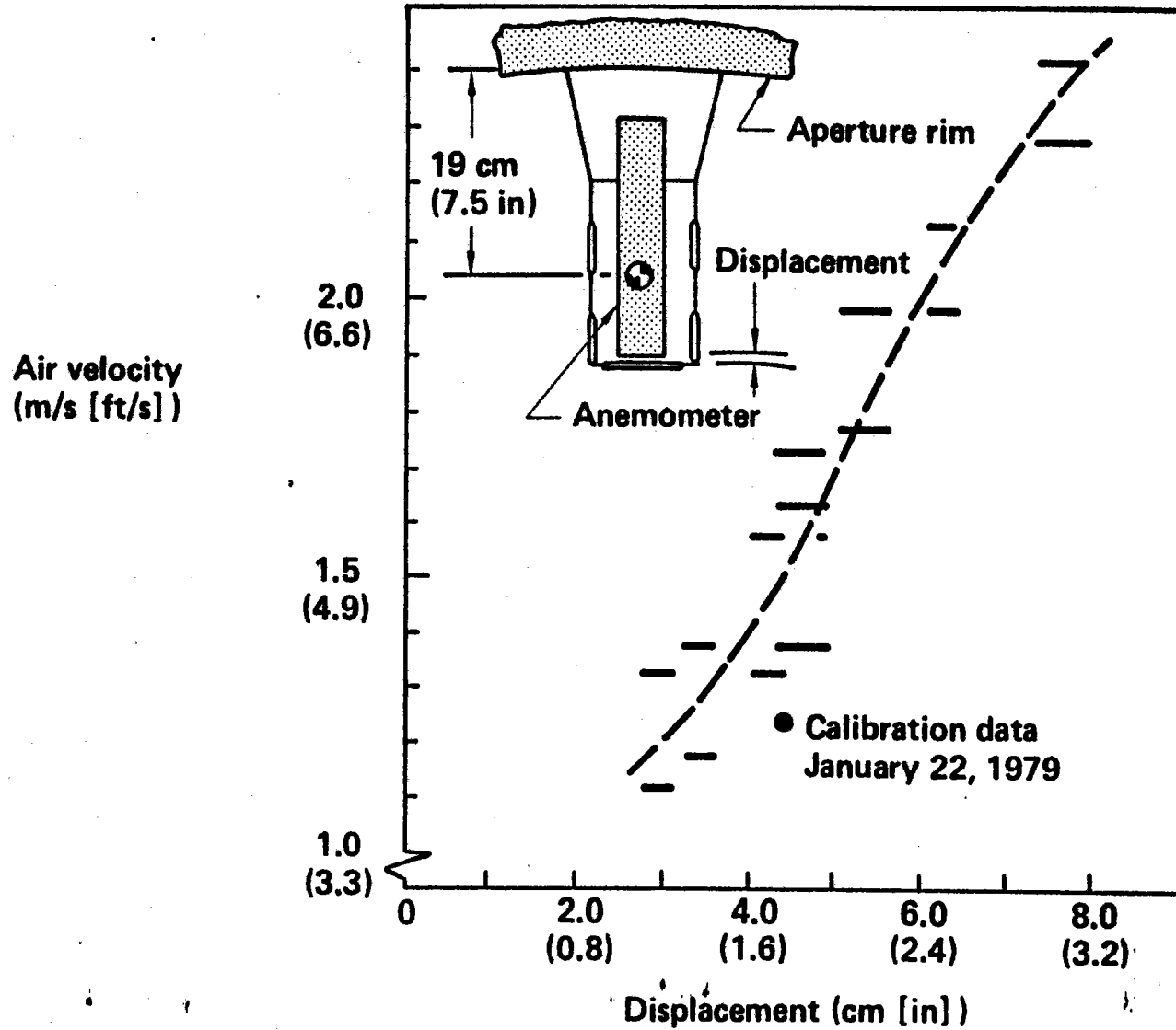
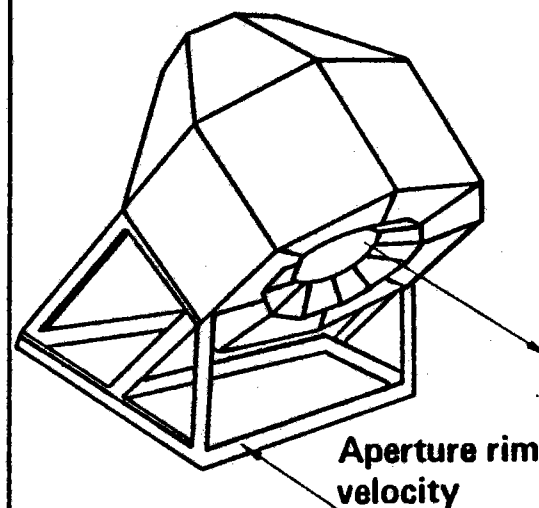
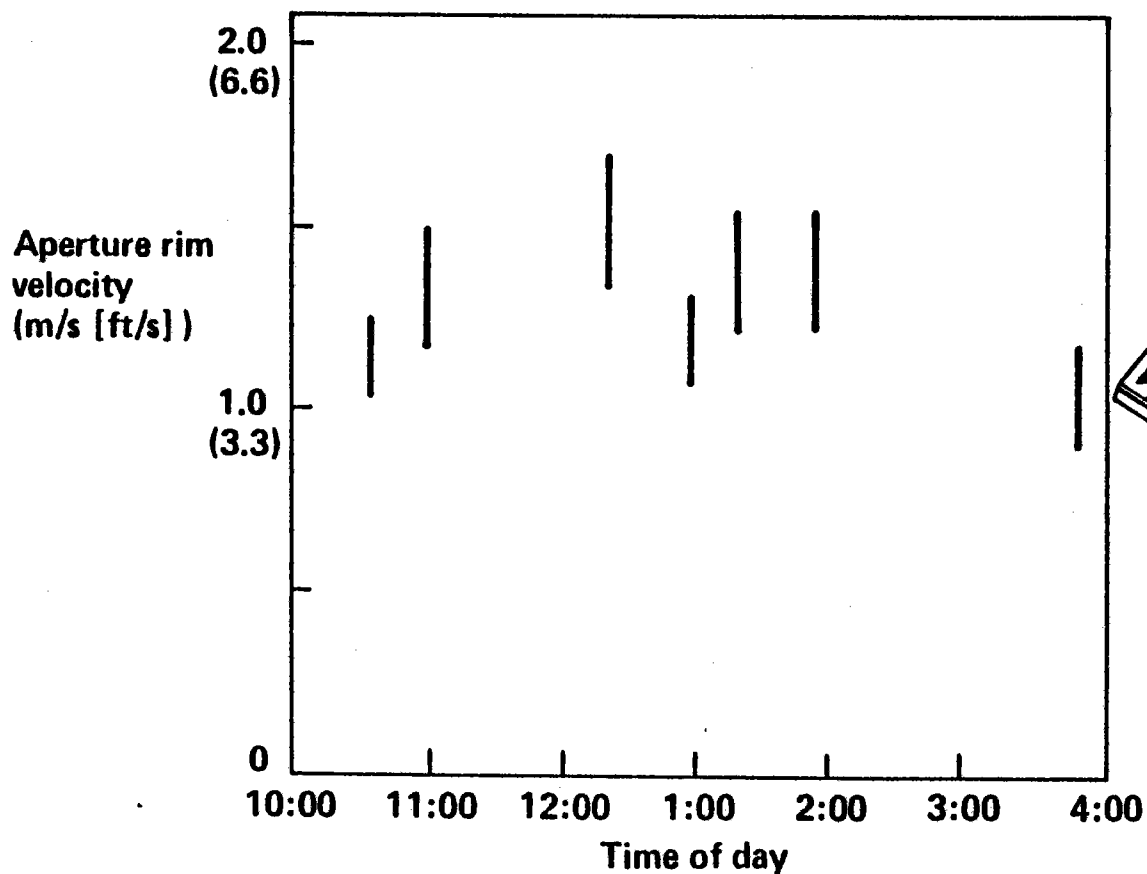


Figure 8.5-4. Aperture Rim Air Velocity Measured on January 20, 1979

# Aperture Rim Air Velocity Measured on January 20, 1979



North wind azimuth is zero

Aperture rim velocity

471

6.5	9.9	7.5	5.0	3.8	Ambient wind velocity (m/s [ft/s])
(21.3)	(32.5)	(24.6)	(16.4)	(12.5)	
8	2	340	336	40	Azimuth (degrees)

## SECTION 9.0

### RESULTS OF THE EXPERIMENT

Solar test data (Section 8.0) was processed and evaluated for each of the six types of solar tests described in Section 7.0. In addition, the test data obtained during BMSR transient cooldown events was processed to substantiate evidence of convective heat transfer through the receiver aperture. These experimental results are reported in Section 9.1 through 9.7. Other direct test results, including the equipment problems encountered during tests, and the review of testing effects on the receiver are discussed in Section 10.0.

#### 9.1 EQUILIBRIUM HEAT BALANCE TESTS

##### 9.1.1 Identification of Equilibrium Heat Balance Conditions in Test Data

During operation, the BMSR accepted solar heat at a high rate and transferred most of this heat to the air flowing through its heat exchangers. Thermal equilibrium conditions existed in the receiver when a steady rate of solar input was balanced by constant rates of heat transfer to the circulating air and to the environment by means of heat-loss mechanisms. This balanced state of heat transfer within the receiver was needed to accurately measure its heat transfer efficiency.

A number of test operating conditions disrupted the heat transfer equilibrium of the receiver. These included changing rate of solar heat input, changing rate of airflow through the receiver heat exchangers, and storage of heat in the receiver by virtue of its thermal capacity when its temperatures were changing.

Stabilization of these conditions was the most important consideration during the tests that determined receiver thermal efficiency.

The BMSR EB tests were conducted to obtain receiver efficiency measurements. Solar test operating conditions suitable for the characterization of

receiver thermal efficiency occurred during other tests as well. The methods used to identify equilibrium conditions in the test data are described herein. The 21 sets of equilibrium test data found in the BMSR test results are also presented.

It was difficult to achieve solar test conditions for which the solar input, thermal output, and temperatures of the receiver remained constant over a several minute period. Receiver solar input was at best, a steadily changing condition. Even when the ambient direct solar flux was constant, the heliostats in the collector field continued to move. As a result, their performance varied because of changes in their projected area and their shadowing and blocking of one another. This caused changes in the receiver solar input. For this reason, most of the equilibrium test conditions occurred within a 2-hour period around solar noon. During this time, the solar elevation angle remained nearly constant. Solar input was also more constant during these periods because the collector field performance was symmetrical. Performance before solar noon was equal to performance at an equal period after noon. This was because the north field optical characteristics simply reversed the roles of east-side and west-side heliostats at noon.

The existence of preferred solar heating conditions at noon is not particularly compatible with other conditions desired during EB tests. It was especially difficult to obtain steady-state-receiver operating temperatures by this time of day. Even though the heat exchanger tubing and the surfaces of the BMSR insulation walls exhibited rapid thermal response, several hours of receiver operation were needed before temperatures within the cavity wall insulation reached steady values.

Fortunately, even though 2 to 3 hrs of operating time were required for the temperatures within the receiver insulation to stabilize, the rate of heat storage in the insulation became negligibly small during the first hour of receiver operation.

The storage of heat in the receiver during startup was determined with the aid of the receiver thermal model (Section 3.0). These data are shown in



Figure 9.1-1. Functionally, the heat stored in the receiver during startup appeared as an additional heat loss. Its effect on test results was to reduce the indicated thermal efficiency of the receiver. The ordinate in Figure 9.1-1 describes the reduction of apparent receiver efficiency caused by neglecting the heat being stored in the receiver by virtue of its thermal capacity. After 1 hr of receiver operation, these errors became small enough to be considered negligible.

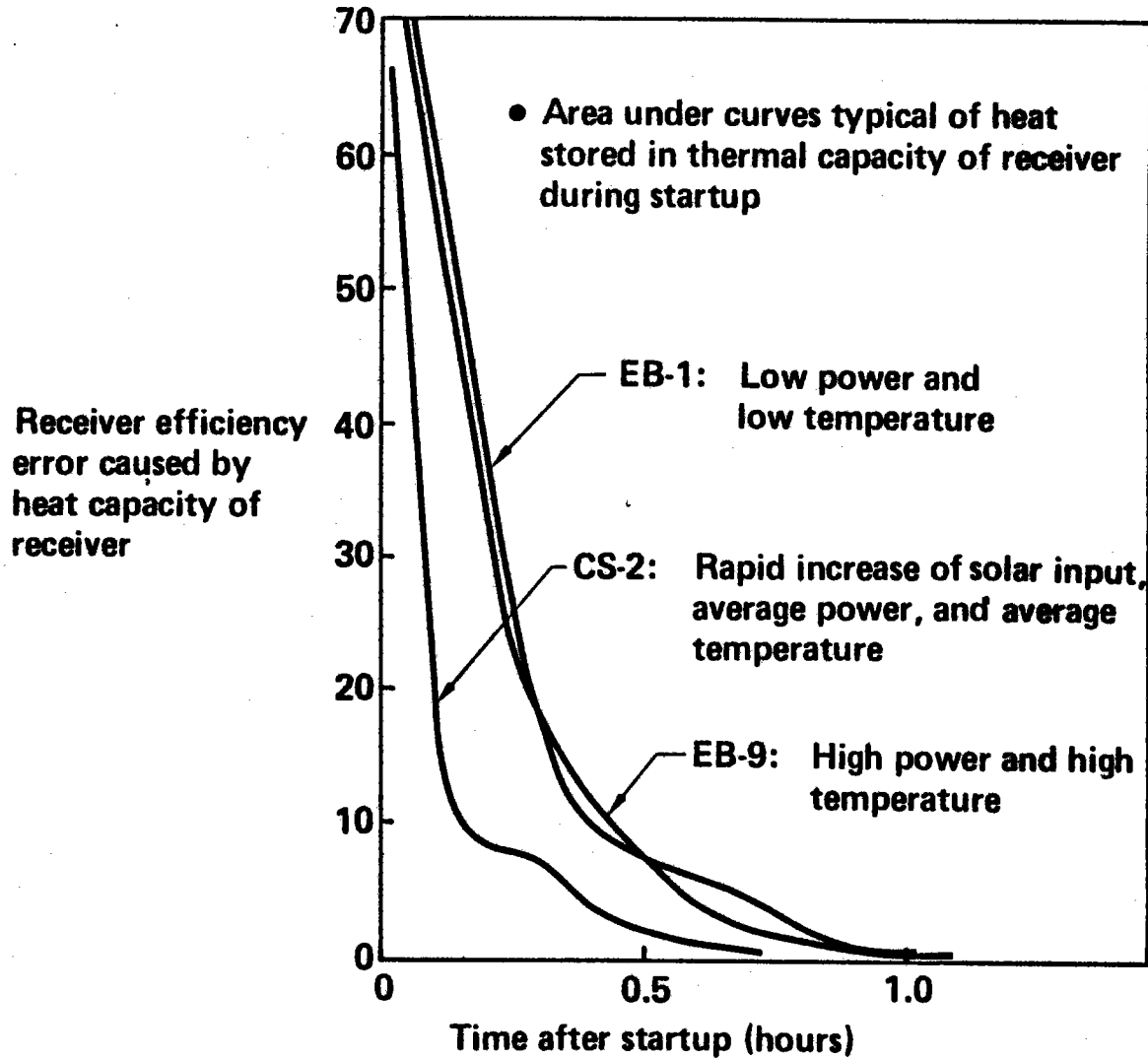
It was also difficult to achieve steady rates of airflow through the receiver heat exchangers. This flow was regulated by the outlet temperature controllers and valves used with the eight receiver heat exchangers. Even when operating alone, these controllers were subject to minor variations of flow within their proportional control limits. In the BMSR test setup, these controllers were also functionally dependent on the action of four other automatic control systems used in the test air supply system. These included compressor speed controls, compressor outlet pressure regulators, and the recuperator bypass and back-pressure valves located on the air supply equipment skid. The receiver flow controls were designed to exhibit response rates many times faster than these other flow and pressure controls. This difference in response rates greatly reduced the interaction between receiver flow controls and the others. Test data showed that these effects caused the airflow rates through the individual heat exchangers to vary in a random manner over a range of 5% to 10% of their average values. However, the period of the oscillations of individual panel flows was quite short (about 10 to 30 sec), so there was no apparent effect on the measured air outlet temperature.

Because of these various difficulties, the task of identifying equilibrium conditions in the solar receiver tests involved the following:

- a. Searching through the test logs to find periods when the receiver solar input was constant. This search was aided by notations that were made in the test log during periods of apparent thermal equilibrium conditions.
- b. Examining the collector-field operating record to verify test log notes and to identify a specific 5-min time span during each of these periods

Figure 9.1-1. Potential Errors in Receiver Thermal Efficiency Measurement Caused by Heat Capacity of Receiver

## Potential Errors in Receiver Thermal Efficiency Measurement Caused by Heat Capacity of Receiver



- that would be suitable for further detailed examination.
- c. Processing the engineering data tape to extract the 25 unique sets of receiver flow and heat transfer data on record for the 5-min period of interest.
  - d. Computing average values and standard deviations of the important receiver flow and heat transfer data including inlet and outlet air temperatures, airflow rate, and heat transfer to the air.

After the 25 data points were processed, the original data, average values, and standard deviations of values were examined to verify the suitability of the data point as an EB condition. Most of the test data processed exhibited average heat exchanger inlet and outlet temperatures that varied less than 3°C (5.4°F) during the 5-min period of interest. The heat transferred to circulating air generally exhibited a standard deviation of about 3%. In particular, the 25 separate measurements were examined to verify that steadily increasing or decreasing receiver heat transfer had not occurred during the 5-min period of interest.

As a result of these examinations of test data, several of the time periods of interest were moved a few minutes earlier or later. Disturbances of receiver flow rate and steady changes of the receiver heat transfer rate were generally avoided by this process.

It should be noted that this process of identifying EB test conditions was an approximate technique. As applied, the technique relied entirely on measured receiver data. Direct measurements of receiver solar input were not available to confirm that this receiver heat input rate was constant during the period of interest. Instead, the technique relied on the assumption that changes in the receiver solar input occurring during these 5-min periods would show up in the receiver heat transfer data, which was available for examination.

The 21 test events for which suitable EB conditions prevailed in the receiver are listed in Table 9.1-1. The table describes pertinent test conditions, including receiver airflow characteristics and solar input to the BMSR. The process of determining receiver solar-input values for these

Table 9.1-1. Twenty-one Sets of Equilibrium Heat Balance Data

## Twenty-one Sets of Equilibrium Heat Balance Data

Equilibrium heat balance test number	Date	Time of day <sup>a</sup> (MST)	No. of heliostats in use	Direct insolation (W/m <sup>2</sup> )	Average heat flux in receiver <sup>b</sup> (kW/m <sup>2</sup> )	Receiver airflow conditions				Receiver solar input <sup>c</sup> (kW)	Remarks
						Inlet (°C[°F])	Outlet (°C[°F])	Flow rate <sup>b</sup> (kg/s)	Heat absorbed <sup>b</sup> (kW)		
EB-1A	11/17/78	12:15	34	1,030	131	334 (833)	620 (1,147)	1.16 ±0.02	384	No data	Single-point BMSR data
EB-2A	11/28/78	12:14	40	930	159 ±2	438 (819)	703 (1,297)	1.16 ±0.03	341 ±8	No data	
EB-3A	11/20/78	14:48	51	940	161 ±3	527 (980)	810 (1,490)	1.03 ±0.03	331 ±11	624	Low panel 5 temperature
EB-4A	12/10/79	14:49	53	970	146 ±5	350 (681)	623 (1,153)	0.99 ±0.03	290 ±10	No data	Single-point BMSR data
EB-4B	1/23/79	12:54	50	1,040	159 ±2	415 (778)	710 (1,310)	1.47 ±0.01	471 ±4	749	
EB-5A	1/4/79	13:06	47	1,000	144 ±1	425 (797)	703 (1,296)	1.35 ±0.04	413 ±11	671	
EB-6A	1/20/79	13:49	53	1,000	181 ±1	527 (980)	816 (1,500)	1.31 ±0.03	425 ±9	744	
EB-7A	1/7/79	14:48	61	900	156 ±2	348 (657)	622 (1,151)	1.62 ±0.04	482 ±13	718	
EB-7B	1/13/79	14:20	65	980	171 ±2	344 (651)	621 (1,150)	2.01 ±0.06	601 ±18	879	
EB-8A	1/10/79	12:21	59	1,000	179 ±4	406 (763)	706 (1,302)	1.75 ±0.04	574 ±11	835	
EB-8B	1/11/79	11:50	65	990	195 ±1	416 (780)	703 (1,296)	2.15 ±0.03	677 ±10	920	
EB-8C	1/30/79	14:20	68	1,020	169 ±2	452 (845)	703 (1,297)	2.16 ±0.02	600 ±8	904	
EB-9A	1/20/79	12:10	62	1,010	220 ±4	500 (931)	816 (1,500)	1.82 ±0.03	644 ±10	945	
EB-9B	1/20/79	12:52	62	1,020	200 ±3	525 (976)	436 (1,500)	1.95 ±0.03	637 ±10	950	
EB-9C	1/28/79	14:33	75	990	209 ±1	520 (967)	799 (1,470)	1.94 ±0.02	604 ±6	947	Panel 5 blocked
EB-9D	1/31/79	12:00	65	1,070	227 ±1	501 (933)	802 (1,475)	2.11 ±0.02	709 ±6	961	
EB-9E	3/23/79	12:00	60	1,010	225 ±2	485 (905)	816 (1,501)	2.05 ±0.02	759 ±7	966	
EB-9F	3/24/79	11:50	58	1,030	226 ±3	487 (908)	813 (1,494)	2.03 ±0.03	739 ±8	944	
EB-9G	3/24/79	15:15	92	940	194 ±3	531 (987)	813 (1,494)	1.87 ±0.03	599 ±9	No data	Large number of heliostats
EB-9H	3/25/79	11:00	55	1,030	202 ±3	385 (725)	803 (1,477)	1.41 ±0.02	651 ±6	902	
EB-9I	3/25/79	11:20	68	1,020	180 ±3	386 (727)	806 (1,483)	1.91 ±0.02	667 ±9	1,128	

<sup>a</sup>Start of 5-min equilibrium period. <sup>b</sup>Value plus root mean square (rms) interval in test data. <sup>c</sup>Helios and RTAF/helios correlation data.

conditions is described in Section 8.4. some of the problems encountered during the reduction and evaluation of data from these test cases are discussed in the following paragraphs.

Three of the test cases of interest occurred in 1978. These were outside the applicable range of HELIOS code data used to analyze January and March test cases. Two of these cases also required the use of single-point BMSR data rather than the RMS averaging of 25 data points, one because of a tape-reading problem and the other because of a short period of apparent steady-state conditions. It was decided that the time required for a specialized HELIOS analysis of these three cases could be more productively used for additional study of the preferred January and March test data.

Two other test cases became suspect while the receiver thermal efficiency data were being evaluated. Both the EB-9C and EB-9G data showed thermal efficiencies that were much lower than other comparable test cases.

Examination of the test log, receiver data, and posttest inspection records for January 28 (EB-9C) revealed major problems with these data. The performance of heat exchanger panel 5, on the bottom of the receiver cavity, was lower than usual. Posttest inspection of the receiver conducted January 29 revealed that pieces of the Saffil insulation from the receiver back cone had broken loose and dropped onto the panel 5 heat exchanger. They were removed. The receiver thermal output during EB-9C had been about 50 kW lower than during similar test conditions with clear heat exchangers. As a result of this performance discrepancy and the strong evidence of cause, the EB-9C test case was not included in the BMSR performance evaluation.

Problems were also encountered with the EB-9G test case. Here, 29 of the Zone B heliostats had been brought on line to maintain the late afternoon solar input to the BMSR. These heliostats were aligned to provide optimum focusing on the CRTF tower-top test site rather than the BMSR aperture. Review of the HELIOS computation procedures used to determine BMSR solar input values in Table 9.1-1 revealed that Zone B collector alignment had not been fully accounted for. Since none of the other tests used more than six of these heliostats, test case EB-9G was the only one subject to this

problem.

Experimental determination of the BMSR thermal efficiency is discussed in Section 9.1.2. Section 9.1.3 presents the results of additional studies conducted with the seven of the EB-9 test cases. These cases were of special interest because they approximated the BMSR design-point operational conditions of 816°C (1500°F) air outlet temperature, solar input of 1 MWt, and thermal output of 750 to 800 kW.

#### 9.1.2 Experimental Measurements of BMSR Thermal Efficiency

Thermal efficiency of the BMSR was about 10% lower than the efficiency predicted for the commercial receiver designed during Contract RP377-1. This fact was realized during the BMSR design activity. The commercial-receiver design used a downward-facing aperture and a surround field of collectors. Its configuration, which was symmetrical around the vertical centerline of the cavity, was most compatible with the circular solar-flux distribution of the surround field of collectors. A circular symmetric design was selected for the BMSR to thermally model the internal heat transfer characteristics of the commercial-size receiver. Increased losses of heat from the BMSR resulted from the adaptation of this design to the north-side collector field and side-facing receiver aperture location required at CRTF. This increased its convective heat losses by air transport through the aperture. Also, the north-field solar input produced more intense heat flux on some of the interior cavity walls. Solar reflective and radiant infrared heat losses in the BMSR had been predicted to be about 50% higher than the comparable losses in the commercial receiver (Section 3.0).

As a result of these BMSR design compromises for test, its thermal efficiency did not represent a typical best effort for 816°C (1500°F) solar receivers. However, the BMSR experiment was viewed as an opportunity to demonstrate typical receiver performance. Most importantly, it constituted an opportunity to improve and validate the analytical skills required for ongoing studies of similar solar receivers.

Pretest predictions of BMSR thermal performance are presented in Sections 3.0 and 7.0. Test results have been used to update and improve these analyses. Test data and the pretest and posttest thermal modeling results are compared and discussed in Section 11.0.

Attempts have been made to limit the contents of Sections 9.0 and 10.0 to purely experimental results. Therefore, the 16 suitable EB test conditions have been exclusively and independently used in defining receiver efficiency. As will be shown in Section 11.0, the best evaluation of test results produced a BMSR performance characterization nearly identical to the analysis data of BMSR design-point operating conditions, but varied significantly at different receiver operating (air outlet) temperatures and at solar-input levels above and below the design point condition.

Receiver thermal efficiency is defined as the ratio of its thermal output to solar input. The receiver solar input data discussed in Section 8.4 and nominally described in Table 9.1-1 incorporates a minimum uncertainty interval of  $\pm 5\%$ . The receiver thermal output data, heat absorbed in Table 9.1-1, include a data system uncertainty of  $\pm 3\%$  (Section 8.3). The test data scatter shown with the nominal heat absorbed values in Table 9.1-1 are assumed to be factored out by the RMS averaging of 25 data points for each test case.

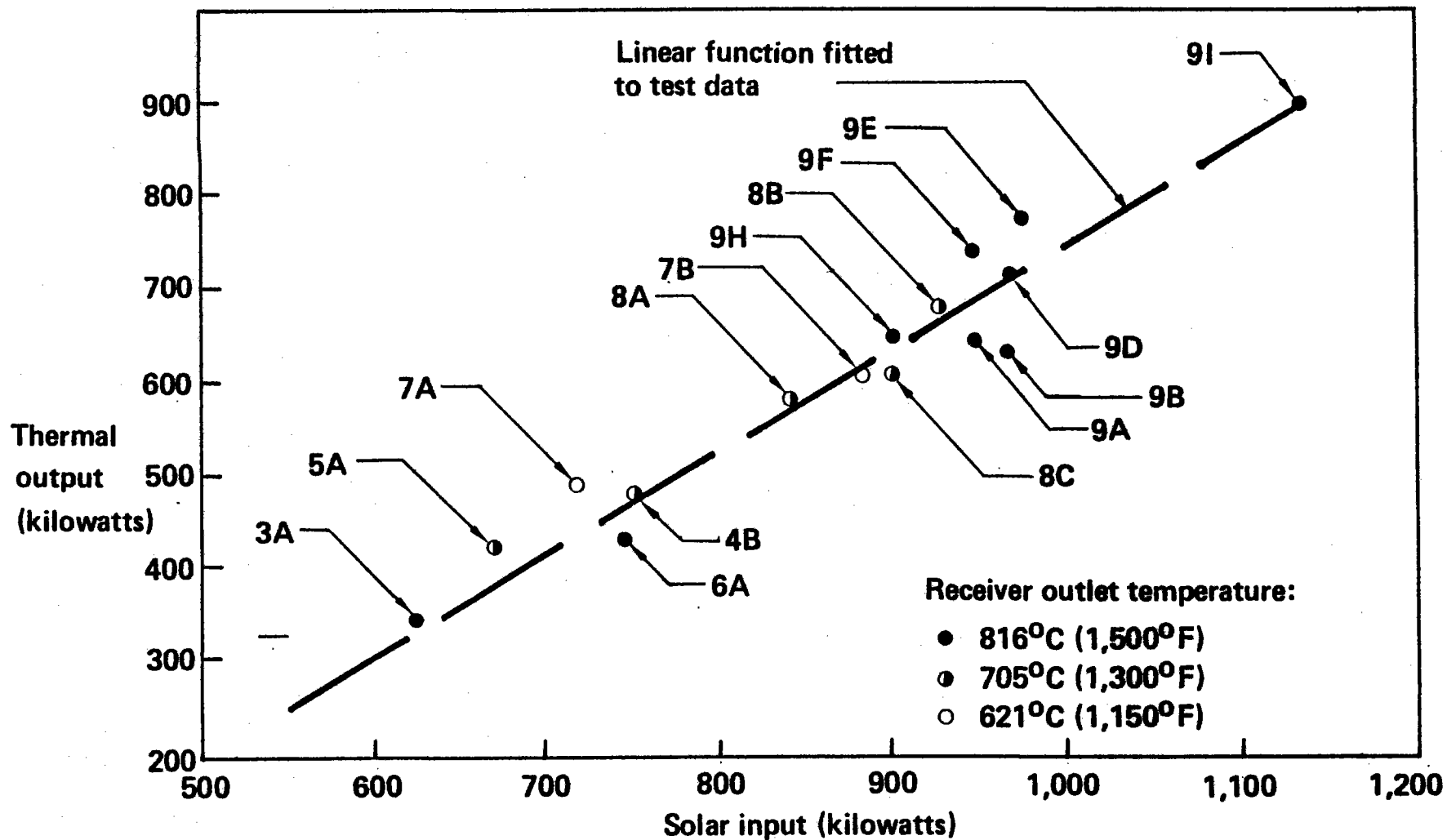
Figure 9.1-2 compares nominal values of receiver solar input and thermal output for the 16 EB-9 test cases. Data points are coded to identify test cases at each of the three levels of receiver outlet temperature experienced during the tests. Significantly higher thermal output was expected for the tests at lower temperatures compared to high-temperature tests at the same solar input level. However, these differences were smaller than the apparently random scatter in the test data.

Test results shown in Figure 9.1-2 were plotted as functions of ambient windspeed during tests. Wind data recorded by the CRTF metrology tower system showed ambient windspeeds at the BMSR test-bay elevation of 0 to 10.5 m/s (0 to 34.5 ft/s) during tests. These winds were always blowing from within 40 deg of a northerly direction. The scatter in the test data at

Figure 9.1-2. BMSR Thermal Output Versus Input Data

## BMSR Thermal Output Versus Input Data

481





equal receiver operating temperatures did not appear to be influenced by ambient wind velocity. Neither did the absence of BMSR thermal output sensitivity to operating temperature appear to be masked out by wind effects.

It was assumed earlier in Section 8.5 that the stagnant air zone produced on the north side of the CRTF tower and the BMSR test bay during a northerly wind protected the receiver from the effects of ambient wind. This conclusion appeared to be confirmed by the absence of systematic effects of ambient wind on BMSR performance.

A straight line has been fitted to the BMSR output versus input data in Figure 9.1-2 by means of a least-squares curve fit. Half the data fits this line to within an error interval of  $\pm 10$  kW. The remainder falls within  $\pm 50$  kW of the fitted curve.

Experimental determinations of receiver thermal efficiency are plotted in Figure 9.1-3. Here the uncertainty intervals associated with solar input and thermal output data are included. The uncertainty interval for thermal efficiency data is computed by the quotient function shown in the error analysis section, equation 8.3-5. These intervals on solar input and efficiency define the probable range of experimental data. Two plotted curves are shown for comparison with these data. One shows thermal efficiency corresponding to the linear curve fitted to data in Figure 9.1-2. The other shows the most recent analytical and experimental efficiency data agree reasonably well in the range of 900- to 1000-kW receiver solar input.

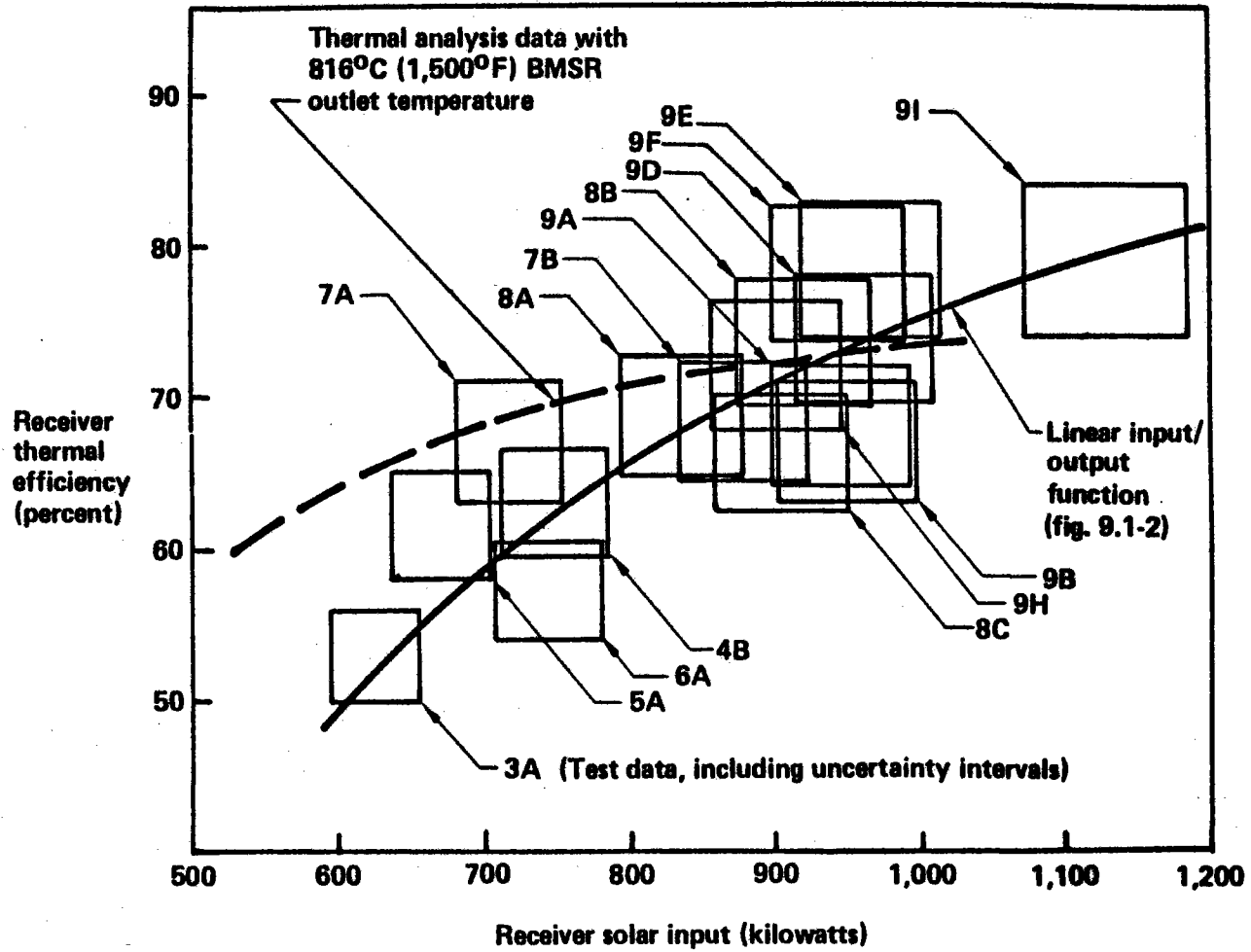
### 9.1.3 Other EB Test Results

In addition to the BMSR thermal efficiency data, the equilibrium heat balance tests provided other valuable measurements of BMSR operating characteristics. The receiver design-point conditions simulated during the EB-9 tests were most useful in this regard.

A total of seven sets of EB-9 test data were obtained during the solar testing program. Detailed BMSR performance data for these tests is

Figure 9.1-3. BMSR Thermal Efficiency

# BMSR Thermal Efficiency



summarized in Tables 9.1-2 through 9.1-8. These tables show heat fluxes, heat transfer rates, and temperatures for the eight separate heat exchanger bays in the receiver. Systematic differences in performance between the upper and lower heat exchanger bays are apparent in these data. Data comparing the overall receiver operating conditions during these seven EB-9 tests are summarized in Table 9.1-9. Pertinent features of these sets of data are discussed in the following paragraphs.

The degree to which the BMSR achieved steady-state thermal equilibrium conditions during these tests can be seen by comparing the average receiver frame insulation temperatures. As mentioned in Section 9.1.1, the amount of energy stored in the heat exchanger tubes and insulation became negligibly small after the first hour of receiver operation. However, as shown in Table 9.1-9, the temperature at a point 5.0 cm (2.0 in) into the insulation continued to change for a period of several hours. These data are plotted in Figure 9.1-4.

The duration of receiver operation before the various sets of EB-9 test data were collected ranged from 2.4 to 4.0 hr. Receiver insulation within the cavity walls ranged from 810° to 898°C. Even at a point 5.0 cm (2.0 in) from the heated face, the insulation temperatures during the various EB-9 test cases were always within about 100°C (180°F) of their final equilibrium values.

The heat transfer to air passing through each of the BMSR heat exchangers was measured by the indicated mass flow rate and temperature change of the air passing through the heat exchanger. As discussed in Section 8.0, the airflow rate was determined by instrumenting and calibrating the heat exchanger flow-control valve to act as a variable area orifice flowmeter. The rates of heat absorbed by each of the BMSR heat exchangers are shown in the individual test data summaries, Tables 9.1-2 through 9.1-8. The average rates of heat absorbed by heat exchangers during each of the tests are shown in Table 9.1-9. Normalized heat exchanger heat transfer rates were obtained by taking the ratios of these values and dividing the individual heat exchanger rates by the average value for each test. These normalized heat transfer rates were then compared on an equal basis with one another for all

Table 9.1-2. Summary of Test Data, Case EB-9A

## Summary of Test Data, Case EB-9A

Receiver bay		1 Top	2	3 East	4	5 Bottom	6	7 West	8
Heat flux on receiver bay calorimeter (kW/m <sup>2</sup> )		247	—	229	—	204	—	200	—
Heat absorbed by heat exchanger (kW)		93	87	85	60	52	75	91	96
Insulation temperature 10 cm from hot face (°C [°F])	Behind heat exchanger	—	805 (1,480)	801 (1,473)	748 (1,377)	763 (1,409)	798 (1,468)	790 (1,454)	821 (1,510)
	On aperture plane	830 (1,526)	—	859 (1,577)	—	831 (1,528)	—	810 (1,489)	—
Indicated outlet air temperature (°C [°F])		816 (1,500)	816 (1,500)	816 (1,500)	818 (1,503)	816 (1,500)	816 (1,500)	818 (1,503)	814 (1,496)
Average indicated tube temperature at outlet (°C [°F])		873 (1,603)	874 (1,604)	861 (1,582)	860 (1,579)	844 (1,551)	856 (1,573)	869 (1,596)	878 (1,612)
Indicated tube-to-air thermal gradient at outlet (°C [°F])		57 (103)	58 (104)	45 (81)	42 (76)	28 (50)	40 (72)	51 (92)	64 (116)

Table 9.1-3. Summary of Test Data, Case EB-9B

## Summary of Test Data, Case EB-9B

Receiver bay		1 Top	2	3 East	4	5 Bottom	6	7 West	8
Heat flux on receiver bay calorimeter (kW/m <sup>2</sup> )		243	—	224	—	202	—	211	—
Heat absorbed by heat exchanger (kW)		92	84	81	59	55	76	92	98
Insulation temperature 10 cm from hot face (°C [°F])	Behind heat exchanger	—	841 (1,546)	834 (1,532)	788 (1,450)	801 (1,473)	833 (1,531)	825 (1,517)	855 (1,570)
	On aperture plane	871 (1,600)	—	899 (1,650)	—	871 (1,600)	—	854 (1,569)	—
Indicated outlet air temperature (°C [°F])		816 (1,500)	816 (1,500)	816 (1,500)	818 (1,503)	816 (1,500)	816 (1,500)	818 (1,503)	814 (1,496)
Average indicated tube temperature at outlet (°C [°F])		872 (1,601)	874 (1,604)	860 (1,580)	852 (1,565)	848 (1,559)	860 (1,580)	869 (1,595)	878 (1,611)
Indicated tube-to-air thermal gradient at outlet (°C [°F])		56 (101)	58 (104)	44 (80)	34 (61)	32 (58)	44 (80)	51 (91)	64 (115)

Table 9.1-4. Summary of Test Data, Case EB-9D

## Summary of Test Data, Case EB-9D

Receiver bay		1 Top	2	3 East	4	5 Bottom	6	7 West	8
Heat flux on receiver bay calorimeter (kW/m <sup>2</sup> )		245	—	233	—	209	—	220	—
Heat absorbed by heat exchanger (kW)		99	108	92	62	50	79	104	109
Insulation temperature 10 cm from hot face (°C [°F])	Behind heat exchanger	—	856 (1,572)	853 (1,567)	816 (1,500)	816 (1,501)	848 (1,558)	847 (1,556)	867 (1,592)
	On aperture plane	895 (1,643)	—	919 (1,686)	—	891 (1,635)	—	883 (1,621)	—
Indicated outlet air temperature (°C [°F])		800 (1,471)	791 (1,455)	801 (1,473)	806 (1,482)	806 (1,482)	803 (1,477)	805 (1,480)	802 (1,475)
Average indicated tube temperature at outlet (°C [°F])		863 (1,584)	855 (1,571)	851 (1,562)	860 (1,580)	833 (1,531)	831 (1,527)	858 (1,577)	872 (1,601)
Indicated tube-to-air thermal gradient at outlet (°C [°F])		63 (113)	64 (115)	50 (89)	54 (97)	27 (49)	28 (50)	53 (96)	70 (126)

Table 9.1-5. Summary of Test Data, Case EB-9E

## Summary of Test Data, Case EB-9E

Receiver bay		1 Top	2	3 East	4	5 Bottom	6	7 West	8
Heat flux on receiver bay calorimeter (kW/m <sup>2</sup> )		230	—	229	—	214	—	226	—
Heat absorbed by heat exchanger (kW)		105	110	96	86	68	78	104	112
Insulation temperature 10 cm from hot face (°C [°F])	Behind heat exchanger	—	857 (1,574)	855 (1,571)	812 (1,493)	825 (1,517)	843 (1,549)	841 (1,546)	867 (1,592)
	On aperture plane	809 (1,487)	—	920 (1,688)	—	891 (1,635)	—	873 (1,602)	—
Indicated outlet air temperature (°C [°F])		816 (1,500)	822 (1,511)	816 (1,500)	816 (1,501)	816 (1,500)	816 (1,501)	815 (1,498)	816 (1,500)
Average indicated tube temperature at outlet (°C [°F])		882 (1,618)	883 (1,622)	868 (1,593)	872 (1,601)	855 (1,571)	857 (1,575)	874 (1,606)	888 (1,629)
Indicated tube-to-air thermal gradient at outlet (°C [°F])		66 (118)	61 (111)	52 (93)	56 (100)	39 (70)	41 (74)	60 (107)	72 (129)

Table 9.1-6. Summary of Test Data, Case EB-9F

## Summary of Test Data, Case EB-9F

Receiver bay		1 Top	2	3 East	4	5 Bottom	6	7 West	8
Heat flux on receiver bay calorimeter (kW/m <sup>2</sup> )		228	—	230	—	213	—	233	—
Heat absorbed by heat exchanger (kW)		109	88	97	77	67	87	104	110
Insulation temperature 10 cm from hot face (°C [°F])	Behind heat exchanger	—	875 (1,606)	871 (1,599)	830 (1,526)	843 (1,549)	866 (1,590)	863 (1,585)	883 (1,621)
	On aperture plane	911 (1,671)	—	940 (1,723)	—	909 (1,668)	—	893 (1,639)	—
Indicated outlet air temperature (°C [°F])		817 (1,502)	805 (1,480)	813 (1,494)	815 (1,498)	813 (1,495)	812 (1,493)	814 (1,497)	810 (1,489)
Average indicated tube temperature at outlet (°C [°F])		882 (1,618)	868 (1,593)	861 (1,581)	864 (1,586)	862 (1,583)	862 (1,583)	872 (1,601)	881 (1,616)
Indicated tube-to-air thermal gradient at outlet (°C [°F])		65 (116)	63 (113)	48 (87)	49 (88)	49 (89)	50 (90)	58 (104)	71 (127)



Table 9.1-7. Summary of Test Data, Case EB-9H

## Summary of Test Data, Case EB-9H

Receiver bay		1 Top	2	3 East	4	5 Bottom	6	7 West	8
Heat flux on receiver bay calorimeter (kW/m <sup>2</sup> )		206	—	—	—	189	—	210	—
Heat absorbed by heat exchanger (kW)		99	94	86	57	47	72	97	99
Insulation temperature 10 cm from hot face (°C [°F])	Behind heat exchanger	—	810 (1,489)	810 (1,489)	766 (1,410)	783 (1,441)	805 (1,480)	804 (1,478)	823 (1,513)
	On aperture plane	842 (1,547)	—	—	—	839 (1,542)	—	825 (1,517)	—
Indicated outlet air temperature (°C [°F])		804 (1,478)	791 (1,455)	805 (1,480)	804 (1,479)	803 (1,477)	801 (1,473)	809 (1,487)	810 (1,490)
Average indicated tube temperature at outlet (°C [°F])		862 (1,583)	846 (1,554)	848 (1,557)	843 (1,549)	834 (1,533)	841 (1,545)	859 (1,578)	873 (1,603)
Indicated tube-to-air thermal gradient at outlet (°C [°F])		58 (104)	55 (99)	43 (77)	39 (70)	32 (57)	40 (72)	50 (90)	63 (114)

Table 9.1-8. Summary of Test Data, Case EB-9I

## Summary of Test Data, Case EB-9I

Receiver bay		1 Top	2	3 East	4	5 Bottom	6	7 West	8
Heat flux on receiver bay calorimeter (kW/m <sup>2</sup> )		248	—	—	—	224	—	247	—
Heat absorbed by heat exchanger (kW)		132	119	114	93	87	96	124	122
Insulation temperature 10 cm from hot face (°C [°F])	Behind heat exchanger	—	834 (1,532)	835 (1,535)	790 (1,454)	810 (1,489)	831 (1,528)	826 (1,519)	849 (1,560)
	On aperture plane	871 (1,599)	—	—	—	871 (1,599)	—	855 (1,570)	—
Indicated outlet air temperature (°C [°F])		803 (1,477)	816 (1,500)	805 (1,480)	804 (1,479)	804 (1,478)	800 (1,472)	809 (1,488)	810 (1,490)
Average indicated tube temperature at outlet (°C [°F])		882 (1,619)	884 (1,623)	866 (1,591)	862 (1,583)	857 (1,574)	860 (1,580)	879 (1,613)	893 (1,639)
Indicated tube-to-air thermal gradient at outlet (°C [°F])		79 (142)	68 (122)	61 (111)	58 (105)	53 (96)	60 (108)	70 (126)	83 (150)

Table 9.1-9. Summary of EB-9 Test Data

## Summary of EB-9 Test Data

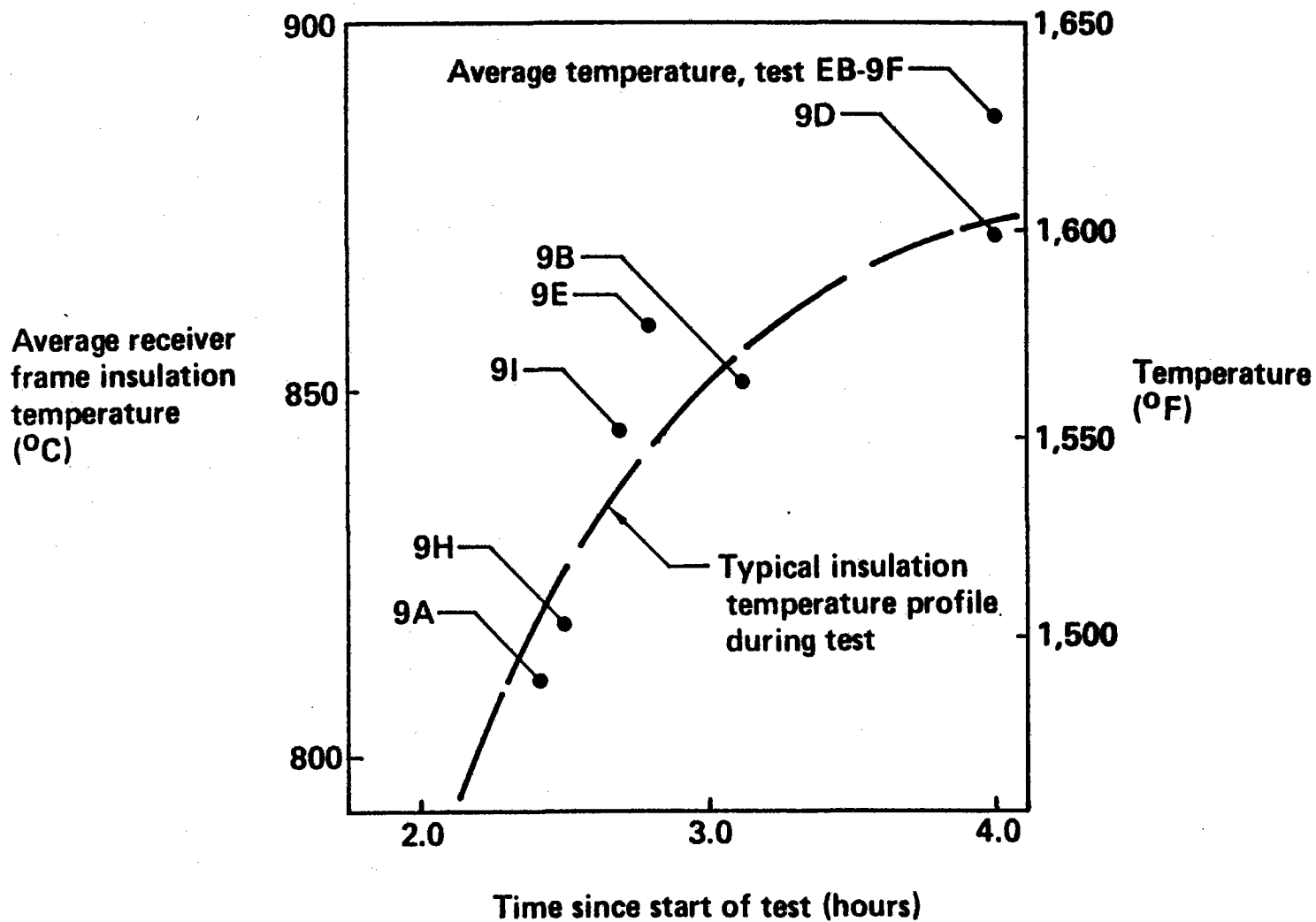
Test case	9A	9B	9D	9E	9F	9H	9I
Time since collectors targeted on receiver (hr)	2.4	3.1	4.0	2.8	4.0	2.5	2.7
Average receiver frame insulation temperature (°C [°F])	811 (1,491)	850 (1,561)	870 (1,598)	858 (1,576)	887 (1,629)	818 (1,503)	845 (1,553)
Apparent average tube-to-air thermal gradient at outlet (°C [°F])	48 (86)	48 (86)	51 (92)	56 (101)	57 (103)	48 (86)	67 (121)
Average heat absorbed by heat exchanger (kW)	81	80	89	95	92	81	111

492

Solar input, thermal output, and airflow through receiver shown in table 9.1-1.

Figure 9.1-4. Comparison of BMSR Insulation Temperatures

# Comparison of BMSR Insulation Temperatures



seven tests. These are the values of relative panel heat transfer that are plotted in Figure 9.1-5.

The plot of relative panel heat transfer showed a systematic variation of heat exchanger performance around the periphery of the BMSR cavity. Heat exchangers located on the top of the receiver (bays 8, 1, and 2) exhibited heat transfer rates 15% to 20% higher than the average. The lower heat exchangers (bays 4, 5, and 6) exhibited rates 15% to 35% lower than average. This large difference in performance between upper and lower heat exchangers was not predicted by the pretest thermal analysis of the receiver.

One concern during the evaluation of the panel heat transfer data (Figure 9.1-5) was that the BMSR manifolds and flow valves could be providing false indications of the airflow distribution to the heat exchanger panels. The reason for this suspicion was that the heat transfer data for panels 6, 7, and 8 on the west side of the receiver were consistently higher than panels 2, 3, and 4 on the east side. This was an extremely unusual condition because the east and west sides of the receiver were symmetrical. An independent verification of individual panel heat transfer rates was desired.

Test data provided this verification of individual panel heat transfer distribution around the receiver. The tube-to-air temperature difference furnished a relative, although nonlinear, measure of panel heat transfer. The only sets of tube-to-air temperature gradient data available for all eight heat exchangers included the three tube temperatures measured near the exit of each heat exchanger panel and the corresponding panel air outlet temperature. The three tube temperatures were averaged in Tables 9.1-2 through 9.1-8, and the individual panel tube-to-air thermal gradients are shown. Receiver average values for these gradients are shown in Table 9.1-9. These values have been ratioed and normalized, similar to the determination of normalized heat transfer values, to provide the desired independent measure of panel heat transfer.

Relative values of the tube-to-air temperature difference are plotted in Figure 9.1-6. The relative values, variations between heat exchangers on

Figure 9.1-5. Relative Panel Heat Transfer

# Relative Panel Heat Transfer

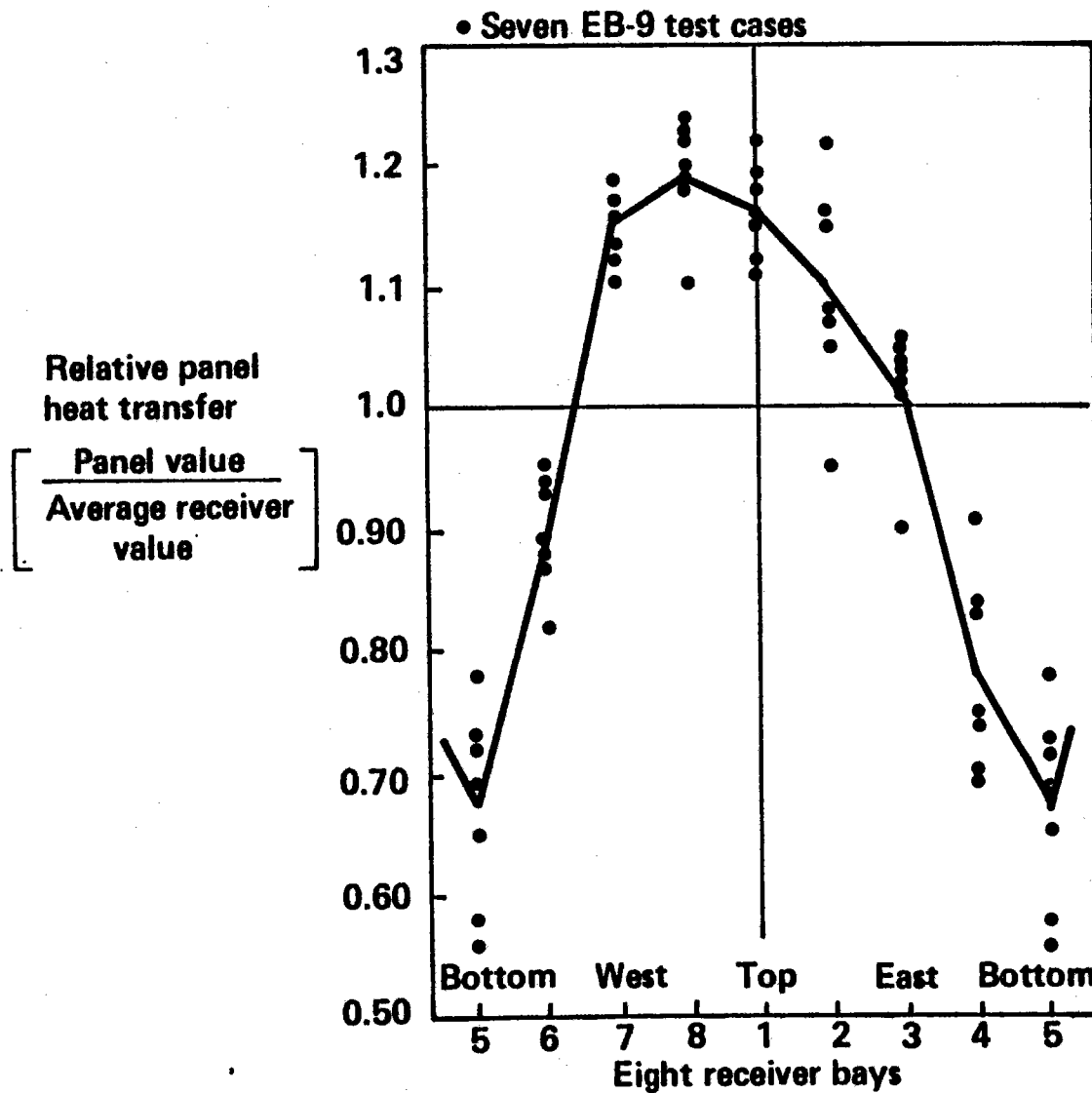
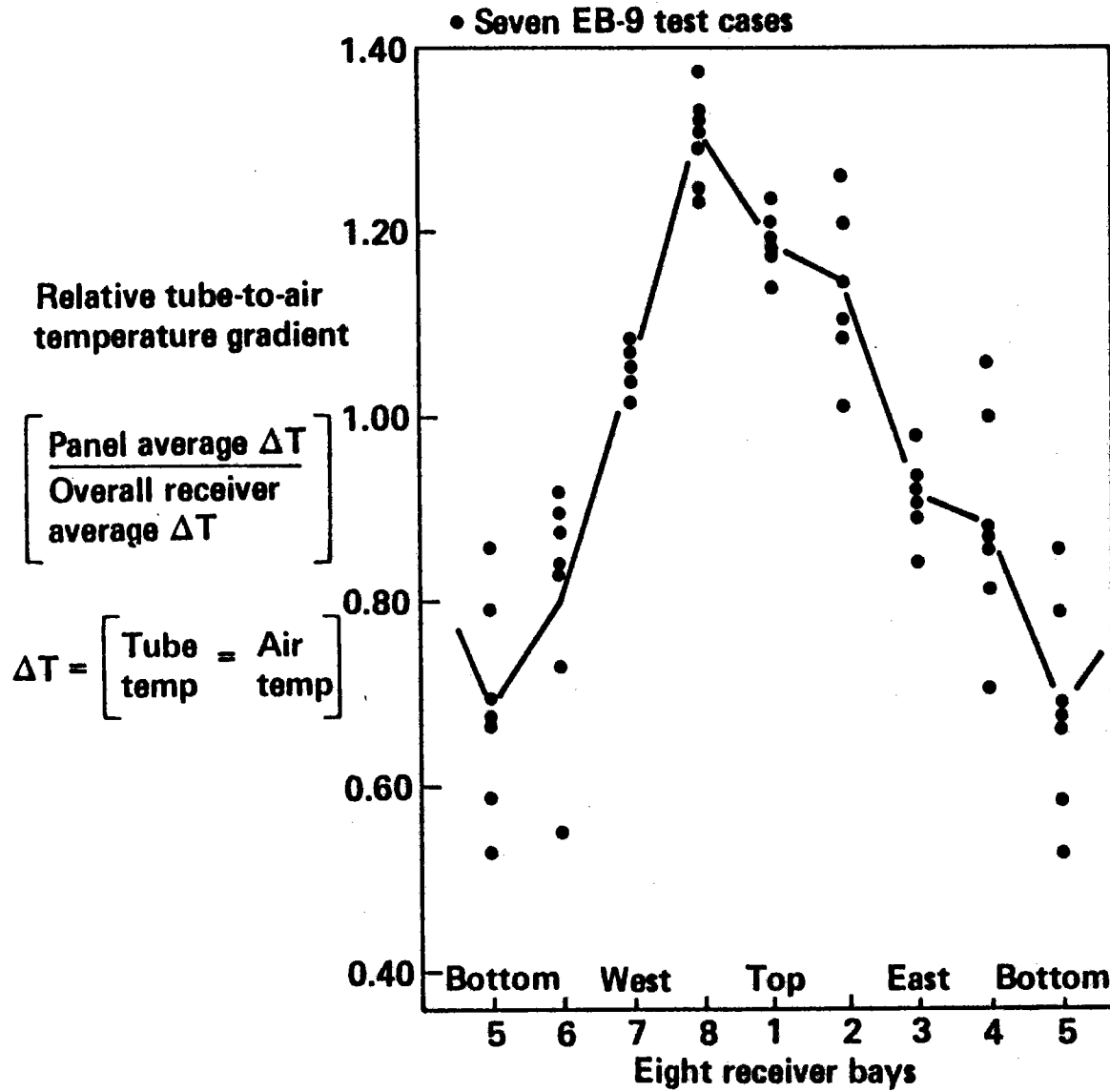


Figure 9.1-6. Relative Panel Tube-to-Air Thermal Gradient

# Relative Panel Tube-to-Air Thermal Gradient



top and bottom of the BMSR, and the higher values of panels 6, 7, and 8 compared to panels 2, 3, and 4 are similar to the other heat transfer data (Figure 9.1-5). These two independent measures of heat transfer distribution among the BMSR heat exchangers verified one another.

Further analyses were made to understand these nonuniform heat exchanger heat transfer rates in the BMSR. One source of variation could be differences in the solar and radiant thermal heat flux on the panels. Heat-flux calorimeters located adjacent to heat exchangers in bays 1, 3, 5, and 7 provided a measure of the relative magnitude of the radiant heat-flux environment. Relative values of the heat flux inside the receiver during EB-9 tests are shown in Figure 9.1-7. These data are for five of the EB-9 test cases as the bay 3 calorimeter was damaged during tests EB-9H and EB-9I. These data show a vertical variation of radiant heat flux within the cavity, partly explaining the differences in individual panel heat transfer rates. However, the total heat-flux variation of about 12% in Figure 9.1-7 was significantly less than the panel heat transfer variation of about 50% in Figure 9.1-5. Also, the radiant heat flux on panel 3 was consistently higher than the radiant heat flux on panel 7. This is the opposite of the panel heat transfer performance trends shown in Figure 9.1-5 and 9.1-6, where panel 7 provided more heat output than panel 3.

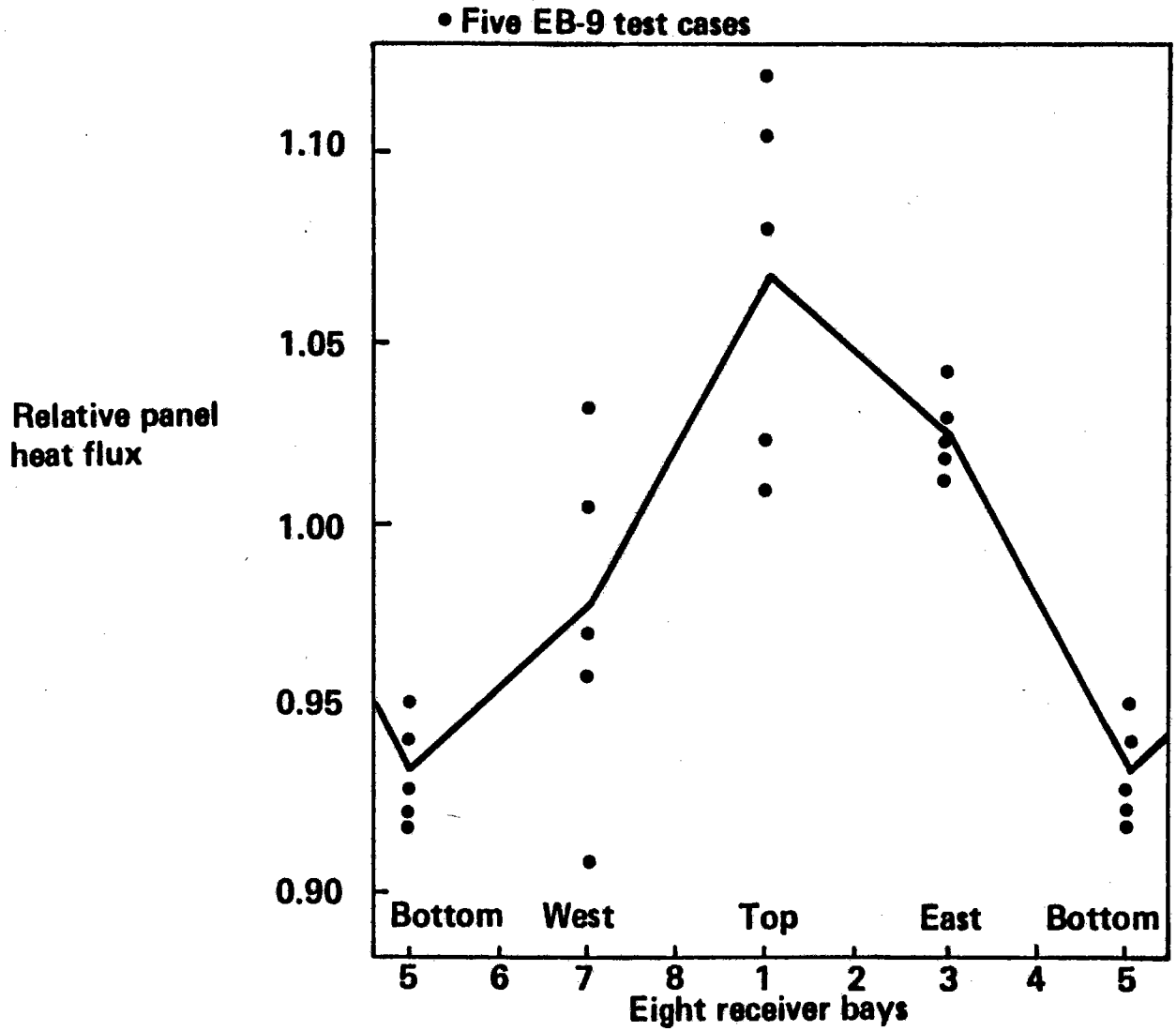
As a result of these studies of the individual panel heat transfer data, it was concluded that a significant natural convection heat transfer mechanism was affecting the relative heat absorbed by the various BMSR heat exchangers. The relatively small bias of radiant heat to the top of the receiver and a significant convective heat transfer from the bottom to the top of the BMSR cavity combined to produce the top-to-bottom distribution in Figures 9.1-5 and 9.1-6. A bias of the convection mechanism to the west side of the cavity was presumed to occur simultaneously. The cause of this bias was not apparent, but the test results clearly showed its effect. In spite of the less intense radiant environment on the west side of the cavity interior, the west-side heat exchangers (panels 6, 7, and 8) absorbed more cavity heat than those on the east side (panels 2, 3, and 4).

Even though these convective heat transfer effects became apparent during



Figure 9.1-7. Relative Heat Flux Inside Receiver

# Relative Heat Flux Inside Receiver



the beginning of the solar testing program, the desire to experimentally measure air velocities within the receiver cavity were frustrated by the lack of airflow sensors capable of operating in the intense radiant thermal environment of the receiver interior. Posttest analyses of the convective heat transfer mechanisms within the BMSR cavity are described in Section 10.0.

## 9.2 NONUNIFORM SOLAR INPUT TESTS

The nonuniform solar input tests determined the ability of the solar reflective cavity design to redistribute and equalize the effects of nonuniform collector-field solar input. A commercial receiver design was desired in which the heat exchangers were uniformly heated in spite of the normal variations of solar input from different regions of the collector field. These variations were caused by the differences in individual heliostat performance that occurred during a typical day of operation. North-side and west-side heliostats provided more solar input during morning hours; the north-side and east-side heliostats become more effective in the afternoon. During a typical nonuniform solar-input test, the CRTF collector field was operated to provide two comparable cases, one with uniform solar-input distribution, and a second with solar input biased to one side (the east side) of the collector field.

Three nonuniform solar input tests were planned and two were conducted. The best of the completed tests, NI-2, was conducted during early afternoon with nearly ideal solar testing conditions. The second test, NI-1, was conducted later on the same day at a lower level of solar input power to the receiver and a lower receiver outlet temperature. Changing solar input caused by the late afternoon optical characteristics of the CRTF collector field made it difficult to accurately define the receiver solar input during this test.

Posttest review of the NI-2 test results indicated that heat loads on the BMSR heat exchangers were not significantly affected by changing the direction of the solar input to the receiver aperture. The results that characterize the BMSR performance during periods of nonuniform solar input are presented here. Because of the high degree of success achieved during

test NI-2, the third test, NI-3, was cancelled.

Test NI-2 was conducted on January 23, 1979. The BMSR was started and brought to operating temperatures by 50 of the CRTF heliostats. A uniform distribution of heliostats throughout Zone A and the first row of Zone B were used during this first phase of the test. The heliostats in use at this time are shown in Figure 9.2-1. A solar input of approximately 750 kW was achieved. A period of approximately 2 hr was required to obtain normal steady-state operating conditions in the BMSR and test air supply system. At the end of this period, the BMSR thermal output stabilized at about 480 kW.

Then, according to the test plan, the heliostats on the west side of the collector field were replaced, one by one, by previously unused collectors on the east side. A period of 10 min was required to accomplish these changes. The collector-field configuration after this transition to east-side heliostats is shown in Figure 9.2-2.

The airflow rate through BMSR heat exchangers was monitored during this collector-field transition period. No significant changes were observed in the receiver operating conditions during this time.

After the new collector-field configuration was attained, the BMSR solar input was measured by means of the RTAF and found to be a few percent higher than the original solar input. This was caused by replacement of west-side collectors with the better performing central and east-side collector. However, a second scan conducted 20 min later showed that afternoon CRTF collector-field performance had degraded just enough to provide a solar input equal to the initial uniform heliostat field value. This point in time was taken as the nonuniform test condition for comparison with the earlier uniform solar-input case.

Test results are summarized in Figure 9.2-3 and 9.2-4. Relative flux values measured by the calorimeters located adjacent to heat exchanger panels 1, 3, 5, and 7 are shown in Figure 9.2-3. These calorimeters were located in cavity wall areas not directly illuminated by sunlight from the collector

Figure 9.2-1. Uniform Collector Field Configuration at State of Test NI-2

# Uniform Collector Field Configuration at Start of Test NI-2

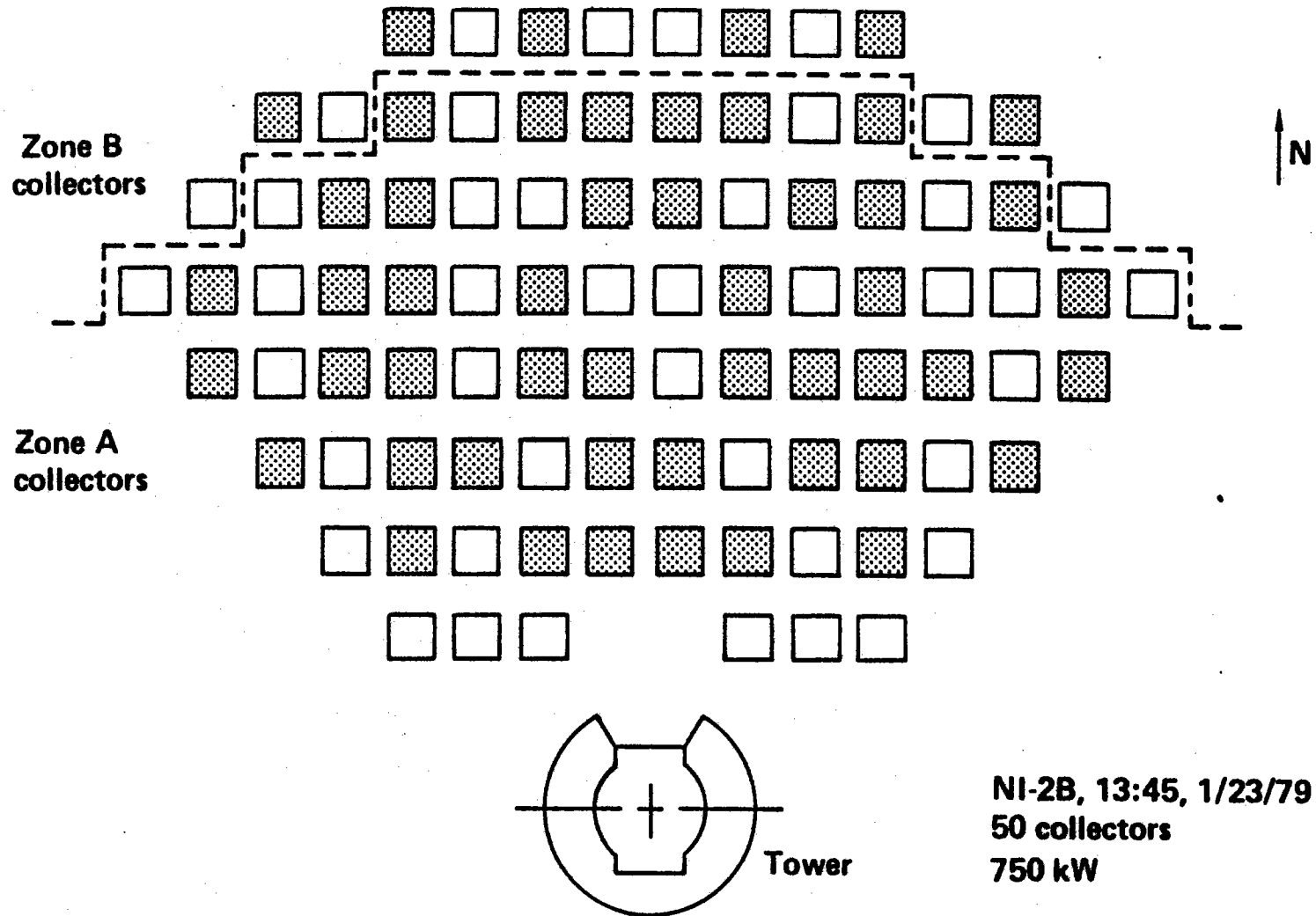


Figure 9.2-2. East Side Collector Field Configuration at End of Test NI-2

# East Side Collector Field Configuration at End of Test NI-2

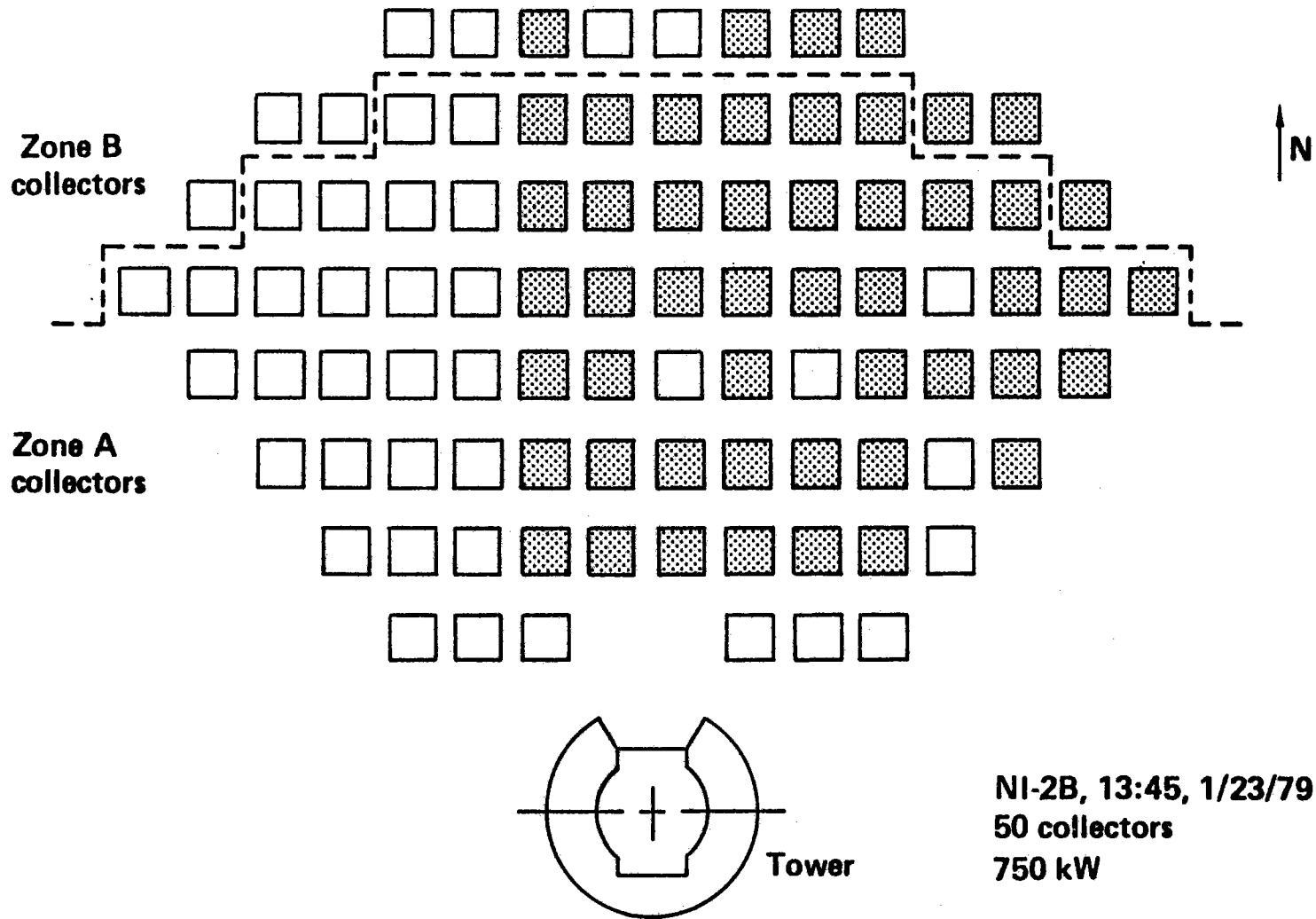


Figure 9.2-3. Comparison of Heat Flux Measurements, Test EB-2

# Comparison of Heat Flux Measurements, Test EB-2

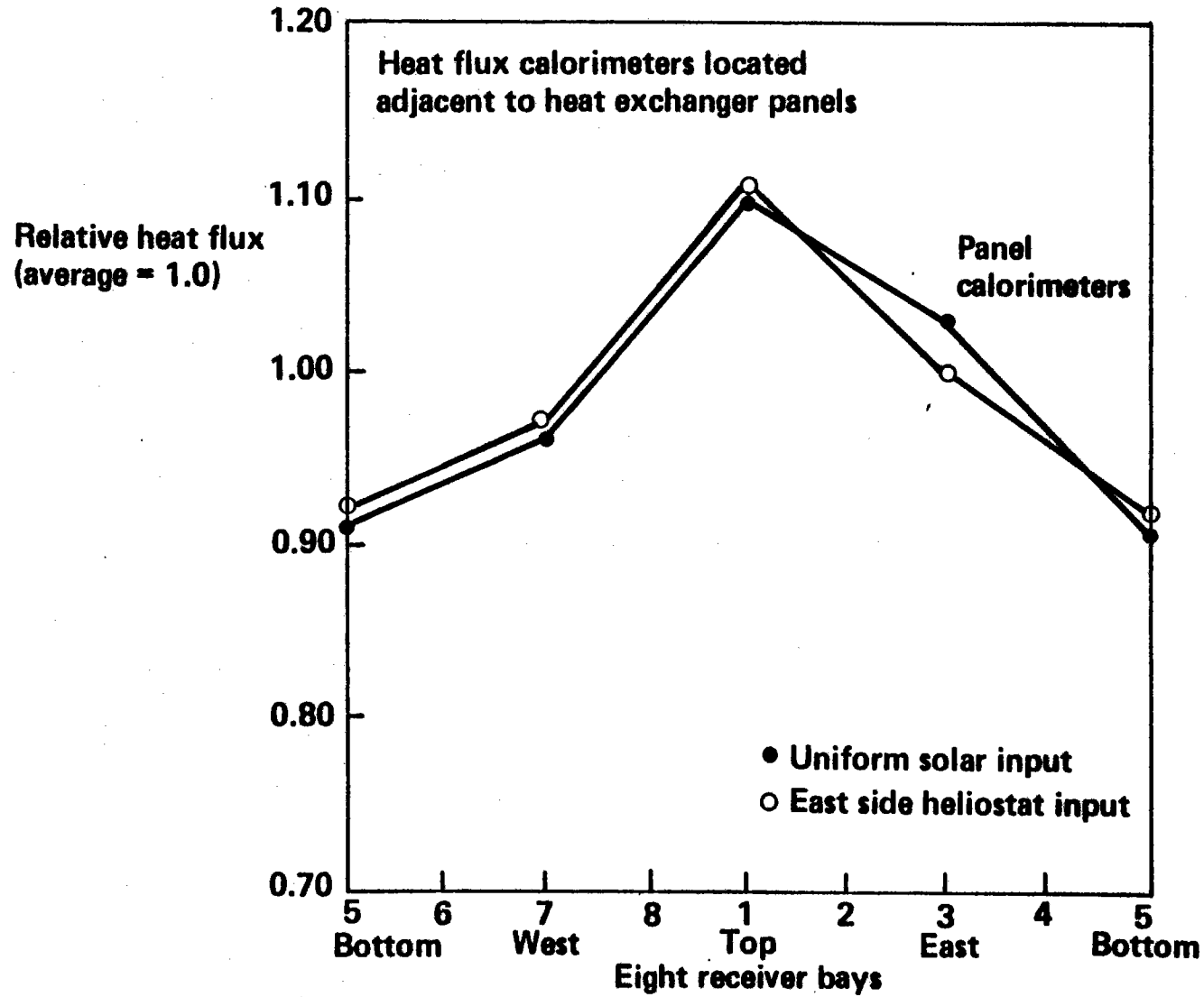
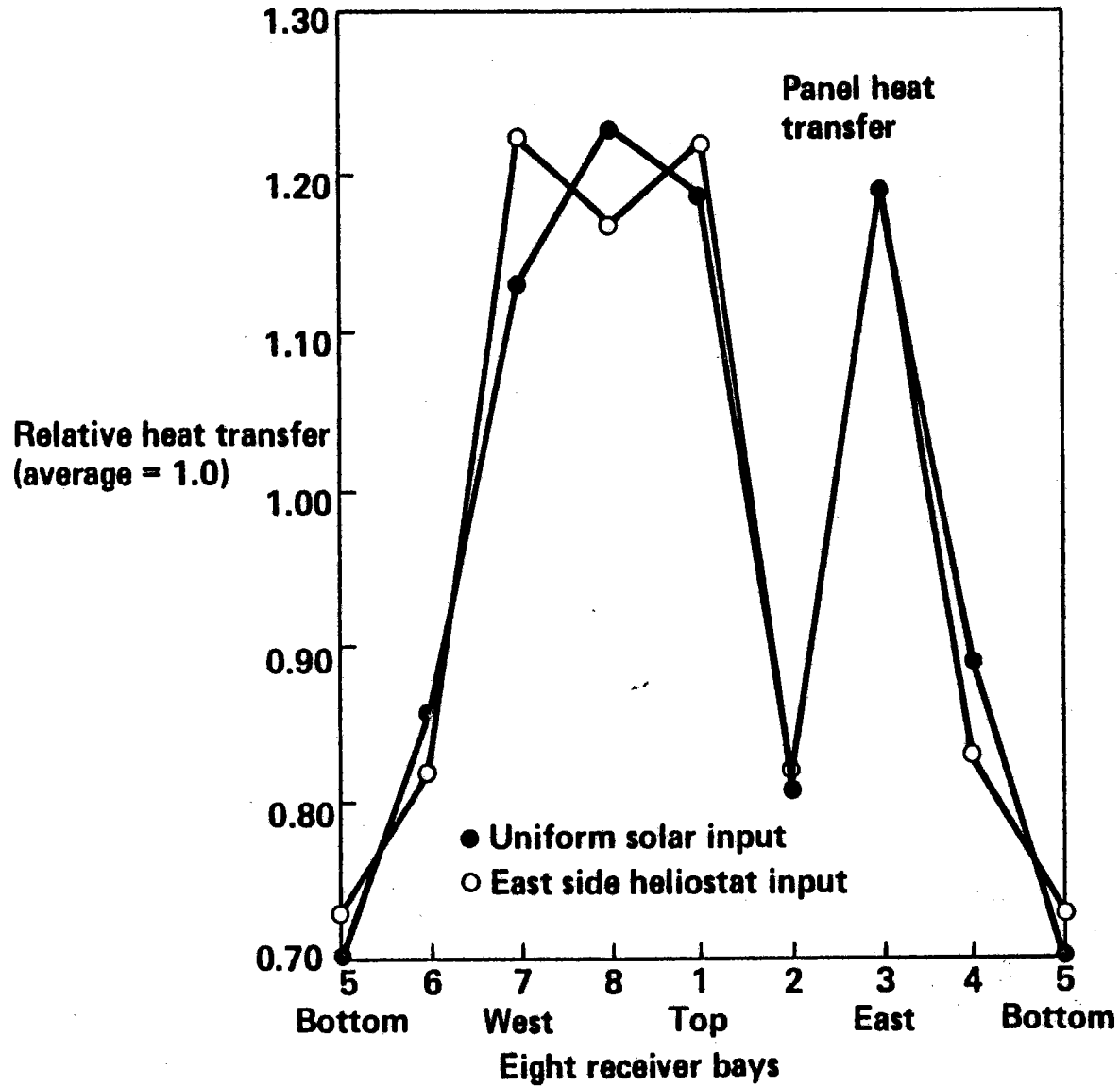


Figure 9.2-4. Comparison of Heat Exchanger Performance, Test EB-2

# Comparison of Heat Exchanger Performance, Test EB-2



field. They measured the heat exchanger thermal environment consisting of reflected sunlight and infrared radiant heat flux. The difference in heat-flux measurements between the two test cases was negligible. The largest change occurred on heat exchanger panel 3 on the east side of the receiver. As expected, its value decreased when west-side heliostats were taken off line. These were the heliostats that preferentially heated the east side of the receiver cavity.

Figure 9.2-4 compares the relative heat absorbed by the eight receiver heat exchangers during the two test conditions. Heat exchanger 2 operated at a lower-than-normal heat load because of a mechanical problem with its flow-control valve. Because it was closed more than usual, it caused a high air outlet temperature and a corresponding reduction in the quantity of heat absorbed by panel 2. Again, the differences in heat exchanger load distributions for these two cases were negligible.

These tests showed that the BMSR was insensitive to the directional distribution of solar input to its aperture. Furthermore, these artificially imposed variations of solar-input distributions were equal in magnitude to the vertical nonsymmetry imposed by testing the receiver in a north-field solar-test facility. However the east-west nonsymmetry experienced did not produce variations in the heat-load distribution in the cavity.

The highly nonuniform top-to-bottom heat-load distributions experienced during all the BMSR tests were most certainly not caused by the unequal vertical distribution of solar inputs from the north-field collector system. Another cause, such as internal natural convection or differences in the radiant or conductive heat losses from top and bottom heat exchanger panels must be sought as their cause.

### 9.3 TRANSIENT HEAT-LOAD TESTS

The purpose of transient heat-load (TH) testing of the BMSR was to determine the effects of rapidly changing solar-input power on the receiver flow and outlet temperature control system. These tests provided an opportunity to



expose the BMSR to simulated solar-input variations designed to be typical of pilot plant and commercial-size powerplant systems. Two rates of changing solar input were defined as typical of cloud-induced transients in these larger systems. A 1.0-kW/s rate of change of BMSR input, full power to zero in 16 min, was considered to be typical for a 200- to 300-MWt commercial system. A 2.0-kW/s rate of change, full power to zero in 8 min, was considered to be typical for a 10- to 40-MWt pilot-plant-size system.

This test plan was accelerated because of operating experience gained during the early portion of the solar testing program. The natural rates of change of solar input at CRTF during passage of clouds was observed to be 2.5 to 4.0 kW/s. The receiver was exposed to these rates of change of solar input on several occasions before the start of transient heat-load tests. Plots of test data taken on January 18, 1979, which are included in Section 12.0, show some of these natural transient events that occurred at CRTF. Because of confidence gained during these unplanned solar transient events, the schedule was changed so that the most severe of the transient heat-load tests, TH-4, was conducted first. This occurred on January 28, 1979. The test schedule allowed a second test, TH-2, to be conducted on January 30. Completion of the two most severe tests accomplished all the TH test program objectives.

Solar heat-load transients for these tests were produced by preprogrammed operation of the CRTF heliostats by the collector system computer. Twenty of the heliostats were programmed to be taken off the receiver at 8-sec intervals. This was to occur on command by the CRTF console operator. Then, after the BMSR had stabilized at the lower solar-input-power level, another operator input initiated a program that returned these same heliostats on target, again at 80-sec intervals.

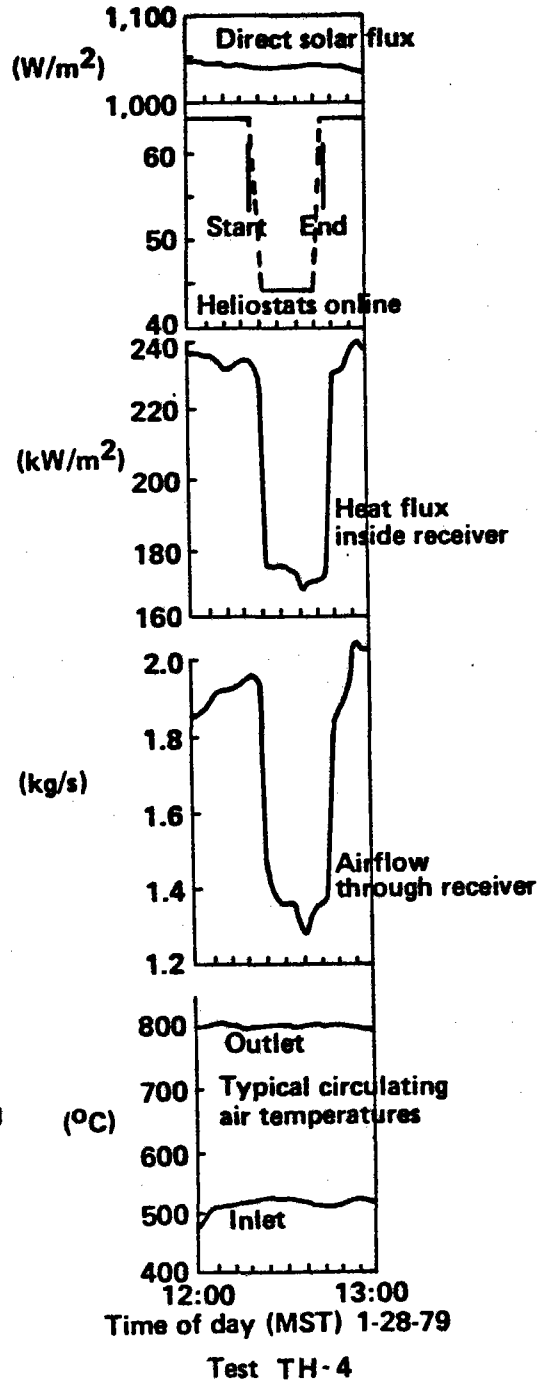
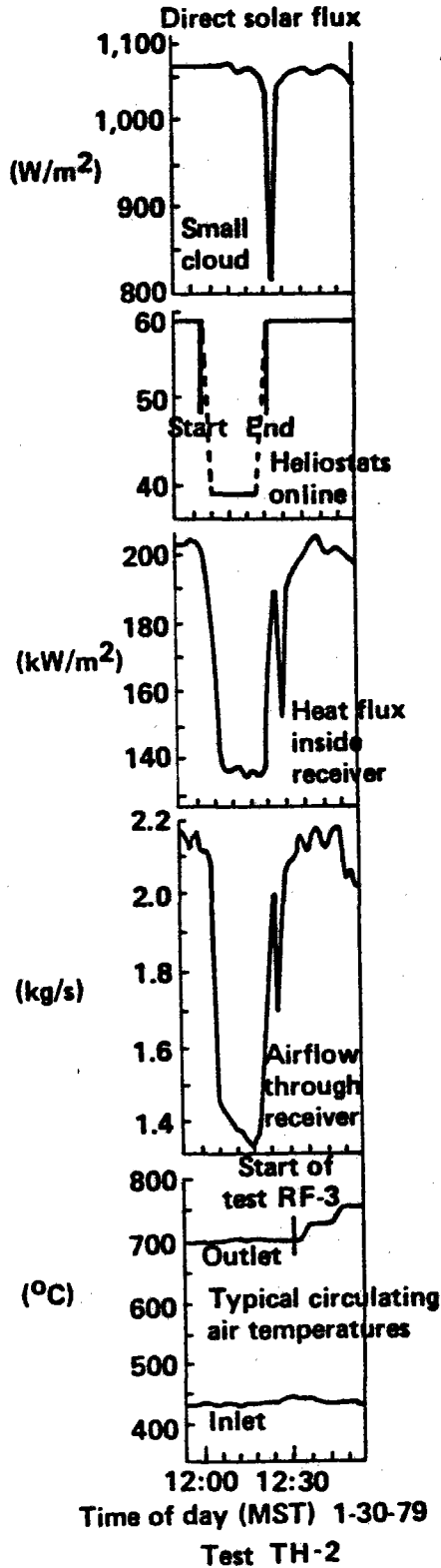
The BMSR was started and brought to operating temperature at about the design-point level of solar input, 1000 kW. The RTAF was not available during these tests so the solar input power had to be estimated from the receiver thermal output data and the number of heliostats in use. Actual solar input values were about 940 kW. Test data are shown in Figures 9.3-1 and 9.3-2.

Figure 9.3-2. Results of Transient Heat Load Test TH-4

# Results of Transient Heat Load Test TH-4

Figure 9.3-1. Results of Transient Heat Load Test TH-2

# Results of Transient Heat Load Test TH-2



The plots of the results were arranged to depict simultaneously occurring test conditions. Direct solar flux as measured by the Eppley pyrhelimoter on top of the CRTF tower and the number of heliostats on line (targeted on the BMSR aperture) characterized the receiver solar input. Because both of these tests were conducted within an hour of noon, the clear-sky direct solar flux was nearly constant. However, just after completion of the collector field activities for TH-2 (Figure 9.3-1), the collector field was partially shaded by a small cloud. This was noted on the plotted pyrhelimoter data. The test log for January 30 noted that small, precisely defined clouds were present during most of the day. This, however, was the only time during the day when the CRTF collector field was shaded.

The plots of heat flux inside the receiver were obtained by means of heat-flux calorimeters located on interior walls adjacent to the heat exchanger panels. These approximated the variation of solar input to the BMSR aperture. Both the variations of collectors on line and the effect of the small cloud during TH-2 can be observed on these plots.

The plots of total airflow rate through the receiver heat exchangers characterized the BMSR thermal output. This was because receiver inlet and outlet air temperatures were constant and the resulting heat removal per pound of airflow was also constant. Some of the variations of heat flux inside the receiver were duplicated on the airflow plots. Large and rapid changes as induced by collector-field activities and the cloud shadow were duplicated. Other airflow rate variations such as the 0.05-kg/s (0.1-lb/s) oscillations prior to the transient event on January 30 were not caused by solar-input changes. These variations in receiver flow rate appeared to be caused by cycling of the inlet temperature and backpressure controls in the test air supply system. As indicated in Figure 9.3-2, this cycling did not always occur.

As shown in the figures, the BMSR flow and temperature control system operated perfectly throughout these tests. Receiver outlet temperatures, representative of turbine inlet temperatures in a closed Brayton-cycle powerplant remained essentially constant.

The step changes in receiver outlet temperature shown in Figure 9.3-1 signaled the beginning of another of the BMSR tests, the restricted flow tests.

#### 9.4 RESTRICTED FLOW TESTS

The restricted flow testing determined the magnitude of tubing temperature increases caused by loss of airflow through one of the eight BMSR heat exchangers. Test conditions simulated the inadvertent partial closure of a heat exchanger flow-control valve in a pilot plant or commercial-size solar receiver. During this event, the remaining operational heat exchangers carried higher-than-normal airflow and continued to maintain the receiver thermal output and to prevent generalized increases in receiver operating temperature. The heat exchanger experiencing reduced flow was no longer cooled by circulating air, and its air outlet and tubing temperatures increased. As the airflow rate through the heat exchanger became small, tubing temperatures approached the effective local cavity temperature.

Effective cavity temperatures in the BMSR, operating at restricted-flow test conditions, ranged from about 1040°C (1900°F) near the U-bend of the heat exchanger tubes to about 900°C (1650°F) near the inlet end of the heat exchanger tubes. The design life of the Inconel 617 heat exchangers was very short at these temperatures. Therefore, the restricted-flow test plan called for gradual reductions of flow through heat exchanger panel 3 until its tubing temperatures reached an indicated temperature level of 982°C (1800°F). This procedure was expected to provide temperature data at a number of reduced rates of heat exchanger airflow that could be plotted and extrapolated to determine temperatures at zero airflow.

To increase the number of airflow step changes before the 982°C (1800°F) temperature was achieved, the receiver outlet temperatures were reduced from the BMSR design-point level of 816°C to 705°C (1500°F to 1300°F) during these tests. The RTAF was not in operation, so the receiver solar input had to be estimated.

Three of the restricted flow tests were planned. Test RF-1, conducted at a

low solar-input power, was deleted to accelerate the BMSR solar testing program. Test RF-2 was conducted on January 27, 1979, at a solar input of about 750 kW, and test RF-3 was conducted on January 30, 1979, at a solar input of about 940 kW.

Figures 9.4-1 and 9.4-2 show typical operating conditions experienced during these two tests. Ambient direct solar flux at CRTF is shown as it was measured by the Eppley pyrhelimeter located on top of the CRTF tower. As shown in Figure 9.4-1, the testing on January 27 was interrupted 18 times by clouds shading the collector field. In spite of these disturbances, the BMSR was brought to operating temperatures and successfully tested for a period of about 1 hr. This allowed test RF-2 to be started. Effects of the restricted-flow test showed up on the plot of outlet temperatures for heat exchanger panel 3. Reductions of airflow rate through the heat exchanger caused the temperature increases occurring after 1300. However, only four sets of data at reduced flow rates and increased panel 3 outlet temperature were obtained before the testing was again interrupted by clouds. As a result, test RF-2 was only a limited success.

Figure 9.4-2 shows similar test data recorded on January 30. This was one of the most successful test days at CRTF. The step changes in panel 3 flow rate and air outlet temperature that defined test RF-3 can be easily identified. Seven of the step changes in airflow rate through heat exchanger 3 were accomplished with the heat exchanger tubing and receiver outlet air temperatures reaching stable operating levels during each step.

Some of the temperature changes occurring during test RF-3 are shown in Figure 9.4-3. Panel 3 airflow and temperature data for the initial normal operating condition and the seven reduced airflow-rate conditions are summarized in Table 9.4-1. Local insulation wall temperatures have been estimated by means of the thermocouple located inside the insulation wall behind panel 3. These temperatures have been used to determine corrections required for tubing thermocouples (Figure 8.3-2) and ranged from 27° to 39°C (49°F to 70°F).

As indicated in Figure 8.3-11, the probable-error interval involved in

Figure 9.4-1. Operating Conditions, Test RF-2

# Operating Conditions, Test RF-2

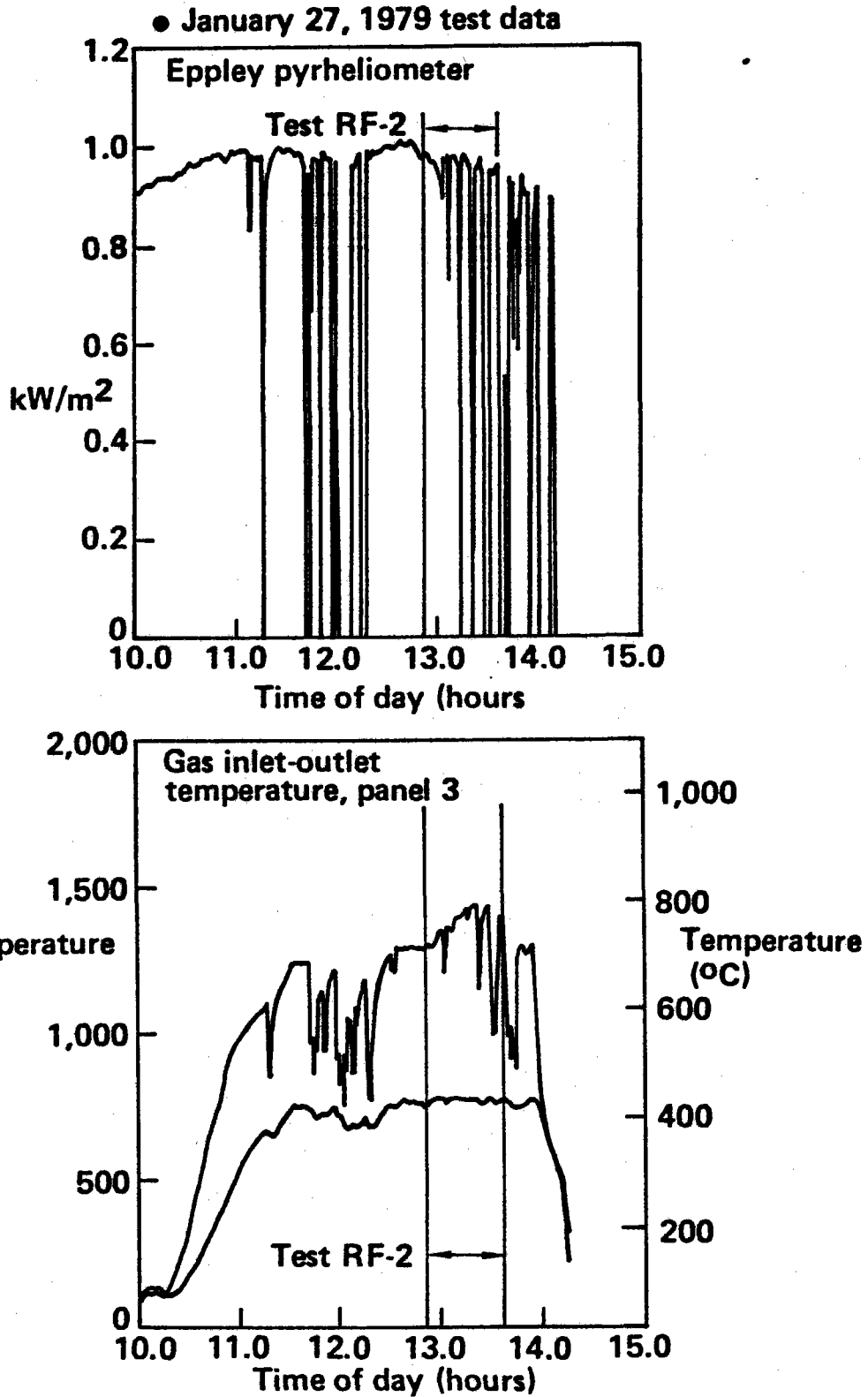


Figure 9.4-2. Operating Conditions, Test RF-3

# Operating Conditions, Test RF-3

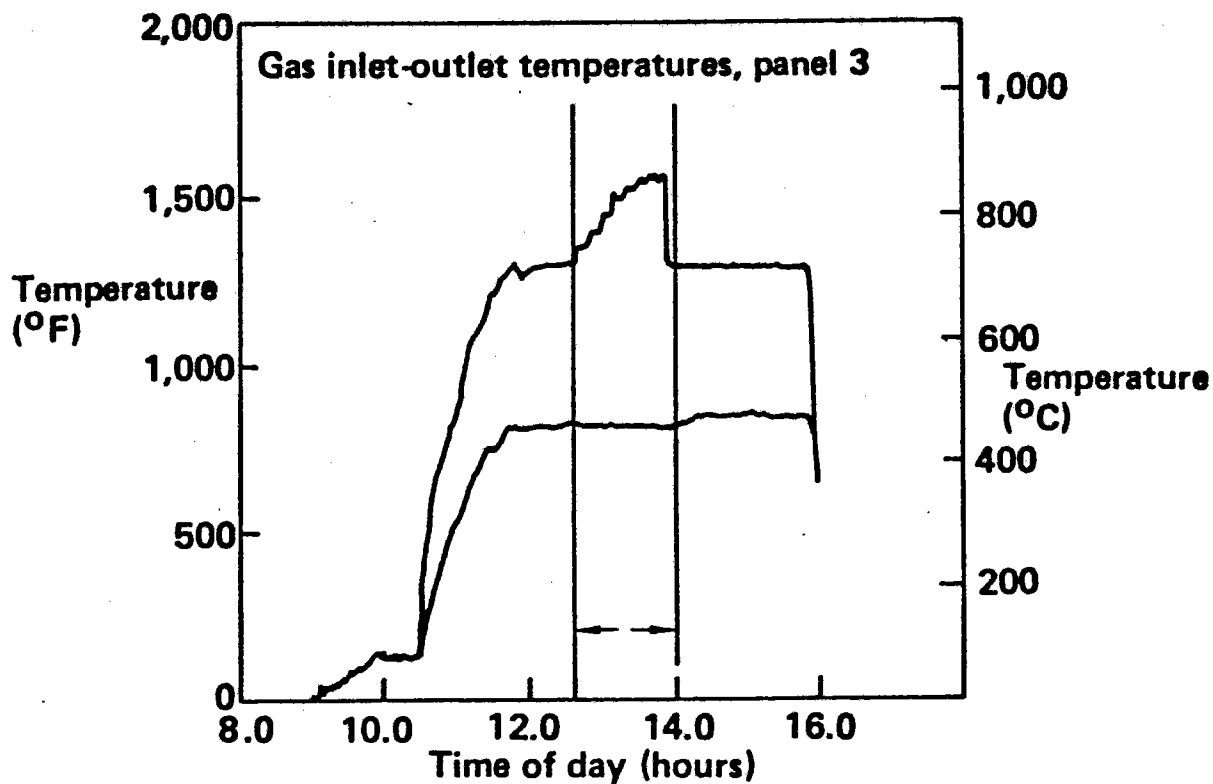
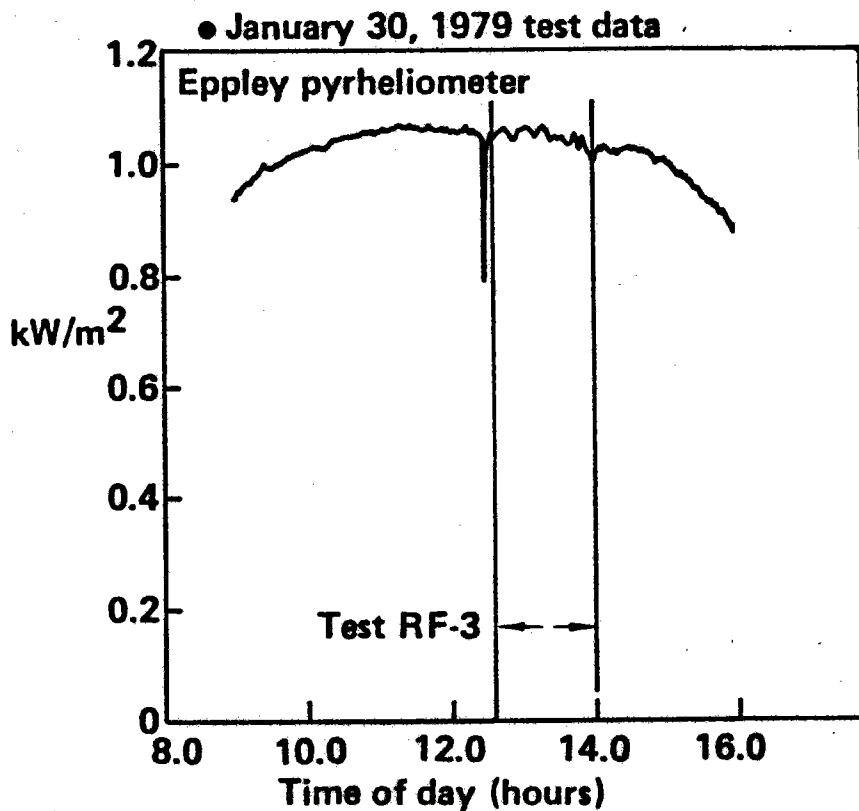


Figure 9.4-3. Heat Exchanger and Air Temperatures During Restricted Flow Test

## Heat Exchanger and Air Temperatures During Restricted Flow Test

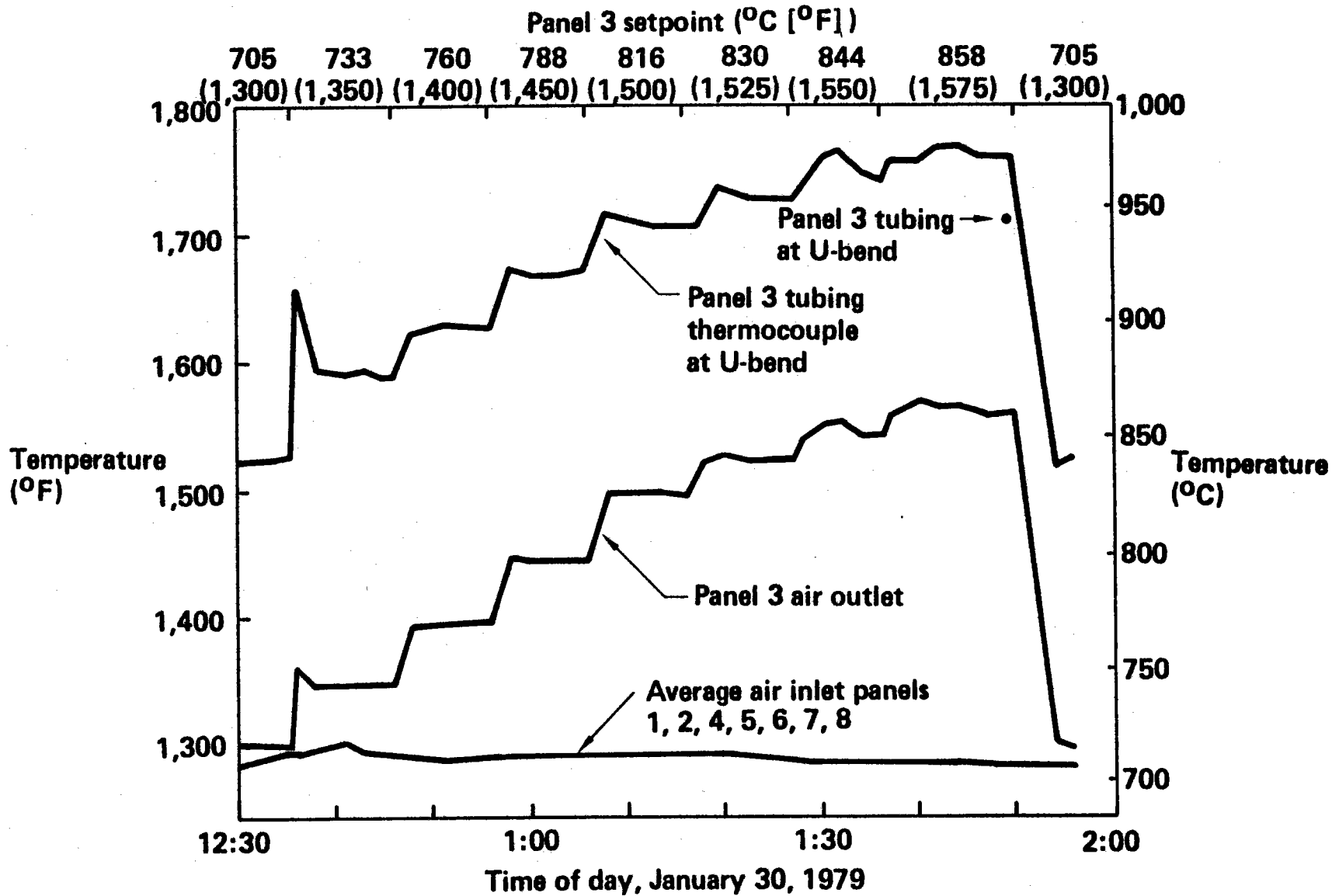




Table 9.4-1. Data Summary, Test RF-3

## Data Summary, Test RF-3

Panel 3 setpoint (°C [°F])		705 (1,300)	733 (1,350)	760 (1,400)	788 (1,450)	816 (1,500)	830 (1,525)	844 (1,550)	858 (1,675)
Panel 3 flow rate (kg/s [lb/s])		0.25 (0.55)	0.23 (0.51)	0.20 (0.44)	0.16 (0.35)	0.14 (0.31)	0.11 (0.24)	0.09 (0.20)	0.07 (0.15)
Panel 3 air outlet temperature (°C [°F])		704 (1,298)	730 (1,346)	758 (1,395)	785 (1,445)	814 (1,496)	829 (1,523)	839 (1,542)	846 (1,554)
Indicated panel 3 tubing temperature (°C [°F])	U-bend	835 (1,534)	856 (1,573)	880 (1,614)	903 (1,656)	924 (1,695)	940 (1,724)	949 (1,739)	956 (1,752)
	Outlet	760 (1,399)	786 (1,446)	807 (1,484)	831 (1,527)	852 (1,565)	866 (1,590)	871 (1,599)	877 (1,610)
Corrected panel 3 tubing temperature (°C [°F])	U-bend	796 (1,464)	819 (1,506)	845 (1,552)	870 (1,597)	893 (1,639)	910 (1,669)	921 (1,689)	929 (1,704)
	Outlet	725 (1,336)	751 (1,383)	772 (1,421)	796 (1,464)	817 (1,502)	831 (1,527)	836 (1,536)	842 (1,547)

measuring normal rates of airflow through individual BMSR heat exchangers was  $\pm 9.2\%$ . An uncertainty interval of  $\pm 0.02$  kg/s ( $\pm 0.4$  lb/s) was assumed for the airflow-rate data in Table 9.4-1. The uncertainty interval for indicated tubing (thermocouple) data was about  $\pm 6^\circ\text{C}$  ( $10.88^\circ\text{F}$ ). However, an additional uncertainty had to be assessed to account for probable errors in the temperature corrections. Because these corrections were all less than the  $40^\circ\text{C}$  ( $72^\circ\text{F}$ ), an additional uncertainty interval of  $\pm 10^\circ\text{C}$  ( $\pm 18^\circ\text{F}$ ) was assumed. The resulting combined uncertainty for corrected tube temperature data was  $\pm 11.7^\circ\text{C}$  ( $\pm 21^\circ\text{F}$ ).

Data from Table 9.4-1 are plotted in Figure 9.4-4 along with these best estimates of test data uncertainty intervals. These data define two functions of tube temperature versus heat exchanger airflow rate. Tube temperatures near the U-bend of the heat exchanger are defined by the upper curve. These temperatures were higher because of the higher local effective temperature level in this region of the BMSR cavity. The lower curve describes tube temperatures at the outlet end of the heat exchanger panel.

Extrapolation of the temperature data in Figure 9.4-4 to zero airflow indicated that loss of airflow through a BMSR heat exchanger panel caused its tubing temperatures to increase by as much as  $170^\circ\text{C}$  ( $306^\circ\text{F}$ ). The maximum tube temperature during normal BMSR design-point operation was  $860^\circ$  to  $890^\circ\text{C}$  ( $1580^\circ$  to  $1633^\circ\text{F}$ ). The temperature expected during loss of airflow through one of the eight heat exchangers could reach as high as  $1060^\circ\text{C}$  ( $1940^\circ\text{F}$ ). Developmental tests of the Inconel 617 heat exchanger tubing (Section 4.0) showed that the heat exchangers could only survive for a few minutes at these temperatures.

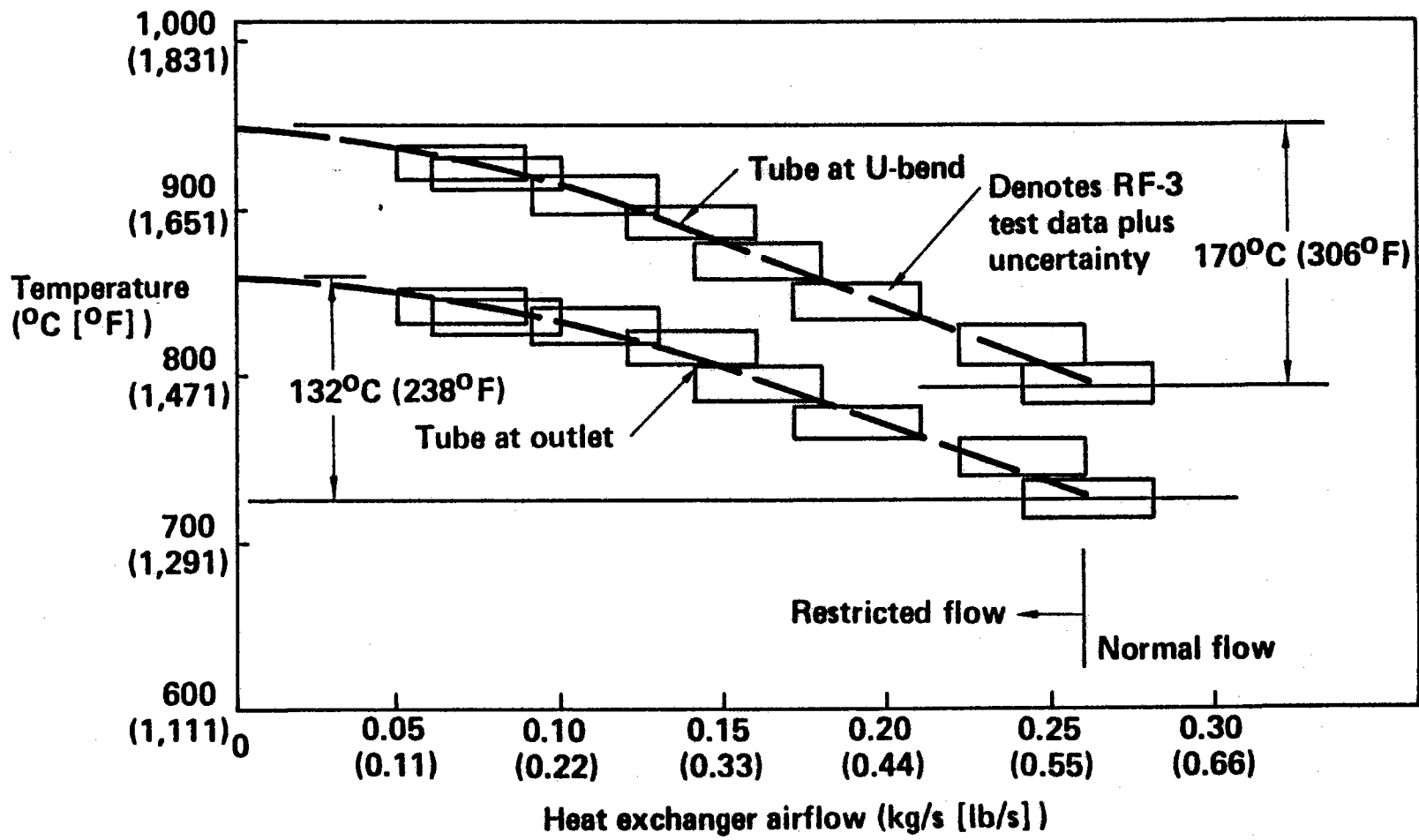
## 9.5 COLD STARTUP AND EMERGENCY COOLDOWN TESTS

During the start of a normal test, the BMSR solar input was increased very gradually. Heliostat solar images were initially aimed at the standby point, a target located about 10m (33 ft) east of the CRTF tower. Then, after the airflow rate through the receiver had been verified, the heliostat solar images were moved onto the receiver aperture. A preprogrammed sequencing was used that brought heliostats on target at about 35-sec

Figure 9.4-4. Results of Test RF-3

# Results of Test RF-3

516



intervals. This gradual heatup rate reduced the exposure of insulation and shielding materials and heat exchanger tubes to thermal shock.

A similar procedure was used during normal shutdown. At the end of tests the heliostats were taken off-target one at a time. This was also preprogrammed to provide 35-sec intervals between heliostats.

The purpose of the planned cold startup and emergency cooldown tests was to investigate the effects of higher rates of heatup and cooldown on the receiver. A collector-field operating program was written that brought heliostats on target at approximately 8-sec intervals. An emergency standby command programmed into the CRTF collector-field computer system was used for rapid heliostat image removal from the BMSR aperture during emergency cooldown tests. This reduced the BMSR solar input to zero in about 3 sec.

#### 9.5.1 Cold Startup Tests

Cold startup tests were conducted on two occasions at CRTF. One portion of CS-3 was conducted on January 28, 1979. The receiver had been to temperature but was shut down for about 16 min allowing cavity temperatures to drop to about 370°C (700°F). Then 66 heliostats were brought on target in a period of 102 sec. This was a unique receiver startup in two respects. First, the solar input went from zero to approximately full power in a very short time. More importantly, because the test air supply system, recuperator, and piping had already been brought to operating temperature, it was possible to leave the BMSR controllers online during the return to operational temperatures. The BMSR control system had to be turned off during startup to prevent receiver flow from being reduced and inlet-to-outlet temperature rise from being hazardous to the heat exchangers. This BMSR operating hazard is discussed in Section 7.5. Because the receiver inlet temperature was allowed to drop to 370°C (700°F), the maximum inlet-to-outlet air temperature rise could not exceed 444°C (800°F). This was judged to be an acceptable risk.

This portion of test CS-3 exposed the BMSR flow and outlet temperature control system to one of its most severe operational tests. During the

16-min precooling period, the BMSR controls closed the receiver valves as far as possible while attempting to maintain the desired outlet temperature. As soon as the solar power was brought up to normal operating conditions, the nearly closed valves and low flow rate caused a rapid increase in BMSR outlet temperature. During this portion of test CS-3, the receiver outlet temperatures increased by 444°C (800°F) in about 4 min. Then, as outlet temperatures passed through the 800°C (1470°F) set-point of the receiver temperature controls, they had to rapidly open the valves and increase the airflow rate through the receiver. The most important thing to be determined was the amount of temperature overshoot that occurred during this onset of control.

These features of test CS-3 are shown in Figure 9.5-1. Data are shown for heat exchanger panel 3. These results are typical of the eight BMSR heat exchangers. The upper plot of panel 3 valve angles shows the valve closed to a minimum angle of 36 deg, which occurred when receiver solar input was reduced to zero. This condition was also indicated by the rapid reduction of panel 3 outlet temperature on the lower data plot. Then, as the solar input to the BMSR was rapidly increased, the panel 3 outlet temperature on the lower data plot increased at the previously mentioned rate of 111°C/min (200°F)/min). The valve motion, opening up to increase the airflow at the time the outlet temperature passed through the set-point, was practically instantaneous.

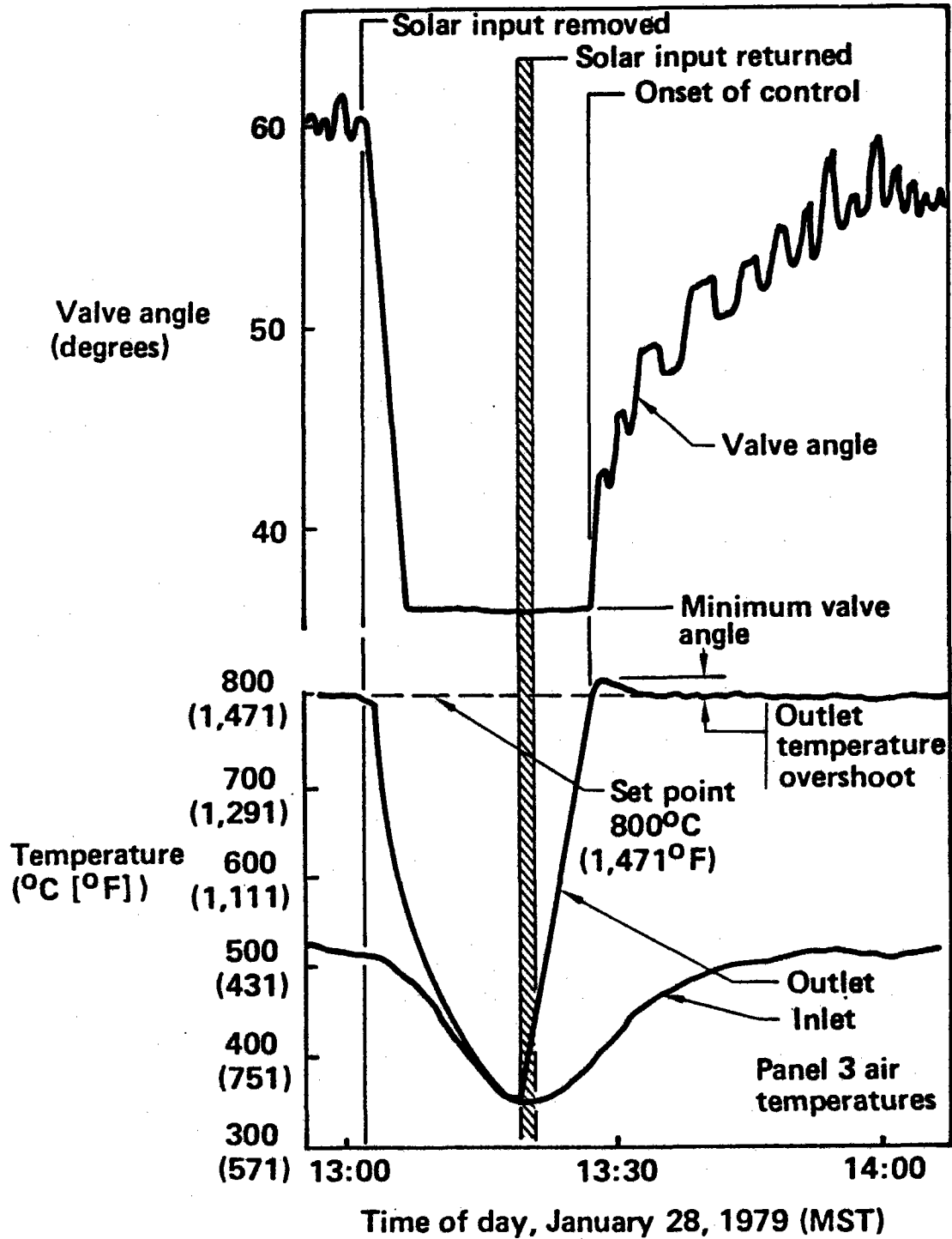
These test results were very satisfactory. The outlet temperature response at the onset of control was well damped with a maximum set-point overshoot of about 14°C (25°F) and no oscillations. The valve angular movements also appeared to be stable.

Test results showed that BMSR airflow temperature controls could handle the rapid temperature increase expected during startup of a pilot plant or commercial solar receiver. Except for the thermal lag of the BMSR test air supply system, it could have been started and brought to operating temperature within a few minutes.

The second portion of test CS-3 was conducted on January 30, 1979. The

Figure 9.5-1. Results of Cold Startup Test, CS-3

## Results of Cold Startup Test CS-3



purpose of this test was to expose the cold BMSR to the thermal shock caused by a high initial rate of solar input power. A normal startup condition with fully open flow-control valves and a high rate of airflow through the receiver was used during this cold startup test. Once the receiver airflow had been verified, the test was initiated by bringing 40 heliostats on target within 4 min. This brought the receiver solar input power up to about 600 kW.

After the cold startup test a number of other tests were conducted throughout the remainder of the day. Subsequent posttest inspection showed that the receiver thermal insulation, solar shielding, and heat exchangers survived with no visible changes.

#### 9.5.2 Emergency Cooldown Tests

The CRTF collector-field control system incorporated several preprogrammed commands that were used to rapidly reduce the solar input power to the receiver under test. Emergency cooldown tests were initiated by the CRTF console operator entering an emergency standby command to the field control computer. This action caused all the heliostats on target to move to the standby point. All the heliostat images would move off the BMSR aperture within about 3 sec of the time this command was input to the field control computer.

The emergency standby command was used several times prior to the commencement of this test series. These were actual test emergencies that occurred during several of the early solar tests and these shutdown events preempted most of the planned tests. Data collected during these events were examined and the receiver was inspected to determine whether heat exchangers were exposed to hazardous temperatures or other conditions were occurring that might damage the BMSR. No problems could be found.

One feature of the planned emergency cooldown tests was not experienced during any of the unplanned emergency shutdown events. This was the provision in test EC-2 that called for simultaneously shutting off the solar input and airflow through the receiver.

Simultaneous removal of airflow and solar-input power was considered to be one of the most important simulations of emergency conditions in pilot plant or commercial solar receivers. These conditions would be imposed on the solar receiver during any emergency that required the turbomachinery to be shut down. The most serious concern was that without airflow to cool the heat exchanger tubes, they could be overheated by radiant heat from the insulation walls of the cavity.

Test EC-2, which incorporated simultaneous shutdown of solar input and receiver airflow, was conducted on January 23, 1979. It was repeated on March 24, 1979, as part of the extended solar testing program. Transient cooldown data from these two tests is discussed in Section 9.7 with respect to analyses of the convective heat losses out the receiver aperture. A thorough review of the data showed that heat exchanger temperatures were not increased by soakback heating. As a result of these tests, soakback heating was not expected to be a problem with other air-cooled solar receivers having similar thermal characteristics and lightweight (120 to 220 kg/m<sup>3</sup>, [8 to 15 lb/ft<sup>3</sup>]) cavity wall insulation.

Objectives of the emergency cooldown tests were accomplished by a mixture of planned and unplanned test events. These events had no visible effects on the receiver. Evidence of soakback heating could not be found in the test data.

#### 9.6 SOLAR LOAD-FOLLOWING TESTS

Most of the BMSR solar tests were conducted by exposing the receiver to specific short-term operating conditions and measuring the response. Four solar load-following tests were included in the test plan to fulfill the need for sustained long-term receiver operation under design-point conditions of solar-input power and temperature. The 4 days of testing were to include clear-sky conditions as well as days with various degrees of cloudiness. The solar load-following test plan included starting the receiver at dawn and operating throughout the day.

Several problems affected the execution of these day-long tests. During



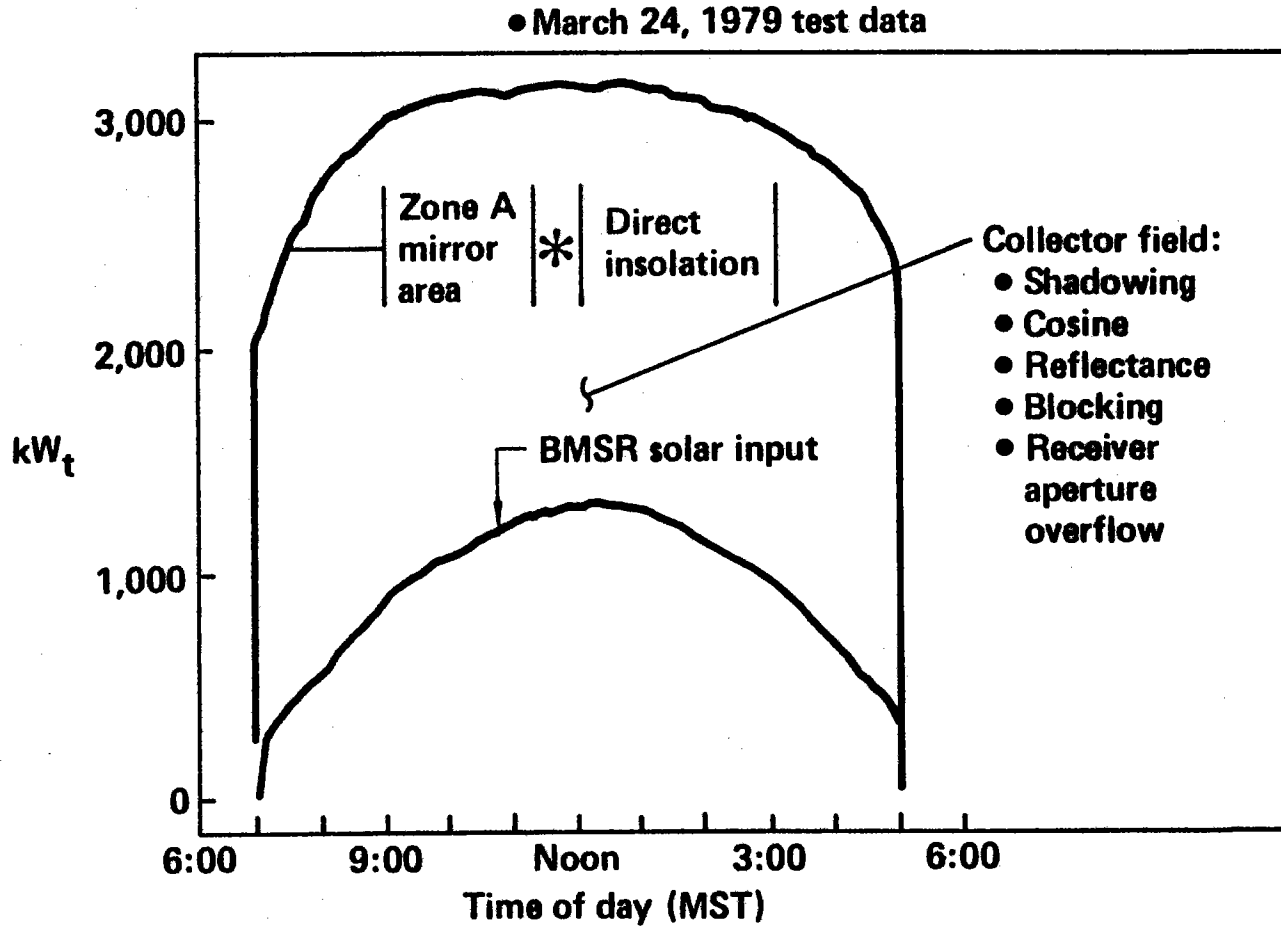
December and January, the start of solar testing was often delayed by cold weather conditions. The unusually cold weather at Albuquerque caused unexpected problems with heliostat tracking, BMSR instrumentation, the electric power generation at CRTF, and the air supply compressors. These problems continued to occur on cold, clear mornings in spite of the best efforts of all persons involved. Specific cold weather problems included ice in instrumentation lines, frozen and hard-to-start engines, failed starting batteries, and excessive numbers of heliostat tracking alarms, which caused the CRTF collector system to shut down.

The optical characteristics of the CRTF heliostats combined with the already-short winter days to reduce the effective solar test day to about 6 hr. This increased to about 7 hr during the tests in March. Figure 9.6-1 shows the day-long performance of the CRTF collector system during one of the March test days. The direct insolation became significant about 7:00 a.m. During the period from 7:00 a.m. to 5:00 p.m., the idealized maximum solar power (intercepted by heliostats pointed at the Sun) ranged from 2000 to 3000 kW. However, the collector system performance and its net solar input to the BMSR was only above 1000 kW during the period from about 9:30 a.m. to 3:00 p.m. It was highly dependent on the time of day. Data were not available to describe the separate effects of variables such as shadowing, cosine, blocking, and overflow losses on this performance. Nevertheless, the receiver aperture overflow was assumed to be the major source of solar transmission losses in the system. Two factors caused these large overflow losses. First, the BMSR aperture was a scale model of the commercial-size receiver. Its 1.1m-diameter (3.6-ft-diameter) aperture was about 30% smaller than the optimum target size at times before and after solar noon. These effects were small from about 10:00 a.m. to 2:00 p.m., but were the major cause of the reduced BMSR solar input in morning and afternoon (shown in Figure 9.6-1).

Large numbers of Zone B heliostats were used during some of the solar load-following tests. They were brought on line in an attempt to extend the period during which the receiver solar input could be maintained at nearly 1000 kW. This procedure was not effective. The Zone B heliostats were aligned for an optimum focus on the tower-top test site. Most of them were

Figure 9.6-1. Typical Daily Performance of CRTF Collector System

# Typical Daily Performance of CRTF Collector System



much further away from the receiver than the Zone A heliostats. Several of the Zone B heliostats equaled the performance of one Zone A heliostat at noon.

In spite of these difficulties, it was possible to obtain a total of about 16 hr of BMSR operation in a solar load-following mode. Partial days of operation were accomplished on January 28 and 30, 1979, after completion of the other scheduled tests. Day-long tests were attempted on January 31 and on March 23, 24, and 25, 1979 with limited success.

Most of the results of these extended periods of BMSR operation show up in the assessments of the physical effects of testing on the receiver. Thermal performance, including thermal output and heliostats in use during the tests, are shown in Figures 9.6-2 through 9.6-6.

The average BMSR thermal output during these periods of solar load-following turned out to be about 610 kW. This was significantly lower than the 750 kW output typical of design-point operating conditions. There were two reasons for this lower level of receiver thermal output. First, the real-time estimates of BMSR solar input turned out to be about 10% high. Second, much of the testing was conducted in the afternoon when the CRTF collector system could not provide the 1 Mwt design-point solar input. Other test results describing BMSR temperatures, airflow rates, and heat-flux levels are included in Section 12.

The total thermal output of the BMSR during solar load-following tests was about 10 Mwt/h. This was about half of the integrated output power considered during the test planning. However, these extended periods of receiver operation did accomplish the test plan objectives. Long periods of operation with constant air outlet temperature were obtained.

These tests increased the duration of exposure of the BMSR to high levels of solar-input power to a total of about 40 hr. This was long enough to verify the short-term structural stability of the BMSR heat exchangers, and to show that the aperture-rim shielding and high-temperature insulation designs used in the BMSR would not be acceptable for pilot plant or commercial solar

Figure 9.6-2. Solar Load Following Test Conditions, January 28, 1979

# Solar Load Following Test Conditions, January 28, 1979

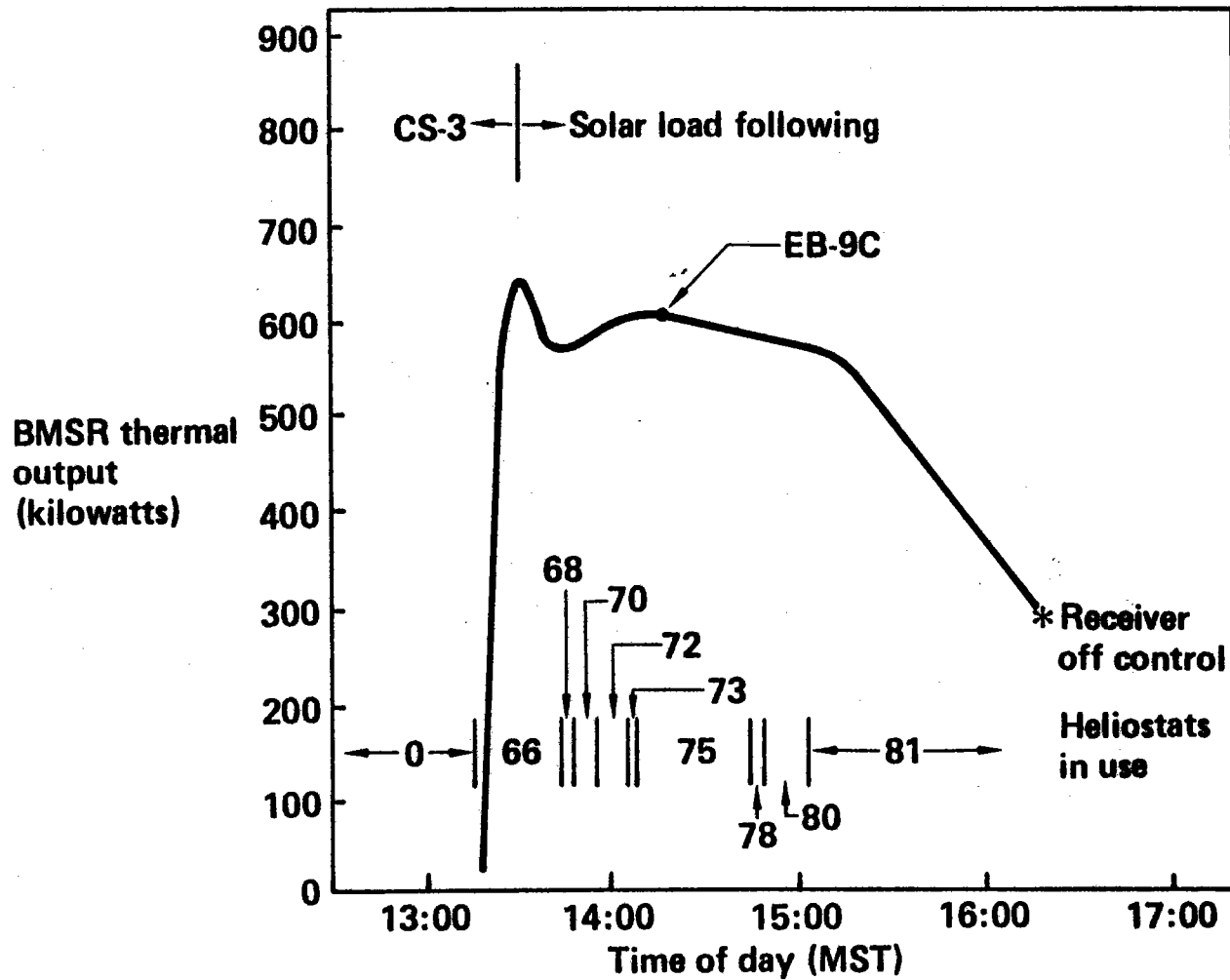


Figure 9.6-3. Solar Load Following Test Conditions, January 30, 1979

## Solar Load Following Test Conditions, January 30, 1979

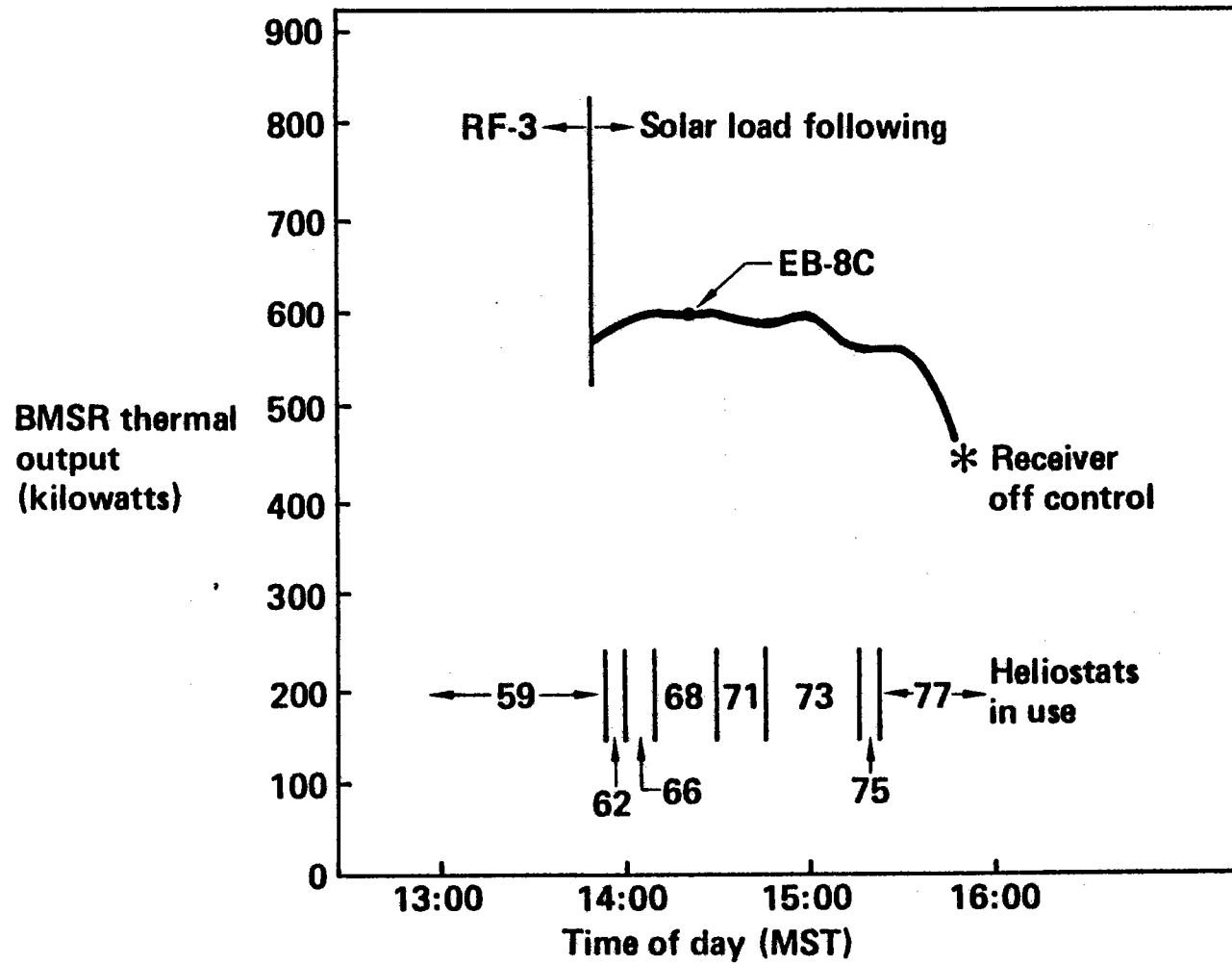


Figure 9.6-4. Solar Load Following Test Conditions, January 31, 1979

# Solar Load Following Test Conditions, January 31, 1979

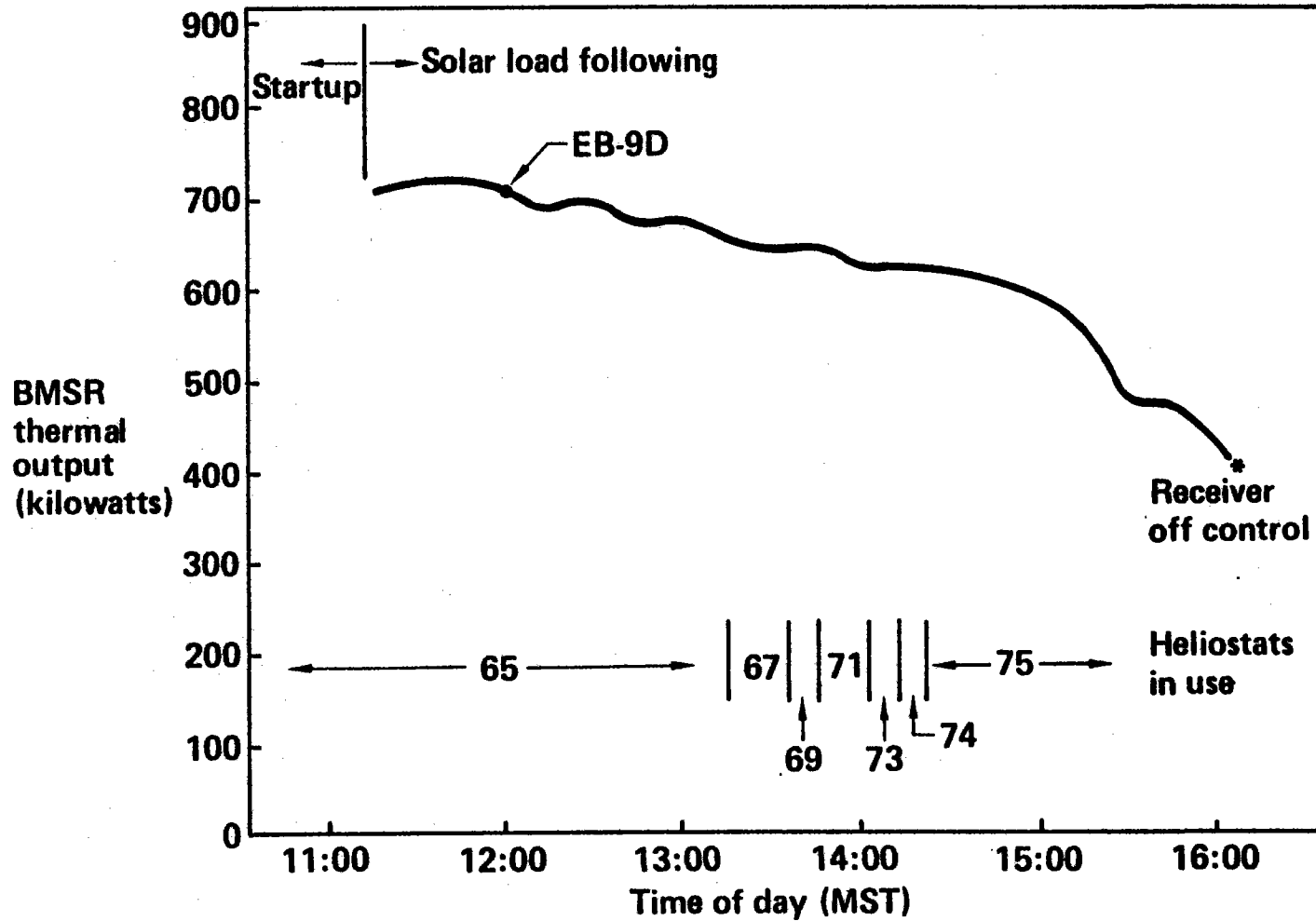
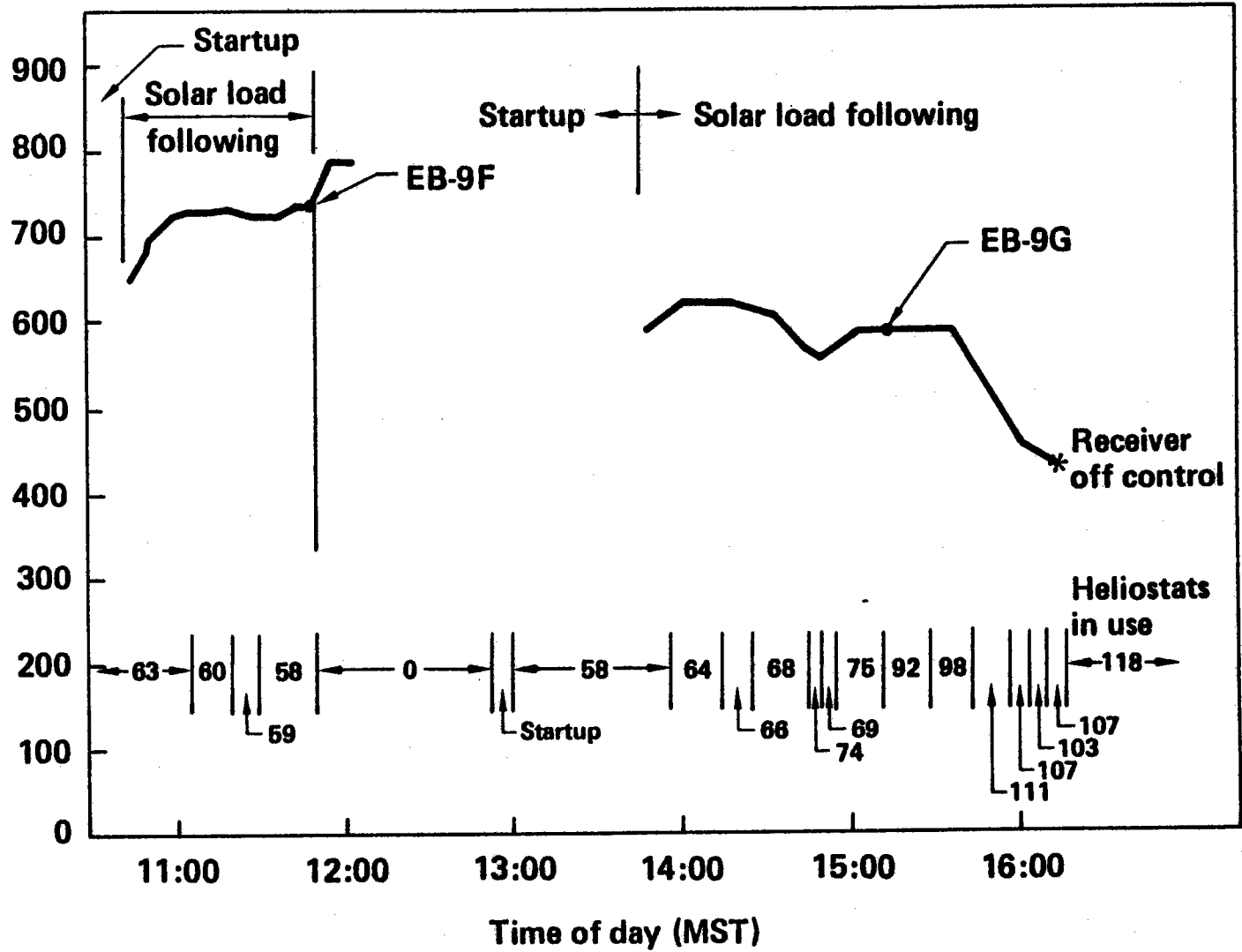


Figure 9.6-5. Solar Load Following Test Conditions, 3/24/79

# Solar Load Following Test Conditions, 3/24/79

528

BMSR thermal output (kilowatts)

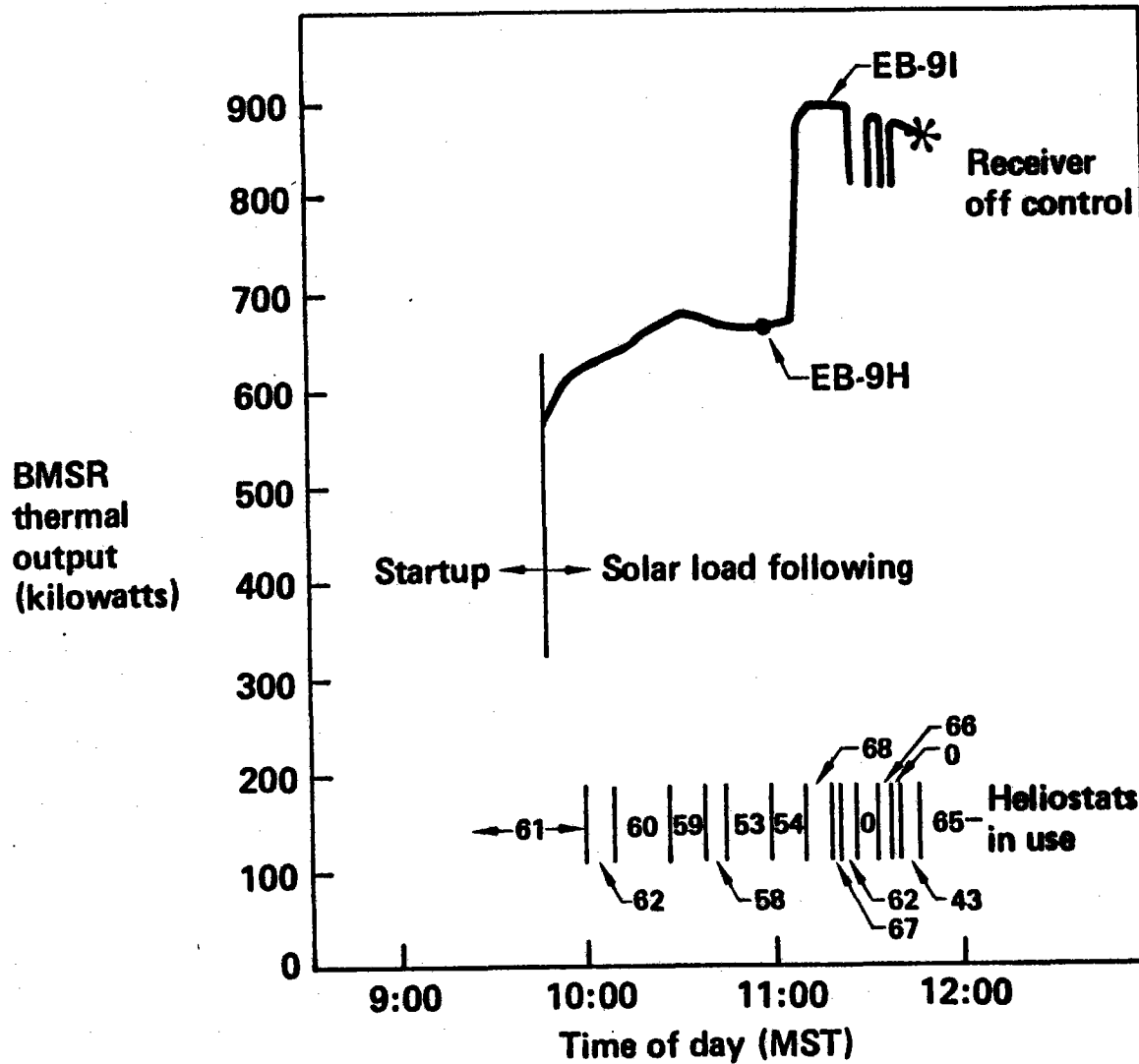


Receiver off control

Heliostats in use

Figure 9.6-6. Solar Load Following Test Conditions, 3/25/79

## Solar Load Following Test Conditions, 3/25/79





receivers.

The physical effects of the solar testing on the BMSR are described and evaluated in Section 10.0.

## 9.7 EVIDENCE OF EXTERIOR CONVECTIVE HEAT TRANSFER

The first inkling of a possible convective mechanism exterior to the heat exchanger tubes was noted when the first equilibrium tests were started, early in the test program. The panel mass flow rates were strongly biased to the top of the receiver. Section 9.1 presented some of these data.

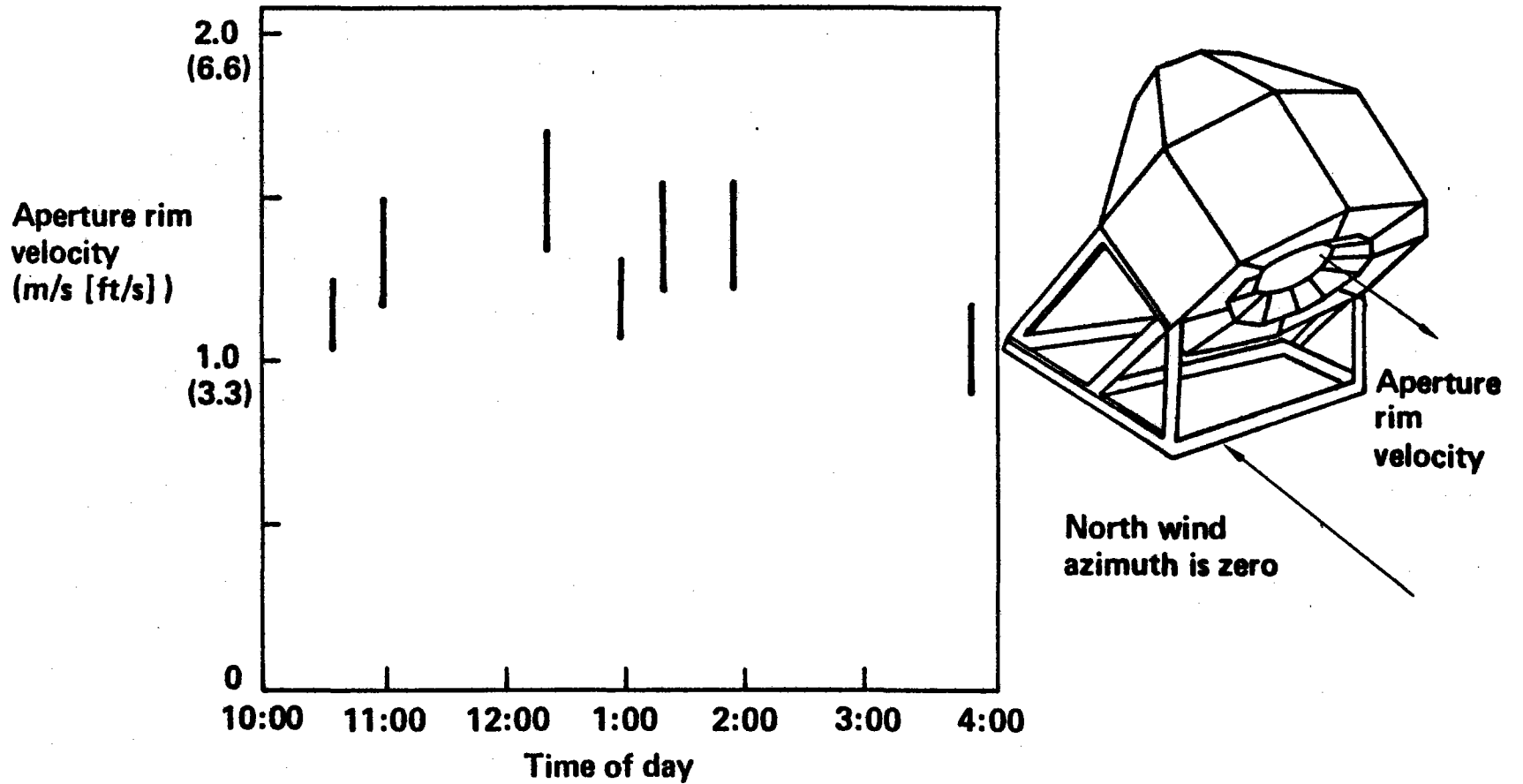
Subsequently, various experimental means were considered to measure any convective flow out the top of the aperture. The method adopted was the aperture anemometer described in detail in Section 8.4. The data collected from this anemometer are presented in Figure 9.7-1. The bands represent the estimates of several different observers. As can be seen, a velocity of about 1.5 m/s (5.0 ft/s) was estimated.

Another evidence of an exterior convective effect was noted during transient cooldown tests. These tests were performed by simultaneously turning off the heliostat field and the receiver mass flow as quickly as possible and monitoring the thermal response of the receiver. Two such tests were performed, one at about 4:30 p.m. on March 24, 1979, and the other at about 4:00 p.m. on January 23, 1979. The calorimeter data for both days are presented in Figures 9.7-2 and 9.7-3. As can be seen, a characteristic of this test was for the calorimeter output (frame and cover) to coalesce into a band that subsequently decayed. Thermocouple data taken from the heat exchanger tubes during this same period are shown in Figure 9.7-4. Because these thermocouples were attached to the thin-wall heat exchanger tubes, they responded rapidly to the cavity environment, and their readings presented an accurate register of the local air temperatures.

Figure 9.7-4 indicates a definite stratification of air temperatures in the receiver as the transient cooldown proceeded. Because heat exchanger thermocouples were located at different vertical positions (Figure 9.7-5),

Figure 9.7-1. Anemometer Data, January 20, 1979

# Anemometer Data, January 20, 1979



531

6.5	9.9	7.5	5.0	3.8	Ambient wind velocity (m/s [ft/s])
(21.3)	(32.5)	(24.6)	(16.4)	(12.5)	
8	2	340	336	40	Azimuth (degrees)

Figure 9.7-2. Calorimeter Data

# Calorimeter Data

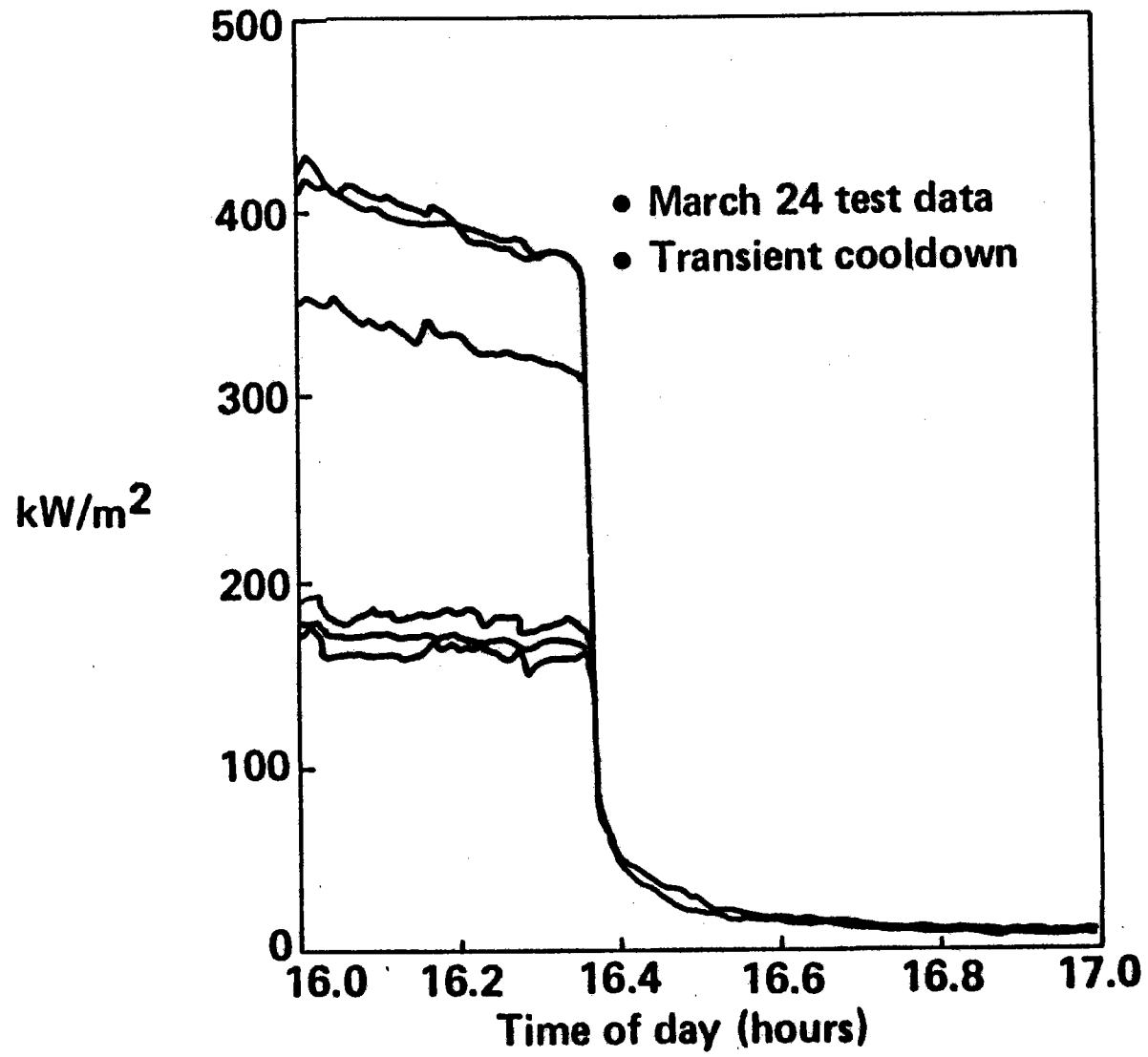


Figure 9.7-3. Calorimeter Data

# Calorimeter Data

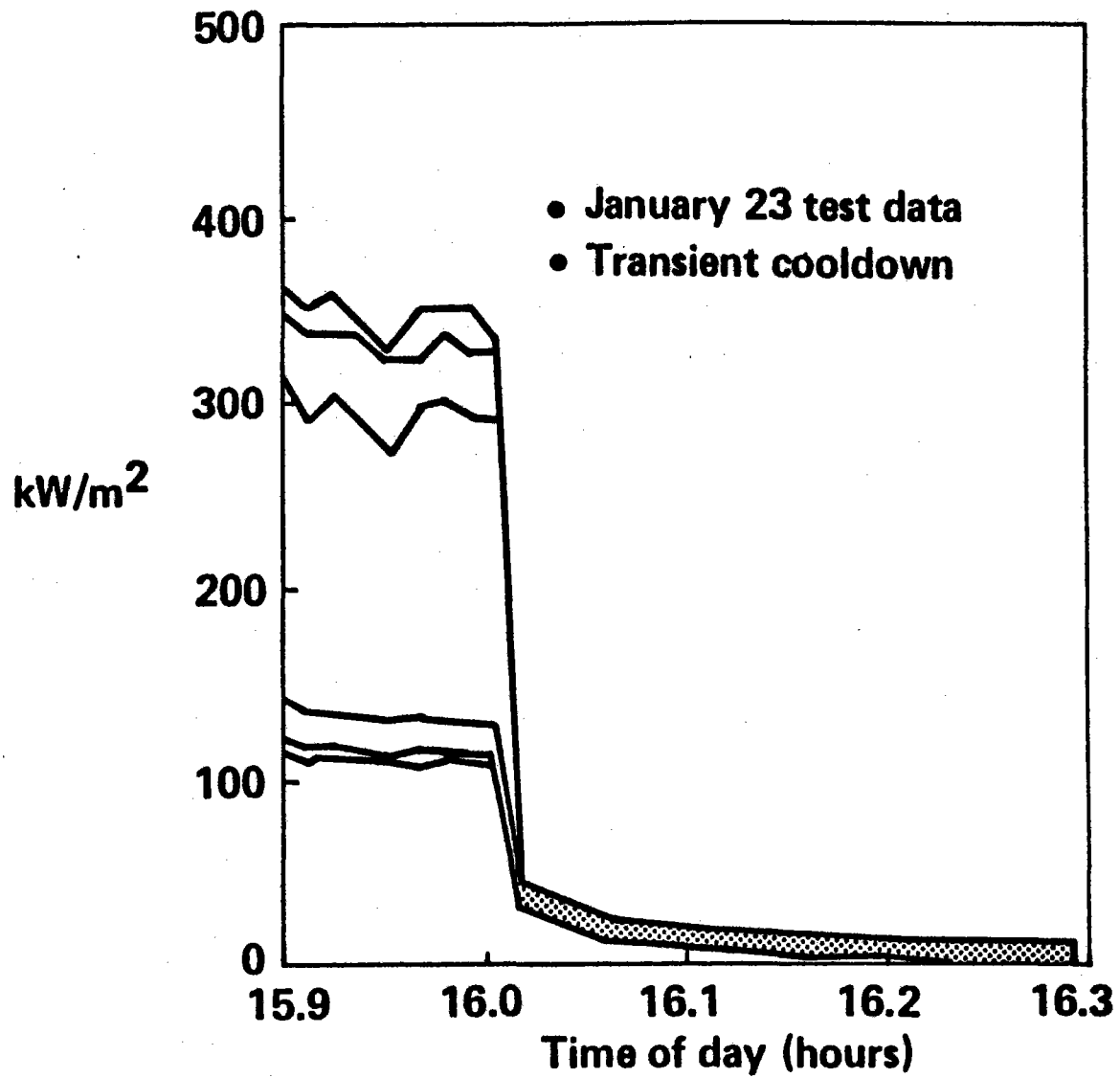


Figure 9.7-4. BMSR Transient Cooldown (Heat Exchanger Temperatures)

# BMSR Transient Cooldown (Heat Exchanger Temperatures)

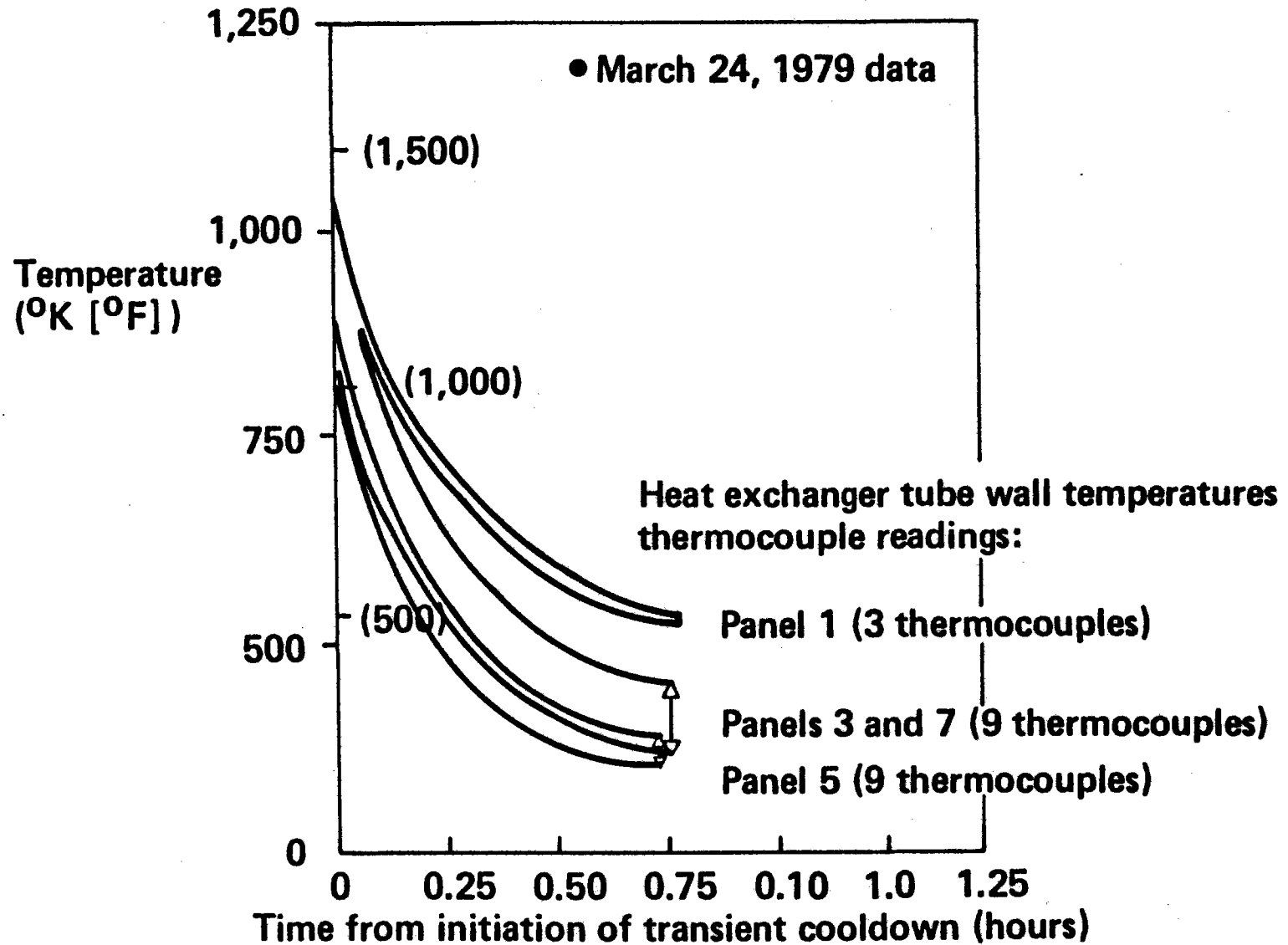
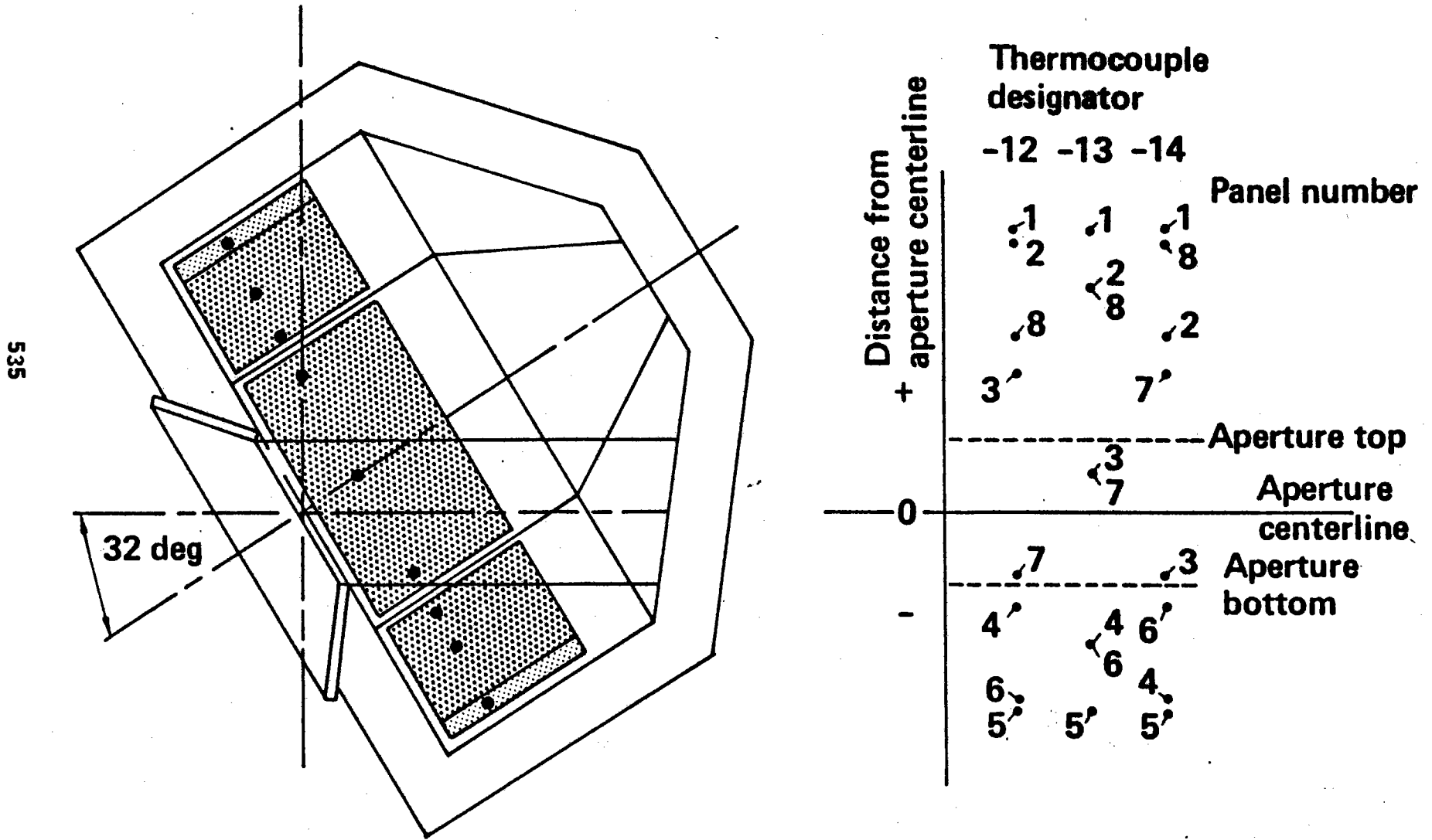


Figure 9.7-5. Receiver Convective Losses

# Receiver Convective Losses



the temperatures during the transient cooldown were plotted against the thermocouple vertical position. To negate the effects of the decaying temperature level from the cooling receiver interior, an average of 29 heat exchanger thermocouples were used for each temperature record. The difference between the thermocouple reading and the average was plotted against the vertical distance from the aperture centerline for several representative times during the March 24 transient cooldown (Figures 9.7-6 to 9.7-10). Also presented in the plots is the time relative to the start of the transient cooldown and the average thermocouple reading.

The plots portray negligible stratification a few seconds before and after the initiation of the transient cooldown. However, stratification increased as the cooldown continued, and approximately a 200°C (360°F) temperature difference is noted after about 0.5 hr.

A similar effect was noted in the January 23, 1979 data. Figure 9.7-11 presents data near the end of the transient cooldown. Again a stratified behavior is noted.

Figure 9.7-12 presents a plot of the average heat exchanger temperature as a function of time for March 24. Also presented is the average cavity temperature as determined from the calorimeter data. As can be seen, the heat exchanger temperatures assumed intermediate values between the cavity temperature,  $T_c$ , and the ambient temperature of about 4.4°C (40°F).

The data in this section furnish the data base for the posttest convective loss analysis presented in Section 11.2.

Figure 9.7-6. BMSR Transient Cooldown

# BMSR Transient Cooldown

Temperature difference versus vertical distance

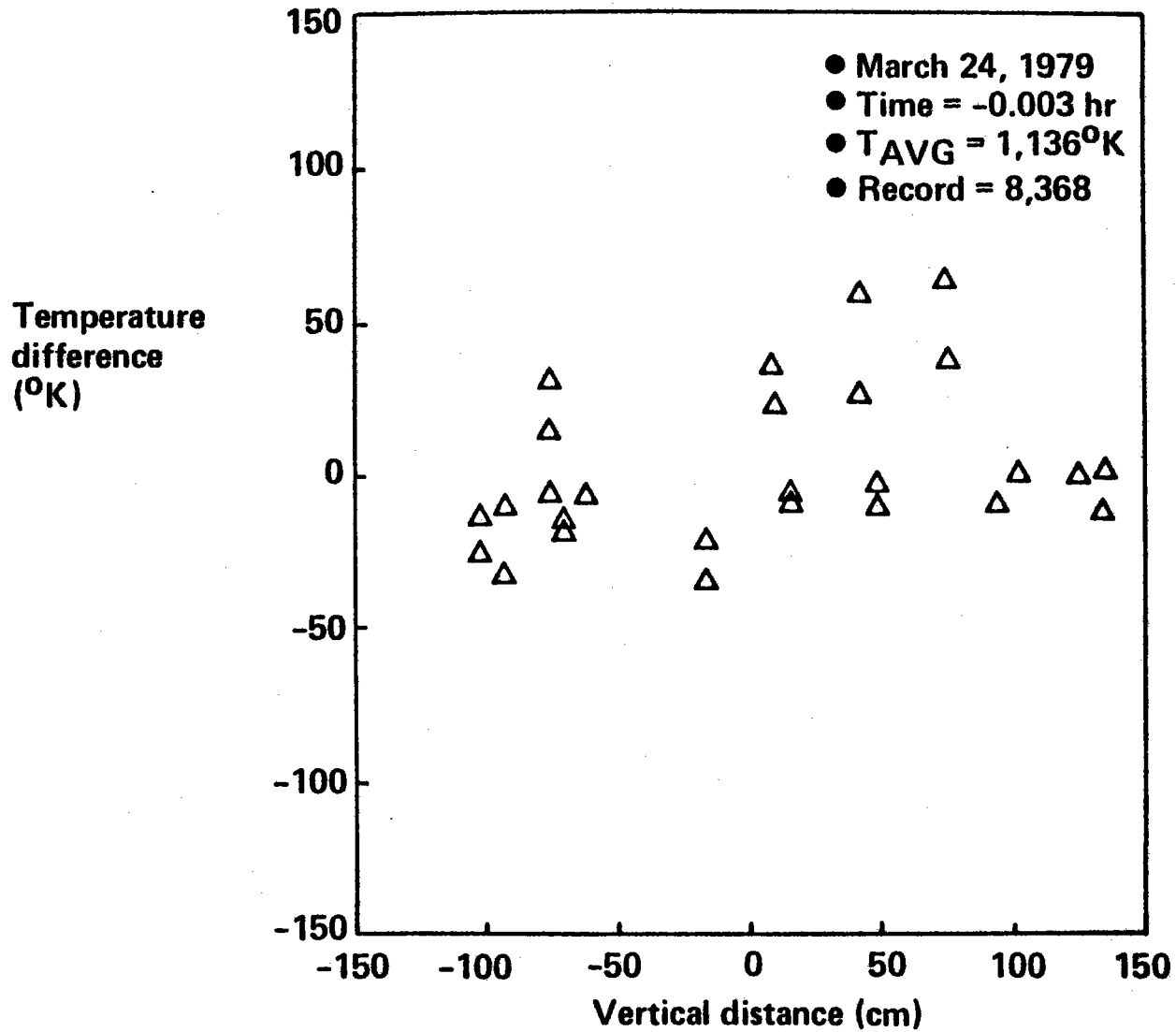




Figure 9.7-7. BMSR Transient Cooldown

# BMSR Transient Cooldown

Temperature difference versus vertical distance

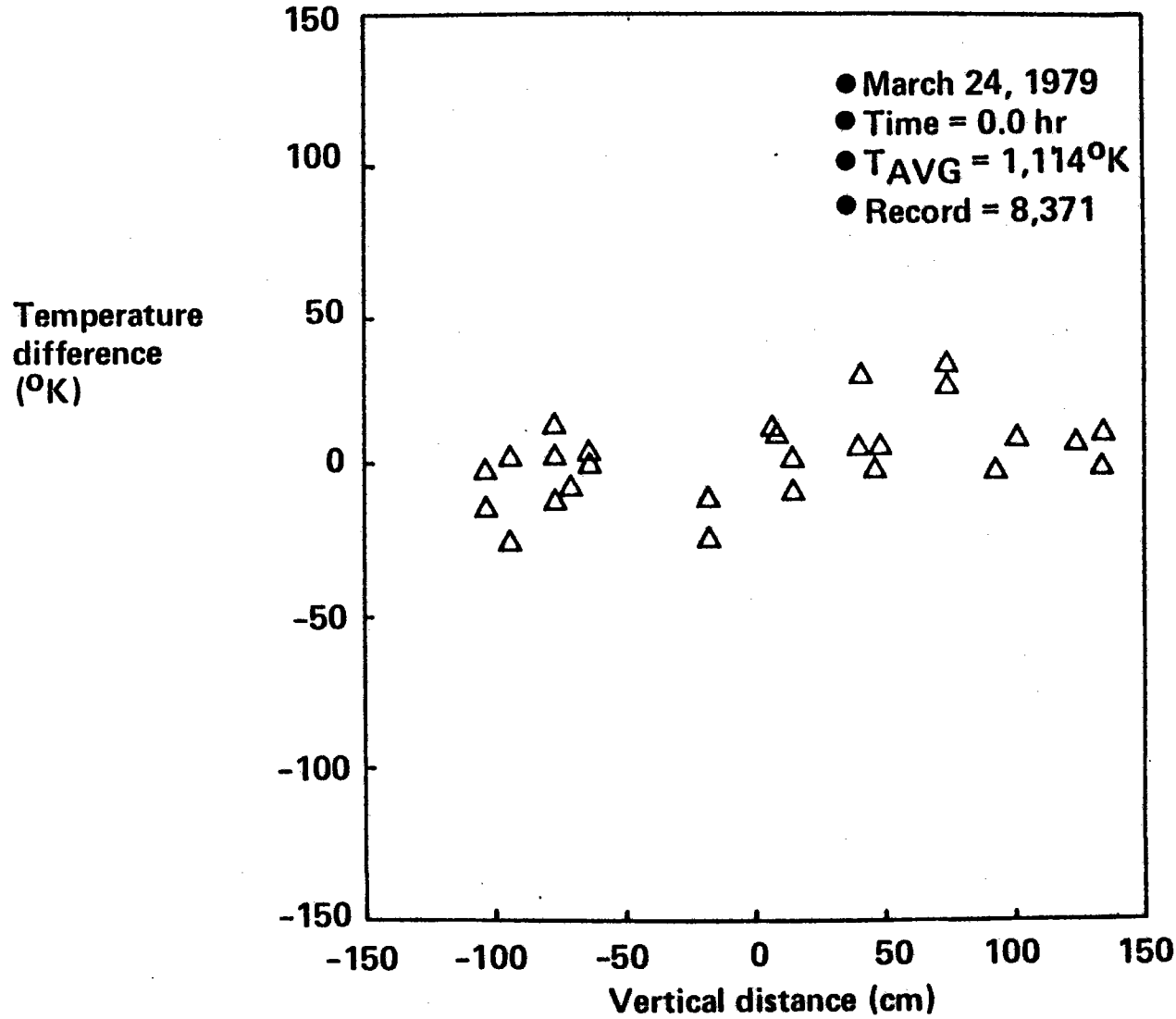


Figure 9.7-8. BMSR Transient Cooldown

# BMSR Transient Cooldown

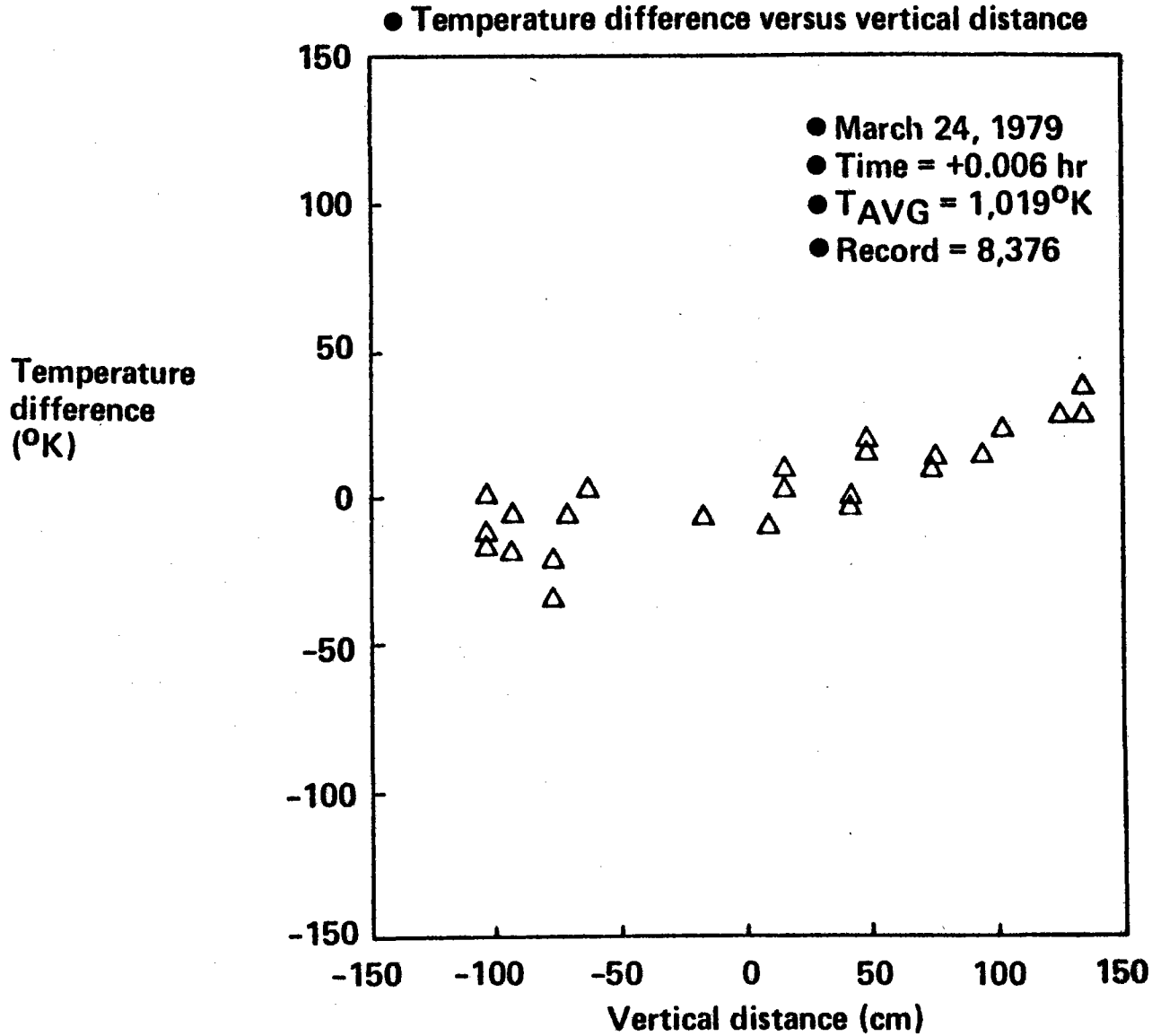


Figure 9.7-9. BMSR Transient Cooldown

# BMSR Transient Cooldown

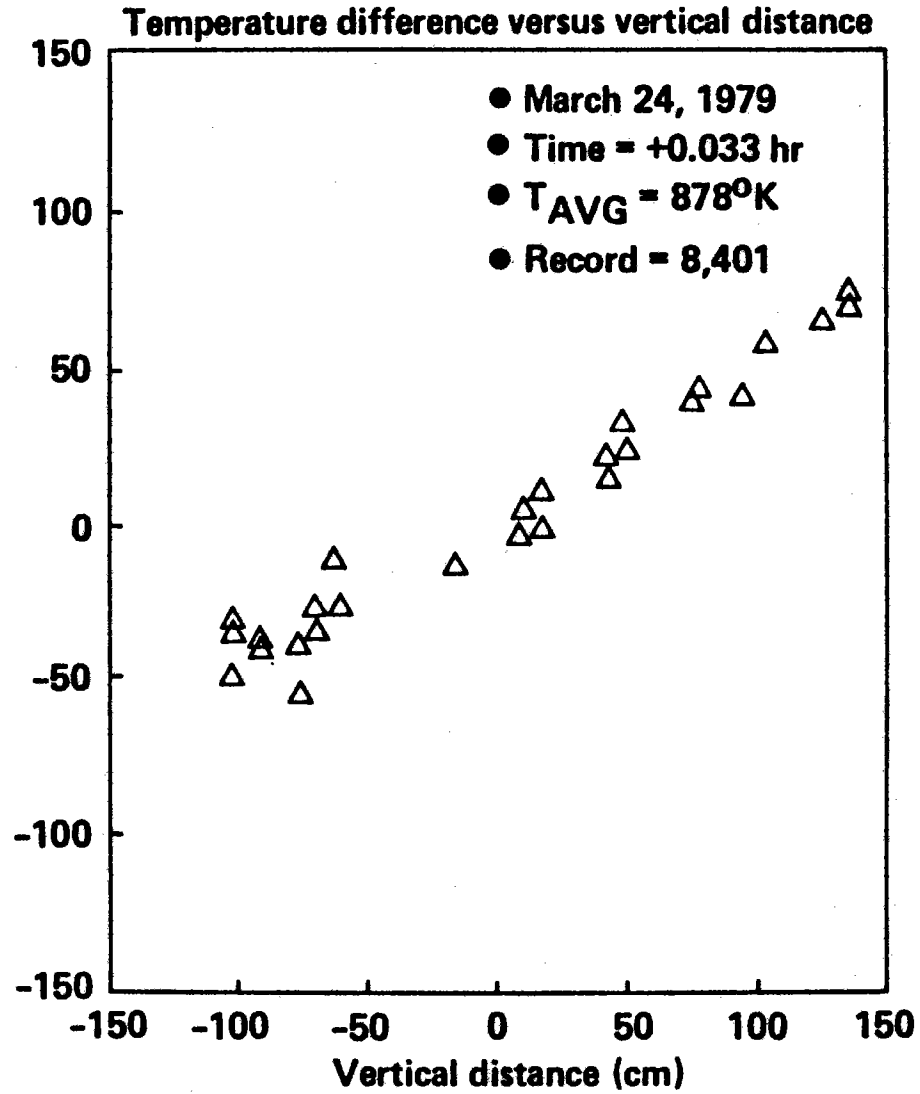
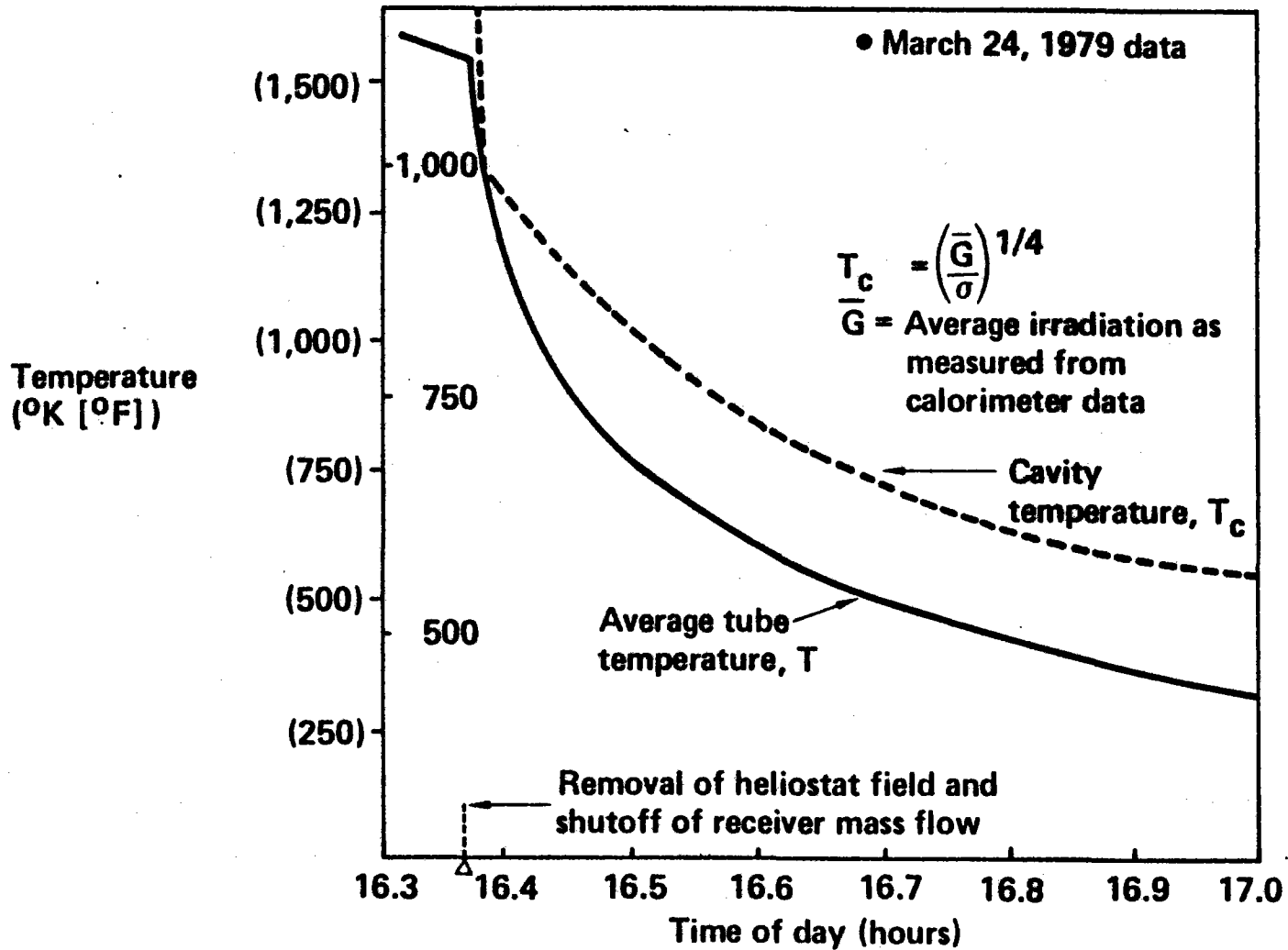


Figure 9.7-12. BMSR Transient Cooldown (Average Receiver Temperatures)

## BMSR Transient Cooldown (Average Receiver Temperatures)



## SECTION 10.0

### ADDITIONAL RESULTS OF THE SOLAR RECEIVER TESTING PROGRAM

BMSR test data were collected and presented in Section 9.0, which described BMSR heat transfer capability and heat losses, operating temperatures, and transient response characteristics. Because of the scale-model-thermal aspects of the BMSR design, these data also provided a direct experimental assessment of the characteristics of the commercial solar receiver. Results of the experiment and corresponding analyses are also of scientific value to the extent that solar and high-temperature radiant heat transfer technology pertinent to the design of cavity receivers for central receiver thermal power systems has been exercised, compared with experimental results, and evaluated. The processes of design, development and testing of the BMSR have also produced a wealth of information concerning other aspects of central receiver solar-thermal powerplant development. This information is made up of events that have been observed, changes detected in the receiver and test system resulting from exposure to solar powerplant operating conditions, and direct experience gained by personnel who operated the BMSR and test system. Additional results of the experiment are described in the following paragraphs.

Section 10.1 gathers a variety of personal observations, notes in test logs, and results of periodic BMSR inspections to produce a historical summary of the solar-testing activity, from November 17, 1978, through March 25, 1979. Important gradual changes are described such as the steady increases in BMSR operating temperature and solar-power level that characterized the early testing conditions. These test environment changes are described in conjunction with the gradual changes observed in the BMSR. The development of receiver problems precipitated by cumulative hours of operation or attainment of damage thresholds of temperature or solar-input power are also described.

A wide variety of weather conditions and solar power system operating problems also affected the execution of the BMSR solar tests. They are described in Section 10.1, although the BMSR testing experience at CRTF

during the first series of tests at the new facility during winter months may not be typical.

Sections 10.2 through 10.5 describe the effects of solar testing activities on the major BMSR subsystems, including cavity thermal insulation, heat exchangers and airflow subsystem, receiver instrumentation, and aperture-rim solar shielding. Problems with this equipment are described, along with conclusions as to its suitability for use in pilot-plant and commercial solar receivers.

#### 10.1 HISTORICAL SUMMARY OF TEST ACTIVITIES, INSPECTIONS, AND OBSERVATIONS DURING THE PRODUCTION SOLAR TESTS

Some aspects of the solar testing activities at CRTF have already been described in Section 7.0. However, the purpose of this earlier discussion was to describe the degree of success achieved in accomplishing the specific objectives of the 29 planned solar tests. Figure 7.6-1, which is reproduced as Figure 10.1-1 here, consists of a calendar of test-site activities, including checkout and production testing. It is a good point of departure for these more detailed discussions of production solar testing activities at CRTF.

As shown in Figure 10.1-1, the BMSR solar tests occupied a period of 105 calendar days. The production solar tests occupied a total of 85 of these days. Of the 85, only 26 were viable test opportunities. This included all the occasions when the receiver and test system could be brought on the line before 11:00 a.m.

The solar testing calendar also shows that all the test objectives were accomplished on just 11 of the 26 test opportunity days. Of the remainder, 3 days were disrupted by test facility problems, 10 were affected by weather conditions, and 2 were disrupted by problems with the experiment. Notes in Figure 10.1-1 also show that test objectives were at least partially accomplished on four of these disrupted test days.

The weather, test operations, and equipment failure problems that occurred

Figure 10.1-1. Solar Testing Calendar

# Solar Testing Calendar

	October	November					December					January					March
	30	6	13	20	27	4	11	18	25	1	8	15	22	29	19		
Checkout testing	[Bar from Oct 30 to Nov 13]																
Production testing			[Bar from Nov 20 to Jan 29]														
Conditions preventing test:																	
Experiment not ready			[ ]	[ ]	[ ]	[ ]	[ ]										
Facility not ready	[ ]	[ ]	[ ]	[ ]		[ ]	[ ]	[ ]			[ ]						
Test personnel not ready	[ ]			[ ]	[ ]	[ ]	[ ]	[ ]	[ ]	[ ]							
Weather prohibitive		[ ]	[ ]	[ ]	[ ]	[ ]	[ ]	[ ]	[ ]	[ ]	[ ]	[ ]	[ ]	[ ]	[ ]	[ ]	
Test opportunities	[ ]	[ ]	[ ]	[ ]	[ ]	[ ]	[ ]	[ ]		[ ]	[ ]	[ ]	[ ]	[ ]	[ ]	[ ]	
Conditions preventing success:																	
Facility problem	[ ]	[ ]		[ ]			[ ]	[ ]									
Weather				[ ]			[ ]	[ ]		[ ]	[ ]	[ ]	[ ]			[ ]	
Experiment problem					[ ]											[ ]	
Usable test data	☆	○ ○ ☆	☆☆		☆	○ ☆				☆☆	☆☆	○ ☆	☆☆☆	☆☆	○ ☆ ○		

546

- ☆ Met test objectives
- Partial results, incomplete test

during these 26 days of production solar tests are of interest in the assessment of operational feasibility of central receiver solar-thermal power systems. Testing activities during these days are described in detail in the following paragraphs.

One aspect of the BMSR test operations not depicted in Figure 10.1-1 is that many of the successful test days were only partially successful efforts to conduct day-long operation of the solar-thermal test system. Each of the production solar testing days included primary as well as secondary objectives sufficient to occupy the available time from start to end of the solar test day. This period was about 6.5 hr long during the months of December and January and 7.5 hr long during the March tests. As mentioned earlier, the optical characteristics of the CRTF collector field and the low solar elevation angles in winter caused the solar input to the receiver to fall below about half of its design level at around 3:30 p.m. during December and January, and 4:15 p.m. during March.

Actual periods of solar test operation during the 26 production test opportunity days are shown in Table 10.1-1. Tests conducted during November and December 1978, were less than half the potential duration of the test operation day. Later, during January 1979, the length of tests increased, with two of the test operating periods extending beyond the normal afternoon stopping time. These extended periods of operation, with the receiver at well below its normal range of solar input power, were conducted to increase BMSR operating time and to observe changes in the late afternoon solar image of the CRTF collector field.

An important feature of the production test activities shown in Table 10.1-1 was the steadily increasing duration of tests during January 1979. Three factors contributed to this increase in the length of daily testing periods: weather, increased test operating experience, and reduced conservatism in the BMSR operating philosophy.

Poor weather and marginal insolation conditions at CRTF during November and December 1978, significantly reduced the effective length of daily test operating periods. Temperatures well below freezing made it extremely



PRODUCTION SOLAR TEST DAY AT CRTF		DURATION OF SOLAR INPUT (HR)	DURATION OF BMSR OPERATION ON CONTROL (HR)
1	11/17/78	2.50	0.65
2	11/19/78	1.75	-0-
3	11/20/78	2.70	-0-
4	11/28/78	2.83	0.30
5	12/5/78	2.80	-0-
6	12/9/78	2.90	-0-
7	12/10/78	2.85	0.87
8	12/16/78	0.50	-0-
9	1/3/79	4.83	-0-
10	1/4/79	3.13	0.53
11	1/7/79	3.50	0.80
12	1/10/79	3.15	0.73
13	1/11/79	3.40	0.71
14	1/13/79	4.13	0.53
15	1/14/79	2.27	-0-
16	1/18/79	4.58	-0-
17	1/20/79	5.65	3.53
18	1/21/79	3.83	-0-
19	1/23/79	4.70	1.75
20	1/27/79	3.62	0.85
21	1/28/79	7.77*	2.83
22	1/30/79	5.30	1.72
23	1/31/79	8.42*	4.61
24	3/23/79	3.05	0.37
25	3/24/79	8.86	3.73
26	3/25/79	4.53	1.93
TOTAL		103.55 HR	26.49 HR

\*TEST CONDUCTED UNTIL SUNSET, AT MUCH REDUCED SOLAR POWER LEVEL

Table 10.1-1: Cumulative BMSR Operating Hours  
During Production Solar Tests

difficult to get test equipment started in the morning. Air-supply compressors, the CRTF electric-power generator, and CRTF heliostats all exhibited cold weather operating problems. Freezing temperatures also caused difficulties with BMSR instrumentation.

The other weather problem of significance during these first few weeks of production solar testing was the early morning cloudiness experienced at the test site. Morning skies were usually cloudy, with a low-level cloud layer extending from the Sandia Mountains a few miles east of the facility, and westward over the desert plain south of Albuquerque. Clear skies could frequently be observed to the west of this low cloud layer. Typically, these clouds would begin to dissipate during the morning hours, clearing from west to east. However, a line of clouds would usually remain adjacent to the north-south line of the mountain range. By about 11:00 the Sun would move westward beyond the edge of the clouds and testing could commence. Later, during January and March, it was more typical for the morning sky to be completely clear of clouds.

Another factor significantly affecting the duration of tests in 1978 and early January 1979, was the conservatism of the BMSR test-operating philosophy. The first tests were conducted at solar-input-power levels and air-outlet temperatures well below the BMSR design levels. The gradual increase in severity of the receiver operating conditions during these early tests is shown in Figures 10.1-2 and 10.1-3. Caution was exercised to minimize the risk of early damage to the receiver that might prevent full-power and full-temperature operation. Any minor disruption of the testing was viewed as a major risk to the test program during this time. For this reason, some of the problems that caused termination of testing during this period were tolerated during the conduct of later tests. Full solar-input-power conditions were achieved during the 13th day of production tests, January 11, 1979; full input power and maximum air outlet temperatures were achieved on the 17th day of production tests, January 20, 1979. Increases in the length of the test operating periods after these dates were partly due to the less conservative testing philosophy adopted.

Changes were observed in the BMSR and test support equipment at CRTF

Figure 10.1-2: BMSR Solar Exposure History

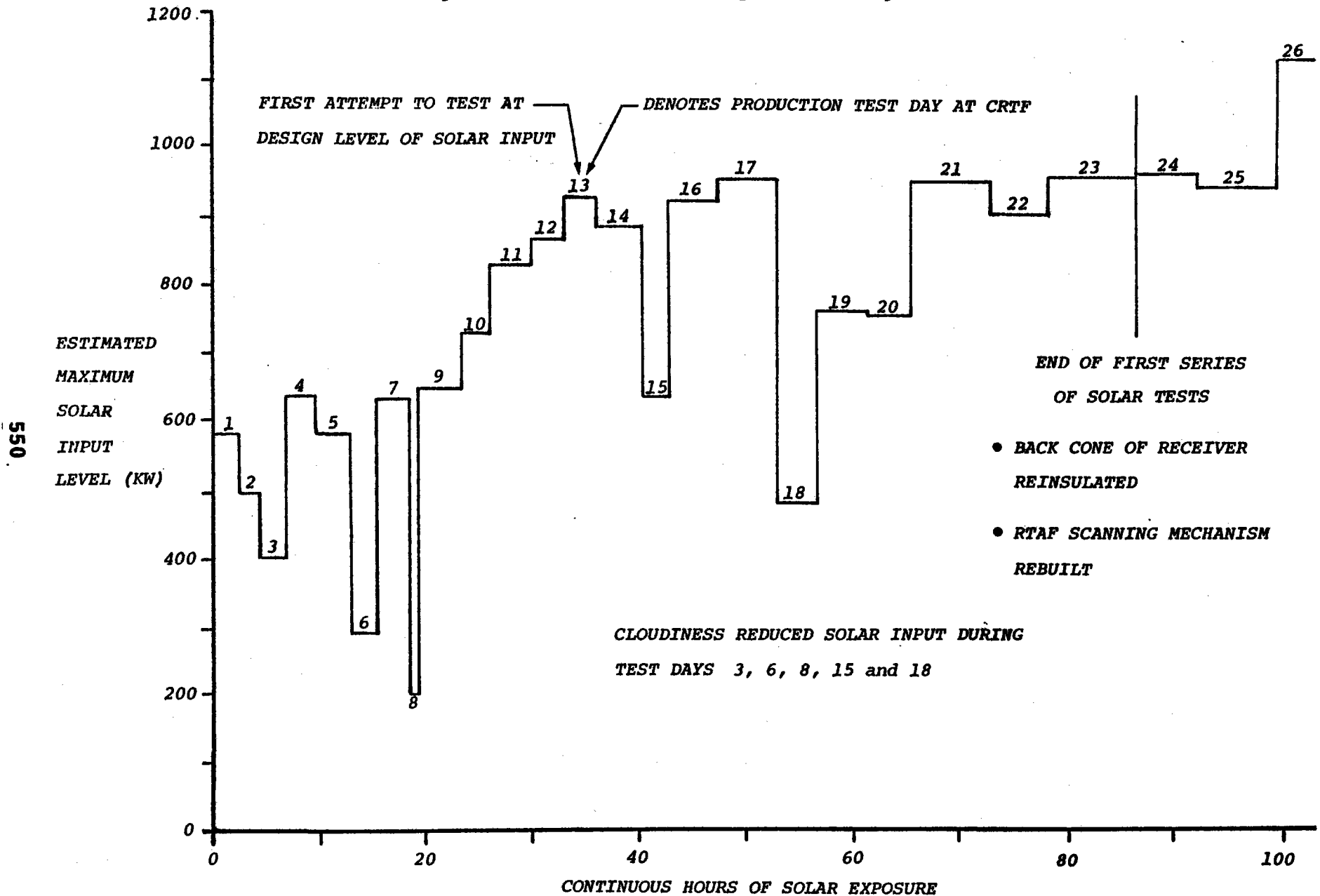
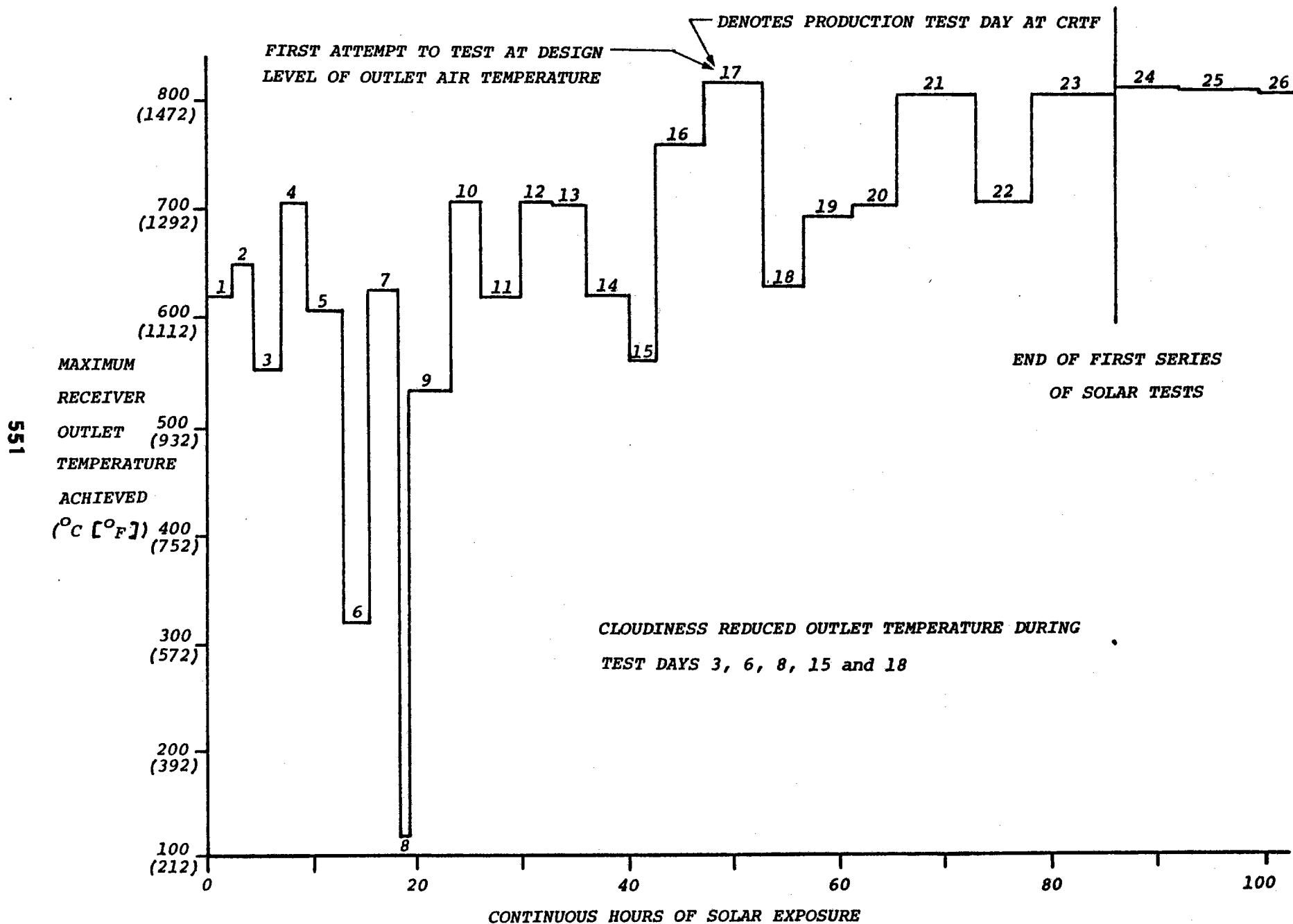


Figure 10.1-3: BMSR Outlet Temperature History



throughout the duration of the solar testing program. A total of 28 significant changes in equipment were noted during the tests. These were distributed throughout the 26 days of production solar tests. Some of these changes consisted of outright failure of components during operation, usually resulting in termination of the day's tests. Others, such as the gradual degradation of the insulation on the back of the receiver and development of air leaks, were detected by visual inspections and functional tests conducted after nearly every day of receiver operation.

These 28 changes observed in the BMSR and test support equipment are described in Table 10.1-2. Description of the receiver insulation, leakage of flanges connecting receiver heat exchangers with the inlet and outlet manifolds, and problems with the BMSR airflow valves are discussed in following subsections. Other problems not involving BMSR subsystems are discussed here.

The primary function of the water-glycol chiller system was to provide coolant to the RTAF scanning bar. This convenient source of coolant was also used for BMSR heat-flux gages. The 13 circular-foil calorimeters located on interior walls of the receiver are shown in Figure 7.3-9. The chiller system consists of a fluid reservoir, a refrigeration unit used to control fluid temperature, and a circulating pump. The temperature of coolant delivered to the calorimeters was instrumented and alarmed by the data acquisition system. This instrumentation, however, failed to detect the loss of coolant flow on November 11, 1978, which resulted from failure of the circulating pump. Loss of flow was followed by draining of coolant out of all but four of the BMSR calorimeters. The dry calorimeters were overheated within seconds. Those with coolant remaining in their supply lines survived the several seconds between detection of pump failure and removal of the BMSR solar input.

The air-supply compressors were subject to a variety of temporary and partial failures caused by vibration. Copper air lines used for compressor instrumentation and pneumatic control had to be replaced by stainless-steel lines and fittings less susceptible to vibration. Wiring terminals frequently failed because of vibration until they were refitted with

Table 10.1-2: Changes Caused By Testing Activity

PRODUCTION TEST DAY AT CRTF	REASON FOR TERMINATION OF TEST	CHANGES CAUSED BY TESTING ACTIVITY	WHEN OBSERVED	REMEDY/REPAIR
1 (11/17/78)	PRESSURE TRANSDUCER FAILURES ON BMSR	WIRING DAMAGED BY HIGH TEMPERATURE	DURING TEST	REPAIR WIRING, PROVIDE FORCED FLOW OF COOLING AIR
2 (11/19/78)	HEAT FLUX GAGES INSIDE RECEIVER OVERHEATED	EIGHT GAGES DAMAGED BY FAILURE OF TRANSFORMER IN "CHILLER" COOLING SYSTEM	DURING TEST	REPAIR CHILLER, PROVIDE BACKUP COOLANT SUPPLY SYSTEM, RELOCATE FRAME GAGES TO BAYS 1, 3, 5, 7, REPLACE GAGES ON BACK COVER
		BILLOWING, 10 CM LONG SURFACE CRACKS OBSERVED ON BACK COVER INSULATION. GLYCOL LEAKAGE FROM DAMAGED BACK COVER GAGES CAUSED LOCALIZED DISCOLORATION AND DAMAGE TO INSULATION	AFTER TEST	
553 3 (11/20/78)	CLOUDINESS	SIGNIFICANT AIR LEAKAGE DEVELOPED AT HEAT EXCHANGER OUTLET FLANGES	AFTER TEST	TIGHTENED BOLTS ON PANEL 4 AND 6 FLANGES. NO ACCESS TO PANEL 2 FOR REPAIR
4 (11/28/78)	INSTRUMENTATION FAILURES SMOKING OBSERVED IN TEST BAY	MAJOR AIR LEAKS DEVELOPED AT HEAT EXCHANGER OUTLET FLANGES. HOT AIR DAMAGED THERMOCOUPLE, PRESSURE TRANSDUCER, AND VALVE ANGLE POTENTIOMETER WIRES ON TOP OF BMSR. SMOKE FROM TEST BAY CLOSURE INSULATION IN VICINITY OF AIR LEAKS.	DURING TEST	REPLACE GASKETS AND RE-TIGHTEN OUTLET FLANGE BOLTS. LEAVE OUT LOCK WASHERS. RE-WIRE VALVE ANGLE AND PRESSURE TRANSDUCERS. DAMAGED THERMOCOUPLE WIRING COULD NOT BE REPAIRED DUE TO BRAZED CONNECTIONS REQUIRED IN SHEATHED THERMOCOUPLE. REPLACE TWO PRESSURE TRANSDUCERS. REPOWER VALVE 8 POTENTIOMETER TO WORK IN SPITE OF UNACCESSABLE SHORT CIRCUIT TO GROUND

PRODUCTION TEST DAY AT CRTF	REASON FOR TERMINATION OF TEST	CHANGES CAUSED BY TESTING ACTIVITY	REMEDY/REPAIR	
5 (12/5/78)	CRTF SCHEDULE FOR OTHER TESTS	ADDITIONAL BILLOWING AND SURFACE CRACKS ON BACK COVER INSULATION	AFTER TEST	
6 (12/9/78)	CLOUDINESS			
7 (12/10/78)	CRTF DATA SYSTEM IN TOWER DELUGED BY WATER FROM TOWER SPRINKLER SYSTEM. FROZEN AND BROKEN PIPE FITTING.	PIPE BREAKAGE UNRELATED TO TESTING	DURING TEST	DRY AND REFURBISH TOWER DATA SYSTEM AND DATA COMPUTER
		AIR FLOW OSCILLATIONS INDUCED BY BYPASS VALVE	DURING TEST	ADJUSTED GAIN OF CONTROLLER. ADJUSTED POSITIONER TO ELIMINATE MOVEMENT BEYOND OPEN AND CLOSED ANGLES OF VALVE
554		BACK COVER INSULATION DAMAGE IN REGION OF WEST HEAT FLUX GAGE CONTINUED TO DETERIORATE	AFTER TEST	CONTINUING EFFECTS OF GLYCOL LEAKAGE ON 11/19/78.
8 (12/16/78)	CLOUDINESS	INSULATION BEING ERODED IN VISCINITY OF WEST HEAT FLUX GAGE ON BACK COVER	AFTER TEST	REMOVE HEAT FLUX GAGE. USE HOLE IN CAVITY WALL TO FASTEN 3000 BOARD PATCH IN DAMAGED AREA.
9 (1/3/79)	CLOUDINESS	BROKEN HEAT FLUX GAGE COOLANT LINE ON OUTSIDE OF RECEIVER	DURING TEST	NO DAMAGE TO HEAT FLUX GAGES. REPLACE COOLANT LINE.
10 (1/4/79)	CLOUDINESS	BROKEN PNEUMATIC CONTROL LINE ON AIR SUPPLY COMPRESSOR	AFTER TEST	REPAIR COPPER LINE. RECOMMEND. TO REPLACE ALL COPPER TUBES WITH STAINLESS STEEL ACCEPTED PENDING ACQUISITION OF MATERIALS.

PRODUCTION TEST DAY AT CRTF	REASON FOR TERMINATION OF TEST	CHANGES CAUSED BY TESTING ACTIVITY	WHEN OBSERVED	REMEDY/REPAIR
11 (1/7/79)	LOW SOLAR ELEVATION ANGLE			
12 (1/10/79)	UNEXPLAINED SHUTDOWN OF CRTF COLLECTOR FIELD			
13 (1/11/79)	LOW SOLAR ELEVATION ANGLE	RTAF SCANNING BAR DOES NOT AUTOMATICALLY RETURN TO EAST. RTAF OUT OF SERVICE.	DURING TEST	ADJUST POSITION OF WEST LIMIT STOP ON RTAF FRAME. SCANNING MECHANISM CONTINUED TO DISTORT
555		ADDITIONAL DAMAGE TO BACK COVER INSULATION. CRACKING AROUND AND PULLING OFF THE CERAMIC FASTENERS	AFTER TEST	
14 (1/13/79)	UNEXPECTED CLOSURE OF BMSR FLOW VALVE ON HEAT EXCHANGER PANEL NUMBER TWO	PANEL TWO TEMPERATURE INCREASED FROM 620°C (1150°F) to 777°C (1430°F). AS RESULT OF VALVE CLOSURE AGAINST LIMIT STOP.	DURING TEST	VALVE ACTUATOR FEEDBACK LINKAGE HAD COME LOOSE. ADJUST AND TIGHTEN LINKAGE.
		RTAF SCANNING BAR STOPPED IN MID-SCAN. OVERHEATING CAUSED LEAK TO DEVELOP.	DURING TEST	ADJUST SCANNING MECHANISM. REPAIR LEAKING SEAL.
15 (1/14/79)	CLOUDINESS			
16 (1/18/79)	CLOUDINESS			



PRODUCTION TEST DAY AT CRTF	REASON FOR TERMINATION OF TEST	CHANGES CAUSED BY TESTING ACTIVITY	WHEN OBSERVED	REMEDY/REPAIR
17 (1/20/79)	LOW SOLAR ELEVATION ANGLE	SMALL PIECES OF INSULATION (LESS THAN 0.5cm THICK) FALLING OFF OF BACK COVER INSULATION SURFACE	AFTER TEST	REMOVE LOOSE PIECES FROM INTERIOR OF RECEIVER
		BMSR FLOW VALVE ON PANEL TWO INOPERATIVE. ACTUATOR DAMAGED	AFTER TEST	MANUALLY POSITION VALVE AT AN ACCEPTABLE ANGLE. FOR RECEIVER OPERATION. REPAIR NOT FEASIBLE BECAUSE OF ACTUATOR LOCATION.
		SIGNIFICANT AIR LEAKS DEVELOPED AT HEAT EXCHANGER INLET FLANGES	AFTER TEST	RECOMMENDATION TO REPLACE GASKETS REMOVE LOCKWASHERS AND RE-TIGHTEN FLANGES ACCEPTED. PANEL 6 REPAIRED ON 1/20. ALL OTHERS (EXCEPT INACCESSIBLE 8, 1, AND 2) REPAIRED ON 1/22.
18 (1/21/79)	CLOUDINESS			
19 (1/23/79)	LOW SOLAR ELEVATION ANGLE	LARGER (SAUCER SIZE) THIN PIECES OF INSULATION BREAKING OFF OF BACK COVER INSULATION. A FEW SQUARE CM OF KAOWOOL SUBLAYER EXPOSED ON WEST SIDE OF BACK COVER.	AFTER TEST	REMOVE LOOSE PIECES FROM INTERIOR OF RECEIVER
20 (1/27/79)	CLOUDINESS	RTAF SCANNING MECHANISM FAILURE	START OF TEST	RTAF MUST BE LOWERED TO GROUND FOR REPAIR. REMOVAL FROM TEST BAY WOULD CAUSE SUSPENSION OF TESTING. CONTINUE TESTING AND ESTIMATE BMSR SOLAR INPUT.

556

PRODUCTION TEST DAY AT CRTF	REASON FOR TERMINATION OF TEST	CHANGES CAUSED BY TESTING ACTIVITY	WHEN OBSERVED	REMEDY/REPAIR
21 (1/28/79)	SUNSET	FURTHER DAMAGE TO BACK COVER INSULATION. PIECES CONTINUING TO BREAK OFF. MORE KAOWOOL SUBLAYER EXPOSED.	AFTER TEST	REMOVE LOOSE PIECES FROM INTERIOR OF RECEIVER.
22 (1/30/79)	LOW SOLAR ELEVATION ANGLE			
23 (1/31/79)	LOW SOLAR ELEVATION ANGLE	SEVERE BUT LOCALIZED DAMAGE TO BACK COVER INSULATION. AREA WHERE KAOWOOL SUBLAYER WAS EXPOSED HAS NOW MELTED. OUTER STEEL WALL NOW EXPOSED TO CAVITY HEAT.	AFTER TEST	BACK COVER MUST BE REMOVED TO GAIN ACCESS FOR REPAIR, TESTING SUSPENDED.
557	END OF FIRST SERIES OF PRODUCTION SOLAR TESTS			BACK COVER REMOVED AND REPAIRED. RTAF MOVED TO GROUND AND SCANNING MECHANISM REBUILT
24 (3/23/79)	CLOUDINESS	RTAF SCANNING BAR STOPPED IN MID SCAN. OUT OF SERVICE	START OF TEST	ADJUSTED SCANNING MECHANISM
		BILLOWING, SURFACE CRACKING AND APPARENT SHRINKAGE OF THE NEW BLANKET INSULATION ON BACK COVER	AFTER TEST	

PRODUCTION TEST DAY AT CRTF	REASON FOR TERMINATION OF TEST	CHANGES CAUSED BY TESTING ACTIVITY	WHEN OBSERVED	REMEDY/REPAIR
25 (3/24/79)	LOW SOLAR ELEVATION ANGLE	PANEL THREE TEMPERATURE INCREASED TO 844°C (1550°F) AS RESULT OF VALVE CLOSURE AGAINST LIMIT STOP. ACTIVATED AUTOMATIC SHUTDOWN OF TEST	DURING TEST	VALVE ACTUATOR FEEDBACK LINKAGE HAD COME LOOSE. ADJUSTED AND TIGHTENED LINKAGE AND RESUMED TESTING.
		INCREASED LOCALIZED DAMAGE TO BLANKET INSULATION ON EAST SIDE OF BACK COVER	AFTER TEST	DECIDED TO BIAS SOLAR INPUT TOWARD WEST SIDE OF CAVITY INTERIOR BY PREFERENTIALLY USING EAST SIDE HELIOSTATS. INCREASES THE HEAT LOAD ON 3000' BOARD PANEL OF BACK COVER.
558 26 (3/25/79)	BACK COVER INSULATION FAILURE	SMALL REGION ON EAST SIDE OF BACK COVER INSULATION HAD PEELED BACK EXPOSING AND CAUSING MELTING OF SUBLAYERS. OUTER STEEL WALL OF RECEIVER NOW EXPOSED TO CAVITY HEAT.	DURING TEST	TESTING SUSPENDED

heavy-duty terminals and the wires were taped down to prevent motion. Because only three of the compressors were required to support receiver operation at up to 950-kW solar input, it was possible to test even when one of the air compressors was out of service. Several tests were disrupted in a minor way, but none of the tests were canceled because of compressor problems.

The RTAF is described in section 7.0. It was a complex device specially designed and constructed for these BMSR tests. Dozens of scans of the solar-flux incident on the face of the BMSR were conducted during the course of these tests. At first the RTAF scans were conducted on quarter-hourly intervals, but after many cycles of operation, the RTAF scanning mechanism began to show signs of use. A continuous link chain was used to simultaneously move the top and bottom ends of the scanning bar across the frame. This chain appeared to stretch with use, initially causing difficulty with the bar engagement of limit and reversing switches, and then beginning to slip on the drive-gear mechanism.

When these scanning problems were first observed, it was decided to reduce the frequency of RTAF scans to 1-hr intervals. This probably increased the life of the RTAF, but as noted in Table 10.1-2, the scanning problems continued to develop. These problems eventually resulted in inadvertent stoppage of the bar in midscan. The result was overheating and damage to coolant seals on the bar itself.

Once installed, the RTAF frame became an integral part of the test bay and test-bay solar shielding. Tests could not be conducted without the RTAF in place. CRTF personnel were able to make some repairs to the RTAF in place. However, when damage exceeded this inplace repair capability, it became necessary to decide whether to continue testing without the RTAF or to stop tests while it was removed for repair. Therefore, the loss of RTAF service during some of the tests was not caused by a lack of desire or inability to effect repairs, but by the tight test schedule at CRTF, which at this time dictated continuing without it in-service. Later, on two occasions during planned breaks in the testing schedule, the RTAF was removed and repaired.

Even though no failures were observed, there were several occasions when the weather conditions caused difficulty in operating the CRTF collector field. One factor noted during the tests in January was the strong correlation between clear skies and high winds at CRTF. Because the strong winds usually came from the north and the winter Sun was quite low in the southern sky, the operating position of the heliostat mirrors was nearly perpendicular to the incident wind. Once they were in this position, the heliostats operated satisfactorily during winds of up to 9.7 m/s (25.8 ft/s). However, the high winds caused major problems while the heliostats were being rotated from their horizontal stowed position. Wind striking the mirrors from their edges would cause enough misalignment to generate alarm signals. When too many simultaneous alarms occurred, the collector field would automatically shut down. This problem was resolved by reducing the number of heliostats in transit during startup. However, the time required to move all heliostats to standby was increased correspondingly. Questions remain as to the usability of the heliostats during weather conditions with strong winds out of the east or west that would be incident on the edges of mirrors in their operational attitude.

Because these tests were the first to use the CRTF, it is safe to assume that the experiences gained represent an early stage in the development of methods of heliostat field operation and control and utilization of the various facility systems. In this or any other respect, the CRTF operation during BMSR tests can only be viewed as a resounding success. As may be noted in Table 10.1-2, the receiver survived these tests with a high degree of success as well. Problems that developed in the insulation wall of the back cover were localized and limited to the 1 or 2 m<sup>2</sup> (1.2 or 2.4 yd<sup>2</sup>) of insulation subjected to the highest incident solar-flux levels. Receiver valve problems were limited to mechanical problems with the actuators that appeared to have been caused by their actuator temperatures being higher than usually recommended for these industrial-quality parts (actuators in valves 2 and 3 were subjected to temperatures in excess of 125°C). The air leaks that developed at the bolted heat exchanger inlet and outlet flanges occurred as soon as these were heated above about 450°C (840°F). Loosening of the flange bolts occurred at this temperature because of the softening of serrated lock washers that were installed during BMSR fabrication. Once

these washers had been removed and the flanges were properly torqued, the air-leakage problems were solved. These and other BMSR changes of lesser significance are discussed in Sections 10.2 through 10.5.

## 10.2 CAVITY THERMAL INSULATION

Because of the arrangement of the BMSR and test bay solar shielding, it was possible to stand in front of the receiver and look through its aperture to inspect or photograph its interior. The condition of the cavity interior was frequently observed and occasionally photographed during the solar test program.

Early solar tests were conducted at about 50 to 75% of the design solar input to the BMSR. Inspections conducted after several of these tests revealed significant changes in the appearance of the Saffil insulation in the center of the receiver back-cone. The rest of the back-cone insulation and the Kaowool insulation on the main body of the receiver cavity remained virtually unchanged throughout the duration of the solar testing program. Initial changes observed at low solar power levels consisted of billowing and surface cracking of the Saffil insulation in the areas of maximum solar heating. These areas also became brilliantly white in color and appeared to become rigid and brittle. A thin (1-2 mm) layer appeared to be shrinking and cracking in the roll-width direction and separating from the remaining bulk of the Saffil blanket. The surface cracks were observed at mid-span between the ceramic insulation fasteners.

Once the billowing and cracking was observed after these first few tests, it did not significantly change during the remaining tests at partial solar input power. However, increasing the test level to full solar input caused a dramatic increase in the insulation damage. Observation after the first full solar power test on January 11, 1979 revealed that the thin damaged surface layer had become extensively separated from the bulk of the Saffil. In some places this thin layer had broken around the edge of the ceramic fasteners and pulled away leaving an opening through which the fastener and the balance of the Saffil blanket could be observed.

Continuing operation at or near the full solar power level caused additional cracking and separation of the damaged layer of Saffil. Small pieces began to break loose and had to be removed from the cavity to prevent blocking of heat exchangers and the cavity wall heat flux gages. These pieces were thin (1-2 mm) and were extremely brittle. When they came loose they exposed additional Saffil material. This material initially appeared to be sound, but after further testing would be observed to separate and break off just as the outer layer had. This flaking-off of thin pieces consumed the full thickness of the Saffil blanket in a few localized areas. This exposed the lower temperature Kaowool layer which quickly gave way causing a localized failure and loss of all the wall insulation in the area corresponding to the missing Saffil.

A contributory factor to the flaking of Saffil was the failure of several ceramic anchors. Radial cracks were observed in fastener heads as testing progressed. Ultimately, the heads fell off and insulation support was lost.

Cracking and separation occurred over a large area, however, testing had to be terminated because of a few square inches of complete loss of the Saffil insulation layer. The back-cone was removed from the BMSR, inspected and re-insulated. Results of the inspection are shown on Figure 10.2-1. Much of the Saffil remained in its original soft and resilient condition. In regions of higher solar flux intensity the material had become crusty and then brittle with a surface layer breaking loose from the bulk of the blanket. The most severe insulation damage had occurred adjacent to free edges and corners of the original blanket layup, particularly at the intersections of trapezoidal and octagonal wall panels. Figure 10.2-2 is a photograph of the receiver back-cone being removed after the first series of BMSR tests.

The back-cone was re-insulated and the BMSR tested again in March 1979. Three days of testing were completed before the insulation was once again subjected to localized mechanical failure and loss of the Saffil layer. Photographs taken before and after each of these tests provide a dramatic portrayal of the progressive mechanical degradation of the Saffil blanket.

# Back Cone Insulation

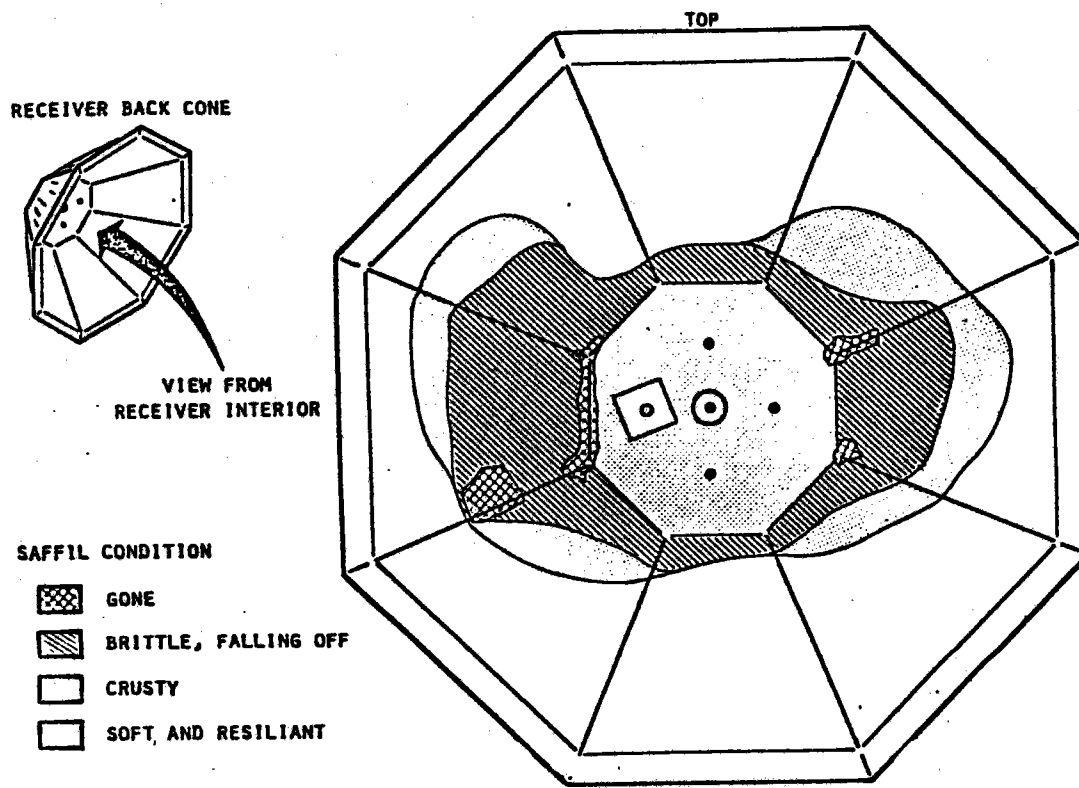


Figure 10.2-1: Posttest Condition of Original Insulation on Back-Cone of BMSR





Figure 10.2-2: Posttest Condition of Original BMSR Insulation

Figure 10.2-3 shows the center of the back-cone prior to exposing the new insulation to testing. The large central dark area is the back-cone radiometer and the three smaller dark spots are heat flux gages. Metal clips, used to hold the back-cone insulation in place during transport and assembly onto the receiver main frame can be observed in this photograph.

Figure 10.2-4 shows the center of the back-cone after about three hours of solar testing conducted on March 23, 1979. The metal clips have become oxidized leaving dark spots on the surrounding insulation.

Cracking of the surface layer of Saffil can be observed around many of the ceramic fasteners and in the free spaces between fasteners.

Figure 10.2-5 shows the same region after a total of about 12 hours of solar testing, including about 9 hours on March 24, 1979. Surface layer cracking and separation are readily apparent. Material in one corner has separated, broken loose and curled back to expose Saffil blanket edges. This curling back from a free edge was a common failure mechanism. Several small pieces of insulation had broken away from the back-cone at this time.

Figure 10.2-6 shows the final condition of the central area of the receiver back cone insulation. This photograph was taken after a total of about 16.5 hours of solar testing. Breaking up and loss of the surface layer of the Saffil blanket had occurred over about one third of the insulation area. Areas are observed where up to four individual layers of Saffil (1-2 mm thick) have separated and broken off.

Figure 10.2-7 shows the condition of most of the receiver back-cone insulation at the conclusion of the second series of tests. Once again, the insulation in the central region receiving intense solar flux was damaged while most of the remainder of the insulation remained intact. The damage to the central region of the back-cone which is described above was a repeat of the initial insulation failure. However, the gross failure of Saffil on the East side of the back-cone and the apparent success of the 3000-board insulation panel on the West side were unique new experiences.

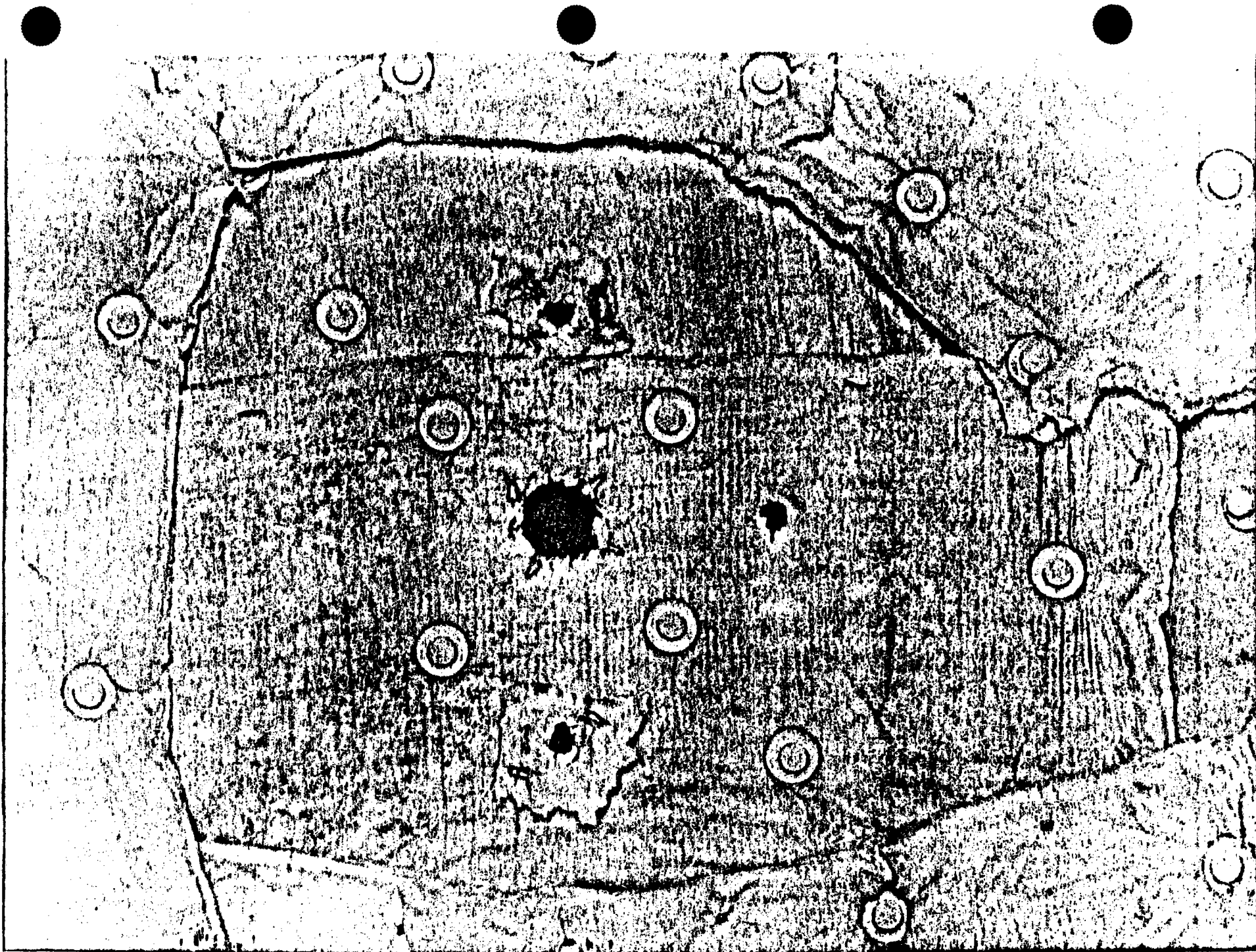


Figure 10.2-3: Pretest Condition of Central Area on Reinsulated Back Cone

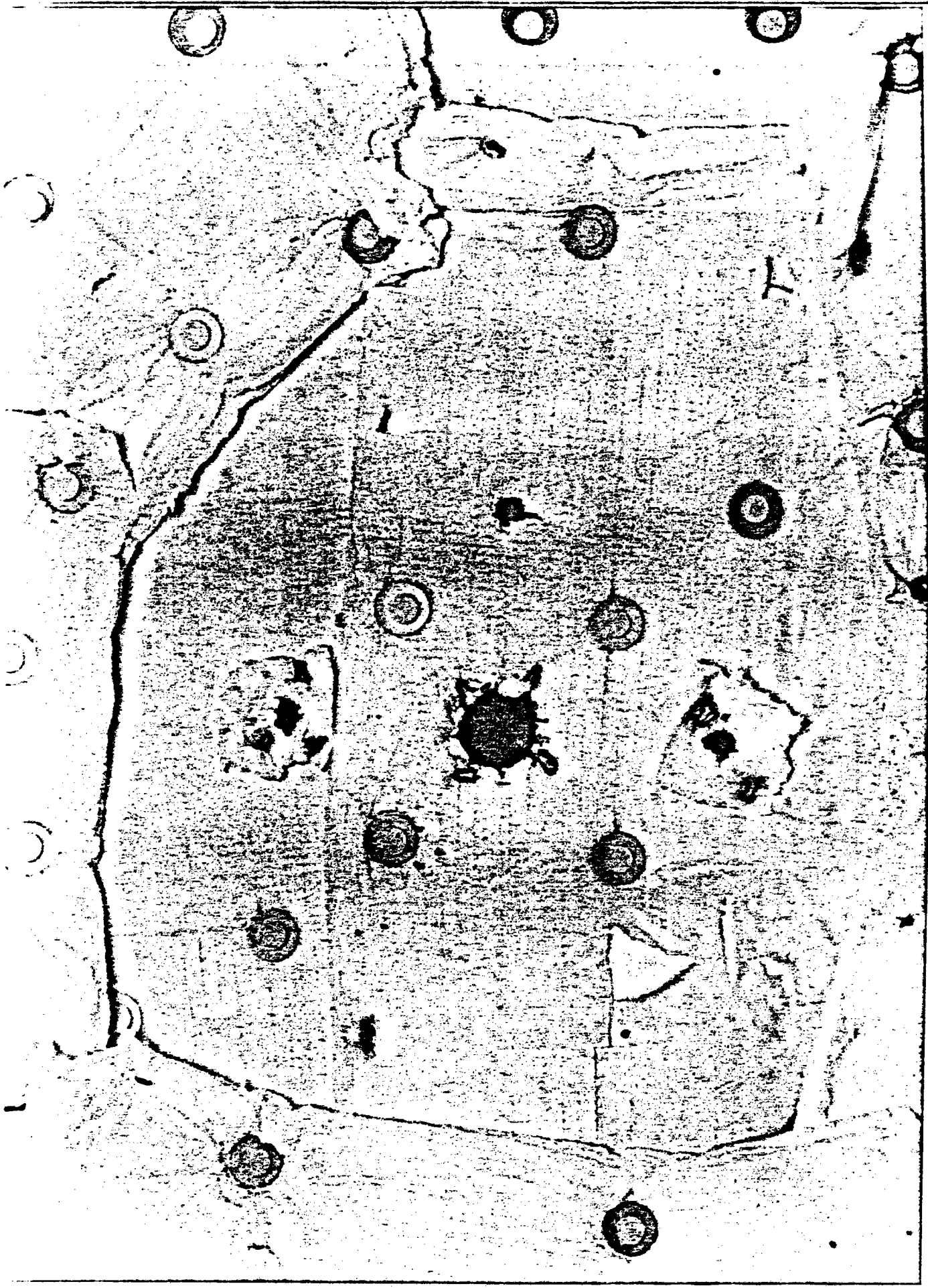


Figure 10.2-4: Condition of Reinscribed Back Cone After 3 Hours Exposure

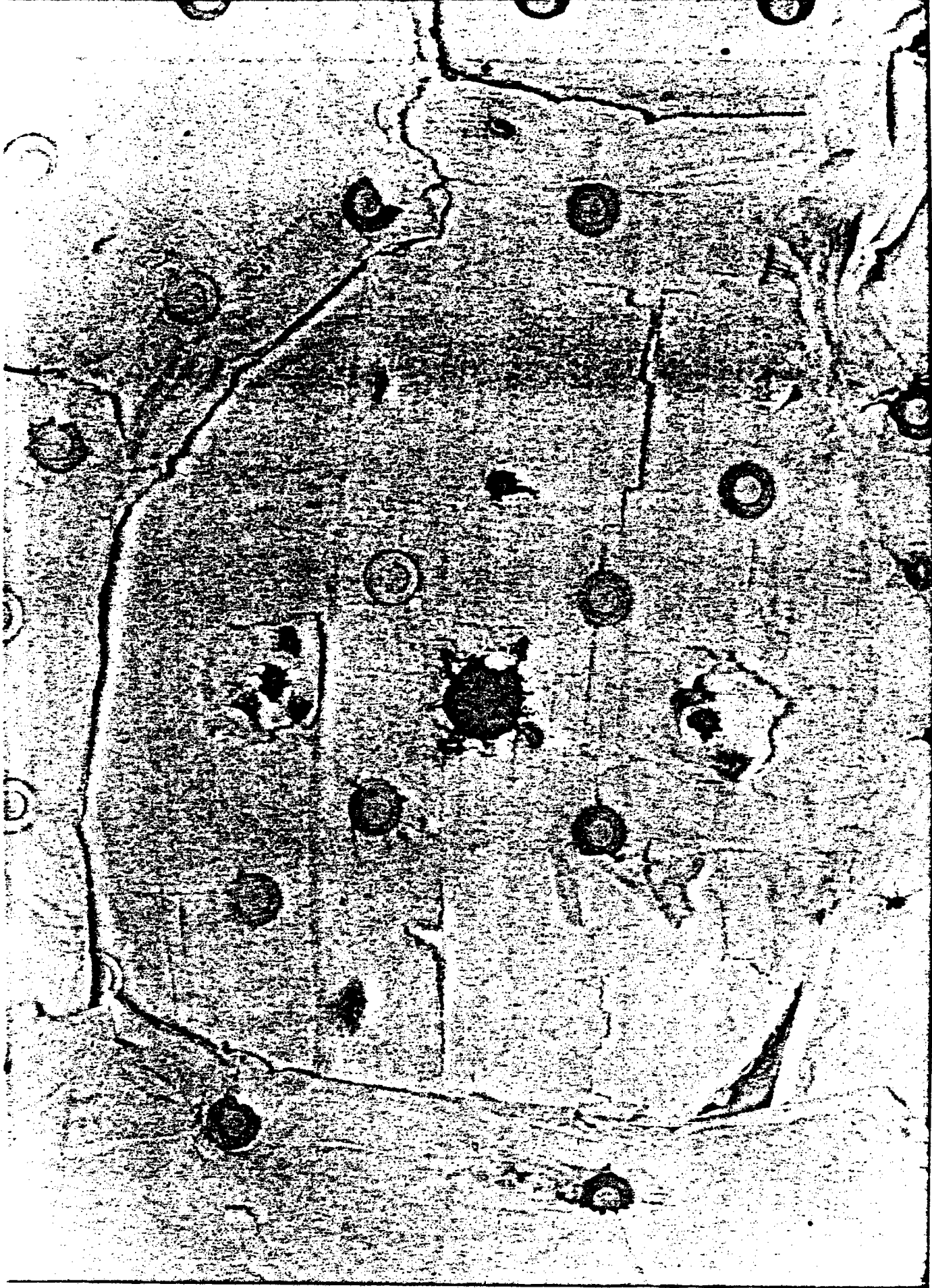


Figure 10.2-5: Condition of Reinsulated Back Cone After 12 Hours Exposure



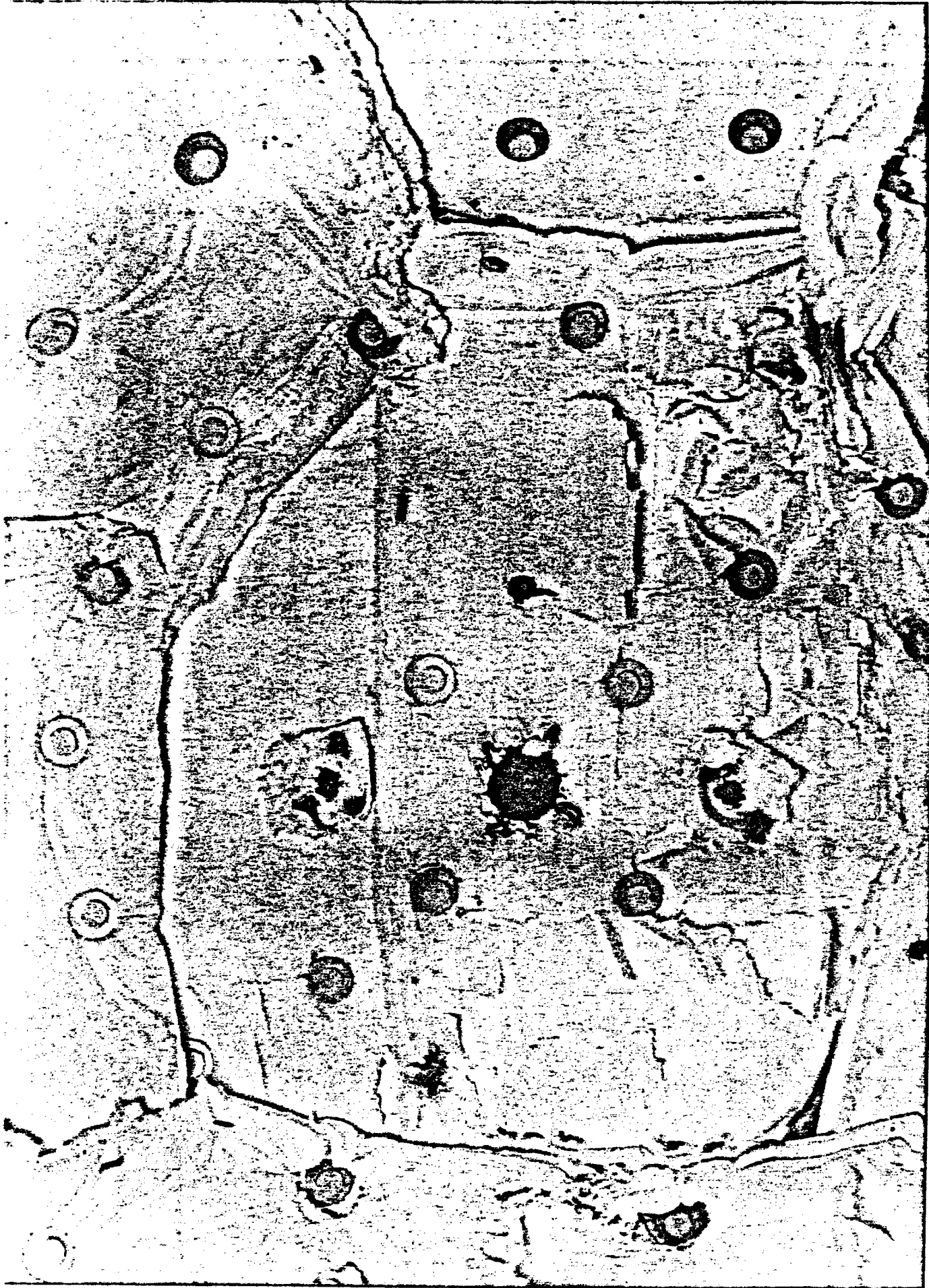


Figure 10.2-6: Condition of Reinforced Back Cone After 16.5 Hours Exposure



Figure 10.2-7: Posttest Condition of Reinsulated BMSR Back Cone

The Saffil failure on the East side of the back-cone apparently resulted from the improper orientation of overlapping layers of insulation. Previously, the lap-joints had been overlapped away from the receiver aperture. This arrangement is apparent in Figure 10.2-2, a photograph of the original back-cone insulation. However, since the original Saffil on the periphery of the back-cone was re-used, it was more convenient to overlap the outer edge of new pieces outward, toward the receiver aperture and the direction of incident sunlight. Figure 10.2-8 shows the pre-test condition of the region of the back-cone which eventually failed. The center of the receiver is toward the right so that incident sunlight (from the left) can enter the gap between layers of insulation.

Figure 10.2-9 shows the East side of the back-cone insulation after about 3 hr of testing. The Saffil blanket along the sunlit lap-joint has been overheated, damaged, and broken. A deep crack has also occurred in the cross-roll direction of the blanket. This damage is much more severe than the effect of 3 hr of tests on the central region of the back-cone shown in Figure 10.2-4.

Figure 10.2-10 shows the East side of the back-cone after about 12 hr of testing. A complete section of Saffil about 0.5m (20 in) across has become almost completely severed along two of its edges. The combination of lap-joint damage and cross-roll shrinkage cracking has almost completely freed one corner of the section.

Figure 10.2-11 shows the final state of the damaged East side of the back-cone. During this last day of BMSR tests the CRTF collector field was used selectively in an attempt to bias the receiver solar input to the West side of the back-cone. However, during the test, the loosened section of Saffil apparently fell away exposing the Kaowool and Mineral Wool sub-layers. These failed with the Mineral Wool melting and flowing into the cavity.

Figure 10.2-7 also shows the board type insulation used on the West side of the reinsulated back-cone. This material was inserted in place of the Saffil blanket in order to obtain comparable performance data. It survived



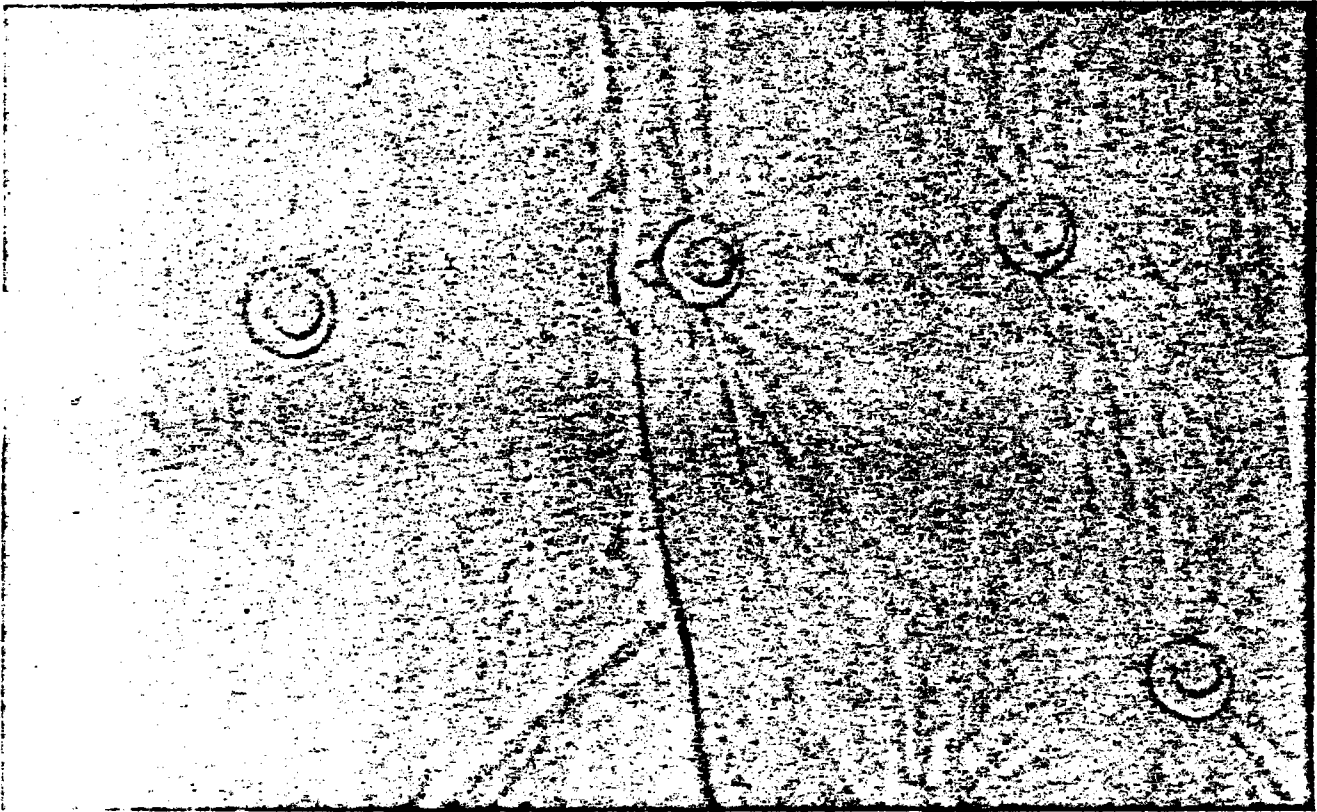


Figure 10.2-8: East Side of Reinsulated Back Cone Prior to Testing

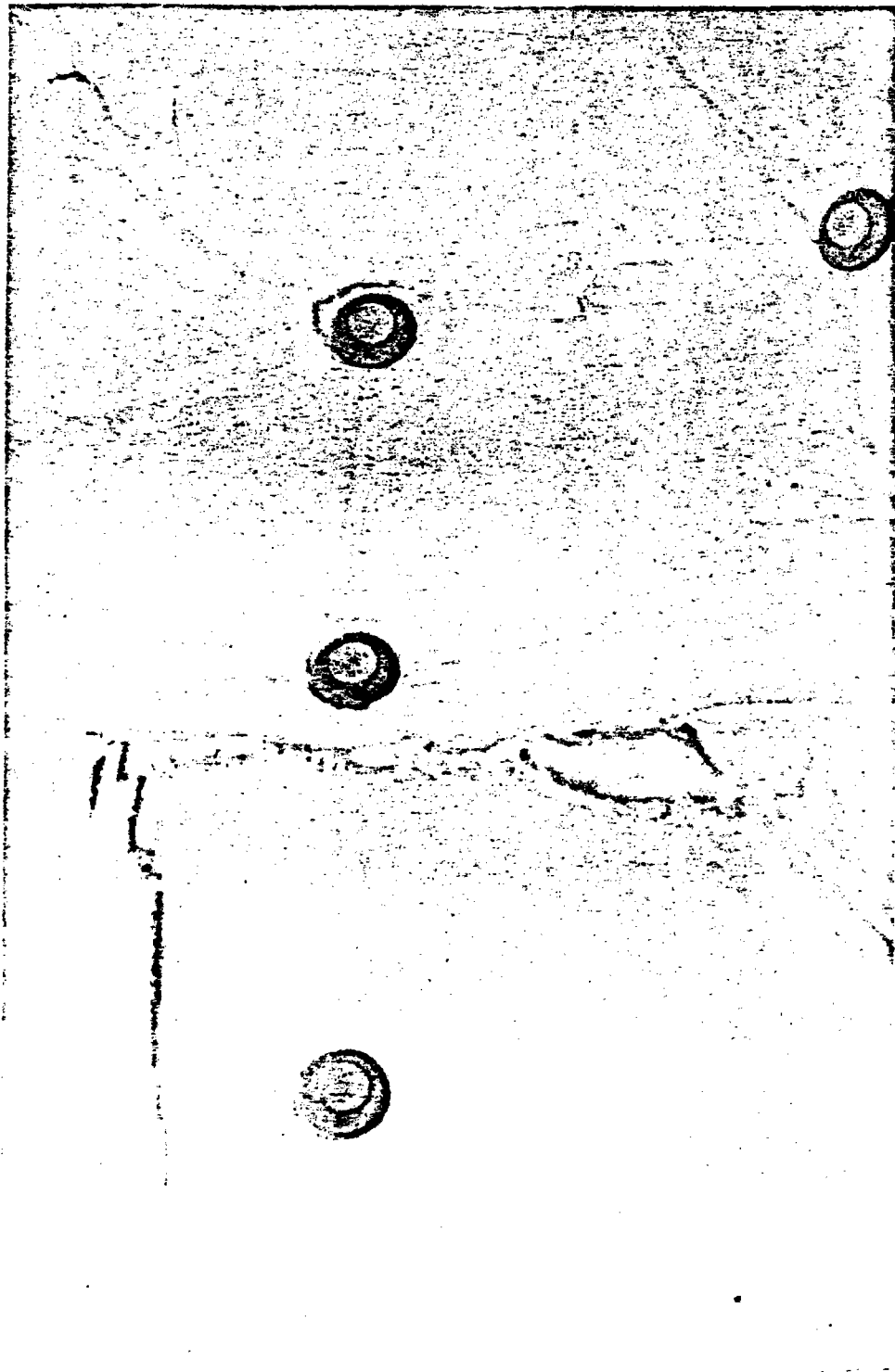


Figure 10.2-9: East Side of Reinsulated Back Cone After 3 Hours of Testing

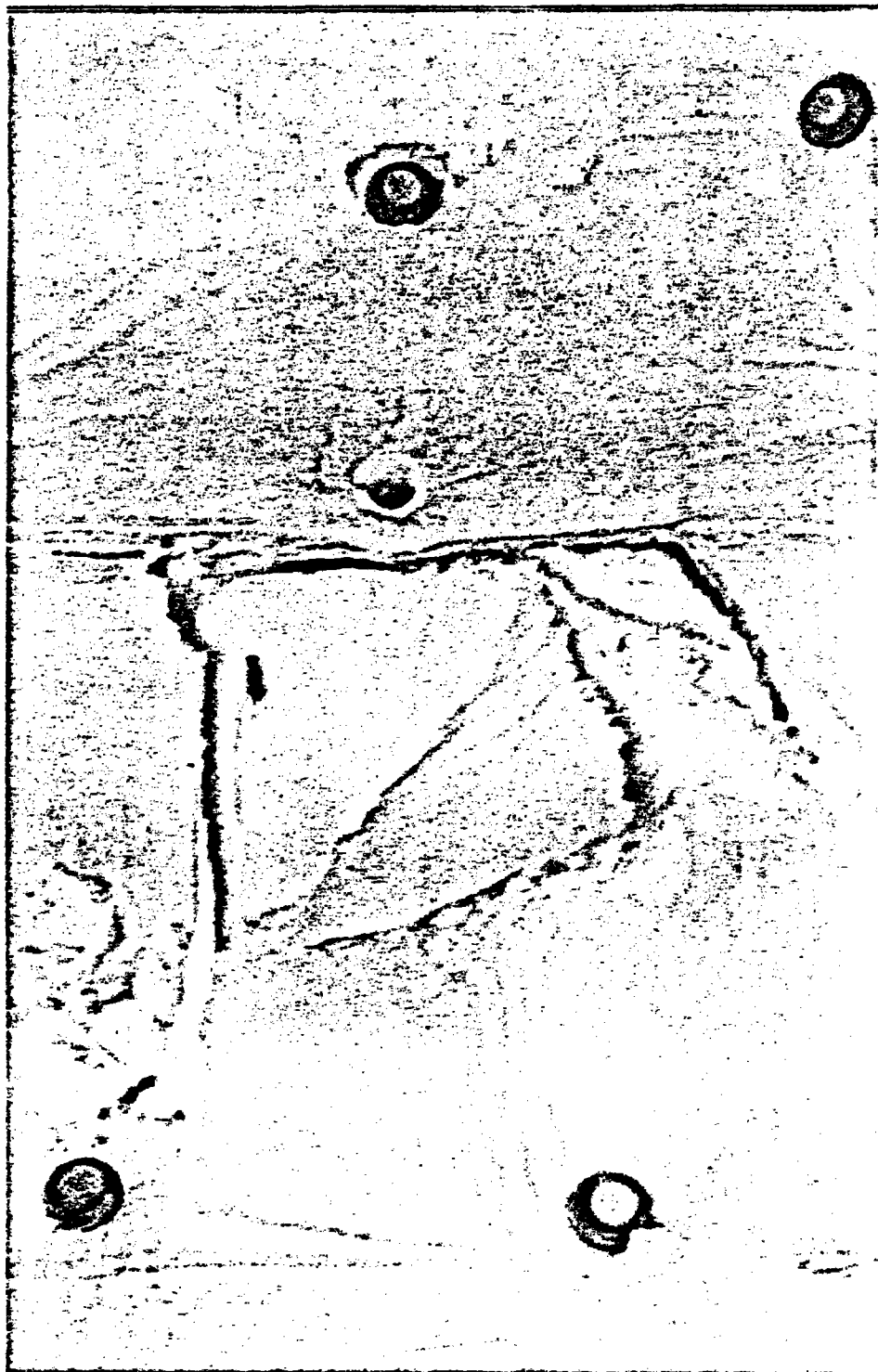


Figure 10.2-10: East Side of Reinsulated Back Cone After 12 Hours of Testing



Figure 10.2-11: East Side of Reinsulated Back Cone After 16.5 Hours of Testing

in good condition except for a small region near the center of the photograph where an outward overlapped layer of Saffil blanket caused a hot spot. A variety of fastener arrangements were investigated with the insulation board material. One, two, and four fasteners were used with the various board segments to determine whether shrinkage would cause multiple attached segments of board to break. No cracking or breakage could be detected after the tests. Gaps between board segments were also of interest because they cause trapping of incident sunlight and potential hot spots. The original fit-up of these boards was carefully done so that gap spacing was negligible (less than 1 mm). However, shrinkage of the boards caused gaps of about 4 mm to develop. Upon disassembly, no melting or other indication of excessive temperature could be detected along these edges of the boards. A 12.5mm (1/2 in) layer of Saffil was used under the board.

Samples of the damaged Saffil insulation were removed from both the first and second insulation assemblies on the back-cone. Extensive testing was conducted to verify composition, melting point temperature, and fiber composition of these samples.

Approximate melting temperatures were determined by heating samples with a CO<sub>2</sub> laser at increasing power settings. These were compared with power settings required to melt pure element samples of Alumina, Chromic Oxide, Silica, Titania, and Sodium Phosphate. The melting point of the Saffil was determined to be above 1340°C (2444°F) and below 1710°C (3110°F). Melted samples were also obtained for comparison with samples taken from the receiver.

An electron microscope was used to examine laser melted samples as well as those removed from the receiver. This survey conclusively proved that fibers had not been melted in the BMSR. Some clumping together of fibers was observed and this may account in part for the rigidity of the damaged Saffil. An Energy Dispersive X-ray analysis was conducted to determine the chemical composition of the samples. This data is summarized in Table 10.2-1, which shows a normal range of constituents and impurities in the insulation samples.

Table 10.2-1: Chemical Composition of Samples Removed From Original BMSR Back-Cone Insulation

		Al	Si	Mg	Ca	Fe	Ti	K	Other
Unused material	Saffil	99	1						
	Kaowool	49	51						
	Mineral block	11	55	3	30			1	
Undamaged area	Saffil	98-1/2	1	-	1/4	-	1/4	-	-
	Kaowool	48	47	-	1/2	1/4	3	1-1/4	-
	Mineral block	-	-	-	-	-	-	-	-
Crusty surface	Saffil	99	3/4	-	-	-	1/4	-	-
	Kaowool	46-1/3	46-1/3	-	1-3/4	1-1/3	3-1/4	1	-
	Mineral block	11	58	2	26	1/4	1/4	2-1/2	-
Severe damage	Saffil	97	1-1/2	-	-	-	1-1/2	-	-
	Kaowool	45	45	-	2-1/2	2-1/2	4	1	-
	Mineral block—burn-through area	26	45	2	26	1	-	-	-
	Mineral block—covered	8-3/4	62-1/4	2	19	3	-	5	-

During the evaluation of the Saffil insulation samples, more was learned about the Saffil fibers which are manufactured by Imperial Chemical Industries Ltd. Upon heating, the crystalline structure of the fibers is changed. This change results in shrinkage and embrittlement. The crystal structure changes occur at rates which are temperature dependent. They occur slowly at temperatures of about 1000°C (1830°F) and more rapidly at higher temperatures up to about 1400°C (2550°F). An intentional crystal phase conversion, by preheating raw fibers at high temperature, has recently been added to the processing of fibers for use in vacuum formed high temperature insulation board materials. However, the process is not practical for blanket materials. Conversion by preheating shrinks the fibers but also makes them brittle causing fiber breakage during handling and layup of blanket insulation.

Shrinkage of up to 5 percent can be expected during complete conversion of Saffil fibers. On the other hand, the converted fiber products such as vacuum formed insulation board, exhibit acceptable shrinkage of less than one percent in use.

The opening of surface cracks in the Saffil which can be seen in Figures 10.2-4 through 10.2-6 was probably the result of shrinkage of fibers in the outer highest temperature layer of the material. Curling-up of free edges, has been noted in several of the Figures. This is one of the mechanisms by which pieces of Saffil broke loose, and it was also explained by temperature dependent shrinkage of the material.

Because of these tests and observations it has been concluded that:

- o Quality of the Saffil insulation used in the BMSR was normal;
- o BMSR insulation temperatures were below the melting temperature of the Saffil;
- o Insulation failure was attributed to the installation design features and the characteristics of the Saffil fibers.

Major factors which induced failure were:

- o Shrinkage of material beneath the heads of fasteners;
- o Fragility of the Saffil fibers after their high temperature conversion;

- o Incorrect arrangement of overlapping joints (in the second installation).

It was also concluded, based on examination of the physical characteristics of Saffil heated to temperatures of 1260°C (2300°F) and above, that the resulting embrittlement of fibers makes it an unacceptable material for commercial solar receiver applications. It should also be noted that the Saffil blanket product is no longer being supplied to industry because of a number of experiences similar to those described here.

### 10.3 APERTURE RIM SOLAR SHIELDING

The solar image of the CRTF collector field was slightly larger than the BMSR aperture. This mismatch caused more severe solar heating of the BMSR aperture rim than would be experienced in the commercial receiver. Estimates of the aperture rim solar flux in the RP 377-1 receiver design ranged from 100 to 300 kW/m<sup>2</sup>, whereas the solar flux on the BMSR was expected to vary from 660 to 1050 kW/m<sup>2</sup>. In addition, collector field lockup due to loss of control or electric power could cause eastward drift of the CRTF solar image. During this emergency condition, the East side of the BMSR aperture shield could be exposed to short term solar heating up to 2100 kW/m<sup>2</sup>. This higher solar flux level was adopted as the design requirement for the BMSR shield.

Section 4.0 describes the testing of candidate materials for the BMSR aperture rim solar shielding. Only one material, the Zirconia tiles supplied by Zircar Products Inc., provided thermal protection at solar flux levels in excess of 1000 kW/m<sup>2</sup>. However, thermal gradients produced during solar exposure caused extensive cracking of the tiles. The cracking appeared to occur in directions perpendicular to the thermal gradient direction, and was thought at the time to be caused by the small area exposed during tests.

The BMSR solar shield was fabricated by bonding a 12 mm (0.50 in) layer of the zirconia tile on top of 25 mm (1 in) thick panels of 3000-board supplied by Babcock and Wilcox. The adhesive utilized for bonding was QF-180 coating



cement supplied by The Carborundum Company. After bonding of tiles, the shield was coated with an approximately 1 mm (0.04 in) layer of QF-180.

The aperture rim shield performed adequately throughout the duration of the BMSR solar test series. Severe cracking of the zirconia tiles was experienced once again in planes perpendicular to the thermal gradient direction. Since the tiles were fairly uniformly heated, the cracking occurred parallel to and just behind the exposed surface. Layers of tile approximately 2 mm (.08 in) thick became loosened but remained attached to the original material. The shield was recoated with QF-180 on two occasions in order to reattach these pieces of tile.

The cracking of the BMSR aperture rim shielding is shown in Figure 10.3-1. This picture was taken at the conclusion of the BMSR test program. Most of the cracking had occurred at an early time in the test program and had progressed only slightly in the interim.

Because of these tests and observations, it has been concluded that; the basic material of the zirconia tiles is acceptable for solar shielding applications, however, the dense tile manufactured by Zircar Products Inc., fractured too readily when exposed to intense solar heat. It was also concluded that the QF-180, a less temperature resistant material, was a poor choice for coating the zirconia tiles and may have contributed to the failures noted.

#### 10.4 HEAT EXCHANGERS AND AIR FLOW SYSTEM

The BMSR air flow system consisted of air supply system components as well as the manifolds, valves and heat exchangers which made up the solar receiver heat exchanger system. These are shown on Figure 10.4-1, a photograph taken prior to shipment of the system to CRTF. In this photograph, the receiver back-cone was removed for shipment and the eight heat exchanger panels are visible within the receiver cavity.

Air supply system problems which occurred during BMSR testing included development of air leaks at gasketed flanges and failure of actuators used



Figure 10.3-1: Condition of Aperture Rim Shielding After Completion of BMSR Solar Tests

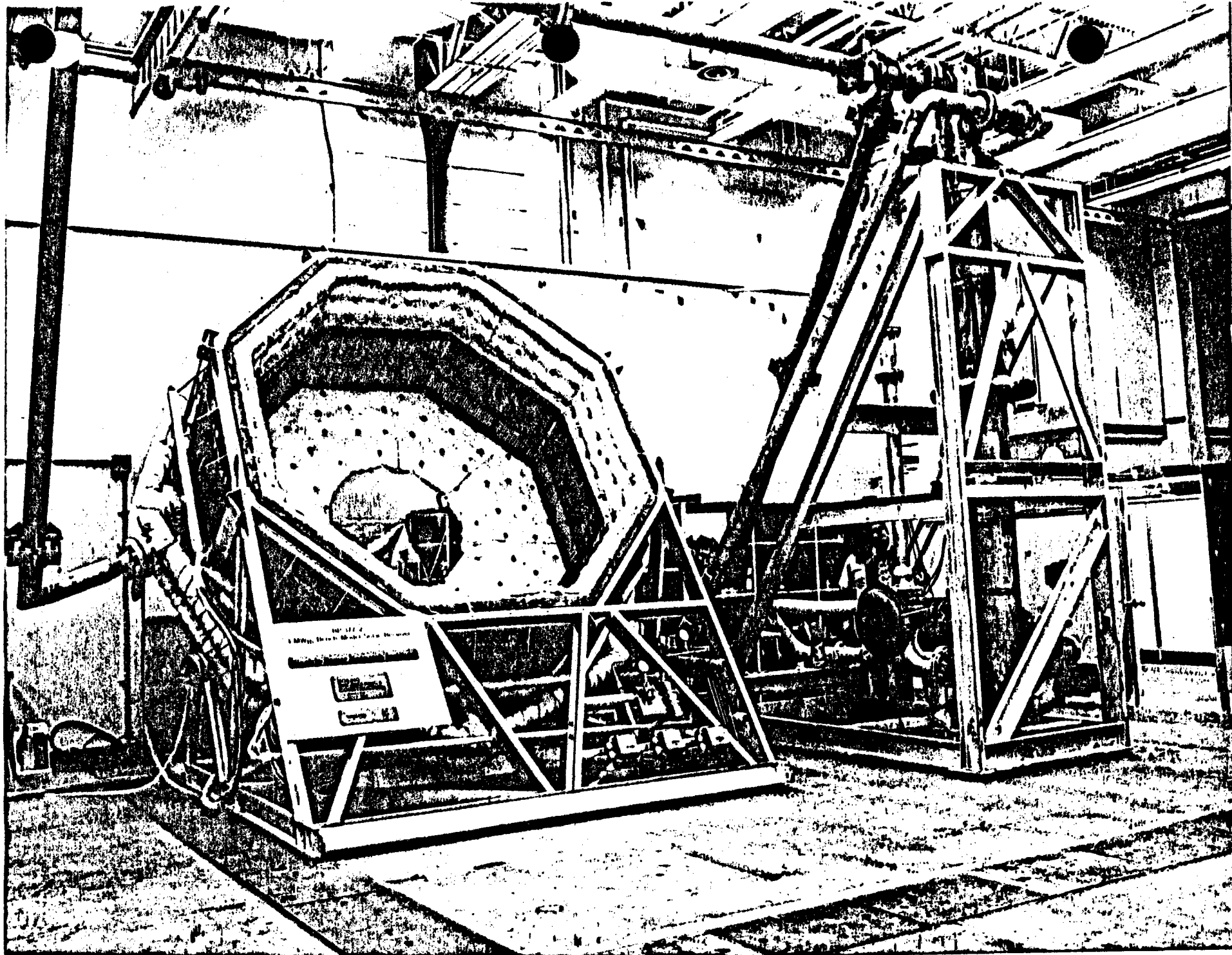


Figure 10.4-1: BMSR Heat Exchangers and Air Flow System Prior to Shipment and Testing at CRTF

to operate flow control valves on heat exchanger panels 2 and 3. Original plans called for removal, disassembly, and metallurgical testing of one of the heat exchanger panels at the completion of solar testing. These activities have been delayed because of the possibility of further utilization of the BMSR in an electrical power generation system. Conclusions as to the posttest status of the heat exchanger panels can only be drawn by reference to visual observations and leak tests of the system.

Figure 10.4-2 is a photograph of portions of heat exchanger panels four and five taken after completion of the solar test program. The final oxide coating on tubes was noticeably darker than the initial oxide coating. This initial coating had been produced during heat treatment of the panels before installation. Nevertheless, the oxide coating continued to be smooth and well adhered to the tubes. There was no evidence of any loss of material in the form of flaking or spalling off of the oxide coating. The original form and spacing of heat exchanger tubes remained unchanged with no visible sagging or warping. Micrometer tube diameter measurements were made before solar exposure and after test. No changes were detected within the measurement accuracy of the hand-held micrometer.

Only one problem was detected in the air supply equipment skid and interface piping used for BMSR tests. The receiver inlet line, the single interconnect pipe on Figure 10.4-1, became deformed. The lower end of this pipe connected to a flexible thermal expansion joint. Because of inadequate lateral constraint, its lower end moved several centimeters closer to the BMSR. This distorted but did not damage the expansion joint.

Leak tests were conducted at frequent intervals throughout the test program to confirm the integrity of the BMSR and air flow system. These were accomplished by pressurizing the system to approximately 0.69 MPa (100 psi), closing valves to isolate the combined volume of the BMSR, the air supply equipment skid, and the pipes built into the CRTF tower, and monitoring the rate of pressure loss. Results of these tests are shown on Table 10.4-1.

An initial air pressure loss rate of 0.5 pounds per minute was measured while using blank flanges to isolate the combined volume of the receiver and



Figure 10.4-2: Condition of BMSR Heat Exchanger Tubes at Conclusion of BMSR Testing

Table 10.4-1: Leak Testing and Repair of Bolted Flanges on BMSR Heat Exchangers

Leakage Test Date*	Pressure Decay Rate (PSI/Minute)	Comments
10/21/78	0.50	Installed Prior to Testing
11/21/78	12.30	Leaking outlet flanges after tests on 11/20/78, repaired by tightening bolts on panel 4 and 6.
11/28/78	-	Audible leaks at flanges, replaced outlet flange gaskets and retorqued bolts
12/1/78	0.40	Verified repair of damage on 11/28
1/4/79	0.57	System Verification
1/12/79	0.57	System Verification
1/17/79	0.94	System Verification
1/20/79	4.31	Leaking inlet flanges on several heat exchanger panels after tests on 1/20/79
1/22/79	3.30	After tightening bolts on panel 3, 4, 5, 6 and 7 inlet flanges
1/28/79	3.00	Acceptable Leak Rate
1/29/79	2.20	Acceptable Leak Rate
3/23/79	3.00	Acceptable Leak Rate

\*Leak test conducted after completion of solar test and system cooldown to less than 205°C (400°F). Some tests conducted at ambient temperature.

the air supply equipment skid. This leak rate is comparable with airflow through a hole about 0.5 mm (0.020 in) in diameter.

The BMSR outlet flanges began to leak severely during testing on November 21 and 28, 1978. The most severe leakage was developed on the 28th when the receiver outlet temperature was increased to 705°C (1300°F) for the first time. The eight heat exchanger outlet flange gaskets were replaced at this time. Serrated steel lockwashers had been used on the flange bolts. Softening and collapse of these washers had relieved clamping pressure and was determined to be cause of the leakage. Since inlet air temperatures were not expected to increase above 538°C (1000°F), the inlet flanges were expected to remain tight in spite of the serrated washers being used.

An increased leakage rate was observed after tests on January 20, 1979. Tightening the bolts on accessible inlet flanges reduced the leakage rate by about 25%. Three of the flanges were inaccessible. Since the leakage rate was only equivalent to a 2mm (0.080 in) diameter hole, it was decided to continue tests and accept the leakage. Pressure loss leak tests conducted throughout the remainder of the solar test program confirmed that leakage remained within acceptable limits.

Figure 10.4-3 shows the type of pneumatic actuator and positioner used to operate air flow control valves on each of the eight heat exchanger panels on the BMSR. The ball valve itself was covered by the inlet manifold insulation blanket. The linkage arm connected to the valve shaft outboard of the actual housing caused two unexpected valve closures during tests. The linkage arm provided a feedback signal to the valve positioner (the black box adjacent to the air cylinder). Differential thermal expansion of the aluminum linkage arm on the steel valve shaft caused it to loosen when heated. At least two of the valve actuators, panels two and three, were heated to temperatures in excess of 240°F (116°C) during tests. Once the linkage arm became loose, the return spring in the positioner caused closure of the valve. This caused excessive air outlet temperature from the panel requiring complete shutdown of the test. Repairs were accomplished by relocation and tightening of the linkage arm on the valve shaft.



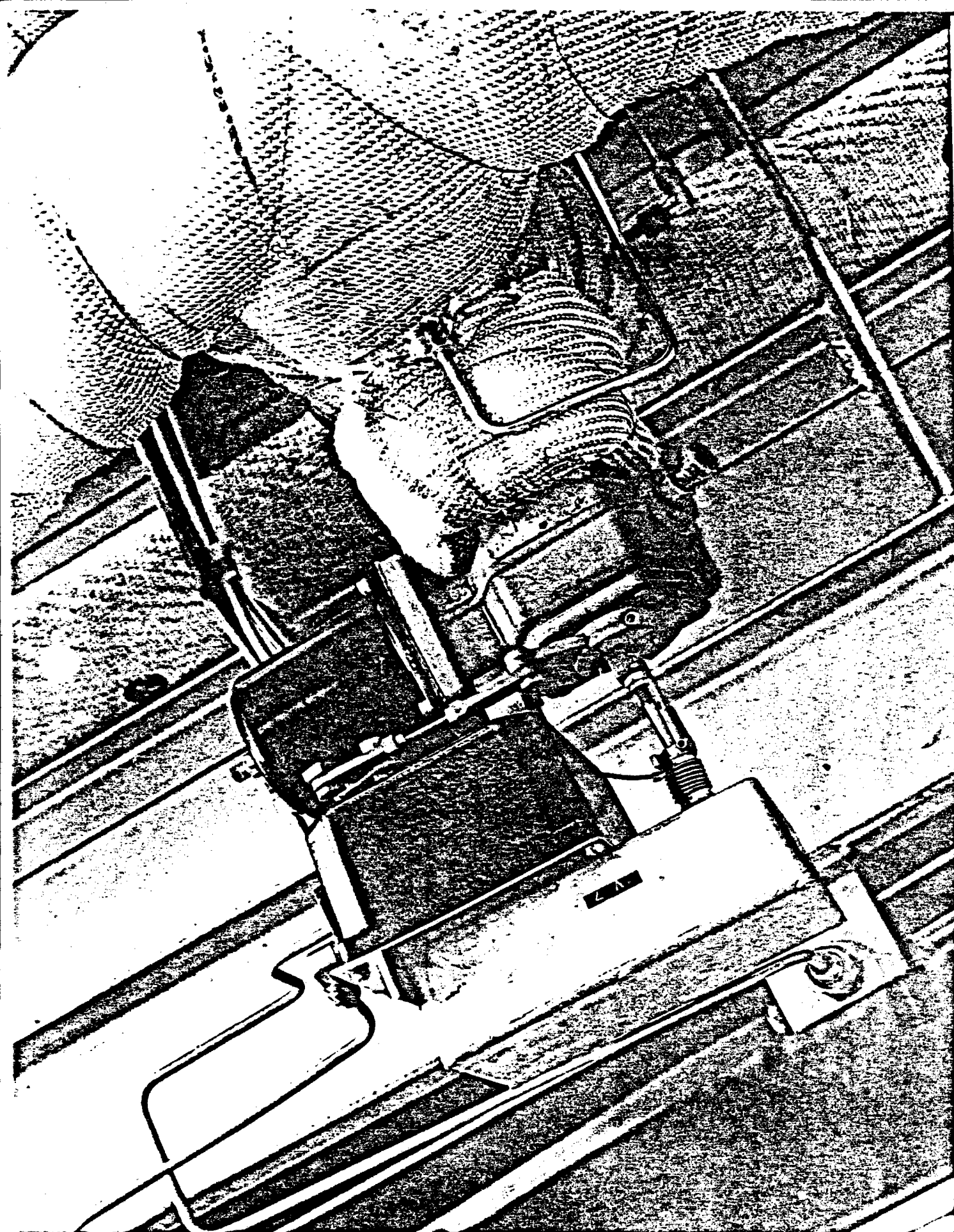


Figure 10.4-3: Valve, Actuator and Positioner Assembly Typical of Eight on the BMSR



The pneumatic actuator on valve 2 failed completely after tests on January 20, 1979. It worked acceptably that day but afterward it would not move from a fully open position. This appeared to be caused by a massive air leak past the piston of the actuating air cylinder. Its air lines were disconnected and the valve was manually positioned at desired valve angles prior to each of the remaining solar tests. Since the problem occurred on panel 2, it was impossible to reach the actuator for removal or repair. A review of the maintenance manual indicated that actuator failure was probably caused by damage to its teflon piston ring.

#### 10.5 BMSR INSTRUMENTATION

The experiment instrumentation consisted of 172 measurements including pressures, temperatures, heat fluxes, and valve angles. A total of 128 thermocouples were used along with 10 valve angle potentiometers, 13 calorimeters, and 21 pressure transducers. Experience gained with these sensors during the solar testing program confirmed most of the instrumentation design decisions and component selections. However, as noted in the following paragraphs, many of the instrumentation problems which were encountered had not been anticipated. As noted earlier, the BMSR test instrumentation provided accurate and reliable test data. However, much more on-site maintenance and repair work was required to achieve this result than was expected.

High temperature sheathed thermocouples were used for 93 of the 128 temperature measurements. These were chromel/alumel thermocouples encased in Inconel 601 sheathing. All the sheathed thermocouples were of the ungrounded type whereby the junction and sheath were separated by a layer of magnesium oxide insulation. This choice of design caused a slight increase in the response time and time constant of the units but the freedom allowed for independent thermal expansion of sheath and thermocouple was probably responsible for the unusually high survival rate of thermocouples used in this test program. Even though none of the thermocouple junctions failed during tests, other problems caused loss of several temperature measurements. A total of seven units, all located near panel 1 on the top of the receiver, were lost because of damage to the transition fitting

between sheathing and flexible extension wire. Air leakage from the panel outlet flange during tests at 705°C (1300°F) impinged directly on the outer shell of the receiver where these fittings were mounted. Thermal expansion of the potting compound within these fittings caused irreparable damage to the fine thermocouple wires. One additional sheathed thermocouple was lost because of damage to the back-cone insulation in which it was mounted.

Pressure measurements were a persistent source of problems with the BMSR instrumentation. Similar industrial quality units were used throughout the test setup. Their zero bias varied on a daily basis requiring recalibration at the completion of each day of testing and continuous updating of the real time and posttest data processing information. The worst offenders in this respect were the differential pressure transducers used to monitor pressure drop across the eight BMSR flow control valves and the two venturi flowmeters on the air supply skid. With system air admitted to both sides of the sensing diaphragm, the strain gages on the diaphragm were exposed to humid system air. They were inadequately protected from this moisture. Electrical resistance variations caused their zero balance to drift even more than the gage pressure transducers and on occasion caused complete failure of the transducer.

Leakage of high temperature air from the heat exchanger outlet flanges also caused problems with some of the pressure transducers. Several transducers as well as their electrical cables were destroyed by hot air leaks on November 28, 1978.

Finally, the pressure transducers were connected to pressure ports on the BMSR by means of small diameter stainless steel tubing. These tubes were coiled to provide flexibility and to accommodate motion of the BMSR manifolds and heat exchangers. Moisture condensing in these lines tended to be trapped in the coils. This probably aggravated the problems with exposed strain gages on the differential transducers. It also caused problems in cold weather when trapped moisture would freeze, blocking the line.

In future designs of compressed air systems it is important to recognize and accommodate the fact that the relative humidity of ambient air is increased

by compression. The added expense of aerospace quality pressure transducers is clearly justified by the maintenance and recalibration required with the industrial quality gages used here.

A total of 13 circular foil heat flux gages were used to measure radiant heat flux on cavity walls. When properly cooled, these gages proved to be reliable and durable. However, the black coating on their exposed surfaces became discolored during the test program. Recommendations for future utilization of these devices include provision for easy removal to clean and recoat the sensors and initial replacement of the vendor supplied coating with a readily available and easily applied black paint. The gages have to be recalibrated with the new paint but once this is done, recoating could restore the initial accuracy of a discolored gage without necessarily requiring recalibration. Utilization of spare gages which could be recoated and recalibrated in a laboratory environment would be an even more desirable, although costly solution to this problem.

High resolution potentiometers were used to measure air flow valve positions on the BMSR and the air supply skid. Their location near the sunlit side of the receiver resulted in exposure to operating temperatures of 94 to 116°C (200 to 240°F). In spite of the unusual high temperatures, the potentiometers operated reliably. Once again, the leakage of 705°C (1300°F) air at heat exchanger outlet flanges on November 28, 1978 severely damaged wiring to these sensors.

## SECTION 11.0

### POSTTEST THERMAL ANALYSIS

This section describes the BMSR thermal analyses performed subsequent to the end of the testing program. Section 11.1 combines the salient pretest predictions and test data. Areas of agreement and disagreement are noted. The areas of disagreement form the basis of discussion for Section 11.2, where revisions to the thermal analysis of the receiver are considered.

#### 11.1 COMPARISON OF PRETEST THERMAL ANALYSIS WITH TEST DATA

The areas that are considered in this comparison are insulation temperatures, the overall receiver thermal performance, the panel-to-panel heat balance distribution, and the transient cooldown data. This section is intended to briefly establish those important areas that indicate the adequacy or inadequacy of pretest analysis. Those areas in which test data corroborate the pretest thermal analyses are considered to be complete. Those comparisons that indicated additional analyses were required form the basis for the following subsection.

##### Insulation Temperatures

A comparison of pretest analytical and test data is given in Table 11.1-1. Significant differences are noted, especially on the cover temperatures. Although the general behavior of higher bay 3 and 7 temperatures are observed in both the experimental and analytical data, the maximum temperature observed in the experimental data is about 550°F above the analytical prediction. This discrepancy is considered in more detail.

##### Overall Receiver Thermal Performance

Figure 11.1-1 presents a comparison of the receiver thermal efficiency for the pretest prediction as compared to seven test data bands. The height of the test band represents the uncertainty in the test data parameters. As can be seen, significant scatter is noted in the test data, all about the

Table 11.1-1. Pretest Analytical and Experimental Insulation Temperature Comparison

## Pretest Analytical and Experimental Insulation Temperature Comparison

		Panel number							
Channel		1	2	3	4	5	6	7	8
TX-2	E	1,147 (2,097)*		1,264 (2,307)		1,209 (2,209)		1,194 (2,182)	
	A	797 (1,466)		797 (1,466)		797 (1,466)		797 (1,466)	
TX-1	E	101 (213)		119 (247)		102 (215)		111 (232)	
	A	73 (164)		73 (164)		73 (164)		73 (164)	
TX-3	E	812 (1,494)	821 (1,509)	1,321 (2,410)	1,209 (2,209)	871 (1,599)	910 (1,670)	1,105 (2,021)	819 (1,507)
	A	844 (1,551)	902 (1,655)	1,018 (1,864)	900 (1,652)	852 (1,566)	900 (1,652)	1,018 (1,864)	902 (1,655)
TX-4	E	59 (138)	138 (281)	240 (464)	89 (192)	72 (162)	83 (181)	117 (242)	107 (224)
	A	91 (196)	97 (207)	110 (230)	97 (206)	92 (197)	97 (206)	110 (230)	97 (207)
TX-6	E	Inoperative	875 (1,607)	871 (1,599)	830 (1,526)	843 (1,549)	866 (1,590)	863 (1,585)	883 (1,621)
	A	824 (1,515)	840 (1,544)	866 (1,591)	832 (1,529)	828 (1,523)	832 (1,529)	866 (1,591)	840 (1,544)
TX-5	E	56 (133)	71 (160)	92 (197)	110 (230)	87 (189)	101 (213)	56 (132)	53 (128)
	A	85 (185)	87 (188)	89 (193)	86 (187)	86 (186)	86 (187)	89 (193)	87 (188)
TX-7	E	911 (1,672)		939 (1,723)		920 (1,668)		893 (1,639)	
	A	814 (1,497)		814 (1,497)		813 (1,496)		813 (1,496)	
TX-8	E	145 (293)		253 (488)		162 (323)		150 (302)	
	A	88 (191)		88 (191)		88 (191)		88 (191)	

592

- Experimental data from March 24, 1979, solar test, 4.0 hr.
- Analytical data from solar load following, 4.0 hr:

$$Q_{IN} = 975 \text{ kW}$$

$$Q_{OUT} = 736 \text{ kW}$$

$$\dot{m} = 2.28 \text{ kg/s (5.02 lb/s)}$$

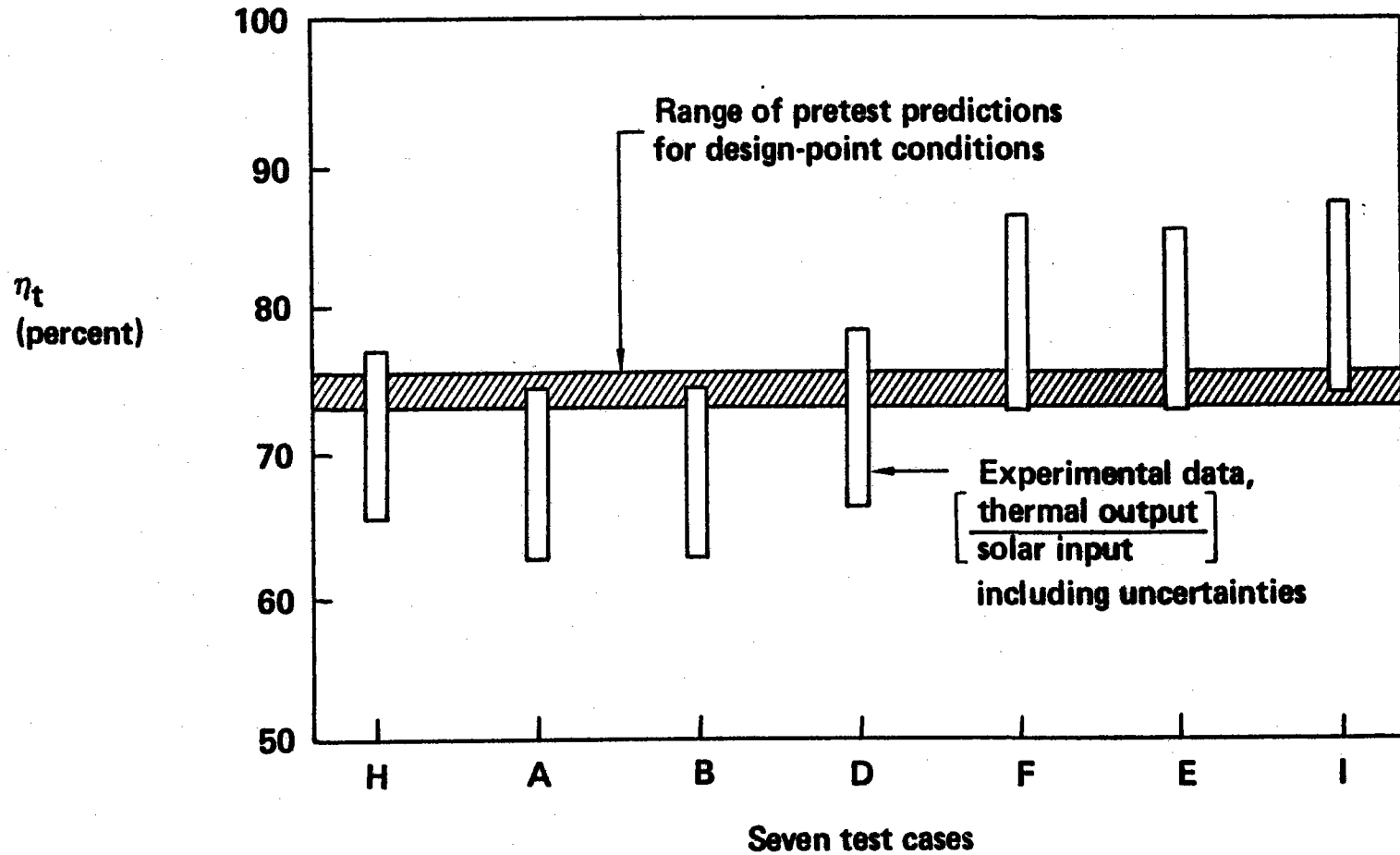
$$T_{AIR (IN)} = 534^{\circ}\text{C (994}^{\circ}\text{F)}$$

$$T_{AIR (OUT)} = 816^{\circ}\text{C (1,500}^{\circ}\text{F)}$$

\*Temperatures  
in °C (°F)

Figure 11.1-1. Receiver Thermal Efficiency Comparison

# Receiver Thermal Efficiency Comparison



design-point prediction. Figure 11.1-2 presents the thermal efficiency as a function of solar power input level. The test data and analysis are seen to agree within the limits of uncertainty for design-point conditions of 1000 kWe. However, at lower power levels, the experimental efficiency is seen to be lower than the pretest prediction.

#### Panel-to-Panel Heat Balance Distribution

Figure 11.1-3 presents the panel-to-panel heat balance distribution for the pretest analysis prediction and test data. The pretest analysis predicted a uniform panel heat balance; experimental data showed not only a total heat transfer less than the prediction, but also a significant nonuniformity from panel to panel. Most importantly, the bottom heat exchanger panels, 4, 5, and 6, performed significantly less than the top panels, 1, 2, and 8. This same trend was noted for differing total power-output levels, as demonstrated in Figure 11.1-4. A comparison of the relative panel heat transfer to the relative heat flux as measured by the panel calorimeters is shown in Figure 11.1-5. This comparison indicates the panel heat imbalance is not accounted for by radiative flux imbalances inside the cavity. This panel-to-panel heat balance distribution is one of the indicators of convective effects occurring inside the cavity.

#### Transient Cooldown

In a transient cooldown test, the working fluid mass flow and the solar input were stopped simultaneously. The receiver cavity environment was then monitored as the cooldown occurred. The pretest analysis prediction for a transient cooldown from the receiver design-point equilibrium conditions is shown in Figure 11.1-6. Test data from the March 24 transient cooldown was not quite at the design-point conditions. A very significant difference between the analysis prediction and the test data can be seen. The pretest analysis prediction showed the heat exchanger temperatures coalescing into a nearly uniform temperature, which then decayed over a period of time. The test data show not only a much more rapid cooldown of heat exchanger temperatures, but also a definite stratification of temperatures from the lowest panel (in a vertical plane), 5, to the top panel, 1, *figures 11.1-7.*

Figure 11.1-2. Receiver Thermal Efficiency as a Function of Solar Input Power

## Receiver Thermal Efficiency as a Function of Solar Input Power

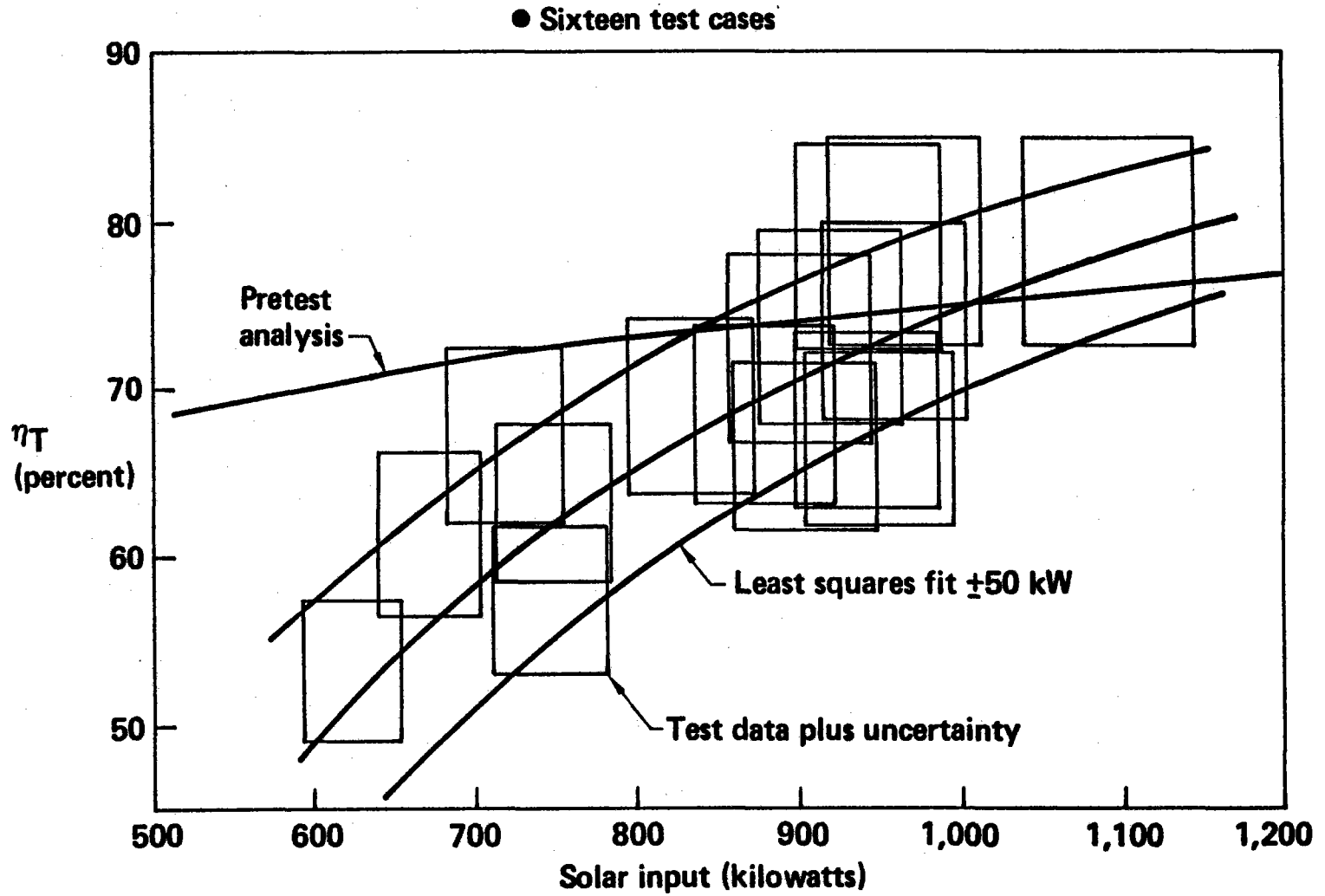
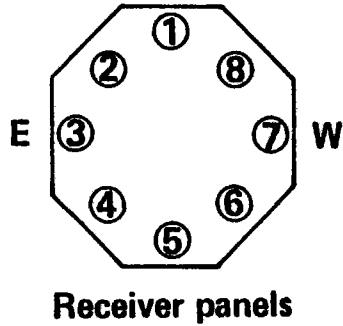




Figure 11.1-3. Panel Heat Balance Comparison

# Panel Heat Balance Comparison



	Experiment	Pretest analysis	Difference
Total heat transfer (kW)	643	718	75
Solar input (kW)	950		

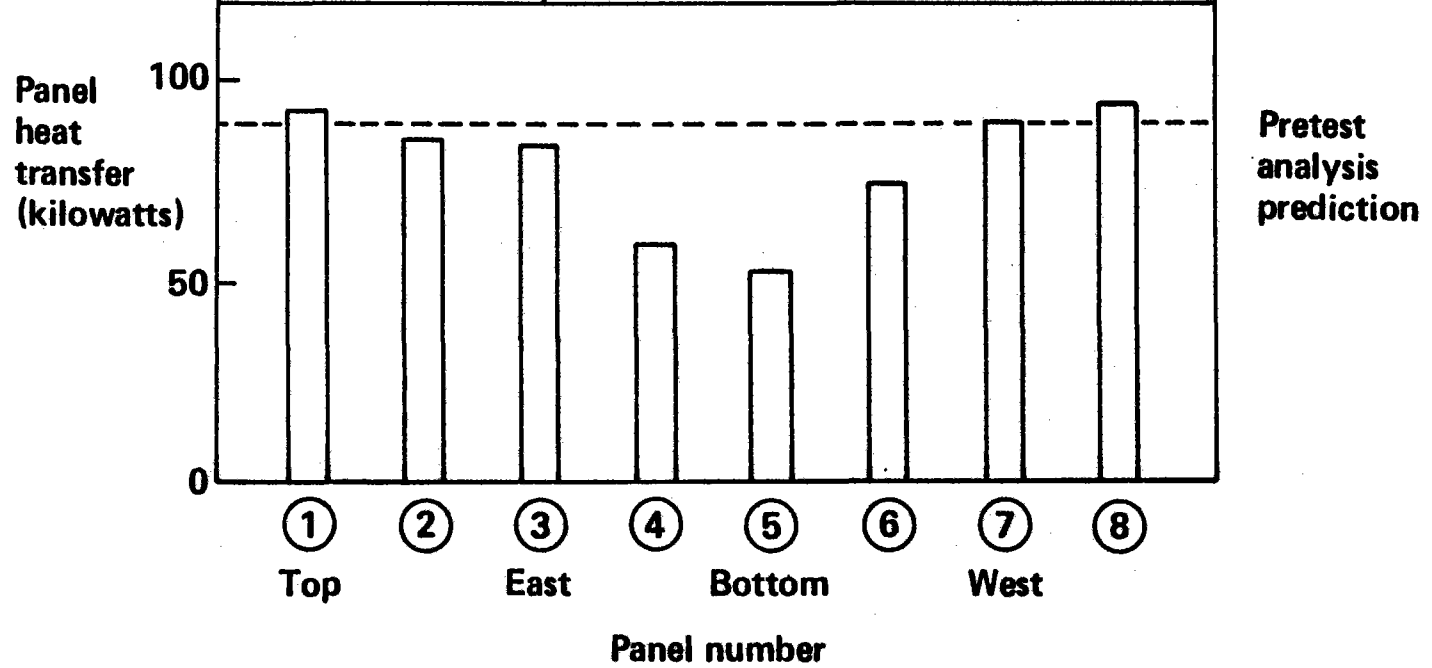


Figure 11.1-4. Panel Heat Balance Data for Different Power Levels, 1/20/79

# Panel Heat Balance Data for Different Power Levels, 1/20/79

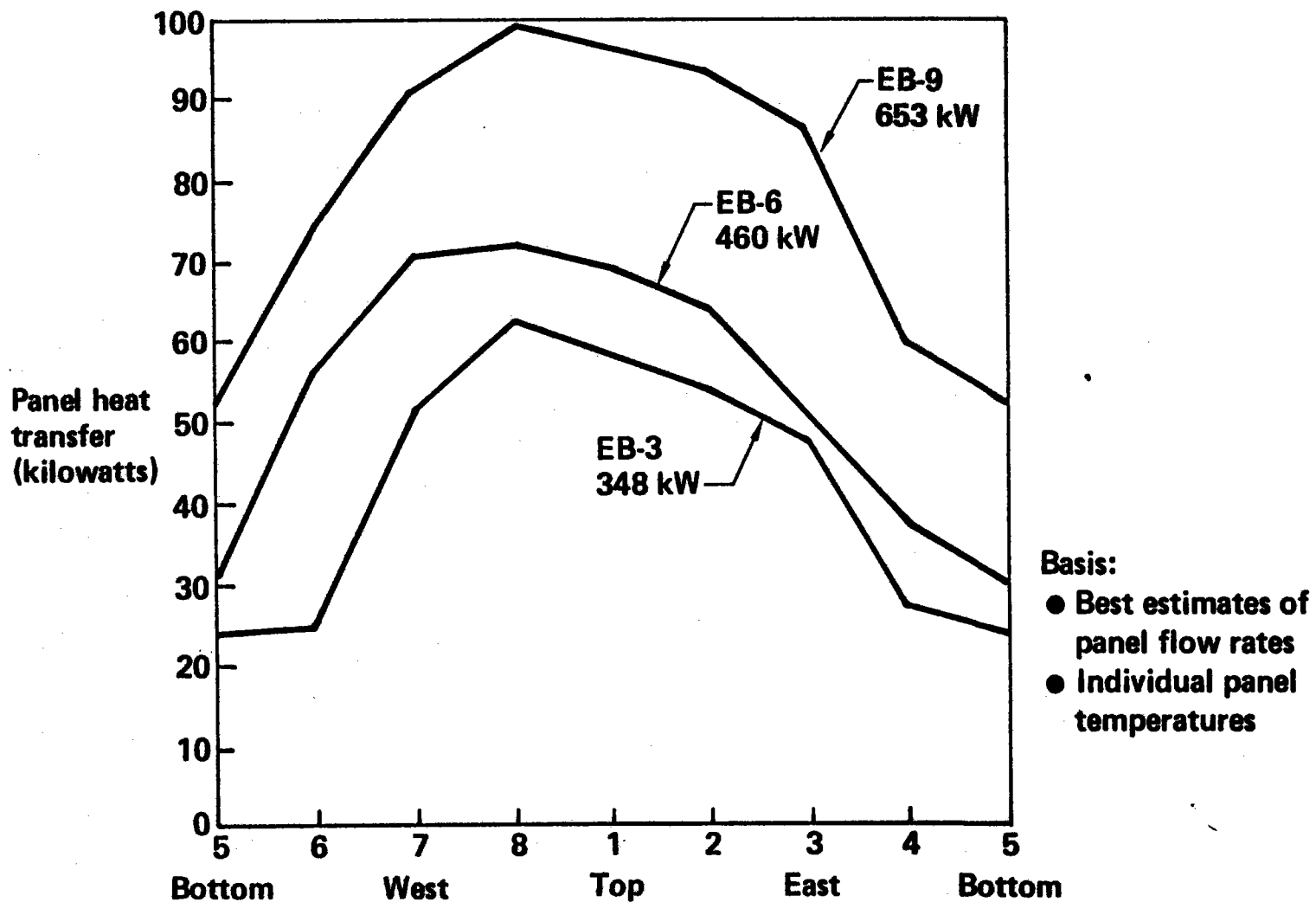


Figure 11.1-5. Comparison of Relative Heat Balance and Relative Heat Flux Test Data

# Comparison of Relative Heat Balance and Relative Heat Flux Test Data

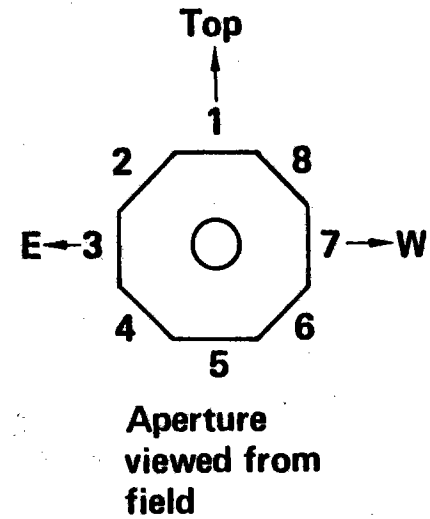
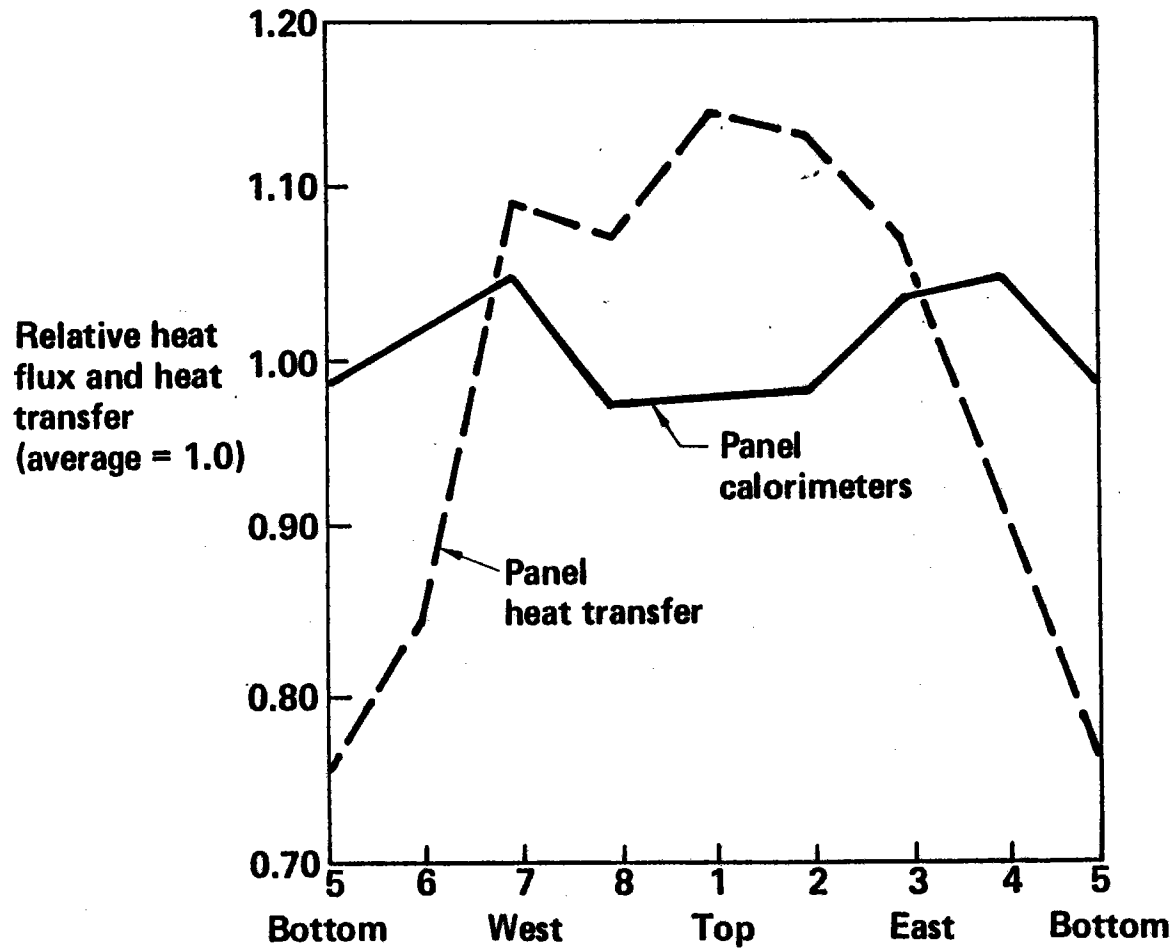


Figure 11.1-6. Pretest Analysis Transient Cooldown From Design Point Conditions

# Pretest Analysis Transient Cooldown From Design Point Conditions

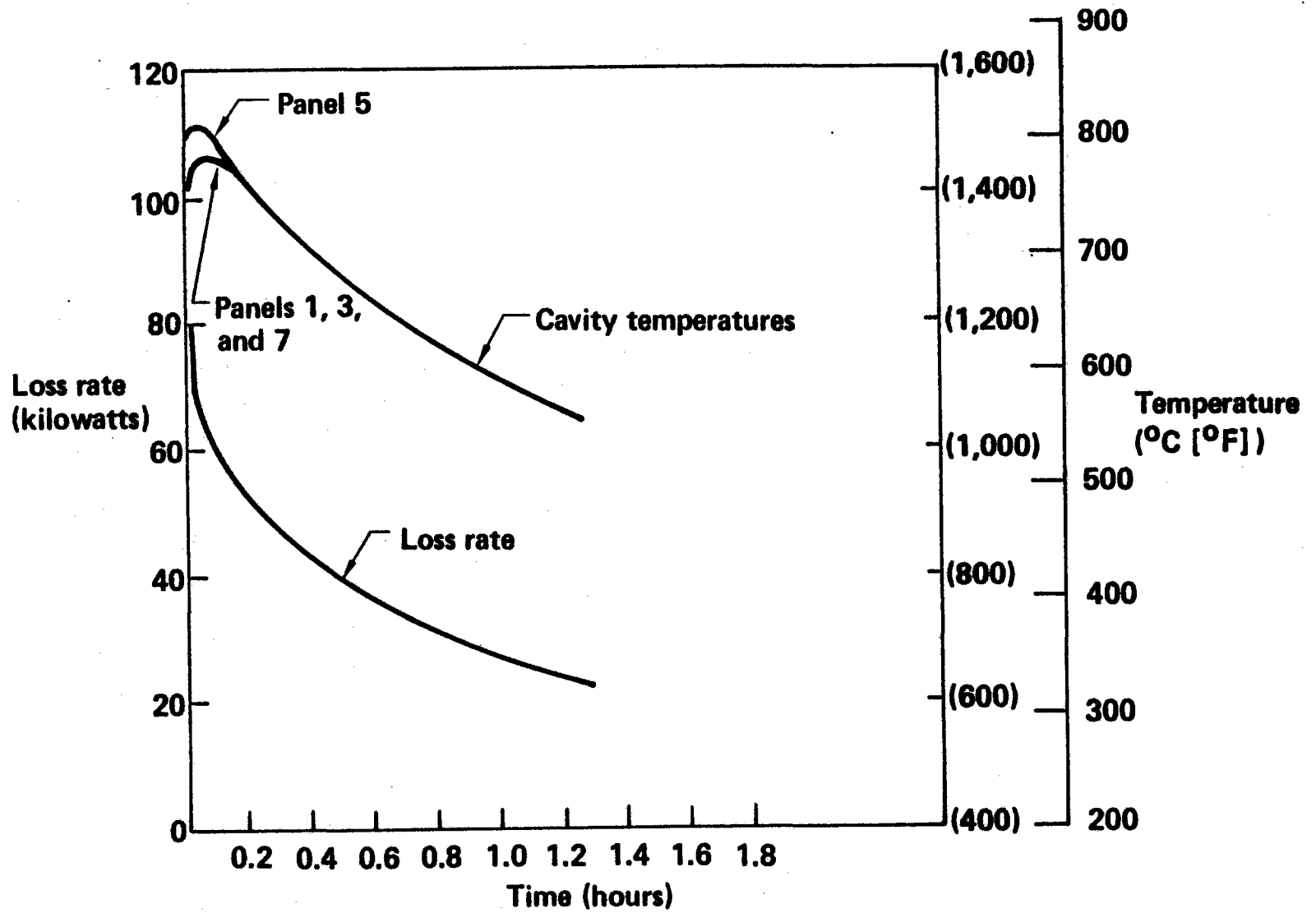
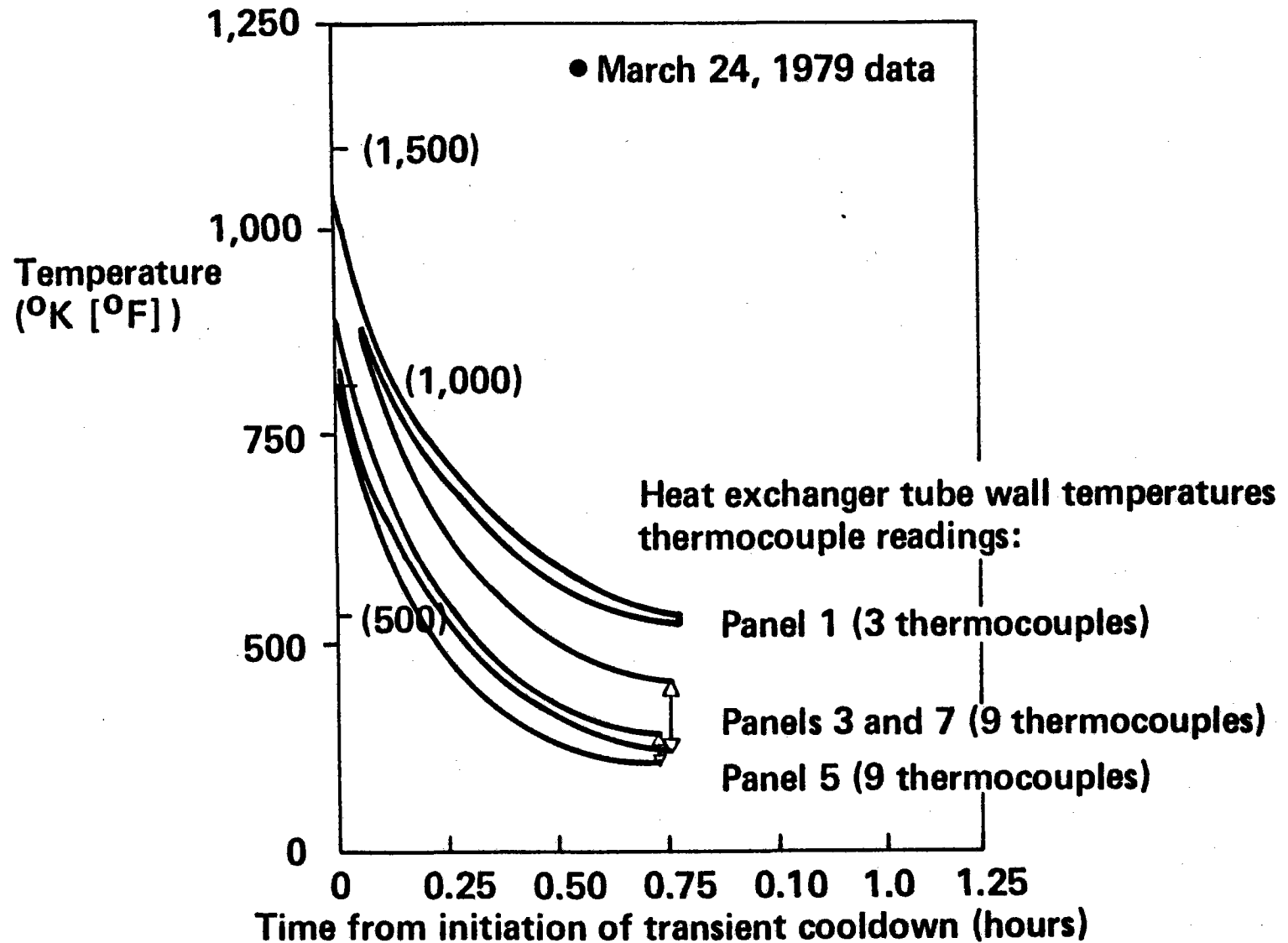


Figure 11.1-7. BMSR Transient Cooldown (Heat Exchanger Temperatures)

# BMSR Transient Cooldown (Heat Exchanger Temperatures)



## 11.2 REVISIONS TO THE PRETEST THERMAL ANALYSIS

As a result of the comparisons in Section 11.1, revisions in the thermal analysis were necessary. The entire area of insulation temperature predictions was considered in more detail, especially with application to the insulation damage noted in Section 10.1. Revision of the receiver thermal model was made to attempt to reproduce the differences in overall receiver performance and the panel-to-panel heat balance. Finally, the implications of the transient cooldown data were considered more closely, especially their implications on the presence of cavity convective phenomena. The results of these additional posttest thermal analyses are presented in the following sections.

### 11.2.1 Insulation Temperature Profile

The BMSR design was chosen based on design temperatures of less than 815°C (1500°F) for the mineral wool block, 1140°C to 1260°C (2100° to 2300°F) for Kaowool, and less than 1649°C (3000°F) for Saffil. After the insulation failures previously described occurred, a concern was raised as to whether these design temperatures were exceeded. The purpose of this section is to present analytical treatment of the insulation temperature profiles using measured experimental temperature data as boundary conditions.

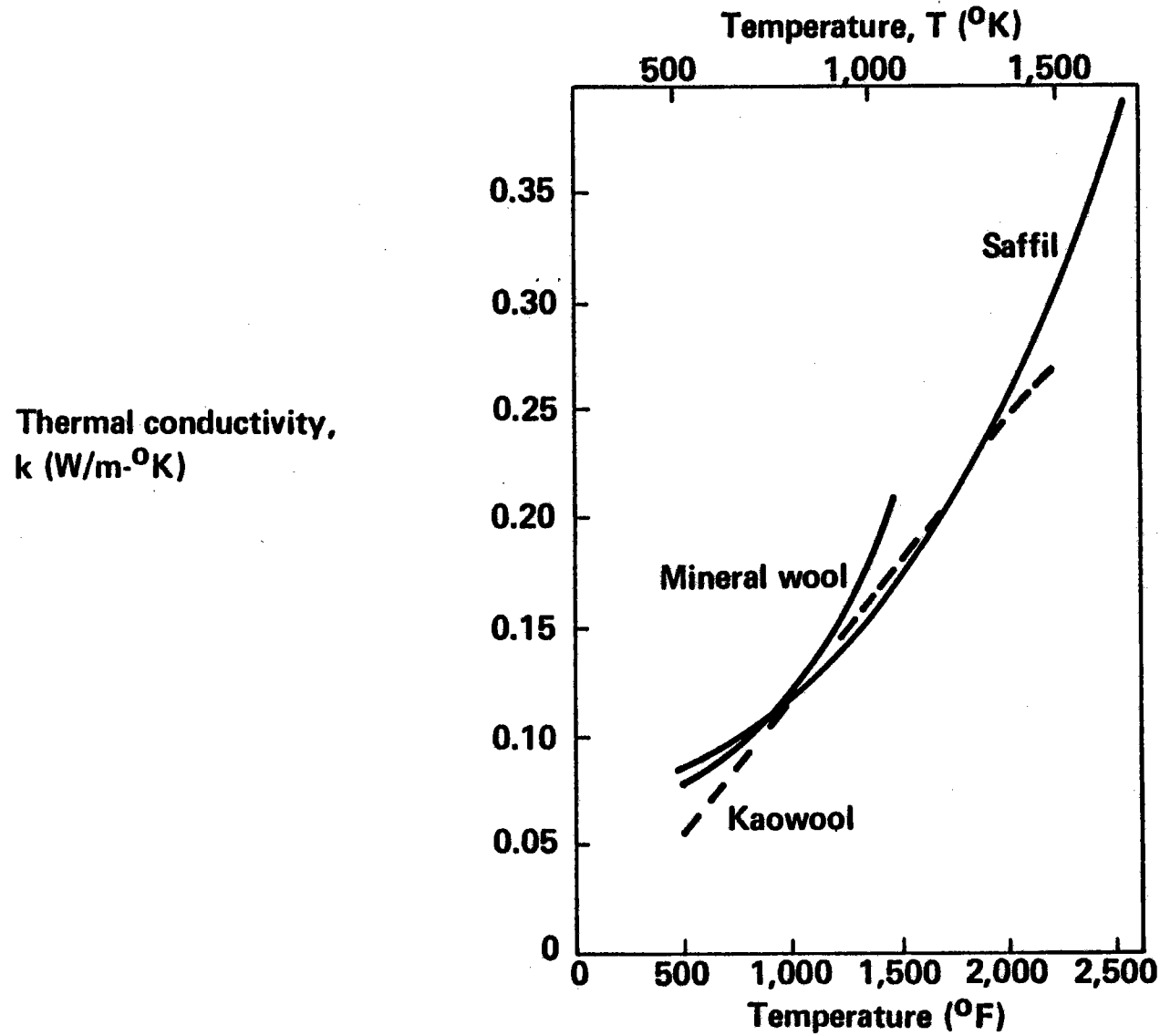
The temperature thermal conductivity data used in the pretest thermal model were based on Babcock and Wilcox product data bulletins. In an attempt to obtain the most precise information on these products, detailed numerical data were obtained from the Babcock and Wilcox research groups. They are presented in Figure 11.2-1.

To solve the one-dimensional energy equation, the functional behavior of the insulation thermal conductivity must be known. Such a functional relationship for high-temperature ceramic-fiber blankets has been suggested by Clausing (Reference 10). The suggested relationship is

$$k(T) = C_1 T^{0.65} + C_2 T^3 \quad (11.2-1)$$

Figure 11.2-1. Insulation Thermal Conductivity Data

# Insulation Thermal Conductivity Data



where the first term represents the conduction through the air at the interstices and the second term represents the thermal radiation across the interstices. This relationship as expressed herein was based on the following assumptions: (1) The insulation material was homogeneous; the contribution to the thermal conductivity due to conduction through the fibers was negligible; (2) the total thermal conductivity was determined by superposition of the radiative transfer and the conduction through the air; (3) the insulation blanket did not contain any binders at its typical utilization temperatures; and (4) the interstices were sufficiently small so that natural convection was not important and large enough so that free molecular flow and accommodation coefficients need not be considered.

The thermal conductivity data presented in Figure 11.2-1 were least-squares curve fit to the functional relationship of equation 11.2.1-1; excellent agreement was found. The resulting coefficients for Saffil, Kaowool, and mineral wool are given in Table 11.2-1.

### Surface Absorption

The model assumed in this analysis is presented in Figure 11.2-2. The net solar energy (after absorption, reflection, re-emission, and re-absorption) was assumed deposited on the insulation surface and conducted through the insulation layers. Thermocouple data 5.1cm (2 in) from the insulation surface and on the steel shell were available from experimental measurements. These thermocouple data served as the boundary conditions, and the temperatures at the insulation layer interfaces and the surface were calculated. The energy equation solved in each insulation layer is given by

$$(C_1 T^{0.65} + C_2 T^3) \frac{d^2 T}{dy^2} = 0 \quad (11.2.1-2)$$

and,

$$\left. \begin{aligned} T(y_3) &= T_3 \\ T(y_5) &= T_5 \end{aligned} \right\} \text{known}$$



Table 11.2-1. Insulation Thermal Conductivity Coefficients

## Insulation Thermal Conductivity Coefficients

$$k(T) = C_1 T^{0.65} + C_2 T^3$$

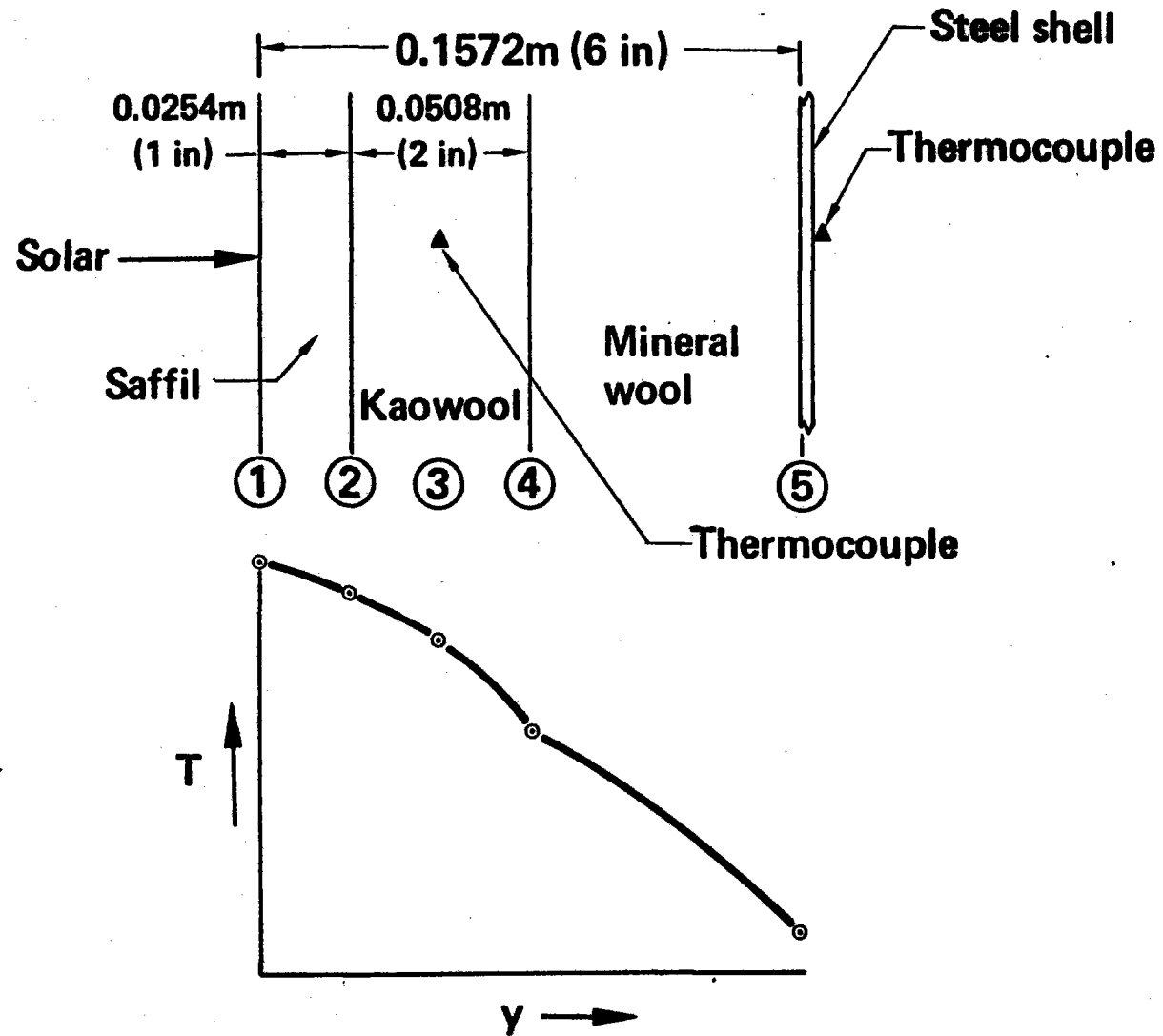
k in W/m<sup>0</sup>K

T in <sup>0</sup>K = <sup>0</sup>C + 273.16<sup>0</sup>

Material	C <sub>1</sub>	C <sub>2</sub>
Saffil	0.001145	5.228 x 10 <sup>-11</sup>
Kaowool	0.001045	5.468 x 10 <sup>-11</sup>
Mineral wool	0.001031	8.177 x 10 <sup>-11</sup>

Figure 11.2-2. Surface Absorption Analysis Model

# Surface Absorption Analysis Model



The solution of this equation also gave the heat flux,  $q_m$ , being conducted through the insulation. The results using experimental data from noon, March 24, 1979, are presented in Figure 11.2-3. They were chosen because they were taken near noon and also near the spring equinox. Also this condition represented a stable operating period at the design-point conditions (equilibrium point EB-9F). The location of the cover octagon, cover trapezoid, and frame rectangle sections are presented in Section 3.2 (Figure 3.2-9).

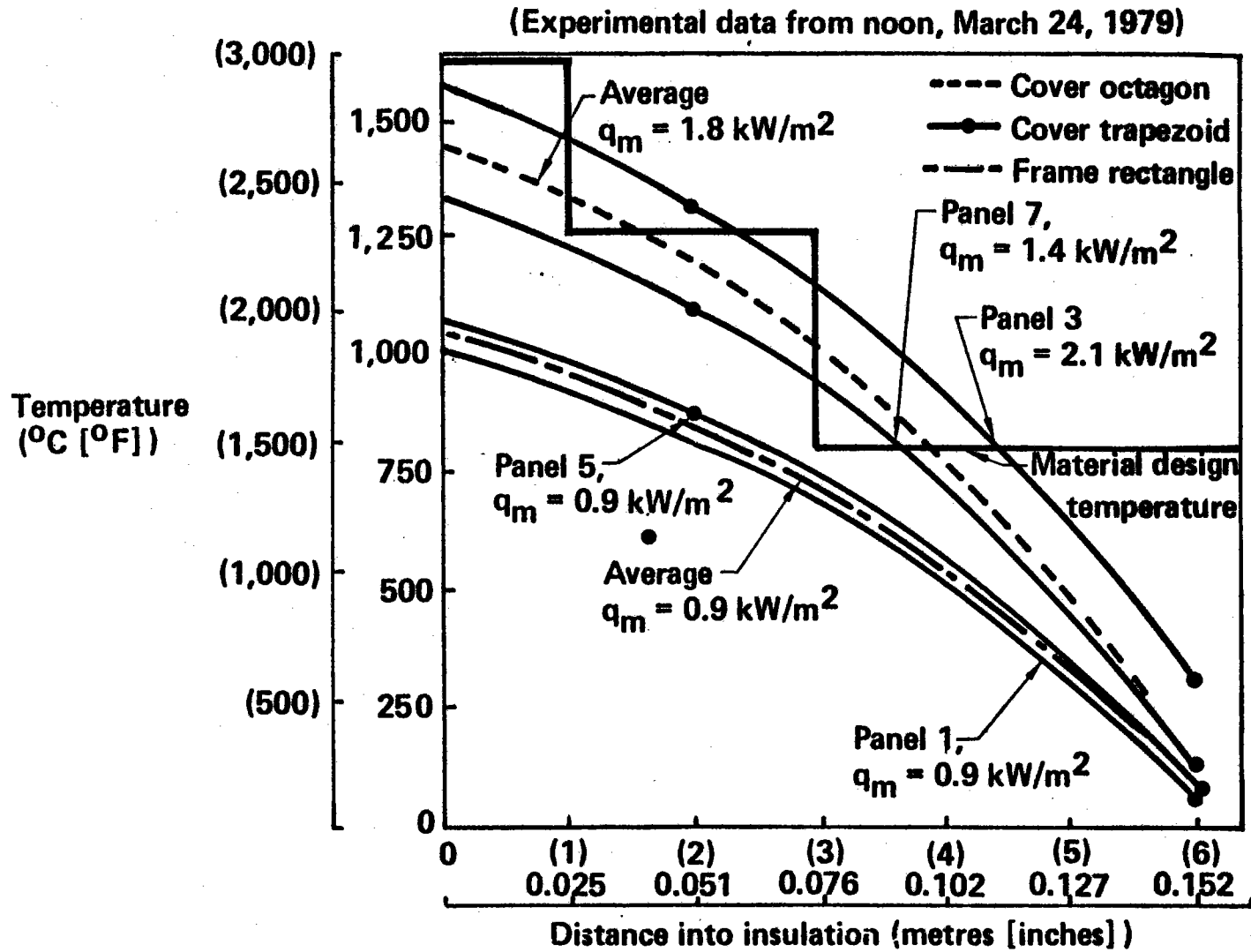
Also presented in Figure 11.2-3 are the material design temperature data presented at the beginning of this section. These data clearly show that the 1649°C (3000°F) value was not exceeded. The panel 3 back cone trapezoid data indicates that some insulation deterioration was beginning to occur. On the following day of testing (March 25, 1979), this panel 3 area was the region of greatest insulation damage. The data from the back cone octagon and the panel 7 back cone trapezoid appear to be more representative of the insulation profile before failure. (Neither panel 7 back cone trapezoid or the back cone octagon regions had major insulation failure). The data indicates a maximum expected insulation temperature from this analytical formulation of 1454°C (2650°F) Figure 11.2-3 also indicates that there were regions where the Kaowool and mineral wool design temperatures were exceeded. The Kaowool and mineral wool in the back cone regions where the greatest first-incident solar flux occurred appear to have been subjected to excessive temperatures. This condition could have been a precipitator for the subsequent insulation problems.

#### Volume Absorption

During the posttest analysis of the Saffil insulation samples, it became apparent that a surface absorption model of the net solar flux might not be accurate. When irradiated with a CO<sub>2</sub> laser, Saffil samples were heated white hot and the visible light permeated the entire blanket. Figures 11.2-4 through 11.2-7 present photos of the laser test setup and the samples under irradiation from the 10.6- $\mu$ m laser. As can be seen, the blanket appeared to be translucent. This led to speculation that a volume absorption analysis in the surface layer should be explored with the idea

Figure 11.2-3. Insulation Temperature Profiles Based on Surface Absorption

# Insulation Temperature Profiles Based on Surface Absorption



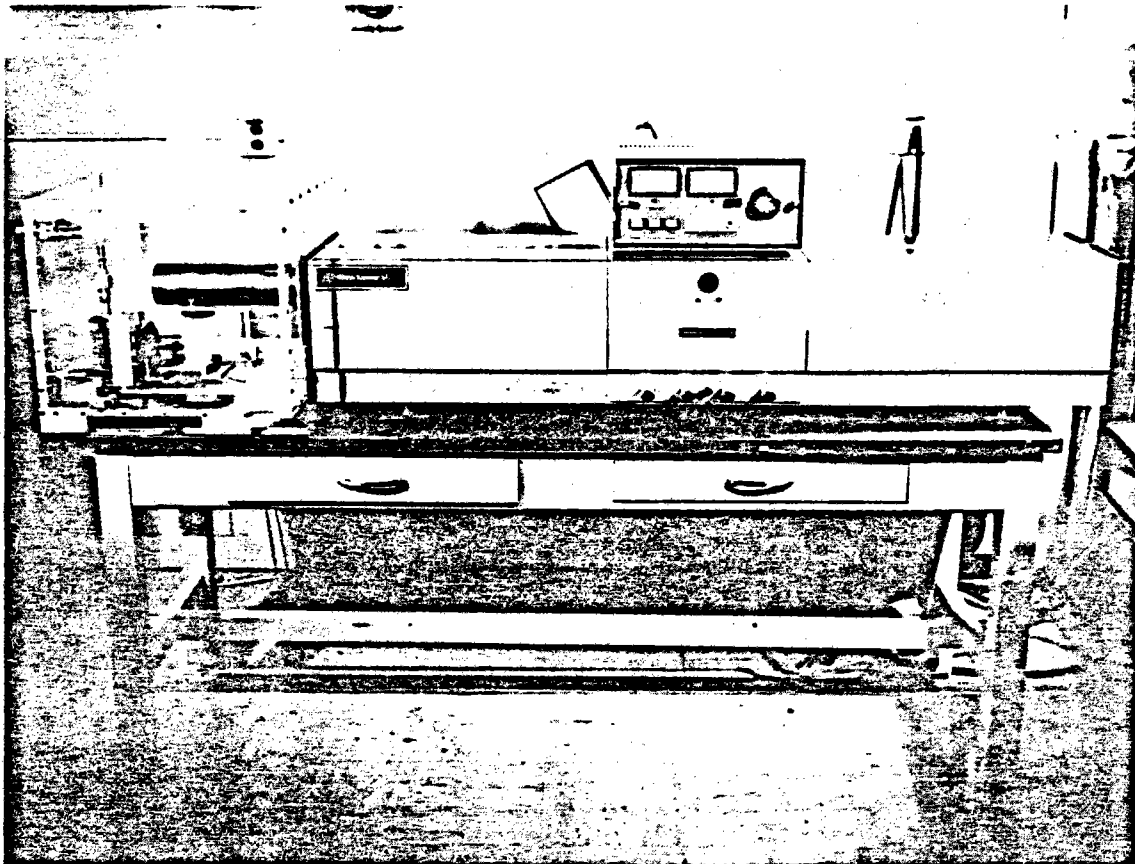


Figure 11.2-4: CO<sub>2</sub> Laser System

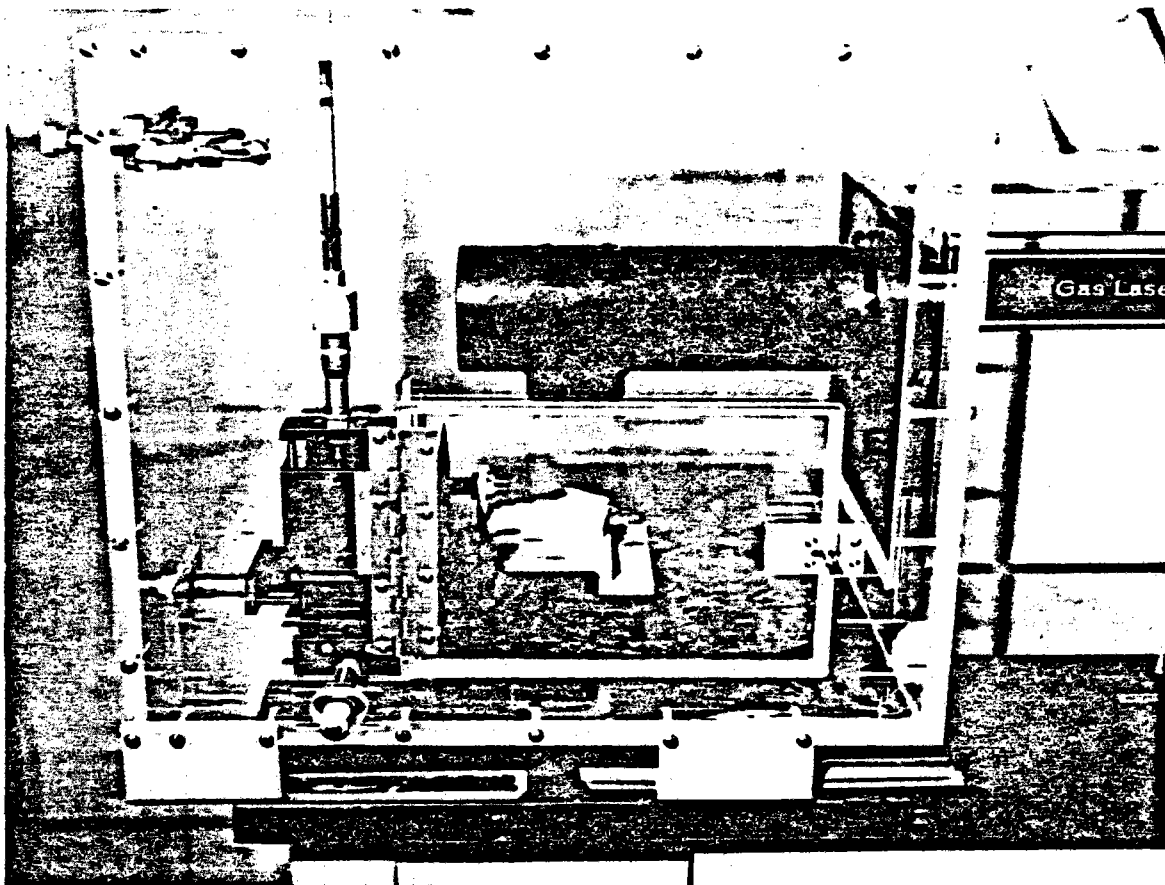


Figure 11.2-5: CO<sub>2</sub> Laser Irradiation of Saffil Sample



Figure 11.2-6: Laser Irradiation Normal to Saffil Fibers



Figure 11.2-7: Laser Irradiation Parallel to Saffil Fibers



that the maximum temperature experienced by the Saffil could be at some distance away from the surface, inside the insulation.

To facilitate this analysis, layers of differing thicknesses of Saffil insulation were placed on a Beckman DK-2A spectrophotometer integrating sphere and the transmission was measured. The resulting data are shown in Table 11.2-2 and Figure 11.2-8. As can be seen, even at 0.9cm (0.375 in) depths, approximately 5% of the solar flux is transmitted. Figure 11.2-9 presents the transmission as a function of thickness. The transmittance would be expected to follow an exponentially decaying functional behavior characterized by some average extinction coefficient appropriate for the main solar spectrum.

The model assumed for this volume absorption analysis is shown in Figure 11.2-10. Only volume absorption through the 2.5cm (1.0 in) Saffil layer was considered. The temperature,  $T^*$ , at the Saffil-Kaowool interface was assumed available from the surface absorption case. The same total solar-power input to the Saffil as in the surface absorption case was assumed for this analysis. The resulting energy equation and boundary conditions are given by

$$(C_1 T^{0.65} + C_2 T^3) \frac{dT}{dy} = \frac{k_s q_0}{e^{-k_s L} - 1} e^{-k_s y} \quad (11.2.1-3)$$

$$T(L) = T^*$$

$$\frac{dT(0)}{dy} = \frac{-q_0}{(C_1 T(0)^{0.65} + C_2 T(0)^3)}$$

The solution details of these series of equations are too laborious to be presented here. The extrema are found by setting  $\frac{dT(y)}{dy} = 0$  and solving for  $\bar{y}$ . If this is done, the important result found is that  $\bar{y}$  is always negative, i.e., outside the insulation for all  $k_s$ . This suggests that there are no temperatures in the insulation from the volume absorption analysis, which are larger than the surface temperature at  $y=0$ . That is, if  $T_v(0) = \hat{T}_v$ , then  $\hat{T}_v$  is the maximum predicted temperature.

Table 11.2-2. Transmission of Saffil

## Transmission of Saffil

Wavelength (micrometres)

Sample thickness	0.3	0.4	0.5	0.6	0.7	0.8	1.0	1.2	1.4	1.6	1.8	2.0	2.2
50 mil	56	55	56	56	56	57	50	50	59	49	49	50	50
100 mil	18	22	25	26	27	30	23	24	25	24	25	26	26
175 mil	10	13	18	19	20	19	19	20	19	19	20	19	18
225 mil	11	7	11	12	10	12	6	7	7	7	8	9	9
275 mil	13	4	8	10	8	10	2	2	2	3	4	4	4
375 mil	12	1	5	6	5	6	1	1	1	2	3	3	3

Transmission—Beckman DK-2A spectrophotometer plus integrating sphere

Figure 11.2-8. Transmission of Saffil

# Transmission of Saffil

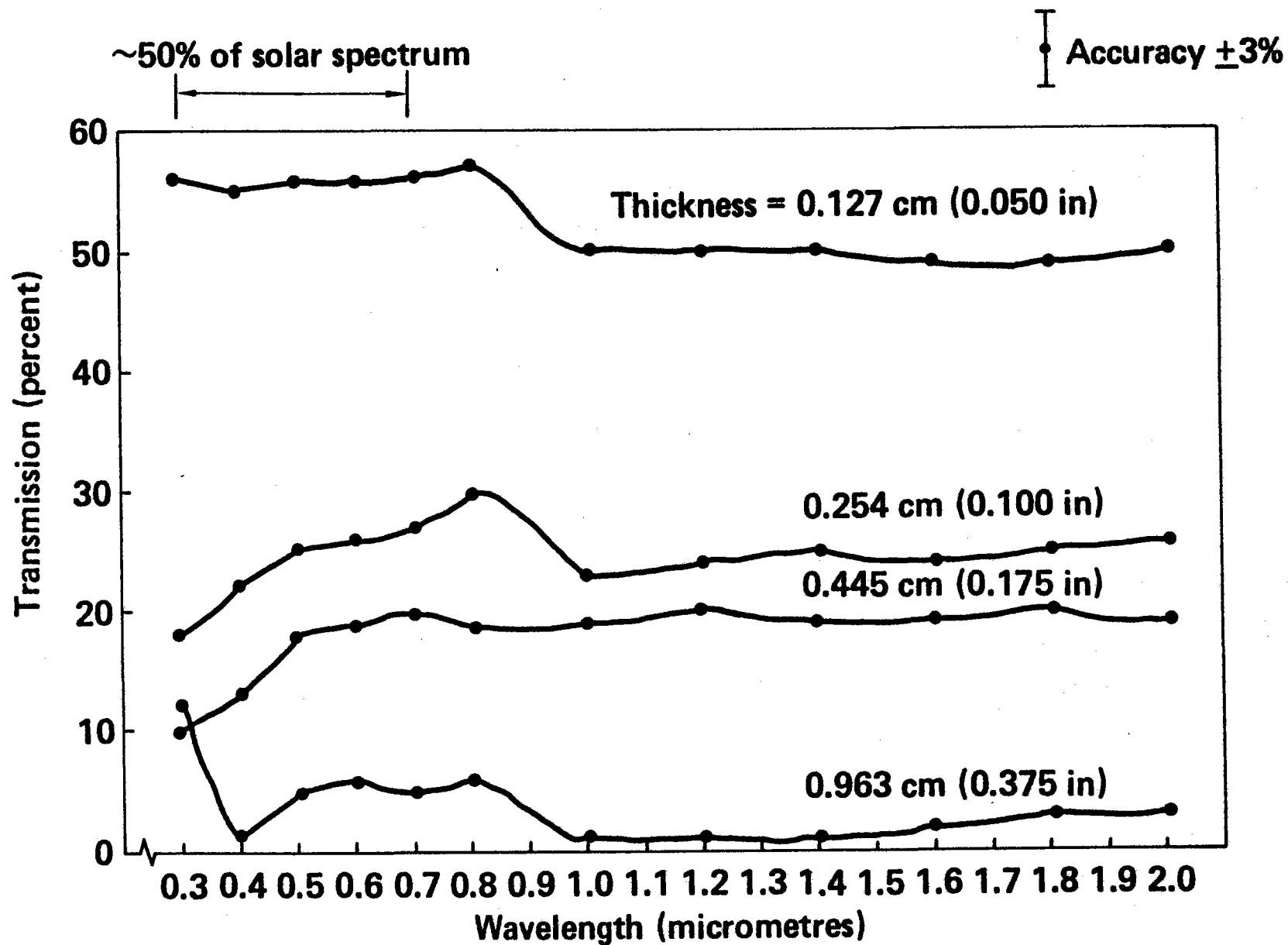


Figure 11.2-9. Saffil Extinction Coefficient  
**Saffil Extinction Coefficient**

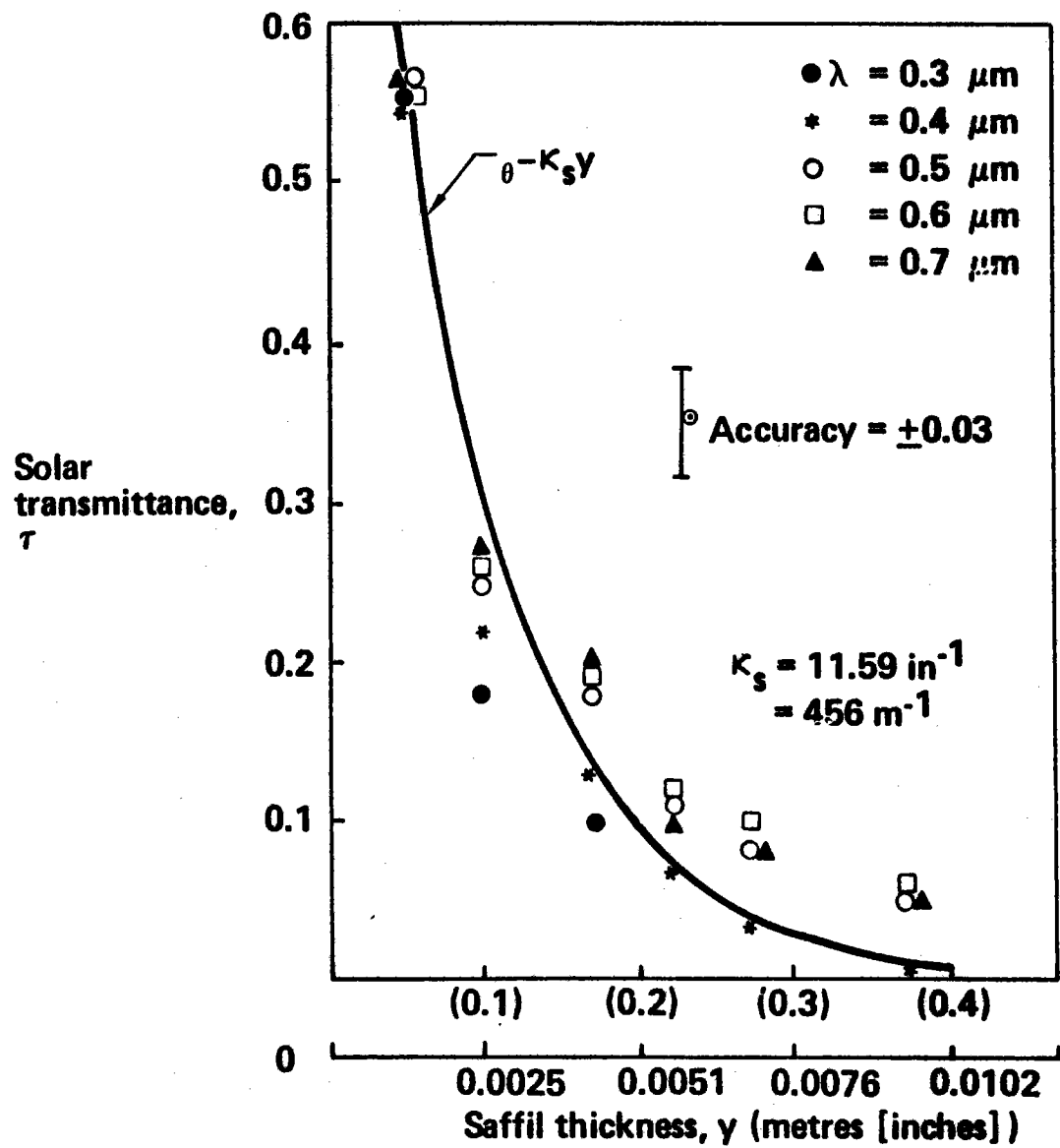
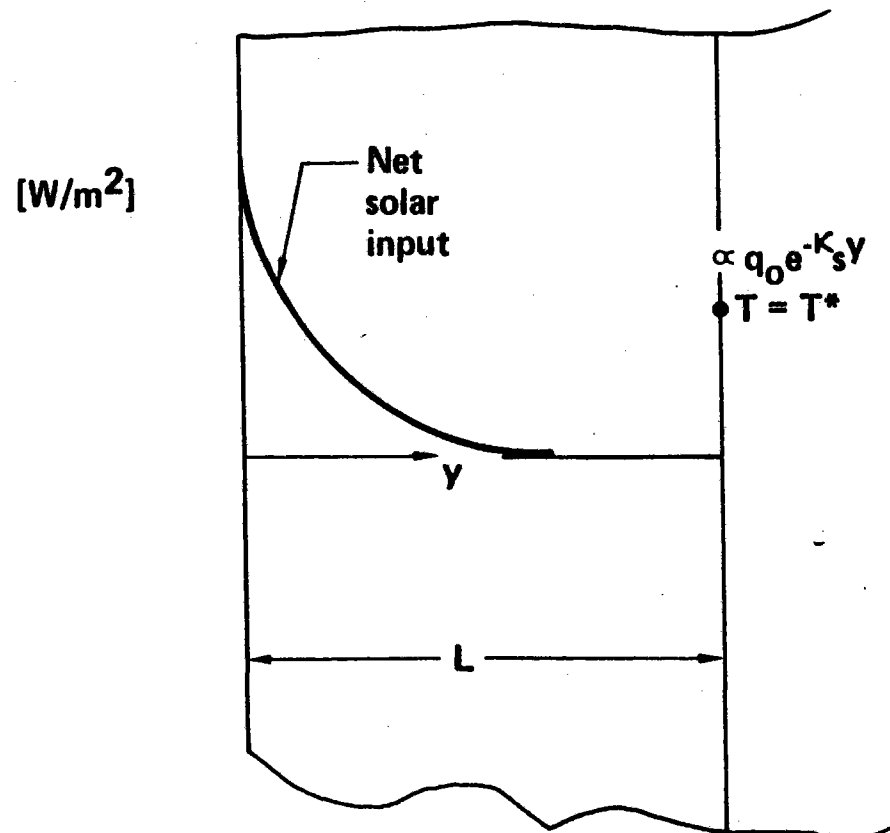


Figure 11.2-10. Volume Absorption Analysis Model

# Volume Absorption Analysis Model



Similarly, if  $\hat{T}_s$  represents the surface absorption temperature at  $y=0$ ,  $\hat{T}_s$  is the maximum predicted temperature from the surface absorption analysis. If  $\hat{T}_s$  and  $\hat{T}_v$  are compared for similar experimental conditions, one finds  $\hat{T}_s > \hat{T}_v$ . In fact, the difference between  $\hat{T}_s$  and  $\hat{T}_v$  is only on the order of  $5.6^\circ\text{C}$  ( $10^\circ\text{F}$ ). Therefore, the previously presented surface absorption case temperature profiles represent the maximum expected temperatures consistent with experimentally measured data and the best thermal conductivity data.

As a result of this insulation temperature analysis and the revisions in the thermal model discussed in the following section, a revised analytical prediction of the insulation temperatures was made. The results are presented in Table 11.2-3. The experimental data shown in Figure 11.2-3 are compared to the posttest analysis data. As can be seen, the predictions for panels 1 and 5 are in good agreement with test data at both thermocouple locations. However, panel 3 test data are still significantly higher than would be expected from analysis. This is caused by two factors. On March 25, the day after the experimental data of Table 11.2-3 were taken, the panel 3 insulation failed dramatically. In fact, visual inspection of the insulation prior to the March 25 test revealed the panel 3 insulation beginning to deteriorate. A portion of the discrepancy between the panel 3 analytical and experimental insulation temperatures was caused by the beginning of deterioration of the insulation itself. This was substantiated by the cold face panel 3 test data showing that the exterior shell of the receiver was significantly warmer than panel 7, thus indicating the onset of the subsequent burnthrough of the insulation.

As pointed out earlier in the report, the panel 7 back cone trapezoid surface insulation material during the March testing was different from the remainder of the receiver back cone surface material. The panel 7 material was 3000 board as opposed to the blanket material used on the remainder of the cavity surface. The panel 7 board did not fail even though it received even more incident flux than panel 3. When the panel 3 insulation began to deteriorate during the March tests, heliostats were chosen that placed as much energy as practical on panel 7 rather than panel 3. In light of this, the experimental temperatures shown for panel 7 would be expected to be those most representative of the trapezoid during testing without insulation

Table 11.2-3. Comparison of Posttest Analytical and Experimental Insulation Temperatures

## Comparison of Posttest Analytical and Experimental Insulation Temperatures

Temperatures in °C [°F]

T/C location		Panel number				
		①	③	⑤	⑦	
Cover trapezoid	Cold face	E	58 (137)	240 (464)	72 (162)	117 (242)
		A	61 (141)	123 (253)	68 (154)	93 (200)
2 in from hot face		E	812 (1,494)	1,321 (2,409)	871 (1,599)	1,105 (2,021)
		A	837 (1,538)	1,107 (2,024)	865 (1,589)	1,029 (1,884)
Frame rectangle	Cold face	E	56 (133)	92 (197)	87 (189)	56 (132)
		A	69 (156)	80 (176)	77 (171)	66 (150)
2 in from hot face		E	—	871 (1,599)	843 (1,549)	863 (1,585)
		A	835 (1,535)	858 (1,576)	829 (1,525)	853 (1,567)

- Experimental data from March 24, 1979, EB-9F, 11.78 hours (instantaneous data).
- Analytical data based on inputs from 10-min average of experimental conditions

failure.

However, a comparison of the panel 7 analytical and experimental temperatures revealed a remaining discrepancy between the two temperatures. Because the cold face experimental temperature agreed well with analytical prediction, the second factor, which accounted for the discrepancy in analytical temperatures for the back cone trapezoid insulation, was found in the thermal model itself. The first incident solar-flux patterns of the receiver back cone surface repeated in Figure 11.2-11 show that panels 3 and 7 received some of the highest incident flux levels. In fact, after absorption-reflection in the cavity, about 37% of all the energy absorbed on the receiver back cone was absorbed on panels 3 and 7, while panels 3 and 7 accounted for only 23% of the surface area. In comparison, panels 1 and 5 absorbed 13% of the total absorbed on the back cone. It appeared that panels 3 and 7 should not have been represented by a single node each, but should have been broken into multiple nodes so that, on the average, the energy absorbed on each cover node would have been uniform. This also applied to the placement of thermocouples. The experimental data of Table 11.2-3 for panels 3 and 7 are responding to localized hot spots on the insulation while the analysis represents an averaged temperature for the entire panel. Apparently the approach used in the thermal model was appropriate for panels 1, 2, 4, 5, 6 and 8 but not so for panels 3 and 7. A revision in the thermal model to account for this factor required a very significant amount of effort and was not considered appropriate at this time.

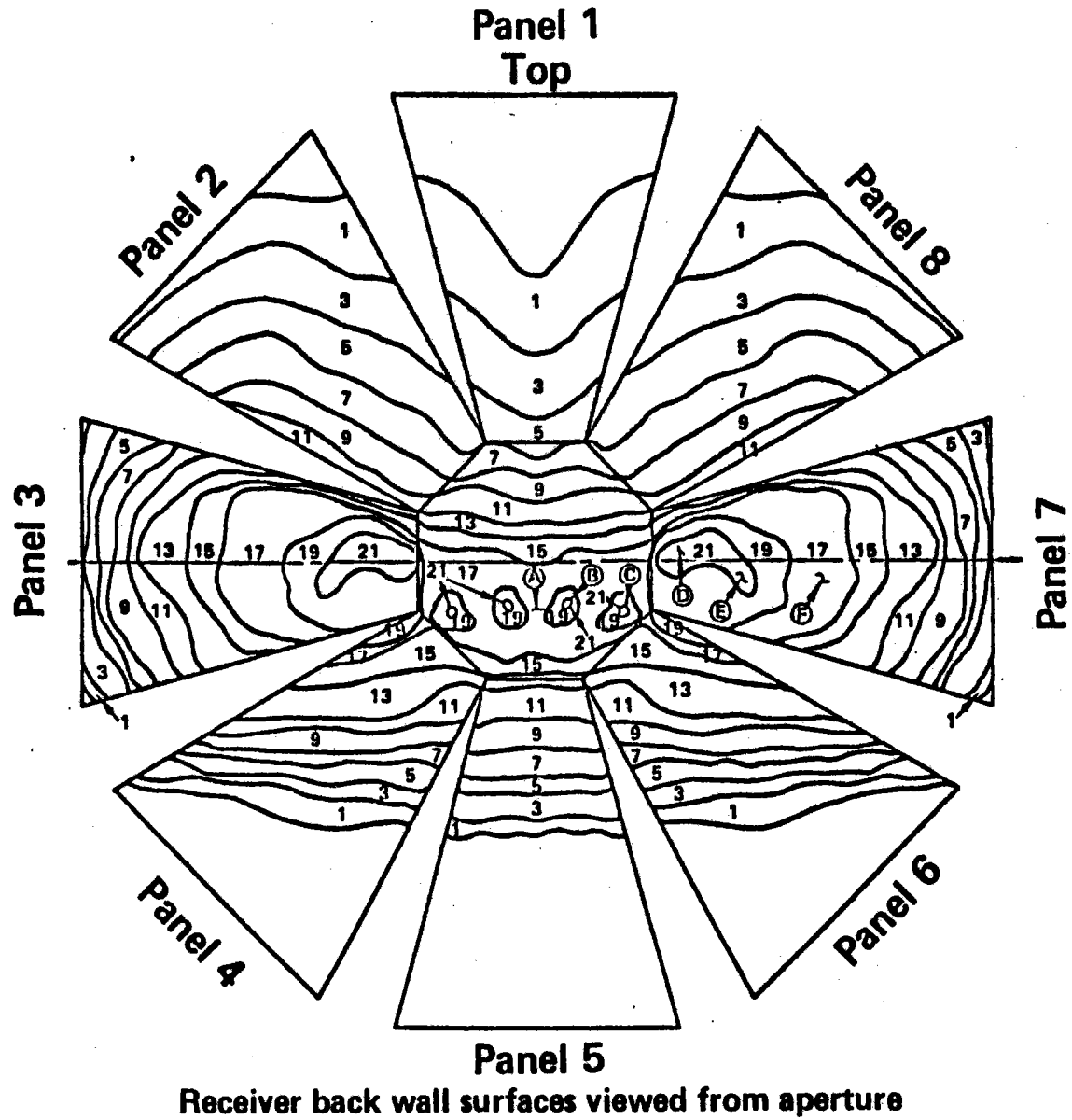
#### 11.2.2 Posttest Thermal Model

The receiver pretest thermal model required specification of postulated test conditions, thereby requiring the modeling of the recuperator and air supply subsystem. During testing, the inlet mass flow rate and gas temperature to the receiver heat exchanger were measured. Therefore, one of the revisions to the pretest thermal model was to remove the recuperator and air supply nodes and fix the receiver panel mass flow rate and inlet gas temperature. Also because heliostat operation was continually monitored, the relative solar input from the various parts of the heliostat field was also fixed. As reported earlier, the total solar input through the receiver aperture



Figure 11.2-11. Receiver Cover Incident Flux Map

# Receiver Cover Incident Flux Map



from the heliostat field was not as easily measured as initially planned. The posttest analysis proceeded with the best available solar input data.

Ideally, to explore the overall receiver performance and panel heat balance discrepancies noted in Section 11.1, an algorithm that could account for any free-forced convection phenomena inside the cavity would be desirable. Unfortunately, at this time no such algorithm was available that could treat the generalized cavity with all the potential interactions. Convective energy losses from solar central receivers are not presently well understood. Programs have been initiated to study and quantify these phenomena (Ref. 11). The approach taken in the BMSR posttest thermal model was to add sources to each receiver panel in such a way as to force agreement of the panel heat balance to the experimental values. The resulting analytical heat exchanger and insulation temperatures were compared to actual test data. If reasonable agreement was obtained, mechanisms to justify the source additions were evaluated.

Although not completely satisfactory and applicable only to these specific receiver conditions, this approach yielded some qualitative insights into the convective effects occurring inside the cavity. Also, in conjunction with the transient cooldown data, an estimate of the convective loss magnitude was available.

The posttest BMSR thermal model is shown in Figure 11.2-12. Included in this model are the updated insulation thermal conductivities presented in Section 11.2-1. Also, minor revisions to the insulation nodal network and heat exchanger gas sources are included.

---

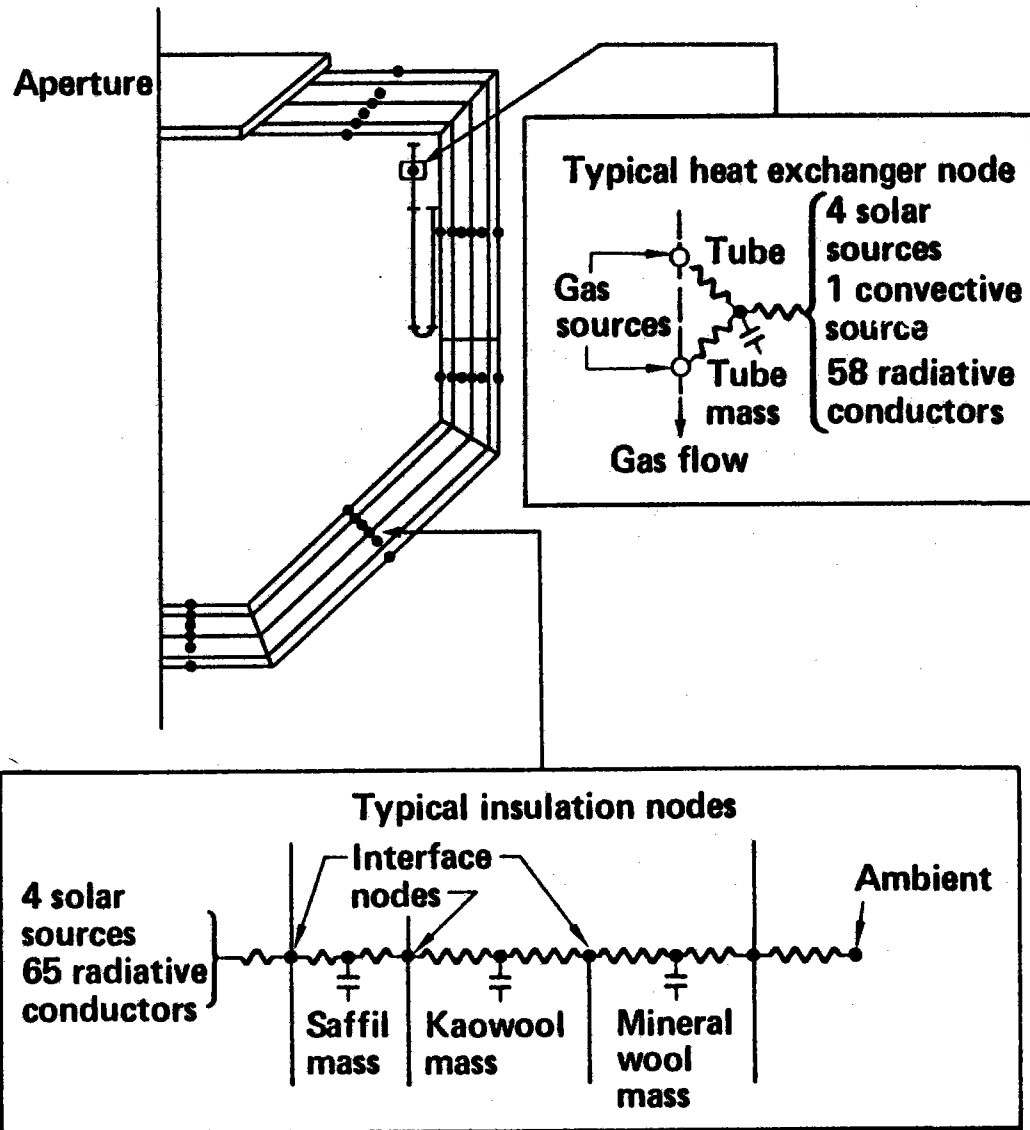
\*M. Abrams. "The Receiver Energy Loss Program." (Sandia Livermore), DOE SemiAnnual Central Receiver Review. Sept. 1979, Williamsburg, Virginia

Figure 11.2-12. Posttest BMSR Thermal Model

# Posttest BMSR Thermal Model

## Details of model

- Receiver structure, 72 nodes
- Insulation, 207 nodes
- Heat exchangers
  - Tubing, 32 nodes
  - Gas, 48 nodes
- 260 solar sources
- 32 gas sources
- 32 convective sources
- 2,121 radiative conductors
- 429 conductors
- Temperature-dependent insulation thermal conductivity
- Temperature-dependent working fluid viscosity, heat capacity, thermal conductivity
- Temperature-dependent insulation emissivity correction
- Time-dependent solar input and ambient temperature
- Heat exchanger thermocouple radiative correction
- Receiver overall heat balance and specialized printouts
- Receiver control logic



A comparison of posttest analytical data with experimental data is given in Table 11.2-4. The inputs to the analysis included the gas inlet, mass flowrate, and applied source, as noted in the table, and also the ambient temperature and solar input. The input values were based on a 10-min average of the experimental data. The experimental data expressed in Table 11.2-4 were obtained from one particular data record and represented an instantaneous data reading. In some instances, several thermocouples were located at the same general area of the panel; the temperature range noted at the particular time is presented. In comparing experimental and analytical tube temperatures, it was important to compare the analytical indicated reading, designated with an I, with the experimental temperature. The indicated reading was based on the calculated tube temperature, but also corrected for the radiation environment of the thermocouple. In general, the indicated analytical tube thermocouple readings were in, or close to, the range of temperatures recorded during testing.

The sum of the applied sources from Table 11.2-4 is -15.7 kW. For other test data points, this net loss ranged as high as 50 kW. An interesting observation is that the applied sources on the bottom panels 4, 5, and 6 were net losses, while the top panels were net additions. Panel 2 was an exception; however, at this time the panel 2 mass flow control was defective and did not allow the mass flow to be adjusted to maintain near 837°C (1500°F) outlet temperature. If operating correctly, one would expect the panel 2 applied source to follow the pattern for the other top panels. This, in fact, was the case for analyses of earlier tests performed with the panel 2 mass flow rate control operative. Because some of the applied sources were positive (net additions) while others were negative (net losses), it appeared there were two distinct effects operative in the cavity interior. One mechanism redistributed energy from the lower panels to the upper panels. A natural convective mechanism would be indicated. A second mechanism was the overall net loss of power from the receiver. This second mechanism was consistent with the observation of flow from the aperture rim as noted by the aperture anemometer (Section 8.5).

Mechanisms that were postulated that would account for the increased losses included radiative-reflective losses, conduction losses, and convection

Table 11.2-4. Comparison of Posttest Analytical and Experimental Data

# Comparison of Posttest Analytical and Experimental Data

		Panel number							
T/C location		①	②	③	④	⑤	⑥	⑦	⑧
Panel heat transfer (kilowatts)	E	103.7	85.9	98.1	83.0	78.7	89.9	99.0	104.7
	A	107.2	87.7	94.5	72.4	65.7	85.6	101.4	107.4
Gas inlet (°C [°F])	E	487 (908)	488 (911)	488 (911)	491 (915)	488 (911)	488 (911)	483 (901)	481 (898)
	*A	487 (908)	488 (911)	489 (912)	490 (914)	488 (911)	488 (911)	484 (903)	481 (898)
Tube inlet (°C [°F])	E	732 (1,349)		728-743 (1,342-1,370)		726-746 (1,339-1,374)		707-726 (1,304-1,339)	
	A	650 (1,202)		652 (1,260)		665 (1,229)		648 (1,199)	
	**I	724 (1,335)		724 (1,336)		734 (1,353)		722 (1,331)	
Tube bend (°C [°F])	E	***		940-956 (1,724-1,752)		884-941 (1,624-1,726)		925-965 (1,697-1,769)	
	A	814 (1,497)		818 (1,504)		816 (1,500)		817 (1,502)	
	I	892 (1,637)		911 (1,671)		894 (1,642)		920 (1,688)	
Tube exit (°C [°F])	E	878-883 (1,613-1,622)		839-876 (1,542-1,608)		859-864 (1,578-1,587)		863-879 (1,585-1,614)	
	A	848 (1,559)		833 (1,532)		823 (1,514)		837 (1,539)	
	I	869 (1,597)		858 (1,576)		851 (1,563)		861 (1,581)	
Gas outlet (°C [°F])	E	817 (1,502)	804 (1,479)	812 (1,493)	816 (1,500)	813 (1,493)	812 (1,493)	813 (1,496)	809 (1,489)
	A	809 (1,489)	802 (1,475)	806 (1,482)	807 (1,485)	806 (1,483)	803 (1,478)	806 (1,482)	802 (1,476)
Mass flow rate (kg/s [lb/s])	E	0.280 (0.618)	0.243 (0.536)	0.271 (0.597)	0.288 (0.502)	0.216 (0.476)	0.248 (0.547)	0.267 (0.589)	0.284 (0.627)
	*A	0.296 (0.653)	0.250 (0.551)	0.266 (0.587)	0.204 (0.449)	0.185 (0.407)	0.243 (0.535)	0.281 (0.620)	0.299 (0.659)
Applied source	*A	+15.0	-5.40	+2.60	-19.0	-25.2	-6.78	+9.3	+13.8

\*Input data (based on 10-min average)

\*\*Indicated reading (includes T/C radiation)

\*\*\*T/C inoperative

● Experimental readings from March 24, 1979, EB-9F, 11.78 hours (instantaneous data)

(natural and forced). Potential increases in the radiative-reflective or conduction losses over the predicted values were investigated. However, none of these could both produce the observed redistribution of energy and net loss of energy consistently measured during testing at all solar power input levels. A convective mechanism was strongly indicated.

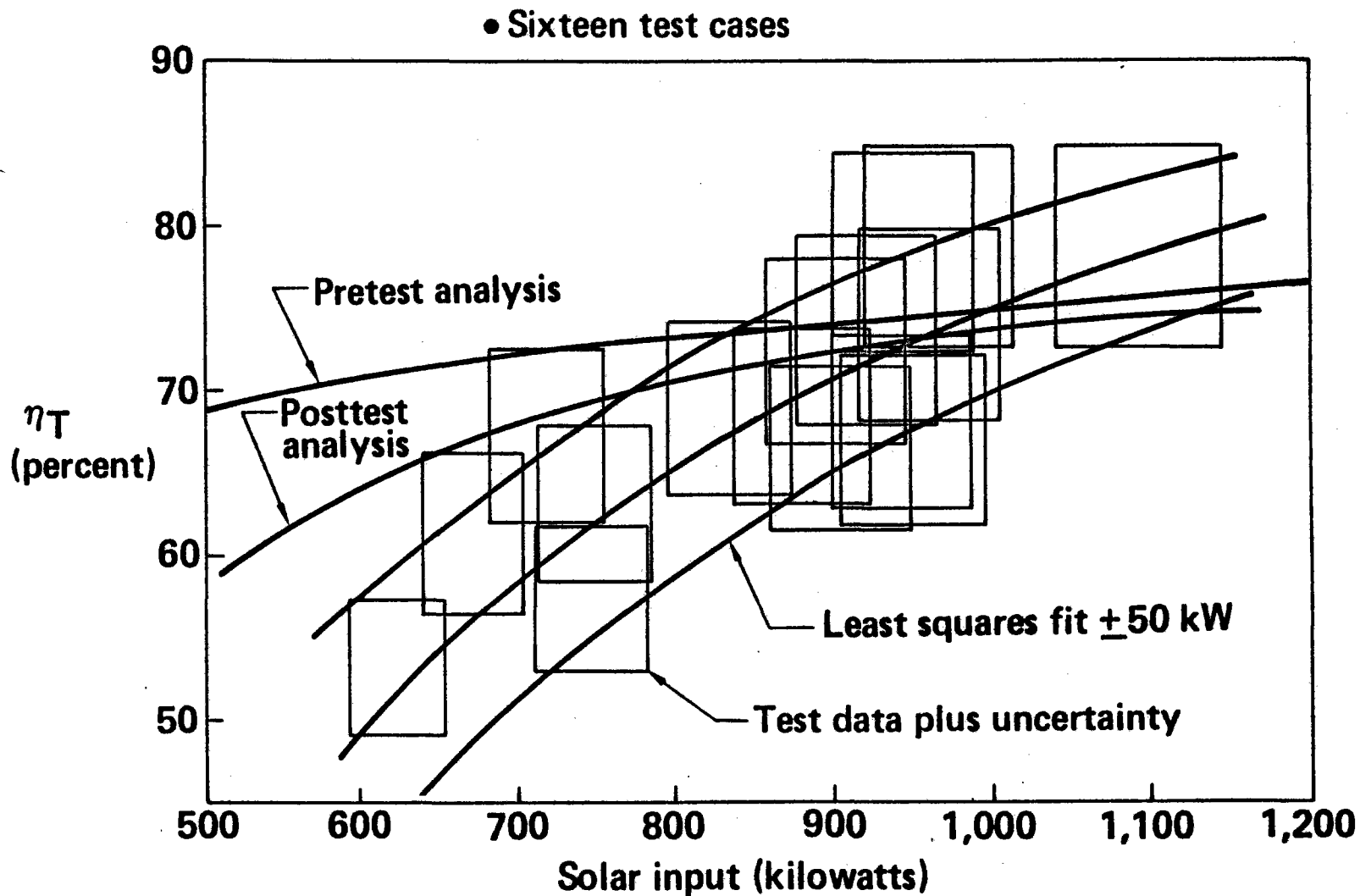
Wind direction and speed were measured at 15-min intervals at several different elevations by the CRTF facility throughout the BMSR testing. During evaluation of the test data, winds were noted over a distribution of  $\pm 40^\circ$  from north. However, no correlation was noted between the projected convective losses and the wind direction or speed. This was to be expected because the CRTF tower was rather large in cross section and the BMSR was somewhat tucked inside the 43m (140 ft) level. This may not have been the case for a receiver situated atop a more slender tower and exposed. The lack of correlation with wind speed or direction for the BMSR tests pointed towards a natural convective mechanism rather than a forced convective mechanism in the cavity interior.

Recognizing that definitive calculations of the natural convective behavior in cavities did not lend itself to simple calculations, a first-order investigation of heat transfer and fluid mechanics revealed that the observed aperture-rim velocity of 1.2m to 1.5m (4 to 5 ft/s) was consistent with net receiver losses as high as 65 kW if a large portion of the aperture area was active in the convective process and the exiting air temperature was in the range of 177 to 204°C (350° to 400°F). Further data on the convective mechanism were noted during the transient cooldown tests and will be discussed in the following section.

A comparison of the posttest analysis and experimental results for changing solar input is presented in Figure 11.2-13. The analytical data were based on the best operating conditions encountered during BMSR testing and with a constant total 50 kW convective loss. As can be seen, the posttest analysis agreed better at lower power levels, but still somewhat above the experimental observations. A potential cause of this would be an increase in convective losses at lower power levels, although no test data or analytical observations presently confirm this hypothesis. Calculation of

Figure 11.2-13. Receiver Thermal Efficiency as a Function of Solar Input Power  
Based on Posttest Analysis

## Receiver Thermal Efficiency as a Function of Solar Input Power Based on Posttest Analysis



the convective loss estimate was hampered because the uncertainty in the solar input (about  $\pm 50$  kW) was on the same order of the expected convective loss. Figure 11.1-1 showed that significant scatter was experienced in the testing. It would be expected that 30 to 40 identical test points would allow a reduction in some of the test uncertainties, giving a better estimate of the convective loss. This number of test data points was not feasible owing to limitations of budget and test facility availability.

### 11.2.3 Transient Cooldown

As noted in Section 11.1 and Figure 11.1-7, a definite stratification of the receiver heat exchanger temperatures was experienced during transient cooldown tests. This section explores these noted phenomena more carefully, especially their implications of convective effects occurring in the cavity.

The energy removal mechanisms acting on the receiver heat exchanger tubes during solar operation are depicted in Figure 11.2-14. The expected order of dominance of these mechanisms was (1) forced convection on the tube interior due to the flow of the working fluid, (2) thermal radiation, and (3) natural convection on the tube exterior. Transient cooldown tests were performed by both turning away the heliostat field and turning off the receiver mass flow as quickly as possible. By removing the forced convection on the tube interior, a relative sizing of the natural convection to radiation loss mechanism was made.

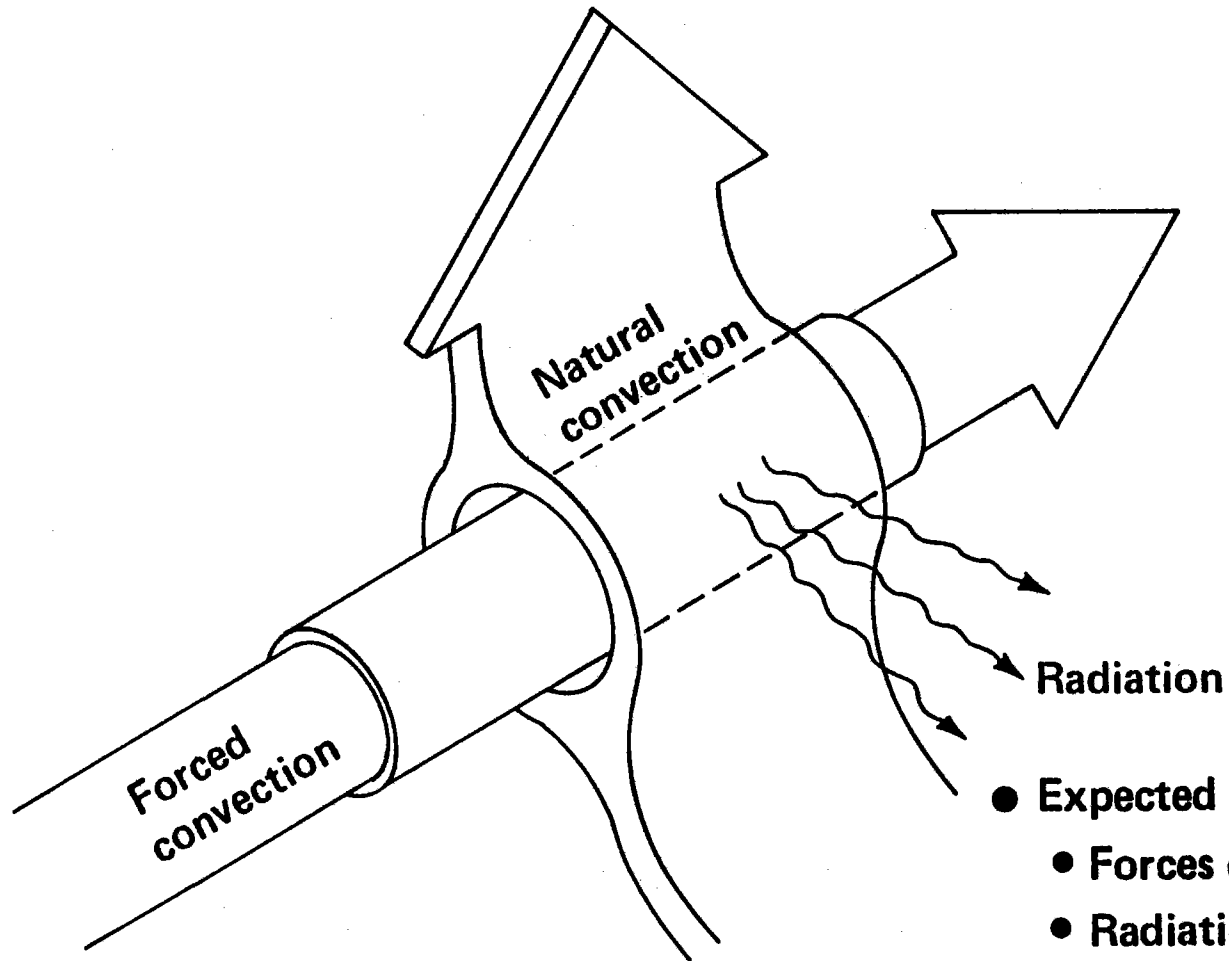
Two transient cooldown tests were performed, one at about 4:30 PM hours on March 24, 1979, and the other at about 4:00 PM hours on January 23, 1979. The calorimeter data for both days are presented in Figures 11.2-15 and 11.2-16. A characteristic of the transient cooldown test was for the calorimeter data, both frame and cover calorimeters, to coalesce into a narrow band that subsequently decayed. This narrow band of calorimeter readings from widely dispersed locations inside the cavity indicated the rapid establishment of a nearly uniform but decaying thermal radiative environment in the receiver cavity.

The tube thermocouples responded rapidly to the cavity environment because



Figure 11.2-14. Receiver Tube Energy Removal Mechanisms

## Receiver Tube Energy Removal Mechanisms



628

- Expected order of dominance:
  - Forces convection
  - Radiation
  - Natural convection

Figure 11.2-15. Calorimeter Data

# Calorimeter Data

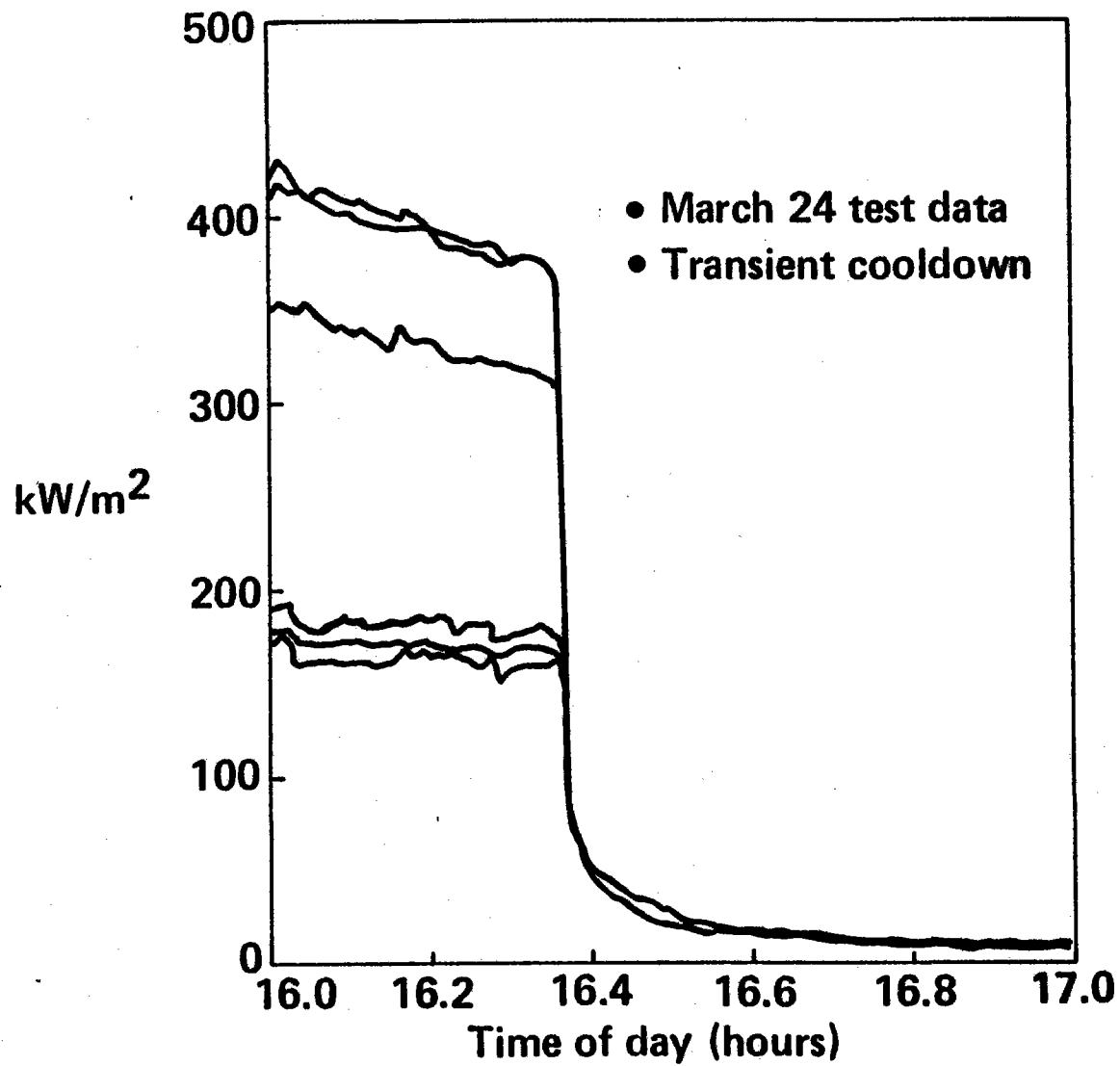
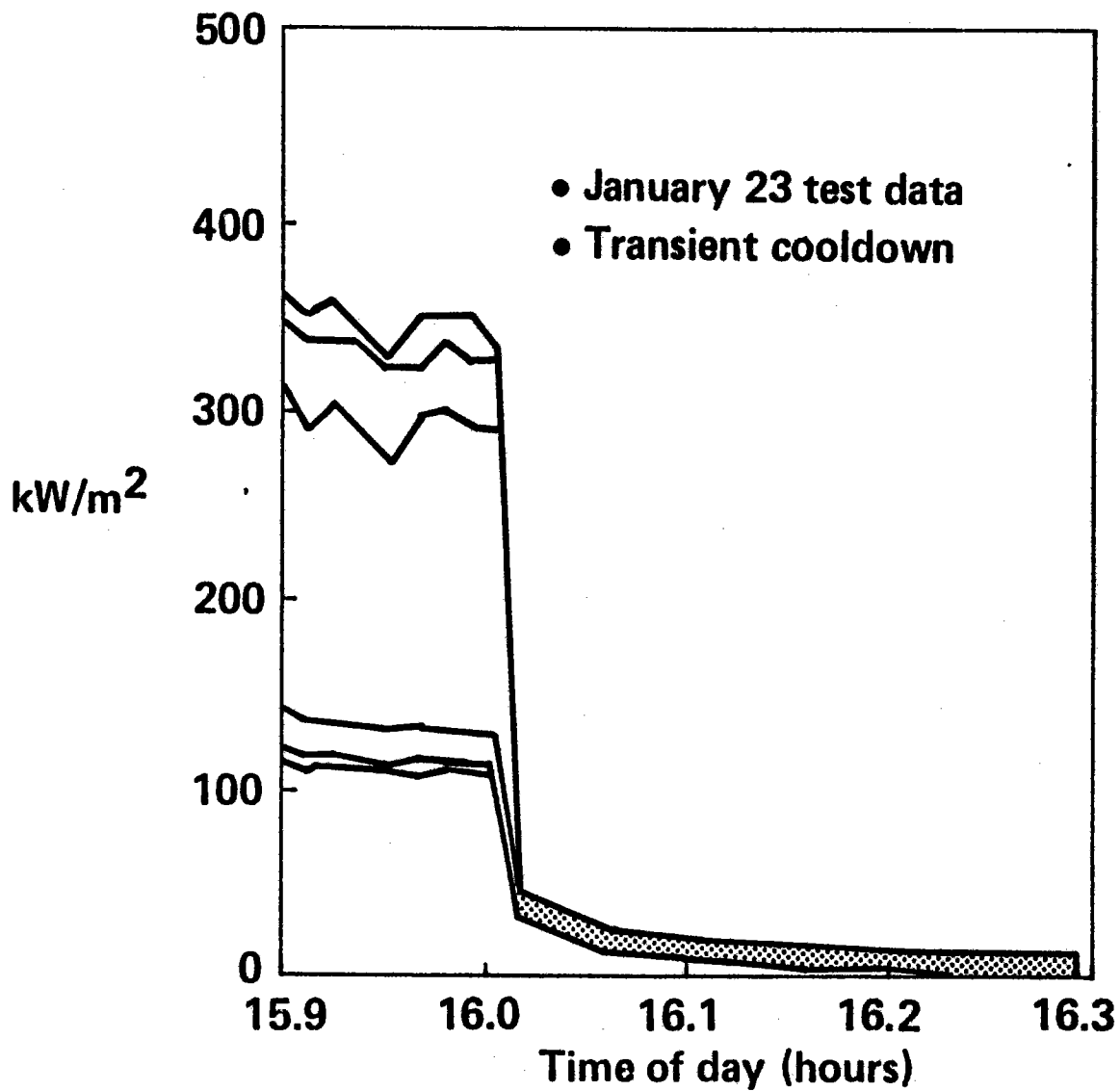


Figure 11.2-16. Calorimeter Data

### Calorimeter Data



630

of their low mass and the low mass of the thin-wall tubes. The tube thermocouple readings during the transient cooldown therefore represented an accurate register of local air temperatures. Because the heat exchanger thermocouples were located at different vertical positions, as demonstrated in Figure 11.2-17, the temperatures could be plotted against the thermocouple vertical position. To take out the effects of the decaying temperature level, an average of 29 heat exchanger thermocouples was formed for each data record. The difference between the individual thermocouple reading and the average is plotted against the vertical distance from the aperture centerline for several representative times during the March 24 transient cooldown in Figures 11.2-18 through 11.2-22. Also presented in the figures are the times relative to the start of the transient cooldown and the average thermocouple reading.

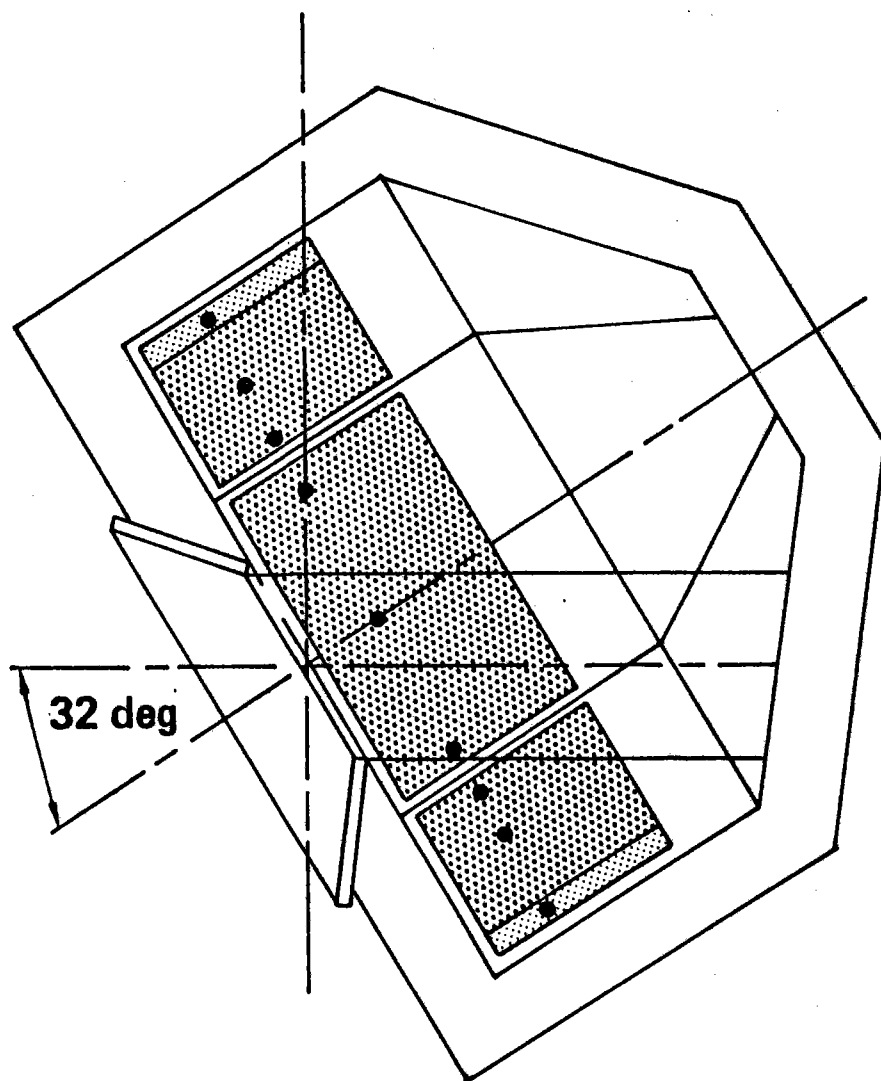
The data from these figures portray negligible stratification about 10 sec before test initiation. At this time, the solar input and the gas mass flow would be expected to dominate the thermocouple reading. Figure 11.2-20 shows that about 20 sec after test initiation, the thermocouple readings were even more uniform. Both solar input and mass flow are known to have been removed in 5 to 10 sec. The time constant of the tube thermocouples was expected to be about 5 to 10 sec. The thermocouple readings of Figure 11.2-20 represent actual experienced local cavity air temperatures. The radiation mechanism was expected to produce more uniform cavity temperatures, whereas a natural convection mechanism was expected to stratify temperatures. Apparently, the radiation mechanism, as expected, exerted more influence on local cavity temperatures during solar operation and just after the initiation of a transient cooldown.

As the transient cooldown continued, Figures 11.2-21 and 11.2-22 demonstrate increasing amounts of stratification, thus indicating the convection mechanism beginning to become more influential. This increasing stratification was also apparent in the January 23 data. Figure 11.2-23 presents January 23 data similar to that of the March 24 data. In all of the transient cooldown tests, the lower and upper heat exchanger temperatures appeared to form nearly uniform layers of temperature. Most of the stratification appeared to occur in the region of the aperture. Based

Figure 11.2-17. Receiver Convective Losses

# Receiver Convective Losses

632



Distance from + aperture centerline	Thermocouple designator			Panel number
	-12	-13	-14	
	.1	.1	.1	
	.2		.8	
	.8	2 8	.2	
	3'		7'	
		3 7		Aperture top
0				Aperture centerline
	.7		.3	Aperture bottom
	4'	4 6	6'	
	6 5'	5'	4 5'	

Figure 11.2-18. BMSR Transient Cooldown

# BMSR Transient Cooldown

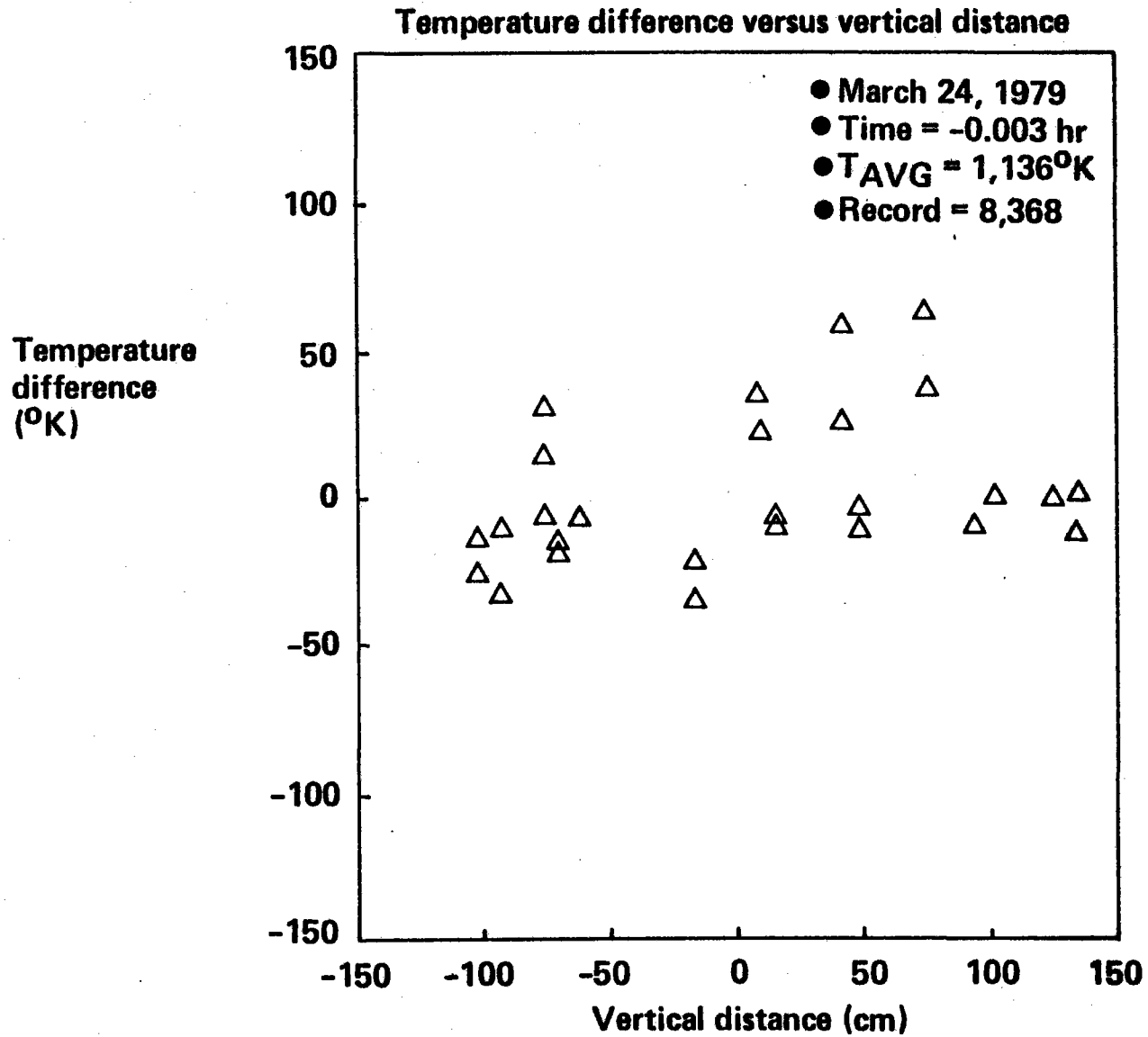


Figure 11.2-19. BMSR Transient Cooldown

# BMSR Transient Cooldown

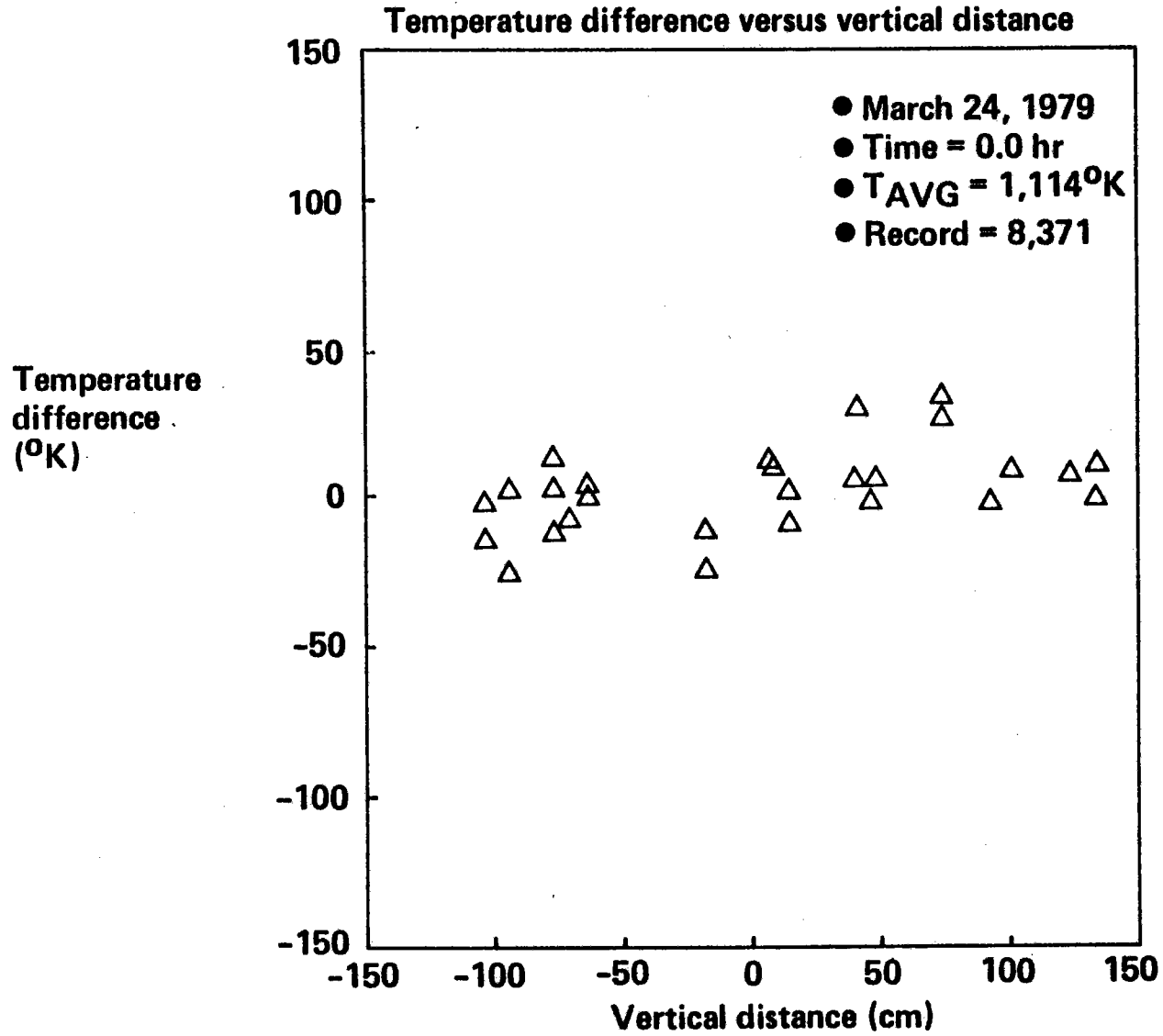


Figure 11.2-20. BMSR Transient Cooldown

# BMSR Transient Cooldown

Temperature difference versus vertical distance

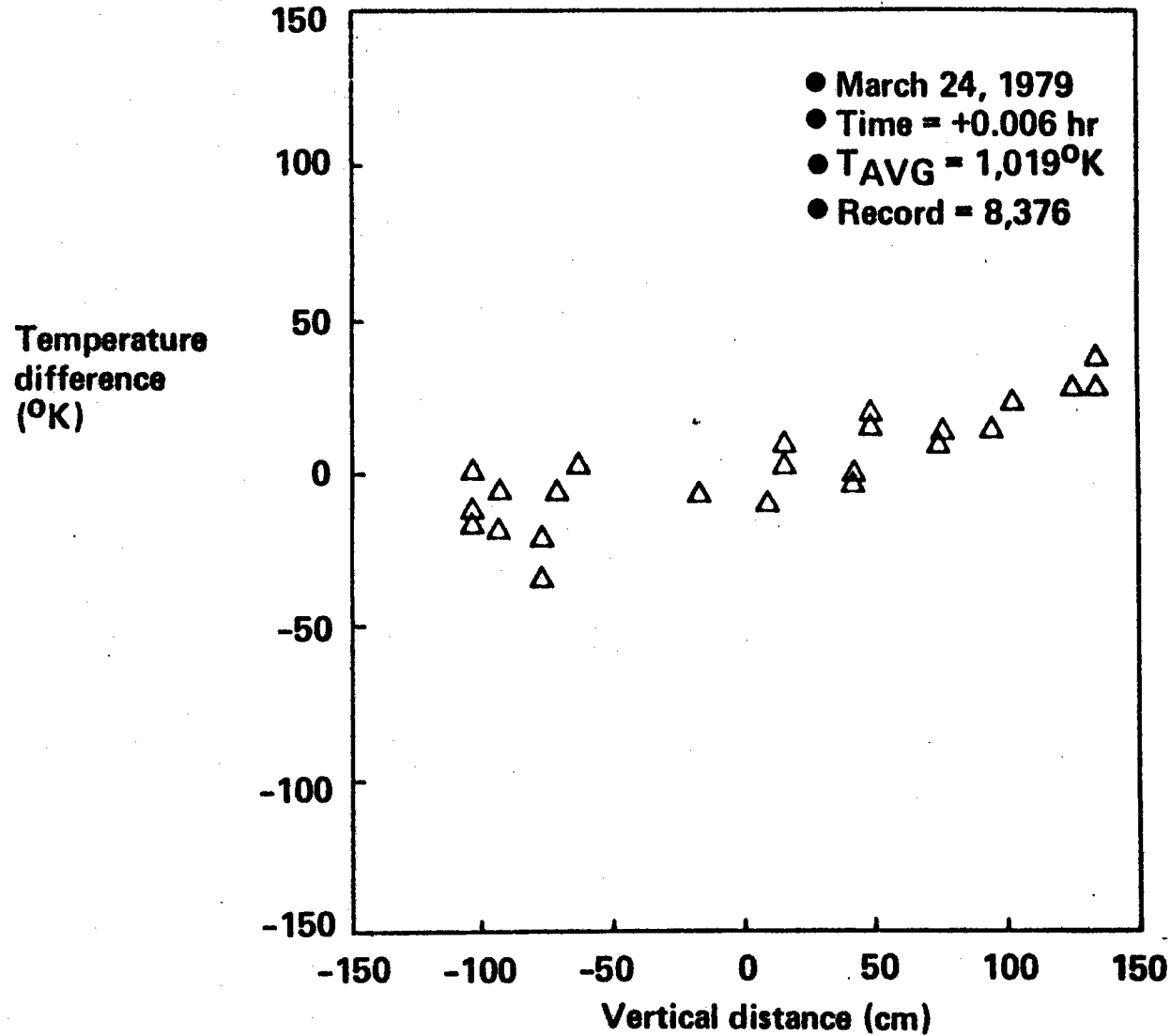




Figure 11.2-21. BMSR Transient Cooldown

# BMSR Transient Cooldown

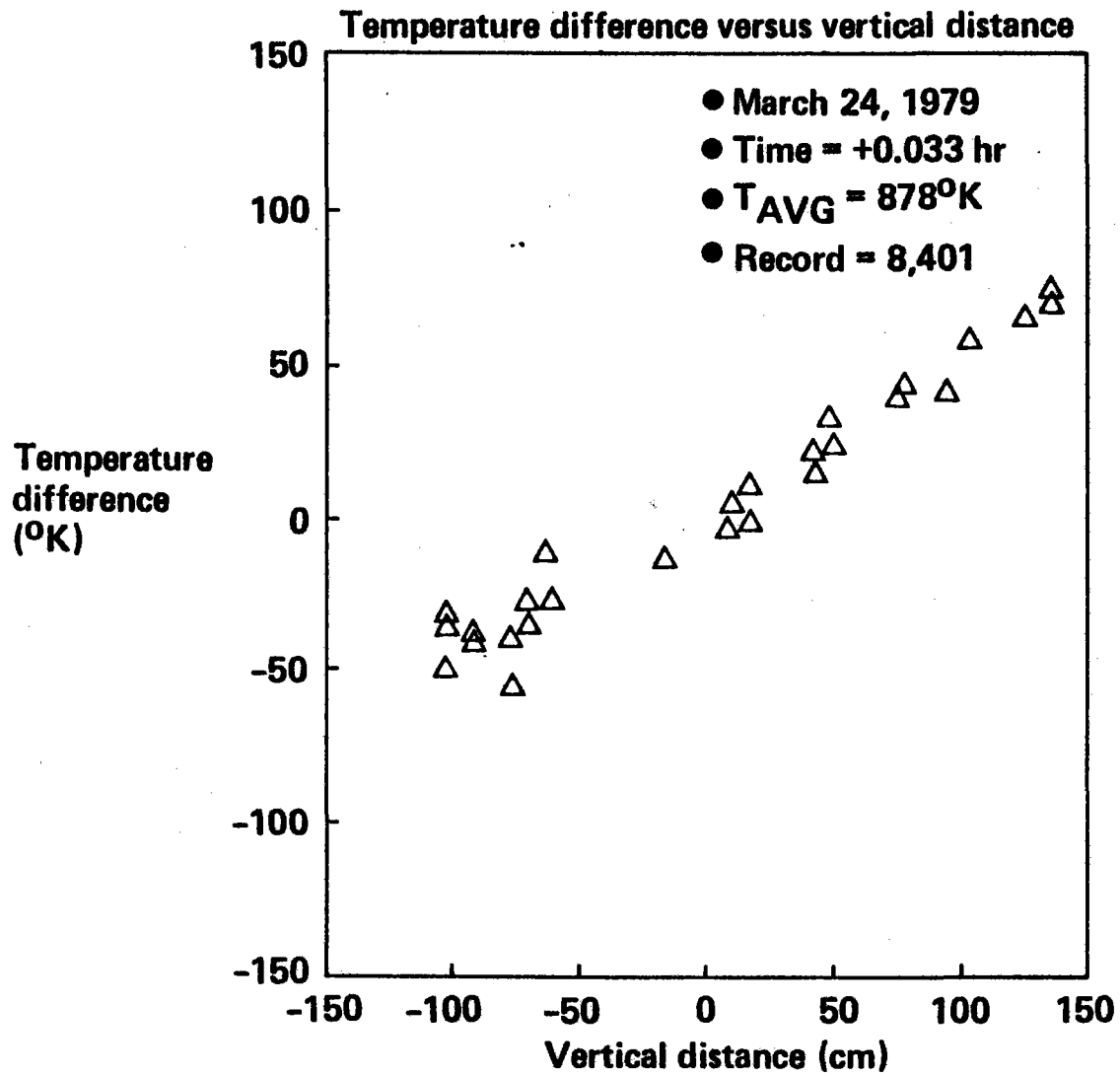


Figure 11.2-22. BMSR Transient Cooldown

# BMSR Transient Cooldown

Temperature difference versus vertical distance

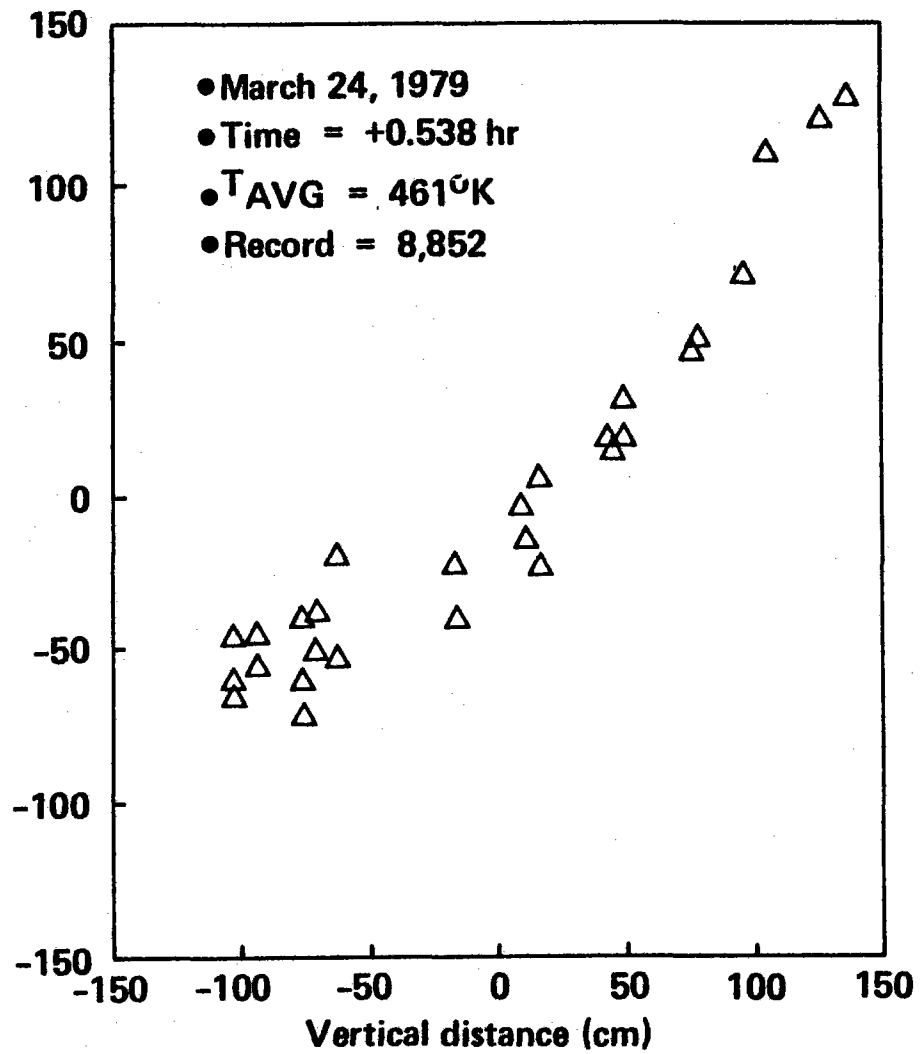
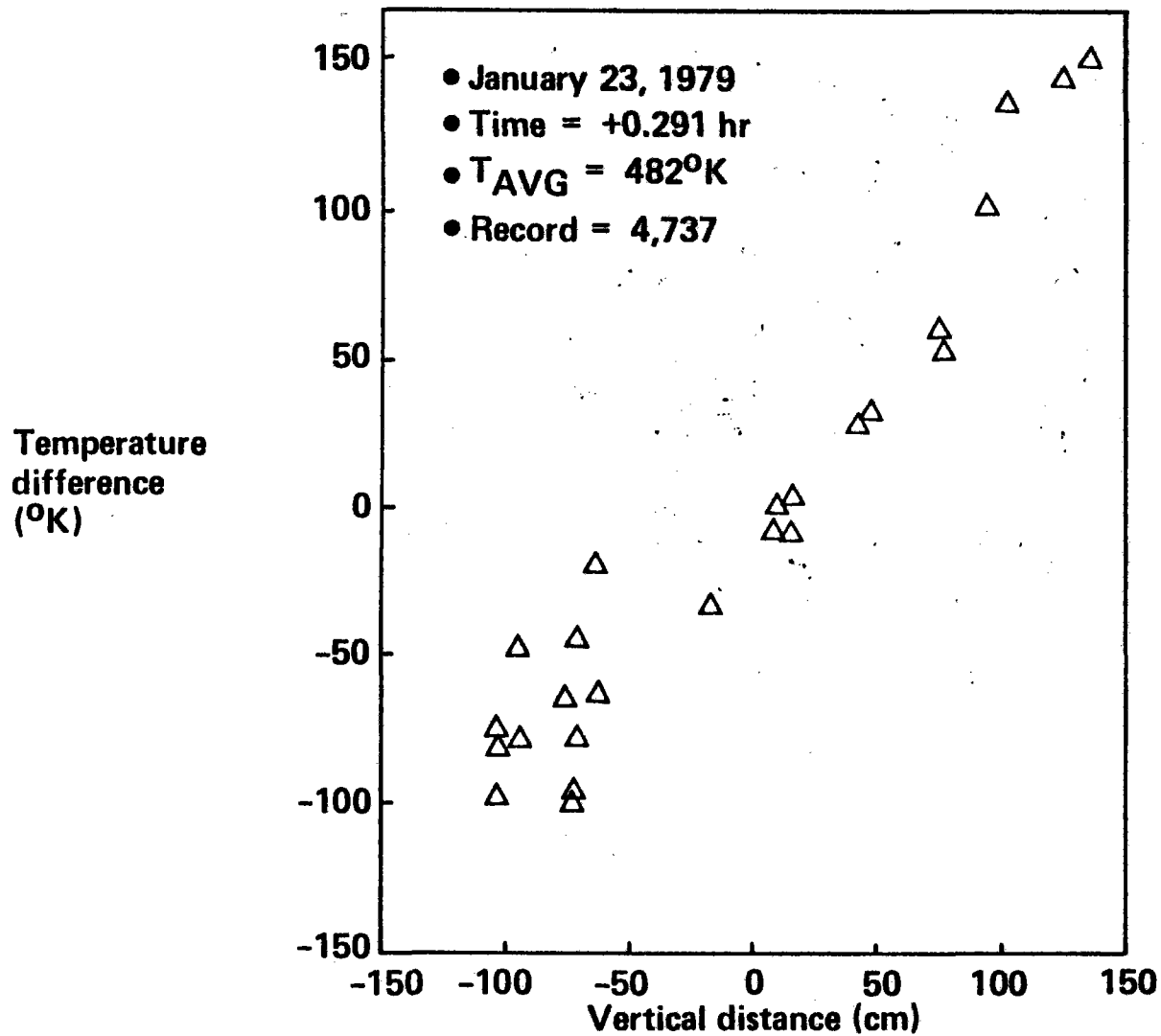


Figure 11.2-23. BMSR Transient Cooldown

# BMSR Transient Cooldown

● Temperature difference versus vertical distance



on the observations of the transient cooldown data, the convective flows of the receiver cavity are postulated in Figure 11.2-24. Although not shown, three-dimensional effects would be expected to be important in the cavity also.

Figure 11.2-25 presents a plot of the average heat exchanger temperature from the data of Figures 11.2-18 through 11.2-22. Also presented is the average cavity temperature as determined from the calorimeter data of Figure 11.2-15. As can be seen, the heat exchanger temperatures assumed intermediate values between the cavity temperature,  $T_c$ , and the ambient temperature of about 4.4°C (40°F). Based on this data, a simplified thermal model was assumed, as shown in Figure 11.2-26. This was a three-node model with radiative input to the tube coming from the higher cavity temperature,  $T_c$ , and losses going to the ambient,  $T_{amb}$ , by radiation and convection. The following functional behavior was assumed:

$$\frac{dT}{d\tau} = A(T_c^4 - T^4) - B(T^4 - T_{ambient}^4) - C(T - T_{ambient})^n$$

The experimental data from the March 24 transient cooldown shown in Figure 11.2.3-12 were least-squares curve fit to this functional behavior. The results are shown below (T in °R):

$$\begin{aligned} \frac{dT}{d\tau} = & 0.656 \times 10^{-9} (T_c^4 - T^4) - 0.698 \times 10^{-9} (T^4 - T_{ambient}^4) \\ & - 0.304 (T - T_{ambient})^{1.33} \end{aligned}$$

Figure 11.2-24. Potential Convective Flows During Receiver Cooldown

# Potential Convective Flows During Receiver Cooldown

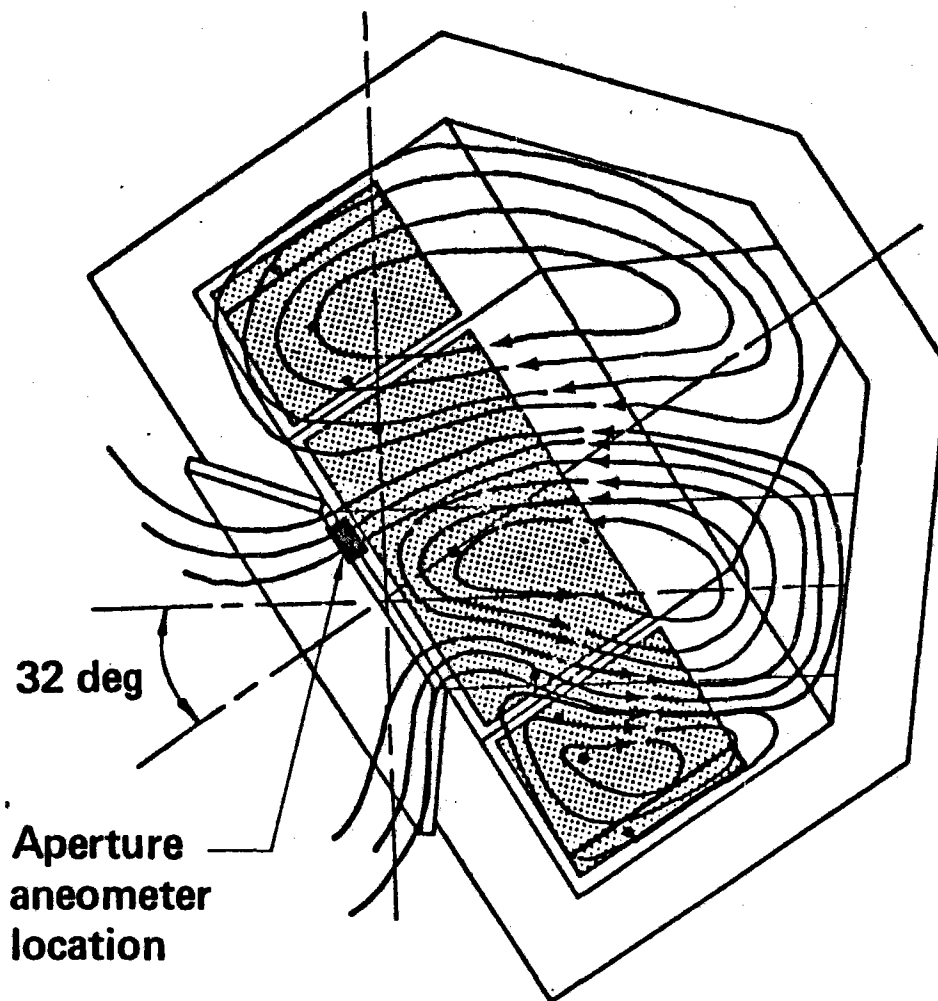


Figure 11.2-25. BMSR Transient Cooldown (Average Receiver Temperatures)

## BMSR Transient Cooldown (Average Receiver Temperatures)

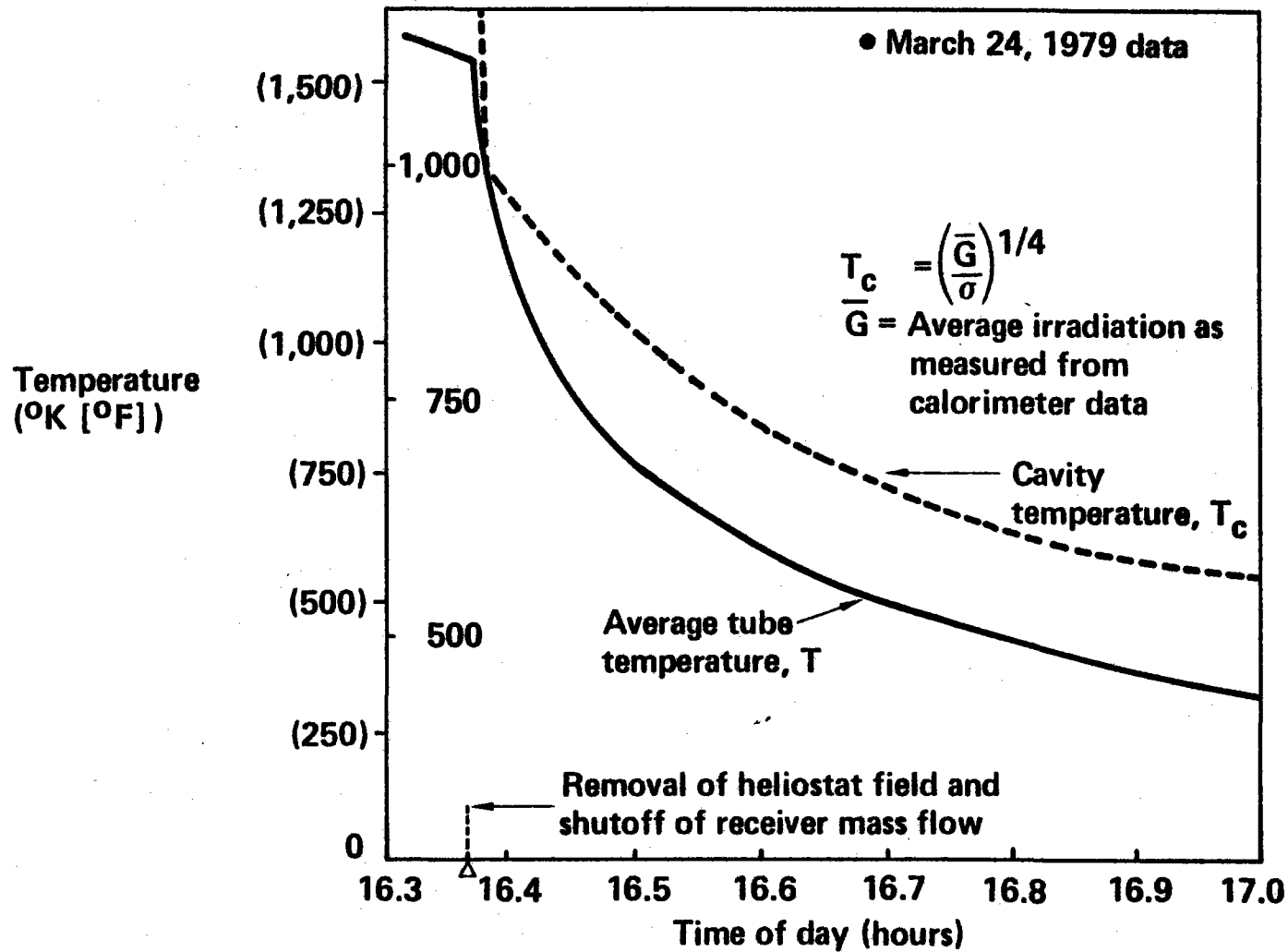
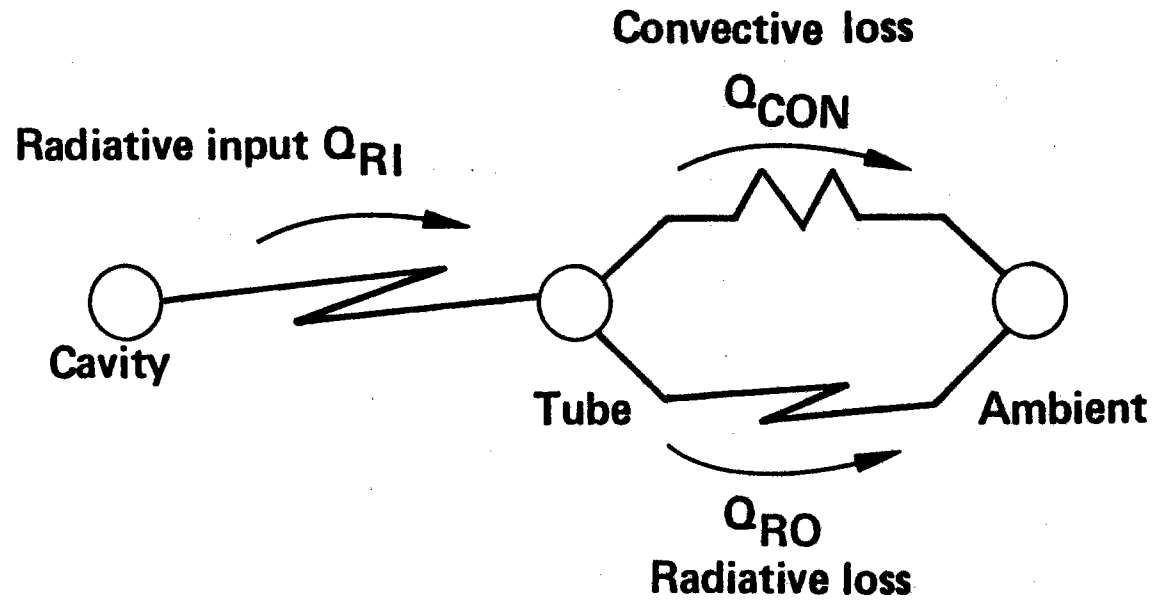


Figure 11.2-26. Simplified Thermal Model of Transient Cooldown

## Simplified Thermal Model of Transient Cooldown



The curve fit residual was 0.2% at  $T = 1726^{\circ}\text{R}$  (992K) and 7.6% at  $T = 1236^{\circ}\text{R}$  (687K), indicating a very reasonable matching of experimental data. The relative behavior of the radiative and convective losses are then

$$\frac{Q_{RO}}{Q_{CON}} = \frac{0.698 \times 10^{-9} (T^4 - T_{\text{ambient}}^4)}{0.304 (T - T_{\text{ambient}})^{1.33}}$$

Extrapolation of this function relationship to the full-power solar operation conditions is shown in Figure 11.2-27. Based on this extrapolation of data, the ratio of radiative to convective losses at full power is 2.33. The posttest thermal analysis predicted at full-power conditions a radiative loss of 120 kW. This simplified analysis would then indicate a convective loss of about 50 kW at full power conditions. This loss estimate was consistent with the best analytical predictions from the posttest thermal analysis.

#### 11.2.4 Independent Convective Flow Analysis

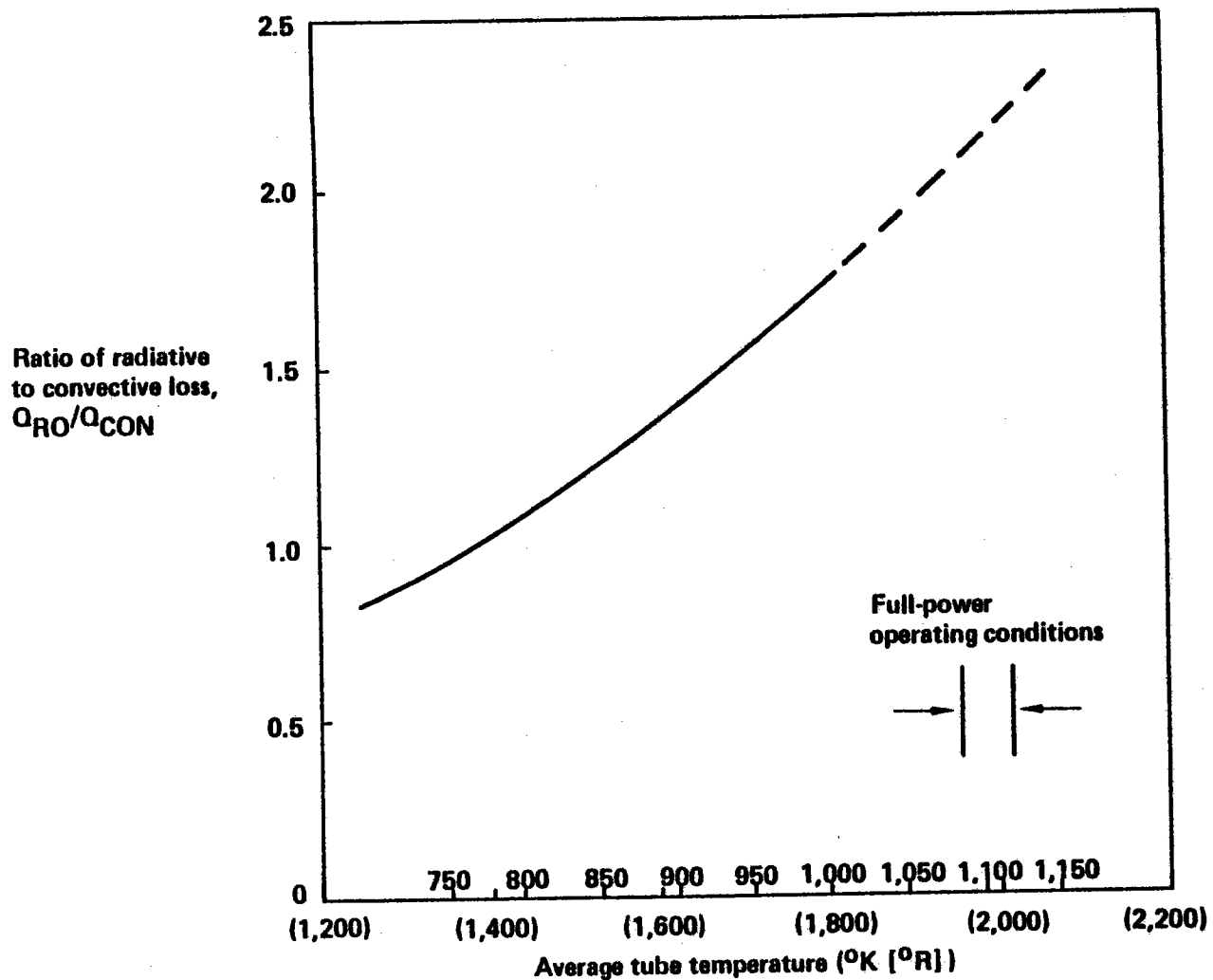
An independent analysis of the convective flow in cavity receivers was performed by Battelle Pacific Northwest Laboratories. BEC supplied PNL with the BMSR cavity geometrical data, cavity temperature data, and results from the aperture anemometer observations. PNL used their TEMPEST computer code to analyze a two-dimensional version of the BMSR cavity geometry. The TEMPEST code is a fully coupled, transient hydrothermal, finite-difference code currently under development at PNL. Although the code is capable of three-dimensional calculations, two-dimensional calculations were considered for simplicity. The results of their calculations point towards a nearly uniform temperature region in the cavity above the top aperture rim and the major amount of stratification occurring across the aperture region.

Although neither BEC or the PNL analyses are totally satisfactory, it appears their first attempts at understanding the convective flows in the cavity do support one another. Also, based on the results of these



Figure 11.2-27. Relative Sizing of Loss Mechanisms

# Relative Sizing of Loss Mechanisms



analyses, location of heat exchanger surfaces above the top aperture rim should minimize natural convection effects on the heat exchanger performance.

### 11.3 THERMAL ANALYSIS CONCLUSIONS

This subsection presents the major conclusions formulated as a result of the posttest thermal analysis.

#### Insulation Temperatures

After the insulation failures noted during testing and the measurement of insulation temperatures significantly above the pretest predictions, the potential for the peak insulation temperature being higher than the assumed 1649°C (3000°F) design limit was strong. However, as detailed in the previous section the peak insulation temperature expected during design point operation was 1455°C (2650°F). The effects of volume absorption of the solar energy in the Saffil layers, if present, were expected to produce a peak or maximum temperature less than the 1455°C (2650°F).

Figure 11.2-3 of the previous section indicated that the Kaowool and mineral wool could have exceeded their respective design temperature limits in the areas of highest incident solar flux. It is a strong possibility that the catastrophic insulation failures noted during testing were caused by mechanical failures (shrinkage) in the Saffil layer. When this shrinking and subsequent tearing of the Saffil occurred, its effective insulative capacity decreased, thus allowing the Kaowool-Saffil interface temperature to rise. Obviously, as soon as the Kaowool melted and removed the remainder of the existing Saffil, the situation became unstable and the Kaowool and mineral wool rapidly failed. Under this hypothesized failure scenario, the catastrophic failure would be thermal in nature (i.e., melting of the Kaowool, initiated by a mechanical failure rather than thermal failure of the Saffil). Appropriate design changes using more rigid insulation products (such as the Kaowool 3000 board insulation used in panel 7 during the March tests) should be able to alleviate the initial mechanical failure and the subsequent catastrophic failure.

### Overall Receiver Thermal Performance

Application of additional sources in the BMSR thermal model to simulate convective losses provided a closer agreement between analysis and experiment. It was concluded that windspeed and direction could not be correlated to the experimental data of this test indicating a natural rather than forced convective mechanism. It was also concluded that additional experimental data would have helped to relieve the experimental uncertainty in the test data evaluation. Also, the accurate measurement of solar input was especially important in determining the magnitude of convective effects, which may be only a few percent of the incident power.

The thermal model used in this RP377 program was concluded to be an accurate model of the receiver temperatures. Updates in the model that could increase its accuracy include a more detailed nodding of the high-incident-flux regions on the receiver back cone sections. Also precise modeling of the natural convective effects in the cavity would also increase its utility.

### Transient Cooldown

Investigation of transient cooldown test data pointed to the relative magnitude of the radiative and convective loss mechanisms. The convective mechanism became more influential at lower receiver cavity temperatures, producing increasing amounts of stratification in the vertical dimension. The largest amounts of stratification occurred across the aperture. It can be concluded that location of heat exchangers above the top of the aperture tend to minimize any convective cooling of the heat exchanger tubes and the resulting loss of receiver efficiency. Based on a first-order analysis of the transient cooldown data, the full-power convective losses for the BMSR configuration were extrapolated to be 3% to 5%. This estimate was concluded to be consistent with the magnitude of applied sources in the thermal model.

GAS COOLED CENTRAL RECEIVER -  
CLOSED CYCLE 1MWt BENCH MODEL TESTING

RP377-3  
FINAL REPORT

Volume: III

June 5, 1980

Prepared for  
Electric Power Research Institute  
3412 Hillview Avenue  
Palo Alto, California 94304

by  
Boeing Engineering and Construction Company  
P.O. Box 3707  
Seattle, Washington 98124

LEGAL NOTICE

This report was prepared by Boeing Engineering and Construction, as an account of work sponsored by the Electric Power Research Institute, Inc. (EPRI). Neither EPRI, members of EPRI, Boeing, nor any person acting on behalf of either: (a) makes any warranty or representation, express or implied with respect to the accuracy, completeness, or usefulness of the information contained in this report, or that the use of any information, apparatus, method, or process disclosed in this report may not infringe privately owned rights; or (b) assumes any liabilities with respect to the use, or for damages resulting from the use of, any information, apparatus, method, or process disclosed in this report.

## SECTION 12.0

### TEST DATA

The acquisition of test data and processing of the test data tapes were discussed in Sections 7.3 and 8.2. The interpretation and use of the test data tapes will be discussed in the following sections. Section 12.1 shows how to interpret and use the BEC version of the data tapes. Included is a "map" of the data layout and an example of a record of data. Section 12.2 demonstrates a typical test day with the use of six data plots. Section 12.3 then summarizes all the test data (from the 17 selected test runs) with data plots and a time chart for each run.

#### 12.1 INTERPRETATION AND USE OF TEST DATA TAPES

Interpretation of the data tapes requires discussion of the format to enable usage of the tapes. The basic data arrangement was maintained when the BEC tapes were created from the CRTF engineering data tapes. Each data record (scan) on the CRTF tapes stored 275 data channels, but only 192 were required for BMSR instrumentation data. The extra channels were for RTAF and cross-reference data, and the remainder were spares. These extra channels were superfluous so they were not carried over to the new tapes. There were also several channels within the data that were not required and were replaced with calculated data. Therefore, 200 data channels held all pertinent recorded and calculated data. To further reduce the amount of superfluous data, any data recorded before or after actual testing was dropped. This varied from between a few minutes to several hours. Therefore, data on file was actual test data in a compacted form. By compacting the data, access time was dramatically increased, thus reducing computer costs.

Each data tape represented one physical file and each file represented one test day. A logical record of data was considered equal to one scan, and the number of records per file varied as to the length of the test day itself. However, all the data on each file was continuous, with no record marks. Therefore, the correct number of channels (200) must be read to

access the data properly. Each record can be thought of as an array of numbers, dimension equal to 200. When accessing the data, it is more efficient to read more than one record at a time into a two-dimensional buffer (temporary) array. Seventy-five records were chosen as an optimum number for access time and costs, representing 5 min of data (75 by 200 array). In this buffer array, data was extracted knowing only relative location within the array. The data buffer array layout (Table 12.1-1) showed the location number within the array, the instrumentation mnemonic, and a description of the data. Figure 12.1-1 shows a layout of the BMSR instrumentation and its numbering system. Each record also contained the date of the test (month, day, year) for test identification; the decimal time, which indicated scan time; and the record number for identification.

The data buffer was logically partitioned into blocks, according to scan rate, called frequency blocks. This was a notation held over from the CRTF engineering tapes and was used to indicate in which scan block the data was contained. Frequency block 1 included channels 1 through 47; frequency block 2 included channels 48 through 108; and frequency block 3 included channels 109 through 200. These blocks are so indicated in Table 12.1-1. Recalling the data acquisition scanning process described in Section 7.3, data were scanned at one of three priority levels. The highest priority level (frequency block 1) was scanned at 4 sec intervals; the next level (frequency block 2) was scanned at 8 sec intervals; and the lowest level (frequency block 3) was scanned at 12 sec intervals. Because each record was of consistent length (200 channels), there was some repetition of data. Level 1 data was new each record; level 2 data was new every second record; and level 3 data was new every third record.

An example of the BMSR data print format is shown in Figure 12.1-2. This format was chosen to print out all data contained in a record, for any given time interval. The data could, of course, be output using any format desired. At the top of the page, the test identification, date, time, record number, and print interval are given. All data was grouped according to what group it fit into: insulation temperatures, control conditions, air supply values, heat exchanger tube temperatures, and miscellaneous values. If there was a blank space, then there was no sensor in that location. The

Figure 12.1-1. Bench Model Instrumentation

# Bench Model Instrumentation

649

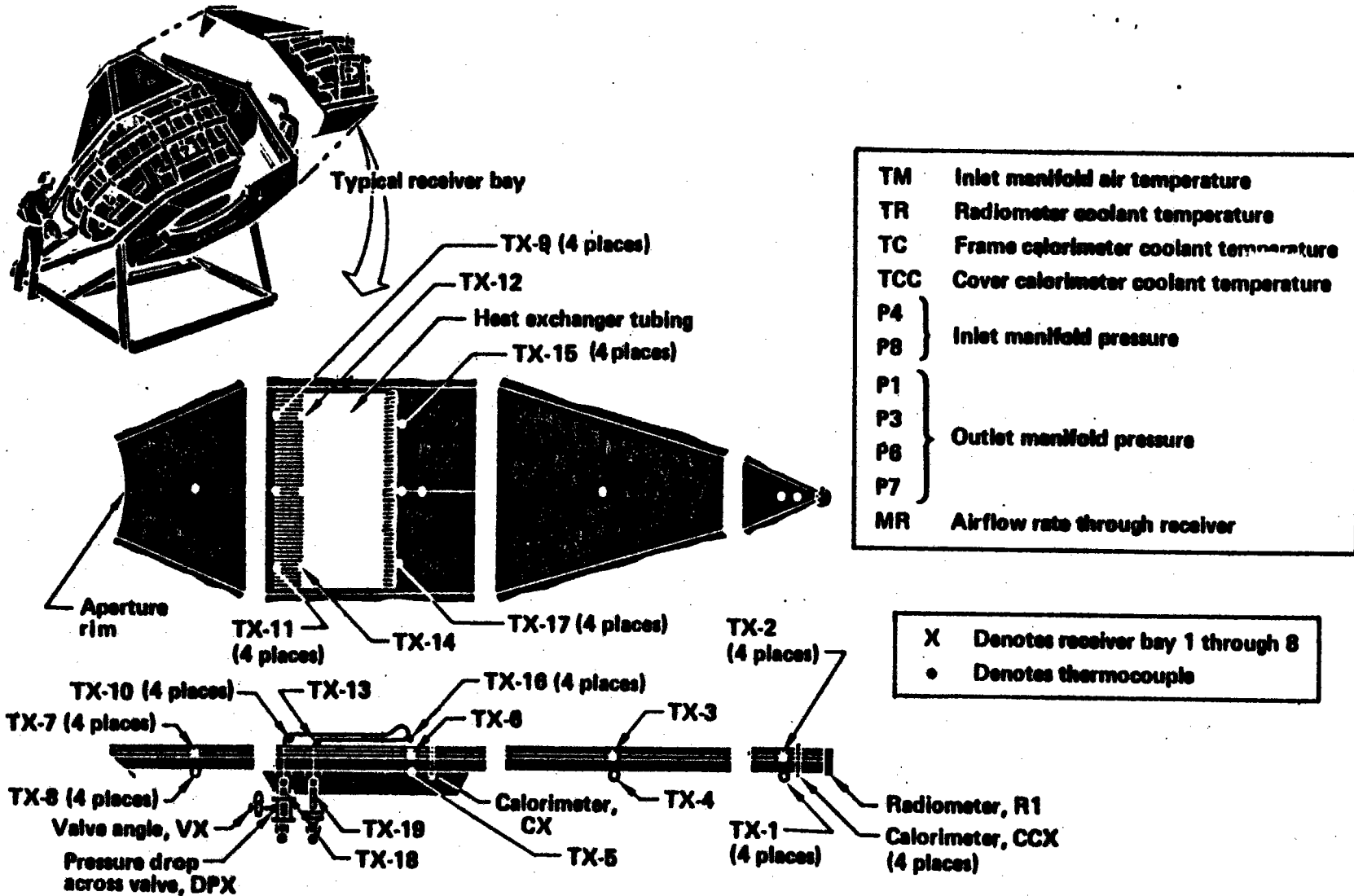


Table 12.1-1. Data Buffer Array Layout

## Data Buffer Array Layout

<u>Buff No.</u>	<u>Mnemonic</u>	<u>Description</u>	
Frequency 1	MO	Month	
Block 1	2	IDAY	} Test identification
	3	IYR	
	4	DTIME	
5	VA1	Decimal time	
6	VA2	Valve angle, bypass	
7	V1	Valve angle, back pressure	
8	V2	Valve angles, receiver	
9	V3	H/X panels	
10	V4		
11	V5		
12	V6		
13	V7		
14	V8		
15	P1	Outlet manifold pressure	
16	P3		
17	P5		
18	P7		
19	P4	Inlet manifold pressure	
20	P8		
21	DP1	Differential pressures,	
22	DP2	H/X panels	
23	DP3		
24	DP4		
25	DP5		
26	DP6		
27	DP7		
28	DP8		
29	REC	Data record number	
30	T1-18	Inlet air temperatures, H/X panels	
31	T2-18		
32	T3-18		
33	T4-18		
34	T5-18		
35	T6-18		
36	T7-18		
37	T8-18		



Table 12.1-1. Data Buffer Array Layout (Continued)

## Data Buffer Array Layout (Continued)

	<u>Buff No.</u>	<u>Mnemonic</u>	<u>Description</u>
	38	T1-19	Outlet air temperatures, H/X panels
	39	T2-19	
	40	T3-19	
	41	T4-19	
	42	T5-19	
	43	T6-19	
	44	T7-19	
	45	T8-19	
	46	TM	Inlet manifold air temperature
	47	MR	Mass flow, total
Frequency Block 2	48	PA1	Air pressure to receiver
	49	PA2	Air pressure from receiver
	50	PA4	Air pressure from compressors
	51	PA5	Air pressure to back pressure
	52	PA6	Air pressure in bypass
	53	DPA4	$\Delta P$ across main flow
	54	DPA6	$\Delta P$ across bypass
	55	MB	Mass flow, bypass
	56	T1-9	Temperature of H/X, inlet (left)
	57	T3-9	
	58	T5-9	
	59	T7-9	
	60	T1-10	Temperature of H/X, inlet (center)
	61	T3-10	
62	T5-10		
63	T7-10	Temperature of H/X, inlet (right)	
64	T1-11		
65	T3-11		
66	T5-11		
67	T7-11	Temperature of H/X, outlet (left)	
68	T1-12		
69	T2-12		
70	T3-12		
71	T4-12		
72	T5-12		
73	T6-12		
74	T7-12		
75	T8-12		

Table 12.1-1. Data Buffer Array Layout (Continued)

## Data Buffer Array Layout (Continued)

<u>Buff No.</u>	<u>Mnemonic</u>	<u>Description</u>	
76	T1-13	Temperature of H/X, outlet (center)	
77	T2-13		
78	T3-13		
79	T4-13		
80	T5-13		
81	T6-13		
82	T7-13		
83	T8-13		
84	T1-14	Temperature of H/X, outlet (right)	
85	T2-14		
86	T3-14		
87	T4-14		
88	T5-14		
89	T6-14		
90	T7-14		
91	T8-14		
92	T1-15	Temperature of H/X, bend (left)	
93	T3-15		
94	T5-15		
95	T7-15	Temperature of H/X, bend (center)	
96	T1-16		
97	T3-16		
98	T5-16		
99	T7-16	Temperature of H/X, bend (right)	
100	T1-17		
101	T3-17		
102	T5-17		
103	T7-17	Air temperature to receiver Air temperature from receiver Air temperature from compressors Air temperature to back pressure Temperature of recuperator shell, outlet	
104	TA-1		
105	TA-2		
106	TA-4		
107	TA-5		
108	TRC0		
Frequency Block 3	109	C1	Calorimeters, sidewall
	110	C2	
	111	C3	
	112	C4	

Table 12.1-1. Data Buffer Array Layout (Continued)

## Data Buffer Array Layout (Continued)

<u>Buff No.</u>	<u>Mnemonic</u>	<u>Description</u>
113	C5	Calorimeters, backwall
114	C6	
115	C7	
116	C8	
117	CC1	
118	CC3	
119	CC5	
120	CC7	
121	R1	Radiometer
122	EPLY	Eppley pyrhelimeter
123	T1-2	Temperature of insulation, back
124	T3-2	
125	T5-2	Temperature of insulation, cone
126	T7-2	
127	T1-3	
128	T2-3	
129	T3-3	
130	T4-3	
131	T5-3	
132	T6-3	
133	T7-3	Temperature of insulation, sidewall
134	T8-3	
135	T1-6	
136	T1-6	
137	T3-6	
138	T4-6	
139	T5-6	
140	T6-6	
141	T7-6	Temperature of insulation, face
142	T8-6	
143	T1-7	
144	T3-7	Temperature of shell, back
145	T5-7	
146	T7-7	
147	T1-1	
148	T3-1	
149	T5-1	
150	T7-1	

Table 12.1-1. Data Buffer Array Layout (Continued)

## Data Buffer Array Layout (Continued)

<u>Buff No.</u>	<u>Mnemonic</u>	<u>Description</u>
151	T1-4	Temperature of shell, cone
152	T2-4	
153	T3-4	
154	T4-4	
155	T5-4	
156	T6-4	
157	T7-4	
158	T8-4	
159	T1-5	Temperature of shell, sidewall
160	T2-5	
161	T3-5	
162	T4-5	
163	T5-5	
164	T6-5	
165	T7-5	
166	T8-5	
167	T1-8	Temperature of shell, face
168	T3-8	
169	T5-8	
170	T7-8	
171	TR	Temperature of radiometer, coolant
172	TCC	Temperature of cover calorimeter coolant
173	TC	Temperature of side calorimeter coolant
174	TS-1 (TCON)	Temperature of potentiometers
175	TS-2 (TP-1)	Temperature of steel, aperture shield
176	TS-3 (TP-2)	
177	TS-4 (TP-3)	
178	TS-5 (TP-4)	
179	TS-6 (TP-5)	
180	TS-7 (TP-6)	
181	TS-8 (TP-7)	
182	TS-9 (TP-8)	
183	SP1	
184	SP2	
185	SP3	
186	SP4	
187	SP5	
188	SP6	

Table 12.1-1. Data Buffer Array Layout (Continued)

## Data Buffer Array Layout (Continued)

<u>Buff No.</u>	<u>Mnemonic</u>	<u>Description</u>
189	SP-7	Setpoint, bypass
190	SP-8	
191	SPT1	Setpoint, back pressure
192	SPP2	
193	M1	Mass flow, H/X panels
194	M2	
195	M3	
196	M4	
197	M5	
198	M6	
199	M7	
200	M8	

Figure 12.1-2. BMSR Data Printout  
**BMSR Data Printout**

BMSR TEST: JA2079\*\*\*\*

DATE: 1/20/1979  
 TIME: 20 :: 12 :: 13 :: 55 = 12.232 HRS.

REC. NO. 2175  
 PRINT INT: 300 SEC.

PAGE 30

CHANNEL	BAY 1	BAY 2	BAY 3	BAY 4	BAY 5	BAY 6	BAY 7	BAY 8
---------	-------	-------	-------	-------	-------	-------	-------	-------

INSULATION TEMPERATURES (DEG F)

TX-2	1789.53		1881.84		1728.58		999.90	
TX-1	116.70		136.59		89.89		1117.58	
TX-3	1487.39	1658.93	999.00	1535.12	1394.89	1448.75	1950.93	1871.85
TX-4	84.99	118.89	178.05	82.33	79.22	86.54	142.24	95.18
TX-6	0.00	1490.34	1473.31	1377.33	1408.80	1468.04	1454.01	1510.32
TX-5	104.42	119.55	130.91	149.42	120.84	138.32	83.17	80.55
TX-7	1528.25		1577.87		15928.02		1489.15	
TX-8	118.05		251.12		159.82		189.46	

MISC. (T - DEG F, C - CC - R - EPPLEY - KW/M 2, M - LB/SEC)

TP-X	69.86	175.87	79.22	85.87	66.73	83.40	39.89	82.99
CX	246.92	0.00	230.82	0.00	203.74	0.00	214.71	0.00
CCX	350.88		0.00		564.37		581.36	

R1 - 182.58 EPLY - 1.01 TM - 946.56 MR - 4.08 MB - 0.00

TR - 39.01 TCC - 37.85 TC - 36.96 TCON - 111.01

CONTROL CONDITIONS (V - DEG, DP - PSID, P - PSIG, T - DEG F, SP - DEG F)

MX	0.63	0.57	0.53	0.41	0.31	0.42	0.80	0.81
PX (IN)				117.02				
VX	59.87	57.49	55.27	49.72	44.94	49.12	56.29	58.25
DPX	18.91	19.37	23.46	28.74	33.01	33.75	27.29	21.32
PX (OUT)	76.81		75.26		75.75		74.88	
TX-18	931.36	934.74	936.43	938.12	934.74	931.36	924.81	914.47
TX-19	1499.73	1499.73	1499.73	1503.26	1501.49	1497.96	1503.26	1498.20
SPX	1499.88	1498.20	1489.81	1494.84	1499.88	1493.18	1493.18	1499.81

Figure 12.1-2. BMSR Data Printout (Continued)

# BMSR Data Printout (Continued)

## H/X PANEL TUBE TEMPERATURES (DEG, F)

H/X PANEL NO. 1			H/X PANEL NO. 2			H/X PANEL NO. 3			H/X PANEL NO. 4		
	931.4			934.7			938.4			938.1	
0.0	0.0	1335.9				1373.9	1358.8	1342.7			
0.0	143.1	0.0				1739.4	1715.5	1788.2			
1608.4	0.0	1597.5	1508.4	1595.9	1410.1	1606.5	1599.4	1538.7	1528.2	1579.7	1538.7
	1499.7			1499.7			1499.7			1503.3	

H/X PANEL NO. 5			H/X PANEL NO. 6			H/X PANEL NO. 7			H/X PANEL NO. 8		
	934.7			931.4			924.8			914.5	
1342.7	1349.5	1380.9				1299.7	1335.9	1332.4			
1638.0	1678.9	1782.7				1684.4	1730.2	1758.1			
1555.4	1538.7	1549.3	1538.9	1598.8	1594.0	1577.9	1599.4	1610.1	1599.4	1617.3	1621.0
	1501.5			1478.0			1503.3			1498.2	

## AIR SUPPLY (T - DEG F, P - PSIG, OP - PSID, M - LB/SEC, V - DEG)

TA4 -	153.54	TRCO -	1125.74	TA1 -	348.25	TA2 -	1440.91	TAS -	673.11
PA4 -	123.98	PAG -	118.13	PA1 -	115.32	PA2 -	73.19	PAS -	71.29
DPA4 -	8.86	DPAG -	-0.18						
MR -	4.08	MB -	0.00						
VA1 -	66.38	VA2 -	38.37						
SPT1 -	925.46	SPP2 -	-11.08						

channel and bay numbers correspond to Figure 12.1-1.

## 12.2 TYPICAL TEST RUN

This section presents a short discussion of the representative plots for a typical test run. The test day of January 20, 1979, was chosen as typical. There were no major problems with instrumentation or hardware, and it was a good example of a high temperature 816°C (1500°F) outlet air test.

Six plots were chosen as representative because they best described, in brief, the test and receiver operation. The data plots were computer generated using the test data tapes and were plotted at 2-minute intervals. The plots are preceded by a time chart (Figure 12.2-1) that gives a brief summary of test events, showing the number of heliostats on target and periods of stable test conditions.

The first plot (Figure 12.2-2) is the output from the Epply pyrhelimeter, which was mounted atop the CRTF tower. The sensor tracked the sun and was a gage of the insolation during the test. The second plot (Figure 12.2-3) is of the air supply equipment skid air temperatures. To be more precise, the four plots correspond to the four inlet and outlet air temperatures of the recuperator. The recuperator outlet-to-receiver (receiver inlet) air temperature was measured at the connection between the air supply piping and receiver inlet manifold. This was the control inlet temperature. The recuperator inlet-from-receiver (receiver outlet) air temperature was measured at the recuperator, meaning by the time the air temperature was measured here, all the receiver panel outlets had mixed and traveled through the air supply piping. Therefore, the temperature measured here varied somewhat from the individual panel outlet temperatures. The third plot (Figure 12.2-4) shows the output from four of the original eight-frame calorimeters. However, there were several occasions when all four calorimeters were not in working condition, therefore some data will be missing. The calorimeters showed the distributed radiant heat within the cavity of the receiver. The fourth plot (Figure 12.2-5) is of the total receiver mass flow. This was the combined flow of all eight heat exchanger panels. The general trend in flow rate, up or down, can be seen. The fifth



*Figure 12.2-1. Time Chart for January 20, 1979 Solar Test*

## **Time Chart for January 20, 1979 Solar Test**

<b>9:45</b>	<b>Field at standby</b>
<b>9:50</b>	<b>First collector on target</b>
<b>10:26</b>	<b>58 collectors on target</b>
<b>10:58</b>	<b>62 collectors on target</b>
<b>11:31</b>	<b>Receiver on control</b>
<b>12:10</b>	<b>Steady test conditions, EB-9A</b>
<b>12:52</b>	<b>Steady test conditions, EB-9B</b>
<b>13:25</b>	<b>53 collectors on target</b>
<b>13:49</b>	<b>Steady test conditions, EB-6A</b>
<b>14:03</b>	<b>47 collectors on target</b>
<b>14:21</b>	<b>49 collectors on target</b>
<b>14:23</b>	<b>55 collectors on target</b>
<b>14:44</b>	<b>51 collectors on target</b>
<b>14:53</b>	<b>Steady test conditions, EB-3A</b>
<b>15:29</b>	<b>Field at standby</b>

Figure 12.2-2. Plot of January 20, 1979 Test Data, Eppley Pyrheliometer

# Plot of January 20, 1979 Test Data, Eppley Pyrheliometer

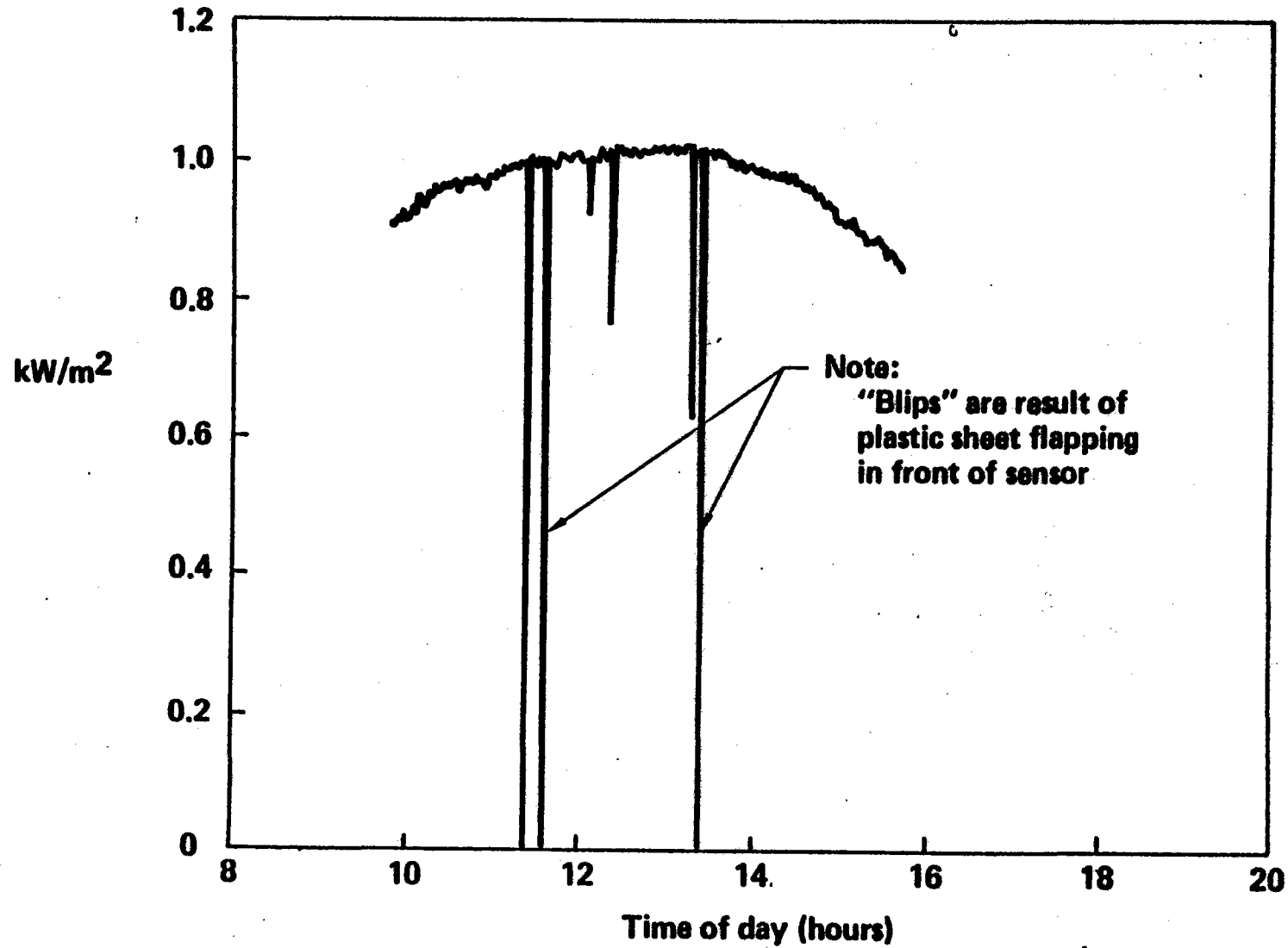


Figure 12.2-3. Plot of January 20, 1979 Test Data, Air Supply Gas Temperatures

# Plot of January 20, 1979 Test Data, Air Supply Gas Temperatures

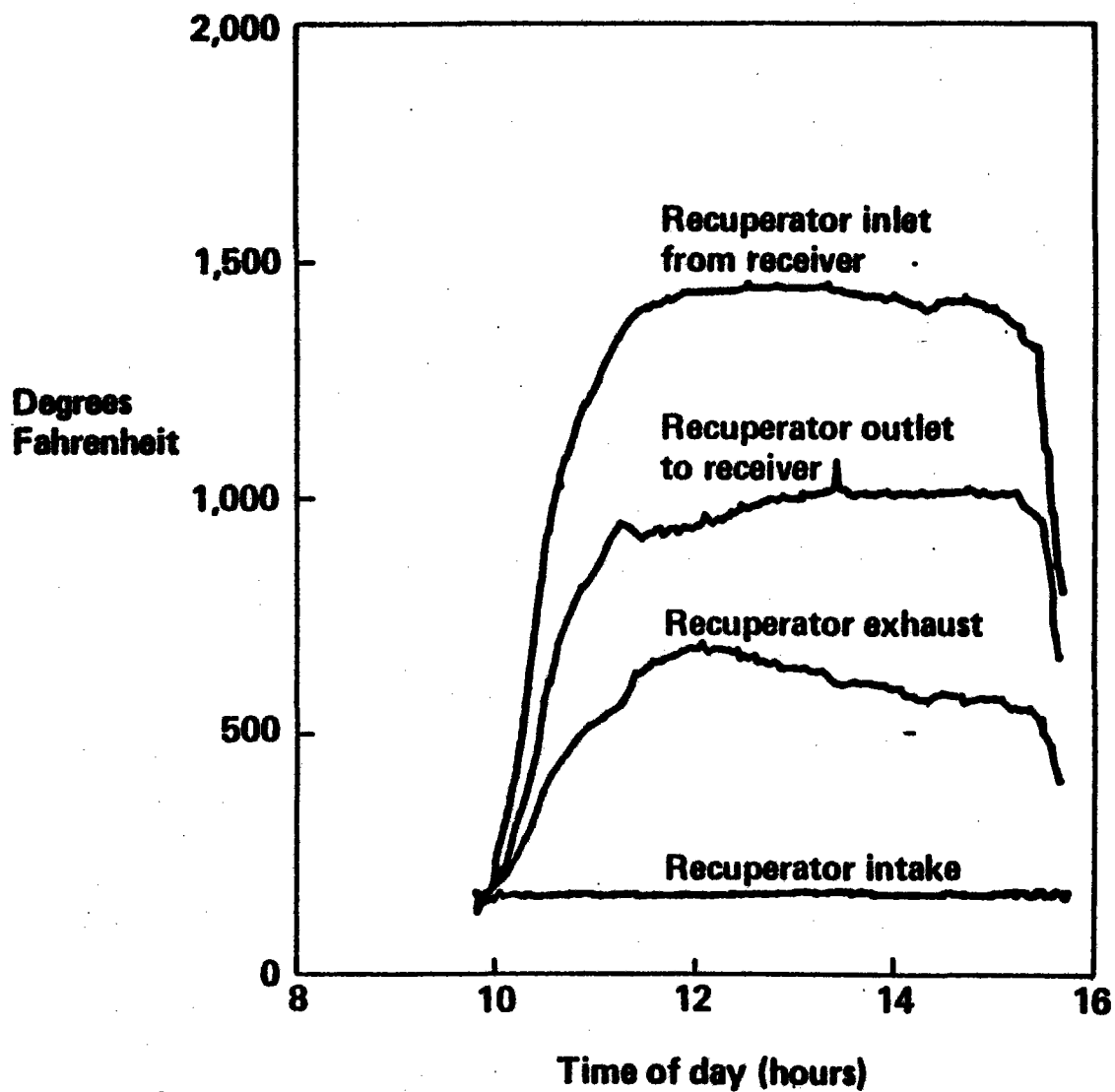


Figure 12.2-4. Plot of January 20, 1979 Test Data, Frame Calorimeters

## Plot of January 20, 1979 Test Data, Frame Calorimeters

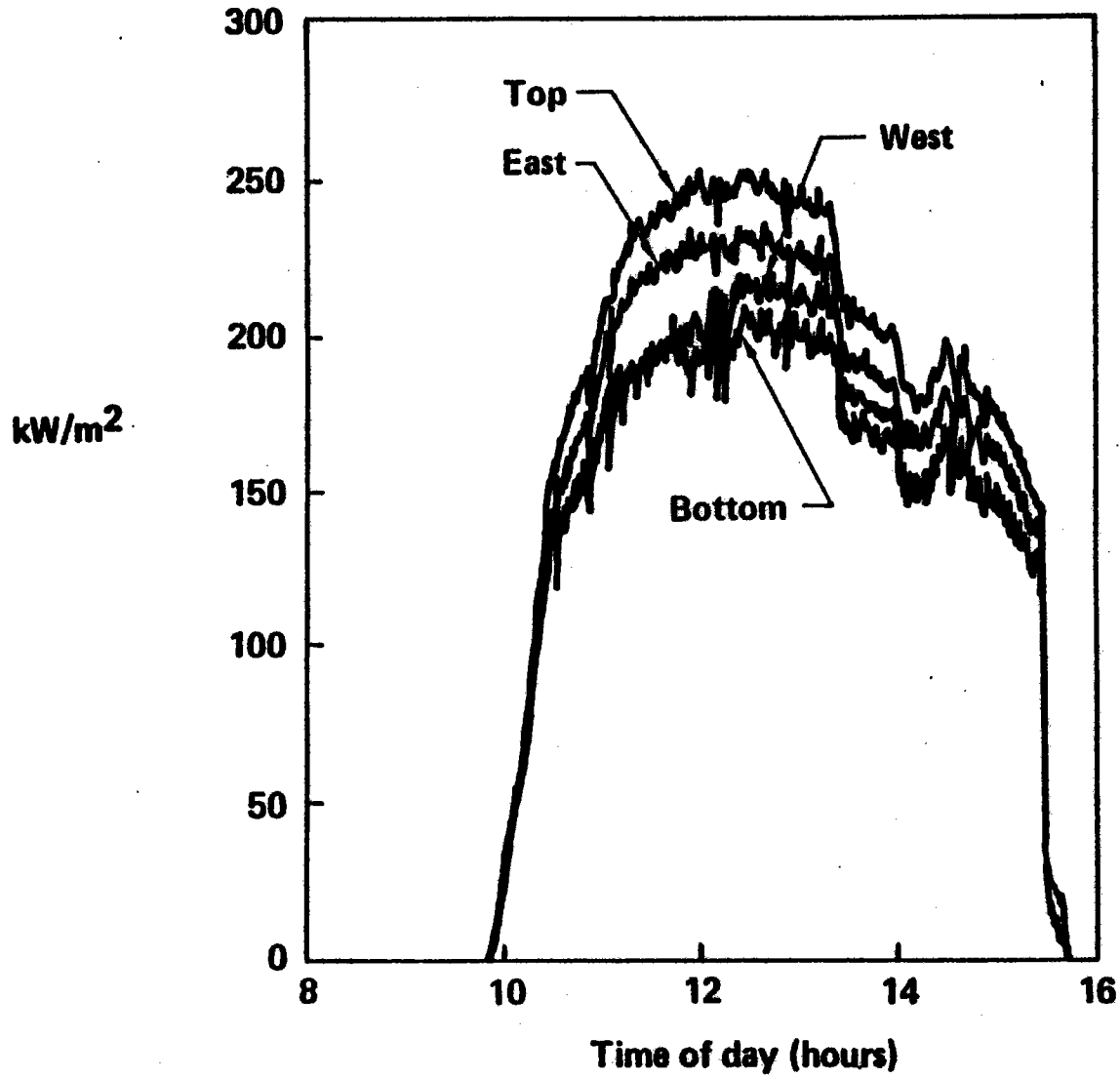
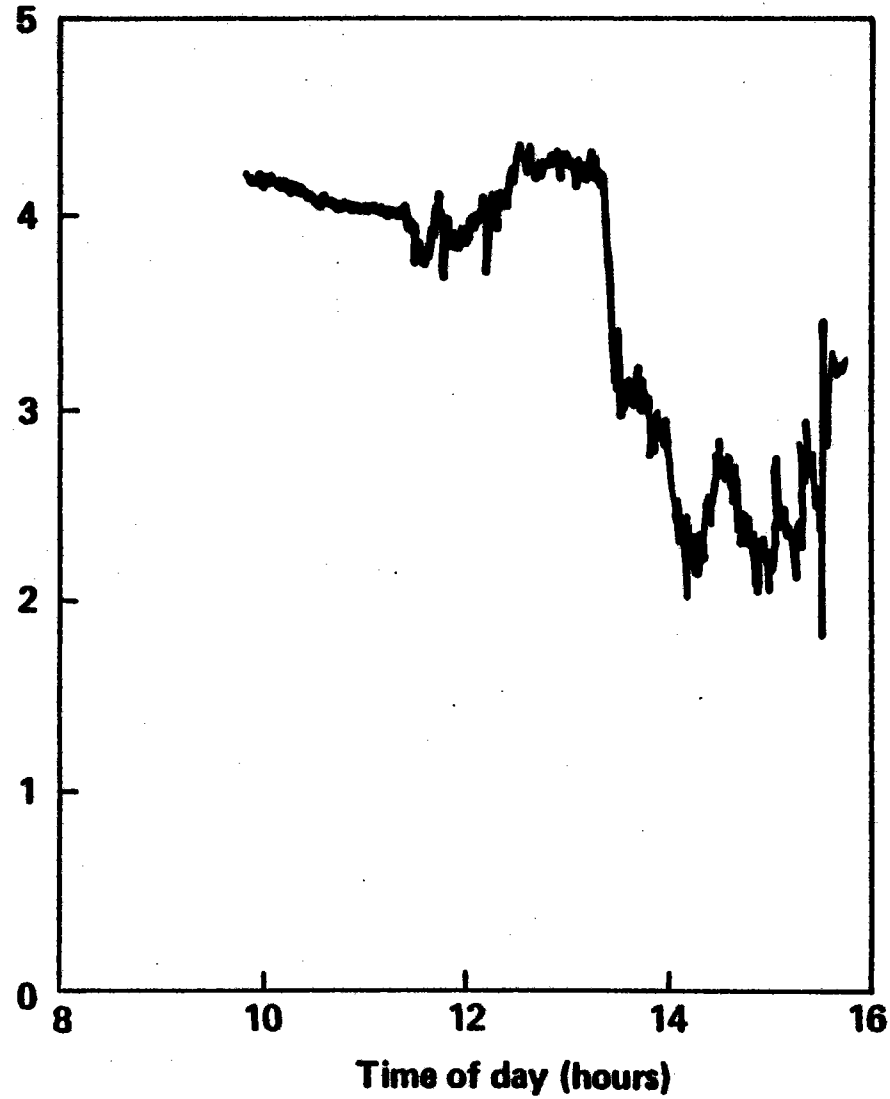


Figure 12.2-5. Plot of January 20, 1979 Test Data, Receiver Mass Flow

# Plot of January 20, 1979 Test Data, Receiver Mass Flow

663

lb/s



plot (Figure 12.2-6) is of one of the heat exchanger valve-angle indicators. Panel 3 was chosen as a representative value. These plots appear somewhat erratic, but the valve moved fast and often to control the outlet temperature. The sixth plot (Figure 12.2-7) shows the receiver air inlet and outlet temperatures for heat exchanger panel 3. The outlet temperature controlled, via a feedback loop, the operation of the inlet valve for each panel.

The operation of the receiver can be visualized from the data plots. For instance, it can be seen that for startup of the receiver, there was full flow with valves wide open at 90 deg (Figures 12.2-5 and 12.2-6). As the collectors were brought on target, the cavity began to heat up (Figure 12.2-4); air in the heat exchanger panels increased in temperature (Figure 12.2-7); and the recuperator started warming up (Figure 12.2-3). Startup proceeded for approximately 1.5 hr, at which point the bypass control valve on the air supply equipment skid and then the panel valves were allowed to come on control. When the bypass valve opened, allowing cold air to mix with hot air, the inlet took a small dip in temperature. It then slowly increased to control temperature. Meanwhile, the outlet temperature recovered quite promptly and held for the remainder of the test. Three steady-state test conditions were run, all high-temperature 816°C (1500°F) runs but requiring various power levels into the receiver. The first steady-state test was EB-9. This condition was held for approximately 1.0 hr. Collectors were then removed to obtain a lower power level for EB-6 (Figure 12.2-4). The valves closed (Figure 12.2-6) and mass flow decreased (Figure 12.2-5) to maintain the same outlet temperature. This condition was maintained for approximately 0.5 hrs, then the process of lowering the power level was started again for EB-3. This final test was maintained for the duration of the test day. During shutdown, the panel valves were opened fully, increasing mass flow, and collectors were removed, causing the receiver and associated components to cool.

### 12.3 DAILY ACTIVITIES AND TEST DATA SUMMARY

This section summarizes the 17 test days chosen for detailed posttest analysis. As in Section 12.2, each data set is represented by six

Figure 12.2-6. Plot of January 20, 1979 Test Data, H/X Panel Three-Valve Angle

### Plot of January 20, 1979 Test Data, H/X Panel Three-Valve Angle

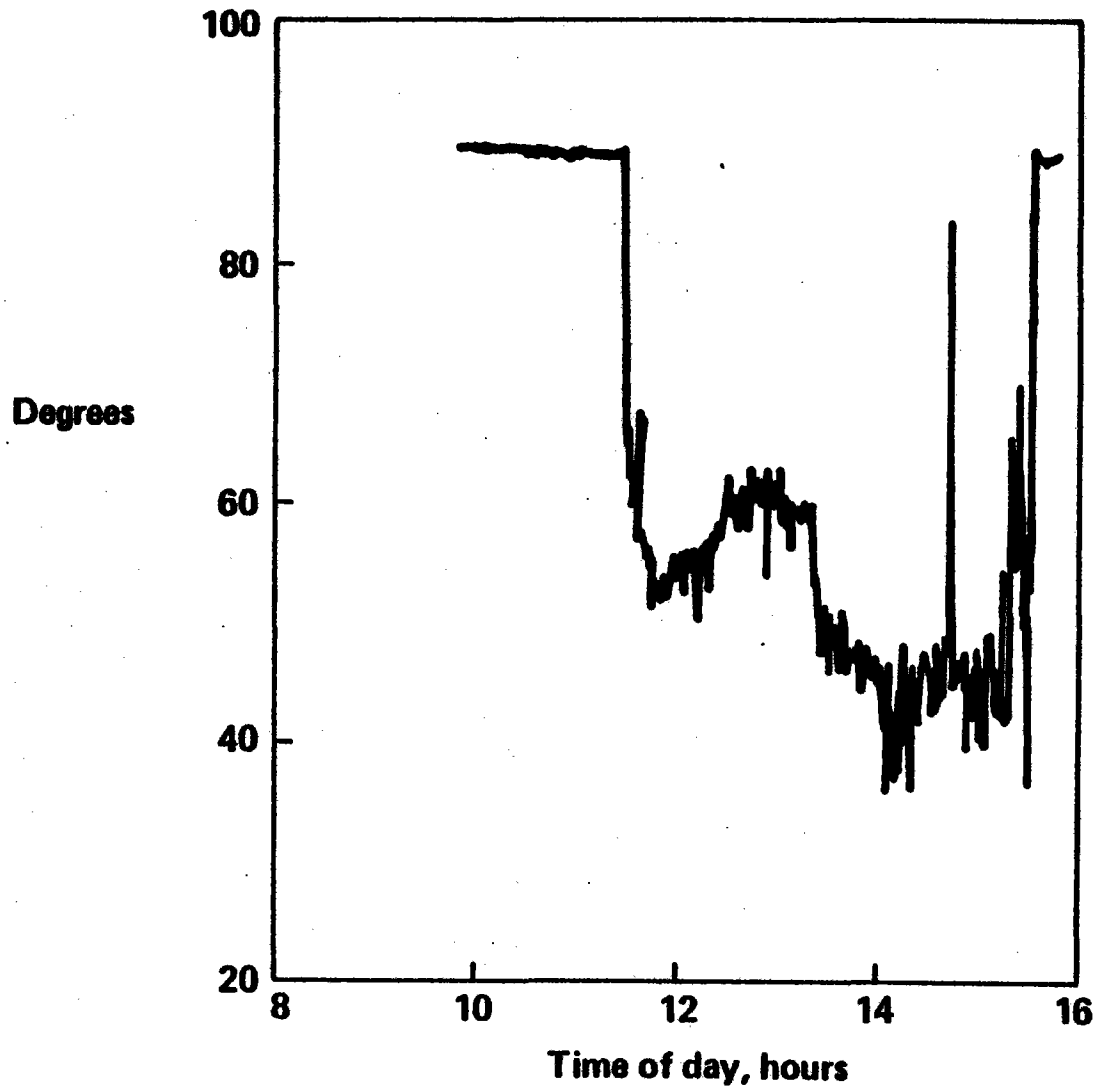
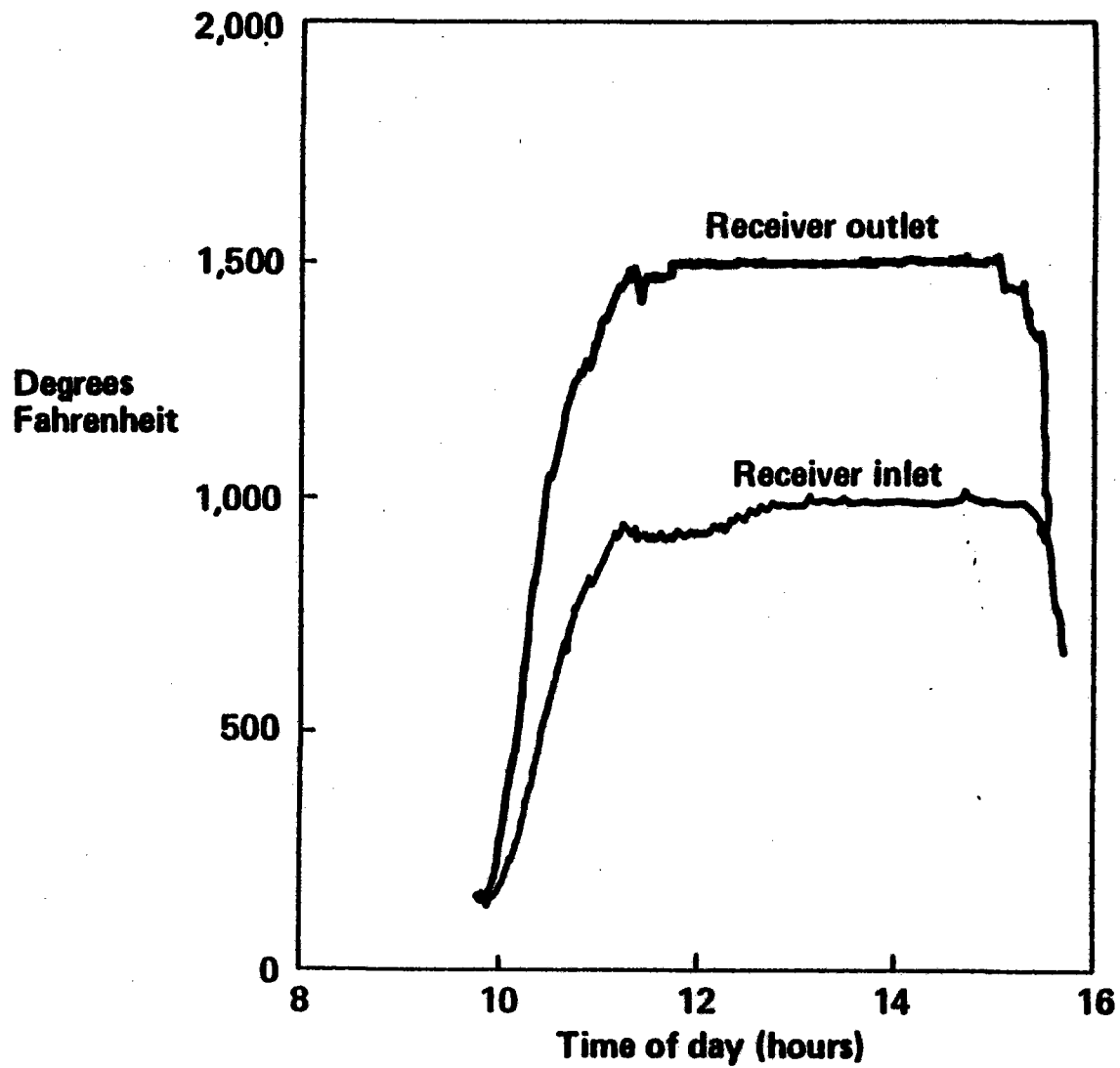


Figure 12.2-7. Plot of January 20, 1979 Test Data, Air Inlet-Outlet Temperatures, Panel 3

## Plot of January 20, 1979 Test Data, Air Inlet-Outlet Temperatures, Panel 3





computer-generated plots, chosen because they represented the typical operation of the receiver and give the reader a good general overview of the data. Section 12.2 describes each of the data plots.

Each set of data plots is preceded by a time chart showing the number of collectors on target, when the receiver was considered on control, and when various test conditions were present.

Table 12.3-1 lists the chosen test days along with tests satisfactorily performed and any remarks appropriate for the day's run.

Table 12.3-1. Seventeen Test Data Tapes Selected for Detailed Analysis

## Seventeen Test Data Tapes Selected for Detailed Analysis

Date	Test(s) accomplished	Remarks
11-28-78	EB-2A	High clouds yielding intermittent insolation; only two frame calorimeters working; test aborted due to burning of instrumentation cables; lost several thermocouples and pressure transducers and all valve angle indication
12-10-78	EB-4A	Good insolation, no clouds; oscillation in bypass valve and inlet temperature control; problem corrected by adjustment of valve controller, then test aborted because fitting broke on sprinkler system in tower, dousing tower DACS
1-4-79	EB-5A	Four frame calorimeters now working; clouds moving in shut test down eventually
1-7-79	EB-7A	Intermittent insolation early in test; steady state not obtained until late in afternoon
1-10-79	EB-8A	Good insolation early in test but eventually deteriorated; could not maintain control
1-11-79	EB-8B	Good insolation early in test but eventually deteriorated; could not maintain control
1-13-79	EB-7	Good start but eventually plagued by many small, dense clouds; receiver would not stay hot; panel valve 2 slammed shut, no control; testing stopped
1-18-79	—	No testing accomplished this day; data inserted to show example of extremely intermittent insolation and its effect
1-20-79	EB-9A EB-9B EB-6A EB-3A	Good test day; prime example of receiver operation

Table 12.3-1. Seventeen Test Data Tapes Selected for Detailed Analysis (Continued)

## Seventeen Test Data Tapes Selected for Detailed Analysis (Continued)

Date	Test(s) accomplished	Remarks
1-23-79	EB-4B NI-2 NI-1	Good test day; panel valve 2 had to be manually set at about 55 deg; panel valve 7 went wide open during test
1-27-79	RF-2 EC-1	Insolation good initially, but became very intermittent; data system went down about noon, brought back up within 10 min
1-28-79	TH-4 EC-3 CS-3 EB-9C	Good test day; managed to run for almost full solar day, until sunset
1-30-79	CS-2 TH-2 RF-3 EB-8C	Good test day
1-31-79	EB-9D	Good test day
3-23-79	EB-9E	Good insolation early in test but eventually deteriorated; collectors taken to standby twice during startup because of RTAF problems
3-24-79	EB-9F EB-9G	Good test day
3-25-79	EB-9H EB-9I	Good test day; lost several more thermocouples, pressure transducers, calorimeters, and valve angle indicators; test eventually shut down because of insulation burnthrough on cone

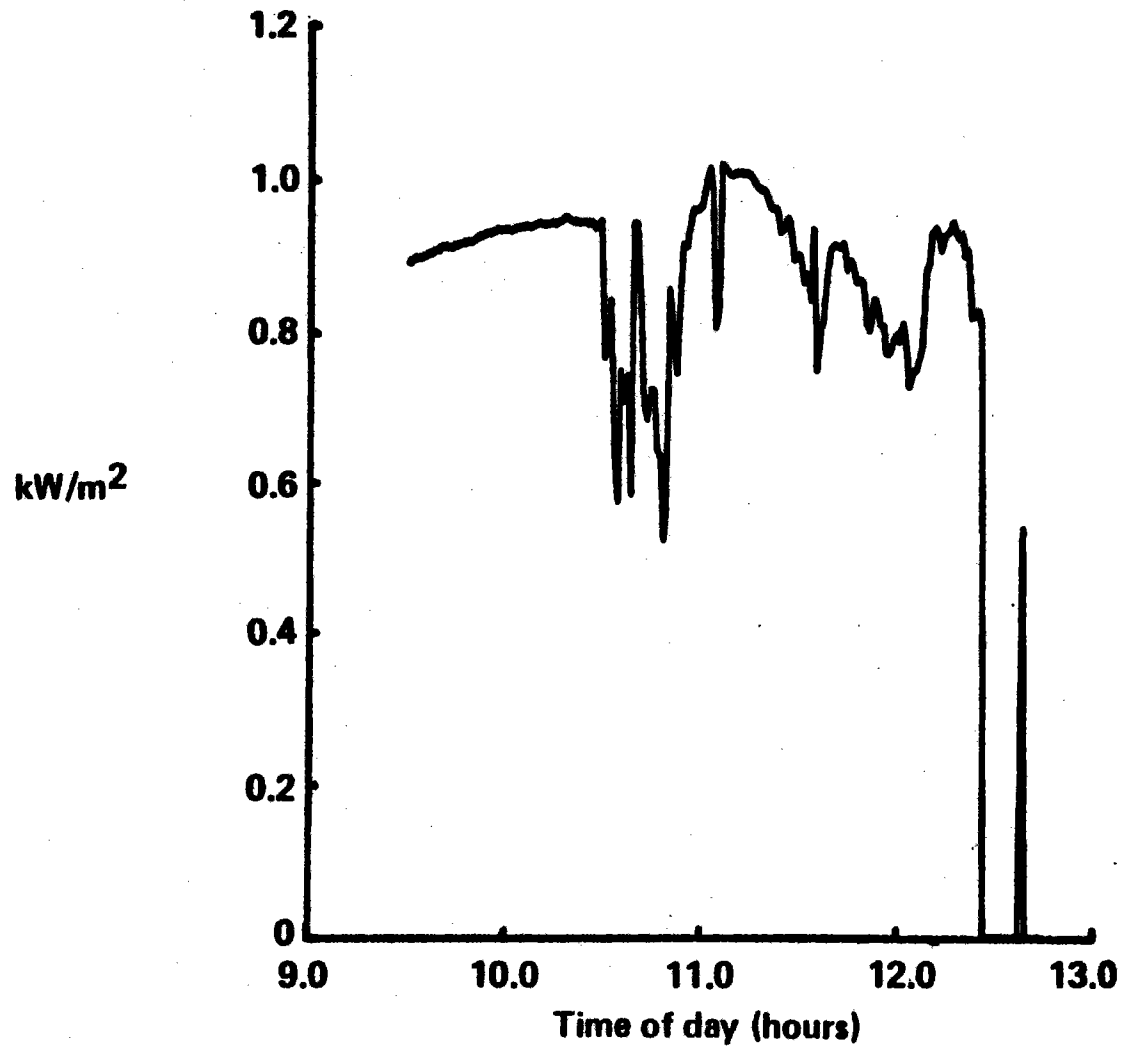
*Figure 12.3-1. Time Chart for November 28, 1978 Solar Test*

## **Time Chart for November 28, 1978 Solar Test**

<b>9:37</b>	<b>Field on standby</b>
<b>9:38</b>	<b>First collector on target</b>
<b>10:10</b>	<b>40 collectors on target</b>
<b>11:34</b>	<b>Receiver on control</b>
<b>12:18</b>	<b>Steady test conditions, EB-2A</b>
<b>12:28</b>	<b>Field to standby</b>
<b>12:33</b>	<b>Field shut down</b>

Figure 12.3-2 Plot of November 28, 1978 Test Data, Eppley Pyrheliometer

## Plot of November 28, 1978 Test Data, Eppley Pyrheliometer



671

Figure 12.3-3 Plot of November 28, 1978 Test Data, Air Supply Gas Temperatures

## Plot of November 28, 1978 Test Data, Air Supply Gas Temperatures

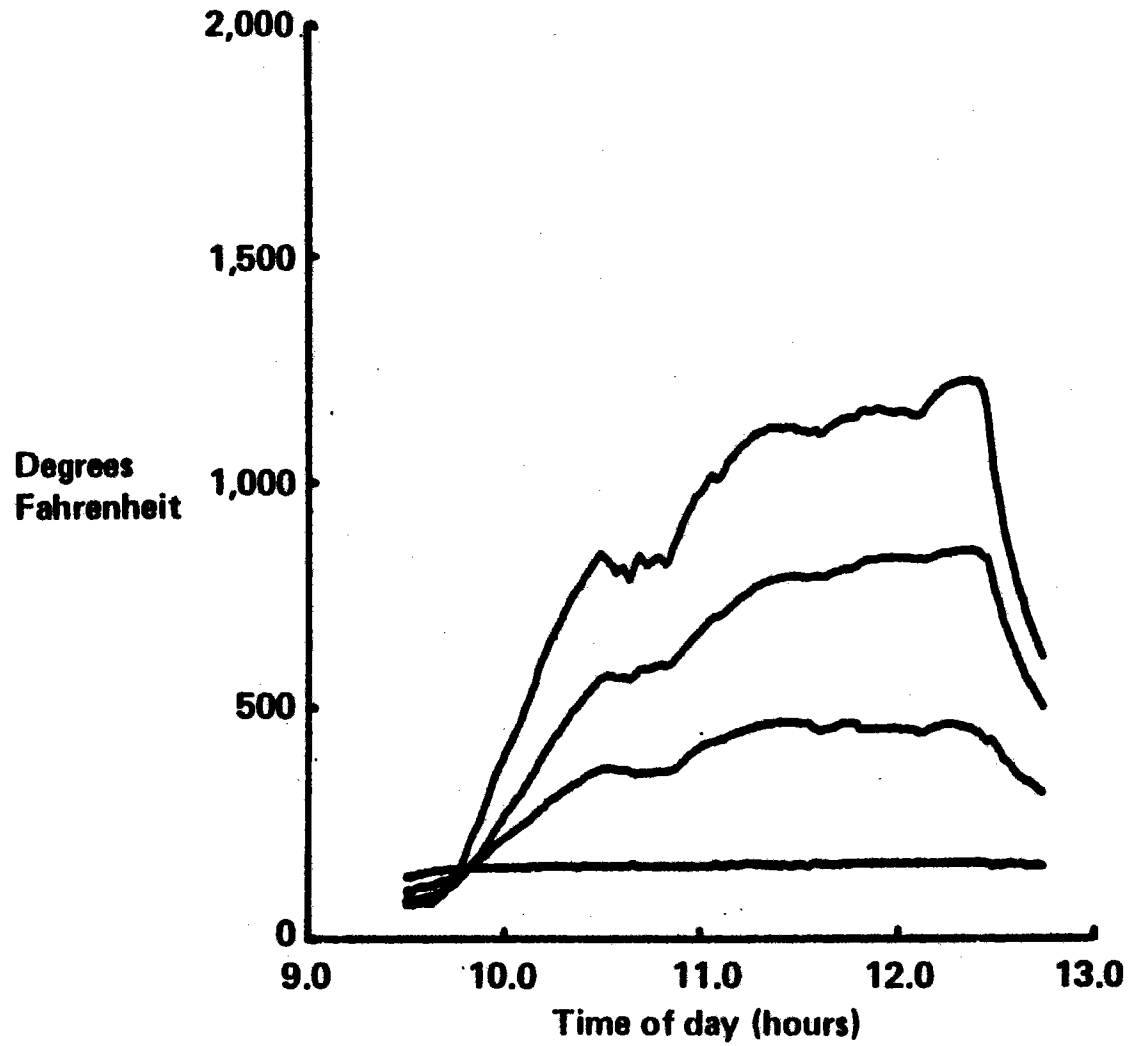
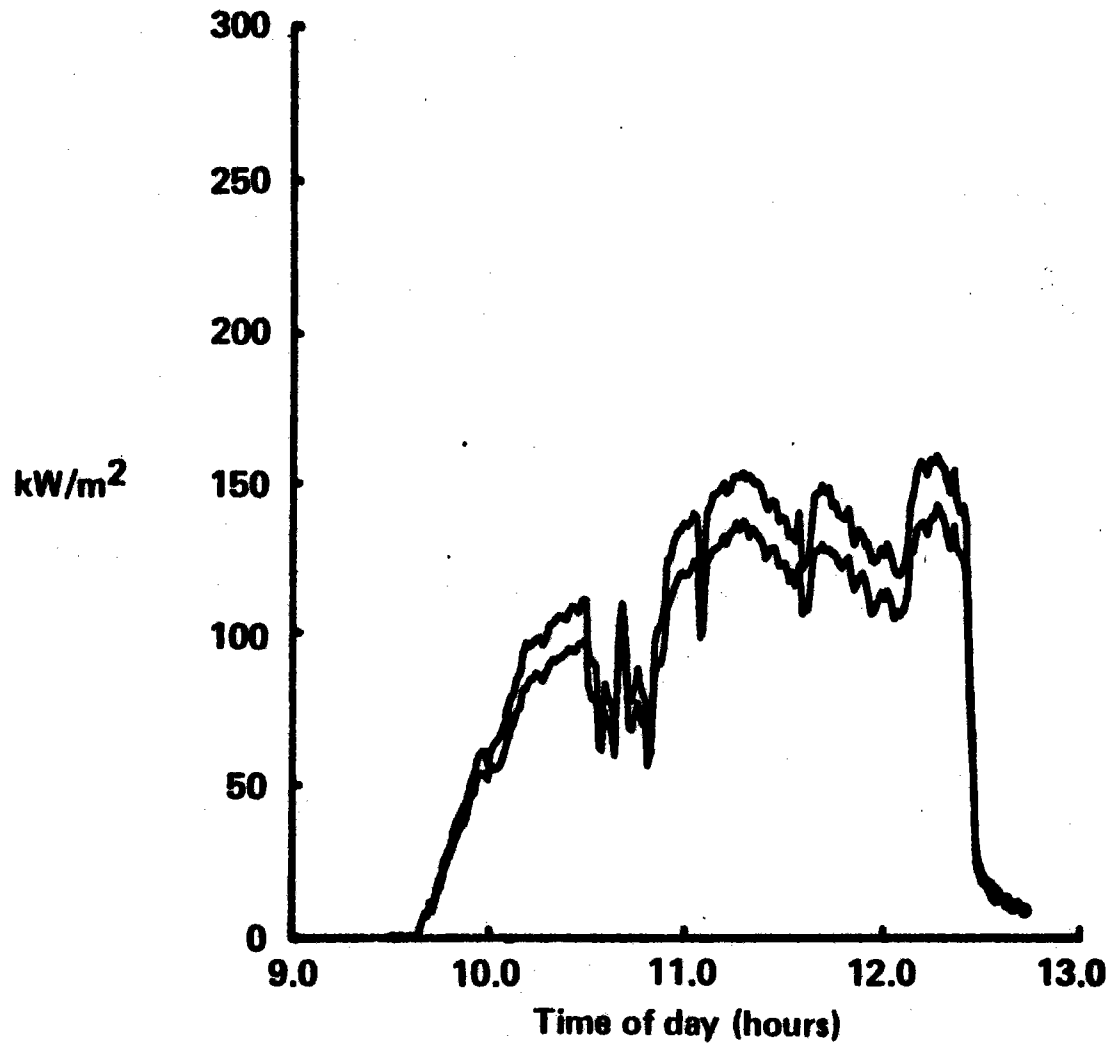


Figure 12.3-4 Plot of November 28, 1978 Test Data, Frame Calorimeters

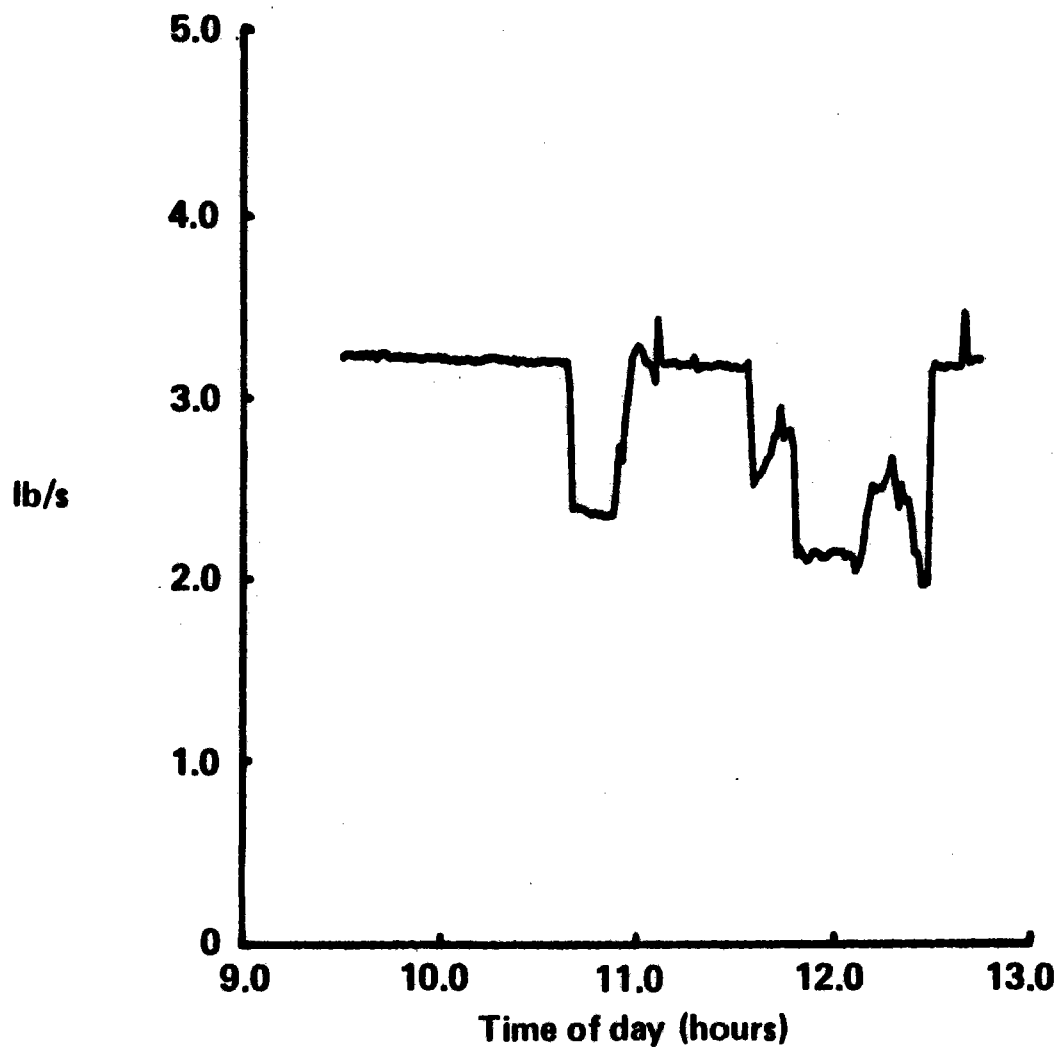
## Plot of November 28, 1978 Test Data, Frame Calorimeters



673

Figure 12.3-5 Plot of November 28, 1978 Test Data, Receiver Mass Flow

### Plot of November 28, 1978 Test Data, Receiver Mass Flow



674



Figure 12.3-6 Plot of November 28, 1978 Test Data, H/X Panel 3 Valve Angle

### Plot of November 28, 1978 Test Data, H/X Panel 3 Valve Angle

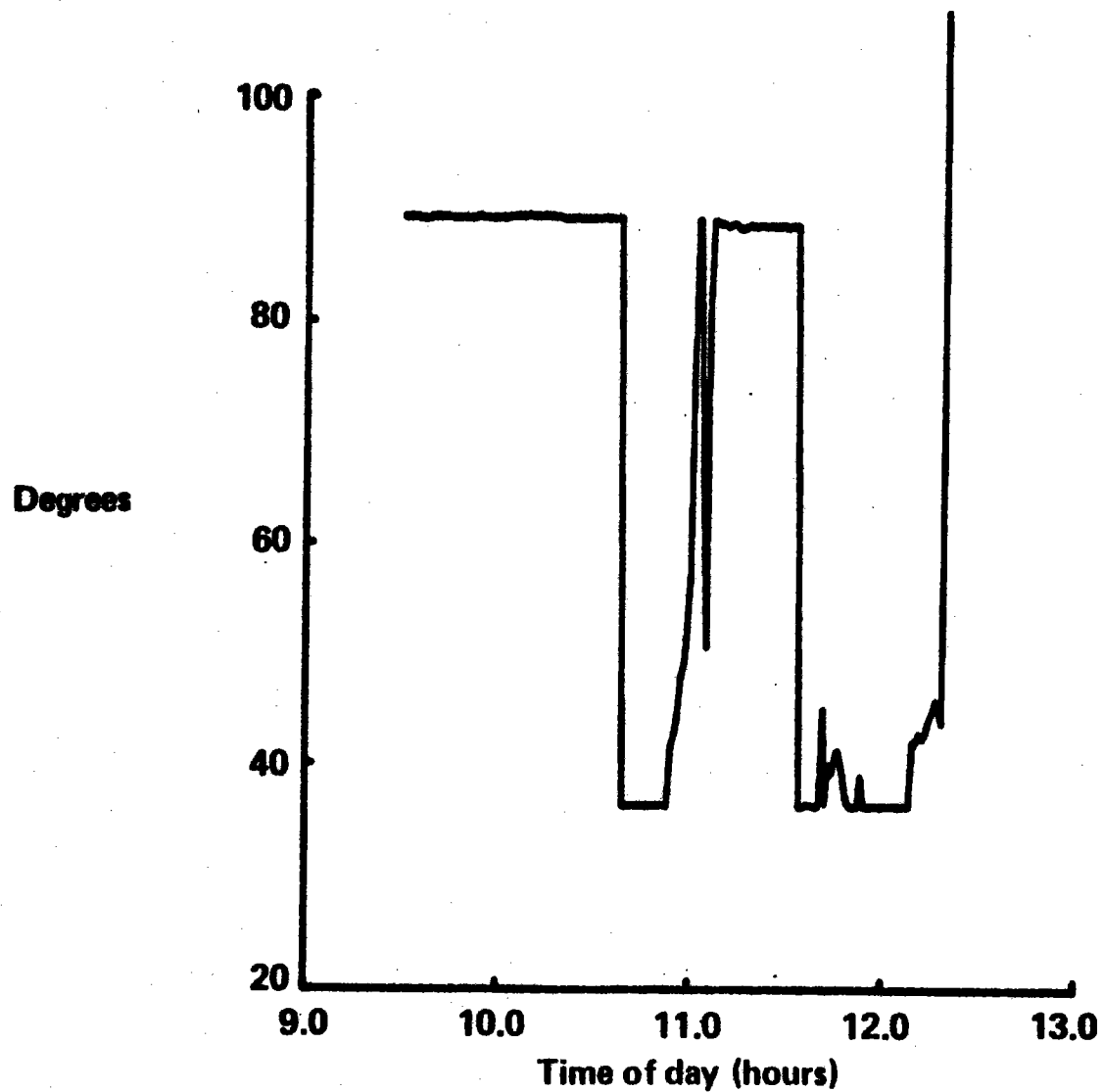
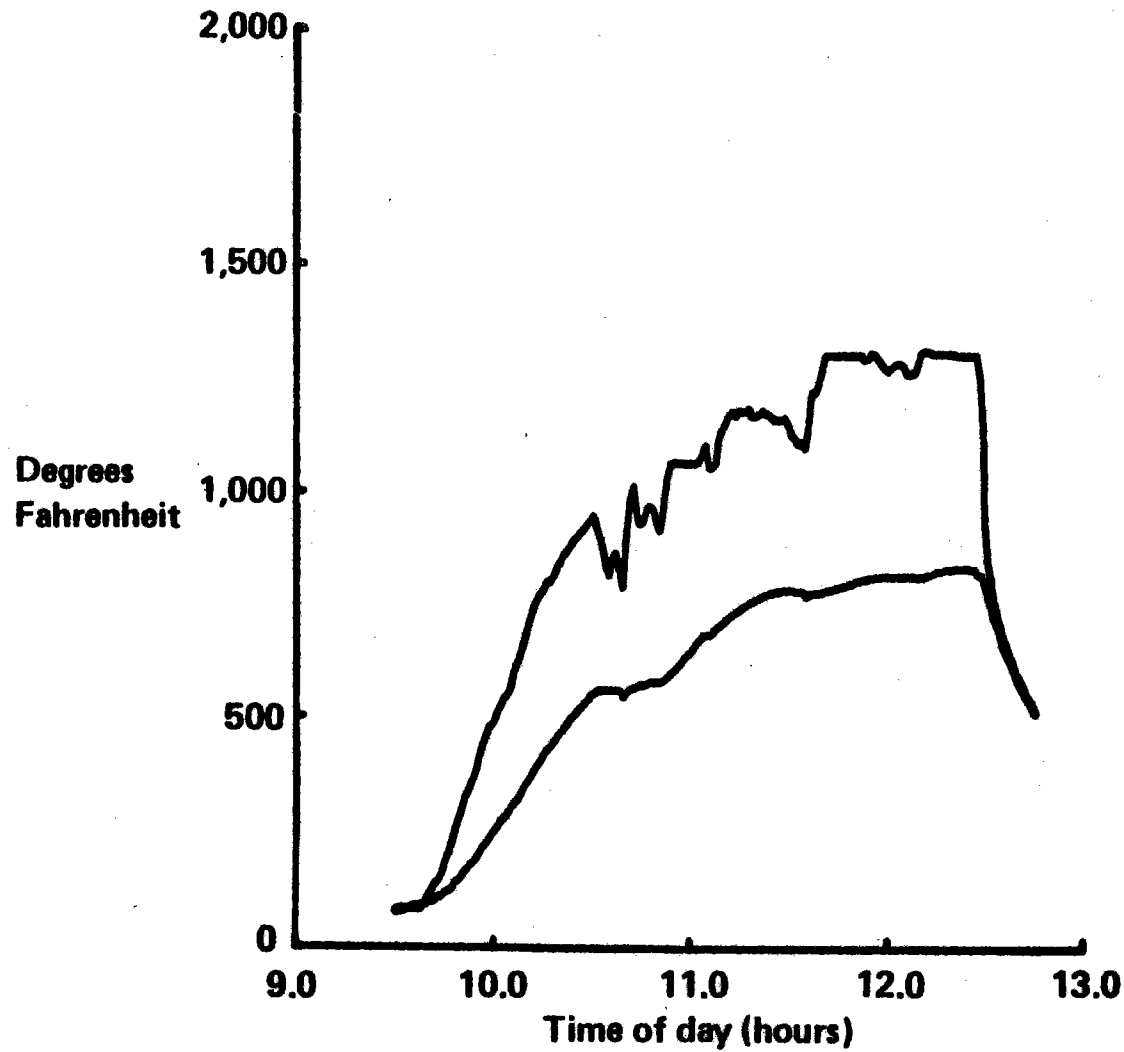


Figure 12.3-7 Plot of November 28, 1978 Test Data, Air Inlet-Outlet Temperatures, Panel 3

### Plot of November 28, 1978 Test Data, Air Inlet-Outlet Temperatures, Panel 3



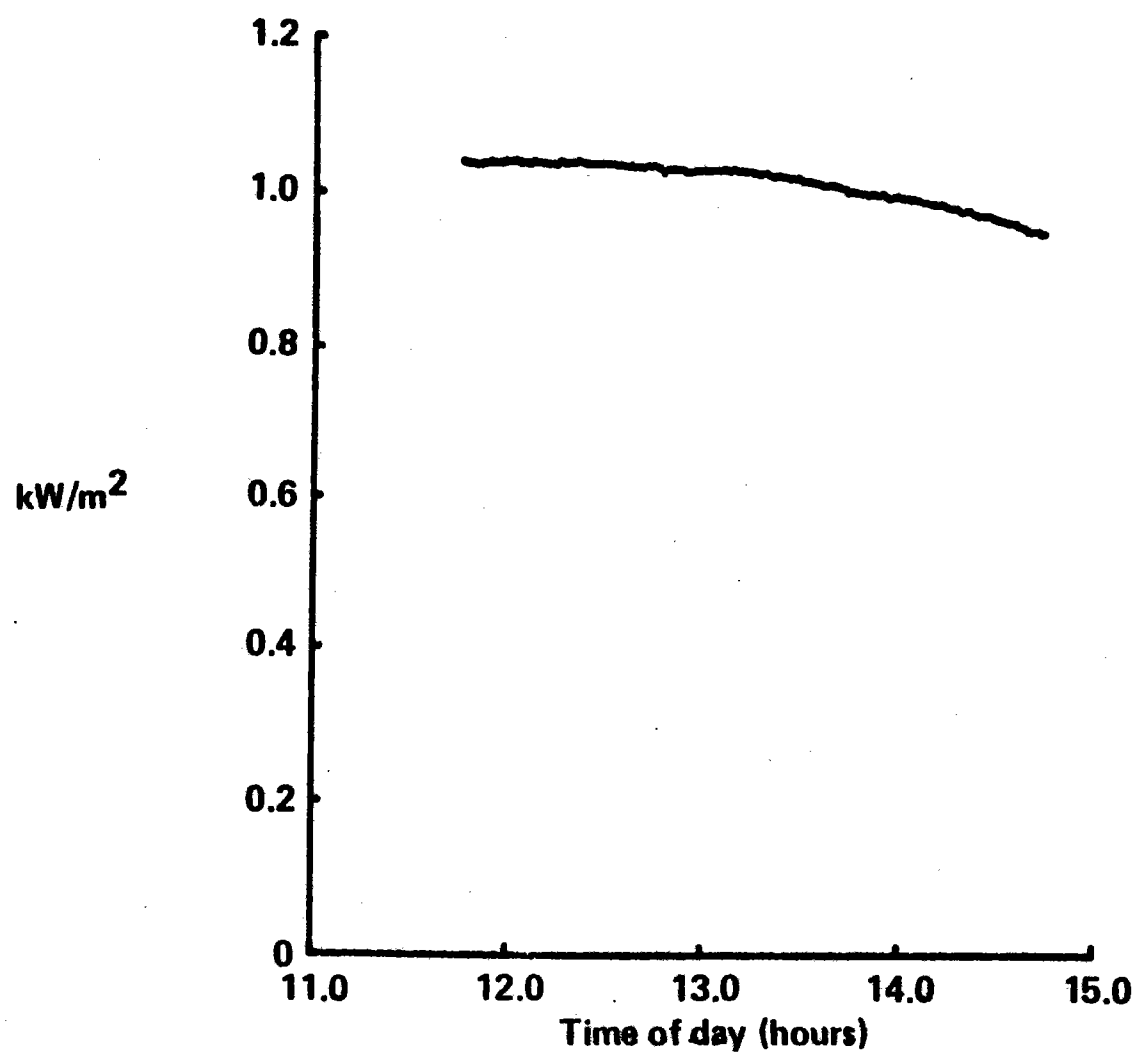
*Figure 12.3-8 Time Chart for December 10, 1978 Solar Test*

## **Time Chart for December 10, 1978 Solar Test**

<b>11:57</b>	<b>Field at standby</b>
<b>11:59</b>	<b>First collector on target</b>
<b>12:11</b>	<b>20 collectors on target</b>
<b>12:31</b>	<b>25 collectors on target</b>
<b>13:04</b>	<b>43 collectors on target</b>
<b>13:21</b>	<b>45 collectors on target</b>
<b>13:35</b>	<b>47 collectors on target</b>
<b>13:46</b>	<b>Receiver on control</b>
<b>14:22</b>	<b>53 collectors on target</b>
<b>14:29</b>	<b>Steady test conditions, EB-4A</b>
<b>14:35</b>	<b>56 collectors on target</b>
<b>14:51</b>	<b>Field shutdown</b>

Figure 12.3-9 Plot of December 10, 1978 Test Data, Eppley Pyrheliometer

### Plot of December 10, 1978 Test Data, Eppley Pyrheliometer



678

Figure 12.3-10 Plot of December 10, 1978 Test Data, Air Supply Gas Temperatures

## Plot of December 10, 1978 Test Data, Air Supply Gas Temperatures

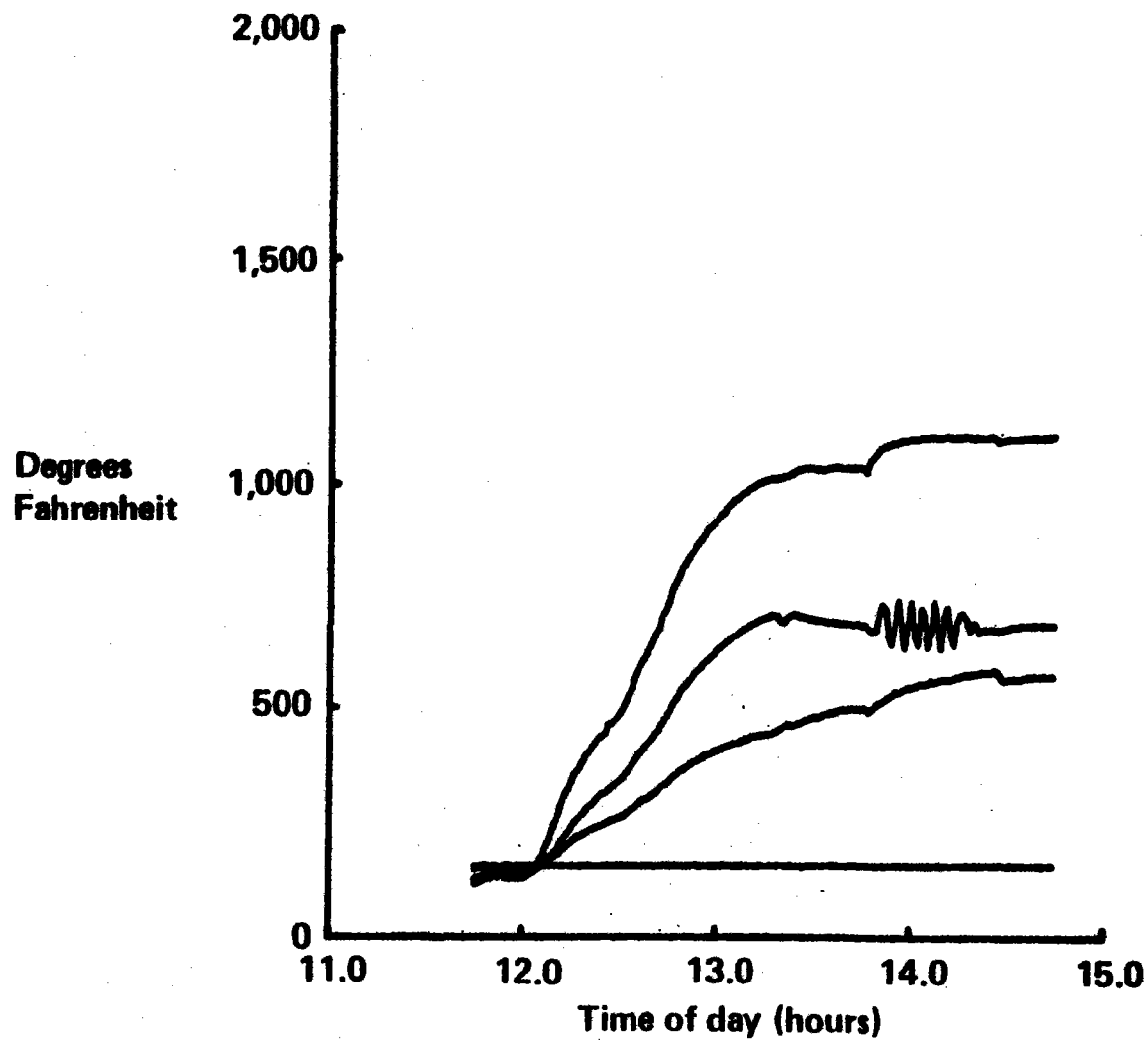
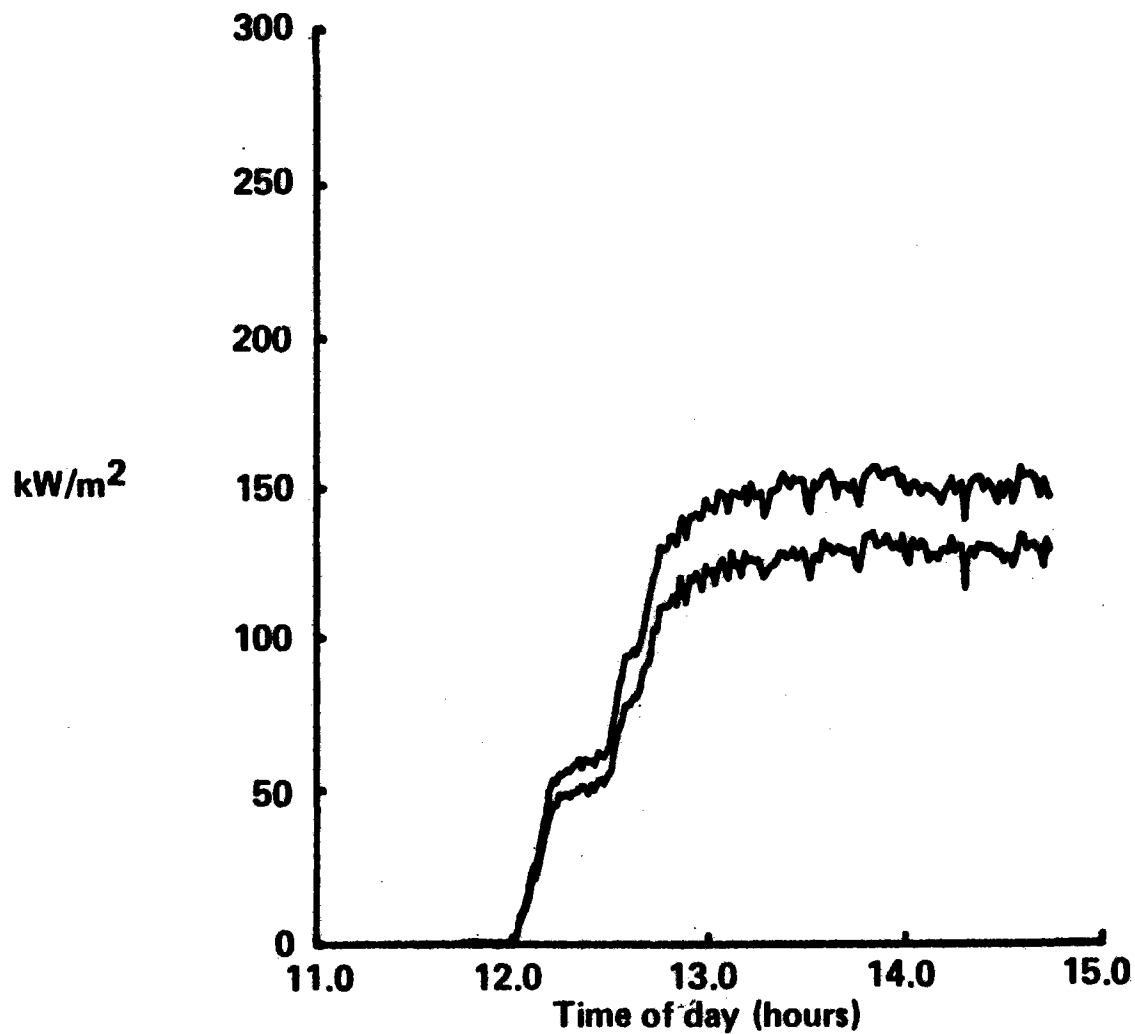


Figure 12.3-11 Plot of December 10, 1978 Test Data, Frame Calorimeters

## Plot of December 10, 1978 Test Data, Frame Calorimeters



089

Figure 12.3-12 Plot of December 10, 1978 Test Data, Receiver Mass Flow

# Plot of December 10, 1978 Test Data, Receiver Mass Flow

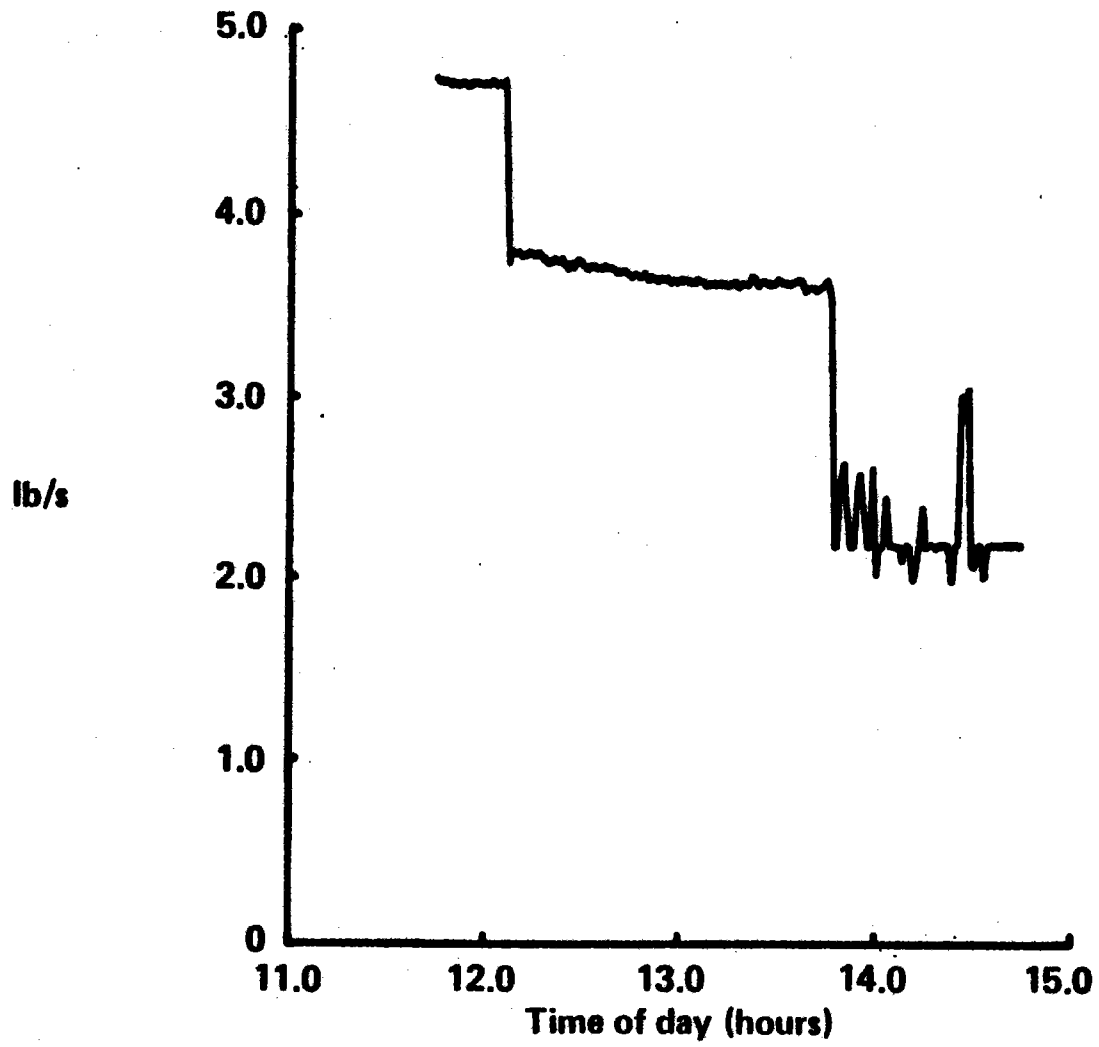


Figure 12.3-13 Plot of December 10, 1978 Test Data, H/X Panel 3 Valve Angle

## Plot of December 10, 1978 Test Data, H/X Panel 3 Valve Angle

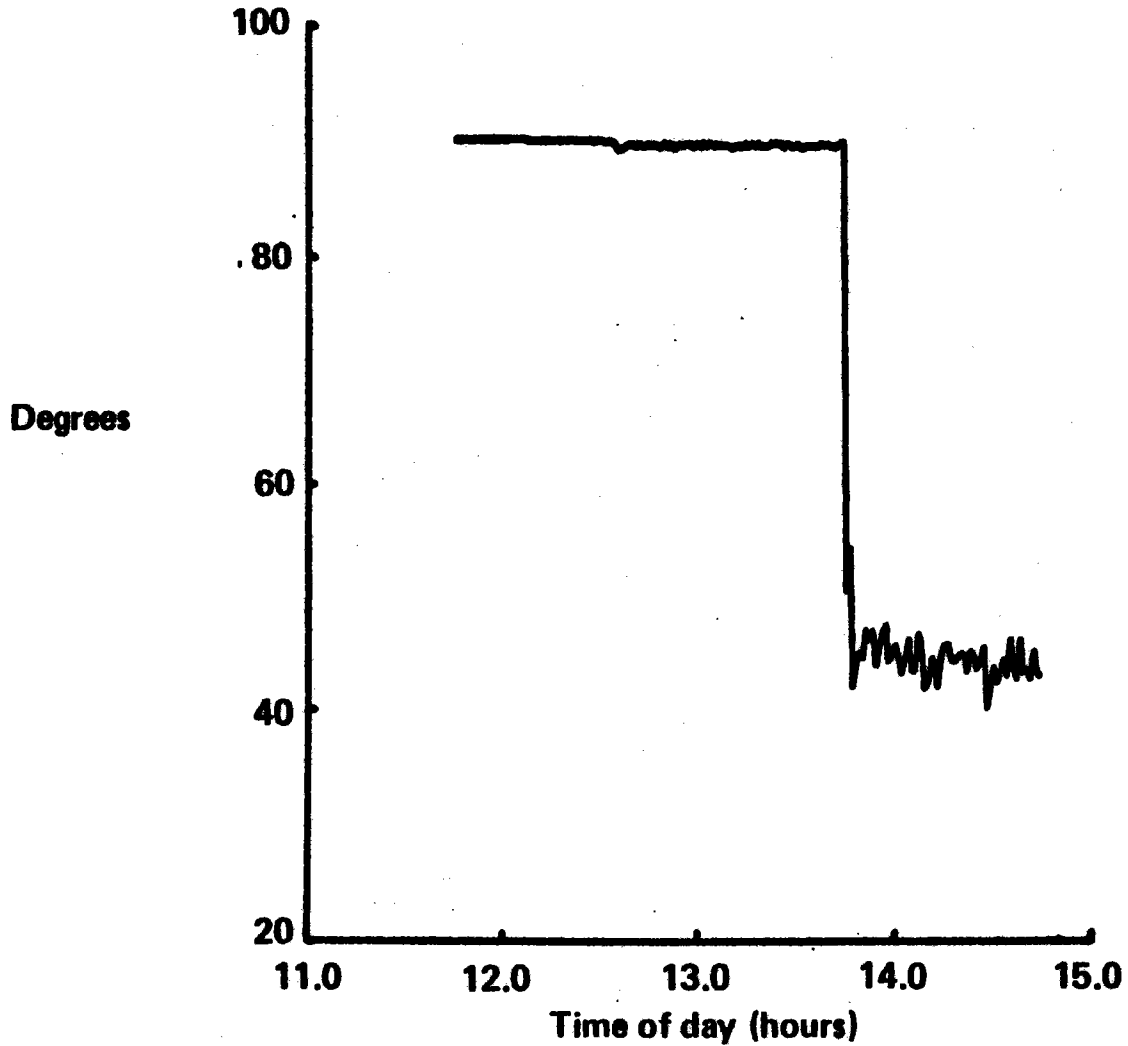
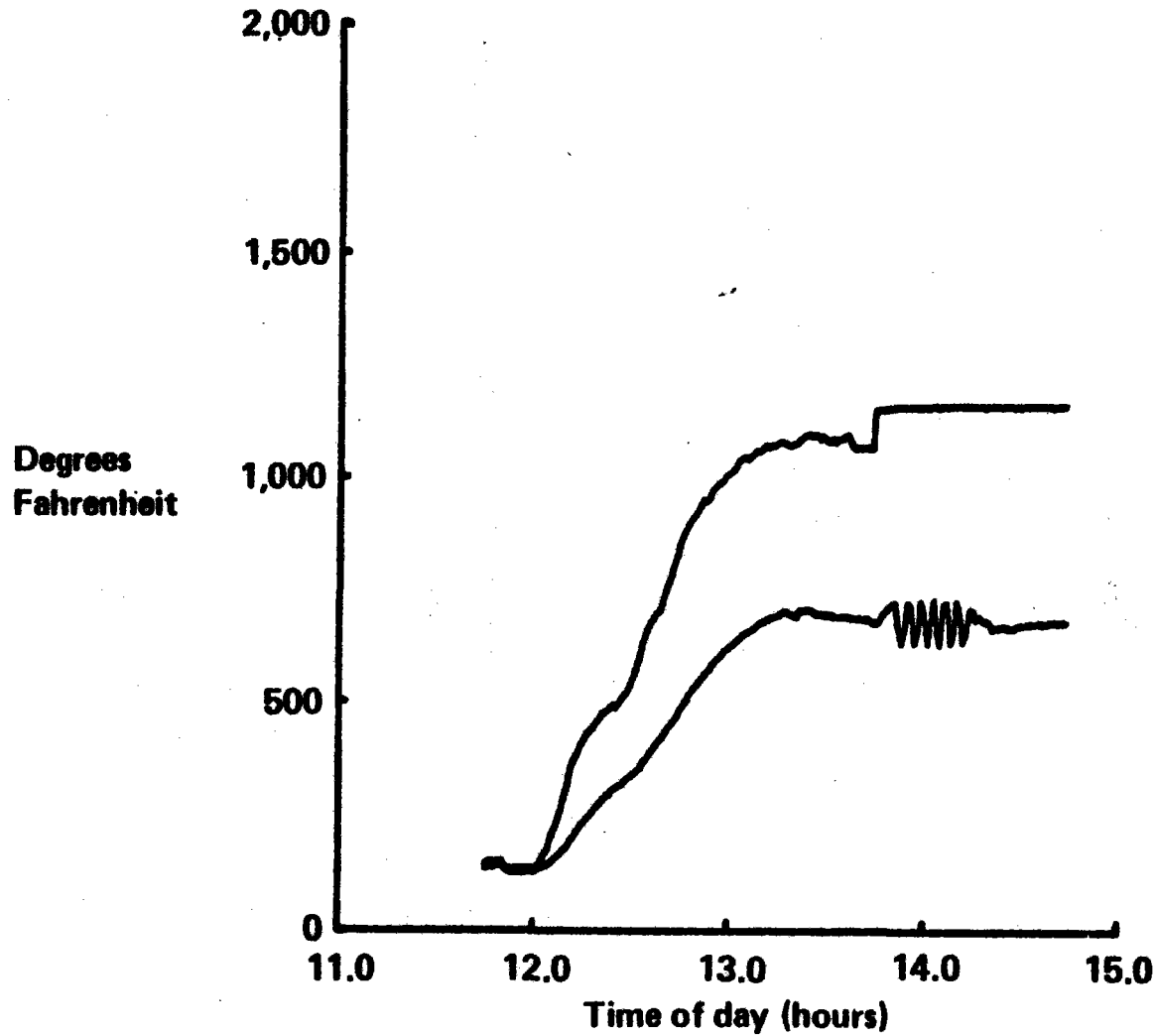




Figure 12.3-14 Plot of December 10, 1978 Test Data, Air Inlet-Outlet Temperatures, Panel 3

## Plot of December 10, 1978 Test Data, Air Inlet-Outlet Temperatures, Panel 3



*Figure 12.3-15 Time Chart for January 4, 1979 Solar Test*

## **Time Chart for January 4, 1979 Solar Test**

<b>11:04</b>	<b>Field at standby</b>
<b>11:05</b>	<b>First collector on target</b>
<b>11:33</b>	<b>45 collectors on target</b>
<b>12:56</b>	<b>Receiver on control</b>
<b>13:06</b>	<b>47 collectors on target</b>
<b>13:06</b>	<b>Steady test conditions, EB-5A</b>
<b>13:31</b>	<b>53 collectors on target</b>
<b>13:32</b>	<b>Field at standby</b>
<b>13:40</b>	<b>First collector on target</b>
<b>13:54</b>	<b>30 collectors on target</b>
<b>14:13</b>	<b>Field shutdown</b>

Figure 12.3-16 Plot of January 4, 1979 Test Data, Eppley Pyrheliometer

### Plot of January 4, 1979 Test Data, Eppley Pyrheliometer

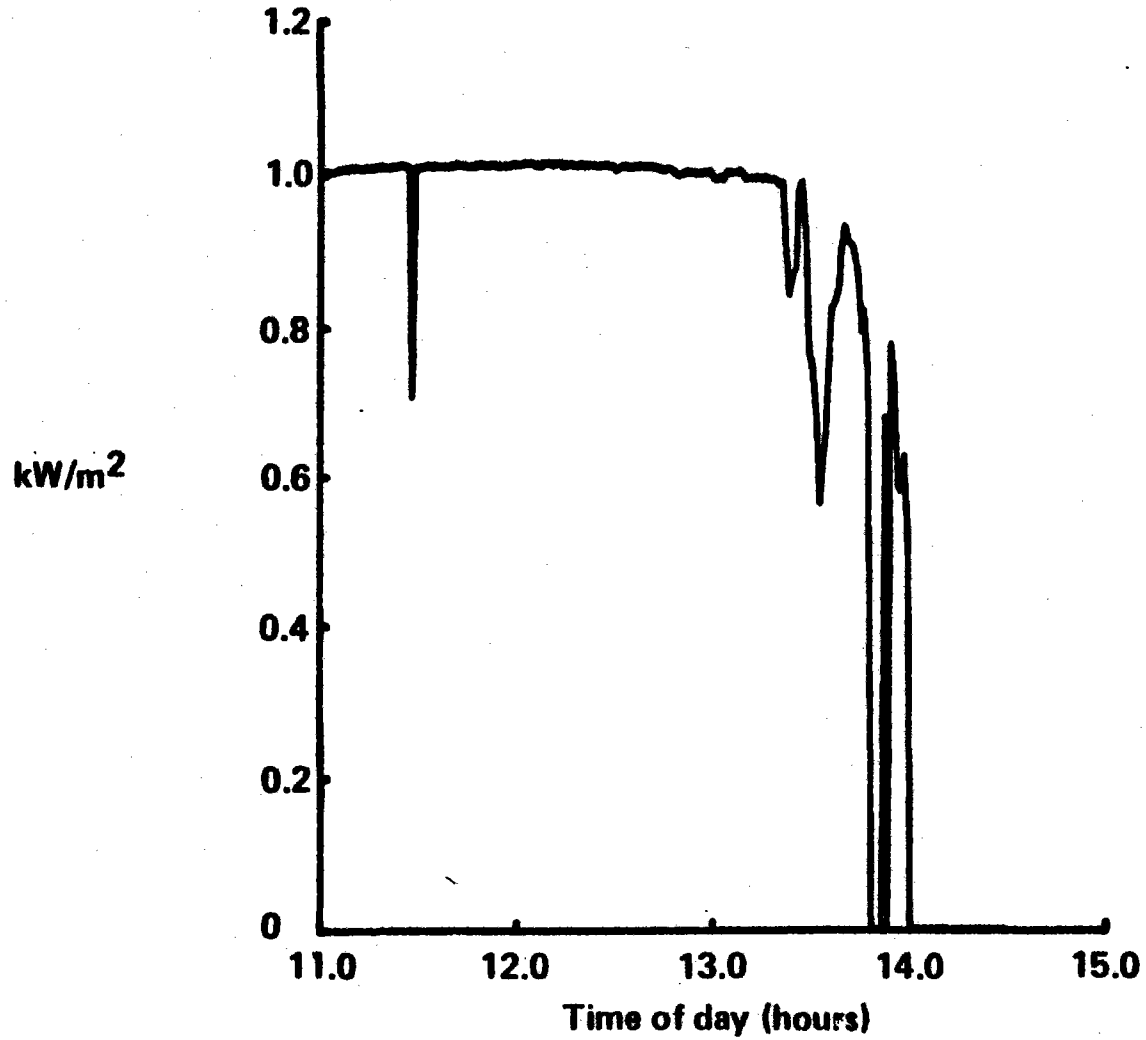


Figure 12.3-17 Plot of January 4, 1979 Test Data, Air Supply Gas Temperatures

## Plot of January 4, 1979 Test Data, Air Supply Gas Temperatures

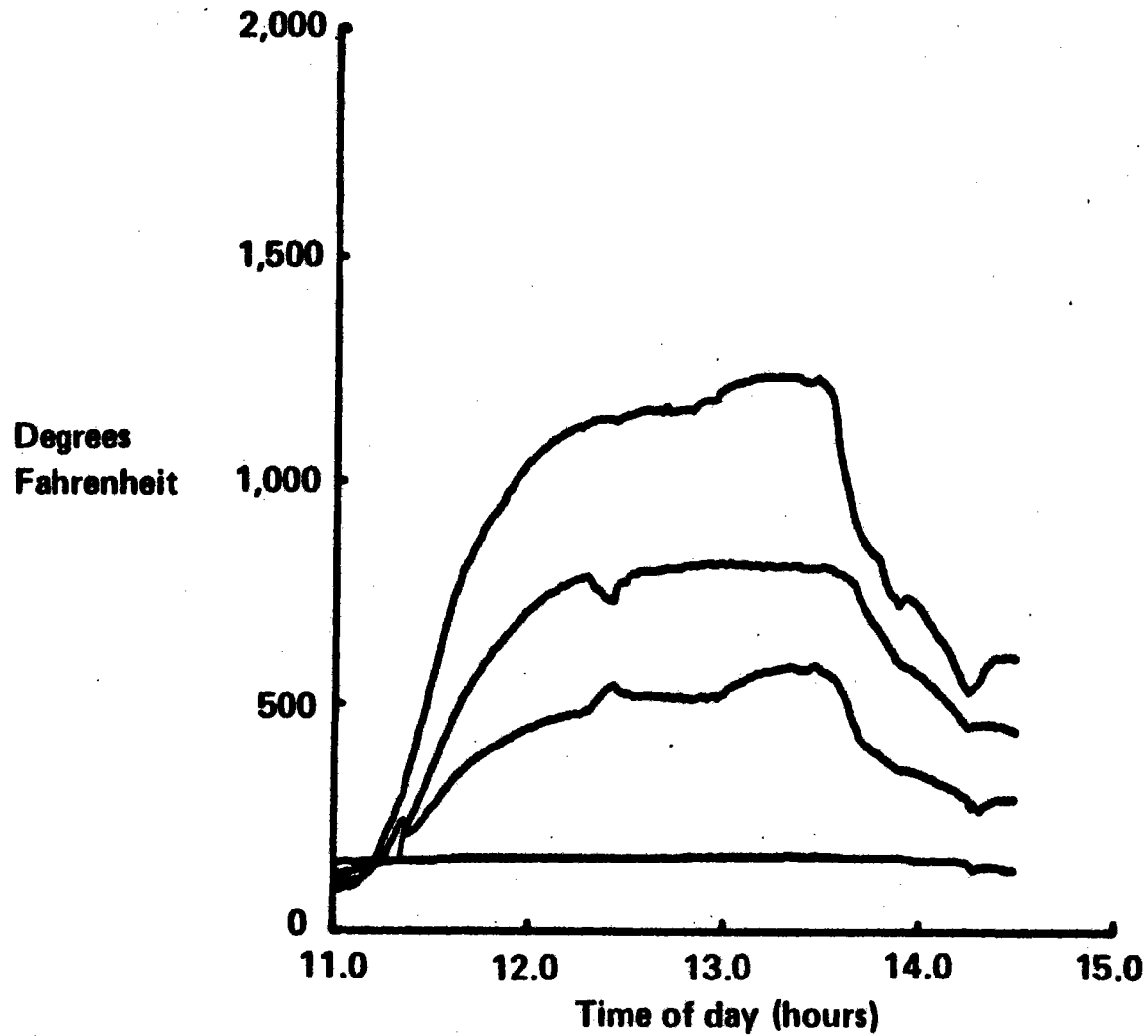


Figure 12.3-18 Plot of January 4, 1979 Test Data, Frame Calorimeters

## Plot of January 4, 1979 Test Data, Frame Calorimeters

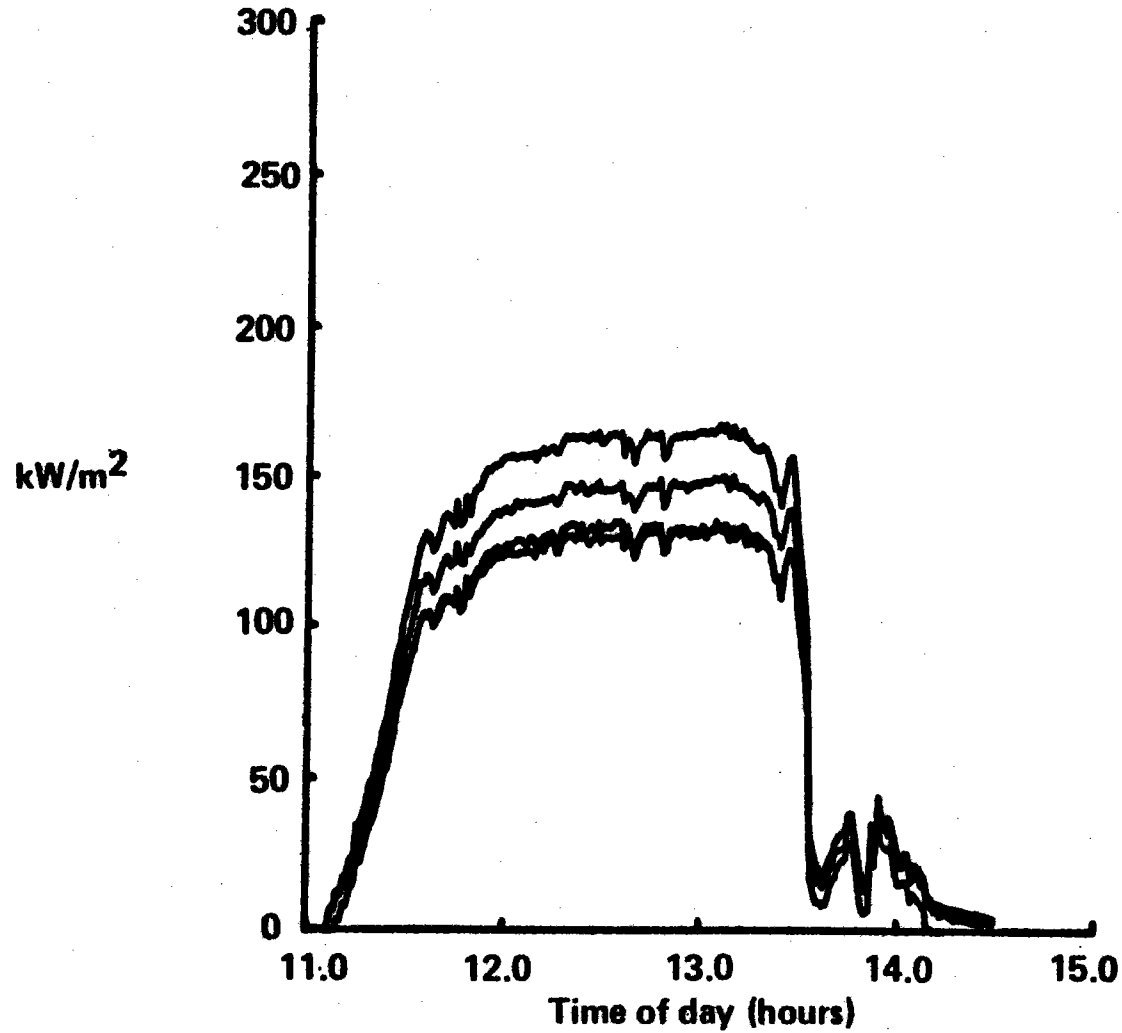
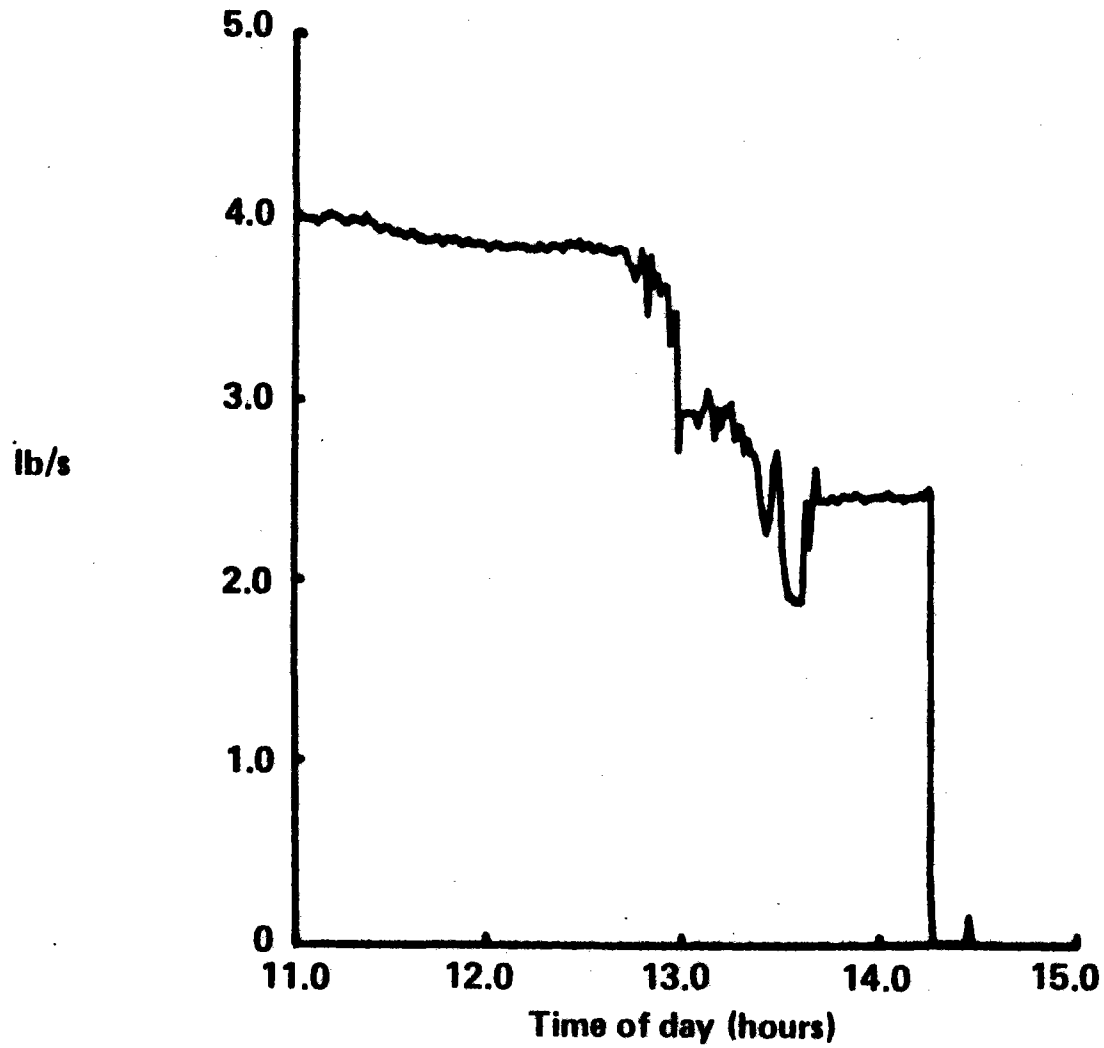


Figure 12.3-19 Plot of January 4, 1979 Test Data, Receiver Mass Flow

# Plot of January 4, 1979 Test Data, Receiver Mass Flow



689

Figure 12.3-20 Plot of January 4, 1979 Test Data, H/X Panel 3 Valve Angle

### Plot of January 4, 1979 Test Data, H/X Panel 3 Valve Angle

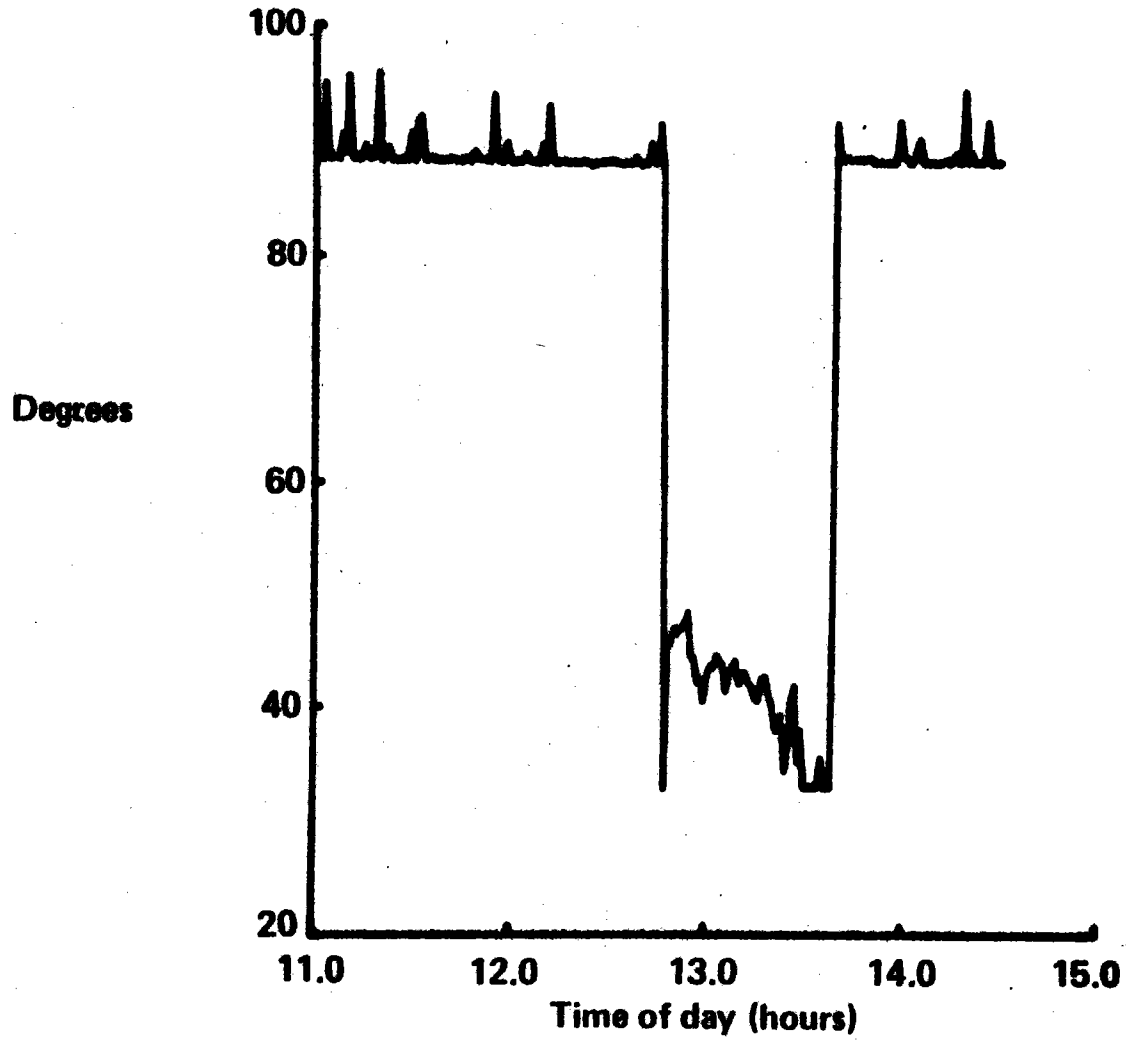
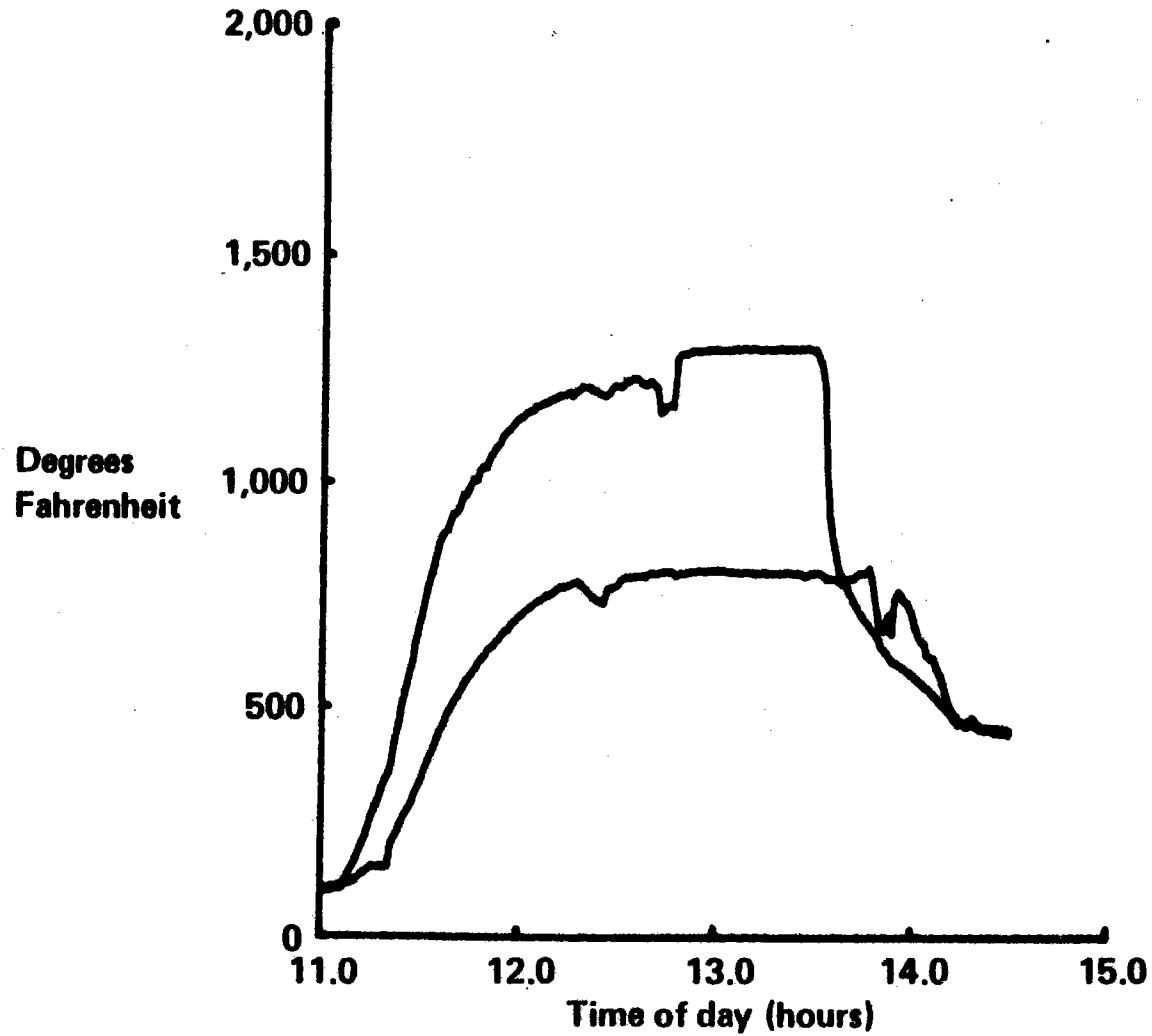


Figure 12.1-21 Plot of January 4, 1979 Test Data, Air Inlet-Outlet Temperatures, Panel 3

### Plot of January 4, 1979 Test Data, Air Inlet-Outlet Temperatures, Panel 3





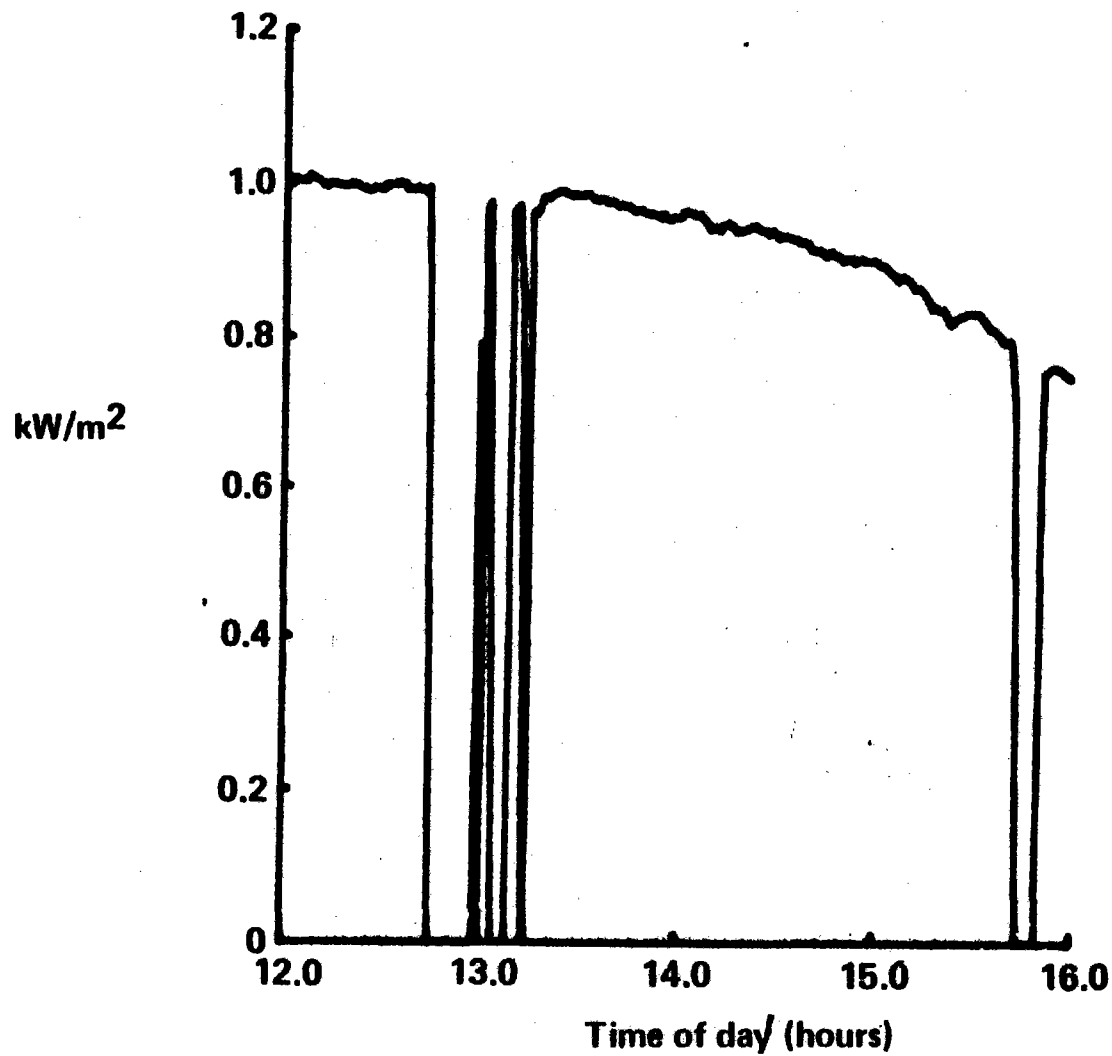
*Figure 12.3-22 Time Chart for January 7, 1979 Solar Test*

## **Time Chart for January 7, 1979 Solar Test**

<b>12:10</b>	<b>Field at standby</b>
<b>12:12</b>	<b>First collector on target</b>
<b>12:45</b>	<b>55 collectors on target</b>
<b>14:05</b>	<b>Receiver on control</b>
<b>14:14</b>	<b>60 collectors on target</b>
<b>14:27</b>	<b>66 collectors on target</b>
<b>14:43</b>	<b>76 collectors on target</b>
<b>14:48</b>	<b>Steady test conditions, EB-7A</b>
<b>14:57</b>	<b>71 collectors on target</b>
<b>15:15</b>	<b>41 collectors on target</b>
<b>15:16</b>	<b>Receiver off control</b>
<b>15:21</b>	<b>31 collectors on target</b>
<b>15:41</b>	<b>Field shutdown</b>

Figure 12.3-23 Plot of January 7, 1979 Test Data, Eppley Pyrheliometer

## Plot of January 7, 1979 Test Data, Eppley Pyrheliometer



692

Figure 12.3-24 Plot of January 7, 1979 Test Data, Air Supply Gas Temperatures

## Plot of January 7, 1979 Test Data, Air Supply Gas Temperatures

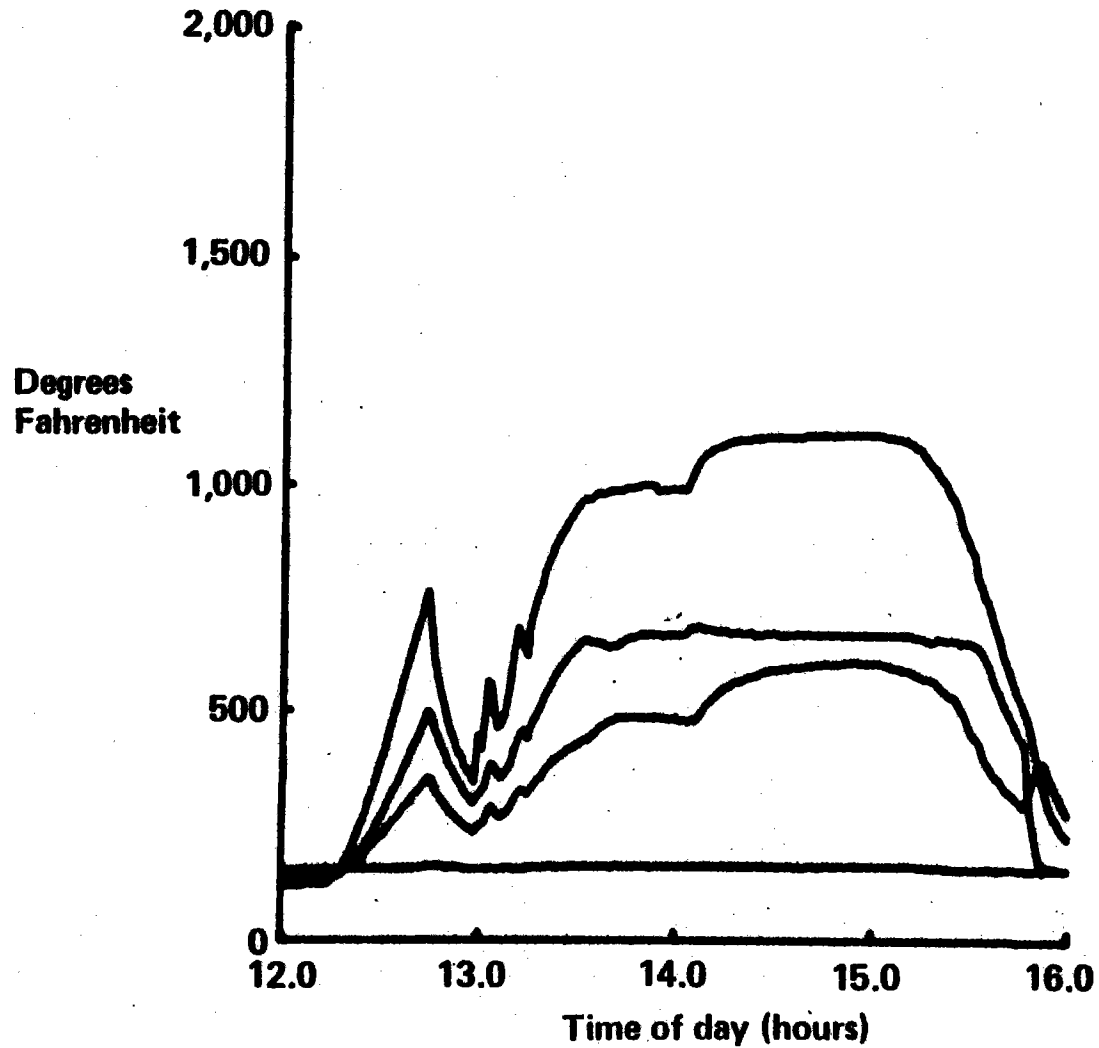
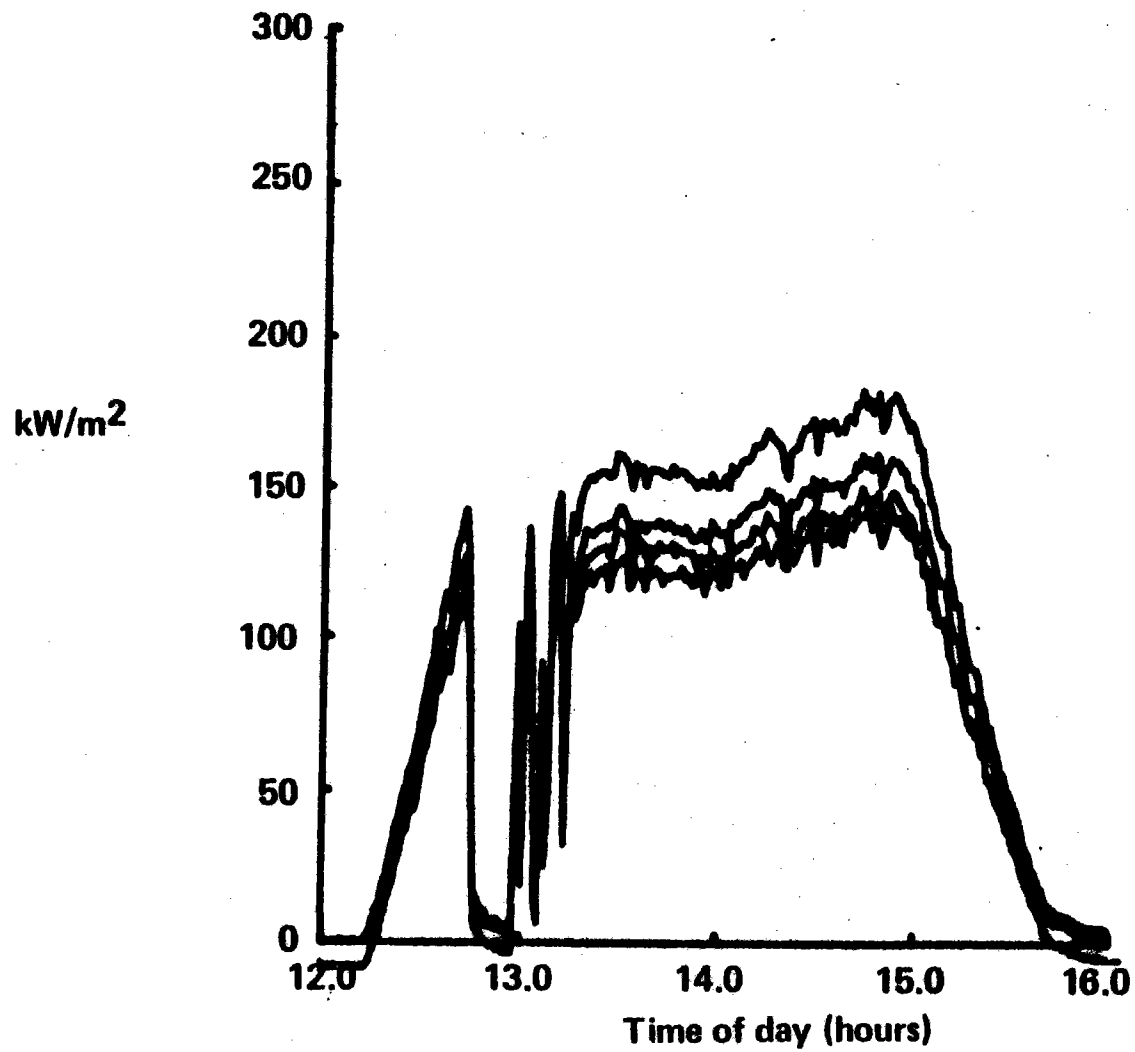


Figure 12.3-25 Plot of January 7, 1979 Test Data, Frame Calorimeters

# Plot of January 7, 1979 Test Data, Frame Calorimeters



694

Figure 12.3-26 Plot of January 7, 1979 Test Data, Receiver Mass Flow

# Plot of January 7, 1979 Test Data, Receiver Mass Flow

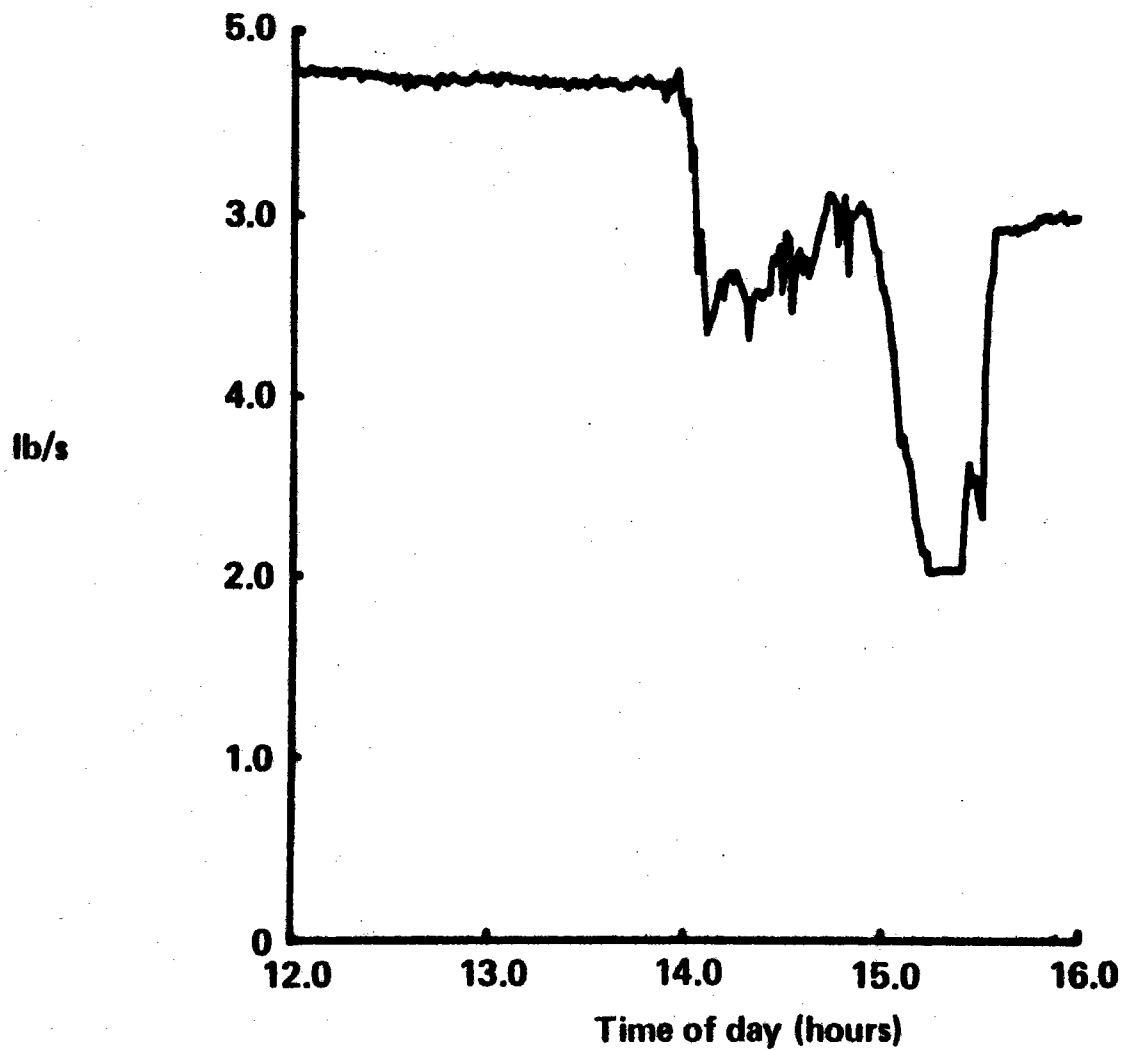
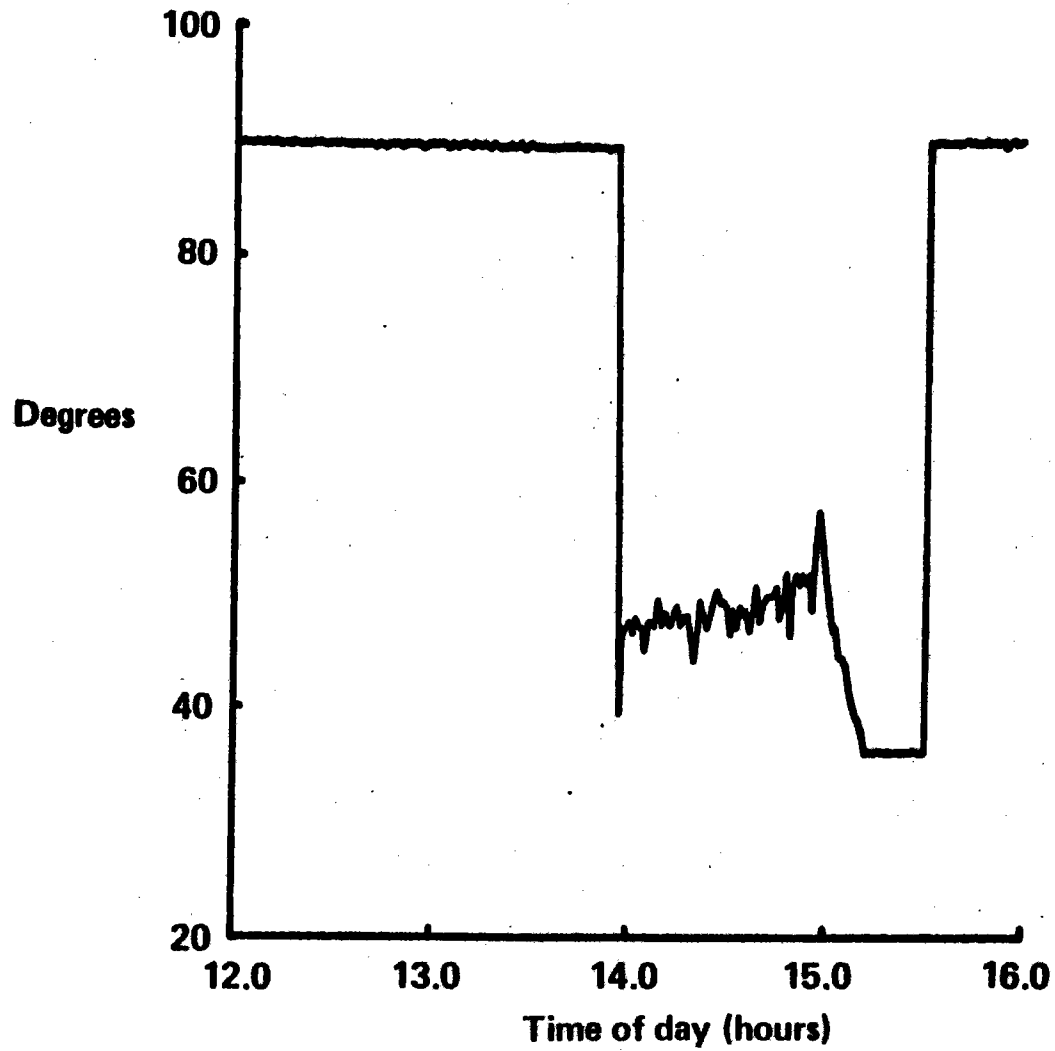


Figure 12.3-27 Plot of January 7, 1979 Test Data, H/X Panel 3 Valve Angle

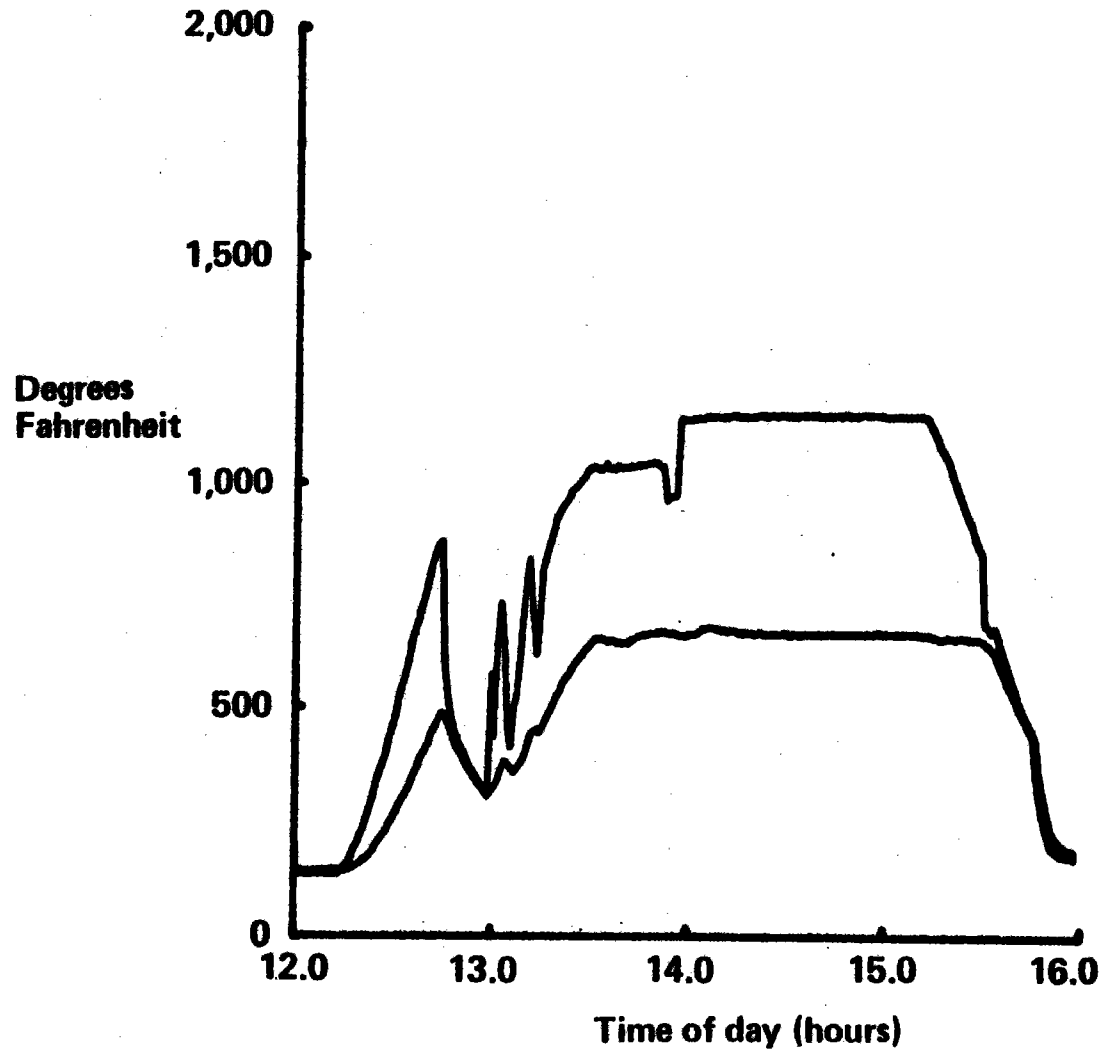
# Plot of January 7, 1979 Test Data, H/X Panel 3 Valve Angle



969

Figure 12.3-28 Plot of January 7, 1979 Test Data, Air Inlet-Outlet Temperatures, Panel 3

### Plot of January 7, 1979 Test Data, Air Inlet-Outlet Temperatures, Panel 3



697

*Figure 12.3-29 Time Chart for January 10, 1979 Solar Test*  
**Time Chart for January 10, 1979 Solar Test**

<b>10:10</b>	<b>Field at standby</b>
<b>10:12</b>	<b>First collector on target</b>
<b>10:47</b>	<b>55 collectors on target</b>
<b>11:35</b>	<b>Receiver on control</b>
<b>11:43</b>	<b>56 collectors on target</b>
<b>11:54</b>	<b>59 collectors on target</b>
<b>12:21</b>	<b>Steady test conditions, EB-8A</b>
<b>12:34</b>	<b>Receiver off control</b>
<b>13:13</b>	<b>Receiver on control</b>
<b>13:22</b>	<b>47 collectors on target</b>
<b>13:43</b>	<b>Lost "A" zone</b>
<b>13:57</b>	<b>Fail-safe initiated, field shutdown</b>



Figure 12.3-30 Plot of January 10, 1979 Test Data, Eppley Pyrheliometer

### Plot of January 10, 1979 Test Data, Eppley Pyrheliometer

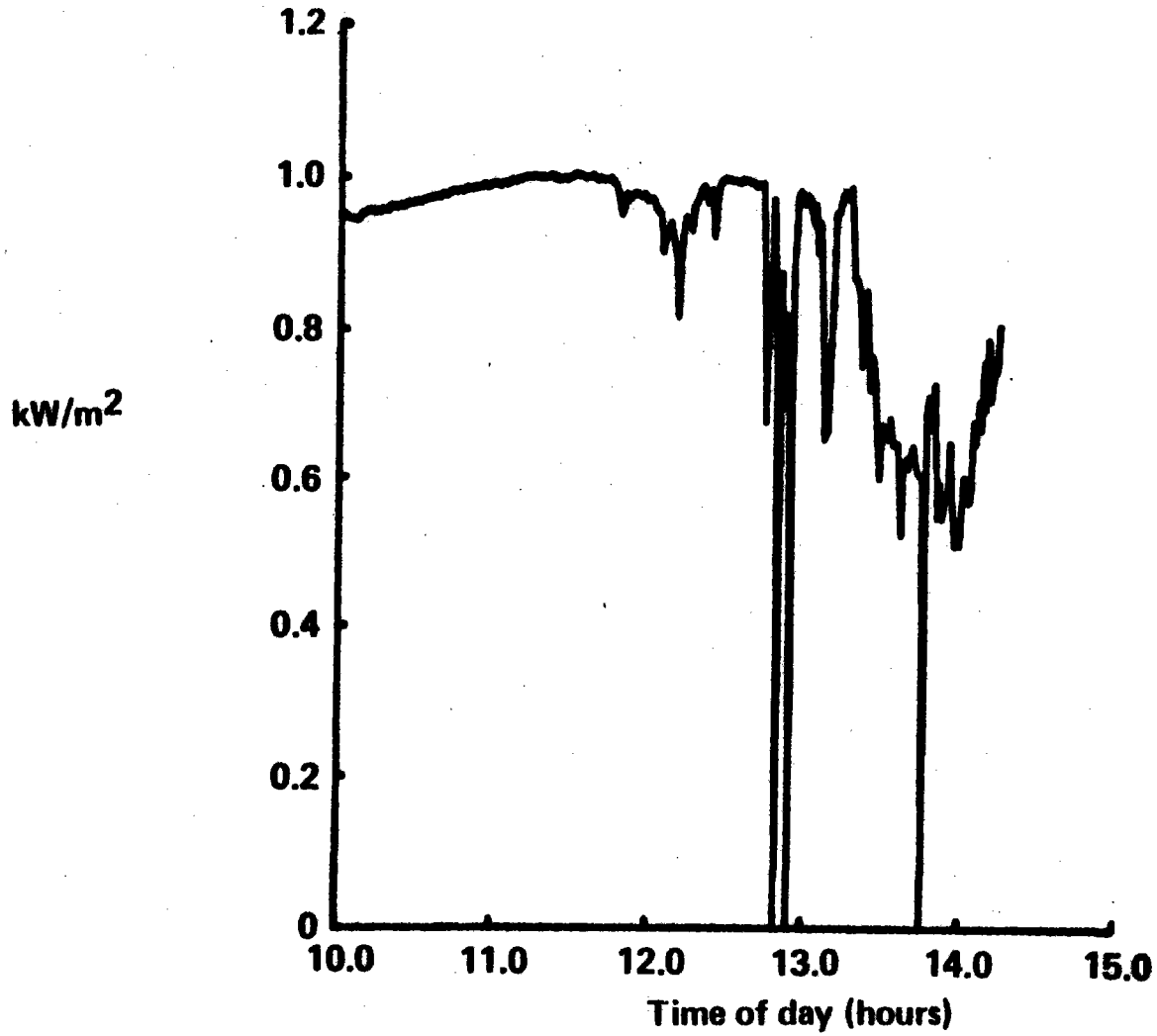
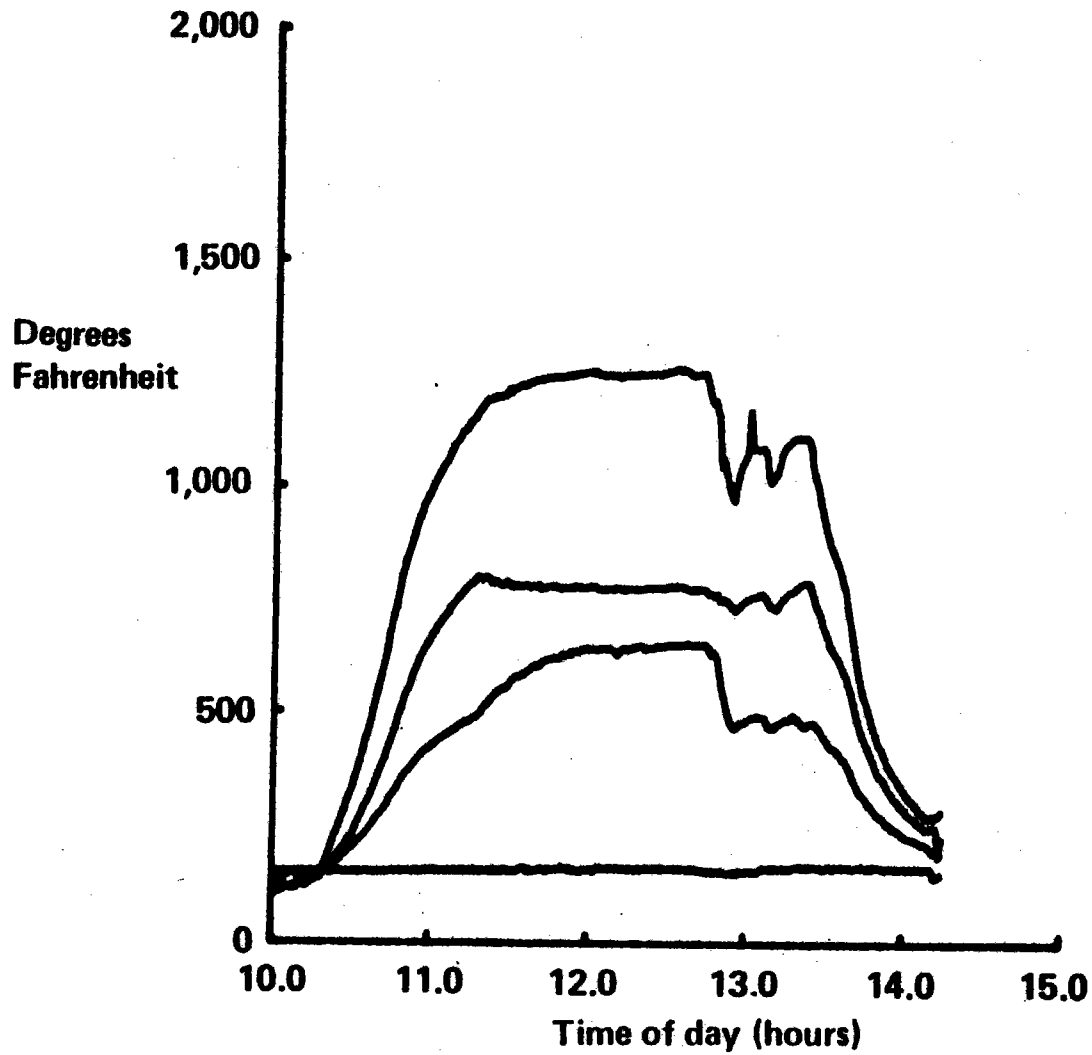


Figure 12.3-31 Plot of January 10, 1979 Test Data, Air Supply Gas Temperatures

## Plot of January 10, 1979 Test Data, Air Supply Gas Temperatures



700

Figure 12.3-32 Plot of January 10, 1979 Test Data, Frame Calorimeters

# Plot of January 10, 1979 Test Data, Frame Calorimeters

701

kW/m<sup>2</sup>

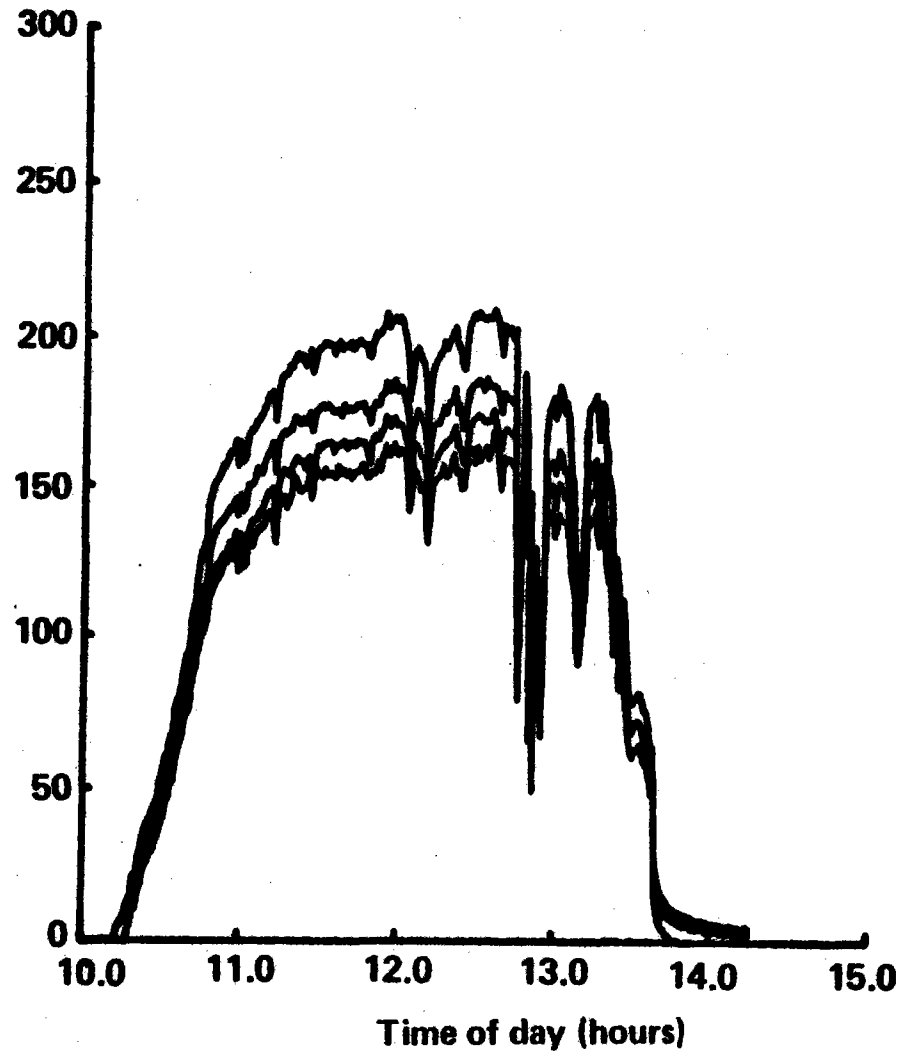
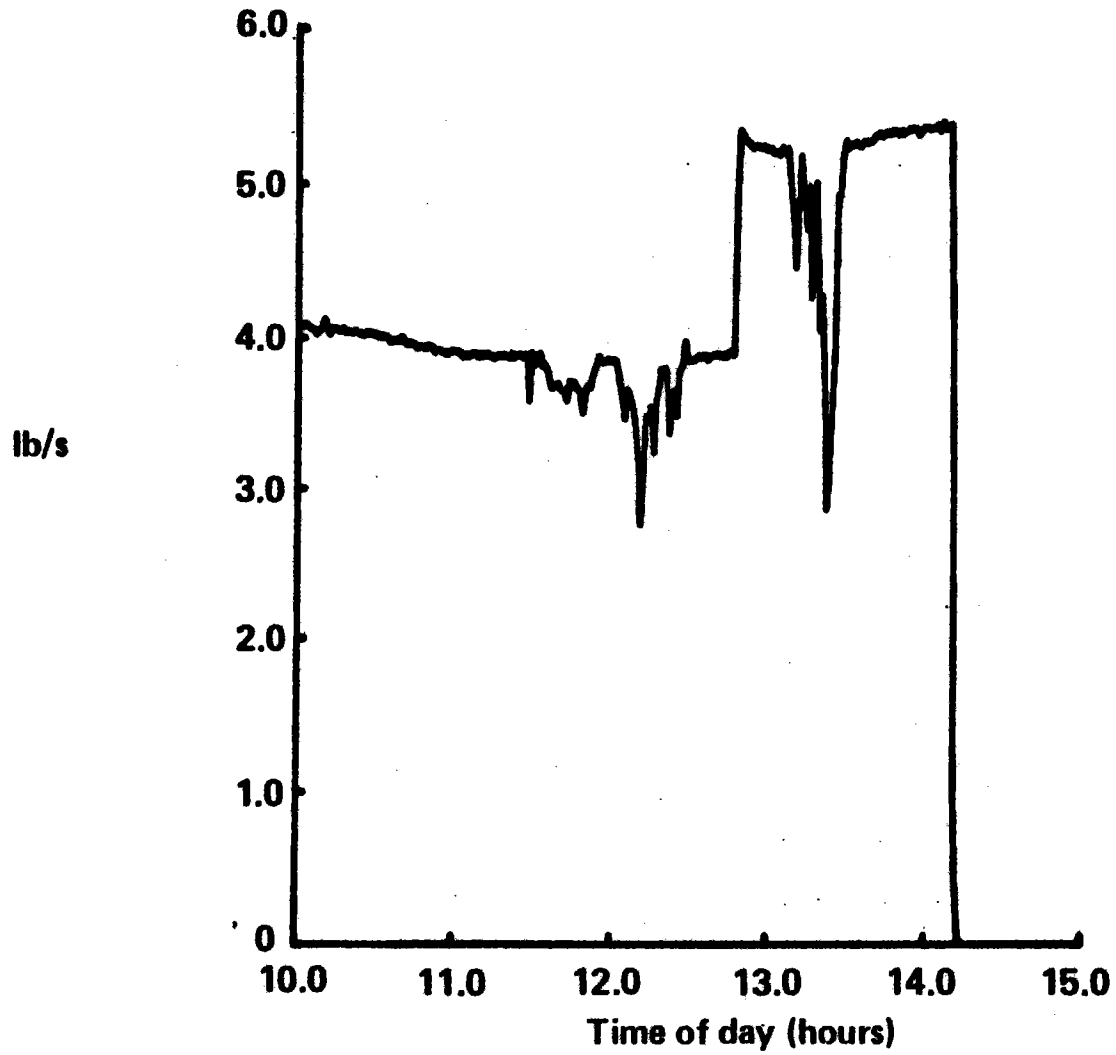


Figure 12.3-33 Plot of January 10, 1979 Test Data, Receiver Mass Flow

## Plot of January 10, 1979 Test Data, Receiver Mass Flow



702

Figure 12.3-34 Plot of January 10, 1979 Test Data, H/X Panel 3 Valve Angle

# Plot of January 10, 1979 Test Data, H/X Panel 3 Valve Angle

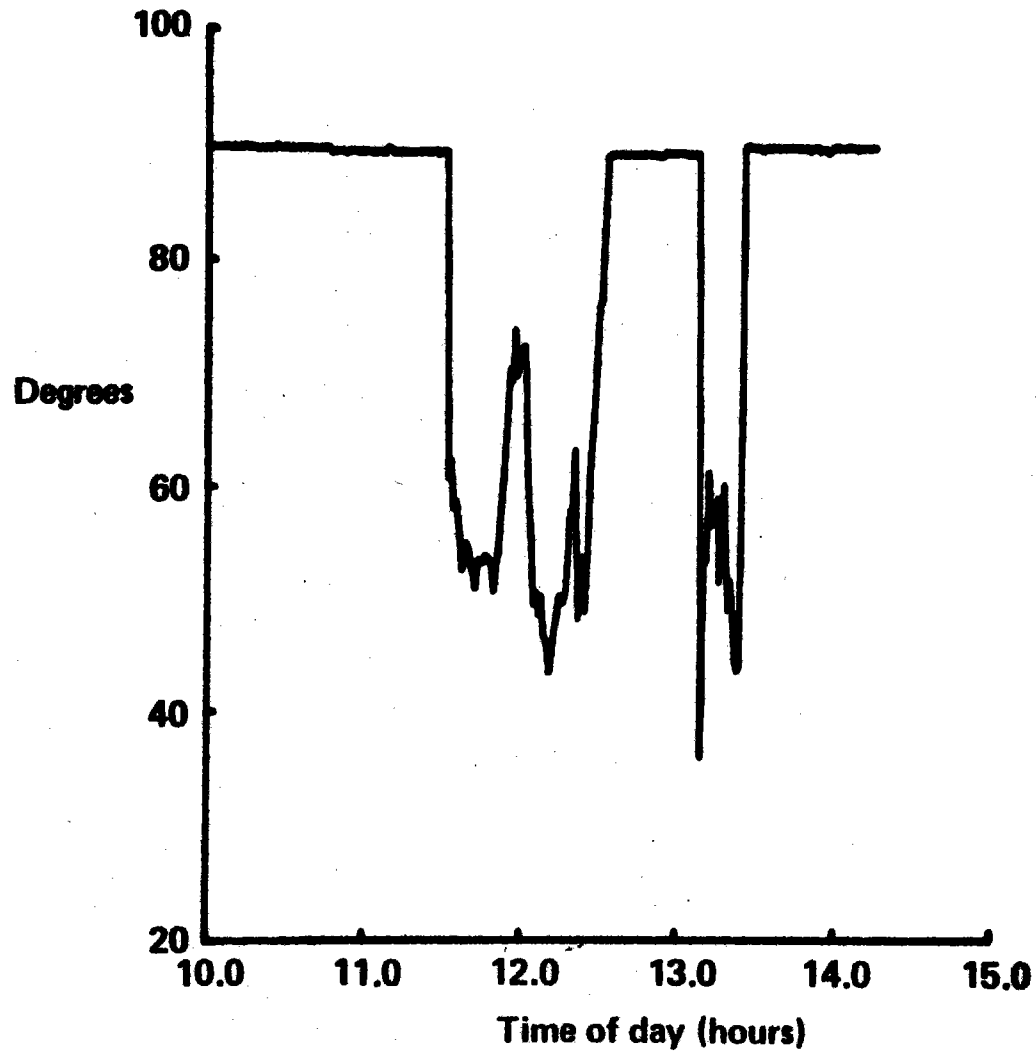
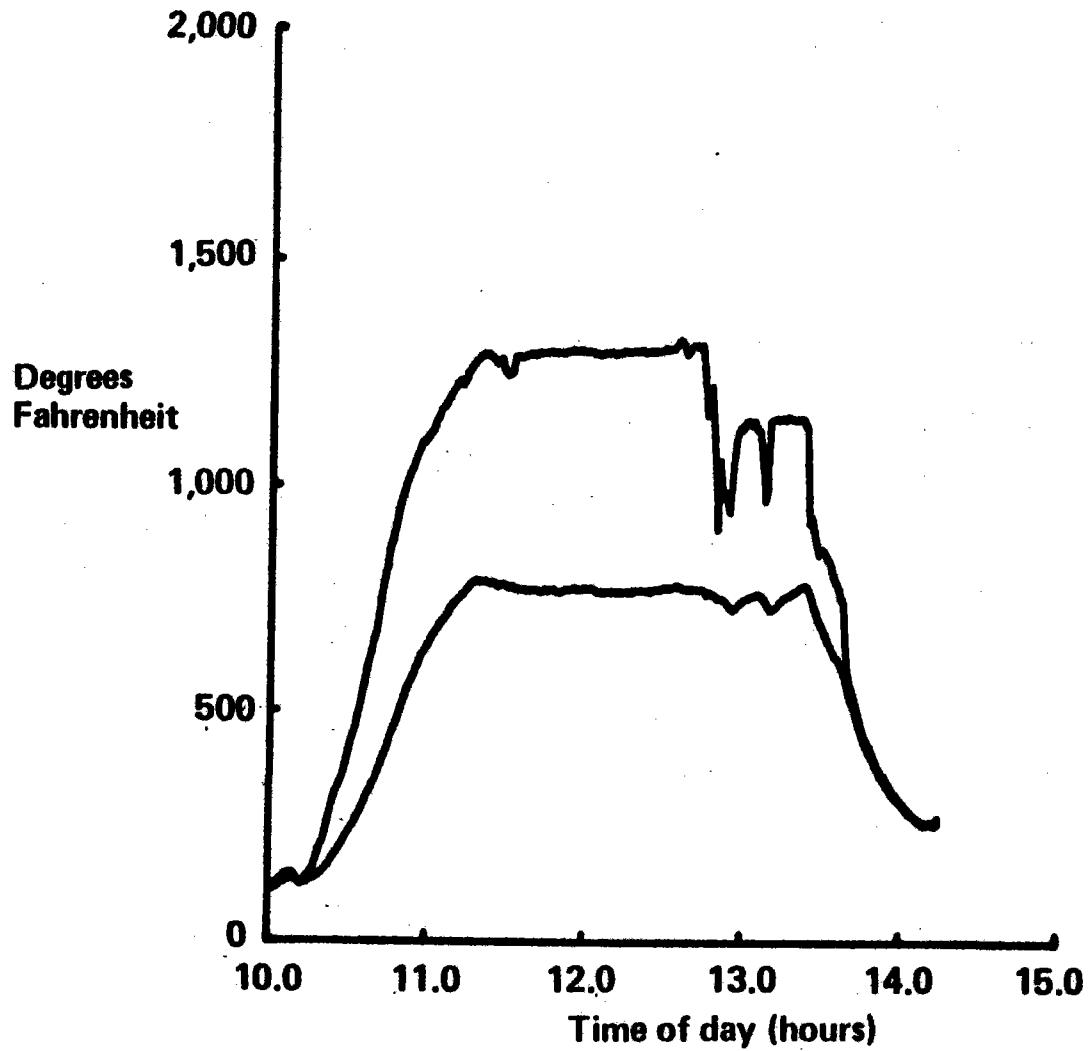


Figure 123-35 Plot of January 10, 1979 Test Data, Air Inlet-Outlet Temperatures, Panel 3

### Plot of January 10, 1979 Test Data, Air Inlet-Outlet Temperatures, Panel 3



*Figure 12.3-36 Time Chart for January 11, 1979 Solar Test*

## **Time Chart for January 11, 1979 Solar Test**

<b>9:55</b>	<b>Field at standby</b>
<b>10:02</b>	<b>10 collectors on target</b>
<b>10:20</b>	<b>40 collectors on target</b>
<b>10:37</b>	<b>50 collectors on target</b>
<b>11:17</b>	<b>60 collectors on target</b>
<b>11:37</b>	<b>Receiver on control</b>
<b>11:49</b>	<b>65 collectors on target</b>
<b>11:50</b>	<b>Steady test conditions, EB-8B</b>
<b>12:13</b>	<b>53 collectors on target</b>
<b>12:26</b>	<b>65 collectors on target</b>
<b>12:31</b>	<b>50 collectors on target</b>
<b>13:24</b>	<b>Field at standby</b>

Figure 12.3-37 Plot of January 11, 1979 Test Data, Eppley Pyrheliometer

# Plot of January 11, 1979 Test Data, Eppley Pyrheliometer

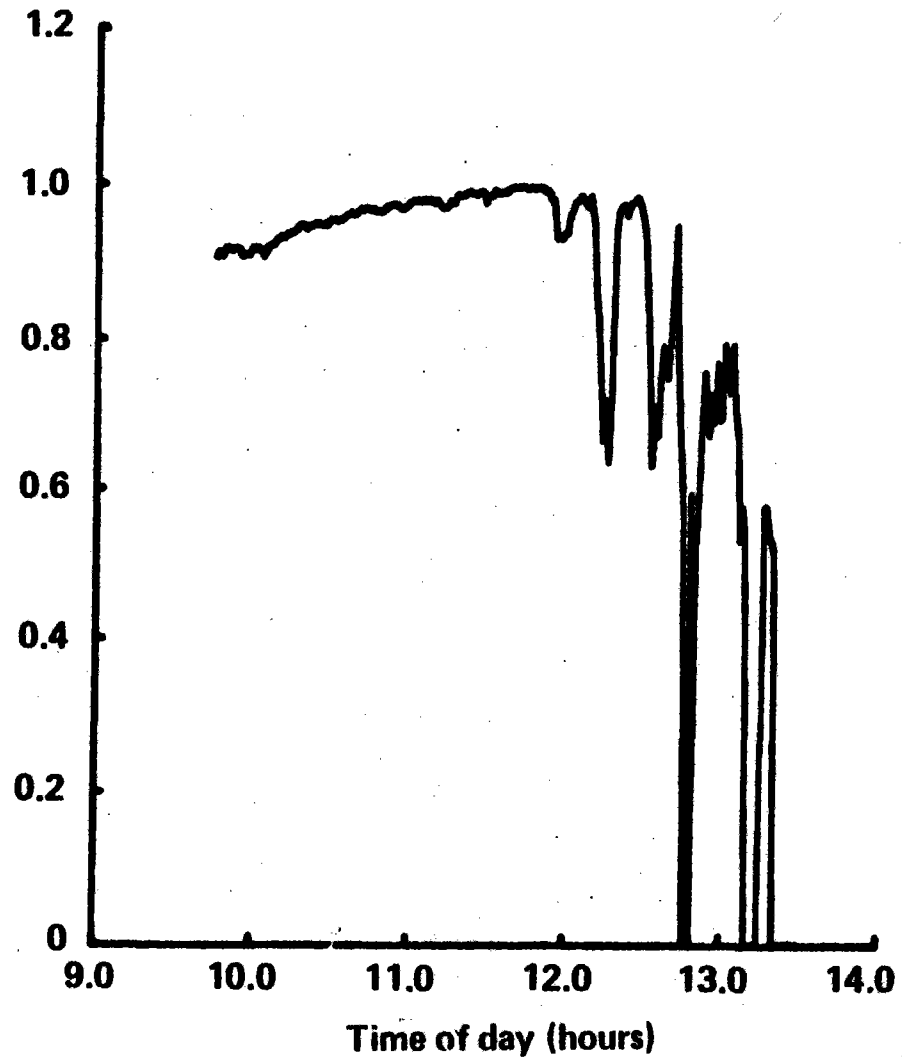




Figure 12.3-38 Plot of January 11, 1979 Test Data, Air Supply Gas Temperatures

## Plot of January 11, 1979 Test Data, Air Supply Gas Temperatures

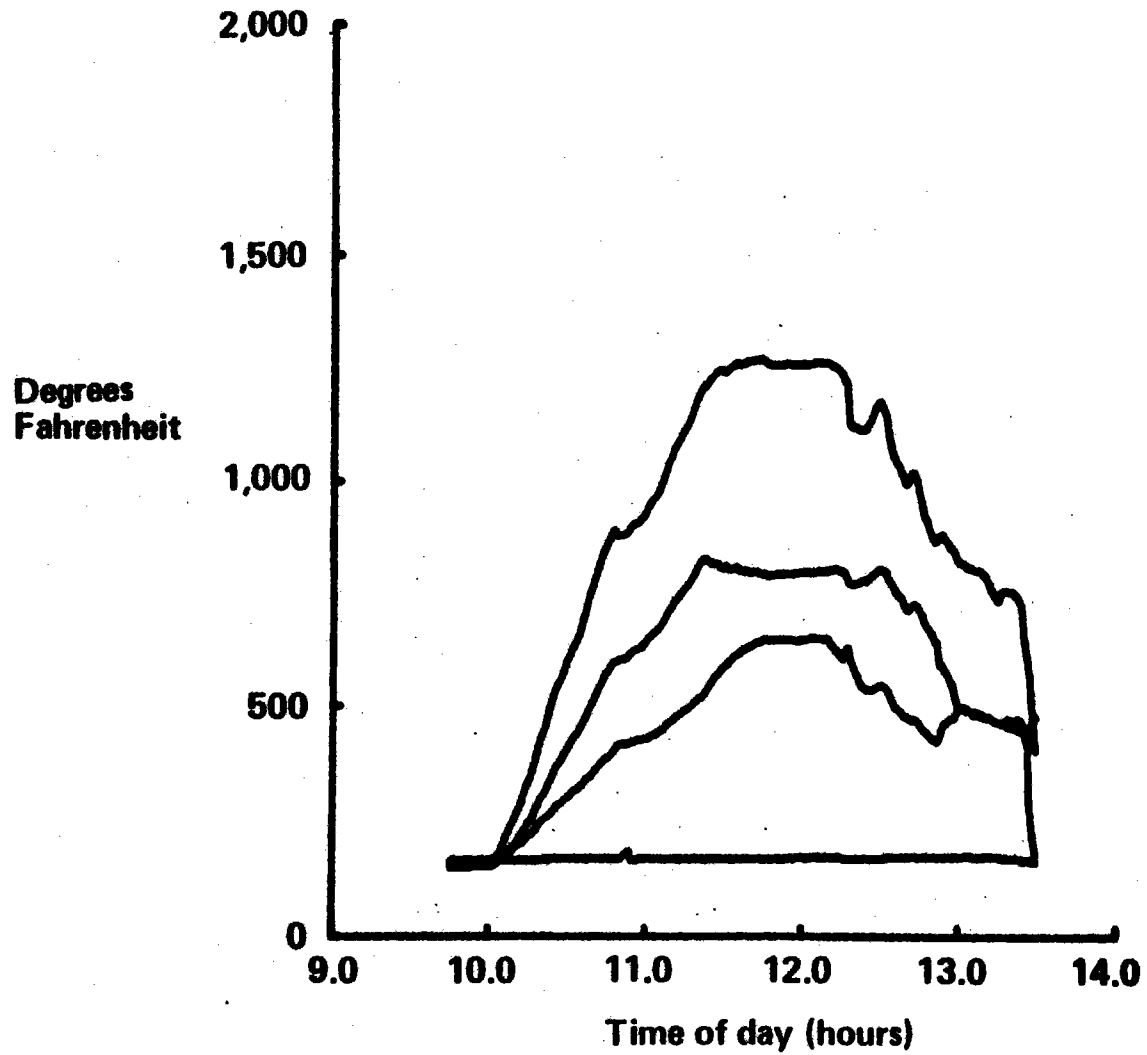


Figure 12.3-39 Plot of January 11, 1979 Test Data, Frame Calorimeters

## Plot of January 11, 1979 Test Data, Frame Calorimeters

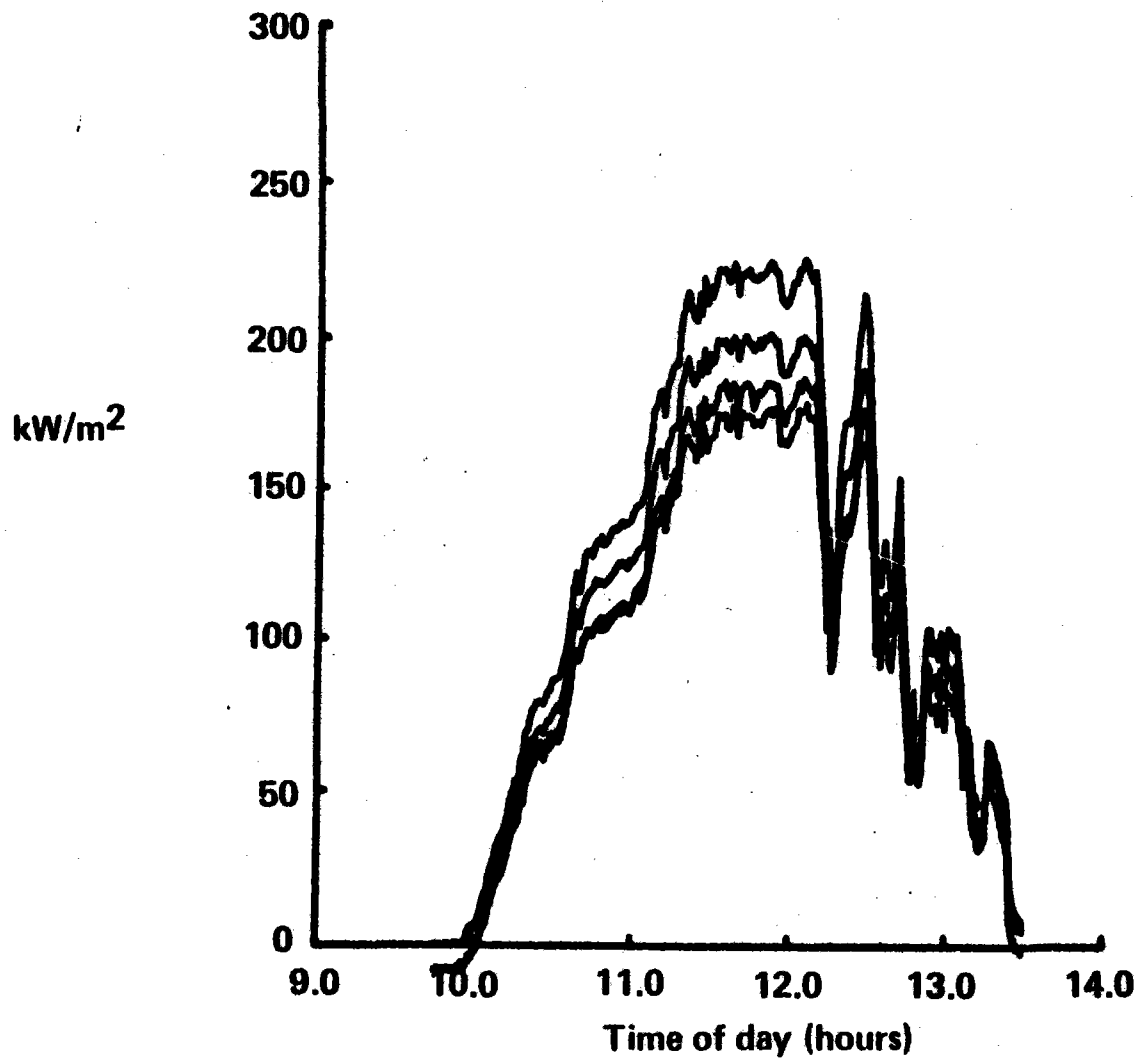
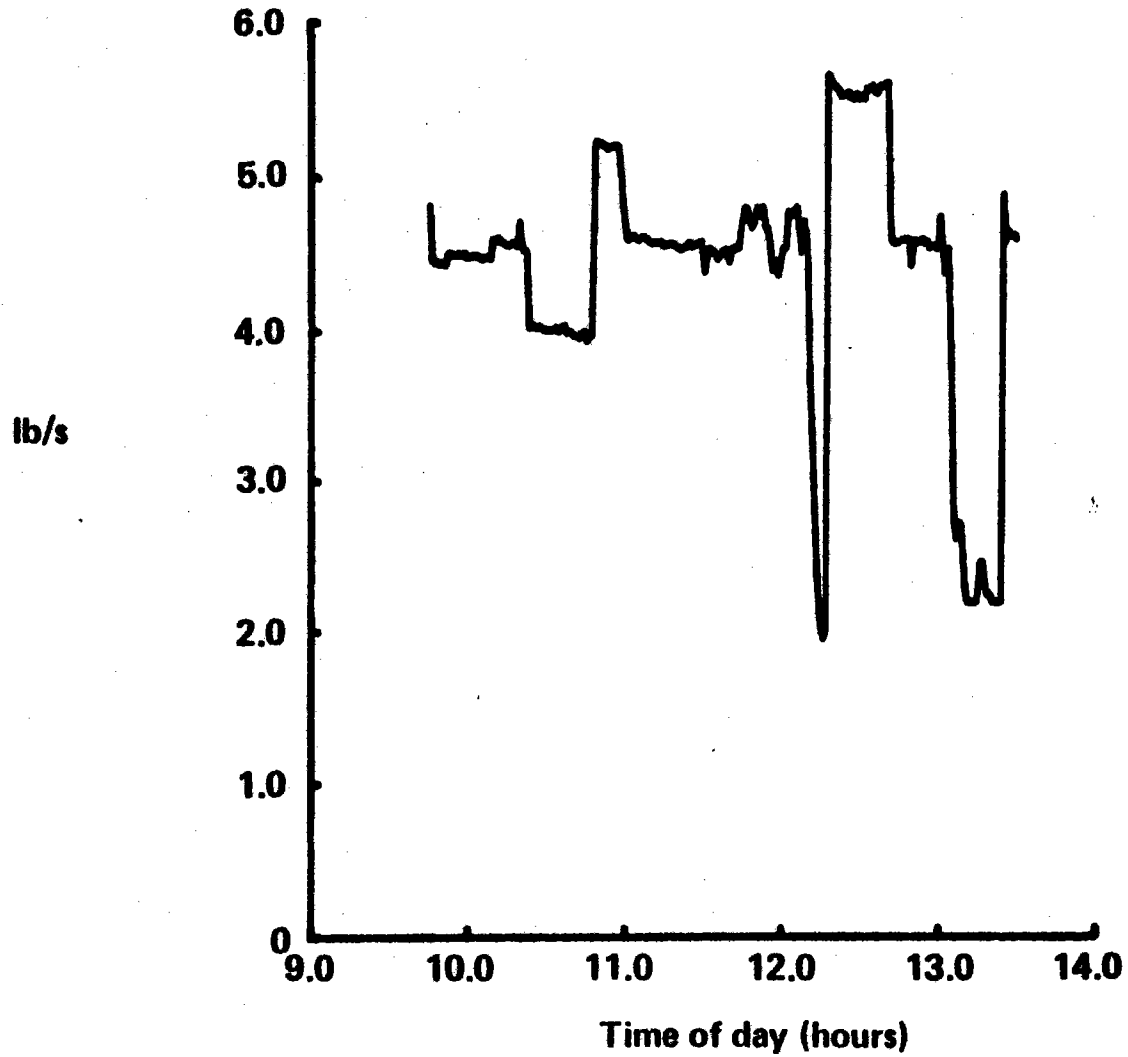


Figure 12.3-40 Plot of January 11, 1979 Test Data, Receiver Mass Flow

## Plot of January 11, 1979 Test Data, Receiver Mass Flow



709

Figure 123-41 Plot of January 11, 1979 Test Data, H/X Panel 3 Valve Angle

# Plot of January 11, 1979 Test Data, H/X Panel 3 Valve Angle

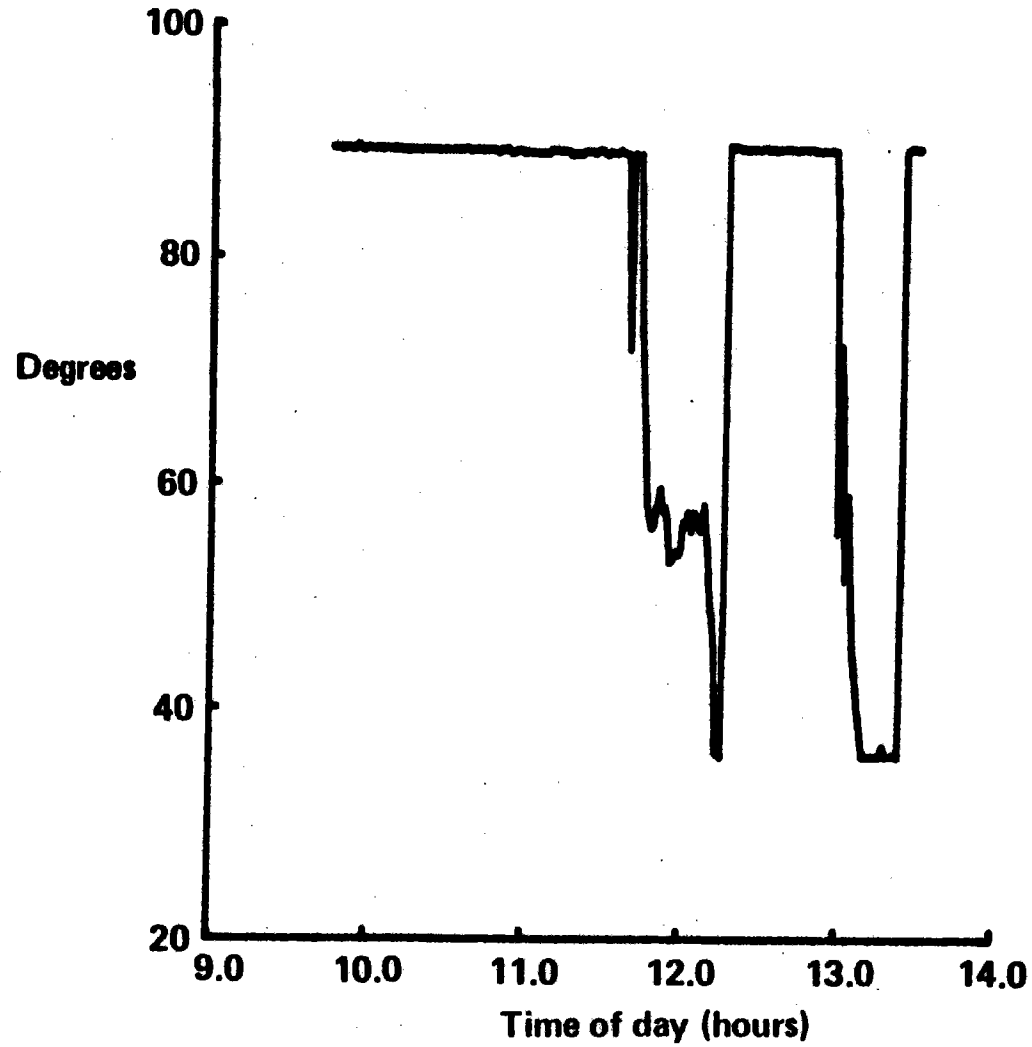
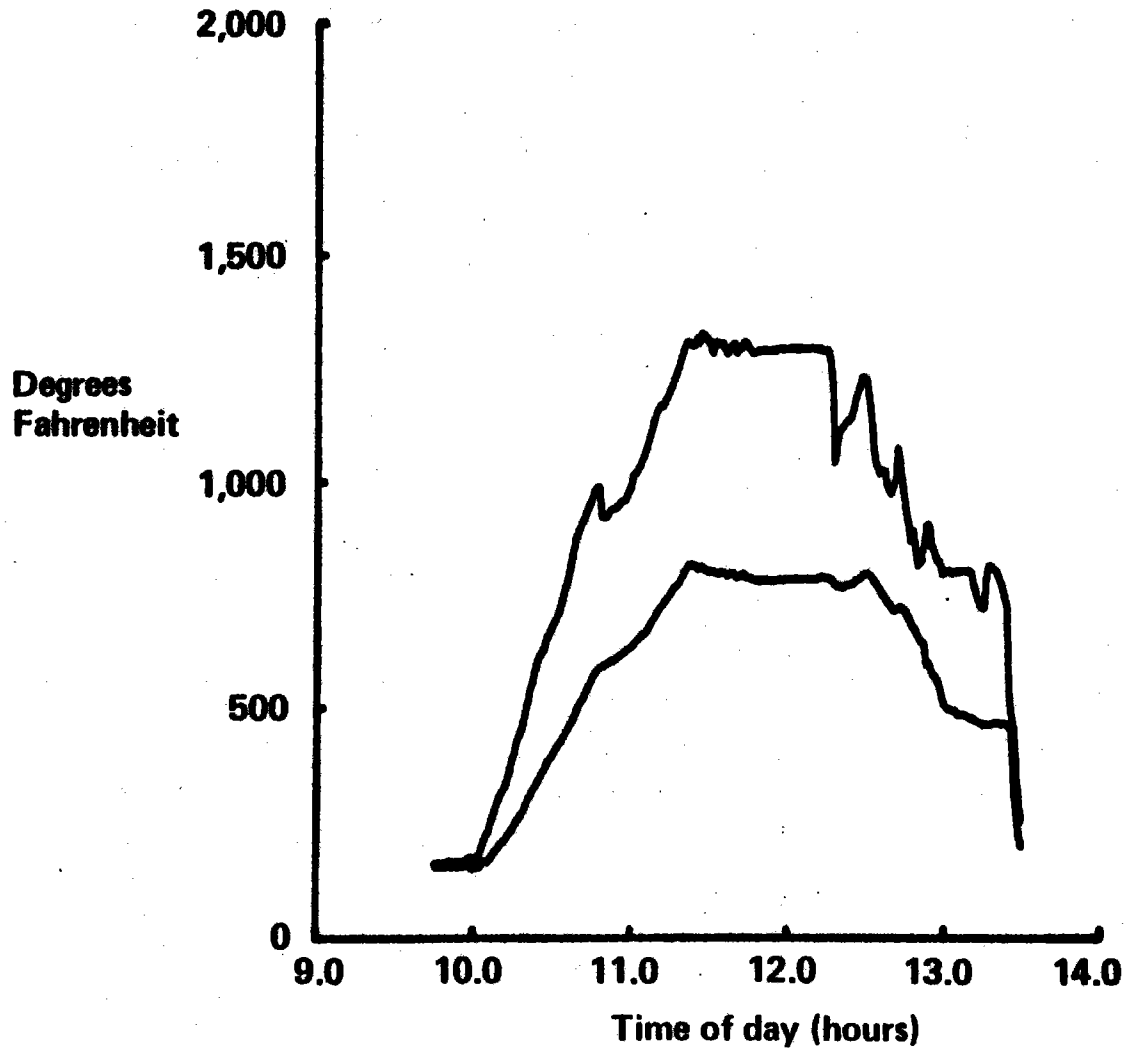


Figure 12.3-42 Plot of January 11, 1979 Test Data, Air Inlet-Outlet Temperatures, Panel 3

### Plot of January 11, 1979 Test Data, Air Inlet-Outlet Temperatures, Panel 3



*Figure 12.3-43 Time Chart for January 13, 1979 Solar Test*

## **Time Chart for January 13, 1979 Solar Test**

<b>10:40</b>	<b>Field at standby</b>
<b>10:41</b>	<b>First collector on target</b>
<b>11:10</b>	<b>45 collectors on target</b>
<b>12:01</b>	<b>50 collectors on target</b>
<b>12:18</b>	<b>54 collectors on target</b>
<b>12:44</b>	<b>58 collectors on target</b>
<b>13:01</b>	<b>63 collectors on target</b>
<b>13:18</b>	<b>65 collectors on target</b>
<b>14:11</b>	<b>Receiver on control</b>
<b>14:18</b>	<b>69 collectors on target</b>
<b>14:20</b>	<b>Steady test conditions, EB-7B</b>
<b>14:26</b>	<b>73 collectors on target</b>
<b>14:34</b>	<b>77 collectors on target</b>
<b>14:46</b>	<b>81 collectors on target</b>
<b>14:48</b>	<b>Collectors to emergency standby</b>

Figure 12.3-44 Plot of January 13, 1979 Test Data, Eppley Pyrheliometer

### Plot of January 13, 1979 Test Data, Eppley Pyrheliometer

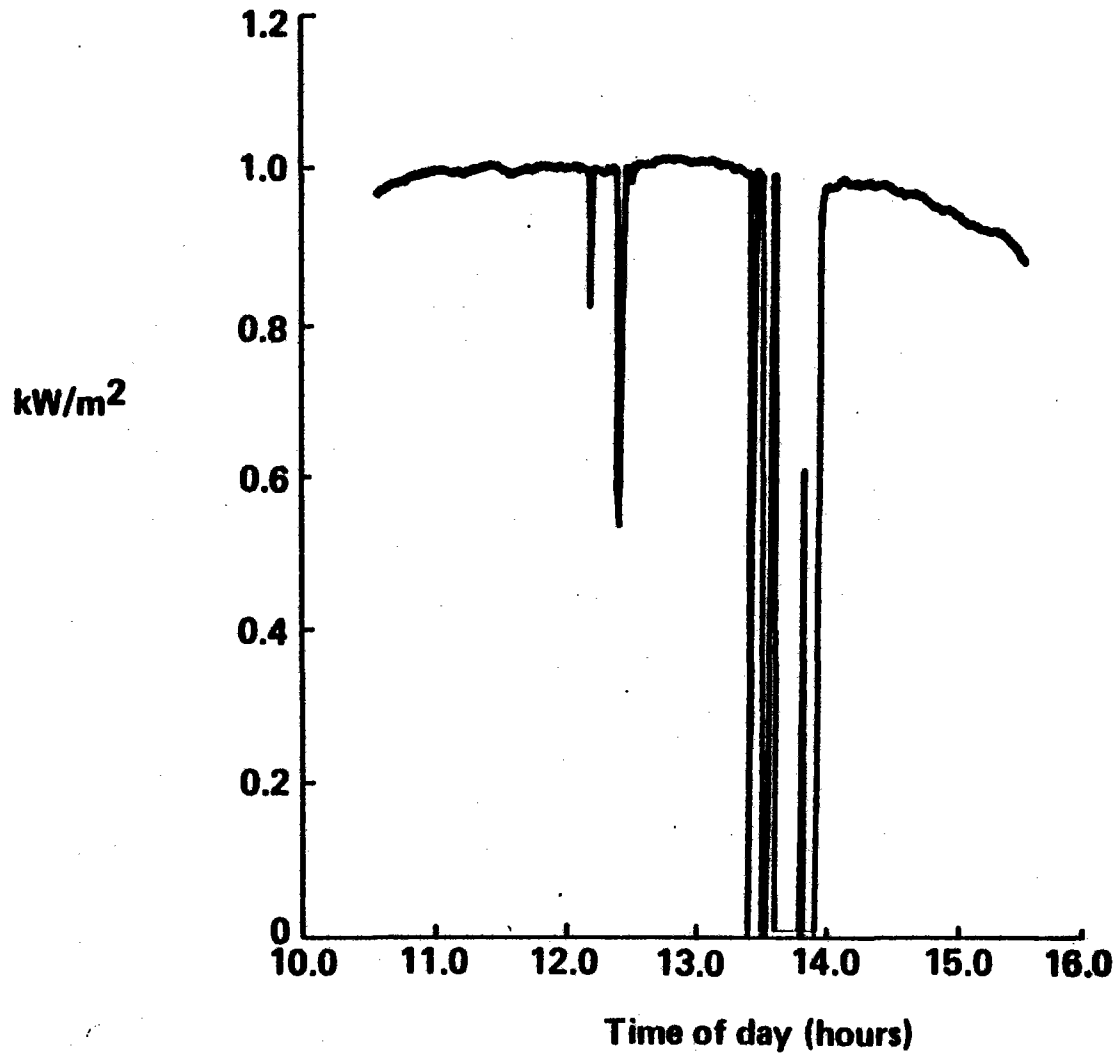


Figure 12.3-45 Plot of January 13, 1979 Test Data, Air Supply Gas Temperatures

## Plot of January 13, 1979 Test Data, Air Supply Gas Temperatures

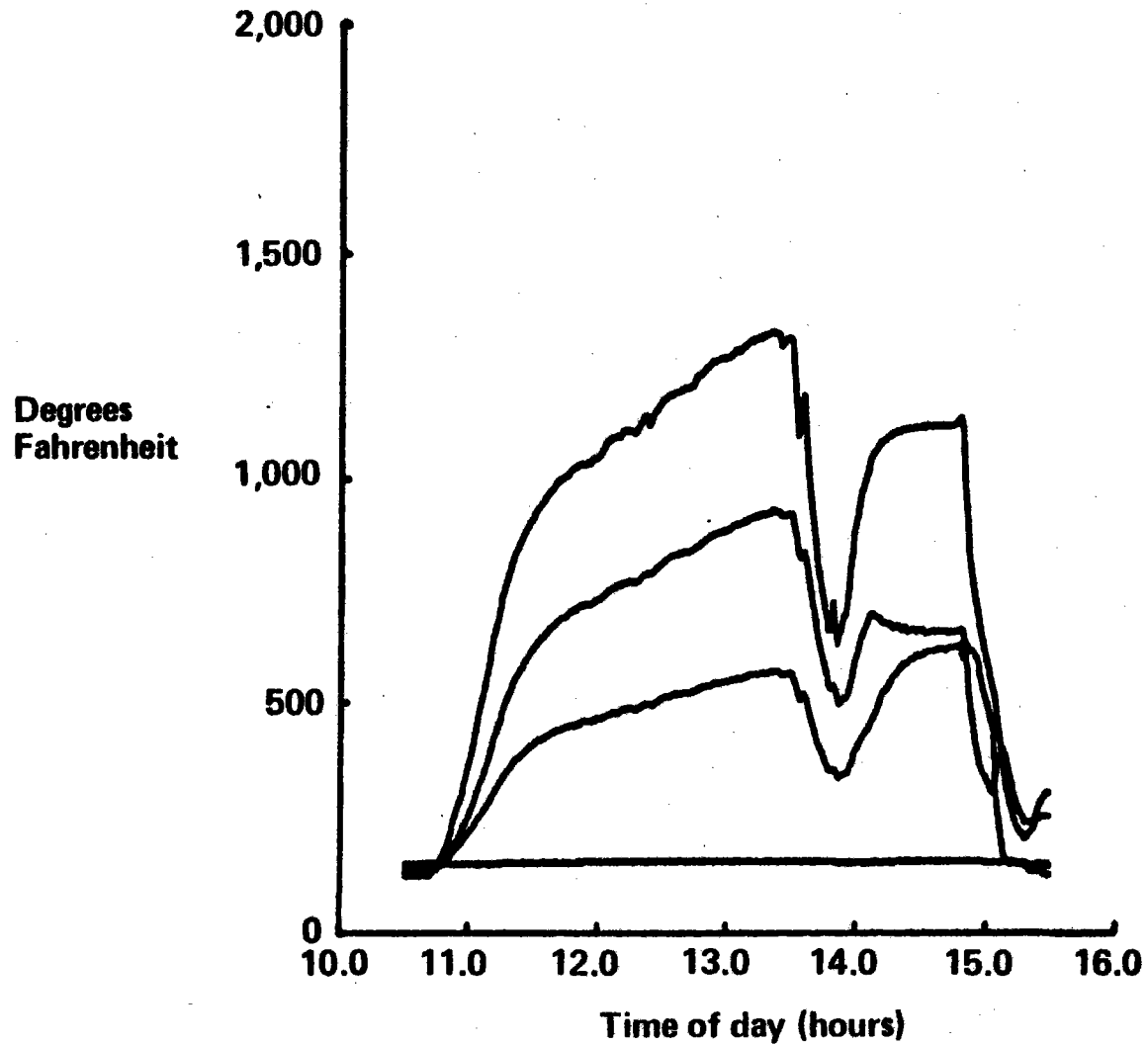




Figure 12.3-46 Plot of January 13, 1979 Test Data, Frame Calorimeters

## Plot of January 13, 1979 Test Data, Frame Calorimeters

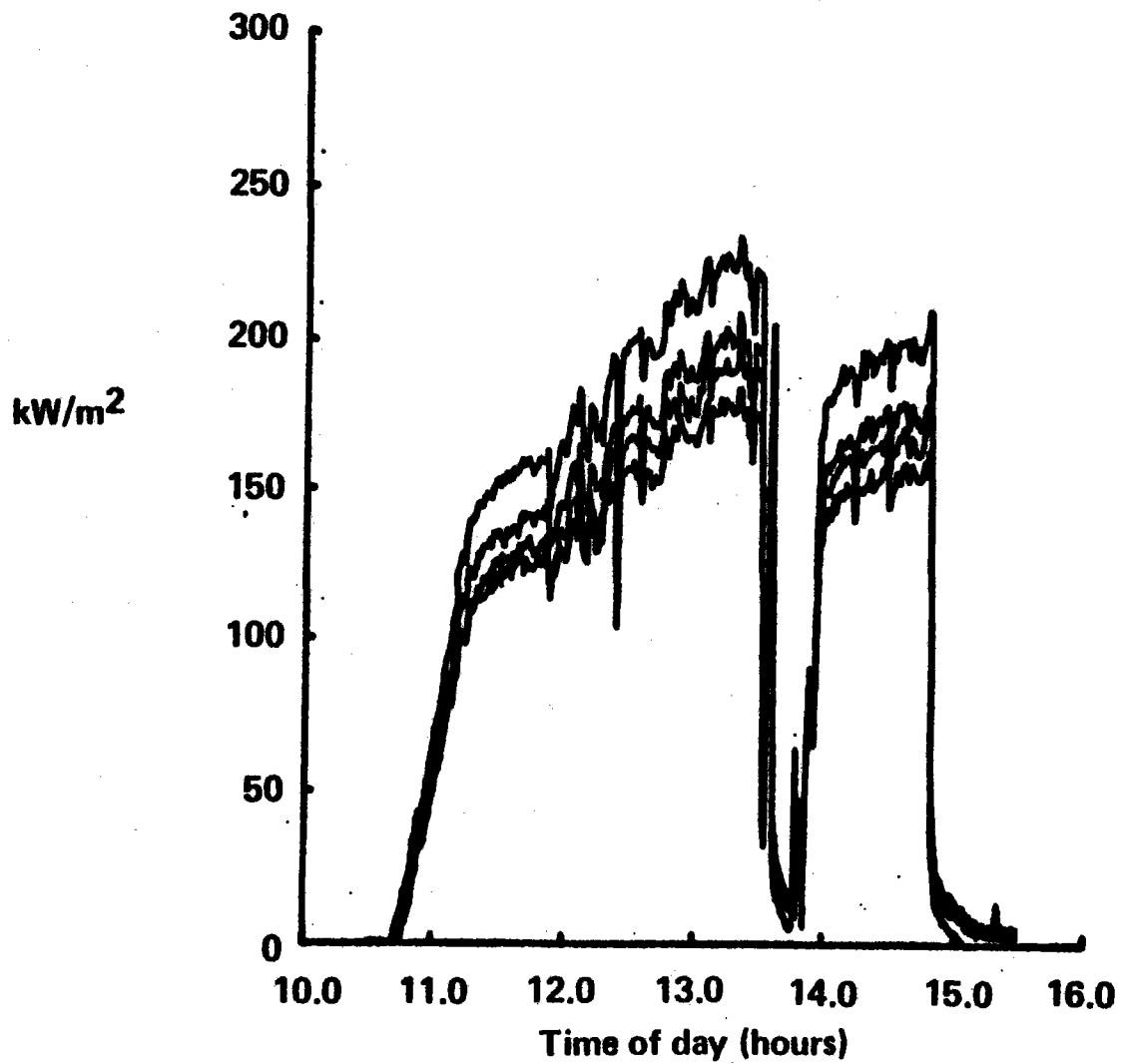


Figure 12.3-47 Plot of January 13, 1979 Test Data, Receiver Mass Flow

### Plot of January 13, 1979 Test Data, Receiver Mass Flow

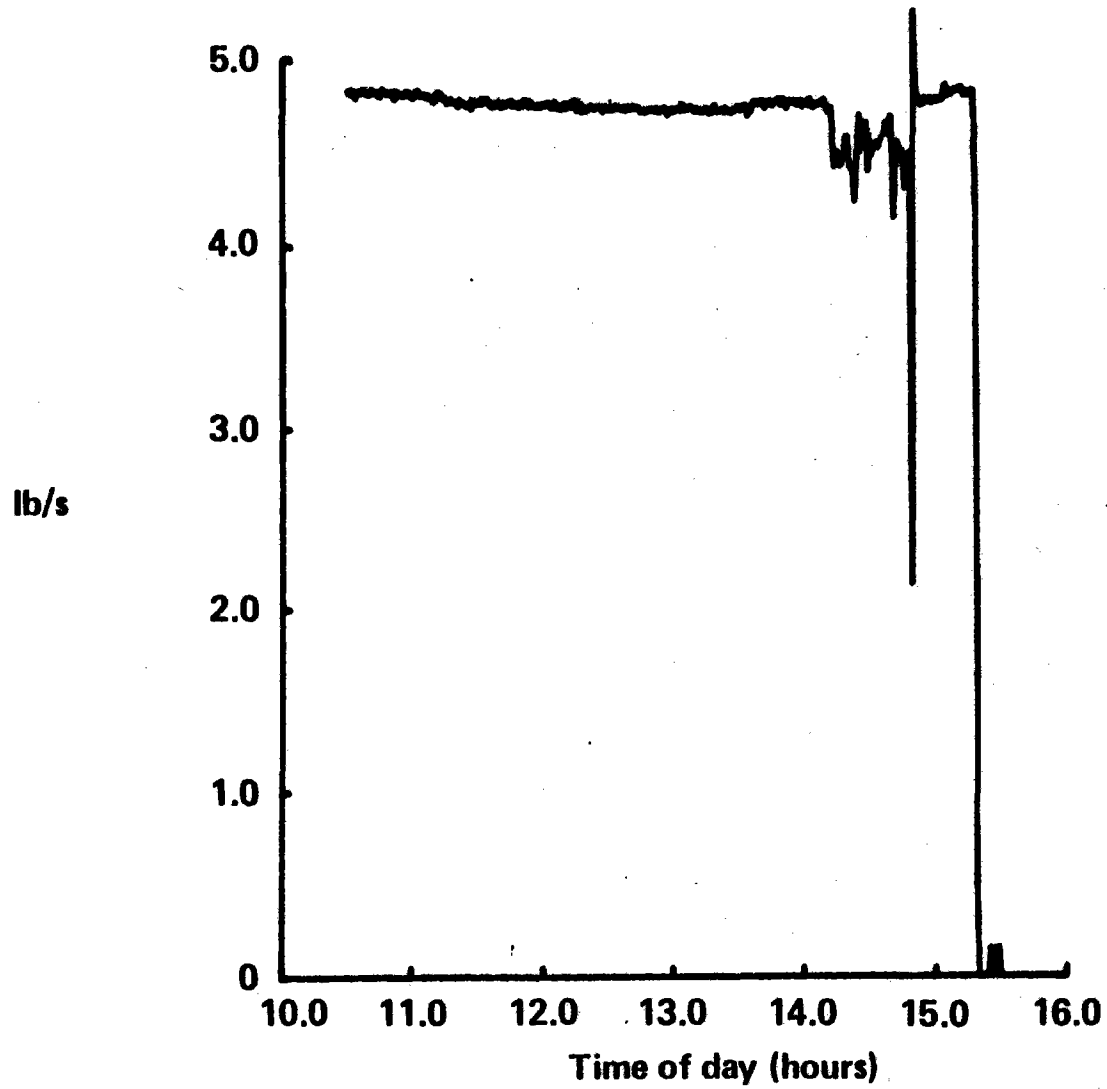


Figure 123-48 Plot of January 13, 1979 Test Data, H/X Panel 3 Valve Angle

# Plot of January 13, 1979 Test Data, H/X Panel 3 Valve Angle

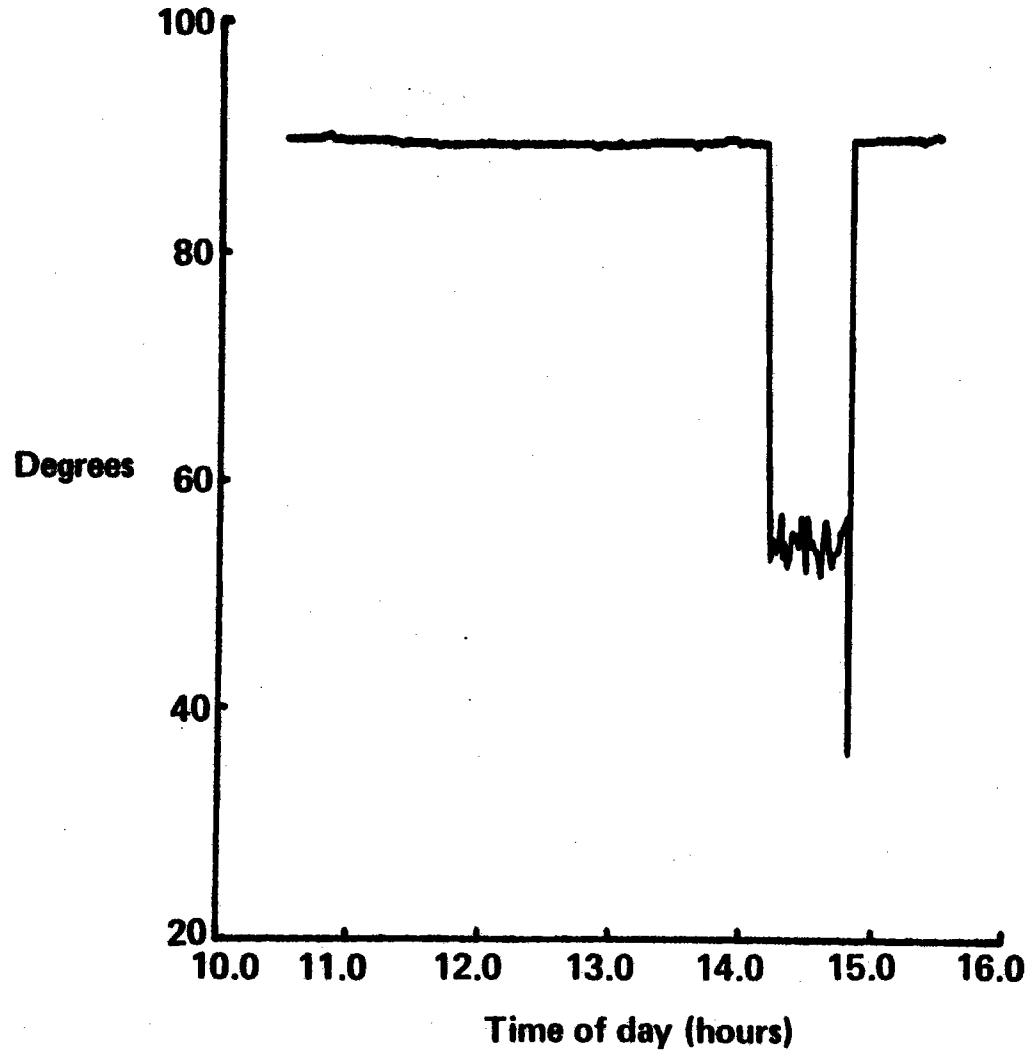
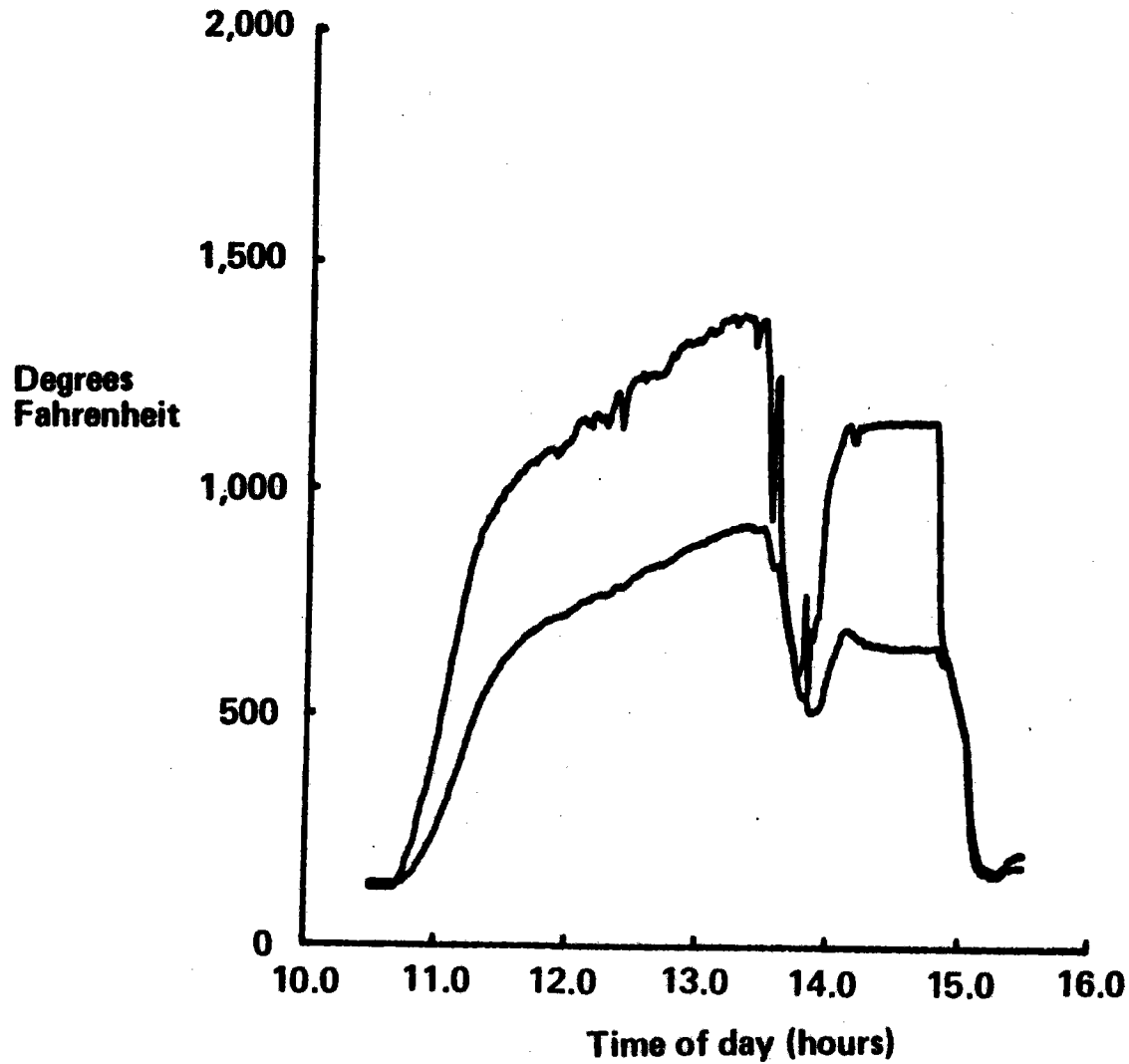


Figure 12.3-49 Plot of January 13, 1979 Test Data, Air Inlet-Outlet Temperatures, Panel 3

## Plot of January 13, 1979 Test Data, Air Inlet-Outlet Temperatures, Panel 3



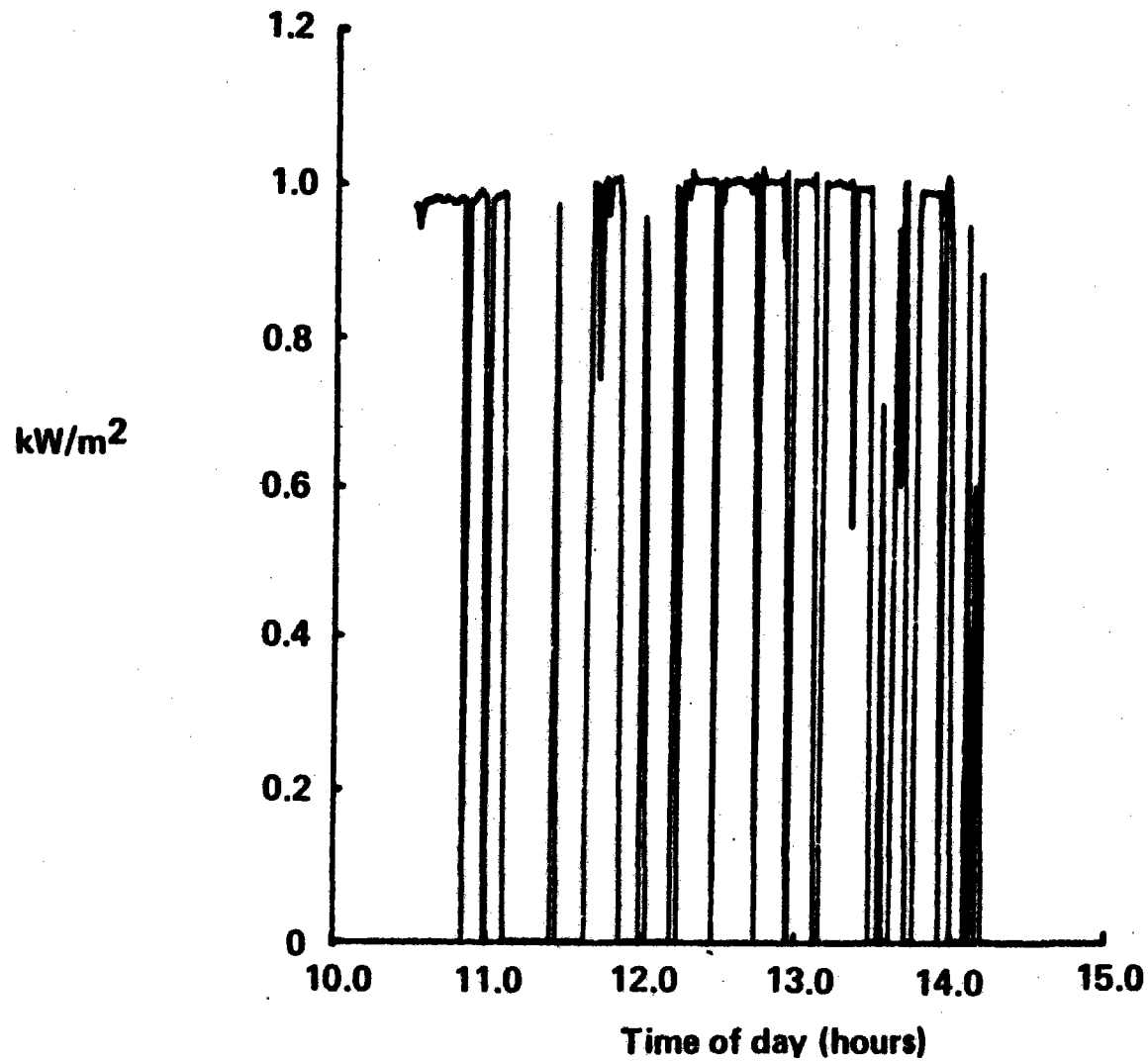
*Figure 12.3-50 Time Chart for January 18, 1979 Solar Test*

## **Time Chart for January 18, 1979 Solar Test**

<b>11:21</b>	<b>Field at standby</b>
<b>11:25</b>	<b>First collector on target</b>
<b>11:58</b>	<b>55 collectors on target</b>
<b>12:52</b>	<b>60 collectors on target</b>
<b>13:26</b>	<b>63 collectors on target</b>
<b>13:50</b>	<b>Field to standby</b>

Figure 12.3-51 Plot of January 18, 1979 Test Data, Eppley Pyrheliometer

## Plot of January 18, 1979 Test Data, Eppley Pyrheliometer



720

Figure 12.3-52 Plot of January 18, 1979 Test Data, Air Supply Gas Temperatures

## Plot of January 18, 1979 Test Data, Air Supply Gas Temperatures

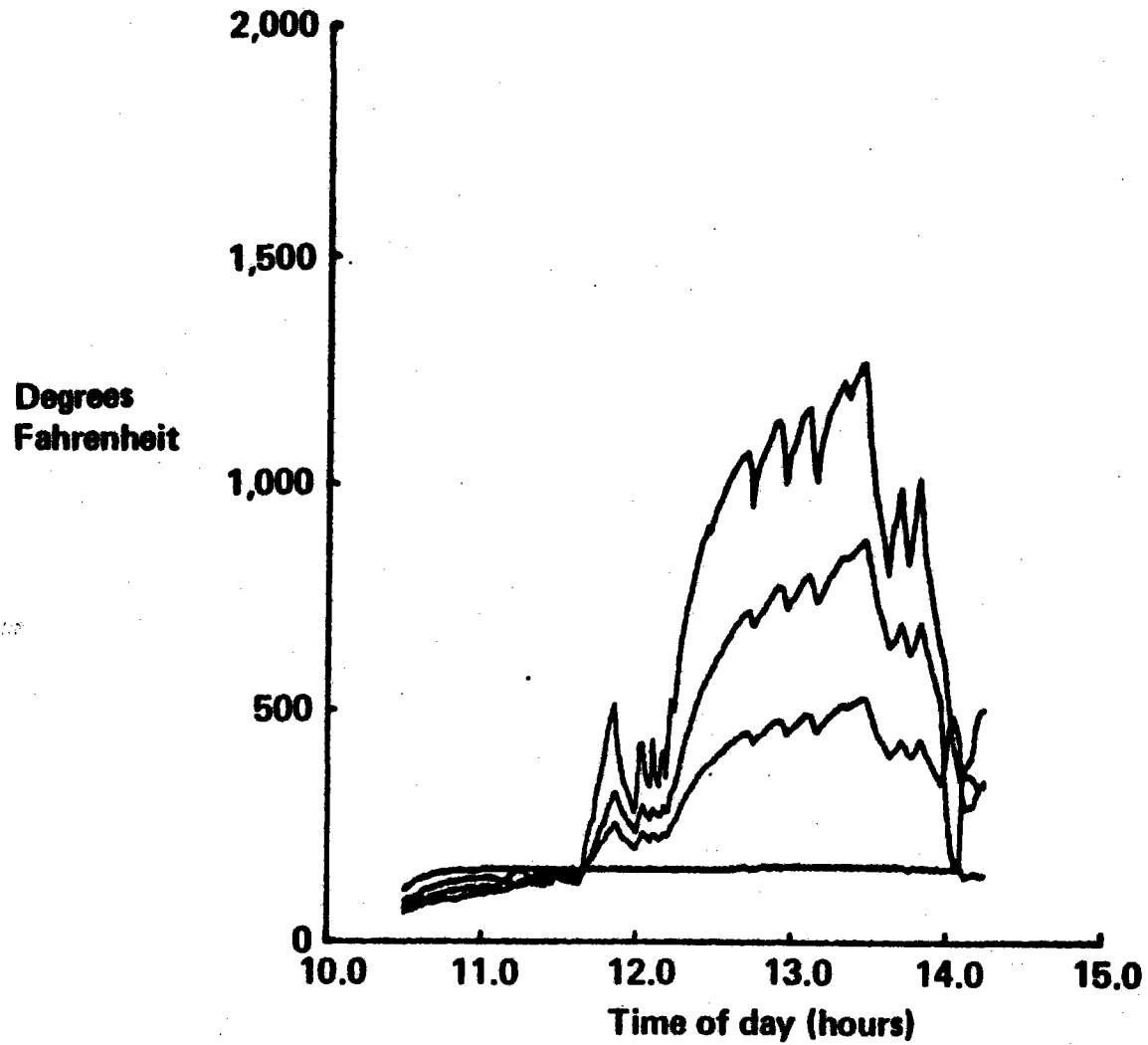


Figure 12.3-53 Plot of January 18, 1979 Test Data, Frame Calorimeters

## Plot of January 18, 1979 Test Data, Frame Calorimeters

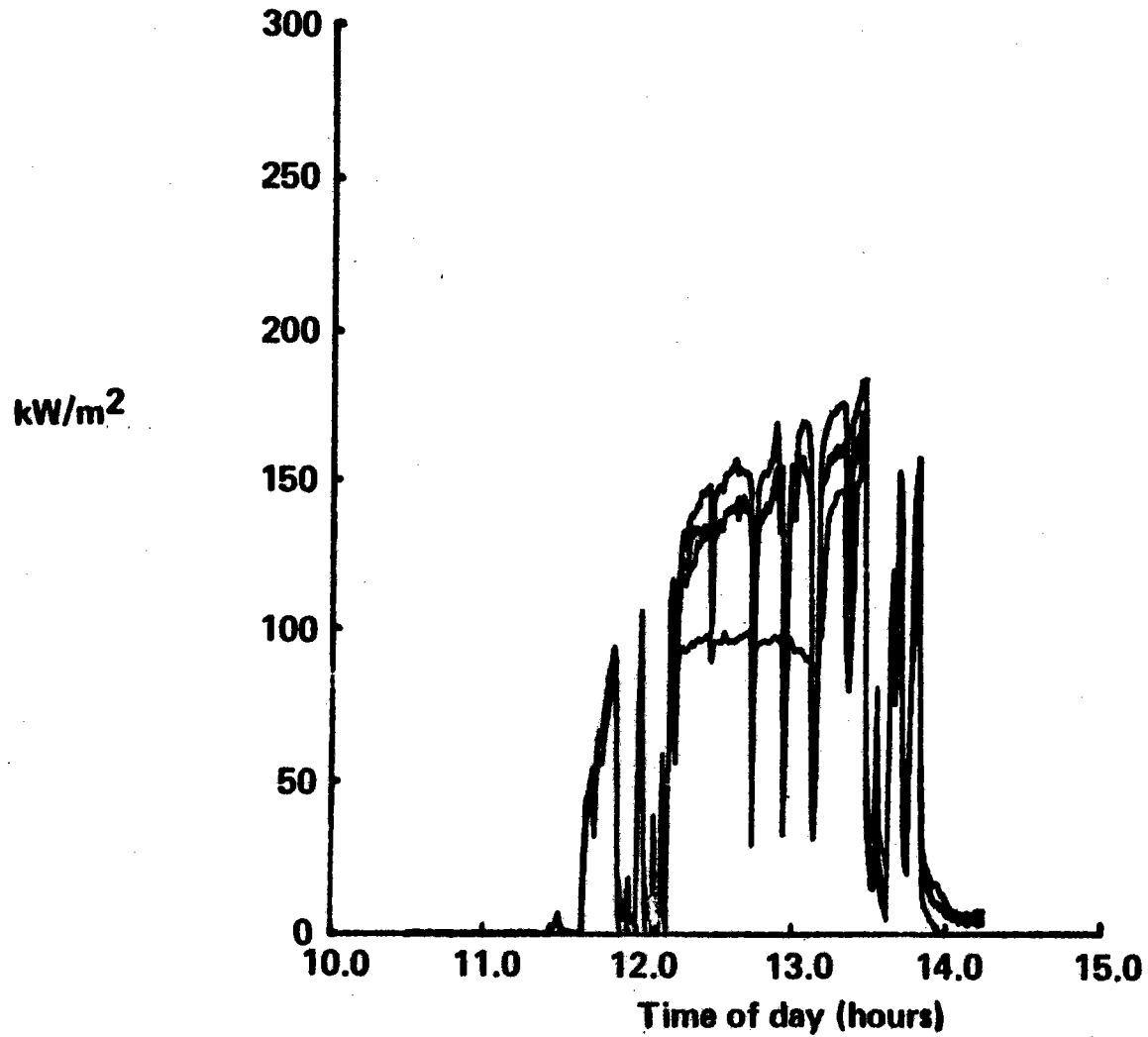
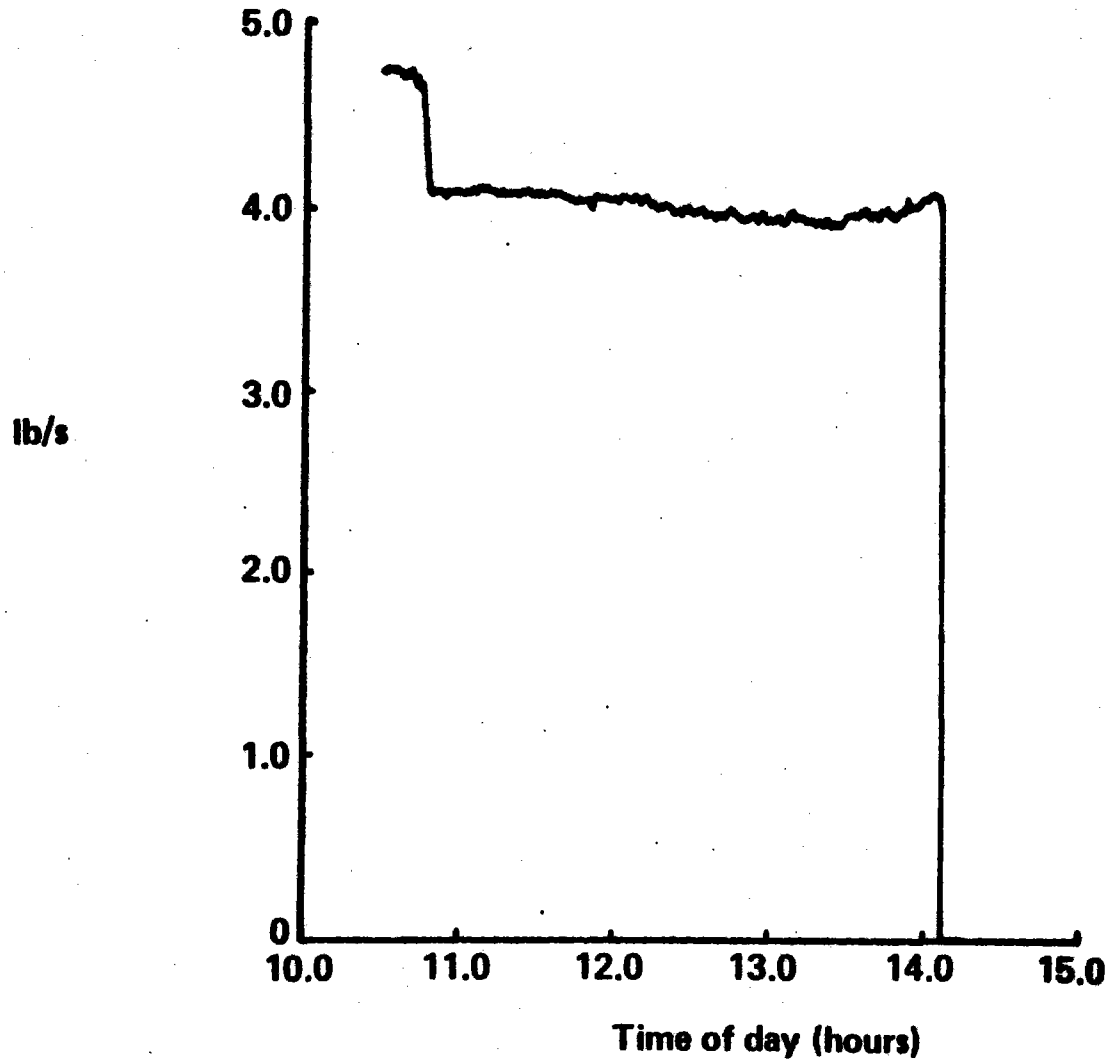




Figure 12.3-54 Plot of January 18, 1979 Test Data, Receiver Mass Flow

### Plot of January 18, 1979 Test Data, Receiver Mass Flow



*Figure 12.3-55 Plot of January 18, 1979 Test Data, H/X Panel 3 Valve Angle*

## **Plot of January 18, 1979 Test Data, H/X Panel 3 Valve Angle**

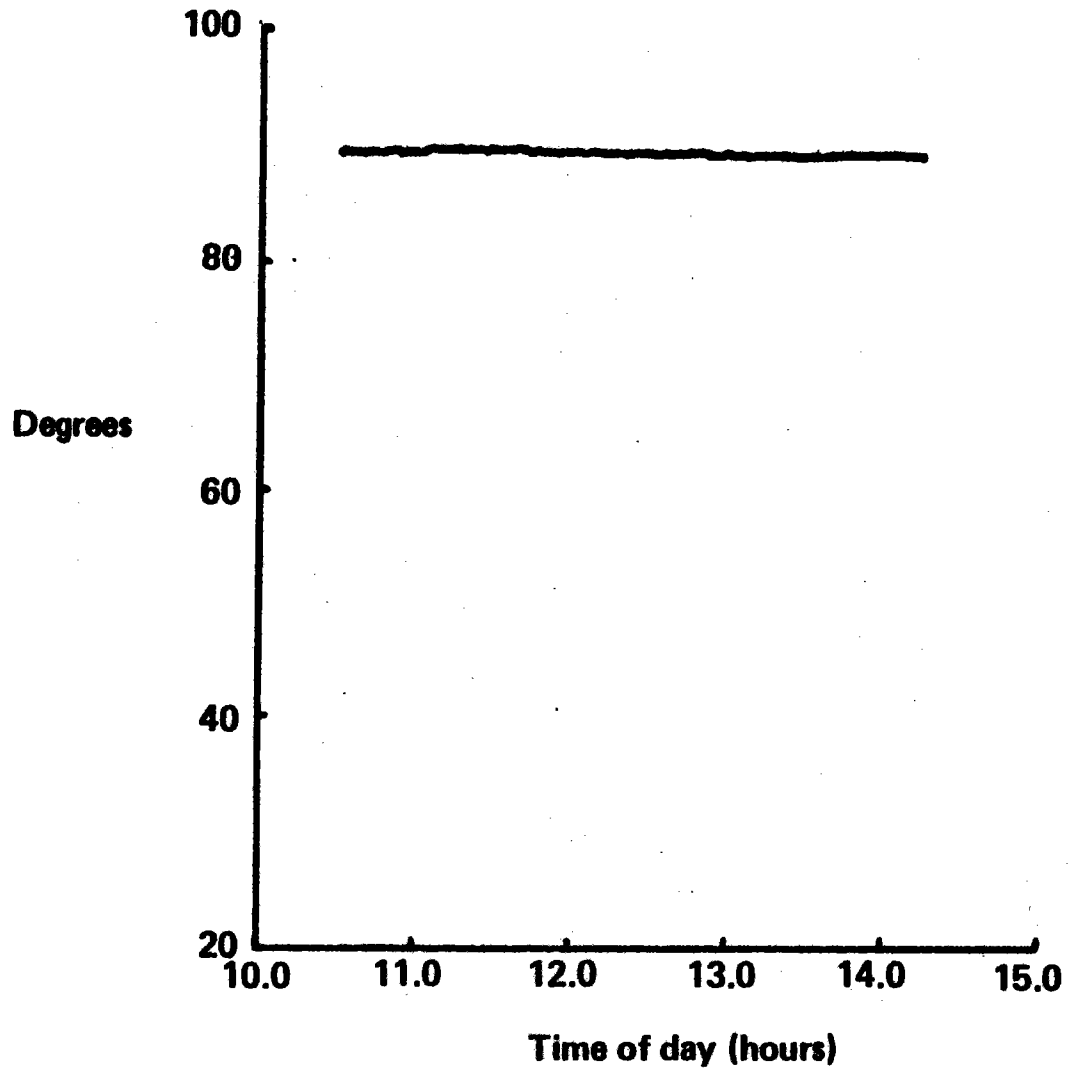
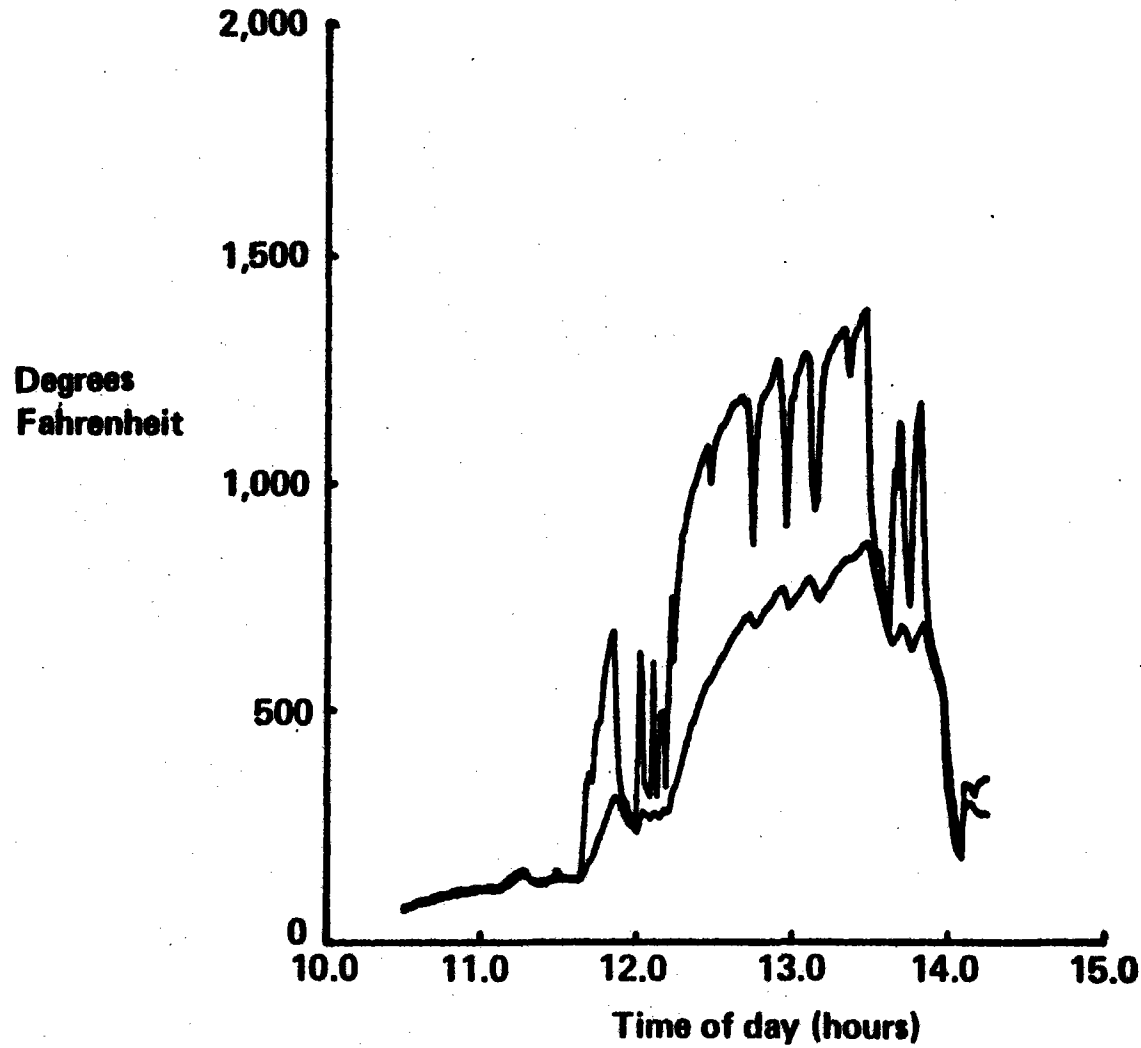


Figure 12.3-56 Plot of January 18, 1979 Test Data, Air Inlet-Outlet Temperatures, Panel 3

### Plot of January 18, 1979 Test Data, Air Inlet-Outlet Temperatures, Panel 3



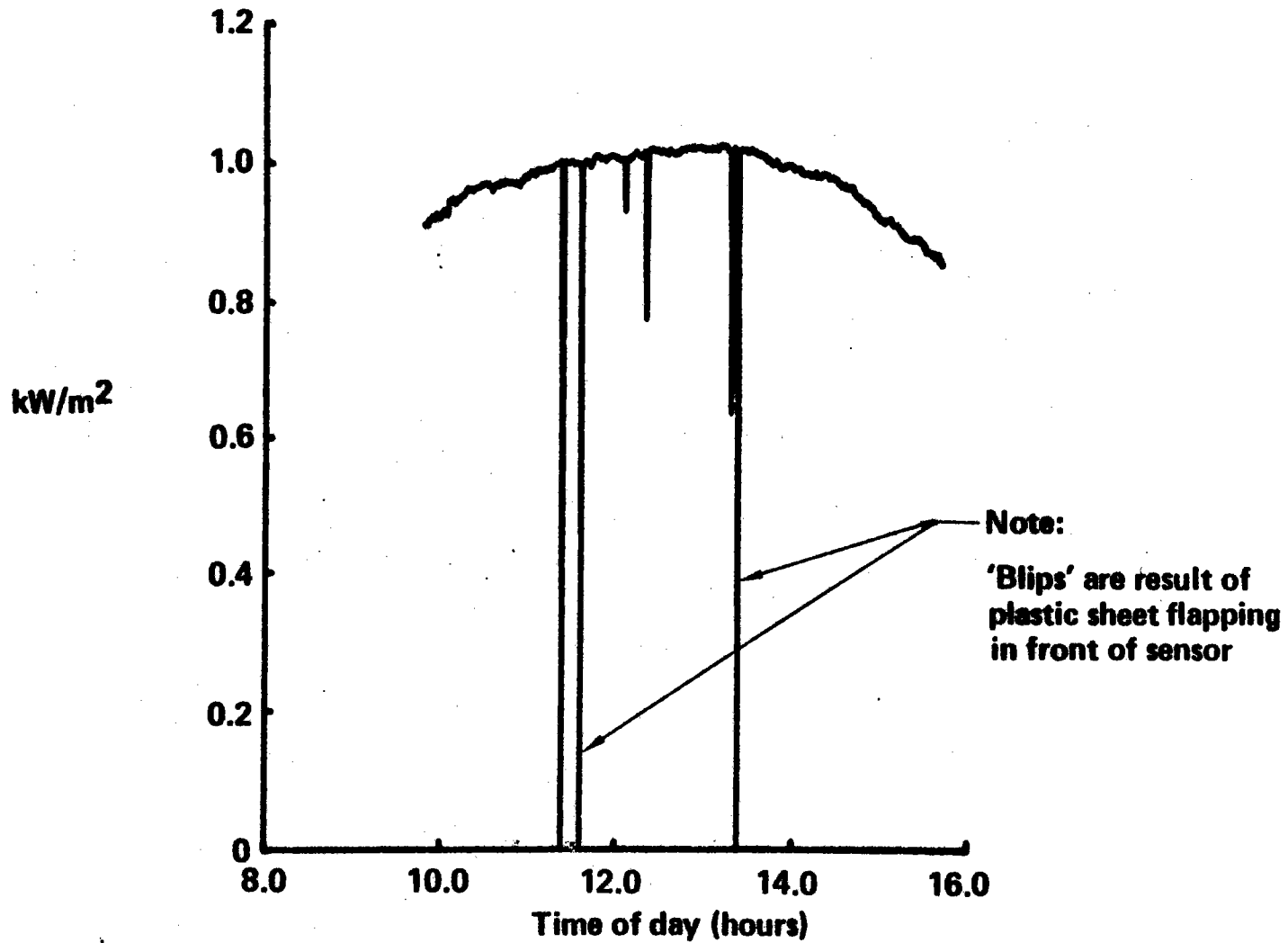
*Figure 12.3-57 Time Chart for January 20, 1979 Solar Test*

## **Time Chart for January 20, 1979 Solar Test**

<b>9:45</b>	<b>Field at standby</b>
<b>9:50</b>	<b>First collector on target</b>
<b>10:26</b>	<b>58 collectors on target</b>
<b>10:58</b>	<b>62 collectors on target</b>
<b>11:31</b>	<b>Receiver on control</b>
<b>12:10</b>	<b>Steady test conditions, EB-9A</b>
<b>12:52</b>	<b>Steady test conditions, EB-9B</b>
<b>13:25</b>	<b>53 collectors on target</b>
<b>13:49</b>	<b>Steady test conditions, EB-6A</b>
<b>14:03</b>	<b>47 collectors on target</b>
<b>14:21</b>	<b>49 collectors on target</b>
<b>14:23</b>	<b>55 collectors on target</b>
<b>14:44</b>	<b>51 collectors on target</b>
<b>14:53</b>	<b>Steady test conditions, EB-3A</b>
<b>15:29</b>	<b>Field at standby</b>

Figure 12.3-58 Plot of January 20, 1979 Test Data, Eppley Pyrheliometer

### Plot of January 20, 1979 Test Data, Eppley Pyrheliometer



727

Figure 12.3-59 Plot of January 20, 1979 Test Data, Air Supply Gas Temperatures

## Plot of January 20, 1979 Test Data, Air Supply Gas Temperatures

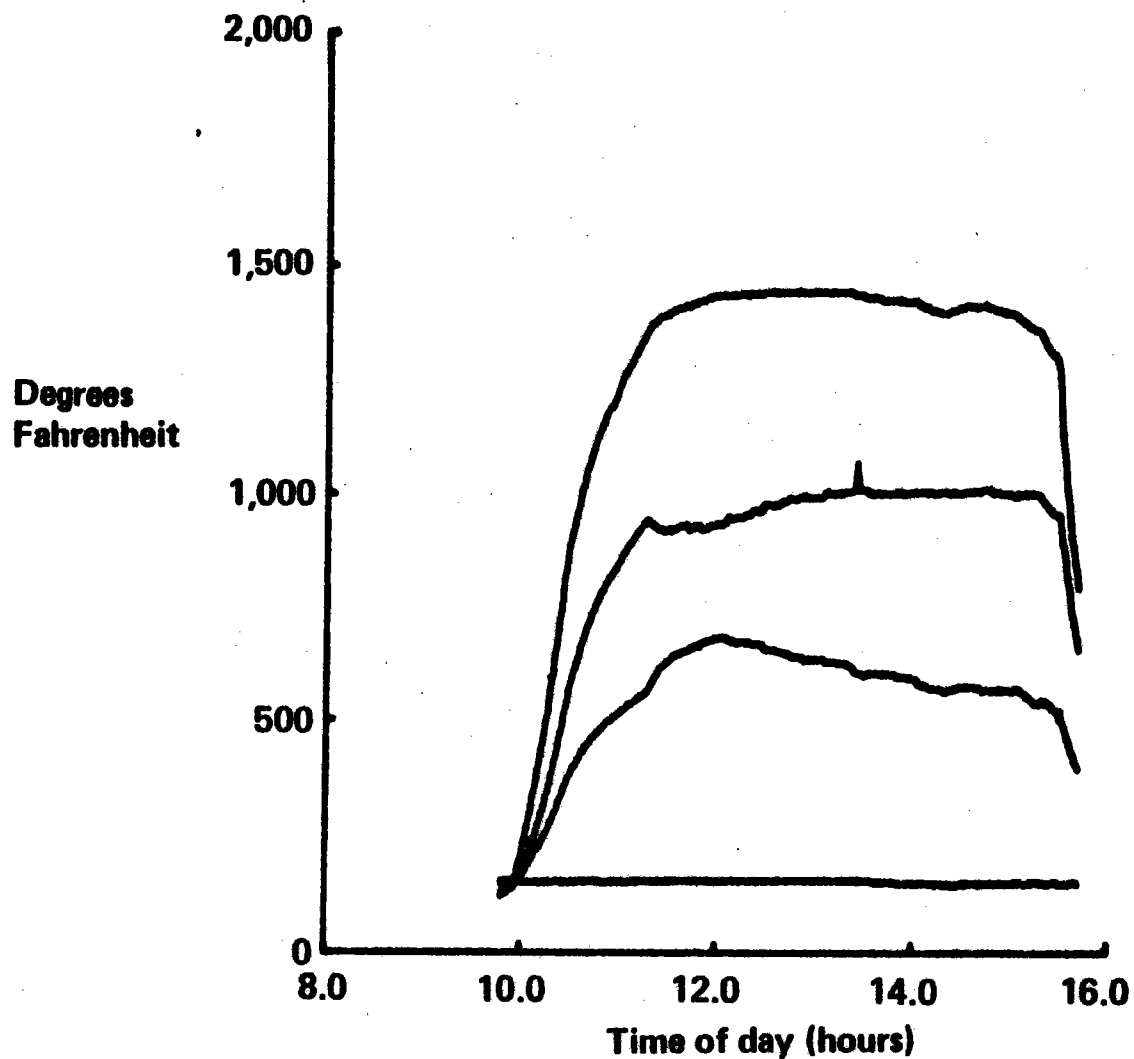


Figure 12.3-60 Plot of January 20, 1979 Test Data, Frame Calorimeters

## Plot of January 20, 1979 Test Data, Frame Calorimeters

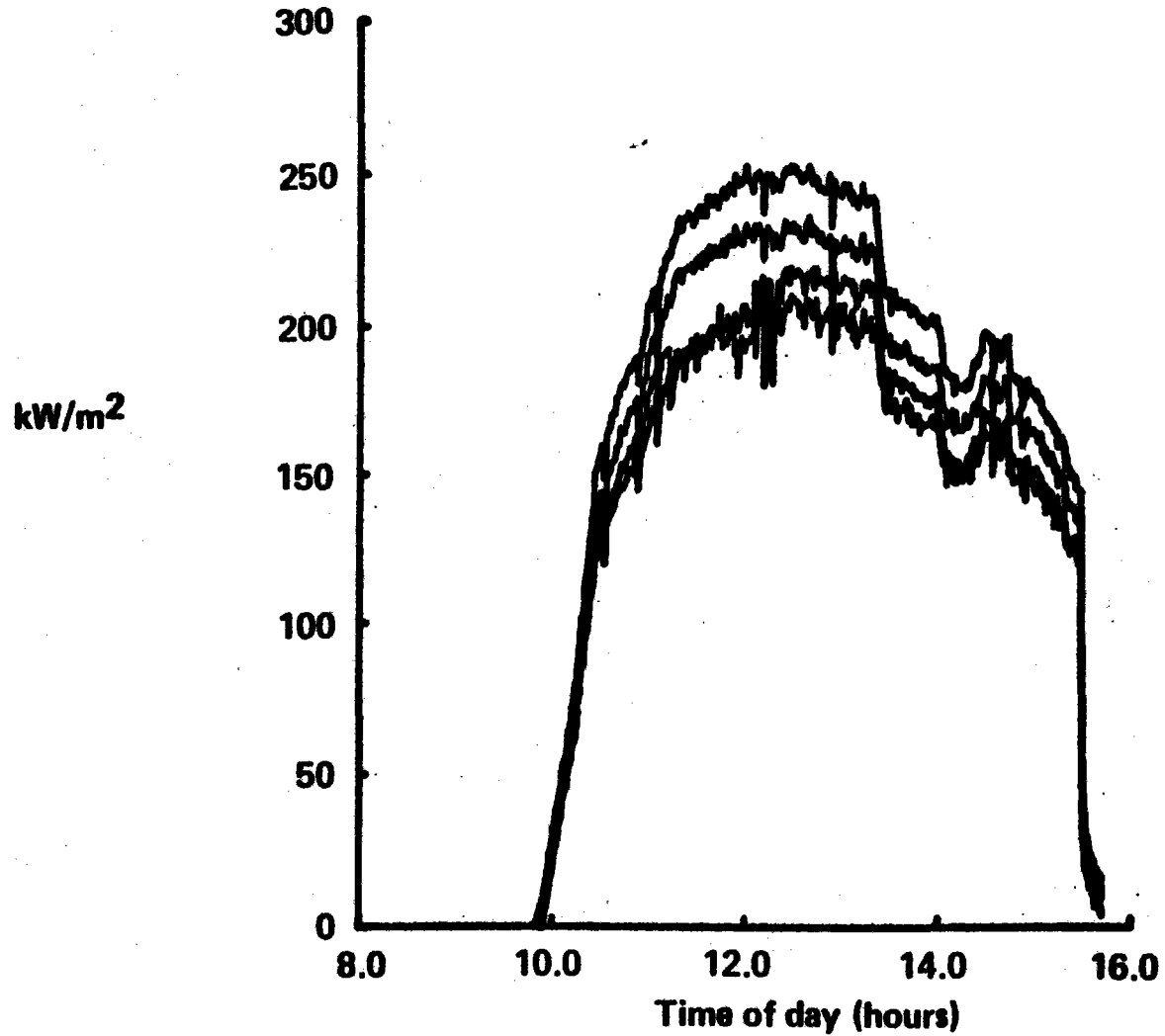
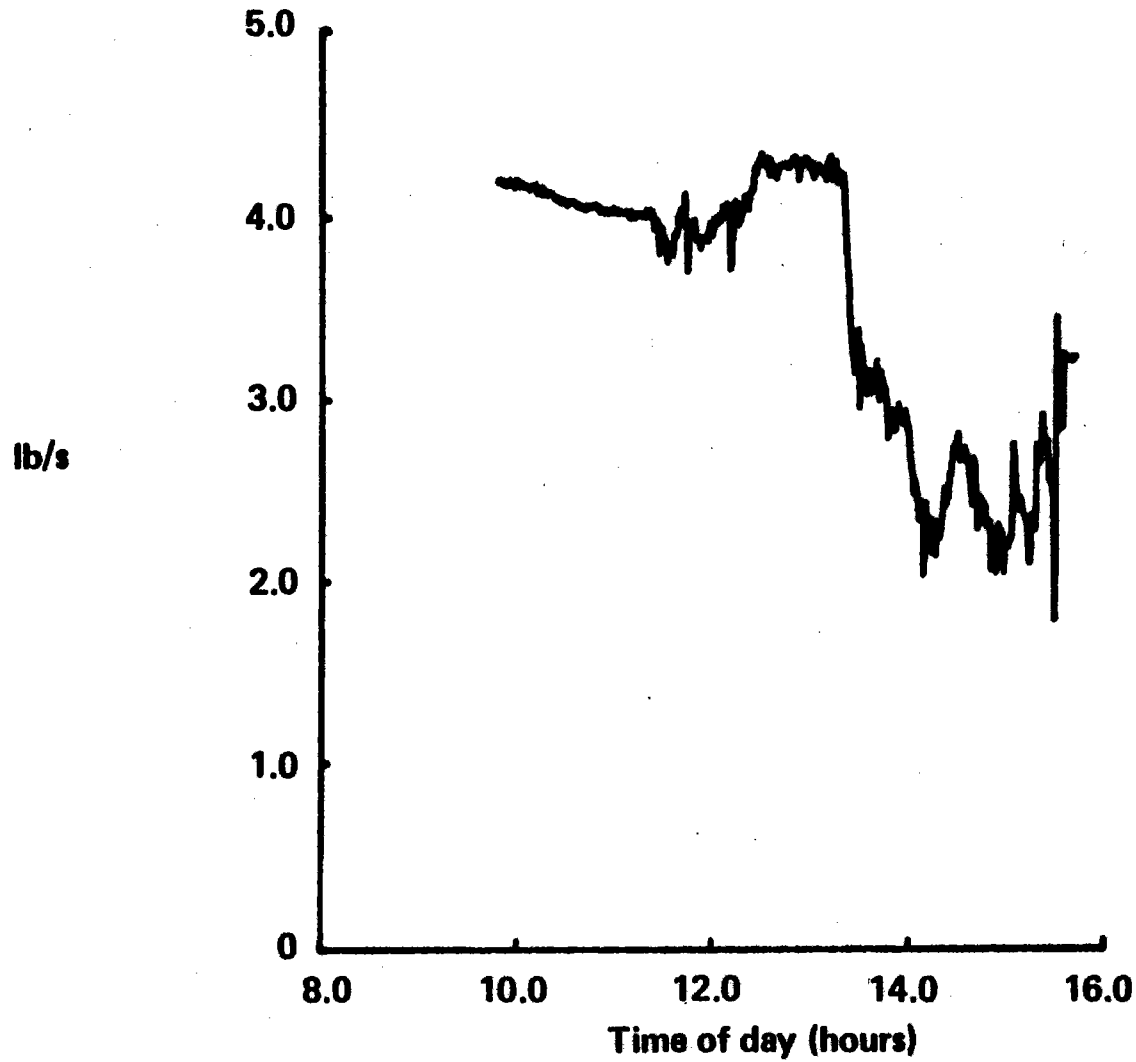


Figure 12.3-61 Plot of January 20, 1979 Test Data, Receiver Mass Flow

# Plot of January 20, 1979 Test Data, Receiver Mass Flow



730



Figure 12.3-62 Plot of January 20, 1979 Test Data, H/X Panel 3 Valve Angle

### Plot of January 20, 1979 Test Data, H/X Panel 3 Valve Angle

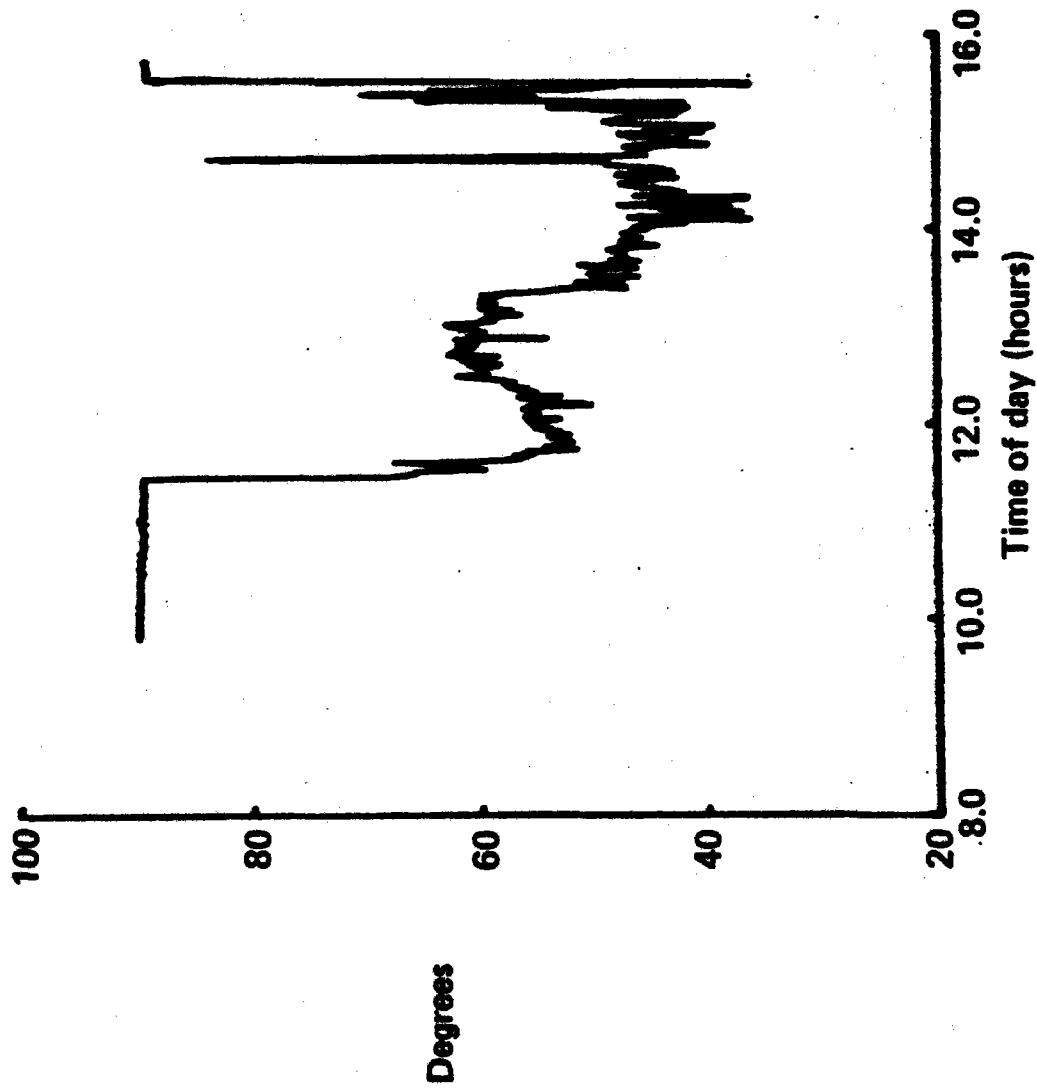
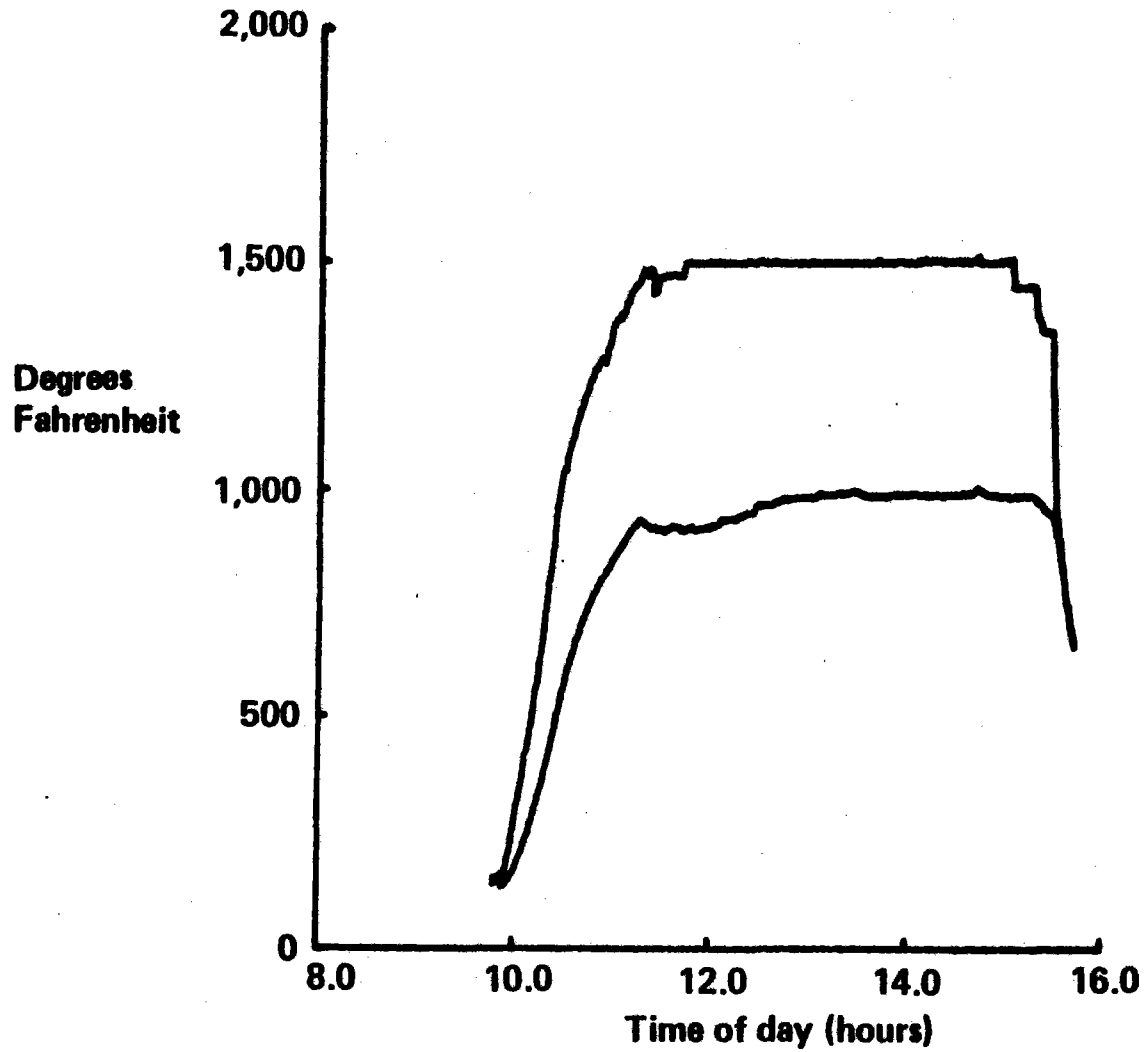


Figure 12.3-63 Plot of January 20, 1979 Test Data, Air Inlet-Outlet Temperatures, Panel 3

## Plot of January 20, 1979 Test Data, Air Inlet-Outlet Temperatures, Panel 3



*Figure 12.3-64 Time Chart for January 23, 1979 Solar Test*

## **Time Chart for January 23, 1979 Solar Test**

<b>11:06</b>	<b>Field at standby</b>
<b>11:18</b>	<b>First collector on target</b>
<b>12:22</b>	<b>44 collectors on target</b>
<b>12:36</b>	<b>Receiver on control</b>
<b>12:48</b>	<b>50 collectors on target</b>
<b>12:54</b>	<b>Steady test conditions, EB-4B</b>
<b>13:11</b>	<b>Started field conditions for NI-2</b>
<b>13:54</b>	<b>Completed test NI-2</b>
<b>14:08</b>	<b>Adjusted receiver temperatures for test NI-1, started NI-1</b>
<b>14:09</b>	<b>51 collectors on target</b>
<b>14:35</b>	<b>Completed test NI-1</b>
<b>14:36</b>	<b>53 collectors on target</b>
<b>14:49</b>	<b>Increased receiver temperature set points</b>
<b>16:00</b>	<b>Field shutdown</b>

Figure 123-65 Plot of January 23, 1979 Test Data, Eppley Pyrheliometer

## Plot of January 23, 1979 Test Data, Eppley Pyrheliometer

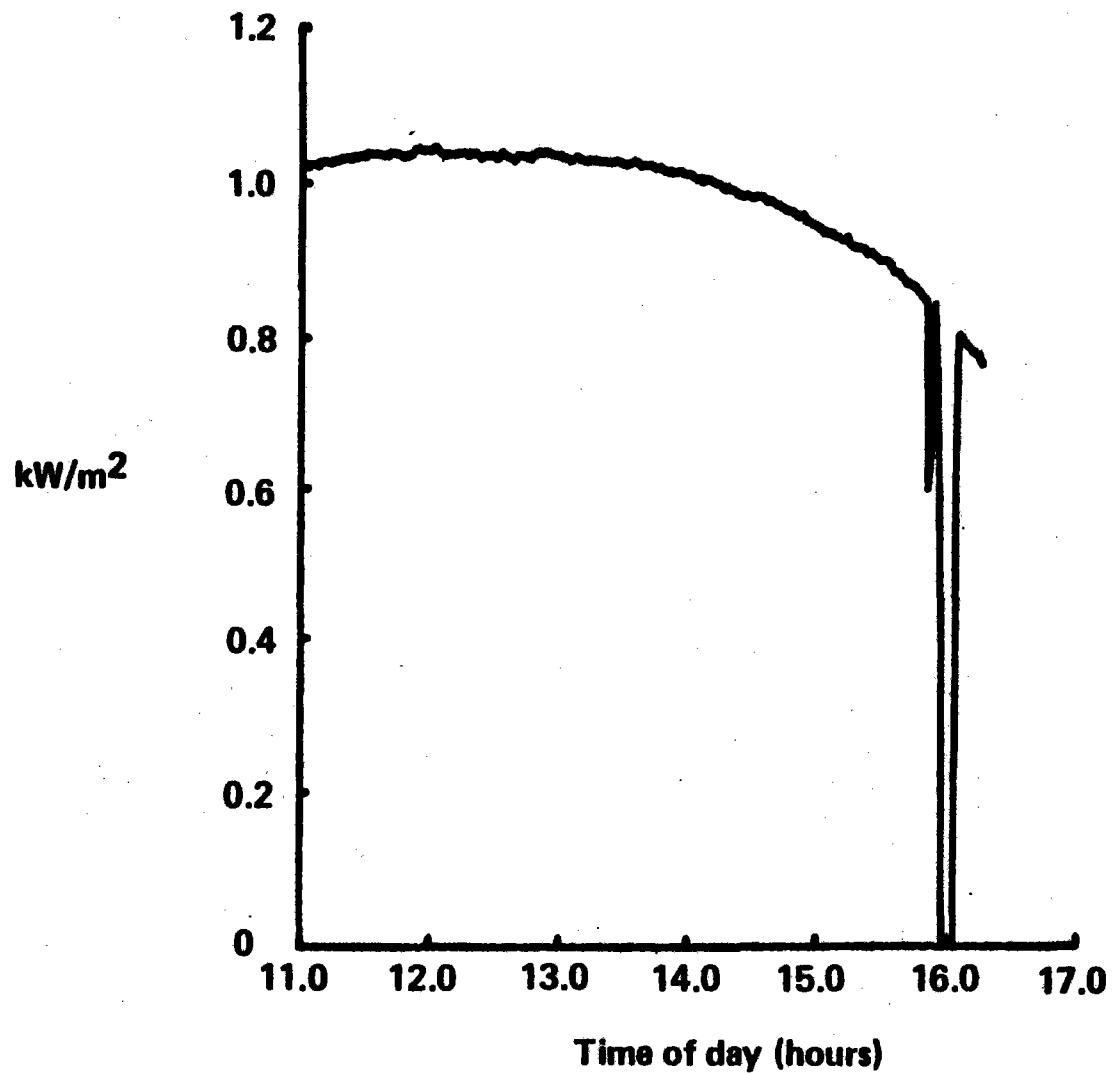


Figure 123-66 Plot of January 23, 1979 Test Data, Air Supply Gas Temperatures

## Plot of January 23, 1979 Test Data, Air Supply Gas Temperatures

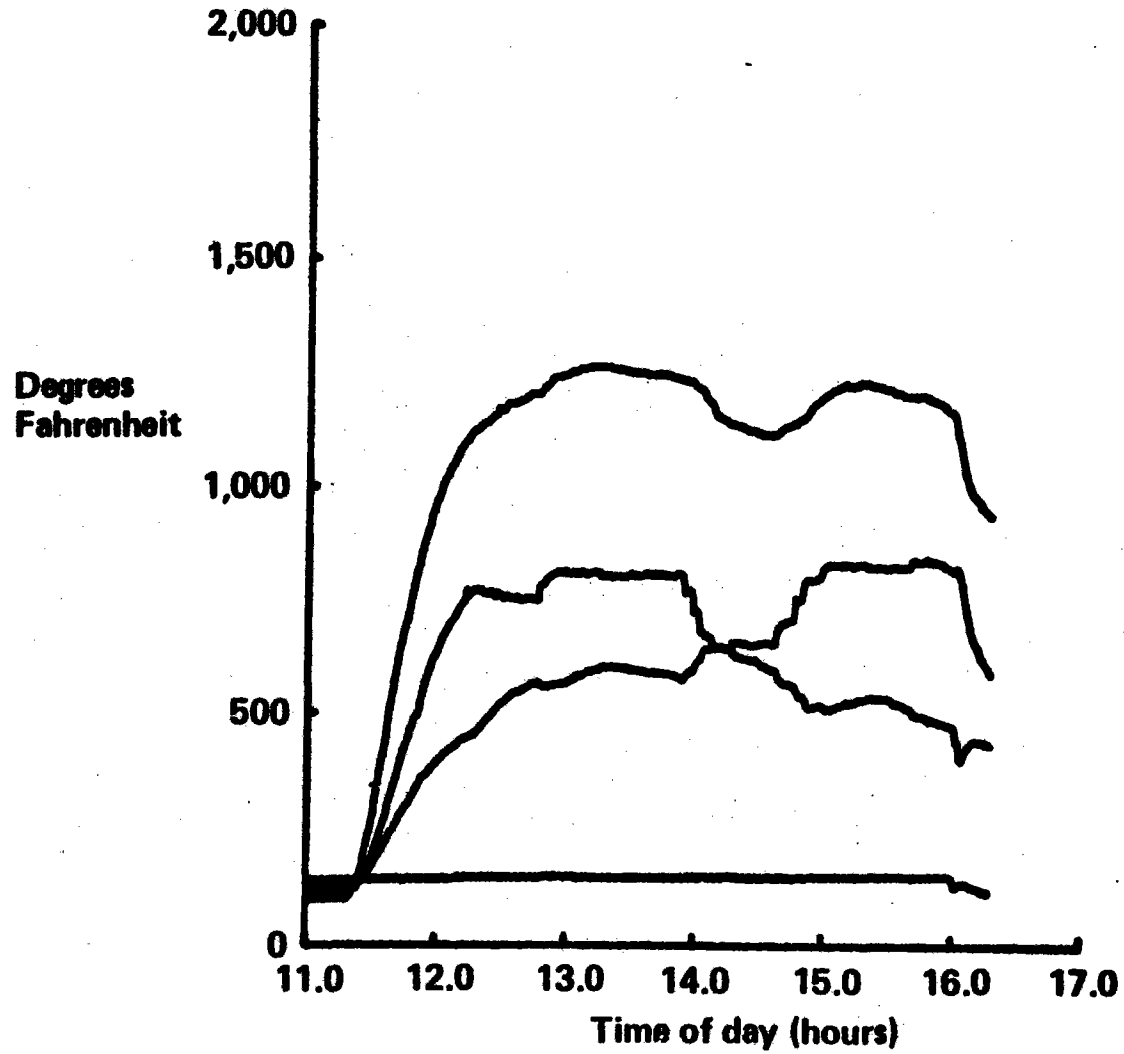


Figure 123-67 Plot of January 23, 1979 Test Data, Frame Calorimeters

# Plot of January 23, 1979 Test Data, Frame Calorimeters

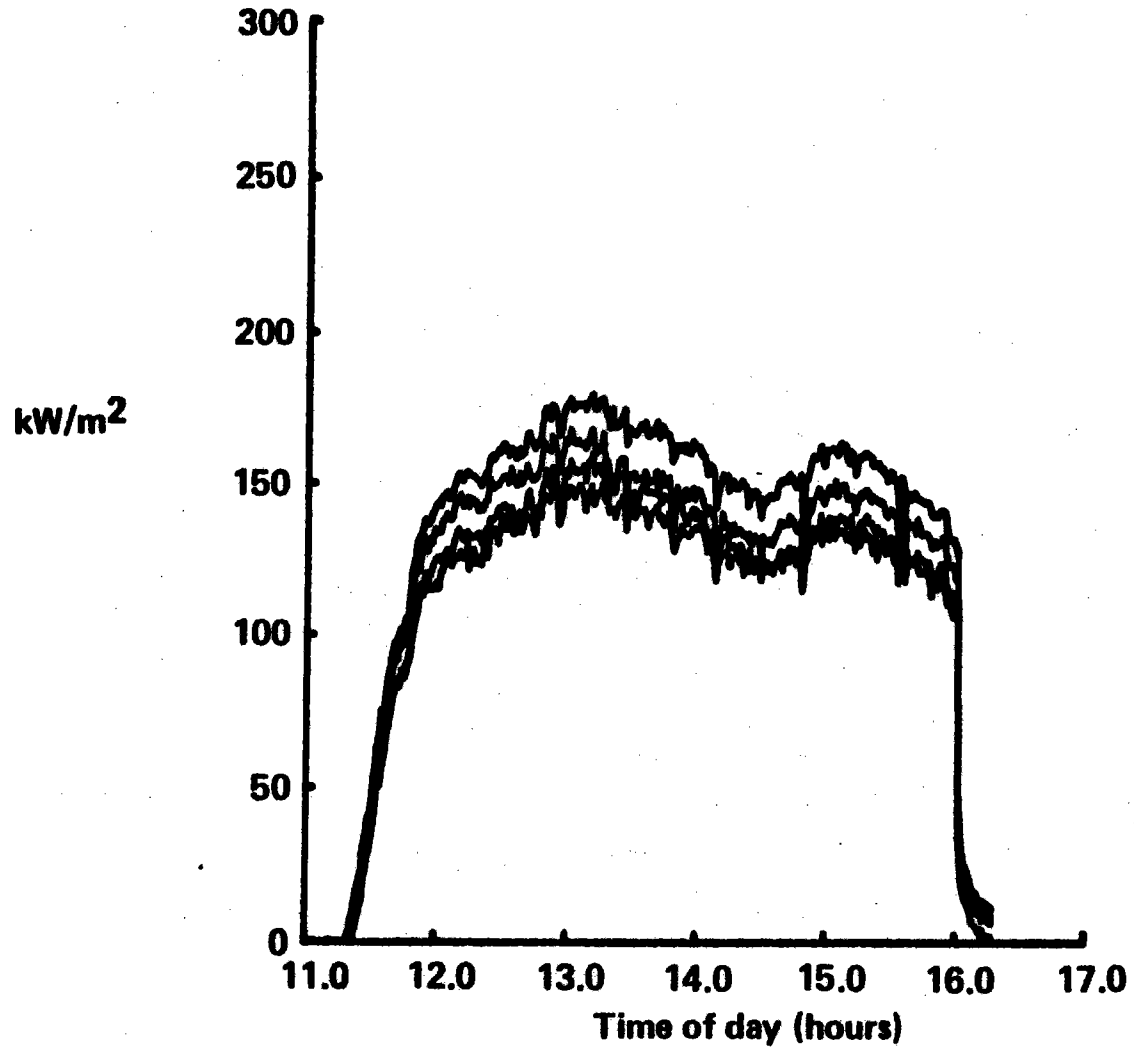
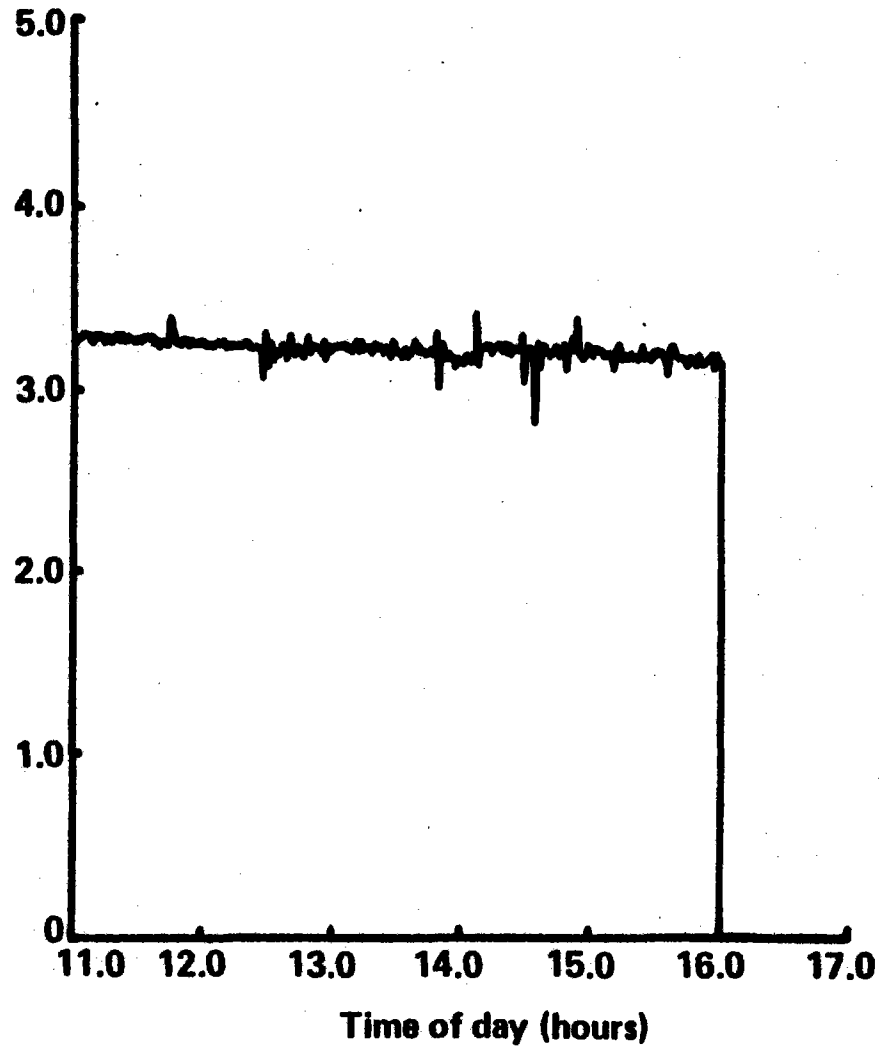


Figure 123-68 Plot of January 23, 1979 Test Data, Receiver Mass Flow

# Plot of January 23, 1979 Test Data, Receiver Mass Flow



737

lb/s

Time of day (hours)

Figure 123-69 Plot of January 23, 1979 Test Data, H/X Panel 3 Valve Angle

## Plot of January 23, 1979 Test Data, H/X Panel 3 Valve Angle

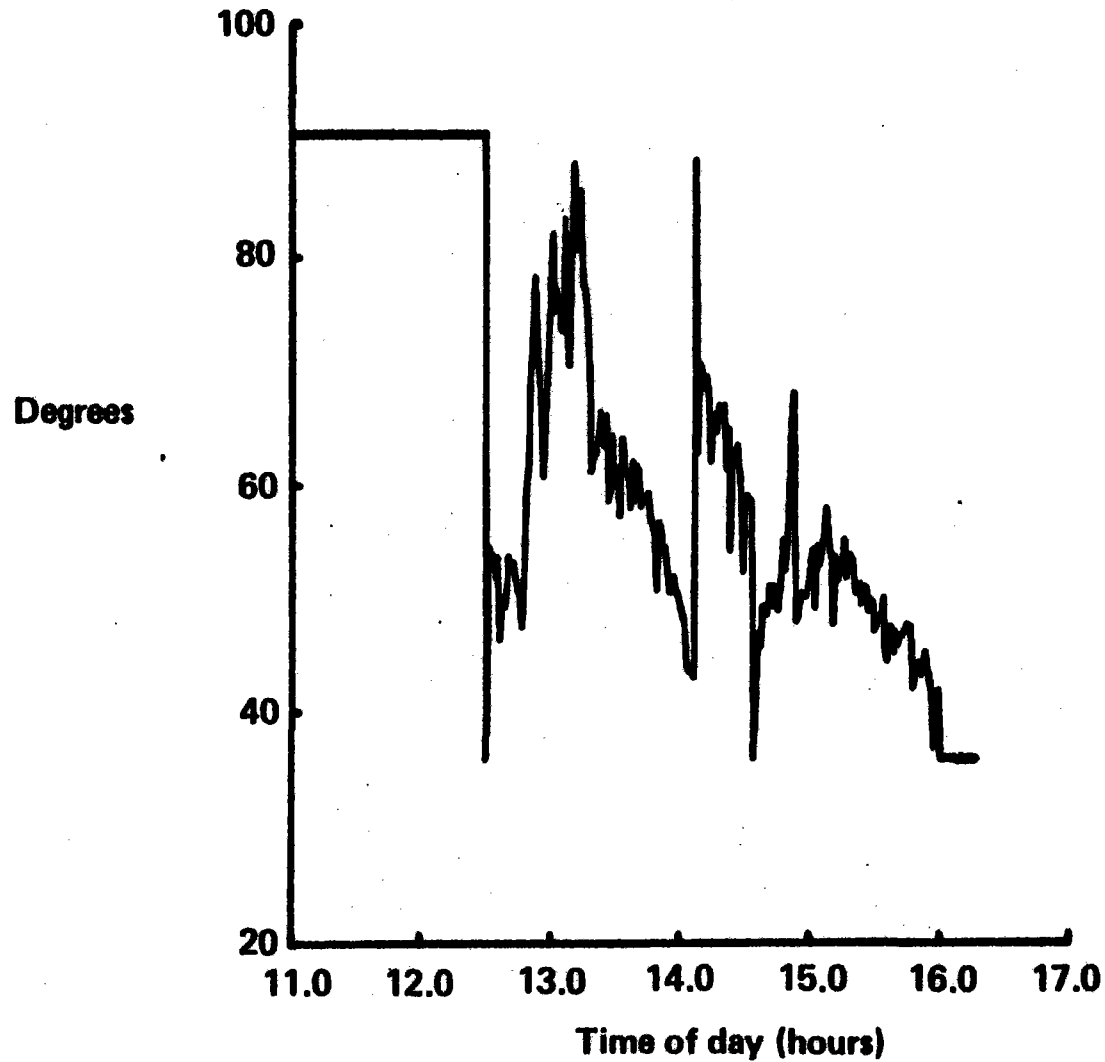
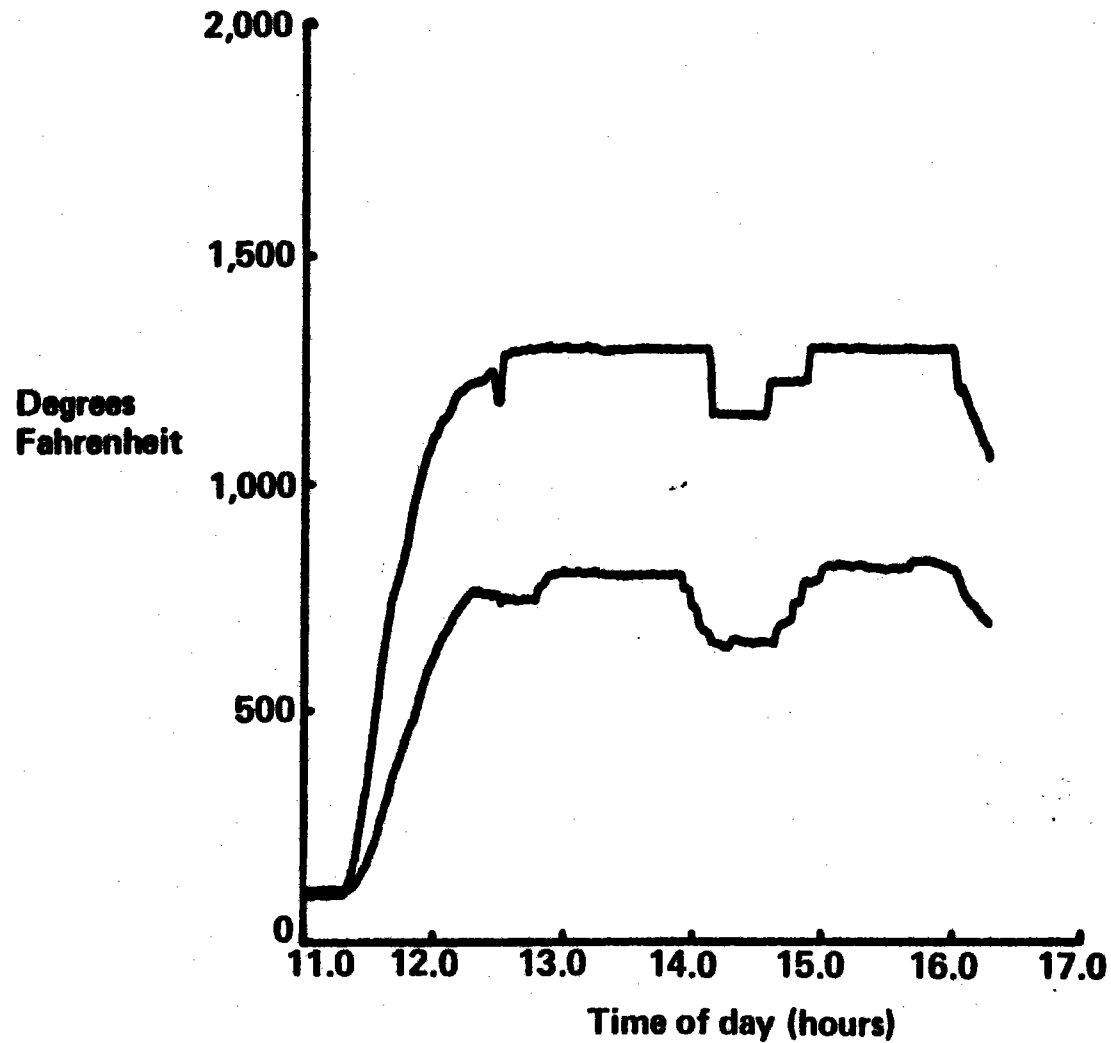




Figure 123-70 Plot of January 23, 1979 Test Data, Air Inlet-Outlet Temperatures, Panel 3

### Plot of January 23, 1979 Test Data, Air Inlet-Outlet Temperatures, Panel 3



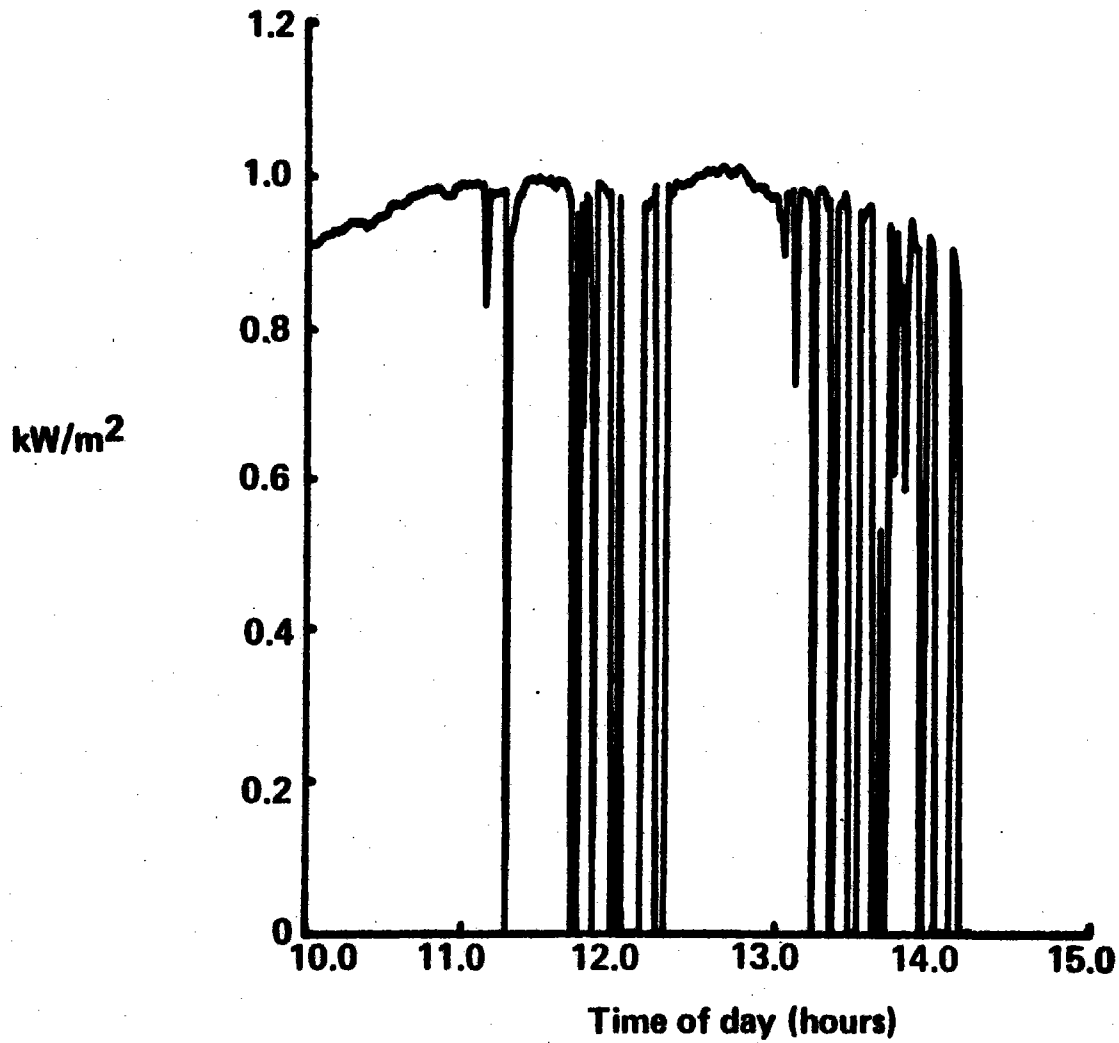
*Figure 123-71 Time Chart for January 27, 1979 Solar Test*

## **Time Chart for January 27, 1979 Solar Test**

<b>10:00</b>	<b>Field at standby</b>
<b>10:17</b>	<b>First collector on target</b>
<b>11:22</b>	<b>50 collectors on target</b>
<b>12:47</b>	<b>Receiver on control</b>
<b>12:55</b>	<b>Started receiver adjustment for RF-2</b>
<b>13:00</b>	<b>Interruption due to clouds</b>
<b>13:13</b>	<b>Interruption due to clouds</b>
<b>13:19</b>	<b>53 collectors on target</b>
<b>13:21</b>	<b>Interruption due to clouds</b>
<b>13:25</b>	<b>56 collectors on target</b>
<b>13:30</b>	<b>Interruption due to clouds</b>
<b>13:37</b>	<b>Interruption due to clouds</b>
<b>13:52</b>	<b>RF-2 complete</b>
<b>13:54</b>	<b>Field to standby simulating EC-1 conditions</b>

Figure 12.3-72 Plot of January 27, 1979 Test Data, Eppley Pyrheliometer

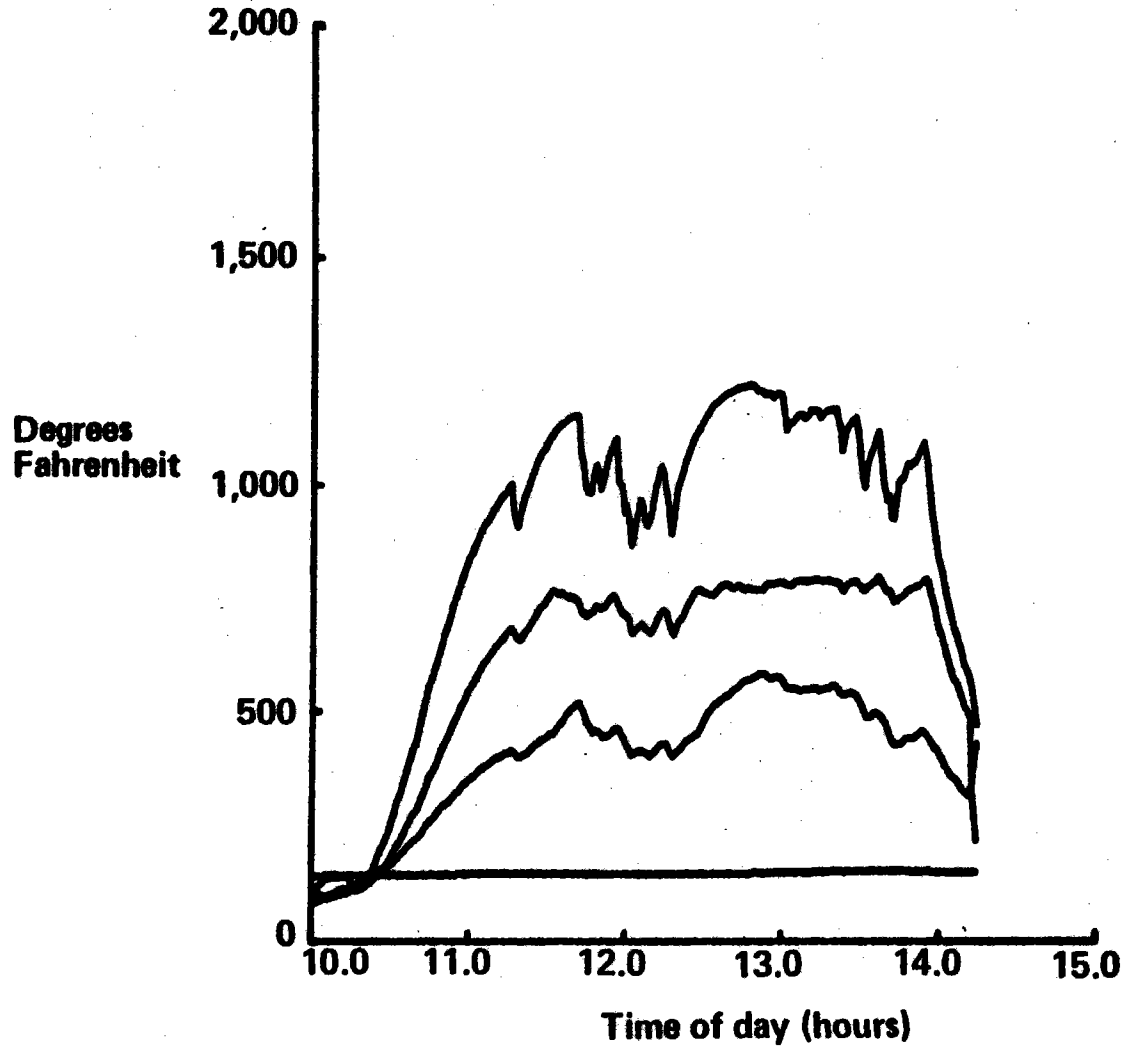
# Plot of January 27, 1979 Test Data, Eppley Pyrheliometer



741

Figure 123-73 Plot of January 27, 1979 Test Data, Air Supply Gas Temperatures

# Plot of January 27, 1979 Test Data, Air Supply Gas Temperatures



742

Figure 12.3-74 Plot of January 27, 1979 Test Data, Frame Calorimeters

## Plot of January 27, 1979 Test Data, Frame Calorimeters

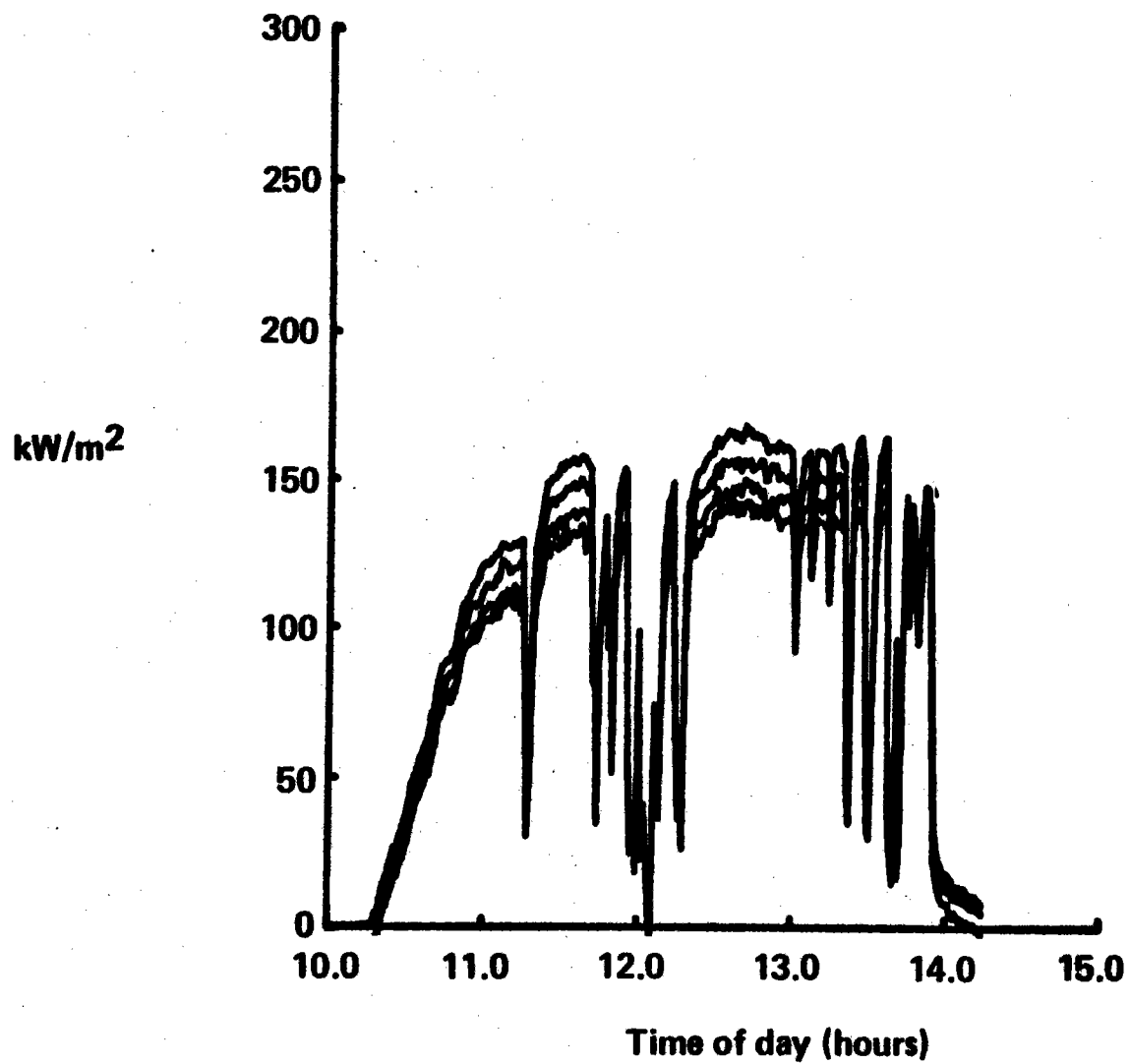
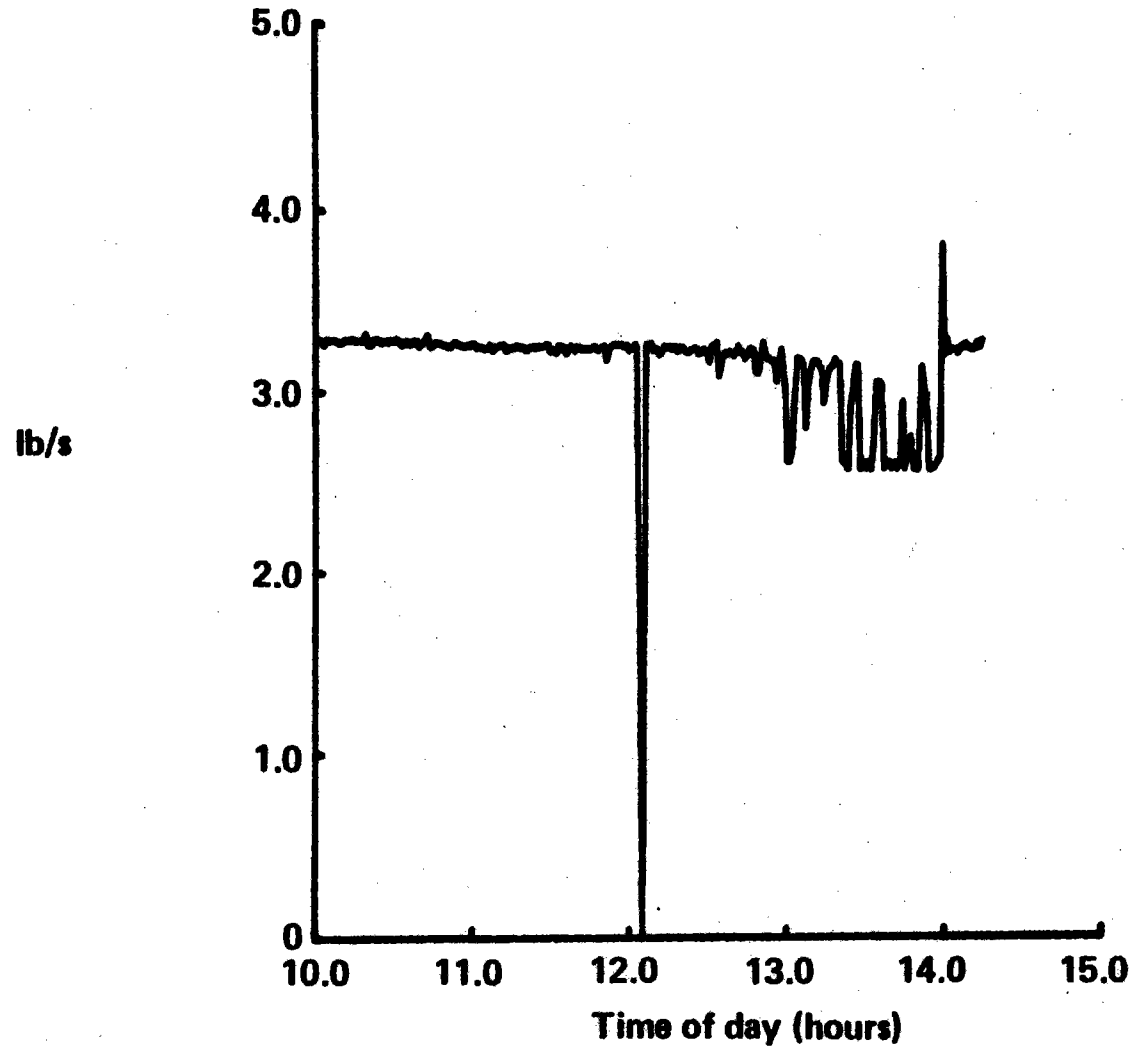


Figure 123-75 Plot of January 27, 1979 Test Data, Receiver Mass Flow

# Plot of January 27, 1979 Test Data, Receiver Mass Flow



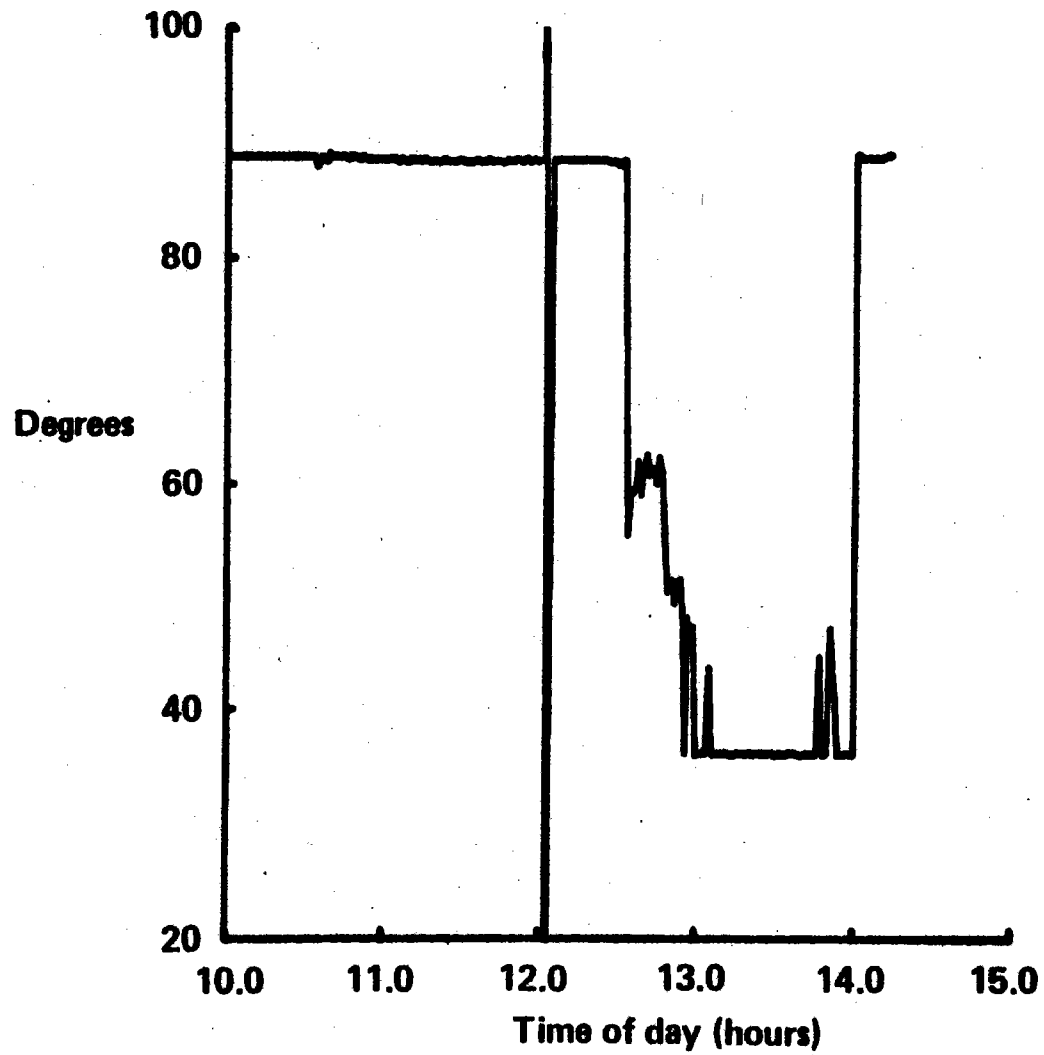
744

lb/s

Time of day (hours)

Figure 123-76 Plot of January 27, 1979 Test Data, H/X Panel 3 Valve Angle

# Plot of January 27, 1979 Test Data, H/X Panel 3 Valve Angle



745

Figure 123-77 Plot of January 27, 1979 Test Data, Air Inlet-Outlet Temperatures, Panel 3

## Plot of January 27, 1979 Test Data, Air Inlet-Outlet Temperatures, Panel 3

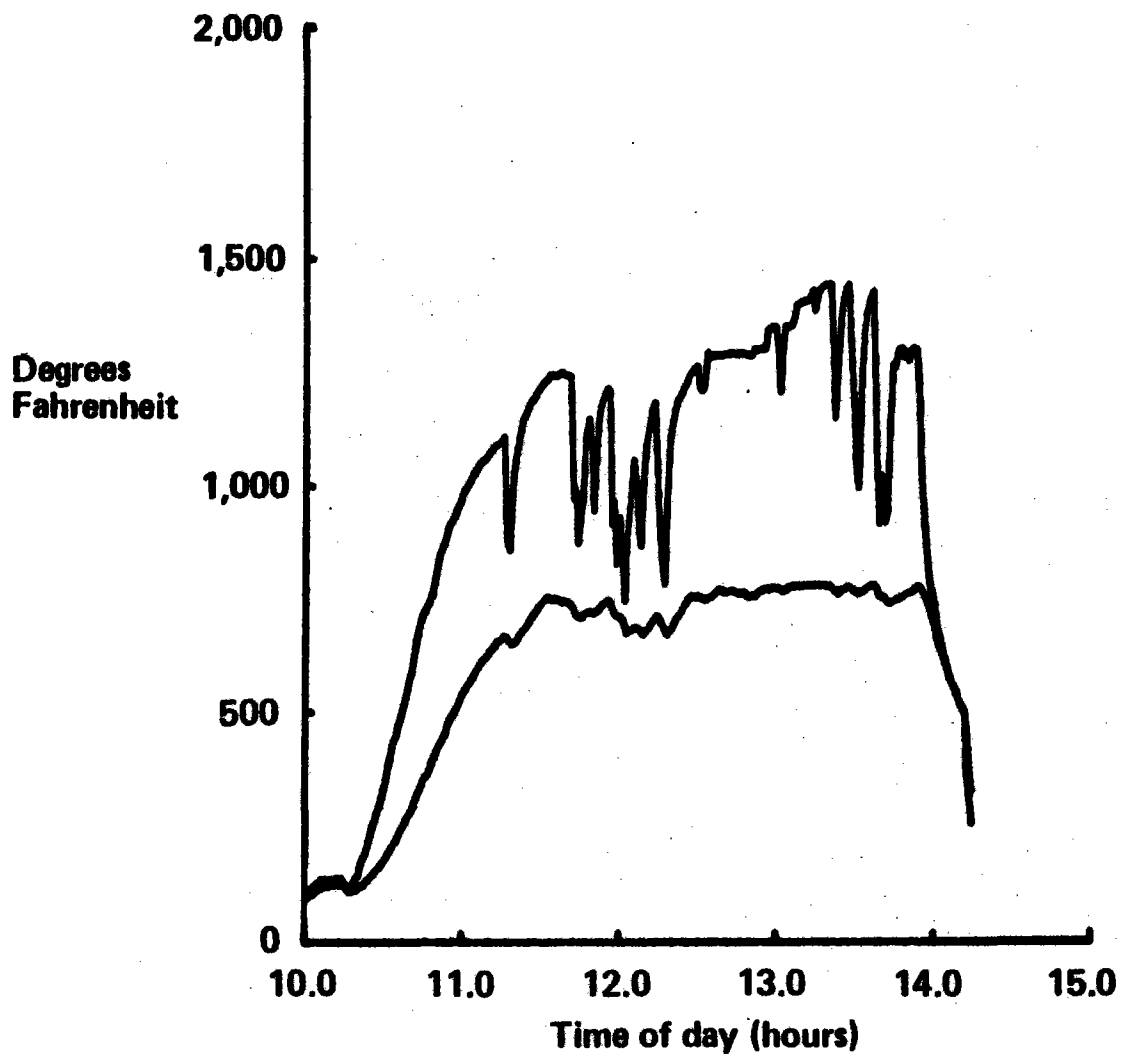




*Figure 12.3-78 Time Chart for January 28, 1979 Solar Test*

## **Time Chart for January 28, 1979 Solar Test**

<b>9:34</b>	<b>Field at standby</b>
<b>9:37</b>	<b>First collector on target</b>
<b>10:13</b>	<b>62 collectors on target</b>
<b>10:18</b>	<b>Unplanned zone A shutdown</b>
<b>10:39</b>	<b>Field at standby</b>
<b>10:40</b>	<b>First collector on target</b>
<b>11:03</b>	<b>62 collectors on target</b>
<b>11:24</b>	<b>66 collectors on target</b>
<b>11:42</b>	<b>64 collectors on target</b>
<b>11:55</b>	<b>Receiver on control</b>
<b>12:21</b>	<b>Start TH-4, reduction of 20 collectors</b>
<b>12:35</b>	<b>38 collectors on target</b>
<b>12:53</b>	<b>66 collectors on target, end TH-4</b>
<b>13:03</b>	<b>Field to standby for EC-3</b>
<b>13:10</b>	<b>EC-3 completed</b>
<b>13:19</b>	<b>Field on target for CS-3</b>
<b>13:21</b>	<b>65 collectors on target</b>
<b>13:27</b>	<b>66 collectors on target</b>
<b>13:45</b>	<b>End of CS-3</b>
<b>14:33</b>	<b>Steady test conditions, EB-9C</b>
<b>14:49</b>	<b>80 collectors on target</b>
<b>15:04</b>	<b>81 collectors on target</b>
<b>17:26</b>	<b>Field shutdown</b>

Figure 12.3-79 Plot of January 28, 1979 Test Data, Eppley Pyrheliometer

## Plot of January 28, 1979 Test Data, Eppley Pyrheliometer

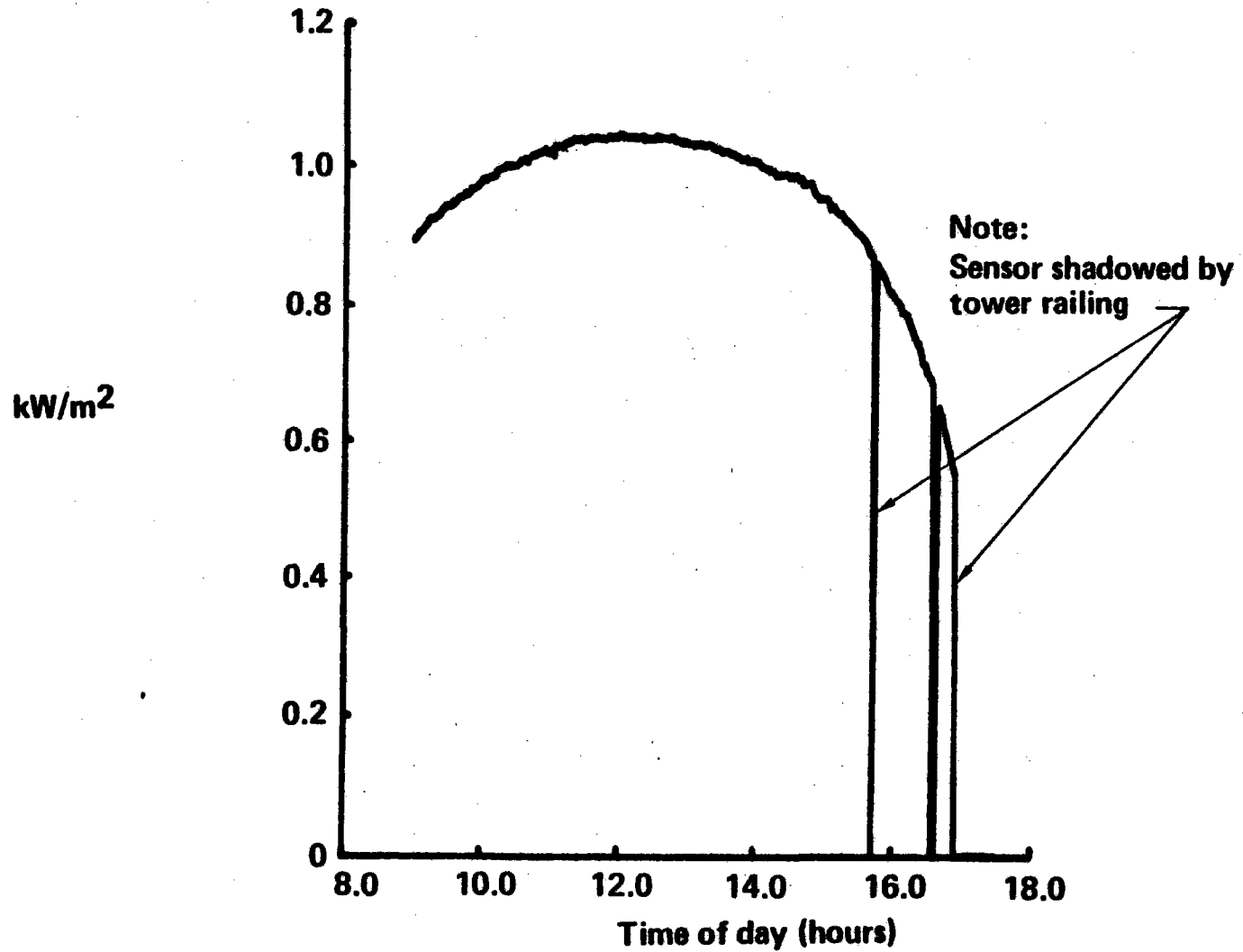


Figure 123-80 Plot of January 28, 1979 Test Data, Air Supply Gas Temperatures

## Plot of January 28, 1979 Test Data, Air Supply Gas Temperatures

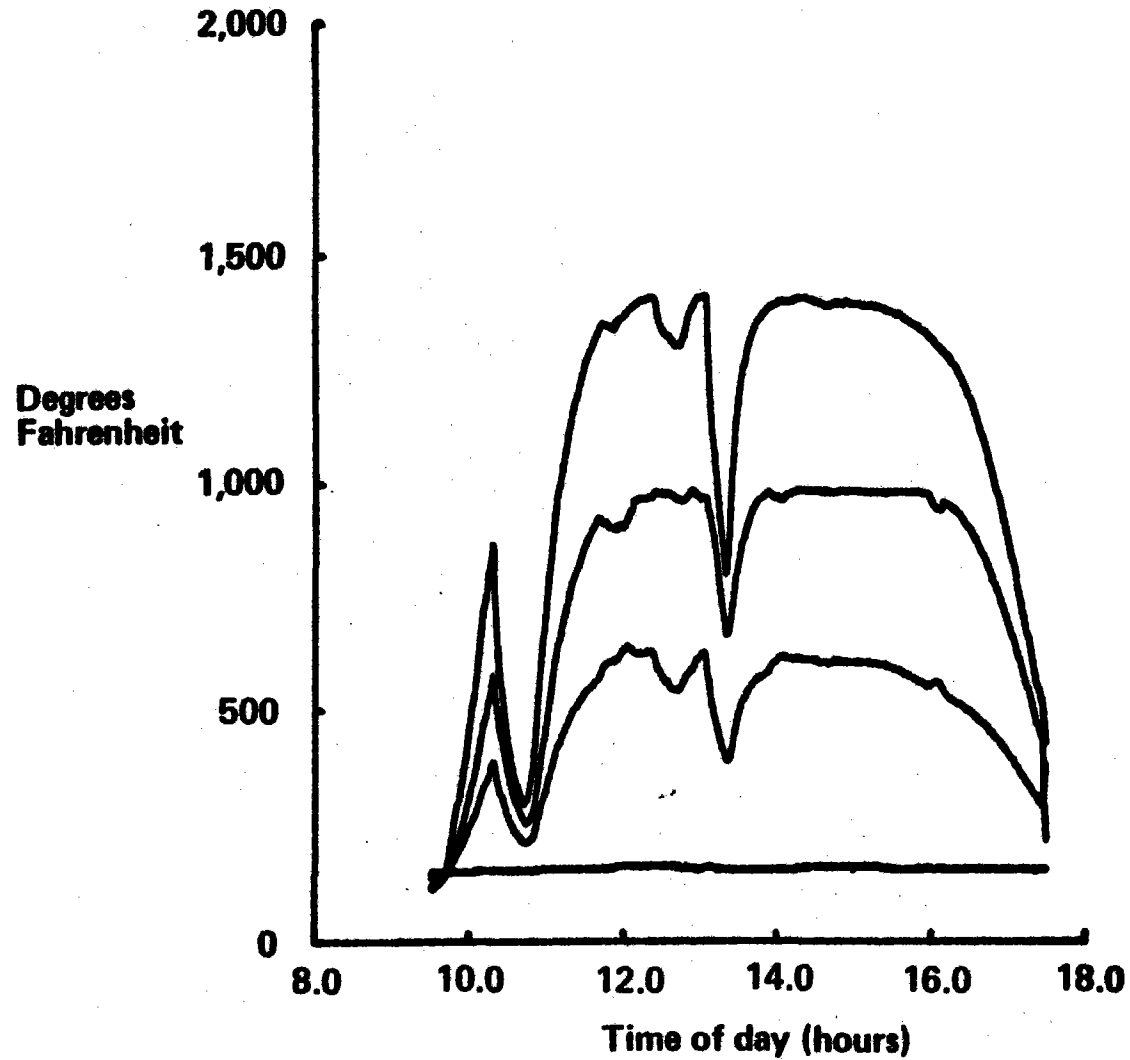


Figure 12.3-81 Plot of January 28, 1979 Test Data, Frame Calorimeters

## Plot of January 28, 1979 Test Data, Frame Calorimeters

750

kW/m<sup>2</sup>

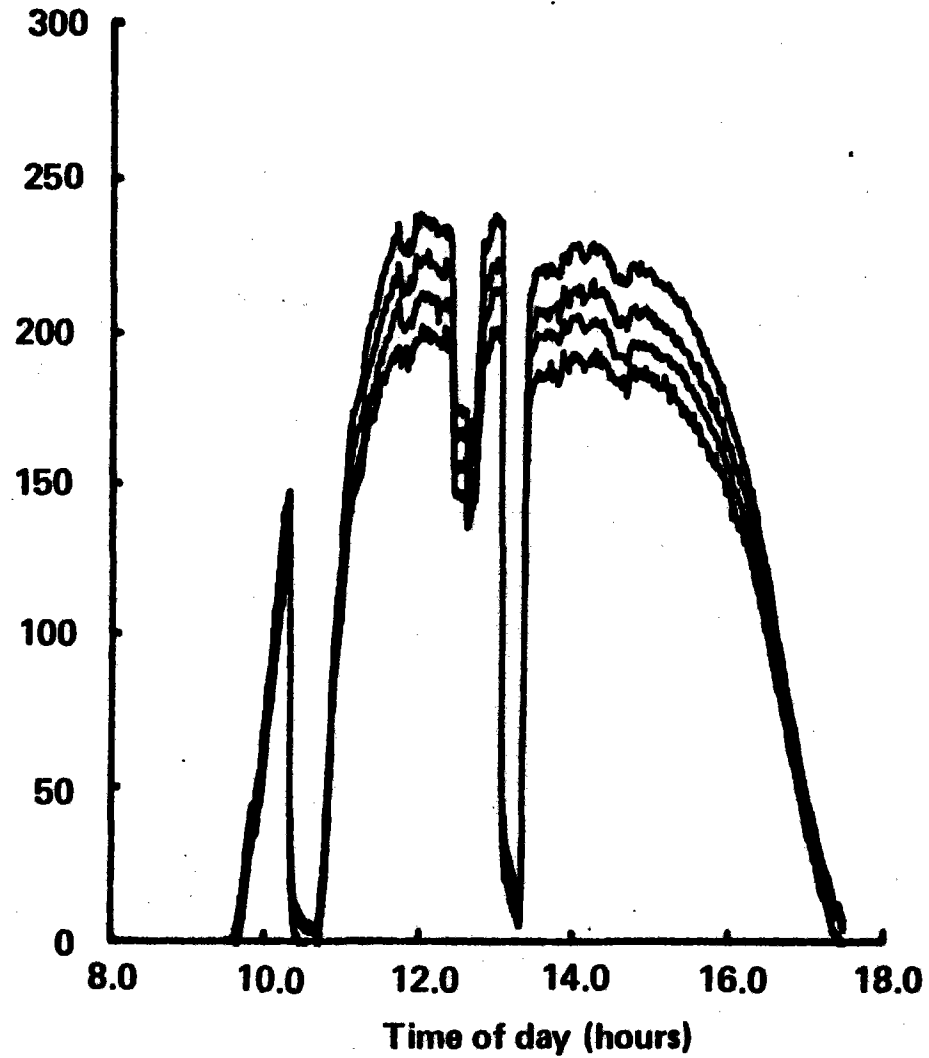
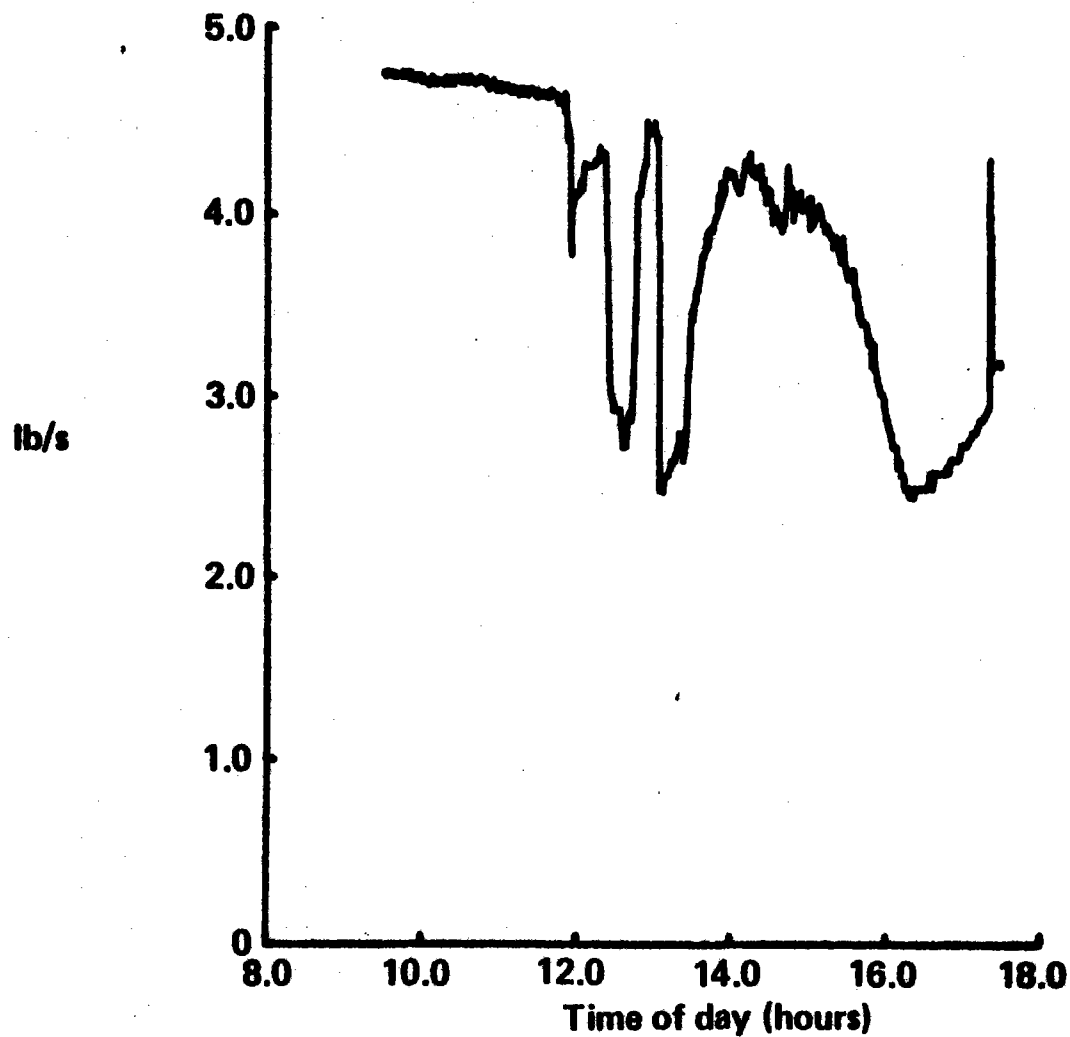


Figure 12.3-82 Plot of January 28, 1979 Test Data, Receiver Mass Flow

## Plot of January 28, 1979 Test Data, Receiver Mass Flow



751

Figure 12.3-83 Plot of January 28, 1979 Test Data, H/X Panel 3 Valve Angle

### Plot of January 28, 1979 Test Data, H/X Panel 3 Valve Angle

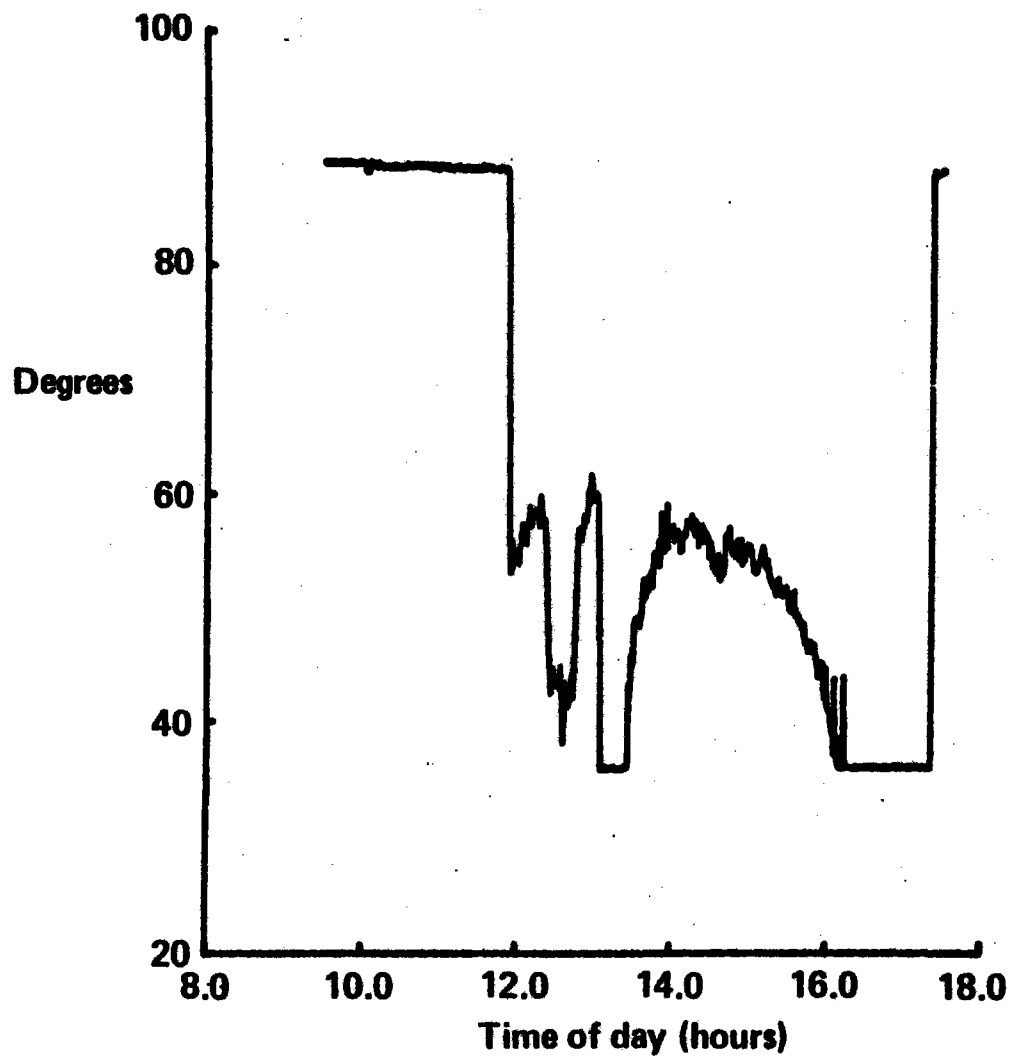
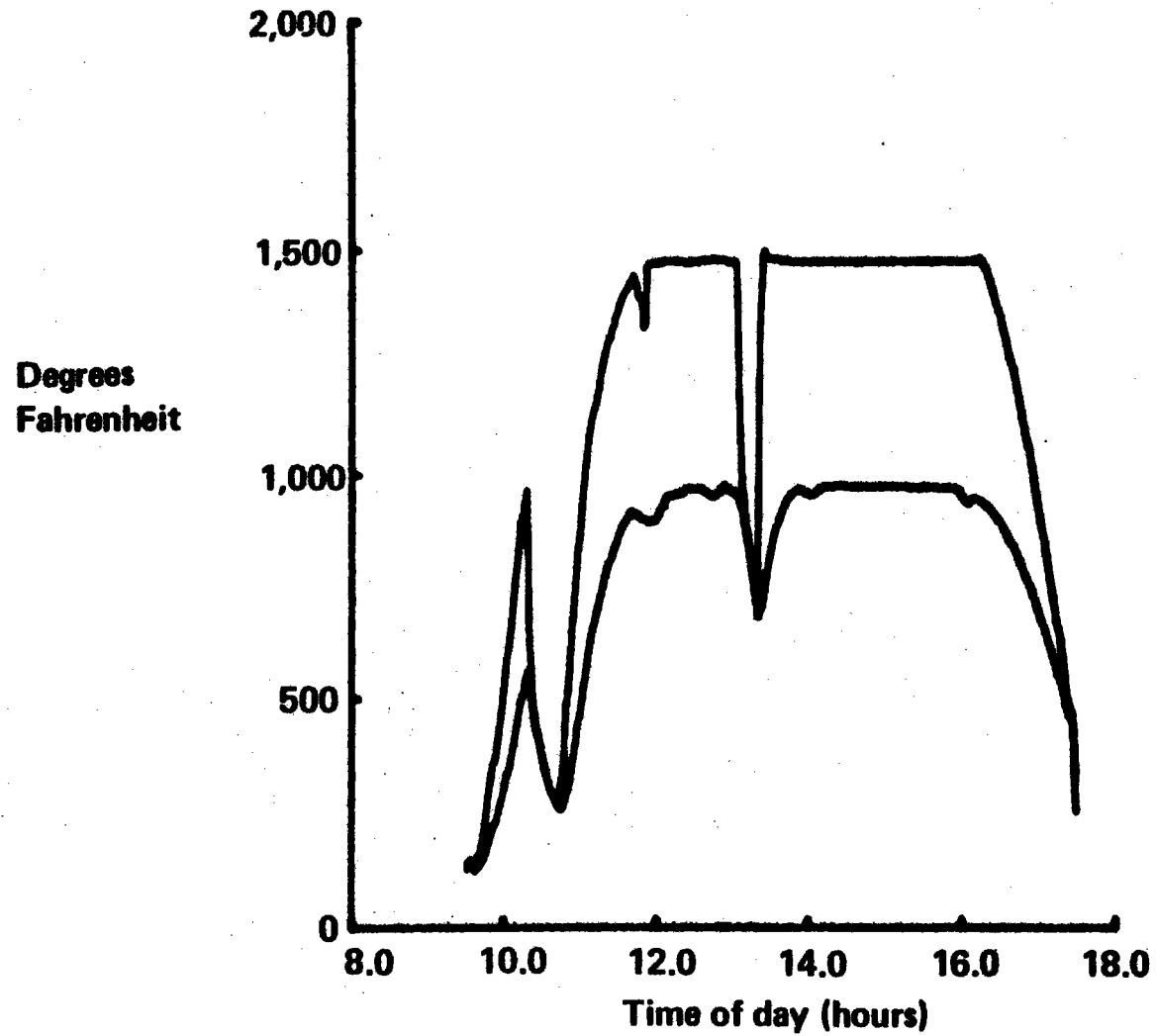


Figure 12.3-84 Plot of January 28, 1979 Test Data, Air Inlet-Outlet Temperatures, Panel 3

### Plot of January 28, 1979 Test Data, Air Inlet-Outlet Temperatures, Panel 3



*Figure 12.3-85 Time Chart for January 30, 1979 Solar Test*

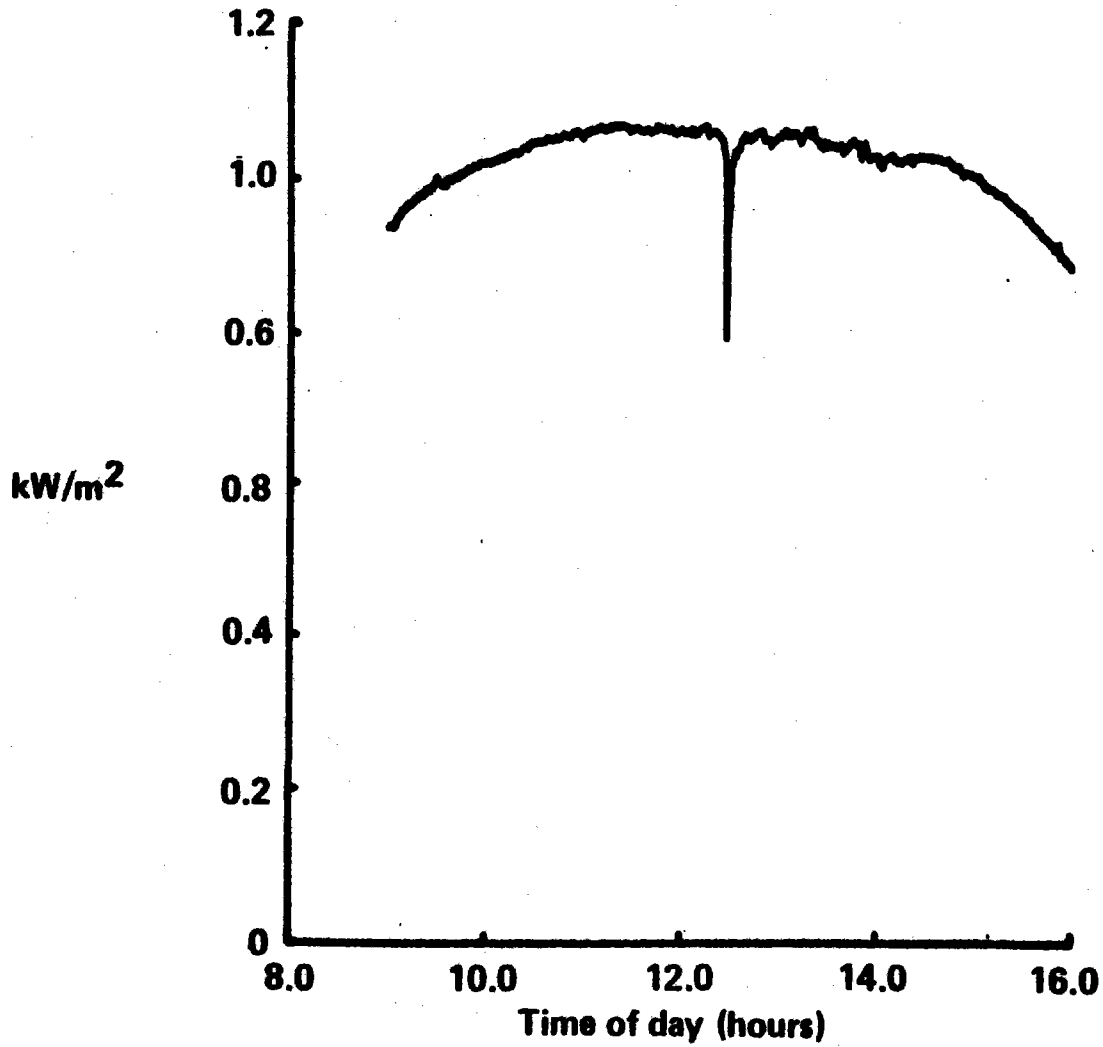
## **Time Chart for January 30, 1979 Solar Test**

<b>10:21</b>	<b>Field at standby</b>
<b>10:28</b>	<b>37 collectors on target</b>
<b>10:32</b>	<b>40 collectors on target</b>
<b>11:03</b>	<b>50 collectors on target</b>
<b>11:21</b>	<b>53 collectors on target</b>
<b>11:24</b>	<b>56 collectors on target</b>
<b>11:32</b>	<b>59 collectors on target</b>
<b>11:56</b>	<b>Receiver on control</b>
<b>12:04</b>	<b>Starting cooldown, TH-2</b>
<b>12:07</b>	<b>39 collectors on target</b>
<b>12:21</b>	<b>Starting heatup, TH-2</b>
<b>12:27</b>	<b>59 collectors on target</b>
<b>12:36</b>	<b>Begin RF-3</b>
<b>13:50</b>	<b>End of RF-3</b>
<b>13:55</b>	<b>62 collectors on target</b>
<b>14:20</b>	<b>Steady test conditions, EB-8C</b>
<b>15:23</b>	<b>77 collectors on target</b>
<b>15:30</b>	<b>Receiver off control due to low power</b>
<b>15:40</b>	<b>76 collectors on target</b>
<b>15:52</b>	<b>36 collectors on target</b>
<b>15:53</b>	<b>Field shutdown</b>



Figure 12.3-86 Plot of January 30, 1979 Test Data, Eppley Pyrheliometer

## Plot of January 30, 1979 Test Data, Eppley Pyrheliometer



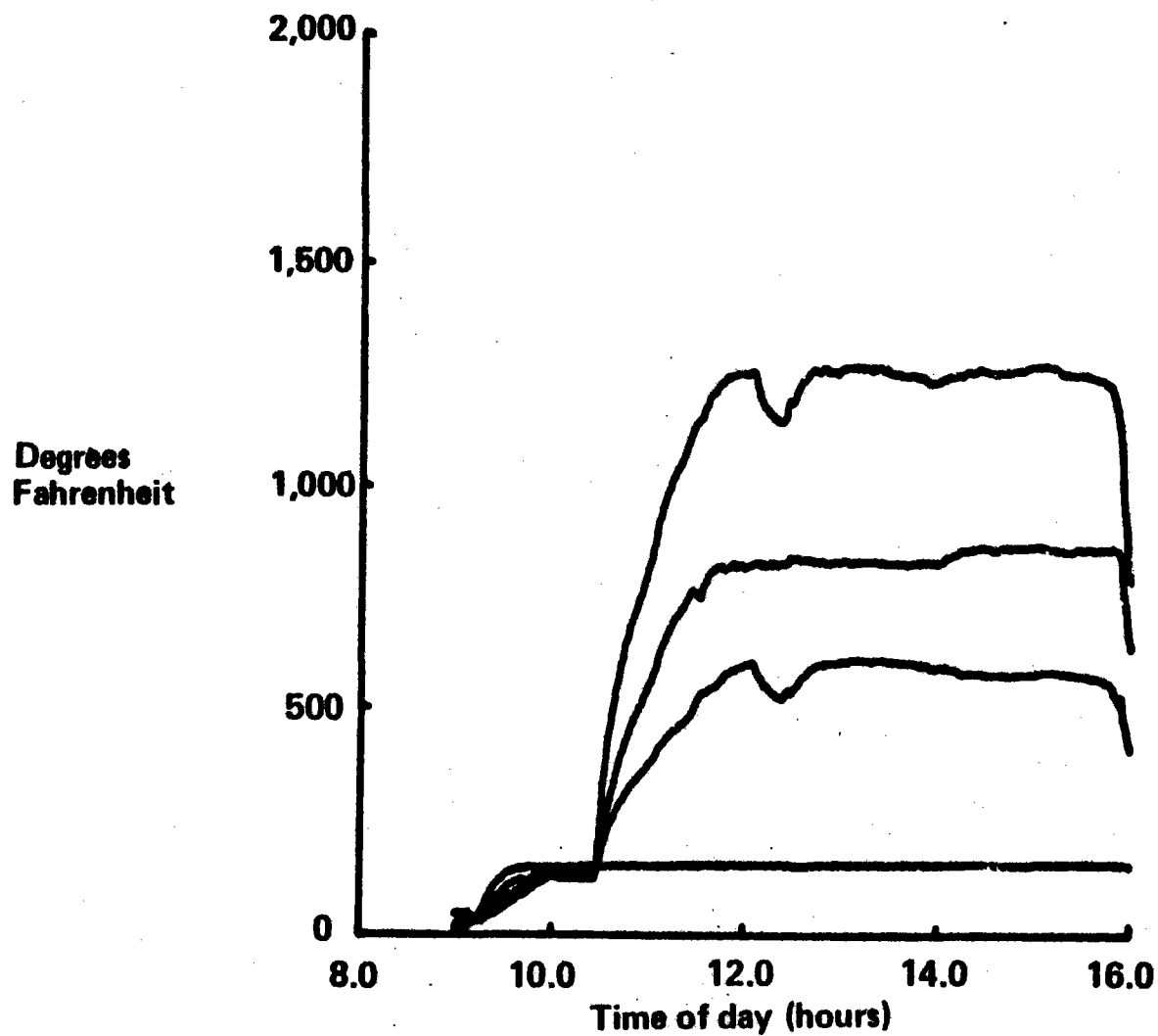
755

kW/m<sup>2</sup>

Time of day (hours)

Figure 12.3-87 Plot of January 30, 1979 Test Data, Air Supply Gas Temperatures

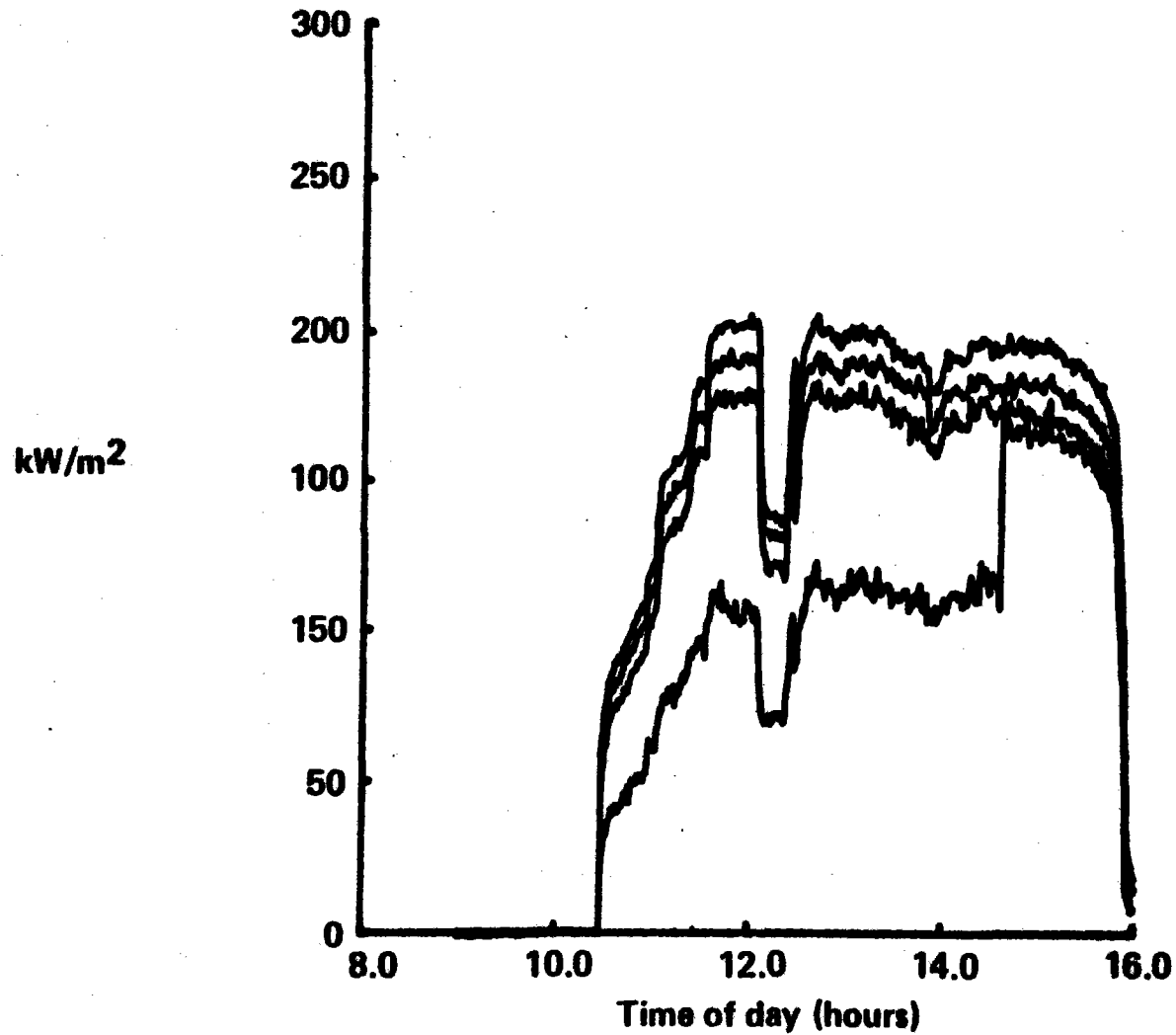
### Plot of January 30, 1979 Test Data, Air Supply Gas Temperatures



756

Figure 12.3-88 Plot of January 30, 1979 Test Data, Frame Calorimeters

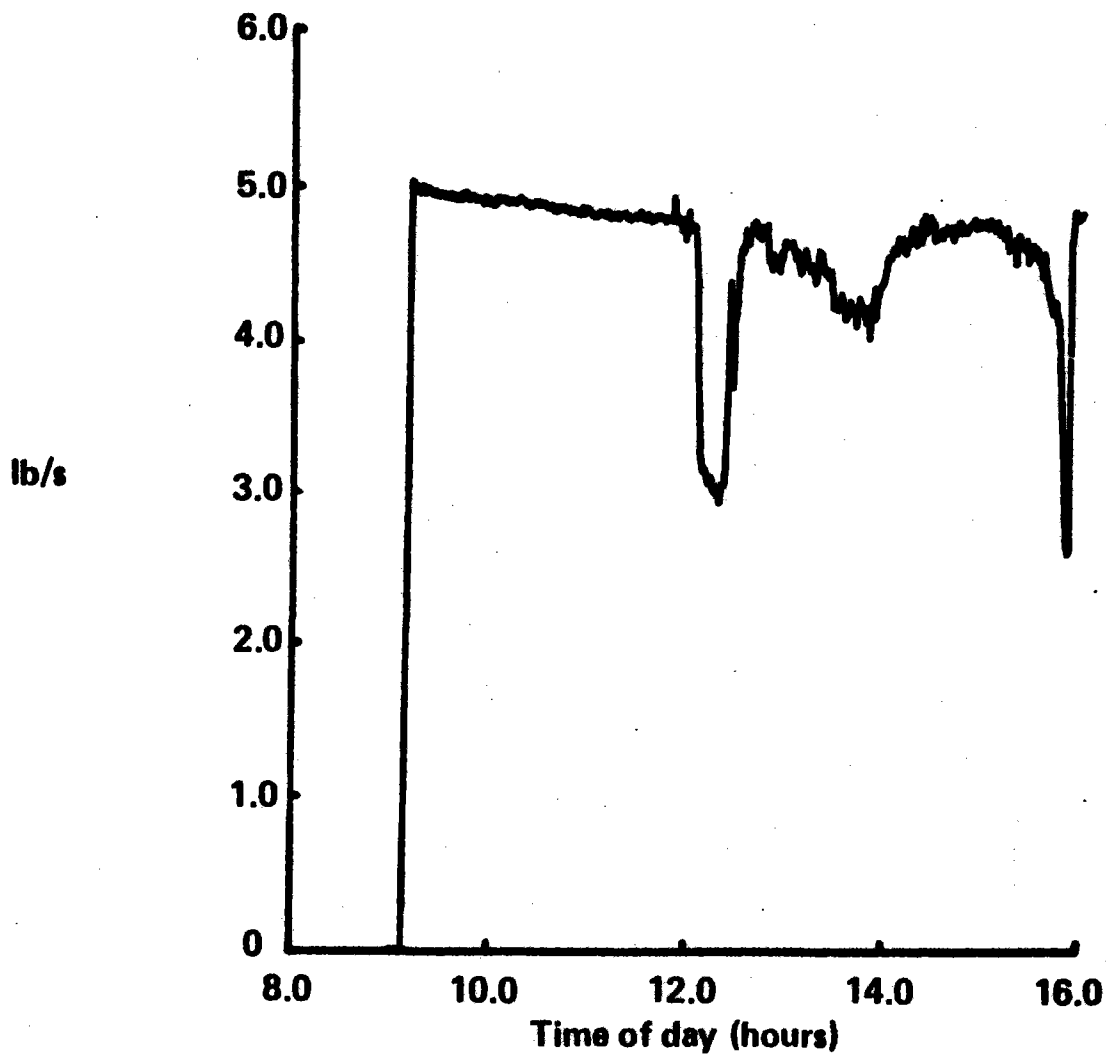
# Plot of January 30, 1979 Test Data, Frame Calorimeters



757

Figure 12.3-89 Plot of January 30, 1979 Test Data, Receiver Mass Flow

## Plot of January 30, 1979 Test Data, Receiver Mass Flow



758

lb/s

Time of day (hours)

Figure 12.3-90 Plot of January 30, 1979 Test Data, H/X Panel 3 Valve Angle

### Plot of January 30, 1979 Test Data, H/X Panel 3 Valve Angle

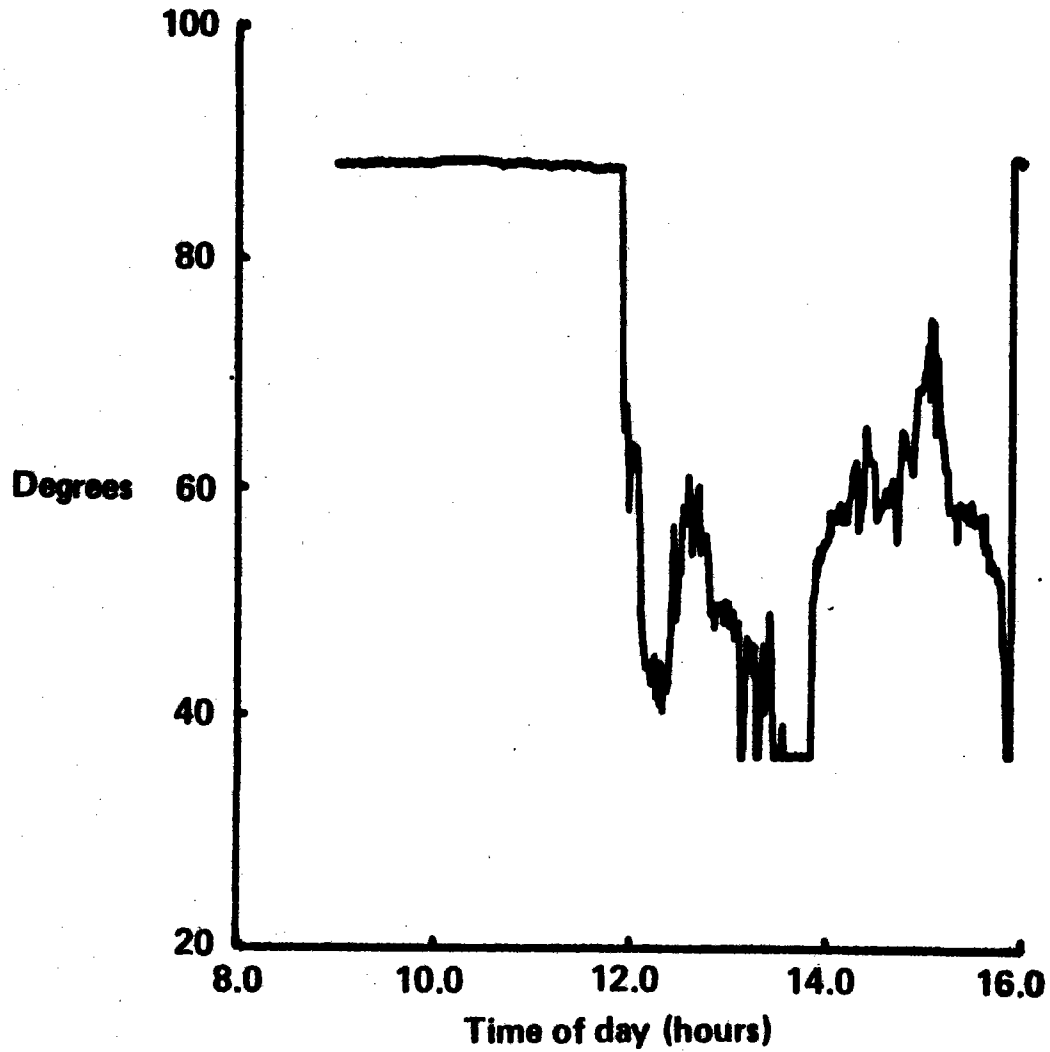


Figure 123-91 Plot of January 30, 1979 Test Data, Air Inlet-Outlet Temperatures, Panel 3

### Plot of January 30, 1979 Test Data, Air Inlet-Outlet Temperatures, Panel 3

760

Degrees  
Fahrenheit

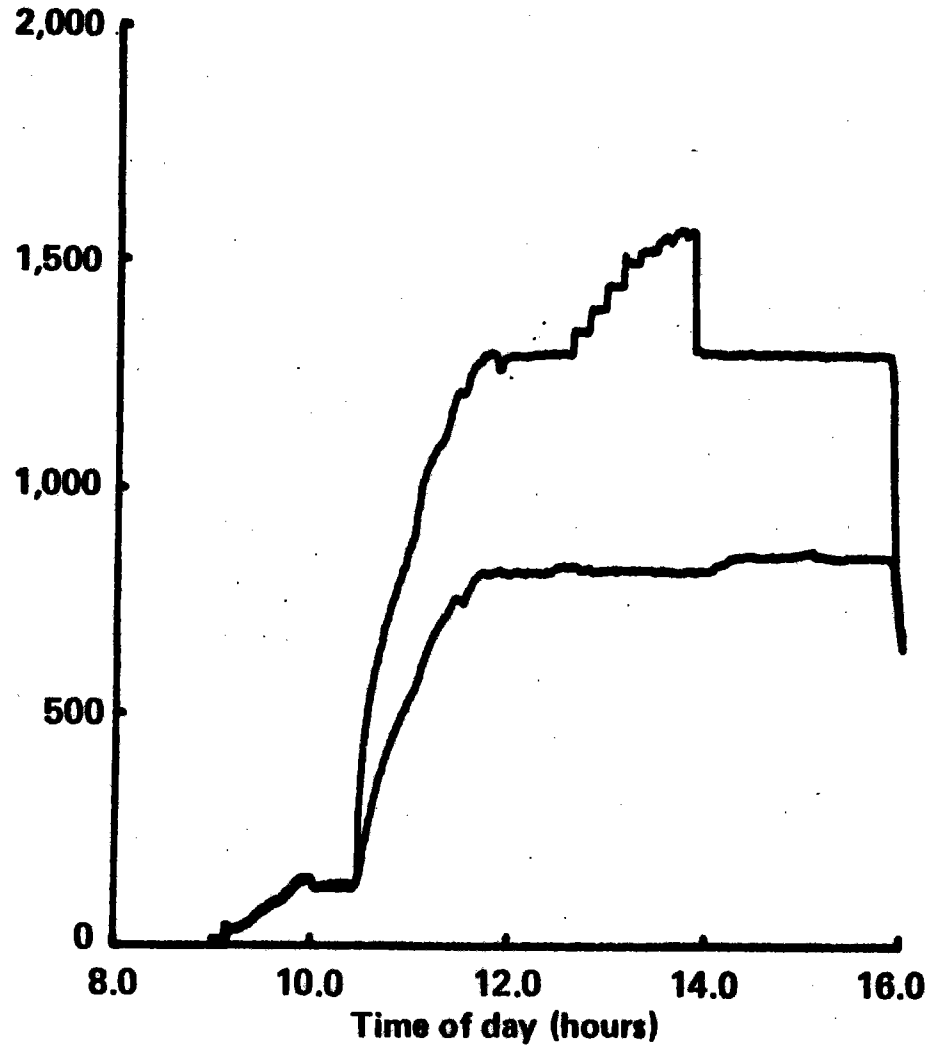


Figure 12.3-92 Time Chart for January 31, 1979 Solar Test

## Time Chart for January 31, 1979 Solar Test

<b>7:39</b>	<b>Field at standby</b>
<b>7:40</b>	<b>First collector on target</b>
<b>7:42</b>	<b>24 collectors on target</b>
<b>7:46</b>	<b>55 collectors on target</b>
<b>7:52</b>	<b>Field (zone A) on emergency standby</b>
	<b>11 collectors (zone B) on target</b>
<b>8:03</b>	<b>50 collectors on target</b>
<b>8:17</b>	<b>68 collectors on target</b>
<b>8:27</b>	<b>69 collectors on target</b>
<b>8:32</b>	<b>68 collectors on target</b>
<b>10:58</b>	<b>65 collectors on target</b>
<b>11:13</b>	<b>Receiver on control</b>
<b>12:00</b>	<b>Steady test conditions, EB-9B</b>
<b>13:16</b>	<b>67 collectors on target</b>
<b>13:35</b>	<b>69 collectors on target</b>
<b>13:43</b>	<b>71 collectors on target</b>
<b>14:02</b>	<b>73 collectors on target</b>
<b>14:12</b>	<b>74 collectors on target</b>
<b>14:20</b>	<b>75 collectors on target</b>
<b>16:05</b>	<b>Field to standby</b>
<b>16:22</b>	<b>Field shutdown</b>

Figure 12.3-93 Plot of January 31, 1979 Test Data, Eppley Pyrheliometer

# Plot of January 31, 1979 Test Data, Eppley Pyrheliometer

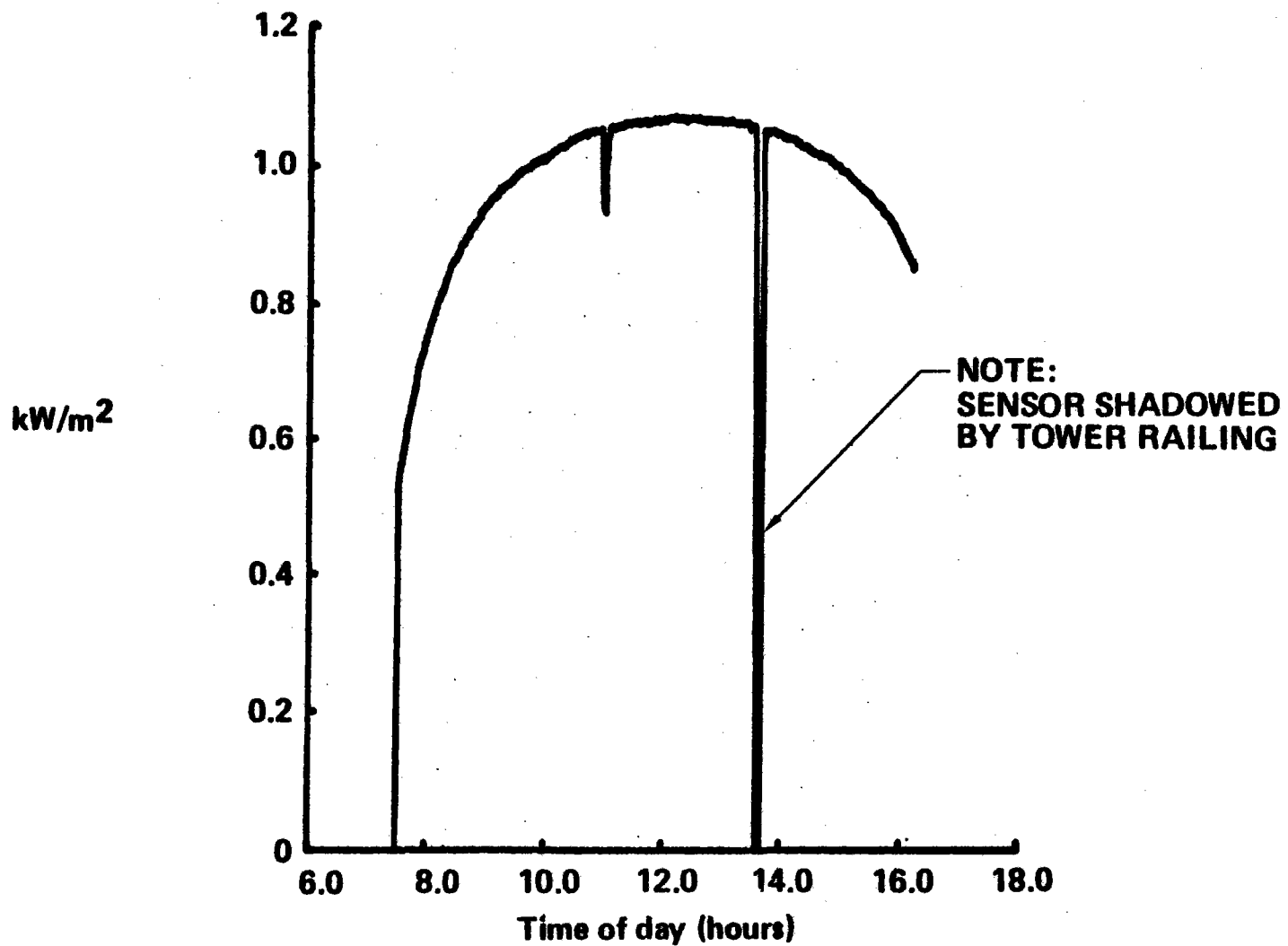




Figure 12.3-94 Plot of January 31, 1979 Test Data , Air Supply Gas Temperatures

## Plot of January 31, 1979 Test Data, Air Supply Gas Temperatures

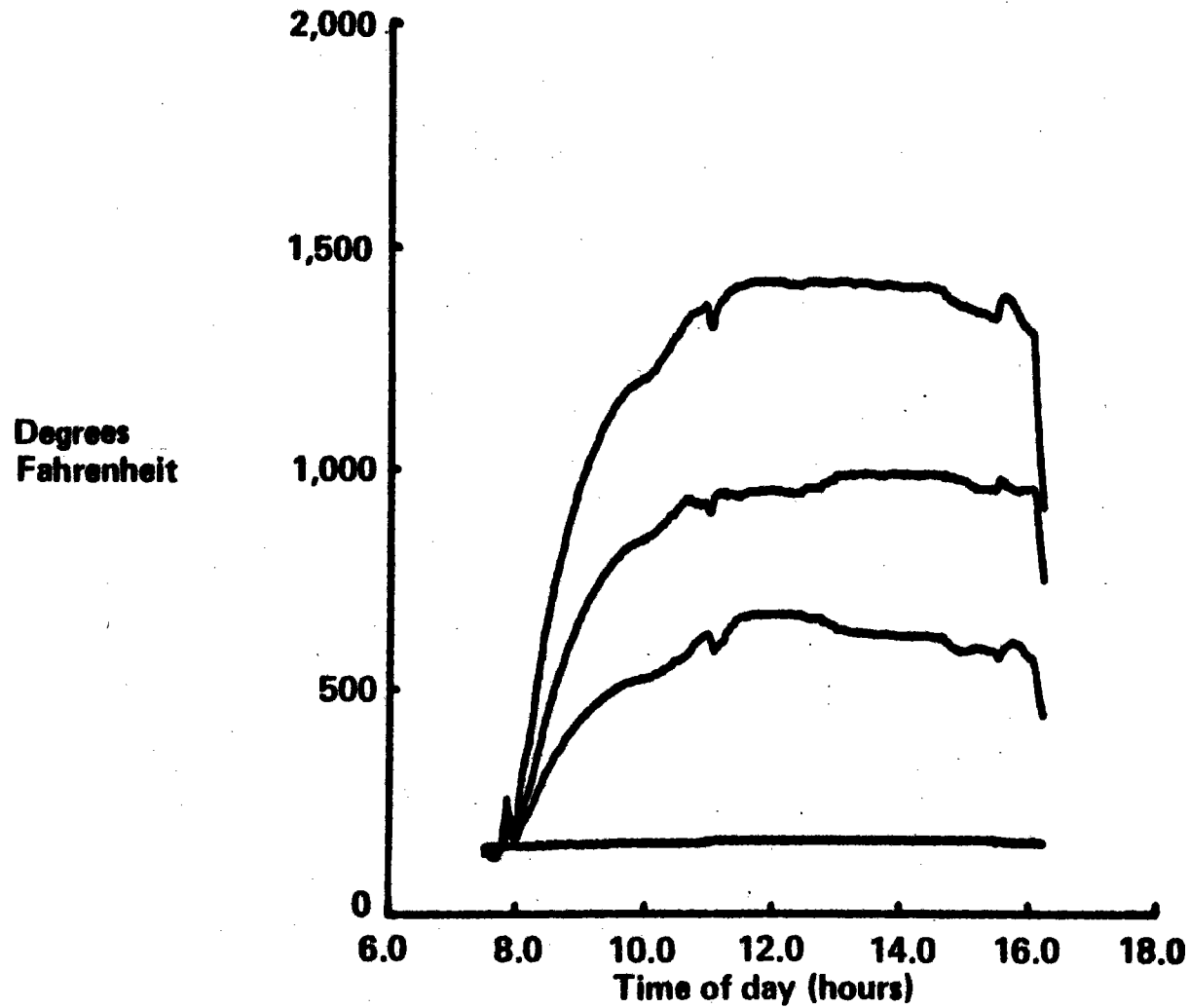
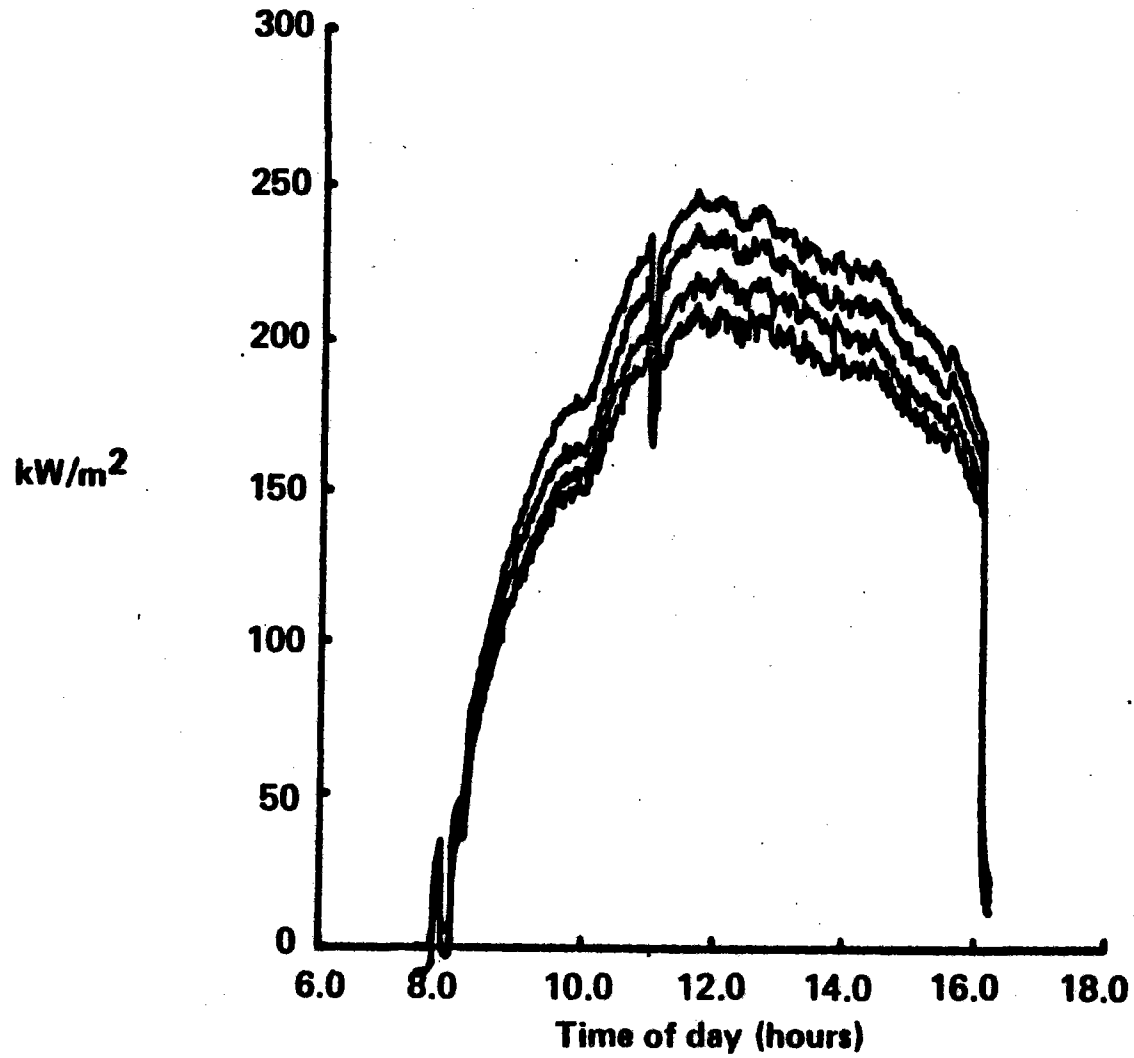


Figure 12.3-95 Plot of January 31, 1979 Test Data, Frame Calorimeters

## Plot of January 31, 1979 Test Data, Frame Calorimeters



764

Figure 12.3-96 Plot of January 31, 1979 Test Data, Receiver Mass Flow

### Plot of January 31, 1979 Test Data, Receiver Mass Flow

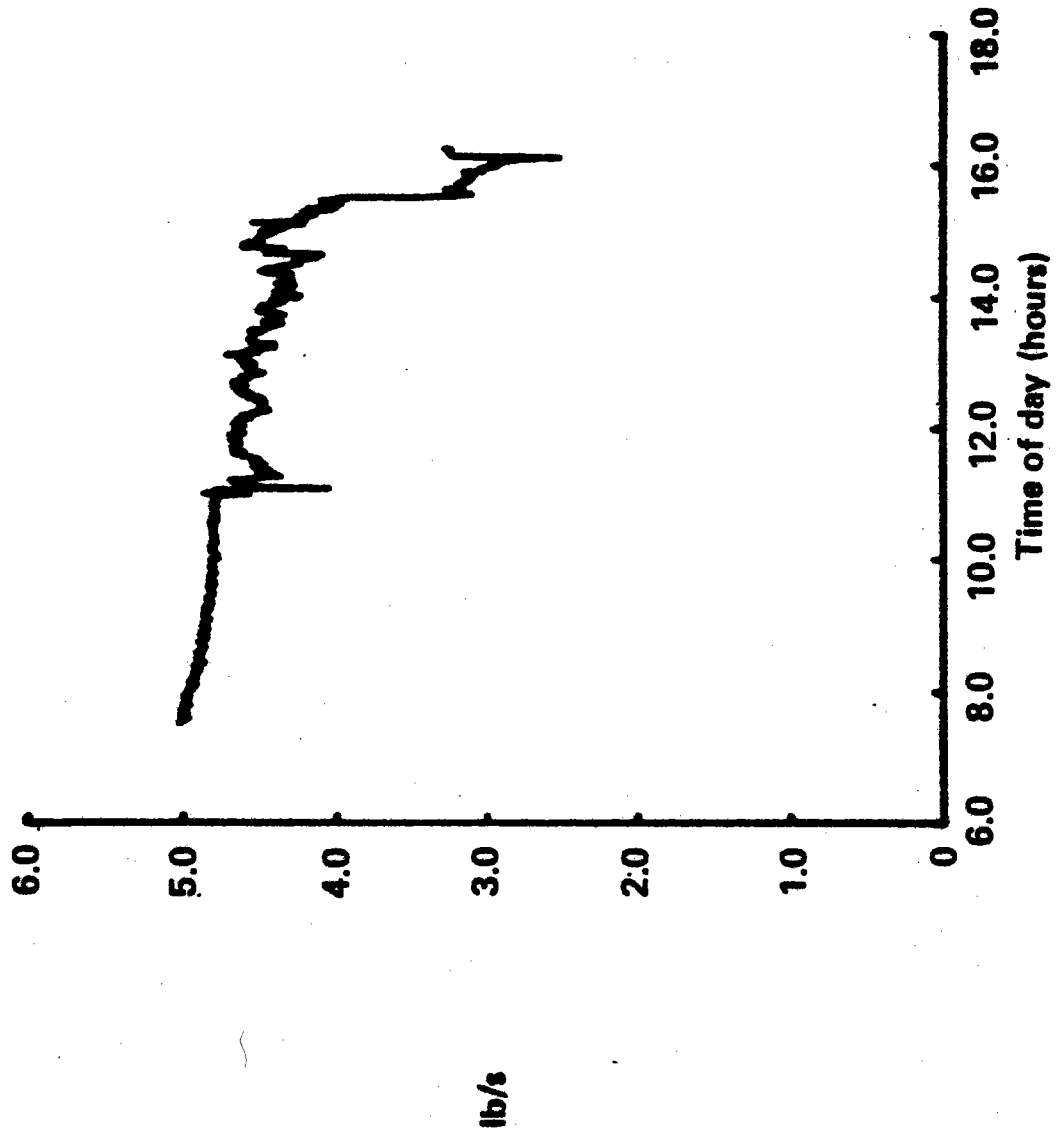
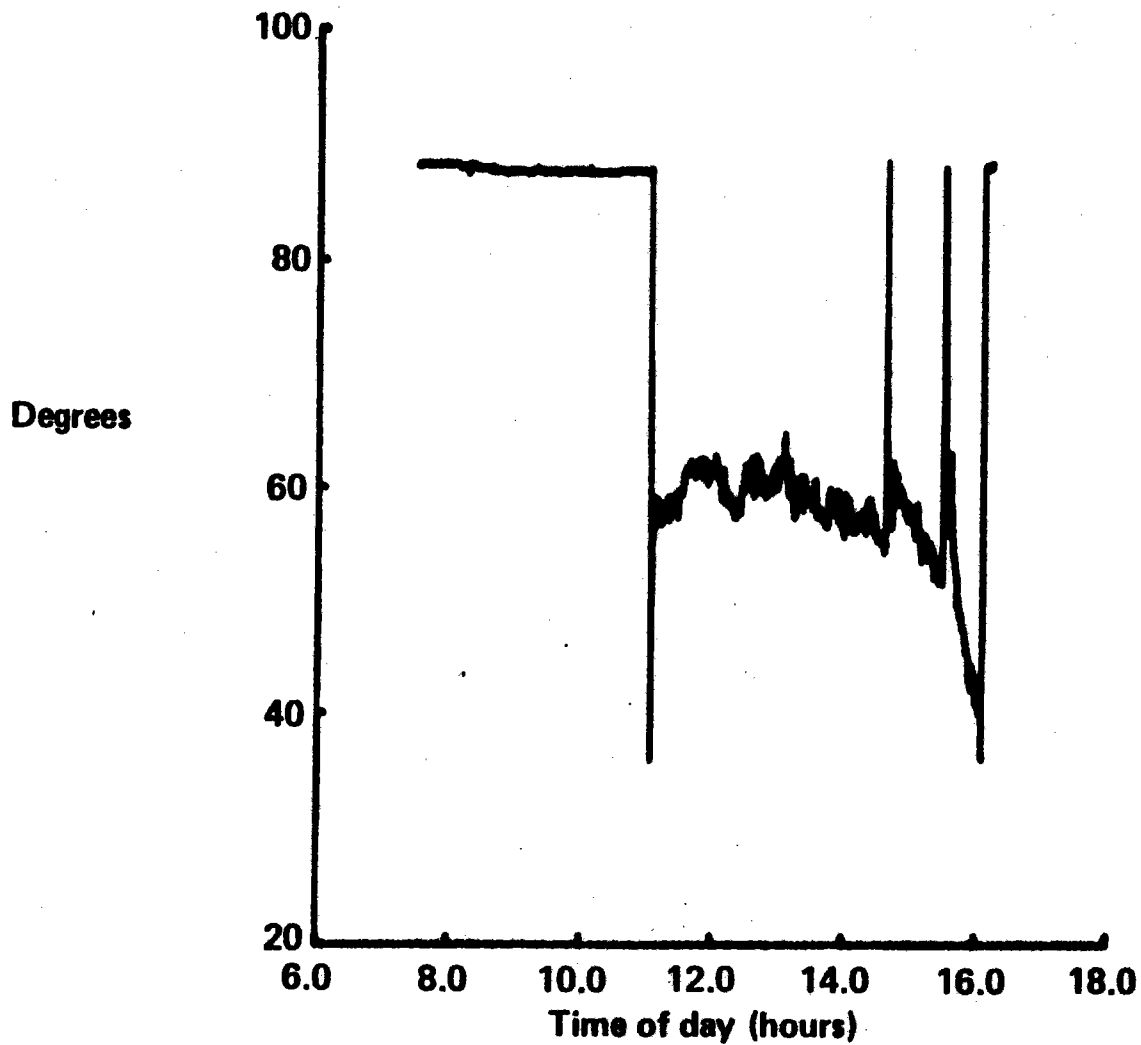


Figure 12.3-97 Plot of January 31, 1979 Test Data, H/X Panel 3 Valve Angle

## Plot of January 31, 1979 Test Data, H/X Panel 3 Valve Angle



767

Figure 12.3-98 Plot of January 31, 1979 Test Data, Air Inlet-Outlet Temperatures, Panel 3

### Plot of January 31, 1979 Test Data, Air Inlet-Outlet Temperatures, Panel 3

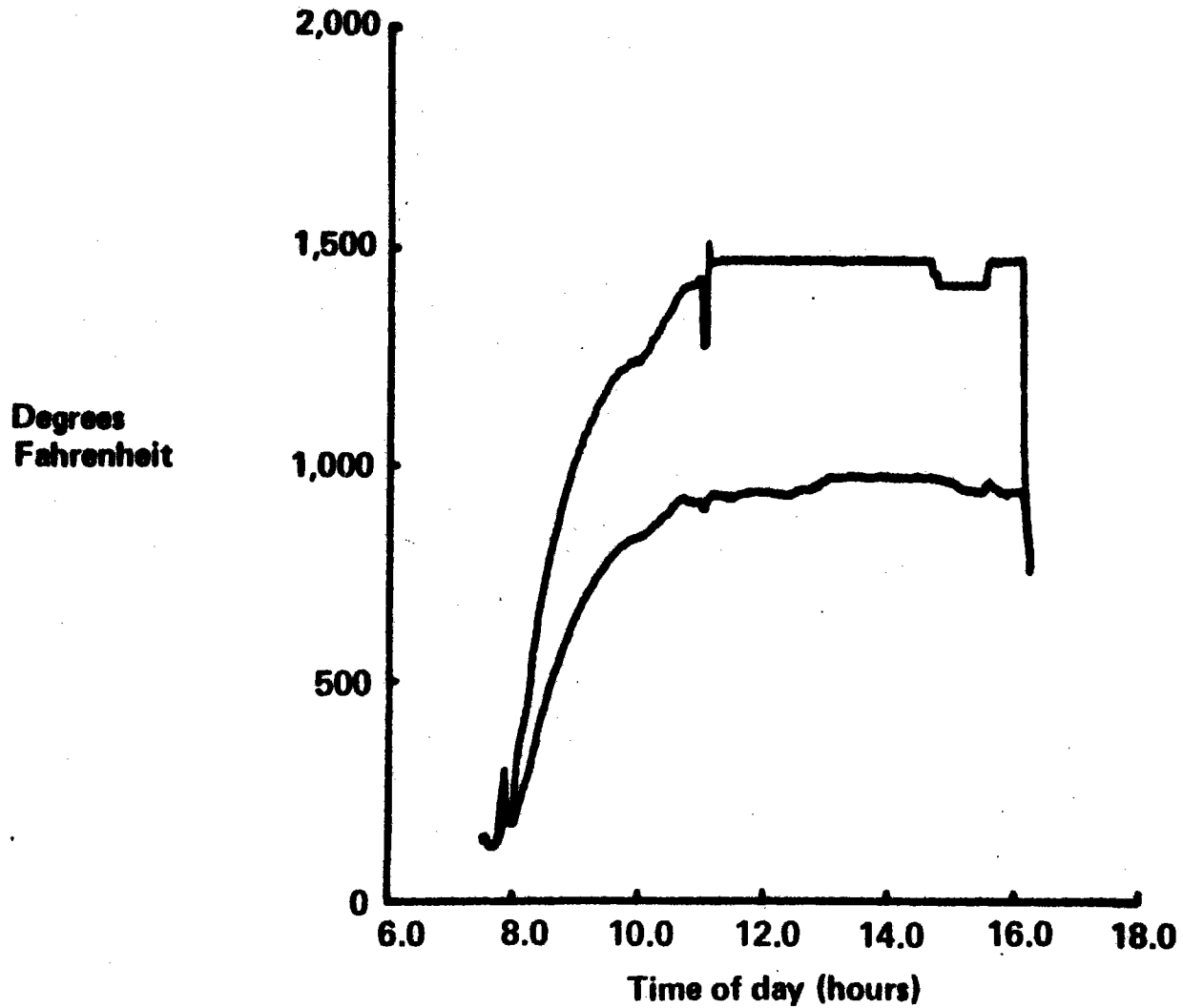


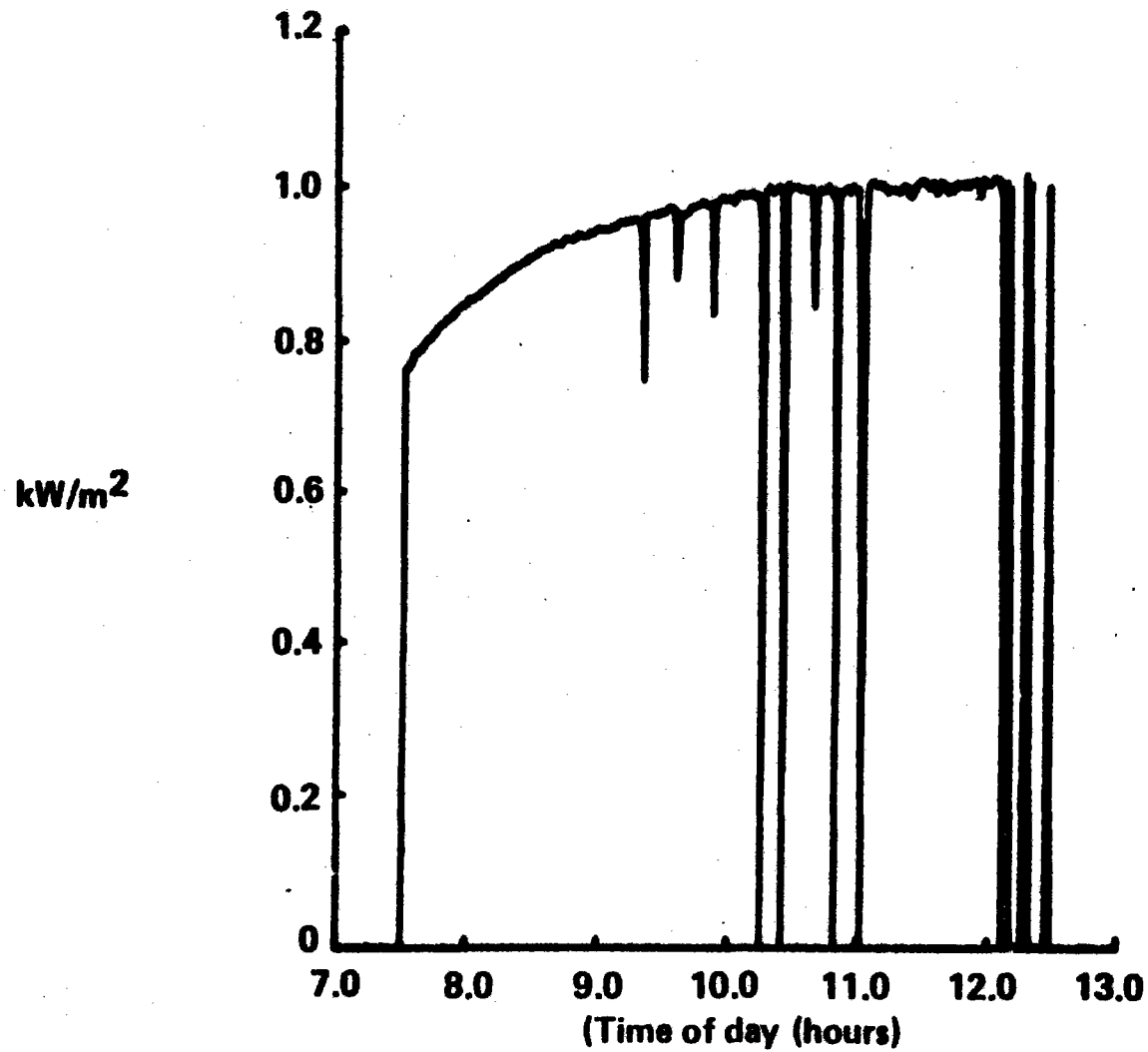
*Figure 12.3-99 Time Chart for March 23, 1979 Solar Test*

## **Time Chart for March 23, 1979 Solar Test**

<b>7:30</b>	<b>Field at standby</b>
<b>7:38</b>	<b>First collector on target</b>
<b>8:06</b>	<b>50 collectors on target</b>
<b>8:14</b>	<b>Field at standby</b>
<b>8:30</b>	<b>First collector on target</b>
<b>8:45</b>	<b>50 collectors on target</b>
<b>8:54</b>	<b>60 collectors on target</b>
<b>9:03</b>	<b>Field at standby</b>
<b>9:15</b>	<b>First collector on target</b>
<b>9:27</b>	<b>60 collectors on target</b>
<b>11:00</b>	<b>Receiver on control</b>
<b>12:00</b>	<b>Steady test conditions, EB-9E</b>
<b>12:17</b>	<b>Lost field</b>
<b>12:23</b>	<b>First collector on target</b>
<b>12:26</b>	<b>17 collectors on target</b>
<b>12:31</b>	<b>Field shutdown</b>

Figure 12.3-100 Plot of March 31, 1979 Test Data, Eppley Pyrheliometer

## Plot of March 31, 1979 Test Data, Eppley Pyrheliometer



770

Figure 123-101 Plot of March 23, 1979 Test, Data, Air Supply Gas Temperatures

## Plot of March 23, 1979 Test, Data, Air Supply Gas Temperatures

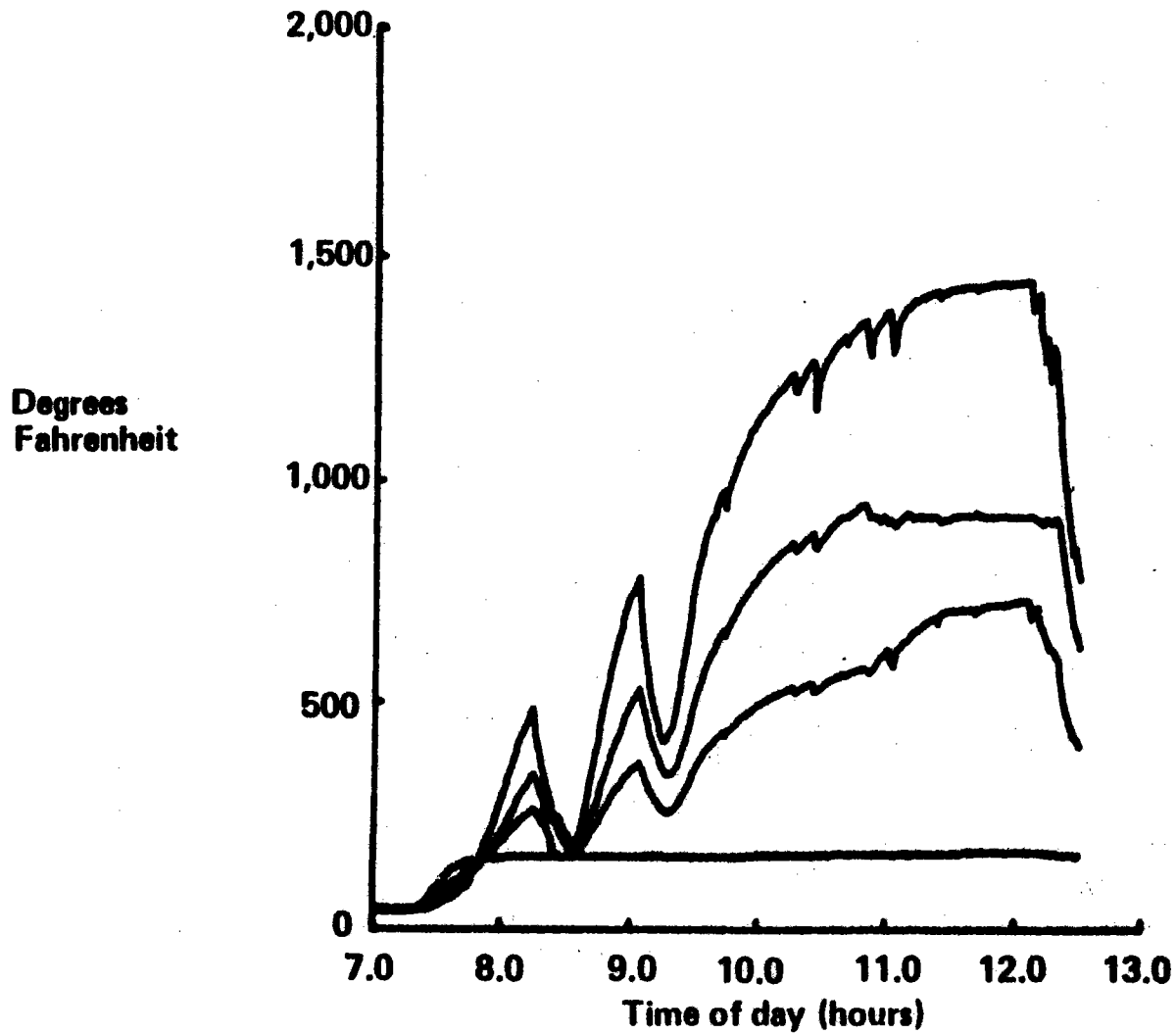
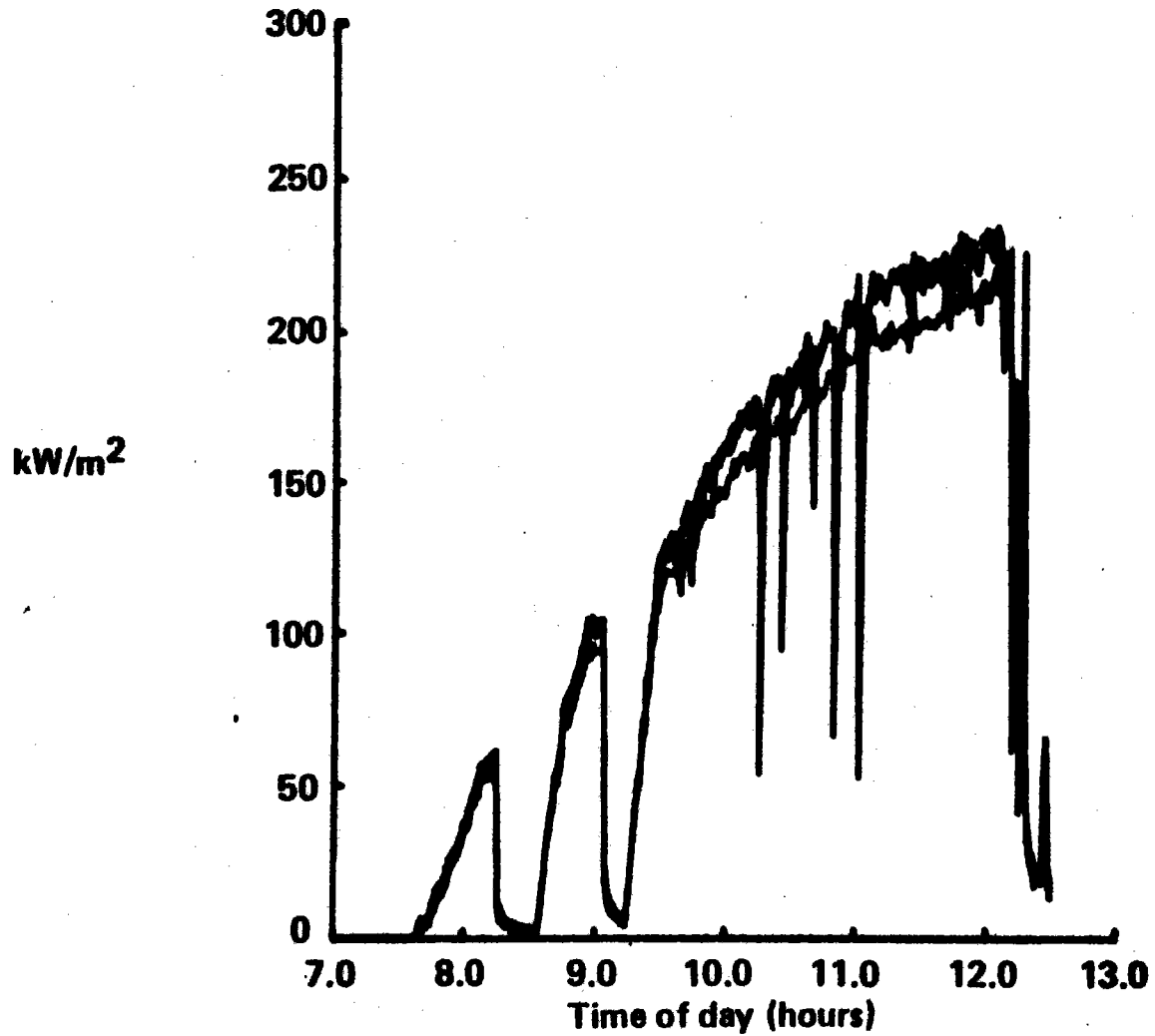




Figure 12.3-102 Plot of March 23, 1979 Test Data, Frame Calorimeters

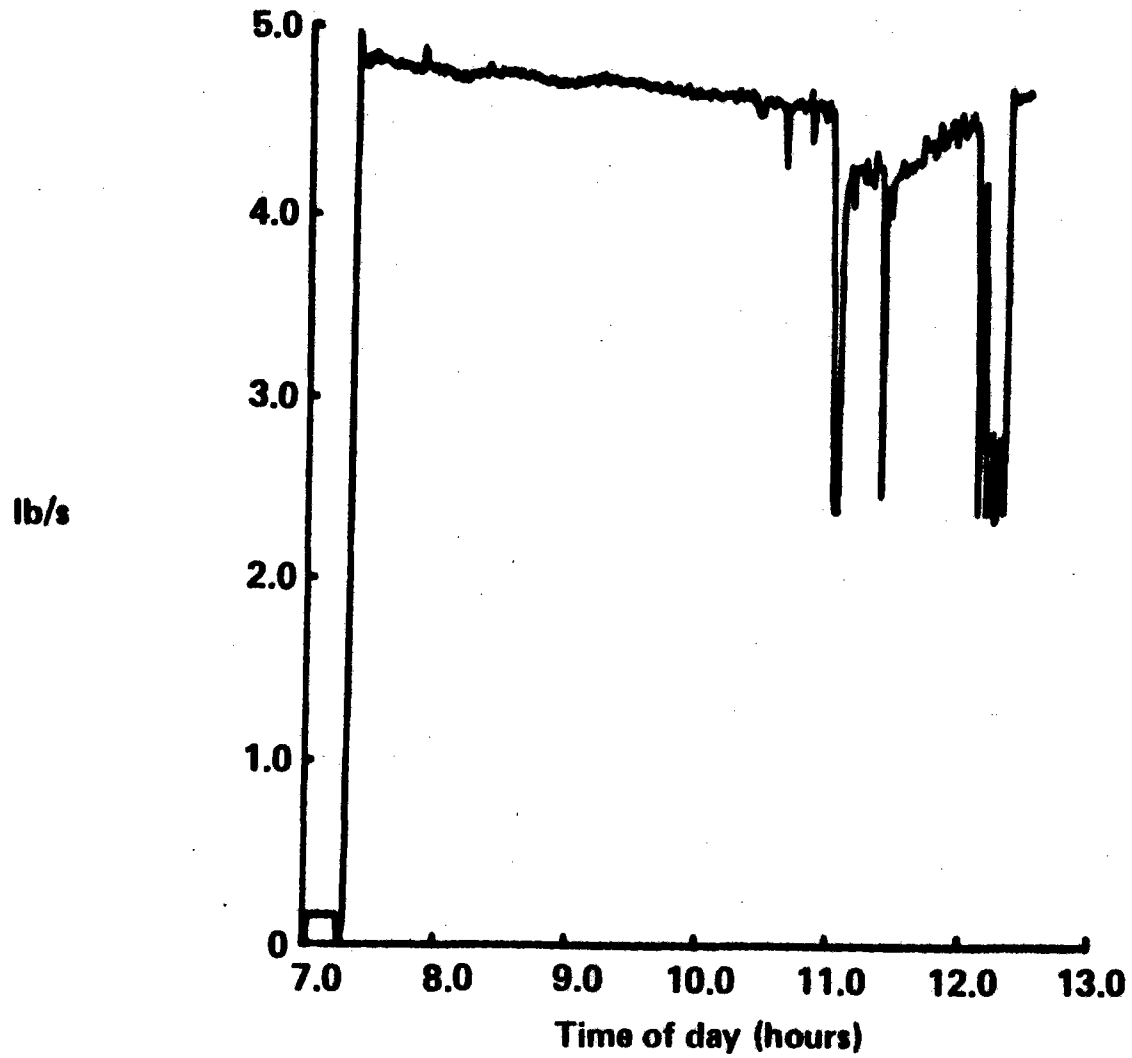
### Plot of March 23, 1979 Test Data, Frame Calorimeters



772

Figure 12.3-103 Plot of March 23, 1979 Test Data, Receiver Mass Flow

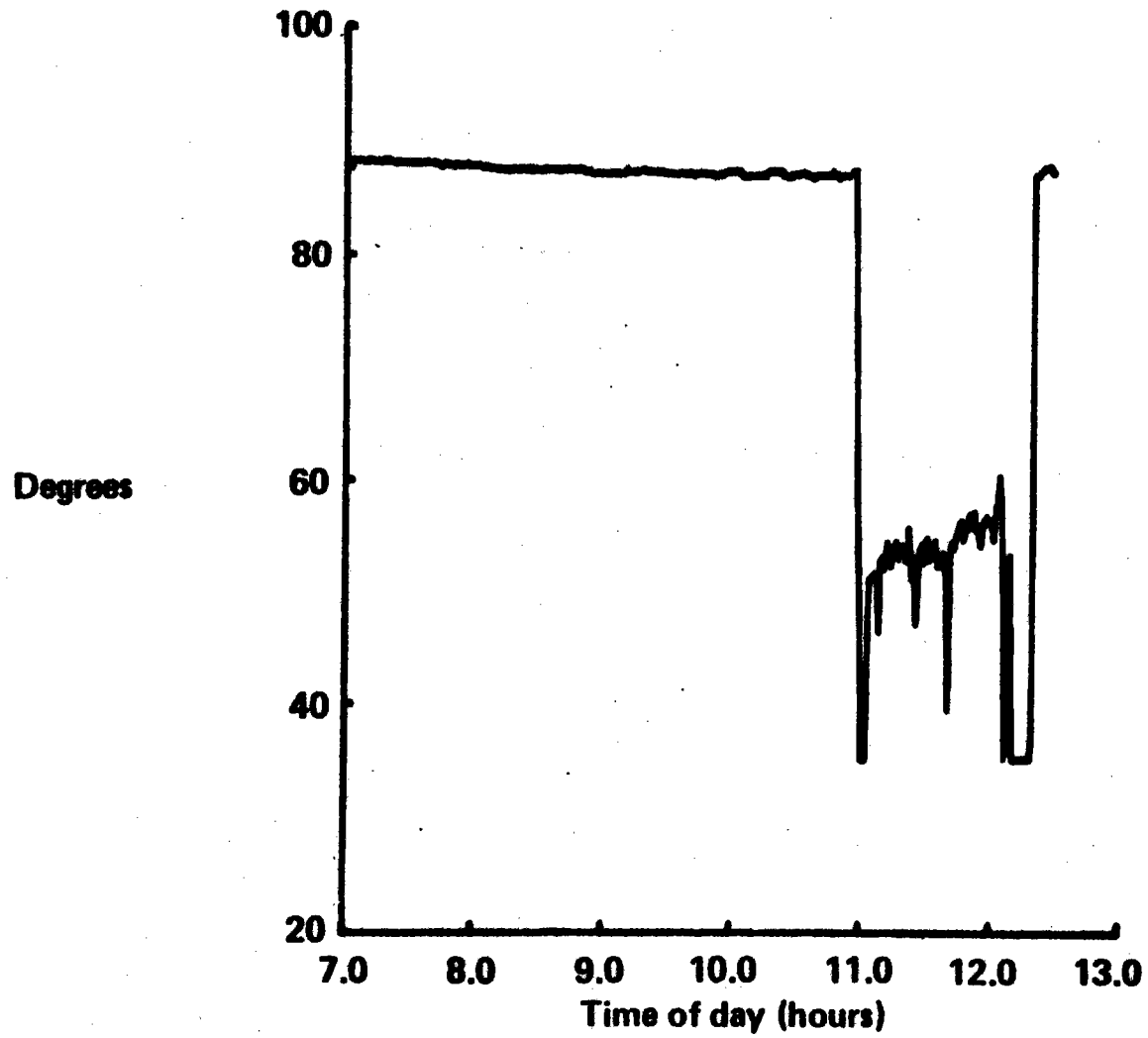
## Plot of March 23, 1979 Test Data, Receiver Mass Flow



773

Figure 12.3-104 Plot of March 23, 1979 Test Data, H/X Panel 3 Valve Angle

# Plot of March 23, 1979 Test Data, H/X Panel 3 Valve Angle



174

Figure 12.3-105 Plot of March 23, 1979 Test Data, Air Inlet-Outlet Temperatures, Panel 3

# Plot of March 23, 1979 Test Data, Air Inlet-Outlet Temperatures, Panel 3

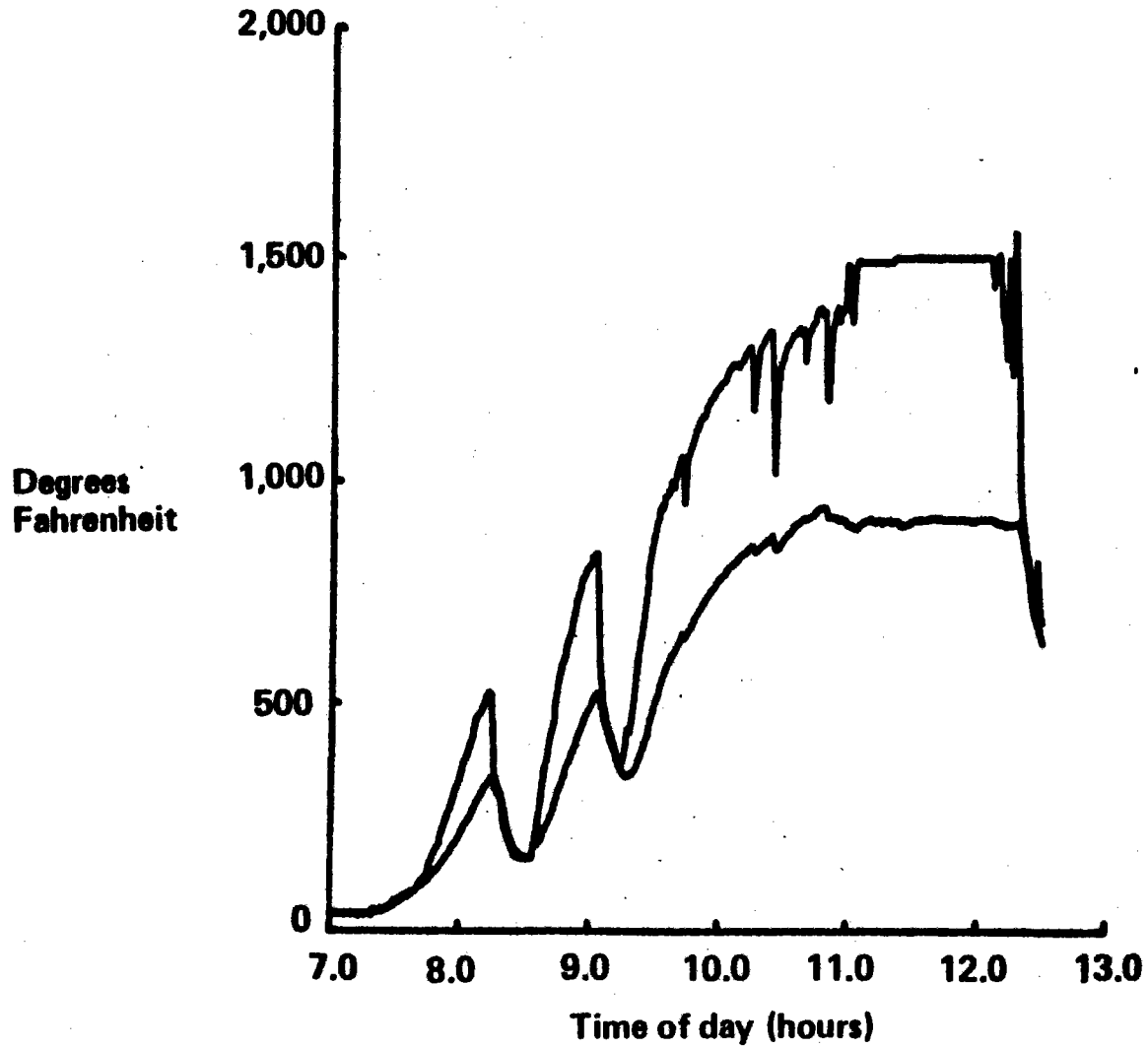


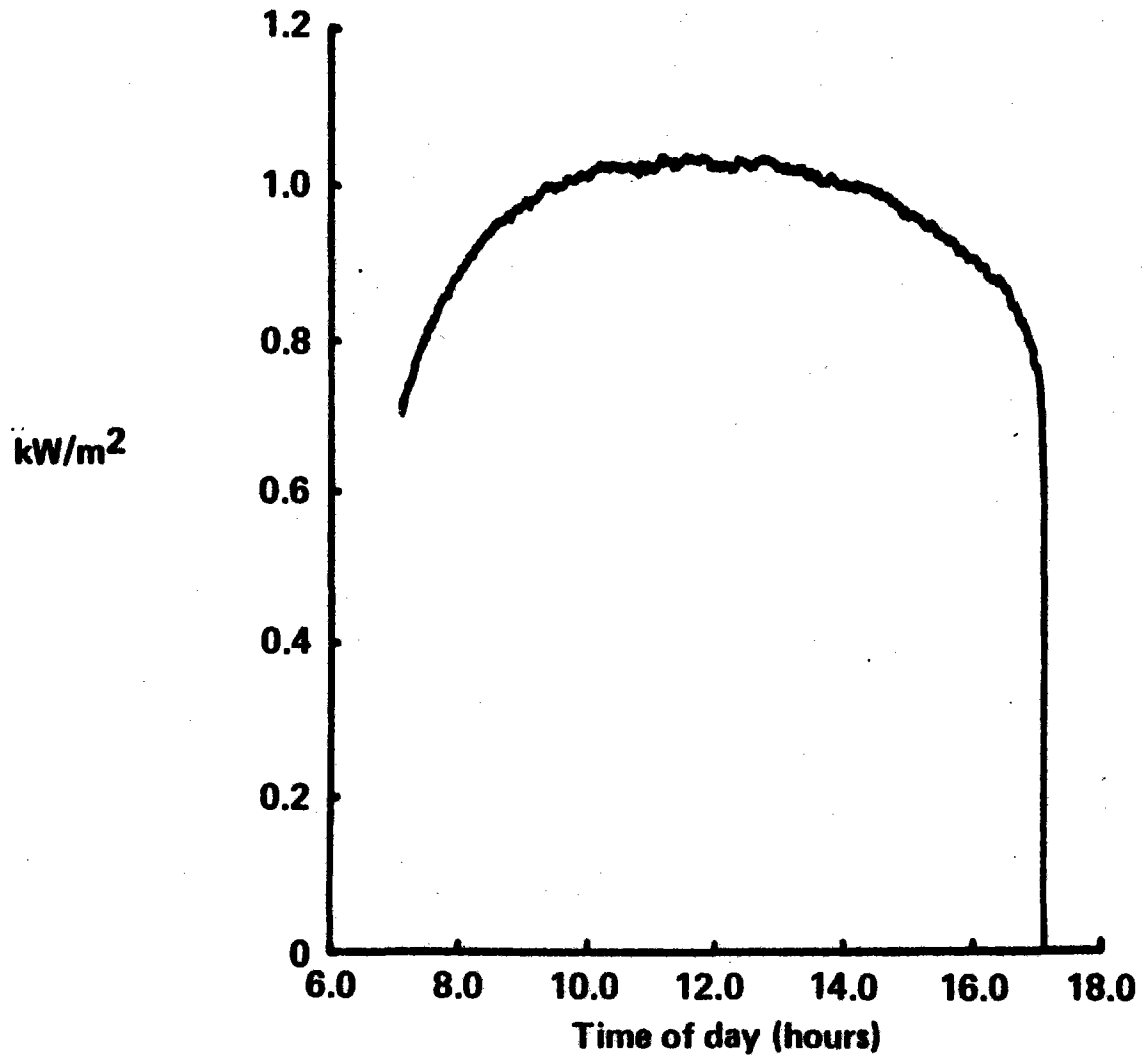
Figure 12.3-106 Time Chart for March 24, 1979 Solar Test

## Time Chart for March 24, 1979 Solar Test

7:00	Field at standby	13:00	58 collectors on target
7:30	First collector on target	13:48	Receiver on control
8:05	60 collectors on target	13:57	64 collectors on target
9:03	66 collectors on target	14:15	66 collectors on target
9:41	60 collectors on target	14:25	68 collectors on target
9:56	63 collectors on target	14:46	74 collectors on target
10:17	Receiver on control	14:50	Lost five collectors
10:24	Several collectors off target	14:54	75 collectors on target
10:27	63 collectors on target	15:12	92 collectors on target
11:06	60 collectors on target	15:15	Steady test condition, EB-9G
11:20	59 collectors on target	15:26	98 collectors on target
11:30	58 collectors on target	15:41	111 collectors on target
11:50	Steady test conditions, EB-9F	15:58	107 collectors on target
11:53	Lost field due to valve 3 failure	16:04	103 collectors on target
12:00	Field at standby	16:18	113 collectors on target
12:49	First collector on target	16:24	Field at standby

Figure 12.3-107 Plot of March 24, 1979 Test Data, Eppley Pyrheliometer

# Plot of March 24, 1979 Test Data, Eppley Pyrheliometer



777

Figure 12.3-108. Plot of March 24, 1979 Test Data, Air Supply Gas Temperatures

## Plot of March 24, 1979 Test Data, Air Supply Gas Temperatures

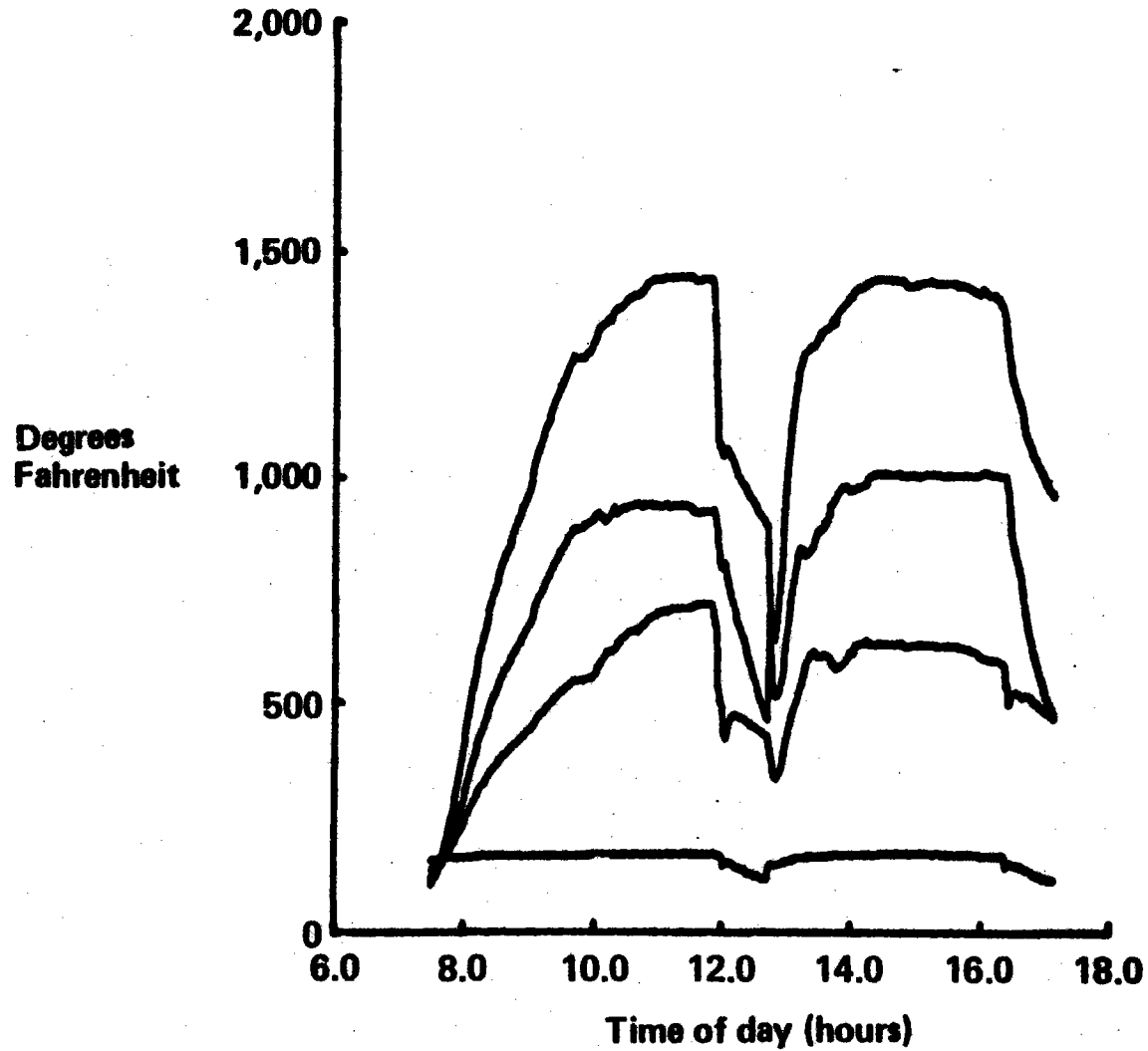
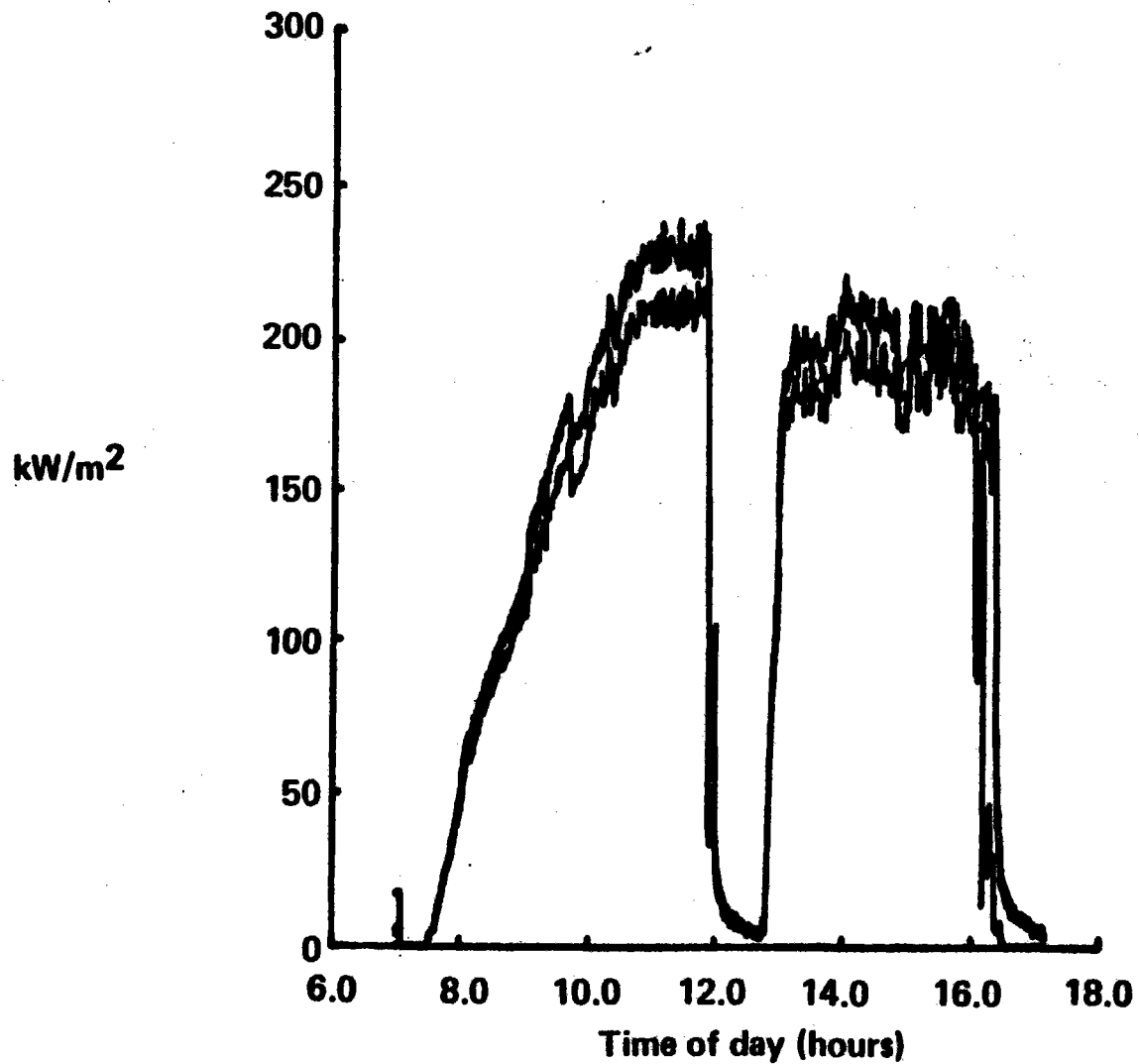


Figure 12.3-109 Plot of March 24, 1979 Test Data, Frame Calorimeters

# Plot of March 24, 1979 Test Data, Frame Calorimeters

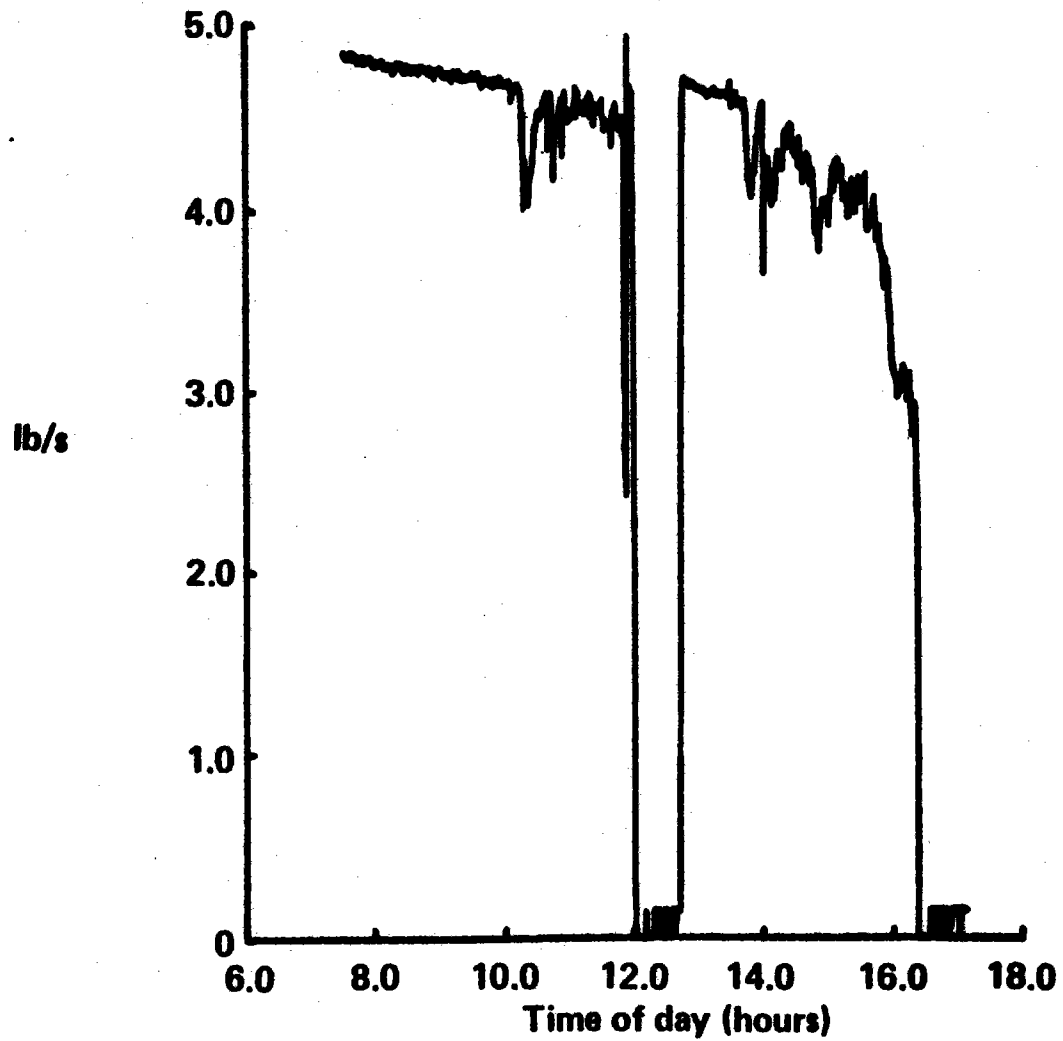


779



Figure 12.3-110 Plot of March 24, 1979 Test Data, Receiver Mass Flow

### Plot of March 24, 1979 Test Data, Receiver Mass Flow



780

Figure 123-111 Plot of March 24, 1979 Test Data, H/X Panel 3 Valve Angle

### Plot of March 24, 1979 Test Data, H/X Panel 3 Valve Angle

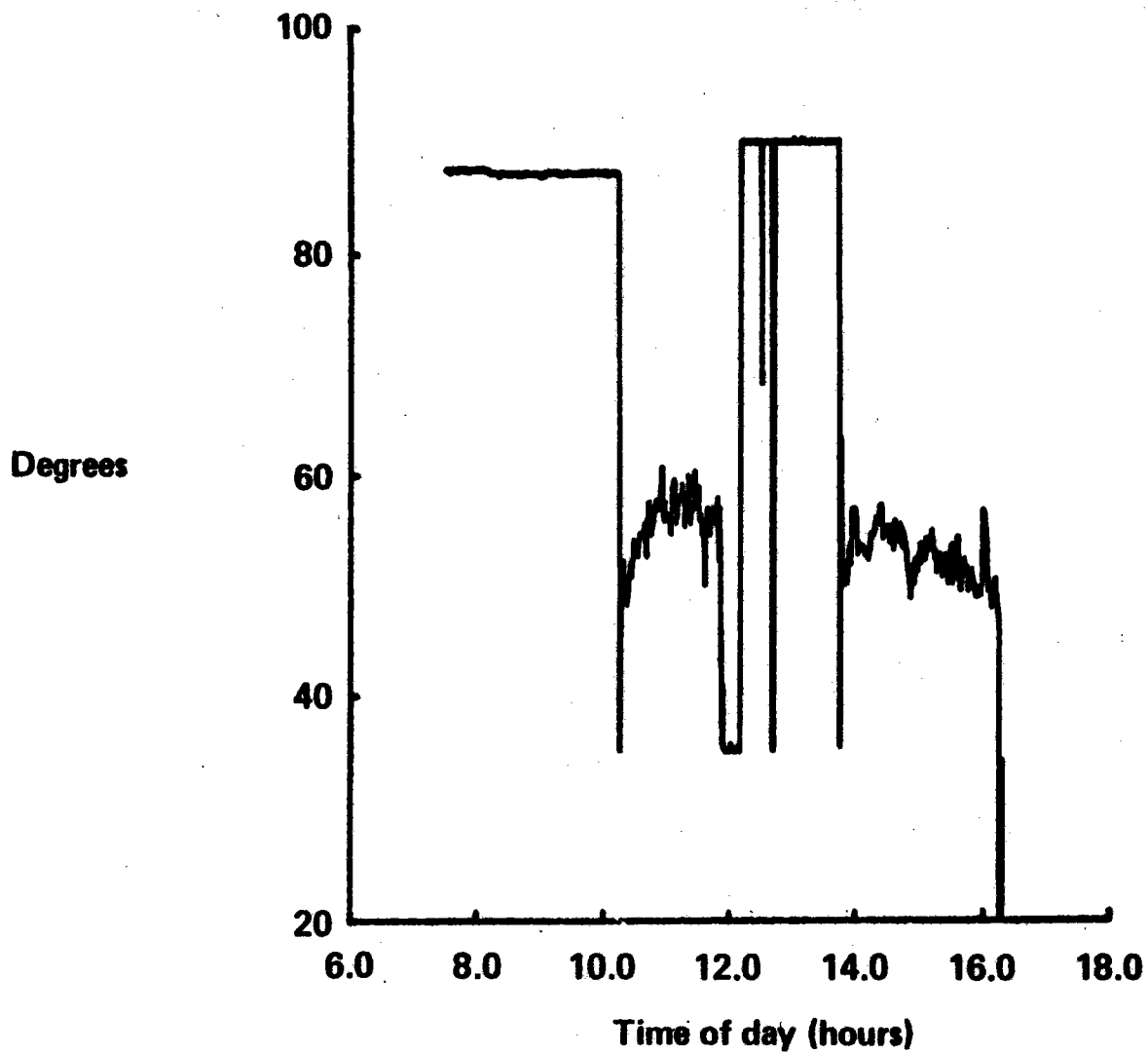


Figure 123-112 Plot of March 24, 1979 Test Data, Air Inlet-Outlet Temperatures, Panel 3

### Plot of March 24, 1979 Test Data, Air Inlet-Outlet Temperatures, Panel 3

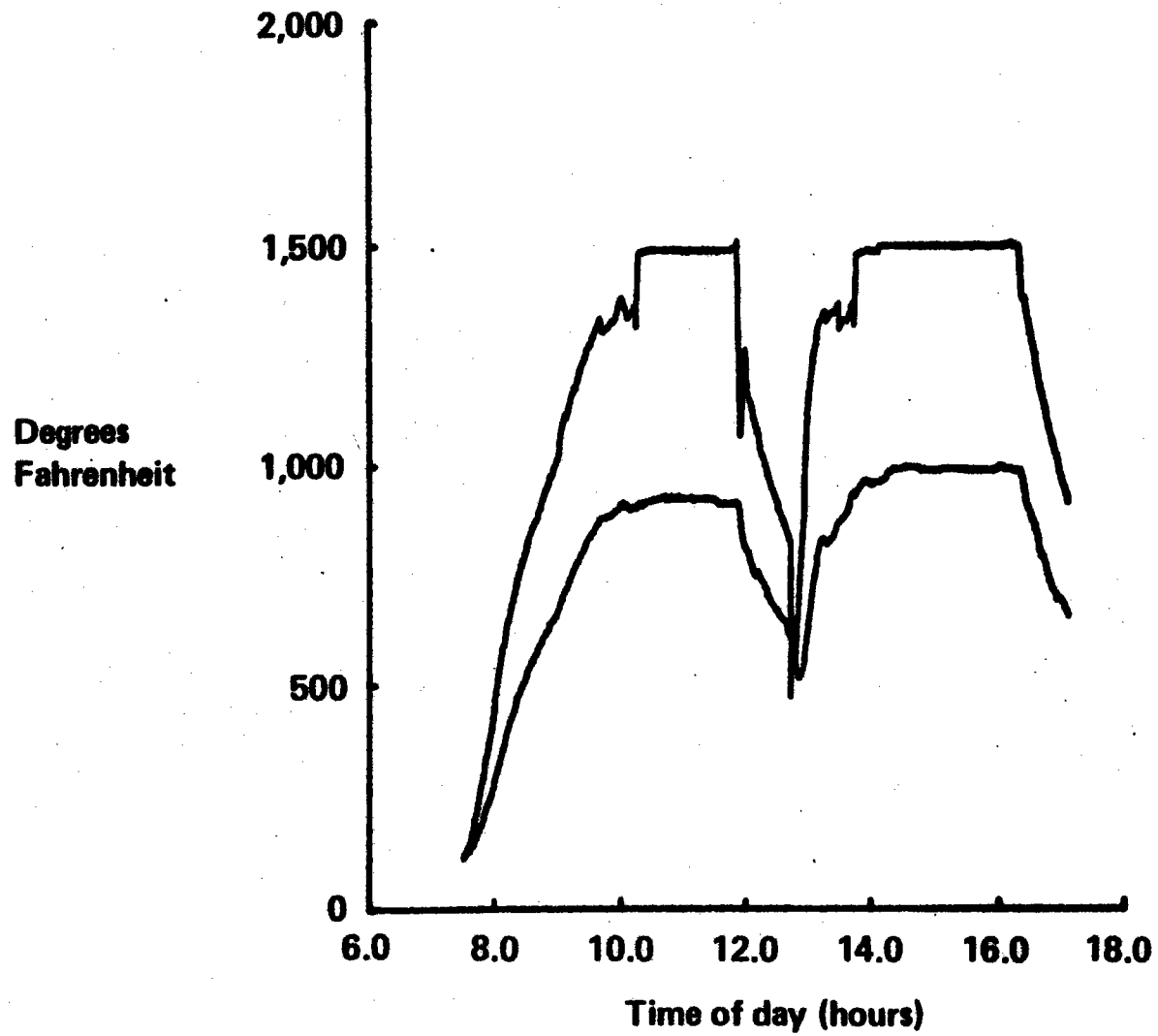


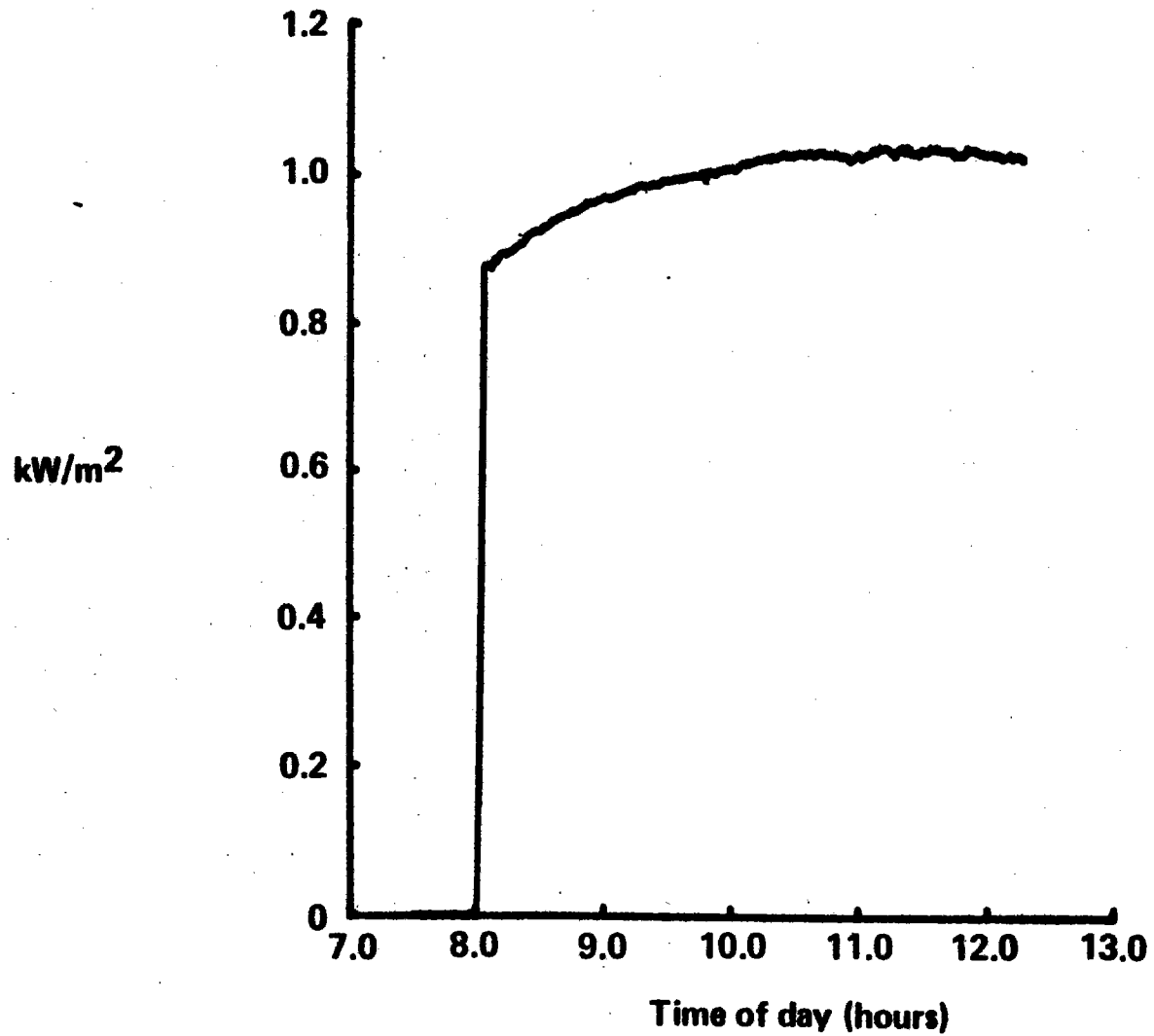
Figure 12.3-113 Time Chart for March 25, 1979 Solar Test

## Time Chart for March 25, 1979 Solar Test

7:30	Field at standby	11:00	Steady test condition, EB-9H
7:58	First collector on target	11:13	69 collectors on target
8:32	50 collectors on target	11:18	67 collectors on target
9:32	57 collectors on target	11:20	Steady test conditions, EB-9I
9:48	61 collectors on target	11:20	62 collectors on target
9:55	Receiver on control	11:26	Lost field due to compressor shutdown
10:00	62 collectors on target	11:33	66 collectors on target
10:09	60 collectors on target	11:35	Lost field due to panel 2
10:26	59 collectors on target	11:38	43 collectors on target
10:37	58 collectors on target	11:48	65 collectors on target
10:43	55 collectors on target	11:51	Emergency shutdown

Figure 123-114 Plot of March 25, 1979 Test Data, Eppley Pyrheliometer

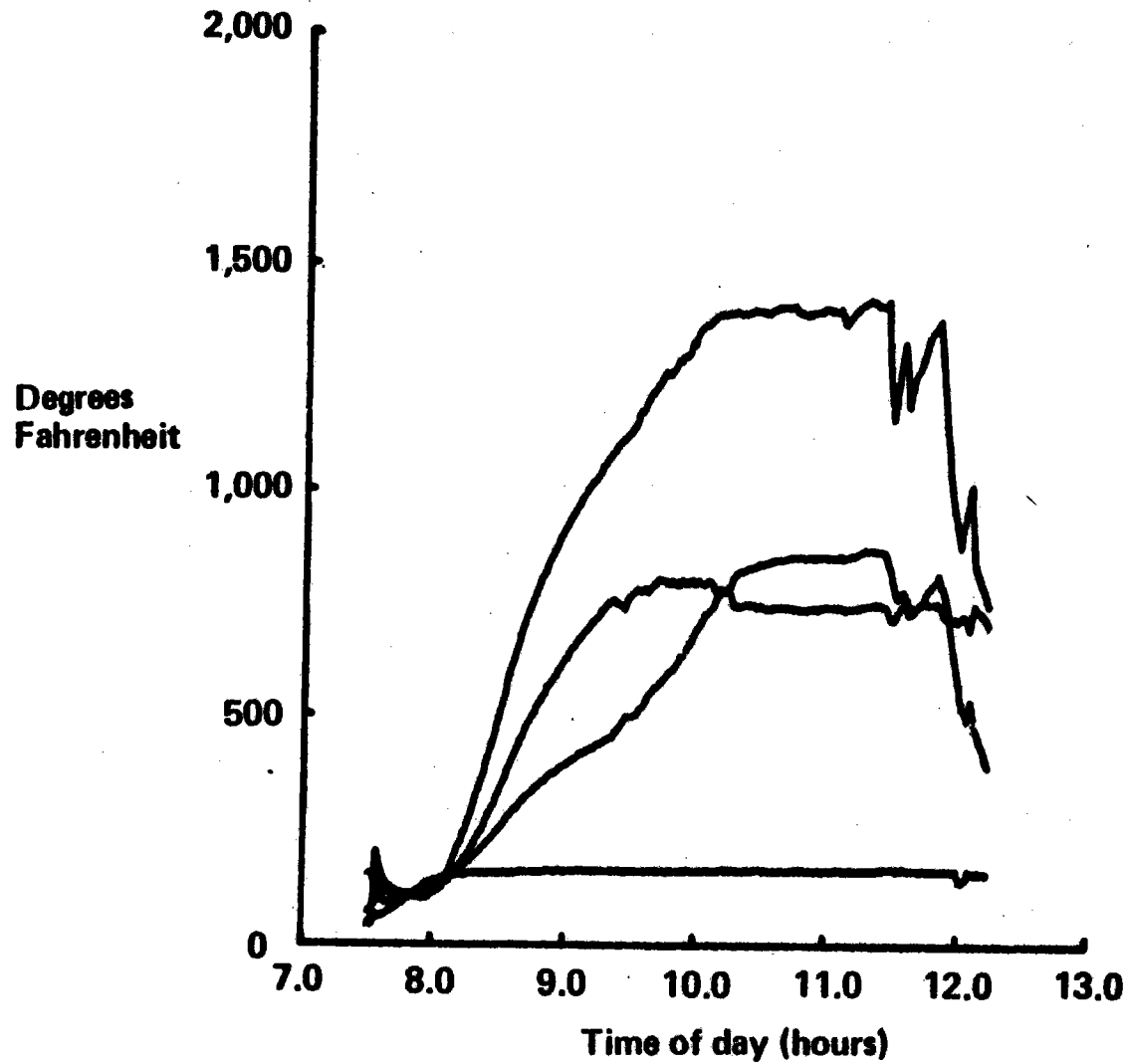
### Plot of March 25, 1979 Test Data, Eppley Pyrheliometer



784

Figure 12.3-115 Plot of March 25, 1979 Test Data, Air Supply Gas Temperatures

### Plot of March 25, 1979 Test Data, Air Supply Gas Temperatures



785

Figure 12.3-116 Plot of March 25, 1979 Test Data, Frame Calorimeters

### Plot of March 25, 1979 Test Data, Frame Calorimeters

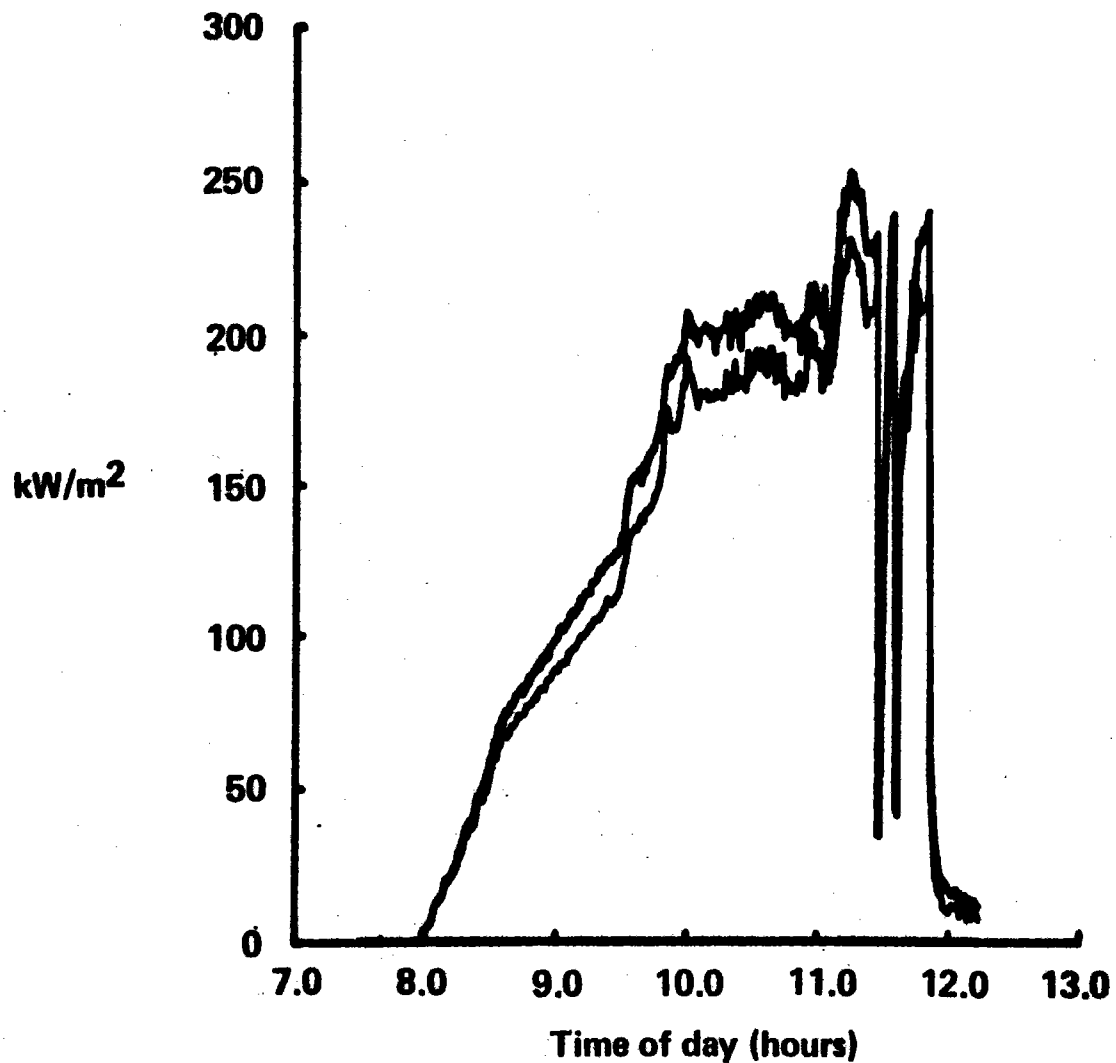
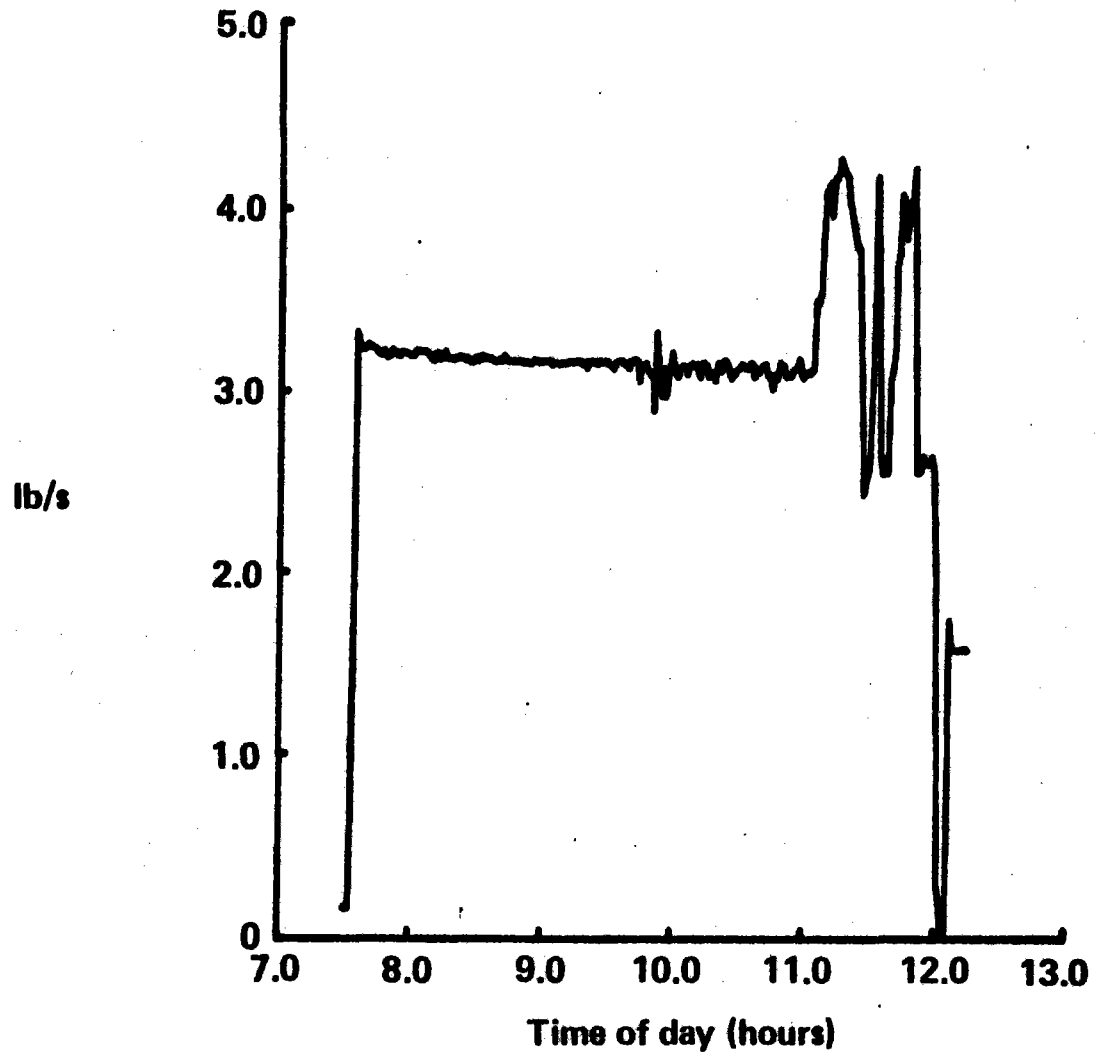


Figure 12.3-117 Plot of March 25, 1979 Test Data, Receiver Mass Flow

### Plot of March 25, 1979 Test Data, Receiver Mass Flow



787



Figure 12.3-118 Plot of March 25, 1979 Test Data, H/X Panel 3 Valve Angle

## Plot of March 25, 1979 Test Data, H/X Panel 3 Valve Angle

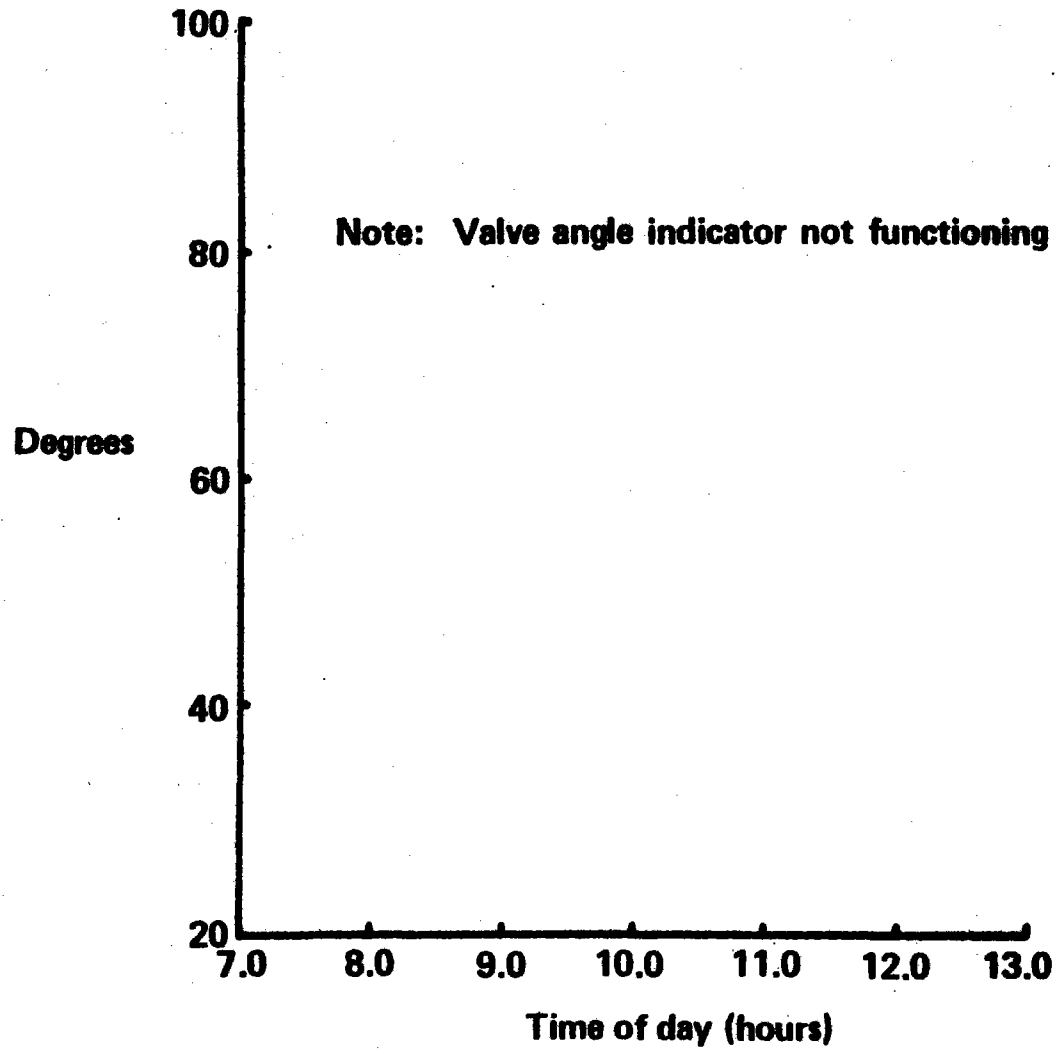
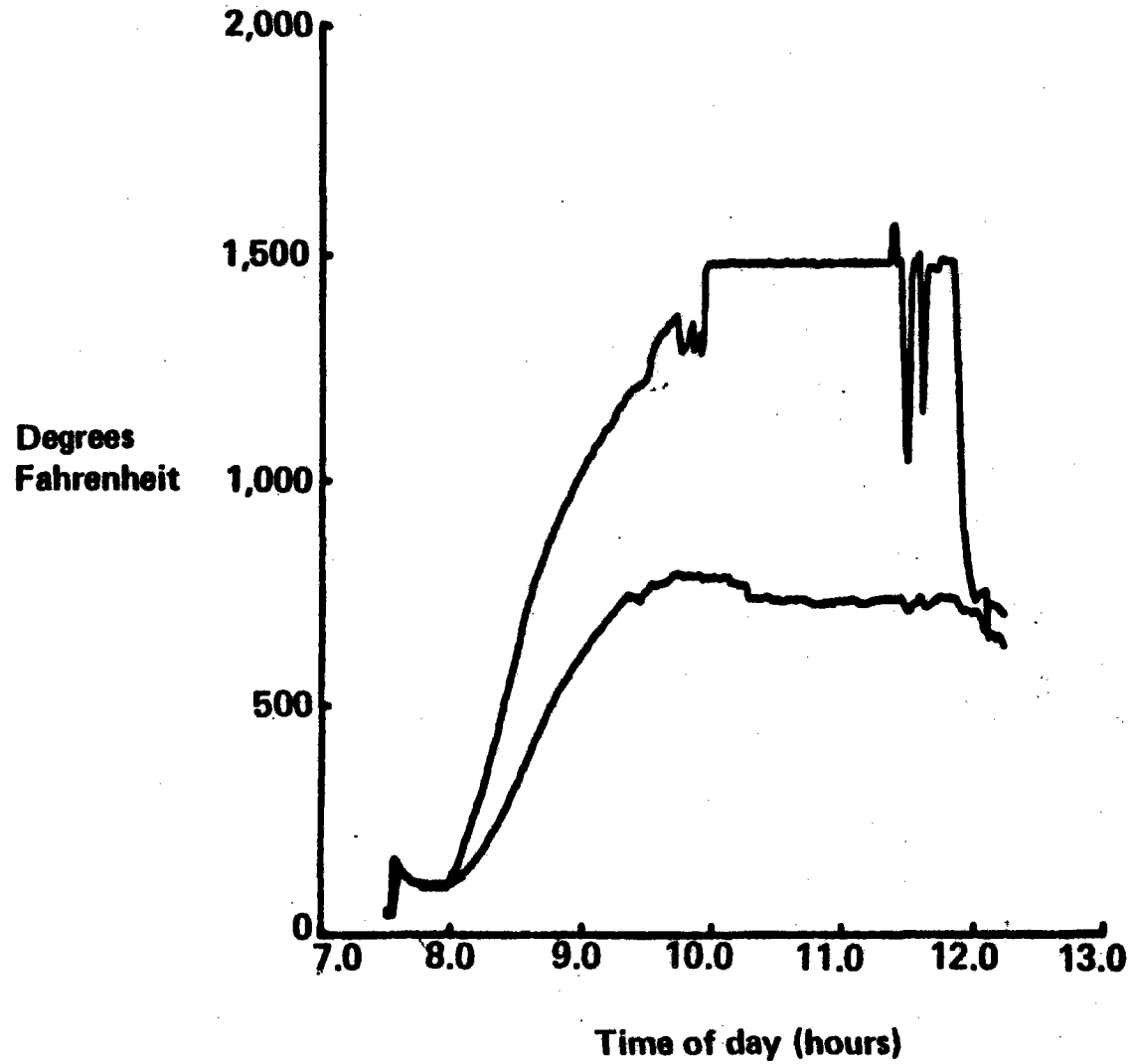


Figure 12.3-119 Plot of March 25, 1979 Test Data, Air Inlet-Outlet Temperatures, Panel 3

## Plot of March 25, 1979 Test Data, Air Inlet-Outlet Temperatures, Panel 3



## REFERENCES

Listing of references to be prepared and verified prior to issue of camera-ready document, citations in text and reference list to be revised consistent with EPRI Style Guide.